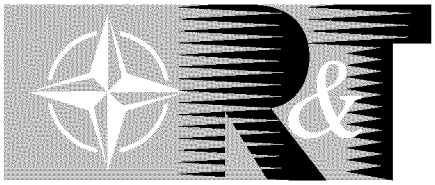
RTO-EN-010
AC/323(AVT-058)TP/45

RTO-EN-010

NORTH ATLANTIC TREATY ORGANISATION



RESEARCH AND TECHNOLOGY ORGANISATION

BP 25, 7 RUE ANCELLE, F-92201 NEUILLY-SUR-SEINE CEDEX, FRANCE

© RTO/NATO 2002

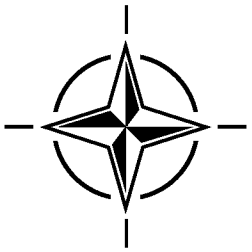
Single copies of this publication or of a part of it may be made for individual use only. The approval of the RTA Information Policy Executive is required for more than one copy to be made or an extract included in another publication. Requests to do so should be sent to the address above.

RTO LECTURE SERIES 005

Supercavitating Flows

(les Ecoulements supercavitants)

The material in this publication was assembled to support a RTO/VKI Lecture Series under the sponsorship of the Applied Vehicle Technology Panel (AVT) and the von Kármán Institute for Fluid Dynamics (VKI) presented from 12-16 February 2001, in Brussels, Belgium.



Published January 2002

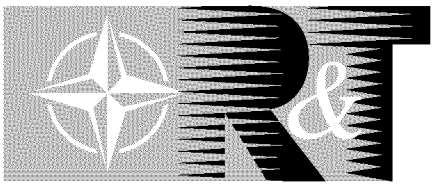
Distribution and Availability on Back Cover

This page has been deliberately left blank

Page intentionnellement blanche

RTO-EN-010
AC/323(AVT-058)TP/45

NORTH ATLANTIC TREATY ORGANISATION



RESEARCH AND TECHNOLOGY ORGANISATION

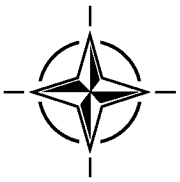
BP 25, 7 RUE ANCELLE, F-92201 NEUILLY-SUR-SEINE CEDEX, FRANCE

RTO LECTURE SERIES 005

Supercavitating Flows

(les Ecoulements supercavitants)

The material in this publication was assembled to support a RTO/VKI Lecture Series under the sponsorship of the Applied Vehicle Technology Panel (AVT) and the von Kármán Institute for Fluid Dynamics (VKI) presented from 12-16 February 2001, in Brussels, Belgium.



The Research and Technology Organisation (RTO) of NATO

RTO is the single focus in NATO for Defence Research and Technology activities. Its mission is to conduct and promote cooperative research and information exchange. The objective is to support the development and effective use of national defence research and technology and to meet the military needs of the Alliance, to maintain a technological lead, and to provide advice to NATO and national decision makers. The RTO performs its mission with the support of an extensive network of national experts. It also ensures effective coordination with other NATO bodies involved in R&T activities.

RTO reports both to the Military Committee of NATO and to the Conference of National Armament Directors. It comprises a Research and Technology Board (RTB) as the highest level of national representation and the Research and Technology Agency (RTA), a dedicated staff with its headquarters in Neuilly, near Paris, France. In order to facilitate contacts with the military users and other NATO activities, a small part of the RTA staff is located in NATO Headquarters in Brussels. The Brussels staff also coordinates RTO's cooperation with nations in Middle and Eastern Europe, to which RTO attaches particular importance especially as working together in the field of research is one of the more promising areas of initial cooperation.

The total spectrum of R&T activities is covered by the following 7 bodies:

- AVT Applied Vehicle Technology Panel
- HFM Human Factors and Medicine Panel
- IST Information Systems Technology Panel
- NMSG NATO Modelling and Simulation Group
- SAS Studies, Analysis and Simulation Panel
- SCI Systems Concepts and Integration Panel
- SET Sensors and Electronics Technology Panel

These bodies are made up of national representatives as well as generally recognised 'world class' scientists. They also provide a communication link to military users and other NATO bodies. RTO's scientific and technological work is carried out by Technical Teams, created for specific activities and with a specific duration. Such Technical Teams can organise workshops, symposia, field trials, lecture series and training courses. An important function of these Technical Teams is to ensure the continuity of the expert networks.

RTO builds upon earlier cooperation in defence research and technology as set-up under the Advisory Group for Aerospace Research and Development (AGARD) and the Defence Research Group (DRG). AGARD and the DRG share common roots in that they were both established at the initiative of Dr Theodore von Kármán, a leading aerospace scientist, who early on recognised the importance of scientific support for the Allied Armed Forces. RTO is capitalising on these common roots in order to provide the Alliance and the NATO nations with a strong scientific and technological basis that will guarantee a solid base for the future.

The content of this publication has been reproduced
directly from material supplied by RTO or the authors.

Published January 2002

Copyright © RTO/NATO 2002
All Rights Reserved

ISBN 92-837-1074-6



Printed by St. Joseph Ottawa/Hull
(A St. Joseph Corporation Company)
45 Sacré-Cœur Blvd., Hull (Québec), Canada J8X 1C6

Supercavitating Flows

(RTO EN-010 / AVT-058)

Executive Summary

This Lecture Series, jointly organised by the Applied Vehicle Technology Panel (AVT) of RTO and the von Kármán Institute (VKI) can be considered as a natural extension of the AGARD Workshop held in Kiev, Ukraine - September 1997 - entitled "High Speed Body Motion in Water" (AGARD Report 827 - February 1998). Indeed, the common topic of these two meetings was: high speed hydrodynamics, the RTO/VKI Special Course focusing exclusively on Supercavitating Flows.

Supercavitating flows are flows of liquids past solid bodies which involve large trailing cavities. They are generally associated with high velocities and these cavities are filled either by the vapour of the surrounding liquid or by a non-condensable foreign gas. This results in a substantial reduction in drag as compared to that of the same fully wetted body.

This publication contains the written versions of twenty out of the twenty three lectures which were prepared, and presented at VKI, by Specialists from France, Russia, Ukraine and the U.S. These lectures describe theoretical aspects, modelling, mathematical approaches, numerical studies as well as test facilities (hydrodynamic tunnels, launching channels, vertical tanks), experimental studies and results of supercavitating flows (true cavitating flows or ventilated flows) concerning:

- 2D foils or struts, 3D hydrofoil wings,
- propellers, cascades, surface piercing propellers,
- axisymmetric (or quasi-axisymmetric) bodies including water entry phenomena,

the velocity range extending up to supersonic Mach number in water.

This publication can be considered as a comprehensive overview of all the works on supercavitating flows carried out in both Western and Eastern countries since World War II. It should be a useful tool for scientists and engineers interested in high-speed hydrodynamics for the following civilian and military applications:

- design of high-speed ships or hydrofoil boats,
- design of high-speed marine propellers, low-head pumps and turbines.

In addition to the above mentioned applications there are the following applications, highly relevant for the military side:

- design of high-speed submarines,
- design of high-speed or very high speed projectiles (for instance torpedoes) to be used in ASW (Anti-Submarine Warfare) or MCM (Mine Counter Measures).

les Ecoulements supercavitants

(RTO EN-010 / AVT-058)

Synthèse

Ce Cycle de Conférences, organisé conjointement par la commission sur la technologie appliquée aux véhicules (AVT) de la RTO et l'Institut von Kármán (VKI), peut être considéré comme la suite naturelle de l'atelier AGARD organisé à Kiev, Ukraine - en septembre 1997 - intitulé "Mouvement des corps évoluant à grande vitesse dans l'eau" (Rapport AGARD 827 - février 1998). Ces deux manifestations, en effet, avaient pour thème commun: l'hydrodynamique des grandes vitesses, le Cours Spécial RTO/VKI étant axé exclusivement sur les écoulements supercavitants.

Les écoulements supercavitants sont les écoulements de liquides qui, au voisinage de corps solides, sont accompagnés de cavités de grandes dimensions généralement associées aux vitesses élevées, des cavités étant remplies par la vapeur du liquide environnant ou par un gaz étranger non condensable.

Cette publication contient les versions écrites de vingt des vingt-trois conférences* qui ont été préparées, et présentées au VKI, par des spécialistes de la France, la Russie, l'Ukraine et les Etats-Unis. Ces conférences décrivent les aspects théoriques, la modélisation, les approches mathématiques, les études numériques ainsi que les installations d'essais (tunnels hydrodynamiques, canaux de tir balistique, réservoirs verticaux), les études expérimentales et leurs résultats pour les écoulements supercavitants (les cavités étant remplies de vapeur ou résultant d'une ventilation) concernant:

- profils ou mâts bidimensionnels, ailes sous-marines tridimensionnelles
- hélices, grilles, hélices de surface
- corps axisymétriques (ou quasi axisymétriques), y compris les phénomènes qui prennent naissance lors de la pénétration dans l'eau.

Cette publication peut être considérée comme une revue exhaustive de l'ensemble des travaux sur les écoulements supercavitants réalisés depuis la seconde guerre mondiale par les pays aussi bien de l'Ouest que de l'Est. Elle devrait jouer un rôle très utile pour les scientifiques et ingénieurs intéressés par l'hydrodynamique des grandes vitesses pour les applications civiles et militaires suivantes:

- projets de vaisseaux rapides ou d'hydroptères
- projets d'hélices marines pour les grandes vitesses, de pompes ou turbines hydrauliques à basse pression.

En plus des applications mentionnées ci-dessus, les applications suivantes sont particulièrement importantes du point de vue militaire:

- projets de sous-marins à grande vitesse
- projets de projectiles sous-marins rapides ou très rapides (par exemple: torpilles) pour emploi dans la lutte anti-sous-marine ou la lutte contre les mines.

Click inside the blue boxes or on the titles to view the corresponding section

(except for items marked in red, which were not available at the time of production)

Contents

	Page
Executive Summary	**iii**
Synthèse	**iv**
List of Authors/Lecturers	**vii**

	Reference
Introduction to Cavitation and Supercavitation by J.M. Michel	**1**
Oscillations of Ventilated Cavities - Experimental Aspects by J.M. Michel	**2**
Overview Supercavitation by M.P. Tulin	**3†**
Experimental Investigation of Supercavitating Motion of Bodies by Yu.N. Savchenko	**4**
Developed Cavitation-Cavity Dynamics by D.R. Stinebring, M.L. Billet, J.W. Lindau and R.F. Kunz	**5**
Mathematical Approaches by M.P. Tulin	**6†**
Variational Methods in Cavitational Flow by P.R. Garabedian	**7**
The Principle of Independence of the Cavity Sections Expansion (Logvinovich's principle) as the basis for Investigation on Cavitation Flows by A.D. Vasin	**8**
Numerical Modeling of Supercavitating Flows by I.N. Kirschner, N.E. Fine, J.S. Uhlman and D.C. Kring	**9**
Review of Theoretical Approaches to Nonlinear Supercavitating Flows by G.M. Fridman and A.S. Achkinadze	**10**
Artificial Supercavitation. Physics and Calculation by V.N. Semenenko	**11**
Dynamic Processes of Supercavitation and Computer Simulation by V.N. Semenenko	**12**
Multiphase CFD Modeling of Developed and Supercavitating Flows by R.F. Kunz, J.W. Lindau, M.L. Billet and D.R. Stinebring	**13**
Control of Supercavitation Flow and Stability of Supercavitating Motion of Bodies by Yu.N. Savchenko	**14**

† Paper not available at time of production.

Results of Selected Experiments Involving Supercavitating Flows **15**
by I.N. Kirschner

Supercavities in Compressible Fluid **16**
by A.D. Vasin

Supercavitating Object Propulsion **17**
by Yu.N. Savchenko

Supercavitating Flows: Small Perturbation Theory and Matched Asymptotics **18**
by K.V. Rozhdestvensky

Supercavitating Nonlinear Flow Problems: Matched Asymptotics **19**
by K.V. Rozhdestvensky and G.M. Fridman

The History and Principles of Operation of Supercavitating Propellers **20†**
by M.P. Tulin

Supercavitating 2-D Hydrofoils: Prediction of Performance and Design **21**
by S.A. Kinnas

Supercavitating Propellers **22**
by A.S. Achkinadze

Supercavitating 3-D Hydrofoils and Propellers: Prediction of Performance and Design **23**
by S.A. Kinnas

† Paper not available at time of production.

List of Authors/Lecturers

Lecture Series Directors

IGA B. Masure
Université d'Orleans
6, rue Eudoxe Marcille
45000 Orléans, France

Prof. M.P. Tulin
University of California
Ocean Engineering Laboratory
6740 Cortona Drive - Santa Barbara
California 93106-1080, USA

LECTURERS

Prof. J-M. Michel
LEGI/IMG
Institut de Mécanique de Grenoble
BP 53, 38041 Grenoble Cedex 9, France

Prof. A.S. Achkinadze
State Marine Technical University
Dept. of Applied Mathematics and
Mathematical Modelling
Lotsmanskaya str. 3
Saint-Petersburg 190 008, Russia

Dr. G.M. Fridman
State Marine Technical University
Dept. of Applied Mathematics and
Mathematical Modelling
Lotsmanskaya str 3
Saint Petersburg 190 008, Russia

Prof. K. Rozhdestvensky
State Marine Technical University
Dept. of Applied Mathematics and
Mathematical Modelling
Lostsmanskaya str. 3
Saint-Petersburg 190 008, Russia

Prof. A.D. Vasin
State Scientific Research Center
TsAGI, Radio Street, 17
Moscow, 107005, Russia

Prof. Yu.N. Savchenko
National Academy of Sciences
Institute of Hydro Mechanics
8/4 Zheliabova str.
Kiev 03057, Ukraine

Dr. V.N. Semenenko
National Academy of Sciences
Institute of Hydro Mechanics
8/4 Zheliabova str.
Kiev 03057, Ukraine

Mr. M. Billet
Gasfield Thomas Water Tunnel
Pennsylvania State University
Applied Research Laboratory
P.O. Box 30, State College
PA 16803, USA

Prof. P. Garabedian
New York University
Courant Institute
251 Mercer St.
New York, NY 10012, USA

Prof. S. Kinnas
University of Texas at Austin
ECJ 8.604, Ocean Eng. Group, EWRE
Civil Engineering
Texas 78712, USA

Dr. I.N. Kirschner
Engineering Technology Centre
Applied Mechanics Department
240 Oral School Road
Mystic, CT 06355, USA

Prof. M.P. Tulin
University of California
Ocean Engineering Laboratory
6740 Cortona Drive - Santa Barbara
California 93106-1080, USA

LOCAL COORDINATOR AND EDITOR

Prof. R. Van den Braembussche
von Kármán Institute for Fluid Dynamics
Chaussee de Waterloo, 72
1640 Rhode-Saint-Genese
Belgium

our thanks also go to Christelle Debeer of VKI
for her invaluable help in assembling the papers published

This page has been deliberately left blank

Page intentionnellement blanche

Introduction to Cavitation and Supercavitation

J.M. Michel
Laboratoire des Ecoulements Géophysiques et Industriels
BP 53 - 38041 Grenoble Cedex 9
France

1. The Physical Phenomenon

1.1. DEFINITION

Cavitation, *i.e.* the appearance of vapour bubbles and pockets inside an initially homogeneous liquid medium, occurs in very different situations. According to the flow configuration (shape and relative motion of the walls limiting the flow field, or physical properties of the liquid), it can take various figures. In order to encompass all possible cases, we propose the following definition :

Cavitation is the breaking of a liquid medium under excessive stresses.

That definition makes cavitation relevant to the field and the methods of continuum mechanics. It is convenient for cases in which the liquid is either *still* or *flowing*.

Examples of the first case :

- An oscillating pressure field is applied above a liquid contained in a bowl : if the oscillation amplitude is large enough, bubbles can appear inside the liquid.
- A solid body with sharp edges (a disk, for example) is suddenly accelerated by a shock in still water. Bubbles can appear at the very first instants in the region neighbouring the edges, when the velocity of the liquid particulates are still negligible.

Examples of flowing liquids :

- Flows in venturis or in narrow passages (valves for hydraulic control).
- Flow near the upper side of a wing or a propeller blade.

Here we will be rather concerned with **flowing liquids.**

In order to solve the problem of excessive stresses, we need a *threshold of stress* : beyond such a threshold, the liquid cohesion is no longer ensured. Ideally, the threshold should be determined from physical consideration at a submicrosopic scale. Taking the actual state of the scientific development into account, together with the need of practical solutions for possibly complicated fluid systems, it is useful to call only on fluid properties at the macroscopic scale.

Concerning the stress, it must be specified that only the normal component $\vec{n}$ of the total stess $\vec{t}$ has to be considered here (recall that $\vec{n} = -p\vec{v}$ for an incompressible Newtonian fluid, where p stands for the **absolute pressure**). Indeed we have no experimental result in which cavitation would be produced uniquely by the shearing stress $\vec{\tau}$, under a large absolute ambient pressure.

Paper presented at the RTO AVT Lecture Series on "Supercavitating Flows", held at the von Kármán Institute (VKI) in Brussels, Belgium, 12-16 February 2001, and published in RTO EN-010.

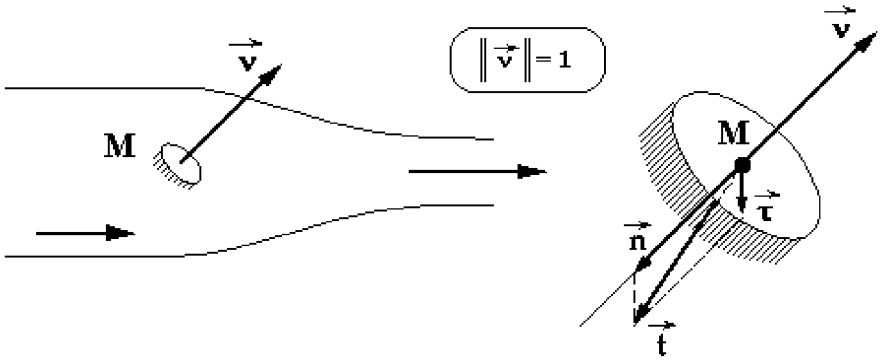


Fig. 1.

For example, the correct filling of a serynge requires that the piston motion is slow : if not, the liquid column is broken and the filling is stopped. That is because, due to the head losses inside the needle, the pressure drops to a value lower than atmospheric pressure, the difference increasing with the liquid velocity, and then with the piston velocity. More, at the serynge inlet, where the flow is a submerged liquid jet, additional turbulent fluctuations of the pressure occur : both mechanisms contribute to lower the pressure, possibly to a value below the liquid vapour pressure, so that vapour is produced. A similar phenomenon can be found in volumetric pumps for fuel injection in engines : head losses and rapid accelerations of the liquid columns result in deep underpressures so that evaporation occurs and only a small part of the chamber is filled with liquid.

1.2. THE VAPOUR PRESSURE

The first (and basic) *threshold* at our disposal is given by the thermodynamic diagram of phase changes (see figure 2). Here, we are interested in the curve T_rC which links the triple point T_r to the critical point C, and separates the liquid and vapour domains. Across that curve. reversible transformations *under static or equilibrium conditions*, result in evaporation or condensation of the fluid, at a level p_V which is a function of the absolute temperature T. We can obtain the phase change by lowering the pressure at an approximately constant temperature (as it actually happens in real flows) to obtain cavitation. Thus at first sight cavitation appears similar to boiling, except that the driving mechanism is different.

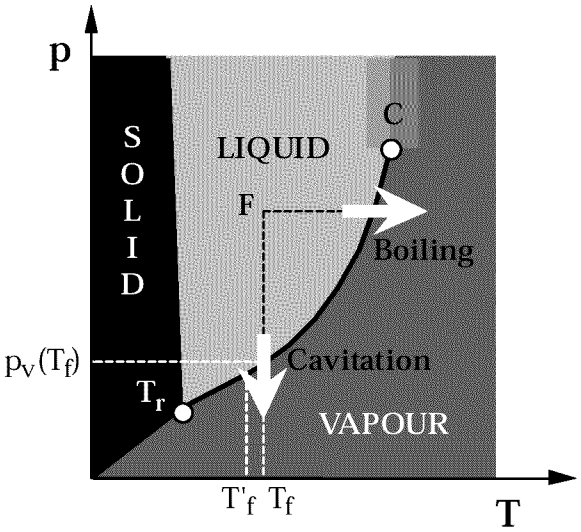


Fig. 2. Diagram for phase changes

In fact, for most of the cases (with cold water, for example), the path in the T – p_V diagram is practically isothermal : here the driving mechanism is the local pressure controlled by the flow dynamics, and only a very small amount of heat is required to the formation of a significant volume of vapour. However, in some cases the heat transfer needed by vaporisation results in the phase change at a temperature T'_f lower than the ambient liquid temperature T_f. The temperature difference $T_f - T'_f$ is called *"thermal delay"* to cavitation. It is greater when the ambient temperature is closer to the fluid critical temperature. For example, that phenomenon may be important when pumping the cryogenic liquids used in rocket engines.

It must be kept in mind that curve $\mathbf{p_V(T)}$ is not *an absolute limit* between the liquid state and the gaseous state. Deviations from that curve may exist in the case of rapid phase changes. Even in almost static conditions, the phase change may occur at a pressure lower than p_V. For example, let us consider the so-called Andrews-isotherms in the v–**p** diagram, where $v = 1/\rho$ and ρ stands for the density (see figure 3). Such curves are well modelled by the Van der Waals law in the liquid and vapour domains. More, the transformation from liquid to vapour on branch **AM** of the Van der Waals curve is possible. On this branch, the liquid is in a metastable equilibrium. We note that this allows the liquid to whithstand *negative absolute pressures, i.e. tensions,* without any phase change. Such considerations are necessary for a correct interpretation of some phenomena occurring in industrial situations as well as in laboratory conditions : it may happen that the interfaces between the liquid and vapour domains undergo very rapid evolution laws so that the reversibility conditions are far from being met.

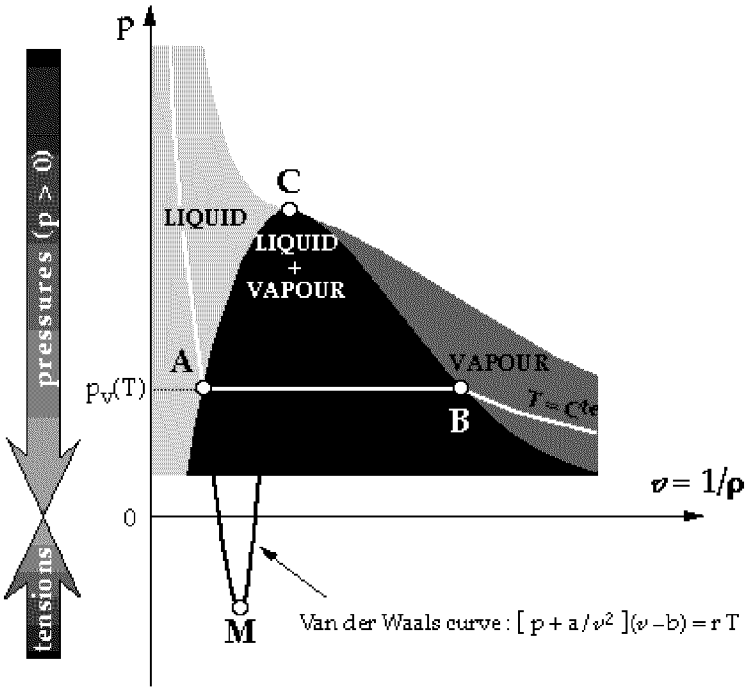


Fig. 3. Andrews-isotherms

In conclusion, it appears that the condition : *"local absolute pressure equal to the vapour pressure at the global temperature of the system"* does not ensure in all cases that cavitation actually appears in the flow. The difference between p_V and the actual pressure at cavitation inception is called *"static delay"* to cavitation. In some cases, we have also to consider a *"dynamic delay"* which is due to inertial phenomena : a "certain" time is necessary to obtain observable vapour cavities.

1.3. THE MAIN PATTERNS OF VAPOUR CAVITIES

Cavitation can take different forms at its inception and in its further development. The main patterns are the following :

a. Transient isolated bubbles

These bubbles appear in the region of low pressures as a result of the rapid growing of very small *air nuclei* present in the liquid. They are convected by the main flow and then disappear subsequently when they encounter adverse pressure gradients.

b. Attached, or sheet, cavities

Such cavities (or vapour pockets) are often attached at the leading edges of such bodies as blades, foils ... on their upper side, *i.e.* on the low pressure side.

c. Cavitating vortices

Cavitation can appear in the low pressure core of vortices in turbulent wakes or, as a more regular pattern, in tip vortices of 3-D wings or propeller blades.

It must be noted that, in cases **b** and **c**, cavitation at its inception is strongly dependent on the basic non-cavitating flow structure. This point will be examined later. In all cases, the development of cavitation tends to disturb and modify this basic flow.

• In some cases, it may happen that some patterns of cavitation are not easily settled in those classes. For example, on upper sides of foils or propeller blades, cavitation figures with a very short life time may appear which are conveyed by the flow as bubbles but are shaped as attached cavities. If needed, it would be possible to give an objective foundation to the classification by appealing the relative velocity of the liquid at interface with respect to the mass centre of the vapour figures : if the velocity is rather normal to the interface, the figure should be considered as a bubble (then attention is mainly paid to the volume variation). On the contrary, if the relative velocity is close to the plane tangent to the interface, the figure should be considered as a cavity (in the absence of circulation), or as a cavitating vortex (with circulation).

2. Cavitation in Hydraulics

2.1. CAVITATION REGIMES

For practical purposes, it is useful to distinguish :

- the *limiting regime* between the non-cavitating flow and the cavitating flow ;
- the *regime of developed cavitation*. In laboratory situations, developed cavitation corresponds to a certain permanency and a certain extent of the cavitation figures, relatively to the size of the system under consideration, while for industry it corresponds to a significant fall of the system performances.

That distinction is in relation with the possibility to accept (or not) cavitation in industrial situations. In the case of limiting regime, the *threshold of cavitation inception or cavitation disappearance* is of interest, while in the second case, assuming that this threshold is overstepped, the consequences of cavitation on the operation of the hydraulic system in question focus attention (see § 2.3).

In the case of attached cavities, another distinction may be useful : either *partial cavities*, which re-attach on the foil or the blade, or ***supercavities***, the closure of which is downstream the foil, inside the liquid domain.

2.2. TYPICAL SITUATIONS FAVOURABLE TO CAVITATION

Some examples of situations favourable to cavitation were previously presented. Here are listed typical situations in which cavitation can appear and grow in a liquid flow :

- The *wall geometry* entails local overvalues of the velocity and then local underpressures in a flow which is globally steady : that is the case for the restriction in the cross-section area of liquid ducts (venturis), or for the curvature imposed to the flow streamlines (bends of pipes, uppersides of blades in propellers and pumps).

- The *shearing* between two neighbouring flows having very different velocities entails *large turbulent fluctuations of the pressure* : that is the case for jets, wakes...

- The strongly *unsteady character* of some flows (*e.g.* water hammer in hydraulic control circuits, in ducts of hydraulic power plants, or in the feeding lines of Diesel engines) results in large values of the temporal terms of the fluid acceleration and then in the production of low pressures at some instants of the flow cycle.

- The *local roughness* of the walls (*e.g.* concrete walls of dam spillways) produces local wakes in which small attached cavities possibly take place.

- The consequence of the *vibratory motion* of the walls (*e.g.* liquid cooling of Diesel engines, standard A.S.T.M.E. erosion device) is the creation of oscillating pressure fields superimposed to the mean pressure field. If the oscillation amplitude is large enough, cavitation can appear at those times when the negative oscillation occurs.

- In mechanical systems such as motors, if water is present in *interstices* due to defects in the joining of neighbouring pieces and if the wall of interstices are moving periodically, cavitation can occur there and erode the walls.

- Finally, attention has to be drawn on the case of solid bodies which are suddenly *accelerated* by a shock in a still liquid field, particularly if they have sharp edges : the liquid acceleration needed for getting round these edges produces low pressures even if the velocities are rather low immediately after the shock.

2.3. THE MAIN EFFECTS OF CAVITATION IN HYDRAULICS

If a hydraulic system is designed to operate with an homogeneous liquid, the additional vapour structures due to cavitation can be interpreted at first sight (by analogy with the case of mechanical systems) as mechanical clearances which increase the number of its freedom degrees. The vapour structures are often unstable, at least the ones which are carried along by the flow : when they reach a region of increasing pressure, they collapse violently since their internal pressure is constant and close to the vapour pressure.

That collapse is analogous to shocks by which clearances between neighbouring pieces disappear in mechanical systems. Thus, it is expected that cavitation results in the main following effects :

- *the alteration of the performance* of the system (reduction of the lift and increase in the foil drag, fall of turbomachinery efficiency , least capacity to evacuate water in spillways, energy dissipation...) ;
- *the appearance of unexpected forces* on the solid structures ;
- *the production of noise and vibrations* ;
- in the case of developed cavitation, if the relative velocities between the liquid and the solid walls are high, the *erosion of these walls.*

Thus, at first glance cavitation appears as a harmful phenomenon which must be avoided. However, in many cases it can be shown that the condition of no cavitation is the most severe among all conditions the designer is faced. It strongly reduces the performances that the given hydraulic system would eslsewere perform. If those performances have to be obtained without any too high financial charge, a "certain" degree of cavitation development should be allowed. Of course, this can be done only if the effects of developed cavitation are known.

Remark : Here, we insist on the negative effects of cavitation. However, cavitation has applications in industrial processes which require energy concentration on small surfaces in order to produce there high pressure peaks. For this purpose, cavitation is often obtained from ultrasonic devices by which bubbles are produced and then implode, without costly spending in energy. For example, we quote the following applications :

- the *cleaning of surfaces* by ultrasonics or with cavitating jets,
- the dispersion of particles in a liquid medium,
- the *production of emulsions* ,
- the *electrolytical deposit* (by cavitation, the ion layers which wrap electrodes are broken, accelerating then the deposit process),
- and in the field of medical engineering, the *therapeutic massage* and the *destruction of bacteria.*

3. Specific Features of Cavitating Flows

3.1. PRESSURE AND PRESSURE GRADIENT

In non-cavitating flows, the ambient pressure has no effect on the flow dynamics and attention is paid only to the *pressure gradient*. On the contrary, the cavitating flows are primarily dependent on the *ambient pressure* (which, for convenience, is taken here as equal to the absolute pressure, as previously mentioned). It will be shown that by only lowering the pressure at a reference point, cavitation can appear and develop in the flow region where the pressure is the lowest. Thus, considering the pressure value, not only its gradient, is essential in cavitation studies and experiments.

If then one looks for the prediction of *cavitation occurrence* by **theoretical or numerical way**, one has to compare the calculated value of the pressure in a sensitive region of the flow to a critical value (for example the vapour pressure) given by physical experience, which expresses the physical properties of the liquid. The method of calculation depends on the flow configuration :

- For *one-dimensional, steady flows in pipes*, the use of the Bernoulli relation, with due account to head losses, is sufficient to obtain the region of minimum pressure together with the value of this minimum.
- *Steady flows without significant shearing stresses* can be considered as potential flows (*e.g.* flows around wings, propeller blades...). Classical methods require that firstly the kinematics problem be solved and then the pressure is still given by the Bernoulli relation. In this case, the pressure minimum occurs on the boundary of the flow. Physical experience confirms that theoretical result fairly well.
- The case of *the turbulent flows with important shearing stresses* is among the most complicated ones and for this reason has been treated only by an experimental way until a recent past. Now, the progress of computational methods in fluid dynamics allows us to envisage a possible prediction of cavitation inception by this way, at least for the simplest configurations : some encouraging results have recently been obtained in this field.

In that case, the pressure field is controlled by the following Poisson equation :

$$\frac{\Delta p}{\rho} = \frac{1}{2}\Omega^2 - e_{ij}e_{ij}$$

which is obtained by applying the divergence operator to the Navier-Stokes equation. The two terms on the right hand represent the respective contributions of the rotation rate vector $\vec{\Omega} = r\vec{o}t\vec{V}$ and the deformation rate tensor $e_{ij} = \frac{1}{2}\left(\partial v_i/\partial x_j + \partial v_j/\partial x_i\right)$. The velocity vector $\vec{V}$ has components v_i, i = 1, 2 or 3. The Poisson equation has to be solved once the velocity field is known. The results of available numerical models, as applied to sheared turbulent flows, exhibit specific features such as the prominent role of the vorticity in the Poisson equation, compared with the deformation rate : the regions of minimum pressure coincide markedly with filaments on which vorticity is concentrated, inside of the flow field. Thus cavitation must appear firstly in those regions, which indeed agrees with physical observation,

- In the case of wings or propeller blades tip vortices, the structure of the flow is well identified and it is possible to use simple models such as the Rankine vortex or the Burger's vortex. Then, the problem reduces to the search for two parameters, the circulation around the vortex and the size of its viscous core.

Of course, the pressure also plays an important role in the case of *developed cavitation*, and this is the source of additional complexity in the modelling of cavitating flows :

- For example, the modelling of *cavities* attached to foils or blades requires a condition on the pressure along the cavity boundary : this modifies the nature of the mathematical problem to solve numerically. On the physical ground, the change in the pressure distribution entails a change in the pressure gradient and then a modification of the boundary layer behaviour.
- When a *large number of bubbles* explode on the upper side of a foil, the initial, non-cavitating, pressure distribution can be deeply modified and the interaction between the basic, non-cavitating flow and the bubbly flow must be taken in account.
- Lastly, the evolution of the *turbulent, cavitating vortices* of a wake cannot be predicted on the usual base of the classical fluid mechanics equations by which mass and intensity conservation of the vortex filaments are expressed : when the core of a vortex filament is changed into vapour, it becomes dependent on the pressure imposed in its vicinity. In other words, cavitation breaks the link (expressed by the relation $\boldsymbol{\omega / \delta\ell = k}$, where k stands for a constant) between the elongation rate and the rotational rate of a rotational filament.

On the **experimental side**, two main difficulties appear with respect to the measurement of the pressure. The first one is of fundamental type, as it appears from numerical simulations of non-cavitating flows : pressure transducers, which can be only flush mounted on the solid frontiers of the flow domain, do not give necessarily a valuable information on the value of the pressure inside of sheared turbulent flows - even although parallel in the mean (Lesieur, 1998). The second difficulty is rather technical : it appears that phenomena connected to bubble collapse have a very small size (less than about 0.1 mm) and a short duration (of the order of the microsecond). Then the transducers must have a very small spatial resolution and a very short rise time. In fact, those requests often are beyond the present technical possibilities. Moreover, in the case of erosion studies, pressures of the order of hundreds of Megapascals, or even Gigapascals, have to be measured : the material resistance of the pressure transducers then becomes a central problem for experimentalists.

In order to study conditions of cavitation inception and physics of developed cavitation, special equipments have been progressively worked out. The most common are made of a vertical closed loop with the test section at the top and a circulating pump at the lower part : that allows to draw benefit from the increase of pressure due to gravity and thus to avoid cavitation in the pump. The absolute pressure at the test section level is adjusted below the atmospheric pressure thanks to a void pump. In some cases, a compressor is used to increase the pressure above the atmospheric pressure. Such test loops are named *Hydrodynamic Tunnels* by analogy with the *Wind Tunnels* used in Aerodynamics.

3.2. THE LIQUID–VAPOUR INTERFACES

The cavitating flows, like other two-phases liquid-gas flows, are characterized by the presence of numerous interfaces. But their response to external perturbations, for example an increase in the pressure, can be very different from the liquid-gas flows response. Two-phase flows containing gas bubbles are usually not subject to rapid changes in their mean density (except for the case of shock waves), just because of the non-condensable character of the gas which ensures a kind of global stability to the flow. On the contrary, in cavitating flows, the interfaces are submitted on one side to a pressure practically equal to the vapour pressure and then to a constant pressure. Thus, (as already mentioned previously) they cannot sustain an increase or decrease of the external pressure without rapidly evolving in both shape and size : they are of deeply unstable nature.

It is not possible to place measurement probes inside a cavitating flow because they would be followed by their own cavity which, in general, would disturb the flow. In compensation, if the liquid is transparent, it is possible to visualise interfaces which reflect the light very efficiently. Generally enough, the interfaces can be considered as material surfaces (see the following paragraph) and thus an idea of the flow dynamics can be obtained by taking photographs (with short flash lighting duration, of the order of one microsecond) or by taking rapid films (at a typical rate of ten thousand frames per second).

When considering the exchange of liquid and vapour through the interface, we can

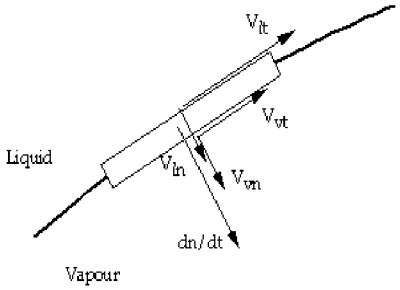


Figure 4

introduce the mass flowrate $\dot{m}$ (per unit of area) which is proportional to the relative normal velocities of either liquid or vapour. Thus we obtain, using mass conservation (see Fig. 4) :

$$\dot{m} = \rho_\ell \left[V_{\ell n} - \frac{dn}{dt} \right] = \rho_v \left[V_{vn} - \frac{dn}{dt} \right]$$

In that equation, indexes ℓ and v are relative to the liquid and vapour phases respectively, while index n means that the velocity component normal to the interface must be considered. The symbol dn/dt is the normal velocity of the interface, the equation of which is : $F(x_1, x_2, x_3, t) = 0$. It is related to $F(x_1, x_2, x_3, t)$ by :

$$\frac{dn}{dt} = - \frac{1}{\| \vec{grad}(F) \|} \frac{\partial F}{\partial t} \qquad \textbf{(2)}$$

If we neglect the flowrate at interface (what is actually made in most of the cases), we consider that the three normal velocities are equal and the surface F = 0 is a *material surface*, *ie* a surface which is made of the same fluid particulates at different instants. Two cases are of particular interest :

- For a spherical bubble with a variable radius R(t), the interface is defined as $F(r, t) = r - R(t) = 0$, which gives dn/dt = dR/dt and, with a negligible flowrate, $V_{\ell n} = V_{vn} = dR/dt$.
- For a steady cavity attached to a wall with a flowing liquid in its vicinity, we have $\partial F / \partial t = 0$ and then $\partial n / \partial t = 0$. If we assume that the mass flowrate is negligible, the normal velocities of the liquid and the vapour near the interface are zero. Then the liquid velocity at interface is reduced to its component $V_{\ell t}$ tangent to the cavity frontier.

3.3. THERMAL EFFECTS

The effects of the liquid temperature on cavitation are diverse :

a- If we consider a system in which the global temperature can evolve under a constant ambient pressure (as for example the case of Diesel engines cooling), the increase of temperature results in a greatest aptitude to cavitate : in the diagram of Figure 2, the distance between the point F and the phase change curve diminishes and thus smaller pressure variations can produce cavitation inception.

b- Now, as said in Section 1.2, the liquid vaporization requires a heat transfer from the bulk of the liquid towards the region of low pressure and the liquid-vapour interface. That results in the temperature difference $T_f - T'_f$ mentioned in the Figure 2, which is commonly called "*thermal delay*" to cavitation.

In order to estimate that delay, one needs to use the energy equation in addition to the mass conservation and the momentum equations (see annex 1 for the case of a spherical bubble). Then the boundary conditions $T'_f(T)$ and $p_V(T'_f)$ are unknown quantities. They are linked through the vaporization curve equation and the Clapeyron's relation :

$$L = T \left[\frac{1}{\rho_V} - \frac{1}{\rho_\ell} \right] \frac{dp_V}{dT}$$

in which L stands for the latent heat of vaporization.

In general, the thermal delay increases with the global temperature because the densities of the liquid and its vapour become closer. Near the critical point C (Fig. 2), they tend to be equal, while the slope dp_V/dT of the vaporization curve tends to become very large. As a result, for water, L decreases slowly on a large range of temperature variations, then it abruptly tends to zero in the close vicinity of the critical temperature.

3.4. SOME TYPICAL ORDERS OF MAGNITUDE

The instabilities of the interfaces result in *explosion* or *implosion* (named also *collapse)* phenomena, with large variations in their typical sizes and velocities during very short times. This character makes their scaling, together with their experimental or numerical analysis, rather difficult. However, we can quote some values which are currently encountered in the field of cavitation :

- the collapse of spherical vapour bubbles in water, with radius one centimeter, under an external pressure of one bar : its duration is approximately one millisecond ;
- the final phase of the collapse of bubbles or cavitating vortices : about one microsecond ;
- the normal velocities of interfaces : between some meters/second and some hundreds m/s ;
- the overpressures due to the implosion of vapour structures (bubbles and vortices) : they can reach several thousand bars.

4. The Non-Dimensional Parameters

4.1. CAVITATION NUMBER σ_V

Let us consider a hydraulic system liable to cavitate, such as a turbine, a pump, a gate, a foil in a hydrodynamic tunnel... and $\mathbf{p_r}$ the pressure at a conventional reference point **r** where the measurement of the pressure is possible. Usually, **r** is chosen in a region close to the one where cavitation inception is expected. If $\mathbf{T_f}$ is the operating temperature of the liquid and $\mathbf{\Delta p}$ a pressure difference which characterises the system, the *cavitation number* (which is also called *cavitation parameter*) is the ratio :

$$\sigma_v = \frac{p_r - p_v(T_f)}{\Delta p} \qquad (3)$$

For example, in the case of a gate, one takes :

$$\sigma_v = \frac{p_{downstream} - p_v(T_f)}{p_{upstream} - p_{downstream}}$$

while, for a foil placed at a submersion depth **h** in a horizontal free surface channel where the pressure on the surface is $\mathbf{p_o}$ and the flow velocity **U** :

$$\sigma_v = \frac{p_o + \rho g h - p_v(T_f)}{\frac{1}{2}\rho U^2}$$

and, for a pump (V_p stands for the velocity at the periphery of the runner) :

$$\sigma_v = \frac{p_{inlet} - p_v(T_f)}{\rho V_p^2}$$

It must be noted that the cavitation number is defined from dynamical parameters only and not from the system geometry. Also, in a non-cavitating flow, this non-dimensional parameter *cannot be considered as a similarity parameter* since, in the upper term of the ratio by which σ_v is defined, the difference between p_r and p_v has no physical significance for the actual flow : it cannot be obtained by integration of the pressure gradient along a real path. It becomes a similarity parameter only at cavitation inception.

4.2. CAVITATION NUMBER AT INCEPTION, σ_{VI}

The number σ_{vi} is the value of the parameter σ_v corresponding to inception of cavitation at any point of the flow system. Cavitation appears as a consequence of either the decrease in the pressure at the reference point (*i.e.* the ambient pressure) or the increase in the Δp-value. In some cases, for better experimental convenience (in particular for a best repeatability), number σ_{vd}, corresponding to cavitation disappearance from an initial regime of developed cavitation, is also used.

Operating in *non-cavitating conditions* then requires that the following condition be satisfied :

$$\sigma_v > \sigma_{vi} \qquad (4)$$

Threshold σ_{vi} depends on all influence factors usually considered in fluid mechanics : flow geometry,viscosity, gravity, surface tension, turbulence rate, thermal parameters, wall roughness and in addition the content of the liquid in gas (dissolved gas and "free gas", i.e. gas nuclei).

In general, a smaller value of σ_{vi} for a given system expresses its better adaptation to the flow. For example, for a circular cylinder with diameter 10 mm in the test section of a hydrodynamic tunnel, one finds about 1.5, while for elliptical cylinders at zero incidence, with chord 80 mm and axe ratios 1/4 and 1/8, the σ_{vi}-values are 0.45 and 0.20 respectively.

When σ_V becomes smaller than σ_{vi}, usually cavitation becomes more and more developed. However, exceptionnally it may happen that after a first development, cavitation finally disappears as the consequence of a further lowering of σ_{Vi}.

NOTE : In many circumstances, particularly for the numerical modelling of cavitating flows, the following estimate is made for σ_{vi} :

$$\sigma_{vi} = -Cp_{min} \qquad (5)$$

where Cp_{min} is the minimum pressure coefficient (a negative value, in general), and **Cp** at a point **M** is defined by the relation :

$$Cp = \frac{p_M - p_r}{\Delta p}$$

In this expression, $\mathbf{p_r}$ still stands for the absolute pressure at the reference point, as in relation (3). Two assumptions underlie that short cut :

- on the one hand, cavitation occurs at the point of minimum pressure
- on the other hand, the threshold of pressure is the vapour pressure.

We know that those assumptions are too restrictive. Thus the estimate resulting from equation (5) must be taken cautiously.

4.3. RELATIVE UNDERPRESSURE OF A CAVITY, σ_C

If a developed cavity is attached to the upperside of a blade (or if a large amount of bubbles is present on the upperside) one observes that the pressure in the region covered by the cavity is uniform. Calling $\mathbf{p_c}$ its value, one defines the non-dimensional parameter :

$$\sigma_c = \frac{p_r - p_c}{\Delta p}$$

which is the "*relative underpressure of the cavity*". It is a *true similarity parameter*, as the numerator in the ratio expresses an actual pressure difference inside the flow domain. In the numerical modelling of flows with developed cavities, a great use is made of this number. It is often (but unduly) named "cavitation number" : indeed, it plays a large role in dynamics due to its "underpressure" character.

Usually, pressure $\mathbf{p_c}$ is the sum of two partial pressures : the vapour pressure $\mathbf{p_v}$ and a term $\mathbf{p_g}$ which expresses the presence of gas inside the cavity. When this last term is negligible, the number $\boldsymbol{\sigma_c}$ becomes equal to $\boldsymbol{\sigma_v}$ (which probably explains the confusion just mentioned).

5. Some Historical Aspects

The word "cavitation" appeared in England at the end of the nineteenth century. Before, it seems that the problem of the behaviour of liquids in rotating machinery was suspected by *Torricelli* then *Euler* and *Newton*. In the middle of the nineteenth century, *Donny* and *Berthelot* have measured the *cohesion of liquids*. The negative effect of cavitation on the performances of a ship propeller was firstly noted by *Parsons* (1893) who built the first experimental loop - the first hydrodynamic tunnel - for its study. The cavitation number was introduced by *Thoma* and *Leroux* around the years 1923-1925.

Subsequently, many experiments were carried out in order to study the physical aspects of the phenomenon and examine its effects on industrial systems. Theoretical and numerical approaches were also largely used. Two main ways of research can roughly been distinguished :

- The first way considered the *Bubble dynamics (Rayleigh 1917 ; Lamb 1923 ; Cole 1948 ; Blake 1949 ; Plesset 1949...)*. The simplicity of the shape of spherical bubbles made their study (either theoretical or experimental) relatively easier. Thus, a large amount of work was devoted to topics related to bubble dynamics.

- The second way related to developed cavities or supercavities and leant on the old *wake theory (Helmholtz 1868 ; Kirchhoff 1869 ; Levi-Civita 1907 ; Villat 1913 ; Riabouchinski 1920* - those references can be found in Jacob's book : *"Introduction mathématique à la mécanique des Fluides").* This theory considered wakes as regions where pressure is uniform and which are limited by surfaces on which the tangential velocity is not continuous. It is more suited to cavitating wakes than to monophasic wakes. Later, *Tulin (1953)* and *Wu (1956)* made use of linearization in order to adapt this theory to the case of slender bodies such as wings and blades.

Vortical cavitation was not considered as deeply from the theoretical point of view. However, we can quote studies made by *Genoux and Chahine (1983)* and by *Ligneul (1989)* concerning torus and tip vortices respectively.

References

BLAKE, F.G. –1949– The tensile strength of liquids : a review of the literature. *Harvard Acoustics Res. Lab.* TM 9, June.

COLE, R.H. –1948– Underwater explosions. *Princetown University Press.*

GENOUX, P. & CHAHINE, G.L. –1983– Équilibre statique et dynamique d'un tore de vapeur tourbillonnaire. *J. Méc. Théor. Appl.,* **2**, N°5, 829-857.

JACOB, C. –1959– Introduction mathématique à la mécanique des fluides. *Gauthier-Villars.*

LAMB, H. –1923– The early stages of a submarine explosion. *Phil. Mag.,* **45**, 257 sq.

LESIEUR, M. –1998– Vorticity and pressure distributions in numerical simulations of turbulent shear flows. *Proceedings of the 3rd Int. Symp. on Cavitation, Grenoble, 7-9 April,* **1**, 9-18.

LIGNEUL, P. –1989– Theoretical tip vortex cavitation inception threshold. *Euro J. Mech. B/Fluids,* **8**, 495-521.

PLESSET, M.S. –1949– The dynamics of cavitation bubbles. *J. Appl. Mech.,* **16**, 277 sq.

RAYLEIGH –1917– The pressure developed in a liquid during the collapse of a spherical cavity. *Phil. Mag.,* **34**, 94 sq.

TULIN, M.P. –1953– Steady two-dimensional cavity flows about slender bodies. *D.T.M.B.* , Rept 834.

WU, T.Y.T. –1956– A free streamline theory for two-dimensional fully cavitated hydrofoils. *J. of Math. and Physics,* **35**, 236-265.

Annex I to Section 3.3

The spherical bubble growing with thermal delay : setting of equations

We assume that a spherical bubble, initially in equilibrium, is compelled to grow under the effect of a sudden decrease of the ambient pressure. The liquid is assumed to be non vsicous and weightless. Inside the bubble, the volume is saturated with vapour only. There the temperature is $T_b(t)$, (t stands for the time), the pressure is $p_v(T_b)$, while the bubble radius is R(t). Note that those quantities are the main unknown of interest.

The liquid domain is described thanks to the distance r, $r \geq R(t)$, the temperature T(r,t), the pressure p(r,t), the liquid density $\rho(r,t)$ and the radial velocity $u_r(r,t)$. Far from the bubble center, the temperature $T(\infty,t)$ is T_∞ the pressure $P(\infty,t)$ is $P_\infty \langle p_v(T_\infty)$, the density is ρ_∞ and the velocity is zero.

At the bubble interface the temperature and the pressure have to meet the following conditions :

$$T(R,t) = T_b(t),$$

$$p(R,t) = p_v(T_b) = p_v(t).$$

Initially (t = 0), the conditions are : $T(r,0) = T_\infty$, $p(r,0) = p_v(T_\infty)$, $\rho(r,0) = \rho_\infty$, $u_r(r,o) = 0$, $R(0) = R_0$.

Taking the sperical symmetry into account, the equations of the problem are the following ones :

- Mass conservation

$$\frac{\partial \rho}{\partial t} + \frac{1}{r^2}\frac{\partial}{\partial r}\left(\rho r^2 u_r\right) = 0$$

- Momentum equation

$$\frac{\partial u_r}{\partial t} + u_r \frac{\partial u_r}{\partial r} = -\frac{1}{\rho}\frac{\partial p}{\partial r}$$

- Liquid state equation (here we assume a barotropic behaviour, as given for example by the Tait's equation)

$$f(p,\rho) = 0 \text{ or } \frac{p + A}{P_0 + A} = \left(\frac{\rho}{\rho_0}\right)^n, \text{with } A \cong 3000\text{bars}, n \cong 7{,}15 \text{ for water.}$$

- Energy equation

$$\frac{1}{r^2}\frac{\partial}{\partial r}\left(r^2\frac{\partial T}{\partial r}\right)=\frac{1}{\alpha}\frac{dT}{dt}$$

In the last equation, the work of the pressure is neglected, as the compressibility of the liquid is very small. In the same way, the thermal diffusivity α, $\alpha = \lambda / \rho c_p$, is assumed to be a constant (λ stands for the thermal conductivity of the liquid and c_p for its heat capacity).

Finally, it is necessary also to consider the following quantities :

- The heat flux ϕ at the distance r : $\phi(r,t) = -4\pi\lambda r^2 \frac{\partial T}{\partial r}$

- The mass exchange $\dot{m}$ at the interface : $m(R,t) = (T_b)\left[u_r(R,t) - \frac{dR}{dt}\right]$

with $\dot{m}(R,t) = \phi(R,t)/L(T_b)$

- L is the latent heat of vaporization which has to meet the Clapeyron's equation :

$$L = T_b\left[\frac{1}{\rho_v} - \frac{1}{\rho_\ell}\right]\frac{dp_v}{dT}$$

Annex 2 to Section 3.3

Vapour Bubble Collapse (Rayleigh problem)

Here we suppose that a vapour bubble, initially at equilibrium, is submitted suddenly to an increase of the ambient pressure from the value p_v to the final value $P_\infty, P_\infty \rangle p_v$. All thermal aspects are neglected and the liquid is assumed to be incompressible. The mass conversation equation reduces to $\mathrm{div}\vec{V} = 0$, which gives :

$$u_r(r,t) = \dot{R}\frac{R^2}{r^2}$$

in which we put $\dot{R} = \frac{dR}{dt} = U$. Then the momentum equation of Annex 1 can be written :

$$\ddot{R}\frac{R^2}{r^2} + 2\dot{R}^2\left(\frac{R}{r^2} - \frac{R^4}{r^5}\right) = -\frac{1}{}\frac{\partial p}{\partial r}$$

and after integration, the equation for the pressure is :

$$\frac{p(r,t) - P_\infty}{\rho} = \ddot{R}\frac{R^2}{r} + 2\dot{R}^2\left(\frac{R}{r} - \frac{R^4}{4r^4}\right)$$

That equation can be rewritten at the interface, r = R , and then integrated, taking into account the fact that the pressure at infinity is assumed to be constant. One obtains :

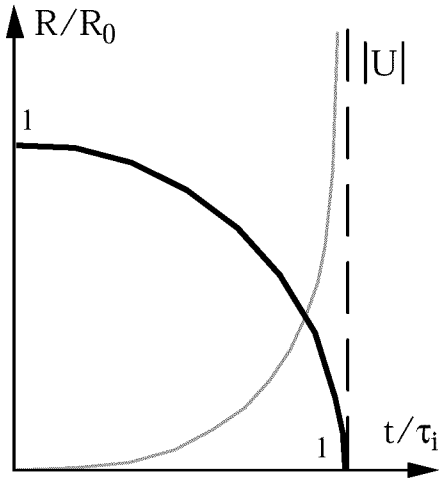
$$\rho \dot{R}^2 R^3 = -\frac{2}{3}(P_\infty - p_v)\left[R^3 - R_0^3\right]$$

From that differential equation the relation R(t) can be obtained.

The radius becomes zero after the time τ_i, which is called "*Rayleigh time*" :

$$\tau_i = -\sqrt{\frac{3\rho}{2(P_\infty - p_v)}} \int_{R_0}^{0} \frac{dR}{\sqrt{\frac{R_0^3}{R^3} - 1}} \cong 0.915 R_0 \sqrt{\frac{\rho}{P_\infty - p_v}}$$

The behaviour of R(t) and the interface velocity U(t) is shown on the figure.



Behaviour of R(t) and U(t) during the bubble collapse

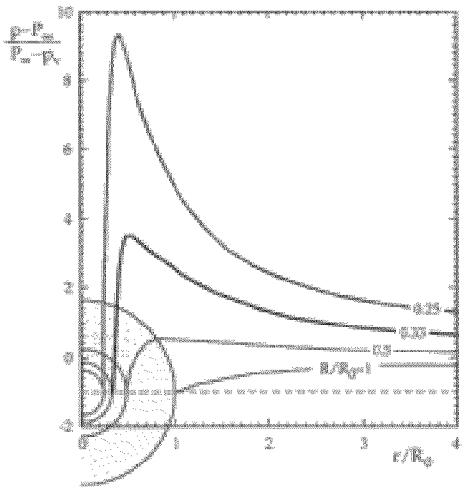
While the mean value of the velocity is R_0/τ_i, U tends to an infinite value at the end of the collapse, the singularity intensity being approximately 1.12 $R_0/\tau_i.(R_0/R)^{3/2}$. In fact, compressibility effects are present at the end of the collapse, which tend to weaken the strength of the singularity.

The pressure equation, together with the equation which gives the velocity $\dot{R}$, allows expressing the pressure field as :

$$\frac{p(r,t) - P_\infty}{P_\infty - P_v} = \frac{R}{3r}\left(\frac{R_0^3}{R^3} - 4\right) - \frac{R^4}{3r^4}\left(\frac{R_0^3}{R^3} - 1\right)$$

The following figure shows the evolution of the pressure distribution at different instants. Attention must be paid to the kind of pressure wave which comes from infinity to the neighbouring of the bubble. That phenomenon is due to the high unsteadiness of the flow, although inertia and pressure forces only are considered here. The pressure wave is still found with more evolved models, although with some modifications.

In the case of water, it is found that at the instant when R/R_0 is equal to 1/20, the interface velocity is 720 m/s (i.e. approximately the half of the sound speed), while the pressure maximum is 1260 bars if the pressure difference $P_\infty - p_v$ is one bar.



Evolution of the pressure field

From the physical point of view, the violent behaviour of the bubble collapse results from two main facts :

- On one hand, the pressure inside the bubble is constant and does not bring any resistance to the liquid motion.

- On the other hand, the conservation of the liquid volume, through the spherical symmetry, tends to concentrate the liquid motion on a smaller and smaller region.

It must be noted that the Rayleigh time is found in various experimental situations, for order of magnitude of R_0 betwen the micrometer and the meter, and for large ranges of the overpressure $P_\infty - p_v$.

This page has been deliberately left blank

Page intentionnellement blanche

Oscillations of Ventilated Cavities Experimental Aspects

J.M. Michel
Laboratoire des Ecoulements Géophysiques et Industriels
BP 53 - 38041 Grenoble Cedex 9
France

1. Introduction

By injecting air in the low pressure regions of water flows, it is possible to obtain cavities similar to the attached cavities due to "true" cavitation. That ventilation is a current practice in the field of spillways for large concrete dams, especially in tropical zones. It is aimed to diminish the risks of erosion, as the speeds of the water flows ordinarily are very large : the stresses between concrete and water are diminished by the injected air, due to its compressibility which increases the characteristic time of contact and diminishes the forces for the same total impulse. Then the main problem is to calculate the ideal dimensions of the ducts by which atmospheric air is sucked up under the water flow (Chanson, 1999).

Here our main concern is rather on the side of ventilated hydrofoils or, possibly, torpedoes. In both cases, the main difference with respect to the case of vapour cavities is due to the non-condensable character of the gas which modifies the closure region of the cavities. For the latter case, the presence of gas inside the cavity can be produced either by the burning of powder for the body propulsion, or by the entrainment of atmospheric air at the body entry in water. Then initially there is a limited amount of gas inside of the cavity which progressively is shed into the cavity wake. On the contrary, hydrofoils are assumed to be supplied continuously with air, so that a steady regime is obtained, at least in the mean, which makes their study easier.

The concept of ventilated hydrofoil was imagined, about forty years ago, for the lift of rapid hydrofoil boats and even their propulsion by ventilated propellers. The shape of such a foil is shown on Figure 1 : it widens downstream as a parabola but can admit a small curvature.

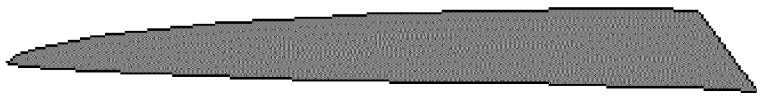


Fig. 1. Truncated foil with a ventilated base

The aft part of the foil is truncated, its upper side usually is shorter than its lower side. It is currently named "base-vented hydrofoil". Ventilation is operated artificially from an air compressor placed on the boat. Air passes by the legs of the boat or by the propeller hub and it is injected at the base of the foils or the propeller blades : the pressure at the base of the foil is increased and the drag is lowered. If the angle of attack becomes important, air tends to invade the region of the flow close to the foil upper side, which results in the decrease of the lift. That flow regime must be avoided, and then the possible range of incidences currently is rather small.

This kind of foil seems to be well enough suited to boat speeds in the range 40-80 knots, for which classical, non-cavitating foils are inoperative. For larger speeds, only supercavitating foils with a non

Paper presented at the RTO AVT Lecture Series on "Supercavitating Flows", held at the von Kármán Institute (VKI) in Brussels, Belgium, 12-16 February 2001, and published in RTO EN-010.

wetted upper side can be used (as for example in pump inducers of cryogenic liquids used in rocket propulsion).

For base-vented hydrofoils with wetted upperside, several problems have to be considered (*Rowe* 1979). Firstly, the global operation of the foil is characterized by the dependence of the cavity length, the lift and drag coefficients on the foil geometry and the relative underpressure of the cavity σ_c (cf chapter 1, § 1.4.3) :

$$\sigma_c = \frac{p_r - p_c}{\frac{1}{2}\rho V^2} \quad \textbf{(1)}$$

Here p_r stands for the reference pressure upstream of the foil and p_c for the cavity pressure, the latter being the sum of the vapour pressure (as it can be assumed that the cavity is saturated in vapour) and the mean pressure of the injected air :

$$p_c = p_v + p_{air} \quad \textbf{(2)}$$

Secondly, we need to know the limits of operation corresponding to cavitation inception near the leading edge or to the venting of the foil upper side. As the radius of curvature at leading edge of such foils usually is very small, the first limit is the strictest one, which justly leads to small possible ranges of incidence.

Finally, in the expression (2) for p_c and then for σ_c, the contribution of p_{air} is not known when the air flowrate is imposed : the balance of pressures depends on the mode by which air is evacuated at the rear of the cavity. The evacuating mode depends on the global flow geometry, particularly the length of the cavity and the circulation, so that all parameters are in mutual dependance. An additional difficulty comes from the fact that several air evacuation regimes are possible, even for a cavity confined at the base of the foil. Thus the non-condensable character of air makes the behaviour of ventilated cavities deeply different from the vapour cavities.

2. Non-Dimensional Parameters

By analysing the experimental results (Michel 1971, 1984) it appears that it is necessary to distinguish two terms in the relative underpressure σ_c, such as $\sigma_c = \sigma_v - \sigma_a$:

- the classical parameter cavitation σ_v, which characterizes the ambient pressure :

$$\sigma_v = \frac{p_r - p_v}{\frac{1}{2}\rho V^2} \quad \textbf{(3)}$$

- the relative mean pressure of air inside the cavity, which takes the elastic behaviour of air into account :

$$\sigma_a = \frac{p_{air}}{\frac{1}{2}\rho V^2} \quad \textbf{(4)}$$

Note that, as σ_c is usually small, the parameters σ_v and σ_a are not very different.

In the case of *pulsating ventilated cavities*, we have also to consider the ratio σ_c/σ_a which compares the cavity underpressure to the mean pressure of air (or, in an almost equivalent way, the parameter σ_c/σ_v, as done by *Silberman* and *al*, 1961, and *Song* (1962), who described the pulsating regime for the first time).

In this case also, if f, ℓ and d stand for the pulsation frequency, the mean cavity length and a fixed reference length respectively (*e.g.* the chord of the forebody for the latter), the phenomena are well enough described when we introduce the non- dimensional frequency :

$$\varphi = \frac{f}{\sqrt{\frac{p_{air}}{\rho d \ell}}} \qquad \textbf{(5)}$$

Finally, considering the mass air flowrate Q_m and a reference area S, we can build the following non-dimensional parameters :

• the mass air flowrate coefficient :

$$C_{Qm} = Q_m / \rho V S \qquad \textbf{(6)}$$

• the volume air flowrate coefficient :

$$C_{Qv} = Q_m / \rho_{air} V S \qquad \textbf{(7)}$$

The mean air density ρ_{air} is known through the measurement of the cavity pressure p_c and the use of the Boyle-Mariotte law. If we consider the mean velocity V_{air} of air inside the cavity and take an area close to the cavity cross-section for S, we have, approximately : $Q_m \cong \rho_{air} V_{air} S$, so that the volume airflow coefficient C_{Qv} more or less represents the ratio of the air velocity to the water velocity : V_{air}/V. Practically, the values of C_{Qv} can be markedly lower than 0.1, and they can also reach values of the order 0.7 to 1.

Of course, other classical non-dimensional parameters must be considered, and among them especially the Froude number $V/\sqrt{gd}$.

3. Experimental Results

3.1. DEPENDENCE BETWEEN NON-DIMENSIONAL PARAMETERS

Experimental tests operated in various configurations (two or three-dimensional wings, cavity formed between an horizontal water jet and a solid wall, free surface channel or closed channel...), bring three main dependences in light (in all those relations, the main influence parameter is in bold type characters) :

- The relative mean cavity length ℓ/d and the global force coefficients depend on the foil incidence, the Froude number and the relative cavity underpressure :

$$\frac{\ell}{d}[\alpha, Fr, \boldsymbol{\sigma_c}] \qquad \textbf{(8)}$$

- The relative air pressure σ_a depends on the incidence, the mean ambient pressure and the mass air flowrate coefficient :

$$\sigma_a[\alpha, \sigma_v, \mathbf{C_{Qm}}] \qquad \textbf{(9)}$$

Note that from the experimental point of view, a more convenient way to express that dependence is :

$$C_{Qv}[\alpha, \sigma_v, \boldsymbol{\sigma_c}] \tag{10}$$

- The non-dimensional frequency φ depends particularly on the ratio σ_c/σ_a :

$$\varphi\left[\frac{\boldsymbol{\sigma_c}}{\boldsymbol{\sigma_a}}\right] \tag{11}$$

Some experimental results which illustrate those relations are presented below. Most of them were obtained with a two-dimensional flow realized in a rectangular, free-surface channel (width 175 mm, height 280 mm). The fore-body was a simple triangular wedge (chord c = 60.5 mm, base b = 17 mm) placed at at a zero mean incidence and different submersion depths : h_1 = 70, 140 or 210 mm. The water velocity V could be varied between 2 and 14 m/s, while the absolute pressure p_0 over the free surface was fixed between a value close to the water vapour pressure and the atmospheric pressure. Then the range of actual values for the cavitation number σ_V was between 0.04 and 20 approximately. It is valuable to note that the hydrodynamic tunnel in which such experiments are carried out must be able to eliminate the large amounts of the injected air so that the water entering the test section be free from all trace of air after recirculation in the tunnel loop.

3.2. RELATIVE CAVITY LENGTH ℓ/C AS A FUNCTION OF σ_C

In Fig. 2, the main dependence of the relation (8) is shown for four values of the velocity V and an immersion depth h = 140 mm. Note that the experimental points correspond to various values of the cavitation number σ_v, between 0.4 and 10 approximately. Thus the influence of the ambient pressure on the different air flow regimes does not appear on such a graph.

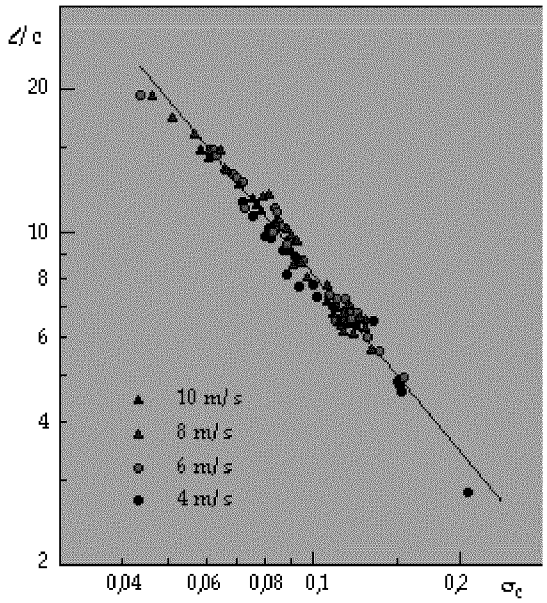


Fig. 2. Variation of the mean non-dimensional length of the cavity versus the relative underpressure σ_c

Considering the almost linear dependence of ℓ/c *vs.* σ_c in logaritmic coordinates, we can adopt a power law : $\ell/c = A\ \sigma_c^{-n}$. The following table gives the values of A and n for the three values of the submersion depth :

h(mm)	A	n	Variations of ℓ/c
70	0.38	1.16	3.4-23
140	0.45	1.26	2.8-19
210	0.34	1.47	3.6-21

Those values are close to the ones corresponding to vapour supercavities. The theoretical asymptotic value of n in an infinite medium is 2 (for small σ_c), while a simple model considering the flow above the wedge and the cavity as a simple jet gives the value n = 1.

The Froude number has a small influence on the cavity length, at least for the present range of velocities and chord length, except for the smallest values of σ_c. In fact, if we consider the Froude number based on the cavity length, we obtain the small value $Fr_\ell = 2.4$ for ℓ/c = 18 (or ℓ = 1.09 m) and V = 8 m/s. which makes likely the gravity effect, as seen on the Figure 2.

3.3. AIR FLOW RATE

The sketch of Figure 3 represents the relation (10), together with the flow behaviour, when the air flowrate is gradually increased then decreased between small and large values. Here we suppose that σ_v is large enough so that there does not exist any vapour cavity before the air injection.

Remark : If such a cavity is present, the initial value of σ_c is equal to σ_v, and the phenomena are practically as in Figure 3. However, for very small values of σ_v, say lower than about 0.2, it was found that a very small amount of air results in a sudden, and large, increase of the cavity length, disclosing a kind of global flow instability. We don't consider that case here.

Roughly speaking, the curve of Figure 3 is L-shaped. For the very small air flowrates, the air escapes downstream of the cavity as separate bubbles which are later entrapped in the alternate Benard-Karman vortices of the body wake. For larger air flowrates, a continuous air cavity appears and it is possible to consider and measure the parameter σ_c (the initial point on the right hand of Figure 3). A subsequent small increase of Q_m produces large variations in the air pressure, the σ_c - value and the length of the cavity : that is due to the difficulty, for air, to escape from the cavity (see below). On the contrary, on the vertical branch of the curve, air is evacuated by big separated bubbles. Those bubbles can leave the cavity upstream of its termination, under the gravity effect. That mode of air evacuation is very efficient, so that usually the parameter σ_c tends to a positive minimum value σ_m (and the cavity length to a maximum value). Subsequent tests (*Laali* and al 1984, see below) gave values between 0.01 and 0.09 for the parameter σ_m. It decreases when the Froude number increases and it depends also on the ambient air pressure *via* the parameter σ_v.

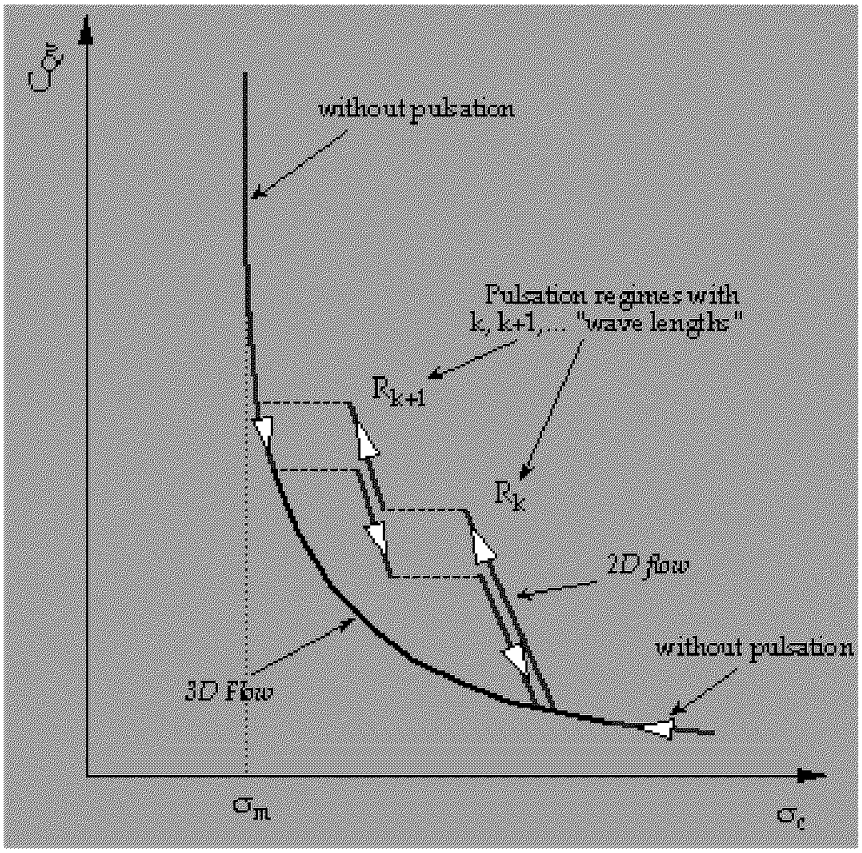


Fig. 3. Typical evolution of the cavity for an increasing, then decreasing, air flow rate (σ_v is constant)

3.4. PULSATING REGIME

In two-dimensional flows, the connecting region between the horizontal and vertical branches of the curve of Figure 3 is characterized by periodic pulsations of the air cavity : undulations are convected, with an increasing amplitude, on both free frontiers. They join at the rear part of the cavity, thus allowing air to escape under the form of separate, periodic, air pockets, as shown on Figure 4 (that figure sketches experimental results which were obtained through a special device for a one wave cavity (*Michel*, 1971). Then the air pressure undergoes periodic, almost sinusoidal, fluctuations. Their minimum occurs at the instants when the air pockets leave the cavity. At the same instants, undulations of the free surfaces, pointed to the cavity interior, arise at the two trailing edges of the wedge. And then the cavity, which passes by its minimum length, has the shape of one or several spindles : the corresponding flow regimes are named R_1, R_2, ..., R_k (Regime R_2 is presented in Figure 4). In general, the largest values of k are obtained for large values of the ambient pressure or, more precisely, for the small values of the parameter σ_c/σ_a.

When the regime R_k is established, a small increase in the ventilation air flowrate can result in the passage to the regime R_{k+1}, as shown in Figure 3. That occurs for threshold values of the parameter C_{Qv}. For decreasing values of the airflow, the passage from regime R_{k+1} to R_k occurs for lower values of C_{Qv}, so that the total evolution of the ventilated cavity exhibits a hysteretic aspect. As indicated on Figure 4, the wake of the cavity is featured by separate, almost periodical, air pockets, which have been emitted during the previous periods.

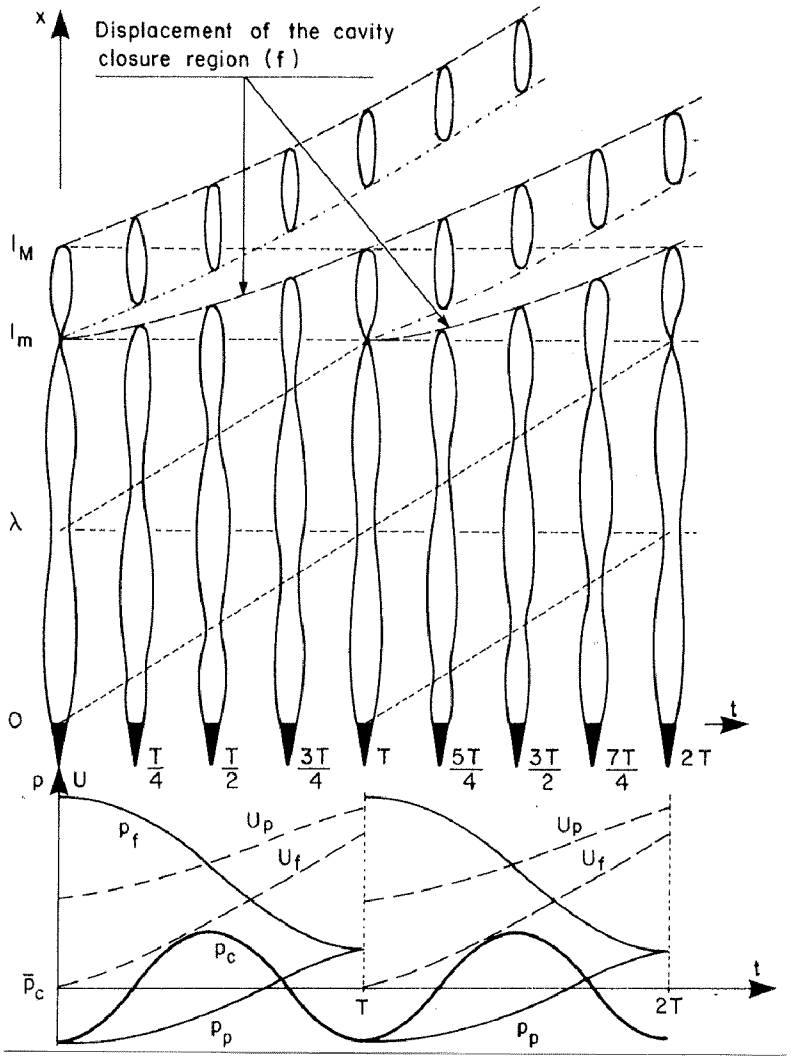


Fig. 4 A schematic view of the evolution of a two-waves cavity over two periods

- For comparison, the above mentioned *Laali* tests (*Laali et al* 1984) were carried out with the so-called "half-cavity" configuration, *i.e.* the cavity formed between an initially horizontal plane water jet, the thickness of which was H, and a solid plate having a small slope β. The distance between the jet and the plate is named h (see the Figure 5).

  Note that here the reference pressure p_r in the definition of σ_c and σ_v is the pressure p_0 above the jet. That configuration is a possible model for the spillway aerated flow mentioned in the Introduction to the present Chapter. The main features of the ventilated cavities downstream bodies were present also in that case : trends of the relations $\ell(\sigma_c)$ and $C_{Qv}(\sigma_c)$, pulsating regimes, relation $\varphi(\sigma_c/\sigma_a)$... In particular :

  a. The dependence between the cavity length ℓ and the relative cavity underpressure σ_c takes the approximate form :

$$\ell \cong \frac{4}{3}\sqrt{\frac{Hh}{\sigma_c}}\left[1+\sqrt{\frac{Hh}{\sigma_c}}\sin\beta\right]$$

b. The threshold value of the volume flowrate coefficient C_{Qv} for the passage of the regime R_1 to the regime R_2 diminishes when the parameter σ_v increases, either by the growing reference pressure p_0 or by the decreasing jet velocity V.

c. The dependence $C_{Qv}(\sigma_c)$ is practically not influenced by the step height h, neither as regards the threshold values of C_{Qv} nor the jumps in the σ_c-values. The maximum value of the jump occurs in the regime R_1 and is of the order 0.01-0.02.

d. Finally, the minimum value σ_m of σ_c seems to be controlled by the transverse pressure gradient inside the water jet, which influences the rising of the air bubbles for the high rates of ventilation.

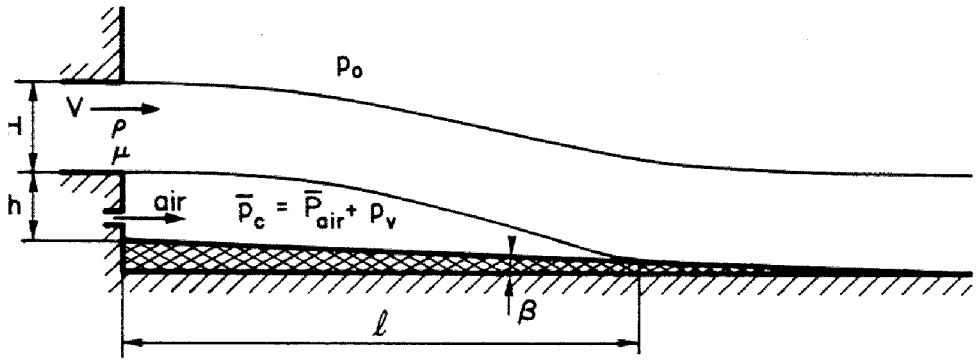


Fig. 5 Sketch of the half-cavity flow

Returning now to the case of the cavities behind the wedge, it is observed that, if the gravity effect is negligible, the air pockets tend initially to be symmetrical with respect to the flow direction. However, further investigations have shown that subsequently air is not present as a continuous medium in the air pocket, rather as small bubbles organized in alternate vortices. When the Froude number is small (for small water velocities), the air pockets are no longer symmetrical and the wake of the cavity looks a "duck file" : that seems to be due to the deviation of the reentrant jet from the axial direction under the gravity effect (see the Figure 6).

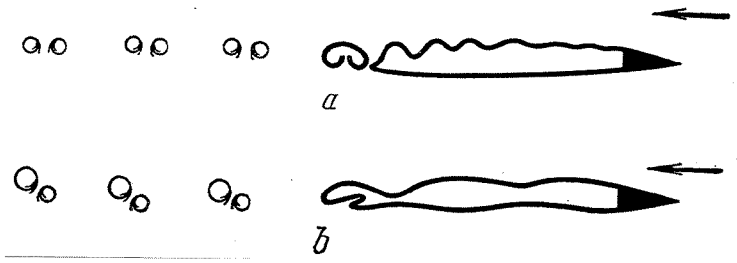


Fig. 6 Influence of gravity on the reentrant jet direction and the arrangement of the vortices in the wake.

3.5. THE AIR BLOCKAGE CONDITION FOR PULSATION

The basic reason for the discontinuous release of air at the rear part of a ventilated cavity is to be looked for in its geometry : since cavity is an underpressure region, the curvature of its frontiers tends to be directed towards its interior so that - in steady, 2D or axisymmetric flow - those surfaces tend to join themselves and to produce a reentrant jet which prevents the outflow of air. That *blockage condition* can be illustrated in an experimental way : if we put two parallel plates downstream a ventilated, pulsating,

cavity (see Figure 7), the curvature of the frontiers is locally reversed and air can flow in a continuous way. Then the pulsations disappear and the global flow becomes steady.

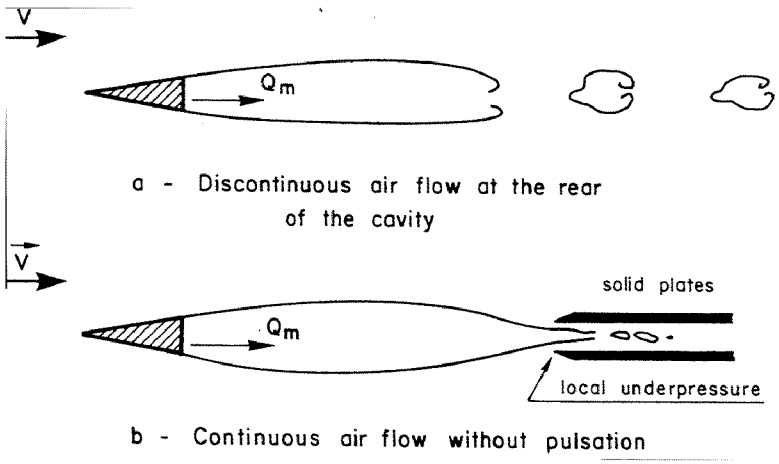


Fig. 7.

Another way for the air escape can be observed in the case of a ventilated three-dimensional hydrofoil with a small aspect ratio : a part of the injected air is evacuated continuously through the tip vortex, which tends to weaken, or even to suppress, pulsations (*Verron*, 1977), and *Verron* and al (1984). A similar observation was made by *Cox et al* (1957) for the horizontal ventilated cavity behind a vertical disk, at low Froude number. In this case the cavity ended by two almost parallel vortices by which air was evacuated into the wake. A physical model taking the gravity in account allowed the authors to give an account of the main flow features, ie the distance between the vortices, their diameter and the air flowrate.

Now, in the case when pulsations do exist, their periodical character results from a phase synchronization between the production of the undulations near the forebody and their coming to the rear part of the cavity (as suggested in Figure 4). Air pressure plays an important role in that mechanism as it conveys information from the rear to the fore part of the cavity (see below).

3.6. PULSATION FREQUENCY

Roughly speaking, the frequency of pulsations varies as $\sqrt{P_{air}}$ in each regime R_k. That result appears in Figure 8 for regime R_1. It leads us to build the non-dimensional frequency φ as defined by relation (5) and study its variation versus the parameter σ_c/σ_a (Figure 9).

It is noticeable that the various pulsating regimes are determined by ranges of σ_c/σ_a. values. In particular, the one-wave regime corresponds to the range 0.06 - 0.25 of that parameter, as well for a closed channel that a free surface channel. Also, higher the rank of the regime, narrower the range of σ_c/σ_a. In each regime, the dependence $\varphi(\sigma_c/\sigma_a)$ is roughly linear. The total variations of φ are between about 0.7 and 1, *i.e.* a small enough range (the limits are slightly smaller in the case of a deeper submersion of the forebody). It follows that the pulsation frequency is roughly proportional to the inverse of the mean length of the cavity.

In case of lifting foils, the circulation around the cavity can also influence the mode of air evacuation at its rear part, as indicated by relations (8) and (10). Then it happens (*Michel* 1984), that under only slight variations of the angle of attack α, (all other parameters being kept constant, in particular σ_v and the mass airflow rate Q_m) , the lift and drag coefficients may change : variations of α may result in a change of regime and then of σ_c.

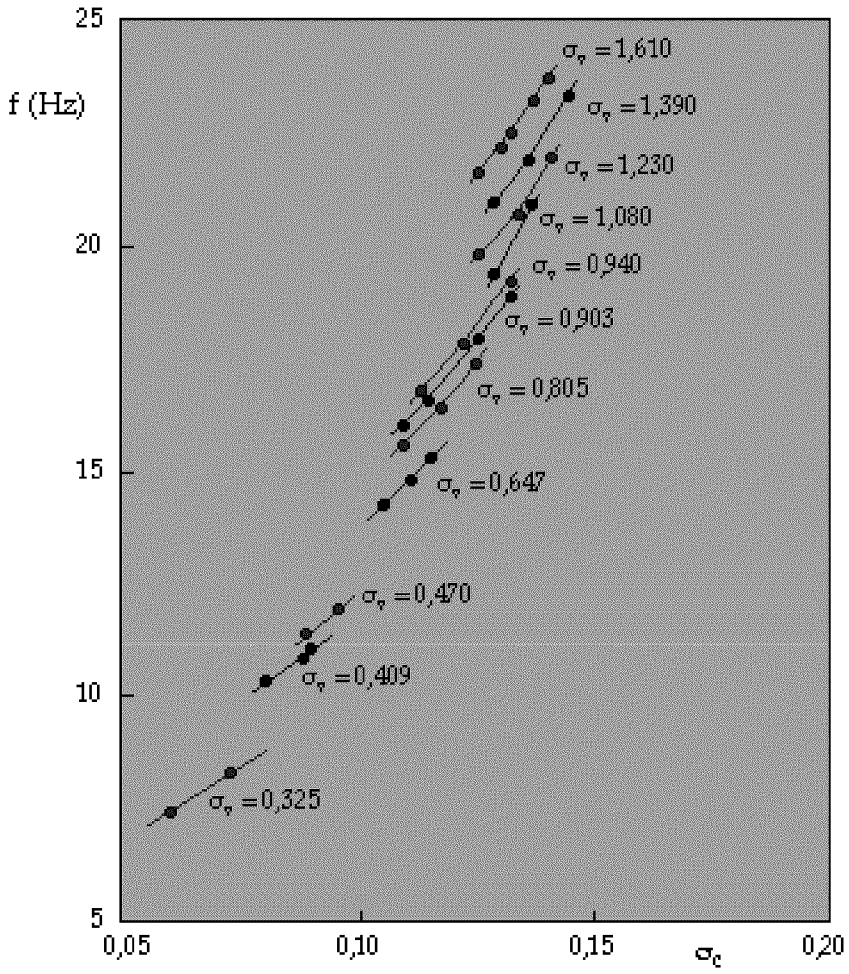


Fig. 8. Variations of the frequency f vs σ_c for increasing values of σ_v (Regime R_1, h_1 = 21 cm, V = 8 m/s)

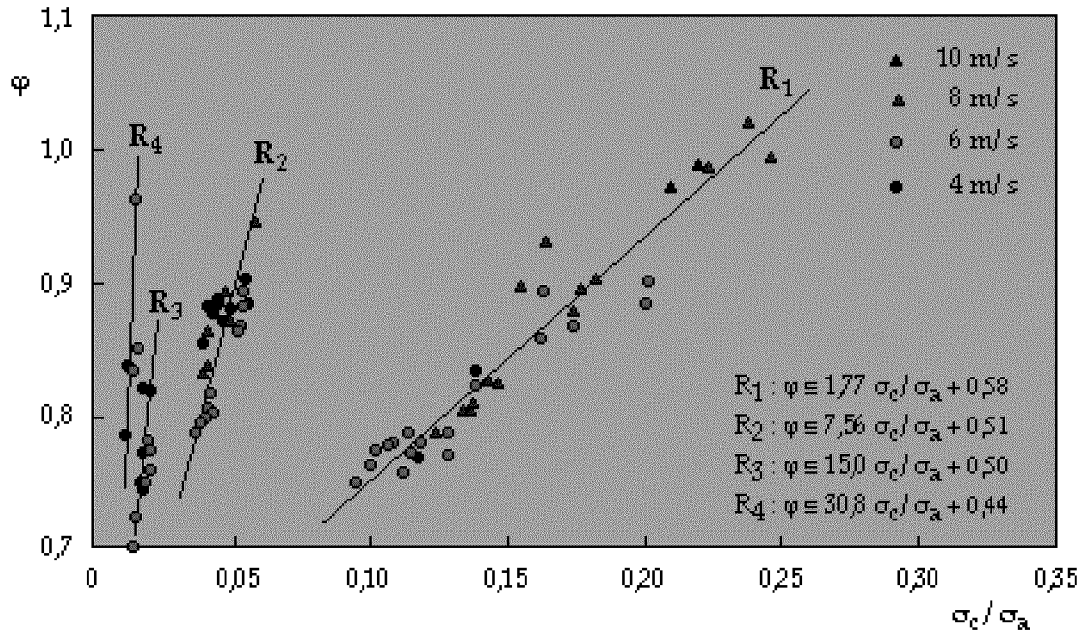


Fig. 9. Non-dimensional frequency vs. σ_c/σ_a (h_1 = 7 cm)

4. On the Pulsation Mechanism

As suggested in the Figure 4, different parameters can be described, as connected to the evolution of a ventilated, pulsating, cavity.

- For the experimental conditions in view, the existence of pressure waves inside the cavity cannot be considered and the pressure p_c is uniform through the cavity. The measurement of p_c shows that it fluctuates practically as a sinusoidal function of time, at the frequency f. Its minimum value corresponds to the instant at which an air pocket is shed in the wake of the cavity.
- The length λ, $\lambda = V_c/f$, where V_c stands for the mean velocity of water at the cavity frontier, *i.e.* $V_c = V (1 + \sigma_c)^{1/2}$, can be considered as a wave length for the cavity pulsation. In a regime R_k, it is connected to the minimum cavity length ℓ_m by the relation :

$$\ell_m = k\lambda \qquad \textbf{(12)}$$

- That relation agrees with the above-mentioned phase relation between the birth of the fluctuations of the free surfaces near the wedge trailing edges and the instant of the shedding of the air pocket.
- The overpressure p_f, which is created in the closure region at the instant of the juncture between both cavity interfaces, diminishes when the air pocket moves away from the cavity with the velocity U_p.
- The pressure p_p in the air pocket, which initially is equal to p_c, grows subsequently until the p_f-value. Then the volume v_p of the pocket decreases while it is accelerated inside the cavity wake.
- The velocity U_f of the rear of the cavity is initially zero and then grows until the velocity-value of the air pocket.

That simple examination shows that all parameters undergo mutually consistent variations. In order to complete the description, we have to invoke several specific relations :

- The air mass in the air pocket is Q_m/f.
- The velocities U_f and U_p are related to the variations of the cavity volume v_c and the virtual mass of the air pocket.
- The variations of v_c result from the perturbations of the transverse velocity v at the interfaces.
- They are connected to the flow rate Q_m by the relation :

$$\frac{d(p_c v_c)}{dt} = Q_m \times \text{constant}$$

- A special condition can be used, as was done by *Woods* (1964,1966), in order to avoid the pressure singularity at infinity in a 2D field of flow : to cancel the variations of the total volume "cavity plus cavity wake". That condition means that energy exchanges between the cavity and its wake have to be considered. Here, it could be approximated by the condition that the variations of the cavity volume are balanced by the volume variations of the first air pocket in the wake.

The Wood's condition meets the experimental observation of pulsating cavities in free surfaces channels : in most of the cases, the free surface is not affected by the pulsations, which suggests that the exchanges are mainly in the streamwise direction, not in the transverse one. It allows understanding that pulsating cavities can be produced in closed channels and in the configuration of the half-cavity, as described by *Laali et al* (1984). Let us note that, for the reduced pulsation ω_k defined by the expression :

$$\omega_k = \frac{\pi f \ell_m}{V_c} = \frac{\pi f \ell_m}{V\sqrt{1+\sigma_c}}$$

Woods gets the theoretical relation :

$$\omega_k = 1.97 + \pi\,(k-1)$$

while the experimental relation (12) can be rewritten as :

$$\omega_k = \pi k.$$

4. Final Remark

The behaviour of ventilated cavities, namely their stability and the pulsating regimes, was theoretically studied in the case of 3D axisymmetrical flows by Parishev (1978), who used several simplifications previously proposed by Serebryakov (1973) and Logvinovich (1976). More recently, Semenenko (1998) and Semenov (1998) proposed theoretical descriptions of the pulsating regimes in the case of 2D, plane flows.

References

CHANSON, H. -1999- The Hydraulics of open channel flow - An Introduction. *Butterworth-Heineman Publishers*. Oxford (England). 544 p.

COX, R.N. & CLAYDEN, W.A. -19575- Air entrainment at the rear of a steady cavity.*Symp. on Cavitation in Hydrodynamics.* NPL, Teddington (England)

LOGVINOVICH, G.V. -1976- Problems of the theory of axixymmetrical cavities. *Tsagi*, **1797.**

LAALI, A.R. & MICHEL, J.M. -1984- Air entrainment in ventilated cavities : case of the fully developed "half-cavity" *J. of Fluids Engineering*; **106, 3**, 327-335.

MICHEL, J.M. -1971- Ventilated cavities : a contribution to the study of pulsation mechanism. *Symposium IUTAM on rapid, non steady liquid flows*, Leningrad.

MICHEL, J.M. -1984- Some features of water flows with ventilated cavities. *J. of Fluids Engineering*; **106, 3**, 319-326.

PARISHEV, E.V. -1978- Theoretical study of the stability and pulsations of axisymmetric cavities. *Tsagi.*

ROWE, A. -1979- Evaluation of a three-speed hydrofoil with wetted upper side. *J. of Ship Research*, **23, 1**, 55-65.

SEMENENKO, V.N. - 1998- Instability and oscillation of gas-filled supercavities. *3rd International Symposium on Cavitation*, Grenoble (France), Proc., Vol 2, 25-30.

SEMENOV, Y.A. - 1998- Exact solution of problem of unsteady cavitation flow past wedge. *3rd International Symposium on Cavitation*, Grenoble (France), Proc., Vol 2, 55-59.

SEREBRYAKOV, V. -1973- Asymptotic solution of the problem of slender axisymmetric cavity. *Reports of the NAS of Ukrainia,* **A 12**, 1119-1122.

SILBERMAN, E. & SONG, C.S. -1961- Instability of ventilated cavities. *J. of Ship Research*. **5, 1**, 13-33.

SONG, C.S. -1962- Pulsation of ventilated cavities. *J. of Ship Research*, **5, 4**, 1-20.

VERRON, J. -1977- Écoulements cavitants autour d'ailes d'envergure finie en présence d'une surface libre. *J. de Mécanique*. **12, 4**, 745-774.

VERRON, J. & MICHEL, J.M. -1984- Base-vented hydrofoils of finite span under a free surface : an experimental investigation. *J. of Ship Research*. **28, 2**, 90-106.

WOODS, L.C. –1964- On the theory of growing cavities behind hydrofoils. *J. Fluid Mech.*, **19-1**, 124-136.

WOODS, L.C. –1966- On the instability of ventilated cavities. *J. Fluid Mech.*, **26-3**, 437-457.

This page has been deliberately left blank

Page intentionnellement blanche

Experimental Investigation of Supercavitating Motion of Bodies

Yu.N. Savchenko
Ukrainian National Academy of Sciences - Institute of Hydromechanics
8/4 Zhelyabov str., 03057 Kiev
Ukraine

1. Modeling the supercavitation processes

1.1. FEATURES OF SUPERCAVITATING FLOWS

Supercavitation naturally occurs when the speed of a subsurface craft increases at fixed pressure P_0. At considerably low speeds (V > 3 m/sec), supercavities form when an object crosses the free water surface. In this case cavities are filled by atmospheric air and refer to artificial cavities formed at low speeds [4, 18].

According to the hydrodynamic scheme of supercavitation flow, the object is placed partially or fully inside a supercavity (Fig. 1a, b) formed by the nose part (cavitator) [1, 4, 6]. In the case of a jet cavitator system the cavity separates from the craft hull (Fig. 1c) and body has no points of contact with cavity [17].

The hydrodynamic drag formulae for continuous and cavitation flow have the form

$$X = C_x(\mathrm{Re})\frac{\rho V^2}{2}S, \qquad X_c = C_c(\sigma)\frac{\rho V^2}{2}S_c \tag{1}$$

and suggest that X_c does not depend on viscosity. Here, $\mathrm{Re} = VL/\nu$ is the Reynolds number; $\sigma = (P - P_c)/(\rho V^2)/2$ is the cavitation number, S and S_c are the characteristics of the wet surface in continuous and cavitation flow, and ρ and ν are the density and viscosity of water.

A qualitative estimation of the respective hydrodynamic drags indicates that with $\sigma = 10^{-4}$ the resistance to motion reduces by a factor of 1/1000.

However, for all its attractiveness due to a low hydrodynamic drag, the motion of an object in a cavity is a more complicated and paradoxical process than that of a space rocket. Moving in a vapor- or gas-filled cavity, the cavitating body loses buoyancy – the main advantage of motion in water, and thus needs dynamic means to maintain its weight inside the cavity [17].

The classical stability condition for motion in a continuum requires that the center of mass of the body should lead the external force application point. In the supercavitation motion scheme, this condition is violated in the most unfavorable way: the hydrodynamic forces are applied in the foremost point of the object – far ahead of the center of mass (Fig. 2). Moving in a cavity with a subsonic speed relative to water (V_a=1430 m/s), the object moves at a supersonic speed V = 4M relative to the vapor filling the cavity as if it were 24 km above the sea level.

Paper presented at the RTO AVT Lecture Series on "Supercavitating Flows", held at the von Kármán Institute (VKI) in Brussels, Belgium, 12-16 February 2001, and published in RTO EN-010.

While, in the continuous flow, the energy expended to overcome the hydrodynamic drag is irreversibly lost in the wake, in the supercavitation flow, the energy of a cavity of length L_c travels with the object of mass m. Their total energy is

$$E_\Sigma = E_0 + E_c = \frac{mV^2}{2} + \int_0^{L_c} X_c \, dl.$$

It is paradoxical that at the moment when the cavity collapses around the body moving in water by inertia with decreasing speed, the velocity suddenly increases. However, this velocity gain occurs in agreement with the energy conservation law. The cavity returns to the body the energy it expended earlier to form the cavity. This effect was found in experiments with cavitating models moving along a wire. In free motion, the imploding cavity can not only disturb motion stability but also destroy the body.

It should be noted that the problem of cavity closure, including hulls of vehicless, is a large field of research with applications to generation of supercavities and reduction of dynamic drag to levels below X_c.

In view of these specific features of supercavitation flows one may conclude that the feasibility of this motion scheme is contingent on the stability of object motion in the cavity. Therefore, in experimental launches in water, spherical bodies have been used more frequently than others [9]. In some flows, cavity embraced only a part of the hull, while the aft remained wet to preserve the stability of motion (see Fig. 1a).

In experimental investigation we realize a processes of physical modeling the supercavitation flows which includes three separate but associate problems:

1) modeling the supercavity shape and dimensions;
2) modeling the main SC processes as gas supply, gas leakage, SC creation, SC control, SC disturbanse;
3) modeling the supercavitating body motion.

We consider sequentially these problems from point of view of the theory of dimensionality and similarity of the hydrodynamic flows. Application of methods of the theory of dimensionality and similarity permits:

– to determine the minimal number of dimensionless parameters describing main sides of the studied process;

– to choose a rational scheme of the laboratory experiment;

– to obtain rules of recalculation of the experimental results for full-sc

ale magnitudes of the parameters.

Foundations of the theory of dimensionality and similarity and this theory application to different fields of the hydromechanics are stated in books

[1, 2].

1.2. MAIN SCALES AND PARAMETERS GOVERNING THE SUPERCAVITATION PROCESSES

For stationary supercavitation flows the process is defined by the following parameters [29]:

– characteristic linear size of the body L;

– pressure difference in the free stream and cavity

$p_\infty - p_c$;

– fluid velocity V_∞;

– fluid density ρ;

– gravity acceleration g;

– kinematic coefficient of the water viscosity υ;

– coefficient of water surface tension ζ.

There are three basic measurement units: length, time and mass. According to Π - theorem of the theory of dimensionality [1], it is possible to give no more than 7 – 3 = 4 independent dimensionless combinations of enumerated parameters. The other flow parameters and acting forces are functions of such four scaling parameters.

The cavitation number σ, the *Froude* number *Fr*, the *Reynolds* number *Re* and the *Weber* number *We* are used as main scaling parameters:

$$\sigma = \frac{2(p_\infty - p_c)}{\rho V_\infty^2}, \qquad Fr = \frac{V_\infty}{\sqrt{gL}}, \qquad \mathrm{Re} = \frac{V_\infty L}{\nu}, \qquad We = \frac{\rho V_\infty^2 L}{\zeta}. \tag{2}$$

Cavitator diameter D_n is usually used as linear scale L for supercavitation flows.

Equality of four scaling parameter guarantee observance of geometric, kinematic and dynamic similarity of stationary supercavitating flows. Namely, the cavity section diameters D and acting forces F may be calculated by formulae:

$$D\left(\frac{x}{D_n}\right) = D_n f_1(\sigma, Fr, \mathrm{Re}, We), \qquad F = \frac{\rho V_\infty}{2} D_n^2 f_2(\sigma, Fr, \mathrm{Re}, We), \tag{3}$$

where f_1, f_2 are dimensionless functions of dimensionless parameters. They can be once and for all determined theoretically and experimentally..

Moreover, only equality of cavitation drag coefficients c_X of the cavitators, but not the geometric similarity of them is necessary for the supercavitating flows. The cavitators with the same diameters D_n and drag coefficients c_X forms cavities of approximately equal sizes. When values of σ are low and values of *Fr* are high, mid-section diameter D_c and length L_c of the axisymmetric cavity past a disk are approximately equal [2, 3]:

$$D_c = D_n \sqrt{\frac{c_x}{\kappa\sigma}}, \qquad L_c = D_n \frac{A\sqrt{c_x}}{\sigma}, \qquad A = \sqrt{\ln\frac{1}{\sigma}}, \tag{4}$$

where κ = 0.9 ÷ 1.0 is the empirical constants. It is shown in [2, 4] that formulae (4) may be used and for non-disk cavitators of different shape, if the universal linear dimension $D_n\sqrt{c_x}$ is accepted as characteristic linear dimension instead D_n.

When values of σ are small, the approximate relation is valid for the drag coefficient of blunted cavitators [2, 3]:

$$c_x(\sigma) = c_{x0}(1+\sigma), \qquad 0 < \sigma < 1.2, \tag{5}$$

where c_{x0} is the cavitator drag coefficient at $\sigma = 0$. For disk cavitator it is established that $c_{x0} = 0.82$.

However, simultaneous equality of numbers σ, Fr, Re, We is impossible to reach in practice. Therefore, investigation of scaling effects, i.e. influences of different deviation from similarity is of great importance in modeling the supercavitation processes.

1.3. SUPERCAVITIES IN STEADY FLOWS: MODELING BY THE σ NUMBER

The cavitation number σ is main scaling criterion of the supercavitation flows. The value of $\sigma <$ 0.1 corresponds to the supercavitation regime. Such values of the cavitation number are reached at velocities V_∞ > 50 m/s. It is established experimentally [2, 3] that the water viscosity influence is practically absent at such velocities in the case of the disk cavitator and free cavity closure. Influence of gravity and surface tension forces also are negligible when

$$Fr > 20 \div 30, \qquad We > 1000. \tag{6}$$

Thus, for natural supercavities the functions f_1, f_2 in (3) depend on only dimensionless parameter σ being unique scaling criterion of the flow.

We obtain the empirical formula for the natural supercavity shape [5]:

$$\overline{R}^2(\overline{x}) = 3.659 + 0.847(\overline{x} - 2.0) - 0.236\sigma(\overline{x} - 2.0)^2, \qquad \overline{x} \geq 2.0 \tag{7}$$

where $\overline{R} = R / R_n$, $\overline{x} = x / R_n$. In this case we used an analysis of the experimental data obtained for the models with D_n = 15 mm and the range of cavitation numbers σ = 0.012 ÷ 0.057. The frontal cavity part $\overline{x}$ < 2.0 is described by the empirical formula [3]

$$\overline{R} = \left(1 + \frac{3x}{R_n}\right)^{1/3}, \qquad \overline{x} < 3 \div 5, \tag{8}$$

The following expressions for the cavity mid-section and length are obtained from the formula (7):

$$\overline{R}_c = \sqrt{3.659 + \frac{0.761}{\sigma}}, \tag{9}$$

$$\overline{L}_c = 4.0 + \frac{3.595}{\sigma}. \tag{10}$$

Expressions (9), (10) are in good agreement with results of our experimental investigations of high-speed motion of small supercavitating models in water [5] (D_n = 1.0 ÷ 3.0 mm). The cavitation numbers $\sigma = 10^{-4} \div 10^{-3}$ and Mach numbers $M = V_\infty / a = 0.3 \div 0.9$ (where a = 1460 m/s is the sound speed in water) correspond to these experiments. Thus, the water compressibility influence on the main cavity dimensions may be considered as nonessential one at motion velocities up to 1200 m/s.

A practical advantage of formula (7) is that it gives the explicit dependence of the cavity shape on the cavitation number.

1.4. ARTIFICIAL SUPERCAVITIES IN STEADY FLOWS: MODELING BY THE *Fr* NUMBER

It follows from the theory of similarity of hydrodynamic flows that the shape and dimensions of natural and artificial (ventilated) cavities must be equal at the same value of σ . However, this is not observed in reality.

The main cause is that the moderate values of the *Froude* number $Fr < 20$ correspond to the flows with artificial cavitation when motion velocity V = 10 ÷ 50 m/s. It means that the gravity importance for artificial cavity is essentially greater at equality of the cavitation numbers.

As it is known , gravity forces influence on the artificial cavity by double ways.

Firstly, the cavity axis is curved (the cavity floating-up), and the cross section shapes calculable by the perturbation method [6] are deformed.

It is known from the experiments, and theoretical investigations confirm that the liquid crest forms below the cavity when the cross gravity field acts. Its top increases in direction from the cavitator to the cavity tail. Sometimes, this crest is small even in the cavity end, and the cavity does not transform into two vortex tubes. In other cases the crest top already past the mid-section may reach the upper cavity part and cleave it on two tubes.

In the work [6] important criterion was obtained by theoretical way:

$$N = \sigma \sqrt{\sigma} Fr^2 \geq 1.5. \qquad (11)$$

It is possible to emphasize the following ranges of changing the parameter N. They corresponds to different conditions of perturbations caused by fluid gravity:

1) range N = 1 ÷ 2 is characterized by high perturbation levels, when all cavity part after the mid-section degenerates in vortex tubes;
2) range N = 2 ÷ 4 corresponds to mean or essential perturbation level, when the water crest height is lower than the unperturbed cavity radius, although may be close to it;
3) range N = 4 ÷ 10 is characterized by low perturbation level, and gravity influence may be egligible when

$N > 10$.

In Fig. 3, a, b, the calculation results of shape of cross cavity sections when cavitation numbers σ = 0.06 and *Froude* numbers Fr = 10 are shown. In this case N = 1.47. In sections 1, 2, 3, when x = 0.25 and x = 0.50, the gravity action yet does not appear, and in section, when x = 0.75, small compression

from below is already appreciable. In sections 4, 5, when x = 1.25, the deformation is considerable. It is close to half of the radius value below the section. The crest directed up is well seen. In the next sections the cavity collapses.

Secondly, the cavity closure behavior and type of gas leakage from the cavity change. It was established experimentally [2, 3], that the influence of viscosity and surface tension is not essential. Thus, in this case the flow is determined by two scaling criteria σ and Fr.

However, it is difficult practically to obtain simultaneous equality of numbers σ and Fr . Modeling by the cavitation number requires simultaneous decrease of the model dimension to save the *Froude* number value. A way of the gravity force compensation in rotating hydro-tunnels is known [2].

A method of physical modeling of the gravity influence on the supercavity shape by means of curving the external flow was proposed in the work [7]. The flow was curved in the vertical plane due to bend of the working part bottom (Fig. 4). For such flow the numbers Fr depends on bottom curvature radius R_b:

$$Fr = \frac{V}{\sqrt{\left(g - \frac{V^2}{R_b}\right) D_n}}. \tag{12}$$

To change fluently the *Froude* number in range $20 < Fr < \infty$ was succeeded by curving the flow in the experiments with artificial cavity past a disk when D_n = 20 mm and free stream velocity V = 9 m/s. In this case the characteristic deformation of the cavity owing to the floating-up was completely eliminated. The cross force arising on the cavitator may be easily compensated by corresponding inclination of the cavitator.

The stream curving method is convenient to use for compensation or, on the contrary, intensification of the gravity force action on the artificial cavity shape in hydrotunnels with horizontal flow. It has advantage compared to a method of the rotating hydro-channel [2], since permits to work with models of large longitudinal dimensions. However, we notice that this method does not model the influence of number Fr on the internal processes in the cavity, such as reentrant jet formation and motion of foam and sprays within the cavity.

In the case of unsteady flow the *Strouhal* number is the additional determining scaling parameter:

$$St = \frac{L}{Vt}. \tag{13}$$

The essential difference between natural (vapor) and ventilated supercavities becomes apparent at unsteady flow. Investigations showed that the parameter characterizing the gas elasticity influence in the cavity is of important in this case.

2. Special equipment for experimental investigation

All installations for experimental investigations may be divided on two parts:

I. Installations of inverse motion:

- water tunnels;
- water flumes;
- rotating channels.

II. Installations of direct motion:

- towing channels;
- test basins;
- launching tanks.

The models with full fixation (without levels of freedom) are mainly used under inverted motion.

The models with partial fixation or models with free motion may be used in direct motion. There are wire riding models and models used as missiles.

The inverted motion is limited by velocity range 3 ÷50 m/s so that the high speed motion of SC models must be investigated at direct motion only [17, 18].

2.1. WATER TUNNELS

Experience of development of experimental high-speed hydrodynamics shows that it is convenient for velocities up to 30 m /s to use the inverted motion, which is realized due to water tunnels [16], water flumes and rotating water channels [2, 9].

There are the closed circuit water tunnels as LCC in Memphis and Garfield Thomas Water Tunnel in Pennsylvania.

The Large Cavitation Channel (LCC) of the David Taylor Model Basin, CDNSWC, is a large variable pressure water tunnel and it is one of the most technologically advanced large cavitation tunnels in the world.

IHM has two unclosed circuit water tunnels.

The small WT has a working section is 0.34×0.34 m, the working part length is 2m, the mainstream velocity is 9 m/s. It is a tunnel of open type with opened working part. Pumps inject water to the upper tank, where free level is sustained constant. The water arrives under constant pressure of water column equal to 4.5 m to the working part.

The big WT (Fig. 5) has a working section 1 – $4 \times 0.5 \times 0.5$ m with maximal admissible velocity up to 30 m/s. The supplying part – 2 of the WT has length 35 m is used as a launching tank. It has 10 pairs of looking windows.

The WT has a gas separator – 3. The water arrives in basin – 4 having volume – 4400 m^3 through the separator for the further degassing and comes to the pumps – 5 with total power 5 000 KWt. The photo Fig. 6 demonstrates WT view from separator.

In experimental supercavitation it is very significant to organize supercavity without extra disturbances in rear part of supercavity. A special device (Fig. 7), which can do this, was elaborated at the IHM.

Supercavity generator (Fig. 7) contains struts – 1, cylindrical section – 2, ring type cavitator – 3 with leading edge to produce free boundary – 4 of supercavity – 5.

To decrease disturbances of supercavity this device contains a special pipe line – 7 for boundary layer suction through the ring gap – 6.

The photo below demonstrate the working supercavity generator in the test section of WT.

It should point that the supercavity is very sensitive to changing of surrounding flow in the working part of WT. This change of the flow is caused by the supercavity and called by Blocking effect and may be estimated experimentally.

Fig. 8 shows change of the supercavity under influence of Blocking effect. General recomendations relating to the maximal cross section of the supercavity S_c has the form

$$\frac{S_c}{S_w} \le 0.01,$$

where S_w is the working part section.

2.2. EXPERIMENTAL EQUIPMENT FOR SELF-PROPELLED WIRE RIDING MODEL TESTING

Considerable experience of the creation of such laboratory equipment and carrying out with the help of it the experiments to study the supercavitating flow around models with caliber 40 – 60 mm, when they free move in water at velocities higher than 100 m/s has been accumulated at the IHM UNAS [28]. Application of different power systems of the models is possible in the experiments. The ecologically pure components: water in various phase states and compressed air are used as working medium in them. The body ride system along a guide wire proved to be the most effective to divide the problems of the cavity dynamics and the motion stability by stabilizing the model trajectory in water.

It is possible to note the following advantages of the described technique of the model testing:

– a possibility of studying the supercavitating flow around models of comparatively large caliber at absence of external perturbations;

– enough wide range of the flow velocities and regimes: from artificial ventilated cavitation to natural vapor cavitation in the velocity range V ≈ 50 – 150 m/s;

– possibility of studying of both stable flow regimes and unsteady processes on initial stages of the cavity, development and also adjustment of regimes of water entry of models;

– comparatively large caliber of the tested models gives considerable variety both in the model constructions and in the hydrodynamic schemes of flow around them;

– system of the model trajectory stabilization by means of the guide wire allows the minimal necessary deepening of the trajectory and, hence, simplifies photo-registration of flow pictures through the free surface;

– when optimal conditions of the water entry of the models are ensured, the stabilization of the supercavitating flow regime is reached on very short distance (about some model length) and requires very limited engine power of the models;

– compact laboratory reservoirs of different types: channels, flumes, basins, tunnels etc. may be used to carry out tests due to short working part of the trajectory and effective system of the ydrodynamic braking of models;

– absence of chemical energy sources and use of the water and compressed air in the model power systems as the working medium at moderate high values of the pressure ensure a possibility of safe exploitation of the experimental equipment in laboratory conditions.

Imperfection of the described technique of the testing is mainly complexity of registration of the process characteristics at the model motion in water with high speeds. In this case the basic information is ensured by studying of the model motion kinematics and photo-cinematography of its flow pictures.

Synchronization of work of the registering apparatuses with certain phases of the model motion in water may have certain technical complexity.

Configuration of the model testing system

Here, we interpret the optimal configuration as such set of the system elements and their composition which ensure a possibility of obtaining of the stable motion regimes in a supercavity for different constructive modifications of the models at rational technical parameters of whole system: general dimensions, material capacity and sizes of equipment, energy consumption etc, including the ecological compatibility and exploitation safety. As it was noticed, the type of reservoir used to create the testing system has no principal significance. The following description is based on materials of tests carried out in the hydrodynamic laboratory at the IHM in opened hydroflume with dimensions 1.0 x 1.0 x 40 m. The model motion trajectory was located on the depth 0.5 m along the flume axis. Photo-cinematography of the flow pictures was realized through the glass windows in walls of the flume and through the free water surface.

One of necessary conditions of the supercavity formation on starting stage of the motion in water is enough high velocity of the model which is ensured by means of the starting catapult, i.e. predominantly owing to "cannon effect". In this case the model mass executes a role of the kinetic energy accumulator being able to ensure the stable motion on inertia. In the given case equipping the model by jet engine has no principal significance for its dynamics. The considered here types of the working medium of the engine at their bounded board reserve are able to ensure only very short-term thrust. It does not give decisive difference of the velocity value and is reached by means of the model mass decrease during motion. In some cases, for example, increase of the inertial mass of the model due to filling the hull by material with higher density, for instance, metal may be the more advantageous to increase the free model passage distance at the same starting velocity instead of the engine with working medium reserve. Therefore, in this case use of models with jet engine is of interest for combined study of hydrodynamic aspects of interaction between the cavity and working engine.

Model with water-vapor jet engine

The water-vapor jet engine represents a kind of propulsive device where the direct transformation of the thermal energy into the thrust work occurs, and, simultaneously, hydrodynamic and thermodynamic processes including the phase changes of the working medium proceed.

Hot water application as the working medium of the jets has considerable history. In various time beginning from antiquity different variants of the devices using the reactive vapor jet to carry out the work appeared. Serious works on application of the hot water for missiles began to be carried out, apparently, before the Second World War in Germany and after the War in West Germany, USA, Italy [19 – 22]. An interest to such type of propulsions is stipulated first of all by their economical parameters and ecological factors.

The considerable volume of investigations on thermal hydrojets including water-vapor jet was carried out at the IHM UNAS [23, 24, 25]. The investigations were being performed as applied to a problem on creation of high-speed underwater vehicles using the outboard water for jet work.

The constructive scheme of the model with water-vapor jet is shown in Fig. 9, a. As a whole the model represents a body of revolution with cone nose and cylindrical parts. The cylindrical part 1 of the model hull is made from stainless steel and contains the working medium reserve for the water-vapor jet. The jet nozzle 2 is installed on the hull end and has a central body with tail 3 protruding from the model hull. The tail is intended for joining with the catapult lock and holding the model during the process of heating and water pressure increasing in the model and catapult. The nose cone part 4 of the model hull is isolated hermetically from the cylindrical part 1 and may be made from aluminum for the model mass

decrease. The changeable cavitator 5 is installed on the cone nose 4. The general view of such model with hull diameter 58 mm is shown in photo of Fig. 9, b.

As it is pointed above, tests of the described models were carried out in the flume with dimensions 1.0 x 1.0 x 42 m. The general scheme of the model testing system is presented in Fig. 10. In the scheme numerals designate: 1 is the flume, 2 is the starting chamber produced in the flume by divider 3. In the scheme the starting chamber is shown filled by water. Respectively, the catapult 4 and the model 5 installed in it are located in underwater position. Cameras 6 and impulse illuminants 7 with divergent screen for uniform light background creation are used to register the picture of flow around the model at its motion in the flume. Disposition of the photo-registration means is shown in the scheme in two positions. The position for recording photo-registration means is shown in the scheme in two positions. The position for recording through the glass windows in the flume walls stipulates disposition of the camera and illuminant on the opposite sides of the flume. The position for recording through the free water surface requires the camera disposition above the flume and underwater disposition of the illuminant.

Conditions of carrying out the experiments differed from the calculation ones by final value of the heated water reserve, which was close to the calculated second rate, and inevitable pressure dropping in the chamber of the jet in moment of the model start from the catapult. However, it is possible to suppose that the pointed differences do not essentially influence the jet thrust value for short term of its work. It is less than 0.2 sec at average model velocity 110 m/s and length of the working part of the trajectory about 20 m. This supposition is confirmed by results of tests where the model motion regimes with practically constant velocity along the distance were registered, and photographs of flow around the model were obtained. In these cases the model moved in the supercavity without washing the hull, i.e. its total drag was equal to the nose cavitator drag and corresponded to the thrust developed by the jet. The maximal parameters of heated water was $P = 150 kgf / cm^2$, $t = 320^\circ C$.

Drag value R_x of the disk cavitator with diameter D_n is determined by formula [3]

$$R_x = c_x F_n \frac{\rho V^2}{2}, \tag{14}$$

where $c_x = 0.82$ is the drag coefficient for a disk; $F_n = \frac{\pi D_n^2}{4}$ is the wetted area of the cavitator; ρ is the water density; $V \approx 110$ m/sec is the model velocity characteristic for considered regimes. For models with disk cavitators at $D_n = 12 \div 16$ mm we obtain the cavitation drag magnitudes in the range $R_x = 57 \div 101$ kgf. This satisfactorily corresponds to pointed above calculated value of the jet thrust $T = 87.5$ kgf.

Mentioned above photographs of supercavitating flow around the model without washing the hull are shown in Fig. 11. The presented photographs are made from the different positions: through the free water surface at model velocity $V = 124$ m/s (Fig. 11, a) and through the glass windows in the flume sides at model velocity $V = 106$ m/s (Fig. 11, b). The photographs shows that in the both cases the model jet works in natural vapor cavity, i.e. in the medium with the saturated vapor pressure corresponding to the value accepted in the calculated example value $P_c = 0.02$ kgf/cm^2.

Auxiliary devices of starting chamber

It was pointed above that the developed cavity formation on starting part of the model trajectory in water is a necessary condition of establishing the supercavitating flow regime on the next part of the trajectory. Experience of tests of cavitating self-propelled models showed that the high starting model velocity not always ensures enough fast axisymmetric cavity formation past the cavitator at the underwater start. This mainly relates to the models with small cavitator diameter compared to the hull

diameter. In this connection different types of auxiliary devices intended to regulate conditions of water entry of model and optimize the cavity formation past the cavitator were tested in the IHM. Such devices were mounted in the start chamber of the flume with the catapult installed in it. It is shown in scheme Fig. 10. Description of some types of pointed auxiliary devices is given below.

One of ways of optimization of the cavity formation process consists in organization of water entry of the model through the initial air bubble. A scheme of such bubble creation for underwater start conditions is presented in Fig. 12. The catapult 1 with installed in it model 2 is shown in the scheme. The ring distributive chamber 3 with ring nozzle 4 is installed coaxial to the model near the cavitator. The compressed air is supplied by the main 5 to the device. The air supply is regulated by the electric valve 6. In the start moment the air bubble 7 may be obtained by choosing the ring chamber and nozzle parameters, the compressed air pressure and moment of its charging into the water. This air bubble maintains orientation along the model axis for short term. In this case the air from the bubble may be entrapped into the cavity and promote its formation process. However, the test showed that the described device does not guarantee stable results. Possible explanation of this consists in non-uniformity of the internal bubble structure with chaotic distribution of the water and air masses.

The most stable results by ensuring the cavity formation were obtained at model start from the dry start chamber according to the scheme given in Fig. 13. In this case in the partition 1 separating the flume 2 filled with water from the dry start chamber the hatch 4 is closed by movable gate opening the hatch 4 just before the start. As a result, the contrary water jet 5 is formed, and the model enters in it after the start from the catapult. Favorable conditions for the supercavity formation past the cavitator are stipulated by two factors: atmospheric air entrapment and that the pressure in free flowing jet is equal to the entrapped atmospheric air.

However, uncontrolled entrapment of the atmospheric air into the cavity is undesirable in a number of cases. Such situation takes place, for example, at studying the quantitative characteristics of the air supply influence on the cavity formation process. In such cases the water entry of the model may be organized according to the scheme presented in Fig. 14. For that the entrance hatch 2 is covered by elastic plastic diaphragm 3 in the partition 1 separating the dry start chamber from the flume filled by water. At start the model 4 punches the diaphragm serving as an elastic seal hindering the atmospheric air penetration into the zone filled by water. In this case the initial cavity 5 forms under influence of a established beforehand value of the supply realized from the model.

Model attachment mechanism

The local features of flow around the cavitator at the model motion along the wire are illustrated by photographs and scheme in Fig. 15, a,b. The presented illustration shows that the zone in front of the cavitator, where the fixed wire is located, must be excluded from the consideration when the quantitative characteristics are determined. Therefore, so called effective value D_{ef} of the cavitator diameter is accepted for calculations. Its area is equal to the wetted area of the real cavitator [2, 3] by formulae

$$D_{ef} = \sqrt{D_n^2 - d_w^2}\ .$$

Such approach validity is illustrated by experimental results of the cavity profile measurements at different conditions of flow around the cavitator. They are given in Fig. 16. The experimental data in the graph are compared with the cavity profile equation proposed by *G.V.Logvinovich* [3]:

$$\frac{D}{D_c} = \sqrt{1 - \left(1 - \frac{D_1^2}{D_c^2}\right)\left(1 - \frac{2x}{L_c}\right)^2}\ ,$$

where D, x are current diameter and coordinate of the cavity section; D_c, L_c are the cavity mid-section diameter and length, respectively; $D_1 = 1.92 D_n$.

Model arresting mechanism

It is necessary to ensure fluent arresting the model up to its stoppage at the model trajectory end. A simple and effective mechanism in the form of installed with some intervals metal disks with diameters scaling up is the most convenient for this purpose. The testing system scheme shown in Fig. 10. gives a general presentation about such mechanism. There are shown the arresting disks 9 in the end part of the flume 1 filled by water on the wire 8. They are coaxial with it. The model in turns meets them on its path. Orifices in the disk centers permit them to be free removed along the wire. In rest water the disks are in given position. After contact with the model they move together with it as cavitators with sequentially increasing diameters and hydrodynamic drag value. During arresting the model pushes on a set of such disks in front of it up to complete stoppage.

The scheme in Fig. 17 shows this process the more in detail. Obviously, the cavity dimensions decreases, the hull washing area increases, and on the end part of the arresting path the model moves in unseparated flow regime as a result of the motion velocity reduction. Correspondingly, three typical parts of the arresting path are shown in the scheme. The regime of flow around the model is qualitatively changes on these parts. There are: part I with predominantly cavitation flow regime, part III with unseparated flow regime and part II between them with transient regime. Thus, hydrodynamic side of the model arresting process is enough complex.

It is important from practical point of view that the described mechanism permits to give by the simplest means any required intensity of the arresting from very fluent reduction of the model velocity to abrupt its stoppage. The necessary effect is reached by choosing the arresting disk diameters and intervals between them The arresting process intensity may be regulated in very wide limits by changing one of the pointed parameters.

2.3. EXPERIMENTS WITH FREELY MOVING MODELS

Vertical vacuum launching tank (VVLT)

VVLT (Fig. 18) consists of cylindrical tank, that is installed under different angles to horizon. There are a catapult, windows and device to capture models on the tank (arresting system). The VVLT contains the system of pressure control and system of underwater launch.

The VVLT gives the possibilities for wide range experiments with freely moving models. It is possible to change an angle between the model velocity and horizon and between the model velocity and the model axis and to investigate the model motion under different trajectory inclination and different model incidence.

The problems of body water entry at supercavitation regime, the ricochet problem, body motion stability on underwater trajectory were investigated successfully by using the VVLT.

The Fig. 18 shows the frames of high speed photo registration of supercavitating body motion at water entry under angle to the free surface of water.

The Fig. 19 shows the instant pictures of water entry investigation with supercavity inception control by using the metal or rubber rings on the body hull. During water entry the rubber ring produces a local pressure field suppressing the supercavity inception.

35 m Launching Tank

At the IHM the supplying part of Big Water Tunnel is used as a 35 m Launching Tank with the cross section is 2.2 ×2.2 m (Fig. 20). This tank has 10 pairs of glass windows and may be supplied by an pneumatic or electrochemical catapult using electrolysis gas energy by electric decomposition of water [30].

$$H_2O \Rightarrow 2H_2 + O_2 \Rightarrow 2H_2O + 152\,kcal.$$

The Fig. 21 shows the scheme of experiments in the launching tank. The launching tank – 1 contains 10 pair of windows – 2. The catapult – 3 may be used in two positions for underwater launch:

Position 1 – out side of tank. The catapult is connected with launching tank only by end of barrel through the hole – 4.

Position 2 – inside of tank. The catapult is placed completely in the water tank.

A steel shield – 6 is used as arresting system for supercavitating models – 5. It is in another end of the launching tank.

Photo-registering system has cameras and sparkle lamps working through the glass windows – 2 (Fig. 20).

The Fig. 22 demonstrates the view of launching tank with catapult in position –1 (out side of water tank).

The Fig. 23 shows the supercavitating model cartridge. There are supercavitating model – 1, container – 2 assembled with two parts with help rubber ring – 3 and piston – 4.

The Fig. 24 demonstrates the frames of high speed photo-registration of supercavity produced by moving projectile having a cone shape and disk cavitator – 3 mm with velocity 1000 m/s when $\sigma = 10^4$. The supercavity length and diameter were 12 m and 0.11 m, respectively.

References

1 Sedov L.I.. Methods of similarity and dimensionality in mechanics. 7th Edition. - Moscow, Nauka, 1972. 428 p., (in Russian).

2 Epshtein L.A. Methods of theory of dimensionality and similarity in problems of ship hydromechanics. – Leningrad: Sudostroenie, 1970. 208 p., (in Russian).

3 Logvinovich G.V. Hydrodynamics of flows with free boundaries. - Kiev, Naukova dumka, 1969. 208 p., (in Russian) .

4. Epshtein L.A. Characteristics of ventilated cavities and some scale effects. // High-speed unsteady water flows (Proc. of international simp. IUTAM) – Moscow, Nauka, 1973. P. 173-185, (in Russian).

5 Savchenko Yu.N., Vlasenko Yu.D., Semenenko V.N. Experimental study of high-speed cavitation flows. //J. Hydromechanics. 1998, # 72. P. 103-111, (in Russian).

6 Buyvol V.N. Slender cavities in flows with perturbations. - Kiev: Naukova dumka, 1980. – 296 p., (in Russian).

7 Savchenko Yu.N. Developed cavitation modeling in flume with curved flow. // J. Hydromechanics. 1974. – # 26. P. 3-5, (in Russian) .

8 Epshtein L.A., Lapin V.M. Approximate calculation of influence of flow boundaries on cavity length in two dimensional problem and past the axisymmetric body. // Trudy TsAGI - 1980. # 2060. P. 3-24, (in Russian).

9 Knapp R.T., Daily I.W. Hammitt F.G. Cavitation. McGraw-Hill Book Co., 1970.

10 Savchenko Yu.N., Semenenko V.N., Osipenko S.B. Mechanism of interaction between cavity and bubble flow. // Reports of AS of Ukraine. 1985. N 9. P. 39 – 42, (in Russian).

11 Savchenko Y.N., Semenenko V.N. The gas absorption into supercavity from liquid–gas bubble mixture. //Proc. Third International Symp. on Cavitation. Vol.2. Grenoble (France). 1998. P. 49-53.

12 Savchenko Yu.N., Semenenko V.N., Putilin S.I. Unsteady processes during supercavitating body motion. // J.Applied Hydromechanics. 1999, Vol. 1, N 1. P.62-80, (in Russian).

13 Semenenko V.N. Computer simulation of supercavitating body dynamics. //J. Applied Hydromechanics. –2000, Vol. 2, N 1. P. 64-69, (in Russian).

14 Pernik A.D. Problems of cavitation. –Leningrad: Sudostroenie, 1966. 335 p. (in Russian) .

15 Levkovsky Yu.L. Structure of cavitating flows. Leningrad: Sudostroenie, 1978. 222 p., (in Russian).

16 Gorshkov A.S., Rusetsky A.A. Cavitation tunnels. – Leningrad, Sudostroenie, 1972.

17 Savchenko Yu.N. On motion in water at supercavitation flow regimes. // J. Hydromechanics, # 70. Kiev: Naukova dumka. 1996. P. 105 – 115.

18 Kirschner Ivan N. Supercavitating projectile experiments at supersonic speeds. High Speed Body Motion in Water. AGARD Report 827. Published February 1998.

19 Kolle H.H. Uber die Wirtschaftlichkeit von Wasserdampfraketen als Horizontal –Starthilfen. – Munchen, 1955.

20 Schwarzler K., Untersudiungen an Hiess Wasserraketen zum Start von Flugzeugen. – Zeitschrift fur Flugwissenschaften 6. Tahrgang, Heft 1. Januar, 1958.

21 Etheimer I.P. Beitrage zu den Problemen der Heisswassseraketen. – Luftfahrt. Forschungsber. 1962, # 12.

22 Tunge Tohn F. Steam rocket successfully tested. Missiles and Rockets. 1962. 11.

23 Babitsky A.F., Ivchenko V.M. Jet theory of thermal hydrojet.// J. Hydromechanics, # 5. Kiev: Naukova dumka. 1968. P. 67 – 78.

24 Logvinovich G.V. Work of jet with ejector nozzle. // J. Hydromechanics, #19. Kiev: Naukova dumka. 1971. P. 3 – 9.

25 Ivchenko V.M., Prihodko N.A., Grigoriev V.A. Optimal jet systems. Krasnoyarsk. Krasnoyarsk University Publishing House. 1985. 218 p.

26 Utkin G.A. Formulation of problems on dynamics of elastic systems with objects moving along them. // Wave dynamics of machines. – Moscow: Nauka, 1991. P. 4 – 14.

27 Kazhayev V.V., Utkin G.A. Motion of mass along wire under action of wave pressure forces. // Differential and integral equations. Gorkiy: Publ. House of GSU, 1989. P. 112 – 117.

28 Vlasenko Yu.D. Supercavitating roket model experiments// Applied Hydromechanics. V. 2, #3. 2000. P. 26 – 39.

29 Savchenko Yu.N. Modeling of supercavitation processes// Applied Hydromechanics. V. 2, #3. 2000. P. 75 – 86.

30 Savchenko Yu. N. Investigation of High-Speed Supercavitating Underwater Motion of Bodies. AGARD Report 827 "High Speed Body Motion in Water", 1998, FDP Wokrshop, Kiev. – P. 20-1 – 20-12.

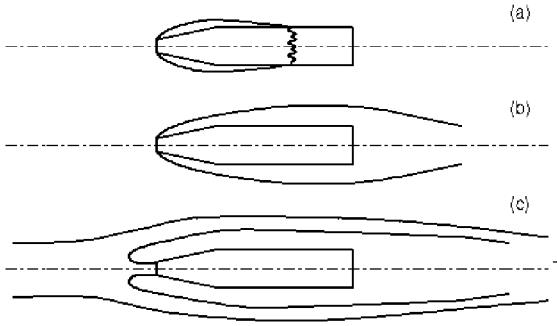


Fig. 1

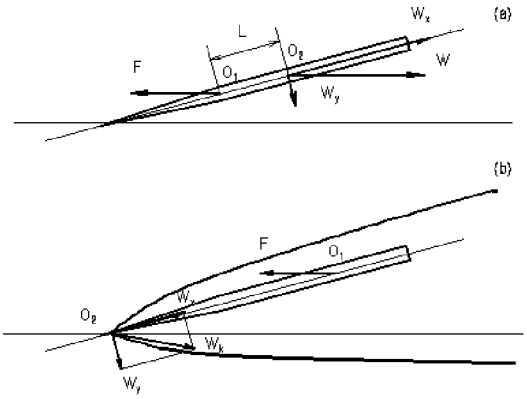


Fig. 2

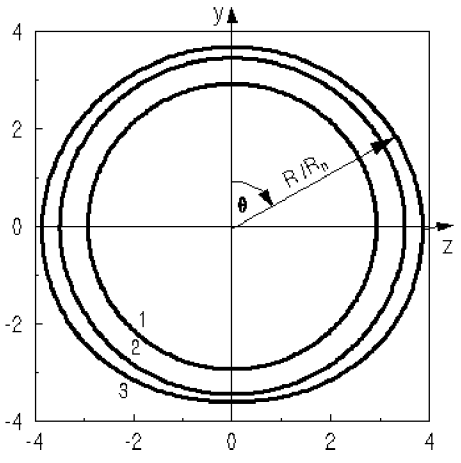


Fig. 3a

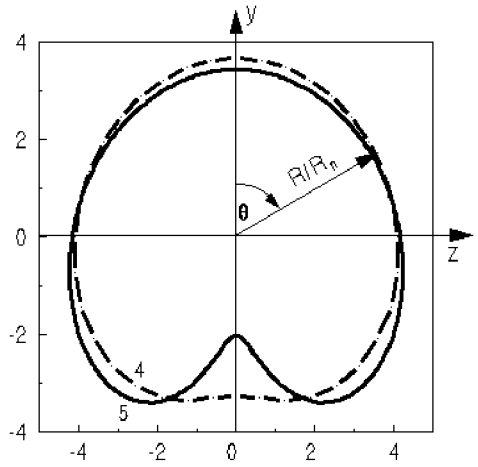


Fig. 3b

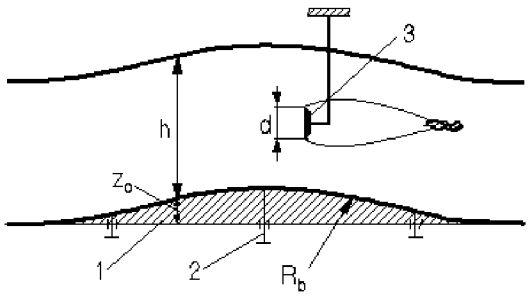


Fig. 4

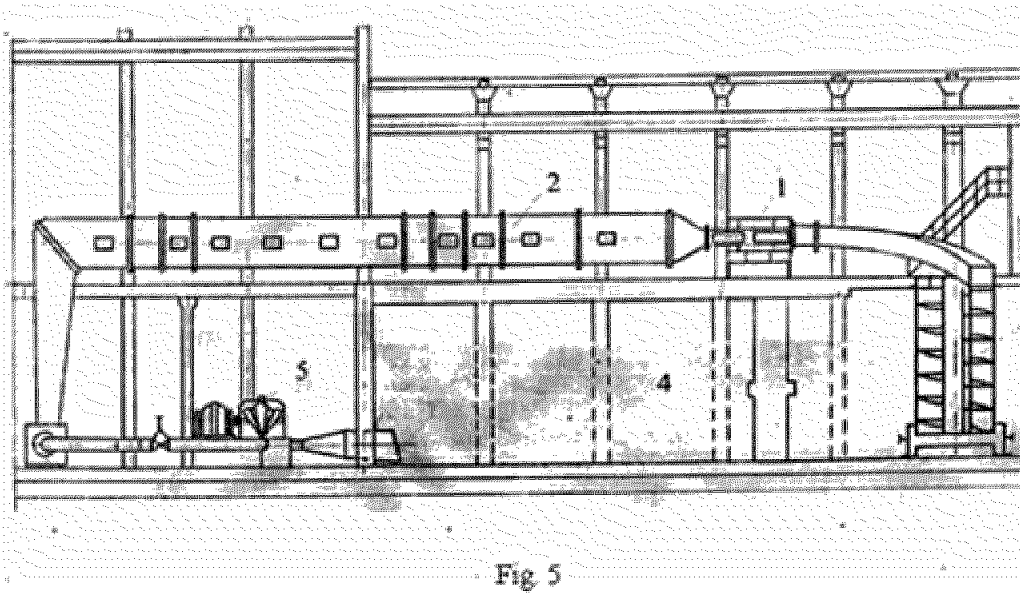


Fig. 5

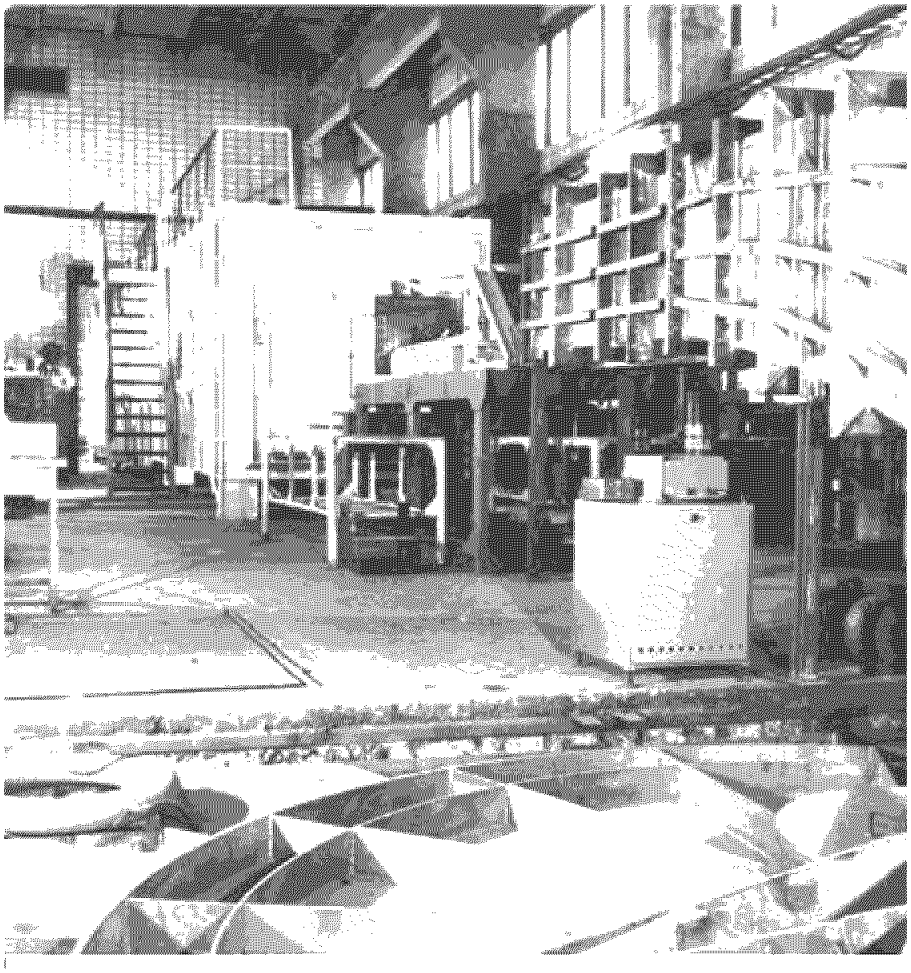


Fig. 6

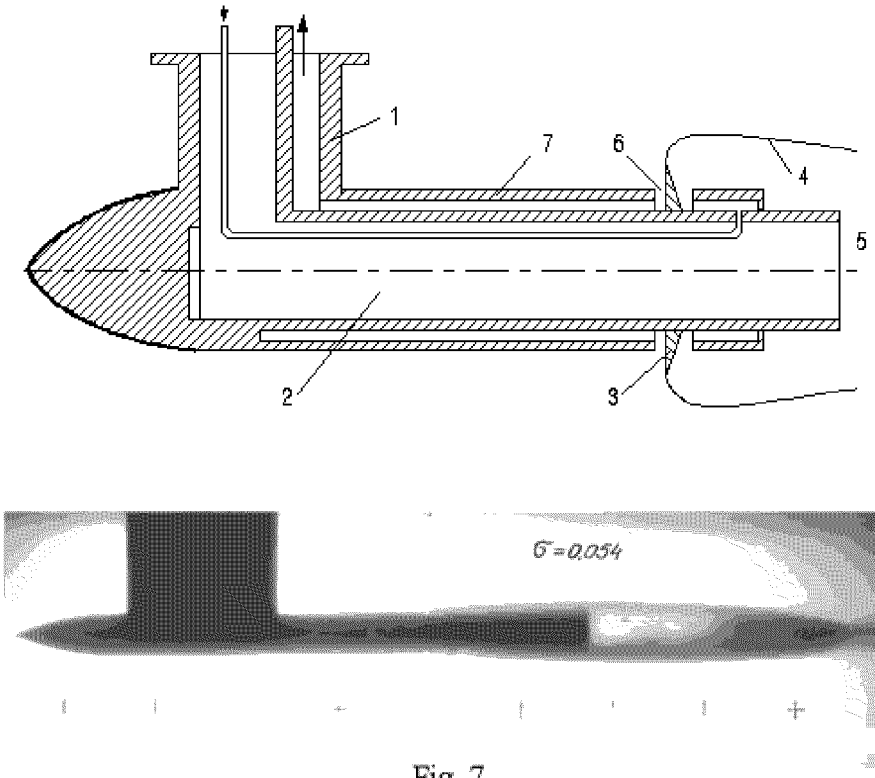

1
7
6
4
5
2
3
σ=0.054

Fig. 7

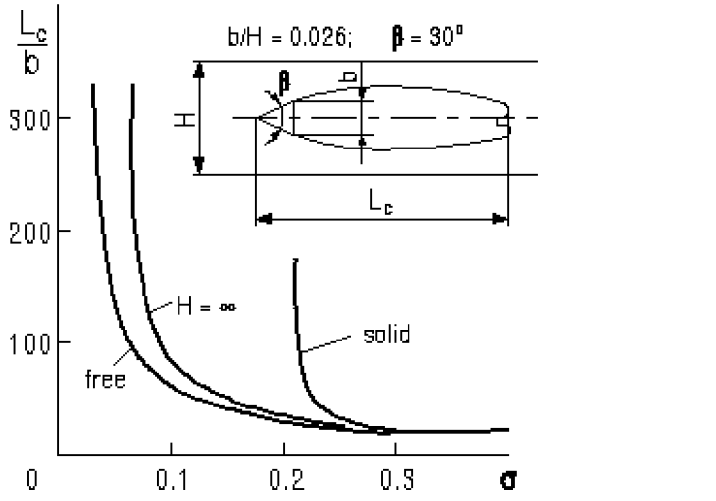

Lc/b
b/H = 0.026;
β = 30°
β
b
H
Lc
300
200
100
0
0.1
0.2
0.3
σ
H = ∞
free
solid

Fig. 8

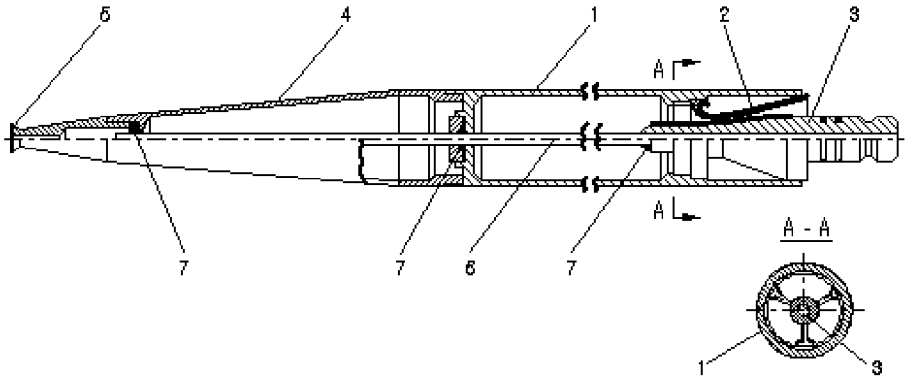


Fig. 9a

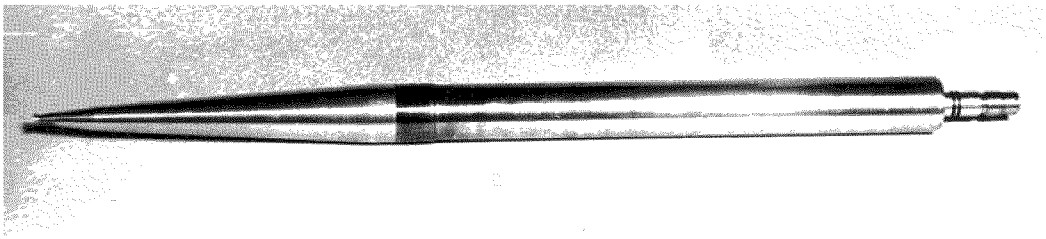


Fig. 9b

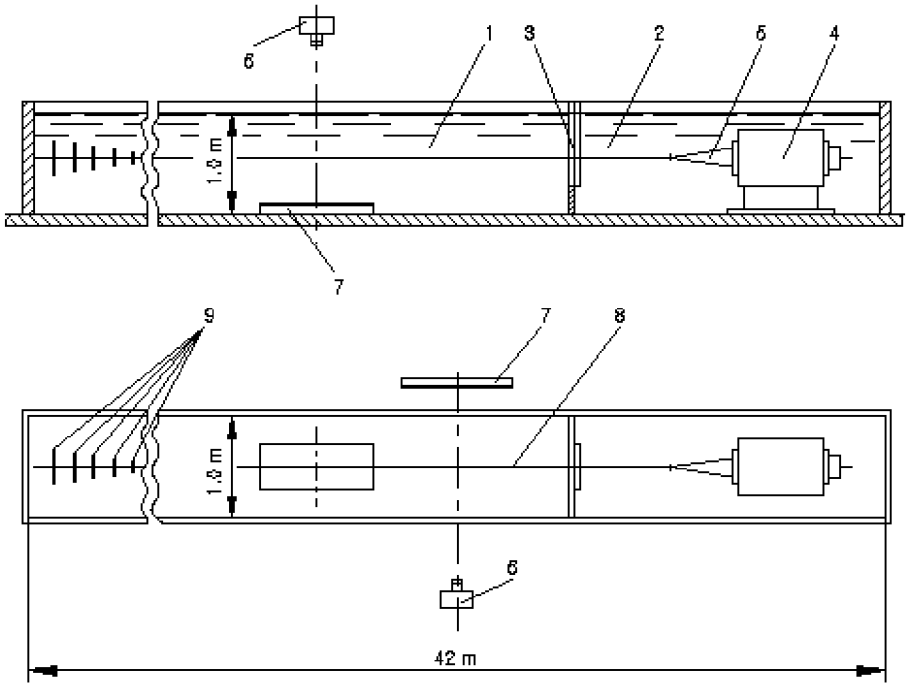


Fig. 10

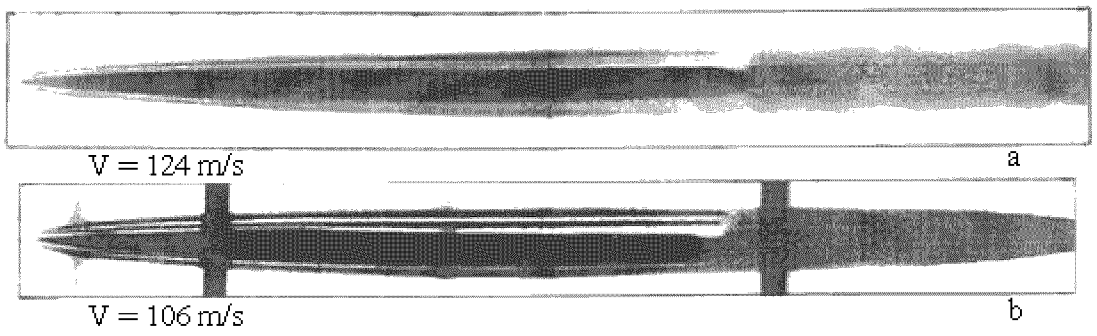


Fig. 11

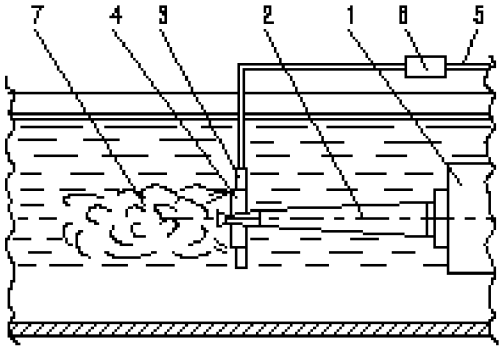


Fig. 12

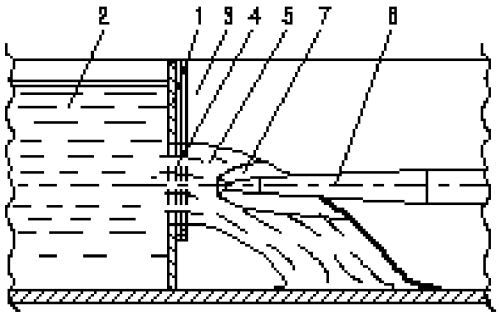


Fig. 13

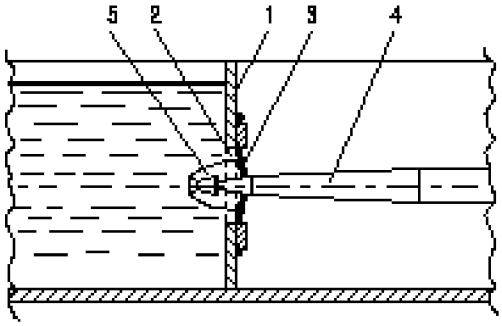


Fig. 14

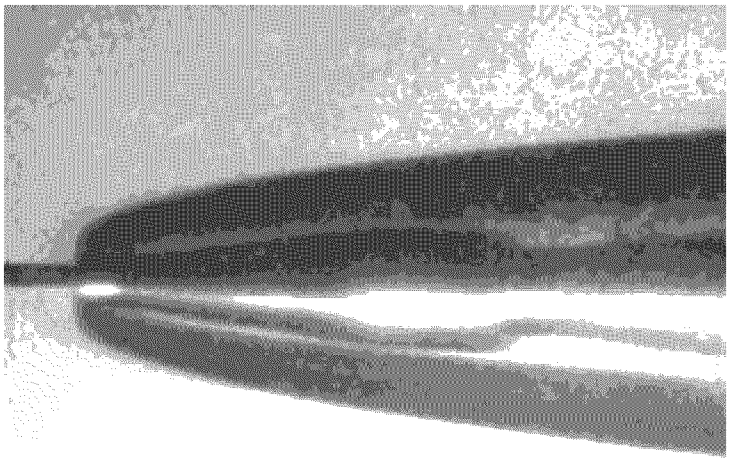


Fig. 15a

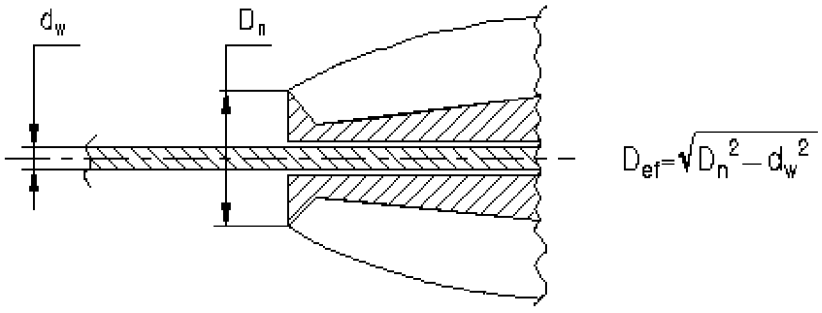


Fig. 15b

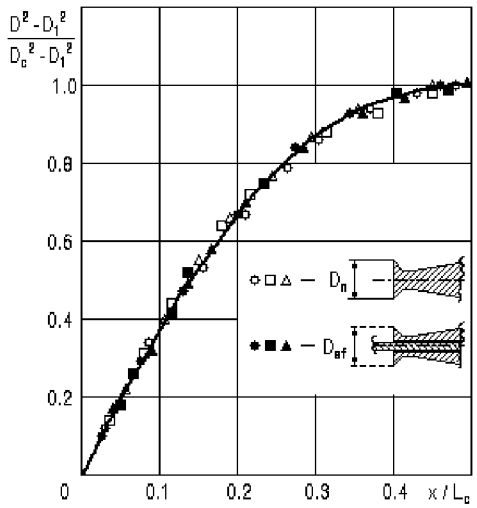


Fig. 16

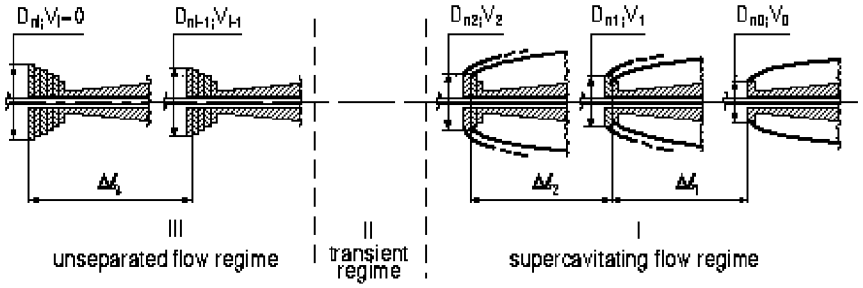

$D_{n};V_{l}=0$
$D_{n1-1};V_{l-1}$
$D_{n2};V_2$
$D_{n1};V_1$
$D_{n0};V_0$
ΔL_3
ΔL_2
ΔL_1
III
unseparated flow regime
II
transient regime
I
supercavitating flow regime

Fig. 17

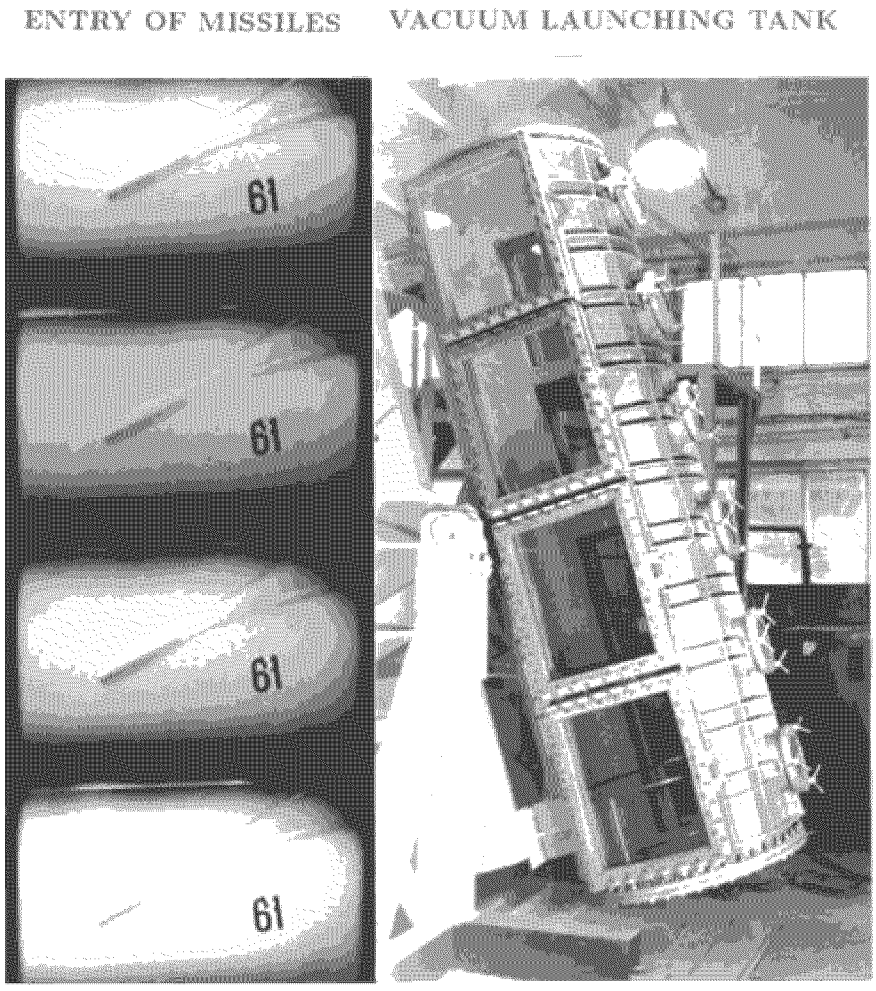

ENTRY OF MISSILES
VACUUM LAUNCHING TANK
61
61
61
61

Fig. 18

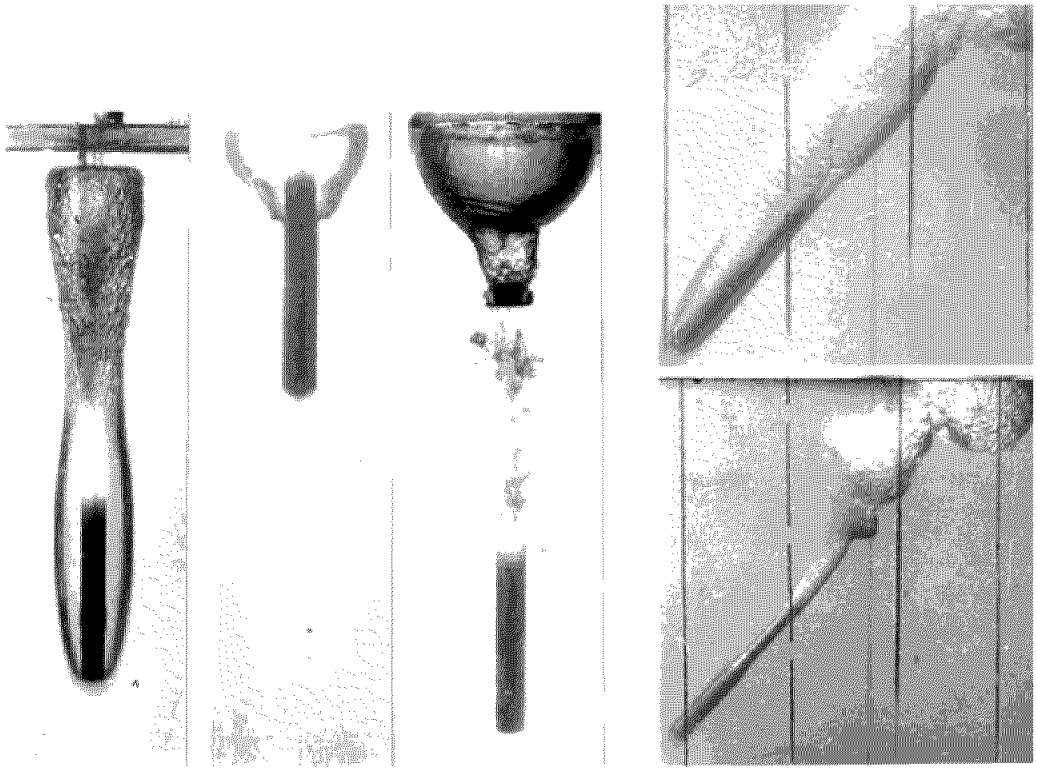


Fig. 19

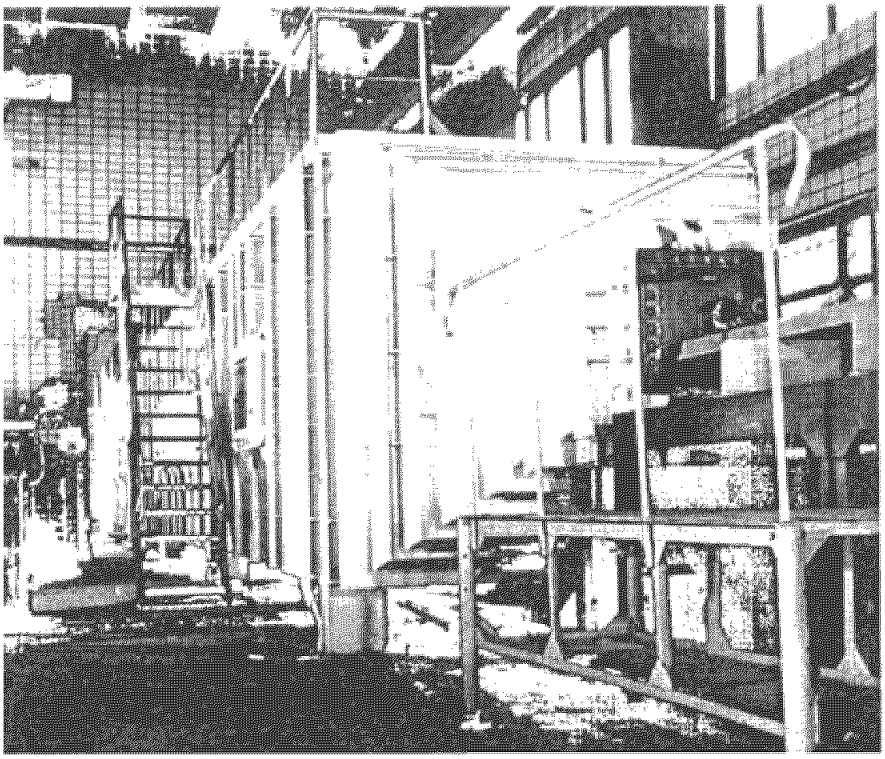


Fig. 20

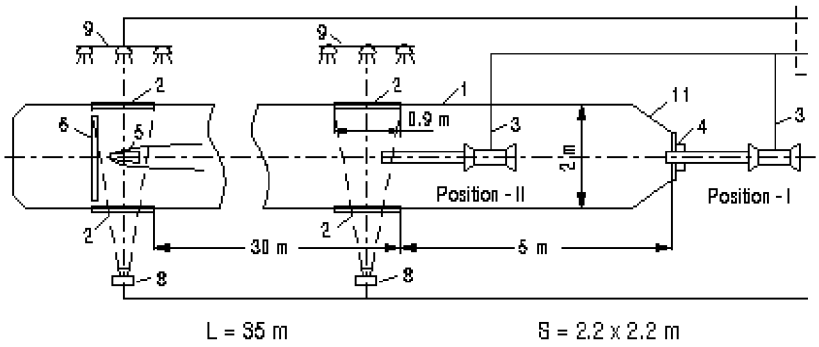


Fig. 21

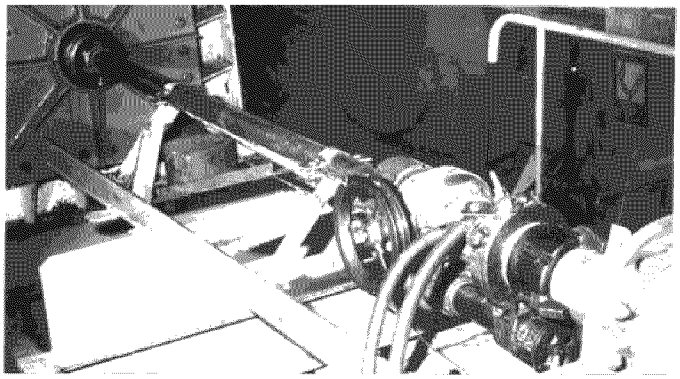


Fig. 22

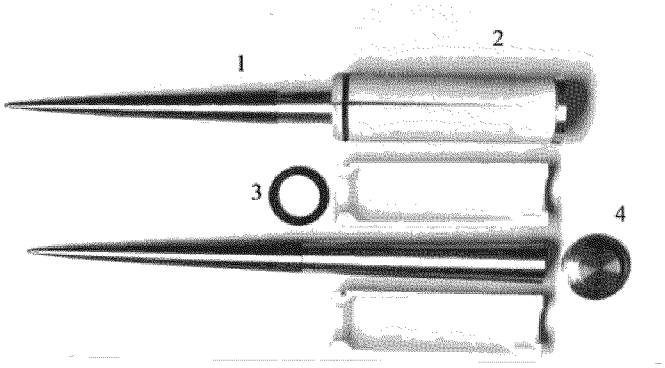


Fig. 23

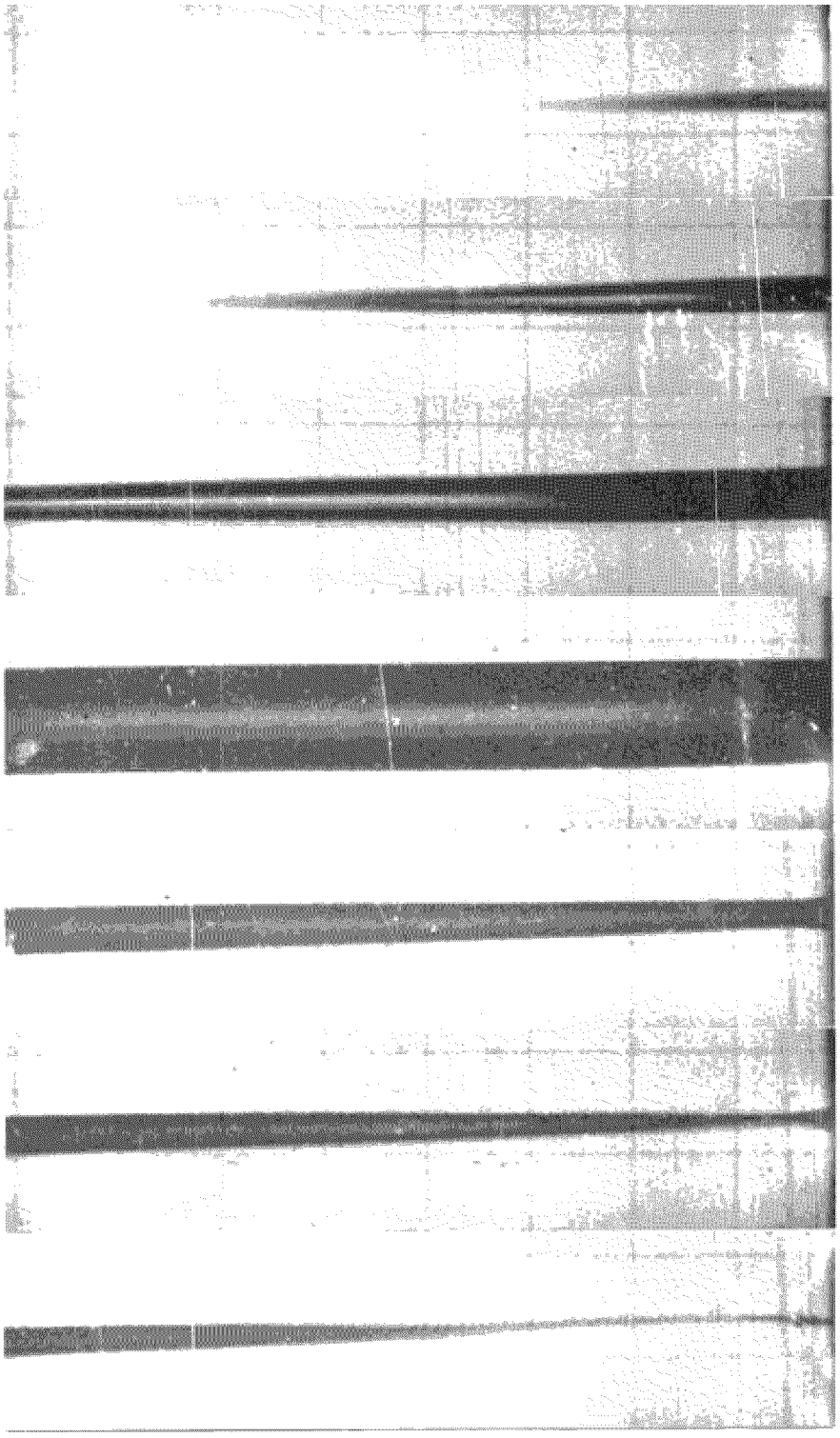


Fig. 24

Developed Cavitation-Cavity Dynamics

David R. Stinebring
Michael L. Billet
Jules W. Lindau
Robert F. Kunz
Applied Research Laboratory
P.O. Box 30
State College, PA 16804
USA

Introduction

When we discuss high-speed supercavitating bodies, it primarily involves the fully developed supercavitating phase. For many cases the body must transition from fully wetted, through the partially cavitating regime before reaching supercavitation. Therefore, an understanding of all phases of cavitation is necessary.

Flow regimes and basic definitions

Cavitating flows are commonly described by the cavitation number, σ, expressed as

$$\sigma \equiv \frac{P - P_v}{\frac{1}{2}\rho V^2} \tag{1}$$

where, P and V are the reference pressure and velocity, respectively, P_v is the vapor pressure at the bulk temperature of the liquid, and ρ is the mass density of the liquid. If a cavitation experiment is conducted by holding the velocity constant and varying the reference pressure, various amounts of cavitation can be observed as shown in Figure (1). Noncavitating flows occur at sufficiently high pressures where there is no evidence of bubbles. Supercavitation occurs at very low pressures where a very long vapor cavity exists and in many cases the cavity wall appears glassy and stable except near the end of the cavity. Between these flow regimes is limited cavitation and developed cavitation.

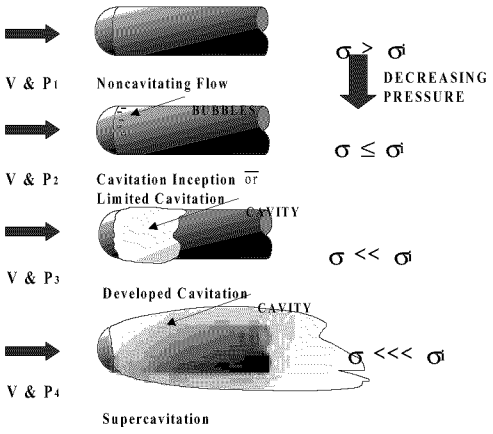


Figure 1: Schematic of cavitation flow regimes

Paper presented at the RTO AVT Lecture Series on "Supercavitating Flows", held at the von Kármán Institute (VKI) in Brussels, Belgium, 12-16 February 2001, and published in RTO EN-010.

Limited cavitation occurs at an intermediate value of the cavitation number where amount of a given type of cavitation is minimized. Limited cavitation can be vaporous or gaseous. The former type of cavitation is caused by the explosive growth of bubbles due to the rapid conversion of liquid to vapor at the bubble wall whereas the latter is due to a slower mode of bubble growth caused by the transport of noncondensible gas into the bubble. The condition at which cavitation initially appears is called cavitation inception.

Of particular importance in the study of cavitation is the minimum pressure coefficient, $C_{p_{min}}$ given by

$$C_{p_{min}} = \frac{p_{min} - P}{\frac{1}{2}\rho V^2} \tag{2}$$

where, P_{min} is the minimum pressure in the liquid. The "classical theory for scaling vaporous limited cavitation" states that, $\sigma = -C_{p_{min}}$ and $C_{p_{min}}$ = constant. This implies that when scaling from one flow state to another, the characteristics of the flow field and its boundaries remain geometrically and kinematically similar. However, real flows often do not obey the classical theory because of so-called "scale effects" which arise from changes in velocity, size, fluid properties and microbubble distribution. Experimental results clearly show that in many cases, the limited cavitation number can be greater or less than the minimum pressure coefficient and in some cases the minimum pressure coefficient is not constant, such as in vortical flows. One example of scale effects can be noted from the "standard" cavitation tests conducted at many facilities for the ITTC. Figure (2) shows some of the cavitation data and the varied appearance of the cavitation data can be noted in Figure (3).

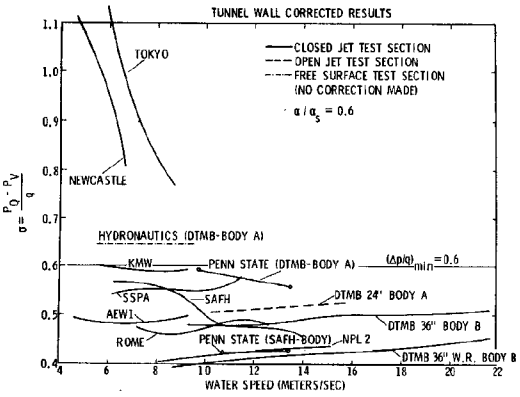


Figure 2: ITTC cavitation data

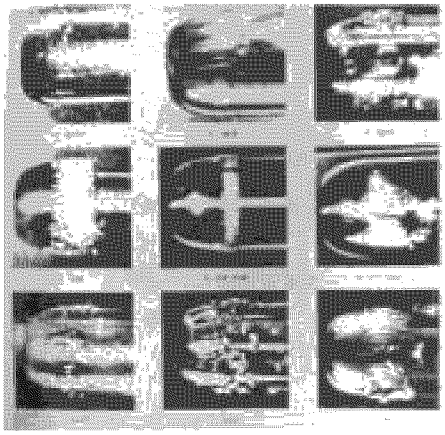


Figure 3: Photographs of cavitation appearance for ITTC data

Extensive research has been conducted into scale effects, such as in References (1), (2), and (3). Also, it is very important to determine the definition of limited cavitation when comparing experimental results. In general, these studies into scale effects can be divided into two general types as follows:

Viscous Effects: Scale effects that act on the flow outside the cavitation bubble which influence the local pressure in the liquid flow.

1. Flow field changes due to variations in Reynolds number, Froude number, and Mach number including steady and turbulent pressure fluctuations.
2. Departures from exact geometric similarity such as those due to roughness and manufacturing.

Bubble Dynamic Effects: Scale effects that act on the bubble growth process which cause the liquid pressure at the cavitation bubbles to depart from the equilibrium vapor pressure corresponding to the bulk temperature of the liquid.

1. Time effects.
2. Heat transfer effects.
3. Surface tension effects
4. Transport of noncondensible gas
5. Liquid tension, i.e., microbubbles.

The various factors which causes scale effects and the influence on the cavitation number can be ascertained by employing the Rayleigh-Plesset equation to describe the growth of a "typical" cavitation bubble. This equation can be written as

$$\rho\left(R\ddot{R}+\frac{3}{2}\dot{R}^2\right)=P_G(t)-\frac{2S}{R}-\frac{4\mu\dot{R}}{R}-\left[C_p(t)+\sigma+C_T(t)\right]\frac{1}{2}\rho V^2 \tag{3}$$

where,

$$C_p(t)=\frac{P(t)-P}{\frac{1}{2}\rho V^2}$$

and,

$$C_T(t)=\frac{P_v(T)-P_v(T_r(t))}{\frac{1}{2}\rho V^2}.$$

Thus $C_p(t)$ is the time varying pressure coefficient which describes the variation of the liquid pressure outside of the bubble. The thermodynamic coefficient (C_T) describes the effect of heat transfer on the vapor pressure in the bubble. The term $\overline{P}_G$ is the partial pressure of gas inside the bubble and the term $\frac{2\overline{S}}{R}$ is the "liquid" tension of the bubble. Multiplying Equation (3) by a time interval (dt), integrating over a time interval (T_c) which is typical of a cavitation process, and solving for σ yields

$$\sigma=-\overline{C}_p+\frac{\overline{P}_G}{\frac{1}{2}\rho V_\infty^2}-\frac{\frac{2\overline{S}}{R}}{\frac{1}{2}\rho V_\infty^2}-\phi-\overline{C}_T \tag{4}$$

where, ϕ is a bubble dynamic parameter. The bars denote averages over the interval T_C. In the absence of significant dynamic effects, Equation (4) reduces to an equilibrium equation

$$\sigma=-\overline{C_p}+\frac{\overline{P}_G-\frac{2\overline{S}}{R}}{\frac{1}{2}\rho V^2}-\overline{C}_T \tag{5}$$

Referring to Equation (5), it is noted that the terms P_G, $\frac{2\overline{S}}{R}$, and C_T all cause bubble dynamic scale effects and the liquid tension effect and thermodynamic coefficient will reduce the cavitation number at inception and the gas pressure in the bubble will increase the cavitation number at inception. Viscous scale effects are contained with the average pressure coefficient $\overline{C}_p$. This can be written as

$$-\overline{C}_p = -\overline{C}_{p_s} + \frac{\overline{\nabla P}_T}{\frac{1}{2}\rho V_\infty^2} + \frac{\overline{\nabla P}_R}{\frac{1}{2}\rho V_\infty^2} + \frac{\overline{\nabla P}_U}{\frac{1}{2}\rho V_\infty^2}$$

where $\overline{C}_{P_R}$ is the average local pressure in the absence of surface roughness $\left(\overline{\Delta P}_R\right)$, turbulence, $\left(\overline{\Delta P}_T\right)$ and flow unsteadiness $\left(\overline{\Delta P}_U\right)$.

Scale effects are very important in understanding the physics of cavitation. They are important as can be noted in Figure (4) for a Schiebe headform and in Figure (5) for a 1/8-caliber ogive. Figure (6) shows the effect of boundary layer transition on limited cavitation.

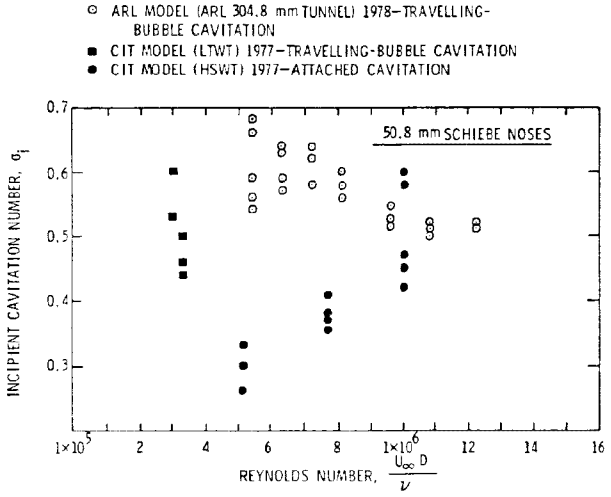


Figure 4: Comparison of CIT and ARL Penn State inception data for 50.8-mm (2.0-inch) Schiebe noses

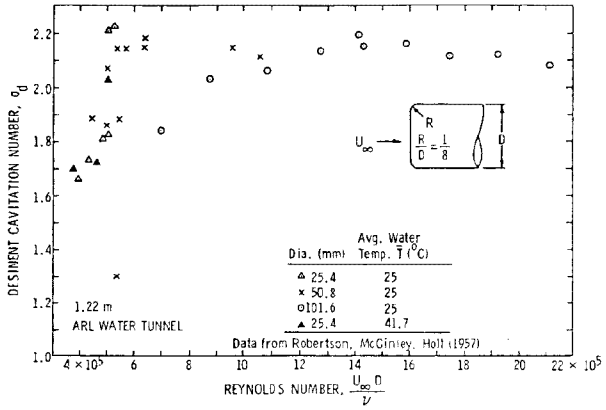


Figure 5: Desinent cavitation number versus Reynolds number for 1/8-caliber ogives

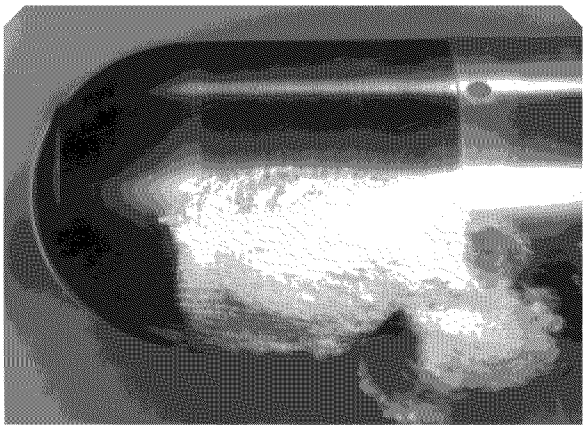


Figure 6: Effect of boundary layer transition on limited cavitation

Developed Cavitation

The subject of a fully developed cavity and the various similarity laws which predict the cavity parameters have been studied by many researchers and some of these results are discussed in other lectures. However, this research has largely been divided into two types of cavity flows: (1) ventilated cavities, and (2) vaporous cavities. These cavities have been shown to have one similar characteristic in that the cavity shape is a single-valued function of the cavitation number based on cavity pressure. Thus, the cavitation number for developed cavitation is based on cavity pressure (P_c) and can be expressed as

$$\sigma = \frac{P - P_c}{\frac{1}{2}\rho V_\infty^2} \tag{6}$$

where $P_c \approx P_V + P_G - \Delta P_V$ for vaporous cavity and P_c would be P_{VE} for the ventilated cavity. The rear of these cavities is a complex and often highly turbulent region of the flow where the contents of the cavity are carried or entrained away. However, in the case of vaporous cavitation where the cavity contains mostly vapor, the loss of vapor is immediately made up by the evaporation from the walls of the cavity. On the other hand, a continual supply of gas is needed to form a ventilated cavity.

Fluid properties of the liquid inherently affect the vaporization process along the cavity wall, which supplies vapor to the cavity in a similar manner as is the case of limited cavitation. This scale effect is given the term "thermodynamic effect," and is noted by the effect of liquid temperature variation on the cavitation number. It is the same as for limited cavitation and it will become more significant as the temperature is increased, resulting in the cavity temperature being lower than the bulk temperature of the fluid. One of the first theoretical and experimental investigations into the variation of cavitation number with temperature has been conducted by Stahl and Stepanoff[4]. A detailed investigation into this effect was conducted by Holl, Billet, and others at Penn State that developed the entrainment theory[5],[6]. This investigation provides insite into the characteristics of developed cavitation.

Most of this thermodynamic scale effect investigation used a zero-caliber-ogive body shown in Figure (7). At small cavity lengths (L/D < 2.0), the cavity is very cyclic and the re-entrant jet formed at the cavity closure strikes the leading edge of the cavity. The photograph of the cavity on the zero-caliber ogive was taken with continuous lighting so the cavity appears like seen to the naked eye. Figures (8 to 11) show cavity behavior seen with high-speed movies and very short-duration strobe flash lighting. The unsteady nature of the cavity is apparent. Observing the cavitation with continuous lighting provides a time average view of the cavity, which also can lead to problems in investigating developed cavitation.

The cavity length is a measure of the cavitation number. However, determination of the cavity length visually is subjective, since an observer is seeing a time average of the cavity, and pressure measurements are affected by the transient nature of the cavity.

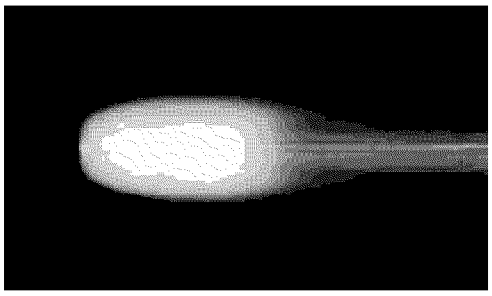


Figure 7: Photograph of cavity on a zero-caliber ogive illuminated with continuous lighting

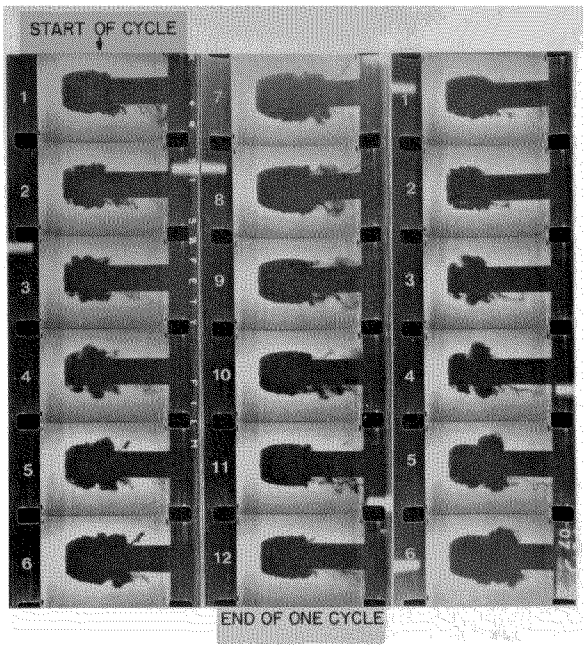


Figure 8: Sequence from a high-speed movie showing a complete cavity cycle- 5000 frames per second- 6.35-mm (0.25-inch) diameter zero-caliber ogive, Velocity = 25 m/sec



Figure 9: Detail of cavity after reentrant jet strikes leading edge, first image in sequence is below

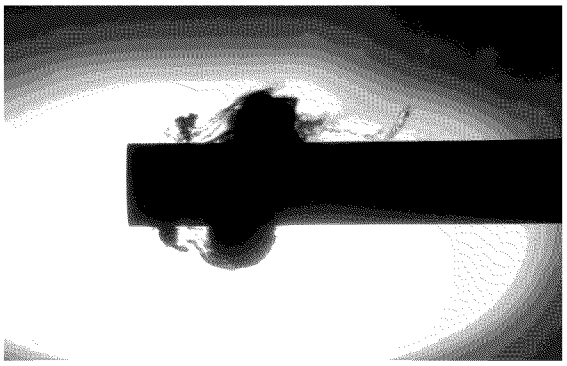


Figure 10: Photograph of cavity on zero-caliber ogive illuminated with a 3-μ sec flash

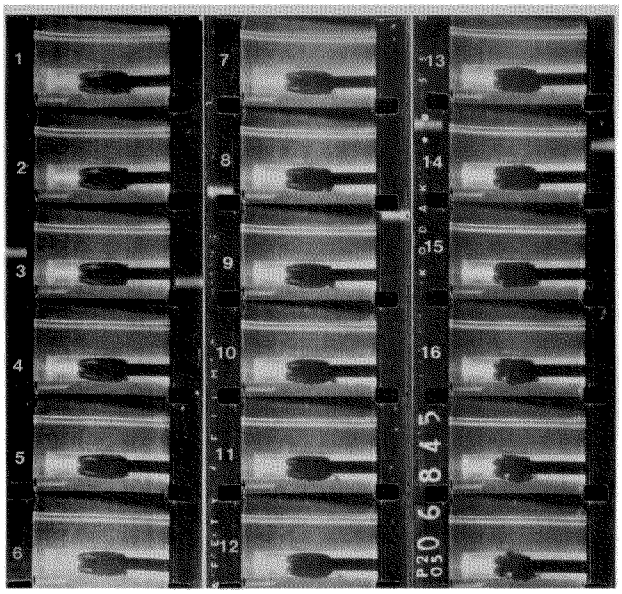


Figure 11: Sequence from high-speed movie showing the reentrant jet moving through the cavity and striking the cavity leading edge (between frames 11 and 12)- 5000 frames per second- 6.35-mm (0.25-inch) diameter zero-caliber ogive, Velocity = 15 m/sec

The high-speed movie sequences show that the unsteady nature of the cavities is due to the reentrant jet moving through the cavity and striking the cavity leading edge. This causes the cavity to detach from the cavitator leading edge and break into helical vortices connected by vortex filaments, Figures 9 and 10.

The cavity on the zero-caliber ogive is similar to the bubble shape of the wake associated with the separated flow from the model nose. At the end of this bubble there is a re-entrant jet and the velocity of this jet of liquid can be expressed as

$$V_j = V(1+\sigma)^{\frac{1}{2}} \tag{7}$$

which can be derived from Bernoulli's equation which assumes that the frictionless fluid. This condition is similar to the vortical flow near the end of the wake bubble. At appropriate values of Reynolds numbers a regular vortex sheet is observed in the wake region aft of bubble closure. At higher Reynolds numbers a turbulent wake with irregular mixing results. For the case of the cavity closure on the body, the re-entrant travels along the body surface to the cavity separation location.

As the re-entrant jet affects the cavity dynamics, the body experiences a time dependent drag. Gilbarg and Serrin[7] show that this change of drag can be related to the momentum of the re-entrant jet and hence a characteristic dimension of this jet.

Measurements made inside of a developed cavity also indicate the physics of the vaporization process. As shown in Figure (12), the maximum temperature depression from inside the cavity indicating that most of the vaporization process is occurring near the beginning of the cavity where the curvature is greatest. This maximum temperature depression is affected by the air content of the liquid as shown in Figure (13). Consequent measurement of the cavity pressure indicates that this is due to the presence of noncondensible gas (partial pressure above vapor pressure). The magnitude of the pressure unsteadiness that occurs in the cavity as shown in Figure (14). This is due to the re-entrant jet.

The geometric characteristics of developed cavities were determined from a series of experiments conducted by Billet and Weir[5],[6]. From measurements of the cavity profiles, the maximum cavity diameter (D_m), cavity half-length (A), and cavity surface area were determined for both natural and ventilated cavities. Data shows that for a given model geometry and cavitation number, ventilated and natural cavities have the same profile, within experimental error. This was found to be independent of reference velocity, and cavity dimension are directly proportional to the model diameter as shown in Figure (15). This is in agreement with several other investigators such as Wade[9].

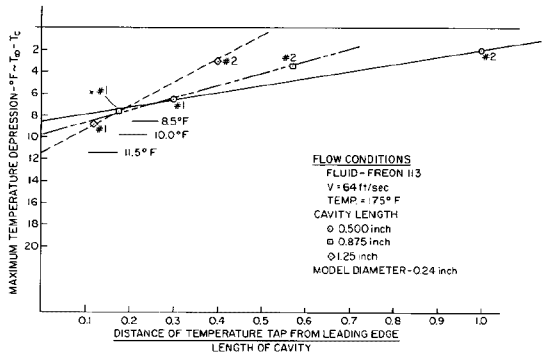


Figure 12: Maximum temperature depression versus cavity tap position for Freon 113; Temperature= 175° F, L= 0.50, 0.875, and 1.25-inch, V=64 ft/sec

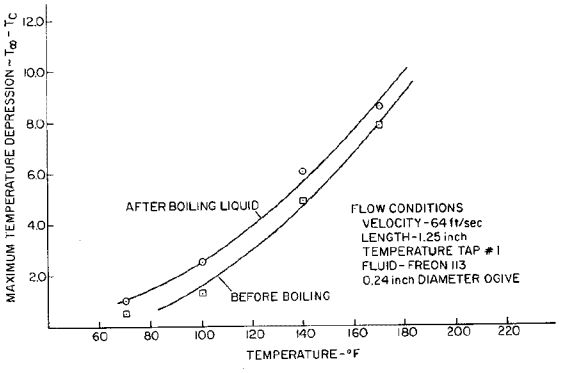


Figure 13: Cavity temperature depression versus temperature for Freon 113, V=19.5 m/sec, L=3.18 cm (1.25-inch), two different air contents

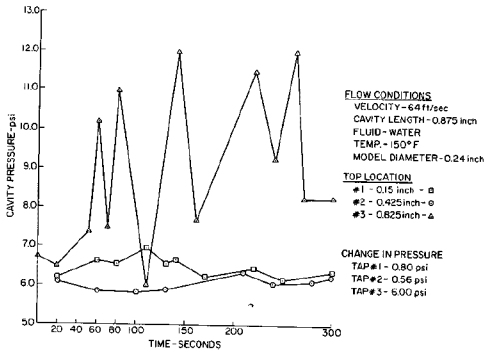


Figure 14: Cavity tap pressures versus time for water; temperature= 66° C, L= 2.2 cm (0.875-inch), V=19.5 m/sec

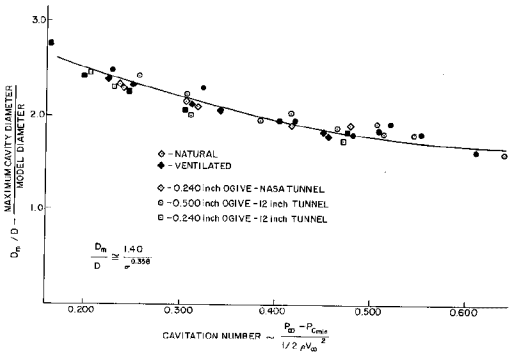


Figure 15: Ratio of maximum cavity to model diameter versus corrected cavitation number

For ventilated cavities, the flow coefficient is defined as

$$C_Q = \frac{Q}{VD^2} \tag{8}$$

where Q is the ventilation rate and D is the reference dimension. This is a dimensional representation of the volume flow rate of gas needed to sustain a cavity. This volume flow rate is the same regardless if it is a ventilated or vapor cavity. This assumption is supported by Reichardt, who demonstrates that the drag and geometry for similar vaporous and ventilated cavities are the same.

One of the first experimental investigations of air entrainment was carried out at the California Institute of Technology in 1951 by Swanson and O'Neill[10]. In their experiments an air filled cavity was maintained behind a 2.54-cm disk over a cavitation number range of 0.25 to 0.08 and a corresponding Froude number range of 10 to 15. Their results show that as the supply of air to the ventilated cavity was decreased from a maximum flow coefficient of 1.6, the cavity size decreased only slightly over a large range of air supply rates until a certain minimum rate of air supply was reached. Thereafter, a slight decrease in the air supply led to a rapid reduction in the size of the cavity for small values of flow coefficients.

In the region where the cavity size varies rapidly with the flow coefficient, the cavity has a re-entrant jet closure. A further increase in flow coefficient causes the re-entrant jet to break down and be replaced by the twin-vortex regime. This demonstrates the existence of two distinct flow coefficient regions which are determined by the cavity closure conditions.

An extensive analysis of the various factors which influence air entrainment for ventilated cavities in the twin-vortex regime is presented by Cox and Clayden[11]. They show theoretically that high rates of air entrainment are associated with the formation of the twin-vortex system. They also present experimental data for ventilated cavities on 2.54-, 1.91-, and 1.27-cm-diameter disks which show that for a given rate of air entrainment, the cavity length to disk diameter ratio increases as the Froude number based on disk diameter increases.

Waid[12] also measured flow coefficients for ventilated cavities on a series of three-dimensional hydrofoils. The results obtained for both the re-entrant jet and two-vortex regimes show the same trends as the data obtained by Swanson and O'Neill[10].

Gas diffusion was found to have a significance on the cavity pressure (above vapor pressure) and on the measured thermodynamic effect. Thus, the entrainment rate needed to sustain a natural cavity has contributions not only from the vapor but also from gas diffusion. Gas diffusion was also found to have a significant effect on the gas needed to sustain a ventilated cavity. Billet and Weir[13] conducted an experimental investigation into this effect. An analysis of this effect was conducted based on a mathematical model of diffusion developed by Brennen[14].

Gas diffusion will occur when there exists a concentration gradient between the freestream and the cavity. This concentration gradient can be calculated from the partial pressures of the gas. The maximum partial pressure of the gas in the freestream can be determined from a knowledge of the air content and Henry's Law

$$P_{FS} = \alpha \cdot \beta \tag{9}$$

where, α is the air content in ppm by moles and β is Henry's Law constant, which depends on temperature. The mass flow rate of diffused gas into the cavity is proportional to the concentration gradient and can be expressed in terms of the difference in partial pressures as

$$M_{DG} = f(\text{transport})\left[P_L \frac{P_{FS} - P_G}{\beta} \right] \tag{10}$$

where, f(transport) is a dimensional function of the parameters influencing the diffusion mechanism and P_G is the partial pressure of noncondensible gas in the cavity. This transport function can be determined from a knowledge of the free shear layer over the cavity surface. A schematic of this process is shown in Figure (16) from Brennen[14].

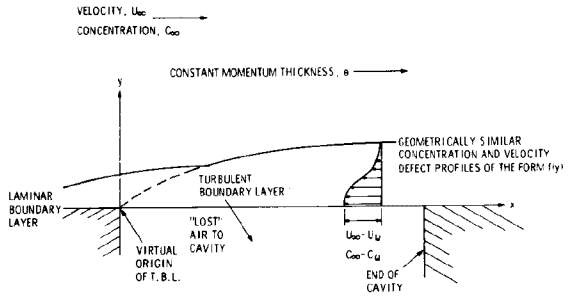


Figure 16: Schematic for an undersaturated cavity (Brennen [14])

The results of this analysis are shown in Figure (17). In this figure, the effect on flow coefficient is given for both an undersaturated and oversaturated condition. These data were then corrected for gas diffusion effects and compare favorably to the data for no gas diffusion.

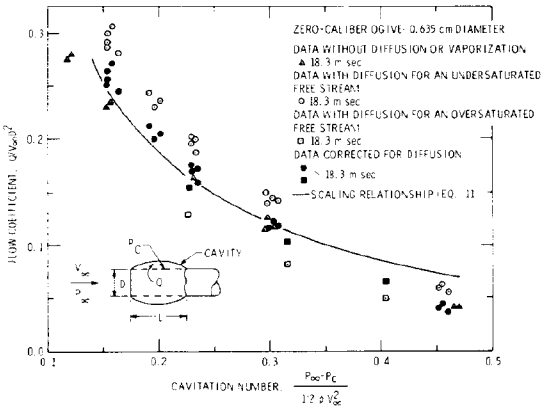


Figure 17: Flow coefficient data with diffusion for 6.35-mm diameter zero-caliber ogive, V= 18.3-m/sec

Supercavitation

When a cavity length is much greater than the body dimensions, this flow regime is described as supercavitation. The cavity stays attached to the body and the cavity closure is far downstream. The length of the cavity does not vary significantly even though considerable oscillations can occur at its closure. However, the cavity acts as if it were an extension of the body. In this case, the same flow field would exist around a solid body having a shape comprising of the wetted nose plus the free-cavity profile. Unlike developed cavities, the gross features of supercavitation on a headform are not only functions of the cavitation number but also the Froude number-gravity becomes important.

Supercavities have many characteristics of classical free streamline flows. The cavity interior is essentially at constant pressure, and the cavity walls are essentially free-stream surfaces of constant velocity. Cavity pressures approach vapor pressure. These assumptions are the basis of many theoretical treatments of cavity geometry and forces. Many of these theories will be presented during this course; however, only cavity dynamics will be discussed in this section.

There exists a transition between the re-entrant jet closure condition and the twin-vortex closure condition. This has been discussed in many previous investigations. However, a study of water-entry modeling by Stinebring and Holl[15] describes this transition of flow regimes in detail and will be discussed briefly.

It has been observed that for a ventilated cavity there exists a condition when the cavity length for a given flow condition suddenly grows to four or five times its original length with only a slight increase in the ventilation air flow rate. This instability in the cavity length may be attributed to the transition between the re-entrant jet and twin-vortex flow regimes.

Previous discussions on developed cavitation are for flows where gravity effects are not important and the re-entrant jet is the gas entrainment mechanism. However, at low velocities or longer cavity lengths and gravity is normal to the flow, the cavity will move upward to the body centerline as a result of buoyancy. The flow velocities of the top surface of the cavity will be different than on the lower surface, which will result in a net circulation. As a result, a new cavity equilibrium system is established where entrainment now occurs through the vortex cores of the twin-vortex structure at cavity closure.

A photograph of the cavity in the re-entrant jet regime is shown in Figure (18). The conical nose is supported by support struts so the aft region the cavity can be investigated with minimum disturbance. The opaque appearance of the cavity is primarily due to the violent mixing caused by the re-entrant jet. As transition to the twin-vortex regime takes place, the cavity becomes clear at the leading edge but with some mixing due to the re-entrant jet. The photograph in Figure (19) shows the cavity in the twin vortex regime. This transitional region between flow regimes was also observed for models which have afterbodies (sting mounted) although this effect was not as pronounced. The full growth of the cavity could not be realized because of interference at the downstream end of the cavity.

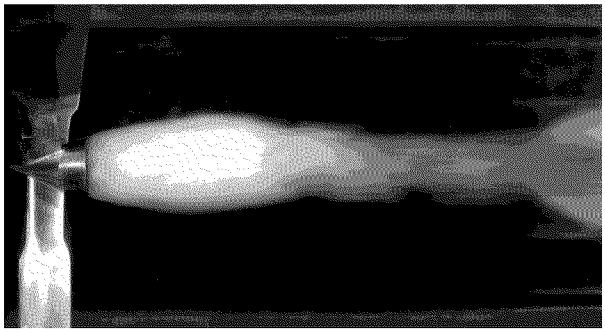


Figure 18: Photograph of cavity for a 45° conical nose illuminated with continuous lighting

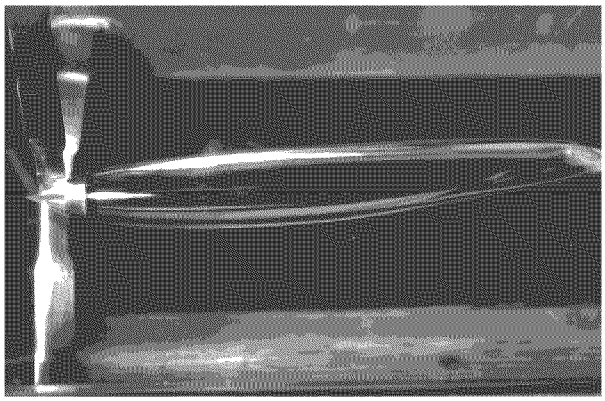


Figure 19: Photograph of twin vortex cavity downstream of a strut-mounted 45° cone

Cavitator hydrodynamics

For supercavitating flow the cavitator is located at the forward most location on the body, and the cavity downstream of the cavitator covers the body. The shape of the cavity is defined by the cavitation number based on cavity pressure. The simplest form of cavitator is a disk where the drag coefficient is defined as,

$$C_d = 0.82(1+\sigma). \tag{11}$$

There have been numerous expressions derived for cavity dimensions as a function of cavitation number. Reichardt (16) showed that the cavity length divided by the cavity diameter is independent of the shape of the cavitator and is only a function of cavitation number,

$$\frac{L}{d_m} = \frac{\sigma + 0.008}{\sigma(0.066 + 1.7\sigma)}. \tag{12}$$

Reichardt also developed an expression for the cavity diameter divided by the cavitator diameter,

$$\frac{d_m}{d} = \left(\frac{C_d}{\sigma - 0.132\sigma^{8/7}} \right)^{0.5}, \tag{13}$$

which is only a function of cavitation number and cavitator drag coefficient, C_d.

By substituting the definition of drag coefficient into equation (13) and rearranging, the drag force required to create an axisymmetric cavity of a given diameter is:

$$D_{cavity} = \frac{\pi}{8} \rho \; V_\infty^{\,2} \; d_m^{\,2} \; (\sigma - 0.132 \, \sigma^{\,8/7}) \tag{14}$$

where, ρ is the mass density of the fluid. For a given velocity and cavity diameter, the drag is only a function of the cavitation number. It is not a function of the geometry of the cavitator.

The shape of the cavity is approximately elliptical. A number of researchers have developed formulas for the cavity, most notably, Logvinovich (17). The cavity radius is given as,

$$R = R_k \sqrt{1 - \left(1 - \frac{R_1^{\,2}}{R_k^{\,2}}\right)\left(1 - \frac{t}{t_k}\right)^{\frac{2}{\chi}}} \tag{15}$$

where, R_k, is the maximum cavity radius, t_k, is the time of formation to the cavity midpoint, χ, is a correction factor, χ = 0.85, and R_1 and t are the radius and time of formation at the matching station, x_1, where,

$$t = \frac{x - x_1}{V_k}$$

and where, x, is the streamwise distance, and V_k, is the cavitator velocity.

Since there is a gas filled cavity over the body, there is a loss of buoyancy so the body must be supported by contact with the cavity wall. The cavitator must be at an angle of attack to provide lift to support the forward section of the body, and the aft section can be supported by the afterbody planing or control surfaces or a combination of both. The cavity shape will be influenced by foreshortening due to the cavitator at angle of attack, and perturbations due to downwash from lift and bouyancy effects. These effects upon the cavity shape are beyond the scope of this paper and are covered in Logvinovich.

Experimental facilities and test programs

These next sections will briefly cover some of the facilities and test programs at ARL Penn State related to cavity dynamics, cavity ventilation requirements, cavitator testing, and control surface testing. They are intended to show the hardware and techniques that have been used to investigate the physics of developed cavitation.

Testing Facilities at ARL Penn State

The Garfield Thomas Water Tunnel of the Applied Research Laboratory Penn State is a complex of hydrodydynamic and hydroacoustic test facilities that are registered with the International Towing Tank Conference, an organization of member counties that design and test ships and other marine structures in tanks and tunnels. Since the 48-inch Diameter Water Tunnel began operation in 1949, many additional facilities and capabilities were added. Many of the smaller water tunnels are utilized to research specific physics problems, so it is especially appropriate for graduate student work.

Three facilities are specially utilized for supercavitation studies and are: (1) 48-inch Diameter Water Tunnel, (2) 12-inch Diameter Water Tunnel, and (3) Ultra-High-Speed Cavitation Tunnel. The 12-inch Diameter Water Tunnel was built in 1951 and the Ultra-High-Speed Cavitation tunnel was built in 1962. These three facilities will be discussed briefly.

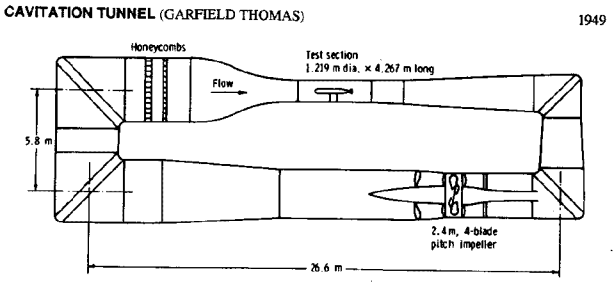
48-INCH (1.22 M) DIAMETER WATER TUNNEL (GARFIELD THOMAS WATER TUNNEL)

This large water tunnel is a variable –speed, variable-pressure tunnel primarily intended for propulsion studies of body-propulsor systems. It is a closed circuit, closed-jet water tunnel. A detailed description of the facility is given in Figure (20).

The tunnel has two honeycombs in the 3.66 m diameter "settling section" to not only straighten the flow, but also reduce the test section turbulence level below 0.1 percent. The cylindrical working section is four feet in diameter and 4.27 m long. The water velocity in the working section is variable up to 24.4 m/sec. And is controlled by a four-bladed, adjustable pitch impeller which is 2.41 m in diameter and is driven by a 1491 kW electric motor.

The pressure in the working section may be reduced to 20.7 kPa, which permits a wide range of cavitation numbers for testing. The air content of the water in the tunnel is controlled through the use of a degasser that permits removal of air from the water. Thus, the water in the working section can be less than air-saturated regardless of the working section.

The degassing system is located in the tunnel by-pass system, which also has filters and the tunnel pressure control systems. This by-pass can handle from 500 gpm to 3000 gpm from the tunnel and can be operated during cavitation testing to remove air and bubbles. Gas removal from the water is accomplished with a Cochrane Cold-Water Degasifier. This degasser consists of an upright cylindrical tank where the upper portion is filled with plastic saddles. Water taken from the tunnel is sprayed into the top of the tank, the interior being maintained at a high vacuum. The water spray falling over the saddles exposes a thin water film to a vacuum, which permits the rapid removal of air. The water collects at the bottom of the degasser and is returned to the bypass system.



Description of Facility: Closed Circuit, Closed Jet

Type of Drive System:4-Blade Adjustable Pitch Impeller

Total Motor Power:2000 HP Variable Speed (1491 kW)

Working Section Max. Velocity: 18.29 m/s

Max. & Min. Abs. Pressures:413.7 to 20.7 kPa

Cavitation number Range:>0.1 dependent on velocity and/or J-range

Instrumentation: Propeller dynamometers, five-hole probes, pitot probes, lasers, pressure sensors, hydroplanes, planar motion mechanism, force balances.

Type and Location of Torque & Thrust Dynamometers: Model internally mounted, 150 hp limit (111.85 kW).

Propeller or Model Size Range: Model size from 76.2 mm to 635.0 mm id.

Tests Performed: Forces, flow field, and pressure distributions on bodies of revolution, hydrofoils, propellers, etc. Cavitation performance and noise measurements of propellers, foils, hydrodynamic shapes, etc. Steady state and time-dependent force and torque measurements on powered models. Flow visualization.

Other Remarks: Tunnel turbulence level is 0.1 percent in test section. Air content can be controlled as low as 1 ppm per mole. Measurement can be made of hydrodynamic functions for stability and control of submerged vehicles. Directional hydrophone system for relative acoustic measurements.

Published description: ARL Penn State Report NORD 16597-56, Lehman, 1959.

Applied Research Laboratory, Fluid Dynamics Department, The Pennsylvania State University, USA

Figure 20: Description of the ARL Penn State 48-inch diameter water tunnel

12-INCH (0.305 M) DIAMETER WATER TUNNEL

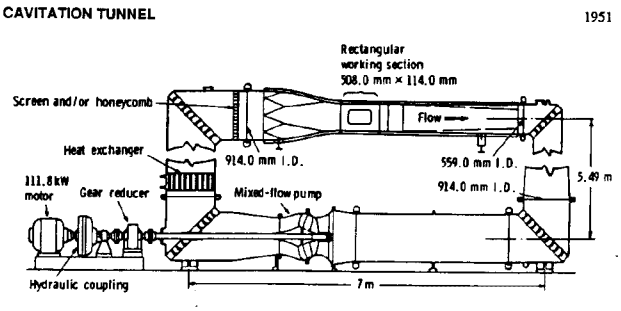
The facility is typically used for flow studies that do not require wake-operating propellers. This is a closed-circuit tunnel, which has the similar working section velocity and pressure range as the Garfield

Thomas Water Tunnel. As is the case of other facilities, the pressure is independent of the working section velocity and details are given in Figure (21),

One of the unusual features of this facility is the use of two interchangeable working sections for different test purposes. A circular section is 0.305 m in diameter, and a rectangular one is 0.51 m high and 11.4 cm wide; each is 0.76 m long. The circular working section is used to study the bodies employed in three-dimensional flow problems. The rectangular one is to study hydrofoils and slots and other two-dimensional flow problems.

The tunnel drive consists of a mixed-flow pump that forms a part of the lower leg and one turn of the tunnel circuit. The pump is driven by a 150 hp electric induction motor through a variable-speed fluid coupling and reducing gear. The method of cooling the tunnel water is by a heat exchanger, which is an integral part of the circuit.

The tunnel is also connected to the by-pass circuit of the 48-inch diameter water tunnel so that the air content and free air can be controlled.



Description of Facility: Closed Circuit, Closed Jet

Test Sections:(1) Circular: 304.8 mm dia x 762.0 mm long

(2) Rectangular: 508.0 mm x 114.3 mm x 762.0 mm long

Type of Drive: Mixed Flow Peerless Pump

Total Motor Power: 150 hp (11.8 kW)

Working Section Max. Velocity:24.38 m/s

Max. & Min. Abs. Pressures: 413.7 to 20.7 kPa

Cavitation Number Range:>0.1 dependent on velocity

Instrumentation:Lasers, pressure sensors, hydrophones

Model Size Range:50.8 mm max. dia.

Tests Performed: Steady and time-dependent force and pressure measurements on unpowered models. Noise measurements on cavitating models. Three-dimensional flow problems (circular section). Two-dimensional flow problems (rectangular section). Axial-flow pump tests.

Other Remarks: Independent gas control of air content. Water filtration with 25-micrometer filters. Intermittent operation with drag-reducing additive injection. Partial neutralization of additive downstream of test section.

Published Description: ARL Penn State Report NORD 16597-56, Lehman, 1959.

Figure 21: Description of the ARL Penn State 12-inch diameter water tunnel

ULTRA-HIGH-SPEED CAVITATION TUNNEL

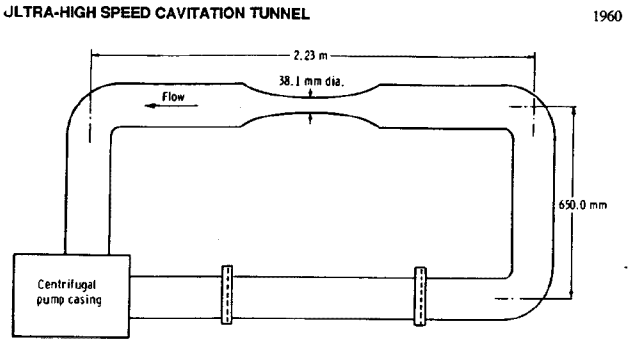
Much of the basic studies on cavitation have been conducted in the Ultra-High-Speed Cavitation Tunnel. The characteristics of this tunnel are given in Figure (22).

This tunnel is a high-speed, high-pressure system which is designed so that the velocity in the test section can be varied from 13.7 to 100 m/sec. The tunnel pressure can be varied to a maximum of 8.3 MPa. The inside diameter of the test section of 3.81 cm.

The entire tunnel circuit is made of stainless steel except for the lucite test section windows and the bronze centrifugal pump. The small amount of corrosion in the system coupled with a bypass filtering circuit allows for a very clean system.

The bearing for the centrifugal pump shaft is lubricated by drawing water from the tunnel circuit through the bearing and thus this method of lubrication avoids possible contamination which would be encountered in a system employing hydrocarbon lubricants. As the fluid leaves the bearing, it enters an accumulator tank and from there is pumped by means of a triplex pump back to the tunnel. Pressure control is obtained by by-passing a portion of the fluid from the discharge of the triplex pump to the accumulator tank and/or bleeding some fluid from the main tunnel circuit. A surge tank is located in the pressure control circuit in order to remove fluctuations caused by the triplex pump. The liquid in the tunnel by-pass is filtered down to remove particles above two microns.

Also, a 14 kw heater is located in the by-pass circuit. It has the capability to heat the liquid to temperatures in excess of 176°C. Water, Freon 113, and alcohol have been used as working fluids in this facility.



Description of Facility:Closed Circuit, Closed Jet

Type of Drive System:Centrifugal Variable Speed Drive

Total Motor Power: 75 hp (55.9 kW)

Working Section Max. Velocity: 83.8 m/s

Max. & Min. Abs. Pressures:8274.0 to 41.4 kPa

Cavitation Number Range:>0.01 dependent on velocity and velocity

*Instrumentation:*Pressure and temperature sensors, lasers

Temperature Range:16°C to 176°C

Model Size Range:12.7 mm max. dia.

Test Medium:Water, Freon 113, Alcohol

Tests Performed: Incipient and desinent cavitation studies. Development cavittion studies. Cavitation damage.

Other Remarks: Stainless steel tunnel. Bronze pump. Three filter banks for removal of water, acides, solid particles (10 micrometers) depend on fluid media.

Published Description: ARL Penn State TM 75-188, Weir, Billet & Holl, 1975.

Figure 22: Description of the ARL Penn State 1.5-inch diameter water tunnel

Measurements of cavity dynamics in the reentrant flow regime

As stated previously, if the product of the cavitation number and Froude number is above a critical value, then the cavity will be in the reentrant flow regime. The oscillation of the cavity in the reentrant regime affects the ventilation gas entrainment and the body dynamics. Therefore, understanding the dynamics of reentrant jet cavities is important.

A 45° conical-nosed model having a 2.54-cm (1.0- inch) diameter afterbody was instrumented with an internally mounted piezoelectric transducer, Figure 23. It was expected that the reentrant jet striking the cavity would cause a significant pressure rise that could be measured with the transducer. Spectral analyses were performed on the transducer output to determine the frequency of the cavity cycling. Tests were conducted with both vaporous and ventilated cavities over a range of cavitation numbers and

velocities of 9.1, 13.7 and 15.2 m/sec (30, 45, and 50 ft/sec). High-speed movies of the cavitation were taken and compared to the spectrum analyzer results. To determine if the boundary layer thickness affects the cycling frequency, a number of tests were conducted with distributed roughness applied to the conical nose. Lastly, the results were compared with the findings of previous investigations in water tunnels covering a wide range of model sizes and geometries.

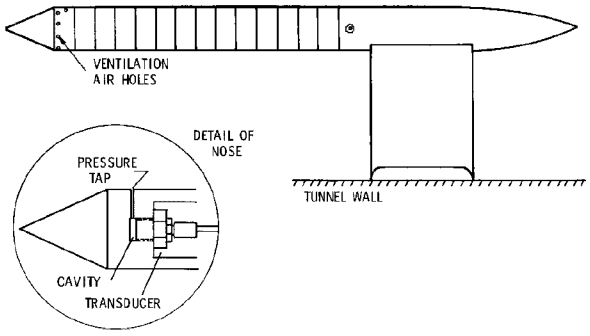


Figure 23: Schematic of model for measuring cavity cycling showing the location of the pressure transducer (inset)

The cavity cycling frequency Strouhal number based on body diameter is defined as

$$S = \frac{f D}{V_\infty}$$

where, f is the cycling frequency, and D is the body diameter. A plot of cycling frequency Strouhal number as a function of cavitation number is presented in Figure (24). The data of Knapp (18) for hemispherical nosed models and from Stinebring (8) for zero caliber ogives are also shown in the figure. The trend of lower cycling frequency for lower cavitation numbers, i.e., larger cavities, is the same for all models for vaporous and ventilated cavities. The Strouhal number can also be defined such that the characteristic length scale is the ratio of cavity length to model diameter, *L/D.* A plot of Strouhal number as a function of *L/D* is presented in Figure (25). The plot shows that the cavity length is the characteristic dimension for cavity cycling and that the Strouhal number based on cavity length is a constant, approximately, $S = 0.16$.

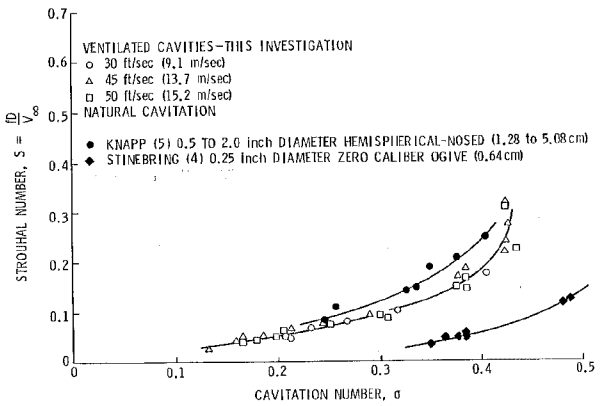


Figure 24: Cavity cycling Strouhal number, based on body diameter, as a function of cavitation number for vaporous and ventilated cavities for a number of investigations having different test geometries

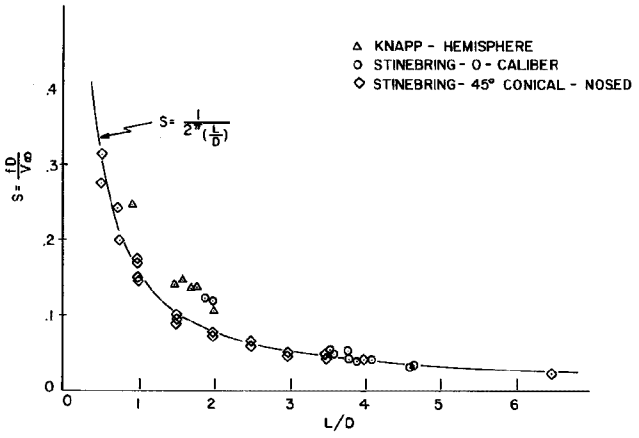


Figure 25: Cavity cycling Strouhal number, based on cavity length divided by body diameter, as a function of cavity length divided by body diameter for vaporous and ventilated cavities for a number of investigations having different test geometries

Effect of afterbody shape upon gas entrainment

Since most of the gas entrainment takes place in the aft region of a body, the afterbody shape should affect the required ventilation rate to generate a cavity. Tests were performed in the ARL Penn State 0.305-m (12-inch) diameter water tunnel to examine afterbody effects upon gas entrainment. The models used for this study are shown in Figure (26). Each model had a 25.4-mm (1.0-inch) diameter 45° apex angle conical nose. One model had a 25.4-mm (1.0-inch) afterbody, the second had a 12.7-mm (0.5-inch) afterbody, and the third model was supported by three struts and had no afterbody. All models had six holes for introduction of ventilation gas and a pressure tap for measuring cavity pressure. Tests were conducted at velocities of 9.1, 13.7, and 15.2-m/sec (30, 45, and 50 ft/sec). To minimize gaseous diffusion across the cavity wall, the test conditions were selected so the cavity pressure was close to the partial pressure of gas in the surrounding water.

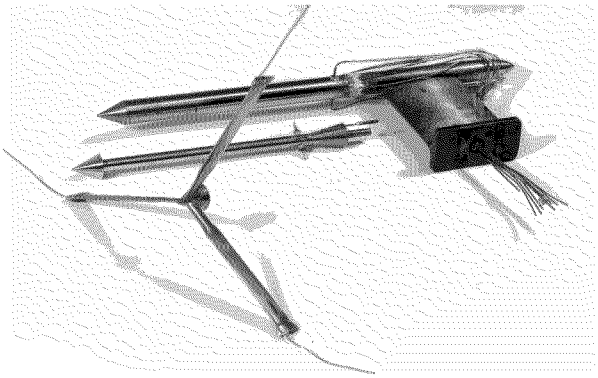


Figure 26: Photograph of the models used to examine the effect of afterbody on gas entrainment

The results of the study for a tunnel velocity of 13.7- m/sec (45-ft/sec) are displayed in Figure (27). The model requiring the lowest flow rate for a given cavitation number was the one with no afterbody. The model having the afterbody one-half of the cone diameter required the largest ventilation flow rate (except at the highest cavitation numbers), and the model with the afterbody equal to the cone diameter

was between the two. It would seem that the model with no afterbody should require the largest flow rate, because of the greater volume of gas inside the cavity, but this was not the case. The reentrant jet behavior could possibly account for this effect. Observations show that gravity causes the reentrant jet to move along the bottom of the cavity for the model with no afterbody. An afterbody causes a "guiding effect" upon the reentrant jet that results in more mixing at the top of the cavity. It is not known why the smaller afterbody required the largest ventilation. The data does show that afterbody design is important to minimize ventilation requirements.

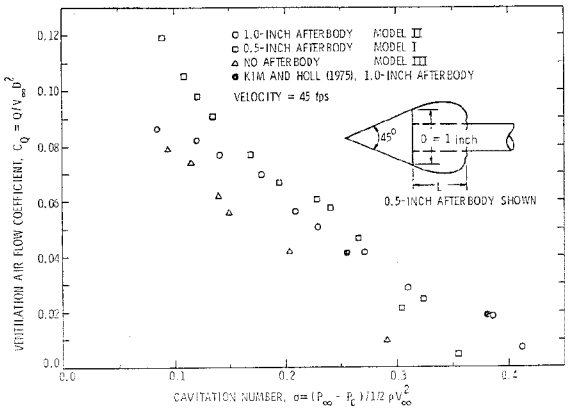


Figure 27: The effects of afterbody arrangement on ventilation requirements

Cavitator testing

A photograph of a model for cavitator testing in the ARL Penn State 12-inch diameter water tunnel is shown in Figure (28). The models can incorporate systems for introducing ventilation gas, cavitator force balances, pressure measurement systems, and other instrumentation. Just downstream of the cavitator in the figure is a gas deflector that redirects the gas flow to minimize disturbances to the cavity. The strut-mounted model is attached to the large dark plate, which is the section that mounts to the water tunnel test section. A typical mounting, for a cavitator at angle of attack, to a force balance, is shown in Figure (29). Care must be taken to ensure that the design for the introduction of ventilation gas does not have a significant effect upon the force measurements.

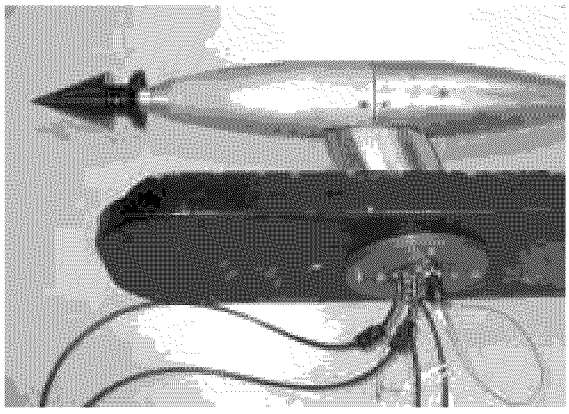


Figure 28: Photograph of model for testing cavitators

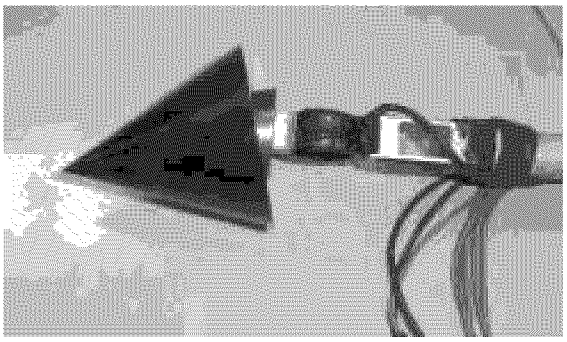


Figure 29: Photograph of cavitator mounted on force cell balance

Photographs of cavities produced by conical and disk cavitators are shown in Figures (30 to 32). The differences in cavity appearance, by using continuous and stroboscopic lighting, are shown in Figures (30 and 31). Short exposure times, such as with stroboscopic lighting, should be used when investigating unsteady cavity dynamics. Strobe lights can be syncronized with the scanning rate of video systems to provide exposure times of a few microseconds for each video frame. The video record of the cavity can then be compared with transient measurements, such as forces, by use of a master clock. The photograph in Figure (32) shows a stable cavity and the effect of the strut mounting on the cavity. When investigating the downstream end of a cavity, a sting mount is used, or as shown in Figure (19) the cavitator can be supported with careful design of the struts.

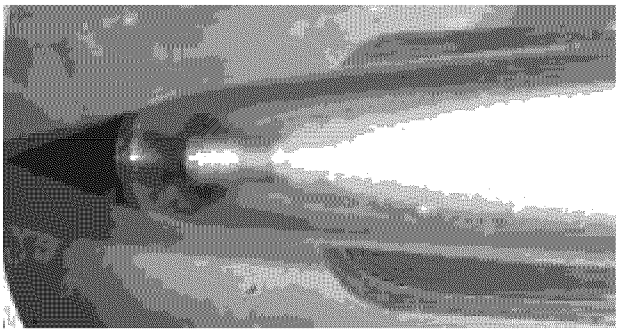


Figure 30: Photograph of cavity formed by a conical nosed cavitator- continuous lighting



Figure 31: Photograph of cavity formed by a conical nosed cavitator- stroboscopic lighting

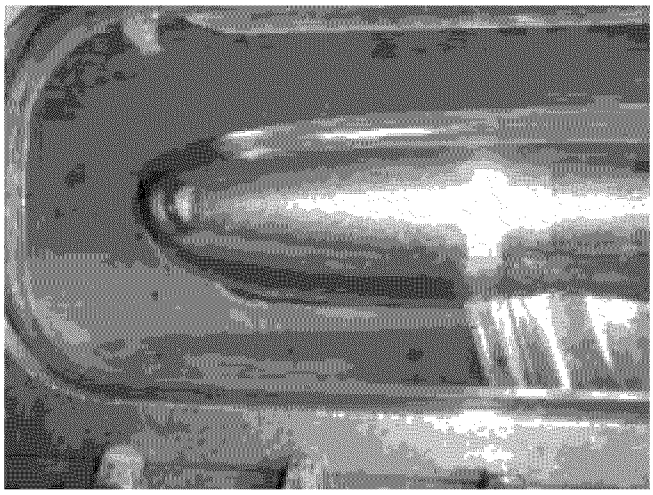


Figure 32: Photograph of cavity formed by a disk at angle of attack

Cavity Piercing Hydrofoil/Control Surface Testing

Cavity piercing supercavitating hydrofoil/control surfaces have been tested in the ARL Penn State 12-inch diameter water tunnel. Some hydrofoils having wedge shaped cross sections are shown in Figure (33). The hydrofoil is mounted to a force balance and test fixture, as shown in Figure (34). The test fixture mounts through the water tunnel test section wall, and is designed so that there is a small gap between the base of the hydrofoil and the test section wall. The hydrofoil angle of attack can be adjusted by rotating the test fixture. A two-dimensional cavity is created along the test section wall upstream of the hydrofoil. This is done by ventilating downstream of a wedge mounted to the tunnel wall. The hydrofoil then pierces the tunnel wall cavity as shown in Figure (35). The wall cavity is approximately 25.4-mm (1.0-inch) thick at the leading edge of the hydrofoil. Reference lines are drawn along the hydrofoil, 25.4-and 38.1-mm (1.0 and 1.5-inches) from the base. The photograph in Figure (35) shows the pressure side view with the hydrofoil at high angle of attack. As shown in the figure, the tunnel wall cavity strikes the hydrofoil leading edge at the 25.4-mm (1.0-inch) reference line. The cavity along the hydrofoil surface is deflected down due to the constant pressure cavity and the pressure gradient along the surface. This deflection of the cavity changes the wetted area and affects the lift and drag forces. The hydrofoil cavity can be seen attached to the trailing edge in the figure.

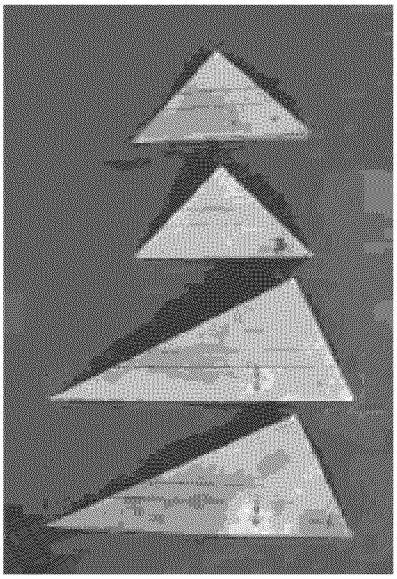


Figure 33: Cavity piercing hydrofoils having wedge shaped cross sections

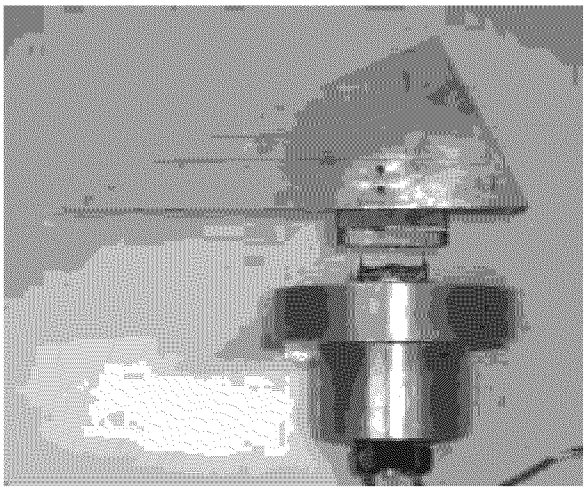


Figure 34: Cavity piercing hydrofoil showing force balance and tunnel mounting fixture

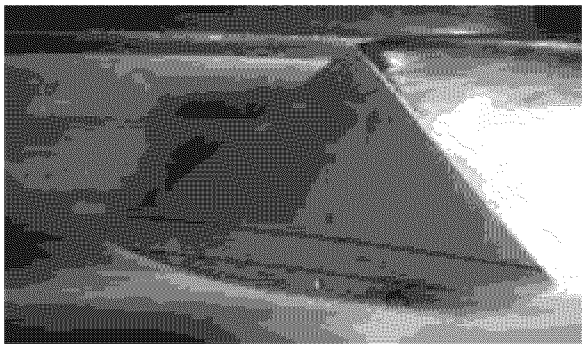


Figure 35: Photograph of pressure side of cavity piercing hydrofoil

The suction side view of a hydrofoil at high angle of attack is shown in Figure (36). This view shows disturbances in the cavity wall due to imperfections along the hydrofoil leading edge. For a hydrofoil with a very sharp leading edge and at large angles of attack, the cavity is transparent and stable near the hydrofoil. At low angles of attack the cavity is attached at the base as shown in Figure (37), and is termed base cavitation. At intermediate angles of attack between base cavitation and supercavitation there can be what is termed partial cavitation. With partial cavitation there may be intermittent cavitation along the suction face, a small, attached cavity or a vortex cavity. Figure (38) shows the stable sheet cavity and supercavitating tip vortex formed by a higher aspect ratio hydrofoil. The forces associated with the different forms of hydrofoil cavitation will be discussed next.

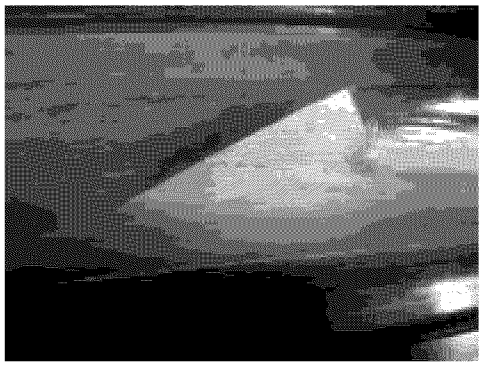


Figure 36: Photograph of suction surface of cavity piercing hydrofoil that shows cavity disturbances due to imperfections along leading edge.

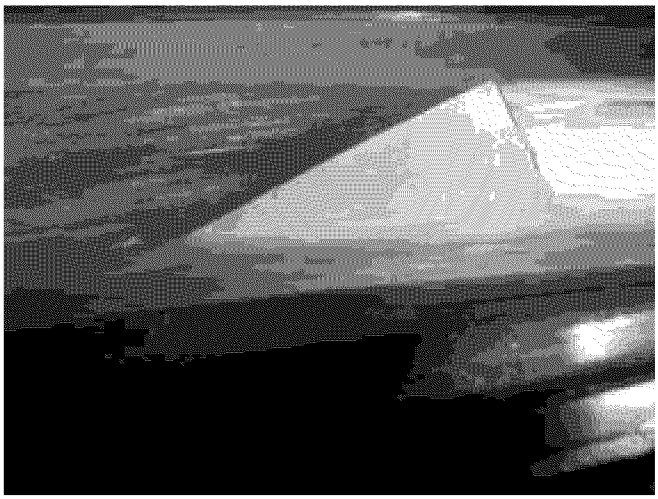


Figure 37: Photograph of cavity piercing hydrofoil at low angle of attack, with base cavitation

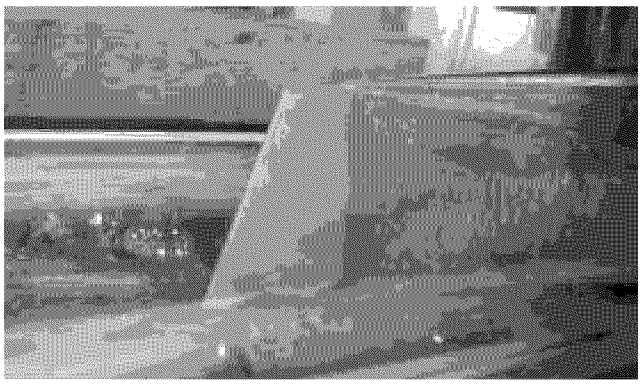


Figure 38: Photograph of cavity from higher aspect ratio cavity piercing hydrofoil

Typical lift and drag coefficient curves as a function of angle of attack for a cavity piercing hydrofoil, are shown in Figure (39). The reference area for reducing forces to coefficient form was the wetted area if the tunnel wall cavity was not affected by the hydrofoil surface pressure gradient. The force coefficients have also been calculated based upon the actual wetted area, as determined from videotapes of the tests, see Figure (35). The complex shape of the force coefficient curves is due in part to the transitions between base, partial, and supercavitating flow regimes.

While the figure shows the averaged force coefficients, the time dependent forces due to cavity fluctuations can also be very important. Time dependent forces for base cavitation are shown in Figures (40 and 41), partial cavitation in Figures (42 and 43), and supercavitating conditions in Figure (44 and 45). For all figures, at time zero the hydrofoil is fully wetted. At approximately 1.25 seconds the tunnel wall cavity is established and the hydrofoil pierces the cavity. After establishment of the tunnel wall cavity, both lift and drag decrease for all conditions, as expected. The primary difference due to the changes in forms of cavitation can be seen in the lift plots. The lift for base cavitation and supercavitation show relatively little fluctuation. However, with partial cavitation there are large changes in lift. All tests in the tunnel were documented with video cameras using stroboscopic lighting synchronized with the video scanning. These changes in lift were associated with intermittent bursts of cavitation on the hydrofoil suction surface. In some cases the lift fluctuations were up to 50%.

For these fins with wedge shaped cross sections, the intermittent cavitation occurred when the relative flow direction near the leading edge was close to the wedge half-angle in the direction of flow. This relative flow direction is affected by the perturbation in the tunnel wall cavity due to the pressure side pressure gradient. The "effective half-angle" is then also affected by the cavity perturbation. Practical designs must take into consideration these factors that affect the unsteady cavity behavior.

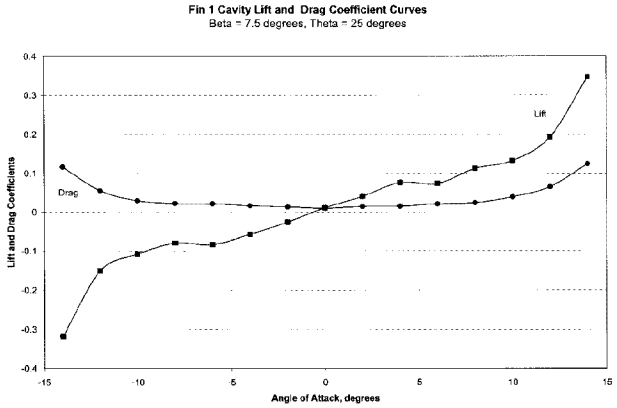


Figure 39: Lift and drag coefficients for a cavity-piercing hydrofoil as a function of angle of attack

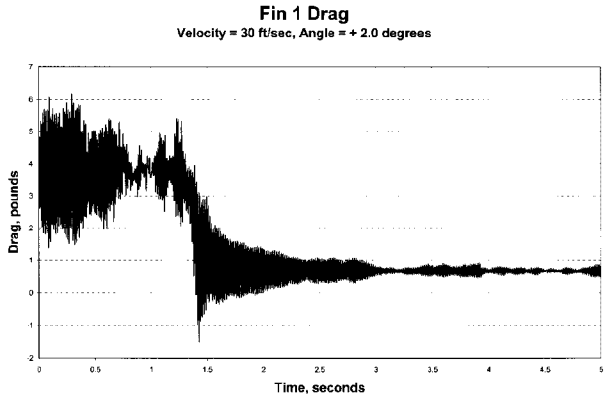


Figure 40: Drag force as a function of time, base cavitation

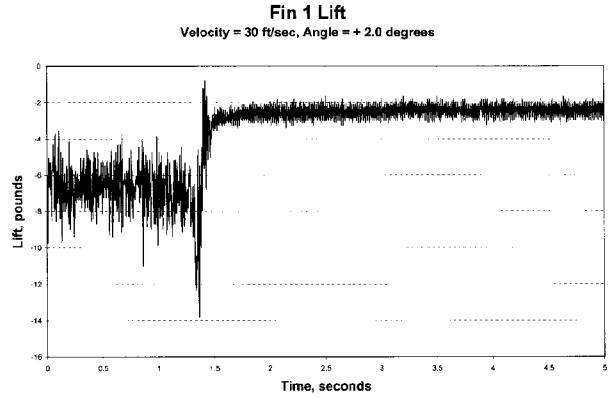


Figure 41: Lift force as a function of time, base cavitation

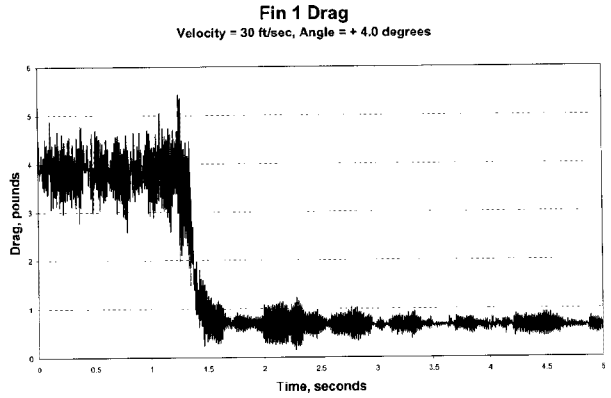


Figure 42: Drag force as a function of time, partial cavitation

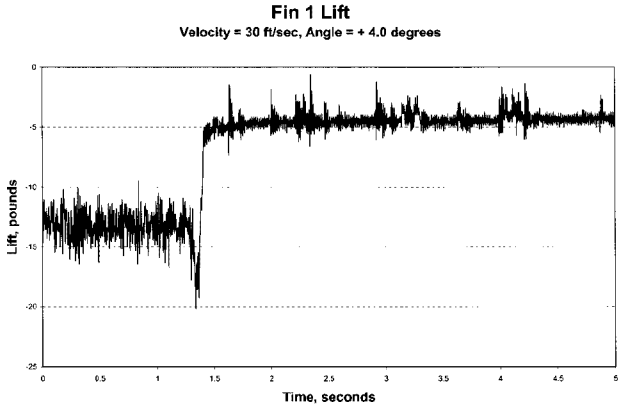


Figure 43: Lift force as a function of time, partial cavitation

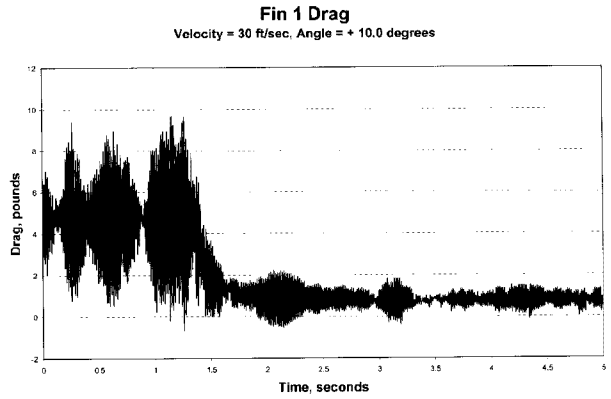


Figure 44: Drag force as a function of time, supercavitation

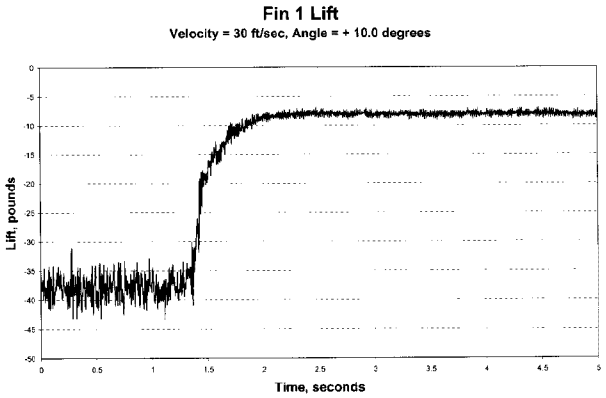


Figure 45: Lift force as a function of time, supercavitation

Summary

This report presents a summary of the cavitation flow regimes and experimental techniques used at ARL Penn State for investigating developed cavitation physics.

References:

1. Arakeri, V. H. and A. J. Acosta, "Viscous Effects in Inception of Cavitation on Axisymmetric Bodies," *J. of Fluids Engr.*, ASME, December 1973, pp. 519-526.
2. Gates, E. M. and M. L. Billet, "Cavitation Nuclei and Inception," IAHR Symposium, Tikyo, Japan, 1980, pp. 3-25.
3. Holl, J. W., R. E. A. Arndt, and M. L. Billet, "Limited Cavitation and the Related Scale Effects Problem, The Second international JSME Symposium on Fluid Machinery and Fluidics, Tokyo, Japan, 1972, pp. 303-314.
4. Stahl, H. A. and A. J. Stephanoff, "Thermodynamic Aspects of Cavitation in Centrifugal Pumps," *J. of Basic Engr.*, ASME, Vol 78, 1956, pp. 1691-1693.
5. Holl, J. W., M. L. Billet, and D. S. Weir, "Thermodynamic Effects on Developed Cavitation," *J. of Fluids Engr.*, Vol. 97, No. 4, Dec. 1975, pp. 507-514.
6. Billet, M. L., J. W. Holl, and D. S. Weir, "Correlations of Thermodynamic Effects for Developed Cavitation," *J. of Fluids Engr.*, Vol. 103, Dec. 1981, pp. 534-542.
7. Gilbarag, D., and J. Serrin, "Free Boundaries and Jets in the Theory of Cavitation," *J. of Math and Physics*, Vol 29, April 1950, pp. 1-12.
8. Stinebring, D. R., M. L. Billet, and J. W. Holl, "An Experimental Study of Cavity Cycling for Ventilated and Vaporous Cavities," International Symposium on Jets and Cavities, ASME, Miami Beach, FL, Nov. 1985, pp. 1-4.
9. Ward, R. L., "Cavity Shapes for Circular Disks at Angles of Attack," CA Inst. of Tech. Hydrodynamic Lab Report, E-73.4, 1957.
10. Swanson, W. M., and J. P. O'Neill, "The Stability of an Air-Maintained Cavity Behind a Stationary Object in Flowing Water," Hydrodynamic laboratory, CA Inst. of tech, M24.3, Sept 1951.

11. Cox, R. N. and W. A. Clayden, "Air Entrainment of the Rear of a Steady Cavity," Symposium on Cavitation in Hydrodynamics, National Physical Laboratory, Sept. 1955.

12. Ward, R. L., "Experimental Investigation of Forced Ventilated Cavities on Hydrofoils of Various Chord Lenths," Report No. LMSC/D243664, Lockheed Missiles and Space Corp, Sunnyvale, CA, Dec. 1968.

13. Billet, M. L. and D. S. Weir, "The Effect of Gas Diffusion on the Flow Coefficient for a Ventilated Cavity," *J. of Fluids Engr.*, ASME, Vol. 97, Dec. 1975, pp. 501-506.

14. Brennen, C., "The Dynamic Balances of Dissolved Air and Heat in Natural Cavity Flows," *J. of Fluid Mechanics,* Vol. 37, Part 1, 1969, pp. 115-127.

15. Stinebring, D. R., and J. W. Holl, "Water tunnel Simulation Study of the Later Stages of Water Entry of Conical Head Bodies: Phase II – Effect of the Afterbody on Steady State Ventilated Cavities," ARL Penn State Report No. TM-79-206, Dec. 1979.

16. May, A., "Water Entry and the Cavity-Running Behavior of Missiles," *SEAHAC Technical Report 75-2*, Naval Surface Weapons Center, White Oak Laboratory, Silver Spring, MD, 1975.

17. Logvinovich, G., "Hydrodynamics of Free-Boundary Flows," *Trudy TsAGI,* 1980.

18. Knapp, R. T., J. W. Daily, and F. G. Hammitt, "Cavitation," McGraw-Hill, 1970.

This page has been deliberately left blank

Page intentionnellement blanche

Variational Methods in Cavitational Flow

P.R. Garabedian
New York University, Courant Institute of Mathematical Sciences
251 Mercer Street
New York, NY 10012, USA

ABSTRACT

The study of cavitational flow is formulated as a free boundary problem for the Laplace equation in three dimensions. Constant pressure free streamlines are determined by a variational principle for the virtual mass. Steepest descent applied to minimization of the potential energy suggests a natural iteration scheme to calculate the shape of the cavity bounded by the free streamlines. Numerical methods enable one to estimate the drag and the geometry of the flow. Another version of the variational principle plays an important role in plasma physics and the theory of magnetic fusion. Novel stellarator configurations for a thermonuclear reactor have been designed by running large computer codes based on these mathematical ideas.

1. Introduction

We shall be concerned with steady, irrotational flow of an incompressible fluid with a free surface on which the pressure is constant. This is a difficult mathematical problem because the shape of the free boundary must be calculated as part of the solution. Our approach is to apply the principle of minimum virtual mass, in which the answer appears as the solution of a problem in the calculus of variations that is easier to treat both theoretically and numerically. The appearance of potential energy in the analysis may be unconventional in fluid dynamics, but we shall show how this can be used to find the drag, and afterwards we shall present another application of the same method in magnetohydrodynamics where the physics becomes more natural.

2. The Riabouchinsky model

Steady irrotational flow of an incompressible fluid in the plane is governed by a complex potential $\zeta = \phi + i\psi$ whose real and imaginary parts satisfy the Cauchy-Riemann equations

$$\phi_x \;=\; \psi_y \;,\; \phi_y \;=\; -\psi_x \;.$$

The horizontal and vertical components of the velocity are found from the derivative

$$w \;=\; u - iv \;=\; d\zeta/dz$$

of ζ as an analytic function of the complex variable $z = x + iy$, and the pressure p is found from Bernoulli's law

$$\frac{q^2}{2} \;+\; \frac{p}{\rho} \;=\; \text{const.}\;,$$

where $q = |w|$ is the speed. Thus along any streamline $\psi = 0$ bordering a cavity we arrive at a free boundary condition of the form

$$p \;=\; \text{const.} \quad , \quad q \;=\; \text{const.}$$

In the Riabouchinsky model of cavitational flow the obstacle consists of two symmetrically located vertical plates joined by a pair of free streamlines. A solution is obtained by mapping the upper half of the ζ-plane conformally onto a semicircle in the hodograph plane slit along a segment of the u-axis. Another interesting method of finding the flow is to study the geometry of the analytic function

$$g(z) \;=\; \int \zeta'(z)^2 \, dz \;=\; \bar{z}\;,$$

Paper presented at the RTO AVT Lecture Series on "Supercavitating Flows", held at the von Kármán Institute (VKI) in Brussels, Belgium, 12-16 February 2001, and published in RTO EN-010.

which has boundary values indicated at the right along a free streamline where $q = 1$. This function has to do with the forces on the vertical plates and is suggested by the conservation of momentum. The solution of the Riabouchinsky free boundary value problem can be obtained by using the Schwarz-Christoffel formula to calculate the two auxiliary functions

$$\Phi(z) \;=\; z + g(z) \;,\; \Psi(z) \;=\; z - g(z) \;,$$

which map the flow conformally onto polygonal domains of the complex plane. These classical methods apply primarily to plane flow and play a significant role in the study of supercavitating hydrofoils. However, we do not discuss them in detail here, but turn our attention instead to three-dimensional flows such as occur in the study of torpedoes.

3. The principle of minimum virtual mass

Let us consider a flow of water past a body followed by a cavity Ω in three-dimmensional space. The velocity potential of the flow is a harmonic function ϕ whose normal derivative vanishes at the boundary, and at infinity it has an expansion of the form

$$\phi \;=\; x + \frac{ax}{r^3} + \ldots$$

with a coefficient a related to the virtual mass. On the free surface Γ bounding the cavity it satisfies the additional condition

$$(\nabla\phi)^2 \;=\; \text{const.}$$

because the pressure is constant there. The shape of the cavity has to be adjusted to meet this nonlinear free boundary condition, and that is what makes the problem hard mathematically.

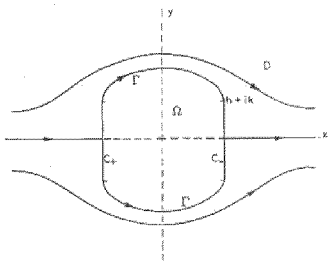


Figure 1: Geometry of the Riabouchinsky model of plane flow around a finite cavity Ω displaying the free stramlines Γ and two vertical fixed boundaries C.

The kinetic energy, or virtual mass,

$$M \;=\; \int\int\int (\nabla\phi - \nabla x)^2 \; dV$$

is a Dirichlet integral over the flow region. We also introduce the volume

$$V \;=\; \int\int\int \; dV \;,$$

which is an integral over the cavity and the body. An application of the divergence theorem leads to the remarkable formula

$$4\pi a \;=\; M + V$$

relating the virtual mass to the coefficient a in the expansion of the velocity potential at infinity.
We proceed to discuss variational formulas for a and V under a suitable hypothesis about smoothness at the boundary of the flow. Let us shift each point on the free surface by an infinitesimal distance

δn along its normal n. It is evident that the first order perturbation of the volume is given by the formula

$$\delta V \;=\; -\int\int \delta n \; dS \;,$$

where integration is performed over the free surface.
Next observe that according to the divergence theorem, the harmonic function ϕ minimizes the Dirichlet integral regardless of conditions at the boundary because its normal derivative vanishes there. It follows that the perturbation of the coefficient a under the shift δn can be computed with ϕ held fixed. Therefore we obtain an equally simply result

$$4\pi\delta a \;=\; -\int\int (\nabla\phi)^2 \delta n \; dS$$

giving the first variation of the virtual mass. This means that a flow satisfying the free boundary condition

$$(\nabla\phi)^2 \;=\; \lambda$$

can be found from the variational principle

$$4\pi\delta a - \lambda\delta V \;=\; 0 \;,$$

where λ is constant. The result is better stated in the form

$$M - \sigma V \;=\; \text{minimum}$$

of an extremal problem, where $\sigma = \lambda - 1$ is the cavitation parameter.
The theorem we have described, which we refer to as the principle of minimum virtual mass, makes sense only when the cavity is finite so the improper integrals that occur are convergent. This becomes the case for the Riabouchinsky model of cavitational flow. In that model two symmetrically situated plates C are connected by the free surface Γ of a cavity Ω. For plane flow the geometry is illustrated in Fig. 1. Note that the cavitation parameter σ is positive.
A physical interpretation of the variational formula for the virtual mass just states that work equals force times displacement. Details of a mathematical proof are easier to understand for the example of a vortex ring, which will come up again in our discussion of magnetohydrodynamics. Suppose ϕ is a harmonic function in a torus D with a unit period and a vanishing normal derivative, and let ϕ^* be the analogous function in a neighboring torus D^* obtained by a shift δn of the boundary. If M now stands for the Dirichlet integral of ϕ over D and M^* stands for the Dirichlet integral of ϕ^* over D^*, what we want to show is that

$$M^* - M \;=\; \int\int (\nabla\phi)^2 \delta n \; dS \;,$$

where higher order terms are neglected and the integration is performed over the surface of D. This is true because the Dirichlet integrals of ϕ^* and ϕ over D differ by a term of second order in δn. To see that we apply the divergence theorem to establish the identity

$$\int\int\int \nabla\phi \cdot (\nabla\phi^* - \nabla\phi) \; dV \;=\; \int\int \frac{\partial\phi}{\partial n}(\phi^* - \phi) \; dS - \int\int\int (\phi^* - \phi) \; \Delta\phi \; dV \;=\; 0 \;,$$

which asserts that because of the natural boundary condition satisfied by ϕ its Dirichlet integral over D is stationary. The desired result now follows because

$$(\nabla\phi + \nabla\phi^* - \nabla\phi)^2 \;=\; (\nabla\phi)^2 + 2\nabla\phi \cdot (\nabla\phi^* - \nabla\phi) + (\nabla\phi^* - \nabla\phi)^2 \;.$$

4. Calculation of the drag

For special shapes of the fixed boundary the principle of minimum virtual mass can be used to calculate the drag. In the Riaboucnsky model suppose that the free surface Γ is a sheath connecting a symmetric pair of circular disks situated in planes perpendicular to the x-axis. Let us magnify the whole configuration by the factor $1+\eta$, where η is a small positive number. For this infinitesimal normal displacement of the boundary of the flow our variational formulas yield the relation

$$\delta M - \sigma \delta V \;=\; \int\int [(\nabla\phi)^2 - \lambda]\delta n \; dS \; .$$

Along the free surface the integrand vanishes, so

$$\delta M - \sigma \delta V \;=\; \eta h \int\int [(\nabla\phi)^2 - \lambda] \; dS \; ,$$

where the integrals are now evaluated only over the disks, and $2h$ is the distance between them. On the other hand, by Bernoulli's law the integral

$$D \;=\; \frac{1}{2} \int\int [1 + \sigma - (\nabla\phi)^2] \; dS$$

over just one disk is the drag. Since V and M have the dimensions of length cubed, and since the shift δn is defined by a magnification, this establishes the remarkable relationship

$$4hD \;=\; 3(\sigma V - M)$$

between the virtual mass and the drag for Riabouchinsky flow past a circular disk.

If the formula we just established for the drag were generalized to the case of two parallel plates of elliptical cross section, then a continuous transition could be made from axially symmetric over to plane flow. It is not hard to see that invariance of the drag under changes of the eccentricity of the ellipse would then lead to a contradiction. We conclude that it is naive to assume that the symmetric model of Riabouchinsky flow always has solutions in three dimensions.

To compute the drag more generally one needs to solve the cavitational flow problem numerically. A systematic scheme to accomplish that is suggested by applying the concept of steepest descent to the principle of minimum virtual mass. This means that to improve on a given approximation of the free surface one should shift it along the normal by an amount δn proportional to the error $(\nabla\phi)^2 - \lambda$ in the free boundary condition. This concept has been implemented in computer codes that run quite succesfully. We shall discuss the matter in more detail when we describe an application to magnetic fusion in the next section.

Another attack on the drag problem has been developed using a stream function ψ which satisfies the partial differential equation

$$\Delta\psi - \frac{\epsilon}{y}\frac{\partial\psi}{\partial y} \;=\; 0$$

with $\epsilon = 0$ for plane flow and $\epsilon = 1$ for axially symmetric flow. For other values of ϵ the boundary value problem still makes sense, and it can be solved in closed form in special cases. That enables one to estimate the drag for a circular disk by interpolation from known values. For a circular disk with an infinite cavity the drag coefficient is found to be $C_D = 0.827$. Similarly, the contraction coefficient for a circular orifice in a plane wall is $C_c = 0.59$, a result differing from the answer obtained in the case of plane flow. Presently of course many more complicated free boundary problems are being investigated computationally by a variety of new methods.

5. Variational principle of magnetohydrodynamics

Another enlightening application of the variational principle plays an important role in the plasma physics of magnetic fusion. The concept of a thermonuclear reactor is based on fusion of hydrogen

at very high temperatures to form helium and release neutrons that penetrate a blanket which is heated up to supply power. The hydrogen is ionized to become a plasma so hot that it should not encounter material walls and must be confined by a magnetic field. The charged particles of the plasma tend to follow lines of force in the magnetic field, whose geometry is therefore usually chosen to be a torus. Most of the magnetic lines sweep out nested flux surfaces rather than ergodic regions so that the confinement of the plasma is adequate for fusion in a power plant. There is an analogy here with vortex rings and rotational flow of an incompressible fluid governed by the Euler equations. We shall review the mathematical theory of equilibrium and stability in magnetohydrodynamics that is required to address this problem.

We study the equilibrium and stability of a plasma by solving magnetostatic equations

$$\nabla \cdot \mathbf{B} \;=\; 0, \quad \mathbf{J} \times \mathbf{B} \;=\; \nabla p$$

analogous to the Euler equations, where $\mathbf{B}$ is the magnetic field, $\mathbf{J} = \nabla \times \mathbf{B}$ is the current density, and p is the pressure. In the analogy the velocity of the flow corresponds to the magnetic field and the stagnation enthalpy from Bernoulli's law corresponds to the pressure of the plasma. We shall explain our variational theory in the context of the plasma problem, which will show how islands whose flux surfaces are shaped like vortices can be modeled in practice by current sheets.

Let us rewrite the partial differential equations of magnetostatics in a conservation form

$$\nabla \cdot \mathbf{B} \;=\; 0, \quad \nabla \cdot \mathbf{T} \;=\; 0$$

involving the Maxwell stress tensor $\mathbf{T}$, which is given by

$$T_{jk} \;=\; B_j B_k - \delta_{jk}(B^2/2 + p) \;,$$

where δ_{jk} is the Kronecker delta. To avoid assuming the existence of partial derivatives, we apply the the divergence theorem and say that $\mathbf{B}$ and p define a weak solution of the equations whenever

$$\int\int\int \sum B_k \frac{\partial \psi}{\partial x_k} dV = 0 \;, \qquad \int\int\int \sum\sum T_{jk} \frac{\partial \psi_j}{\partial x_k} dV = 0$$

over any volume of integration, where ψ_1, ψ_2, ψ_3 and ψ are arbitrary continuously differentiable functions of compact support. The simplest example of a weak solution is a magnetic field with just one nontrivial component B_1 that is a nondifferentiable function of x_2 and x_3, while the pressure satisfies the condition $B_1^2/2 + p = \text{const}$.

These formulas are comparable to the conservation of mass

$$\sum \frac{\partial u_k}{\partial x_k} \;=\; 0$$

and the conservation of momemtum

$$\sum \frac{\partial}{\partial x_k}\, u_j u_k + \frac{\partial p}{\rho \partial x_j} \;=\; 0$$

for steady flow of an incompressible fluid without viscosity in hydrodynamics. Another application of the divergence theorem establishes that any smooth surface of discontinuity of a weak solution of the magnetostatic equations must be a current sheet in the sense that it is a flux surface of the magnetic field across which $\mathbf{B}$ may have jumps, but $B^2/2 + p$ remains continuous. It is our contention that small magnetic islands can be modeled computationally by such current sheets when a finite difference scheme with adequate numerical viscosity is applied. We use the variational principle of magnetohydrodynamics to show how this concept has been implemented in practice. The analogy with the problem of cavitational flow is evident.

The variational principle of magnetohydrodynamics enables one to study questions of toroidal equilibrium and stability in plasma physics by considering the extremal problem

$$\int\int\int [B^2/2 - p] dV = \text{minimum}$$

for the potential energy subject to appropriate flux constraints on the vector field $\mathbf{B}$, which is supposed to be divergence free. This leads in a natural way to the Clebsch representations

$$\mathbf{B} \;=\; \nabla s \times \nabla \theta$$

of $\mathbf{B}$ in terms of flux functions s and θ and potentials ϕ and ζ. We make a nested surface hypothesis under which s becomes the single-valued toroidal flux and p is a prescribed function of s. The flux function θ is multiple-valued on each torus $s = \text{const.}$, with periods related to the rotational transform $\iota = \iota(s)$, which measures how much a magnetic line turns in the poloidal direction during a complete circuit in the toroidal direction. For fully three-dimensional equilibria called stellarators no constraint is imposed on ι in the variational principle and the potential ϕ has no poloidal period, whereas for an axially symmetric tokamak ι is a prescribed function of the toroidal flux s and ϕ acquires a nontrivial poloidal period equal to the net current.

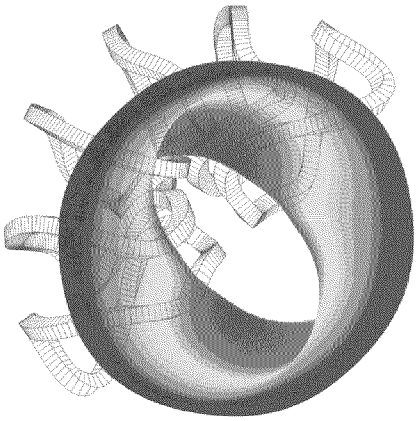


Figure 2: Computational model of fusion plasma in a thermonuclear reactor based on the stellarator concept for magnetic confinement of hot ions and electrons. Twelve moderately twisted modular coils, half of which are plotted, produce a magnetic field whose strength has a desirable symmetry displayed by the color map of the plasma surface.

Straightforward perturbations of the potential energy lead to variational equations that are equivalent to classical magnetostatics. Before a standard integration by parts they furnish a practical definition, essentially in conservation form, of what we mean by a weak solution without derivatives. For a stellarator at zero $\beta = 2\langle p \rangle / B^2$ the result reduces to Dirichlet's principle for harmonic functions, so the configuration is stable. The NSTAB computer code has been written to implement the variational principle of magnetohydrodynamics numerically and perform an analysis of nonlinear stability for positive β. It enables us to capture small magnetic islands in a convincing way when we use a mesh size for s larger than the island width.

In stellarators it is convenient to renormalize the multiple-valued flux function θ and the Clebsch potential ϕ so they become invariant poloidal and toroidal angles. If one then represents the magnetic field strength by a Fourier series of the form

$$\frac{1}{B^2} = \sum B_{mn} \cos(m\theta - [n - \iota m]\phi) \;,$$

the coefficients B_{mn}, which depend on the toroidal flux s, are known collectively as the magnetic spectrum. By solving the magnetostatic equations for J and taking a divergence we can show that there is a comparable expansion

$$\frac{\mathbf{J}\cdot\mathbf{B}}{B^2} = p' \sum \frac{mB_{mn}}{n-\iota m} \cos(m\theta - [n-\iota m]\phi)$$

for the parallel current, which is analogous to the swirl in fluid dynamics. In three dimensions the small denominators $n - \iota m$ are seen to vanish at a dense set of rational surfaces where $\iota = n/m$. Therefore smooth solutions of the equilibrium problem that have three-dimensional asymmetry do not in general exist, so that one should only try to construct weak solutions. Correspondingly, the only smooth vortex rings in steady flow must be axially symmetric.

The NSTAB code includes a remarkably robust calculation of the coefficients B_{mn}. In the spectral method that has been used it is helpful to filter the Fourier series defining the solution. This is especially true in the case of the parallel current, which requires evaluation of a divergent series. It turns out that many aspects of equilibrium, stability and transport just depend on the magnetic spectrum, together with the profiles of pressure and rotational transform. For tokamaks there is a two-dimensional symmetry such that only the column B_{m0} differs from zero, and similarly for straight two-dimensional stellarators only the diagonal B_{mm} is present. Because of their two-dimensional magnetic symmetry, these equilibria have excellent transport properties. The problem of design is to exploit this theory to arrive at configurations for a fusion reactor that meet a broad range of physics and engineering requirements.

6. Quasiaxially symmetric stellarators

Fast computer codes with a three-dimensional capability are an essential tool for the design of efficient stellarators. Here we shall discuss in some detail a stellarator called the Modular Helias-like Heliac 2 (MHH2) that has quasiaxial symmetry characterized by very small coefficients B_{mn} with $n \neq 0$. This was discovered recently by running the NSTAB code. It has just two field periods and the aspect ratio of the plasma is only 2.5. Transport is almost as good as that in a tokamak because of the comparable symmetry. Moderately twisted modular coils to generate the required magnetic field can be wound on a control surface surrounding the plasma, whose shape brings the total rotational transform into an acceptable range $0.5 \geq \iota \geq 0.4$. Ample space is available for the hardware requirements of a power plant (cf. Fig. 2).

We studied nonlinear stability of the MHH2 stellarator by looking for bifurcated equilibria over the full torus that do not have the helical symmetry of the solution with two field periods. The most dangerous mode we found running the NSTAB code has a complicated ballooning structure that is localized in an outer rim of the plasma. Equilibrium seems to impose a more severe limitation on β for the MHH2 than stability. Only for broad pressure profiles do good magnetic surfaces prevail when β is raised as high as 5%. Thus calculations by the NSTAB code used to invent the MHH2 establish that its equilibrium and stability limits on average β for a relatively broad pressure profile lie somewhere between 4% and 5%. The configuration is sufficiently robust to allow for further optimization. Less painstaking computations of linear or local stability that ignore the difficulties with parallel current at magnetic resonances give misleading predictions about performance. Numerical simulations built around the construction of weak solutions seem to be the best that mathematical theory can contribute to the problem of design in this situation.

Acknowledgments

We wish to express our appreciation for helpful discussions with Frances Bauer and Marshall Tulin. This work has been supported by the United States Department of Energy under Grant DE-FG02-86ER53223.

References

1. Bauer, F., Betancourt, O. and Garabedian, P., *A Computational Method in Plasma Physics,* Springer-Verlag, New York, 1978.

2. Garabedian, P., *Calculation of axially symmetric cavites and jets,* Pacific J. Math. 6, 1956, pp. 611-684.

3. Garabedian, P., *Nonparametric solution of the Euler equations for steady flow,* Comm. Pure Appl. Math. 36, 1983, pp. 529-535.

4. Garabedian, P., *Stellarators with the magnetic symmetry of a tokamak,* Phys. Plasmas 3, 1996, pp. 2483-2485.

5. Garabedian, P., *Partial Differential Equations,* AMS Chelsea, Providence, 1998.

6. Garabedian, P. and Schiffer, M., *Convexity of domain functionals,* J. Anal. Math. 2, 1953, pp. 281-368.

7. Garabedian, P., and Spencer, D., *Extremal methods in cavitational flow,* J. Ratl. Mech. Anal. 1, 1952, pp. 359-409.

8. Riabouchinsky, D., *Sur un probleme de variation,* C. R. Acad. Sci. Paris 185, 1927, pp. 840-841.

9. Taylor, M., *A high performance spectral code for nonlinear MHD stability,* J. Comp. Phys. 110, 1994, pp. 407-418.

10. Tulin, M., *Supercavitating flows - small perturbation theory,* J. Ship Research 7, 1964.

The Principle of Independence of the Cavity Sections Expansion (Logvinovich's Principle) as the Basis for Investigation on Cavitation Flows

A. D. Vasin

State SRC TsAGI, Moscow, Russia
17, Radio str., Moscow, Russia

Summary

For the investigation of complex non-steady cavitation flows in three dimensions it is extremely important to find a simple model which on one hand would correspond to the basic laws of a fluid stream (the laws of conservation of energy and momentum) and on the other hand would be simple enough for the numerical calculation. This model was presented by G. V. Logvinovich, and was called "The Principle of Independence of the Cavity Sections Expansion". In the present lecture the deduction of the principle of independence from the equation of conservation of energy is adduced. It is shown that for the stationary cavities the results obtained on the basis of the principle of independence agree with the results obtained on the basis of the slender body theory and the numerical methods as well as with the experimental data. It is shown that for the special case - the cavitation number equals zero - the cavity shape determined on the basis of the principle of independence agrees with the well-known Levinson-Gurevich asymptotic. The application of the principle of independence for the calculation of some types of the non-stationary cavities and cavities with variable external pressure (the vertical cavities in the gravitational field) is considered.

Introduction

In the case of high-speed motion in water, cavities filled with gas or vapor are formed behind the body-cavitator. The mathematical problem on the determination of the cavity shape is stated as the inverse problem on the flow around a body – the free boundary shape is found from the constant pressure condition. In case of the non-stationary cavities, the cavities with variable external pressure along their length or the asymmetrical cavities, the problem on the determination of the cavity shape becomes extremely complex. For the practical problems it is very important to have a simple method of calculation of non-stationary cavitation flows that corresponds with the basic laws of a fluid stream. Such a method was suggested by Logvinovich and was called "The Principle of Independence of the Cavity Sections Expansion".

The principle of independence is stated as following. Each cross section of a cavity expands relatively to the trajectory of the center of a cavitator which happens almost independently from the following or the previous body motion. The expansion occurs according to the definite law which is dependent only upon the difference between the pressure at infinity and the pressure within the cavity, the speed, the size, and the drag of a body at the moment when a body passes the plane of the considered section [1]. The law of expansion of the cavity fixed section can be determined using the principle of conservation of energy in the wake. The thin cavity in ideal fluid can be considered as the wake. Each unit of the wake length keeps the energy which was expended by the cavitator at the moment when it passes this unit of the length of the trajectory [2,3]. This theory applied to the cavity with the constant difference of pressures gives results which are very similar to the results observed in the experiments. Therefore, we can suggest that this theory is also applicable for the case of variable difference of pressures.

Paper presented at the RTO AVT Lecture Series on "Supercavitating Flows", held at the von Kármán Institute (VKI) in Brussels, Belgium, 12-16 February 2001, and published in RTO EN-010.

1. The Deduction of the Principle of Independence from the Equation of Conservation of Energy

We designate the coordinate along the arc of the trajectory of the cavitator center as h (Fig. 1). This coordinate is fixed relatively to the motionless fluid. At the point h let us draw the plane Σ that is perpendicular to the trajectory. We will observe the development of the cavity cross section arisen on this plane at the moment t=0.

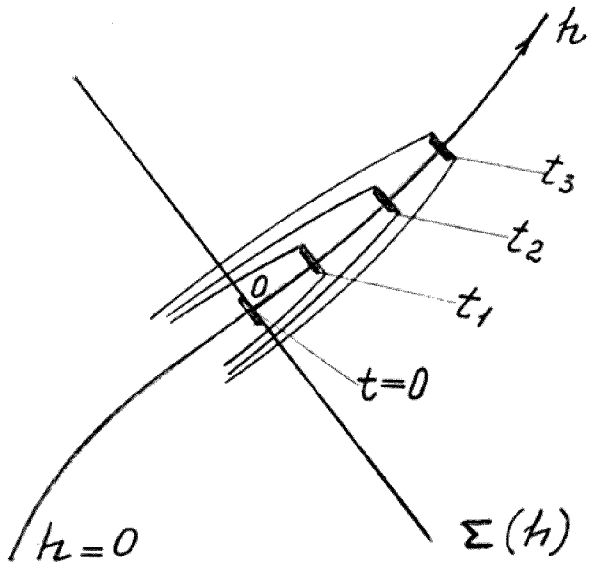


Fig. 1 The scheme of development of the non-stationary cavity

Let us introduce the following designations: the radius of the cavity section $R=R(h,t)$, the area of the cavity section $S(h,t)=\pi R^2$, the pressure within the cavity $P_k=P_k(h,t)$, the pressure at infinity $P_\infty(h,t)$. We can consider the pressure $P_\infty(h,t)$ to be the pressure at the point "0" of the intersection of the trajectory with the plane Σ when the cavity is absent or to be the hydrostatic pressure on the depth of the point '0'.

The cavitator passing the path Δh performs certain work and gives the energy $W\Delta h$ to the fluid (where W is the drag force acting on the cavitator at the moment t=0). Proceeding from the physical scheme of the flow we can accept that approximately the energy $W\Delta h$ is conserved in the considered section at the same segment Δh in the form of the kinetic energy $T\Delta h$ и potential energy $E\Delta h$ up to the moment of this section closure. Therefore, we can write an approximate equation for each cavity cross section

$$T(h,t)+E(h,t)=W(h,0) \tag{1.1}$$

Equation (1.1) can be applied to the whole cavity length and signifies that the energy that was imparted by the cavitator at the point of the trajectory h is conserved on the cavity at this point. Proceeding from the first Green's formula [4] we can express the kinetic energy that fits the unit of the cavity length by the following equation

$$T = -\frac{1}{2}\rho\varphi\, 2\pi R\,\frac{\partial\varphi}{\partial n} \tag{1.2}$$

where φ is the potential of the absolute velocity at the boundary, R and $\dot{R} \approx \partial\varphi / \partial n$ are the radius and the radial velocity of cavity boundary at the point of the trajectory h, ρ is the fluid density.

The potential energy of a cavity section is determined as follows

$$E = \int_o^t \Delta P\,(h, t)\, 2\pi R \dot{R}\, dt \tag{1.3}$$

where $\Delta P(h,t) = P_\infty(h,t) - P_k(h,t)$. After substitution of (1.2) and (1.3) in (1.1) we obtain an approximate equation of energy

$$-\frac{1}{2}\rho\varphi\dot{S} + \int_o^t \Delta P(h,t)\dot{S}dt = W(h,0) \tag{1.4}$$

where $\dot{S} = 2\pi R\dot{R}$ is the time derivative of the area of a cavity cross section.

The kinetic energy is determined along the stream tubes that lean on the expanding cavity hole in the motionless plane. The trajectory of a cavitator intersects this plane along normal at the point h. The dynamic boundary condition is written in a form of the general Bernoulli equation applied to the points of space that coincide with the cavity boundary at the considered moment (later on we will be writing ΔP instead of $\Delta P(h,t)$)

$$\frac{\partial\varphi}{\partial t} + \frac{v^2}{2} = \frac{\Delta P}{\rho} \tag{1.5}$$

where v is the absolute velocity of the fluid particles on the cavity boundary. In the middle section of the cavity $v \approx \dot{R}$ is the small quantity and we neglect the value of v^2 compared to the value of $\Delta P/\rho$. Then equation (1.5) is written in the form

$$\frac{\partial\varphi}{\partial t} = \frac{\Delta P}{\rho} \tag{1.6}$$

Let us differentiate equation (1.4) with respect to t and using expression (1.6) we obtain

$$\varphi\ddot{S} = \frac{\Delta P}{\rho}\dot{S} \tag{1.7}$$

From equation (1.6) the value of the potential on the cavity section boundary is determined as follows

$$\varphi = \varphi_n + \int_o^t \frac{\Delta P}{\rho} dt \tag{1.8}$$

where φ_n is the value of the potential at the edge of a cavitator at the moment of generation of the cavity section *(t*=0*)*. After substitution of (1.8) in (1.7) we obtain the following differential equation

$$\left[\rho\varphi_n + \int_o^t \Delta P dt \right] \ddot{S} = \Delta P \dot{S} \tag{1.9}$$

Taking into account that $d\int_o^t \Delta P dt = \Delta P dt$, as a result of dividing variables and integrating we obtain

$$\dot{S} = A\left[\rho\varphi_n + \int_o^t \Delta P dt \right] \tag{1.10}$$

where A is the constant connected with the initial velocity of expansion of the cavity section by dependence $A = \dot{S}_o / \rho\varphi_n$; $\dot{S}_o$ is the initial velocity of expansion. As a result equation (1.10) is represented in the following form

$$\dot{S} = \dot{S}_o \left[1 + \frac{1}{\varphi_n} \int_o^t \frac{\Delta P}{\rho} dt \right] \tag{1.11}$$

The value of the potential at the edge of a cavitator we can write as following: $\varphi_n = -\frac{1}{2} a R_n V(0)$, where a is some constant, R_n is the radius of a cavitator, *V(0)* is the velocity of a cavitator at the moment t=0. Since for the stationary cavity the flow is symmetrical the value of the potential on the mid-section equals zero, consequently for the stationary cavity equation (1.8) can be written in the following form

$$\varphi_n = -\int_o^{t_k} \frac{\Delta P}{\rho} dt = -\frac{\Delta P}{\rho} t_k = -\frac{1}{2} a R_n V(0) \tag{1.12}$$

where t_k is the time of expansion of a cavity section to the maximum size. In case of the stationary cavity we can obtain the expression of the constant a from equation (1.12)

$$a = \frac{\sigma L_k}{2R_n} \tag{1.13}$$

where $\sigma = \frac{2\Delta P}{\rho V^2}$ is the cavitation number, V is the velocity of stationary motion of a cavitator, $L_k = 2Vt_k$ is the cavity length. Let us determine the initial velocity of expansion $\dot{S}_o$ from the equation of energy (1.4) at the moment t=0. Taking into account that $W = C_x \pi R_n^2 \frac{\rho V^2(0)}{2}$, where C_x is the drag coefficient of a cavitator we obtain

$$\dot{S}_o = \frac{2\pi C_x R_n V(0)}{a}, k = -\frac{\dot{S}_o}{\varphi_n} = \frac{4\pi C_x}{a^2} \tag{1.14}$$

As a result we go on from equations (1.11) and (1.14) to the well-known mathematical entry expressing the principle of independence of the cavity sections expansion in the form of

$$\ddot{S} = -\frac{k\Delta P}{\rho} \tag{1.15}$$

Equation (1.15) with the coefficient (1.14) (the constant a is slightly dependent on the cavitation number and its value is selected from the range 1.5÷2) is widely applied for the investigation of non-stationary cavities and cavities with variable external pressure along their length. The velocity of expansion of a cavity section is determined from equation (1.11)

$$\dot{S} = \dot{S}_o - k\int_o^t \frac{\Delta P}{\rho} dt \tag{1.16}$$

Integrating equation (1.16) we obtain the dependence of the area of a cavity section on time

$$S = S_0 + \dot{S}_0 t - k\int_0^t \int_0^t \frac{\Delta P}{\rho} dt dt \tag{1.17}$$

where S_0 is the initial area of a cavity cross section. In particular for the stationary cavity the value $\frac{\Delta P}{\rho}$ is constant and from (1.17), (1.14) and (1.13) we obtain the well-known result

$$\frac{S - S_0}{S_k - S_0} = \frac{t}{t_k}\left(2 - \frac{t}{t_k}\right) \tag{1.18}$$

where S_k is the maximum quantity of the area of a cavity cross section (the area of the mid-section).

If as the quantity S_0 we choose the quantity of the area of the cross section on which the incline of a cavity boundary is sufficiently small (slightly deviating from a disk-cavitator), then the calculations from formula (1.18) agree very well with the experimental data as shown in Fig. 2 (in this figure the points show the experimental data for the different cavitation numbers).

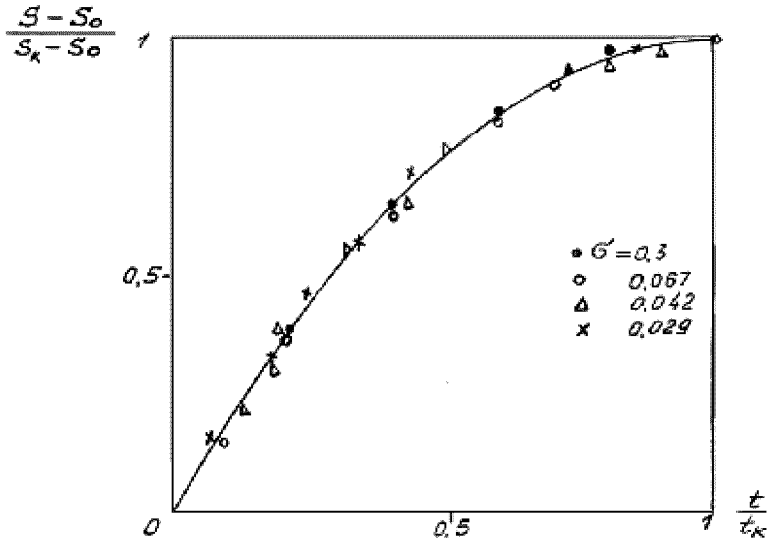


Fig. 2 The comparison of the stationary cavity profile obtained on the basis of the principle of independence with the experimental data

Usually the profile of the stationary cavity past a disk is constructed as follows. In the vicinity of the disk the cavity shape is not dependent on the cavitation number and can be expressed in the form [1]

$$R(x) = R_n\left(1 + \frac{3x}{R_n}\right)^{1/3} \tag{1.19}$$

where x is the coordinate measured along the axis of symmetry from the center of a disk. The cavity shape determined from equation (1.18) joins with the shape expressed by the dependence $R(x)$ (1.19). We can consider the point with the coordinates: $x=2R_n$, $R(x)=1.92R_n$ to be the point of contact.

2. The comparison of the results obtained for stationary cavitation flows on the basis of the principle of independence with the results obtained on the basis of the slender body theory and the numerical methods

In this chapter we will demonstrate that the shape of the stationary cavity represented by expression (1.18) can be obtained from the slender body theory. As an example we use the cavitation flow past a thin cone. Let us consider a more general case - the supercavity past a thin cone in subsonic compressible fluid flow. We apply the Riabouchinsky scheme (Fig. 3, the cavity is closed by a body with the same dimensions as the caivtator).

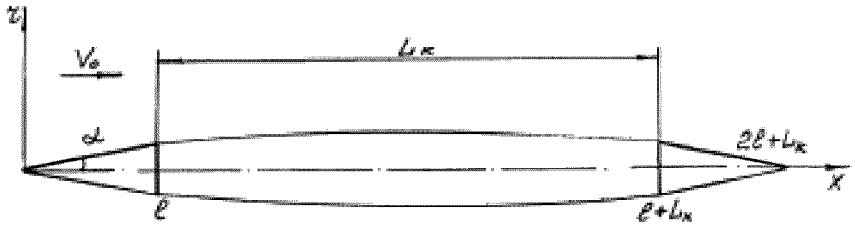


Fig. 3 The Riabouchinsky scheme for the cavitation flow past a thin cone

The origin of the orthogonal system x, r is placed at the apex of the cone, the geometric dimensions are scaled by the radius of the cone base (the radius of the cone base R_n equals unity, l is the altitude of the cone, α is the apex half-angle, L_k is the cavity length, $l+L_k$ and $2l+L_k$ are the coordinates of the base and the apex of the closing cone respectively, $L=2l+L_k$ is the total length).

Let us apply the linearized equation of the flow in the cylindrical coordinate system [5]

$$\left(1-M^2\right)\frac{\partial^2\Phi}{\partial x^2}+\frac{\partial^2\Phi}{\partial r^2}+\frac{1}{r}\frac{\partial\Phi}{\partial r}=0 \qquad (2.1)$$

where $\Phi=\Phi^*/V_0R_n$ is the dimensionless flow velocity potential,

Φ^* is the flow velocity potential,

V_0 is the free stream velocity,

$M=V_0/a_0$ is the Mach number,

a_0 is the free stream speed of sound

We assume that the parameter of the cavity thinness has the same order as the parameter of the cone-cavitator thinness. The parameter of thinness ε equals the ratio of the cone radius to its altitude $(\varepsilon=1/l=tg\alpha)$. Let us represent the potential Φ in the following way: $\Phi=\varphi+x$, where φ is the dimensionless perturbed velocity potential which is aimed at zero when x and r are aimed at infinity. The dynamical boundary condition on the cavity surface is written as follows [6,7] (we neglect the members that have the order of trifle exceeding $\varepsilon^4 ln^2\varepsilon$)

$$2\frac{\partial\varphi}{\partial x}+\left(\frac{\partial\varphi}{\partial r}\right)^2=\sigma \qquad (2.2)$$

For the slender axisymmetrical bodies the perturbed velocity potential is defined by the method of sources and sinks distributed along the axis of symmetry. For the subsonic flow the potential φ satisfying the equation (2.1) has the form [5]

$$\varphi = -\frac{1}{4\pi}\int_0^L \frac{q(x_1)dx_1}{\sqrt{(x-x_1)^2 + (1-M^2)r^2}} \tag{2.3}$$

where $q(x_1)$ is the intensity of sources and sinks on the axis of symmetry. Near the axis of symmetry the perturbed velocity potential is represented by the following asymptotic equation [6,7]

$$\varphi = \frac{1}{2\pi} S'(x)\ln r + g(x) \tag{2.4}$$

where $S'(x)$ is the derivative of the dimensionless area of the slender body cross section with respect to x coordinate.

The logarithmic potential is the main part of expression (2.4), and some function $g(x)$ is added to it. The function $g(x)$ is determined from the condition of matching with the potential of the distributed sources (2.3) since the logarithmic potential does not satisfy the condition at infinity. Also, the function $g(x)$ takes into account the influence of compressibility. After substitution $g(x)$ we obtain the following expression for the perturbed velocity potential near the surface of the body and the cavity [7]

$$\varphi = \frac{1}{4\pi} S'(x)\ln\frac{(1-M^2)r^2}{4x(L-x)} - \frac{1}{4\pi}\int_0^L \frac{S'(x_1)-S'(x)}{|x-x_1|}dx_1 \tag{2.5}$$

Substituting equation (2.5) in (2.2) we obtain the integro-differential equation for the cavity profile [8]

$$\frac{u'^2}{2u} + u''\ln\frac{(1-M^2)u}{4x(L-x)} - \int_0^l \frac{u_1''(x_1)-u''(x)}{|x-x_1|}dx_1 -$$

$$-\int_l^{l+L_k} \frac{u''(x_1)-u''(x)}{|x-x_1|}dx_1 - \int_{l+L_k}^{L} \frac{u_1''(x_1)-u''(x)}{|x-x_1|}dx_1 = 2\sigma \tag{2.6}$$

$$u = R^2, u_1 = R_1^2, u_1'(0) = 0, u_1'(L) = 0$$

The cavity profile is determined by altering its radius along the coordinate x: $R(x)$. Along the coordinate x the radius R_1 of the cone-cavitator and the closing cone respectively change to $R_1=\varepsilon x$ and $R_1=\varepsilon(L-x)$. The following boundary conditions are added to the integro-differential equation (2.6)

$$x = l : R = 1, R' = \varepsilon$$
$$x = l + L_k : R = 1, R' = -\varepsilon$$

We seek the solution for the whole area of the cavity by expanding the asymptotic rows with the small parameter ε.

$$R^2 = \varepsilon^2\left[R_0^2 + R_{-1}^2\left(\ln\frac{1}{\varepsilon^2}\right)^{-1} + R_{-2}^2\left(\ln\frac{1}{\varepsilon^2}\right)^{-2} + \ldots\right]$$
$$\sigma = \varepsilon^2\left[\sigma_1\left(\ln\frac{1}{\varepsilon^2}\right) + \sigma_0 + \sigma_{-1}\left(\ln\frac{1}{\varepsilon^2}\right)^{-1} + \ldots\right] \qquad (2.7)$$

After substitution of the rows (2.7) into (2.6) and conservation of the two members of the rows the integro-differential equation (2.6) is transformed to two differential equations. The first equation is obtained from the equality of the members at $\varepsilon^4 ln1/\varepsilon^2$, the second one follows from the equality of the members at ε^4. The first differential equation with the boundary conditions is written as follows

$$\frac{d^2R_0^2}{dx^2} = -2\sigma_1$$
$$R_0^2(l) = l^2, R_0^2(l + L_k) = l^2, \frac{dR_0^2}{dx}\Big|_{x=l} = 2l \qquad (2.8)$$

The solution of the equation (2.8) has the form

$$R_0^2 = \sigma_1(a-x)(x-b)$$
$$\sigma_1 = \frac{2l}{L_k}, a = \frac{L}{2} + \sqrt{\frac{L^2}{4} - \frac{lL}{2}}, b = \frac{L}{2} - \sqrt{\frac{L^2}{4} - \frac{lL}{2}} \qquad (2.9)$$

After reduction of equations (2.7) and (2.9) to the dimensional form and some transformations the first approximation of the cavity shape is written as follows

$$R^2 = \frac{2R_n^2}{lL_k}\left(-x^2 + xL - \frac{lL}{2}\right) \qquad (2.10)$$

If we transfer the origin of the coordinate system from the apex of the cone to its base then the cavity profile takes the form of

$$R^2 = \frac{2R_n^2}{lL_k}\left(-x^2 + xL_k + \frac{lL_k}{2}\right) \tag{2.11}$$

For the stationary cavity we can write the coordinate x and the length L_k as following: $x = V_0 t, L_k = 2V_0 t_k$, where t is the time. Substituting x and L_k in (2.11) and taking into account that when $t=t_k$ the equality $R=R_k$ is satisfied, where R_k is the cavity mid-section radius, we obtain the following equation

$$\frac{R^2 - R_n^2}{R_k^2 - R_n^2} = \frac{t}{t_k}\left(2 - \frac{t}{t_k}\right) \tag{2.12}$$

Equation (2.12) corresponds with equation (1.18) if $S_0 = \pi R_n^2$. Thus, the principle of independence of the cavity sections expansion and the slender body theory give the same result - we can consider an ellipsoid of revolution to be the first approximation of the shape of the stationary cavity. Taking into account that the first approximation is obtained for the compressible fluid we can draw a more general conclusion – the principle of independence of the cavity sections expansion is satisfied in the subsonic flow of the compressible fluid. For the case of the non-stationary cavities in the incompressible fluid the conclusion of the principle of independence from the slender body theory has been performed in [9] where the so-called "circular model" was applied.

Let us consider the results obtained for the stationary cavities by the numerical methods. We can divide the numerical methods into three groups. The first group can be called 'the boundary integral equation method'. In this method the stream function is applied and the surfaces of a cavity and a cavitator are represented by the vortex layer. The cavitation flow is found with the help of the numerical solution of the vortex layer integral equations [10,11,12]. The boundary element method based on the Green's integral is related to the second group. In this method on the cavitator surface the sought function is the perturbed velocity potential; on the cavity surface the sought function is the normal derivative of the perturbed velocity potential [13,14]. The finite-difference method represents the third group [15,16].

The published works on the numerical calculations of the stationary cavitation flows contain the results on the cavitation drag coefficient of a cavitator, the cavity mid-section radius and the cavity length. In these works the difference in the results of the numerical calculations does not exceed several percent. The numerical calculations have shown that the stationary cavity shape is close to an ellipsoid of revolution for the cavitation numbers that have the order $10^{-2} \div 10^{-1}$. This result agrees with the principle of independence of the cavity sections expansion.

As an example, let us consider the results of the numerical calculations obtained by the author [16]. Using the finite-difference method the author has calculated the cavities past a disk in the subsonic flow of the compressible fluid. The Riabouchinsky scheme was applied and the Mach numbers were located on the range $0 \le M \le 0.95$. The numerical calculation has shown that on the whole range of the Mach numbers the cavity profile is close to an ellipsoid of revolution which is represented by the equation (1.18). An ellipsoid joins with the cavity profile in the vicinity of the disk; as the point of contact we can take the point with the coordinates: $x=2R_n$, $R=2\ R_n$. Figure 4 illustrates the cavity profile in the vicinity of the disk (the geometric dimensions are scaled by the radius of the disk R_n).

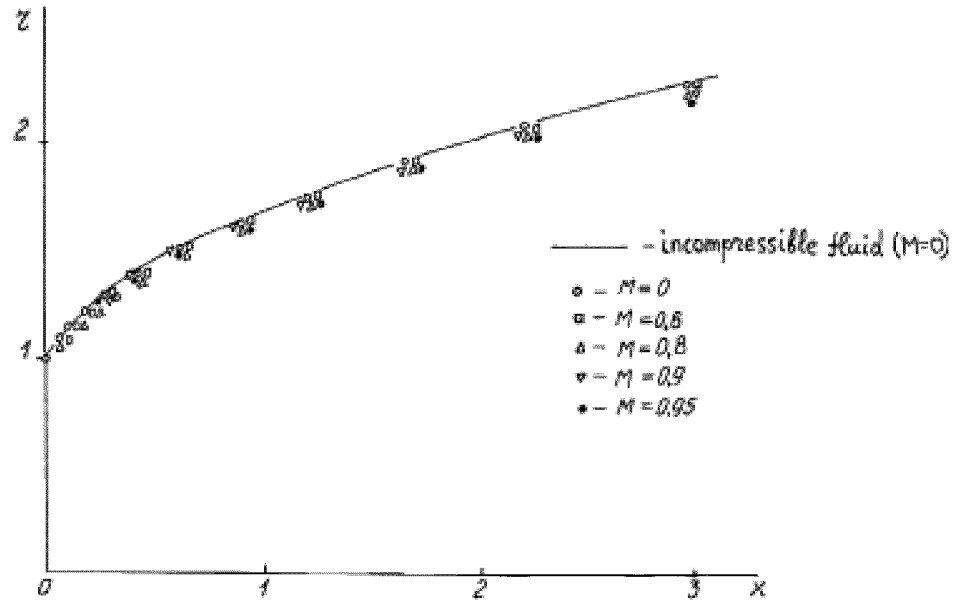


Fig. 4 The front of the caivty

In Fig. 4 the continuous curve represents the result of the numerical calculation by the boundary integral equation method for the incompressible fluid [10], the author's numerical results in the subsonic flow for the different Mach numbers are shown by the points [16]. Figure 5 shows the cavity profiles in the compressible fluid (M=0.8) and in the incompressible fluid (M=0) for the same cavitation number σ=0.0235 [16].

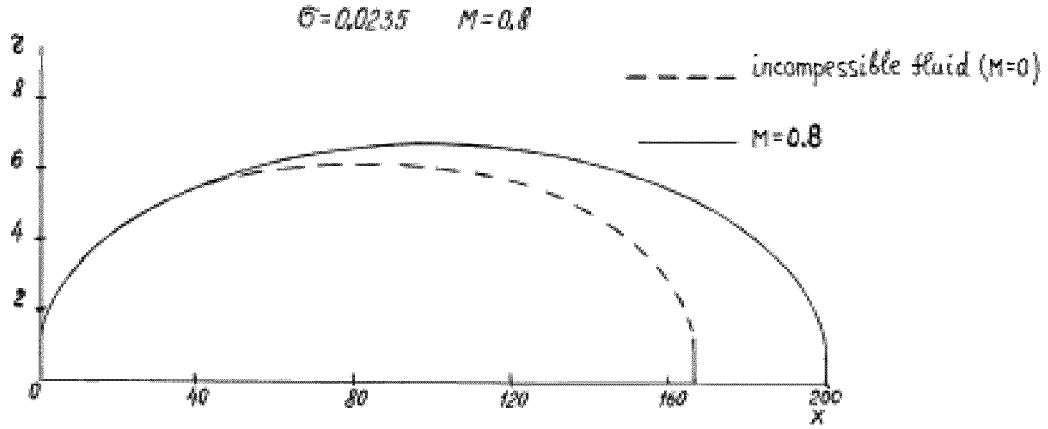


Fig. 5 Cavity profile

Both of the cavity profiles are close to an ellipsoid of revolution. The dimensions of an ellipsoid for M=0.8 exceed the analogous dimensions for M=0 since the cavitation drag coefficient for M=0.8 exceeds that for M=0.

3. The application of the equation of conservation of energy for determining the stationary cavity shape at $\sigma \to 0$

The equation of conservation of energy on the given cavity section (1.1) is equivalent to the principle of independence of the cavity sections expansion since all the three quantities that construct equation (1.1) are independent from both the following and the previous cavitator motion. The sum of the kinetic and potential energies on the section Σ (Fig. 1) is determined by the value of the cavitator drag W at the moment when a cavitator passes the section Σ. The law of the cavity section expansion (1.15) obtained from the energy equation (1.1) is independent from the following and the previous cavitator motion. This law represents the principle of independence. It should be noted that the energy equation similar to equation (1.1) was applied in [17] in order to estimate the axisymmetric cavity shape. However, in [17] the kinetic energy in the wake was determined for the radial flow on the plane circular layer. In chapter 1 in contrast to [17] the kinetic energy (formula (1.2)) is determined along the stream tube leaning on the expanding cavity hole.

The principle of independence is some approximation to the reality. However, a large number of experiments have confirmed its accuracy for both the stationary and non-stationary cavities. The principle of independence agrees with the results obtained from the slender body theory for the stationary and non-stationary cavitation flows. Furthermore, the calculation results of the stationary cavities using the numerical methods show that the cavity shape is close to an ellipsoid of revolution for the cavitation number that have the order $10^{-2} \div 10^{-1}$. Also, the ellipsoidal form of the stationary cavity has been obtained from the principle of independence as we neglect the value of $v^2/2$ compared to the value of $\Delta P/\rho$ in equation (1.5). Let us prove that the principle of independence of the cavity sections expansion or the energy equation (1.1) are applicable for the special case. That is the cavitation number is equal to zero (the infinite cavity length).

When the cavitation number equals to zero then $\Delta \mathrm{P} = P_\infty - P_k = 0$ and the potential energy in the wake E (equation (1.1)) also equals zero. The kinetic energy in the wake is determined by formula (1.2). Let us determine the quantities of the velocities on the cavity surface at the zero cavitation number (Fig. 6).

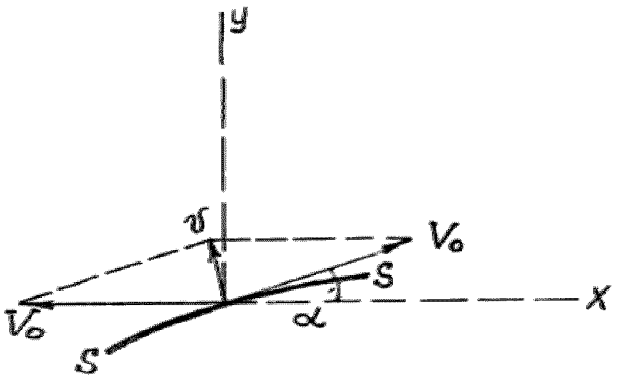


Fig. 6 The absolute velocity of the fluid particle on the cavity surface at σ=0

The absolute velocity of the fluid particles on the cavity surface v is determined as the vector sum of the transport velocity V_0 directed along the x axis and the relative velocity directed along the tangent to the cavity surface (for the zero cavitation number the relative velocity is equal to V_0). In Fig. 6 the section of

the cavity surface is designated as s-s. From Fig. 6 we obtain the following correlations for the velocity components.

$$v = 2V_0 \sin\frac{\alpha}{2}, \quad v_y = \dot{R} = V_0 \sin\alpha, \quad v_n = \frac{\partial\varphi}{\partial n} = V_0 \sin\alpha$$
$$v_n = v_y = \dot{R}, \quad v \approx \dot{R} \tag{3.1}$$

where α is the angle of inclination of the cavity surface to x axis. Correlations (3.1) are approximately satisfied for the small cavitation numbers different from zero. They were used in chapter 1. For the zero cavitation number the energy equation (1.1) we can write in the following form (taking into account equation (1.2) and correlations (3.1))

$$-\rho\varphi\pi R\dot{R} = W \tag{3.2}$$

Let us substitute φ from equation (3.2) in the boundary condition (1.5). We assume that the approximate equality $v \approx \dot{R}$ is satisfied as α is a small quantity (correlations (3.1)). As a result we obtain the equation

$$-\frac{W}{\pi\rho}\frac{d}{dt}\left(\frac{1}{R\dot{R}}\right) + \frac{\dot{R}^2}{2} = 0 \tag{3.3}$$

The first integral of the differential equation (3.3) has the form [1]

$$\dot{R} = \frac{1}{R}\sqrt{\frac{W}{\pi\rho(\ln R / R_n + A)}} \tag{3.4}$$

where A is some constant.

For the stationary cavity the equality $dx=Vdt$ is satisfied. Let us introduce the following designations: $x^*=x/R_n$, $R^*=R/R_n$. Equation (3.4) is written as follows

$$\frac{dR^*}{dx^*} = \sqrt{\frac{C_x}{2}}\frac{1}{R^*\sqrt{\ln R^* + A}} \tag{3.5}$$

Let us join the cavity profile (3.5) with the cavity profile in the vicinity of the disk (1.19). As the point of contact we take the point with the coordinates $x^*=2$, $R^*=1.92$. At the point of contact we determine the derivative dR^*/dx^* from equation (1.19) and substitute it in equation (3.5). As a result we determine the constant A. According to the data presented in [1] the constant A equals 0.845. We obtain the cavity profile from equation (3.5) in the form of

$$x^* = 2 + \sqrt{\frac{2}{C_x}}\int_{\sqrt[3]{7}}^{R^*} u\sqrt{\ln u + A}\,du \tag{3.6}$$

where u is the variable of integration. The asymptotic law of the axisymmetric cavity expansion has been obtained for the zero cavitation number in [18,19]. This law can be presented as follows

$$R^* \sim \sqrt[4]{4C_x}\,\frac{\sqrt{x^*}}{\sqrt[4]{\ln x^*}} \tag{3.7}$$

In [20] the law of the cavity expansion was generalized for the case of subsonic compressible fluid flow. In [20] it is shown that equation (3.7) has the same form for both incompressible and compressible fluid. The compressibility exerts influence on the law of the cavity expansion by means of the drag coefficient C_x, which is dependent upon the Mach number.

Let us compare the cavity profiles past a disk in incompressible fluid for the zero cavitation number (C_x=0.82). We compare the profile obtained from the law of conservation of energy in the wake (equation (3.6)) with the profile expressed by the asymptotic law (3.7). The results of this comparison are shown in the table.

TABLE

x^*	R^* eq. (3.7)	R^* eq. (3.6)
5	2.67	2.59
10	3.45	3.36
25	5.02	4.90
50	6.77	6.63
100	9.19	9.03
250	13.88	13.70
500	19.06	18.86
1000	26.25	26.04
1500	31.69	31.48

It is evident from the table that the difference in the cavity profiles does not exceed several percent. We can conclude here that for the zero cavitation number the results obtained based on the energy equation in the wake (the principle of independence) agree with the well-known Levinson-Gurevich asymptotic (3.7).

In chapters 1 and 3 we have determined the cavitation profiles based on the energy equation (the principle of independence) and have applied the dynamical boundary condition (1.5) for two cases:

1. when we can neglect the value of $v^2/2$ compared to the value of $\Delta P/\rho$ in the middle section of the cavity
2. when the value ΔP equals zero (the zero cavitation number).

In the first case the cavity shape agrees with the experimental data and the theoretical results for the cavitation numbers that have the order $10^{-2} \div 10^{-1}$. In the second case the cavity shape agrees with the Levinson-Gurevich asymptotic at $\sigma=0$. Thus, we do not investigate the cavities on the range $0<\sigma<0.005$. Let us extend the application of the principle of independence to this range of the cavitation numbers.

Recently G. V. Logvinovich has considered the general case – two members $v^2/2$ and $\Delta P/\rho$ are taken into account in the dynamical boundary condition (1.5) [21]. Let us determine the stationary cavity shape for this case. The potential energy is defined as $E=\pi R^2 \Delta P$ and equation (1.4) is written in the following form

$$-\rho\varphi\pi R\dot{R} + \pi R^2 \Delta \mathrm{P} = W \tag{3.8}$$

After substitution of φ from equation (3.8) into the dynamical boundary condition (1.5) using the approximate equality $v \approx \dot{R}$ we obtain the following equation

$$-\frac{W}{\pi\rho}\frac{d}{dt}\left(\frac{1}{R\dot{R}}\right)+\frac{\Delta \mathrm{P}}{\rho}\frac{d}{dt}\left(\frac{R}{\dot{R}}\right)=\frac{\Delta \mathrm{P}}{\rho}-\frac{\dot{R}^2}{2} \tag{3.9}$$

As a result of the transformations the first integral of differential equation (3.9) for the stationary cavity can be written as follows [21]

$$\frac{dR^*}{dx^*}=\sqrt{\frac{C_x}{2}}\frac{1}{R^*}\sqrt{\frac{1-\sigma R^{*2}/C_x}{\ln R^*+A}} \tag{3.10}$$

At $\sigma=0$ differential equation (3.10) is transformed to equation (3.5). Using equation (3.10) the cavity profiles were calculated for the wide range of cavitation numbers [21]. For the cavitation numbers that have the order 10^{-2} the calculations on the basis of equation (3.10) have shown that the cavity shape is close to an ellipsoid of revolution. This result agrees with the well-known experimental and theoretical results.

Thus, on the basis of the carried out investigations we can conclude that the principle of independence of the cavity sections expansion deduced from the equation of conservation of energy in the wake is applicable to the wide range of the cavitation numbers $0 \le \sigma \le 0.1$. On this range the stationary cavity profiles can be calculated by the single formula (3.10).

4. The calculations of the cavities in the gravitational field on the basis of the principle of independence of the cavity sections expansion

The principle of independence of the cavity sections expansion makes the calculation of the cavity profile easier in the arbitrary variable pressure fields. Based on this principle the cavity shape is determined if we know the law of the cavitator motion and the values of the pressure at infinity and within the cavity. Let us apply the principle of independence for the calculation of the vertical cavities in the gravitational field [22].

Let us consider the vertical axisymmetrical cavity formed by the stream around the motionless disk-cavitator in the gravitational field. The stream can be descending or ascending, the value of the stream velocity V is the constant (Fig. 7).

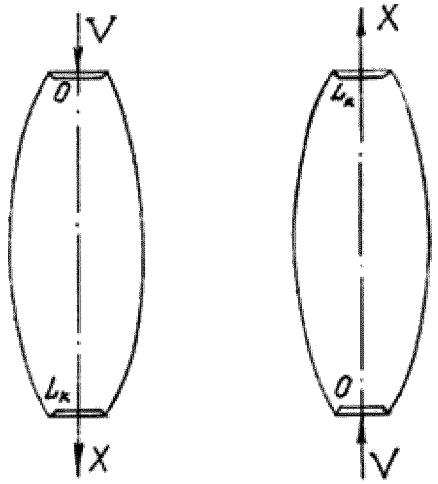


Fig. 7 The coordinate systems for the calculation of the cavity profile in the gravitational field

At the level of the cavitator the free stream pressure P_n (the pressure at infinity) is the constant. Let us introduce the vertical coordinate axis x directed along the stream velocity and the symmetry axis of the cavity from the cavitator center. On the section with coordinate x the free stream pressure (the pressure at infinity) is expressed as following

$$P_\infty(x) = P_n \pm \rho g x \tag{4.1}$$

where g is the gravitational acceleration, the sign 'plus' corresponds with the descending stream, the sign 'minus' corresponds to the ascending stream.

We determine the profile of the stationary vertical cavity. For the stationary cavity the pressure within it is the constant - $P_к$=*const*. The area of the cavity cross section fixed relatively the motionless fluid changes according to equation (1.15). Integral of equation (1.15) is equation (1.17) which describes the change of the area of the cavity fixed cross section. In this example we consider the cavitator to be motionless and observe the cavity section which has been formed at the edge of the cavitator at the moment t=0 and moves at the velocity V along with the stream. The area change of this section can be represented by the following expression

$$S(t) = S_0 + \dot{S}_0 t - \frac{k}{\rho}\int_0^t du \int_0^u \Delta P(v)\,dv \tag{4.2}$$

where v and u are the variables of integration, S_0 is the section initial area equal to the cavitator area. Let us substitute the expression of the external pressure (4.1) in dependence (4.2). Note that in (4.1) x is written as $x(v)=Vv$. After integration of equation (4.2) we obtain

$$S(t)= S_0 + \dot{S}_0 t - \frac{kt^2}{2\rho}\left(\Delta P_0 \pm \frac{1}{3}\rho g V t\right) \tag{4.3}$$

Expression (4.3) contains the difference ΔP_0 of the pressure at infinity and the pressure within the cavity $\Delta P_0 = P_n - P_k$. This difference is related to the section at the level of the cavitator.

Let us consider the case of the descending stream. For the stationary cavity the variable x is written as $x=Vt$. After substitution of (1.14) into (4.3) and certain transformations we obtain the expression for the vertical cavity profile in the dimensionless form

$$R^{*2} = 1 + \frac{2C_x}{a}x^* - \frac{C_x x^{*2}}{a^2}\left(\sigma_0 + \frac{x^*}{3Fr^2}\right) \tag{4.4}$$

where R^*, x^* are the dimensionless cavity radius and coordinate x scaled by the disk radius R_n,

$\sigma_0 = 2\Delta P_0 / \rho V^2$ is the cavitation number at the level of the cavitator,

$Fr = V / \sqrt{2R_n g}$ is the Froude number.

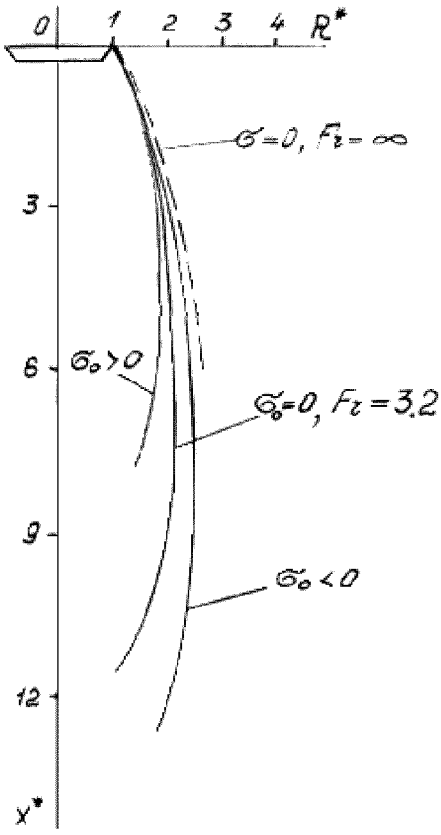


Fig. 8 The vertical cavity profiles in the descending stream

As an example, in Fig. 8 the cavity profiles calculated by formula (4.4) are represented by the continuous curves for the three values of the cavitation number σ_0: –0.1; 0; 0.1. The Froude number equals 3.2 and it remains the same for all the three cavities, the constant a equals 1.5. The Levinson-Gurevich asymptotic (3.7) for the zero cavitation number and weightless fluid ($Fr=\infty$) is represented by the broken curve.

Let us determine the length L_k. of the stationary vertical cavity for the Riabouchinsky scheme (Fig. 7). We assume that the cavity is closed by the disk of the same dimensions as the disk cavitator, i.e. $R^*=1$ at $x^*=L_k/R_n$. From expression (4.4) we obtain the quadratic equation for determining the cavity length

$$\left(\frac{L_k}{R_n}\right)^2 \frac{1}{3aFr^2} + \left(\frac{L_k}{R_n}\right)\frac{\sigma_0}{a} - 2 = 0 \tag{4.5}$$

The solution of equation (4.5) can be represented in the following form

$$\frac{L_k}{2R_n Fr} = -\frac{3}{4}\sigma_0 Fr + \sqrt{\frac{9}{16}\sigma_0^2 Fr^2 + \frac{3a}{2}} \tag{4.6}$$

In Fig. 9 dependence (4.6) is represented by the continuous curve, the points show the experimental data obtained for different values of the Froude and the cavitation numbers [22]. Figure 9 shows good agreement between the theoretical dependence (4.6) and the experimental data.

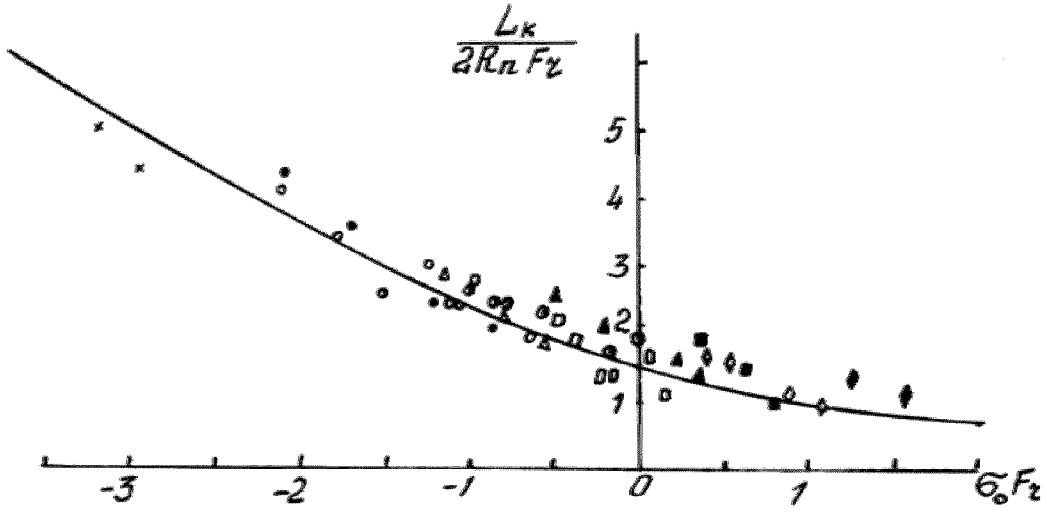


Fig. 9 The comparison of the calculation of the vertical cavity length based on formula (4.6) with the experimental data

Let us apply the principle of independence for the investigation of the cavity deep closure which occurs at the water entry of bodies [23]. At the moment of intersection of the water surface the cavity is formed past a body. This cavity communicates with the atmosphere, consequently in the initial period of submersion the gas pressure within the cavity is close to atmospheric pressure and the cavitation number is close to zero. However, as the body sinks the external hydrostatic pressure increases and under the influence of the excess pressure the cavity section closes. The cavity detaches from the atmosphere and the so-called deep closure occurs (Fig. 10).

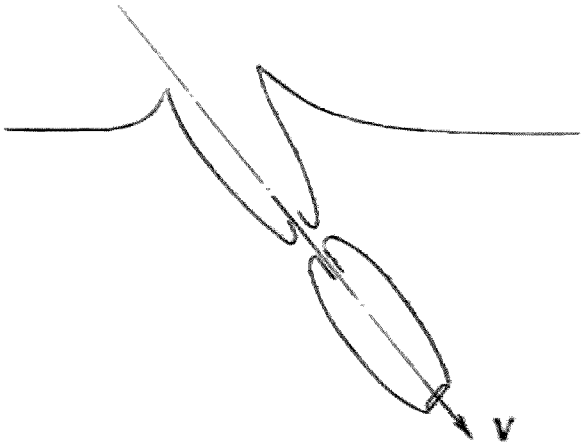


Fig. 10 The cavity deep closure at the water entry of a cavitator

Let us consider the inclined rectilinear water entry of the cavitator at the constant velocity V. We designate the entry angle as θ (the angle of inclination of the trajectory to the free surface). The time t is measured from the instant of the cavitator's initial contact with the water surface. We observe the section which has been formed at the moment t_1 on the depth H_1 (Fig. 11).

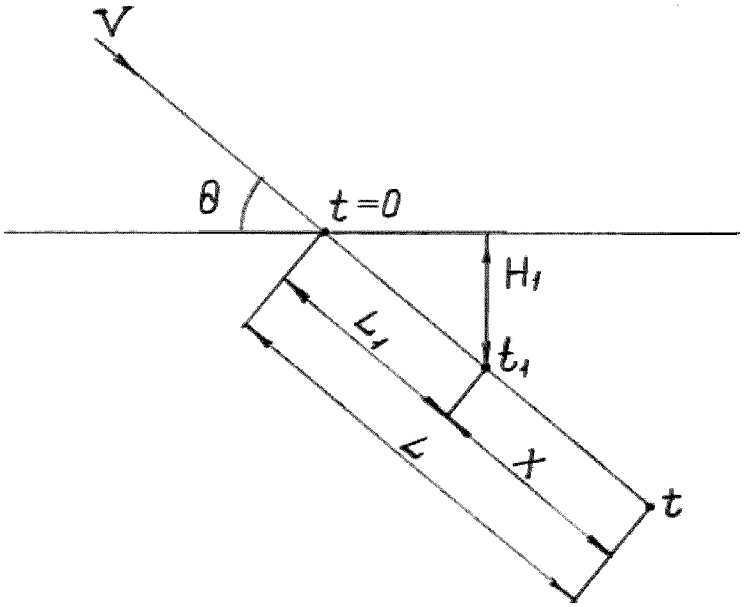


Fig. 11 The scheme for the calculation of the deep closure

We consider the pressure within the cavity equal to the atmospheric pressure then the excess pressure on the considered section is the constant and can be written in the form of

$$\Delta P = \rho g H_1 = \rho g L_1 \sin\theta \qquad (4.7)$$

The equation of the cavity section expansion is described by equation (1.15). The integral of equation (1.15) is written as follows

$$S(H_1,t)=S_0+\dot{S}_0(t-t_1)-\frac{k\Delta\mathrm{P}}{2\rho}(t-t_1)^2 \tag{4.8}$$

where S_0 is the cross section initial area equal to the cavitator area. From equations (4.7) and (4.8) we can determine the cavity profile at the water entry of the disk-cavitator if we apply the obvious correlations - $x=V(t-t_1)$; $L_1=L-x$ where x is the coordinate measured from the cavitator center along the trajectory of the cavitator, L is the cavitator path passed after the intersection of the water surface.

$$S(x)=S_0+\frac{\dot{S}_0}{V}x-\frac{kgL\sin\theta}{2V^2}x^2+\frac{kg\sin\theta}{2V^2}x^3 \tag{4.9}$$

We determine the cavity length from the condition that the cavity is closed by the disk with the same dimensions as the disk-cavitator. From (4.9) we obtain the quadratic equation for determining the cavity length

$$\frac{kg\sin\theta}{2V^2}L_k^2-\frac{kgL\sin\theta}{2V^2}L_k+\frac{\dot{S}_0}{V}=0 \tag{4.10}$$

The solution of equation (4.10) is written in the form of

$$L_k=\frac{L}{2}-\frac{L}{2}\sqrt{1-\frac{8\dot{S}_0V}{kgL^2\sin\theta}} \tag{4.11}$$

It is obvious that the maximum cavity length corresponds to the deep closure. It follows from (4.11) that the value of L_k is maximum when the radicand expression equals zero. Then the value of L_k equals $L/2$, i.e. the cavity closes halfway passed by the cavitator. The moment of the deep closure is determined from the equation

$$\frac{8\dot{S}_0V}{kgL^2\sin\theta}=1 \tag{4.12}$$

After substitution of correlations (1.14) and the equality $L=Vt_d$ in (4.12), for the dimensionless deep closure time we obtain the expression

$$t_d^*=2Fr\sqrt{\frac{2a}{\sin\theta}} \tag{4.13}$$

where $t_d^* = Vt_d / R_n$ is the dimensionless deep closure time, t_d is the deep closure time.

Previously expression (4.13) was obtained in a different way in [24]. The path passed by the cavitator at the moment of the deep closure is determined from the equality $L = R_n t_d^*$.

5. The application of the principle of independence for the calculation of the non-stationary cavities with variable internal pressure

The area of the cavity cross section fixed relatively to the motionless fluid changes according to equation (1.15). Equation (1.15) expresses the principle of independence. The integral of equation (1.15) is equation (1.17) that describes the area change of the cavity fixed cross section. Let us go on from equation (1.17) to the expression that represents the cavity profile at the fixed time [25]. In order to do that in equation (1.17) we introduce the time t which is common for all the sections. At the moment t the cavitator has the coordinate H. Let us designate the moment of the section formation with the coordinate h as t_1 ($t_1=t_1(h)<t=t_1(H)$). Then equation (1.17) transforms to

$$S(h,t) = S_0 + \dot{S}_0(t - t_1) - \frac{k}{\rho}\int_{t_1}^{t} du \int_{t_1}^{u} \Delta P(h,v)\,dv \tag{5.1}$$

where S_0 is the cavitator area, $\dot{S}_0$ is the constant that defines the initial velocity of the cavity expansion, v and u are the variables of integration. At the fixed moment t equation (5.1) expresses the cavity profile $S(h)$. At the fixed moment t_1, i.e. h=const, equation (5.1) describes the expansion of the fixed cavity cross section. We can transform the double integral in (5.1) to the line one as follows. Let us change the order of integration in the double integral

$$\int_{t_1}^{t} du \int_{t_1}^{u} \Delta P(h,v)\,dv = \int_{t_1}^{t} \Delta P(h,v)\,dv \int_{v}^{t} du = \int_{t_1}^{t} (t - v)\Delta P(h,v)\,dv \tag{5.2}$$

After substitution of (5.2) in (5.1) we obtain

$$S(h,t) = S_0 + \dot{S}_0(t - t_1) - \frac{k}{\rho}\int_{t_1}^{t} (t - v)\Delta P(h,v)\,dv \tag{5.3}$$

Equation (5.3) is especially convenient for the numerical calculation of the cavity profile when the pressure within it changes arbitrarily. As an example we consider the calculation of the cavity profile when the gas pressure within it changes according to the harmonic oscillations [26]. The time dependence of the gas pressure is written as follows

$$P_k(t) = P_{k_0} + A\sin\omega t \tag{5.4}$$

where P_{k_0} is some constant pressure, ω is the circular frequency, A is the amplitude of oscillations. We consider the external pressure $P_\infty(h,t)$ to be a constant and equal to P_∞. After substitution of (5.4) in (5.3) or (5.1) we obtain the profile of the pulsating cavity

$$S(x,t)=S_0+\frac{\dot{S}_0}{V}x-\frac{k\Delta P_0}{2\rho V^2}x^2-\frac{kA}{\rho\omega^2}F\left(\frac{\omega x}{V}\right)\sin[\omega t+\varphi(x)] \tag{5.5}$$

where $x=V(t-t_1)$ is the coordinate measured from the cavitator along the stream velocity, $\Delta P_0=P_\infty-P_{k_0}$ is the stationary excess pressure

$$F^2\left(\frac{\omega x}{V}\right)=2\left(1-\cos\frac{\omega x}{V}\right)+\frac{\omega x}{V}\left(\frac{\omega x}{V}-2\sin\frac{\omega x}{V}\right) \tag{5.6}$$

The first three members in (5.5) express the profile of the stationary cavity, the last member describes the perturbation of the cavity profile. The amplitude of the perturbation of the cavity profile increases to the downstream end of the cavity. The increase of the perturbations to the downstream end of the cavity is illustrated by Fig. 12 which shows the dependence (5.6).

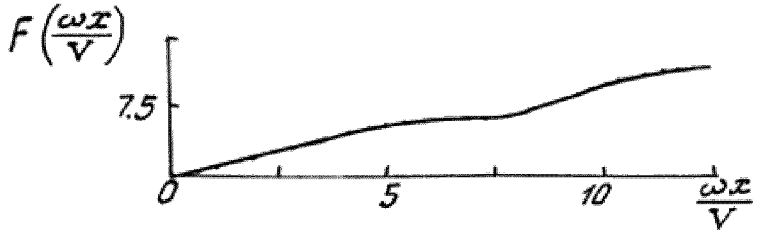


FIG. 12 THE INCREASE OF THE PERTURBATIONS TO THE DOWNSTREAM END OF THE CAVITY

Also, the increase of the perturbations to the downstream end of the cavity is confirmed by the experiments performed with the pulsating cavities [26].

If beforehand the gas pressure within the cavity is not known then it is necessary to add the subsidiary equations to equation (5.3) or (1.15). The equation for calculating the gas volume within the cavity is one of them

$$Q(t)=\int_{H(t)}^{h_c(t)}[S(h,t)-S_b(h,t)]dh \tag{5.7}$$

where $Q(t)$ is the volume contained between the cavity boundary and the body within the cavity,

$S_b(h,t)$ is the area of the body cross section;

$H(t)$ is the coordinate of the cavitator,

$h_c(t)$ is the coordinate of the cavity closure.

The equation of the gas mass change within the cavity has the form of

$$\frac{dm(t)}{dt} = \dot{m}_s - \dot{m}_l \tag{5.8}$$

m(t) is the gas mass within the cavity;

$\dot{m}_s$ is the mass gas-supply rate to the cavity;

$\dot{m}_l$ is the mass-leakage rate from the cavity.

The following is the equation of the gas state within the cavity

$$\frac{P_k(t)\ \ Q(t)}{m(t)} = RT(t) \tag{5.9}$$

where *R* is the gas constant,

T(t) is the gas temperature within the cavity. This temperature is dependent upon the thermodynamic process. In most cases we can consider the thermodynamic processes within the cavity to be isothermal and assume that the gas temperature within the cavity is equal to the temperature of the surrounding fluid.

In general the equation of the cavitator motion appears like

$$\frac{dV}{dt} = F(V, H, P_k, h_c, ...) \tag{5.10}$$

where *V* is the velocity vector.

The system of the equations (5.3), (5.7)-(5.10) describes the dynamics of the non-stationary cavity in the closed form. In fact, we can solve this system by the numerical method at each time step substituting the cavity profile for the discrete set of the cross sections. Also, in this case using the numerical method we can solve equation (1.15) instead of equation (5.3).

E. V. Parishev [25] has transformed the integral correlations (5.3) and (5.7) in the nonlinear differential equations with the lagging argument. It turned out that in general the dynamics of the non-stationary cavity is described by the system of the nonlinear differential equations of the sixth order with the variable lag (excluding the equations of the cavitator motion). In particular cases these equations are simplified. For example, in case of the axisymmetric cavity formed past a cavitator which is moving at the constant velocity in the weightless fluid and with the assumption that the gas mass within the cavity is the constant (gas-supply and gas-leakage are absent), the equation for the small pressure oscillations of the gas within the cavity has the form [27]

$$P_k'''(t^*) + P_k'(t^*) + P_k'(t^* - \tau^*) - \frac{2}{\tau^*} P_k(t^*) + \frac{2}{\tau^*} P_k(t^* - \tau^*) = 0 \tag{5.11}$$

where P_k is the gas pressure within the cavity (small oscillations relatively to the equilibrium), $t^*=t/T$ – is the dimensionless time, $\tau^*=\tau/T$ is the dimensionless lag, $\tau=L_k/V$ is the dimensional lag, L_k is the cavity length at the equilibrium, V is the cavitator velocity. The time scale T is determined by the expression

$$T = \sqrt{\frac{nQ_0\rho}{P_{k_0} kV\tau}} \tag{5.12}$$

where Q_0 is the cavity volume at the equilibrium, P_{k_0} is the gas pressure within the cavity at the equilibrium, $1/n$ is the polytropic index of the thermodynamic process within the cavity, for the isothermal process n equals 1.

Equation (5.11) has the single basic parameter equal to the dimensionless lag τ^*. As a result of transforming equation (5.12) this parameter can be represented as following

$$\tau^* = \sqrt{\frac{12}{n}\left(\frac{Eu}{\sigma} - 1\right)}$$

where $Eu = 2P_\infty / \rho V^2$ is the Euler number, σ is the average cavitation number defined by the pressure P_{k_0}.

Thus, all the cavity properties described by equation (5.11) are defined by the value of the ratio Eu/σ. Also the experimental works [28,29] show that the phenomenon of the artificially inflated cavity pulsation is defined by the ratio σ/Eu. Equation (5.11) has both the steady and unsteady (pulsating) solutions. For the vapor cavities ($\sigma \approx Eu$) and the ones close to them the solutions are steady. However, when $\tau^* > \pi\sqrt{2}$ the solutions are unsteady. This result corresponds to the well-known features of the vapor cavity which does not pulsate. Also, the experiments in [28,29] show that the cavities with a weak gas-supply, i.e. those that are close to the vapor ones, are steady.

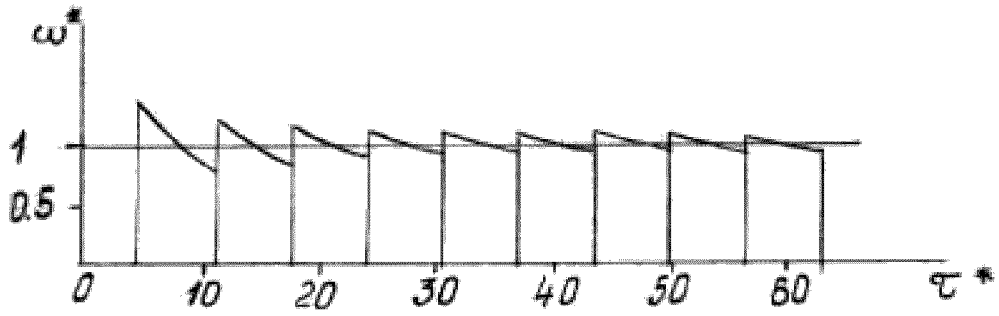


Fig. 13 The dependence of the dimensionless circular frequency of cavity pulsation ω^* on the parameter τ^*

In Fig. 13 the dependence of the dimensionless circular frequency of the cavity pulsation ω^* ($\omega^*=\omega L_k/\tau^* V$, where ω is the dimensional circular frequency) on τ^* is represented by the discontinuous serrate

function with the average value equal to 1. Knowing the dimensionless frequency of pulsation we can determine the number of the waves N going into the cavity length

$$N = \frac{L_k}{\lambda} = \frac{\omega^* \tau^*}{2\pi}$$

where λ is the wave length. Since the dependence $\omega^*(\tau^*)$ is discontinuous the dependence $N(\tau^*)$ is discontinuous too and the number of the waves going into the cavity length is close to integer. At the continuous change of τ^* the value of N changes as the stepped function. The dependence $N(\tau^*)$ is represented in Fig. 14. The points show the experimental data [26].

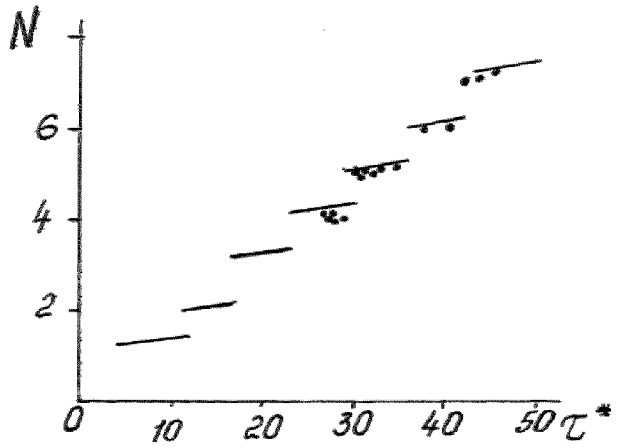


Fig. 14 The dependence of the number of the waves going into the cavity length N on the parameter τ^*

The discontinuous properties of the dependences $\omega^*(\tau^*)$ and $N(\tau^*)$ agree with the well-known experimental data [29]. The experiments have shown [29] that the pulsating cavities have the regimes with the fixed number of waves close to integer. The experiments have also shown [29] that at the smooth value change of the gas-supply the number of waves changes as the stepped function.

Thus, the cavity instability is connected with the gas elasticity within it. The underwater bubble has the analogous instability when it is internally supplied by gas. We can consider the cavity to be a dynamic system with infinite degrees of freedom. The cavity cross section changes influenced by the difference between the free stream pressure and the pressure within the cavity; the cavity volume changes as well. The cavity volume change leads to the pressure change within the cavity, etc. The cavity being a dynamic system with these properties is analogous to the vibration of a body on a spring. The coordinate of a body is analogous to the cavity cross section area. The elastic force of a spring is analogous to the pressure within the cavity. However, in case of a cavity we have an infinite quantity of these bodies (sections) and the pressures within the cavity is a function of the whole cavity volume, i.e. the cross sections are connected by means of the gas that fills the cavity. The gas-leakage from the cavity is the factor of stability. When this factor is active the parameter τ^* that corresponds to the cavity stability, exceeds the value of $\pi\sqrt{2}$. In addition to the mathematical model Parishev removed the gas along the bound vortexes and obtained the accordance with Epshtein's experimental data [26].

Conclusions

The principle of independence of the cavity sections expansion stated by G. V. Logvinovich provides an easier way for investigating the non-stationary cavities and the cavities with the variable external pressure. This principle corresponds to the flow's property around slender bodies and it is stated as following – each cavity cross section expands relatively to the trajectory of the cavitator center according to the certain law which is dependent on the conditions at the moment as a cavitator passes the plane of the considered section. The cross section expands almost independently from the following or the previous cavitator motion.

The principle of independence is equivalent to the equation of conservation of energy applied to the given cavity section. The sum of the kinetic and potential energies on the cavity section is determined only by the value of the cavitation drag at the moment of intersection with this section. The law of the cavity section expansion (1.15) obtained from the energy equation (1.1) is independent from the following and the previous cavitation motion.

The principle of independence is some approximation to the reality. However, the numerous experiments have confirmed it being accurate for both the stationary and non-stationary cavities. The principle of independence agrees with the results obtained from the slender body theory for the stationary and non-stationary cavitation flows.

Furthermore, the results of the stationary cavity calculation by the numerical methods demonstrate that the cavity shape is close to an ellipsoid of revolution for the cavitation numbers that have the order $10^{2} \div 10^{-1}$. The ellipsoidal form of the stationary cavity has also been obtained from the principle of independence. The principle of independence of the cavity section expansion and the energy equation are applicable for a special case – the cavitation number equals zero (the infinite cavity length).

References

1. Logvinovich G. V., "Hydrodynamics of Flows with Free Boundaries", Naukova Dumka, Kiev, 1969, 215 p. (in Russian)
2. Logvinovich G. V., "Questions on Theory of Slender Axisymmetric Cavities", Tr. TsAGI, #1797, 1976, pp 3-17. (in Russian)
3. Logvinovich G. V., Buyvol V. N., Dudko A. S., Putilin S. I. and Shevchuk Yu.R., "Flows with Free Boundaries", Naukova Dumka, Kiev, 1985, 296 p. (in Russian)
4. Lamb H., "Hydrodynamics", 6th ed., New York, Dover, 1932.
5. Liepmann H. W. and Roshko A., "Elements of Gasdynamics", John Wiley & Sons, Inc., New York, 1957.
6. Frankl F. I. and Karpovich E. A., "Gasdynamics of Slender Bodies", Gostechizdat, Moscow – Leningrad, 1948, 175 p. (in Russian)
7. Ashley H. and Landahl M., "Aerodynamics of Wings and Bodies", Addison-Wesley Publishing Com., Inc., Massachusetts. 1966.
8. Vasin A. D., "Application of the Slender Body Theory to Investigate Developed Axisymmetric Cavitation Flows in a Subsonic Stream of Compressible Fluid", Applied hydromechanics, Kiev, v.2 (74), #3, 2000, pp 17-25. (in Russian)
9. Serebryakov V. V., "The Circular Model for Calculation of Axisymmetric Supercavitation Flows", Hydromechanics, Kiev, #27, 1974, pp 25-29. (in Russian)

10. Guzevskii L. G. "Plane and Axisymmetric Problems of Hydrodynamics with Free Surfaces", Dissertation for a doctor's degree, Institute of the Thermal Physics, Siberian Branch of the USSR Academy of Science, Novosibirsk, 1987, 300 p. (in Russian)

11. Kozhuro L. A., "Calculation of Axisymmetric Jet Flows past Bodies in Accordance with the Riabouchinsky Scheme", Uch. Zap. TsAGI, v. 11, #5, 1980, pp 109-115 (in Russian)

12. Amromin E. L. and Ivanov A. N., "Axisymmetric Flow around Bodies at Supercavitation Regime", Izv. Akad. Nauk SSSR, Mech. Zhidk. Gaza, #3, 1975, pp 37-42. (reprinted in the USA)

13. Subhankulov G. I. and Homyakov A. N., "Application of the Boundary Element Method for Calculation of Axisymmetric Cavities", in Hydrodynamics of High Speeds, Chuvash. University Press, Cheboksari, 1990, pp 124-132. (in Russian)

14. Gonor A. L., Zabutnaya V. I. and Yasko N. N., "On the Existence of the Optimal Cavitator", Izv. Akad. Nauk SSSR, Mech. Zhidk. Gaza, #2, 1991, pp 63-68. (reprinted in the USA)

15. Brennen C., "A Numerical Solution of Axisymmetric Cavity Flows", J. Fluid Mech., 37, 4, 1969, pp 671-688.

16. Vasin A. D., "Calculation of Axisymmetric Cavities Downstream of a Disk in Subsonic Compressible Fluid Flow", Izv. Rus. Akad. Nauk, Mekh. Zhidk. Gaza, #2, 1996, pp 94-103. . (reprinted in the USA)

17. Birkhoff G. and Zarantonello E. H., "Jets, wakes and cavities", Academic Press, Inc., New York, 1957.

18. Levinson N., "On Asymptotic Shape of Cavity behind an Axially Symmetric Nose Moving through an Ideal Fluid", Ann. Math., 47, 1946, pp 704-730.

19. Gurevich M. I., "Flow around Axisymmetric Half-Body with Finite Drag", Prikl. Mat. Mekh., 11, 1, 1947, pp 97-104 (in Russian).

20. Gurevich M. I., "Half-Body with Finite Drag in Subsonic Flow", Tr. TsAGI, #653, 1947, pp 1-12 (in Russian).

21. Logvinovich G. V., "On Law of an Unsteady Cavity Expansion", Applied hydromechanics, Kiev, v. 2(74), #3, 2000, pp 60-64 (in Russian).

22. Parishev E. V., "Pulsations of Vertical Cavities in Ponderous Fluid", Uch. Zap. TsAGI, v.12, #3, 1981, pp 1-9 (in Russian).

23. Knapp R. T., Daily J. W. and Hammitt F.G., "Cavitation", McGraw-Hill Book Comp., New York, 1970.

24. Zhuravlev Yu. F., "Perturbation Methods in Three Dimensional Jet Flows", Tr. TsAGI, #1532, 1973, pp 1-24. (in Russian)

25. Parishev E. V., "The System of Nonlinear Differential Equations with Lagging Argument Describing Dynamics of Non-Stationary Axisymmetric Cavities", Tr. TsAGI, #1907, 1978, pp 3-16. (in Russian).

26. Parishev E. V., "The Principle of Independence of Cavity Expansion as the Method for Investigation of Non-Stationary Cavitation Flows", Tr. TsAGI, #2256, 1985, pp 43-50. (in Russian).

27. Parishev E. V., "Theoretical Investigation on Stability and Pulsations of Axisymmetric Cavities", Tr. TsAGI, #1907, 1978, pp 17-40. (in Russian).

28. Silberman E. and Song C. S., "Instability of Ventilated Cavities", J. Ship Res., 5, #1, 1961, pp 13-33.

29. Michel J. M., "Ventilated Cavities. A Contribution to the Study of Pulsation Mechanism", in Proceedings of the IUTAM Symposium held in Leningrad on "Non-steady Flow of Water at High Speeds", 1971, pp 343-360.

This page has been deliberately left blank

Page intentionnellement blanche

Numerical Modeling of Supercavitating Flows

I.N. Kirschner, PhD • Neal E. Fine, PhD • James S. Uhlman, PhD • David C. Kring, PhD

Anteon/Engineering Technology Center
240 Oral School Road, Suite 105
Mystic, CT 06355
United States of America

SUMMARY

Supercavitating bodies can achieve very high speeds under water by virtue of reduced drag: with proper design, a cavitation bubble is generated at the nose and skin friction drag is drastically reduced. Depending on the type of supercavitating vehicle under consideration, the overall drag coefficient can be an order of magnitude less than that of a fully wetted vehicle. Slender-body theory and boundary element methods are two modern computational methods applied to the design of supercavitating vehicles. These course notes present recent advances in the theory behind these two computational approaches, as well as results and application of the methods to the simulation and control of supercavitating vehicles.

1 INTRODUCTION

Naval hydrodynamics and the marine engineering sciences have been characterized by centuries of evolutionary innovation punctuated by several revolutionary performance improvements. The relatively continuous improvement in early paddle wheel technology, for example, became obsolete very quickly upon introduction of the screw propeller in the late nineteenth century. The development of undersea vehicles has seen several similar paradigm shifts, such as the introduction of piston engines appropriately packaged to fit within a typical vehicle envelope, and the application of acoustical homing techniques. However, until recently, there has been little interest in very high speeds for undersea applications.

There are two primary impediments to increasing underwater vehicle speeds: current propulsion capability and the relatively high drag of current underwater vehicle configurations. For most of the last century in this country, relatively little research has been devoted to significantly opening the performance envelope in these areas. Over the last decade, however, high-speed capability has received increased attention, and dramatic advancements have been made. These achievements have been supplemented with information concerning international development (LEGI, 2000).

The history of hydrodynamics research displays an emphasis on eliminating cavitation, chiefly because of the erosion, vibration, and acoustical signatures that often accompany the effect. The drag-reducing benefits of cavitation, however, were noted during the first half of the last century, and have received significant attention over the last decade.

Supercavitation is a hydrodynamic process by which a submerged body is almost entirely enveloped in a layer of gas. Because the density and viscosity of the gas is dramatically lower than that of seawater, skin friction drag can be reduced dramatically. If the body is shaped properly, the attendant pressure drag can be maintained at a very low value, so that the overall body drag is also reduced significantly. The process of designing a supercavitating body for minimum pressure drag, while addressing issues of control and maneuvering, is greatly aided by the use of modern computational methods.

This document presents details of two computational methods that have been applied extensively during the past decade to the analysis and design of supercavitating bodies: boundary element methods and slender- body theory. Section 2 lays the groundwork with a discussion of several issues pertinent to the numerical modeling, including a motivation for the application of

Paper presented at the RTO AVT Lecture Series on "Supercavitating Flows", held at the von Kármán Institute (VKI) in Brussels, Belgium, 12-16 February 2001, and published in RTO EN-010.

potential flow techniques to prediction of supercavitating flows. Section 3 presents results from several applications of boundary element methods, including steady axisymmetric flows, unsteady flows, and cavitating fins. Section 4 contains a discussion of slender-body theory and some pertinent results. In section 5, we present the results of numerical flight simulation for supercavitating vehicles that incorporates some of the computational methods discussed in previous sections in determining the forces experienced by the vehicle in maneuvers.

These lecture notes were derived from several previous publications. The nomenclature schemes of the original publications have been retained, but each sub-section is reasonably self-consistent.

2 PRELIMINARY REMARKS

2.1 Vehicle Control

A properly shaped supercavitating body will have a very small pressure drag, so that the overall body drag is also reduced dramatically over that of a fully wetted body. However, because the center of pressure is typically located well forward with respect to the center of gravity, control and maneuvering present special challenges. Also, whereas a fully wetted vehicle develops substantial lift in a turn due to vortex shedding off the hull, a supercavitating vehicle does not develop significant lift over the gas-enveloped surfaces. This requires a different approach to effecting hydrodynamic control, and increases the relative advantage of a banked maneuvering strategy.

A supercavity can be maintained in one of two ways: (1) by achieving such a high speed that the water vaporizes near the nose of the body, generating a cavity that grows to exceed the length of the body; or, (2) by supplying gas to the cavity at nearly ambient pressure at more moderate (but still very high) speeds. The first technique is known as vaporous cavitation; the second is termed ventilation, or artificial cavitation. Schematic views of two types of notional supercavitating bodies are shown in Figure 1. Note that each concept involves a cavitator (in this case a disk) with a salient edge that ensures clean cavity formation near the nose of the body. The relatively small diameter of the cavitator with respect to that of the vehicle is also important: it is this feature that allows the pressure drag to be maintained at a manageable level. An important step in the design of a supercavitating body is selection of a cavitator that is appropriately sized for the vehicle and speed of interest.

Control of supercavitating vehicles presents special challenges not normally associated with fully wetted vehicle dynamics. These arise from the absence of certain physical effects such as lift on the body and from the presence of other effects such as the nonlinear interaction of the control surfaces and the body with the cavity wall.

In contrast with the controlled vehicle depicted in Figure 1b, a projectile of the type shown in Figure 1a need not have fins, since the global stability of the trajectory is maintained via occasional tail-slap contact of the afterbody with the cavity boundary (or, at extremely high speeds, by the forces due to the relative motion between the vapor and the body). Since the vehicle shown in Figure 1b would incorporate some sort of guidance system, fins have been indicated that would provide hydrodynamic control in concert with actuation of the cavitator. The blast tube (that is, the small-diameter section of the vehicle aft of the fins) shown in Figure 1b is expected to represent a more optimal shape than a cylinder of constant radius for certain classes of supercavitating vehicles: if range is critical, then drag must be minimized, which (in turn) entails minimization of the cavity diameter. The step at the after end of the mid-body allows for this.

2.2 Drag Components for Submerged Bodies

For simplicity, consider an undersea vehicle with constant mass. This excludes rocket propulsion, but is illustrative of the physics of supercavitation drag reduction. The following analysis of the drag force is equally applicable to rocket-propelled vehicles; however, the basic equation of vehicle motion (equation 2.1) must be modified to account for the ejection of mass (Greenwood, 1965).

Newton's second law of motion applied to undersea vehicles can be written (Greenwood, 1965) as

$$T - D = \frac{d}{dt}(mU) \tag{2.1}$$

where m is the vehicle mass plus the hydrodynamic added mass (Newman, 1980) and U is the velocity of the vehicle in straight and level flight along a trajectory parallel to the thrust vector. Under steady conditions, the thrust provided by the propulsion system, T, balances the vehicle drag, D. For this simple case, the dynamics and hydrodynamics of the vehicle are usually analyzed in a body-fixed frame of reference, as shown in Figure 2.

The drag represents an integration over the vehicle surface of all components of stress acting opposite to the direction of travel (Newman, 1980):

$$D = \oiint_S \left(p n_x + n_y \tau_{yx} + n_z \tau_{zx} \right) dS \tag{2.2}$$

where p is the pressure, τ_{yx} and τ_{zx} are the components of the shear stress in the x-direction, and $n = (n_x, n_y, n_z)$ is the unit vector normal to the surface of the vehicle.

It is often convenient to separate the total drag force into components representing the pressure and skin-friction contributions:

$D=D_P+D_F$ where D_P is the pressure drag and D_F is the skin-friction drag.

It should be noted that, for vehicles traveling close to a free surface, generation of gravity and capillary waves is associated with a modification of the pressure and velocity fields on the vehicle hull, causing a drag increase. Also, at speeds greater than the lower critical Mach number, there is a drag increase associated with the shock wave system (Ashley and Landahl, 1965). In most cases of interest, the primary drag component affected is the pressure drag. For purposes of analysis, each contribution is often treated as a separate component, although some coupling of the terms occurs. Free-surface drag will not be considered in the following discussion. A compressible flow formulation using slender-body theory is presented in a later section, but discussion of the associated effects on drag is relegated to the originating publication, Varghese, et al, (1997).

Denoting the fluid density as ρ and the free stream speed as U_∞, the drag is typically normalized on the product of the dynamic pressure of the free stream, $\frac{1}{2}\rho U_\infty^2$, and a characteristic area, A. For axisymmetric undersea vehicles, A is usually chosen as the maximum sectional area. Thus,

$$C_D \stackrel{\Delta}{=} \frac{D}{\frac{1}{2}\rho U_\infty^2 A}. \tag{2.3}$$

2.3 Governing Equations

Neglecting the effect of gravity (assuming that free-surface and stratification effects are unimportant for the case under consideration), the equations of motion of a fluid in a volume V in the incompressible limit describe conservation of mass:

$$\nabla \cdot \boldsymbol{U} \equiv 0 \tag{2.4}$$

and conservation of momentum:

$$\left[\frac{\partial}{\partial t} + (\boldsymbol{U} \cdot \nabla) \right] \boldsymbol{U} = -\frac{\nabla p}{\rho} + \nu \nabla^2 \boldsymbol{U}, \tag{2.5}$$

where ν is the fluid kinematic viscosity. The momentum conservation equations are referred to as the Navier-Stokes equations.

The relative importance of the terms on the right-hand side of equation 2.6 can be gleaned by making the entire system dimensionless, as follows:

$$\tilde{\boldsymbol{U}} \overset{\Delta}{=} \frac{\boldsymbol{U}}{U_\infty} \qquad \tilde{t} \overset{\Delta}{=} \frac{U_\infty t}{L} \qquad \tilde{\nabla} \overset{\Delta}{=} L\nabla \quad ,$$

where L is some length characterizing the flow. For axisymmetric undersea vehicles, this length is usually chosen as the maximum diameter. Making these substitutions into equations 2.5 and 2.6, rearranging, and dropping the tildes gives

$$\nabla \cdot \boldsymbol{U} \equiv 0 \tag{2.6}$$

$$\left[\frac{\partial}{\partial t} + (\boldsymbol{U}\cdot\nabla)\right]\boldsymbol{U} = -\frac{L}{2}\nabla C_p + \frac{1}{\mathrm{R}}\nabla^2\boldsymbol{U}, \tag{2.7}$$

where

$$C_p \overset{\Delta}{=} \frac{p - p_\infty}{\frac{1}{2}\rho U_\infty^2} \overset{\Delta}{=} \text{pressure coefficient} \tag{2.8}$$

and

$$\mathcal{R} \overset{\Delta}{=} \frac{U_\infty L}{\nu} \overset{\Delta}{=} \text{Reynolds number.} \tag{2.9}$$

Prandtl noted that, as the Reynolds number increases, viscous effects become increasingly confined to a thin boundary layer near the body surface (Schlichting, 1979). This fact, in conjunction with certain mathematically provable laws of fluid motion (Yih, 1979), allows use of potential flow techniques in predicting the motion of high-Reynolds-number flows past bodies (Newman, 1980). Under these conditions, the velocity field can be determined based solely on kinematic considerations and knowledge of conditions at the boundaries of the fluid. Once the irrotational velocity field is known, an auxiliary equation for pressure is given by a simple form of Bernoulli's equation (Aris, 1962):

$$p + \frac{1}{2}\rho U^2 = p_\infty + \frac{1}{2}\rho U_\infty^2 \quad . \tag{2.10}$$

The far field pressure, p_∞, is simply the hydrostatic pressure at the operating depth of the vehicle.

When the pressure of a liquid is reduced below some threshold level at constant temperature it vaporizes. This change of phase is known as cavitation (Newman, 1980). The threshold value for a pure liquid undergoing quasi-static pressure reduction is known as the vapor pressure, p_V. Cavitation inception is often enhanced in the field due to various perturbations of ideal conditions, including the amount of gases absorbed in the liquid, contamination by other liquids or solids, or the presence of bubbles. The vapor pressure provides an excellent measure of the cavitation inception pressure under most conditions of interest, however.

As fluid flows past a fully wetted body, the pressure increases to stagnation pressure at the forward stagnation point, decreases below ambient pressure, then increases toward stagnation pressure over the afterbody. The actual pressure recovery depends on the development of the boundary layer and the extent of separation.

If the pressure falls below the fluid vapor pressure at any point, a vapor cavity will form. The density of the vapor within the cavity is orders of magnitude less than that of the ambient liquid. The dimensionless quantity characterizing the tendency of a given flow to cavitate is known as the cavitation number:

$$\sigma \overset{\Delta}{=} \frac{p_\infty - p_c}{\frac{1}{2}\rho U_\infty^2} \tag{2.11}$$

where p_c is the cavity pressure. For non-ventilated flows, the cavity pressure is approximately equal to the vapor pressure of the ambient liquid under most conditions of current interest.

As the velocity increases, the cavitation number and the minimum pressure on the body surface decrease, and the fluid tends to cavitate. Below a certain cavitation number, an experimentally observed fact (one that may be explained by considering the various terms in the momentum equation, equation 2.5) is that the velocity within the vapor cavity is very small. Consequently, to lowest order, the pressure within the vapor cavity is constant, with a value nearly equal to the vapor pressure of the fluid. At high Reynolds number, the shear layer forming the cavity boundary is thin. In that case, potential flow techniques may be used to predict such flows (Newman, 1980). It should be noted that recent results of high-Mach-number research indicate that the assumption of negligible velocities within the cavity is not valid at very high speeds (say, at Mach numbers approaching unity). However, for cavity-riding vehicles, the pressure can be taken as constant within the vapor cavity.

In terms of velocity, the boundary-value problem describing the ideal supercavitating flow shown in Figure 3 is given by the field equation describing conservation of mass (equation 2.4) along with boundary conditions on velocity:

$$\boldsymbol{U} \cdot \boldsymbol{n} \equiv 0 \quad \text{on } S_W \cup S_C \tag{2.12}$$

$$\boldsymbol{U} \cdot \boldsymbol{s} \equiv U_\infty \sqrt{1 + \sigma} \quad \text{on } S_C \tag{2.13}$$

where S_w is the wetted surface of the body and S_c is the cavity boundary.

The dynamic condition results from applying Bernoulli's equation (equation 2.10) along the cavity streamline, under the constraint that the pressure within the cavity is constant with a value equal to the cavity pressure, p_c. Various techniques exist for solving such a problem, including panel methods and slender-body theory (Kuethe and Chow, 1976). These two approaches will be discussed in the following sections.

3 APPLICATION OF THE BOUNDARY-ELEMENT METHOD

This section describes application of the boundary element method to prediction of supercavitating flows. Three sample problems are discussed: (1) steady, subsonic flow around an axisymmetric disk; (2) unsteady, subsonic flow around general cavitator shapes; and (3) steady flow around cavitating control effector fins for application to supercavitating vehicle flight control.

3.1 Steady Axisymmetric Flows

This sub-section is derived from Kirschner, et al, (1995).

The physical problem is shown in the schematic drawing of Figure 4. The body is axisymmetric and oriented parallel to the flow. The geometries under consideration in these lecture notes include only those for which a salient cavity detachment point can be identified, although the solution techniques described could be extended to more general shapes.

The position vector in a meridonal plane is denoted as $\boldsymbol{x} = x\boldsymbol{i} + r\boldsymbol{j}$. The inner boundary of the flow problem is the union of the wetted portion of the body and the boundary of the cavity:

$$S = S_B \cup S_C. \tag{3.1}$$

The lengths of the body and cavity are denoted as ℓ_B and ℓ_C, respectively. The total length of the combined body-cavity system is denoted as ℓ.

Only steady flows are considered in this sub-section. The difficulties of representing cavity closure under this assumption are discussed below.

Unit vectors normal and tangent to the body-cavity surface in a meridonal plane are denoted as $\boldsymbol{n} = n_x\boldsymbol{i} + n_r\boldsymbol{j}$ and $\boldsymbol{s} = s_x\boldsymbol{i} + s_r\boldsymbol{j}$, respectively. The unit normal vector is directed into the liquid; the unit tangent vector is directed positive aft. $\boldsymbol{U}_\infty = U_\infty\boldsymbol{i}$ is the free stream velocity. The total velocity at any point outside of the body-cavity surface is decomposed as

$$\boldsymbol{U} = U_\infty\boldsymbol{i} + \boldsymbol{u} \tag{3.2}$$

where $\boldsymbol{u(x)}=u_x\,\boldsymbol{i}+u_r\,\boldsymbol{j}$ is the disturbance velocity. As discussed above, to lowest order the cavity pressure, p_c

Potential Flow Formulation

The fluid is assumed to be incompressible and the flow is taken to be irrotational. The last assumption guarantees the existence of a velocity potential. Under this condition, the flow field is governed by Laplace's equation,

$$\nabla^2 \Phi = \Phi_{xx} + \Phi_{rr} + \frac{\Phi_r}{r} = 0 \quad , \tag{3.3}$$

where Φ is the total potential.

A disturbance potential, ϕ, can be defined from the total potential by

$$\Phi = \boldsymbol{U}_\infty \cdot \boldsymbol{x} + \phi \quad , \tag{3.4}$$

so that the disturbance velocity, $\boldsymbol{u}$, is given by the gradient of the disturbance potential. The disturbance potential also obeys the Laplace equation. This boundary value problem is shown in the schematic drawing of Figure 5.

Kinematic Condition

The requirement that the flow be tangential to the body and cavity surfaces, equation 2.12, combined with the definition of the potential in equation 3.4, gives the following kinematic condition on the body-cavity surface, S:

$$\frac{\partial \phi}{\partial n} = -\boldsymbol{n} \cdot \boldsymbol{U}_\infty \text{ on } S \quad . \tag{3.5}$$

Dynamic Condition On The Cavity

Bernoulli's equation applied along the cavity surface can be expressed as follows:

$$C_p = -\sigma \quad \text{on } S_C \quad . \tag{3.6}$$

The magnitude of the total velocity on the cavity surface is given by equation 2.13. From this, the following expression for the disturbance potential may be applied on the cavity surface:

$$\frac{\partial \phi}{\partial s} = U_\infty \sqrt{1+\sigma} - U_\infty s_x \quad \text{on } S_C \quad . \tag{3.7}$$

Cavity Termination

For a given wetted body shape and cavity length, Laplace's equation for the disturbance potential can be solved subject to the kinematic condition, equation 3.5, and the dynamic condition, equation 3.7. A cavity termination model is also required.

In this work, a modified Riabouchinsky cavity termination model is used. The cavity is closed with a Riabouchinsky wall or endplate extending from the axis of symmetry to the point at which the cavity streamline becomes perpendicular to the axis. Along the endplate, denoted as S_W, the kinematic condition is satisfied. In the current case, since the flow is axisymmetric, the endplate is always perpendicular to the axis of symmetry.

It should be noted that this termination model has been chosen as a compromise between simplicity and physical validity. The reentrant jet model is a closer representation of the physical flow, but is more difficult to implement numerically. The reentrant jet model is discussed in further detail below.

Solution Procedure using Boundary Elements

The disturbance velocity potential in equation 3.4 satisfies Green's third identity, a Fredholm integral equation of the second kind, along the body, cavity, and endplate (Lamb, 1945). Thus, for

any field point $\boldsymbol{x}$ on the body-cavity surface, the disturbance velocity potential can be computed from

$$2\pi\phi(\boldsymbol{x}) = -\iint\left[\phi(\boldsymbol{x}')\frac{\partial}{\partial n}G(\boldsymbol{x};\boldsymbol{x}') - \frac{\partial}{\partial n}\phi(\boldsymbol{x}')G(\boldsymbol{x};\boldsymbol{x}')\right]dS(\boldsymbol{x}') \tag{3.8}$$

where the integration is performed over source points, $\boldsymbol{x}'$, along the entire body, cavity, and endplate surface. Green's function for this problem, $G(\boldsymbol{x};\boldsymbol{x}')$, is

$$G(\boldsymbol{x};\boldsymbol{x}') = \frac{1}{|\boldsymbol{x}-\boldsymbol{x}'|}. \tag{3.9}$$

Along the body and the endplate surfaces, the source strength distribution, $\partial\phi/\partial n$, is known and given by equation 3.5. Along the cavity surface, an expression for the dipole strength distribution, ϕ, can be found by integrating equation 3.7:

$$\phi(s) = \phi(s_0) + U_\infty\sqrt{1+\sigma}\,(s-s_0) - U_\infty(x-x_0) \text{ on } S_C. \tag{3.10}$$

where s_0 is the arc length coordinate at an arbitrary fixed point on the body-cavity surface, S.

To solve for the dipole strength distribution, ϕ, along the body and endplate surfaces, and the source strength distribution, $\partial\phi/\partial n$, along the cavity boundary, the computational domain is discretized into M_B panels along the body, M_C panels along the cavity, and M_W panels along the endplate. Unequal spacing of the panels is utilized to ensure that more panels are concentrated where large velocity gradients are expected.

The source and dipole strengths are taken to be constant on each panel. Integral equation 3.8 is satisfied at control points on every panel. These are chosen such that each trapezoidal panel is divided into equal areas upstream and downstream of its control point.

The unknowns to be determined are therefore

- M_B dipole strengths on the body panels;
- M_C source strengths on the cavity panels;
- M_W dipole strengths on the endplate panels; and,
- the dimensionless cavity surface velocity, $\sqrt{1+\sigma}$.

There are $M_B + M_C + M_W + 1$ quantities to be determined. Equation 3.8 gives $M_B + M_C + M_W$ equations. The zero net flux condition,

$$\oiint_S \frac{\partial\phi}{\partial n}\,dS = 0 \tag{3.11}$$

is used as another condition to form a determinate system.

Cavity Shape For Fixed Cavity Length

For the body shapes considered in these lecture notes, the cavity detachment point is known. For a specified cavity length, a cavity profile is assumed, and the potential-based boundary element method used to solve for the dimensionless cavity surface velocity, $\sqrt{1+\sigma}$, and the source and dipole strengths. A new estimate of the cavity profile is then determined by applying the kinematic condition on the cavity surface, S_C. The boundary value problem is then re-solved, and the process repeated until the cavity profile converges.

The kinematic condition, equation 3.5, can be written as

$$n_x(u_x + U_\infty) = -n_r u_r. \tag{3.12}$$

For example, if the body cavity surface profile is defined by $y = b(x)$, then

$$\frac{db}{dx} = -\frac{n_x}{n_r} = \frac{u_r}{u_x + U_\infty} \tag{3.13}$$

along the cavity surface.

Prior to convergence of the cavity profile, the kinematic condition on the cavity boundary has not been imposed. Thus, the object is to change the cavity shape such that the flux across the boundary is minimized. Two methods have been tested for modifying the cavity shape including (1) modification of the profile offset; and, (2) sequential modification of each panel angle followed by re-scaling of the cavity to its original length. In practice, the latter approach has proven to be more general and robust than the former.

Pressure and Drag

Once the potential flow problem outlined in the previous section has been solved, the pressure coefficient on the body surface, S_B, can be computed as

$$C_p = 1 - \left(\frac{U_s}{U_\infty}\right)^2 = 1 - \left(s_x + \frac{1}{U_\infty}\frac{\partial \phi}{\partial s}\right)^2 . \tag{3.14}$$

The body drag is the integral of the x-component of the differential pressure force over the wetted portion of the body and the base:

$$D = -\left[\iint_{S_B} p n_x \, dS + \pi B^2 p_C\right] . \tag{3.15}$$

Where B is the radius of the cavitator at the cavity detachment point. The drag coefficient is computed as:

$$C_D = \sigma - \frac{1}{\pi B^2}\iint_{S_B} n_x C_p \, dS \tag{3.16}$$

Selected Results – Steady Flows

Sample results of the fully axisymmetric boundary element method for incompressible flow are presented in Figure 6 through Figure 8. For additional results and discussion, refer to Kirschner, et al, (1995).

The body-cavity profiles predicted for a 15° cone at several cavitation numbers are shown in Figure 6. The predicted drag coefficients at each cavitation number are plotted in Figure 7 and compared with the empirical curve fit of May (1975):

$$C_D = 0.151 + 0.587\sigma . \tag{3.17}$$

It can be seen that the trend is very accurate. Since the publication of Kirschner, et al (1995), a coding error was discovered which, when corrected, virtually eliminated the offset seen in Figure 7.

The predicted maximum cavity diameter is compared with the empirical curve fit of May (1975) in Figure 8. The following equation represents the curve fit:

$$\frac{1}{C_D}\left(\frac{b_{max}}{B}\right)^2 \cong 1.28\sigma^{-0.91} \tag{3.18}$$

The left-hand side of equation 3.18 is the function plotted on the ordinate of Figure 8. The prediction appears to be excellent. Note from the figures that, if the predicted drag coefficient used in equation 3.18 is replaced with that given by equation 3.17, the prediction of values characterizing the cavity geometry is improved. It should be noted that May's equation over-predicts experimental cavity lengths at higher cavitation numbers.

Reentrant Jet Termination Model

A termination model that better represents the physics for typical supercavitating flows of interest is the reentrant jet model, a description of which may be found in Tulin (1964). The current formulation is based on Uhlman, et al, (1998).

For axisymmetric flows, the presence of the reentrant jet may be handled quite simply by truncating an axisymmetric reentrant surface at a jet face, and assuming that, at this axial location, this surface is asymptotic to a cylinder of constant diameter and the cavity surface velocity has approached a constant limit. In the absence of gravity, and assuming that the truncated jet face is perpendicular to the velocity, the conditions at the jet face are

$$\frac{\partial \Phi}{\partial n} = U_\infty \sqrt{1+\sigma} \tag{3.20}$$

and

$$\frac{\partial \Phi}{\partial s} = 0. \tag{3.21}$$

With the disturbance potential defined by equation 3.4, the conditions to be applied at the jet face become

$$\frac{\partial \varphi}{\partial n} = U_\infty \left(\sqrt{1+\sigma} + 1 \right) \tag{3.22}$$

and

$$\frac{\partial \varphi}{\partial s} = 0. \tag{3.23}$$

Note that for two-dimensional reentrant jets with lift the conditions are more complicated. Figure 9 shows a sample computed cavity shape for a two-dimensional flat plate cavitator at an angle of attack.

3.2 General Incompressible Flows

This section, which is based on Kring et al (2000), presents some initial results for a fully three-dimensional time-domain simulation of the flow about general supercavitating bodies. The intent of the effort is to study various ventilated cavitators, lifting appendages, and bodies that may penetrate the cavity wall. The time-domain approach, useful for the formulation of the nonlinear boundary conditions on the cavity free surface, will also allow the application of this method to flight simulation and control studies (see section 5).

In this fully three-dimensional initial value problem for a moving, cavitating body, several boundary conditions must be specified. These include the body boundary condition, nonlinear cavity conditions on the moving free surface, a reentrant jet closure, and a shed wake sheet. At each time step, these conditions are integrated both in time and in space and combined with the governing Laplace equation to produce a boundary value problem that is formulated as a boundary integral equation of the mixed Neumann-Dirichlet type.

The numerical scheme in this paper has been adapted from a boundary-element method developed for free-surface gravity waves interacting with submerged and floating bodies (Kring, et al, 1999), with guidance for the cavity boundary and jet closure conditions from Uhlman (1987 and 1989) and Fine and Kinnas (1993). The free surface scheme was designed in accordance with the numerical stability analysis of Vada and Nakos (1993). A key result of that analysis was the demonstration that both high-order elements and mixed explicit-implicit time marching are needed for numerical stability. The boundary-element method employed here is a high-order, B-spline-based approach developed originally by Maniar (1995) with a so-called fast or accelerated solver

developed by Phillips and White (1997) and applied in Kring, et al, (1999b). Whereas direct solution of full matrices requires computational effort proportional to the cube of the number of unknowns, N, -- that is, effort of order N^3, or $O(N^3)$ -- and other traditional methods may show improved performance of $O(N^2)$, the accelerated method discussed in this section is $O(N)$.

Figure 10 illustrates the potential flow, initial boundary-value problem for a cavitating disk with a trailing cavity, reentrant jet closure, and shed wake. The body may have any shape and the method may be extended to add lifting appendages and planing bodies.

In order to provide a computational window to track this moving body, the three-dimensional problem is defined with respect to a mean-body frame of reference, $\vec{x}$. Points in the inertial frame, $\vec{x}_I$, are related to the mean-body frame by the relation:

$$\vec{x}_I = \vec{x} + \int_{t_0}^{t} \vec{U}(\vec{x},\tau)d\tau, \tag{3.24}$$

where t is time. The motion of the mean-body frame, $\vec{U}(\vec{x},t)$, is a function of space since it may be rotating with respect to the inertial frame, so that

$$\vec{U}(\vec{x},t) = \vec{U}(0,t) + \Omega(t)\vec{x}, \tag{3.25}$$

where $\vec{\Omega}(t)$ is a rotational transformation matrix and $\vec{U}(0,t)$ is the translation at the origin. The mean-body frame is defined about the assumed mean position of the disk cavitator, so that the disk tends to oscillate around $x = 0$.

Initial Conditions

The problem is started impulsively from an assumed initial geometry and distribution of potential. Two initial conditions have been considered. In the first case, the potential on the cavity is set to zero on an assumed surface. Physically, this can be considered as an artificial pressure and cavity location that is released at $t = 0$. If the cavitator disk is set in steady motion, the transients due to this artificial start-up should eventually decay. The second case involves solution of a Neumann problem in which the cavity is considered to be a fixed wall. The potential from this solution is then used as the initial condition for the time-domain simulation. The intent is to reduce the size of the startup transient.

Governing Equation

The potential flow exterior to the surface S (the union of the cavity S_{C^+} and S_{C^-}; the body, S_B; and the jet, S_J) is governed by the Laplace equation with allowance for the wake cuts collapsed onto the surface S_W. Hence,

$$\nabla^2\phi = 0 \tag{3.26}$$

where ϕ is the disturbance potential.

Green's third identity, equation 3.8, is applied in a manner similar to that described for steady axisymmetric flows. In this case, however, we explicitly include an integration over the wake surface, S_W, as follows:

$$2\pi\phi(\vec{x}) + \iint_S \left(\phi(\vec{x}')G(\vec{x};\vec{x}') - \phi_n(\vec{x}')G_n(\vec{x};\vec{x}')\right)d\vec{x}' + \iint_{S_W} \Delta\phi(\vec{x}')G_n(\vec{x};\vec{x}')d\vec{x}' = 0 \tag{3.27}$$

where the Green's function is defined by equation 3.9.

Cavity Conditions

The cavity conditions on S_{C^+} and S_{C^-} are posed in the curvilinear frame of reference defined by the parametric surface, $\vec{\xi}(u,v,t)$. The parametric coordinates, (u,v), are the presumed streamwise and circumferential directions, respectively. This semi-Eulerian formulation is important for a numerically consistent representation of the boundary condition on the moving surface. Surface potentials, $\varphi(u,v,t)$ and $\varphi_0(v,t)$, are defined through the decomposition of the perturbation potential:

$$\phi(\vec{\xi}(u,v,t),t) = \varphi(u,v,t) + \varphi_0(v,t) \tag{3.28}$$

The first part of the surface potential, φ, satisfies the dynamic cavity condition implicitly in the numerical scheme. The second part, φ_0, which is constant along the presumed streamline direction, u, satisfies continuity of the disturbance potential at the cavity detachment locus and appears explicitly in the dynamic cavity condition on the leading cavity surface.

Applying the chain rule to the decomposition leads to relations for the time-derivative and gradient:

$$\frac{\partial \phi}{\partial t} = \frac{\partial(\varphi+\varphi_0)}{\partial t} - \nabla_u(\varphi+\varphi_0)\cdot\nabla_u\vec{\xi} \tag{3.29}$$

and

$$\nabla\phi = \nabla_u(\varphi+\varphi_0) + \frac{\partial\phi}{\partial n}\hat{n} \tag{3.30}$$

where $\hat{n}$ is the unit vector normal to the surface and ∇_u is the surface gradient operator defined by

$$\nabla_u f = \frac{\frac{\partial f}{\partial u}\left[\hat{u}-(\hat{u}\cdot\hat{v})\hat{v}\right] + \frac{\partial f}{\partial v}\left[\hat{v}-(\hat{u}\cdot\hat{v})\hat{u}\right]}{\|\hat{u}\times\hat{v}\|^2} . \tag{3.31}$$

Here $\hat{u}$ and $\hat{v}$ are unit vectors that are non-orthogonal in general.

Kinematic Boundary Condition

The total time derivative of the function that defines the cavity surface must vanish. Applying the Gallilean transform from the inertial to the mean-body frame and defining the normal coordinate, n, and the surface displacement in the normal direction, $h(u,v,t) = \vec{\xi}(u,v,t)\cdot\hat{n}(u,v,t)$, yields the kinematic condition:

$$\frac{\partial h}{\partial t} - \vec{U}\cdot\nabla_u h = -\nabla_u(\varphi+\varphi_0)\cdot\nabla_u h - \vec{U}\cdot\hat{n} + \frac{\partial\phi}{\partial n} \tag{3.32}$$

Dynamic Boundary Condition

The dynamic condition specifies a constant pressure on the cavity surface at all times. The derivation of this condition begins with the unsteady Bernoulli condition in the inertial frame (referencing atmospheric pressure as zero). With $z=0$ representing the mean ocean surface:

$$p_c = -\rho\left(\frac{\partial\phi}{\partial t} + \frac{1}{2}\nabla\phi\cdot\nabla\phi + gz\right) \tag{3.33}$$

where p_c is the cavity pressure.

Applying the Gallilean transform from the inertial to the mean-body frame and substituting relations for the surface potential yields

$$\frac{\partial \varphi}{\partial t} - \vec{U} \cdot \nabla_u \varphi = -\frac{\partial \varphi_0}{\partial t} + \vec{U} \cdot \nabla_u \varphi_0 + \left[\left(\vec{U} \cdot \hat{n} \right) \frac{\partial \phi}{\partial n} - \frac{1}{2} \nabla \phi \cdot \nabla \phi \right] - gz - \frac{p_c}{\rho} \tag{3.34}$$

Cavitator Wetted-Surface Condition

A Neumann body-boundary condition similar to equation 3.5 is applied to the cavitator wetted surface, S_B.

Jet Condition

The reentrant jet is artificially truncated (cut perpendicular to the streamline) and assumed to have reached a steady diameter with no cross-flow components and a pressure equal to the cavity pressure across the face of the cut. Thus, it has an imposed flux and an imposed pressure. Although this is intended to be a time-accurate formulation for the cavity problem, a steady-state jet condition has been used to date.

We start with the steady, dynamic boundary condition: equation 3.34 with the time derivative set to zero. If there is no cross-flow, then $\nabla \phi = \phi_n \hat{n}$ on the jet. Therefore, the jet condition becomes

$$U_n \frac{\partial \phi}{\partial n} - \frac{1}{2} \left(\frac{\partial \phi}{\partial n} \right)^2 = gz + \frac{p_c}{\rho}, \tag{3.35}$$

where $U_n = \vec{U} \cdot \hat{n}$.

Choosing the positive root, consistent with the cavity conditions, the jet flux then becomes:

$$\frac{\partial \phi}{\partial n} = U_n + \sqrt{U_n^{\,2} - 2\left(gz + \frac{p_c}{\rho} \right)} \tag{3.36}$$

With no cross-flow, the potential across the jet face must be constant at a given depth and is set equal to the potential on the adjacent cavity.

Cavity Detachment and Kutta Conditions

The additional potential, φ_0, on the leading cavity surface, S_{C^+}, that detaches from the cavitator body boundary is specified by a detachment condition across the body-cavity intersection, $\vec{x}\,|_{BE}$. With the further constraint that the first surface potential vanishes at the cavity detachment line, $\varphi\left(u\,|_{BE}, v, t\right) = 0$, the additional potential is,

$$\varphi_0(v,t) = \phi(\vec{x}\,|_{BE}, t), \tag{3.37}$$

which represents the cavity detachment condition. A cavity trailing edge is defined at the junction of the leading and lagging cavity surfaces where the potential jump across the wake is specified as

$$\Delta\phi\,|_{TE}\,(v,t) = \left(\varphi^+\,|_{TE} - \varphi^-\,|_{TE} \right) + \varphi_0, \tag{3.38}$$

which comprises the Kutta condition. For a time-dependent wake, a nonlinear evolution equation should govern the propagation of the shed vorticity downstream, but, to date, a simplifying assumption has been used: The wake position is fixed and a steady state asymptotic distribution is assumed for the shed vorticity.

Numerical Implementation

The scheme begins with initial conditions for the geometry and the surface potential, φ, at time $t = 0$. The detachment conditions, the Kutta conditions, and the mixed boundary-integral equation are then solved simultaneously to find the normal velocity on the cavity surface and the potential on the body. This is referred to as the mixed BVP, which will be solved at each time step as the surface evolves. The cavity conditions and the mixed BVP must be integrated in time and space.

After the impulsive start, each step in the temporal integration begins by first satisfying the kinematic and dynamic boundary conditions to update the geometry and surface potential on the cavity. The mixed BVP is then solved to update the potential on the body and the normal velocity on the cavity.

To summarize, at the start-up $\left(t = 0^+\right)$:

0. Given initial conditions $\varphi^0, \vec{\xi}^0$ on S_C solve mixed BVP for $\phi_n{}^0$ on S_C.

At each subsequent time-step:

1. Determine body motion: impose or solve equation of motion.
2. Integrate the kinematic condition on the cavity to find $\vec{\xi}^{n+1}$ on S_C.
3. Update the cavity and body geometry.
4. Integrate the dynamic condition on the cavity to find φ^{n+1} on S_C.
5. Set the body and jet conditions for $\phi_n{}^{n+1}$ on S_B and S_J.
6. Solve mixed BVP to find $\phi_n{}^{n+1}, \varphi_0{}^{n+1}$ on S_C and ϕ^{n+1} on S_B.

The continuous problem is discretized by a set of high-order B-spline patches that represent the geometry of the body and cavity and another set that represent the flow quantities of potential, φ, normal velocity, ϕ_n, and cavity displacement, h.

Third- to fifth-order splines and Galerkin schemes are used to spatially integrate both the cavity conditions and the mixed BVP. The use of a high-order discretization has been shown to be stable for the free-surface gravity wave problem where more typical flat panel methods have failed. Initial work with low-order, three-dimensional panel methods indicated that this would hold for cavity free-surface flows also.

The kinematic cavity condition is integrated in time using a forward (explicit) Euler method and the dynamic cavity condition is integrated in time using a backward (implicit) Euler method. For the dynamic condition, only the linear terms for the surface potential are treated implicitly. This mix of explicit and implicit methods was selected based on a stability analysis for wave propagation over discretized free surfaces.

The geometry and surface potential are represented by B-spline basis functions in space that overlap with their neighbors. These conditions produce a banded system of linear equations that must be solved at each time-step.

The unknown normal velocity on the cavity and potential on the body are obtained from the solution of the boundary integral equation, which contains the detachment and Kutta conditions. On the cavity, the disturbance potential at any instant is the sum of the known surface potential and an unknown additional potential.

The solution of the integral equation at each time-step represents the largest computational burden in the problem. To maintain high local accuracy and satisfy numerical stability requirements, a high-order, B-spline, Galerkin boundary-element method is used for this integral equation and two solvers are adopted. The first is a traditional dense matrix solver that requires $O(N^2)$ computational memory and operations. The second is an accelerated solver, using a precorrected fast Fourier transform (FFT) algorithm that is similar to the fast multipole method. This involves a sparse matrix requiring only $O(N)$ computational memory and operations.

Selected Results – General Flows

To date, the high-order boundary-element method has been adapted for the mixed BVP with the detachment and Kutta conditions. In Figure 11 an initial solution of the problem at the startup has been computed. In this figure, the high negative values of the normal velocity at the trailing end of the cavity show that the assumed geometry is too small and the cavity will lengthen along the side in the next time step. Work on the complete simulation is in progress.

This boundary-element method is numerically convergent, has been compared to analytic solutions for simple geometries, and has been validated experimentally in its original ship seakeeping manifestation, but it is too early to judge the performance of the cavity time-marching scheme and the wake sheet.

3.3 Cavitating Fins

In this section, we describe a tool used to predict the flow around cavitating fins, particularly fins with wedge-shaped cross-sections. The tool uses a boundary element method to predict six-degree-of-freedom forces for steady flight. The computed forces have been used as input to guidance and control simulations, as described below. The basic computational approach is summarized in Fine and Kinnas (1993).

A simple wedge-shaped fin geometry was considered for this investigation. It would be easily fabricated and appropriate to operation in the supercavitating regime, but is probably not optimal, although the wedge shape provides good strength characteristics. It is also convenient for comparison of the boundary-element results with preliminary predictions based on two-dimensional theory such as that of Uhlman (1987, 1989) or Wu (1956), or the various experimental data presented in May (1975). Also, for small wedge angles, the unsteady effects associated with the transition between partial cavitation and supercavitation are confined to a very limited range of deflection angles.

In computing the forces, a high level of detail was required over even the limited operational range considered, because several cavity detachment modes must be taken into account. The forces acting on cavitating fins are complicated by these different flow regimes. For wedge-shaped fins, four regimes must be considered. If the flow is symmetric about the symmetric fin, and the cavitation number is low enough, a cavity develops at the base of the wedge. Of course the fin does not develop lift in this case. At small angles of attack and moderately low cavitation numbers, a partial cavity develops at the leading edge separately from the base cavity. At larger angles of attack or lower cavitation numbers, the cavity originating at the leading edge becomes large enough to merge with the base cavity, forming a supercavity that envelopes all the surfaces except the pressure face. The lift curve slope in the supercavitating regime is less than in the partially cavitating regime. The final regime (which has not been modeled for the current effort) involves very high cavitation numbers. In that case, the cavities are eliminated and replaced with separation regions. The three regimes are shown in Figure 12.

Brief Description of LScav

ETC's Lifting Surface Cavitation code (LScav) computes the first iteration of the fully nonlinear cavity solution for a general three-dimensional wing attached to a non-lifting "center-body" at arbitrary cavitation number. The flow is assumed to be steady, inviscid, incompressible, and irrotational (outside of a thin vortex sheet trailing behind the lifting surface). The solution is found by applying a disturbance-potential-based panel method that involves a numerical solution of Green's third identity. The method is described in the context of cavitating propellers in Fine (1992).

The wing and center-body are assumed to be symmetric about a vertical plane intersecting the body centerline. The cavity solution represents the first iteration of a fully nonlinear solution. In order to understand the difference between the first iteration solution and the fully nonlinear solution, consider a two-dimensional hydrofoil and assume that the cavity length is known. Since the cavity length is a single-valued function of the cavitation number for all stable two-dimensional cavities, the cavitation number may not be specified in this canonical problem and, in fact, must be

considered an unknown to be determined as part of the solution. To solve the nonlinear problem, one must first guess the location of the cavity boundary and satisfy the boundary conditions on that approximate surface. However, since we cannot say beforehand that our approximate location of the cavity boundary is the correct one, we can only satisfy the dynamic boundary condition (the condition that the pressure be constant on the boundary and equal to the cavity pressure) in the solution. In general, the kinematic boundary condition (the condition that the normal velocity vanish on the cavity surface) will not be satisfied. However, we may use the kinematic boundary condition to update the location of the cavity surface.

Since the first guess of the cavity location is arbitrary, it is numerically convenient to first solve the boundary conditions on the wing surface and, for supercavities, on a zero-thickness sheet downstream of the wing. To find the nonlinear solution, one simply re-solves the problem with the new body shape defined from the first iteration (see Figure 13). The fully nonlinear solution is found when the solution converges to some preset tolerance. In previous work (Fine, 1992), extensive studies showed that the accuracy of the first iteration solution relative to the fully nonlinear solution was very good over a reasonably large range of operating conditions. As a result (and motivated by the significant computational savings of solving only the first iteration) LScav was configured to compute only the first iteration of the nonlinear solution.

Sample LScav results are shown in Figure 14, which indicates the convergence of the cavity planform for a fin with a triangular planform and a wedge-shaped cross-section. Table 1 shows the convergence of the corresponding lift and drag coefficients and the cavity volume. Convergence to three significant digits occurs with about 1300 total panels. The total amount of memory that is required for this size problem is roughly 108 MB.

LScav has been validated through comparison of computed lift and drag coefficients to measurements made in a water tunnel. A sample of the validation is shown in Figure 15.

4 APPLICATION OF SLENDER-BODY-THEORY

This section is based on Varghese, et al, (1997).

In slender-body theory (SBT), the slenderness ratio, ε, of the body is defined as the ratio of the maximum radius to the total length. It is assumed that $\varepsilon << 1$ and that the cavitation number and the inverse square of the Froude number are of order $\varepsilon^2 \ln \varepsilon$ (Chou, 1974). The axial gradient of the body-cavity radius should be of the same order as the slenderness parameter, restricting the analysis to certain classes of cavitators using this approach.

In the following sections, Chou's formulation is extended to subsonic compressible fluid flows. Also presented are selected results for an incompressible fluid. Chou's original method incorporated terms accounting for an axisymmetric gravitational field, and these have been retained in the following presentation. Results may be found in Varghese, et al, (1997).

4.1 Mathematical Formulation

The present SBT analysis assumes an axisymmetric body with a conical cavity closure. A salient cavity detachment point is specified in the model as is shown in Figure 16. The free-stream velocity, U_∞, is at zero angle of attack. The body length is ℓ_b, the cavity length is ℓ_c, and the total length is ℓ. In the following formulation, all lengths are made dimensionless with body length, velocities with free stream velocity, and potential with body length and free stream velocity.

Incompressible Flow

The total potential is

$$\Phi = x + \phi \,, \tag{4.1}$$

where ϕ is the perturbation velocity potential. The axial and radial components of the perturbation velocity are

$$u_x = \frac{\partial \phi}{\partial x} \quad \text{and} \quad u_r = \frac{\partial \phi}{\partial r}, \tag{4.2}$$

respectively.

The SBT outer expansion results in Laplace's equation for the perturbation potential:

$$\phi(x,r)+\frac{\phi_r}{r}+\phi_{rr}=0 \quad . \tag{4.3}$$

For a continuous distribution of sources along the x-axis, the solution for equation 4.3 can be written as

$$\phi(x,r)=-\frac{1}{4\pi}\int_0^{\ell}\frac{q(\xi)d\xi}{\sqrt{(x-\xi)^2+r^2}} \quad , \tag{4.4}$$

where $q(\xi)$ is the source strength defined along the axis at location ξ. From the SBT inner expansion, assuming $db/dx = O(\varepsilon)$, the source strength is

$$q(x)=\pi\frac{d\left(b^2\right)}{dx} \tag{4.5}$$

The kinematic boundary condition,

$$u_r=\frac{db}{dx} \quad , \tag{4.6}$$

is formed from the no-flux condition on the body and cavity surfaces. The cavity pressure is assumed to be constant. The dynamic boundary condition is derived from Bernoulli's equation:

$$\sigma=-C_p=2u_x+{u_r}^2-\frac{2(x-1)}{F_b^2}. \tag{4.7}$$

Here, σ is the cavitation number, C_p, is the pressure coefficient, and

$$F_b\overset{\Delta}{=}\frac{U\infty}{\sqrt{g\ell_b}}$$

is the Froude number based on body length. Here g is the gravitational acceleration.

Let $\zeta_b=b_b^2$ and $\zeta_c=b_c^2$. Substituting expressions for the radial and axial velocity components defined at the body-cavity surface, in the dynamic boundary condition, equation 4.7, results in a non-linear integro-differential equation:

$$\sigma=\frac{1}{2\pi}\int_0^{\ell}\frac{q(\xi)(x-\xi)d\xi}{\left[(x-\xi)^2+\zeta_c\right]^{\frac{3}{2}}}+\left(\frac{db_c}{dx}\right)^2-\frac{2(x-1)}{F_b^2}, \quad 1\le x\le\ell, \tag{4.8}$$

where b_c is the cavity radius. Integrating by parts and using equation 4.5 for the source strength yields (Chou, 1974):

$$\frac{1}{2}\int_1^{\ell}\frac{\frac{d^2\zeta_c}{d\xi^2}d\xi}{\sqrt{(x-\xi)^2+\zeta_c}}=-\sigma-\frac{1}{2}\int_0^1\frac{\frac{d^2\zeta_b}{d\xi^2}d\xi}{\sqrt{(x-\xi)^2+\zeta_c}}+\frac{\frac{d\zeta_c}{dx}\Big|_{\ell}}{\sqrt{(x-\ell)^2+\zeta_c}}-\frac{\frac{d\zeta_b}{dx}\Big|_0}{\sqrt{x^2+\zeta_c}}+\left(\frac{db_c}{dx}\right)^2-\frac{2(x-1)}{F_b^2}. \tag{4.9}$$

With the assumption that the cavity closes as a cone, the above equation can be written for a conical body as:

$$\frac{1}{2}\int_1^{\ell}\frac{\frac{d^2\zeta_c}{d\xi^2}d\xi}{\sqrt{(x-\xi)^2+\zeta_c}}=-\left[\sigma+\frac{1}{2}\int_0^1\frac{\frac{d^2\zeta_b}{d\xi^2}d\xi}{\sqrt{(x-\xi)^2+\zeta_c}}-\frac{\left(\frac{d\zeta_c}{dx}\right)^2}{4\zeta_c^2}+\frac{2(x-1)}{F_b^2}\right]. \tag{4.10}$$

In this equation, the right hand side is known for a given cavity shape. In the current approach, the cavity shape is approximated and updated iteratively. With an assumed initial cavity shape, equation 4.10 is solved for a new cavity shape. For that procedure, the cavity axial length is discretized into *n* panels. In each panel, a locally quadratic polynomial is used to approximate ζ_c. Varghese, et al, (1997) presents the details of building and solving a system of equeations to update the discretized cavity geometry.

Pressure and Drag Coefficients for the Case of an Incompressible Fluid

Upon convergence, the pressure coefficient along the body is computed as follows:

$$C_p(x) = -\frac{1}{2}\int_0^{\ell} \frac{\frac{d\zeta}{d\xi}(x-\xi)d\xi}{\left[(x-\xi)^2+\zeta_b\right]^{\frac{3}{2}}} - \left(\frac{db_b}{dx}\right)^2 + \frac{2(x-1)}{F_b^2}, \qquad 0 \le x \le 1. \tag{4.11}$$

The pressure coefficient along the cavity is the negative of the cavitation number. The base drag coefficient, based on the maximum body cross-sectional area, is found by integrating the pressure coefficients over the body:

$$C_{db} = \frac{1}{\zeta_b(1)}\int_0^1 C_p(x)\frac{d\zeta_b}{dx}dx + \sigma \ . \tag{4.12}$$

In Varghese, et al, (1997), viscous drag corrections for axisymmetric bodies were developed based on three different methods: (1) Thwaites' method with a linear velocity profile; (2) Thwaites' method with a shear function; and, (3) the method of Falkner and Skan. Moderate improvement to the comparison of the predicted total cavitator drag to experimental data was obtained for certain cases.

Subsonic Compressible Flow

In this section we extend the previous formulation to the case of compressible flows. Results may be found in Varghese, et al, (1997). A method is proposed in Kirschner, et al, (1995) for extending the axisymmetric boundary-element method presented above to compressible subsonic flows.

The outer expansion for the perturbation potential for slender bodies in a compressible fluid results in the following governing equation (Ashley and Landahl, 1965):

$$\left(1-M_\infty^2\right)\phi_{\hat{x}\hat{x}} + \frac{\phi_{\hat{r}}}{\hat{r}} + \phi_{\hat{r}\hat{r}} = 0 \ , \tag{4.13}$$

where the hatted variables represent the physical coordinate for the subsonic flows. With a transformation to $x = \hat{x}$ and $r = \beta\hat{r}$ where $\beta = \sqrt{1-M_\infty^2}$, equation 4.13 reduces to Laplace's equation. Thus the solution for a continuous source distribution is

$$\phi(x,r) = -\frac{1}{4\pi}\int_0^{\ell} \frac{q(\xi)d\xi}{\sqrt{(x-\xi)^2+\beta^2 r^2}} \ . \tag{4.14}$$

Here $q(x)$ is defined by equation 4.5. The radial velocity component is given by equation 4.6. However, the axial velocity component depends on β as follows:

$$u_x(x,r) = \frac{1}{4\pi}\int_0^{\ell} \frac{q(\xi)(x-\xi)d\xi}{\left[(x-\xi)^2+\beta^2 r^2\right]^{\frac{3}{2}}}. \tag{4.15}$$

With the constant.cavity pressure assumption, the dynamic boundary condition is derived from the compressible Bernoulli equation:

$$\sigma = \frac{2}{\gamma M_\infty^2}\left\{1-\left[1-(\gamma-1)M_\infty^2\left(u_x+\frac{u_r^2}{2}\right)\right]^{\gamma/\gamma-1}\right\}. \tag{4.16}$$

As for the case of incompressible flow, substitution of equations 4.6 and 4.15 respectively for the radial and the axial velocity components of equation 4.16 yields an integro-differential equation:

$$\left[1-\frac{\gamma M_\infty^2}{2}\sigma\right]^{\frac{\gamma-1}{\gamma}} = 1-(\gamma-1)M_\infty^2\left[\frac{1}{4\pi}\int_0^\ell \frac{q(\xi)(x-\xi)}{\left[(x-\xi)^2+\beta^2\zeta_c\right]^{\frac{3}{2}}}d\xi+\frac{1}{2}\left(\frac{db_c}{dx}\right)^2\right],\ 1\le x\le \ell, \tag{4.17}$$

Integrating by parts and substituting equation 4.5 for the source strength, the governing equation becomes

$$\int_1^\ell \frac{\frac{d^2\zeta_c}{d\xi^2}d\xi}{\sqrt{(x-\xi)^2+\beta^2\zeta_c}} = \frac{4}{(\gamma-1)M_\infty^2}\left\{\left[1-\frac{\gamma M_\infty^2}{2}\sigma\right]^{\frac{\gamma-1}{\gamma}}-1\right\}$$
$$-\int_0^1 \frac{\frac{d^2\zeta_b}{d\xi^2}d\xi}{\sqrt{(x-\xi)^2+\beta^2\zeta_c}} - \frac{\frac{d\zeta_c}{dx}\Big|_\ell}{\sqrt{(x-\ell)^2+\beta^2\zeta_c}} + \frac{\frac{d\zeta_b}{dx}\Big|_0}{\sqrt{x^2+\beta^2\zeta_c}} + \left(\frac{db_c}{dx}\right)^2 \tag{4.18}$$

For a conical body with a conical cavity closure, this equation becomes

$$\int_1^\ell \frac{\frac{d^2\zeta_c}{d\xi^2}d\xi}{\sqrt{(x-\xi)^2+\beta^2\zeta_c}} = \frac{4}{(\gamma-1)M_\infty^2}\left\{\left[1-\frac{\gamma M_\infty^2}{2}\sigma\right]^{\frac{\gamma-1}{\gamma}}-1\right\}-\int_0^1 \frac{\frac{d^2\zeta_c}{d\xi^2}}{\sqrt{(x-\xi)^2+\beta^2\zeta_c}}d\xi+\frac{\left(\frac{d\zeta_c}{dx}\right)^2}{2\zeta_c}. \tag{4.19}$$

Pressure and Drag Coefficients for the Case of a Compressible Fluid

The pressure coefficient along the body is given by

$$\frac{\gamma M_\infty^2}{2}C_p(x) = \left[1-(\gamma-1)M_\infty^2\left(\frac{1}{4}\int_0^\ell \frac{\frac{d\zeta_b}{d\xi}(x-\xi)d\xi}{\left[(x-\xi)^2+\beta^2\zeta_b\right]^{\frac{3}{2}}}+\frac{1}{2}\left(\frac{db_b}{dx}\right)^2\right)\right]^{\frac{\gamma}{\gamma-1}}-1,\quad 0\le x\le 1. \tag{4.20}$$

Using this form to compute the pressure coefficient, the base drag coefficient, C_{db}, for the compressible case can be calculated using equation 4.12.

4.2 Selected Results – Slender Body Theory

The SBT model was used to predict supercavitating flows of both compressible and incompressible fluids at various cavitation numbers. All the results shown here are for a 10°-cone angle. The cavity shapes (scaled to show cavities enlarged in the radial direction) for cavitation numbers ranging from 0.005 to 0.05 are shown in Figure 17 for the incompressible case. The cavity length increases as the cavitation number decreases, as expected. The predicted surface pressure distributions are plotted in Figure 18 for different cavitation numbers. This quantity decreases as the cavitation number increases. Results have been compared with curve fits of empirical data (May, 1975). In Figure 19, the maximum cavity radius has been plotted, made dimensionless with

respect to the radius at cavity detachment. Figure 19 illustrates an excellent match with experimental values, particularly at low cavitation numbers where SBT is more valid.

4.3 Summary – SBT

Formulations have been presented for applying Chou's SBT model to both incompressible and compressible flows. Selected results have been presented for the incompressible case. Some comparison with experimental data has been presented.

In Varghese, et al, (1997), additional formulation, results, discussion, and comparison are presented for the effects of both an axisymmetric gravity field and viscous drag.

5 NUMERICAL FLIGHT AND CONTROL SYSTEM SIMULATION

In this section, which is based on Kirschner, et al, (2001), we describe numerical flight simulation for supercavitating vehicles. We first discuss the nonlinear forces acting on the cavitator, the fins (if present), and any portions of the hull that penetrate the cavity boundary during excursions from the fully-enveloped condition. Next, we describe simulation of vehicle flight, including system stability and system performance during execution of a banked turn. Without control, some vehicle configurations can be unstable, whereas a feedforward-feedback strategy can control some configurations over a range of turn rates.

5.1 Hydrodynamical Model

The behavior of the cavity is central to the dynamics of a supercavitating vehicle. The nominally steady cavity behavior forms the basis of the quasi-time-dependent model implemented for the current investigation. This model affects not only the forces acting at the nose of the vehicle, but also the immersion of the fins and any planing forces due to contact between the body and the cavity boundary. It is the cavity that makes this dynamical system not only nonlinear, but also dependent on strong memory effects that link the history of motion to the instantaneous cavity shape.

The three parameters that characterize time-averaged or quasi-steady ventilated flows are the cavitation number, the cavity Froude number, and the ventilation coefficient. The cavitation number is defined in equation 2.11, and has been discussed extensively in the formulations above. The cavity Froude number (not to be confused with the related Froude number based on body length discussed above) and the ventilation coefficient are defined as

$$\mathcal{F} \stackrel{\Delta}{=} \frac{V}{\sqrt{g d_c}} \tag{5.1}$$

and

$$C_Q \stackrel{\Delta}{=} \frac{Q}{V d_c^2}, \tag{5.2}$$

respectively. Again, g is the gravitational acceleration. The cavitator diameter is d_c. p_∞ and p_c are the ambient and cavity pressures, respectively. V is the vehicle velocity and Q is the volumetric rate at which ventilation gas is supplied to the cavity. The cavitation number expresses the tendency of cavitation to occur in a flow, and is thus a principal quantity governing cavity dimensions. The Froude number characterizes the importance of gravity to the flow, and therefore governs distortions from a nominally axisymmetrical shape. The ventilation coefficient governs the time-dependent behavior of the cavity as ventilation gas is entrained by the flow.

For the horizontal trajectories considered in these lecture notes, the cavitation number is very low (on the order of 0.015 to 0.030) and the cavity Froude number is typically rather high (on the order of 50 to 100). The cavity is slender, and its maximum diameter is at least 5 times greater than the cavitator diameter. Cavity tail-up under the influence of gravity is small, but not insignificant to the vehicle design.

The nomenclature used for basic vehicle dynamics during the remainder of these lecture notes is presented in Figure 20. The x-axis is directed forward along the nominal vehicle long axis, y is to starboard, and z completes an orthogonal system obeying the right-hand rule. The origin of this coordinate system is located at the cavitator pivot point. Following Kiceniuk (1954), the following relationships have been employed to estimate the hydrodynamic forces and moment acting on the circular disk cavitator selected for investigation:

$$C_D(\sigma,\alpha_c)=\frac{D_c(\sigma,\alpha_c)}{1/2\,\rho V^2 A_c}\cong C_{D0}(1+\sigma)\cos^2\alpha_c$$

$$C_L(\sigma,\alpha_c)=\frac{L_c(\sigma,\alpha_c)}{1/2\,\rho V^2 A_c}\cong C_{D0}(1+\sigma)\cos\alpha_c\ \sin\alpha_c$$

$$C_M(\sigma,\alpha_c)=\frac{M_c(\sigma,\alpha_c)}{1/2\,\rho V^2 d_c A_c}\cong 0 \quad . \tag{5.3}$$

where D_c and L_c are the drag and lift forces acting on the cavitator, M_c is the hydrodynamic moment, and A_c is the disk area. The drag coefficient at zero angle of attack and cavitation number, C_{D0}, is taken as approximately 0.805 based on empirical data (May, 1975).

Various analytical, numerical, and semi- and fully-empirical models have been developed that provide estimates of the maximum cavity diameter, d_{max}, and the cavity length, ℓ_c. The analytical formulae of Garabedian (1956) provide useful and reasonably accurate approximations for investigation of vehicle dynamics:

$$\frac{d_{max}}{d_c}=\sqrt{\frac{C_D(\sigma,0)}{\sigma}} \tag{5.4}$$

and,

$$\frac{\ell_c}{d_c}=\sqrt{\frac{C_D(\sigma,0)}{\sigma}\ln\frac{1}{\sigma}} \tag{5.5}$$

For purposes of time-domain simulation of vehicle dynamics, it is desirable to use simple models. In a cylindrical-polar system with coordinates x, r, and θ, the nominal axisymmetric shape can be approximated as:

$$\frac{r_c}{d_c}=\frac{d_{max}}{2d_c}\left[1-\left(\frac{x/d_c-\ell_c/2d_c}{\ell_c/2d_c}\right)^2\right]^{1/2.4} \tag{5.6}$$

where $r_c(x,\theta)$ is the cavity offset (Münzer and Reichardt, 1950, derived from a low-order potential flow model).

The effects of gravity and turning on this generalized ellipsoidal cavity shape can be approximated as a distortion of the line of centers (y_c,z_c), described by

$$y_c(x)=\mp\frac{1}{\mathcal{F}^2}\frac{a_{turn}}{g}\left(\frac{x}{d_c}\right)^2 \tag{5.7a}$$

and

$$z_c(x)=-\frac{1}{\mathcal{F}^2}\frac{a_g}{g}\left(\frac{x}{d_c}\right)^2 . \tag{5.7b}$$

where a_{turn} is the turn acceleration and a_g is the tail-up acceleration of the cavity, here approximated using the semi-empirical formula recommended by Waid (1957). A binomial expansion (retaining the second term) has been used to simplify the term associated with turning, applying the principle of independent development of cavity sections (Logvinovich, 1985) and assuming that the cavitator traces a circular path in a horizontal plane. Although the distortion of the cavity line of centers due to turning and gravity has been considered, distortions associated with cavitator lift have been ignored. Cavity foreshortening has also been neglected, and distortions of the cavity sections from their nominal circular shapes have been ignored for the current investigation. Under these assumptions, the cavity locus of section centers is coincident with the cavitator trajectory.

Equations 5.7 apply to a steady horizontal turn with gravity acting in the vertical direction. Although generalization to more complicated trajectories would not be difficult, the current formula provides insight concerning the behavior and limitations of a supercavitating vehicle in a turn. The consistent formulation shows the relative influences of turning and gravity, both of which become increasingly important at low cavity Froude numbers. To the order of terms retained in equations 5.7, the locus of cavity section centers is quadratic in the axial coordinate.

The importance of cavity distortion in high turn rates is apparent in Figure 21, which presents results for an extreme turn (in this case, a 5-g turn that is probably impractical, but is illustrative of the cavity-body interactions important to the problem). The nonlinear behavior is clear from this figure. Firstly, as the cavity distorts from a nominally axisymmetric configuration, the immersion of the fins into the ambient liquid outside the cavity becomes asymmetric. Therefore, the couple associated with symmetric or anti-symmetric fin trim will result in nonlinear system response. Secondly, a system designed for close envelopment of the vehicle by a nominally axisymmetric cavity (or even one designed for cavity tail-up in straight and level flight) will be subject to nonlinear forces associated with afterbody planing.

Only the most essential aspects of the unsteady hydrodynamics have been modeled. Self-pulsation of the cavity has been ignored, but changes in cavity shape due to cavitator motion have been taken into account via a convolution scheme. The fin forces are evaluated at each time step via a look-up algorithm. Thus, the three basic cavitating fin flow regimes (base- and partially cavitating and supercavitating) contribute to the unsteady fin forces, but various higher-order hydrodynamic effects in the evolution of the fin cavity are not modeled. Most importantly, hydrodynamic added mass effects have been ignored.

Secondary flows – notably, those due to the fins and to afterbody planing – have been ignored in the current effort, although the theory used to estimate the afterbody planing forces accounts for the lowest-order effect of the spray jet.

In the nominal condition of straight and level flight, the supercavitating vehicle configurations of interest in these lecture notes are supported in the vertical direction by a lift force acting on the cavitator and by a combination of planing and lift on the fins near the after end of the vehicle. The optimal support by afterbody planing forces has not yet been determined with certainty, although the results presented below are enlightening. This secondary function of the cavitator as a lifting surface is essential to operation of a supercavitating vehicle. Since virtually no lift is provided by the gas-enveloped hull, the vehicle weight must be supported by the control surfaces both forward and aft of the mass center. It is natural to provide the forward lift vector by orienting the cavitator at an appropriate angle of attack. Moreover, accounting for changes in vehicle mass and mass center as fuel is consumed, and maintaining optimal vehicle orientation with respect to the cavity during a maneuver, require that this trim angle be variable and controlled.

The forces acting on the fins were predicted using a fully three-dimensional boundary-element method of the type described above, supplemented with a viscous drag correction.

Afterbody forces in the case where planing on the cavity surface occurs were computed using an extension of Wagner planing theory developed by Logvinovich (for example, 1980). The cavity

in way of the planing region is approximated as a cylindrical free surface. The pressure force normal to the inclined longitudinal axis of the cylindrical hull is given by

$$F_b = \pi \ \rho \ \bar{r}_c^2 \ V^2 \sin \ \bar{\alpha}_b \ \cos \ \bar{\alpha}_b \frac{r_b + h_0}{r_b + 2h_0} \left(1 - \left(\frac{\Delta}{h_0 + \Delta} \right)^2 \right), \tag{5.8}$$

where: r_b is the hull radius (assumed to be constant over the planing region); $\bar{r}_c$, $\bar{\alpha}_b$, and Δ are (respectively) the cavity radius, the angle of attack between the longitudinal axes of the body and the cavity, and the difference between the cavity and hull radii (all averaged along the planing region); and h_0 is the immersion depth at the transom measured normal to the cavity centerline. Similarly, the moment of pressure forces about the transom can be expressed as

$$M_0 = \pi \ \rho \ \bar{r}_c^2 \ V^2 \ \cos^2 \ \bar{\alpha}_b \frac{r_b + h_0}{r_b + 2h_0} \frac{h_0^2}{h_0 + \Delta}. \tag{5.9}$$

A viscous drag correction was applied for the current investigation. Forces on the blast tube were neglected, since the fluid outside the time-averaged cavity boundary in that region is characterized by a significant void fraction, so that the overall planing forces acting on the reduced sectional area are expected to be rather small.

5.2 Candidate Vehicle Configuration

Several design issues must be addressed to completely understand the dynamics and control of supercavitating vehicles. One concern is the optimal allocation of fin lift relative to planing force to support the vehicle afterbody. A related question is the need for fin support: if stable flight can be maintained with the afterbody completely supported by the planing force, the elevators and their attendant drag and complexity become unnecessary.

Simulation was conducted on a vehicle with the following characteristics: 4.0 m in length, 0.2 m in diameter, and with a cavitator diameter of 0.07 m. The fins were located 3.5 m aft of the cavitator, and were swept back 15°. Although the mass properties of the vehicle will change as the rocket and ventilation fuels are consumed, they were assumed constant for purposes of the current analysis. A cruciform fin arrangement has been assumed: A pair of horizontal elevators provide some component of steady lift to support the afterbody and would be important to depth changes, while a pair of vertical rudders stabilize the vehicle in roll, but are otherwise deflected only during maneuvers.

As is discussed in Kirschner (2001), under certain conditions, a banked maneuvering strategy might be advantageous for a self-propelled supercavitating vehicle. This strategy was adopted for the investigation described herein.

5.3 Simulation of Underwater Flight

The current investigation focused on the simplified system of Figure 22, for which high frequency hydrodynamic noise excitation and other noise sources have been ignored. Moreover, it is assumed that knowledge of the system state is accurate, eliminating the requirement for a state estimator. However, the nonlinearity of the vehicle-cavity system has been retained. Nonlinearity enters the system via the vehicle, fin, and cavity behavior, due both to the nonlinear force coefficients and to memory effects associated with cavity evolution. Control has been implemented via a linear-quadratic regulator (LQR). Cavity memory effects and the discontinuities in the force coefficients require incorporation of the feedforward model (discussed below) to maintain acceptable system performance.

For the simplified system, the input to the regulator is the error vector, $\boldsymbol{x} = \boldsymbol{x}_d - \boldsymbol{y}$, computed as the difference between the commanded state vector, $\boldsymbol{x}_d$, and the corresponding actual state vector, $\boldsymbol{y}$. Both the actual and commanded state vectors have the form

$$\left\{ \begin{array}{cccccc|l} x & y & z & \phi & \theta & \psi & \leftarrow \text{displacements} \\ \text{surge} & \text{sway} & \text{heave} & \text{roll} & \text{pitch} & \text{yaw} & \end{array} \right.$$

$$\text{rates} \rightarrow \left. \begin{array}{cccccc} u & v & w & p & q & r \\ \text{surge} & \text{sway} & \text{heave} & \text{roll} & \text{pitch} & \text{yaw} \end{array} \right\}^T$$

However, several of these states might not be measured on a vehicle. Thus, for the simulations discussed below, several of the state variables were eliminated from the system. Typically, a 7-state system was investigated, assuming that both rates and displacements in roll, pitch, and yaw are available from an inertial measurement unit and that some measurement of vehicle depth, z, can be obtained.

A classical regulator would provide a control vector, $\boldsymbol{u}$, directly to the hydrodynamic control effectors (in this case, the fins and the cavitator):

$$\boldsymbol{u} = \begin{Bmatrix} u_1 & u_2 & u_3 & u_4 & u_5 \\ \text{starboard} & \text{lower} & \text{port} & \text{upper} & \text{cavitator} \end{Bmatrix}^{\mathrm{T}} . \tag{5.10}$$

However, the control vector of interest involves both the feedback output from the LQR, $\boldsymbol{u}_{\mathrm{b}}$, and output from the feedforward model, $\boldsymbol{u}_{\mathrm{f}}$:

$$\boldsymbol{u} = \boldsymbol{u}_{\mathrm{b}} + \boldsymbol{u}_{\mathrm{f}} . \tag{5.11}$$

Prior to flight simulation of a supercavitating body, the thrust and nominal speed are specified. Values of the state and control vectors are then determined for four basic flow conditions:

- Two trim conditions: fin-supported with pitch equal to zero, and planing-supported with fin deflection (relative to the vehicle axis) equal to zero; and, for each trim condition,
- Two maneuvering conditions: straight and level flight, and level turning at a specified constant turn rate.

Determination of these equilibrium conditions involves a nonlinear root search. In consideration of the discontinuity that can occur at the angle where planing first occurs, a Nelder-Mead scheme has been adopted.

The feedforward model investigated in this effort is specialized for supercavitating vehicle dynamics. A scheme has been selected for which the system is regulated about one of four distinct fixed points. The point selected depends on the user-specified operating condition. The first two fixed points are defined by the nominal condition of straight-line flight for either fin or planing support of the afterbody. The other two are similar, except that they are selected as equilibrium conditions for steady turning in the horizontal plane. Thus the output from the feedforward model is

$$\boldsymbol{u}_{\mathrm{f}} \in \begin{cases} \boldsymbol{u}_1 & \text{fin supported, zero pitch, straight flight} \\ \boldsymbol{u}_2 & \text{planing, zero fin deflection, straight flight} \\ \boldsymbol{u}_3 & \text{fin supported, banking pitch, turn rate } a_{\text{turn}} \\ \boldsymbol{u}_4 & \text{planing, zero fin deflection, turn rate } a_{\text{turn}} \end{cases} \tag{5.12}$$

and feedback control is optimized to regulate motion about one of these equilibrium conditions as the vehicle traverses its commanded trajectory.

The nonlinear equation of motion involves not only the present state, but also the history of cavitator motion, $\boldsymbol{c}(t)$:

$$\dot{\boldsymbol{x}} = \boldsymbol{f}(\boldsymbol{x}, \boldsymbol{c}(t-\tau), \boldsymbol{u})$$
$$\boldsymbol{y} = \boldsymbol{g}(\boldsymbol{x})$$

where τ represents the delay between motion at the cavitator and action along the afterbody. For each flow condition, s, the state-space model for the simplified system is defined in the usual manner as:

$$\begin{aligned} \dot{\boldsymbol{x}} &= \mathbf{A}_s \boldsymbol{x} + \mathbf{B}_s \boldsymbol{u} \\ \boldsymbol{y} &= \mathbf{C}_s \boldsymbol{x} + \mathbf{D}_s \boldsymbol{u} \end{aligned} \quad s \in \{1, \cdots, 4\} . \tag{5.13}$$

The Jacobian matrices are computed numerically prior to flight simulation as (for example)

$$A_{ij} = \frac{\partial f_i}{\partial x_j} \quad s \in \{1, \cdots, 4\} , \tag{5.14}$$

where the indices i and j vary from 1 through 12 for the complete state vector and from 1 through 5 for the control vector in each flow condition. For the simplified system, the Jacobian matrices in the second of equations 5.13 are simply

$$\mathbf{C}_s = \mathbf{I} \quad s \in \{1, \cdots, 4\} \tag{5.15}$$

(the identity matrix), and

$$\mathbf{D}_s = \mathbf{0} \quad s \in \{1,\cdots,4\} \tag{5.16}$$

Regulation for the general LQR is measured by the quadratic performance criterion

$$J(\boldsymbol{u}) = \int_{t=0}^{\infty} \left(\boldsymbol{x}^{\mathrm{T}} \mathbf{Q} \boldsymbol{x} + 2\boldsymbol{x}^{\mathrm{T}} \mathbf{N} \boldsymbol{u}_{\mathrm{b}} + \boldsymbol{u}_{\mathrm{b}}{}^{\mathrm{T}} \mathbf{R} \boldsymbol{u}_{\mathrm{b}} \right) dt \tag{5.17}$$

where the user-specified weighting matrices, $\mathbf{Q}$, $\mathbf{N}$, and $\mathbf{R}$, define the trade-off between regulation performance and control effort. For the current investigation, the cross-weighting matrix $\mathbf{N}$ was taken as zero, as were all off-diagonal elements of the state and control weighting matrices, $\mathbf{Q}$ and $\mathbf{R}$. A MATLAB® Control System Toolbox routine is used to determine the gain matrices, $\mathbf{K}_s$, that minimize the cost function, $J(\boldsymbol{u})$, for use in the state feedforward-feedback control law (MATH WORKS, 1998) for each of the 4 fixed points considered. The control law is then expressed as:

$$\boldsymbol{u} = \boldsymbol{u}_{\mathrm{fs}} - \mathbf{K}_s \boldsymbol{x} \quad s \in \{1,\cdots,4\} \tag{5.18}$$

A substantial effort was devoted to testing various combinations of the weighting matrices $\mathbf{Q}$ and $\mathbf{R}$ to achieve acceptable performance, although a more systematic and rigorous effort is warranted. The weighting and gain matrices are all computed prior to flight simulation.

A 4th-order Runge-Kutta scheme was used to integrate the equations of motion in time. At each time step the cavity geometry is updated to account for the motion of the cavitator. The forces acting on the cavitator, fins, and afterbody are then updated, and vehicle accelerations in each of the 6 degrees of freedom are computed. The state and error vectors are updated. The control vector is then updated using the gain matrix appropriate to the specified desired operational condition and the control equation is applied.

5.4 Selected Results - Simulations

For all cases discussed below, the operating speed and cavitation number were 75 m/s and 0.03, respectively.

Figure 23 shows the total lift margin (the difference between the total lift and the vehicle weight) as a function of vehicle pitch and elevator deflection angle. The cavitator angle for each curve was selected to provide equilibrium for a pitch angle of zero. Equilibrium is achieved in the fin-supported case at elevator deflection angles between approximately 0.30° and 0.55°; below elevator deflection angles or approximately 0.30° the afterbody is primarily supported by planing forces. Note the discontinuity in lift curve slope when afterbody planing first occurs (at a pitch angle of approximately 0.23°); this represents a tremendous increase in the effective system stiffness and the characteristic response frequencies. The small fin deflections required to produce a substantial change in the forces acting on the body might present an additional challenge for control.

The open- and closed-loop eigenvalues of the system, linearized about the fixed points associated with the fin and planing supported cases for straight-line flight, are shown in Figure 24. For both types of afterbody support, the uncontrolled system has one unstable mode. Preliminary analysis suggests that this is a corkscrew motion associated with cavity tail-up under the influence of gravity: roll and sway are unstably coupled due to asymmetry in the fin immersion as the body rolls about its long axis, which is eccentrically located with respect to the line of cavity centers in way of the fins. This effect can be eliminated in the controlled system, provided some measurement of depth is available; if not, the unstable mode is present even for the controlled system. As expected, the most important remaining difference between the controlled and uncontrolled systems is a significant increase in the damping of each mode in the controlled case. Similarly, the primary difference between the fin and planing supported cases is a significant increase in the frequency of the oscillatory modes in the planing supported case. In all cases, several lightly damped modes are present.

The vehicle motion predicted by time-domain simulation of free decay in pitch for the fin-supported case in straight and level flight is presented in Figure 25. Two types of behavior are presented: essentially linear behavior associated with a small initial pitch rate perturbation of 1°/s, and the clearly nonlinear behavior due to a large perturbation of 20°/s. In both cases, control is required to recover from the perturbation and return to the original depth. More interestingly, the

linear behavior is non-oscillatory for both the controlled and uncontrolled cases, whereas, in the nonlinear case, the perturbation initiates a rather violent pitch oscillation at a frequency of approximately 9.5 Hz that is modulated by a second, gentler, higher-frequency oscillation. The shapes of the peaks and troughs indicate that the vehicle is skipping off the bottom of the cavity in the nonlinear case.

Simulation of vehicle motion in steady, planing-supported, straight and level flight predicts behavior such as that shown in Figure 26. It can be seen that pitch increases with time, but that a 7-state controller both eliminates the tendency of the vehicle to dive and reduces the violent tail-slap behavior. The frequencies characterizing the two types of response are markedly different: the uncontrolled case is dominated by a relatively long-period skipping mode, whereas control eliminates this mode, leaving the higher modulating frequency. The planing force history indicates that skipping occurs in both cases – apparently the controlled response during the planing portion of the cycle is sufficient to mitigate the unsteady cavity behavior in such a manner that the afterbody excursions are not so extreme.

5.5 Summary – Simulation

This section presented strategies for the control of the highly coupled nonlinear system comprising a supercavitating vehicle. A simple hydrodynamic model was implemented for simulating the behavior of such a system. In consideration of the nature of the forces acting on a gas-enveloped body, and in order to maintain mechanical simplicity of the cavitator, a banked maneuvering strategy was investigated. Results of dynamical simulation for a specific vehicle were presented both for uncontrolled flight and with LQR-based feedforward-feedback control.

The system behavior is dominated by the distinct change in the nature of the forces as the afterbody moves between a planing and a non-planing condition. The system eigenvalues strongly depend on the type of afterbody support specified for vehicle operation, but that (under the assumptions made for the simplified hydrodynamics model) a 7-state controller can eliminate the most undesirable behavior in either case. Additional discussion, including description of the simulation of banked maneuvers in steady turns, may be found in Kirschner, et al, (2001).

ACKNOWLEDGEMENTS

The authors are very grateful to Dr. Kam Ng (Office of Naval Research, ONR), who supported the development and presentation of these lecture notes. Many other sponsors supported the work presented herein, including Mr. James Fein (then of ONR), Drs. William Carey and Theo Kooij (formerly and currently of the Defense Advanced Research Projects Agency, DARPA), Dr. Stuart Dickinson (then manager of the NUWC Independent Research Program), and Mr. Bernard Myers (then manager of the NUWC Bid and Proposal Program).

Dr. Abraham Varghese (Naval Undersea Warfare Center, NUWC) participated in the development of many of the computation tools presented herein. Dr. Scott Hassan (NUWC) contributed to the afterbody planing model used in the dynamical simulations. The fin force measurements used to validate the boundary-element predictions presented in these lecture notes were obtained by Mr. D. Stinebring (Applied Research Laboratory / The Pennsylvania State University, ARL/PSU).

The notional concepts presented herein, and the assessment of their status and potential value, represent the authors' opinions only; they do not in any way reflect the policies of the U.S. Government, the Department of Defense, the U.S. Navy, ONR, DARPA, NUWC, or any sponsoring or subsidiary organization.

REFERENCES AND BIBLIOGRAPHY

Aris, R., (1962) Vectors, Tensors, and the Basic Equations of Fluid Mechanics, Prentice-Hall, Englewood Cliffs, NJ.

Ashley, H., and M. Landahl (1965) Aerodynamics of Wings and Bodies, Dover, New York, NY.

Birkgof, G., and E. Sarantonello (1957), Jets, Wakes, and Cavities, Academic Press, New York.

Brennen, C.A. (1969), "Numerical Solution for Axisymmetric Cavity Flows," J. Fluid Mech., 37.

Brodetsky, S., (1923) "Discontinuous Fluid Motion past Circular and Elliptic Cylinders," Proceedings of the Royal Societ,y A102 (as summarized in May, 1975).

Chou, Y.S., (1974) "Axisymmetric Cavity Flows past Slender Bodies of Revolution," *J Hydronautics,* 8(1).

Dieval, L., C. Pellone, and M. Arnaud (2000) "Advantages and Disadvantages of Different Techniques of Modeling of Supercavitation," in LEGI (2000).

Etkin, B., (1972) Dynamics of Atmospheric Flight, John Wiley & Sons, New York, NY.

Fedorov, Y.A. (1960), "Motion of Wedge with Cheekbones Under Free Surface in Ideal Weightless Fluid," Tr. TzAGI. (In Russian.)

Fine, N.E., (1992) *Nonlinear Analysis of Cavitating Propellers in Non-Uniform Flow,* PhD thesis, Massachusetts Institute of Technology, Cambridge, MA.

Fine, N.E., and S.A. Kinnas, (1993) "A Boundary Element Method for the Analysis of the Flow Around 3-D Cavitating Hydrofoils," J. Ship Research, 37(1).

Garabedian, P.R., (1956) "Calculation of Axially Symmetric Cavities and Jets," Pacific J. of Math. 6 (as summarized in May, 1975).

Gieseke, T.J., editor, (1997) Proceedings of the Third International Symposium on Performance Enhancement for Marine Applications, Naval Undersea Warfare Center Division, Newport, RI.

Greenwood, D.T., (1965) Principles of Dynamics, Prentice-Hall, Englewood Cliffs, NJ.

Gregory, I.M., and R. Chowdhry (1994) "Hypersonic Vehicle Model and Control Law Development Using H_∞ and μ Synthesis," NASA TM 4562, National Aeronautics and Space Administration, Washington, DC.

Kiceniuk, T., (1954) "An Experimental Study of the Hydrodynamic Forces Acting on a Family of Cavity-Producing Conical Bodies of Revolution Inclined to the Flow," CIT Hydrodynamics Report E-12.17, California Institute of Technology, Pasadena, CA (as summarized in May, 1975).

Kirschner, I.N., D.C. Kring, A.W. Stokes, N.E. Fine, and J.S. Uhlman (2001) "Control Strategies For Supercavitating Vehicles," *J Vibration and Control,* accepted for publication.

Kirschner, I.N., J.S. Uhlman, Jr., A.N. Varghese, and I.M. Kuria (1995) "Supercavitating Projectiles in Axisymmetric Subsonic Liquid Flows," Proceedings of the ASME & JSME Fluids Engineering Annual Conference & Exhibition, Cavitation and Multiphase Flow Forum, FED 210, J. Katz and Y. Matsumoto, editors, American Society of Mechanical Engineers, New York, NY.

Kramer, F.S., (1998) "Multivariable Autopilot Design and Implementation for Tactical Missiles," Proceedings of the 1998 AIAA Missile Sciences Conference, American Institute of Aeronautics and Astronautics, Reston, VA.

Kring, D.C., N.E. Fine, J.S. Uhlman, and I.N. Kirschner (2000) "A Time-Domain Cavitation Model using a Three-Dimensional Boundary-Element Method," submitted for a publication in honor of Prof. Y.N. Savchenko, Institute of Hydromechanics, Kiev, Ukraine.

Kring, D.C., T. Korsmeyer, J. Singer, D. Danmeier, and J. White (1999) "Accelerated, Nonlinear Wave Simulations for Large Structures," Proceedings of the 7'th Int'l Conference on Numerical Ship Hydrodynamics, Nantes, France.

Kuethe, A.M., and C-Y. Chow (1976) Foundations of Aerodynamics: Bases of Aerodynamic Design, Wiley, New York, NY.

Lamb, H., (1945) Hydrodynamics, Dover, New York, NY.

LEGI (2000) Proceedings of the Scientific Meeting on High-Speed Hydromechanics and Supercavitation, Laboratoire des Ecoulements Géophysiques et Industriels, Grenoble, France.

Logvinovich, G.V. (1969), Hydrodynamics of Flows with Free Boundaries, Naukova Dumka, Kiev. (In Russian.)

Logvinovich, G.V., (1980) "Some Problems in Planing Surfaces [sic]," translated from "Nekotoryyi voprosy glissirovaniya i kavitatsii [Some Problems in Planing and Cavitation]," Trudy TsAGI 2052, Moscow, Russia.

Logvinovich, G.V., V.N. Buivol, A.S. Dudko, S.I. Putilin, and Y.R. Shevchuk (1985) Flows with Free Surfaces, Naukova Dumka, Kiev, Ukraine (in Russian).

Maniar, H.D., (1995) *A Three-Dimensional Higher-Order Panel Method Based on B-Splines,* PhD thesis, Massachusetts Institute of Technology, Cambridge, MA.

MATH WORKS (1998) Control System Toolbox for Use with MATLAB®, The Math Works, Inc., Natick, MA.

May, A., (1975) "Water Entry and the Cavity-Running Behavior of Missiles," SEAHAC TR 75-2, Naval Sea Systems Command, Arlington, VA.

Michel, J.M., "Overview of Former Researches on Supercavitation Carried Out at LEGI/IMG [sic]," in LEGI (2000).

Münzer, H., and H. Reichardt, (1950) "Rotational Symmetric Source-Sink Bodies with Predominantly Constant Pressure Distributions [sic]," ARE Translation 1/50, Aerospace Research Establishment, England, (as summarized in May, 1975).

Newman, J.N., (1980) Marine Hydrodynamics, MIT Press, Cambridge, MA.

Phillips, J.R., and J. White (1997) "A Precorrected-FFT Method for Electrostatic Analysis of Complicated 3D Structures," IEEE Trans. on Computer-Aided Design, 16(10).

Plesset, M.S., and P.A. Shaffer (1948), "Cavity Drag in Two and Three Dimensions," J. Appl. Phys. 19.

Raven, F.H., (1961) Automatic Control Engineering, McGraw-Hill Book Company, New York, NY.

Reichardt, H., (1946) "The Laws of Cavitation Bubbles at Axially Symmetrical Bodies in a Flow [sic]," Ministry of Aircraft Production Volkenrode, MAP-VG, Reports and Translations 766, Office of Naval Research, Arlington, VA, (as summarized in May, 1975).

Romanovsky, B.I., Y.A. Fedorov, and Z.I. Kramina (1970), "Calculation of Hydrodynamic Characteristics of Wedges in a Boundless, Weightless Fluid," Tr. TzAGI. (In Russian.)

Savchenko, Y.N., V.N. Semenenko, and V.V. Serebryakov (1992), "Experimental Research into Supercavitating Flows at Subsonic Speeds," Doklady AN Ukranini. (In Russian.)

Savchenko, Y.N., (2000) "Supercavitation: Applications and Perspectives," in LEGI (2000).

Savchenko, Y.N., V.N. Semenenko, Y.I. Naumova, A.N. Varghese, J.S. Uhlman, and I.N. Kirschner (1997) "Hydrodynamic Characteristics of Polygonal Contours in Supercavitating Flow," in Gieseke (1997).

Schlichting, H., (1979) Boundary-Layer Theory, McGraw-Hill, New York, NY. Translated by J. Kestin.

Semenenko, V.N., (2000) "Dynamics of Supercavitating Bodies," in LEGI (2000).

Stokes, A.W., and D.C. Kring (2000) ETC_Supercav, underwater flight simulation software package, Engineering Technology Center, Mystic, CT.

Tulin, M.P., (1958) "New Developments in the Theory of Supercavitating Flows," Proceedings of the Second Symposium on Naval Hydrodynamics, Office of Naval Research, Arlington, VA, (as summarized in May, 1975).

Tulin, M.P., (1959) "Supercavitating Flow Past Slender Delta Wings," J Ship Research, 3(3).

Tulin, M.P., (1964) "Supercavitating Flows – Small Perturbation Theory," J Ship Research.

Uhlman, J.S., (1987), "The Surface Singularity Method Applied to Partially Cavitating Hydrofoils", Journal of Ship Research, 31(2).

Uhlman, J.S., (1989), "The Surface Singularity or Boundary Element Method Applied to Supercavitating Hydrofoils", Journal of Ship Research, 33(1).

Uhlman, J.S., A.N. Varghese, and I.N. Kirschner (1998) "Boundary-Element Modeling of Axisymmetric Supercavitating Bodies," Proceedings of the 1st HHTC CFD Conference, Naval Surface Warfare Center Carderock Division, Carderock, MD.

Vada, T., and D.E. Nakos (1993) "Time-Marching Schemes for Ship Motion Simulations," 8th Int'l Workshop on Water Waves and Floating Bodies.

Varghese, A.N., J.S. Uhlman, Jr., and I.N. Kirschner (1997) "Axisymmetric Slender-Body Analysis of Supercavitating High-Speed Bodies in Subsonic Flow," in Gieseke (1997).

Waid, R.L., (1957) "Cavity Shapes for Circular Disks at Angles of Attack," CIT Hydrodynamics Report E-73.4, California Institute of Technology, Pasadena, CA (as summarized in May, 1975).

Wang, Q., and R.F. Stengel (1998) "Robust Control of Nonlinear Systems with Parametric Uncertainty," Proceedings of the 37th IEEE Conference on Decision and Control, Institute of Electrical and Electronics Engineers, Inc., New York, NY.

Wu, T.Y-T, "A Free Streamline Theory for Two-Dimensional Fully Cavitated Hydrofoils [sic]," Journal of Mathematics and Physics 35 (as summarized in May, 1975).

Yih, C-S., (1979) Fluid Mechanics, West River Press, Ann Arbor, MI.

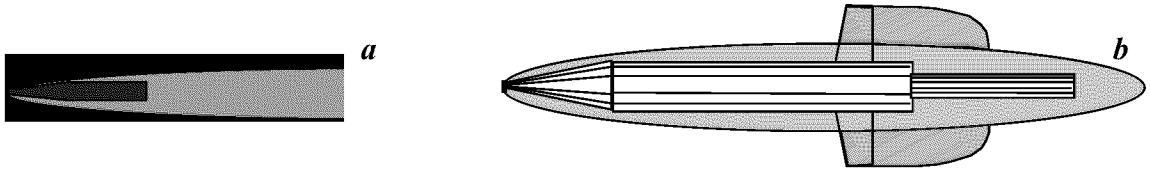


Figure 1. Two classes of supercavitating high-speed bodies: (a) Free-flying projectiles; (b) Self-propelled vehicles



Figure 2. Free-Body Diagram for Undersea Vehicle Drag Analysis

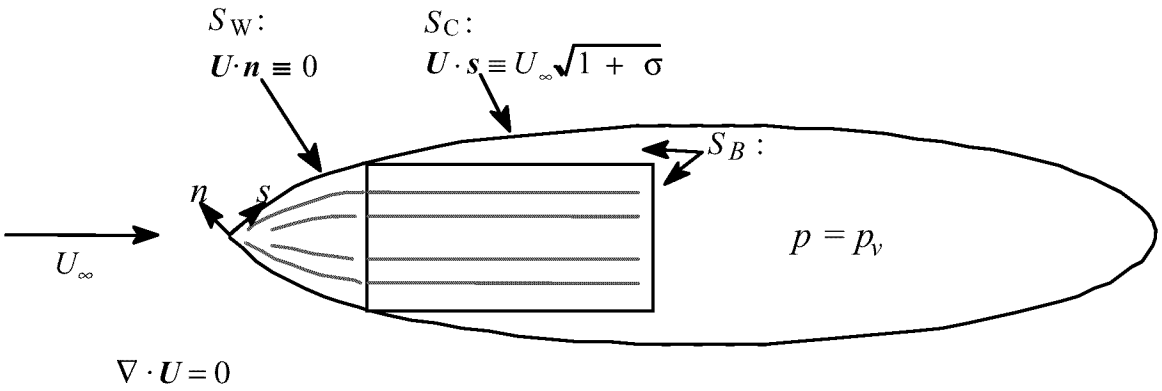
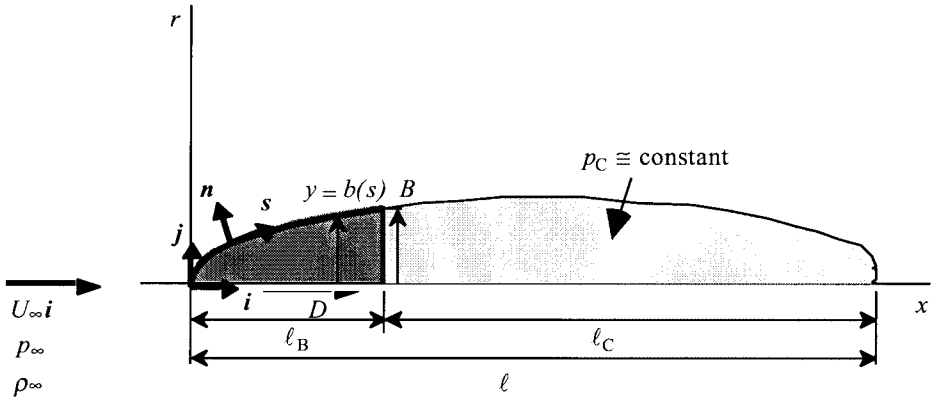


Figure 3. A Boundary-Value Problem for Ideal Supercavitating Flow.



5.5...1.1.1.1

Figure 4. Physics problem for axisymmetric supercavitating flow.

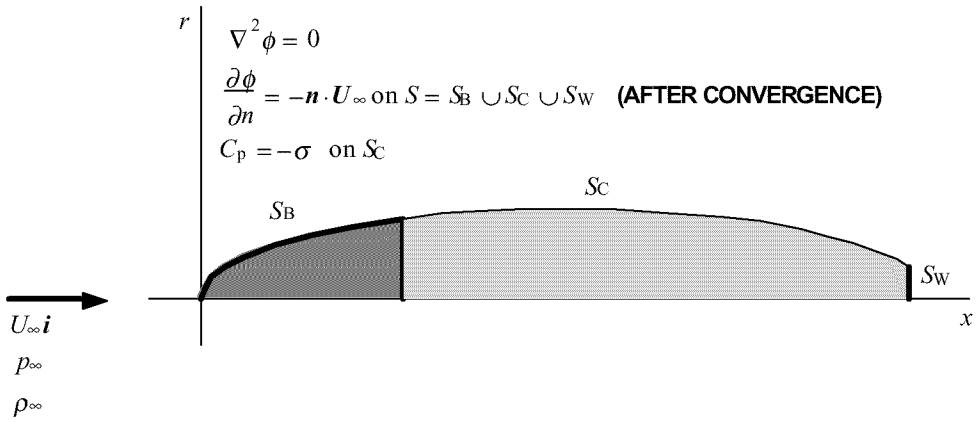


Figure 5. Boundary-value problem for axisymmetric supercavitating flow.

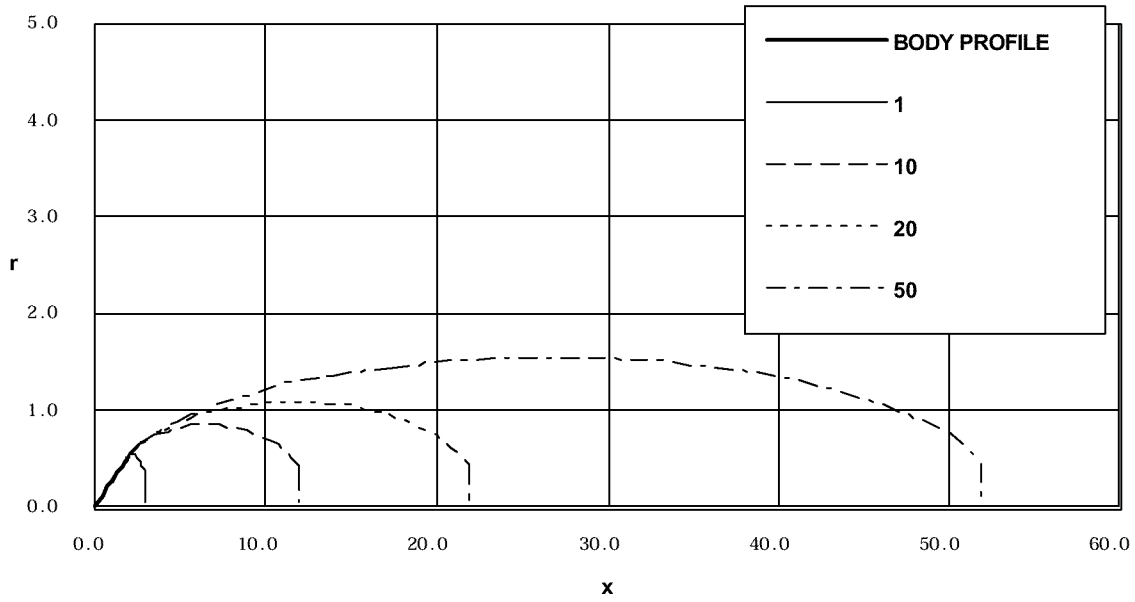


Figure 6. Body-cavity profiles for a 15° cone for dimensionless cavity lengths shown (scaled for viewing). The corresponding predicted cavitation numbers (decreasing with length) are 0.501, 0.070, 0.038, and 0.017

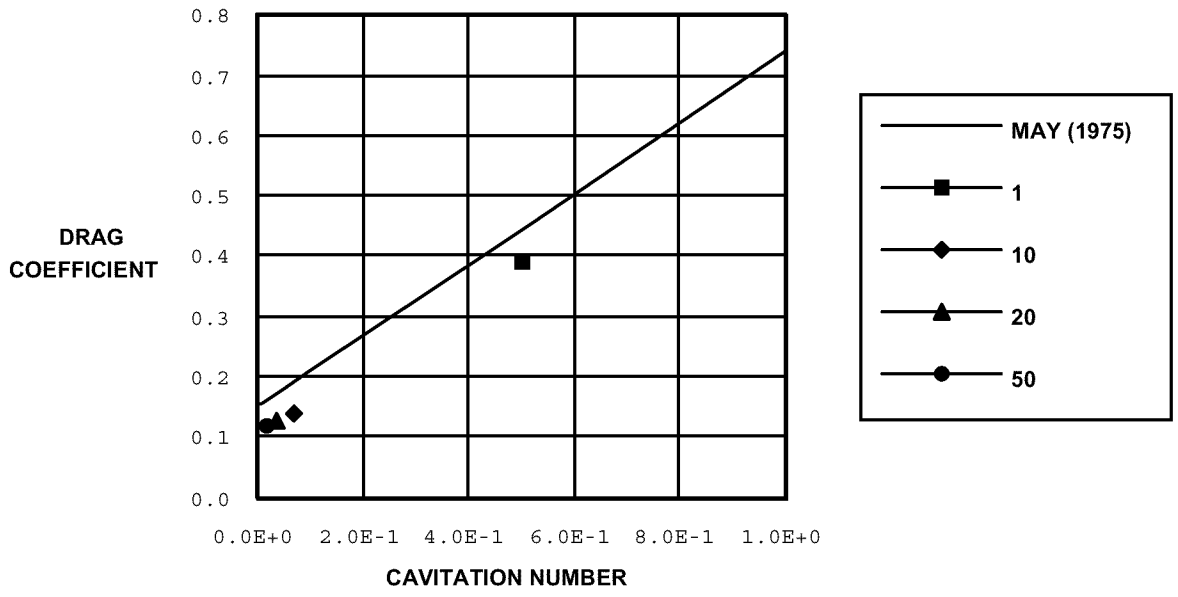


Figure 7. Predicted drag coefficients versus cavitation number for a 15° cone at dimensionless cavity lengths shown. The empirical curve fit of May (1975) is based on results of experiments by various researchers.

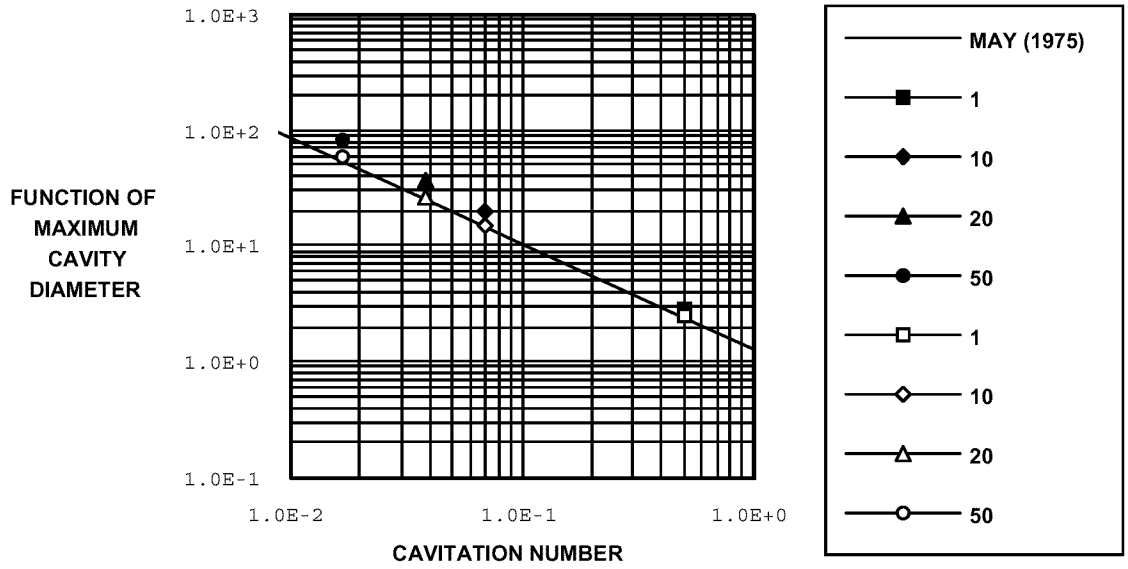


Figure 8. Predicted cavity diameter versus cavitation number for a 15° cone at dimensionless cavity lengths shown. The empirical fit of May (1975) is based on results of experiments by various researchers. Solid markers are based on the computed drag coefficient; open markers are based on the drag coefficient given by the empirical curve fit of May (1975). The function of diameter is given in the text at equation 3.18.

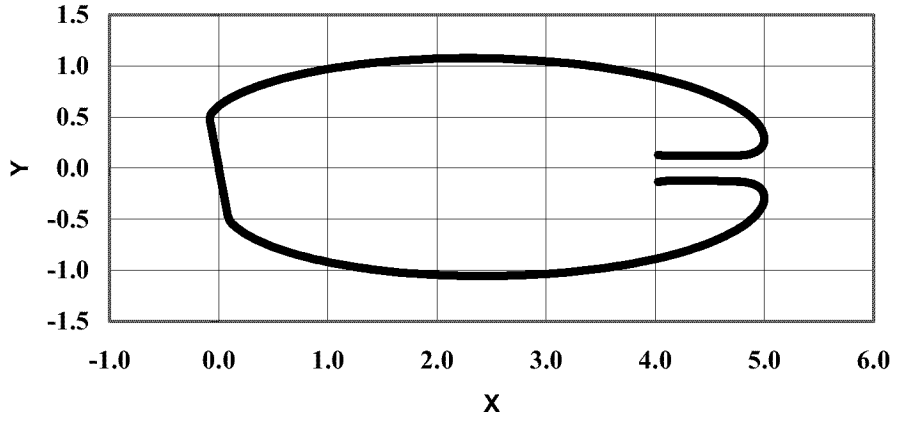


Figure 9. 2D cavity shape for a flat plate cavitator with $l/d = 5.0$ *and* $\alpha = 10°$.

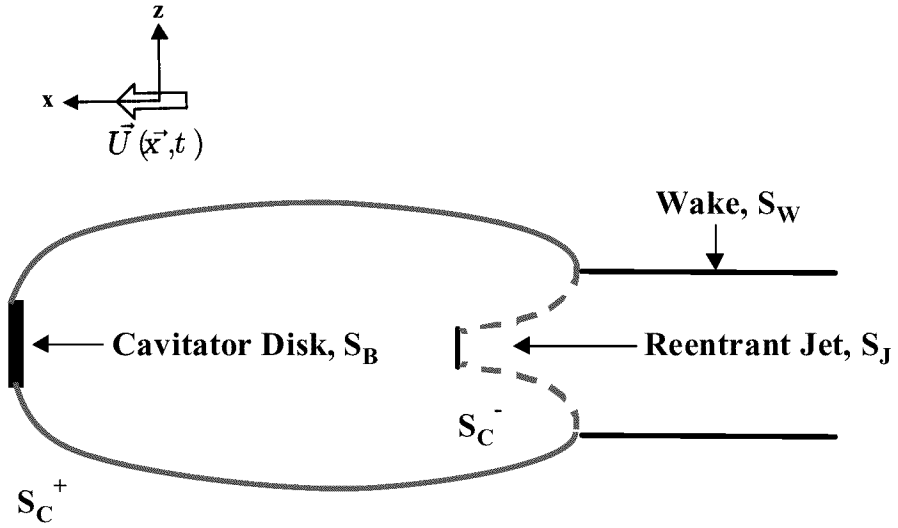


Figure 10. The initial boundary-value problem for unsteady boundary element simulations.

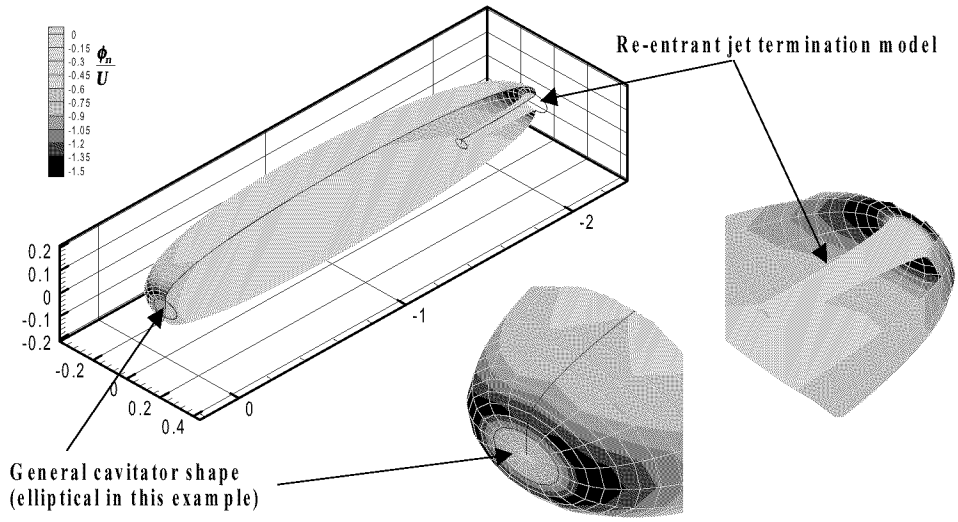


Figure 11. Normal velocity at start-up, with a homogenous initial condition for the cavity potential and an assumed initial geometry.

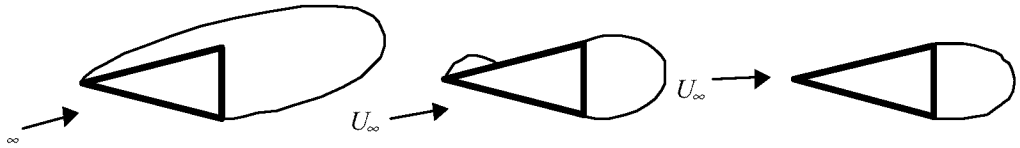


Figure 12. The three regimes of cavitating wedges, fully-, partially- and base cavitating.

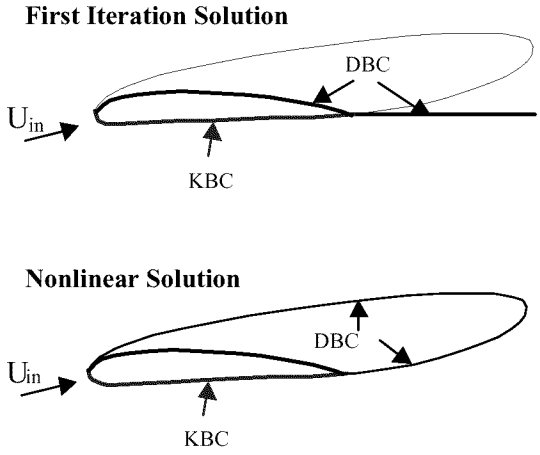


Figure 13. Sketch demonstrating the difference between the first iteration and nonlinear solutions. LScav solves for the first iteration solution.

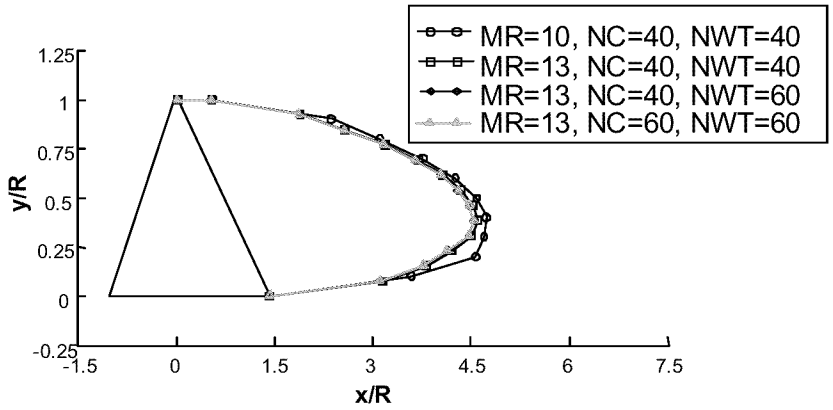


Figure 14. Convergence of cavity planform a fin with 45° sweepback and 7.5° wedge angle (note: the plot is not drawn to scale).

Table 1. Sample LScav results showing convergence of cavity volume, lift, and drag coefficients with number of panels

# Panels	Volume	C_L	C_D
800	1.218	.1032	.0174
1040	1.129	.1024	.0174
1300	1.106	.1031	.0174
1560	1.104	.1036	.0175

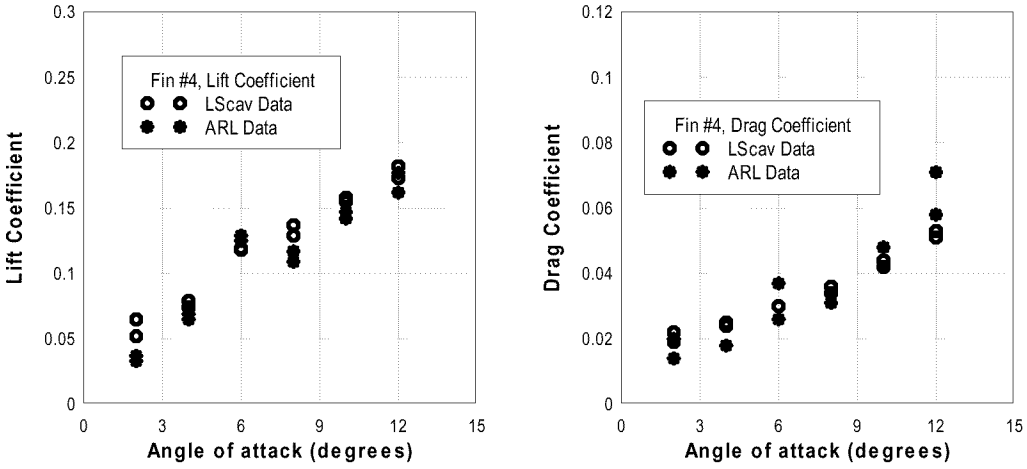


Figure 15. Comparison of measured and computed lift and drag coefficients (measured data provided by D. Stinebring, ARL/PSU)

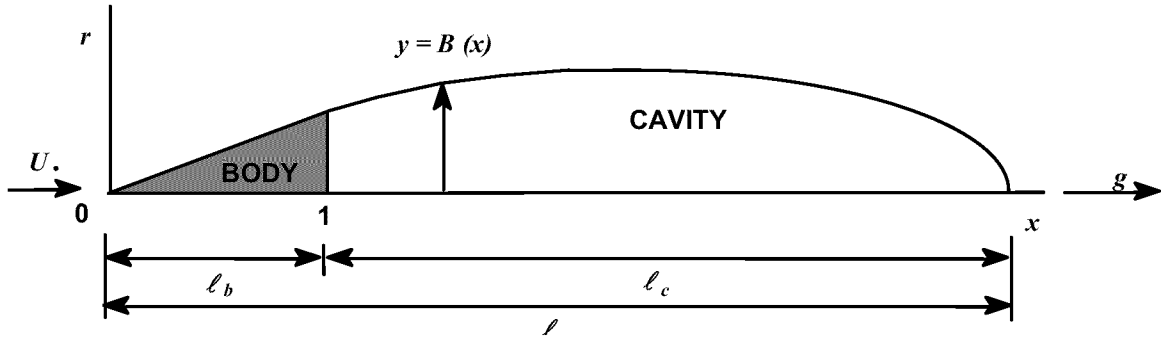


Figure 16. Physical problem addressed by slender body theory.

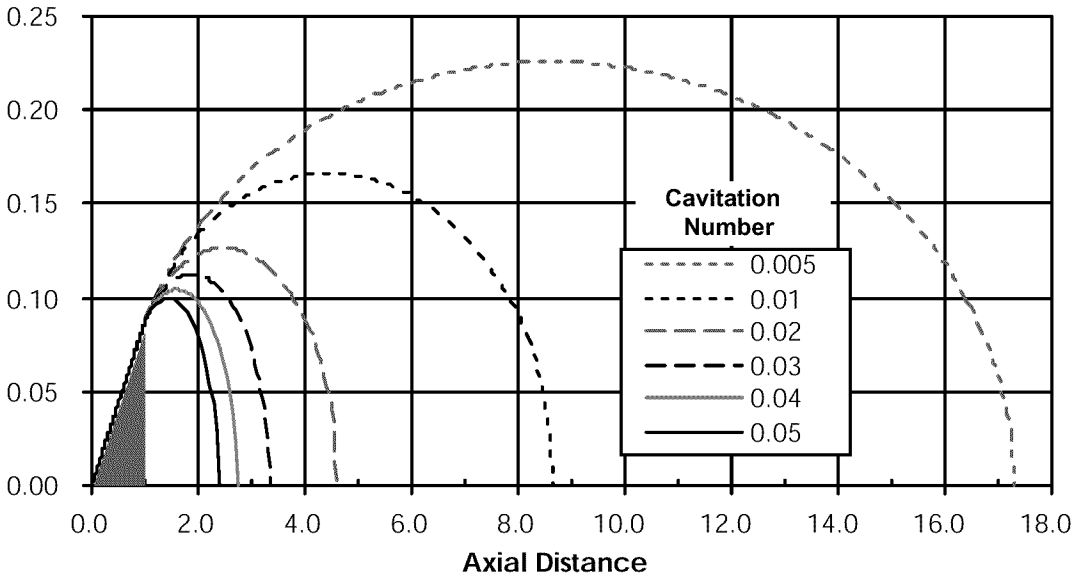


Figure 17. Cavity shapes for different cavitation numbers for axisymmetric supercavitating flow past a 10° cone in an incompressible fluid.

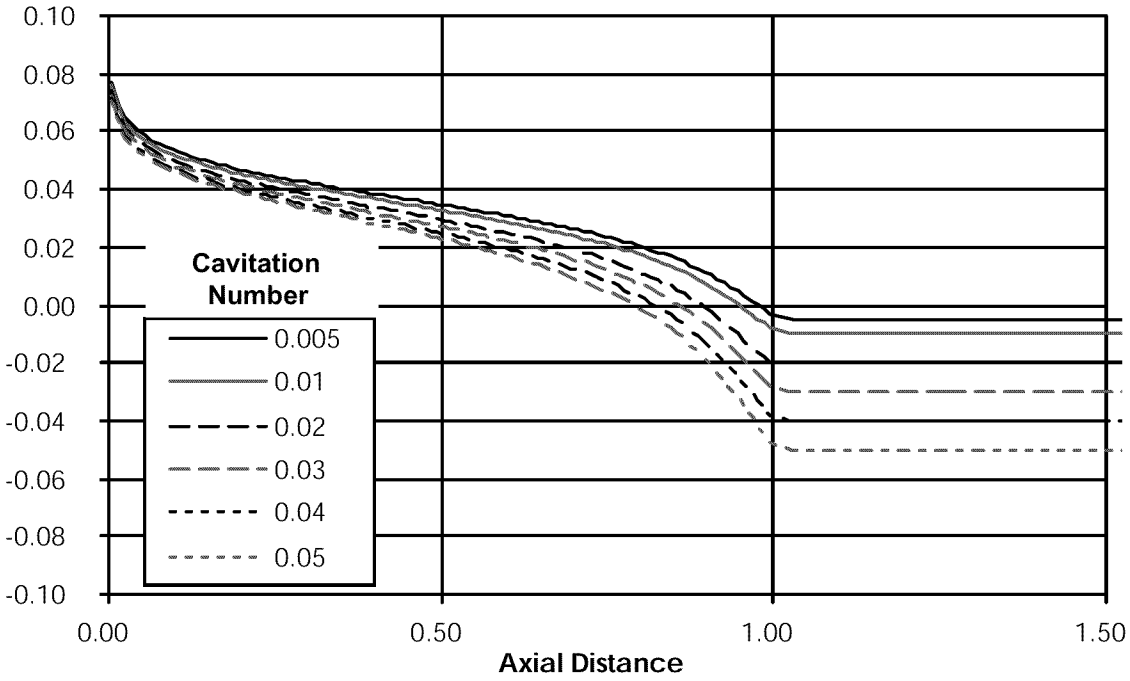


Figure 18. Predicted Surface Pressure Distributions for Various Cavitation Numbers for Axisymmetric Supercavitating Flow Past a 10° Cone in an Incompressible Fluid

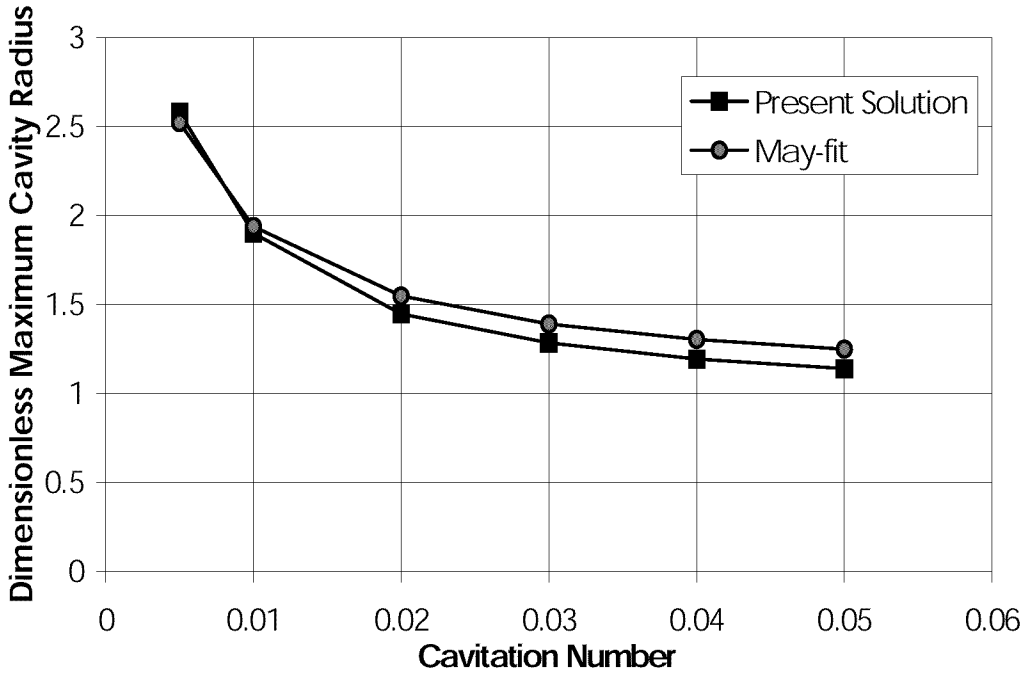


Figure 19. Cavity Maximum Radius Versus Cavitation Number for Axisymmetric Supercavitating Flow Past a 10° Cone in an Incompressible Fluid

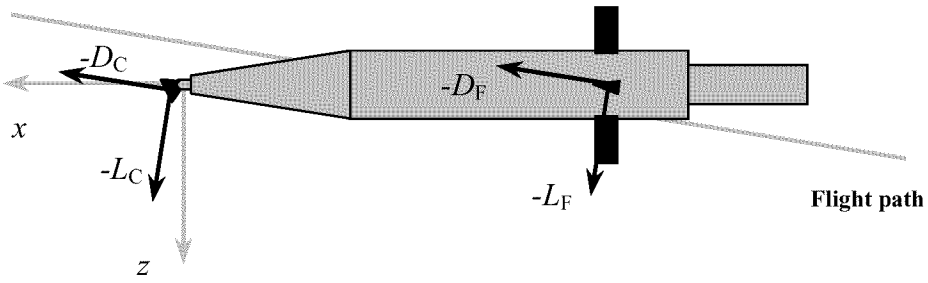


Figure 20. Nomenclature

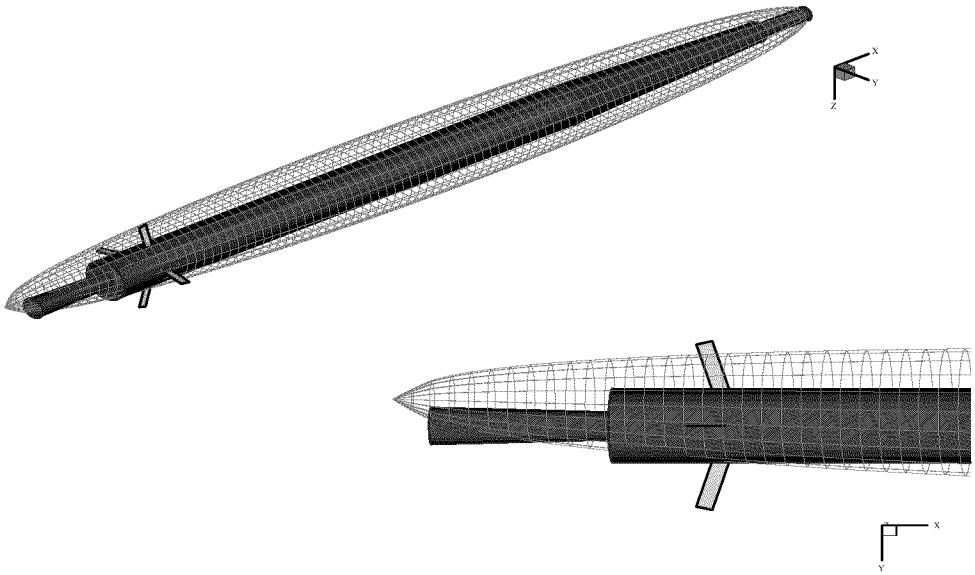


Figure 21. Cavity behavior in an extreme turn

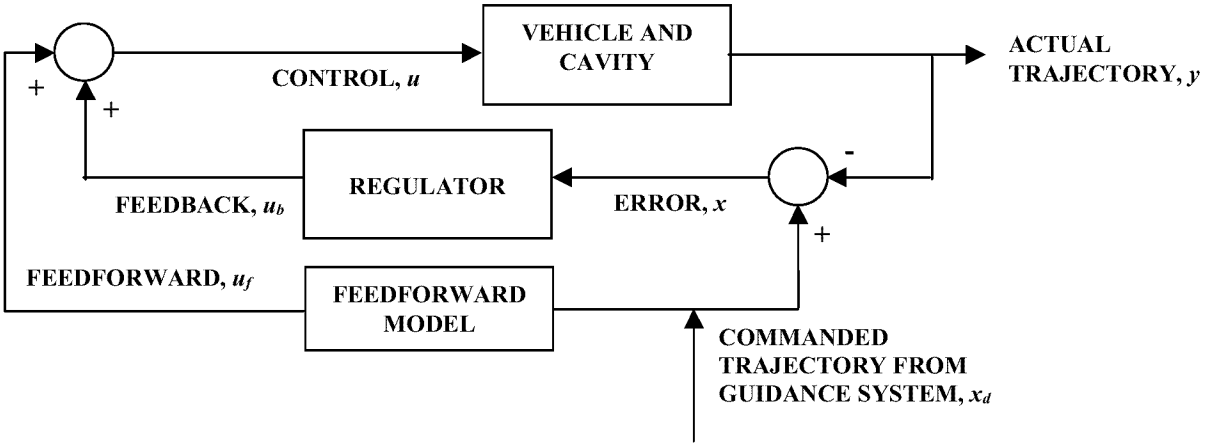


Figure 22. Simplified dynamical systems model of a supercavitating vehicle.

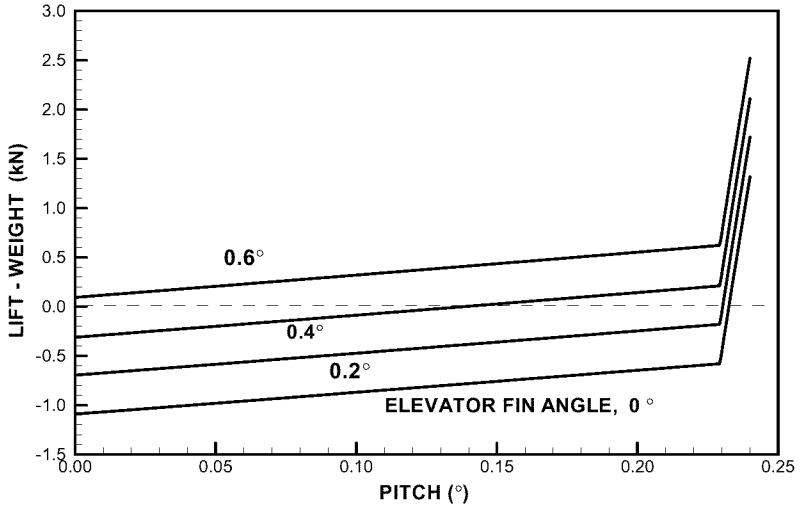


Figure 23. Lift margin as a function of pitch and elevator angles.

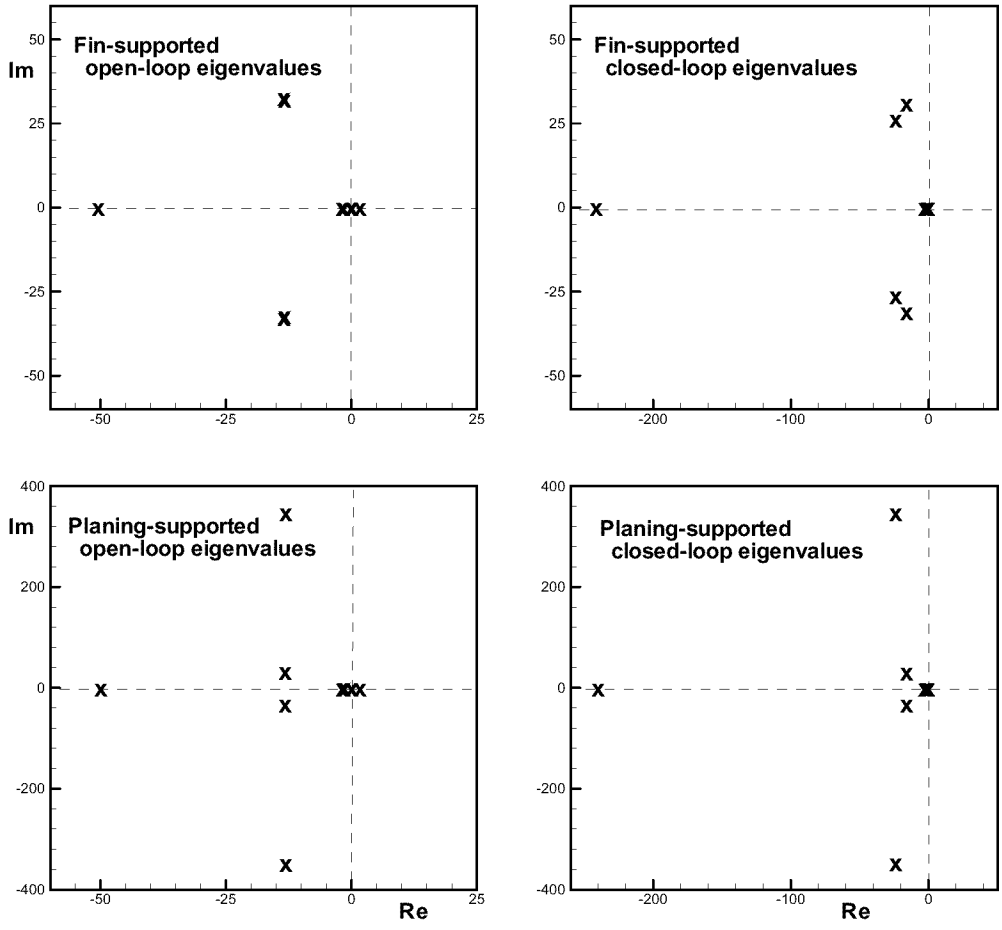


Figure 24. Open- and closed-loop eigenvalues for two modes of afterbody support.

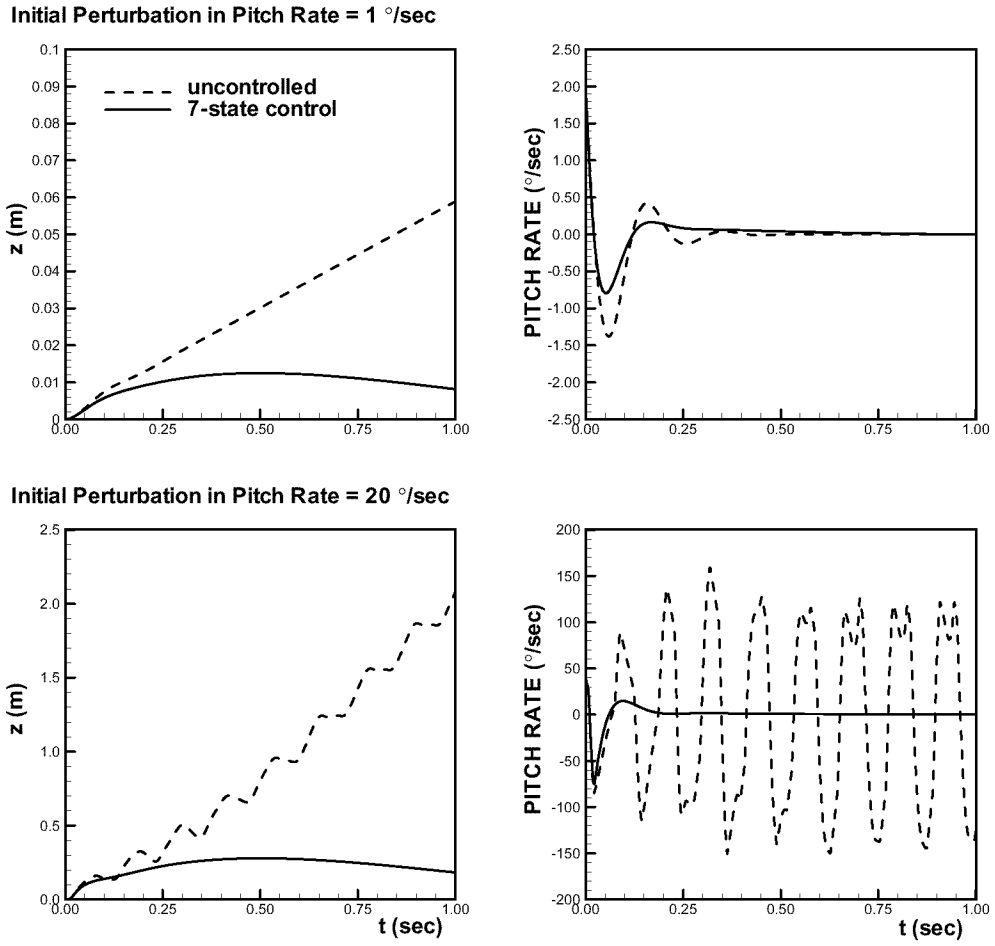


Figure 25. Fin-supported straight and level flight with small and large perturbations.

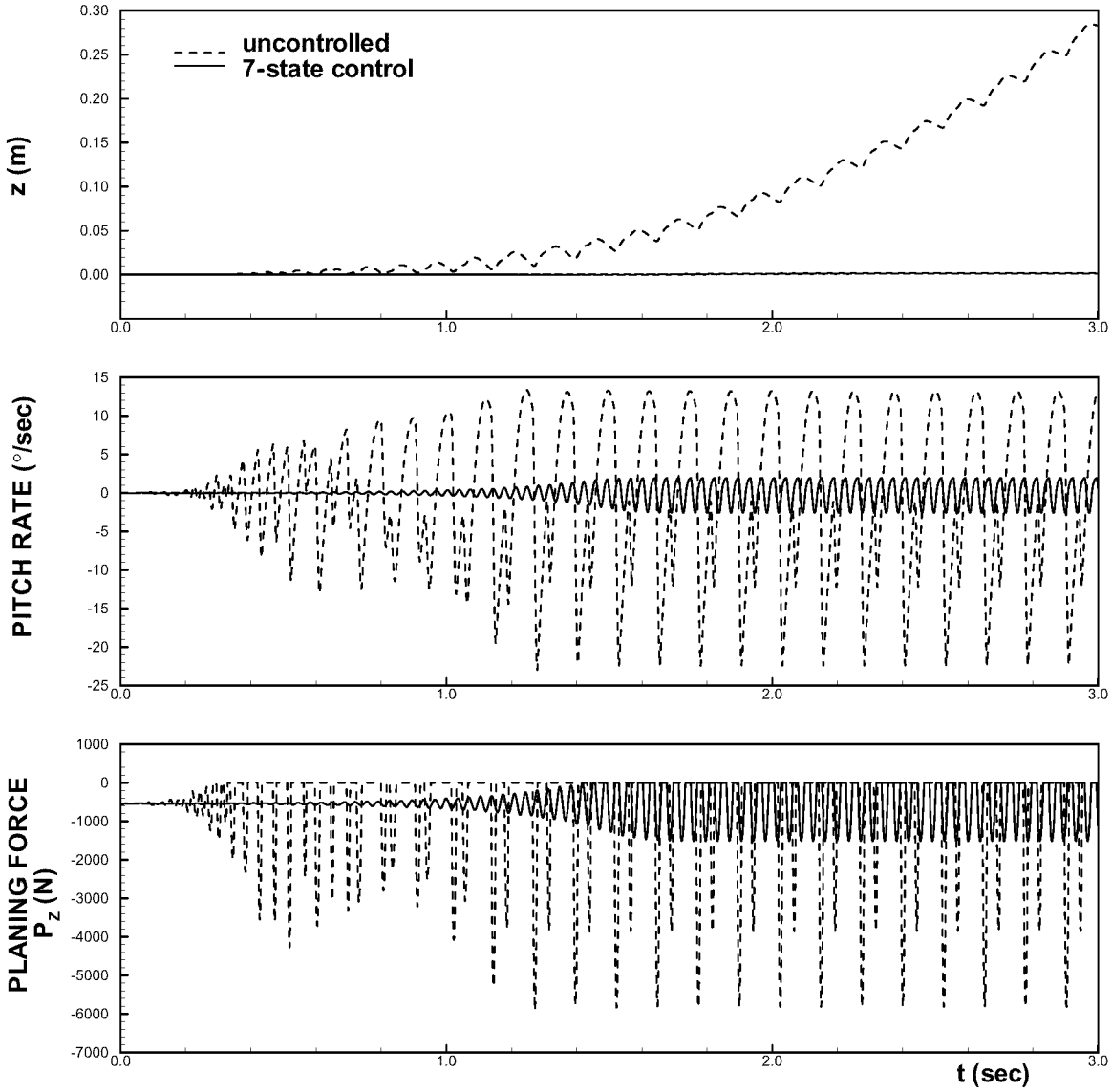


Figure 26. Planing-supported straight and level flight with an initial pitch rate perturbation of 0.01°/s with 7-state control.

This page has been deliberately left blank

Page intentionnellement blanche

Review of Theoretical Approaches to Nonlinear Supercavitating Flows

G.M. Fridman* **& A.S. Achkinadze****
*Department of Applied Mathematics & Mathematical Modelling
**Department of Ship Theory
St.Petersburg State Marine Technical University
Lotsmanskaya str., 3
190008, St.Petersburg
Russia

Summary: The purpose of the paper is to present a brief review of basic theoretical approaches to two-dimensional (2D) nonlinear supercavitating flows in the framework of theory of jets in an ideal fluid. In this connection discussed are Kirchhoff and Zhukovsky methods, Chaplygin method of "singular points", method of integral equation, *etc*. A simple model problem of a supercavitating (SC) flat plate at zero cavitation number $\sigma = 0$ is chosen to illustrate the core of the methods and their comparative effectiveness. Some mathematical aspects of open and closed cavity closure schemes are studied as well with use of Chaplygin method applied to a SC plate with a spoiler at nonzero cavitation number. An influence is demonstrated of free and solid boundaries onto the cavity volume and hydrodynamic characteristics of the plate. *Mathematica 4.0* software is used as a main tool for the flow pattern visualization of the problems under consideration. An analytical exact solution is presented to the 2D nonlinear flow problem of an arbitrary supercavitating foil and numerical results are discussed.

1. Basic assumptions of theory of jets in an ideal fluid

Theory of jets in an ideal fluid is appeared to be one of the best-studied fields of theoretical hydrodynamics dealing with flows confined by free and solid boundaries, the pressure constancy condition being satisfied on the former. H. Helmholtz [8] and G. Kirchhoff [12] were the first to formulate and solve some relatively simple problems of the theory of jets. Nowadays one can find brilliant surveys of the advances and development in the theory in books by Birkhoff & Zarantanello [1], Gilbarg [5] and Gurevich [7] (see also English translation of the book [6]). The works by Tulin [23], Terentev [21] and Maklakov [16] should also be distinguished.
As it follows from the name of the theory itself, we suppose a fluid to be an ideal one. For simplicity we neglect the gravity influence and specify that the flow be 2D, steady and incompressible. The flow has a velocity potential φ if

$$\boldsymbol{v} = \operatorname{grad}\varphi \ ,$$

where $\boldsymbol{v} = v_x + \mathrm{i}v_y$ is the total velocity vector in the flow. The harmonic function $\varphi(x, y)$ is the real part of an analytical function of complex potential (or characteristic function) $w(z) = \varphi + i\psi$, where $z = x + \mathrm{i}y$ and (x, y) denote axes of rectangular Cartesian coordinate system. The imaginary part of w is called stream function ψ, the velocity vector being given by

$$v_x = \frac{\partial\varphi}{\partial x} = \frac{\partial\psi}{\partial y} \ ; \qquad v_y = \frac{\partial\varphi}{\partial y} = -\frac{\partial\psi}{\partial x} \ .$$

Function ψ has a constant value on each separate streamline including free surfaces while φ increases along a streamline in downstream direction. A so called conjugate velocity can be introduced as follows

$$\frac{\mathrm{d}w}{\mathrm{d}z} = v_x + \mathrm{i}v_y = v\,\mathrm{e}^{-\mathrm{i}\theta} \ , \tag{1}$$

which is a mirror image of velocity vector $\boldsymbol{v}$ with respect to y-axis. In formula (1) v denotes absolute value of the vector $\boldsymbol{v}$ and θ is an angle made by the vector to x-axis.
As a result, a problem in question is considered to be solved when the complex potential function $w(z) = w(x+\mathrm{i}y)$ is found. As is customary, on all the solid boundaries of a given topography the kinematic (flow tangency) condition is applied, which requires the fluid flow to be tangent to the surface of the boundary, that is derivative of φ with respect to normal vector $\boldsymbol{n}$ be equal to zero. On the other hand the free streamline condition of constant speed is satisfied on all the free surfaces. The main difficulty of such free surface flow problems is connected to nonlinearity of the boundary conditions which are, moreover, to be satisfied on the surfaces of unknown geometry.

Paper presented at the RTO AVT Lecture Series on "Supercavitating Flows", held at the von Kármán Institute (VKI) in Brussels, Belgium, 12-16 February 2001, and published in RTO EN-010.

2. Model problem – cavitating plate at zero cavitation number

Consider a 2D cavitating flat plate in a uniform flow with velocity absolute value at infinity v_∞ and angle of attack α, see figure 1. The origin of the Cartesian coordinate system is taken at the plate's trailing edge, x–axis being directed downstream and y upwards. There is an incident stream with speed v_∞ coming from the left. The region occupied by the fluid is bounded by the plate $[AB]$ and by two semi-infinite free surfaces (AC) and (BC).

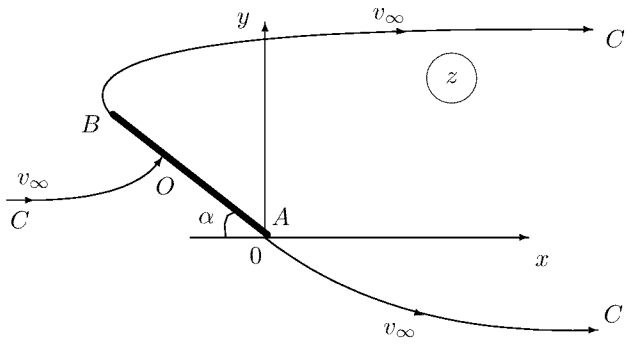


Figure 1: Flow pattern for the cavitating flat plate at zero cavitation number.

Assume the velocity on the streamlines v_0 to be equal to v_∞ and therefore the cavitation number

$$\sigma = \frac{p_\infty - p_0}{\rho v_\infty^2/2} = 0\,,$$

where p_∞ and p_0 denote the pressure at infinity and within the cavity correspondingly. It readily follows from the Bernoulli equation for an upstream reference point and free surface-boundary point

$$p_0 + \frac{1}{2}\rho v_0^2 = p_\infty + \frac{1}{2}\rho v_\infty^2\,.$$

We render all the parameters of the problem nondimensional by a suitable choice of scale so that $v_\infty = 1$ and plate length equals to unit $l = 1$.

2.1. Kirchhoff method

To solve the problem under consideration, it is convenient to determine the function

$$\zeta(w) = v_\infty \frac{\mathrm{d}z}{\mathrm{d}w} \tag{2}$$

rather than the complex potential $w(z) = \varphi + \mathrm{i}\psi$ itself. Indeed, if function $\zeta(w)$ is found then $z(w)$ is easily defined as

$$z = \frac{1}{v_\infty}\int \frac{v_\infty \mathrm{d}z}{\mathrm{d}w}\,\mathrm{d}w = \frac{1}{v_\infty}\int \zeta \mathrm{d}w\,. \tag{3}$$

Note that it's often no sense in reversing function $z(w)$ to find $w(z)$, all the more so that the operation is rather cumbersome.

So the erux of the problem is to determine w and ζ as functions of the same single variable so that equation (3) can be integrated. Since function $\zeta(w)$ defines a conformal mapping of w-plane onto the ζ-plane, one has to determine these regions and map one to another.

If one choses the stream function ψ to have the value zero on the dividing streamline $(COAC)$ and $(COBC)$ and since all the streamlines are by definition lines of constant ψ and therefore become lines parallel to the φ-axis, then the w-plane has the form shown in figure 2. The plate–cavity combination appears as a semi-infinite slit in this plane. The velocity potential φ at the edges of the plate (points A and B) has the values φ_A and φ_B.

It is easy to see that

$$\zeta = \frac{v_\infty}{v}\mathrm{e}^{\mathrm{i}\,\theta}\,.$$

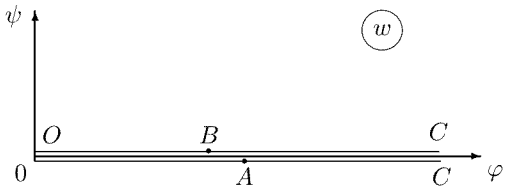


Figure 2: The complex velocity potential w.

On $[OA]$ one has $\theta = -\alpha$ and v_∞/v ratio varies from infinity at point O to unit value at point A. On the ζ-plane interval $[OA]$ corresponds to a semi-infinite line inclined at angle $-\alpha$ to the positive direction of x-axis and starting from the point $\zeta_A = \mathrm{e}^{-\mathrm{i}\alpha}$. A symmetrical line inclined at angle $\pi - \alpha$ and starting from the point $\zeta_B = -\mathrm{e}^{-\mathrm{i}\alpha}$ corresponds to another part of the plate $[BO]$. Angle θ varies from $-\alpha$ to zero and ratio $v_\infty/v = 1$ on streamline (AC). Further on, on streamline (CA) angle θ increases from zero to $\pi - \alpha$ and v_∞/v remains the same. Thus free surface on the z-plane becomes a half-circle of unit radius on the ζ-plane. The ζ-plane is depicted in figure 3. A stagnation point C on the z-plane corresponds to $\zeta_C = 1$.

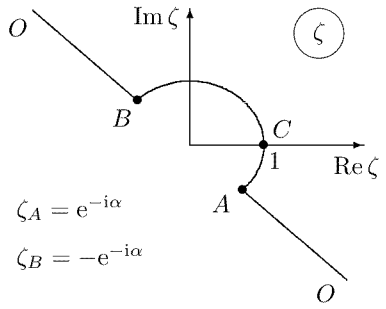


Figure 3: The ζ plane.

To obtain a solution to the problem under consideration it is sufficient to transform w-plane onto ζ-plane, both being given in figures 2 and 3. Such a problem is fairly simple and much easier than that of determining harmonic function φ in the region z with unknown free boundaries. The substitution of the complicated boundary value problem by a simple problem of conformal mapping is the core of the Kirchhoff method.
The appropriate $w - \zeta$ mapping can be found step by step.
First, one transforms ζ-plane to the first quadrant of the auxiliary τ-plane, see figure 4, by conformal mapping

$$\tau = a\,\frac{\zeta - \zeta_A}{\zeta + \zeta_A} = a\,\frac{\zeta - \mathrm{e}^{-\mathrm{i}\alpha}}{\zeta + \mathrm{e}^{-\mathrm{i}\alpha}}\,.$$

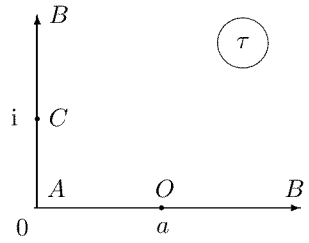


Figure 4: The τ plane.

With the correspondence between ζ and τ planes we have for point C

$$\mathrm{i} = a\,\frac{1 - \mathrm{e}^{-\mathrm{i}\alpha}}{1 + \mathrm{e}^{-\mathrm{i}\alpha}}\,, \quad \text{therefore} \quad a = \cot\frac{\alpha}{2}\,.$$

Second, a new variable $\tau_1 = \tau^2$ varies in the upper semi-plane, see figure 5.

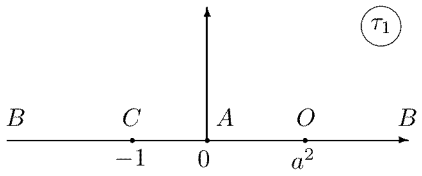


Figure 5: The τ_1 plane.

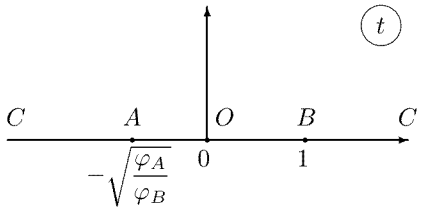


Figure 6: The t plane.

On the other hand, transformation $t = \sqrt{w/\varphi_B}$ transforms w-plane onto the upper semi-plane, see figure 6. Finally, all we need do is to transform t-plane onto τ_1-plane by using formula

$$\tau_1 = \frac{a^2 + t}{1 - t}\,,$$

which results in

$$\zeta = \zeta_A \frac{a\sqrt{\sqrt{\varphi_B} - \sqrt{w}} + \sqrt{\sqrt{\varphi_A} + \sqrt{w}}}{a\sqrt{\sqrt{\varphi_B} - \sqrt{w}} - \sqrt{\sqrt{\varphi_A} + \sqrt{w}}}\,, \tag{4}$$

where radical $\sqrt{w}$ is positive on the interval $[OB]$ and negative on $[OA]$, $\zeta_A = -\zeta_B = \mathrm{e}^{-\mathrm{i}\alpha}$ and $a = \cot(\alpha/2)$. Referring to figures 5 and 6, it is obvious that

$$\sqrt{\frac{\varphi_A}{\varphi_B}} = a^2 = \cot^2\frac{\alpha}{2}\,,$$

while parameter φ_A remains still unknown.
To determine the unknown parameter we have a condition connected with plate length, see figure 1:

$$z_B = l\,\mathrm{e}^{\mathrm{i}(\pi-\alpha)}\,.$$

That is why from equation (3) we find

$$z_B = \frac{1}{v_\infty}\int_{\varphi_A}^{\varphi_B}\zeta\mathrm{d}w = \frac{\zeta_A}{v_\infty}\int_{\varphi_A}^{\varphi_B}\frac{a\sqrt{\sqrt{\varphi_B} - \sqrt{w}} + \sqrt{\sqrt{\varphi_A} + \sqrt{w}}}{a\sqrt{\sqrt{\varphi_B} - \sqrt{w}} - \sqrt{\sqrt{\varphi_A} + \sqrt{w}}}\,\mathrm{d}w\,.$$

It is a complicated integration but it is seen that

$$\frac{1}{v_\infty}\int_{\varphi_A}^{\varphi_B}\zeta\mathrm{d}w = \frac{1}{v_\infty}\int_0^\infty \zeta(\tau)\frac{\mathrm{d}w}{\mathrm{d}t}(\tau)\frac{\mathrm{d}t}{\mathrm{d}\tau_1}(\tau)\frac{\mathrm{d}\tau_1}{\mathrm{d}\tau}(\tau)\,\mathrm{d}\tau\,,$$

where

$$\zeta(\tau) = \zeta_A\frac{a+\tau}{a-\tau}\,; \qquad \frac{\mathrm{d}w}{\mathrm{d}t}(\tau) = 2\varphi_B\frac{\tau^2 - a^2}{\tau^2+1}\,; \qquad \frac{\mathrm{d}t}{\mathrm{d}\tau_1}(\tau) = \frac{1+a^2}{(\tau^2+1)^2}\,; \qquad \frac{\mathrm{d}\tau_1}{\mathrm{d}\tau}(\tau) = 2\tau$$

and the following relation holds:

$$l\,\mathrm{e}^{\mathrm{i}(\pi-\alpha)} = -4\zeta_A\frac{\varphi_B}{v_\infty}(1+a^2)\int_0^\infty \frac{\tau(\tau+a)^2}{(\tau^2+1)^3}\,\mathrm{d}\tau\,.$$

As a result one obtains

$$\varphi_B = l\, v_\infty \frac{2\sin^4\dfrac{\alpha}{2}}{2+\pi\sin\dfrac{\alpha}{2}\cos\dfrac{\alpha}{2}}\,. \tag{5}$$

The total force F acting on the cavitating flat plate is calculated by integration of pressure distribution coefficient C_p

$$F = -\frac{\mathrm{i}\rho v_\infty^2}{2}\int\limits_{z_A}^{z_B} C_p\,\mathrm{d}z\,, \tag{6}$$

where

$$C_p = \frac{p-p_\infty}{\rho v_\infty^2/2}$$

is given by Bernoulli equation

$$p - p_\infty = \frac{\rho}{2}\left(v_\infty^2 - v^2\right) = \frac{\rho v_\infty^2}{2}\left(1-\frac{1}{|\zeta|^2}\right).$$

Taking into account that $\zeta \mathrm{d}w = v_\infty \mathrm{d}z$ on the plate, we find

$$F = -\frac{\mathrm{i}\rho v_\infty}{2}\int\limits_{\varphi_A}^{\varphi_B}\left(1-\frac{1}{|\zeta|^2}\right)\zeta\,\mathrm{d}w\,.$$

Using the same technique as above, we arrive at the following expression for the force coefficient

$$C_F = C_D + \mathrm{i}\,C_L = \frac{F}{\rho v_\infty^2 l/2} = \ = \mathrm{e}^{\mathrm{i}(\pi/2-\alpha)}\,\frac{2\pi\sin\alpha}{4+\pi\sin\alpha}\,. \tag{7}$$

It is obvious from what was dealt with above that Kirchhoff method is quite complicated even for such a simple problem of a cavitating flat plate at zero cavitation number. Nevertheless it was the first to enable one to solve free surface flow problems. A new important step in this direction was made by N. Zhukovsky in 1890 [26]. He proposed a new approach to solution of theory of jets in an ideal fluid problem, which was significantly improved as compared to Kirchhoff one.

2.2. Zhukovsky method

A method proposed by Zhukovsky can be applied to the 2D free surface flow problems with 1-connected flow region bounded by only straight solid boundaries. A new function (so-called Zhukovsky function)

$$\omega = \log\zeta = -\log\frac{\mathrm{d}w}{v_\infty \mathrm{d}z} = -\log\frac{v}{v_\infty} + \mathrm{i}\theta \tag{8}$$

is introduced instead of Kirchhoff's $\zeta = v_\infty \mathrm{d}z/\mathrm{d}w$ function. Another improvement, following to Zhukovsky method, is that one has to connect functions w and ω through variable t varying in the upper semi-plane rather than directly determine a relationship between the two functions. Being aware of dependences $w(t)$ and $\omega(t)$, one can eliminate variable t and hence get a Kirchhoff's solution to the problem. However, this operation is quite aimless because of the following relationships

$$\zeta = \mathrm{e}^{\omega(t)}\,, \quad z = \frac{1}{v_\infty}\int \zeta \mathrm{d}w = \frac{1}{v_\infty}\int \mathrm{e}^{\omega}\frac{\mathrm{d}w}{\mathrm{d}t}\,\mathrm{d}t\,, \tag{9}$$

enabling one to solve the problem.

The meaning of a novel approach is as follows. It was shown in the previous section that w-plane is bounded by horizontal lines $\psi = \text{const}$ which are images of streamlines in the physical z-plane. On the other hand, ω-plane is bounded by vertical and horizontal lines in the case of straight solid walls in z-plane. Indeed, such solid boundaries are lines of constant θ, that is imaginary part of ω, while free surfaces, where pressure (speed) constancy condition is satisfied, are lines of constant real part of ω. Therefore w and ω planes are bounded by polygonal segments. As a result, both w and ω domains can be transformed onto the upper half of auxiliary t-plane by using Schwarz–Christoffel transformation.

Schwarz–Christoffel formula allows one to transform half-plane t into interiority of a polygon with n vertexes (n-gon) on the ω-plane. It is assumed that each vertex is of angle $\alpha_i \leq 2\pi$, $i = 1, \ldots, n$ and

$$\sum_{i=1}^{n} \alpha_i = \pi(n-2)\,.$$

It this case the formula is as follows:

$$\omega = C_1 \int \prod_{i=1}^{n} (t - t_i)^{\alpha_i/\pi - 1}\,\mathrm{d}t + C_2\,, \tag{10}$$

where points t_i correspond to the polygon vertexes. If $t_k = \infty$ then term $(t - t_k)^{\alpha_k/\pi - 1}$ in the integrand should be excluded. Right-hand side of formula (10) includes $2n + 3$ unknowns, namely, n real parameters $t_1, \ldots, t_n$, $n - 1$ of n real parameters α_i, $i = 1, \ldots, n$ and four real parameters in two complex ones C_1 and C_2. An n-gon is totally described by $2n$ coordinates of its vertexes on ω-plane what generates $2n$ conditions. Therefore one can arbitrarily chose three of $2n + 3$ unknown parameters, say t_1, t_2 and t_3. This fact is a version of a well-known postulate that any conformal mapping is determined by three preassigned boundary points.
Consider the same model problem of cavitating flat plate at zero cavitation number formulated above.
We already have got the relationship between w and t planes, see figures 2 and 6:

$$w = \varphi_B t^2\,. \tag{11}$$

It is to be emphasized that in a neighborhood of point $t = 0$

$$\frac{\mathrm{d}w}{\mathrm{d}t} = 2\varphi_B t = \mathrm{O}(t)\,,$$

where $\mathrm{O}(t)$ denotes a quantity which is of the same order of magnitude as t.
On streamline (AC), $v = v_\infty$ wherefrom $\log(v_\infty/v) = 0$ while angle θ increases from $-\alpha$ up to value zero and therefore $\omega = -\log(v/v_\infty) + \mathrm{i}\theta$ varies from $-\mathrm{i}\alpha$ to 0. On streamline (BC) function ω varies from $\mathrm{i}(\pi - \alpha)$ to zero. On the interval $[OA]$ of the cavitating plate imaginary part of ω is a constant: $\operatorname{Im}\omega = -\alpha$ while its real part decreases from infinity down to zero. At point C angle θ varies in a jump–like manner from $-\alpha$ up to $\pi - \alpha$, see figure 7.

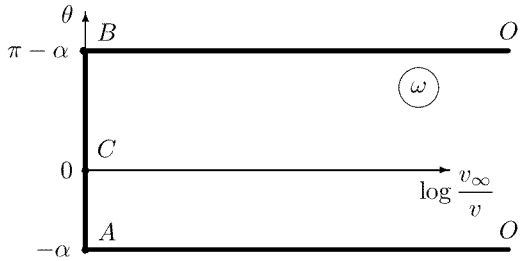


Figure 7: The ω plane.

Thus, domain on ω-plane corresponding to a region occupied by the fluid on z-plane is a triangle OAB with zero angle at infinite point O and right angles at points A and B. Assume that $t_O = 0$, $t_B = 1$ and $t_C = \infty$, see figure 6, (a postulate about three preassigned boundary points). Then Schwarz–Christoffel formula (10) reduces to

$$\omega(t) = C_1 \int_1^t \frac{\mathrm{d}t}{t\sqrt{(t-1)(t+a^2)}} + C_2\,,$$

where $a^2 = \sqrt{\varphi_A/\varphi_B}$. At point B, $\omega(1) = \mathrm{i}(\pi - \alpha)$, that is why $C_2 = \mathrm{i}(\pi - \alpha)$. The integral above yields

$$\omega(t) = C_1 \left(-\frac{1}{a} \arcsin \frac{(1-a^2)t + 2a^2}{(1+a^2)\,t} + \frac{\pi}{2a} \right) + \mathrm{i}(\pi - \alpha)$$

At point A, $\omega(-a^2) = -\mathrm{i}\alpha$, that is why $C_1 = -\mathrm{i}a$ and, finally,

$$\omega(t) = \mathrm{i}\,\arcsin\frac{(1-a^2)\,t + 2a^2}{(1+a^2)\,t} + \mathrm{i}\left(\frac{\pi}{2} - \alpha\right) . \tag{12}$$

Using a relationship between the arc sine function and natural logarithm, expression (12) can be re-written as

$$\omega(t) = \log\frac{(1+a^2)\,t}{\mathrm{i}a^2(t-2) - \mathrm{i}t + 2a\sqrt{(t-1)(t+a^2)}} + \mathrm{i}\left(\frac{\pi}{2} - \alpha\right) . \tag{13}$$

The system of two nonlinear conditions

$$\omega(\infty) = 0\,; \quad \text{and} \quad z_B = l\,\mathrm{e}^{\mathrm{i}(\pi-\alpha)}$$

allows the two unknowns φ_A and φ_B to be derived. The former gives

$$a = \sqrt[4]{\frac{\varphi_A}{\varphi_B}} = \cot\frac{\alpha}{2}\,,$$

while the latter merit some additional explanation. Equations (9), (11) and (13) can be combined to give

$$z_B = \frac{1}{v_\infty}\int\limits_{-a^2}^{1}\frac{v_\infty \mathrm{d}z}{\mathrm{d}w}\cdot\frac{\mathrm{d}w}{\mathrm{d}t}\,\mathrm{d}t\,,$$

wherefrom

$$l = \frac{\varphi_B}{v_\infty}\left(1 + \frac{\pi}{4}\sin\alpha\right)\sin^{-4}\frac{\alpha}{2}\,,$$

what coincides with expression (5).
The total force F acting on the cavitating flat plate is calculated in a manner of the previous section

$$F = -\frac{\mathrm{i}\rho v_\infty^2}{2}\int\limits_{z_A}^{z_B} C_p\,\mathrm{d}z = -\frac{\mathrm{i}\rho v_\infty^2}{2}\int\limits_{-a^2}^{1} C_p\,\frac{\mathrm{d}z}{\mathrm{d}w}\,\frac{\mathrm{d}w}{\mathrm{d}t}\,\mathrm{d}t\,,$$

where

$$C_p = 1 - \left|\mathrm{e}^{-2\omega(t)}\right| \quad \text{and} \quad \frac{\mathrm{d}z}{\mathrm{d}w} = \frac{1}{v_\infty}\,\mathrm{e}^{\omega(t)}$$

and give the same result just as above.
Nowadays some modifications of Zhukovsky method (so-called hodograph method) is widely used and, for instance, was applied to flow domains bounded by not only polygonal segments but by smooth curves as well [11]. Note that the first adaptation of the classical Zhukovsky (hodograph) method to flow past a body with a curved topography was considered by Levi-Civita [15] and Villat [24].

2.3. Mixed boundary value problem method

This method seems to be easy to understand and is very often used. The solution is derived in two steps. The first one allows us to find complex potential $w(\zeta)$ or its derivative $\mathrm{d}w/\mathrm{d}\zeta$ by mapping w-plane onto the preassigned auxiliary ζ-domain (in a manner of Zhukovsky method). In the case of a cavitating plate, using w-plane (depicted in figure 2) and auxiliary ζ upper half-plane, see figure 8, we get

$$\frac{\mathrm{d}w}{\mathrm{d}\zeta} = N\zeta\,, \tag{14}$$

where N denotes a real parameter to be determined.
The second step is formulation of a mixed boundary value problem for Levi-Civita [15] function

$$\omega_{\mathrm{LC}} = \mathrm{i}\log\frac{\mathrm{d}w}{v_\infty \mathrm{d}z} = \theta + \mathrm{i}\log\frac{v}{v_\infty} = \theta + \mathrm{i}\tau\,. \tag{15}$$

It is obvious that Levi-Civita function is a product of the imaginary unit $-\mathrm{i}$ and Zhukovsky function (8).

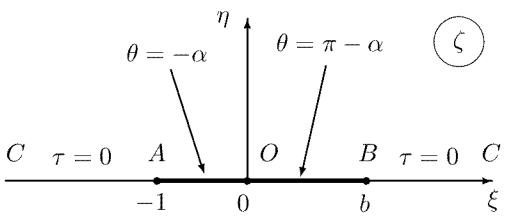


Figure 8: The ζ plane.

With the correspondence between physical z and auxiliary ζ planes the mixed boundary value problem, see figure 8, is:

$$\tau = 0 \quad \text{as} \quad \xi \le -1 \quad \text{and} \quad \xi \ge b$$

$$\theta = \begin{cases} -\alpha\,, & \text{as} \quad -1 \le \xi \le 0\,; \\ \pi - \alpha\,, & \text{as} \quad 0 \le \xi \le b\,. \end{cases}$$

where b is a coordinate (to be determined) of image of point B in ζ-plane.
The solution to the mixed boundary value problem (Riemann–Hilbert problem [17]) is obtained via formulae proposed by Keldysh and Sedov [10]. The formulae are extremely useful for both nonlinear and linearized cavitating flow problem and used also in many other fields of fluid mechanics and so merit some additional explanation.
Below presented are Keldysh–Sedov formulae in the case of the upper semi-plane. It can be readily re-written for another ζ-regions like circle, *etc.*
The Riemann–Hilbert problem is formulated for a function $f(z) = u(z) + \mathrm{i}v(z)$ which is holomorphic in upper semi-plane $z = x + \mathrm{i}y$, its real part $u(z)$ being given on a set of segments $[a_k\,, b_k]$, $k = 1, \ldots, N$ on the x-axis and its imaginary part $v(z)$ being given on the other portion of x-axis. Following to [10], three types of solution to the problem exist:
$\star$ solution unbounded at all points a_k, b_k ($\infty - \infty$ class):

$$f(z) = \frac{1}{\pi\mathrm{i}\,R(z)} \left\{ \sum_{k=1}^{N} \int_{a_k}^{b_k} \frac{u(\zeta)R(\zeta)}{\zeta - z}\,\mathrm{d}\zeta + \mathrm{i} \sum_{k=1}^{N} \int_{b_k}^{a_{k+1}} \frac{v(\zeta)R(\zeta)}{\zeta - z}\,\mathrm{d}\zeta + P_N(x) \right\}, \tag{16}$$

where $a_1 = a_N + 1$, $P_N(x)$ is a polynomial of degree N or $N-1$ depending on behaviour of $f(z)$ at infinity, and

$$R(z) = \sqrt{\prod_{k=1}^{N} (z - a_k)(z - b_k)}\ ;$$

$\star$ solution bounded at all points a_k and unbounded at all b_k ($0 - \infty$ class) as $f(\infty) = 0$:

$$f(z) = \frac{1}{\pi\mathrm{i}} \frac{R_a(z)}{R_b(z)} \left\{ \sum_{k=1}^{N} \int_{a_k}^{b_k} \frac{u(\zeta)}{\zeta - z} \frac{R_b(\zeta)}{R_a(\zeta)}\,\mathrm{d}\zeta + \mathrm{i} \sum_{k=1}^{N} \int_{b_k}^{a_{k+1}} \frac{v(\zeta)}{\zeta - z} \frac{R_b(\zeta)}{R_a(\zeta)}\,\mathrm{d}\zeta \right\}, \tag{17}$$

where

$$R_a(z) = \sqrt{\prod_{k=1}^{N} (z - a_k)}\ ,\ R_b(z) = \sqrt{\prod_{k=1}^{N} (z - b_k)}\ ;$$

$\star$ solution bounded at all points a_k, b_k ($0 - 0$ class) as $f(\infty) = 0$:

$$f(z) = \frac{R(z)}{\pi\mathrm{i}} \left\{ \sum_{k=1}^{N} \int_{a_k}^{b_k} \frac{u(\zeta)}{\zeta - z} \frac{\mathrm{d}\zeta}{R(z)} + \mathrm{i} \sum_{k=1}^{N} \int_{b_k}^{a_{k+1}} \frac{v(\zeta)}{\zeta - z} \frac{\mathrm{d}\zeta}{R(z)} \right\}. \tag{18}$$

The latter solution exists if and only if the relationship holds

$$\sum_{k=1}^{N} \int_{a_k}^{b_k} \frac{u(\zeta)}{R(z)}\,\mathrm{d}\zeta + \mathrm{i}\sum_{k=1}^{N} \int_{b_k}^{a_{k+1}} \frac{v(\zeta)}{R(z)}\,\mathrm{d}\zeta = 0\,. \tag{19}$$

Coming back to solution of the model problem, one has to use the latter formula (18) along with additional condition (19) to derive $\omega_{\mathrm{LC}}(\zeta)$ for the free surfaces detaches smoothly from the edges of the plate A and B and therefore velocity absolute value is finite there. Thus, using boundary conditions, one arrives at the expression

$$\omega_{\mathrm{LC}}(\zeta) = -\frac{1}{\pi}\sqrt{(\zeta+1)(\zeta-b)} \int_{-1}^{b} \frac{\theta(t)}{\sqrt{(1+t)(b-t)}}\,\frac{\mathrm{d}t}{t-\zeta}$$

which yields

$$\omega_{\mathrm{LC}}(\zeta) = \mathrm{i}\log\frac{\sqrt{b-\zeta}-\sqrt{b}\,\sqrt{1+\zeta}}{\sqrt{b-\zeta}+\sqrt{b}\,\sqrt{1+\zeta}} - \alpha\,. \tag{20}$$

Condition (19) gives

$$-\alpha + \frac{\pi}{2} + \arcsin\frac{1-b}{1+b} = 0\,, \tag{21}$$

or $b = \tan^2(\alpha/2)$.
Expressions (14) and (20) give analytical solution to the problem. Conformal mapping is

$$z(\zeta) = \int_{-1}^{\zeta} \frac{\mathrm{d}w}{\mathrm{d}\zeta}\,\exp(\mathrm{i}\,\omega_{\mathrm{LC}}(\zeta))\,\mathrm{d}\zeta\,.$$

Condition $z_B = z(b) = l\,\mathrm{e}^{\mathrm{i}(\pi-\alpha)}$ enables one to find unknown parameter N in the form

$$N = \frac{8\,l\,v_\infty}{4+\pi\sin\alpha}\,\cos^4\frac{\alpha}{2}\,.$$

Taking into account that $\varphi_B = w(b) = Nb^2/2$, one obtains the relationship coinciding with (5).
Note that the method of mixed boundary value problem is effectively applicable to free streamline problems with curved topography of an obstacle. Actually in this case just $\theta(z)$ is given and function $\theta(\zeta) = \mathrm{Re}\,\omega_{\mathrm{LC}}$ is unknown on ξ-axis because it is not a constant and the relationship $z(\zeta)$ is yet to be found. A special integral equation is formulated is a manner presented below in section 5.

2.4. Chaplygin method of singular points.

Chaplygin method of singular points based on the idea of determining of a holomorphic function in flow domain and therefore in auxiliary complex plane, the function's zeros and poles being known and Liuville's theorem applied. The theorem guarantees uniqueness of a solution obtained. The auxiliary region, being the image of the flow region, is chosen to be bounded by straight lines, segments and circular arcs so that one could cover all the auxiliary complex plane by mirror images of the initial domain of auxiliary variable range. Quadrants, rectangles, disk sectors, *etc.* are usually used as such ranges depending on special features of a problem under consideration.
To get the desired solution to the problem, one has to determine two analytical functions, namely derivatives of the complex potential with respect of physical z and auxiliary u variables as functions of u:

$$\frac{\mathrm{d}w}{\mathrm{d}u}(u) \quad \text{and} \quad \chi(u) = \frac{\mathrm{d}w}{v_\infty \mathrm{d}z} = \frac{v}{v_\infty}\,\mathrm{e}^{-\mathrm{i}\theta}\,.$$

Conformal mapping which transform flow region into an auxiliary one, then, is

$$z(u) = \int \frac{\mathrm{d}z}{\mathrm{d}u}\,\mathrm{d}u = \int \frac{\mathrm{d}z}{\mathrm{d}w}\cdot\frac{\mathrm{d}w}{\mathrm{d}u}\,\mathrm{d}u\,.$$

Chaplygin practically introduced some basic postulates (though he had never published them) which of considerable assistance while finding a derivative of w. If $w(u)$ transforms w-region into u-region then:

• a third-order pole of function $\mathrm{d}w/\mathrm{d}u$ corresponds to a jet of infinite width;
• a second-order pole of function $\mathrm{d}w/\mathrm{d}u$ corresponds to a jet of semi-infinite width (that is, jet bounded by a free or rigid surface). Such a semi-infinite jet is called "ocean" in [1];
• a first order pole of function $\mathrm{d}w/\mathrm{d}u$ corresponds to a jet of a finite width;
• in points of auxiliary u-plane corresponding to a vertex of solid wall bounding flow region, function $\chi(u)$ has an exponential zero or singularity depending on angle of the vertex;
• function $\mathrm{d}w/\mathrm{d}u$ has a zero, more precisely behaves like $\mathrm{O}(t-t_0)$, in point t_0 corresponding to a point on physical z-plane where a streamline divides. It can be a stagnation point or leading edge of stagnation zone, *etc.*;
• conformality condition for derivative of complex potential $\mathrm{d}w/\mathrm{d}u$ often does not satisfied at points where free streamlines spring from the body (jet detachment points). To avoid this, one has to chose a form of auxiliary u-region so that its boundary in points corresponding to jet detachment points makes right angles.
• function $\mathrm{d}w/\mathrm{d}u$ has a zero or pole (depending on specific features of the problem) in points where conformality condition does not satisfied for $w-u$ transformation.

Now apply the method of singular point to the model problem considered above with Kirchhoff and Zhukovsky methods, see figure 1. The first quadrant of auxiliary u-plane is chosen as a region to be transformed into the flow domain, see figure 9. As is customary, the coordinates of three points O, B and C on the boundary of the first quadrant of u-plane are chosen arbitrarily and location of point A is to be found. Actually the figure coincides with figure 4 for τ-plane used in section 'Kirchhoff method'.

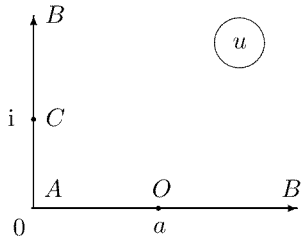


Figure 9: The auxiliary u-plane.

Following to the main postulate of Chaplygin method, find both derivatives of w with respect of z and u as functions of $u=\xi+\mathrm{i}\eta$.
Function $\chi(u)=\mathrm{d}w/(v_\infty \mathrm{d}z)$ is a bounded function in the flow region. It becomes zero in just one stagnation point O, where $u=a$. On the plate $[AOB]$ corresponding to real ξ-axis of u

$$\arg\chi(u)=-\theta(u)=\begin{cases}\alpha\,, & \text{as} \quad 0\le u\le a\,;\\ \alpha-\pi\,, & \text{as} \quad a\le u\le\infty\,,\end{cases}$$

while on free streamlines (AC) and (BC) (imaginary η-axis of u), $|\chi(u)|=1$. Due to the Schwarz principle of symmetry, all the zeros of $\chi(u)$ becomes zeros in corresponding mirror points with respect to the imaginary axis and poles in corresponding mirror points with respect to the real axis. That is why, being continued onto the whole u-plane, function $\chi(u)$ has a zero at point $u=a$ and a pole in $u=-a$. Then the following ratio

$$\left(\frac{u-a}{u+a}\,\Big/\,\chi(u)\right)$$

is a bounded and holomorphic function everywhere including infinite point and therefore is a constant due to Liouville theorem. Thus

$$\chi(u)=\frac{\mathrm{d}w}{v_\infty \mathrm{d}z}=\frac{v}{v_\infty}\,\mathrm{e}^{-\mathrm{i}\theta}=N_1\,\frac{u-a}{u+a}\,,$$

where N_1 is a constant defined by condition $\chi(0)=\mathrm{e}^{\mathrm{i}\alpha}$ which yields $N_1=\mathrm{e}^{\mathrm{i}(\alpha-\pi)}$ and finally

$$\chi(u)=\frac{\mathrm{d}w}{v_\infty \mathrm{d}z}=v\,\mathrm{e}^{-\mathrm{i}\theta}=\mathrm{e}^{\mathrm{i}(\alpha-\pi)}\,\frac{u-a}{u+a}\,. \tag{22}$$

Derivative $\mathrm{d}w/\mathrm{d}u$ has a third-order pole at infinite point C, where $u = \mathrm{i}$, and zeros at stagnation point O ($u = a$) and at point A ($u = 0$) where conformality condition does not satisfied. There is no other pole or zero in the first quadrant of u-plane for $\mathrm{d}w/\mathrm{d}u$. On continuation of the function into the whole u-plane by mirror mapping of the first quadrant with respect to real and imaginary axes of u (where $\psi = \operatorname{Im} w = \text{const}$) we get additional third-order pole at point $u = -\mathrm{i}$ and zero at point $u = -a$. Just as above, the ratio

$$\left(\frac{u(u^2 - a^2)}{(u^2+1)^3} \Big/ \frac{\mathrm{d}w}{\mathrm{d}u} \right)$$

is a bounded and holomorphic function everywhere including infinite point and therefore is a constant due to Liouville theorem. Therefore

$$\frac{\mathrm{d}w}{\mathrm{d}u} = N \, \frac{u(u^2 - a^2)}{(u^2+1)^3} \,, \tag{23}$$

where N is a real constant.
Two expressions (22) and (23) allows one to solve the problem under consideration which has two unknown parameters a and N. With the correspondence between z-plane and u-plane, the conformal mapping transforming latter into former is as follows

$$z(u) = \int\limits_0^u \frac{\mathrm{d}z}{\mathrm{d}w} \, \frac{\mathrm{d}w}{\mathrm{d}u} \, \mathrm{d}u = \frac{N}{v_\infty} \mathrm{e}^{\mathrm{i}(\pi - \alpha)} \int\limits_0^u \frac{u \, (u+a)^2}{(u^2+1)^3} \, \mathrm{d}u \,. \tag{24}$$

Note that (23) and (24) can be readily integrated to give

$$w(u) = \frac{N}{4(1+a^2)} \left(\frac{u^2 - a^2}{u^2 + 1} \right)^2 ; \tag{25}$$

$$z(u) = \frac{N}{4v_\infty} \, \mathrm{e}^{\mathrm{i}(\pi - \alpha)} \left(a \arctan u + \frac{u\big(u^3 + a(u^2-1) + a^2 u(u^2+2)\big)}{(1+u^2)^2} \right). \tag{26}$$

Two conditions

$$\chi(\mathrm{i}) = 1 \,, \quad \text{and} \quad z_B = z(\infty) = l \, \mathrm{e}^{\mathrm{i}(\pi - \alpha)}$$

generate the following nonlinear system in two unknowns

$$\mathrm{e}^{\mathrm{i}(\alpha - \pi)} \, \frac{\mathrm{i} - a}{\mathrm{i} + a} = 1 \,; \quad \frac{N}{v_\infty} \int\limits_0^u \frac{u \, (u+a)^2}{(u^2+1)^3} \, \mathrm{d}u = l \, \mathrm{e}^{\mathrm{i}(\pi - \alpha)}$$

which can be rewritten to yield

$$a = \cot \frac{\alpha}{2} \,; \quad N = v_\infty \, l \, \sin^2 \frac{\alpha}{2} \, \frac{16}{4 + \pi \sin \alpha} \,. \tag{27}$$

It is seen from (25) that

$$\varphi_B = w(\infty) = \frac{1}{4} \, N \, \sin^2 \frac{\alpha}{2} \,, \qquad \varphi_A = w(0) = \frac{1}{4} \, N \, \cos^2 \frac{\alpha}{2} \, \cot^2 \frac{\alpha}{2} \,,$$

what coincides with expression (5).
Taking into account that on the plate $[AB]$

$$C_p = 1 - \frac{v^2}{v_\infty^2} = 1 - |\chi(u)|^2 = 1 - \frac{1}{v_\infty^2} \frac{\mathrm{d}w}{\mathrm{d}z} \overline{\frac{\mathrm{d}w}{\mathrm{d}z}} \,, \tag{28}$$

the total force F can be derived (6):

$$F = -\frac{\mathrm{i}\rho v_\infty^2}{2} \int\limits_{z_A}^{z_B} C_p \, \mathrm{d}z$$

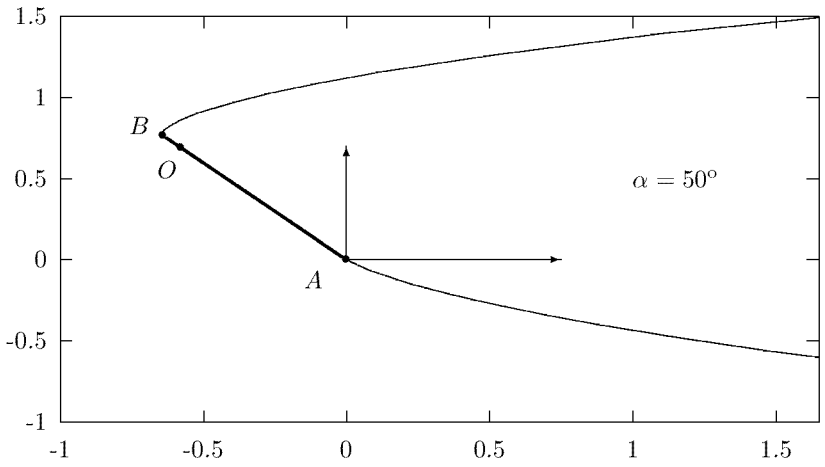


Figure 10: Flow pattern for the cavitating flat plate at zero cavitation number and $\alpha = 50^{\circ}$.

to give the force coefficient in the form

$$C_F = -\frac{\mathrm{i}}{l}\int_0^{\infty}\left(1-\frac{1}{v_\infty^2}\frac{\mathrm{d}w}{\mathrm{d}z}\frac{\overline{\mathrm{d}w}}{\overline{\mathrm{d}z}}\right)\frac{\mathrm{d}z}{\mathrm{d}w}\frac{\mathrm{d}w}{\mathrm{d}u}\mathrm{d}u = -\frac{\mathrm{i}}{l}\left(\int_0^{\infty}\frac{\mathrm{d}z}{\mathrm{d}u}\mathrm{d}u - \frac{1}{v_\infty^2}\int_0^{\infty}\frac{\mathrm{d}w}{\mathrm{d}u}\frac{\overline{\mathrm{d}w}}{\overline{\mathrm{d}z}}\mathrm{d}u\right) = \\ = -\frac{\mathrm{i}}{l}\left(z_B - z_A - \frac{1}{v_\infty^2}\int_0^{\infty}\frac{\mathrm{d}w}{\mathrm{d}u}\frac{\overline{\mathrm{d}w}}{\overline{\mathrm{d}z}}\mathrm{d}u\right). \tag{29}$$

Using expressions (22) and (23) one easily obtains coefficient C_F, see (7).

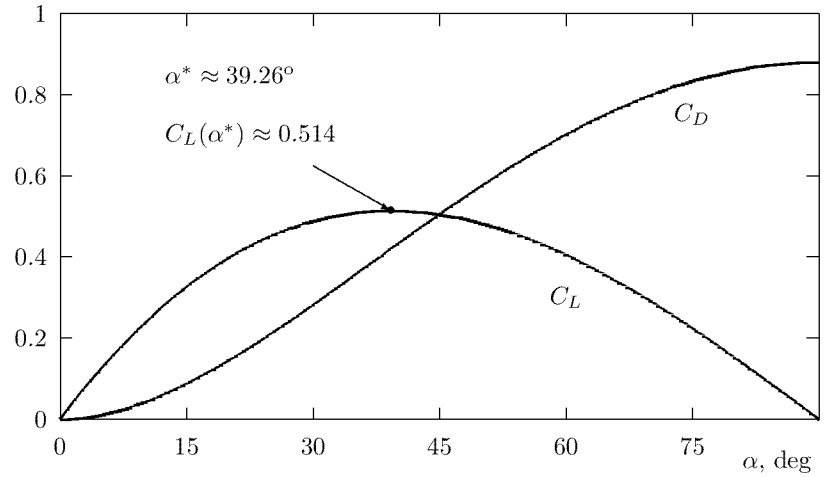


Figure 11: Lift and drag coefficients C_L and C_D versus angle of attack α.

Flow pattern $z(u) = x+iy$ can be calculated in a parametric form from expression (24) or (26). The coordinates of the stagnation point O are as follows

$$z_O = z(a) = l\,\mathrm{e}^{\mathrm{i}(\pi-\alpha)}\,\frac{\sin\alpha}{4+\pi\sin\alpha}\left(\pi-\alpha+2\cot\frac{\alpha}{2}+\sin 2\alpha\right).$$

Flow pattern for the cavitating plate at $\alpha = 50^{\circ}$ and zero cavitation number is depicted in figure 10. Stagnation point O is shown as well. Figure 11 illustrates behaviour of lift and drag coefficients C_L and C_D versus angle

of attack. It is obvious that the lift equals to zero for $\alpha = 0$ and $\pi/2$. The corresponding curve attains its maximum value $C_L \approx 0.514$ at $\alpha^* \approx 39.26^o$. Hydrodynamic fineness

$$Q = \frac{C_L}{C_D + C_f}$$

where C_f denotes friction coefficient is shown in figure 12 for $C_f = 0.003$ and 0.008. The former curve attains its maximum (11.237) at $\alpha_{\max 1} = 2.5^o$ while the latter one (6.798) at $\alpha_{\max 2} \approx 4.07^o$.

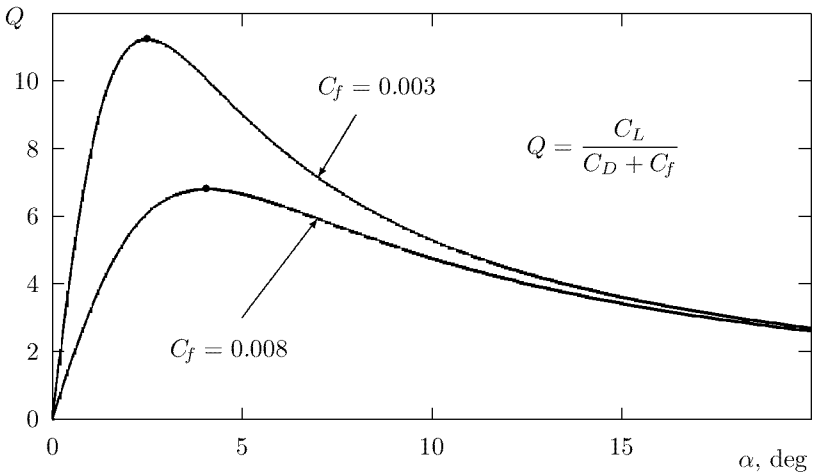


Figure 12: Hydrodynamic fineness versus angle of attack α for friction coefficient $C_f = 0.003$ and 0.008.

It is to be underlined that Chaplygin method of singular point appears to be the most effective while solving 2D nonlinear problems of theory of jets in an ideal fluid. It can be readily applied to considerably more complicated problems than that discussed above and gives quite satisfactory results.

3. A variety of cavity closure schemes

Consider a flat plate with attached cavity, the pressure within the cavity being $p = p_0$. In the flow region the following dynamic condition is satisfied $p \geq p_0$, or using Bernoulli integral

$$v = v_0 \quad \text{on the cavity boundary}; \qquad v < v_0 \quad \text{in the ambient fluid}.$$

Then the cavitation number σ can be rewritten as

$$\sigma = \frac{p_\infty - p_0}{\rho v_\infty^2/2} = \frac{v_0^2}{v_\infty^2} - 1 > 0\,,$$

where v_0 is an absolute velocity value on the cavity boundary. As a result, the cavity length becomes finite because of the cavity pressure is less than ambient, including that at infinity. The smaller the cavitation number, the larger the cavity extent and in a limiting case, as $\sigma \to 0$, the cavitation flow coincides with a streamline one considered above.

The Brillouin paradox [2] is well-known: cavity of finite length with closed continuous boundary is mathematically impossible. Indeed, if the upper and lower parts of the cavity make a closed contour then a stagnation point should appear. That is impossible due to the requirement of a constant absolute velocity value on the cavity boundary. That is why a set of cavity closure models has been developed, for the definitions and properties of which reference may be made to [1, 5, 7, 23]. Each scheme has its own advantages and disadvantages from the mathematical and physical viewpoint and should be chosen depending on specific features of the problem at hand.

The section contains a set of analytical solutions to the nonlinear problem of a supercavitating flow past a flat plate of chord l, with angle of attack α and cavitation number $\sigma > 0$, the cavity closure scheme being varied. The schemes considered are as follows: Tulin–Terentev (single spiral vortex termination), Efros–Kreisel–Gilbarg (re-entrant jet termination), Riabouchinsky (symmetrical plate termination), Tulin (double spiral vortex termination), Zhukovsky–Roshko (horizontal plates termination). All the analytical solution were derived via Chaplygin method of singular points. Numerical results were obtained in *Mathematica for Windows* computer mathematical environment.

3.1. Tulin–Terentev scheme: single spiral vortex termination

Consider a cavitating plate, see figure 13. A cavity closure scheme involving single spiral vortex is accepted as a model of cavity termination. Tulin [23] was the first to propose the scheme which was later thoroughly analysed by Terentev [7]. In the point of cavity 'collapse' the model requires

$$\omega(w) \sim -\frac{\mathcal{A}}{\sqrt{w}}\,,$$

where $\mathcal{A} > 0$.

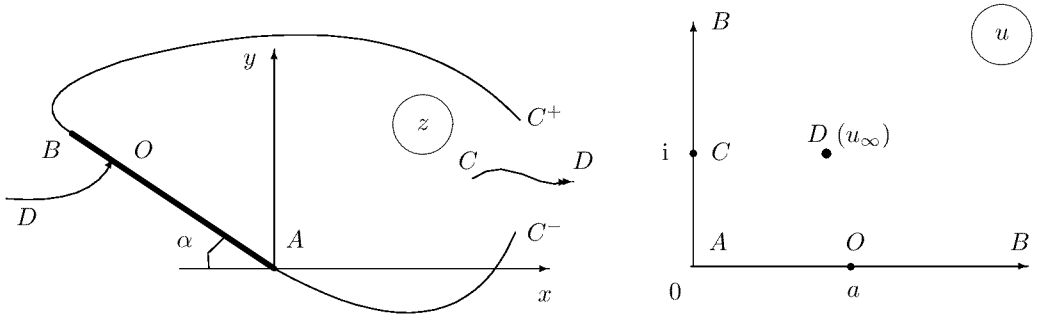


Figure 13: Flow pattern (z-plane) and auxiliary u-plane for the cavitating flat plate, Tulin–Terentev scheme.

On the dividing ('zero') streamline, where $\psi = 0$, the following relationship holds in a neighborhood of point C

$$\lim\left(\arg\frac{\mathrm{d}w}{\mathrm{d}z}\right) = \pm\infty\,,$$

what corresponds to two spiral streamlines with centers at points C^+ and C^-. Sketch of the flow in the region of the cavity termination is shown in figure 14.

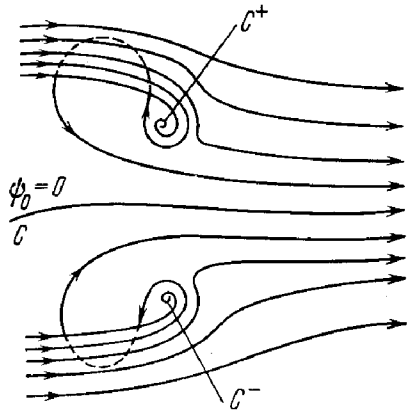


Figure 14: Schematics of the flow in the vicinity of the cavity termination, from [7].

Following to the main postulates of Chaplygin method, with the correspondence between physical z-plane and first quadrant of auxiliary u-plane, see figure 13, and applying Schwarz principle of symmetry to cover all the u-plane, one obtains derivatives of complex potential w in the form

$$\begin{gathered}\frac{\mathrm{d}w}{\mathrm{d}z} = v_0\,\mathrm{e}^{\mathrm{i}(\alpha-\pi)}\,\frac{u-a}{u+a}\,\exp\left(\frac{2bu}{u^2+1}\right);\\ \frac{\mathrm{d}w}{\mathrm{d}u} = N\,\frac{u(u^2+1)(u^2-a^2)}{(u^2-u_\infty^2)^2(u^2-\overline{u_\infty}^2)^2}\,,\end{gathered} \tag{30}$$

wherefrom

$$z(u) = \frac{N}{v_0}\,\mathrm{e}^{\mathrm{i}(\pi-\alpha)} \int\limits_0^u \frac{u(u^2+1)(u+a)^2}{(u^2-u_\infty^2)^2(u^2-\overline{u_\infty}^2)^2} \times \exp\left(-\frac{2bu}{u^2+1}\right) \mathrm{d}u\,. \tag{31}$$

It is easy to see that stagnation point O generates zeros at point $u = a$ for both the derivatives, point at infinity D corresponding to $u = u_i nfty = c + \mathrm{i}d$ generates second-order pole of $\mathrm{d}w/\mathrm{d}u$ and at point $u = \mathrm{i}$ (image of points C, C^+ and C^-), $\mathrm{d}w/\mathrm{d}u = \mathrm{O}(u-i)$ and $\omega = \mathrm{O}(u-\mathrm{i})^{-1}$.
Three conditions

$$\frac{\mathrm{d}w}{\mathrm{d}z}(u_\infty) = v_\infty\,; \qquad z_B = z(\infty) = l\mathrm{e}^{\mathrm{i}(\pi-\alpha)}\,; \qquad \oint\limits_{u_\infty} \frac{\mathrm{d}z}{\mathrm{d}u}\,\mathrm{d}u = 0 \tag{32}$$

give a nonlinear system of five equations in five unknown parameters of the problem a, b, c, d and N to be derived. The latter condition implies an existence of a contour completely surrounding the plate and the cavity on the first Riemann sheet and actually is a cavity closure condition. Terentev was the first to propose such a relationship [20] which can be used to tell so-called closed cavity closure schemes from 'open' ones. All the calculations are effectively accomplished with use of *Mathematica for Windows* software.

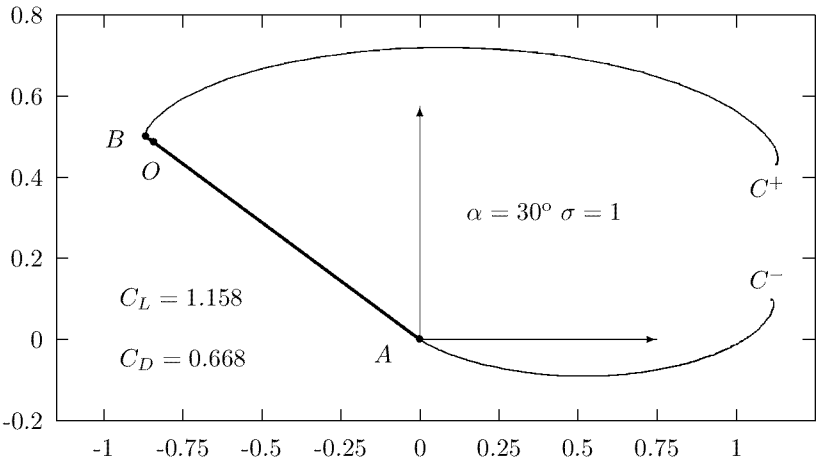


Figure 15: Flow pattern for the cavitating flat plate at $\sigma = 1$ and $\alpha = 30^\mathrm{o}$.

Force coefficient C_F is derived in a similar manner of formula (29):

$$C_F = -\mathrm{i}\frac{1+\sigma}{l}\left(z_B - z_A - \frac{1}{v_0^2}\int\limits_0^\infty \frac{\mathrm{d}w}{\mathrm{d}u}\frac{\overline{\mathrm{d}w}}{\mathrm{d}z}\mathrm{d}u\right) \tag{33}$$

Figure 15 illustrates the flow patter for $\alpha = 30^\mathrm{o}$ and $\sigma = 1$. It is to be emphasized that single spirals at point C shrink very rapidly and so the region of double-sheeted flow is quite small. The flow region in the vicinity of point C^- is shown in figure 16. Note that vertical distance δ between C^+ and C^- is directly connected with drag coefficient C_D:

$$C_D = (1+\sigma)\,\frac{\delta}{l}\,.$$

3.2. Efros–Kreisel–Gilbarg model: re-entrant jet termination

The flow pattern is depicted in figure 17. The model proposed almost simultaneously by Efros, Kreisel and Gilbarg [1] involves a re-entrant jet of unknown width δ and direction μ at infinity point C which lies on the second Riemann sheet. Gurevich [7] was the first to successfully apply the scheme to the problem of a supercavitating plate which is perpendicular to an inflow. An additional stagnation point E is appeared in the vicinity of the cavity trailing edge.

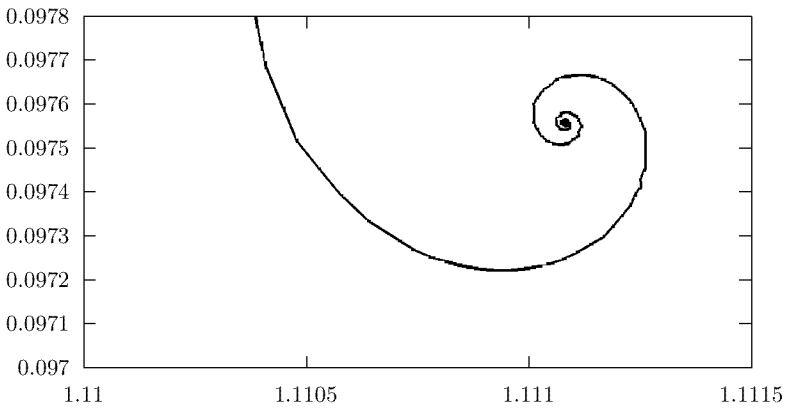


Figure 16: Flow region in the vicinity of lower single spiral vortex.

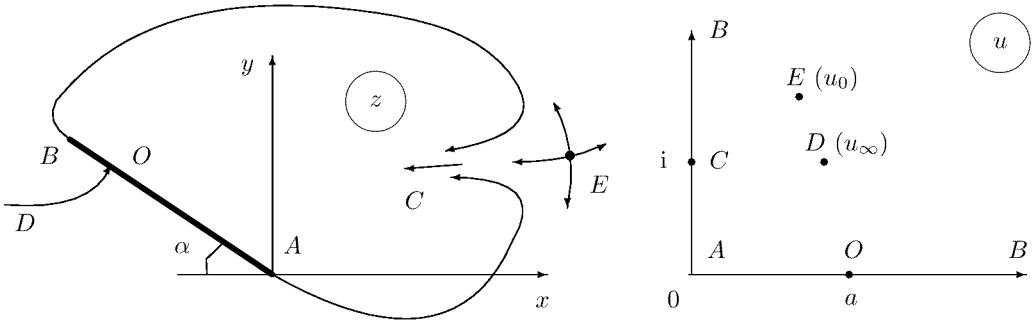


Figure 17: Flow pattern (z-plane) and auxiliary u-plane for the cavitating flat plate, Efros–Gilbarg scheme.

Adopting first quadrant of auxiliary u-plane as an image of the flow region, with the correspondence between physical z and auxiliary u planes (see figure 17) solution to the problem is as follows:

$$\begin{aligned} \frac{\mathrm{d}w}{\mathrm{d}z} &= v_0\,\mathrm{e}^{\mathrm{i}(\alpha-\pi)}\,\frac{u-a}{u+a}\,\frac{(u-u_0)(u-\overline{u_0})}{(u+u_0)(u+\overline{u_0})}\,; \\ \frac{\mathrm{d}w}{\mathrm{d}u} &= N\,\frac{u(u^2-a^2)(u^2-u_0^2)(u^2-\overline{u_0}^2)}{(u^2+1)(u^2-u_\infty^2)^2(u^2-\overline{u_\infty}^2)^2}\,, \end{aligned} \tag{34}$$

where $u_0 = b + \mathrm{i}c$ and $u_\infty = d + \mathrm{i}f$. These two expressions can be combined to give

$$z(u) = \frac{N}{v_0}\,\mathrm{e}^{\mathrm{i}(\pi-\alpha)} \int\limits_0^u \frac{u(u+a)^2}{(u^2+1)} \times \frac{(u+u_0)^2(u+\overline{u_0})^2}{(u^2-u_\infty^2)^2(u^2-\overline{u_\infty}^2)^2}\,\mathrm{d}u\,. \tag{35}$$

The same conditions (32) yield a nonlinear system of five equations in six unknowns a, b, c, d, f and N. It is easy to see that the solution is not unique for the number of unknowns is greater than the number of conditions. Nevertheless, one can use an additional condition connected with the direction of the re-entrant jet at the point of infinity C, see figure 18. Both the asymptotic analysis and numerical results for the cavitating flat plate have shown angle μ not to significantly affect the hydrodynamic coefficients and even most of the flow pattern. That is why it seems reasonable to consider the parameter as a given one. Thus, an additional condition is as follows

$$\frac{\mathrm{d}w}{\mathrm{d}z}(\mathrm{i}) = v_0\,\mathrm{e}^{-\mathrm{i}\mu}\,.$$

Using residue theory, one arrives at the following relationships (which are correct for an arbitrary cavitating hydrofoil):

$$C_D = \frac{2q}{v_\infty l}\left(1 - \frac{v_0}{v_\infty}\cos\mu\right)\,; \qquad C_L = \frac{2q}{v_\infty l}\left(\frac{\Gamma}{q} - \frac{v_0}{v_\infty}\sin\mu\right)\,, \tag{36}$$

where q denotes the flow rate in the re-entrant jet C and Γ is circulation along a large contour completely surrounding the cavitating foil and the cavity and enclosing most of the flow. Note that

$$\mathrm{res} = \oint\limits_{u_\infty} \frac{\mathrm{d}F}{\mathrm{d}\zeta}\mathrm{d}\zeta = \Gamma + iq$$

and, moreover,

$$q = \pi N \frac{(1+a^2)\left((1+b^2-c^2)^2+4b^2c^2\right)}{2\left((1+d^2-f^2)^2+4d^2f^2\right)^2} .$$

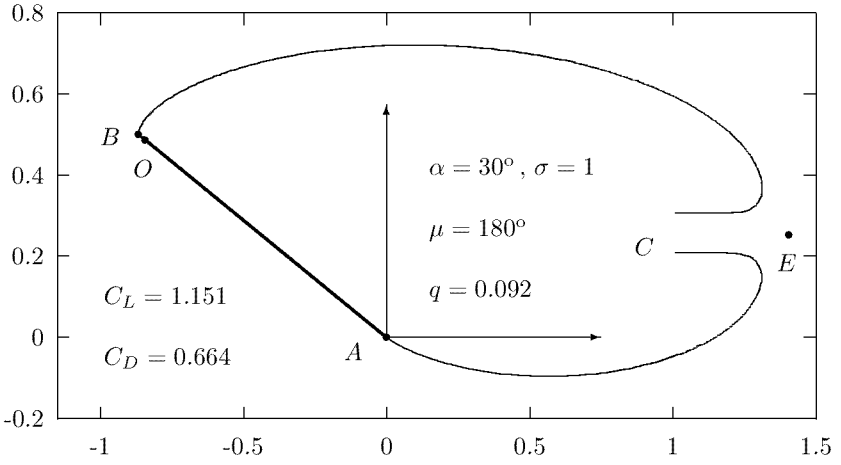


Figure 18: Flow pattern for the cavitating flat plate at $\sigma = 1$, $\alpha = 30^\circ$ and $\mu = 180^\circ$.

Another form of the force coefficient is

$$C_F = \frac{2}{v_\infty l}\left(-\sqrt{1+\sigma}\,\mathrm{e}^{\mathrm{i}\mu}\mathrm{Im}\,(\mathrm{res}) + \mathrm{i}\,\overline{\mathrm{res}}\right). \tag{37}$$

Flow pattern for the cavitating flat plate at $\sigma = 1$ and $\alpha = 30^\circ$ is shown in figure 18 along with hydrodynamic coefficients and position of stagnation points O and E. The direction of re-entrant jet is chosen to be $\mu = 180^\circ$.

3.3. Riabouchinsky model: symmetrical plate termination

The model introduced by D. Riabouchinsky [19] assumes the flow region to be symmetric and so the cavity terminates on the symmetrical plate. Another version of the scheme was proposed [21] with central symmetry, see figure 19, which is more convenient from the viewpoint of mathematical analysis. Adopting this scheme, transform flow region into the rectangular $\pi/2 \times \pi|\tau|/2$, where τ is purely imaginary, on the auxiliary u-plane, see figure 19.

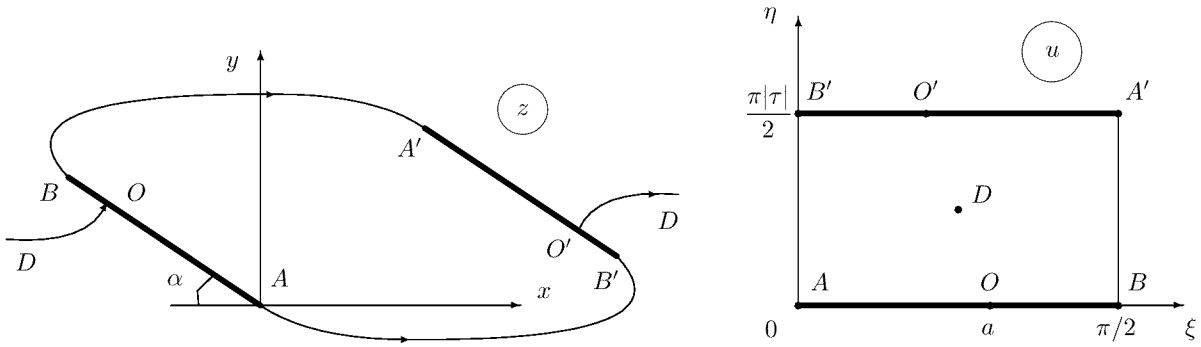


Figure 19: Flow pattern (z-plane) and auxiliary u-plane for the cavitating flat plate, Riabouchinsky scheme.

Conjugate velocity $\mathrm{d}w/\mathrm{d}z$ has constant absolute value v_0 of both vertical sides of the rectangular, while on the horizontal sides its argument is a step function with a jump-like behaviour in stagnation points O and O' (argument varies by π). That is why $\mathrm{d}w/\mathrm{d}z$ has zeros at points $u = a$ and $u = \pi - a + \pi\tau/2$. Using Schwarz principle of symmetry, one arrives at the conclusion that $\mathrm{d}w/\mathrm{d}z$ is a doubly periodic elliptic function with periods π and $\pi\tau$. Basing on the Liouville theorem and accepting notation of Whittaker & Watson [25] one can write down such a functions as a ratio of elliptic theta-function ϑ_i, $i = 1, \ldots, 4$ which *nome* $0 < q < 1$ is real. Function $\mathrm{d}w/\mathrm{d}u$ is real on horizontal sides of the rectangular and must be purely imaginary on vertical sides. That is why this derivative is also a doubly periodic elliptic function with periods π and $\pi\tau$. The point D at infinity becomes the rectangular center $u = \pi/4 + \pi\tau/4$ where $\mathrm{d}w/\mathrm{d}u$ has a second order pole. Stagnation points generates simple zeros and so do points where conformality condition does not satisfied, that is all the rectangle vertexes.

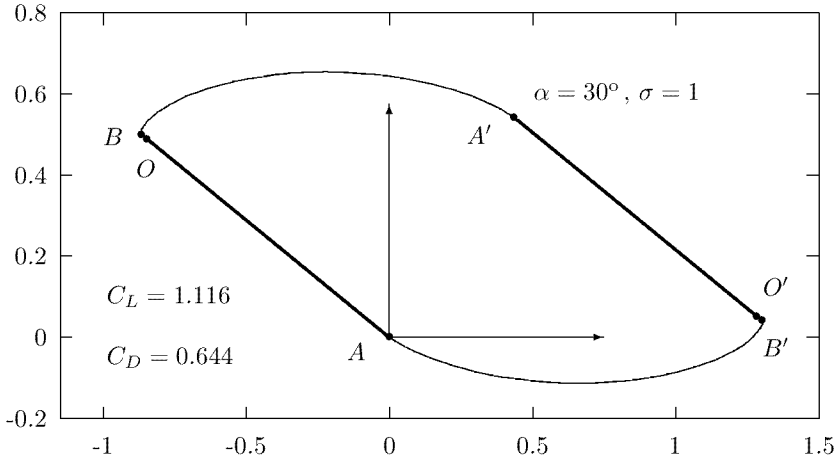


Figure 20: Flow pattern for the cavitating flat plate at $\sigma = 1$, $\alpha = 30^\circ$.

The solution to the problem is as follows

$$\frac{\mathrm{d}w}{\mathrm{d}z} = v_0\,\mathrm{e}^{\mathrm{i}(\alpha-\pi)}\,\frac{\vartheta_1(u-a)\vartheta_3(u+a)}{\vartheta_1(u+a)\vartheta_3(u-a)}\,.$$
$$\frac{\mathrm{d}w}{\mathrm{d}u} = N\,\frac{\vartheta_1(2u)}{\vartheta_3^2(2u)} \times \vartheta_1(u-a)\vartheta_1(u+a)\vartheta_3(u-a)\vartheta_3(u+a)\,. \tag{38}$$

wherefrom

$$z(u) = \frac{N}{v_0}\,\mathrm{e}^{\mathrm{i}(\pi-\alpha)} \int\limits_0^u \frac{\vartheta_1(2u)\vartheta_1^2(u+a)\vartheta_3^2(u-a)}{\vartheta_3^2(2u)}\,\mathrm{d}u\,. \tag{39}$$

An advantage of the model proposed is that it always involves less number of unknown parameters then the other schemes. Indeed, one has to determine just three unknowns a, τ and N in the problem under consideration instead of $5 - 6$ in other cases. Two former out of three conditions (32) give the nonlinear system of three equations in three unknowns, where $u_\infty = \pi/4 + \pi\tau/4$, the latter condition (32) being satisfied due to the central symmetry of the flow region.
Force coefficient and flow pattern are calculated using expressions (33) and (39) correspondingly. Figure 20 illustrates some numerical results obtained in *Mathematica* package for the same set of the flow parameters which was considered in the previous sections.

3.4. Tulin model: double spiral vortex termination

The scheme was proposed by M. Tulin [23] and involves two double spiral-like streamlines at the trailing edge of the cavity. Such a double spiral vortex flow is known to be a unique opportunity to conjugate smoothly two streamlines with different absolute velocity values [1], see figure 21. The scheme is appeared to be especially efficient for confined streamline problems with one/two free surfaces which bounded the flow region [14, 22].

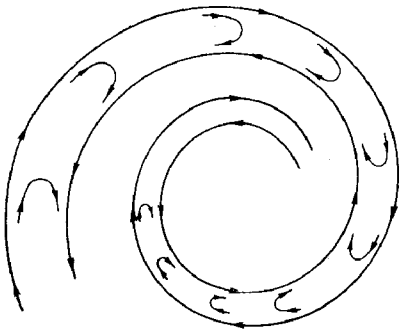


Figure 21: Flow pattern in the vicinity of a double spiral streamline, from [1].

In the case of the cavitating flat plate, first quadrant of auxiliary u-plane is chosen as image of the region occupied by the fluid in z-plane, see figure 22. The wake behind the cavity begins at points C and E and thins continuously in the downstream direction.
Using Chaplygin method of singular points one obtains that function $\mathrm{d}w/\mathrm{d}u$ is real on ξ-axis and purely imaginary on η-axis. It has zeros at stagnation point O ($u = a$) and at point A where conformality condition does not satisfied and three-order pole at point at infinity D ($u = \mathrm{i}$).

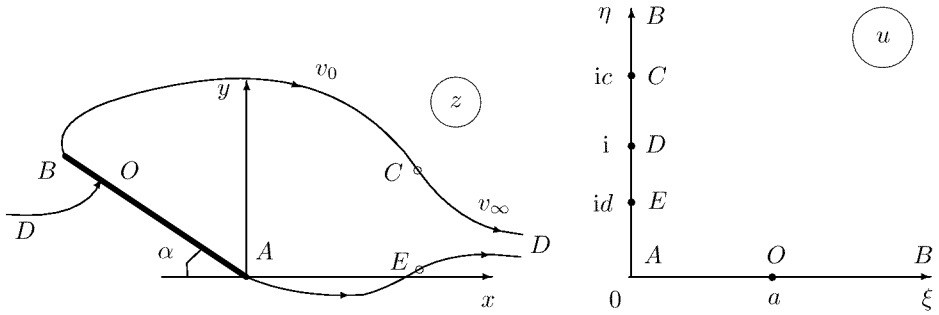


Figure 22: Flow pattern (z-plane) and auxiliary u-plane for the cavitating flat plate, Tulin scheme.

Another derivative $\mathrm{d}w/\mathrm{d}z$ has a zero at stagnation point O and behaves in a special manner at points C and E. Consider a function

$$\left(\frac{\mathrm{d}w}{\mathrm{d}z}\right)^{\mathrm{i}} = \mathrm{e}^{\theta+\mathrm{i}\log v}$$

which is a step function on ξ-axis. Tracing small semi-circles described about points C ($u = \mathrm{i}c$ and E ($u = \mathrm{i}d$) in the counter-clockwise direction, one arrives at the conclusion that the argument of the function has an increment $(1/\pi)(\log(v_0/v_\infty)$ and $(1/\pi)(\log(v_\infty/v_0)$ correspondingly. That is why

$$\begin{aligned} \frac{\mathrm{d}w}{\mathrm{d}z} &= v_0\,\mathrm{e}^{\mathrm{i}(\alpha-\pi)}\frac{u-a}{u+a}\left(\frac{u-\mathrm{i}c}{u+\mathrm{i}c}\frac{u+\mathrm{i}d}{u-\mathrm{i}d}\right)^{\kappa} \\ \frac{\mathrm{d}w}{\mathrm{d}u} &= N\,\frac{u(u^2-a^2)}{(u^2+1)^3}\,, \end{aligned} \tag{40}$$

where

$$\kappa = \frac{\mathrm{i}}{\pi}\,\log\frac{v_\infty}{v_0}$$

and

$$z(u) = \int_0^u \frac{\mathrm{d}z}{\mathrm{d}w}\,\frac{\mathrm{d}w}{\mathrm{d}u}\,\mathrm{d}u = \frac{N}{v_0}\,\mathrm{e}^{\mathrm{i}(\pi-\alpha)}\int_0^u \frac{u(u+a)^2}{(u^2+1)^3}\,\left(\frac{u+\mathrm{i}c}{u-\mathrm{i}c}\frac{u-\mathrm{i}d}{u+\mathrm{i}d}\right)^{\kappa}\,\mathrm{d}u\,.$$

The problem involves four unknown parameters a, c, d and N. On the other hand, just two 'direct' conditions can be imposed:

$$\frac{\mathrm{d}w}{\mathrm{d}z}(u_\infty) = v_\infty \quad \text{and} \quad z_B = z(\infty) = l\mathrm{e}^{\mathrm{i}(\pi-\alpha)}\,. \tag{41}$$

Cavity closure condition applied in the previous sections

$$\oint\limits_{u_\infty} \frac{\mathrm{d}z}{\mathrm{d}u}\,\mathrm{d}u = 0$$

does not satisfied.

Thus this scheme is appeared to be the most indeterminate cavity closure model. Nevertheless, two additional conditions should be formulated:

$$\varphi_C = \varphi_E \quad \text{and} \quad \left.\frac{\mathrm{d}\theta}{\mathrm{d}\eta}\right|_{\eta=1} = 0 \tag{42}$$

to close the problem. The former implies the velocity potential to be the same at the end of the cavity at upper and lower boundaries. The latter specifies the angle θ (direction of the velocity vector) along the wake boundaries be minimal at point D. Note that both conditions are arbitrarily chosen and can be substituted by a pair of others, for instance $y_C = y_E$ and $\mathrm{d}^2w/\mathrm{d}\eta^2 = 0$ as $\eta = 1$.

Numerical results obtained with use of conditions (41) and (42) are shown in figure 23.

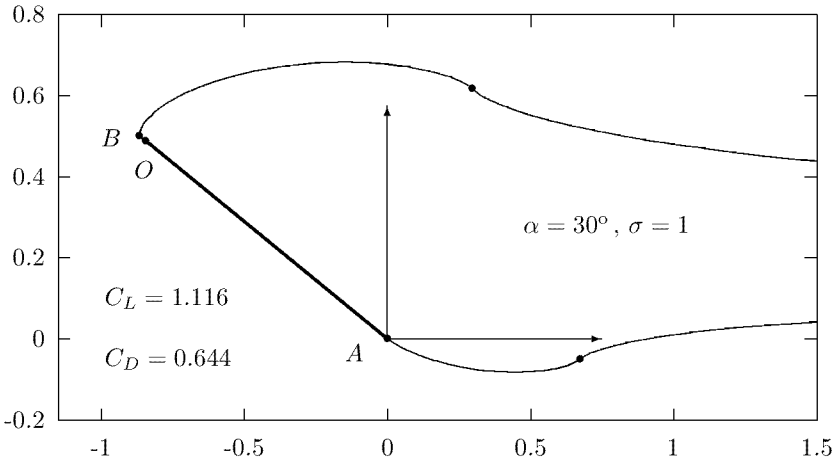


Figure 23: Flow pattern for the cavitating flat plate at $\sigma = 1$, $\alpha = 30^\circ$.

3.5. Zhukovsky–Eppler–Roshko model: horizontal plates termination

The model is often called 'open' one and assumes that free streamlines conjugate smoothly with two solid semi-infinite plates which are parallel to the inflow. The absolute velocity value monotonically decreases from v_0 down to v_∞ along this plate. This cavity closure model is very effective for streamline problems either under gravity or with one/two solid boundaries [7]. Zhukovsky [26] was the first to introduce the model.

Following to Chaplygin method, transform flow region into the rectangular $\pi/2 \times \pi|\tau|/2$, where τ is purely imaginary, on the auxiliary u-plane, see figure 24. Determining zeros and poles, one arrives at the following solution to the problem

$$\begin{gathered}\frac{\mathrm{d}w}{\mathrm{d}z} = v_0\,\mathrm{e}^{\mathrm{i}(\alpha-\pi)}\,\frac{\vartheta_1(u-a)}{\vartheta_1(u+a)}\,;\\ \frac{\mathrm{d}w}{\mathrm{d}u} = N\,\frac{\vartheta_1(2u)\,\vartheta_1(u-a)\,\vartheta_1(u+a)}{\vartheta_4^3(u-b)\,\vartheta_4^3(u+b)}\,,\end{gathered} \tag{43}$$

wherefrom

$$z(u) = \frac{N}{v_0}\,\mathrm{e}^{\mathrm{i}(\pi-\alpha)} \int\limits_0^u \frac{\vartheta_1(2u)\,\vartheta_1^2(u+a)}{\vartheta_4^3(u-b)\,\vartheta_4^3(u+b)}\,\mathrm{d}u\,. \tag{44}$$

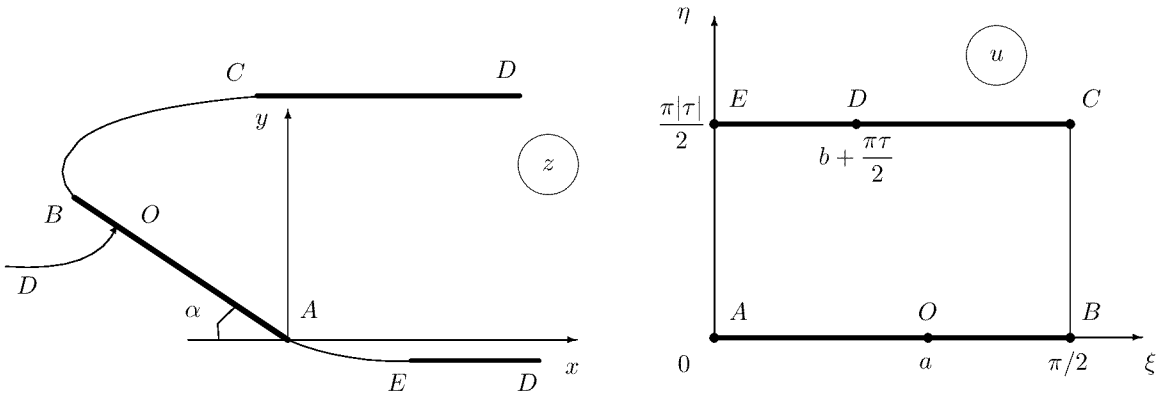


Figure 24: Flow pattern (z-plane) and auxiliary u-plane for the cavitating flat plate, Zhukovsky–Roshko–Eppler scheme.

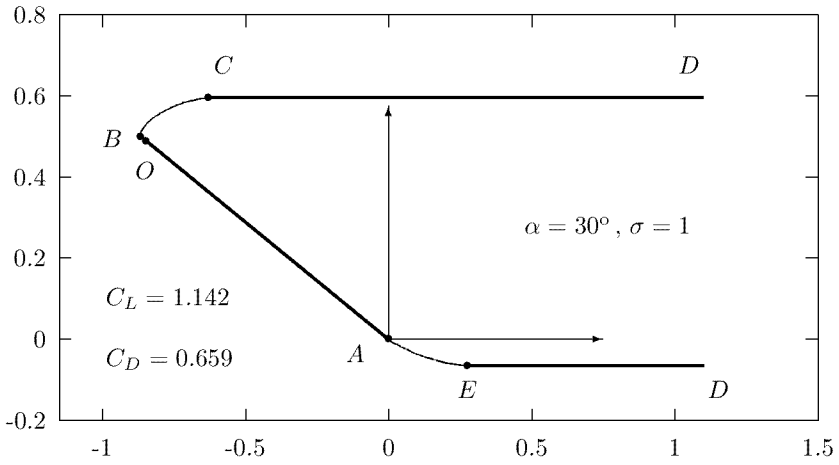


Figure 25: Flow pattern for the cavitating flat plate at $\sigma = 1$, $\alpha = 30^\circ$.

First two out of three conditions (32) where $u_\infty = b + \pi\tau/2$, along with two additional conditions

$$\frac{\mathrm{d}w}{\mathrm{d}z}\left(\frac{\pi}{2} + \frac{\pi\tau}{2}\right) = v_\infty \quad \text{and} \quad \left(\frac{\mathrm{d}w}{\mathrm{d}z}\right)'_u (u_\infty) = 0$$

allow four unknowns a, b, τ and N to be derived. The former of the additional conditions implies that the semi-infinite plates are horizontal and the latter specify the velocity absolute value be a monotone decreasing function having its minimum at point D ($u = u_\infty$).
The corresponding flow pattern and hydrodynamic coefficients are shown in figure 25. Note that this open cavity closure scheme give significantly smaller cavity length than so called closed models, such as Riabouchinsky, Tulin–Terentev, Efros–Kreisel–Gilbarg. As a result, the hydrodynamic coefficients become somewhat larger.

4. Free and solid boundaries

All the previous section has demonstrated an effectiveness of Chaplygin method of singular points applied to nonlinear cavitating problems of theory of jets in an ideal fluid. This section contains another documentation of the fact dealing with two somewhat more complicated problems: first one being that of the flow past a cavitating flat plate in the channel and second one – cavitating plate in the uniform jet of finite width. It was shown by Terentev [21] that Zhukovsky–Roshko and Tulin (double spiral vortex) schemes are to be used for the problems. We shall not dwell on the solution procedure and just describe the final results and some limiting cases.

4.1. Cavitating plate in a channel

The flow pattern $z = x + \mathrm{i}y$ and the auxiliary u-plane are depicted in figure 26. Given are the following parameters: angle of attack α, plate length l, channel width H, cavitation number σ and a distance between the lower wall of the channel and point A (trailing edge of the plate). It is also assumed that velocity v_1 at points D_1 and D_3 is the same (though it is an unknown value).

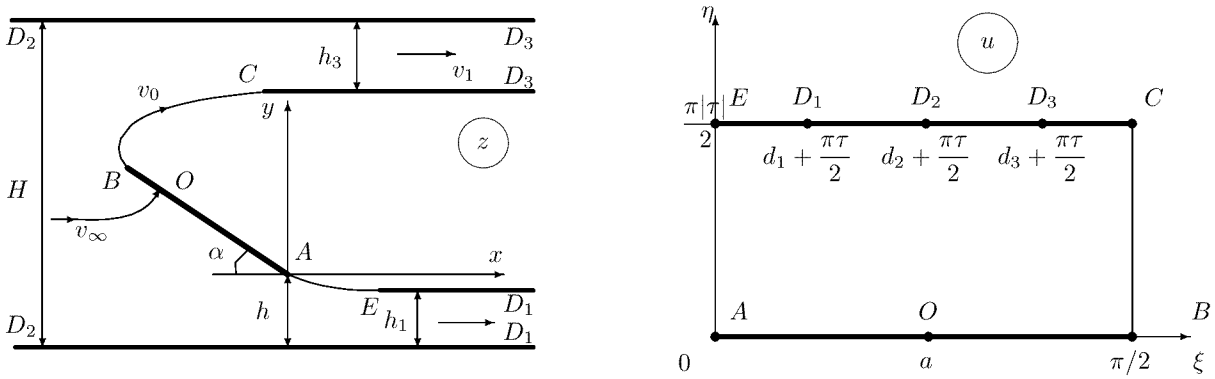


Figure 26: Flow pattern (z-plane) and auxiliary u-plane for the cavitating flat plate in the channel.

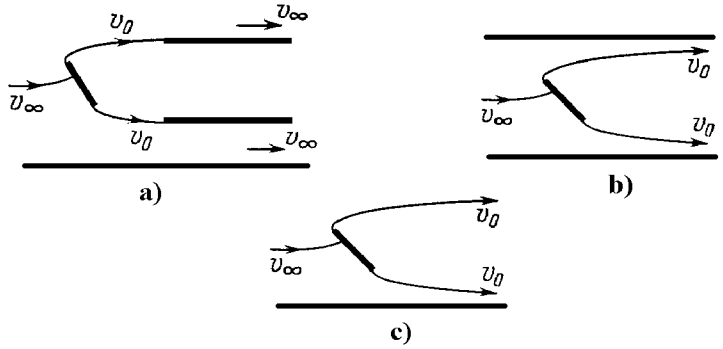


Figure 27: Some special cases of the problem for the cavitating plate in the channel.

The analytical solution to the problem is readily given by Chaplygin method [22]:

$$\frac{\mathrm{d}w}{\mathrm{d}z} = v_0\,\mathrm{e}^{\mathrm{i}(\alpha-\pi)}\,\frac{\vartheta_1(u-a)}{\vartheta_1(u+a)}\,;$$

$$\frac{\mathrm{d}w}{\mathrm{d}u} = N\,\frac{\vartheta_1(2u)\,\vartheta_1(u-a)\,\vartheta_1(u+a)}{\prod\limits_{i=1}^{3}\vartheta_4(u-d_i)\,\vartheta_4(u+b_i)}\,, \tag{45}$$

wherefrom

$$z(u) = \frac{N}{v_0}\,\mathrm{e}^{\mathrm{i}(\pi-\alpha)}\int\limits_0^u \frac{\vartheta_1(2u)\,\vartheta_1^2(u+a)}{\prod\limits_{i=1}^{3}\vartheta_4(u-d_i)\,\vartheta_4(u+b_i)}\,\mathrm{d}u\,. \tag{46}$$

Unknown parameters of the problem a, b_1, b_2, b_3, N, q, velocity v_1, widths h_1 and h_3 are derived from a quite complicated system of transcendental equations obtained on the base of the following conditions

$$\begin{gathered}\frac{\mathrm{d}w}{\mathrm{d}z}(u_\infty) = v_\infty\,; \quad \frac{\mathrm{d}w}{\mathrm{d}z}(u_1) = v_1\,; \quad \frac{\mathrm{d}w}{\mathrm{d}z}(u_2) = v_1\,; \quad Hv_\infty = v_1(h_1+h_3)\,; \quad z_B = z(\infty) = l\mathrm{e}^{\mathrm{i}(\pi-\alpha)}\,; \\ \frac{1}{2}\oint\limits_{u_\infty}\frac{\mathrm{d}w}{\mathrm{d}u}\,\mathrm{d}u = \mathrm{i}v_\infty H\,; \quad \frac{1}{2}\oint\limits_{u_1}\frac{\mathrm{d}w}{\mathrm{d}u}\,\mathrm{d}u = \mathrm{i}v_1 h_1\,; \quad \frac{\mathrm{d}w}{\mathrm{d}z}\left(\frac{\pi}{2}+\frac{\pi\tau}{2}\right) = v_0\,; \quad \operatorname{Im} z_E = \mathrm{i}(h_1-h)\,,\end{gathered} \tag{47}$$

where $u_\infty = u_2 = d_2 + \pi\tau/2$, $u_i = d_i + \pi\tau/2$, $i = 1, 3$.
After some algebra the number of unknowns (and equations) can be reduced from nine down to six and even to four, but the system remains complicated.
The general problem has lots of interesting special cases as h_1 or h_3 tends to infinity (one solid wall), $d_1 = 0$ and $d_3 = \pi/2$ (Kirchhoff scheme in the channel, when point C coincides with D_3 and E with D_1), *etc.*, see figure 27.

4.1. Cavitating plate in a jet of finite width

The flow region and the corresponding auxiliary u-plane are shown in figure 28. Tulin cavity closure model with double spiral vortex is adopted for it seems to be the most efficient from the mathematical viewpoint. The jet width is assumed to be H and submergence of the plate is h. Actually submergence is a distance between a dividing streamline and the upper jet boundary far upstream. The velocity on the jet boundary is v_∞.

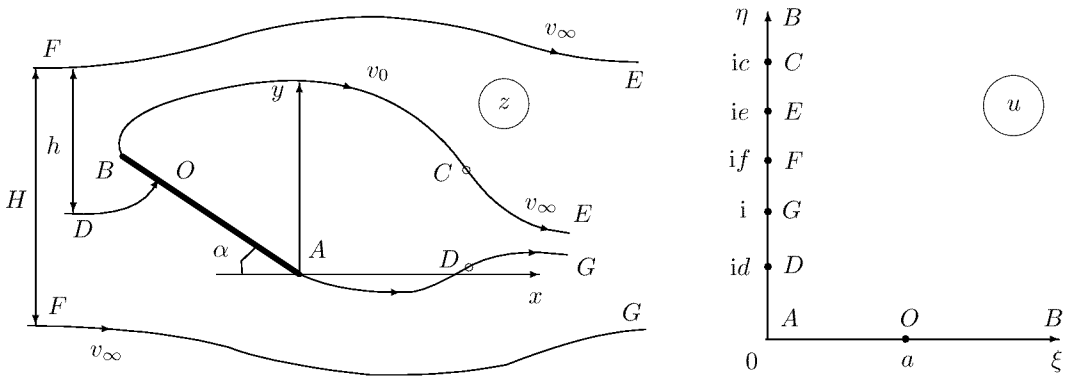


Figure 28: Flow pattern (z-plane) and auxiliary u-plane for the cavitating flat plate in the jet of finite width.

If one choses a first quadrant of the auxiliary u-plane as an image of the flow region, then solution to the problem is found through Chaplygin method in the form:

$$\frac{\mathrm{d}w}{\mathrm{d}z} = v_0\,\mathrm{e}^{\mathrm{i}(\alpha-\pi)}\,\frac{u-a}{u+a}\left(\frac{u-\mathrm{i}c}{u+\mathrm{i}c}\,\frac{u+\mathrm{i}d}{u-\mathrm{i}d}\right)^{\kappa};$$
$$\frac{\mathrm{d}w}{\mathrm{d}u} = N\,\frac{u(u^2-a^2)}{(u^2+1)(u^2+e^2)(u^2+f^2)}, \tag{48}$$

where, as beforehand

$$\kappa = \frac{\mathrm{i}}{\pi}\,\log\frac{v_\infty}{v_0}$$

and

$$z(u) = \int_0^u \frac{\mathrm{d}z}{\mathrm{d}u}\,\mathrm{d}u = \int_0^u \frac{\mathrm{d}z}{\mathrm{d}w}\cdot\frac{\mathrm{d}w}{\mathrm{d}u}\,\mathrm{d}u\,.$$

Conditions

$$\frac{\mathrm{d}w}{\mathrm{d}z}(u_\infty) = v_\infty;\quad z_B = z(\infty) = l\mathrm{e}^{\mathrm{i}(\pi-\alpha)};\quad \arg\frac{\mathrm{d}w}{\mathrm{d}z}(\mathrm{i}) = \arg\frac{\mathrm{d}w}{\mathrm{d}z}(\mathrm{ie});$$

$$w(\mathrm{id}) = w(\mathrm{ic});\quad \frac{1}{2}\oint_{u_\infty}\frac{\mathrm{d}w}{\mathrm{d}u}\,\mathrm{d}u = \mathrm{i}Hv_\infty;\quad \frac{1}{2}\oint_{\mathrm{ie}}\frac{\mathrm{d}w}{\mathrm{d}u}\,\mathrm{d}u = \mathrm{i}hv_\infty$$

allow the unknowns a, c, d, e, f and N/V_∞ to be derived. Again, the third and fourth conditions (which specify the velocity vector be of the same direction at points E and G at infinity downstream and complex potential be of the same value at the ends of the cavity C and D correspondingly) are quite artificial and can be substituted by other reasonable relationships.

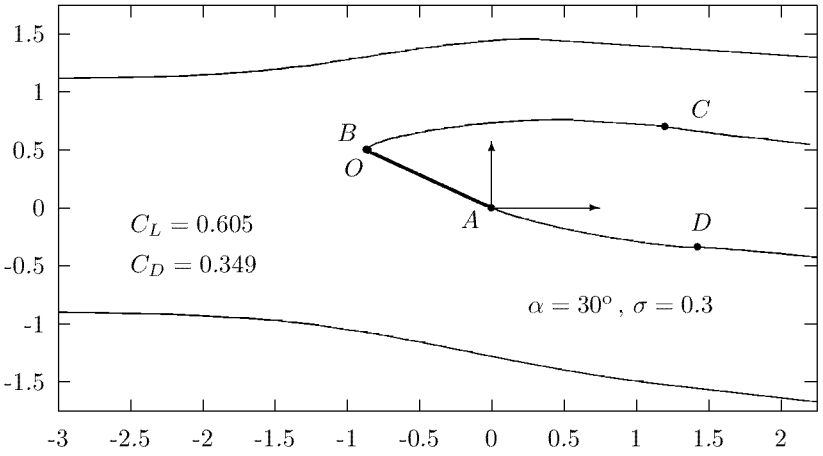


Figure 29: Flow pattern for the cavitating flat plate in the jet.

Note that solution (48) produces a solution by Larock and Street [14] for the cavitating plate beneath the free surface as its special case as $H \to \infty$ and $f \to 1^+$. Solution for the cavitating plate in unbounded inflow (40) is also a special case if $H\,, h \to \infty$ and $d\,, e \to 1^+$ as well.
Figure 29 illustrates numerical results (flow pattern in the vicinity of the plate and hydrodynamic coefficients) obtained with use of *Mathematica* for the cavitating plate with a following set of given parameters: $H = 2$, $h = 0.75$, $\alpha = 30^o$, $\sigma = 0.3$.

5. Separated free streamline flow around a body with a curved boundary

5.1. Levi-Civita approach

Levi-Civita [15] was the first to propose an approach to solution of the plane free surface flow problems for obstacles of a curved topography. Such problems are significantly more complicated than those with flow regions bounded by polygonal segments. For the latter the imaginary part $\theta(u)$ of the Zhukovsky function $\omega(u)$ is given on the portion of the auxiliary u-domain boundary corresponding to the straight solid walls and its real part (velocity absolute value) is given on the other portion of the boundary. In the case of a curved obstacle all information one possesses is just the function $\theta(z)$ on the wetted portion on the body (which is sometimes also unknown) and velocity absolute value on free surfaces. The main difficulty of the problem is that it is impossible to set $\theta(u)$ without conformal mapping $z(u)$, if $\theta(z)$ is not a step function.
Following to Levi-Civita approach, flow region z is transformed into the semi-circle in auxiliary u-plane (one can also chose another domain as well) and Levi-Civita function (15) is written down in the form

$$\omega_{\rm LC} = \omega_0 + \Omega\,,$$

where ω_0 denotes Levi-Civita function for a polygonal body. Additional term is

$$\Omega(u) = \sum_{k=-n}^{\infty} A_k u^k\,,$$

where A_k are real coefficients to be found from the imposed conditions including Brillouin one (smooth detachment condition).
Brodetsky [3] calculated a flow around a circular and elliptic cylinder for $\sigma = 0$, three coefficients A_k being taken into account. In the case of circular cylinder the relationship holds

$$\frac{{\rm d}\theta}{{\rm d}s} = \kappa\,,$$

where s denotes an arc coordinate of the body boundary and κ is its curvature. Collocation method can be used to derive the coefficients A_k. Significantly more detailed numerical analysis of the problem was done in [7] by Terentev and Dmitrieva for an arbitrary cavitation number σ, more than 30 terms being taken into account. Two points were determined satisfying the Brillouin condition. The points correspond to two maxima on curves C_x versus detachment angle γ for a given σ, see figure 30.

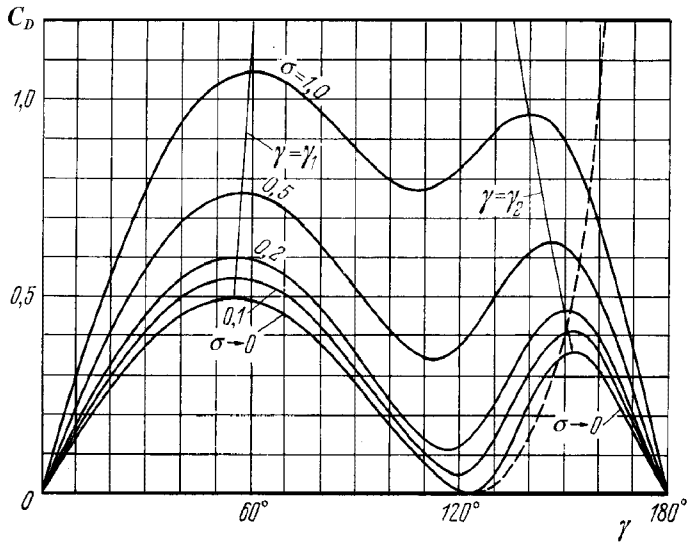


Figure 30: Drag coefficient of a circular cylinder versus detachment angle γ, from [7].

5.2. Method of integral equation

This method is an adaptation of mixed boundary value problem method (see section 2.3) to flow around an obstacle of a curved topography. By a conformal mapping of the flow region into the semi-plane (or semi-circle, *etc.*), the solution to the problem is reduced to an integral (or integro-differential) equation of Villat type [24] for a function $\lambda(u)$ characterizing the angle made by the fluid velocity vector. Using another form of such an integral equation, Nekrasov [18] was the first to prove both existence and uniqueness of flows around a small circular arc.

Consider the method applied to a free streamline problem for an arched contour, see figure 31, and transform the region in z plane occupied by the fluid into the upper semi-plane ζ, see figure 8.

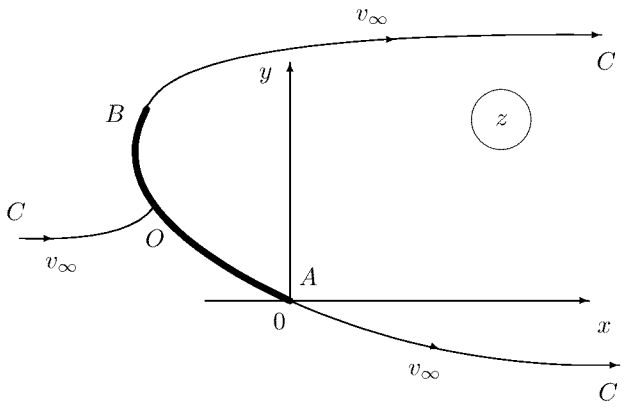


Figure 31: Flow pattern for the cavitating arc contour at zero cavitation number.

Then, again,

$$\frac{\mathrm{d}w}{\mathrm{d}\zeta} = N\zeta\,, \tag{49}$$

where N is a real parameter to be determined and the mixed boundary value problem for Levi-Civita func-

tion (15) arising in ζ-plane:

$$\tau = 0 \quad \text{as} \quad \xi \le -1 \quad \text{and} \quad \xi \ge b$$

$$\theta(\xi) = \begin{cases} -\alpha(\xi)\,, & \text{as} \quad -1 \le \xi \le 0\,; \\ \pi - \alpha(\xi)\,, & \text{as} \quad 0 \le \xi \le b\,. \end{cases}$$

where b is a coordinate (to be determined) of image of point B in ζ-plane and $\alpha(\xi)$ is the body angle at point $\zeta = \xi$, relationship $\alpha(s)$ being given, where s is an arc coordinate of the contour, $s = 0$ at point A and $s = S$ at point B.
The Keldysh–Sedov formula gives the solution to this problem in the $0 - 0$ class

$$\omega_{\rm LC}(\zeta) = -\frac{1}{\pi}\sqrt{(\zeta+1)(\zeta-b)} \times \left\{ -\int\limits_{-1}^{b} \frac{\alpha(t)}{\sqrt{(1+t)(b-t)}} \frac{{\rm d}t}{t-\zeta} + \int\limits_{0}^{b} \frac{\pi}{\sqrt{(1+t)(b-t)}} \frac{{\rm d}t}{t-\zeta} \right\}$$

which exists if and only if

$$-\frac{1}{\pi}\int\limits_{-1}^{b} \frac{\alpha(t){\rm d}t}{\sqrt{(1+t)(b-t)}} + \frac{\pi}{2} - \arcsin\frac{1-b}{1+b} = 0\,. \qquad (\star)$$

It is seen that

$$\alpha = \arctan\left(\frac{{\rm d}y/{\rm d}s}{{\rm d}x/{\rm d}s}\right)$$

This equation can be used in conjunction with the equality

$$\frac{{\rm d}z}{{\rm d}s} = \exp({\rm i}\,\alpha)$$

to give

$$s(\xi) = \int\limits_{0}^{z} \exp(-{\rm i}\,\alpha)\,{\rm d}z = \frac{N}{v_\infty}\int\limits_{-1}^{\xi} \exp\{-{\rm i}\alpha(t)\}\,\exp\{{\rm i}\,\omega_{\rm LC}(t)\}\,t\,{\rm d}t\,.$$

Substituting the solution for $\omega_{\rm LC}$ into this equation finally gives

$$s(\xi) = \frac{N}{v_\infty}\int\limits_{-1}^{\xi} G(t,b)\,{\rm d}t\,, \qquad (50)$$

where

$$G(t,b) = \frac{2\sqrt{b(1+t)(b-t)} + t(b-1) + 2b}{1+b} \times \exp\left\{ \frac{\sqrt{(1+t)(b-t)}}{\pi}{\rm v.p.}\int\limits_{-1}^{b} \frac{\alpha(t)}{\sqrt{(1+t)(b-t)}} \frac{dt}{t-\xi} \right\}$$

This integral equation along with relation ($\star$) and an obvious condition

$$s(b) = S$$

allows unknown parameters b, N and function $\alpha(\xi)$ to be determined.

5.3. Arbitrary 2D supercavitating hydrofoil: analytical solution

Both the Levi-Civita and integral equation methods are known to connect with significant difficulties while considering a flow past an obstacle with a boundary of large curvature κ. At the same time, hydrofoils have such a region in the vicinity of the leading edge. One can find some theoretical analysis of the nonlinear problems of an arbitrary supercavitating hydrofoil and numerical results as well in [9, 4].
That is why an approach proposed by Maklakov [16] for arbitrary cavitating hydrofoil, see figure 32, is of interest as an improvement of Levi-Civita method.

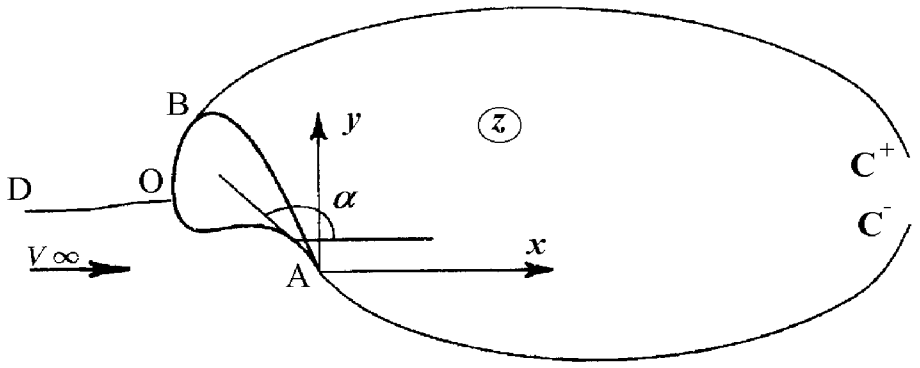


Figure 32: Flow region around a cavitating hydrofoil (Tulin–Terentev cavity closure scheme).

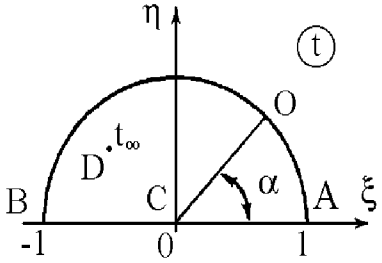


Figure 33: Auxiliary ζ-plane for cavitating hydrofoil.

Consider a cavitating hydrofoil which boundary is given by relation $\alpha = F(s)$, where s – arc coordinate ($s = 0$ at point A) and α is the tangential angle to the foil. Tulin–Terentev cavity closure scheme with a single spiral vortex model of cavity termination is adopted (subsection 3.1). Following to Maklakov, transform flow region z into the upper semi-circle $|t| \le 1$, Im ≥ 0 on auxiliary plane $t = \xi + \mathrm{i}\eta$, see figure 33. Stagnation point O corresponds to $t_0 = \exp(\mathrm{i}\delta_0)$, point C – to the origin of the coordinate system in t-plane and point at infinity D has the image at $t_\infty = r_\infty \exp(\mathrm{i}\delta_\infty)$.
Chaplygin method of singular points gives the derivative

$$\frac{\mathrm{d}w}{\mathrm{d}t} = kv_0 f(t) = \frac{kv_0}{r_\infty} \frac{t(t^2-1)(t^2-2t\cos\delta_0+1)}{(t-t_\infty)^2(t-\overline{t_\infty})^2(t-1/t_\infty)^2(t-1/\overline{t_\infty})^2}\,, \tag{51}$$

where k is a real parameter to be determined.
Levi-Civita function is

$$\omega_{\mathrm{LC}}(t) = \omega_0(t) + M\,\frac{t^2-1}{t} + \Omega(t)\,, \tag{52}$$

where M denotes a real constant, $\omega_0(t)$ is Levi-Civita function for a flat plate at zero cavitation number

$$\omega_0(t) = \alpha_0 - \pi + \mathrm{i}\,\log\frac{t-\exp(\mathrm{i}\,\delta_0)}{1-t\,\exp(\mathrm{i}\,\delta_0)}\,,$$

and $\Omega(t)$ is analytic and continuous function in upper semi-circle. That is why conformal mapping can be written as

$$z(t) = \int\limits_1^t \frac{\mathrm{d}z}{\mathrm{d}w}\,\frac{\mathrm{d}w}{\mathrm{d}t}\,\mathrm{d}t = \int\limits_1^t \exp\left\{\mathrm{i}\,\omega_0(t) + \mathrm{i}\,M\,\frac{t^2-1}{t} + \mathrm{i}\Omega(t)\right\} f(t)\,\mathrm{d}t\,.$$

Levi-Civita method requires the expansion

$$\Omega(t) = \sum_{k=1}^{\infty} A_k t^k\,,$$

where A_k are real coefficients to be found. Maklakov [16] proposed another representation of Ω. If

$$\Omega(\mathrm{e}^{\mathrm{i}\,\delta}) = \lambda(\delta) + \mathrm{i}\,\mu(\delta)$$

then Schwarz formula for a circle gives a relation between Ω and its real part λ given on the semi-circle boundary

$$\Omega(t) = \frac{1-t^2}{\pi} \int\limits_0^\pi \frac{\lambda(\delta)\,\mathrm{d}\delta}{1-2t\cos\delta+t^2}\,.$$

Imaginary part of $\Omega(t)$ is

$$\mu(\gamma) = \boldsymbol{C}\,\lambda = \frac{1}{2\pi} \int\limits_0^\pi \big(\lambda(\varepsilon)-\lambda(\gamma)\big)\,\left(\cot\frac{\varepsilon+\gamma}{2} - \cot\frac{\varepsilon-\gamma}{2}\right)\mathrm{d}\varepsilon\,.$$

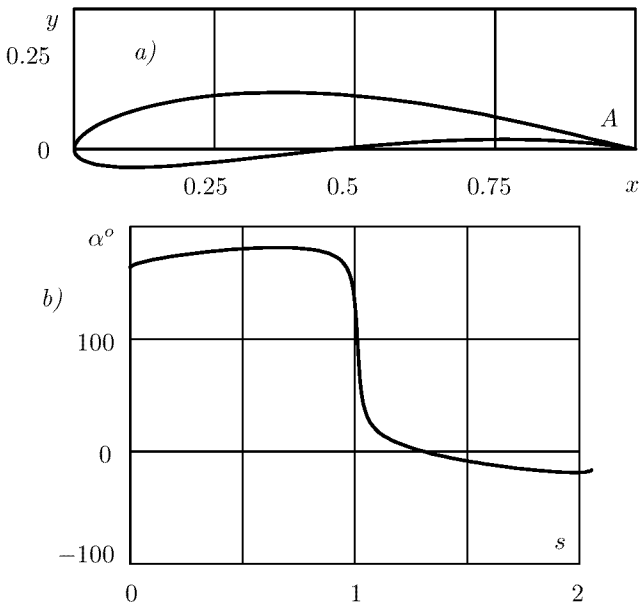


Figure 34: Zhukovsky hydrofoil (a) and relation $\alpha = F(s)$.

Using expression $\mathrm{d}s/\mathrm{d}\delta = |\mathrm{d}z/\mathrm{d}t|$ and conformal mapping $z(t)$ write down the relation between arc coordinate s and polar angle δ:

$$s(\delta) = k \int\limits_0^\delta g(\gamma)\,\exp\big(-\boldsymbol{C}\lambda - 2M\sin\gamma\big)\,\mathrm{d}\gamma\,,$$

where

$$g(\gamma) = 4\sin\gamma\,(1-\cos(\gamma+\delta_0)) \times \frac{1}{\big(1+r_\infty^2-2r_\infty\cos(\gamma-\delta_\infty)\big)^2} \times \frac{1}{\big(1+r_\infty^2-2r_\infty\cos(\gamma+\delta_\infty)\big)^2}\,.$$

It is easy to see that $\lambda = \alpha - \alpha_0$ and therefore, finally, one arrives at the following integral equation

$$\lambda(\delta) = -\alpha_0 + F\left(k \int\limits_0^\delta g(\gamma)\exp\big(-\boldsymbol{C}\lambda - 2M\sin\gamma\big)\mathrm{d}\gamma\right) \tag{53}$$

Five unknown parameters k, M, δ_0, r_∞, δ_∞ are derived from the conditions

$$\oint\limits_{t_\infty} \frac{\mathrm{d}z}{\mathrm{d}t}\,\mathrm{d}t = 0\,, \quad \frac{\mathrm{d}w}{\mathrm{d}z}(t_\infty) = v_\infty\,, \quad s(-1) = S\,,$$

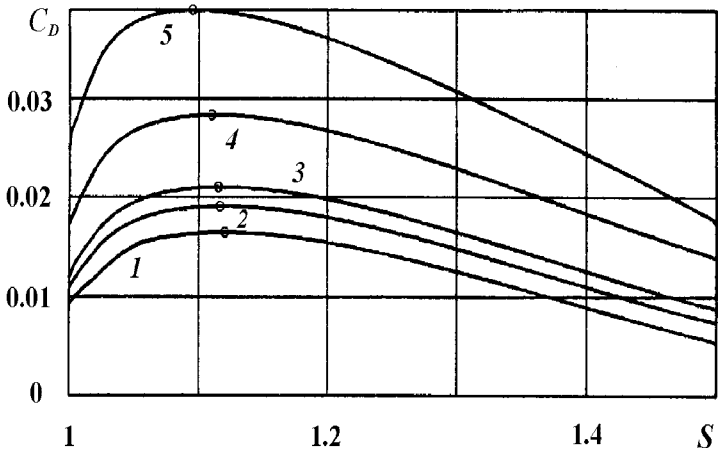


Figure 35: Drag coefficient C_D versus wetted length S.

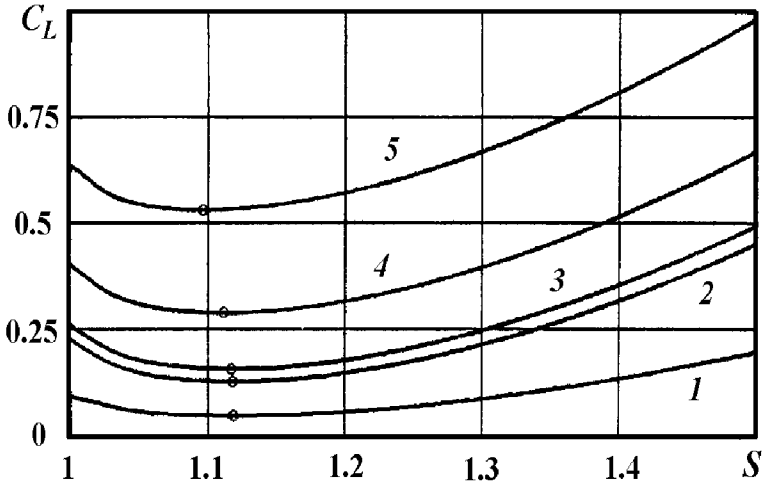


Figure 36: Lift coefficient C_L versus wetted length S.

where S denotes the whole (given) wetted length of the hydrofoil. The latter condition can be substituted by Brillouin condition at point B which specify the curvature of the cavity and hydrofoil be the same at detachment point B ($t = -1$). It was demonstrated [1] that this condition is equivalent to $\Omega'(-1) = 0$ which yields [16]

$$\pi \tan\frac{\delta_0}{2} + \int_0^\pi \lambda'(\gamma) \tan\frac{\gamma}{2} \mathrm{d}\gamma = 2\pi M\,.$$

Naturally, in this case the wetted length S is unknown because z-coordinates of point B are unknown as well. Some numerical results for a supercavitating Zhukovsky hydrofoil are shown in figures 34–36. Zhukovsky hydrofoil of unit chord length is chosen to have maximum thickness 11.82%, perimeter $P = 2.053$ and curvature radius at the leading edge $\rho = 0.016$, see figure 34, where the foil geometry and relation $\alpha = F(s)$ for the tangential angle to the foil versus arc coordinate s are shown. Figures 35 and 36 demonstrate drag and lift coefficient versus wetted length S (Brilllouin condition is not imposed) in the case of angle of attack $\alpha = 5^\circ$ for a set of cavitation number $\sigma = 0$, 0.1, 0.15, 0.3 and 0.5 (curves '1' corresponds to $\sigma = 0$). It was found that drag (lift) coefficient attains its maximum (minimum) value at points where Brilllouin condition was satisfied.

Conclusion

A brief review of the main theoretical approaches to problems of the theory of jets in an ideal fluid was conveyed, including hodograph (Kirchhoff and Zhukovsky) methods, Chaplygin method of singular points, mixed boundary value problem method, some modifications of Levi-Civita approach and method of integral equations. Every analytical solution is illustrated by numerical results, including flow patterns.

References

[1] Birkhoff G. & Zarantonello E.H. 1957 Jets, wakes and cavities. Academic Press, New York.

[2] Brillouin M. Les surfaces de glissement de Helmholtz et la resistance des fluides. Annual chemie et phys., vol. 23.

[3] Brodetsky S. 1923 Discounituous fluid motion past circular and elliptic cylinders. Proc. Royal Soc. London, S.A., vol. CII, No. A718.

[4] Furuya O. 1975 Nonlinear calculation of arbitrary shaped supercavitating hydrofoils near a free surface. *J. Fluid Mech.*, **68**, 21–40.

[5] Gilbarg D. 1960 Jets and Cavities. Handbuch der Physik, vol. 9, Springer–Verlag, 311 p.

[6] Gurevich M.I. 1965 Theory of jets in an Ideal fluid, Academic Press, New York.

[7] Gurevich M.I. 1979 Theory of jets in an Ideal fluid, Nauka Publishing, Moscow, 2-nd edition, (in Russian).

[8] Helmholtz H. 1868 Ueber discontinuirliche Flüssigkeitsbewegungen. Monastber, Köngl. Akad. Wissenscheften, 215, Berlin.

[9] Ivanov A.N. 1979 Hydrodynamics of Supercavitating Flows. Sudostroenie Publ., Leningrad, USSR (in Russian).

[10] Keldysh M.V. & Sedov L.I. 1937 An effective solution to some boundary problems for harmonic functions. Dokladi Akademii Nauk SSSR, vol. XVI, No. 1.

[11] King A.C. & Bloor M.I.G. 1990 Free streamline flow over curved topography. Quarterly of Applied Mathematics, vol. XLVII, pp. 281–293.

[12] Kirchhoff G. 1869 Zur Theorie freier Flüssigkeitsstrahlen. Borchardt's Journal, Bd. 70, 289.

[13] Könhauser P. 1984 Berechnung zweidimensionaler Totwasserströmungen um vorgegeben Konturen. Dissertation Institut A für Mechanik der Universität Stuttgart.

[14] Larock B.E. & Street R.L. 1967 Cambered bodies in cavitating flow – a nonlinear analysis and design procedure. J. Ship Research, **12** (1), pp. 131–139.

[15] Levi-Civita T. 1907 Scie e leggi de resistenza. Rend. Circolo Math. Palermo, vol. XXIII.

[16] Maklakov D.V. 1997 Nonlinear problems of potential flows with unknown boundaries. Yanus-K Publishing, Moscow (in Russian).

[17] Muskhelishvili N.I. 1946 Singular integral equations. P. Noordhoff Ltd. Publ., Gröningen, Holland.

[18] N.A. Nekrasov 1922 Sur la mouvement discontinu a deux dimensions de fluid autour d'un obstacle en form d'arc de cercle. Publ. Plytechnical Institute of Ivanovo–Voznesensk (in Russian).

[19] Riabouchinsky D. 1920 On steady fluid motion with free surfaces. Proceedings of London Mathematical Society, vol. 19, ser. 2.

[20] Terentev A.G. 1976 On nonlinear theory of cavitating flows. Izvestia AN SSSR, Mekhanika zhidkosti i gaza, vol. 1, pp. 158–161.

[21] Terentev A.G. 1981 Mathematical problems of cavitation. Chuvash University Publishing, Cheboksary (in Russian).

[22] Terentev A.G. & Lazarev V.A. 1969 Cavitating plate in a confined flow. In book 'Fiziko–tekhnicheskie problemy', Chuvash University Publishing, Cheboksary (in Russian).

[23] Tulin M.P. 1964 Supercavitating flows – small perturbation theory. J. Ship Res., **7** (3), 16–37.

[24] Villat H. 1911 Sur la re'sistance des fluides. Ann. Sci. Ecole Normal Superior, vol. 28 (3).

[25] Whittaker E.T. & Watson G.N. 1940 A course of modern analysis. 4-th edition, Cambridge University Press.

[26] Zhukovsky N.E. 1890 An improvement of Kirchhoff method for determining the fluid motion in two dimensions for a constant speed given on unknown streamline. Matematichesky sbornik, vol. XV (in Russian).

This page has been deliberately left blank

Page intentionnellement blanche

Artificial Supercavitation. Physics and Calculation

Vladimir N. Semenenko
National Academy of Sciences - Institute of Hydromechanics
8/4 Zhelyabov str., Kyiv, 03057
Ukraine

Summary

This lecture is devoted to the basic physical properties and the calculation methods of the artificial cavitation (ventilation) flows. Main attention is paid to the three-dimensional ventilated supercavities past the disk and blunted cavitators.

Derivation of approximate equations of the axially symmetric supercavities with using the theorem of momentum and also the asymptotic theory of slender body is presented.

The G.V.Logvinovich independence principle of the cavity expansion is stated and grounded. It gives a simple and general method of investigating the unsteady problems.

Calculation of the ventilated cavities has some peculiarities caused by gravity effect, presence of the cavitator angle of attack and taking account of balance between the gas-supply into the cavity and the gas-leakage from the cavity. They are discussed here as well.

Introduction

The basic similarity parameter of cavitation flows is the cavitation number [1–4]:

$$\sigma = \frac{2(p_\infty - p_c)}{\rho V_\infty^2}, \tag{1}$$

where p_∞ is the pressure at infinity; p_c is the cavity pressure; ρ is the water density; V_∞ is the mainstream velocity. When a body moves horizontally on the immersion depth H, we have $p_\infty = \rho g H$, where g is the gravity acceleration. The supercavitation flow regime corresponds to small magnitudes $\sigma < 0.1$. When the magnitude of σ decreases, the supercavity dimensions increase.

When ρ = const, there are three possibilities of the σ reduction:

1) **Increasing the mainstream velocity** V_∞. With decreasing the mainstream velocity the rarefaction past bodies increases, and cavities are created by natural way when the pressure decreases to a value close to the saturated water vapor pressure p_v = 2350 Pascal (at the temperature 20°C). Such supercavities are called the natural or vapor supercavities. The parameter

$$\sigma_v = \frac{2(p_\infty - p_v)}{\rho V_\infty^2} \tag{2}$$

is called the natural or vapor cavitation number. The natural supercavities are filled by water vapor under pressure $p_c = p_v$. The natural cavitation regime, when $\sigma_v < 0.1$, is attained when the mainstream velocity is very high: $V_\infty > 50$ m/sec.

Paper presented at the RTO AVT Lecture Series on "Supercavitating Flows", held at the von Kármán Institute (VKI) in Brussels, Belgium, 12-16 February 2001, and published in RTO EN-010.

2) **Decreasing the difference** $\Delta p = p_\infty - p_c$ owing to decreasing the ambient pressure p_∞, for example, in closed cavitation hydro-tunnels [4, 5]. The super-cavitation flows in the stream with artificially reduced pressure are sometimes called the artificial ones, although they do not distinguish on natural vapor supercavities by their physical properties.

3) **Decreasing the difference** $\Delta p = p_\infty - p_c$ owing to increasing the cavity pressure p_c. This is easy attained by blowing the air or another gas into the rarefaction zone past a non-streamlined body. Such supercavitation regime is called the artificial cavitation or ventilation. The method of obtaining the ventilated cavities was proposed independently by L.A.Epshtein and H.Reichardt in 1944 – 1945.

The ventilated cavitation regime $\sigma < 0.1$ is easy obtained at the significantly lower mainstream velocities $V_\infty \sim 10$ m/sec. That is why, it is widely applied in bench investigations of the supercavitation flows. The Fig. 1 presents a typical scheme of an experimental apparatus to investigate the ventilated cavities.

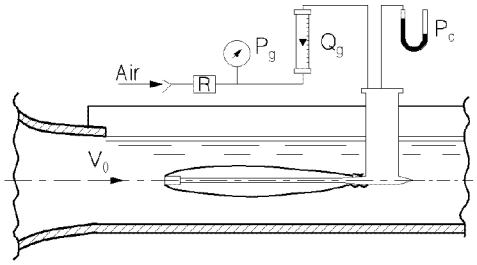


Fig. 1. Scheme of apparatus to create a ventilated supercavity

1 Main problems of artificial cavitation

It follows from the similarity theory of hydrodynamic flows [3] that the shape and dimensions of both the natural vapor supercavity and the artificial ventilated cavity must be the same when the cavity number is equal. However, in reality the full similarity does not fulfil due to a number of causes.

The main peculiarity of the artificial cavitation flows is a consequence of comparatively small values of the velocity $V = 10 \div 100$ m/sec. In this case the Froude number

$$Fr = \frac{V_\infty}{\sqrt{gD_n}} \tag{3}$$

where D_n is the cavitator diameter, has moderate magnitude.

This means that the gravity effect is considerably more for the artificial cavity when the cavitation number is the same. It causes to the more essential deformation of the artificial cavity shape. The floating-up the ventilated cavity tail may be essential so that it completely determines the cavity closure character and type of the gas leakage from the cavity.

Thus, the Froude number (3) together with the cavitation number (1) is the basic similarity parameter for the artificial supercavitation flows.

1.1 METHODS OF CREATION OF THE VENTILATED SUPER-CAVITIES

We know the following methods of creating the artificial ventilated cavities (Fig. 2):

1) **Method of a gas source** [6] consists in creating a gas envelope around a body by the air jet ejection from the body nose opposite to the stream (Fig. 2, a). It is obvious that in this case the gas pressure must exceed the pressure of the water in the nose stagnation point. From the Bernoulli equation [7], we obtain estimation of the necessary velocity of the air V_g:

$$V_g > V_\infty \sqrt{\frac{\rho}{\rho_g}(1+\sigma)} \approx 28.6\left(1+\frac{\sigma}{2}\right)V_\infty, \tag{4}$$

where ρ_g is the air density. One can see that the gas jet velocity and, hence, the gas rate must be very high.

Owing to the high velocity of the gas flow in the cavity, the cavity walls are strongly perturbed (the cavity is nontransparent). The flow represents a strongly turbulized two-phase zone at the tail cavity part and in the wake.

This way of the artifitial supercavity creation is not applied in practice due to its lacks.

2) **L.I.Sedov scheme** [7] consists in ejecting the slender water jet from the body nose opposite to the stream with simultaneous air-supply into the stagnation zone (so called "jet cavitator", Fig. 2, b). This flow scheme represents the inverted cavitation flow by Efros-Gilbarg with the reentrant jet [7]. The nose stagnation point is displaced into the stream, and in the ideal case of complete recovery of the pressure in the tail part, the body must suffer thrust

$$T = \rho S_j V_j V_\infty, \tag{5}$$

where S_j is the jet section area; V_j is the average velocity in the jet.

In real flows, it is impossible to attain smooth closure of the cavity on the body tail and complete recovery of the pressure. Therefore, the arising thrust will be smaller. Nevertheless, this scheme is very perspective. When $\sigma \to 0$, we obtain the infinite Kirchhoff's cavity. In this case the body with the jet cavitator suffers half drag in comparison with the body with the solid cavitator.

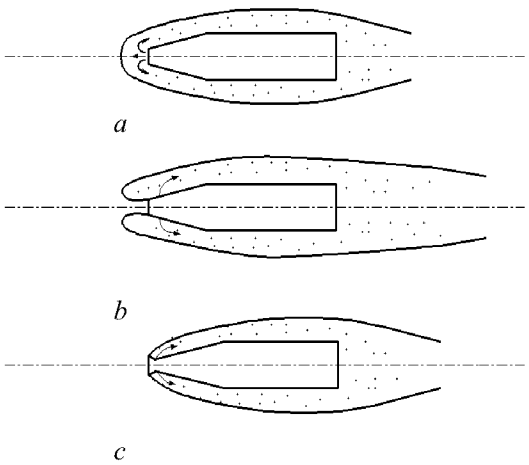


Fig. 2. Ways of creation of ventilated cavities: a – gas source; b – L.I.Sedov's scheme; c – blowing past a sharp edge

3) **Gas-supply past a sharp edge**. The most stable and smooth surface of the cavity is observed, if the cavity separation occurs on the sharp cavitator edge with simultaneous gas-supply to the separation place (Fig. 2, c). It is possible to supply gas in any point of the body after the fully development of the supercavity (so called "distributed gas-supply"). Experiments showed that location of the place of the gas-supply into the steady cavity has no essential significance.

The way of creation of ventilated cavities past cavitators with the sharp edge (for example a disk) is the most frequently used.

1.2 COEFFICIENT OF GAS-SUPPLY RATE INTO THE CAVITY

The main problem for the ventilated cavitation flows is a problem on the gas quantity necessary for supply into the cavity to maintain the supercavity of given dimension (i.e. to attain the given σ). In the case of axisymmetric cavitator, the dimensionless coefficient of the rate is introduced [2, 3]:

$$\overline{Q} = \frac{\dot{Q}}{V_\infty D_n^2}, \tag{6}$$

where $\dot{Q}$ is the volumetric gas rate at the pressure p_c, its dimensionality is m^3 / sec.

Obviously, the gas-supply rate $\dot{Q}_{in}$ must be equal to the gas-leakage rate $\dot{Q}_{out}$ when motion is steady. For unsteady ventilated cavities, the gas leakage from the cavity is the unknown time function depending on the variable pressure in the cavity $p_c(t)$ and on the gas-leakage type. Determination of the function $\dot{Q}_{out}(t)$ for concrete conditions represents a basic problem of the artificial cavitation theory.

A unified theory of the gas leakage from the ventilated cavity, that allows to calculate the function $\overline{Q}(\sigma)$ for any values of the flow parameters, does not exist. The mechanism of the gas-leakage may be considerably distinguished in dependence on the parameters Fr, σ, σ_v. The gas-leakage rate is also different in the cases of free cavity closure and the cavity closure on a body. Approximate estimations were obtained for some types of the gas-leakage.

1.3 HYDRODYNAMIC SCHEMES OF GAS LEAKAGE FROM THE CAVITY

Observations show that two principally different mechanisms of the gas leakage from the stable artificial cavities exist when the cavity closure is free [2, 3].

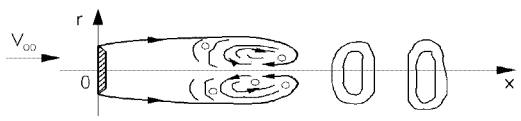


Fig. 3. Scheme of the portion gas-leakage

When magnitudes of the numbers Fr and σ are high, i.e. the gravity effect is not considerable and the cavity shape is close to the axisymmetric one, the cavity tail is filled by a foam which is periodically rejected by portions in the form of toroidal vortices (so called the portion leakage or the first type of gas leakage from the cavity, Fig. 3).

When Fr is fixed and σ is small, i.e. the gravity influence is considerable, the flow in the cavity end becomes well-ordered. The cavity ends by two hollow vortex tubes carrying over the gas from the cavity (so called leakage by vortex tubes or the second type of the gas leakage from the cavity, Fig. 4).

Besides the first and second types of the gas leakage from stable cavities, the third type of the gas leakage exists owing to pulsation of the unsteady ventilated cavities [8, 9].

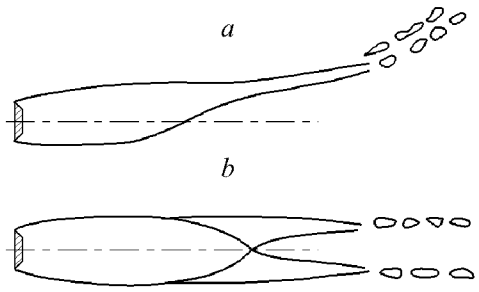


Fig. 4. Scheme of the gas-leakage by vortex tubes: *a* – view from side, *b* – view from above

1.3.1 THE FIRST TYPE (PORTION GAS-LEAKAGE)

The first type of the gas leakage from the artificial cavities is not well studied. This is explained by that in this case the processes at the cavity end are considerably non-stationary and multi-parametric ones. It was shown [3, 10] that they are determined by not only the similarity parameters σ, Fr but depend on both the Reynolds number Re and the Weber number We:

$$Re = \frac{D_n V_\infty}{\nu}, \quad We = \frac{\alpha}{2\rho V_\infty^2 D_n}, \tag{7}$$

where ν is the kinematic coefficient of viscosity; α is the coefficient of water surface tension. They also depend on degree of the free stream turbulence and other external perturbations:

$$\overline{Q} = F(\sigma, \sigma_\upsilon, Fr, \mathrm{Re}, We, \ldots). \tag{8}$$

It was shown experimentally that decrease of numbers Re and We, i.e. increase of viscosity and surface tension of liquid, causes to decrease of the gas leakage rate from the cavity. Some data and hypothesises about the first type of the gas leakage are presented in the papers by L.A. Epshtein [10, 11].

Qualitatively, in this case processes may be described in the following way. Fluid particles flowing around the axisymmetric cavitator in the radial planes collide in the cavity closure zone and create a non-stationary unstable reentrant jet. When the reentrant jet is distorted, the two-phase medium (foam) is formed. It partially fills the cavity and moves within the cavity in the form of a toroidal vortex. The outer part of this vortex moves along the flow direction under action of viscous shears on the cavity boundary. Its central part moves opposite to the stream under action of the pressure gradient. The vortex continuously grows owing to new foam portions. The foam rejection occurs in the form of a ring toroidal vortex or its part, or separate foam portions (see Fig. 3), when the friction forces become equal to the reentrant motion momentum. Also, the continuous foam leakage from the zone past the rear stagnation point exists simultaneously with the portion leakage.

In the work [10] was shown using the methods of the similarity theory that the expression for a dimensionless period of the foam portions rejection should be in the form:

$$\overline{T} = \frac{V_\infty T}{D_n} = \frac{c_x}{\varsigma}\left(\frac{B_1}{\sqrt{\sigma}} + B_2\right), \tag{9}$$

where c_x is the cavitation drag coefficient, ς is the friction coefficient, B_1, B_2 are the function of Re, We.

It follows from the experimental data [12] that an evaluation of Strouhal number Sh for this process is :

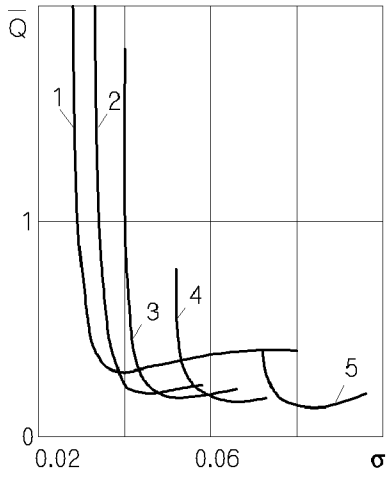
$$Sh = \frac{f L_m}{V_\infty} \approx 0.315,$$

where L_m is the average cavity length. The real process frequency f has values $10 \div 100$ Hz for various tests. It is possible to observe the portion gas-leakage with a stroboscope or using photography with the short exposure time 10^{-4} - 10^{-5} sec.

In the case of the flow close to the natural vapor cavitation when the gravity effect is insignificant, G.V.Logvinovich established the semi-empirical law of the gas-leakage [2]:

$$\dot{Q} = \gamma V_\infty S_c \left(\frac{\sigma_v}{\sigma} - 1 \right), \tag{10}$$

where $\gamma = 0.01 \div 0.02$ is the empirical constant, S_c is the area of the cavity mid-section.



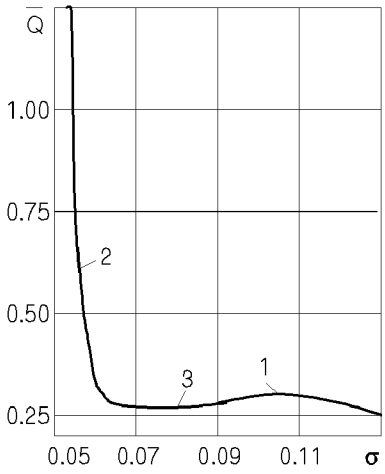


Fig. 5. Influence of the Froude number on $\overline{Q}(\sigma)$: 1 - Fr = 19.3; 2 - 16.5; 3 - 14.6; 4 - 12.7; 5 - 11.0

Fig. 6. Experimental dependence $\overline{Q}(\sigma)$ Fr = 13.3

The portion type of the gas-leakage with the periodically arising and distorting reentrant jet is characteristic also in the case of supercavitation flow around hydrofoils with great aspect ratio [6].

1.3.2 THE SECOND TYPE (GAS-LEAKAGE BY VORTEX TUBES)

When the second type of the gas leakage from the artificial cavity, the process is stationary and completely determined by the gravity effect on the cavity. The second leakage type is the most studied both theoretically and experimentally. As is shown in [3, 4], in this case the viscosity and capillarity forces are not considerable. Therefore, from point of view of the similarity theory the dimensionless coefficient of the gas-supply rate into the cavity $\overline{Q}$ must be determined by the dependence:

$$\overline{Q} = F(\sigma, Fr). \tag{11}$$

The calculation method of $\overline{Q}$ for the second type of the gas-leakage was proposed for the first time by R.N.Cox and W.A.Clayden [13].

Now the semi-empirical formula by L.A.Epshtein [3] is supposed the most reliable:

$$\overline{Q} = \frac{0.42 c_{x0}^2}{\sigma\left(\sigma^3 Fr^4 - 2.5 c_{x0}\right)}. \tag{12}$$

Here, c_{x0} is the coefficient of the cavitator drag when σ = 0:

$$c_{x0} = \frac{2F_{x0}}{\rho V_\infty^2 S_n}, \tag{13}$$

where F_x is the cavitation drag; $S_n = \pi D_n^2 / 4$ is the cavitator area. For the disk cavitator $c_{x0} = 0.82$. Also, the more exact semi-empirical formulae were obtained taking into account the cavitator immersion depth H

and density of the gas supplied into the cavity ρ_g, for example [6]:

$$\overline{Q} = \frac{0.271\sqrt{\frac{\rho}{\rho_g}}\, c_{x0}^{2.75}\sqrt{2 - \frac{\sigma Fr^2}{\overline{H}}}}{\left(Fr - 1.35\right)\sigma^{1.75} Fr^2\left(\sigma^3 Fr^4 - 2.38 c_{x0}\right)^{1.25}}, \tag{14}$$

where $\overline{H} = H / D_n$. Computations by the formula (14) give satisfactory coincidence with experimental data when $Fr = 4.8 \div 20$.

The experimental dependencies $\overline{Q}(\sigma, Fr)$ showing the influence of Froude number on the gas leakage by vortex tubes are presented in Fig.5 [3].

The gas-leakage type by vortex tubes is characteristic also for the case of supercavitation flow around hydrofoils with small aspect ratio.

A criterion of transition from the first type of the gas leakage to second type is given by the empirical Campbell-Hilborne's criterion [14]:

$$\sigma Fr \approx 1; \quad Fr = 5 \div 25 . \tag{15}$$

Values of $\sigma Fr > 1$ correspond to the first (portion) type of the gas-leakage, values $\sigma Fr < 1$ correspond to the second type of the leakage (by vortex tubes). As the experiments show, both the mechanisms of the gas leakage from the cavity can act at range of intermediate values of $\sigma Fr \approx 1$. Such transient regimes of the gas leakage are very unstable.

A typical experimental dependence of the gas rate coefficient $\overline{Q}$ on the cavitation number σ obtained at testing a series of cones with angles from 30° to 180° (disk) is shown in Fig. 6 [3]. In this case the value of the Froude number was Fr = 13.3. In the expressions for Fr and $\overline{Q}$, so called "universal linear dimension" $D_1 = D_n\sqrt{c_{x0}}$ was used instead D_n to analyze the experimental data. As a result, the relation (11) does not depend on c_{x0}, and all the experimental points for various cones lie on the only curve.

The right part of the graph 1 corresponds to the first portion type of the gas leakage, the left part of the graph 2 corresponds to the second type of the leakage by vortex tubes, the middle part of the graph 3 corresponds to the transient regime. The value σ = 0.081 corresponds to a boundary between the types (15) in this graph.

1.3.3 THE THIRD TYPE (GAS-LEAKAGE FROM PULSATING SUPERCAVITIES)

Denominator in the formula (13) must not be equal to zero. It follows from here that it is impossible to obtain the cavitation number lower than some minimal value at any increase of the gas-supply rate into the cavity:

$$\sigma_{\min} \approx 1.34 \sqrt[3]{\frac{c_{x0}}{Fr^4}} . \tag{16}$$

In practice, when the gas rates are very great, the cavity stability is lost and cardinal change of the mechanism of the gas leakage from the cavity occurs [8, 9].

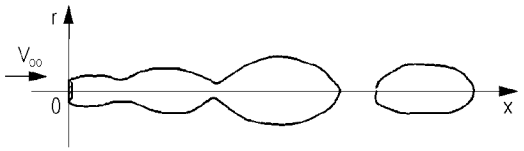


Fig. 7. Scheme of the gas-leakage from the pulsating cavity

Theory of linear stability of the gas-filled axially symmetric cavities was developed by E.V.Paryshev [15]. Analysis showed that the dynamic properties of gas-filled supercavities are mainly determined by the dimensionless parameter

$$\beta = \frac{\sigma_v}{\sigma} . \tag{17}$$

The cavity has a series of fundamental reduced frequencies

$$k = \frac{\omega L_c}{V_\infty} = 2\pi n \qquad n = 1,2,\ldots, \tag{18}$$

where ω is the circular oscillation frequency; L_c is the cavity length. The following value of the parameter β corresponds to each fundamental frequency

$$\beta_n = 1 + \frac{(\pi n)^2}{6} . \tag{19}$$

Supercavities are stable when $1 \le \beta < \beta_1 = 2.645$ and unstable when $\beta > 2.645$.

Thus, the similarity parameter $\beta \ge 1$, that is equal to ratio of vapor cavition number at given velocity and its real value, is the basic similarity parameter for cavitation flows together with the cavitation number (1) and the Froude number (3). The value $\beta = 1$ corresponds to the natural vapor supercavitation. When the parameter β increases, significance of elasticity of the gas filling the artificial cavity increases as well.

The separated self-induced oscillations of the cavity are established as a result of the stability loss when the supply is permanent. In this case the gas-supply occurs owing to periodic separation of great portions of the cavity (air pockets) (see Fig. 7).

The instability phenomenon and arising the self-induced oscillations take place both for 3-D (in particular, axially symmetric) and for 2-D ventilated cavities. In the work [16], a simple "kinematic" theory of gas-leakage from pulsating cavities was proposed. It gives satisfactory correspondence to the experiment.

1.3.4 GAS-LEAKAGE WHEN THE CAVITY CLOSES ON A BODY

The mechanism of gas leakage from the cavity when the cavity closes on a body is very complicate and depends on number of factors such as:

a) **cavity perturbations**: its floating-up, wave deformations, natural distortion of the free boundary;

b) **body parameters**: shape in the closure place, surface roughness, vibrations;

c) **closure conditions**: angle of free boundary inflow, presence of the liquid and gas jets, radial velocity at the closure place.

According to the known theoretical schemes of the supercavity closure [17] the cavity may close on a solid body in the following ways (see Fig. 8):

a) **Riabouchinsky scheme**. The cavity smoothly closes on a solid surface–closurer located in the cavity end. In the closure place, the body diameter is $D_b < D_c$.

b) **Joukowski–Roshko scheme**. The cavity closes on a cylinder with diameter equal to the diameter of the biggest cavity section D_c.

c) **Gilbarg–Efros scheme**. The cavity closes on a cylinder with diameter $D_b < D_c$ with forming the ring reentrant jet.

The experience of work with the artificial cavity shows that the gas leakage may be compared with the rate of fluid supplied into the cavity with the reentrant jet. Physically, this may be explained that the fluid inflowing into the cavity aerates, mixes with the gas and rejects from the cavity as a mixture of gas and water.

Using the momentum conservation equation, the cross section area of the reentrant jet when the cavity closure is free is equal [7]:

$$S_j = \frac{c_x}{4}\frac{\pi D_n^2}{4}. \tag{20}$$

In the case of the cavity closure on the body, the section area of the ring reentrant jet remains the same. It was established experimentally that when the cavity closes on a circular cylinder with diameter D_b, the gas leakage is proportional to a ratio of section areas of the middle cavity part $\pi D_c^2/4$ and one of the cylinder $\pi D_b^2/4$:

$$\dot{Q} = k_2 V_\infty S_j \left(1 - \frac{D_b^2}{D_c^2}\right), \quad D_b \le D_c, \tag{21}$$

where k_2 is some empirical coefficient. When $D_b = 0$, we have free closure of the cavity by the first type of the gas-leakage. When $D_b = D_c$, we obtain the cavity closure by the Joukowski–Roshko scheme with the zero gas leakage (see Fig. 8, b).

Theoretically, we can also obtain the zero gas leakage when the cavity closes on the body by the Riabouchinsky scheme (see Fig. 8, a) when $D_b < D_c$, if the cavity and body curvatures are coordinated at the closure point $\alpha = \alpha_b$ (Fig. 9).

Practically, it is impossible to obtain the zero gas leakage at high magnitudes of *We* and *Re* numbers. However, it may be reduced to the minimal value caused by presence of unremovable small-scale perturbations. Blowing or suction of fluid is applied at the closure place to realize the stable cavity closure [18]. For example, the works [18, 19] propose a scheme of stable closure of the cavity on the liquid jet outflowing from the slot in the closurer of the elliptic shape.

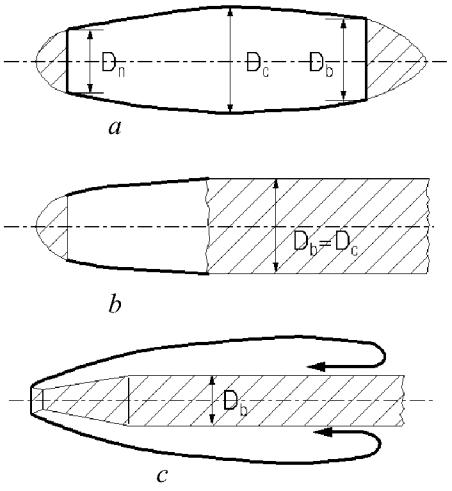


Fig. 8. Schemes of the supercavity closure on a body: *a* – Riabouchinsky; *b* – Joukowski-Roshko; *c* – Efros-Gilbarg

We have discovered experimentally the interesting phenomenon of hysteresis at the control of the ventilated cavity closing on the body by regulating the gas-supply. This effect increases with increasing the body surface curvature.

The control of ventilated cavity is possible, if single-valued dependence of the cavity length on the gas supply rate exists: $L_c = L_c(\dot{Q})$. If we consider neighborhood of the point of the cavity closure on rectilinear generatrix of the body $y = y_b$ (Fig. 10), we can note that the closure angle α will be increased with increasing the cavity dimensions:

$$\alpha(L_1) < \alpha(L_2) < \alpha(L_3), \qquad L_1 < L_2 < L_3$$

due to increasing both the ratio D_c / y_b and the relative cavity dimensions. In this case the velocity on the cavity boundary changes insignificantly due to the cavitation number varies weakly. Thus, the gas-leakage value $\dot{Q}$ depends mainly on the local angle of the cavity closure on the body:

$$\dot{Q} \approx \dot{Q}(\alpha).$$

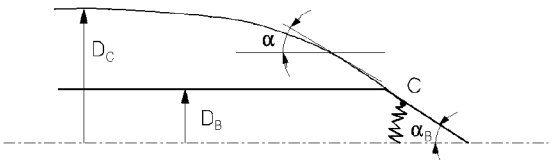


Fig. 9. Scheme of the fluent cavity closure on a body

Dependence of the gas-leakage on the cavity length $\dot{Q}_1(L_c)$ is schematically shown by dotted line in Fig. 10 when the cavity closes on the rectilinear generatrix of the body $y = y_b$.

Qualitatively, appearance of hysteresis behaviour may be explained by locating an additional triangle-shaped body on the rectilinear generatrix (it is dashed in Fig. 10). The cavity length increases with increasing the gas-supply from the value $\dot{Q}_1$. When the cavity closes on the frontal surface of the triangle

$x_1 \div x_2$, the cavity forms bigger angles of closure than at closure on the rectilinear generatrix. For example, $\alpha(x_2)$ is bigger than ones when the cavity closes between the points x_1 and x_4. We have $\alpha(x_2) = \alpha(x_4)$ only in the point x_4. Therefore, the gas rate $\dot{Q}_2$ for maintenance of the cavity closing in the point x_2 will exceed rates when the cavity closes in the points $x_2 \div x_4$ and equal to the rate for maintenance of the cavity closing in the point x_4. As a result, the cavity length will very rapidly increase from $L_c = L_2$ to $L_c = L_4$.

With decreasing the supply from the value $\dot{Q}_2$, when the cavity closure point is on the back side of the triangle $x_2 \div x_3$, the closure angle will be smaller than one when the cavity closes on the rectilinear generatrix. When the cavity closes in the point x_2, the rate $\dot{Q}_1$ will be smaller than one when it closes between the points x_1 and x_2. As a result, the cavity length will decrease very rapidly from the value $L_c = L_2$ to the value $L_c < L_1$.

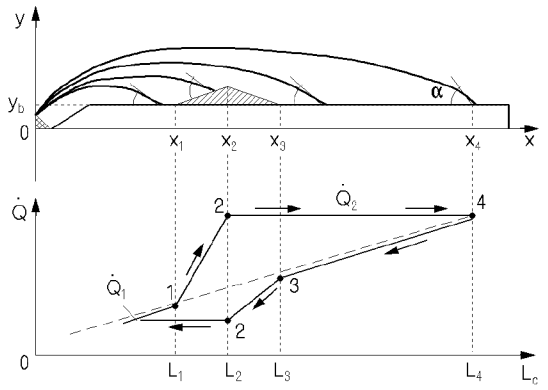


Fig. 10. Scheme of a hysteresis when the cavity closes on a body

Thus, a hysteresis loop appears in the graph $\dot{Q}(L_c)$ that is formed when the gas supply into the cavity increases or decreases.

The hysteresis property of the function of the gas supply into the ventilated cavity may by practically used to stabilize the cavity closure on the body by respective designing the body shape.

2 Approximate calculation of the steady axisymmetric supercavity

As it is known, main properties of supercavitation flows are well described by the potential theory of ideal incompresssible fluid. The respective mathematical problems are related to the class of mixed boundary value problems for harmonic functions. The flow area is bounded by the solid and free boundaries. The velocity distribution is given on the solid boundaries (cavitator or hydrofoil), the constant pressure p_c is given on the unknown free boundaries. For stationary problems, the velocity constancy along the free boundaries follows from the pressure constancy:

$$V_c = V_\infty \sqrt{1+\sigma} = const\,. \tag{22}$$

In this case the free boundaries are lines of flow.

Potential models of developed cavitation flows do not describe a real flow in the cavity closure zone where capillarity and viscosity are considerable. According to the known Brilluene paradox, existence of a closed cavity in the imponderable flow is impossible [1]. This resulted in creation of a number of schemes of "mathematical" closure of the supercavity: by Riabouchinsky, Joukowski-Roshko, Efros-Gilbarg et al [17].

2.1 FORMULATION OF PROBLEM

We consider steady axially symmetric flow around a supercavitating disk in unbounded imponderable fluid with the velocity at infinity V_∞. We introduce the cylindrical coordinate system Oxr connected with the cavitator (Fig. 11). Let $r = R(x)$ is the equation of the cavity generatrix.

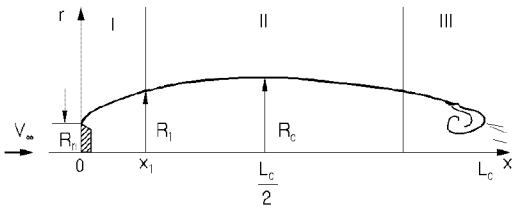


Fig. 11. Scheme of an axisymmetrical supercavity

The Laplace equation for the perturbed velocity potential $\varphi(x,r)$ is valid for all the flow area:

$$\frac{\partial^2\varphi}{\partial x^2}+\frac{\partial\varphi}{\partial r^2}+\frac{1}{r}\frac{\partial\varphi}{\partial r}=0. \tag{23}$$

On the cavity surface, the potential φ must satisfy both the boundary condition of zero normal velocity (the kinematic boundary condition)

$$\frac{\partial\varphi}{\partial r}=\left(V_\infty+\frac{\partial\varphi}{\partial x}\right)\frac{dR}{dx}, \qquad r=R(x) \tag{24}$$

and the cavity pressure to be constant $p = p_c$ (the dynamic boundary condition). Applying the Bernoulli equation on the liquid contour, we can write the dynamic boundary condition in the form:

$$\left(\frac{\partial\varphi}{\partial r}\right)^2+\left(\frac{\partial\varphi}{\partial x}\right)^2+2V_\infty\frac{\partial\varphi}{\partial x}=\frac{2\Delta p}{\rho}, \quad r=R(x), \tag{25}$$

where $\Delta p = p_\infty - p_c$. The third condition is the condition of the perturbations to be vanished at infinity

$$\varphi\to 0, \qquad x^2+r^2\to\infty \tag{26}$$

Owing to great mathematical difficulties an exact solution of the boundary value problem (23)-(26) has been not obtained. In contrast to two-dimensional problems on supercavitation flows, it is impossible to apply the power mathematical theory of analytical functions and conformal mapping in this case. Some progress of applying the theory of generalized analytical functions to axisymmetric problems was outlined last years [20].

All known results of the theory of axisymmetric cavities have been obtained by numerical methods or by approximate asymptotic and semi-empirical methods and perturbation method as well.

P.Garabedian's works [21] are very important and imperishable for the theory of axisymmetric super-cavitation flows. He sought a solution of the axisymmetric problem for stream-function $\psi(x,r)$ and consider it as the plane flow perturbation. As a result, he obtained the asymptotic solution for main dimensions of the supercavity past a disk when $\sigma \to 0$:

$$D_c = D_n\sqrt{\frac{c_x}{\sigma}}, \quad L_c = D_n\frac{A\sqrt{c_x}}{\sigma}, \quad A = \sqrt{\ln\frac{1}{\sigma}}, \quad c_x(\sigma) = c_x(0)(1+\sigma), \quad c_x(0) = 0.827, \tag{27}$$

where D_n is the disk diameter; D_c is the biggest cavity section diameter; L_c is the cavity length.

A comparison of the asymptotic formulae (27) with both the experimental data and the "exact" numerical calculations showed their high precision and physical accuracy.

2.2 APPROXIMATION RELATIONS

A combined approach using reliable physical representations, general conservation laws (such as the momentum and energy theorems) and generalized experimental data proved to be the historically first and most productive in practical calculations. G.V. Logvi-novich was a founder of this direction of the super-cavitation flow investigation.

We present firstly some useful relations for the axisymmetric supercavities obtained by approximating both the experimental data and the "exact" numerical calculations

For main dimensions of the axisymmetric cavity (the mid-section diameter D_c and the cavity length L_c) in the case of the cavitation number is small and the gravity influence is negligible, it was obtained semi-empirical relations of the same structure as in (27) [2, 3]:

$$D_c = D_n\sqrt{\frac{c_x}{k\sigma}}, \qquad L_c = D_n\frac{A\sqrt{c_x}}{\sigma}, \tag{28}$$

where $k = 0.9 \div 1.0$, A are empirical constants. When σ is not very small, it is usually accepted $A \approx 2$.

Formulae (28) are valid not only for the disk but for any blunted cavitators. For a non-disk cavitator D_n is a diameter of the cavity separation line. For the drag coefficient of the blunted cavitators when σ is sufficient small, the approximate Reichardt formula is valid [1-4]:

$$c_x(\sigma) = c_{x0}(1+\sigma), \qquad 0 < \sigma < 1.2, \tag{29}$$

where c_{x0} is the cavitator drag coefficient when σ = 0. Value $c_{x0} \approx 0.82$ was established experimentally for the disk cavitator. For cavitators in the form of a blunted cone with cone angle $120^\circ \le \beta \le 180^\circ$, it is possible to use the formula:

$$c_{x0} = 0.13 + \sqrt{0.0036\beta - 0.1719}, \tag{30}$$

that was obtained by approximating the experimental data for the disk and cones [3].

Analysis of photographs of supercavities past the blunted cavitators when σ is small permits to distinguish three characteristic parts of the cavity (Fig. 11). The frontal part I adjoining to the cavitator has length of order of D_n. It is characterized by strong curvature of the free boundary. The next main part II occupies approximately ¾ of the cavity length L_c. Finally, the tail part III has unstable unsteady boundaries at the moderate magnitudes of σ. It is impossible to determine them using the potential theory.

The frontal part boundaries have great curvature and are determined by the cavitator shape. They do not depend on the cavitation number. For the disk cavitator, the empirical "1/3 law" is usually used [2]:

$$\frac{R}{R_n}=\left(1+\frac{3x}{R_n}\right)^{\frac{1}{3}}, \qquad \frac{x}{R_n}<3\div 5, \tag{31}$$

where $R(x)$ is the current cavity radius, $R_n = D_n / 2$ is the disk radius.

The IHM of Ukrainian NAS accumulated great experimental material on the free motion of supercavitating models with the disk cavitators in wide range of velocities V = 50 ÷1400 m/sec. The corresponding cavitation numbers are $\sigma = 1.4 \cdot 10^{4} \div 10^{2}$. Natural vapor cavities are formed for all the pointed velocity range. They are axially symmetric along the whole their length, i.e. are not deformed under the gravity effect.

For the main supercavity part past the disk, we obtained the semi-empirical formula [22]:

$$\overline{R}^2 = 3.659 + 0.847(\overline{x} - 2.0) - 0.236\sigma(\overline{x} - 2.0)^2, \qquad \overline{x} \geq 2.0 \tag{32}$$

where $\overline{R} = R / R_n$, $\overline{x} = x / R_n$. In this case, the experimental data was used which were obtained for natural vapor supercavities in range of the cavitation number σ = 0.012 ÷ 0.057. Results of measuring the profile of the steady vapor cavities corresponding to various values of σ are presented in Fig. 12. Fig. 13 presents a photograph of the vapor supercavity closing on the jet out-flowing from the model nozzle. The frontal cavity part at $\overline{x} < 2.0$ is described by formula (31).

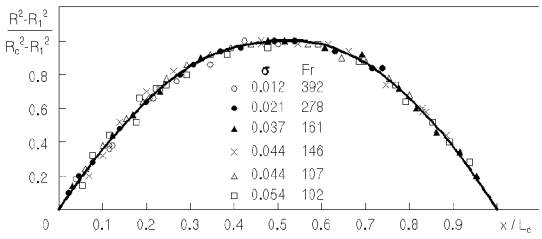


Fig. 12. Universal contour of the axisymmetrical supercavity

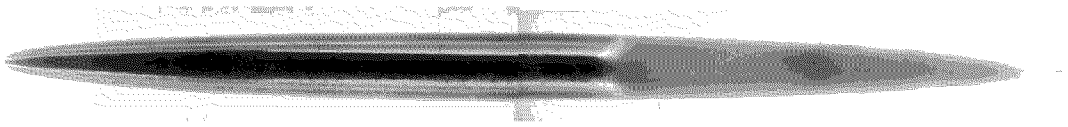


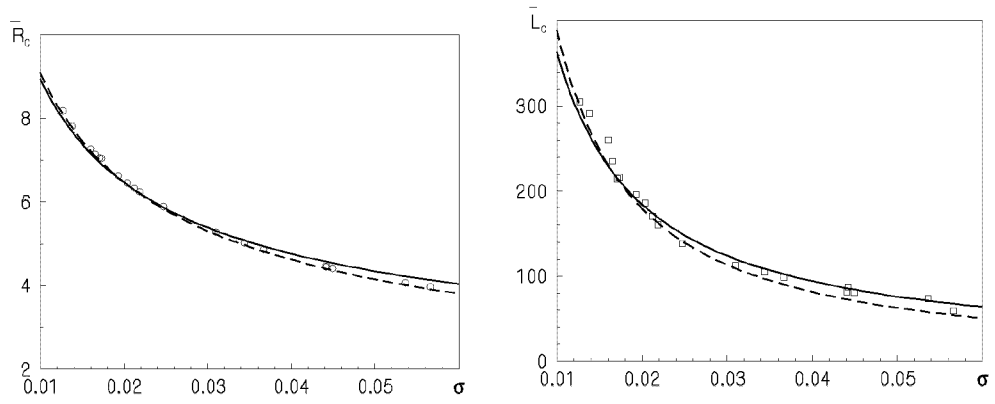
Fig. 13. View of the natural vapor supercavity past the disk: D_n = 15 mm, V = 105 m/sec, σ = 0.0204.

From the formula (32) one has the following expressions for both the cavity mid-section radius and the cavity length:

$$\overline{R}_c = \frac{R_c}{R_n} = \sqrt{3.659 + \frac{0.761}{\sigma}}, \tag{33}$$

$$\overline{L}_c = \frac{L_c}{R_n} = 4.0 + \frac{3.595}{\sigma}. \tag{34}$$

The functions $\overline{R}_c(\sigma)$ and $\overline{L}_c(\sigma)$ which are calculated by formulae (33), (34) in range of cavitation number σ = 0.01 ÷ 0.06 are shown by solid lines in Fig. 14. The experimental data of Fig. 12 also are plotted there. For comparison, the same functions given by asymptotic formulae by P.Garabedian (27) are plotted by dotted lines.



a *b*

Fig. 14. Approximate dependencies $\bar{R}_c(\sigma)$ (a) and $\bar{L}_c(\sigma)$ (b) calculated by formulae (33) and (34)

An advantage of approximation formula (32) is that it gives explicit dependence of the cavity shape on the cavitation number.

We also present other approximation formulae for the main dimensions of stationary axisymmetric super-cavities past cones and the cavitation drag coefficient of cones. They were obtained based on the numerical calculations in "exact formulation" [23, 24]:

$$\frac{D_c}{D_n}=\sqrt{\frac{c_x}{\kappa\sigma}}, \qquad \kappa=\frac{1+50\sigma}{1+56.2\sigma}, \qquad \frac{L_c}{D_n}=\left[\frac{1.1}{\sigma}-\frac{4(1-2\alpha)}{1+144\alpha^2}\right]\sqrt{c_x\ln\frac{1}{\sigma}}, \tag{35}$$

where D_n is the cone base diameter.

$$c_x=c_{x0}+(0.524+0.672\alpha)\sigma, \qquad 0\le\sigma\le 0.25, \qquad \frac{1}{12}\le\alpha\le\frac{1}{2}, \tag{36}$$

$$c_{x0}=0.5+1.81(\alpha-0.25)-2(\alpha-0.25)^2, \quad \frac{1}{12}\le\alpha\le\frac{1}{2}, \qquad c_{x0}=\alpha(0.915+9.5\alpha), \qquad 0<\alpha<\frac{1}{2},$$

where $\alpha\pi$ is the cone half-angle. When $\sigma\to 0$, the formulae (35), (36) transform into the asymptotic relations by P.Garabedian (27).

2.3 ENERGY APPROACH

According to G.V.Logvinovich work [2] we use the theorem of momentum to obtain the approximate equation for the main supercavity part. We display the check volume of liquid (Fig. 15). It has such boundaries:

S_1 is a plane perpendicular to the symmetry axis and located far up-stream ;

S_2 is a plane perpendicular to the symmetry axis and passed through an arbitrary point of the cavity axis before the biggest cavity section;

S_3 is a cylindrical surface with the axis coinciding with the cavity symmetry axis and with radius $R_2\to\infty$. Let $R(x)$ is the radius of the cavity section by the plane S_2, so that $S=\pi R^2$ is the cross-

section area. We write the theorem of momentum for the displayed fluid volume in projection on the x-axis:

$$\int_{S_2-S} \rho(V_\infty + v_x)^2\, ds - \int_{S_1} \rho V_\infty^2\, ds = \int_{S_1} p_\infty^2\, ds - \int_{S_2-S} p\, ds - Sp_c - F_x, \tag{37}$$

where F_x is the cavitation drag. Integrals with respect to the cylindrical surface S_3 vanish, since the perturbed velocity reduces as $1/r^3$ when $r \to \infty$ (like a flow of a dipole).

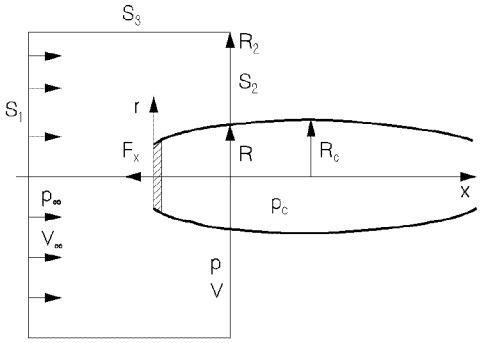


Fig. 15. Scheme of application of the theorem of momentum

From the Bernoulli equation, we obtain the pressure:

$$p = p_\infty - \rho V_\infty v_x - \frac{1}{2}\rho v_r^2, \tag{38}$$

and use condition of conservation of the mass of fluid flowing through the sections S_1 and $S_2 - S$:

$$\int_{S_1} \rho V_\infty^2 ds = \int_{S_2-S} \rho(V_\infty + v_x)^2\, ds.$$

It follows from this that

$$\int_{S_2-S} v_x ds = V_\infty S. \tag{39}$$

Substituting (38) and (39) in the Eq. (37), we obtain the relation for cavitation drag:

$$F_x = \Delta p S - \int_{S_2-S} \frac{\rho v_x^2}{2} dx + \int_{S_2-S} \frac{\rho v_r^2}{2} ds, \tag{40}$$

where $\Delta p = p_\infty - p_c$.

If, in particular, we draw the plane S_2 through the cavity mid-section, then $S = S_c$ and $v_r = 0$. Hence, the second integral in the Eq. (40) is strictly equal to zero. It is possible to show that the first integral in the Eq. (40) is small compared to the first term when $\sigma \to 0$ [2]. That is why, we also cast it out introducing a correcting multiplier *k*. After that, the law of the supercavitation drag may be written in the form:

$$F_x = k\Delta p S_c = k\sigma S_c \frac{\rho V_\infty^2}{2}. \tag{41}$$

Introducing the cavitation drag coefficient of the cavitator (13) in the Eq. (41), we obtain the formula (28) for the supercavity mid-section radius:

$$R_c = R_n \sqrt{\frac{c_x}{k\sigma}}.$$

Experimental check and comparison with numerical calculations showed that the correcting multiplier k weakly depends on σ and has magnitude in range 0.9 ÷ 1.0. It is usually accepted $k = 1$ for practical calculations.

Then, we transform the Eq. (40) to the differential equation of the supercavity section expansion. Neglecting the first integral in the Eq. (40), we may consider the flow in the plane S_2 as pure radial one. We have the boundary condition for the mean part of the slender supercavity surface

$$v_x \approx V_\infty R'(x). \tag{42}$$

The radial velocity of fluid at the arbitrary radius r is determined from the condition of the mass conservation:

$$2\pi R v_r(R) = 2\pi r v_r(r),$$

then we obtain taking into account the Eq. (42):

$$v_r(r) = V_\infty \frac{RR'}{r}. \tag{43}$$

The integral in the Eq. (40) represents the kinetic energy of the flow in the fluid layer E_k. It is equal to

$$E_k = \int\limits_{S_2 - S} \frac{\rho v_r^2}{2} ds = \pi \rho V_\infty (RR')^2 \ln r \Big|_{r=R}^{r=\infty}. \tag{44}$$

One can see that this integral value is equal to infinity, i.e. infinite energy is necessary for the radial expansion of the cavity in the two-dimensional problem. That is why we accept two non-strict but plausible assumptions:

1) Let, according to [1], the outer radius of the flow area R_2 has high but finite magnitude. In other words, we suppose that all perturbations of the fluid motion are concentrated in a ring with the inner radius R and the outer radius R_2. This supposition is plausible, because the velocity perturbation decay very rapidly (as $1 / r^3$) in the three-dimensional problem.

2) Let the logarithm magnitude

$$\mu = \ln \frac{R_2(x)}{R(x)} \tag{45}$$

does not depend on the coordinate x. This assumption is plausible for the mean part of the slender cavity when $\sigma \to 0$.

Then the relation (40) may be rewritten in the form

$$F_x = \Delta p S + \frac{\mu}{4\pi} \rho V_\infty^2 (S')^2. \tag{46}$$

Differentiating the Eq. (46) with respect to S, we obtain another form of the equation of the supercavity section expansion that does not contain the cavitation drag:

$$\mu \frac{\partial^2 S}{\partial x^2} = -\frac{2\pi \Delta p}{\rho V_\infty^2}. \tag{47}$$

Passing to the fixed coordinate system in the Eq. (47) with the independent variable substitution $x = V_\infty t$, we rewrite it in the form

$$\mu \frac{\partial^2 S(\tau, t)}{\partial t^2} = -\frac{2\pi \Delta p}{\rho}. \tag{48}$$

The Eq. (48) assumes the obvious mechanical explanation:

The cavitator passes the fixed "observation plane" at the time $t = \tau$ and makes an orifice with diameter D_n in that plane. Considerable radial velocities arise on that orifice boundaries. Then, that orifice expands on inertia overcoming the pressure difference Δp up to its maximal diameter D_c at the time $t = \tau + t_c$. After that, the orifice decreases and closes again at the time $t = \tau + 2t_c$.

The time interval $t_c = L_c / 2V_\infty$ is called "the time of the complete cavity expansion". After the cavity collapse, the wake remains past it where the mechanical energy transmitted by the cavitator to the fluid disperses into heat.

The Eq. (48) allows to calculate an expansion of each cavity section separately, i.e. it is an expression of the independence principle for expansion of the slender axisymmetric cavity sections by G.V.Logvinovich [2].

A full cavity profile at fixed t may be calculated when $t - 2t_c \le r \le t$. In this case x-coordinates of the cavity sections are $x(\tau) = V_\infty \tau$, and the cavity length is equal to $L_c = 2t_c V_\infty$.

The more strict analysis of the Eq. (40) [2] permits to transform it to the following form (in the fixed coordinate system):

$$\frac{\kappa}{2}(t - t_c)\frac{\partial S}{\partial t} + (S_c - S) = 0, \tag{49}$$

where κ is some correcting coefficient. The integral of the Eq. (49) is

$$S(t) = S_c + C(t - t_c)^{2/\kappa}.$$

Determining the arbitrary constant C from the initial condition $S(0) = S_n$, we finally obtain the law of the cavity section expansion:

$$S(t) = S_c \left[1 - \left(1 - \frac{S_n}{S_c} \right) \left(1 - \frac{t}{t_c} \right)^{2/\kappa} \right]. \tag{50}$$

Passing in the Eq. (50) to the coordinate system related with the cavitator $x = V_\infty t$, we obtain:

$$R(x) = R_c \sqrt{1 - \left(1 - \frac{R_n^2}{R_c^2} \right) \left(1 - \frac{2x}{L_c} \right)^{2/\kappa}}. \tag{51}$$

For non-disk cavitators, the coordinate $x = 0$ corresponds to the plane of the cavity separation.

A comparison with experiments showed that value of the correcting coefficient is $\kappa \approx 0.85$. However, the exact enough results are obtained when $\kappa = 1$.

It is easy to see that the shape of the main part of the axisymmetric supercavity represents an ellipsoid of revolution when $\kappa = 1$, and one is very close to it when $\kappa = 0.85$.

Experience of calculation shows that the expressions (31), (51) must be "matched" on the boundary between the frontal and the main cavity parts when $x = x_1 \approx D_n$. As a result, we obtain so called formula of the G.V.Logvinovich's composed cavity:

$$R(x) = R_n\left(1 + \frac{3x}{R_n}\right)^{\frac{1}{3}}, \qquad x \le x_1, \qquad R(x) = R_c\sqrt{1 - \left(1 - \frac{R_1^2}{R_c^2}\right)\left(1 - 2\frac{x - x_1}{L_c - 2x_1}\right)^{2/\kappa}}, \tag{52}$$

where $R_1 = R(x_1)$ is the "agreement section" radius. When $x_1 = D_n$, we just obtain from the Eq. (31) that $R_1 = 1.913$.

The "universal contour" of the ellipsoidal cavity is plotted by solid line in the Fig. 12. It was calculated by the formula (52) when $\kappa = 1$. A comparison with the experimental data shows good coincidence along the whole cavity length right up to the point of the cavity closure on the body.

2.4 ASYMPTOTIC APPROACH

Great aspect ratio of supercavities when σ is small gives background to apply the theory of flow around slender bodies [25, 26] to calculate them. Basing on this theory, the asymptotic theory of a slender axisymmetric cavity was developed [27-30]. The basic mathematical tool of this theory is asymptotic method of singular perturbations [26]. A solution of the axisymmetric boundary value problem is sought in the form of decomposition by the small parameter ε. Its value is inverse to the cavity aspect ratio.

It is well known from the theory of slender bodies that the potential decomposition near the x-axis is [26]:

$$\varphi = \frac{V_\infty}{2}\frac{dR^2}{dx}\ln r + \dots$$

To evaluate the order of smallness of terms in the Eqs. (23)-(25), we substitute there orders of smallness for all the variables:

$$r \sim \varepsilon, \quad R \sim \varepsilon, \quad x \sim 1, \quad \varphi \sim \varepsilon^2 \ln\varepsilon, \quad \Delta p \sim \varepsilon.$$

As a result, neglecting the terms of high order of smallness, we come to the "internal" problem of the first approximation:

$$\frac{\partial^2\varphi}{\partial r^2} + \frac{1}{r}\frac{\partial\varphi}{\partial r} = 0, \tag{53}$$

$$\frac{\partial\varphi}{\partial r} = V_\infty\frac{dR}{dx}, \qquad when \quad r = R(x), \tag{54}$$

$$V_\infty\frac{\partial\varphi}{\partial x} = \frac{\Delta p}{\rho}, \qquad when \quad r = R(x). \tag{55}$$

We note that the condition (26) proves to be lost in the internal problem.

We verify by direct substitution that the general solution of the Eq. (53) satisfying to the kinematic condition (54) is:

$$\varphi(x) = \frac{V_\infty}{2}\frac{dR^2}{dx}\ln r + C(x), \tag{56}$$

where $C(x)$ is some arbitrary function that may be determined by matching with the "external" solution satisfying to the condition (26) [26].

Substituting the solution (56) to the dynamic boundary condition (55), we obtain the equation:

$$\frac{d^2R^2}{dx^2}\ln R+\frac{2C'(x)}{V_\infty}=\frac{2\Delta p}{\rho V_\infty^2}. \tag{57}$$

We introduce a new arbitrary function $\Psi(x)$ instead $C(x)$ using the equality:

$$C'(x)=-\frac{V_\infty}{2}\frac{d^2R^2}{dx^2}\ln\Psi(x).$$

Then the Eq. (57) becomes the same form as the Eq. (47):

$$\frac{d^2R^2}{dx^2}\ln\frac{R(x)}{\Psi(x)}=\frac{2\Delta p}{\rho V_\infty^2}, \tag{58}$$

if we consider that

$$\ln\frac{\Psi(x)}{R(x)}=\mu=const.$$

Thus, both the energy theory and the asymptotic theory of slender axisymmetric cavities yield the same equation in the first approximation.

The more strict analysis of the boundary value problem (53)-(55) permits to obtain the differential equation

$$\frac{\partial^2R^2}{\partial x^2}\ln\frac{R}{\Psi}+\left(\frac{dR}{dx}\right)^2=\frac{2\Delta p}{\rho V_\infty^2}, \tag{59}$$

having the higher precision $\varepsilon^2\ln\varepsilon$ than the Eq. (58).

In the work [30], its solution was constructed by the method of matched asymptotic decomposition.

However, the equation of the first approximation (48) is the more convenient for practical calculations. It must be integrated when $t>\tau$ with the starting conditions:

$$S(\tau,\tau)=\frac{\pi D_n^2}{4},\qquad \frac{\partial S(\tau,\tau)}{\partial t}=\dot S_0, \tag{60}$$

where $\dot S_0$ is the starting velocity of the cavity section expansion. It is determined by the cavitator shape, i.e. by D_n and c_{x0}, and also by the model velocity V and does not depend on the cavitation number.

The Eq. (48) reminds the Newton equation of motion. The constant μ may have certain physical sense of the additional mass coefficient of the expanding cavity section (so called the ring model of the slender axisymmetric cavity [1, 30]). This assumption allows to determine the starting velocity of the cavity section expansion [29]:

$$\frac{\partial R^2}{\partial t}=2\sqrt{\frac{F_x}{k\pi\mu\rho}},\qquad t=\tau. \tag{61}$$

However, for practical calculations it is rational to determine both the constant μ and the initial velocity of the section expansion $\dot S_0$ in such way that the semi-empirical relations (28) are fulfilled. Integrating twice the Eq. (48), we obtain:

$$\frac{\partial S}{\partial t}=\dot S_0-\frac{k_1\Delta p}{\rho}(t-\tau), \tag{62}$$

$$S=S(\tau,\tau)+\dot S_0(t-\tau)-\frac{k_1\Delta p}{2\rho}(t-\tau)^2, \tag{63}$$

where $k_1 = 2\pi / \mu$. Substituting the expressions (62) and (63) into obvious relations:

$$S(\tau, \tau + t_c) = \frac{\pi D_c^2}{4}, \qquad \frac{\partial S(\tau, \tau + t_c)}{\partial t} = 0,$$

and taking the Eq. (28) into account, we finally obtain:

$$\dot{S}_0 = \frac{k_1 A}{4} D_n V_\infty \sqrt{c_{x0}}, \qquad k_1 = \frac{4\pi}{A^2}. \tag{64}$$

The Eq. (48) is an equation of the ellipsoid of revolution, i.e. it correctly describes the shape of the main cavity part. To take into account the frontal part (31), it is necessary to use the condition $S(\tau, \tau) = \pi D_1^2 / 4$ (here, D_1 is the "agreement section" diameter) instead the first of starting conditions (60).

Fig. 16 gives a comparison of the cavity shape calculated by formulae (52), (63) and (32) when $\sigma = 0.02$.

If $\sigma < 0.01$, all three curves coincide. The cavity contour approaches to the ellipsoidal cavity shape (52) when σ decreases and practically coincides with the latter when $\sigma < 0.01$.

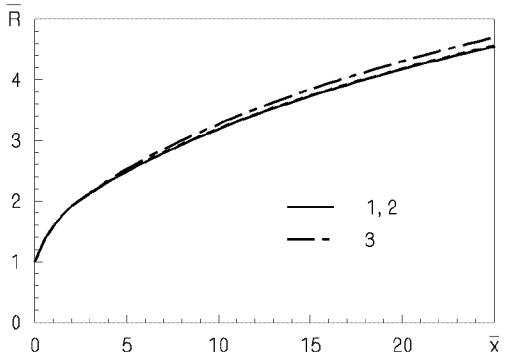


Fig. 16. Supercavity shape calculated by formulae: 1- (32); 2 - (52); 3 - (63)

3 Calculation of unsteady supercavities

3.1 Independence principle of cavity expansion by G.V. Logvinovich

In 50s G.V.Logvinovich proposed and grounded so named principle of independence of the slender axisymmetric cavity section expansion. It may be treated as a partial case of the general mechanical principle of plane sections. That principle consists in that the law of the cavity section expansion almost does not depend on the previous and the next motion of the cavitator. That law is determined by the instantaneous velocity of the cavitator at passing through this section plane and by the pressure difference $\Delta p = p_\infty - p_c$ as well. The independence principle of the cavity expansion is of very importance to research the unsteady supercavitation flows.

3.2 Equation of an unsteady supercavity

In the case of unsteady axisymmetric cavities the independence principle consists in that the law of arbitrary section expansion about the trajectory of the cavitator center is determined by the cavitator instantaneous velocity at passing this section $V(t)$, and also the pressure difference $\Delta p = p_\infty - p_c$ that can

depend on time at fluctuating the external pressure $p_\infty(t)$ or the cavity pressure $p_c(t)$ as well. The mathematical expression of the independence principle is the equation of expansion of the unsteady cavity section [29]:

$$\frac{\partial^2 S(\tau,t)}{\partial t^2} = -\frac{k_1 \Delta p(\tau,t)}{\rho}, \quad x(t) - L_c(t) \le \xi \le x(t), \tag{65}$$

where $\Delta p(\tau,t) = p_\infty(\xi) + p_1(t) - p_c(t)$. Here, $\tau \le t$ is the time of the section ξ formation; $x(t)$ is the current absolute coordinate of the cavitator (see Fig. 17); $p_1(t)$ is the perturbation of the ambient pressure. The hydrostatic pressure p_∞ can change from a section to section in case of the vertical cavity in ponderable fluid.

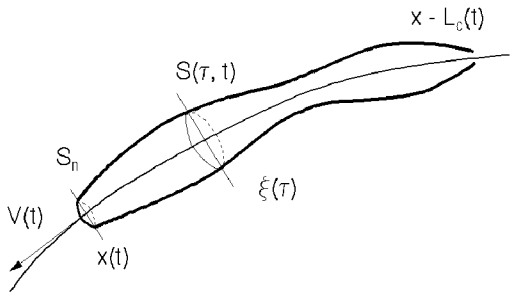


Fig. 17. Calculation scheme of an unsteady supercavity

According to the independence principle, the equations of expansion of the steady cavity (48) and the nonsteady cavity (65) are identical. The constant $k_1 = 2\pi/\mu$ and the initial velocity of the section expansion $\dot{S}(t,t) = \dot{S}_0$ have the same magnitudes (64). In this case $V = V(\tau)$ is the instantaneous cavitator velocity at the time of the section ξ formation.

We introduce the dimensionless variables by formulae:

$$x = D_n x', \quad L_c = D_n L_c', \quad S = D_n^2 S', \quad t = \frac{D_n}{V_\infty} t', \quad p = \rho V_\infty^2 p'.$$

The Eq. (65) for the dimensionless variables is (the primes are omitted):

$$\frac{\partial^2 S(\tau,t)}{\partial t^2} = -k_1 \Delta p(\tau,t) = -\frac{k_1 \sigma(\tau,t)}{2} V^2(\tau), \quad t - L_c(t) \le \tau \le t. \tag{66}$$

The Eq. (66) must be integrated with dimensionless initial conditions:

$$S = \frac{\pi}{4}, \qquad \frac{\partial S}{\partial t} = \frac{k_1 A}{4} V(\tau)\sqrt{c_{x0}}, \qquad t = \tau. \tag{67}$$

The cavitation number is a time function, if the external pressure $p_\infty(t)$ and/or the cavity pressure $p_c(t)$ fluctuate. The cavitator velocity V also is a time function in the general case. For example, in case of the vertical motion of the supercaviating model under action of only cavitation drag the cavitator velocity and the cavitator position are determined by the equations:

$$m\frac{dV}{dt} = -\frac{\rho V_\infty^2}{2} S_n c_{x0}\left[1 + \frac{p_{atm} + \rho g H(t) - p_c(t)}{\rho V_\infty^2/2}\right], \qquad H(t) = \int_0^1 V(s)ds,$$

where m is the body mass; p_{atm} is the atmospheric pressure; H is the cavitator immersion depth.

Twice integrating the Eq. (66) with taking into account the initial conditions (67), we obtain the formula:

$$S(\tau,t)=\frac{\pi}{4}+\frac{k_1V(\tau)}{4}\left[A\sqrt{c_{x0}}\,(t-\tau)-2V(\tau)\int_{\tau}^{t}(t-u)\sigma(u)\,du\right]. \tag{68}$$

The cavity length $L_c(t)$ is determined for each moment by the equation:

$$S(t-L_c(t),t)=\frac{\pi}{4}. \tag{69}$$

An application of formula (68) has, naturally, restricted limits of applicability. However, the experimental tests justify its adequacy for a wide range of parameters.

3.3 EXPERIMENTAL CONFIRMATION OF THE INDEPENDENCE PRINCIPLE

The experimental test of the independence principle was carried out repeatedly and always gave good results. So, it was shown in the specially performed experiments [2] that in case of the model impact acceleration or stoppage, the cavity sections remote from the cavitator expanded some time in the same way as if the uniform motion continued.

Examples of calculation of the cavity shape at the variable cavitator velocity and also along the curvilinear trajectory are given there as well. The work [30] presents results of experimental testing the calculation of the unsteady cavity past the disk with periodically varying angle of slope. A comparison of the experimental and calculated cavity shape at the vertical water entry of bodies is given there as well.

A number of methodical experiments on testing the independence principle was carried out at the IHM UNAS including experiments at very high velocity of the models [31].

Fig. 18 shows a sequence of motion-picture frames of the deformation of the cavity caused by rapid reducing the cavitator drag without changing the cavitator diameter. The experiment was performed in the hydro-tunnel at the free-stream velocity V_∞ = 8.9 m/sec, the diameter D_n of the cavitator with variable drag [22] was equal to 20 mm. In the frames, a well expressed "stepped" boundary separating the initial and new-formed cavity parts is observed. This boundary moved with velocity V_∞ in full accordance with the independence principle.

We confirmed the independence principle validity at the very high velocity of motion in the special experiments on passage of the supercavitating model through a solid steel sheet with thickness 1.5 mm and through a hollow obstacle filled by air as well.

Fig. 19 shows a sequence of motion-picture frames of the process of the model passage through the thin steel sheet. The motion velocity is V = 1000 m/sec, the cavitator diameter is D_n = 1.3 mm. One can see in the frames that the presence of the obstacle preventing the water motion in longitudinal direction did not influence on the cavity development past the obstacle. This testifies that:

1) the fluid motion near the slender supercavity occurs predominantly in radial direction;

2) the adjoining supercavity sections separating by the steel sheet develop in such way as in the case of a flow without the sheet;

3) the longitudinal gas motion together with the supercavity is absent. If not, it would cease at passing of the model through the steel sheet. It could influence on the supercavity development just past the obstacle.

The flow directed to the model motion direction was observed only after the cavity closure.

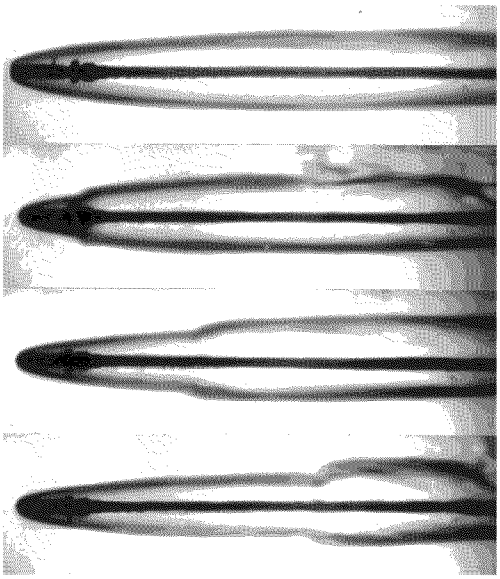


Fig. 18. Supercavity shape at rapid reducing the drag: through the obstacle:

D_n = 20 mm, V_∞ = 8.9 m/sec

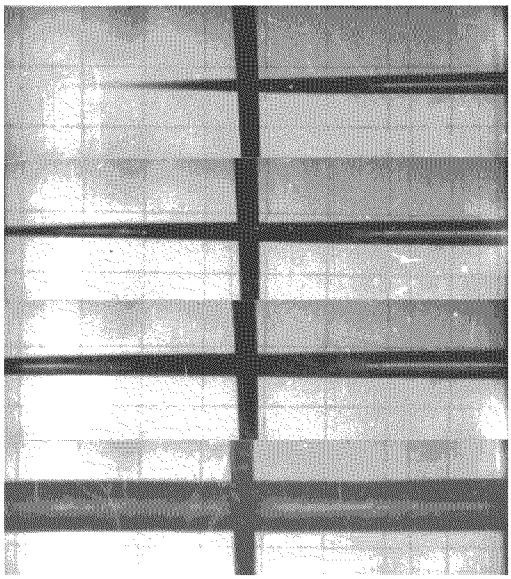


Fig. 19. Passing of supercavitating model

D_n = 1.3 mm, V = 1000 m/sec

The experiment on passing of the supercavitating model through the hollow air space is especially demonstrative one. The obstacle represented a box with the frontal and back walls made of steel sheets having thickness 1 mm and the side walls made of glass having e thickness 10 mm (Fig. 20). In the experiment, we used the model with the length 280 mm and the cavitator diameter D_n = 3.3 mm.

A sequence of frames of shooting the experiments is given in Fig. 21. Passing through the complex obstacle containing the air space between the solid walls excluded the transition of both the pressure pulse and the velocity pulse in longitudinal direction. However, the cavity developed some time before and after the hollow box as if it was absent.

The presented sequences of frames visually demonstrate validity of the principle of independence of the cavity section expansion and, hence, adequacy of the approximate calculation method based on that principle.

4 Peculiarities of calculation of ventilated cavities

4.1 SIMILARITY PARAMETERS IN THE ARTIFICIAL SUPERCAVITATION

It follows from the above that the basic similarity parameters in artificial supercavitation are the cavitation number (1), the Froude number (3) and the dynamic parameter β (17). The cavitation number magnitudes in range $10^{-2} < \sigma < 0.1$ correspond to this type of flow.

The Froude number Fr characterizes the distorting effect of the gravity on the cavity shape. Estimations show that it is considerable when $\sigma Fr < 2$ [2].

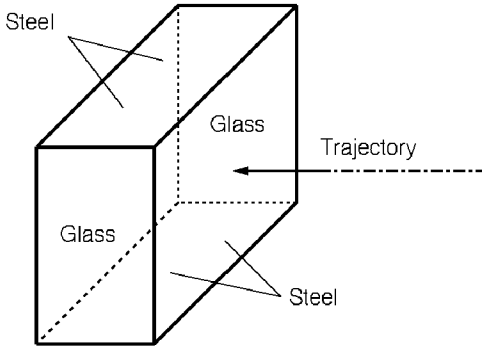


Fig. 20. Sketch of the hollow obstacle

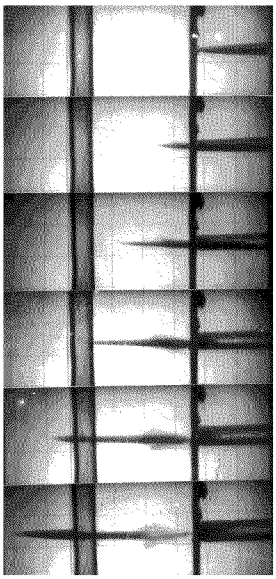


Fig. 21. Passing of supercavitating model through the air space: D_n = 3.3 mm, V = 550 m/sec

The parameter $\beta > 1$ characterizes the significance of elasticity of the gas filling the ventilated cavity. It is the basic similarity parameter at investigation of stability and unsteady behavior of gas-filled cavities [15]. When the parameter β increases, the gas elasticity significance increases as well. The ventilated cavities are stable when $1 \le \beta < 2.645$ and unstable when $\beta > 2.645$.

In practice, it is impossible to attain simultaneous equality of all the numbers σ, Fr, β for the full-scale model and the bench testing one. That is why, investigation of scale effects (i.e. influences of different deviations from the similarity) is of importance in modeling the supercavitation processes.

We enumerate some possible causes of the scale effect at the physical modeling of the artificial cavitation flows.

1) **Influence of the flow boundaries.** The bench testing of the supercavitation flows usually are carried out in hydro-tunnels and hydro-channels in condition of the bounded flow. It is necessary to take into account the influence of the flow boundaries when the experimental data are recalculated to the motion in unbounded fluid.

The influence of the flow boundaries on the supercavity shape and dimensions has been well studied. The solid boundary closeness results in increasing the cavity dimension, and the free boundary closeness results in decreasing them at the same value of the cavitation number.

The influence of the flow boundaries on the gas rate coefficient is of importance in the case of ventilated cavities. It was shown experimentally that the approach to the free boundary results in decreasing the gas-leakage rate at the same values of σ and Fr [3, 10]. The influence of the cavity immersion depth on the gas-leakage coefficient at the second type of the gas-leakage was taken into account in the empirical formula (14).

2) **Influence of the gas flow in the cavity.** The experience shows that in the most of cases the influence of gas flow within the artificial cavity may be neglected. For steady cavities, it becomes considerable only in that cases when the gas flows in a narrow clearance between the body and the cavity wall. According to the Bernoulli equation the pressure in the clearance reduces, and the cavity boundaries may be deformed negatively. In this case local deformation of the cavity wall may be approximately calculated by the perturbation method [32].

3) **Supercavities in a bubble flow.** A peculiar scale effect may arise in the case of the gas-liquid bubble flow around the supercavitating bodies. We showed experimentally and theoretically that the supercavities can absorb gas from the two-phase bubble flow [33].

When the gas concentration is sufficient, this process causes to the considerable gas supply into the cavity and, as a result, to increasing the cavity dimension.

4.2 TAKING INTO ACCOUNT OF GRAVITY EFFECT

As was said above, the gravity effect on the horizontal supercavity consists in:

1) the cavity axis deformation upwards (floating-up of the cavity tail);
2) the cavity section shape deformation.

The cavity axis deformation in ponderable fluid is the main and greatest perturbation of the cavity.

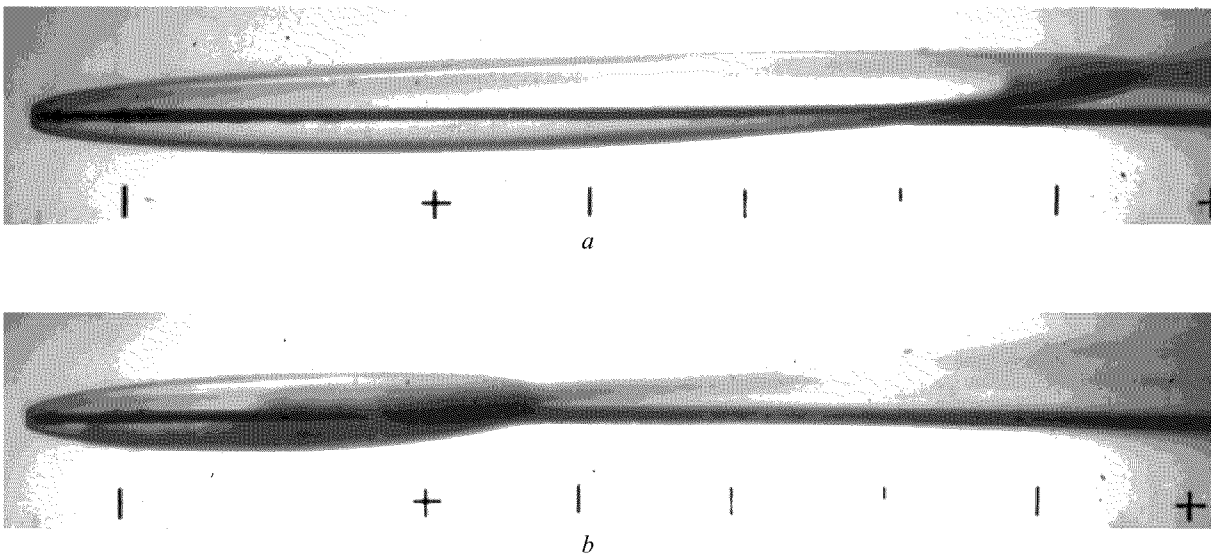


Fig. 22. View of the ventilated supercavities: V_∞ = 8.9 m/sec, Fr = 24.5; *a* - σ = 0.0334, *b* - σ = 0.0644

Fig. 22 demonstrates photographs of ventilated cavities at the same Froude number and the different cavitation numbers. The first form of the gas leakage from the cavity was observed in both cases.

In the works [31, 33] these deformations have been investigated in detail by the perturbation method.

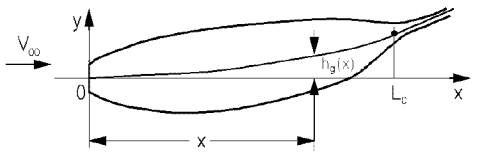


Fig. 23. Scheme of a supercavity in ponderable fluid

However, for practical calculations it is usually enough to evaluate the axis deformation in the first approximation by the theorem of momentum [2]. The calculation scheme is presented in Fig. 23.

We consider the balance of the cavity length element with the radius $R(x)$. Its momentum $\rho\pi R^2 V_\infty \dot{h}_g$ must be equal to the buoyancy force $\rho g Q$. Thus, we have:

$$\dot{h}_g(x) = \frac{gQ(x)}{\pi V_\infty R^2(x)}.$$

Integrating this equation along the x-axis, we obtain

$$h_g(x) = \frac{g}{\pi V_\infty}\int_0^x \frac{Q(s)}{R^2(s)}ds. \tag{70}$$

Here, $Q(x)$ is the cavity part volume from 0 to x, $R(x)$ is the current cavity radius.

In the work [33], the simple approximate formula was obtained for the axis deformation caused to the gravity effect:

$$h_g(x) = \frac{(1+\sigma)x^2}{3Fr_l^2}, \quad Fr_l = \frac{V_\infty}{\sqrt{gL_c}}. \tag{71}$$

Here, Fr_l is the Froude number with respect to the cavity length. Formula (71) may be used in ranges $0.05 \le \sigma \le 0.1$, $2.0 \le Fr_l \le 3.5$. Fig. 24 gives a comparison of calculation by formulae (70) (curve 1) and (71) (curve 2) with the experimental data [30]. Different marks correspond to different experimental conditions.

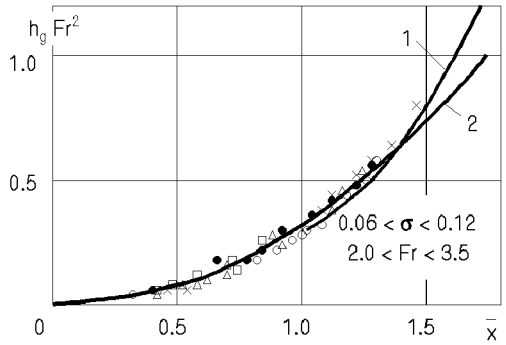


Fig. 24. A supercavity axis deformation in ponderable fluid

Deformation of the cavity section shape in the cross gravity field was investigated by the perturbation method in the works [30, 32]. The calculations showed and the experiments confirmed that a liquid crest with top directed up into the cavity is formed at the bottom cavity wall in this case. The crest height increases from the cavitator to the tail. Sometimes, this crest is small even at the cavity end. In other cases the crest top may attain the upper cavity wall and divide cavity on two tubes just past the mid-section (see Fig. 25)

A criterion of the gravity effect on the supercavity was obtained by theoretical way in the work [32]:

$$\nu = \sigma\sqrt{\sigma}Fr^2 \ge 1.5. \tag{72}$$

When this condition is fulfilled, the cavity is not destroyed, and the water crest does not close up with its upper wall even at the cavity end. With approaching the parameter ν to the limiting magnitude ν = 1.5, two vortex tubes become the more expressed at the cavity end.

A comparison with the experiment showed that the criterion (72) is the more exact than the Campbell-Hilborne criterion (15). Indeed, we have σFr =0.82 < 1; ν = 3.73 > 1.5 for the experiment in Fig. 22, a. For the experiment in Fig. 22, b, we have σFr = 1.58 > 1; ν = 9.82 > 1.5. Thus, in the first case the Campbell-Hilborne criterion does not allow confidently to determine the gas-leakage type. Simultaneously, the criterion (72) determines the portion gas-leakage.

It is possible to determine the following intervals of changing the parameter ν that correspond to different levels of perturbation caused by gravity:

1) interval $\nu = 1 \div 2$ is characterized by high level of perturbation, when the cavity past the mid-section transforms into the vortex tubes;

2) interval $\nu = 2 \div 4$ corresponds to the moderate or considerable level of perturbation. In this case the water crest height is lower than the unperturbed cavity radius, although may be close to it.

3) interval $\nu = 4 \div 10$ is characterized by weak level of perturbation. The gravity effect may be neglected at all when $\nu > 10$.

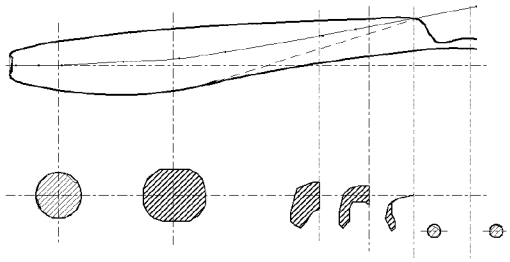


Fig. 25. Deformation of a ventilated supercavity axis in ponderable fluid

Fig. 26 represents the calculation by the perturbation method of the cross cavity section shapes when σ = 0.06, Fr = 10.0 [33]. In this case ν = 1.47. The dimensionless coordinate $\overline{x} = 2x/L_c$ was used at the calculation. In the sections $\overline{x}$ = 0.25 and $\overline{x}$ = 0.50 the gravity effect does not yet become apparent, in the section $\overline{x}$ = 0.75 the small compression from the bottom is appreciable. In the cavity mid-section $\overline{x}$ =1.00 the section shape differs from the circular one. When $\overline{x}$ = 1.25, the deformation is considerable. On the bottom it is close to the half of the cavity radius. The crest directed to up is well visible. The cavity is destroyed in the next sections.

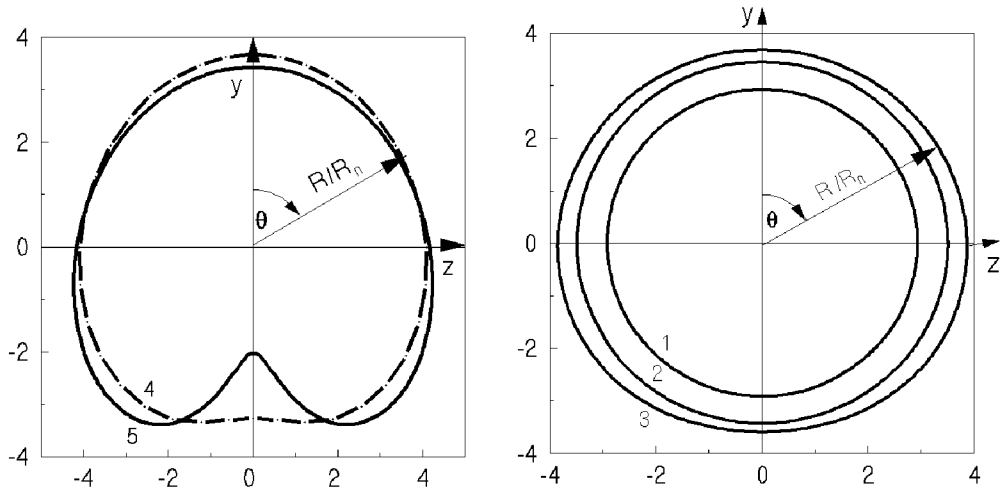


Fig. 26. Gravity effect on the cross cavity section shape: σ = 0.06, Fr = 10.0
1 - $\overline{x}$ = 0.25, 2 - $\overline{x}$ = 0.50, 3 - $\overline{x}$ = 0.75, 4 - $\overline{x}$ = 1.00, 5- $\overline{x}$ = 1.25

4.3 TAKING INTO ACCOUNT OF ANGLE OF ATTACK

The transverse force F_y arising on the cavitator non-symmetric about the free-stream results in the cavity axis deformation (Fig. 27). According to the theorem of momentum, the impulse of the transverse force on the cavitator must correspond to change of the momentum in the wake that is the same by magnitude and opposite by direction. This means that if the force on the cavitator is directed to up, then the cavity axis must be deflected to down (see Fig. 27) and vise versa.

Applying the theorem of momentum allows to estimate easily this bend [1]. The impulse $F_y\ t$ must be equal to momentum of the cavity length unit $-\rho\pi R^2 V_\infty \dot{h}_v$. Hence, we have:

$$\dot{h}_f(x) = -\frac{F_y}{\rho\pi V_\infty^2 R^2(x)}.$$

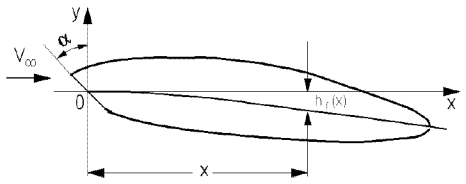


Fig. 27. Scheme of a supercavity past an inclined cavitator

Integrating this equation along the x-axis, we obtain

$$h_f(x) = -\frac{F_y}{\pi\rho V_\infty^2}\int_0^x \frac{ds}{R^2(s)}. \tag{73}$$

Components of the force acting on the cavitator-disk inclined to the stream with the angle α can be approximately calculated by formulae [1]:

$$F_x = F_{x0}\cos^2\alpha, \quad F_y = F_{x0}\sin\alpha\cos\alpha, \tag{74}$$

where F_{x0} is the disk drag when $\alpha = 0$. The formulae (74) well coordinates with experiment when $\alpha < 50°$. They may be applied not only for a disk but also for blunted cavitators of other shapes.

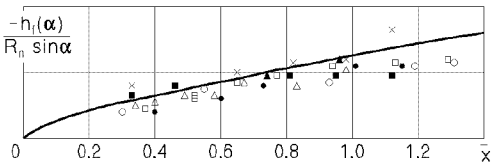


Fig. 28. A superavity axis deformation past the inclined cavitator: $\sigma = 0.08$, $\alpha = 33.5°$

An analysis of the cavitator orientation effect on the cavity shape using the perturbation method was given in the work [34]. As a result, the simple approximate formula was obtained to determine the cavity axis deformation under action of the lift on the cavitator:

$$h_f(x) = -c_y R_n\,(0.46 - \sigma + \bar{x}), \quad c_y = \frac{8F_y}{\rho V^2 \pi D_n^2}, \tag{75}$$

where $\bar{x} = 2x / L_c$. Fig. 28 gives a comparison of the calculation by the formula (75) with the experimental data [31].

Comparing the formulae (74) and (78), we can see that the cavity axis bend caused by the gravity increases according to the quadratic law, and one caused by the lift on the cavitator increases according to the linear law. Therefore, it is impossible to neutralize the gravity effect using the inclined cavitator along the whole cavity length.

In skewed stream, the cross cavity sections also are deformed. Since a projection of the inclined disk on the vertical plane is an ellipse, then the cross cavity sections before the mid-section will be elliptic with ratio of the half-axes

$$\frac{R_y}{R_z} = \cos\alpha. \tag{76}$$

In this case, the average radii in the middle cavity part before the mid-section are approximately equal to:

$$R(x) = R_0(x)\cos\alpha, \tag{77}$$

where R_0 is the radius of axisymmetric unperturbed cavity [2].

The simple formulae (71), (75) may be used for approximate calculation of both the stationary and non-stationary supercavities (using the independence principle). They are very convenient for using in codes for computer simulation of the cavitation flows.

4.4 EQUATION OF THE MASS OF GAS IN THE CAVITY BALANCE

The mathematical model of the unsteady ventilated cavity must include the equation of the mass of gas in the cavity balance [15]:

$$\frac{dm_g}{dt} = \dot{m}_{in} - \dot{m}_{out}, \tag{78}$$

where $m_g(t) = \rho_g(t)Q(t)$ is the mass of gas in the cavity; $Q(t)$ is the cavity volume; ρ_g is the density of gas in the cavity; $\dot{m}_{in}$ and $\dot{m}_{out}$ are the mass rates of the gas blowing into the cavity and carrying away from the cavity, respectively. Owing to the water thermal capacity, the process of the gas expansion in the cavity usually may be considered as isothermal one:

$$\rho_g(t) = C\,p_c(t), \tag{79}$$

where C is the constant. Taking the relation (79) into account, we rewrite the equation of the mass of gas in the cavity balance in the form:

$$\frac{d}{dt}[p_c(t)Q(t)] = p_\infty\left[\dot{Q}_{in} - \dot{Q}_{out}(t)\right], \tag{80}$$

where $\dot{Q}_{in}$ is the volumetric air-supply rate referred to the ambient pressure p_∞; $\dot{Q}_{out}(t)$ is the volumetric air-leakage rate from the cavity. The cavity pressure $p_c(t)$ is assumed to change synchronously along the cavity length.

Strictly speaking, the Eq. (80) may be applied when the parameters change not very rapidly. Really, the pressure perturbations $p_c(t)$ extend along the cavity with the sound speed in the vapor-gas medium filling the cavity a_g. Characteristic time of changing the pressure in the cavity with length L_c is equal: $T_1 = L_c / a_g$. Let the characteristic frequency of the unsteady process is f Hz. Then, supposition about the synchronism of changing the pressure along the cavity is equivalent to the inequality $T_1 << 1/f$. From

here we derive estimations for both the admissible frequency of the process and the dimensionless Strouhal number (10):

$$f << \frac{a_g}{L_c}, \qquad Sh << \frac{a_g}{V_\infty}. \tag{81}$$

The cavity pressure is constant in the case of the natural vapor supercavity, i.e. σ = const. Therefore, the Eq. (80) becomes needless.

In practice, we usually have $\dot{Q}_{in}$ = const. The value of the gas-leakage from the cavity $\dot{Q}_{out}$ depends on both the cavitation number and the Froude number and on a number of other factors as well [3, 6]. It is obvious for steady ventilated cavity that $\dot{Q}_{in} = \dot{Q}_{out}$.

The function $\dot{Q}_{in}(t)$ is given, and $\dot{Q}_{out}(t)$ is an unknown time function in problems of the ventilated cavities control by regulating the gas supply. As has been said yet, determining the form of function $\dot{Q}_{out}(t)$ for the concrete flow conditions is the most difficult problem of the artificial cavitation theory.

Conclusion

The described approximate mathematical model of the unsteady axisymmetric cavity is very convenient to develop fast calculation algorithms and codes permitting to perform computer experiments with dynamic display of the unsteady cavity shape and other necessary information on the computer screen immediately during run-time. The existing methods of "exact" numerical calculation of the unsteady supercavities are useless for these purposes due to their awkwardness and long run-time. Accuracy of the obtained results is established by direct comparison with experiment.

In our next lecture, results of computer simulation of the unsteady supercavitation processes of different types will be presented.

References

1. Birkhoff, G., Zarantonello, E.H., *Jets, Wakes and Cavities,* Academic Press Inc. Publishers, New York, 1957.

2. Logvinovich, G.V., *Hydrodynamics of Flows with Free Boundaries,* Halsted Press, 1973.

3. Epshtein, L.A., *Methods of Theory of Dimensionality and Similarity in Problems of Ship Hydromechanics,* Sudostroenie Publishing House, Leningrad, 1970 [in Russian].

4. Knapp, R.T., Daily J.W., Hammitt, F.G., *Cavitation*, McGraw-Hill, New-York, 1970.

5. Gorshkov, A.S., Rusetski, A.A., *Cavitation Tunnels,* Sudostroenie Publishing House, Leningrad, 1972 [in Russian].

6. Yegorov, I.T., Sadovnikov, Yu.M., Isayev, I.I., Basin M.A., *Artificial Cavitation,* Sudostroenie Publishing House, Leningrad, 1971 [in Russian].

7. Sedov L.I. *Mechanics of Continuum. Vol. 2.,* Nauka Publishing House, Moscow, 1976 [in Russian].

8. Silberman, E., Song, C.S., Instability of Ventilated Cavities, *J. of Ship Res*., 1961, **5,** No. 1, pp. 13-33.

9. Michel, J.M., Ventilated Cavities. A Contributian to the Study of Pulsation Mechanism, *Unsteady Water Flow with High Velocities, Proc. of Int. Symposium IUTAM,* Nauka Publishing House, Moscow, 1973.

10. Epshtein, L.A., Characteristics of Ventilated Cavities and Some Scale Effects, *Unsteady Water Flow with High Velocities, Proc. of Int. Symposium IUTAM,* Nauka Publishing House, Moscow, 1973.

11. Epshtein, L.A., On Mechanism of Pulse Processes in End Zone of Attached Cavities, *Proc. of Symp. on Physics of Acoustic-Hydrodynamic Phenomena*, Nauka Publishing House, Moscow, 1975 [in Russian].

12. Levkovsky, Yu.L., *Structure of Cavitation Flows*, Sudostroenie Publishing House, Leningrad, 1978 [in Russian].

13. Cox, R.N., Clayden, W.A., *Air Entraiment at the Rear of a Steady Cavity*, Cavitation in Hydrodynamics, London, 1956.

14. Campbell, I.J., Hilborne, D.V., Air Entrainment behind Artificially Inflated Cavities, *Second Symposium on Cavitation on Naval Hydrodynamics,* Washington, 1958.

15. Paryshev, E.V., Theoretical Investigation of Stability and Pulsations of Axisymmetric Cavities, *Trudy TsAGI,* 1978, No. 1907, pp. 17-40 [in Russian].

16. Lapin, V.M., Epshtein, L.A., On Gas Leakage Caused by Cavity Pulsation, Uchenye Zapiski TsAGI, **15**, No. 3, pp. 23-30 [in Russian].

17. Gurevich, M.I., *Theory of Jets in Ideal Fluid.* 2nd Edition, Nauka Publishing House, Moscow, 1979 [in Russian].

18. Migirenko, G.S., Kozyuk, G.S., Maltsev, V.I., Novikov, B.G., Some Methods of Control of Cavitation Flow at Low Magnitudes of Froude numbers, *Unsteady water flow with high velocities, Proc. of Int. Symposium IUTAM,* Nauka Publishing House, Moscow, 1973 [in Russian].

19. Maltsev, L.I., Migirenko, G.S., Mikuta, V.I., Cavitation flows with Cavity Closure on Fluid Jet, In: *Investigations on Developed Cavitation*, In-t of Thermal Physics, Novosibirsk, 1976 [in Russian].

20. Terentiev, A.G., Dimitrieva, N.A. Theoretical Investigation of Cavitating Flows, *Proc. of Third International Symp. on Cavitation*, Grenoble, France, 1998, Vol. 2, pp. 275-280.

21. Garabedian, P.R., Calculation of axially symmetric cavities and jets. *Pac. J. Math.,* 1956, **6**, No. 4, pp. 611-684.

22. Savchenko, Yu.N., Vlasenko, Yu.D., Semenenko, V.N., Experimental study of high–speed cavitated flows, *Int. J. of Fluid Mechanics Research,* 1999, **26**, No. 3, pp. 365-374.

23. Guzevsky, A.G., *Numerical Analysis of Cavitation Flows*, Preprint of In-t of Thermal Physics, Novosibirsk, 1979, pp. 40-79 [in Russian].

24. Guzevsky L.G., Approximation Dependencies for Axisymmetric Cavities past Cones, In: *Hydrodynamic Flows and Wave Processes,* In-t of Thermal Physics, Novosibirsk, 1983, pp. 82-91 [in Russian].

25. Adams, M.C., Sears, W.R., Slender Body Theory. Review and Extensions, *J. of Aeron. Sci.*, 1953, **20**, No. 2., pp. 85-98.

26. Ashley, H., Landahl, M., *Aerodynamics of Wings and Bodies,* Addison-Wesley Publ. Co. Inc., 1968.

27. Grigoryan, S.S., Approximate Solution on Separated Flow around Axisymmetric Body. *Prikladnaya matematika i mehanika,*1959, **23,** No. 5, pp. 951-953 [in Russian].

28. Yakimov, Yu. L. On Axially Symmetric Separated Flow around a Body of revolution at Small Cavitation Numbers, *Prikladnaya matematika i mehanika,* 1968, No. 32, pp. 499-501 [in Russian].

29. Logvinovich, G.V., Serebryakov, V.V., On Methods of Calculating a Shape of Slender Axisymmetric Cavities, *Gidromehanika,* 1975, No. 32, pp. 47-54 [in Russian].

30. Zhuravlyov, Yu.F. Methods of Theory of Perturbations in 3D Jet Flows, *Trudy TsAGI,* 1973, No. 1532, pp. 8-12 [in Russian].

31. Savchenko, Yu.N., Semenenko, V.N., Putilin, S.I., Unsteady Supercavitated Motion of Bodies, *Int. J. of Fluid Mechanics Research*, 2000, **27,** No. 1., pp. 109-137.

32. Buyvol, V.N., *Slender Cavities in Flows with Perturbations*, Naukova Dumka Publishing House, Kiev, 1980 [in Russian].

33. Savchenko, Y.N., Semenenko, V.N., The Gas Absorption into Supercavity from Liquid-Gas Bubble Mixture, *Proc. Third Internat. Symp. on Cavita-tion.* Grenoble, France, 1998, Vol.2, pp. 49-53.

34. Logvinovich, G.V., Buyvol, V.N., Dudko, A.S., et al, *Free Boundary Flows*, Naukova Dumka Publishing House, 1985 [in Russian].

This page has been deliberately left blank

Page intentionnellement blanche

Dynamic Processes of Supercavitation and Computer Simulation

Vladimir N. Semenenko
National Academy of Sciences – Institute of Hydromechanics
8/4 Zhelyabov str., Kyiv, 03057
Ukraine

Summary

This lecture is devoted to unsteady processes in the flows with natural and artificial supercavitation. We consider two classes of phenomena:

1) forced non-stationarity of the flow which is induced by external causes – a model velocity change, an ambient pressure impulse, a variation of gas supply into a cavity etc.;

2) self-exited oscillation arising due to internal instability of gas-filled supercavities.

Results of computer simulation of the dynamic supercavitation processes are presented. They were obtained by using the approximate mathematical model based on the G.Logvinovich independence principle of the supercavity expansion.

A comparison of unsteady behaviour of axisymmetric and two-dimensional supercavities is given. Formulation and solution of two 2-D problems are presented:

1) the problem on instability of the 2-D gas-filled supercavity;

2) the problem on evolution of the 2-D supercavity past an oscillating wedge.

The solutions are based on the M.Tulin's linearized cavitation scheme.

The lecture material is illustrated by sequences of motion-picture frames and photographs of the unsteady supercavitation processes. They were obtained at the hydrodynamic laboratory of the Institute of Hydromechanics of NAS of Ukraine (IHM UNAS).

1 Main types of dynamic supercavitation processes

We consider main types of the supercavitation flows and characteristic for each of them unsteady phenomena which are well simulated by using the accepted mathematical model.

1.1 SUPERCAVITY FORMATION DURING HIGH–SPEED WATER ENTRY

When the high-speed motion in water is experimentally investigated at the IHM UNAS, models are accelerated with the vapor-gas catapult up to velocities 500 ÷ 1400 m/sec, enter into water through the membrane and then move under water on inertia in the natural super-cavitation regime [1, 2]. Length of the distance is 35 m.

Fig. 1 shows consecutive frames of the initial period of the model motion. The cell of the coordinate mesh is 0.2 × 0.2 m. The cavitator diameter of model is D_n = 1.5 mm, the model velocity is V_0 = 980 m/sec. One can see that the cavity formation process has a stage of cavity closure caused by rapid increase of the water pressure when the model and gases penetrate into water. In this case, if a stability of the model motion does not loss, then the normal formation of the supercavity goes on in further.

Paper presented at the RTO AVT Lecture Series on "Supercavitating Flows", held at the von Kármán Institute (VKI) in Brussels, Belgium, 12-16 February 2001, and published in RTO EN-010.

1.2 NATURAL HIGH–SPEED SUPERCAVITIES

A main characteristic peculiarity of high-speed super-cavities is their very huge aspect ratio $\lambda = L_c / D_c$ = 70 ÷ 200, where L_c is the cavity length; D_c is the cavity mid-section diameter. The vapor cavitation number is unique similarity parameter for such flows:

$$\sigma = \frac{2(p_\infty - p_v)}{\rho V^2}, \qquad (1)$$

where p_∞ is the pressure at infinity; p_v = 2350 Pascal is the saturated water vapor pressure (at the temperature 20 °C); ρ is the water density. This type of flow corresponds to the cavitation numbers $\sigma < 10^{-3}$.

Fig. 2 shows a sequence of frames of shooting the high-speed supercavity (D_n = 1.2 mm; V = 1075 m/sec; L_c = 18 m). The shooting frequency in this experiment was N = 4200 frames/sec, the time interval between the frames was $1 / N$ = 0.24 msec.

A typical unsteady process at the high-speed motion of the supercavitating model on inertia is fast decrease of both the velocity and the cavity length. The super-cavitation regime of motion remains until the model is fully placed within the cavity.

The second peculiarity of the high-speed super-cavities is the cavity closure mechanism. The cavities in the described experiments fluently closed practically in a point in contrast to the vapor cavities when cavitation numbers $\sigma < 0.01$. For latter, the unsteady closure with periodic arising reentrant jet is characteristic. It is seen from sequential frames of the experiments that the wake past the cavities has periodic bubble structure. Absolute frequencies of the periodic structure in the wake were in range 80 ÷ 140 kHz in various experiments when D_n = 1.2 ÷ 1.5. In Fig. 2, the frequency is equal to 140 kHz .

The analysis showed that one of causes of the periodic bubble wake formation may be elastic vibrations of the model.

The third peculiarity of the high-speed supercavitation motion in water is the stability mechanism of motion. For the supercavitating models, the classical condition of the motion stability in continuum is not fulfilled. It consists in location of the point of the hydrodynamic force application past the center of the body mass. The experiments showed that the stabilization of free motion of the supercavitating models is attained owing to ricocheting the model tail from the inner cavity walls when $V > 300$ m/sec [1, 2].

In the experiment, action of this stabilization mechanism appears in periodic perturbations of the supercavity surface that develop according to the independence principle. In Fig. 3, two experimental photographs are showed: the model at the time of touching the upper internal cavity wall (a) and the cavity part perturbed owing to contact with the model (b). Exposure time for shooting was $3 \cdot 10^{-6}$ sec.

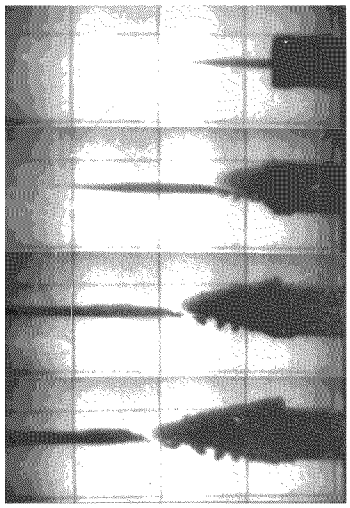


Fig. 1. High-speed water entry: D_n = 1.5 mm, V_0 = 980 m/sec

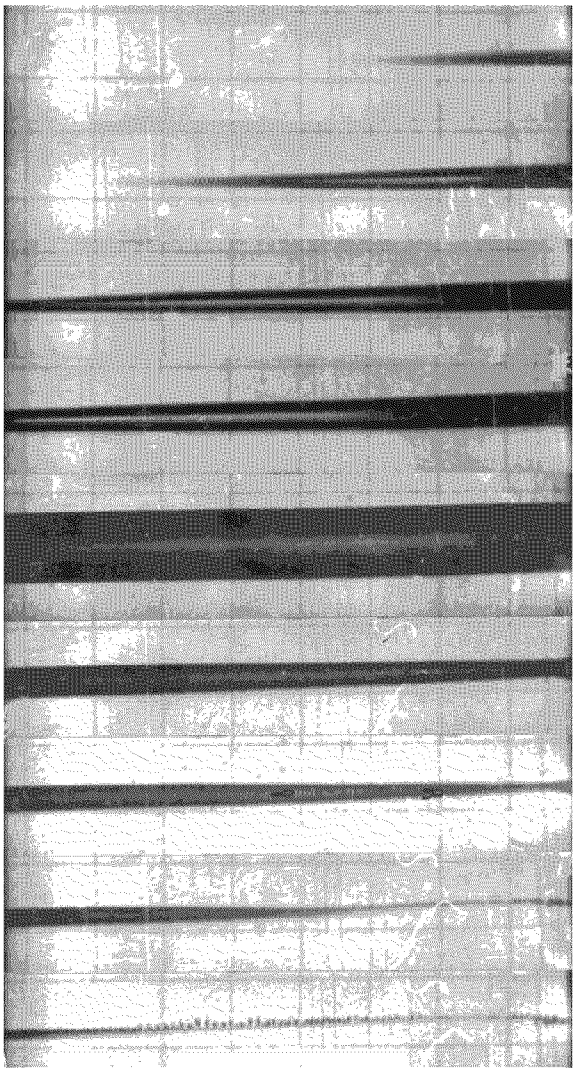


Fig. 2. High-speed supercavity: D_n = 1.2 mm; V = 1075 m/sec

1.3. ARTIFICIAL VENTILATED CAVITIES

The supercavitation regime may be created in water at the moderate velocities $V = 10 \div 100$ m/sec. The basic similarity parameters of the ventilation flow are:

$$\sigma = \frac{2(p_\infty - p_c)}{\rho V^2}, \quad Fr = \frac{V}{\sqrt{gD_n}}, \quad \beta = \frac{\sigma_v}{\sigma}, \tag{2}$$

where $p_c > p_v$ is the cavity pressure; Fr is the Froude number; g is the gravity acceleration; D_n is the cavitator diameter. The cavitation numbers $10^{-2} < \sigma < 0.1$ correspond to this type of flow.

The Froude number Fr characterizes the distorting effect of the gravity on the cavity shape. Estimations show that it is considerable when $\sigma Fr < 2$ [3].

The dynamic similarity parameter $\beta \geq 1$, that is equal to relation of the vapor cavitation number σ_v and its real value σ, plays an important role at calculation of the unsteady ventilation flow.

The value $\beta = 1$ corresponds to the natural supercavitation. When the parameter β increases, significance of elasticity of the gas filling the ventilated cavity increases as well.

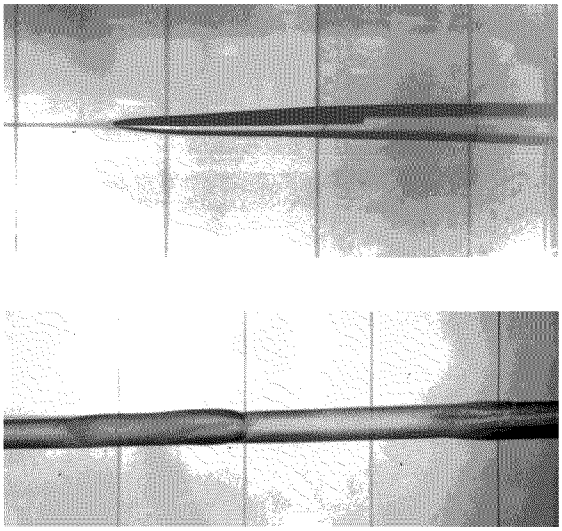


Fig. 3. Cavity perturbation at ricocheting: $D_n = 3$ mm, $V = 690$ m/ sec

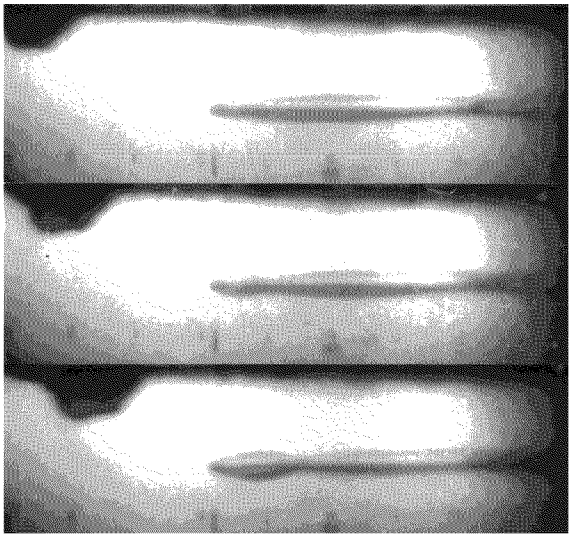


Fig. 4. Ventilated cavity reaction on the pressure impulse: $D_n = 20$ mm, $V = 9$ m/sec

Fig. 4 shows a sequence of motion-picture frames of the ventilated cavity deformation under action of the ambient pressure impulse. The pressure impulse in water was created with the compressed-air catapult. The air bubble created by the catapult is seen in the upper part of the frames. The frames show that the pressure impulse results in the axisymmetric pinch of the cavity.

A characteristic unsteady process for ventilated cavities is the cavity evolution at changing or ceasing the gas-supply. The experiments show that this process is determined by type of the gas-leakage from the cavity [3, 4]. In Fig.5, the typical experimental graphs of $L_c(t)$, $D_c(t)$ are shown when the air-supply was instantly turned on and turned off [5]. The portion type of the air-leakage from the cavity was maintained during this test. It is seen that the cavity length increased by linear law. This process was

decelerated only at approach to the stationary regime. On the contrary, the cavity decreased with increasing speed when the cavity closes.

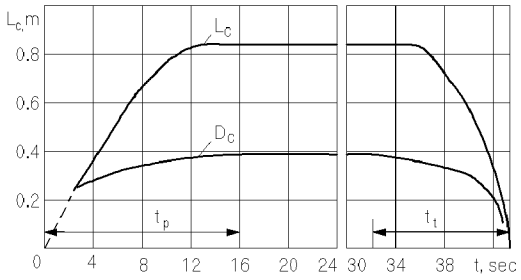


Fig. 5. Ventilated cavity history at air-supply change

1.4 INSTABILITY OF VENTILATED CAVITIES

Arising the self-induced oscillations of the ventilated cavities [6, 7] is interesting unsteady phenomenon. If too many gas is supplied into the cavity, then it can become unstable. In this case waves arise on the cavity surface, it pulsates along the its length and width, the gas-leakage from the cavity is realized by separation of great cavity portions (air pockets). A photograph of pulsating axisymmetric cavity is presented in Fig. 6 (Yu.F.Zhuravlev).

Theoretically, this phenomenon was explained by E.V.Paryshev [8, 9] on the basis of both the G.V.Logvinovich independence principle and the equation of the mass of gas in the cavity balance.

1.5 CAVITIES AFTER THE WATER ENTRY FROM THE ATMOSPHERE

The air cavity forming after water entry of bodies from the atmosphere, closes on the depth or at the water surface depending on the initial conditions [10]. The cavity pressure is lower than atmospheric one at the cavity closure time. During further immersion of the body, the cavity fast decreases because of both the static pressure growth and the loss of the air entrapped from the atmosphere.

The unsteady process of the depth cavity closure is well described by the approximated mathematical model based on the independence principle [11].

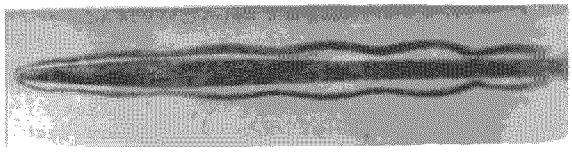


Fig. 6. Pulsating axisymmetric cavity

We have investigated experimentally the interesting phenomenon of wave-shaped deformation of the cavities forming after vertical water entry of bodies with velocity about 10 m/sec [12] (Fig. 7). We showed that cause of this phenomenon consists in excitation of one of fundamental frequencies of the cavity filled by air entrapped from the atmosphere.

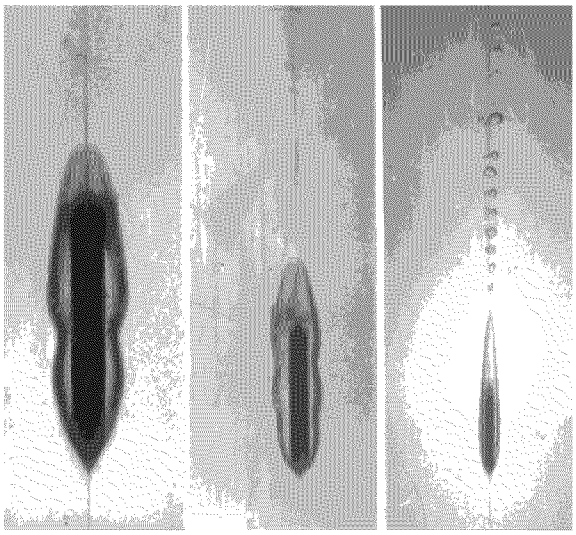


Fig. 7. Cavities after water entry from the atmosphere

2. Mathematical model and calculation algorithm

We use the approximate mathematical model based on the G.V.Logvinovich independence principle of the cavity section expansion for computer simulation of all the mentioned unsteady processes. The mathematical model includes the following equations:

1) The equation of expansion of the unsteady cavity section [13]:

$$\frac{\partial^2 S(\tau,t)}{\partial t^2} = -\frac{k_1 \Delta p(\tau,t)}{\rho}, \quad x(t) - l(t) \le \xi \le x(t), \qquad S(\tau,\tau) = \frac{\pi D_n^2}{4}, \qquad \frac{\partial S(\tau,\tau)}{\partial t} = \frac{k_1 A}{4} D_n V \sqrt{c_x}, \qquad (3)$$

where $\Delta p(\tau,t) = p_\infty(\xi) + p_1(t) - p_c(t)$. Here, $\tau \le t$ is time of section ξ creation; $x(t)$ is the current absolute x-coordinate of the cavitator; $p_1(t)$ is the perturbation of the ambient pressure; $l(t)$ is the cavity length; c_x is the cavitation drag coefficient; $k_1 = 4\pi / A^2$; $A \approx 2$ is the empirical constant. The hydrostatic pressure p_∞ can vary from one section to another when the body moves with the variable depth in ponderable fluid.

2) The equation of the mass of gas in the cavity balance when the gas expands by the isothermal law [8]:

$$\frac{d}{dt}[\overline{p}_c(t)\, Q(t)] = \beta [\dot{q}_{in} - \dot{q}_{out}(t)], \qquad (4)$$

where $\overline{p}_c(t) = p_c(t)/\sigma_0$; σ_0 is the initial cavitation number; Q is the cavity volume; $\dot{q}_{in}$ and $\dot{q}_{out}(t)$ are volumetric rates of air-supply to the cavity and air-leakage from the cavity, respectively, referred to p_∞. We assume that the cavity pressure $p_c(t)$ changes synchronously along the cavity length.

3) The equation of rectilinear motion of the supercavitating model:

$$m\frac{dU}{dt} = \sum F, \qquad (5)$$

where m is the model mass; $U(x,t)$ is the model speed; $\sum F$ is a sum of acting forces (cavitation drag, propeller thrust, gravity when vertical motion etc.). In problems on the supercavitating model dynamics, we use a complete set of the dynamic equation of axisymmetric model [14].

This mathematical model may be applied, strictly speaking, when the parameters change not very fast. In the case of oscillation, we have estimation for dimensionless angular frequency $k << 2\pi\, a / V_\infty$, where a is the sound speed in the gas filling the cavity. It follows from the assumption that the cavity pressure $p_c(t)$ changes synchronously along the cavity length.

We have developed a "fast" numerical algorithm and a number of computer codes on the basis of the Eqs. (3), (4) and (5). That codes allow to reproduce the unsteady supercavitation processes of the mentioned types on a computer screen [2, 15, 16]. Examples of the computer simulation are given below.

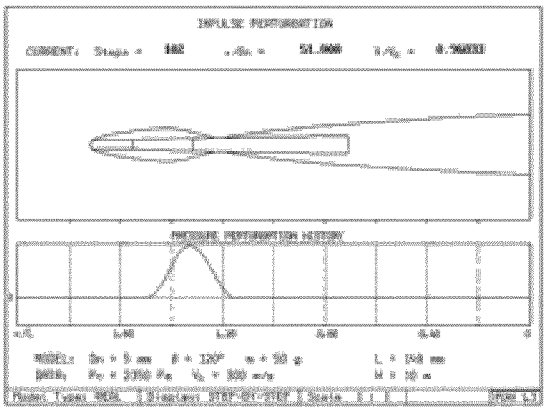


Fig. 8. Result of the PCAV code operation: cavity reaction on the water pressure impulse

3. Cavity deformation under action of the external pressure perturbation

The PCAV code (PerturbedCavity) is intended for computer simulation of supercavity deformation under action of the ambient pressure perturbations in water.

Fig. 8 presents the computer simulation of action of the external pressure impulse imitating the underwater explosion. In this case the cavity pinch occurs when the pressure impulse amplitude is enough. It qualitatively corresponds to the experimental shooting in Fig. 4.

In Fig. 9, a result of computer simulation of the supercavity formation after high-speed water entry through the solid wall is shown. The extra pressure impulse shape $p_1(t)$ in Eq. (3) was evaluated by numerical solving the problem on water penetration of a solid body of revolution. In each time its shape coincides with the cavity shape ("principle of freezing the free boundaries") . The model contour is plotted by thin lines, the cavity contour is plotted by bold lines. The cavity contour at absence of the pressure perturbation is shown by dashed line for comparison. In this case the pressure impulse arising at the water entry of the model results in local pinch of the cavity as well. A comparison with the Fig. 1 shows qualitatively agreement of the calculation and experiment.

The same kind of deformation of the cavity occurs at computer simulation of water entry of the model from within an expanding gas bubble (Fig. 10). In this case the pressure in the fluid may be computed exactly. The model velocity is assumed to be much more than the bubble expansion velocity. The pressure in the cavity is equal to the pressure in the bubble for the starting penetration period.

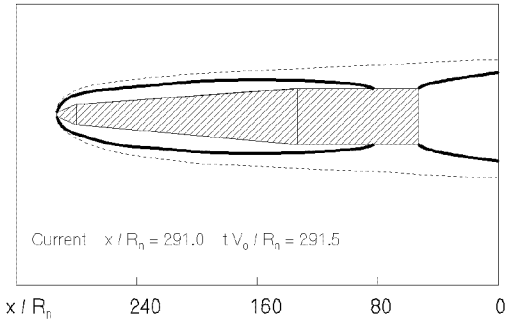


Fig. 9. Result of PCAV code operation: high-speed water entry through a wall

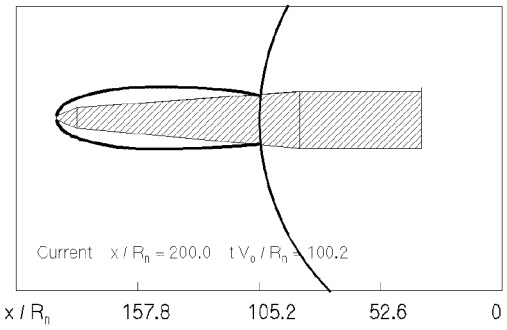


Fig. 10. Result of PCAV code operation: water entry from within an expanding gas bubble

4. Dynamic properties of gas–filled super-cavities

We describe briefly a procedure of the stability analysis and calculation of self-induced oscillation of the axisymmetric gas-filled cavities according to the works [8, 9, 14].

We make dimensionless the Eq. (3) using the initial cavity length l_0 and the velocity V_∞ as scales:

$$\frac{\partial^2 S(\tau,t)}{\partial t^2} = -\frac{k_1 \sigma(t)}{2}, \qquad t - l(t) \le \tau \le t. \tag{6}$$

We consider for simplicity that the cavitator is negligibly small compared to the cavity:

$$S(t,t) = S(t - l(t),t) \to 0, \tag{7}$$

Twice integrating the Eq. (6) with taking account of (7) and using the Dirichlet formula for interchanging integrals, we obtain:

$$S(\tau,t) = \frac{k_1 \sigma_0}{4}\left[t - \tau - 2\int_\tau^t (t-u)\overline{\sigma}(u)du, \right] \tag{8}$$

where $\overline{\sigma}(t) = \sigma(t)/\sigma_0$. Substituting (8) into the cavity closure condition (7), we obtain the equation connecting two unknown functions $\overline{\sigma}(t)$ and $l(t)$:

$$l(t) = 2\int_{t-l(t)}^{t} (t-u)\,\overline{\sigma}(u)du\,. \tag{9}$$

The dimensionless equation of the mass of gas in the cavity balance (4) has the form:

$$\frac{d}{dt}[(\beta - \overline{\sigma}(t))Q(t)] = \beta[\dot{q}_{in} - \dot{q}_{out}(t)]. \tag{10}$$

We calculate the cavity volume, integrating the Eq. (8) along the cavity length and using again the Dirichlet formula:

$$Q(t) = \frac{k_1 \sigma_0}{4}\left[-\frac{l^2(t)}{2} + \int_{t-l(t)}^{t} (t-u)^2\,\overline{\sigma}(u)du \right].$$

The work [3] presents the empirical law of the air-supply for steady axisymmetric cavities when effect of gravity is weak:

$$\dot{q}_{in} = \gamma V_\infty S_c \left(\frac{\sigma_v}{\sigma_0} - 1 \right), \qquad \gamma \approx 0.01 \div 0.02,$$

where $S_c = \pi D_c^2 / 4$ is the cavity mid-section area. We have for the considered processes $p_v << p_\infty$. For the weakly perturbed unsteady cavities, we accept the quasistationary law of the gas-leakage of the same structure [8]:

$$\dot{q}_{out}(t) = \gamma S_c(t) \left(\frac{\beta}{\overline{\sigma}(t)} - 1 \right). \tag{11}$$

The values β = 1, $\overline{\sigma} \equiv 1$ correspond to the natural vapor supercavity. In this case the Eq. (10) is satisfied identically.

4.1 INSTABILITY OF AXISYMMETRIC VENTILATED CAVITIES

A set of the Eqs. (9) and (10) is related to the class of dynamic system with distributed lag [17]. It has the only stationary point $\overline{\sigma}$ = 1, l = 1. We investigate it on stability relatively to small oscillations. Representing the unknown functions in the form:

$$\overline{\sigma}(t) = 1 + \varepsilon \sigma_1(t), \quad l(t) = 1 + \varepsilon l_1(t), \quad \varepsilon \approx o(1),$$

and linearizing the equations and excepting $l_1(t)$, we obtain the uniform equation with respect to $\sigma_1(t)$:

$$\dot{\sigma}_1(t) - 12(\beta - 1) \int_0^1 \theta(\theta - 1) \dot{\sigma}_1(t - \theta) d\theta + \frac{3}{2} \gamma \beta (2\beta - 1) \sigma_1(t) = 0. \tag{12}$$

Following to a usual procedure of investigation of solutions of the equations on stability with respect to small oscillations, we do the substitution in the Eq. (12)

$$\sigma_1(t) = a e^{\mu t}, \qquad \mu = \lambda + jk$$

and obtain its characteristic equation:

$$\mu^3 + \frac{3}{2} \gamma \beta (2\beta - 1) \mu^2 + 12(\beta - 1)[\mu(e^{-\mu} + 1) + 2(e^{-\mu} - 1)] = 0. \tag{13}$$

Here, k is the reduced oscillation frequency, $k = \omega l_0 / V_\infty$; λ is the oscillation increment. The oscillation with frequency k damps when $\lambda < 0$ and increases indefinitely when $\lambda > 0$.

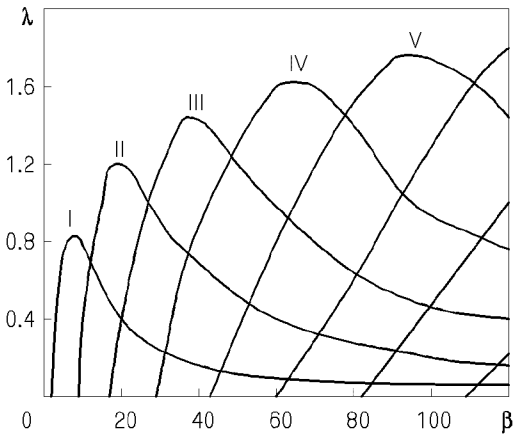


Fig. 11. Real part of the characteristic Eq. (13) roots

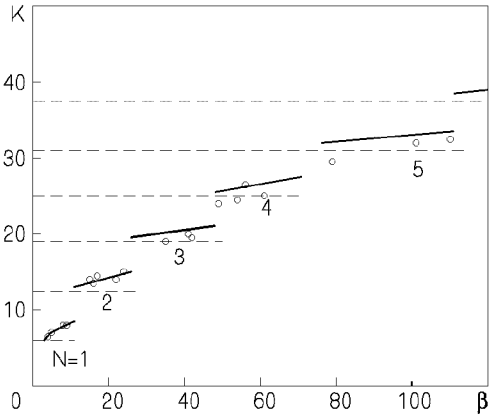


Fig. 12. Modes of the axisymmetric cavity pulsation

In the first case the solution of the Eq. (12) is asymptotically stable, in the second case it is unstable. The frequency k which corresponds to the increment value $\lambda = 0$ is called the fundamental frequency of the dynamic system.

The Eq. (13) contains two physical parameters γ and β. When $\gamma \neq 0$, it has the double root $\mu = 0$ which transforms into threefold one when $\gamma = 0$. It is not difficult to make sure by direct checking that the corresponding secular solutions [17] do not satisfy the Eq. (12). When $\gamma = 0$, the Eq. (13) has a series of the pure imaginary roots, i.e. the fundamental frequencies:

$$k_n = 2\pi n, \qquad \beta_n = 1 + \frac{(\pi n)^2}{6}, \qquad n = 1, 2, \ldots \tag{14}$$

Fig. 11 presents graphs of distribution of the real part of the Eq. (13) roots when $\gamma = 0$. When $\beta \to \infty$, the curves asymptotically approaches to the x-axis. We suppose that the frequency corresponding to the maximal linear increment λ "survives" among severe fundamental frequencies for the given value of β. In a result we obtain estimation of the mode boundaries of the cavity self-induced oscillation (solid lines in Fig. 12).

Thus, when $\gamma = 0$, the cavity is asymptotically stable when $1 \leq \beta < 2.645$ and unstable when $\beta > 2.645$. The value $\gamma = 0$ corresponds to the case when the mass of gas in the cavity is constant. An analysis of the characteristic Eq. (13) shows that it is possible to point a finite interval of changing the value β for each $0 < \gamma < 0.08$. Outside this interval, the zero solution of the Eq. (12) is asymptotically stable, and within this interval it is unstable (Fig. 13). Within the instability zone and when $\gamma \neq 0$, the characteristic equation has the finite number of pure imaginary roots. Their quantity decreases with increasing γ. When $\gamma > 0.08$, roots are absent in general, i.e. the cavity is asymptotically stable for any β.

The established behaviour of effect of the gas-leakage variability on the cavity stability qualitatively explains the experimental fact that the cavity pulsation ceases when the gas-supply becomes very great. So, in the experiments [6, 7], five waves on the pulsating cavities ($N = 5$) have been observed at most.

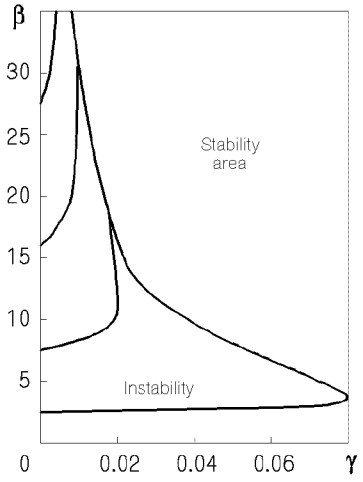


Fig. 13. Influence of the parameter γ

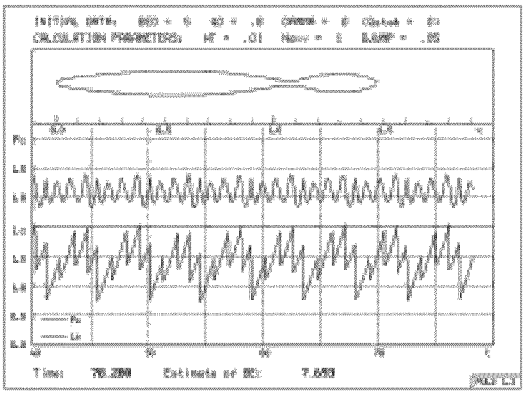


Fig. 14. Result of the PULSE code operation (mode II)

4.2 SELF-INDUCED OSCILLATION OF VENTILATED CAVITIES

For the first time, calculation of self-induced oscillations developing after the stability loss of the ventilated cavity was performed by E.V.Paryshev [9]. We have developed the computer code PULSE that allows to reproduce the cavity pulsation on a computer screen "in real run-time" and to carry out its Fourier analysis [15].

Calculation showed that pulsation arises in the dynamic system described by Eqs. (3) and (4) when the parameter β is in the linear instability zone ($\beta > \beta_1 = 2.645$) . The oscillation develops until the establishment of the periodic or the quasiperiodic pulsation with discontinuous dependence l(t). Fig. 14 shows a view of the computer screen during run-time of the code PULSE. Fig. 15 shows evolution of spectrum of the cavity pressure when the bifurcation parameter $q_0 = \beta_0 \dot{q}_{in}$ increases. Increasing the bifurcation parameter q_0 is accompanied by spasmodic appearance of new frequencies and their linear combinations in the spectrum $\overline{p}_c$. This corresponds to passage up to higher modes of the cavity pulsation. The spectrum $\overline{p}_c$ becomes complicated within each mode, remaining the line one. In this case the basic harmonic changes weakly.

The same behaviour of unsteady ventilated cavities is observed experimentally [6, 7].

Fig. 16 shows spectra of the cavity pressure oscillation under action of forced oscillation of the external pressure $\overline{p}_1(t) = \kappa \sin k_f t$ (q_0 = 0.8, κ = 0.1). The corresponding spectrum $\overline{p}_c(t)$ when the external perturbation is absent is given in Fig. 15, a. We have the modulation when $\tilde{k}_f << \tilde{k}_I$ (a), the synchronization when $\tilde{k}_f \approx \tilde{k}_I$ (b) or the "chaotization" when $\tilde{k}_f > \tilde{k}_I$ (c) of the periodic mode I in depending on a ratio of the forcing frequency $\tilde{k}_f$ to the cavity oscillation frequency $\tilde{k}_I$ (they both are referred to the average cavity length l_m).

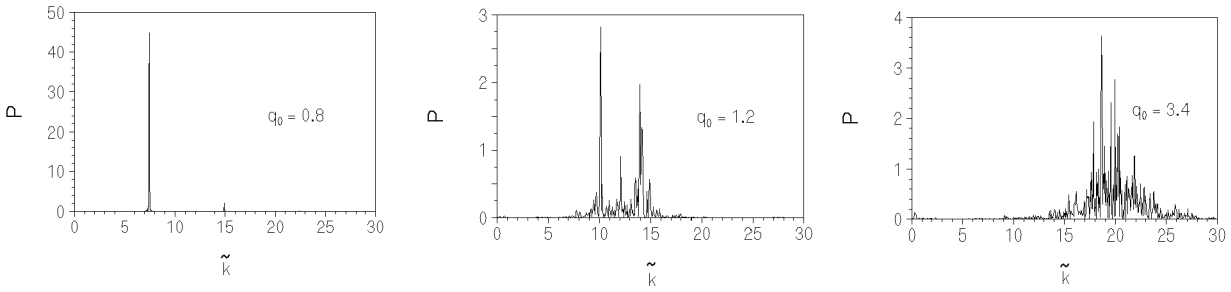


Fig. 15. Power spectral density of $p_c(t)$ at the self-induced oscillation

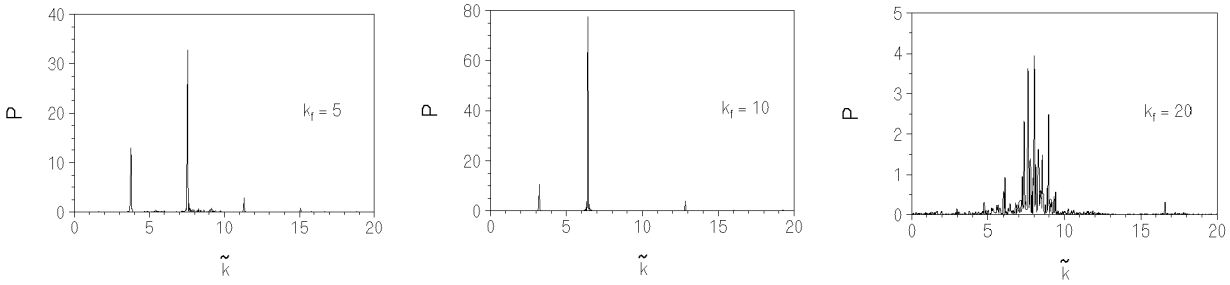


Fig. 16. Power spectral density of $p_c(t)$ at the forced oscillation

4.3 WAVE FORMATION ON THE CAVITY AFTER WATER ENTRY FROM THE ATMOSPHERE

We already spoke of the wave formation phenomenon on the cavities forming at vertical water entry of bodies through the free surface from the atmosphere with the velocities 5 ÷ 10 m/sec [12].

It was established experimentally [18] that the free water surface influence on the drag coefficient c_x and on the cavity shape near the cavitator propagates only on the depth of 1.5 ÷ 2 cavitator diameters. This result gives background to use the approximate Eq. (3) for computer simulation of penetration of the bodies through the free surface into water.

To explain this phenomenon we have applied results of the linear theory of gas-filled supercavity instability. We showed that its cause consists in excitation of one of the fundamental frequencies of the cavity filled by air entrapped from the atmosphere. In the case of enough high both the body mass and the initial Froude number Fr_0, we obtain a priori estimation of the wave number N on the cavity:

$$N = \left[\frac{1}{\pi} \sqrt{\frac{2Eu_0 Fr_0}{B}} \right], \quad B = \sqrt{\sqrt{c_x}}, \tag{15}$$

where $Eu_0 = 2p_{atm} / \rho V_0^2$ is the Euler number. The estimation (15) is in good agreement with the experimental data.

The calculation model of that process after the cavity depth closure includes three Eqs. (3), (4) and (5). Their solution is sought numerically by iteration process for each time step. Fig. 17 presents graphs of both the cavity length and the cavity pressure as functions of the cavitator immersion x. The graph of the dependence $l(x)$ which was calculated without taking account of the air elasticity is plotted by a dashed line. A comparison of the calculated shape and the experimental shape of the cavity for three sequential times is given in Fig. 18.

The obtained good agreement of the calculation and experiment for such complicated unsteady process confirms adequacy of the accepted approximate mathematical model of the unsteady axially symmetric supercavity.

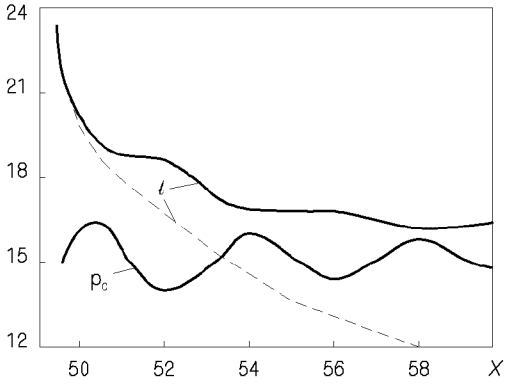


Fig. 17. Cavity history after vertical water entry: graphs of $\overline{p}_c(t)$ and $l(t)$

5. Control of the ventilated cavities

A problem of control of the ventilated cavity is the problem of maintaining the cavity dimensions or of varying the cavity dimensions according to the given law by regulating the gas-supply into the cavity. Examples of the typical control problems are:

1) How should the gas-supply rate be varied for maintenance of the invariable cavity if the motion velocity and/or the motion depth change?

2) What is the law governing the cavity collapse if the gas-supply to the cavity is rapidly stopped?

The difficulty of the problem on the ventilated cavity control is caused by non-linearity and non-monotonicity of the dependence $\dot{q}_{in}(t) = f(\sigma)$ [3, 4] and by the multiparametric nature and lack of knowledge of the gas-leakage laws as well.

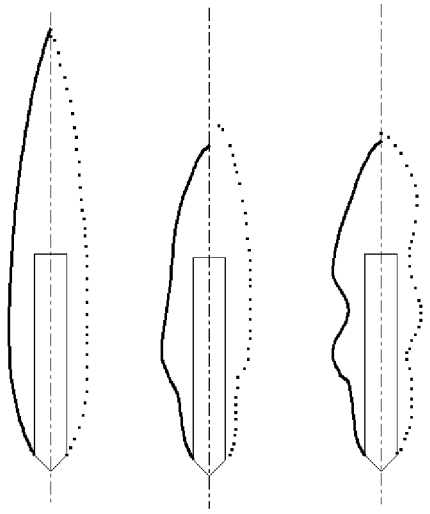


Fig. 18. Cavity history after vertical water entry: ------ - calculation, - - - - experiment

We have developed the computer code ACAV (ArtificialCavitation) for computer simulation of unsteady processes at the ventilated cavity control. It allows to use any laws of varying the air-supply, the air-leakage and the model velocity as well.

Fig. 19 shows a view of the computer screen during run-time of the code ACAV. In this case, the model quasi-stationary law of the gas-leakage from the cavity was used:

$$\dot{q}_{out}(t) = \frac{2 \cdot 10^{-5}}{\sigma^4(t)}. \tag{16}$$

It corresponds to the second type of the gas-leakage by vortex tubes.

In the code ACAV, the set of the Eqs. (3) and (4) is integrated with the constant step with respect to dimensionless longitudinal variable x. During computation in Fig. 19, the gas-supply rate into the cavity increases in 2.4 times on the distance $\Delta x = 0.5$, then remains constant on the distance $\Delta x = 1.0$ and than decreases to its initial value. The calculation gives a characteristic lagging reaction of the cavity on the changing the rate which is observed in experiments.

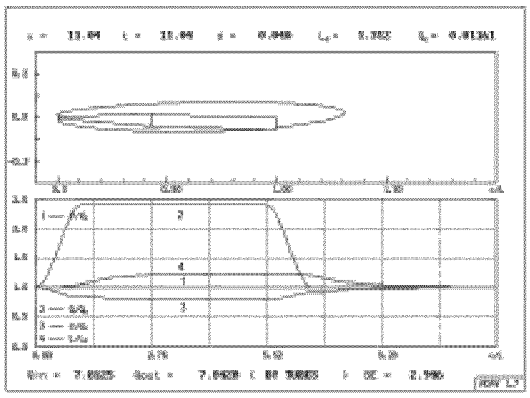


Fig. 19. Result of the ACAV code operation

5.1 CAVITY REACTION ON CHANGING THE GAS–SUPPLY RATE

Firstly we consider peculiarities of the ventilated cavity reaction on changing the air-supply rate $\dot{q}_{in}(t)$ when the model velocity is constant: $V_0 = \text{const}$. Here we present results of computer simulation for two types of changing the supply: 1) impulse increase of the air-supply; 2) rapid single decrease of the air-supply.

At the calculation, we used the following parameters of the model: the disk cavitator with diameter $D_n = 200$ mm; the cavitator slope angle $\delta = 10°$; the model tail diameter $D_s = 350$ mm; the model length $L = 7$ m. Also, we used the following common starting values of the parameters: $V_0 = 100$ m/c; the motion depth $H = 5$ m; $\sigma_0 = 0.04$; the model pitch angle $\psi = 2°$. In this case the starting cavity length is $L_c = 9.06$ m when the balanced air-supply coefficient is $\dot{q}_0 = 7.813$.

In Figs. 20, 21, the following legends are used for marking the curves: 1 – $\dot{q}(t)$; 2 – $\sigma(t)$; 3 – $l(t)$; 4 – $V(t)$.

Fig. 20,a demonstrates a calculation result of the cavity reaction on the impulse increase of the air-supply. One can see that the cavity length reacts on the rate change with greater lagging than the cavity pressure. All the cavity parameters return to their starting values after the impulse end.

A calculation result of the cavity reaction on the rapid decreasing the air-supply is shown in Fig. 20, b. In this case the cavity does a number damped oscillations (a transient process), then establishes new balanced values of the parameters: L_c = 6.09 m; σ =0.06 m; $\dot{q}_{in}$ = 1.563.

A cause of the transient process is the elasticity effect of the gas filling the cavity when the cavity volume rapidly decreases. We note that self-induced oscillations of the cavity may arise for other starting parameters (smaller values of V_0 and higher values of σ_0).

5.2 CAVITY REACTION ON CHANGING THE MODEL VELOCITY

Now we consider peculiarities of the ventilated cavity reaction on varying the model velocity V when the gas-supply rate is constant: $\dot{q}_{in}$ = const.

The calculation result of the ventilated cavity reaction on increasing the model velocity is shown in Fig. 21, a. One can see that the cavity length increases very significantly (in quasi-stationary approximation it is proportional to the velocity square), but the cavity pressure changes weakly. It is typical for this case that the unsteady cavity length considerably exceeds the new balanced level L_c = 13.0 m.

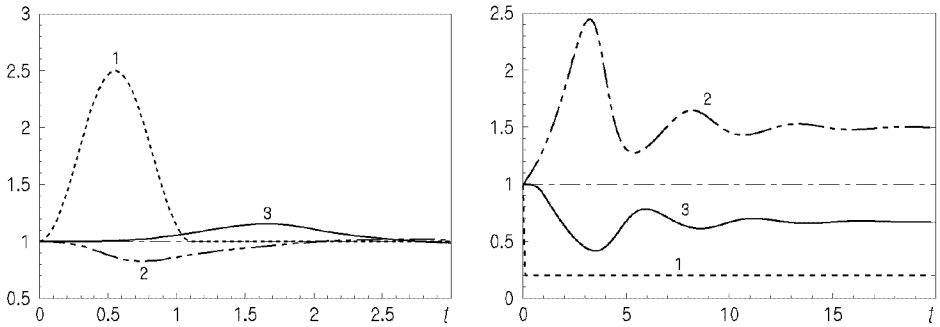
The calculation result of the ventilated cavity reaction on decreasing the model velocity is shown in Fig. 20, b. A comparison with Fig. 20, a shows a difference from the cavity reaction on the air-supply decrease that consists in absence of the transient process. The new balanced cavity length is L_c=2.34m.

We can investigate with the ACAV code the ventilated supercavity behavior when the model motion velocity $V(t)$ and the air-rate into the cavity $\dot{q}_{in}(t)$ change simultaneous. In this case we can try to obtain answers for two practically important questions:

1) May we accelerate the cavity development on the accelerating phase of the body motion by means of increasing the gas-supply into the cavity ?

2) How long may we maintain the cavity with given dimension by means of increasing the gas-supply when the body velocity decreases?

The computer simulation allows to conclude that the air-supply increase when the model velocity increase does not result in considerable decrease of time of the cavity development to the balanced length at the accepted law of the gas-leakage from the cavity (16). This conclusion is valid in the case when the model velocity is already high, and the supercavity already exists.



a *b*

Fig. 20. Cavity reaction on varying the gas-supply rate
a – impulse increasing the gas-supply rate; *b* – rapid decreasing the gas-supply rate

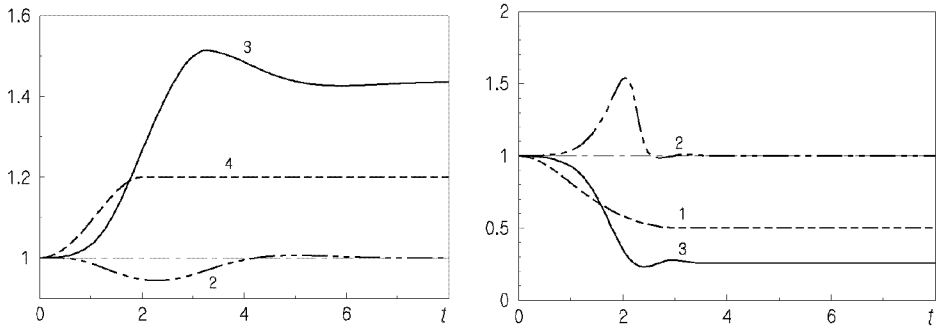


Fig. 21. Cavity reaction on varying the model velocity: *a* – increasing the velocity; *b* – decreasing the velocity

5.3 INFLUENCE OF THE PARAMETER β AND THE GAS–LEAKAGE TYPE

Considerable difference between the natural vapor and ventilated supercavities appears in the case of the unsteady flow. In this case the parameter β is of importance that characterizes effect of elasticity of the gas filling the cavity.

A dependence of changing the cavity length L_c on the parameter β_0 is shown in Fig. 22. The calculation was performed with the code ACAV when D_n = 200 mm. The free cavity closure and the gas-leakage law (16) were accepted at calculation. The cavitation number was constant and equal to σ = 0.06. The starting cavity dimensions were: L_c = 6.04 m, D_c = 0.74 m.

The model velocity firstly increases on 50% along the distance 10 m, then remains constant along the distance 100 m, next decreases to its starting value. A graph of the model velocity variation is shown by dotted line.

The curve 1 corresponds to the natural cavitation regime $\beta \equiv 1$. In this case the starting model velocity was V_0 = 69.5 m/sec.

In the artificial cavitation regime, changing the parameter β at the constant σ is attained by changing the starting model velocity V_0. We used the data:

curve 2 – V_0 = 50 m/sec, β_0 = 1.96;

curve 3 – V_0 = 30 m/sec, β_0 = 5.45.

The presented graphs visually demonstrate increasing the effect of the gas elasticity with increasing the parameter β. In the last case (the curve 3) undamped self-induced oscillations of the cavity develop according to the theory of instability of gas-filled cavities. In this case the starting value of the parameter is β = 7.358 > 2.645, i.e. the cavity is unstable according to (14).

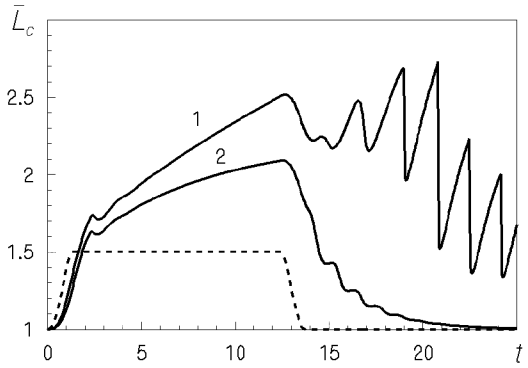


Fig. 22. Influence of the parameter β the cavity behaviour

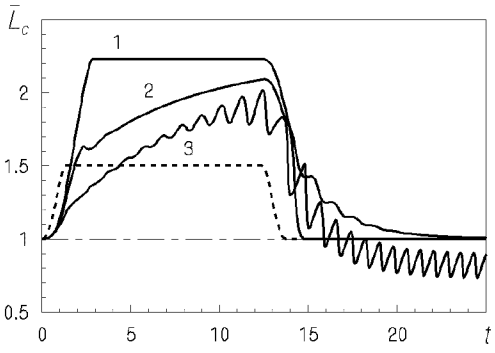


Fig. 23. Cavity behaviour at various on types of the gas-leakage

In Fig. 23, the dependence $L_c(t)$ which has been calculated for different laws of the gas-leakage from the cavity is shown. The model velocity changed in the same way as in Fig. 22. In calculation we assumed that the leakage coefficient is a single-valued function of the cavity pressure: $\overline{Q} = \overline{Q}(p_c)$. Different curves in the figure correspond to the following gas-leakage laws:

curve 1 – the 1st type of the portion gas-leakage ;

curve 2 – the 2nd type of the gas-leakage by vortex tubes, the formula (16).

For the 1st type of the gas-leakage we used a function obtained by the experimental data [4] approximation:

$$\overline{Q} = \frac{5\sigma}{100\sigma^2 + 1}. \tag{17}$$

Considerable difference of the cavity behaviour confirms importance of observance of the gas-leakage type similarity at both the physical modeling and the computer simulation of unsteady ventilated cavities.

Presence of the model body within the cavity decreases active volume of the cavity filled by gas. This does not influence on the cavity dimension in the case of the steady flow at the cavity free closure (if we do not take into account the possible interaction between the model and the reentrant jet). In the non-stationary case we have quite another situation. It is necessary to take into account decreasing the active cavity volume in the equation of the mass of gas balance (4). This causes to changing the dynamic cavity behaviour.

6. Comparison of unsteady behaviour of 2-D and axisymmetric supercavities

It follows from said before that the approximate equation of the cavity section expansion (3) based on the G.V.Logvinovich independence principle gives an effective (and usually unique) method of calculation of the unsteady supercavitation flows.

The independence principle is approximate one, and its verification has great methodological significance. The experimental tests justify its validity in wide range of the parameters [2].

The Eq. (3) well describes the mean part of the supercavity, i.e. it is in essence linear one. A comparison of calculation results of the unsteady cavity shape by the Eq. (3) with the theoretical solutions, which are obtained in the linearized theory of two-dimensional super-cavitation flows [19–22], is of interest.

We use the solutions of two 2-D problems for comparison:

1) the problem on instability of the 2-D gas-filled supercavity;

2) the problem on evolution of the 2-D supercavity at the forced oscillations.

The linear theory application to this problems is correct, because the ventilated cavities always have very great aspect ratio at the time of the stability loss [6, 7].

6.1 MATHEMATICAL MODELS OF THE 2-D UNSTEADY SUPERCAVITY

Two alternative approaches are applied to solve the steady and non-stationary 2-D linearized problems on the supercavitation flow [23, 24]:

1) the method of boundary value problems for analytical functions;

2) the method of integral equations (a variant of the method of boundary integral equations).

The first method gives a solution in the form of quadratures. It is convenient for analytical investigation of stability of the 2-D gas-filled cavity .

The second method is more convenient for numerical calculations when the cavity length is variable. It is easy generalized for the bounded flows, for the super-cavitating hydrofoils in hydrodynamic cascades and for the hydrofoils of finite span as well.

6.1.1 Method of boundary value problem for analytical functions

We construct firstly a solution of the linear unsteady problem by the 1st M.Tulin's scheme (Fig. 24). For simplicity, we consider so called "pure" supercavity, i.e. we assume that the cavitator dimension is negligibly small compared to the cavity.

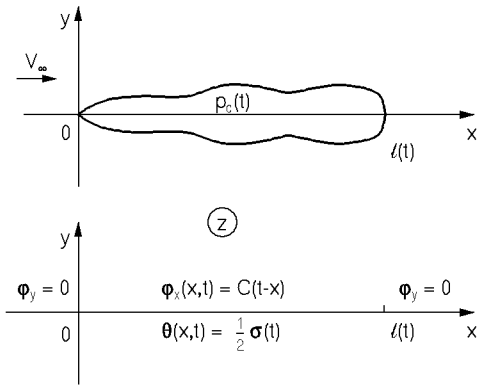


Fig. 24. Two-dimensional "pure" unsteady supercavity
by the 1st M.Tulin's scheme

All the variables are assumed to be dimensionless. The initial cavity length l_0 and the velocity V_∞ are accepted as the length scale and the velocity scale, respectively. We consider two analytical functions:

the complex velocity $\overline{V}(z,t)=\varphi_x-i\varphi_y$ and the complex acceleration potential $\Phi(z,t)=\theta+i\chi$. We have:

$$\theta(x,y,t)=\frac{p_\infty-p(x,y,t)}{\rho}=N\varphi(x,y,t),\quad N=\frac{\partial}{\partial t}+\frac{\partial}{\partial x}. \tag{18}$$

On the *x*-axis, the components of $\Phi(z,t)$ and $\overline{V}(z,t)$ are connected by relations:

$$\theta(x,t)=\theta(-\infty,t)+\varphi_x(x,t)+\int_{-\infty}^{x}\varphi_{xt}(s,t)ds, \tag{19}$$

$$\chi(x,t)=\chi(-\infty,t)-\varphi_y(x,t)-\int_{-\infty}^{x}\varphi_{yt}(s,t)ds. \tag{20}$$

The cavity pressure $p_c(t)$ must be constant at each time along the cavity length. Thus, we have the boundary condition for the acceleration potential:

$$\theta(x,t)=\frac{\sigma(t)}{2},\qquad 0<x<l(t). \tag{21}$$

The cavity length $l(t)$ is an unknown time function. The cavity pressure p_c and, therefore, the cavitation number σ are unknown time functions in the case of the gas-filled supercavity.

Differentiating the Eq. (21) with respect to *x* and applying the inverse operator N^{-1}, we obtain the boundary condition for perturbed horizontal velocity:

$$\varphi_x(x,t)=C(t-x),\qquad 0<x<l(t),$$

where $C(t)$ is an arbitrary time function. Out the interval $[0,l(t)]$ we have $\varphi_y=0$ because of the flow symmetry and absence of sources in the cavity wake.

According to the 1st M.Tulin scheme, the "pure" super-cavity has a shape of ellipse in the stationary case:

$$F(x)/\sigma_0=\frac{1}{2}\sqrt{x(l_0-x)},\qquad 0\le x\le l_0.$$

In the points $z=0,\ z=l_0$, the complex velocity has singularities of the order $O\left(x^{-\frac{1}{2}}\right)$ and $O\left((l_0-x)^{-\frac{1}{2}}\right)$. We assume that the solution must have singularities of the same order for unsteady supercavity in each time on the ends of the interval $[0,l(t)]$.

Thus, we have the mixed boundary value problem for the function $\overline{V}(z,t)$ in the upper half-plane $\operatorname{Im} z>0$:

$$\varphi_y=0,\quad at\quad -\infty<x<0,\quad \varphi_x=C(t),\quad at\quad 0<x<l(t),\quad \varphi_y=0,\quad at\quad l(t)<x<\infty. \tag{22}$$

The solution of this problem in the class of functions unlimited on the ends of interval $[0,l(t)]$ is given by Keldysh-Sedov formula [25]:

$$\overline{V}(z,t)=\frac{1}{4}\sqrt{\frac{l}{z(z-1)}}+\frac{1}{\pi}\sqrt{\frac{z}{z-l}}\int_0^l C(t-s)\sqrt{\frac{l-s}{s}}\frac{ds}{s-z}. \tag{23}$$

Here and later, functions $\overline{V}$ and *C* are related to σ_0.

The solution (23) gives a logarithmic singularity of the pressure at infinity. It is caused by variability of the 2-D closed cavity in unbounded fluid. This methodological paradox disappears when the free boundary is in the flow.

To determine the cavity shape $F(x,t)$ we use the linearized kinematic condition on the cavity boundary [24]

$$\varphi_y(x,t) = N F(x,t), \qquad 0 < x < l(t). \tag{24}$$

From here, using the relation (20) and the Dirichlet formula for interchanging integrals, we obtain the expression for both the shape and the volume of the unsteady symmetric cavity:

$$F(x,t) = \int_0^x (x-s)\chi_t(s,t-x+s)ds - \int_0^x \chi(s,t-x+s)ds, \tag{25}$$

$$Q(t) = -2\int_0^l (l-s)\chi(s,t-l+s)ds, \tag{26}$$

where

$$\chi(x,t) = -\frac{1}{4}\sqrt{\frac{l}{x(l-x)}} + \left(\frac{\overline{\sigma}}{2} + \frac{\dot{q}}{\pi}\ln\frac{2}{\sqrt{l}}\right)\sqrt{\frac{x}{l-x}} - \frac{\dot{q}}{\pi}\arctan\sqrt{\frac{x}{l-x}},$$

$$q(t) = 2\pi\left[\frac{\sqrt{l}}{4} - \frac{1}{\pi}\int_0^l C(t-s)\sqrt{\frac{l-s}{s}}\,ds\right].$$

It is necessary to fulfill the natural boundary condition (21) to eliminate the auxiliary function $C(t)$. Calculating the acceleration potential on the interval $[0, l(t)]$ by the formula (19), we obtain the equation:

$$\frac{\dot{l}}{4\sqrt{l}} + \frac{1-\dot{l}}{\pi}\int_0^l \frac{C(t-s)ds}{\sqrt{s(l-s)}} - \frac{\dot{q}}{\pi}\ln\frac{2}{\sqrt{l}} = \frac{\overline{\sigma}}{2}. \tag{27}$$

The constructed solution of the unsteady problem (23), (27) contains two unknown time functions $\overline{\sigma}(t)$ and $l(t)$. To determinate them we use the condition of the cavity to be close in each time:

$$\int_0^l (l-s)\chi_t(s,t-l+s)ds - \int_0^l \chi(s,t-l+s)ds = 0 \tag{28}$$

and equation of the mass of gas in the cavity balance (4).

In the case of steady flow, the solution (23) has the form:

$$\overline{V}(z) = \frac{1}{2}\left[\frac{l_0}{2\sqrt{z(z-l_0)}} + 1 - \sqrt{\frac{z}{z-l_0}}\right]. \tag{29}$$

We note that the parameters σ_0 and l_0 are independent for stationary "pure" supercavity.

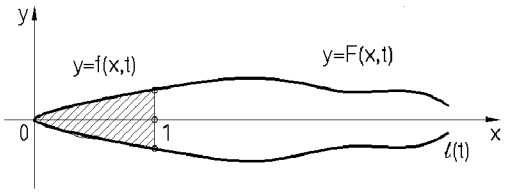


Fig. 25. Unsteady flow around supercavitating wedge

6.1.2. Method of integral equations

Now we construct the solution by the method of integral equations for the unsteady problem on supercavitation flow around a thin symmetric wedge with unit length (Fig. 25). Let the unsteady perturbation of the flow caused by deformation of the wedge sides so that a shape of the wedge is given by the function:

$$y = \pm f(x,t) \sim O(\varepsilon), \quad 0 < x < 1, \tag{30}$$

where ε is the small parameter. In this case the kinematic boundary condition on the upper side of the wedge is added to the boundary conditions (22), (24):

$$\varphi_y = N f(x,t), \quad 0 < x < 1; \qquad y = +0\ . \tag{31}$$

Because of the flow symmetry, we can obtain the flow satisfying the boundary conditions (24), (31) when we place a layer of 2-D sources with the linear intensity $q(x,t)$ on the interval $[0, l(t)]$ of the x-axis. At the arbitrary point (x, y) of the flow, the sources induce the total potential:

$$\varphi(x,y,t) = \frac{1}{2\pi} \int_0^{l(t)} q(s,t) \ln \sqrt{(x-s)^2 + y^2}\, ds. \tag{32}$$

The source intensity is equal to a jump of the normal velocity of the fluid φ_y at passage through the x-axis. We have for the flow symmetric about the x-axis:

$$q(s,t) = 2\varphi_y(s,t), \qquad 0 < s < l(t). \tag{33}$$

Applying the linear operator N to the expression (32), we obtain the acceleration potential of unsteady sources distributed along an interval with a variable length:

$$\theta(x,y,t) = \frac{1}{2\pi} \int_0^{l(t)} q(s,t) \frac{x-s}{(x-s)^2 + y^2} ds + \frac{1}{2\pi} \frac{\partial}{\partial t} \int_0^{l(t)} q(s,t) \ln \sqrt{(x-s)^2 + y^2}\, ds. \tag{34}$$

Passing to the limit $y \to 0$ in Eq. (34) and substituting it in the boundary condition (24), we obtain the integro-differential equation

$$\int_0^{l(t)} \frac{q(s,t)ds}{x-s} + \frac{\partial}{\partial t} \int_0^{l(t)} q(s,t) \ln|x-s|\, ds - \pi\sigma(t) = 0\ , \tag{35}$$

where $1 < x < l(t)$. The intensity of the sources distributed along the interval [0, 1] is known:

$$q(x,t) = 2Nf(x,t), \qquad 0 \le x \le 1.$$

Thus, the Eq. (35) may be finally rewritten in the form:

$$\int_1^{l(t)} \frac{q(s,t)ds}{x-s} + \frac{\partial}{\partial t} \int_1^{l(t)} q(s,t) \ln|x-s|\, ds - \pi\sigma(t) = A_1(x,t), \tag{36}$$

where the function $A_1(x,t)$ in the right part is easy calculated for the concrete law of unsteady deformations of the wedge (30):

$$A_1(x,t) = -2\int_0^1 \frac{Nq(s,t)ds}{x-s} - 2\int_0^1 N\dot{q}(s,t) \ln|x-s|\, ds. \tag{37}$$

Then, we obtain the equation of the upper cavity boundary from the kinematic condition on the cavity (24) when $1 \le x \le l(t)$:

$$F(x,t) = N^{-1}\varphi_y(x,t) = \frac{1}{2}\int_0^x q(s,t-x+s)ds. \tag{38}$$

Since the cavity length $l(t)$ and the cavitation number $\sigma(t)$ are unknown time functions in the general case, it is necessary to add two relations to the Eq. (36):

1) the condition of solvability of the Newmann's external boundary value problem for the velocity potential

$$\int_0^{l(t)} q(s,t)ds = 0; \tag{39}$$

2) the equation of the mass of gas in the cavity balance (4) for gas-filled cavities. In the case of natural vapor supercavities the Eq. (4) is replaced by the condition $p_c = \text{const}$.

As a result, we obtain a set of three equations to determine the functions $q(x,t)$, $l(t)$ and $\sigma(t)$. It must be integrated with respect to time with the initial conditions

$$q(x,0) = q_0(x), \quad l(0) = l_0, \quad \sigma(0) = \sigma_0. \tag{40}$$

The condition (39) ensures limitation of the pressure at infinity. In the partial case of the steady flow, the Eq. (39) is the cavity closure condition. In the case of the unsteady flow, the cavity is unclosed.

It is necessary to distribute 2-D vortexes with the linear intensity $\gamma(x,t)$ along the projection of the foil on the x-axis [24] together with the sources in the general case of nonsymmetric flow around the supercavitating hydrofoil. This adds one more singular integral equation to the set of equations. Our paper [26] presented results of solving the problem on supercavitating flow around an oscillating hydrofoil near the water surface.

6.2. INSTABILITY OF THE 2-D VENTILATED CAVITY

Using the solution of the equation set (27), (28) and (4), we investigate stability of the "pure" 2-D supercavity in the unbounded flow.

According to the experimental data [6] for the steady plane supercavities, the air-supply rate may be approximated by the linear function (in the dimensional form):

$$\dot{q}_{in} = \gamma b_0 V_\infty \left(1 - \frac{\sigma_0}{\sigma_v}\right), \tag{41}$$

where γ is the empirical coefficient; b_0 is the cavity mid-section. It is valid for the steady "pure" cavity (29) that

$$b_0 = \frac{\sigma_0 l_0}{2}.$$

We assume that when oscillation of the cavity pressure is small, the air-leakage rate depends in quasi-stationary way on $p_c(t)$:

$$\dot{q}_{out}(t) = \gamma b(t) V_\infty \left(1 - \frac{\sigma(t)}{\sigma_v}\right). \tag{42}$$

Passing to the dimensionless variables and using the quasi-stationary dependence $b(\sigma)$, we obtain from the Eq. (4):

$$\frac{d}{dt}[(\beta - \overline{\sigma}(t))Q(t)] = \frac{\gamma}{2}(\beta - \overline{\sigma})\left[1 - \frac{1}{\beta} - \frac{1}{\overline{\sigma}}\left(1 - \frac{\overline{\sigma}}{\beta}\right)\right]. \tag{43}$$

The set of equations (27), (28) and (43) relates to the class of nonlinear autonomous equations with distributed lag of Volterra type. Their properties are similar to properties of ordinary differential equations with a lagging argument [17].

This set has the only stationary point $\overline{\sigma} = 1, \quad l = 1, C = 0.5$. It corresponds to the steady supercavity (29). We linearize the equations in the stationary point neighbourhood, representing the unknown functions in the form:

$$\overline{\sigma}(t) = 1 + \varepsilon a e^{\mu t}, \qquad l(t) = 1 + \varepsilon b e^{\mu t}, \qquad C(t) = \frac{1}{2} + \varepsilon c e^{\mu t}$$

and saving the only terms of order $O(\varepsilon)$. Here, $\mu = \lambda + jk, \quad k = \omega l_0 / V_\infty$ is the reduced frequency of the oscillations; *a, b, c* are constants. In this case the integrals in the equations are expressed by the modified Bessel functions of the 1st kind $I_0(\mu/2)$ and $I_1(\mu/2)$ [27]. As a result, we obtain the set of the linear uniform equations with respect to unknowns *a, b, c*. We do not present it here because its awkwardness. Equating the determinant of the equation set to zero, we obtain the characteristic equation:

$$A[\mu^2(I_0^2 - I_1^2) + 2\mu I_0(2I_0 + I_1) + 2I_0^2] + [\mu A \ln 2 + 4(\beta - 1)][2I_0 I_1 + \mu(I_0 + I_1)(I_0 + 3I_1)] = 0, \tag{44}$$

$$A = 8[\mu Q_0 + \gamma(\beta - 1)]/\pi.$$

where $Q_0 = \pi\sigma_0 l_0^2 / 8$ is the volume of the stationary pure" cavity (29).

We suppose firstly that the mass of gas in the cavity is constant, i.e. $\gamma = 0$. In this case the Eq. (44) contains the only physical parameter β. It is easy to make sure that $\mu = 0$ is the only real root of the Eq. (44). Assuming $\lambda = 0$ and using the relations:

$$I_0\left(\frac{jk}{2}\right) = J_0\left(\frac{k}{2}\right), \qquad I_1\left(\frac{jk}{2}\right) = jJ_1\left(\frac{k}{2}\right),$$

where J_0, J_1 are the Bessel functions of the 1st kind, we establish that the Eq. (44) has two series of alternating pure imaginary roots, i.e. frequencies of the fundamental oscillations $k_n^{(1)}, k_n^{(2)}, \ldots$ They satisfy the equations:

$$J_0\left(\frac{k_n^2}{2}\right) = 0, \qquad kJ_1(J_0^2 + J_1^2) + J_0(J_0^2 - J_1^2) = 0.$$

Corresponding values of the parameter β are:

$$\beta_n^{(1)} = 1 + \frac{2Q_0(3\ln 2 - 1)}{3\pi}k^2, \quad \beta_n^{(2)} = 1 + \frac{2Q_0}{\pi}\left[k^2 \ln 2 - \frac{kJ_0(k/2)}{J_1(k/2)}\right]. \tag{45}$$

A numerical analysis of the complex roots of the Eq. (44) shows that we have $\lambda > 0$ when $k_n^{(1)} < k < k_n^{(2)}, \quad n = 1, 2, \ldots,$ i.e. oscillation with such frequencies is unstable. A graph of the dependence

of $\lambda(\beta)$ is presented in Fig. 26. A comparison with Fig. 11 shows that the distributions of the characteristic equation roots is qualitatively similar for the dynamic models of both the two-dimensional and the axisymmetric gas-filled cavities.

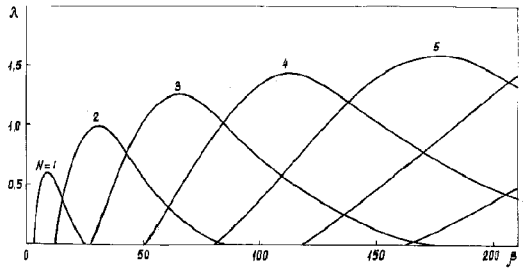


Fig. 26. Real part of the characteristic Eq. (44) roots

When $1 \le \beta < \beta_1^{(1)}$, the steady cavity is asymptotically stable, and when $\beta > \beta_1^{(1)}$, it is unstable. When the parameter β increases and passes through the values $\beta_n^{(1)}$, the oscillations with frequencies $k_n^{(1)}$ are excited. We may suppose that if several frequencies simultaneously exist for the given value of β, the frequency corresponding to the highest coefficient of growth λ becomes dominate when the nonlinear self-induced oscillation of the cavity is establishing. This allows to estimate the limits of modes of the cavity oscillation. A graph of dependence $k(\beta)$ is presented for the first five modes in Fig. 27 (solid lines).

When $\gamma \neq 0$ as in the case of axisymmetric cavities, number of the fundamental cavity frequencies becomes finite. When $\gamma > 0.2153$, the cavity is asymptotically stable for any values of β. According to the data [6] for the stationary cavities past a flat plate perpendicular to the mainstream $\gamma = 2.5 \cdot 10^{-4}$ and effect of taking into account the gas-leakage variability is small.

Table 1. Comparison with experiment (the 1st M.Tulin's scheme)

Unbounded flow				Jet H = 0.254 m				Experiment [6]	
$\beta_N^{(1)}$	$\beta_N^{(2)}$	$k_N^{(1)}$	$k_N^{(2)}$	l_j / H	l_j / l_0	$\beta_N^{(1)}$	$\beta_N^{(2)}$	β_N	k_N
3.081	15.40	4.810	7.088	1.875	0.589	2.226	9.485	5.06	6.15
15.40	42.70	11.28	13.38	2.125	0.515	8.418	22.48	16.1	12.9
42.70	83.60	17.74	19.64	2.000	0.551	23.97	46.51	33.5	18.8
83.60	138.1	24.12	25.90	2.000	0.551	46.51	76.55	55.5	22.9
138.1	206.5	30.47	32.17	1.875	0.589	81.74	122.0	88.7	30.3

The experiments [6] were carried out in a falling jet with the width H = 25.4 cm at the decreased external pressure p_∞. Closeness of the free boundaries of the flow results in decreasing both the length l_j and the volume Q_j of the steady cavity. According to the relations (45) this should affect on the parameter β values. Using the results of the work [28], we obtain the estimation of influence of the jet boundaries on the "pure" supercavity volume when $\sigma \to 0$:

$$\frac{Q_j}{Q_0} \approx \frac{l_j}{l_0}, \qquad \frac{l_j}{l_0} = \frac{l_j}{H} \Big/ \sinh\frac{l_j}{H}.$$

Table 1 represents theoretical values of the parameters β and k for unbounded flow which correspond to the limits of the cavity pulsation modes The parameter β values are recalculated by formulae (45) with taking account of influence of the jet boundaries.

A graph of the theoretical dependence $k(\beta)$ with taking account of the jet boundaries for five modes of the cavity pulsation are plotted in Fig. 27 by dotted lines. Experimental points from [6] also are plotted there by circles. We have a good agreement with taking account of the experimental data dispersion.

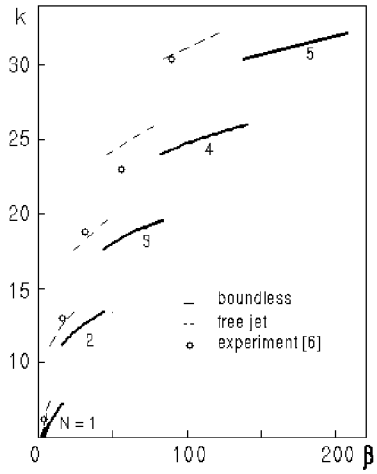


Fig. 27. Modes of the two-dimensional supercavity pulsation

In our work [21], we have investigated stability of the 2-D ventilated supercavities in a free jet with using the 2nd linearized M.Tulin's scheme with the infinite wake and limited pressure at the infinity. We shown that the dynamic properties of both the cavitation schemes are identical.

6.3 THE 2-D SUPERCAVITY SHAPE AT SINUSOIDAL TIME PERTURBATIONS

Now we describe a method of calculation of the length and the shape of the unsteady 2-D supercavity with using the integral Eqs. (36) and (39).

The set of the equations (36), (39) and (4) is nonlinear one, if the cavity length $l(t)$ is considered as an unknown time function. The cause is that variation of the function $l(t)$ has order $l(t) \sim O(1)$ even if $\sigma \sim O(\varepsilon)$ and $\varphi_y(x,t) \sim O(\varepsilon)$, where ε is the small parameter.

We consider a practically important case of periodical dependence of the flow on time [22]. Let the upper wedge side oscillates and deforms sinusoidally

$$f(x,t) = \alpha x + \kappa \operatorname{Re}\{f^*(x)e^{jkt}\}, \tag{46}$$

where $\alpha \sim \kappa \sim O(\varepsilon)$. Here and below, values which are complex with respect to j, are marked by the star. These are named the complex amplitudes.

In the Eq. (36), we replace the time derivative inside the integral and use exponential representation for the time functions with variation of order $O(\varepsilon)$:

$$q(x,t) = \alpha\, q_0(x,l) + \kappa \operatorname{Re}\{q^*(x)e^{jkt}\},\ \sigma(t) = \alpha\sigma_0(l) + \kappa \operatorname{Re}\{\sigma^* e^{jkt}\},$$
$$F(x,t) = \alpha F_0(x,l) + \kappa \operatorname{Re}\{F^*(x)e^{jkt}\}. \tag{47}$$

The first terms in the relations (47) represent quasi-stationary components of the solution, which depend on time only via $l(t)$. The second terms represent non-stationary perturbed components of the solution.

One can show that replacing the time derivative inside the integral and also representation of the solution in the form (47) is equivalent to neglecting some terms. The effect of the latter is essentially decreased with increasing the average cavity length l.

Substituting the expressions (47) into the Eqs. (36) and (39), we obtain a set of the singular integral equations with respect to the complex amplitudes $q^*(x) = q_1(x) + jq_2(x)$ and $\sigma^* = \sigma_1 + j\sigma_2$:

$$\int_1^{l(t)} q^*(s)\left(\frac{1}{x-s} + jk\ln|x-s|\right)ds - \pi\sigma^* = A_1^*(x), \tag{48}$$

$$\int_1^{l(t)} q^*(s)ds = A_2^*, \tag{49}$$

where $A_1^*(x)$, $A_2^*(x)$ are known. When k = 0, we obtain from the Eqs. (48) and (49) the equations to determine the quasi-stationary components $q_0(x)$, σ_0.

We consider the cavity length $l(t)$ as a free time parameter and determine it at the sequential times $t^{(n)} = t^{(n-1)} + \Delta t$ by numerical solving the equation of the mass of gas in the cavity balance (4). In this case the unsteady cavity volume $Q(t^{(n)})$ is calculated by integrating the expression (38). Using the Eq. (38) for the sinusoidal oscillation, we have

$$F^*(x) = \frac{1}{2}e^{-jkx}\int_0^x q^*(s)e^{jks}ds. \tag{50}$$

For each iteration, both the quasi-stationary and the non-stationary parts of the solution are calculated at the same fixed value $l^{(n)}$ from the set of Eqs. (48) and (49) by the numerical method of discrete singularities [24].

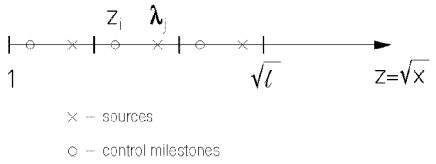


Fig. 28. Discretization of the problem

The numerical method of discrete singularities consists in approximation of the integral Eqs. (48) and (49) by a set of linear algebraic equations. In this case the continuous distribution of sources along the x-axis is replaced by discrete one, and then the quadrature formula of rectangles is applied. Change of variables $x \to z^2$, $s \to \lambda^2$ is preliminarily realized in the integrals to improve the method convergence [24]. The cavity projection is divided into M equal intervals. A point source and a collocation point (control milestones) are located in each interval. The boundary condition (24) is satisfied at the collocation points. Order of location of singularities λ_j and collocation points z_i is determined by the

class of the solution of the singular integral Eq. (48). This solution must be limited at the point of the cavity separation $x = 1$, and it is unlimited at the point $x = l^{(n)}$:

$$z_i = 1 + \Delta z(i - 0.75), \quad \lambda_j = 1 + \Delta z(j - 0.25)\ \Delta z = \frac{\sqrt{l^{(n)}} - 1}{M}, \qquad i, j = 1, 2, \ldots, M. \tag{51}$$

A scheme of the problem discretization is shown in Fig. 28 when $M = 3$.

As a result, separating the real part and the imaginary part, we obtain a set of $2(M + 1)$ linear algebraic equations:

$$\Delta z \sum_{j=1}^{M} \left(\frac{q_{1j}^{(n)}}{z_i^2 - \lambda_j^2} - k q_{2j}^{(n)} \ln \left| z_i^2 - t_j^2 \right| \right) t_j - \frac{\pi}{2} \sigma_1^{(n)} = \frac{1}{2} A_{1,1}^{(n)}(z_i), \qquad i = 1, 2, \ldots, M,$$

$$\Delta z \sum_{j=1}^{M} \left(\frac{q_{2j}^{(n)}}{z_i^2 - \lambda_j^2} - k q_{1j}^{(n)} \ln \left| z_i^2 - t_j^2 \right| \right) t_j - \frac{\pi}{2} \sigma_2^{(n)} = \frac{1}{2} A_{1,2}^{(n)}(z_i), \qquad i = 1, 2, \ldots, M,$$

$$\Delta z \sum_{j=1}^{M} q_{1j}^{(n)} \lambda_j = \frac{1}{2} A_{2,1}^{(n)}$$

$$\Delta z \sum_{j=1}^{M} q_{2j}^{(n)} \lambda_j = \frac{1}{2} A_{2,2}^{(n)}$$

Fig. 29 shows the characteristic wave-like shape of the cavity past the wedge when its sides are performing pitching oscillations about the nose

$$f^*(x) = x$$

for three values of the reduced frequency k.

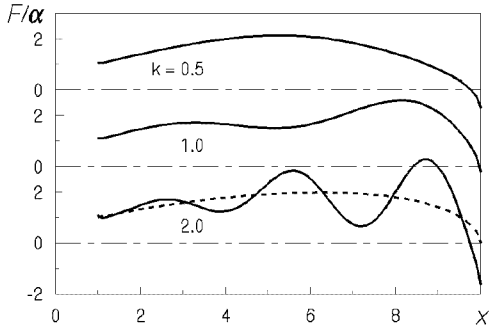


Fig. 29. The cavity shape in dependence on the oscillation frequency: $l_0 = 10.0$, $\overline{\kappa} = 0.1$

In each case the cavity shape was calculated by the Eqs. (47) and (50) at the time t_k when $l(t_k) = l_0$ for convenience of comparison. A shape of the closed stationary supercavity when $k = 0$ is shown by dashed line. When $k > 0$, the cavity is unclosed.

Character of the cavity deformation is the same for different types of oscillations of the wedge. Kinematic waves, which are formed by oscillation of the points of the cavity boundary separation, move along the cavity with the velocity V_∞. Their amplitude increases approximately by linear law.

Graphs of the functions $l(t)$ and $Q(t)$, which are calculated for only period of the oscillation and various values of the relative amplitude $\overline{\kappa} = \kappa / \alpha$, are given in Fig. 30. The wedge sides are wave-likely deformed according to the law (for the upper side):

$$f^*(x) = xe^{-jkx}.$$

One can see that the cavity length oscillation distinguishes more and more from sinusoidal one when the amplitude $\overline{\kappa}$ increases. The same occurs when the reduced frequency k increases. The functions $l(t)$ and $Q(t)$ become discontinuous when $\overline{\kappa}$ and/or k exceed the some critical values.

Fig. 31 shows time dependence of the axisymmetric cavity length and volume that calculated with the code PULSE. Here, a cause of the cavity unsteady perturbation is the ambient pressure oscillation:

$$\beta(t) = \beta_0(1 + \overline{\kappa}\cos kt).$$

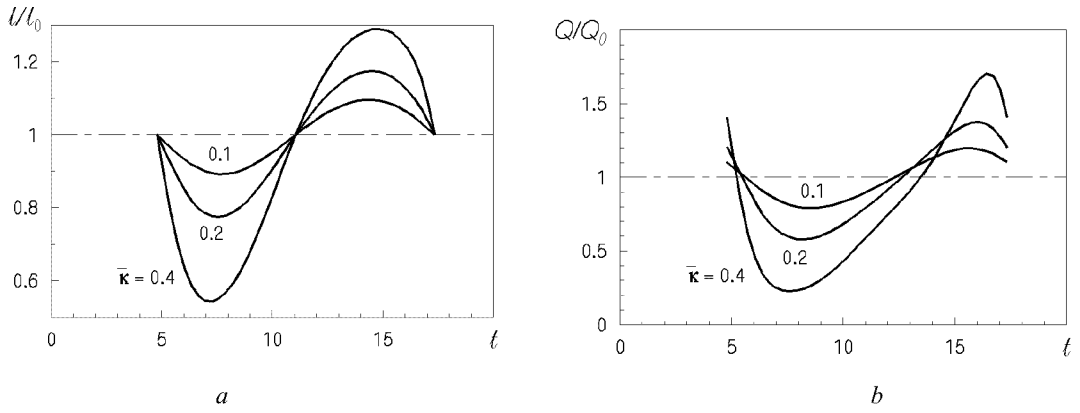


Fig. 30. Influence of the oscillation amplitude on the functions $l(t)$ (a) and $Q(t)$ (b): $l_0 = 6.0$, $k = 0.5$ (wave-like deformation of the wedge)

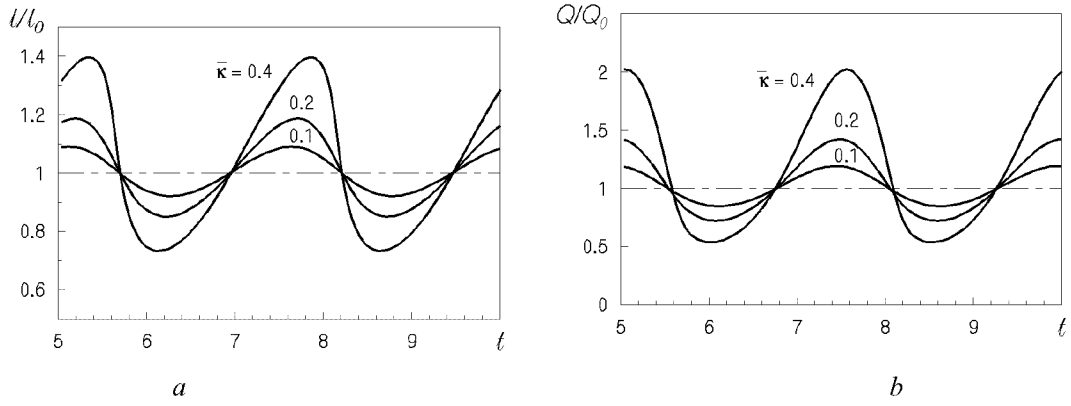


Fig. 31. History of the length (a) and the volume (b) of the axisymmetrical supercavity: $\beta_0 = 1.0$; $k = 2.5$ (the ambient pressure pulsation)

A comparison of graphs in Figs. 30 and 31 shows that shape of the graphs of $l(t)$ and $Q(t)$ for the axisymmetric and the two-dimensional cavities is qualitatively similar in the case of nonlinear

oscillations. When the oscillation frequency and amplitude increases, their shape more and more deviates from sinusoidal one having a shape of a "falling wave". When the frequency and/or the amplitude exceed some critical values k_{cr} and $\bar{\kappa}_{cr}$, the functions $l(t)$ and $Q(t)$ become discontinuous.

The same kind of behaviour of the unsteady supercavities is observed at the experiments for both the axisymmetric and two-dimensional cavities [29].

References

1. Savchenko, Yu.N., Vlasenko, Yu.D. and Semenenko, V.N., Experimental Study of High-Speed Cavitated Flows, *Int. J. of Fluid Mechanics Research*, 1999, **26**, No. 3, pp. 365-374.

2. Savchenko, Yu.N., Semenenko, V.N., and Putilin, S.I., Unsteady Supercavitated Motion of Bodies, *Int. J. of Fluid Mechanics Research,* 2000, **27**, No. 1, pp.109-137.

3. Logvinovich G.V., *Hydromechanics of Free-Boundary Flows*, Halsted Press, 1973.

4. Epshtein, L.A., *Methods of Theory of Dimensionality and Similarity in Problems of Ship Hydromechanics*, Sudostroenie Publishing. House, Leningrad, 1970 [in Russian].

5. Korolyev, V.I., Vlasenko, Yu.D., and Boyko, V.T., Experimental Investigation of the Cavity Development at Unsteady Gas Cavitation, *Gidromehanika*, 1973, No. 24, pp. 79-83 [in Russian].

6. Silberman, E., Song, C.S. Instability of Ventilated Cavities , *J. of Ship Res*., 1961, **5**, No. 1, pp. 13-33.

7. Michel, J.M., Ventilated Cavities. A Contribution to the Study of Pulsation Mechanism, *Unsteady water flows with high velocities, Proc. of International Symp. IUTAM*, Nauka Publishing House, 1973, pp. 343-360.

8. Paryshev, E.V., Theoretical Investigation of Stability and Pulsations of Axially Symmetric Cavities, *Trudy TsAGI,* 1978, No. 1907, pp. 17-40 [in Russian].

9. Paryshev, E.V., Numerical Modeling of Ventilated Cavity Pulsations, *Trudy TsAGI,* 1985, No. 2272, pp. 19-28 [in Russian].

10. Knapp, R.T., Daily, J.W., Hammitt, F.G., *Cavitation*, McGraw-Hill, New York, 1970.

11. Zhuravlyev, Yu.F., Methods of Theory of Perurbations in Three-Dimensional Jet Flows, *Trudy TsAGI,* 1973, No. 1532, pp. 8-12 [in Russian].

12. Savchenko, Yu.N., Semenenko, B.H. Wave Formation on the Boundaries of Cavities Forming at Water Entry of a Disk and Cones, In: *Problems of High-speed Fluid Mechanics,* Chyvashi University Press, Cheboksary, 1993, pp. 231-239 [in Russian].

13. Logvinovich, G.V., Syeryebryakov, V.V., On Methods of Calculations of Slender Asisymmetric Cavities, *Gidromehanika,* 1975, No. 32, pp. 47-54 [in Russian].

14. Semenenko, V.N., Computer Simulation of Dynamics of Supercavitating Bodies, *Prykladna gidromehanika,* 2000, **2**, No. 1, pp. 64-69 [in Russian].

15. Semenenko, V.N., Computer Modeling of Pulsations of Ventilated Supercavities, *Int. J. of Fluid Mechanics Research*, 1996, **23**, Nos. 3 & 4, pp. 302-312.

16. Semenenko, V.N., Computer Simulation of the Unsteady Supercavitating Flows, *High Speed Body Motion in Water (AGARD Report 827), Proc. Fluid Dynamics Panel Workshop*, Kiev, 1997.

17. Elsgolts, L.E., Norkin, S.B., *Introduction in Theory of Differential-Delay Equations*, Nauka Publishing House, Moscow, 1971 [in Russian].

18. Logvinovich, G.V., Yakimov Yu.L., High-Speed Immersion of Bodies in Fluid, *Unsteady water flows with high velocities, Proc. of International Symp. IUTAM*, Nauka Publishing House, Moscow, 1973, pp. 85-92.

19. Semenenko, V.N., Instability of a Plane Ventilated Supercavity in an Infinite Stream, *Int. J. of Fluid Mechanics Research*, 1996, **23,** Nos. 1 & 2, pp. 134-143.

20. Semenenko, V.N., Instability and Oscillation of Gas-Filled Supercavities, *Proc. Third International Symp. on Cavitation,* Grenoble (France), 1998, **2,** pp. 25-30.

21. Semenenko, V.N., Instability of a Plane Ventilated Supercavity in an Free Jet, *Prykladna gidromehanika,* 1999, **1**, No. 2, pp. 45-52 [in Russian].

22. Semenenko, V.N., Calculation of Shape of Plane Supercavities at Harmonic Oscillations, *Prykladna gidromehanika,* 2000, **2**, No. 3, pp. 87-93 [in Russian].

23. Tulin, M.P., Supercavitating Flows – Small Perturbation Theory, *J. of Ship Research,* 1964, **7,** No. 3, pp. 16-37.

24. Yefremov, I.I. *Linearized Theory of Cavitation Flow,* Naukova Dumka Publishing House, Kiev, 1974 [in Ukrainian].

25. Gakhov, F.D., *Boundary value problems,* 3rd Revised and Supplemented Edition, Fizmatgiz Publishing House, 1977 [in Russian].

26. Semenenko, V.N., Unsteady Flow Calculations Past Ventilated Hydrofoils, *Proc. Seventh International Conf. on Numerical Ship Hydrodynamics,* Nantes (France), 1999.

27. Abramovitz, M., Stegun, I. (Editors), *Handbook of mathematical functions with formulae, graphs and mathematical tables*, National Bureau of Standards, Applied Mathematics Series, 1964.

28. Epshtein, L.A., Lapin, V.M. Approximate calculation of influence of Flow Boundaries in Two-Dimensional Problem and past an Axisymmetric Body, *Trudy TsAGI,* 1980, No. 2060, pp. 3-24 [in Russian].

29. Nishiyama, T., Unsteady Cavity Flow Model for Two Dimensional Super-cavitating Hydrofoils in Oscillation, *Technology Reports*, Tohoku Univ., 1982, **46,** No. 2, pp. 199-216.

Multiphase CFD Modeling of Developed and Supercavitating Flows

Robert F. Kunz

Jules W. Lindau

Michael L. Billet

David R. Stinebring

The Pennsylvania State University Applied Research Laboratory

PO Box 30

University Park, PA 16804

USA

Abstract

Engineering interest in natural and ventilated cavities about submerged bodies and in turbomachinery has led researchers to study and attempt to model large scale cavitation for decades. Comparatively simple analytical methods have been used widely and successfully to model developed cavitation, since the hydrodynamics of these flows are often dominated by irrotational and rotational inviscid effects. However, a range of more complex physical phenomena are often associated with such cavities, including viscous effects, unsteadiness, mass transfer, three-dimensionality and compressibility. Though some of these complicating physics can be accommodated in simpler physical models, the ongoing maturation and increased generality of multiphase Computational Fluid Dynamic (CFD) methods has motivated recent research by a number of groups in the application of these methods for developed cavitation analysis. This paper focuses on the authors' recent research activities in this area.

The authors have developed an implicit algorithm for the computation of viscous two-phase flows. The baseline differential equation system is the multi-phase Navier-Stokes equations, comprised of the mixture volume, mixture momentum and constituent volume fraction equations. Though further generalization is straightforward, a three-species formulation is pursued here, which separately accounts for the liquid and vapor (which exchange mass) as well as a non-condensable gas field. The implicit method developed employs a dual-time, preconditioned, three-dimensional algorithm, with multi-block and parallel execution capabilities. Time-derivative preconditioning is employed to ensure well-conditioned eigenvalues, which is important for the computational efficiency of the method. Special care is taken to ensure that the resulting eigensystem is independent of the density ratio and the local volume fraction, which renders the scheme well-suited to high density ratio, largely phase-separated two-phase flows characteristic of developed and supercavitating systems. A dual-time formulation is employed to accommodate the inherently unsteady physics of developed and super-cavities. We have recently extended the formulation for compressible constituents to accommodate analysis of high speed projectiles and rocket plumes, and these formulation elements are also summarized. To demonstrate the validation status and general capabilities of the scheme, numerous examples are presented.

Nomenclature

Symbols

A_j	flux Jacobians
C_μ, C_1, C_2	turbulence model constants
C_{dest}, C_{prod}	mass transfer model constants
C_i	pseudo-sound speed
C_P	pressure coefficient
C_D	drag coefficient
D	source Jacobian

Paper presented at the RTO AVT Lecture Series on "Supercavitating Flows", held at the von Kármán Institute (VKI) in Brussels, Belgium, 12-16 February 2001, and published in RTO EN-010.

d	body diameter
d_m	bubble diameter
e	total energy per unit volume
E, F, G	flux vectors
f	frequency
g_i	gravity vector
h	enthalpy
H	source vector
I	identity matrix
J	metric Jacobian
K_j	transform matrix
k	turbulent kinetic energy
L	bubble length
$M, M_j, +$	Mach number, similarity transform matrices
$\dot{m}$, $\dot{m}$	mass transfer rates
P	turbulent kinetic energy production
$Pr_{tk}, Pr_{t\varepsilon}$	turbulent Prandtl numbers for k and ε
p	pressure
Q	transport variable vector
Re	Reynolds number
Str	Strouhal number
s	arc length along configuration
t, t_∞	time coordinate, mean flow time scale (d/U_∞)
U_j	velocity magnitude, contravariant velocity components
u_i, u, v, w	Cartesian velocity components
x_j	Cartesian coordinates
Y	mass fraction
α	volume fraction, angle-of-attack
β	preconditioning parameter
Γ, Γ_e	time derivative preconditioning and transform matrices
ε	turbulence dissipation rate, numerical Jacobian parameter, internal energy per unit mass
κ, ϕ	MUSCL parameters
Λ_j, λ_j	eigenvalues
μ	molecular viscosity
ρ	density
σ	cavitation number
τ	pseudo-time coordinate
ν	dissipation sensor
ξ_j	curvilinear coordinates

Subscripts, Superscripts

1ϕ	single-phase value
i, j	coordinate indices
k	constituent index, pseudo-time-step index
L, R	dependent variable values on left and right of face
l	liquid
m	mixture
ng	non-condensable gas
t	turbulent
v	condensable vapor, viscous
∞	free stream value
$\hat{}$	transformed to curvilinear coordinates
+/-	production/destruction, right/left running
~	with respect to mixture
Y	mass fraction form

Introduction

Multi-phase flows have received growing research attention among CFD practitioners due in large measure to the evolving maturity of single-phase algorithms that have been adapted to the increased complexity of multi-component systems. However, there remain a number of numerical and physical modeling challenges that arise in multi-phase CFD analysis beyond those present in single-phase methods. Principal among these are large constituent density ratios, the presence of discrete interfaces, significant mass transfer rates, non-equilibrium interfacial dynamics, compressibility effects associated with the very low mixture sound speeds which can arise, the presence of multiple constituents (viz. more than two) and void wave propagation. These naturally deserve special attention when a numerical method is constructed or adapted for multi-phase flows.

The class of multiphase flows under consideration here is developed- and super-cavitating flows, wherein significant regions of the flow are occupied by gas phase. Depending on the configuration, such "developed" [38] cavities are composed of vapor and/or injected non-condensable gas.

Historically, most efforts to model large cavities relied on potential flow methods applied to the liquid flow, while the bubble shape and closure conditions were specified. Adaptations of potential flow methods remain in widespread use today ([15]), due to their inherent computational efficiency, and their proven effectiveness in predicting numerous first order dynamics of supercavitating configurations.

Recently, more general CFD approaches have been developed to analyze these flows. In one class of methods, a single continuity equation is considered with the density varying abruptly between vapor and liquid densities through an equation of state. Such "single-continuity-equation-homogeneous" methods have become fairly widely used for sheet and supercavitation analysis ([8], [9], [25], [35], [43], for example). Although these methods can directly model viscous effects, they are inherently unable to distinguish between condensable vapor and non-condensable gas, a requirement of ventilated supercavitating vehicle analysis.

By solving separate continuity equations for liquid and gas phase fields, one can account for and model the separate dynamics and thermodynamics of the liquid, condensable vapor, and non-condensable gas fields. Such multi-species methods are also termed homogeneous because interfacial dynamics are neglected, that is, there is assumed to be no-slip between constituents residing in the same control volume. A number of researchers have adopted this level of differential modeling, mostly for the analysis of natural cavitation where two phases/constituents are accounted for ([1], [23], [32], for example). This is the level of modeling employed here, though a three-species formulation is used to account for two gaseous fields. For two phases/constituents these methods are very closely related to the "single-continuity-equation-homogeneous" methods addressed above with interfacial mass transfer modeling supplanting an equation of state.

Full-two-fluid modeling, wherein separate momentum (and in principle energy) equations are employed for the liquid and vapor constituents, have also been utilized for natural cavitation [12]. However, in sheet-cavity flows, the gas-liquid interface is known to be nearly in dynamic equilibrium; for this reason, we do not pursue a full two-fluid level of modeling.

Sheet- and super-cavitating flows are characterized by large density ratios ($\rho_l/\rho_v > 10^4$ is observed in near-atmospheric water applications), relatively discrete cavity-free stream interfaces and, due to ventilation, multiple gas phase constituents. Accordingly, the CFD method employed must accommodate these physics effectively.

Most relevant applications exhibit large scale unsteadiness associated with re-entrant jets, periodic ejection of non-condensable gas, and cavity "pulsations". Accordingly, we and others ([23], [26], [32], [35], for example) employ a time-accurate formulation in the analysis of large scale cavitation.

Compressibility

The compressibility of the liquid and gas phase constituents can significantly influence supercavitating flow configurations in three ways. First, regions of high gas volume fraction *bubbly* flow can exist if the cavity does not fully envelop the body, or if the cavitator is either poorly designed or operating off-design. In these circumstances the two-phase mixture can have a sound speed significantly lower than that of either liquid or gas constituents, as illustrated in Figure 1. This can affect hydrodynamic performance and gives rise to the cloud collapse physics responsible for cavitation damage.

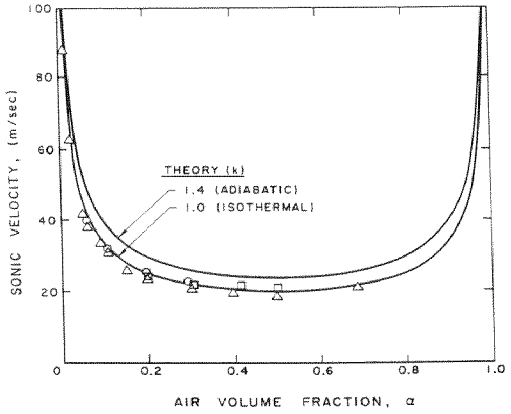


Figure 1. Variation of mixture sound speed in a bubbly air/water mixture. (From Brennan[4].)

The second compressibility issue arises in candidate rocket propulsion systems for very high speed underwater vehicles where exhaust velocities are supersonic (relative to propellant sound speed). Thirdly, very high speed underwater projectiles (i.e., unpropelled supercavitating darts) can be deployed at speeds which are supersonic with respect to the local sound speed of water. This application also requires a compressible CFD formulation ([30], for example). These compressibility effects have motivated several authors to employ compressible formulations ([1], [3], [30], [43] for example) and the present authors have recently extended our baseline formulation to accommodate compressible constituents.

The purpose of this paper is to present the numerical methods and physical models employed, and many of the applications pursued in the authors' research. The paper is organized as follows: The theoretical formulation of the method is summarized, including the baseline differential model, inviscid eigensystem, physical models, compressibility and key elements of the numerical method. Particular emphasis is placed on unique aspects of the numerics including the preconditioning strategy, resultant eigensystem characteristics, and flux evaluation and limiting strategies associated with the resolution of interfaces. This is followed by three sets of results. The first set includes axisymmetric steady-state and transient analyses of natural and ventilated cavitation about several configurations. These solutions are compared to experimental measurements to demonstrate the capability of the modeling employed. The second set of results includes a variety of three-dimensional analyses of sheet- and supercavitating flows of relevance to high speed vehicles and turbomachinery. The third set of results includes compressible simulations of a vehicle propulsion plume and a high speed supercavitating projectile.

Theoretical Formulation

Governing Equations

The baseline governing differential system employed is cast in Cartesian coordinates as:

$$\left(\frac{1}{\rho_m \beta^2}\right)\frac{\partial p}{\partial \tau}+\frac{\partial u_j}{\partial x_j} = (\dot{m}^+ + \dot{m}^-)\left(\frac{1}{\rho_l}-\frac{1}{\rho_v}\right)$$

$$\frac{\partial}{\partial t}(\rho_m u_i)+\frac{\partial}{\partial \tau}(\rho_m u_i)+\frac{\partial}{\partial x_j}(\rho_m u_i u_j) =$$

$$-\frac{\partial p}{\partial x_i}+\frac{\partial}{\partial x_j}\left(\mu_{m,t}\left[\frac{\partial u_i}{\partial x_j}+\frac{\partial u_j}{\partial x_i}\right]\right)+\rho_m g_i$$

$$\frac{\partial \alpha_l}{\partial t}+\left(\frac{\alpha_l}{\rho_m \beta^2}\right)\frac{\partial p}{\partial \tau}+\frac{\partial \alpha_l}{\partial \tau}+\frac{\partial}{\partial x_j}(\alpha_l u_j) = (\dot{m}^+ + \dot{m}^-)\left(\frac{1}{\rho_l}\right)$$

$$\frac{\partial \alpha_{ng}}{\partial t}+\left(\frac{\alpha_{ng}}{\rho_m \beta^2}\right)\frac{\partial p}{\partial \tau}+\frac{\partial \alpha_{ng}}{\partial \tau}+\frac{\partial}{\partial x_j}(\alpha_{ng} u_j) = 0 \quad , \tag{1}$$

where α_l and α_{ng} represent the liquid phase and non-condensable gas volume fractions, and mixture density and mixture turbulent viscosity are defined as:

$$\rho_m \equiv \rho_l \alpha_l + \rho_v \alpha_v + \rho_{ng} \alpha_{ng}$$

$$\mu_{m,t} = \frac{\rho_m C_\mu k^2}{\varepsilon} \tag{2}$$

In this *baseline* formulation, the density of each constituent is taken as constant. The mass transfer rates from vapor to liquid and from liquid to vapor are denoted $\dot{m}^+$ and $\dot{m}^-$, respectively. Mass transfer terms appear in the mixture continuity equation because this equation is a statement of mixture volume conservation. Also, note that each of the equations contains two sets of time-derivatives - those written in terms of the variable "t" correspond to physical time terms, while those written in terms of "τ" correspond to pseudo-time terms that are employed in the time-iterative solution procedure. The forms of the pseudo-time terms will be discussed presently.

In the development of the differential system presented above, a number of physical, numerical, and practical issues were considered. First, a mixture *volume* continuity equation is employed rather than a mixture mass equation. This initial choice was made based on the authors' experience that the *nonlinear* performance of segregated pressure based algorithms [17] is improved by doing so for high density ratio multi-phase systems. Because of this choice, neither a physical time derivative nor mixture density appears in the continuity equation, although the mixture density can vary in space and time. To render the system hyperbolic and to facilitate the use of time-marching procedures, we then introduce a pseudo-time derivative term (signified by "τ") in the mixture continuity equation, a strategy that derives from the work of Chorin [7] and others.

Second, corresponding artificial time-derivative terms are also introduced in the component phasic continuity equations, which ensures that the proper differential equation (in non-conservative form) is satisfied. That is, combining equations [1]a and [1]c:

$$\frac{\partial \alpha_l}{\partial t}+\left(\frac{\alpha_l}{\rho_m \beta^2}\right)\frac{\partial p}{\partial \tau}+\frac{\partial \alpha_l}{\partial \tau}+\frac{\partial}{\partial x_j}(\alpha_l u_j) =$$

$$\frac{\partial \alpha_l}{\partial t}+\left(\frac{\alpha_l}{\rho_m \beta^2}\right)\frac{\partial p}{\partial \tau}+\frac{\partial \alpha_l}{\partial \tau}+\alpha_l\left(\frac{-1}{\rho_m \beta^2}\right)\frac{\partial p}{\partial \tau}+u_j\frac{\partial \alpha_l}{\partial x_j} = \tag{3}$$

$$\frac{\partial \alpha_l}{\partial t}+\frac{\partial \alpha_l}{\partial \tau}+u_j\frac{\partial \alpha_l}{\partial x_j} \equiv 0$$

Inclusion of such "phasic continuity enforcing" terms has a favorable impact on the nonlinear performance of multi-phase algorithms when mass transfer is present [34].

Third, we desired an eigensystem that is independent of density ratio and volume fractions so that the performance of the algorithm would be commensurate with that of single-phase for a wide range of multi-phase conditions. These considerations give rise to the preconditioned system in equation [1].

In generalized coordinates, equations [1] can be written in vector form as:

$$\Gamma_e \frac{\partial}{\partial t}\hat{Q} + \Gamma \frac{\partial}{\partial \tau}\hat{Q} + \frac{\partial \hat{E}_j}{\partial \xi_j} - \frac{\partial \hat{E}_j^v}{\partial \xi_j} - \hat{H} = 0, \tag{4}$$

where the primitive solution variable, flux, and source vectors are written:

$$\begin{aligned}
\hat{Q} &= JQ = J(p, u_i, \alpha_l, \alpha_{ng})^T \\
\hat{E}_j &= J(U_j, \rho_m u_i U_j + \xi_{j,i} p, \alpha_l U_j, \alpha_{ng} U_j)^T \\
\hat{E}_j^v &= J\left(0, \mu_{m,t}(\nabla\xi_j \bullet \nabla\xi_j)\frac{\partial u_i}{\partial \xi_j} + \xi_{j,i}\frac{\partial u_k}{\partial \xi_j}\xi_{j,k}, 0, 0\right)^T \\
\hat{H} &= J\left((\dot{m}^+ + \dot{m}^-)\left(\frac{1}{\rho_l} - \frac{1}{\rho_v}\right), \rho_m g_i, (\dot{m}^+ + \dot{m}^-)\left(\frac{1}{\rho_l}\right), 0\right)^T,
\end{aligned} \tag{5}$$

and J is the metric Jacobian, $J \equiv \partial(x, y, z)/\partial(\xi, \eta, \zeta)$.

Matrix Γ_e is defined by:

$$\Gamma_e \equiv \begin{bmatrix}
0 & 0 & 0 & 0 & 0 & 0 \\
0 & \rho_m & 0 & 0 & u\Delta\rho_1 & u\Delta\rho_2 \\
0 & 0 & \rho_m & 0 & v\Delta\rho_1 & v\Delta\rho_2 \\
0 & 0 & 0 & \rho_m & w\Delta\rho_1 & w\Delta\rho_2 \\
0 & 0 & 0 & 0 & 1 & 0 \\
0 & 0 & 0 & 0 & 0 & 1
\end{bmatrix}, \tag{6}$$

and the preconditioning matrix, Γ, takes the form:

$$\Gamma \equiv \begin{bmatrix}
\left(\frac{1}{\rho_m \beta^2}\right) & 0 & 0 & 0 & 0 & 0 \\
0 & \rho_m & 0 & 0 & u\Delta\rho_1 & u\Delta\rho_2 \\
0 & 0 & \rho_m & 0 & v\Delta\rho_1 & v\Delta\rho_2 \\
0 & 0 & 0 & \rho_m & w\Delta\rho_1 & w\Delta\rho_2 \\
\left(\frac{\alpha_l}{\rho_m \beta^2}\right) & 0 & 0 & 0 & 1 & 0 \\
\left(\frac{\alpha_{ng}}{\rho_m \beta^2}\right) & 0 & 0 & 0 & 0 & 1
\end{bmatrix} \tag{7}$$

where $\Delta\rho_1 \equiv \rho_l - \rho_v$ and $\Delta\rho_2 \equiv \rho_{ng} - \rho_v$. The compatibility condition, $\alpha_l + \alpha_v + \alpha_{ng} = 1$, is incorporated implicitly in definitions 6 and 7.

Eigensystem

Of interest in the construction and analysis of a scheme to discretize and solve equation [4] is its inviscid eigensystem. In particular, the eigenvalues and eigenvectors of matrix $\tilde{A}_j$ are required, where

$$\tilde{A}_j \equiv \Gamma^{-1} A_j, \quad A_j \equiv \frac{\partial \hat{E}_j}{\partial \hat{Q}}. \tag{8}$$

A_j, Γ^{-1}, and $\tilde{A}_j$ can be computed straightforwardly, and expressions for these are available in [18]. The eigenvalues and eigenvectors of $\tilde{A}_j$ can be found by first considering the reduction of equation [4] to a single-phase system. With $\alpha_l = 1$, $\rho_m = \rho_l = \rho_v = \rho_{ng}$ (= constant), $\dot{m}^{+/-} = 0$, equation [4] collapses to the widely used single-phase "pseudo-compressibility" scheme, which can be written for inviscid flow as

$$\frac{\partial \hat{Q}^{1\phi}}{\partial t} + \frac{\partial \hat{E}_j^{1\phi}}{\partial \xi_j} = 0$$

$$\hat{Q}^{1\phi} = J(p, u_i)^T$$

$$\hat{E}_j^{1\phi} = (U_j, u_i U_j + \xi_{j,i} p)^T$$

$$A_j^{1\phi} \equiv \frac{\partial \hat{E}_j^{1\phi}}{\partial \hat{Q}^{1\phi}}. \tag{9}$$

Flux Jacobian matrix $A_j^{1\phi}$ has a well known form ([28], for example) and is also given in [18].

Comparing the expressions for $A_j^{1\phi}$ and $\tilde{A}_j$, one can write:

$$\tilde{A}_j = \begin{bmatrix} K^{-1}\{A_j^{1\phi}\}K & 0 & 0 \\ 0 & U_j & 0 \\ 0 & 0 & U_j \end{bmatrix}, K \equiv \begin{bmatrix} \frac{1}{\rho_m} & 0 \\ 0 & I \end{bmatrix} \quad . \tag{10}$$

Diagonalizing $\tilde{A}_j$:

$$\tilde{A}_j = M_j \Lambda_j M_j^{-1} \quad . \tag{11}$$

The elements of the diagonal matrix Λ_j are the eigenvalues of $\tilde{A}_j$. Similarity transform matrices M_j and M_j^{-1} contain the right and left eigenvectors of $\tilde{A}_j$. Forms for these matrices are sought. Using equation [10], we can write equation [11] as

$$\begin{bmatrix} K^{-1}\left\{A_j^{1\phi}\right\}K & 0 & 0 \\ 0 & U_j & 0 \\ 0 & 0 & U_j \end{bmatrix} = \begin{bmatrix} K^{-1}\left\{M_j^{1\phi}\right\} & 0 & 0 \\ 0 & 1 & 0 \\ 0 & 0 & 1 \end{bmatrix} \times$$

$$\begin{bmatrix} \left\{\Lambda_j^{1\phi}\right\} & 0 & 0 \\ 0 & U_j & 0 \\ 0 & 0 & U_j \end{bmatrix} \begin{bmatrix} \left\{M_j^{1\phi}\right\}K & 0 & 0 \\ 0 & 1 & 0 \\ 0 & 0 & 1 \end{bmatrix} \quad . \tag{12}$$

This brief analysis illustrates that the inviscid eigenvalues of the present preconditioned multi-phase system

are the same as the standard single-phase pseudo-compressibility system with two additional eigenvalues introduced, U_j, U_j. That is,

$$\Lambda_j = (U_j, U_j, U_j + C_j, U_j - C_j, U_j, U_j)^T$$
$$C_j = \sqrt{U_j^2 + \beta^2(\xi_{j,i}\xi_{j,i})} \quad . \tag{13}$$

Equation [12] also illustrates that a complete set of linearly independent eigenvectors exists for the present three-component system. These results generalize for an arbitrary number of constituents. The eigenvalues are seen to be independent of the volume fractions and density ratio. This is not the case for other choices of pre-conditioning matrix, Γ, or if a mixture mass conservation equation is chosen instead of the mixture volume equation.

The local time-steps and matrix dissipation operators presented below are derived from the inviscid multi-phase eigensystem above, which has been shown to be closely related to the known single-phase eigensystem. This has had the practical advantage of making the single-phase predecessor code easier to adapt to the multi-phase system.

Physical Modeling

Mass Transfer

For transformation of liquid to vapor, $\dot{m}^-$ is modeled as being proportional to the liquid volume fraction and the amount by which the pressure is below the vapor pressure. This model is similar to that used by Merkle et al. [23] for both evaporation and condensation. For transformation of vapor to liquid, $\dot{m}^+$, a simplified form of the Ginzburg-Landau potential is employed:

$$\dot{m}^- = \frac{C_{dest}\rho_v\alpha_l \mathrm{MIN}[0, p - p_v]}{(1/2\rho_l U_\infty^2)t_\infty}$$
$$\dot{m}^+ = \frac{C_{prod}\rho_v(\alpha_l - \alpha_{ng})^2(1 - \alpha_l - \alpha_{ng})}{t_\infty} \quad . \tag{14}$$

In this work, C_{dest} and C_{prod} are empirical constants (here $C_{dest} = 10^5$, $C_{prod} = 10^5$). α_{ng} appears in the production term to enforce that $\dot{m}^+ \to 0$ as $\alpha_v \to 0$. Both mass transfer rates are non-dimensionalized with respect to a mean flow time scale.

The mass transfer model presented in equation [14] retains the physically observed characteristic that cavity sizes, and thereby the dynamics of the two-fluid motion, are nearly independent of liquid-vapor density ratio. One outcome of the eigensystem characteristics summarized above is that the numerical behavior of the code parallels this physical behavior. This is illustrated in Figure 2 There, the convergence histories are provided for six simulations of cavitating flow over a hemispherical forebody with cylindrical afterbody (1/2 caliber ogive, $\sigma = 0.3$, from series of results presented below). As the density ratio is increased from 1 to 10, the convergence history is modified somewhat, but beyond $\rho_l/\rho_v = 10$, the performance of the solver is virtually independent of density ratio up to $\rho_l/\rho_v = 10^5$. This behavior is consistent with the modeled physics of this problem as shown in Figure 3. There, drag coefficient and number of predicted vaporous cells are seen to reach a nearly constant value at $\rho_l/\rho_v > 10$.

As the authors have evolved this work into the analysis of turbomachinery, it has become evident that the present mass transfer model has some shortcomings in that it does not accommodate thermal effects on cavitation breakdown performance in turbomachinery [5]. This is discussed further in the pump cavitation results

section below.

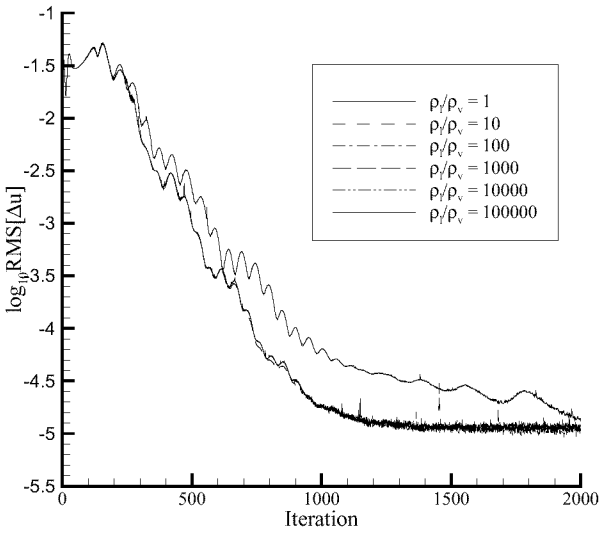


Figure 2. Comparison of convergence histories with density ratio for hemispherical forebody simulation.

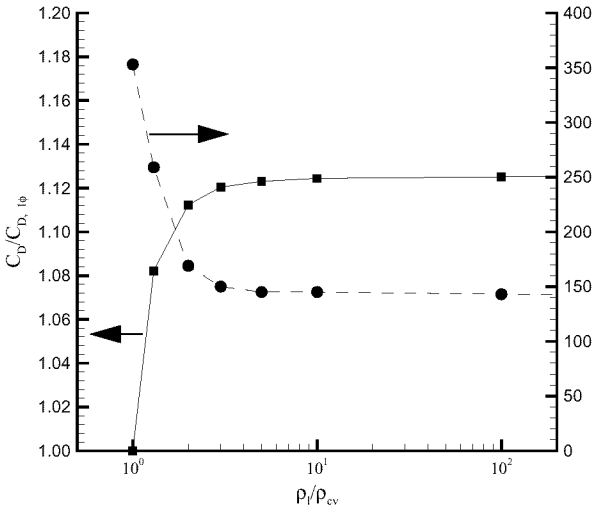


Figure 3. Comparison of predicted drag coefficient and number of vaporous cells with density ratio for hemispherical forebody simulation.

Turbulence Closure

A high Reynolds number form k-ε model (Jones and Launder [16]) with standard wall functions is implemented to provide turbulence closure:

$$\frac{\partial}{\partial t}(\rho_m k) + \frac{\partial}{\partial x_j}(\rho_m k u_j) = \frac{\partial}{\partial x_j}\left(\frac{\mu_{m,t}}{Pr_{tk}}\frac{\partial k}{\partial x_j}\right) + P - \rho\varepsilon$$

$$\frac{\partial}{\partial t}(\rho_m \varepsilon) + \frac{\partial}{\partial x_j}(\rho_m \varepsilon u_j) = \frac{\partial}{\partial x_j}\left(\frac{\mu_{m,t}}{Pr_{t\varepsilon}}\frac{\partial \varepsilon}{\partial x_j}\right) + [C_1 P - C_2 \rho\varepsilon]\left(\frac{\varepsilon}{k}\right) \quad (15)$$

As with velocity, the turbulence scalars are interpreted as being mixture quantities. Other two-equation turbulence models have also been employed as discussed below.

Compressible Constituent Phases

As mentioned above, a complicating phenomena associated with underwater multiphase flows is the presence and effect of compressibility in a flow that is largely incompressible. To directly model flows containing homogeneously mixed bubbly flow regions and/or shock-expansion wave systems, a suitable representation of compressible flow is necessary. Also, in flows of relevance here, liquid vapor mass transfer is important and by virtue of ventilation, a noncondensable gas phase is present.

For the purposes of analysis and development of appropriate preconditioning, the inviscid one-dimensional two-phase form of the governing equations are presented in equation [16]. Here, with no loss of generality, the equations are presented in mass-fraction form. In this form, the governing equations for two-phase flow resemble the equations employed in single-phase multi-component reacting-gas-mixture flows. The eigenvalues of the associated system and the preconditioning forms are well known and have been widely used [40]. The equations corresponding to a preferred set of primitive variables may be achieved and then interpreted in the context of multi-phase flows of interest. A more complete development with applications is given in references [20], [21] and [41].

Compressible Equations of Motion

The fully compressible form of the two-phase equations in 1D is given as,

$$\frac{\partial Q_Y}{\partial \tau} + \frac{\partial E}{\partial x} = 0 \tag{16}$$

which represents the following set of equations in conservation form,

$$\frac{\partial \rho Y_v}{\partial \tau} + \frac{\partial \rho Y_v u}{\partial x} = 0 \tag{17}$$

$$\frac{\partial \rho Y_l}{\partial \tau} + \frac{\partial \rho Y_l u}{\partial x} = 0 \tag{18}$$

$$\frac{\partial \rho u}{\partial \tau} + \frac{\partial \rho u^2}{\partial x} + \frac{\partial p}{\partial x} = 0 \tag{19}$$

$$\frac{\partial e}{\partial \tau} + \frac{\partial (e+p)u}{\partial x} = 0 \tag{20}$$

The mixture density is defined as:

$$\rho = \tilde{\rho}_v + \tilde{\rho}_l = \rho_l \alpha_l + \rho_v \alpha_v \tag{21}$$

where,

$$\tilde{\rho}_v = \rho Y_v = \rho_v \alpha_v \quad \text{and} \quad \tilde{\rho}_l = \rho Y_l = \rho_l \alpha_l \tag{22}$$

The total internal energy of the two-phase mixture may be expressed as,

$$e = \rho \varepsilon + \frac{1}{2}\rho u^2 = \rho h - p + \frac{1}{2}\rho u^2 \tag{23}$$

and the specific enthalpy of the mixture is given as,

$$h = \sum_{i=l,v} h_i Y_i \tag{24}$$

and h_l and h_v are the phasic enthalpies, which are also generally known functions of the temperature and the pressure. The $\tilde{\rho}$ indicates where, in equations [21] and [22], the mass fraction based, Dalton model, of species density is to be used, rather than the volume fraction based, Amagat model. For development of the compressible preconditioning form, the Dalton model for intensive properties is used here.

The system in equations [17]-[20] may equivalently be expressed in the following vector form:

$$\tilde{\Gamma}_e \frac{\partial \tilde{Q}}{\partial \tau} + \frac{\partial E}{\partial x} = 0 \tag{25}$$

where we have adopted a set of primitive variables, $\tilde{Q}$, as the primary dependent vector:

$$\tilde{Q} = \begin{bmatrix} p \\ Y_v \\ u \\ T \end{bmatrix} \qquad E = \begin{bmatrix} \rho Y_v u \\ \rho Y_l u \\ \rho u^2 + p \\ (e+p)u \end{bmatrix}$$

$$\tilde{\Gamma}_e = \begin{bmatrix} Y_v \frac{\partial \rho}{\partial p}\Big|_{\tilde{Q}} & \rho + Y_v \frac{\partial \rho}{\partial Y_v}\Big|_{\tilde{Q}} & 0 & Y_v \frac{\partial \rho}{\partial T}\Big|_{\tilde{Q}} \\ Y_l \frac{\partial \rho}{\partial p}\Big|_{\tilde{Q}} & -\rho + Y_l \frac{\partial \rho}{\partial Y_v}\Big|_{\tilde{Q}} & 0 & Y_l \frac{\partial \rho}{\partial T}\Big|_{\tilde{Q}} \\ u \frac{\partial \rho}{\partial p}\Big|_{\tilde{Q}} & u \frac{\partial \rho}{\partial Y_v}\Big|_{\tilde{Q}} & \rho & u \frac{\partial \rho}{\partial T}\Big|_{\tilde{Q}} \\ -\left(1 - \rho \frac{\partial h}{\partial p}\Big|_{\tilde{Q}}\right) + h_0 \frac{\partial \rho}{\partial p}\Big|_{\tilde{Q}} & \rho \frac{\partial h}{\partial Y_v}\Big|_{\tilde{Q}} + h_0 \frac{\partial \rho}{\partial Y_v}\Big|_{\tilde{Q}} & \rho u & \rho \frac{\partial h}{\partial T}\Big|_{\tilde{Q}} + h_0 \frac{\partial \rho}{\partial T}\Big|_{\tilde{Q}} \end{bmatrix}$$

The corresponding system flux Jacobian is defined as:

$$\tilde{A} = \begin{bmatrix} u Y_v \frac{\partial \rho}{\partial p}\Big|_{\tilde{Q}} & \rho u + u Y_v \frac{\partial \rho}{\partial Y_v}\Big|_{\tilde{Q}} & \rho Y_v & u Y_v \frac{\partial \rho}{\partial T}\Big|_{\tilde{Q}} \\ u Y_l \frac{\partial \rho}{\partial p}\Big|_{\tilde{Q}} & -\rho u + u Y_l \frac{\partial \rho}{\partial Y_v}\Big|_{\tilde{Q}} & \rho Y_l & u Y_l \frac{\partial \rho}{\partial T}\Big|_{\tilde{Q}} \\ 1 + u^2 \frac{\partial \rho}{\partial p}\Big|_{\tilde{Q}} & u^2 \frac{\partial \rho}{\partial Y_v}\Big|_{\tilde{Q}} & 2\rho u & u^2 \frac{\partial \rho}{\partial T}\Big|_{\tilde{Q}} \\ \rho u \frac{\partial h}{\partial p}\Big|_{\tilde{Q}} + u h_0 \frac{\partial \rho}{\partial p}\Big|_{\tilde{Q}} & \rho u \frac{\partial h}{\partial Y_v}\Big|_{\tilde{Q}} + u h_0 \frac{\partial \rho}{\partial Y_v}\Big|_{\tilde{Q}} & \rho(h_0 + u^2) & \rho u \frac{\partial h}{\partial T}\Big|_{\tilde{Q}} + u h_0 \frac{\partial \rho}{\partial T}\Big|_{\tilde{Q}} \end{bmatrix} \tag{26}$$

Note that a standard notation has been used to indicate partial differentiation with respect to the variables in $\tilde{Q}$. The eigenvalues of the above system are:

$$\lambda([\tilde{\Gamma}_e]^{-1}\tilde{A}) = u, u, u \pm c \tag{27}$$

where the speed of sound is given by:.

$$c^2 = \frac{\rho \frac{\partial h}{\partial T}\Big|_{\tilde{Q}}}{\rho \frac{\partial \rho}{\partial p}\Big|_{\tilde{Q}} \frac{\partial h}{\partial T}\Big|_{\tilde{Q}} + \frac{\partial \rho}{\partial T}\Big|_{\tilde{Q}} \left(1 - \rho \frac{\partial h}{\partial p}\Big|_{\tilde{Q}}\right)}$$

For the multi-phase system, the above partial derivatives need to be obtained in terms of the known volume fraction based properties, i.e., $\rho_V = \rho_V(p, T)$ and $\rho_l = \rho_l(p, T)$. Their evaluation is therefore not as straight-forward as for single-phase multi-component mixtures.

The relation for the *isothermal* sound speed is given in equation [28].

$$\left.\frac{\partial \rho}{\partial p}\right|_{\tilde{Q}} = \rho\left[\left.\frac{\alpha_l}{\rho_l}\frac{\partial \rho_L}{\partial p}\right|_{\tilde{Q}} + \left.\frac{\alpha_v}{\rho_v}\frac{\partial \rho_v}{\partial p}\right|_{\tilde{Q}}\right]$$
$$\left.\frac{1}{c^2}\right|_T = \left.\frac{\partial \rho}{\partial p}\right|_{\tilde{Q}} \tag{28}$$

Preconditioned Compressible Equations of Motion

The preconditioned version of equation [25] may be written as:

$$\tilde{\Gamma}\frac{\partial \tilde{Q}}{\partial \tau} + \frac{\partial E}{\partial x} = 0 \tag{29}$$

where the preconditioning matrix is given by:

$$\tilde{\Gamma} = \begin{bmatrix} Y_v\left.\frac{\partial \rho'}{\partial p}\right|_{\tilde{Q}} & \rho + Y_v\left.\frac{\partial \rho}{\partial Y_v}\right|_{\tilde{Q}} & 0 & Y_v\left.\frac{\partial \rho}{\partial T}\right|_{\tilde{Q}} \\ Y_l\left.\frac{\partial \rho'}{\partial p}\right|_{\tilde{Q}} & -\rho + Y_l\left.\frac{\partial \rho}{\partial Y_v}\right|_{\tilde{Q}} & 0 & Y_l\left.\frac{\partial \rho}{\partial T}\right|_{\tilde{Q}} \\ u\left.\frac{\partial \rho'}{\partial p}\right|_{\tilde{Q}} & u\left.\frac{\partial \rho}{\partial Y_v}\right|_{\tilde{Q}} & \rho & u\left.\frac{\partial \rho}{\partial T}\right|_{\tilde{Q}} \\ -\left(1-\rho\left.\frac{\partial h}{\partial p}\right|_{\tilde{Q}}\right)+h_0\left.\frac{\partial \rho'}{\partial p}\right|_{\tilde{Q}} & \rho\left.\frac{\partial h}{\partial Y_v}\right|_{\tilde{Q}}+h_0\left.\frac{\partial \rho}{\partial Y_v}\right|_{\tilde{Q}} & \rho u & \rho\left.\frac{\partial h}{\partial T}\right|_{\tilde{Q}}+h_0\left.\frac{\partial \rho}{\partial T}\right|_{\tilde{Q}} \end{bmatrix} \tag{30}$$

The eigenvalues of the preconditioned system can be shown to be:

$$\lambda(\tilde{\Gamma}^{-1}A) = u, u, \frac{1}{2}\left[u\left(1+\left(\frac{c'}{c}\right)^2\right) \pm \sqrt{u^2\left(1-\left(\frac{c'}{c}\right)^2\right)^2 + 4c'^2}\right] \tag{31}$$

where the preconditioned pseudo-sound-speed is:

$$(c')^2 = \frac{\rho\left.\frac{\partial h}{\partial T}\right|_{\tilde{Q}}}{\rho\left.\frac{\partial \rho'}{\partial p}\right|_{\tilde{Q}}\left.\frac{\partial h}{\partial T}\right|_{\tilde{Q}} + \left.\frac{\partial \rho}{\partial T}\right|_{\tilde{Q}}\left(1-\rho\left.\frac{\partial h}{\partial p}\right|_{\tilde{Q}}\right)} \tag{32}$$

Definition of Pseudo-Sound Speed

The definition of the pseudo-sound speed is selected to render the eigenvalues of the preconditioned system well conditioned. Examining equation [31], we note that this is readily achieved by choosing:

$$(c')^2 = \mathrm{Min}(V^2, c^2) \tag{33}$$

where V is local convective velocity magnitude. This form corresponds to the standard inviscid choice of this parameter. From equation [32], we may thus express the preconditioning parameter in equation [30]:

$$\left.\frac{\partial \rho'}{\partial p}\right|_{\tilde{Q}} = \frac{1}{(c')^2} - \frac{\left.\frac{\partial \rho}{\partial T}\right|_{\tilde{Q}} \left(1 - \rho \left.\frac{\partial h}{\partial p}\right|_{\tilde{Q}}\right)}{\rho \left.\frac{\partial h}{\partial T}\right|_{\tilde{Q}}} \tag{34}$$

Numerical Method

The baseline numerical method is evolved from the UNCLE code of Taylor and his co-workers at Mississippi State University ([39], for example). UNCLE is based on a single-phase, pseudo-compressibility formulation. Roe-based flux difference splitting is utilized for convection term discretization. An implicit procedure is adopted with inviscid and viscous flux Jacobians approximated numerically. A block-symmetric Gauss-Seidel iteration is used to solve the approximate Newton system at each time-step.

The multi-phase extension of the code retains these underlying numerics but also incorporates two volume fraction transport equations, mass transfer, non-diagonal preconditioning, flux limiting, dual-time-stepping, and two-equation turbulence modeling. The fully compressible version incorporates an energy conservation equation.

Discretization

The transformed system of governing equations is discretized using a cell centered finite volume procedure. Flux derivatives are computed as

$$\partial \hat{E}/\partial \xi = (\hat{E}_{i+1/2} - \hat{E}_{i-1/2}), \tag{35}$$

with similar expressions for $\partial \hat{F}/\partial \eta$, $\partial \hat{G}/\partial \zeta$, and the corresponding viscous fluxes. The inviscid numerical fluxes are evaluated using a flux difference splitting procedure [45]:

$$\begin{aligned} \hat{E}_{i+1/2} = \frac{1}{2}[&\hat{E}(Q^L_{i+1/2}) + \hat{E}(Q^R_{i+1/2}) + \\ &|\hat{A}|(Q^R_{i+1/2}, Q^L_{i+1/2}) \bullet (Q^R_{i+1/2} - Q^L_{i+1/2})] \end{aligned} \tag{36}$$

where, with the non-diagonal preconditioner used here, the matrix dissipation operator is defined by $|\hat{A}| = \Gamma(M|\Lambda|M^{-1})$.

The extrapolated Riemann variables, $Q^R_{i+1/2}$ and $Q^L_{i+1/2}$ are obtained using a MUSCL procedure ([2], for example):

$$\begin{aligned} Q^R_{i+1/2} &= Q_{i+1} - \frac{\phi}{4}[(1-\kappa)(Q_{i+2} - Q_{i+1}) + (1+\kappa)(Q_{i+1} - Q_i)] \\ Q^L_{i+1/2} &= Q_i + \frac{\phi}{4}[(1-\kappa)(Q_i - Q_{i-1}) + (1+\kappa)(Q_{i+1} - Q_i)] \end{aligned} \tag{37}$$

For first order accuracy, $\phi = 0$. The choice $\phi = 1$, $\kappa = 1/3$, yields the third order accurate upwind bias scheme used for the results presented in this paper.

The flows of interest here typically contain regions with sharp interfaces between liquid and gas phases. In addition, compressible flows admit shock waves and contact discontinuities. Accordingly, higher order discretization practices are required to retain adequate interface fidelity in the simulations. This is particularly important in three-dimensional super-cavitating vehicle or control surface computations such as those presented below. There, predicted lift and drag can be severely over-predicted if liquid phase (and its much higher inertia) diffuses numerically into low-lift gaseous regions of the lifting surface.

Attendant to the third order upwind bias scheme employed are overshoots in solution variables at these interfaces. These can be highly destabilizing, particularly for the volume fraction equations, if sufficient mass transfer or non-condensable vapor is present to yield $\alpha_l \to 0$ locally. To ameliorate this difficulty, the flux evaluation is rendered locally first order in the presence of large gradients in α_l or α_{ng}. In solutions obtained for incompressible phasic constituents, this is affected through the use of a "dissipation sensor" in the spirit of Jameson et al. [14]. Specifically, a sensor is formulated for each coordinate direction as

$$\nu_i \equiv \frac{\left|\alpha_{i+1} - 2\alpha_i + \alpha_{i-1}\right|}{\alpha_{i+1} + 2\alpha_i + \alpha_{i-1}} \quad . \tag{38}$$

This parameter is very small except in the immediate vicinity of liquid-gas interfaces. In this work, the higher order component of the numerical flux in equation [37], i.e. term ϕ, is multiplied by $(1\text{-}\nu_i)$. In compressible solutions, shocks and contact discontinuities are admissible. Hence, it is necessary to limit interpolations based on the entire primitive vector. A standard form of the van Albada limiter [13] has been employed.

To illustrate the foregoing discretization issues, consider adjacent parallel streams of two constituents. In the absence of shear, if a flow-aligned Cartesian mesh is employed, the mixing layer interface will be perfectly preserved using the present modeling (no mass diffusion). This is true independent of the density ratio of the streams and whether first or higher order discretization is employed. However, if the interface encounters a region of significant grid non-orthogonality, the interface will be smeared.

We consider a two-dimensional grid slice extracted from the three-dimensional fin computation presented below, as illustrated in Figure 4a. Two-dimensional inviscid computations of a high density ratio mixing stream were computed on this grid. Gas and liquid ($\rho_l/\rho_g = 1000$) were injected axially, at the same velocity, above and below an inlet location seen in Figure 4b. No solid boundaries are specified, so ideally, the interface would be perfectly preserved through the domain. However, the initially sharp mixing layer interface encounters severe grid non-orthogonality, as it does in full scale three-dimensional computations, even well away from solid boundaries, due to grid topology. Though this case is particularly pathological, regions where local grid quality suffers due to the geometry of the problem are inescapable in structured multiblock analyses of complex aerodynamic configurations.

Downstream of the grid "stripe" associated with the fin leading edge, Figures 4b and c show that the interface is badly smeared when first order discretization is employed ($0.05 < \alpha_l < 0.95$ for 11-12 nodes). This is largely remedied when the 3rd order flux difference with dissipation sensor is employed ($0.05 < \alpha_l < 0.95$ for 3-4 nodes).

The dissipation sensor used does not completely eliminate overshoots, as illustrated in Figure 4c. If the volume fractions are "clipped" at 1.0 after each pseudo-time-step the impact on the solution accuracy is minimal, as illustrated in Figure 4c. But, clipping causes the non-linear convergence to flat-line, so in general, we accept the modest overshoots in volume fraction.

Second order accurate backward differencing is used to discretize the physical transient term as

$$\Gamma_e \frac{\partial Q}{\partial t} \to \Gamma_e \frac{(3Q^{n+1,k} - 4Q^n + Q^{n-1})}{2\Delta t}, \tag{39}$$

where index n designates the physical time-step. Second order accurate central differencing is utilized for the viscous flux terms.

Implicit Solution Procedure

Adopting Euler implicit differencing for the pseudo-transient term, equation [4] can be written in Δ-form as

$$\left(\Gamma_e\left(\frac{3}{2\Delta t}\right)+\Gamma\left(\frac{1}{\Delta\tau}\right)+\frac{\partial}{\partial\xi_j}A_j-\frac{\partial}{\partial\xi_j}A_j^v-\hat{D}^-\right)\Delta\hat{Q}\;=$$
$$-\Gamma_e\left(\frac{3Q^{n+1,k}-4Q^n+Q^{n-1}}{2\Delta t}\right)-\frac{\partial}{\partial\xi_j}\hat{E}_j+\left(\frac{\partial}{\partial\xi_j}\right)\hat{E}_j^v+\hat{H}\;, \tag{40}$$

where $\Delta\hat{Q}\equiv\hat{Q}^{n+1,k+1}-\hat{Q}^{n+1,k}$, with index n designating the physical time-step and index k designating the pseudo-time-step. Terms A_j, A_j^v and $\hat{D}^-$ are the inviscid flux, viscous flux, and source Jacobians. The source Jacobian is evaluated analytically as illustrated below. The inviscid and viscous flux Jacobians are evaluated numerically as:

$$(A_j\Delta\hat{Q})_{i+1/2}=\frac{\partial\hat{E}}{\partial\hat{Q}_L}\Delta\hat{Q}_L+\frac{\partial\hat{E}}{\partial\hat{Q}_R}\Delta\hat{Q}_R\approx$$
$$\frac{\partial\hat{E}}{\partial\hat{Q}_L}\Delta\hat{Q}_i+\frac{\partial\hat{E}}{\partial\hat{Q}_R}\Delta\hat{Q}_{i+1}\;=$$
$$\left[\frac{\hat{E}(\hat{Q}_L+\varepsilon,\hat{Q}_R)-\hat{E}(\hat{Q}_L,\hat{Q}_R)}{\varepsilon}\right]\Delta\hat{Q}_i+ \tag{41}$$
$$\left[\frac{\hat{E}(\hat{Q}_L,\hat{Q}_R+\varepsilon)-\hat{E}(\hat{Q}_L,\hat{Q}_R)}{\varepsilon}\right]\Delta\hat{Q}_{i+1}\;,$$

where ε is taken as the square root of a floating point number close to the smallest resolvable by the hardware.

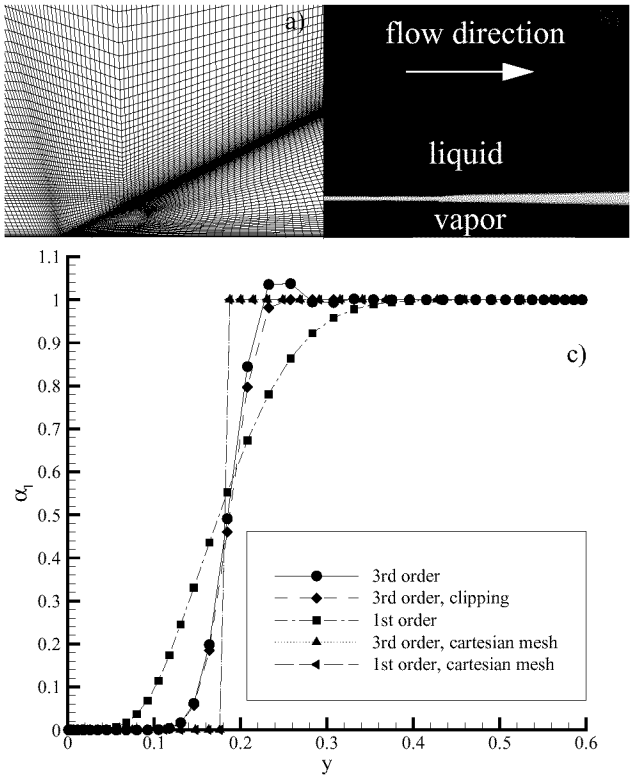


Figure 4. a) Two-dimensional grid slice extracted from three-dimensional control fin model. b) Predicted liquid volume fraction contours using present third order discretization. c) Predicted liquid volume fraction profiles for various grids and discretizations.

The pseudo-time-step is defined based on the spectral radii of $\Gamma^{-1}A_j$ as

$$\Delta\tau = \frac{CFL}{\sum_j |U_j + C_j|}. \tag{42}$$

For steady state computations, the physical time-step, Δt, is set to infinity, and a CFL number of 3-5 is typically used.

In the present work, we seek to resolve transient features characterized by the quasi-periodic shedding of vorticity and gas from the cavity. Strouhal numbers on the order of 0.1 are encountered in practice. Accordingly, non-dimensional physical time-steps on the order of .005 - .01 are required. A CFL number of 3-5 is typically used for the inner iterates in transient computations. As illustrated below, this gives rise to a dual-time scheme that provides a 1 to 3 order-of-magnitude drop in residuals in 5-10 pseudo-time-steps.

Optimum non-linear convergence is obtained using a pseudo-compressibility parameter, $\beta^2/U^2_\infty \cong 10$.

Upon application of the discretization and numerical linearization strategies defined, equation [40] represents an algebraic system of equations for ΔQ. This block (6x6 blocks) septadiagonal system is solved iteratively using a block symmetric Gauss-Seidel method. Five sweeps of the BSGS scheme are applied at each pseudo-time-step.

Source Terms

Following the strategy of Venkateswaran et al. [40] for the numerical treatment of mass transfer source terms in reacting flow computations, we identify a source and sink component of the mass transfer model and treat the sink term implicitly and the source term explicitly. Specifically, with reference to equation [1] we have

$$H^{+/-} = \left[\dot{m}^{+/-}\left(\frac{1}{\rho_l} - \frac{1}{\rho_v}\right), 0, 0, 0, \dot{m}^{+/-}\left(\frac{1}{\rho_l}\right), 0\right]^T. \tag{43}$$

With $\dot{m}^-$ from equation [14] we have

$$\Delta H^- \equiv D^- \Delta Q, \text{ with } D^- \equiv \partial H^- / \partial Q. \tag{44}$$

It can easily be shown that the non-zero eigenvalue of D^- is

$$\lambda(D^-) = C_{dest}\rho_v\left[\left(\frac{1}{\rho_l} - \frac{1}{\rho_v}\right)\alpha_l + \left(\frac{1}{\rho_l}\right)(p - p_v)\right] \tag{45}$$

which is less than zero for $\rho_v < \rho_l$. Hence, the identification of $\dot{m}^-$ as a sink is numerically valid. Implicit treatment of this term provides that α_l approaches zero exponentially, so that cases like those considered below, where significant mass transfer results in extremely low liquid volume fractions, remain stable.

The production mass transfer term is treated explicitly. A relaxation factor of 0.1 is applied at each pseudo-time-step to keep this term from destabilizing the code in early iterations.

Turbulence Model Implementation

The turbulence transport equations are solved subsequent to the mean flow equations at each pseudo-time-step. A first order accurate flux difference splitting procedure similar to that outlined above for the mean flow equations is utilized for convection term discretization. The k and ε equations are solved implicitly using conventional implicit source term treatments and a 2x2 block symmetric Gauss-Seidel procedure.

Boundary Conditions

Velocity components, volume fractions, turbulence intensity, and turbulence length scale are specified at inflow boundaries and extrapolated at outflow boundaries. Pressure distribution is specified at outflow boundaries (p=0 for single-phase or non-buoyant multi-phase computations) and extrapolated at inflow boundaries. At walls, pressure and volume fractions are extrapolated, and velocity components and turbulence quantities are enforced using conventional wall functions. Boundary conditions are imposed in a purely explicit fashion by loading "dummy" cells with appropriate values at each pseudo-time-step.

Parallel Implementation

The multiblock code is instrumented with MPI for parallel execution based on domain decomposition. Inter-block communication is affected at the non-linear level through boundary condition updates and at the linear solver level by loading ΔQ from adjacent blocks into "dummy" cells at each SGS sweep. This is not as implicit as solving an optimally ordered linear system for the entire domain at each SGS sweep, but, as demonstrated below, this potential shortcoming will not deteriorate the non-linear performance of the scheme if the linear solver residuals are reduced adequately at each pseudo-time-step. The authors routinely employ 48-80 processors for three-dimensional, unsteady analyses.

Results

Three sets of results from the authors' recent research are presented. The first set includes axisymmetric steady-state and transient analyses of natural and ventilated cavitation about several configurations. These solutions are compared to experimental measurements to demonstrate the capability of the modeling employed. The second set of results includes a variety three-dimensional analyses of sheet- and supercavitating flows of relevance to high speed vehicles and turbomachinery. The third set of results includes compressible simulations of a vehicle propulsion plume and a high speed supercavitating projectile.

Axisymmetric Analyses

Steady State and Transient Natural and Ventilated Cavitation about a Series of Axisymmetric Forebodies

Due to the authors' principal research interests in supercavitating vehicles, an emphasis of our CFD development and validation efforts has been on axisymmetric bodies. In this regard, we have used data due to Rouse and McNown [29] as well as that due to Stinebring et al. [36], [37] for validation purposes.

Rouse and McNown [29] carried out a series of experiments wherein cavitation induced by convex curvature aft of various axisymmetric forebodies with cylindrical afterbodies was investigated. At low cavitation numbers, these flows exhibit natural cavitation initiating near or just aft of the intersection between the forebody, or *cavitator*, and the cylindrical body. For each configuration, measurements were made across a range of cavitation numbers, including a single phase case (large σ). Surface static pressure measurements were taken along the cavitator and after-body. Photographs were also taken from which approximate bubble size and shape were deduced.

Several of the Rouse-McNown configurations were analyzed. These included 0-caliber (blunt), 1/4-caliber, 1/2-caliber (hemispherical), 1-caliber, and 2-caliber ogives and conical (22.5^{o} cone half-angle) cavitator shapes. The experiments were performed at Reynolds numbers greater than 100,000 based on maximum cavitator (i.e., after-body) diameter. A value of Re = 136000 was used for the simulations. In order to properly assess grid resolution requirements, a range of grid sizes was used. For the hemispherical and conical configurations, grid sizes of 65x17, 129x33 and 257x65 were run. Figure 5 demonstrates that differences between predicted surface pressures for the medium and fine meshes are small. The fine meshes were used for all subsequent calculations presented here. For the blunt fore-body, a two-block grid topology had to be used, and a

mesh consistent with the resolution and clustering of the other head-forms was utilized (65x49, 257x65 for blocks 1 and 2; see Figure 9b).

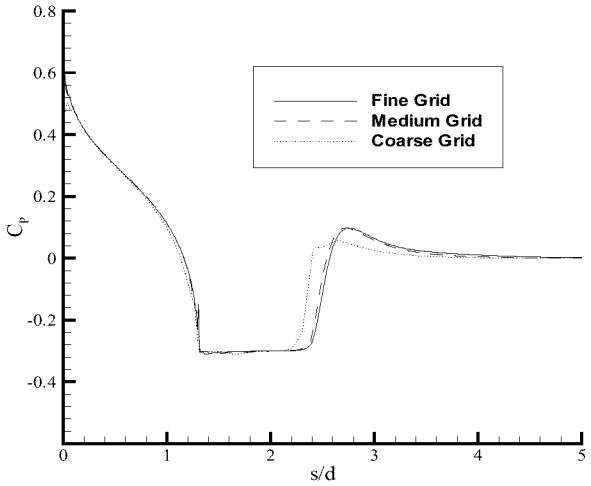


Figure 5. Comparison of predicted surface pressure distributions for naturally cavitating axisymmetric flow over a conical cavitator-cylindrical after-body configuration, $\sigma = 0.3$. Coarse (65x17), medium (129x33) and fine (257x65) mesh solutions are plotted.

Figures 6 through 24 show sample results for these axisymmetric computations. Figure 6a shows predicted and measured surface pressure distributions at several cavitation numbers for the 1-caliber ogive forebody with cylindrical afterbody. As the cavitation number is decreased from near a critical "inception" value, a cavitation bubble forms and grows. The presence of the bubble manifests itself as a decrease in magnitude, flattening and lengthening of the pressure minimum along the surface. Also, bubble closure gives rise to an overshoot in pressure recovery due to the local stagnation associated with free-stream liquid flowing over the convex curvature at the aft end of the bubble. The code is seen to accurately capture these physics as evidenced by the close correspondence between predicted and measured pressure distributions. Figure 6b illustrates the qualitative physics as captured by the model. There, surface pressure contours, field liquid volume fraction contours, selected streamlines and the grid used are shown for the 1-caliber case at $\sigma = 0.15$. For this case, the cavitation bubble is quite long ($L/d > 3$). As with all large cavitation bubbles, the closure region is characterized by an unsteady "re-entrant" jet. The significant flow recirculation and associated shedding of vorticity and vapor in these flows require that a transient simulation be carried out. This is discussed further below. The solution depicted in Figure 6b represents a snapshot in time of an unsteady simulation.

Figures 7-9 provide similar comparisons for hemispherical, conical and blunt ogives. Specifically, Figures 7a, 8a and 9a show comparisons between predicted and measured surface pressure distributions for these three configurations at a range of cavitation numbers. In Figures 7b, 8b and 9b, surface pressure contours, field liquid volume fraction contours, selected streamlines and the grid are illustrated for selected cavitation numbers. In each case, a discrete bubble shape is observed, but the aft end of the predicted bubble does not exhibit a smooth "ellipsoidal" closure. Indeed, due to local flow reversal (reentrant jet), liquid is swept back underneath the vapor pocket. The pressure in this region retains the nearly constant free stream liquid flow value impressed through the bubble. Similar closure region observations have been made by Chen and Heister [6] and others.

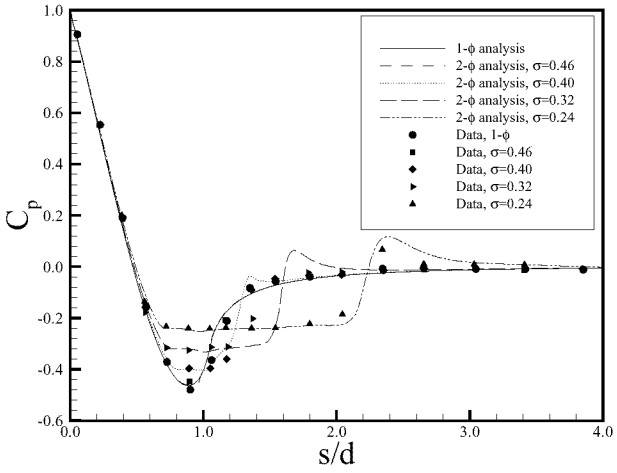


Figure 6a. Comparison of predicted and measured surface pressure distributions at several cavitation numbers for a 1-caliber ogive forebody.

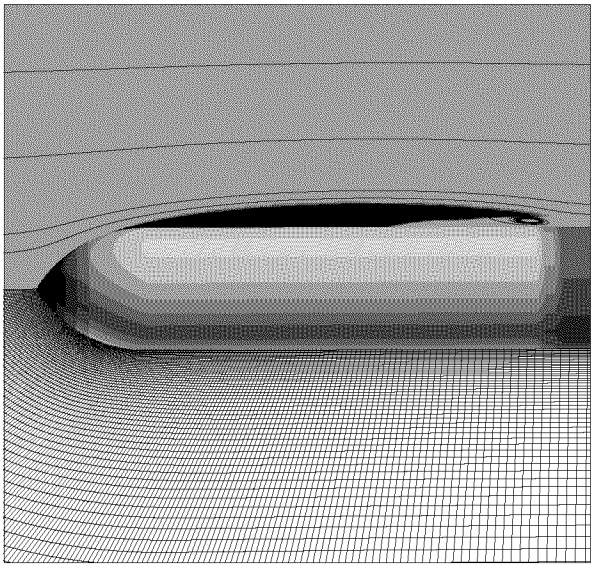


Figure 6b. Predicted liquid volume fraction and surface pressure contours, selected streamlines and computational grid for a 1-caliber ogive forebody,

As with the 1-caliber ogive, the predicted pressure distribution for the hemispherical cavitator is very well predicted, but Figure 8b illustrates that the simulations underpredict the length of the bubble for the 22.5° half-angle conical head form at all cavitation numbers, though qualitative trends remain correctly predicted. Although fairly good quantitative agreement is obtained for the blunt fore-body at low cavitation numbers, shortcomings of the present modeling are evident. First, even the single phase pressure distribution shows significant discrepancy from the data. In particular, the characteristic flattening of the measured pressure distribution due to a large recirculation zone aft of the corner is significantly underpredicted. Such a "forward facing step" flow is well known to provide significant challenges to single phase turbulence models. The conventional model employed here (high Reynolds number k-ε) has well-documented difficulties with stagnated, high strain and recirculating flows. All of these characteristics are embodied in the blunt head-form flow. Our efforts to "remedy" these single phase turbulence modeling shortcomings by deploying several approaches that have appeared in the literature (q-ω, sublayer modeling, RNG) have yet to yield a fully satisfactory resolution. As observed by Shyy [33], ["there are no quick, practical solutions to handle this challenge. However, models capable of handling (i) substantial departure from equilibrium between production and dissipation of the turbulent kinetic energy, (ii) anisotropy between main Reynolds stress components, and (iii) turbulence-enhanced mass transfer across the phase inter-face, should be emphasized".]

Several parameters of relevance in the characterization of cavitation bubbles include body diameter, d, bubble length, L, bubble diameter, d_m, and form drag coefficient associated with the cavitator, C_D. Some ambiguity is inherent in both the experimental and computational definition of the latter three of these parameters. Bubble closure location is difficult to define due to unsteadiness and its dependence on after-body diameter (which can range from 0 [isolated cavitator] to the cavitator diameter). Accordingly, bubble length is often, and here, taken as twice the distance from cavity leading edge to the location of maximum bubble diameter (see Figure 10). The form drag coefficient is taken as the pressure drag on an isolated cavitator shape. For cavitators with afterbodies, such as here, the pressure contribution to C_D associated with the back of the cavitator is assumed equal to the cavity pressure ($\cong p_v$). For the simulations, d_m is determined by examining the $\alpha_l = 0.5$ contour and determining its maximum radial location.

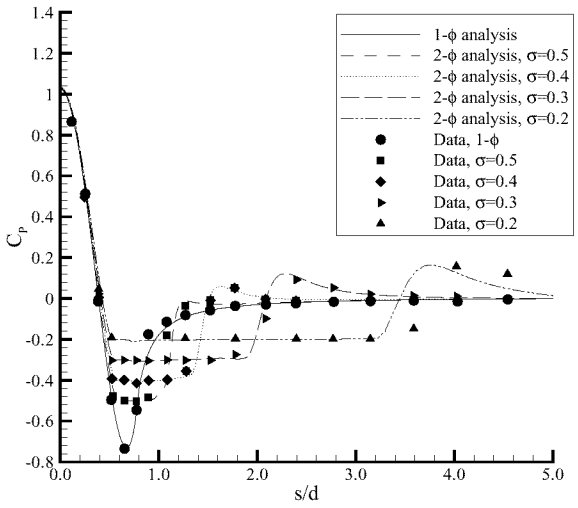


Figure 7a. Comparison of predicted and measured surface pressure distributions at several cavitation numbers for a hemispherical fore-body.

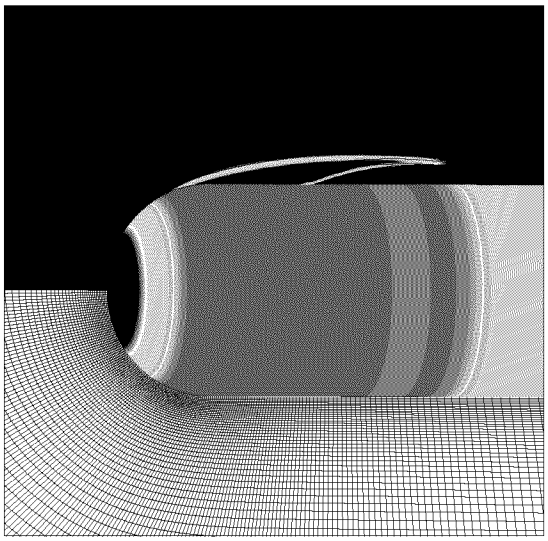


Figure 7b. Predicted liquid volume fraction and surface pressure contours, selected streamlines and computational grid for a hemispherical fore-body, σ=0.3.

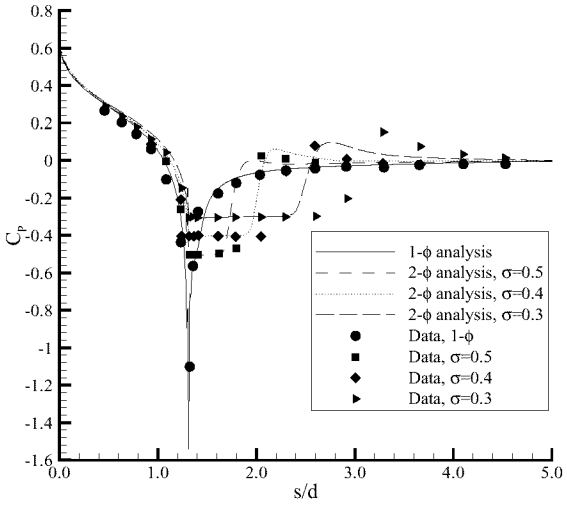


Figure 8a. Comparison of predicted and measured surface pressure distributions at several cavitation numbers for a conical fore-body.

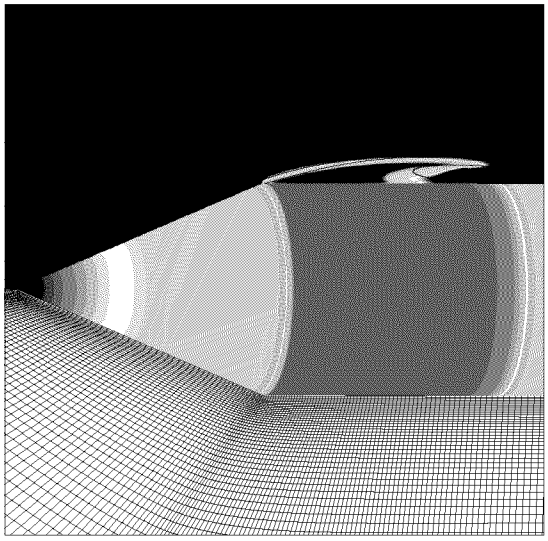


Figure 8b. Predicted liquid volume fraction and surface pressure contours, selected streamlines and computational grid for a conical fore-body, σ=0.3.

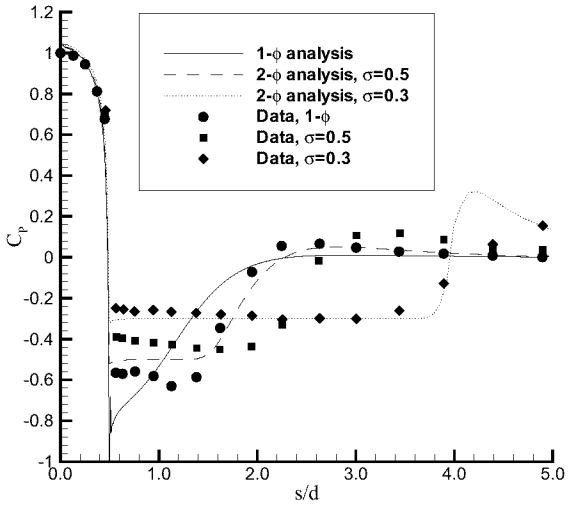


Figure 9a. Comparison of predicted and measured surface pressure distributions at several cavitation numbers for a blunt fore-body.

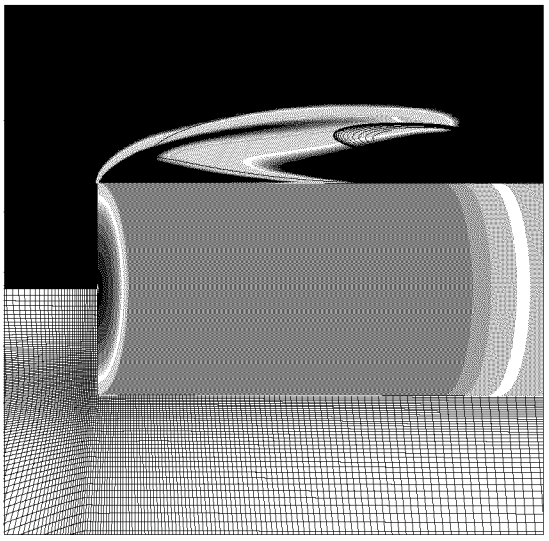


Figure 9b. Predicted liquid volume fraction and surface pressure contours, selected streamlines and computational grid for a blunt fore-body, σ=0.4.

In Figure 11a, the quantity $L/(dC_D^{1/2})$ is plotted against cavitation number for a large number of experimental data sets assembled by May [22] from a variety of sources and for numerous simulations made with six cavitator shapes. That $L/(dC_D^{1/2})$ should correlate with σ has been long established theoretically and experimentally (Reichardt [27], Garabedian [11], for example). Despite the significant uncertainties associated with experimental and computational evaluation of L and C_D, the data and simulations do correlate well, close to independently of cavitator shape. The cone shaped cavitator exhibits some underprediction of this parameter at higher cavitation numbers, consistent with the bubble length underprediction observed in the pressure distribution comparisons presented above.

The so-called *fineness ratio* of the cavity, L/d_m, is plotted against cavitation number in Figure 11b for the same experimental and computational data sets. These parameters again correlate well for both experiment and simulation, though at higher cavitation numbers there is a spread in both. Considering the difficulties in quantifying smaller bubble sizes, we hesitate to draw any conclusions as to the possible sources of this spread.

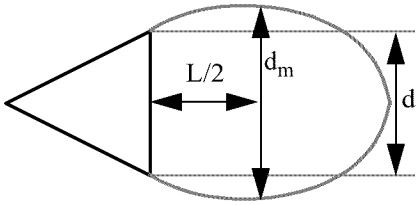


Figure 10. Bubble length and bubble diameter definitions.

In the cases considered so far, steady-state solutions were obtained for higher cavitation numbers. At lower cavitation numbers (i.e. larger bubbles), significant large scale unsteadiness appears in the aft region of the bubble/reentrant jet region. Vorticity and condensable vapor are shed from this region. Accordingly, transient simulations (dual-time stepping) were performed when pseudo-timestepping failed to converge. For the 0-, 1/4-, 1/2-, 1- and 2-caliber and conical cavitator shapes, transient computations were performed for cavitation numbers less than or equal to σ = 0.5, 0.3, 0.35, 0.15, 0.05and 0.4, respectively. Non-dimensional physical time steps of $\Delta t/t_\infty = 0.007$ were utilized for these computations. In Figures 11a and 11b, time accurate CFD results are represented with filled symbols, steady state results with open symbols.

Ventilated Cavitation

Ventilated cavities are also of interest to the authors because for large enough values of free stream pressure the only way to generate large cavities is to inject some mixture of condensable and non-condensable gases into the flow near the body leading edge. In general, ventilated cavities exhibit similar dynamics to natural cavities (May [22]). Ventilated cavities do, however, tend to be more stable than natural cavities near the aft end of the cavitation bubble. Also, as discussed in the authors' companion paper [38] all non-condensable gas must mix with the free stream liquid and be transported downstream.

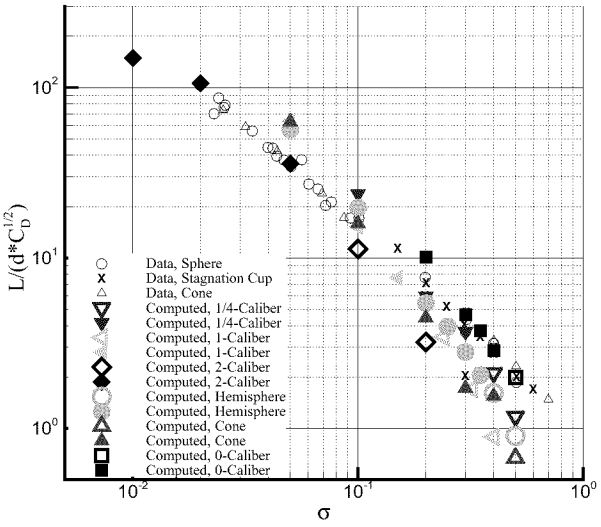


Figure 11a. Comparison of $L/(dC_D^{1/2})$ vs. σ for numerous fore-body shapes. Experimental data adapted from May [22]. Open symbols represent steady computations, filled symbols represent transient computations.

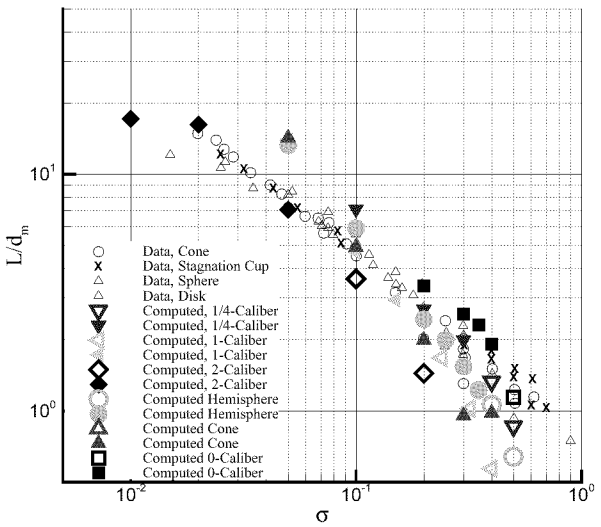


Figure 11b. Comparison of L/d_m vs. σ for numerous fore-body shapes. Experimental data adapted from May [22]. Open symbols represent steady computations, filled symbols represent transient computations.

The axisymmetric blunt fore-body configuration presented above was run with no mass transfer but with non-condensable gas injection just aft of the leading edge. A range of injection mass flow rates were specified, yielding a range of ventilated cavity sizes. The resulting cavities do not close in the sense that all vapor is condensed, however a distinct bubble shape is observed whose geometry is quantified as detailed above. This is illustrated in Figure 12, where the predicted liquid volume fraction fields are shown for the blunt head-form natural and vented cavities at $\sigma = 0.4$. (The cavitation number in ventilated cavities is defined not from the vapor pressure but from the cavity pressure.)

In Figures 13a and 13b, $L/(dC_D^{1/2})$ and L/d_m are plotted for the blunt head-form at a range of cavitation numbers. The natural cavity results presented above are reproduced in these plots along with the results of six ventilated cavity runs. (Note that the cavitation number is not explicitly specified in the ventilated case; rather it is an outcome of specified ventilation flow rate. This is why the ventilated data predictions in Figures 13a and 13b are not at precisely the same cavitations numbers as the natural ventilation cases.) The similarity between the natural and ventilated cavity results are generally affirmed by the simulations, in that these parameters cor-

relate well with each other and with the experimental data provided in Figures 11a and 11b.

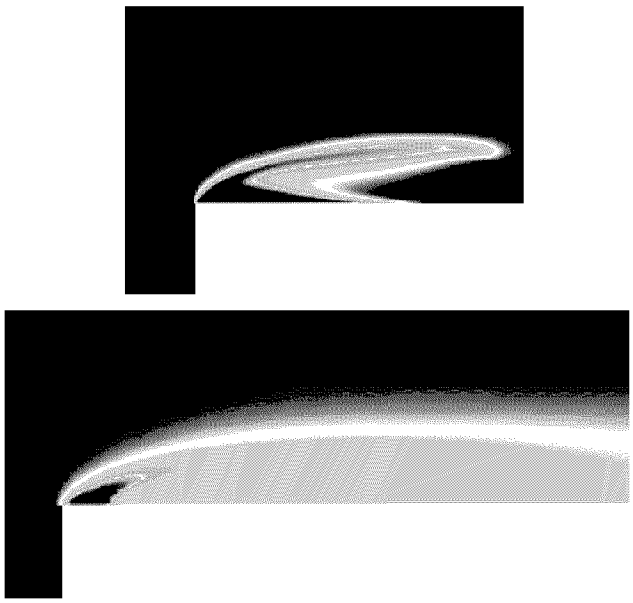


Figure 12. Predicted liquid volume fraction contours for axisymmetric natural and ventilated cavities about a cylindrical configuration with blunt fore-body ($\sigma = 0.4$).

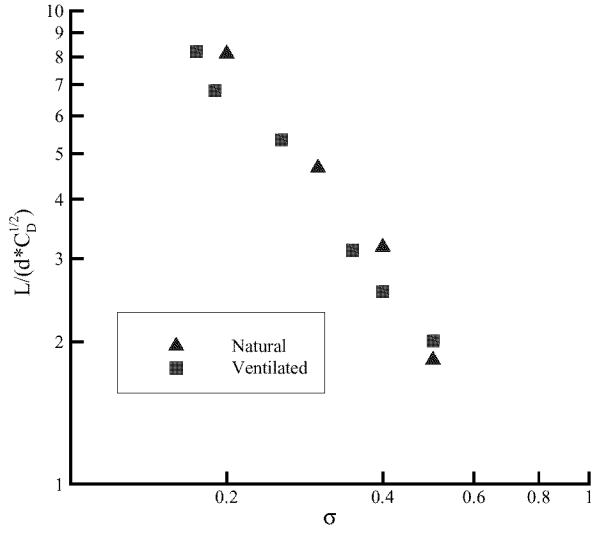


Figure 13a. Comparison of $L/(dC_D^{1/2})$ vs. σ for natural and ventilated cavities about a blunt fore-body.

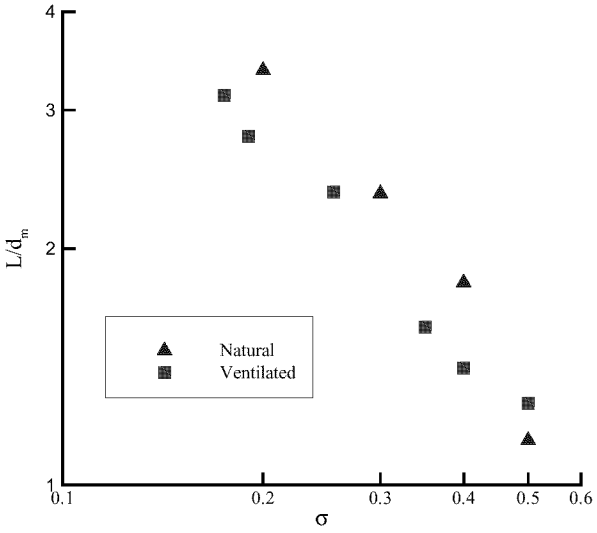


Figure 13b. Comparison of L/d_m vs. σ for natural and ventilated cavities about a blunt fore-body.

Unsteady Characteristics of Cavities

As mentioned above, developed cavities exhibit large scale unsteadiness associated with re-entrant jets, periodic ejection of non-condensable gas, and cavity "pulsations". Accordingly, we have employed a time-accurate formulation in the analysis of developed cavitation. Our particular interest in cavitator design has motivated the hydrodynamic performance parameter model assessments and validation carried out above. There, most of the simulations were unsteady and the presented results were time averaged.

There is also particular interest in the time dependent (as opposed to time averaged) characteristics of devel-

oped cavities, as these physics play importantly in vehicle acoustics, body wetting and bubble cloud collapse. Motivated by the former two, we have carried out an assessment of the accuracy of the predicted temporal statistics provided by the code.

We first illustrate the qualitative temporal characteristics of an analysis of a bluff forebody shape at moderate cavitation numbers. In such flows it is well known that the entire cavity can be highly unsteady, with "re-entrant" liquid issuing quasi-periodically from the aft end of the bubble and traveling all the way to the front of the bubble. In Figure 14, a time-sequence of predicted vapor volume fraction is reproduced for a 1/4-caliber ogive simulation at a Reynolds number of 1.36×10^5 and a cavitation number of 0.3. A 193 x 65 mesh and a non-dimensional physical time-step of 0.007 was used for this computation. Clearly captured is the transport of a region of liquid towards the front of the cavity. There, the liquid interacts with the bubble leading edge, the top of this liquid region being sheared aftward while the bulk of the fluid proceeds upstream "pinching off" the bubble near the leading edge.

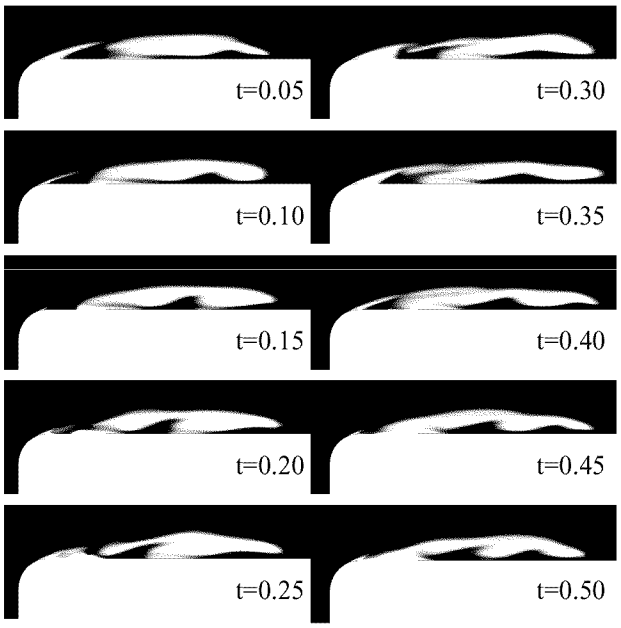


Figure 14. Time sequence of predicted vapor volume fraction for flow over a 1/4 caliber ogive with cylindrical afterbody, $\sigma = 0.3$

.

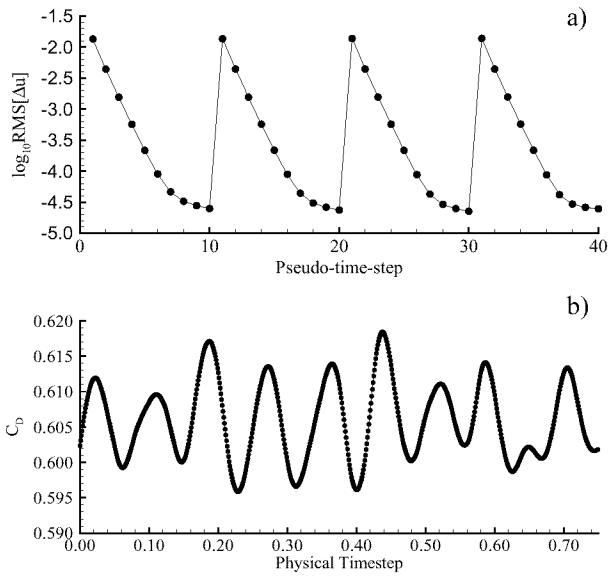


Figure 15. a) Pseudo-time convergence history at four successive physical time steps for transient flow over a 1/4 caliber ogive with cylindrical afterbody, $\sigma = 0.3$. b) Segment of time history of predicted C_D for this case.

Figure 15 shows two other elements of this particular transient simulation. The inner- or pseudo-time convergence history for four successive physical time steps is shown in Figure 15a. Nearly a three order-of-magnitude drop in the axial velocity residuals is obtained at each physical time step using 10 pseudo-time-steps. Figure 15b shows a segment of the time history of predicted drag coefficient for this case

Stinebring et al. [36] documented the unsteady cycling behavior of several axisymmetric cavitators. Their report included results for both ventilated and natural cavitation. The unsteady performance of 45° (22.5° half-angle) conical, hemispherical, and 0-caliber ogival cavitators at a range of cavitation numbers were documented. Natural cavitation analysis comparisons have been included here.

Figure 16 contains a series of snapshots of the predicted volume fraction field from an unsteady model computation of flow over a 0-caliber (blunt) cavitator. Here the Reynolds number (based on diameter) was 1.46×10^5 and the cavitation number was 0.3. This result is presented over an approximate model cycle. The figure also includes the corresponding time segment of drag coefficient. Note that the spikes in drag near t=37.725 and t=38.925 seconds correspond to reductions in the relative amount of vapor near the sharp leading edge. This marks the progress of a bulk volume of liquid from the closure region to the forward end of the cavity as part of the reentrant jet process. Although far from regular, these spikes also delineate the approximate model cycle.

The computed physics in Figures 14 and 23 correspond qualitatively to film footage of blunt cavitators at intermediate cavitation numbers. This is illustrated in Figure 17 which is a photograph (adapted from Stinebring [37]) of a 0-caliber axisymmetric cavitator operating at $Re_D = 2.9 \times 10^5$, $\sigma \cong 0.35$. This picture serves to illustrate the basic phenomenon of natural sheet cavitation as it is captured by the model. This result is notable for the spatially and temporally irregular nature of the computed flow field. Even after significant integration effort, a clearly periodic result had not emerged. Thus, to deduce the dominant frequency with some confidence, it was necessary to apply ensemble averaging.

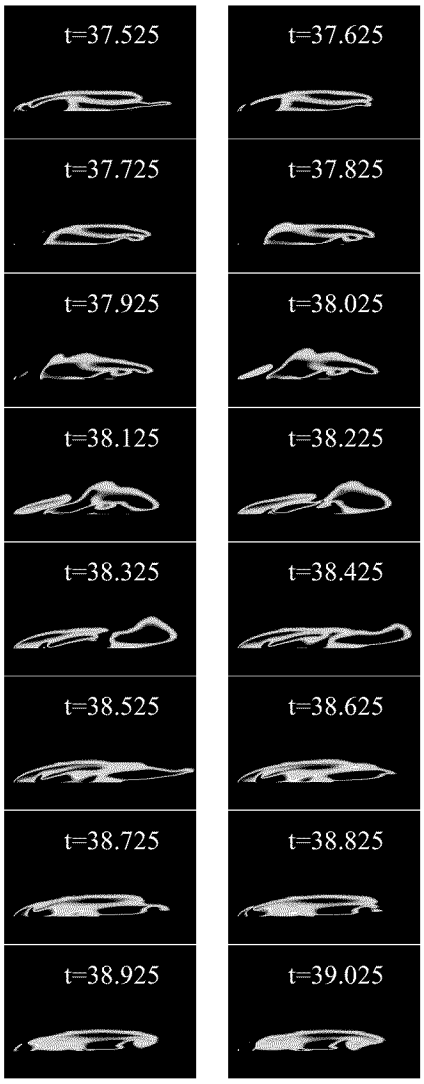
Note, in Figure 16 that over a significant portion of the sequence, the leading, or formative, edge of the cavity sits slightly downstream from and not attached to the sharp corner. In their experiments, Rouse and McNown observed this phenomenon. They suggested that this delay in cavity formation was due to the tight separation

eddy which forms immediately downstream of the corner and, hence, locally increases the pressure. The corresponding evolution of cavitation further downstream, at the separation interface, was proposed to be due to tiny vortices. These vortices, after some time, subsequently initiate the cavity.

Figure 18 shows a single frame at t=37.8 seconds from the same model calculation (as shown in Figure 23). Here, to clarify what is captured, the volume fraction contours have been enhanced with illustrative streamlines. Note that these are streamlines drawn from a frozen time slice. Nonetheless, if all of the details envisioned by Rouse and McNown were present, the streamlines should indicate smaller/tighter vortical flows. The current level of modeling was unable to capture small vortical structures in the flow. However, the overall computation was apparently able to capture the gross affects of these phenomena and reproduce a delayed cavity. In fact from examination of the cavity cycle evolution shown in Figure 23, and the streamlines shown in the snapshot, it appears that gross unsteadiness is driven by a combination of a reentrant jet and some type of cavity pinching. The pinching process is particularly well demonstrated in Figure 23 from t=38.125 to 38.325 seconds. However, rather than complete division and convection into the free stream, it should be noted that, in later frames of Figure 23, the pinched portion of the cavity appears to rejoin the main cavity region.

The low frequency mode apparent in most of the experimental 0-caliber results appears to have been captured at the lowest cavitation number (σ=0.3), as shown in Figure 23, and is evidenced in the test photograph (Figure 17). In Figure 19, the drag coefficient history for a 40 model second interval from the same computation as in Figure 23 is shown. Here, a clear picture of the persistence, over a long integration time, of the irregular flow behavior is documented. At higher cavitation numbers, the current set of 0-caliber cavitator results indicate a more regular periodic motion. This is contrary to the experimental data. However, as Figure 18 indicates, the ability to capture this motion at any cavitation number may not necessarily require the explicit capture of the finer flow details of the vortical flow structure. This is encouraging and suggests that with increased computational effort, without altering the current physical model, the representation of this phenomenon could be improved over a greater range of cavitation numbers.

Figure 20 presents the spectral content of the result given in Figure 19. This power spectral density plot is based on four averaged Hanning windowed data blocks of the time domain result. To eliminate the start-up transient effect, the record was truncated, starting at t=10 seconds and, to tighten the resulting confidence intervals, more time domain results, after t=40 seconds were included. As is typical of highly nonlinear sequences, the experience of this unsteady time integration demonstrated that, additional time records merely enrich the power spectral density function. However, the additional records do serve to improve the confidence intervals, and, therefore, add reliability to the numerical convergence process. The model result used was, as indicated by the confidence intervals, sufficient for a comparison to experimental, unsteady results.



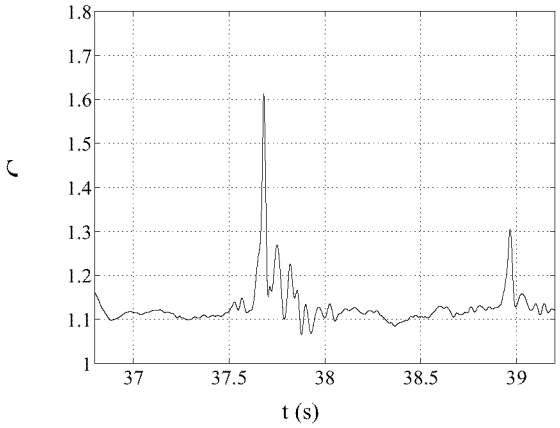


Figure 16. Modeled flow over a 0-caliber ogive. Liquid volume fraction contours and corresponding drag history. σ=0.3. Re_D=1.46x10^5.



Figure 17. Zero caliber ogive in water tunnel at Re_D=2.9x10^5, $\sigma\cong$0.35 (adapted from Stinebring [37]).

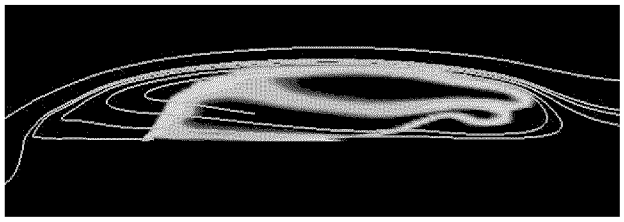


Figure 18. Snapshot of modeled flow over a 0-caliber ogive. Liquid volume fraction contours and selected streamlines. σ=0.3. Re_D=1.46x10^5.

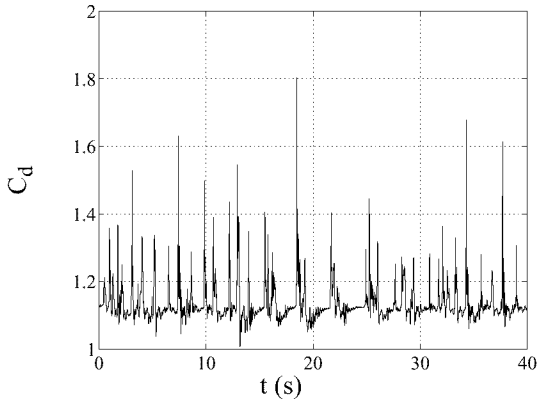


Figure 19. Model time record of drag coefficient for flow over a 0-caliber ogive at Re_D=1.46x10^5 and σ=0.3. In model units, D/U_∞ = 0.146 (s), physical time step, Δt = 0.001 (s).

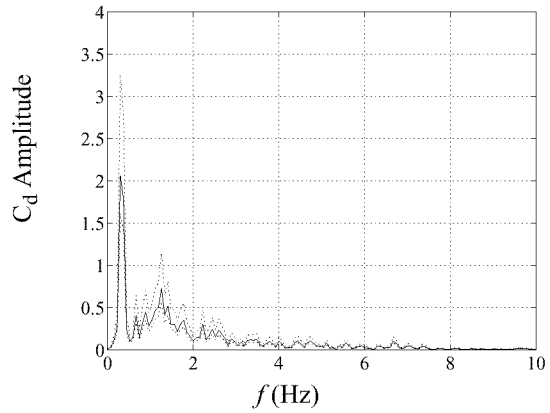


Figure 20. Results for 0-caliber ogive at Re_D=1.46x10^5 and σ=0.3. Power spectral density function with 50% confidence intervals shown.

Figure 21 contains a series of snapshots from the unsteady model computation of a hemispherical cavitator at a Reynolds number (based on diameter) of 1.36x10^5 and a cavitation number of 0.2. This result is presented over a period slightly longer than the approximate model cycle. In this case the model Strouhal frequency is 0.0326. There are ten frames presented, and the first (or last) nine of those ten constitute an approximate model cycle. The drag history trace in Figure 22 demonstrates how, relative to the modeled flow over the blunt forebody, the pattern of flow over the hemispherical forebody is regular and periodic. This is consistent with experimental observations made (for example) by Rouse and Mcnown [29]. Note the evolution of flow shown in Figure 21 as it compares to the drag history shown in Figure 22. As would be expected, the large

spike in drag corresponds to the minimum in vapor shown near the modeled t=1.6 seconds.

Figure 23 contains a time record of drag coefficient during modeled flow over a conical forebody and cylinder at a Reynolds number of 1.36×10^5 and cavitation number of 0.2. The Strouhal frequency based on this result is 0.0383. As anticipated, due to the expected stability of cavities about this shape, this model flow exhibited very regular cycling with little additional strong components from secondary modes.

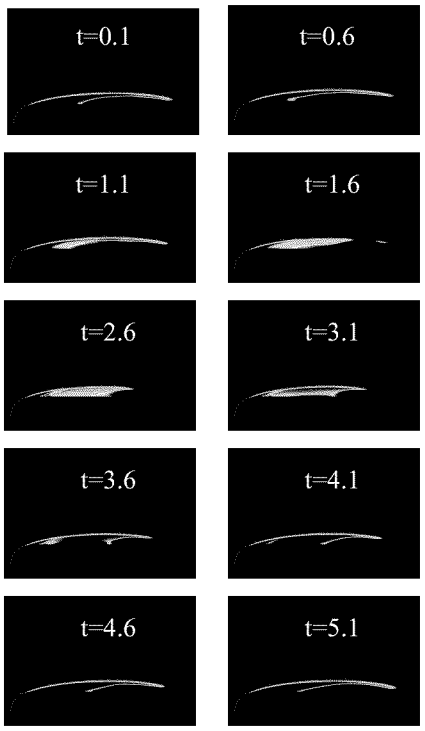


Figure 21. Liquid volume fraction countours. Modeled flow over a hemispherical forebody and cylinder. σ=0.2, Re_D=1.36×10^5.

Figure 24 contains a large survey of unsteady computational and experimentally obtained data [36]. The numerical results in this figure summarize this validation effort. Here, Strouhal frequency is shown over a range of cavitation numbers. Computational results are given for hemispherical, 1/4-caliber, conical, and 0-caliber forebodies. Unsteady experimental data is included for the hemispherical, conical and 0-caliber shapes. Computational results for the hemisphere, 1/4-caliber and conical forebodies, were obtained at a Reynolds number based on diameter of 1.36×10^5. For the 0-caliber ogive, computations were made at a Reynolds number of 1.46×10^5. In addition, for the hemisphere, results are included for Reynolds numbers of 1.36×10^6 and 1.36×10^7. The experimental results included in the figure were obtained at Reynolds numbers ranging from 3.5×10^5 to 1.55×10^6.

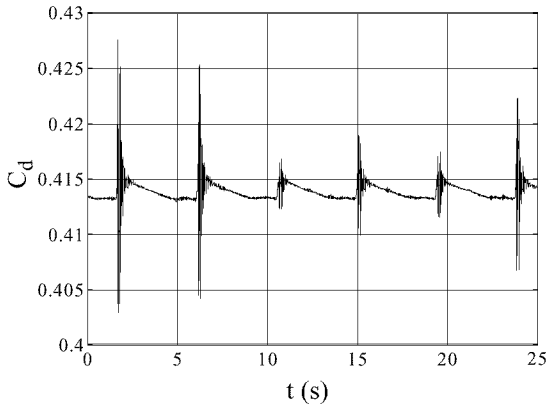


Figure 22. Unsteady drag coefficient. Flow over a hemispherical forebody and cylinder. σ=0.2, Re_D=1.36x10^5. In model units, D/U_∞ = 0.136 (s), physical time step, Δt = 0.001 (s).

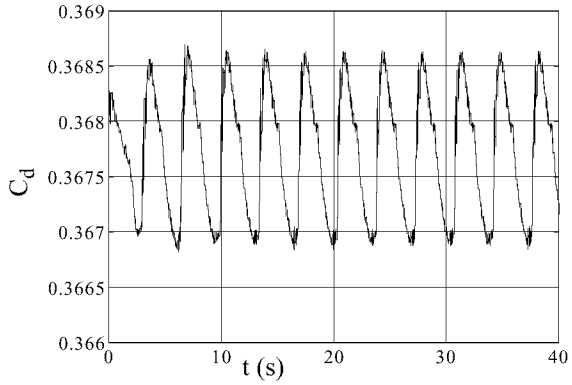


Figure 23. Predicted time record of drag coefficient for flow over a conical forebody and cylinder at Re_D=1.36x10^5 and σ=0.3. In model units, D/U_∞ = 0.136 (s), physical time step, Δt = 0.0025

As a blanket observation, the spread of data between the experiments and computations in Figure 24 is significant. However, there are several encouraging items to be reviewed. It is clear that (for a given cavitation number) the computational results are bounded by the experimental data, and the proper trends (rate of change of Strouhal frequency with cavitation number) are well captured. More insight into the physical relevance of the data requires examination of specific results.

For the hemispherical forebody results, as may be seen in Figure 24, there is a significant but almost constant offset between the measured unsteady data and the modeled results both of which appear to follow a linear trend over the range presented. An interesting result occurs in the model data for the hemispherical forebody with a Reynolds number of 1.36x10^7 (pentagrams in Figure 24). Here the numerical results appear to agree quite well with the experimental data for hemispherical forebodies. The experiments were taken at an order of magnitude lower Reynolds number, but the agreement is apparent in both cases where model results have been obtained. For design purposes, this may suggest an avenue towards model calibration.

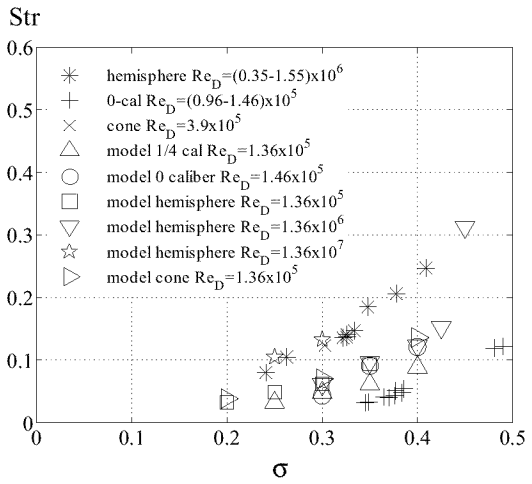


Figure 24. Axisymmetric running cavitators with cylindrical afterbodies. Strouhal frequency and cavitation number. Model results (open symbols) and data reported in Stinebring 36.

Another result found in the Str versus σ plot (Figure 24) is the tendency of the modeled flows to become steady at higher cavitation numbers. For the 0-caliber or the conical cavitators, this is the reason model results are not included for cavitation numbers greater than 0.4. For the modeled hemisphere, the upper limit of cavitation number to yield unsteady model results was found to be Reynolds number dependent. At a $Re_D=1.36x10^5$, the maximum cavitation number yielding an unsteady result was $\sigma \approx 0.35$, at $Re_D=1.36x10^6$, that number was $\sigma \approx 0.45$, and at $Re_D=1.36x10^7$, the maximum cavitation number for unsteady computations was not determined. This result may indicate a limit of the computational grid applied to the problems rather than a limit of the level of physical modeling. In addition, physically in the mode of unsteadiness present, a transition does occur from cavity driven to separated, turbulent, but single phase driven flow.

For the conical forebody, the datum shown in Figure 24 suggests that the cycling frequency should be higher, 0.123. It is worth considering that the Reynolds number of the experimental flow was $3.9x10^5$ and that the general trend with increasing Reynolds numbers is to increased frequency. However, based on the standard level of dependence of Strouhal frequency (see Schlichting [31] for example) on Reynolds number for bluff body flows, it would seem unlikely that the rate of change in frequency with Reynolds number (at $Re_D \approx 10^5$) would be as high as three to two. In addition, compared to shapes with geometrically smooth surfaces, the nature of unsteady flow over a conical shape is not expected to be nearly so dependent on Reynolds number. In the case of a cone, at low values of cavitation number (i.e. σ=0.3), the separation location, and, hence, the likely forward location of the cavity, is rarely in question.

A trend that is captured in the model results but not represented in the experimental data included here, is the tendency for the Strouhal frequency of a given cavitator shape to exhibit two distinct flow regimes. The first regime exists at moderate cavitation numbers and is indicated by a low Strouhal frequency where the value of Str will have an apparent linear dependence on σ. The second regime tends toward much higher cycling frequencies. Here the dependent Strouhal frequency appears to asymptotically approach a vertical line with higher cavitation number, just prior to the complete elimination of the cavity. This is documented in Stinebring [36] and demonstrated in Figure 24 for the modeled hemisphere at $Re_D=1.36x10^6$. Based on the model results, it appears that this is characteristic of a change from a flow mode dominated by a large unsteady cavity to one dominated by other, single-phase, turbulent, sources of unsteadiness.

During this investigation, some effort towards the establishment of temporal and spatial discretization independence was made. As a requirement of the model, to accommodate the use of wall functions, for regions of attached liquid flow, fine-grid near-wall points were established at locations yielding $10<y^+<100$.

Temporal convergence was established by the successive reduction of time integration step for several

selected cases. Figure 25 contains a comparison of the spectral content of results for flow over a hemispherical forebody and cylindrical afterbody, with Re_D=1.36x10^5 and σ=0.3, for three, successively smaller, integration step sizes. Here, with a physical time step, $\Delta t = 0.005$ seconds, the computation resulted in a Strouhal frequency, Str=0.0680, with a time step, $\Delta t = 0.0025$ seconds, Str=0.0622, and with $\Delta t = 0.001$ seconds, Str=0.0680. More significantly, as demonstrated in the figure, for the smaller two integration step sizes, over the range of relevant (shown) frequencies, there was very similar modal behavior.

Unfortunately only the fine-grid models tended to provide unsteady results. Thus time and spatial fidelity were judged independently. A demonstration of the steady-state spatial convergence of the modeled conical forebody and cylindrical afterbody is given in Figure 5.

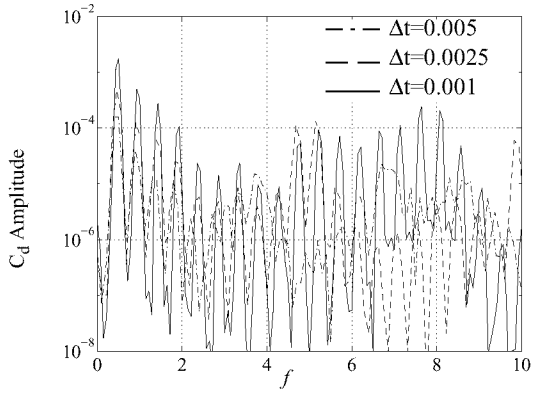


Figure 25. Spectral comparison of effect of physical integration time step size on C_d history. Flow over a hemispherical forebody with cylindrical afterbody. Re_D=1.36x10^5. σ=0.3.

Three-Dimensional Analyses

Natural Cavitation about 1/2- and 1-Caliber Ogives

In order to demonstrate the three-dimensional capability of the method, a model of the hemispherical forebody configuration studied above was run at numerous angles of attack and a cavitation number of 0.3. A 97x33x65 mesh was utilized (corresponding to the "medium" mesh size discussed in grid studies above). The domain was decomposed into 8 subdomains azimuthally and run on 8 SGI RS10K Octane machines. Parallel efficiencies of 85% were achieved for these problems.

Figure 26 provides sample results for angles of attack of 0.0^o, 2.5^o, 5.0^o and 7.5^o. These plots include pressure contours on the plane of symmetry, sample streamlines and the cavitation bubble shape as identified with an isosurface of α_l = 0.99. Several interesting features are observed in the predictions. In particular, the flows are seen to be highly three-dimensional in nature at angle-of-attack. A recirculation zone aft of the bubble, grows with angle of attack. This diminishes the local pressure recovery associated with the bubble-induced blockage and this in turn leads to a local collapse of the bubble on the top of the body. Indeed at angle-of-attack the bubble is seen to have its greatest axial extent off of the symmetry plane of the geometry.

Figure 27 shows the results of a three-dimensional simulation of cavitating flow over a 1-caliber ogive forebody with cylindrical afterbody at a 10° angle-of-attack. A cavitation number of 0.32 was specified. Again a 97 x 33 x 65 mesh was utilized, the domain was decomposed into eight subdomains azimuthally and run on eight processors and at this cavitation number using this grid a steady state solution could be obtained. Figure 27 illustrates the predicted bubble shape and streamline pattern for this simulation. The bubble shape is highly three-dimensional in nature; it does not close on the pressure side of the body. The streamline pattern is characterized by a large recirculation zone aft of the bubble and significant azimuthally oriented vortical struc-

tures.

Figure 28 shows the convergence history for this case. A three order-of-magnitude drop in the axial velocity residual is achieved in 800 pseudo-time-steps. It is observed that the 8-block/8-processor simulation exhibits nearly identical convergence behavior to a 1-block/1-processor run.

Interaction of a Control Surface with Phase-Separated Non-condensable Gas and Liquid Impingement Streams

The second three-dimensional simulation presented is that of a wedge shaped control surface interacting with an incoming stream of phase-separated water and air. This configuration was tested by the fourth author in the 12" water tunnel at the Penn State Applied Research Laboratory (unpublished). The test was run with co-directed air and water streams. Air was injected along the bottom of the tunnel such that the unperturbed gas-liquid interface impinged upon the sharp leading edge at about 25% span from the base of the fin. Air and water velocities were approximately the same. The configuration was tested at a range of angles-of-attack.

A 189,546 vertex grid was used for the results presented here. The simulation was run on 16 processors with a 10° angle-of-attack and a cavitation number of 0.15. Using this relatively coarse mesh and the k-ε model, a steady-state solution was obtained, despite the presence of a blunt trailing edge and its associated recirculation zone along the span. As we refine our analyses of this class of application, time accurate simulations using upwards of 10^{6} nodes will be required.

These flows are characterized by several physical features of academic and practical interest. At angle-of-attack, the liquid and gas streams are turned through approximately the same angle, but because the density ratio is high (≅1000 here), significant spanwise pressure gradients arise along the lifting surfaces. Accordingly, on the pressure side, the gas-liquid interface is deflected downward, giving rise to deceleration and acceleration of the liquid and gas streams respectively. On the suction surface the lower pressure in the liquid gives rise to an upward deflection of the gas interface. Attendant to these interface deflections is a loss in lift.

Adjacent to the sharp leading edge on the suction side, the local static pressure becomes low due to leading edge separation. Local natural cavitation occurs, and this vapor merges with the swept up non-condensable interface so that the entire suction side is enveloped in gas phase. Aft of the blunt trailing edge, the flow is recirculating and therefore the local static pressure is also low. This gives rise to a sweeping up of the pressure side cavity and some natural cavitation so that the entire wake region is principally gas phase.

Figure 29 shows an oblique front/top view of the predicted flow field. Each of the flow features discussed above is clearly observed in the simulation. Of particular note is that the three-species formulation enables the separate prediction and identification of vaporous and non-condensable regions of the flow. Figure 30a shows a suction side video frame of the tested flow configuration at this angle-of-attack. The enveloping of the suction surface in gas phase and the primarily gas phase wake are observed. Figure 30b shows a pressure side photograph. A similar view of the simulation is presented in Figure 30c which shows that the pressure surface interface deflection and gas-vapor wake region are qualitatively consistent with experimental observation.

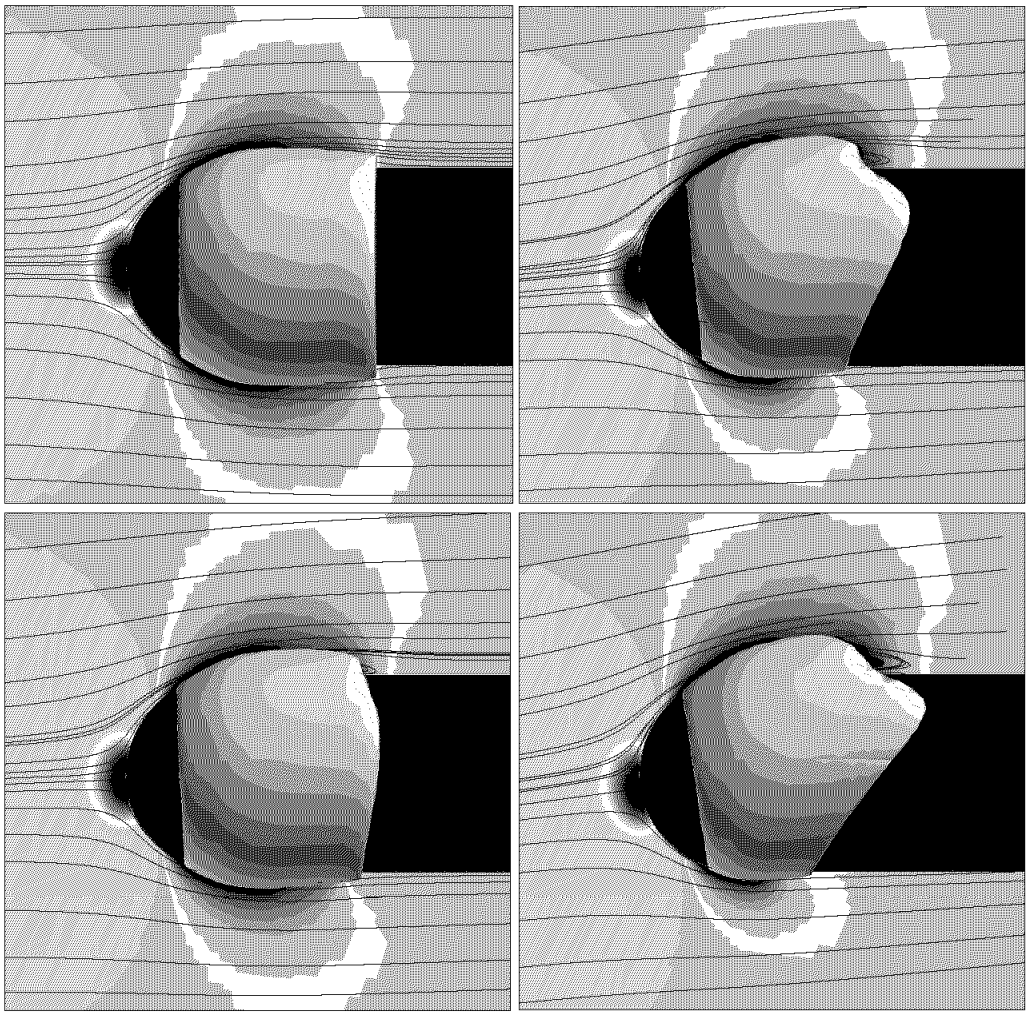


Figure 26. Predicted 3-D flow field with natural cavitation about hemispherical fore-body at several angles of attack. $\sigma = 0.3$. Liquid volume fraction = 0.99 isosurface.

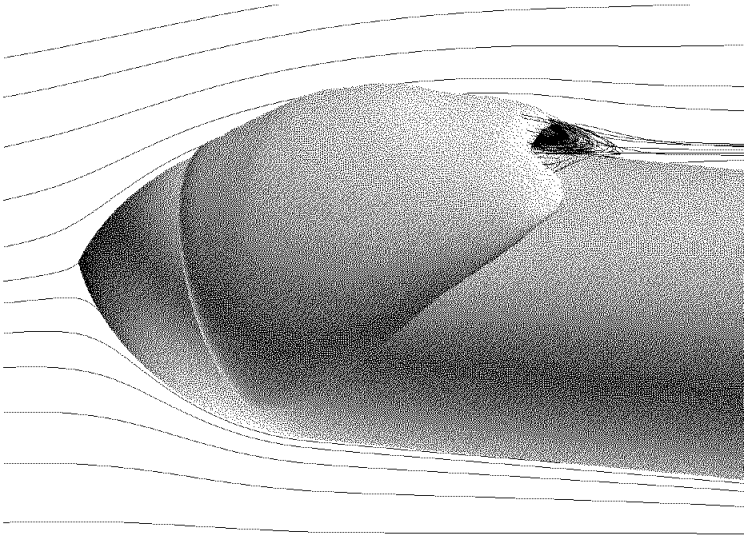


Figure 27. Predicted bubble shape (designated by $\alpha_l = 0.99$ isosurface) and streamlines for a 1-caliber ogive at a 10° angle-of-attack.

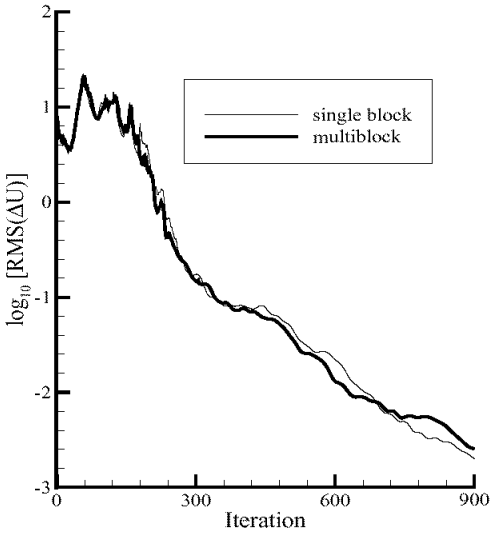


Figure 28. Comparison of 1-block/1-processor and 8-block/8-processor convergence histories for a 1-caliber ogive at a 10° angle-of-attack.

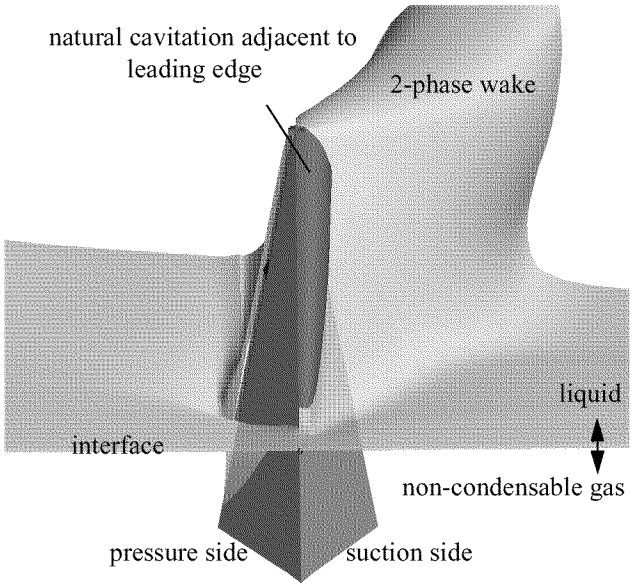


Figure 29. Front/top view of CFD simulation of supercavitating fin configuration at 10° angle-of-attack. Isocontours of $\alpha_{ng} = 0.9$, $\alpha_v = 0.9$ designate non-condensable gas and vapor regions respectively.

Three-dimensional Flow over a Vehicle with Ventilation and Natural Cavitation

Practical high speed supercavitating vehicle designs employ ventilation at or near the cavitator leading edge, where natural cavitation will likely also occur. Figure 31 illustrates elements of a 48-processor three-dimensional analysis of a notional vehicle with natural cavitation, noncondensable gas injection and propulsion stream. This illustrates the three-species nature of the formulation.

Unsteady Three-Dimensional Flow Over a 0-Caliber Ogive

As pointed out by Edwards [10], a potential cause of the discrepancies observed between predicted and measured Strouhal numbers for the cavitator series simulations is the axisymmetric nature of the unsteady runs. We have begun to investigate this by simulating these flows three-dimensionally. Figure 32 illustrates elements of a 1,245,184 cell, 78 processor unsteady simulation of flow over a blunt ogive at σ=0.30. Re_D=1.46x10^5. Clearly observable are non-axisymmetric predicted cavity shapes. We continue to investigate these modes in the hope of quantifying them.

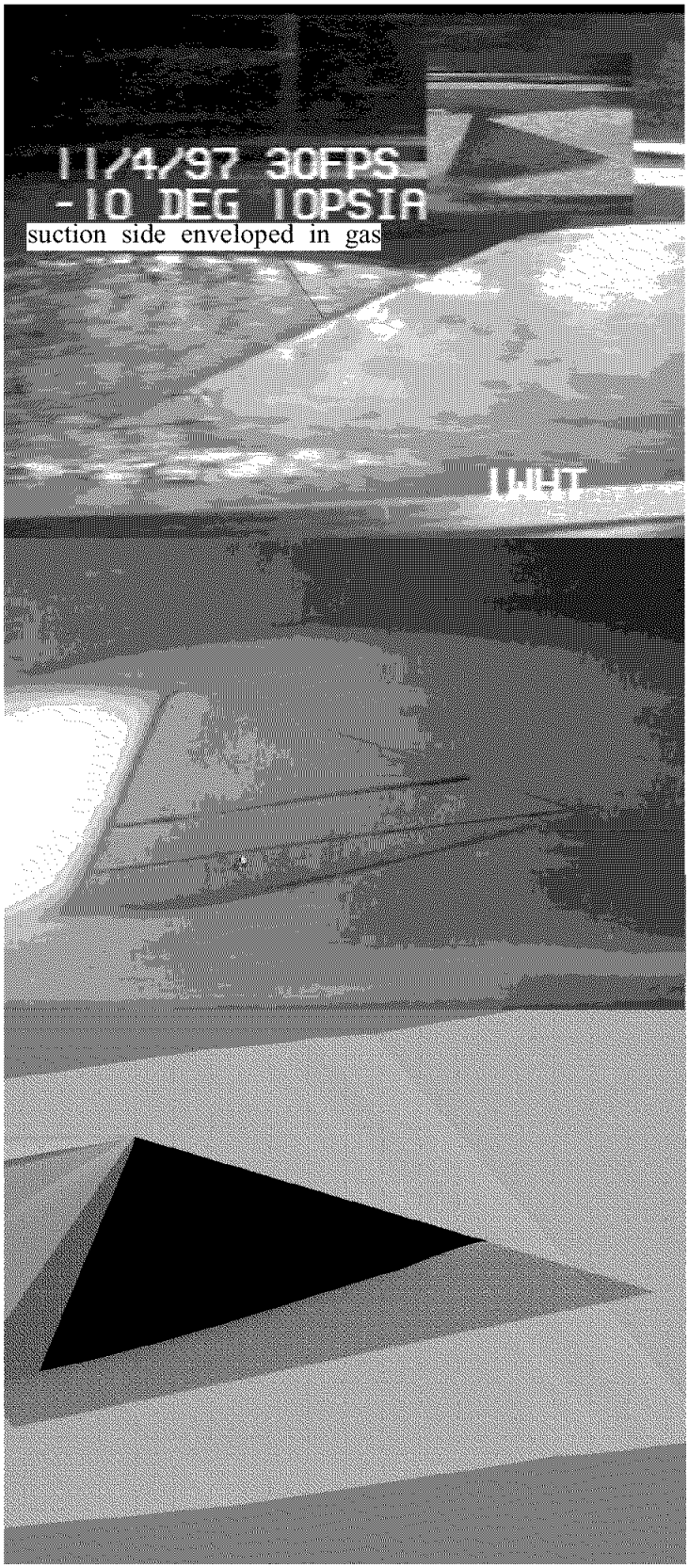


Figure 30. a) Suction side video frame of super-cavitating fin at 10° angle-of-attack. b) Pressure side photograph. c) Pressure side view of CFD simulation.

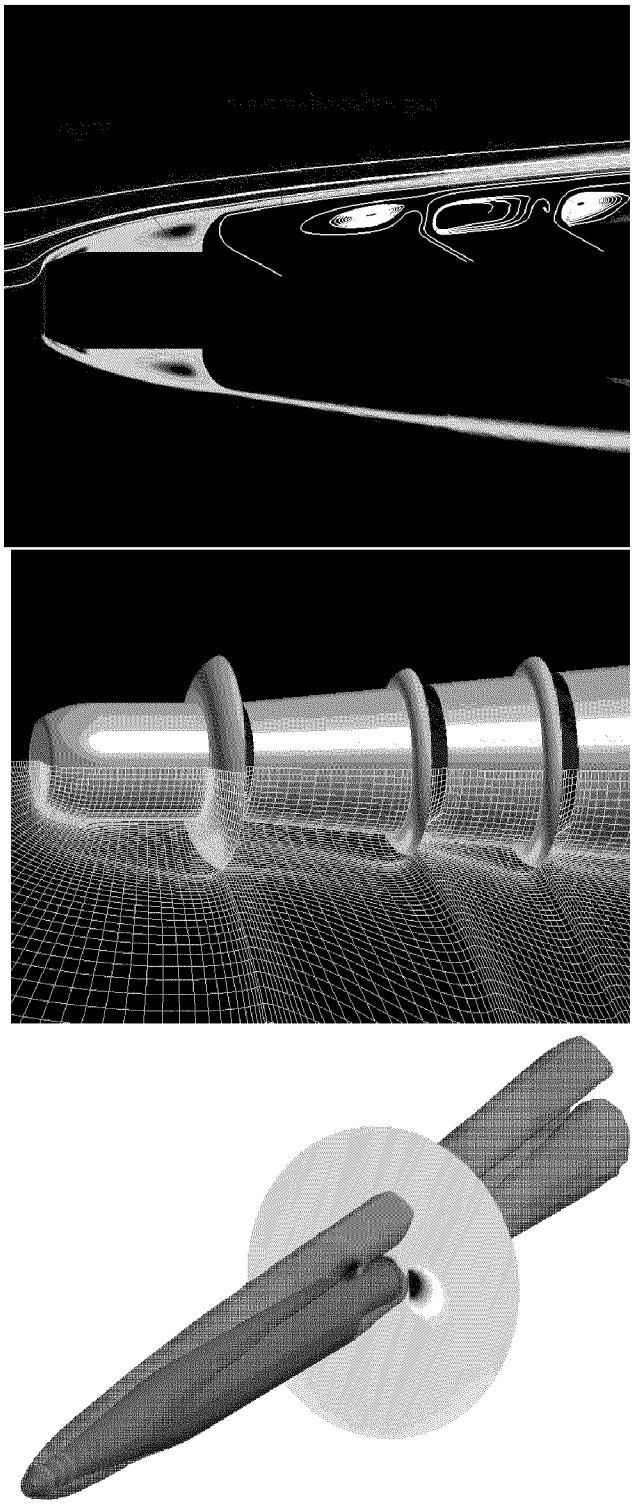


Figure 31. Elements of three-dimensional supercavitating vehicle simulations with ventilated and natural cavitation. a) liquid volume fraction contours and stream lines ($\alpha = 0^{o}$), b) view of 3D geometry and grid, c) liquid volume fraction = 0.9 isovolume and vertical velocity contour plane ($\alpha = 5^{o}$).

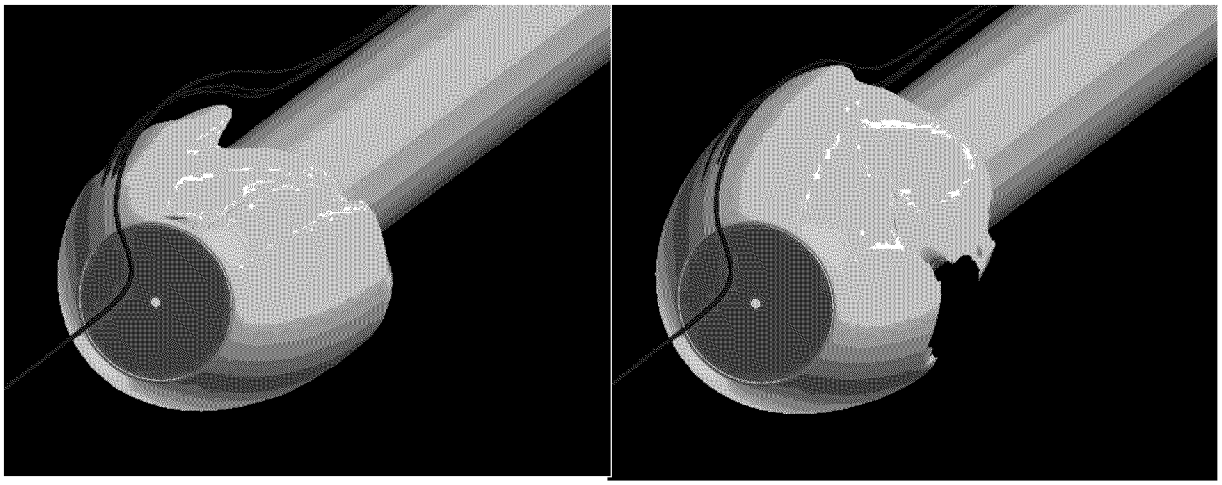


Figure 32. Three-dimensional, turbulent, unsteady, two-phase result. 1,245,184 cell grid. Flow over blunt ogive with an isosurface of volume fraction, α_l=0.9, and selected streamlines at two timesteps. σ=0.30. Re_D=1.46x10^5.

Sheet Cavitation in a Centrifugal Pump

The authors have recently extended our efforts towards the analysis of sheet cavitation in turbomachinery. Some representative results are presented here. Figure 33 shows three simulations of a generic backswept impeller at three cavitation numbers. These plots show a front view of the impeller, with surface pressure contours on the blade surfaces and hub. Also shown are the predicted sheet cavities on the blade surfaces as designated with an isovolume contour of liquid volume fraction = 0.9. A single blade passage was computed; the results have been copied several times to yield a complete annulus view.

We have not yet analyzed the cavitation *performance* of this three dimensional configuration. This is because when employing the higher order convection differencing and fine grids required for accurate cavitation bubble size predictions for a specified cavitation number, the cavities and thereby the simulation are unsteady. As a step towards the goal of predicting cavitation performance in pumps, we have analyzed a quasi-three-dimensional midspan streamsheet representation of the same configuration. Performance predictions for this series of analyses are shown in Figure 34. In Figure 34a, head coefficient versus flow coefficient is plotted for a spectrum of flow coefficients and cavitation numbers. Single phase results are plotted as solid red diamonds. A characteristic head drop off is observed off design (though clearly efficiency levels and off design trends are unrealistic due to the quasi-three-dimensional modeling employed). A sequence of successively lower cavitation numbers were run for several flow coefficients. The reduction in predicted head attendant to the sheet cavitation are also plotted in Figure 34a. Figure 34b illustrates the ability of the analysis to capture incipient cavitation breakdown physics. There, head coefficient is plotted versus cavitation number for the series of quasi-three-dimensional simulations. At each flow coefficient, a rapid drop-off in head is observed at a critical cavitation number.

The authors point out that these pump cavitation results are preliminary and several issues remain to be resolved including the need for improved mass transfer modeling to account for thermal effects on cavitation breakdown, and three-dimensional performance analysis.

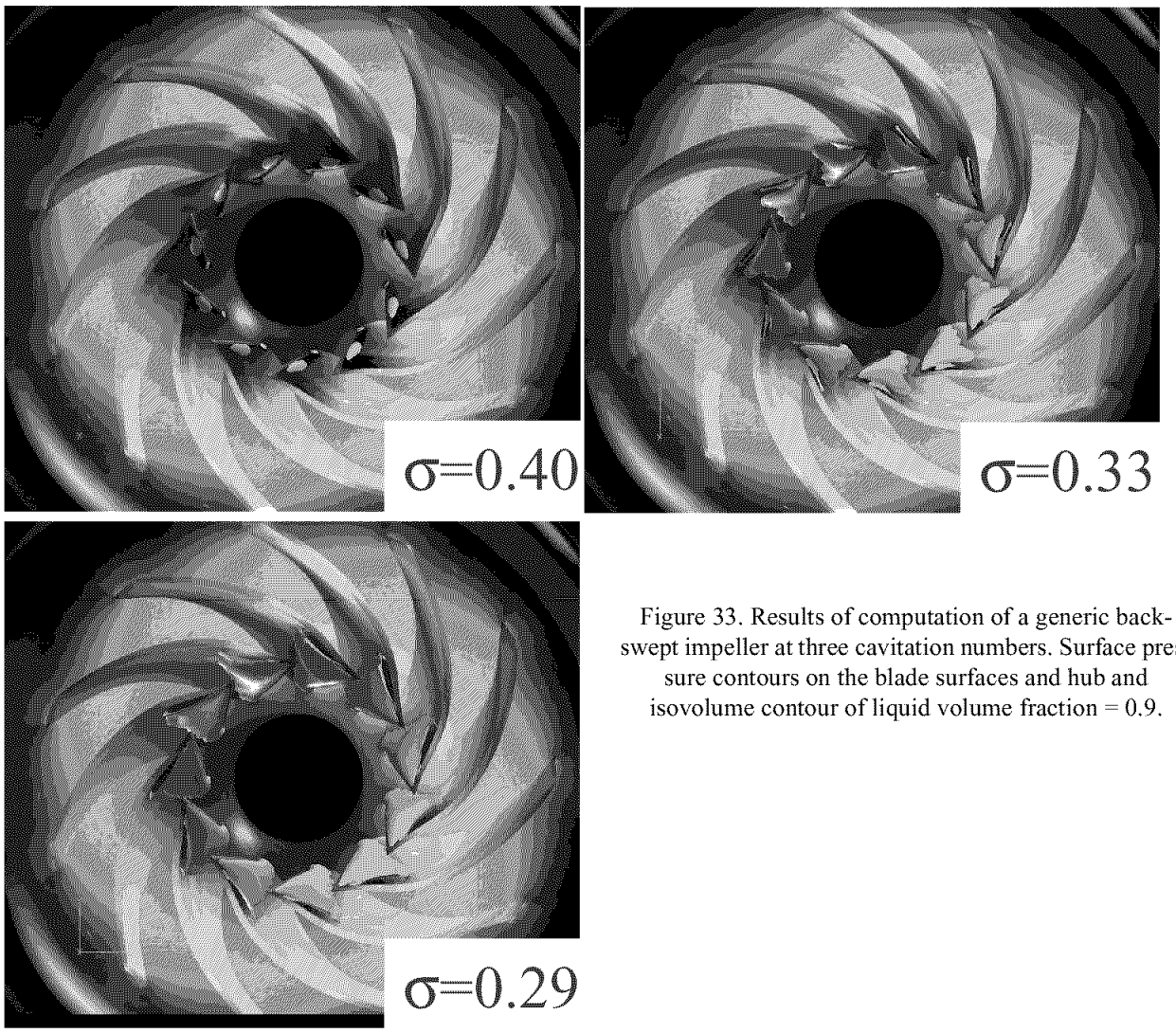


Figure 33. Results of computation of a generic back-swept impeller at three cavitation numbers. Surface pressure contours on the blade surfaces and hub and isovolume contour of liquid volume fraction = 0.9.

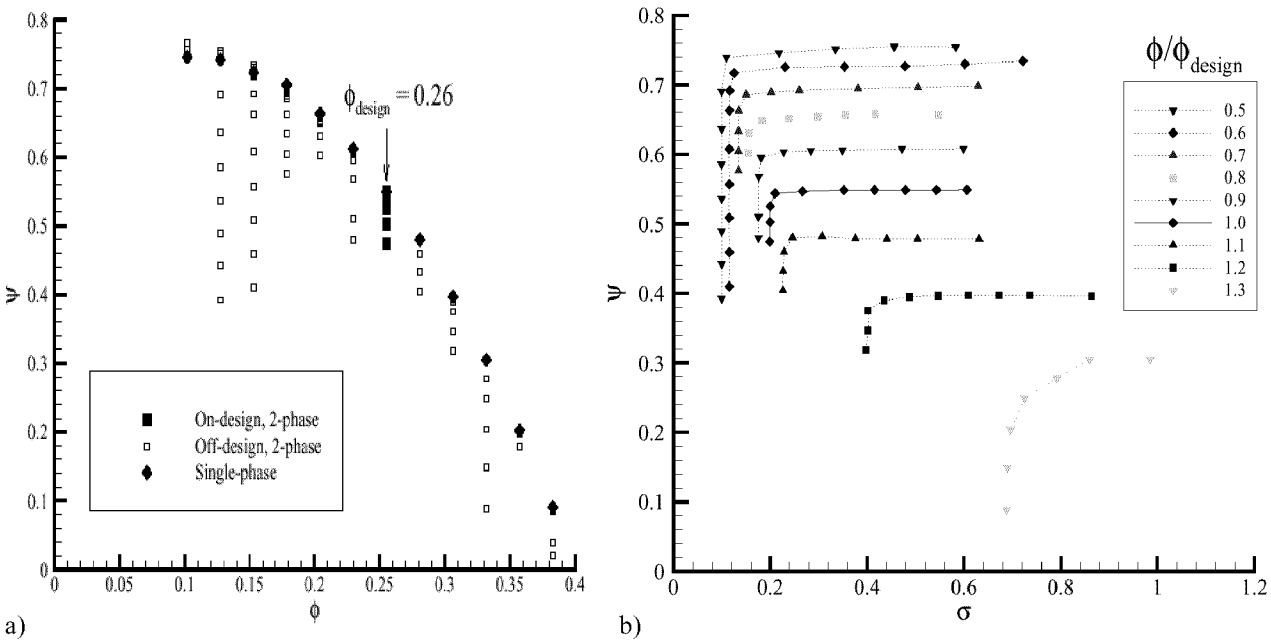


Figure 34. Results of quasi-three-dimensional midspan streamsheet analyses of a generic backswept impeller. a) predicted efficiency vs. flow coefficient, b) predicted head coefficient vs. cavitation number at several flow coefficients.

Compressible Simulations

Some recently obtained compressible flow results are presented in Figures 35 and 36. Figure 35 contains an illustrative result of a projectile traveling supersonically relative to the speed of sound in water. On the left is a photograph of the actual test. At right is the model result for this case. In the model result, the liquid to vapor density ratio is nominally 1000, and the Mach Number is 1.03. The example is illustrative of challenging modeling issues. In the liquid flow, there are shock waves. These are resolved with MUSCL interpolation and the van Albada limiter. In addition, due to the high flow velocity, the cavitation index is approximately 10^{-4}. In the figure, dark blue indicates density of less than one and red indicates density of nominally 1000. Thus, most of the flow immediately adjacent to the object is completely vaporized as is the downstream wake. This is exhibited in both the photograph and the model result.

Figure 36 contains a modeled axisymmetric plume from a hypothetical rocket operating underwater. Here the jet is supersonic and slightly underexpanded. It is surrounded by a second gas stream which is subsonic (notionally the vehicle cavity) and finally by a subsonic water free stream. In this case the nominal liquid to gas density ratio is again 1000. In the density field, red indicates a density of nominally 1000, and blue indicates a density of one or less. In the shock function field, the classic expansion pattern followed by shocks are exhibited. The interaction of the compressible gas stream with the nearly incompressible liquid is demonstrated by the contraction and expansion, from top to bottom in the figure, of the gas stream. In addition, the interface between the gas and liquid contains fully supersonic flow. This region is highlighted by the shock function due to the density gradient, but does not necessarily contain shocks. A line segment drawn locally normal to the interface would be nearly isobaric. Further results of our compressible multiphase efforts are available in [20] and [41].

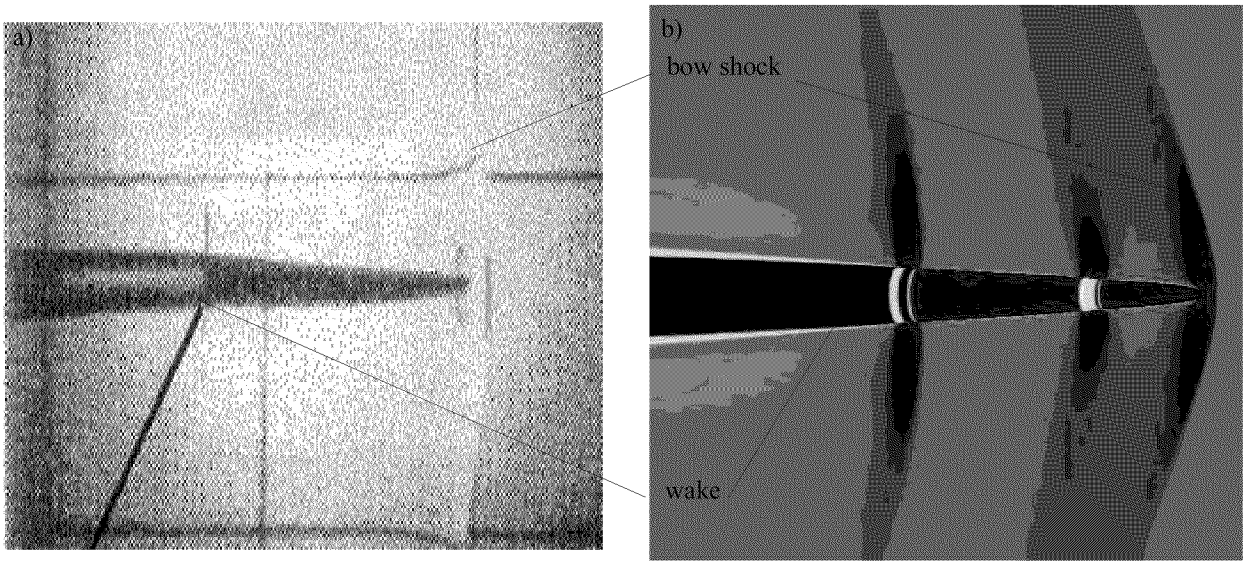


Figure 35. Hypervelocity projectile test and computation. a) Photograph of a projectile at M=1.03 with respect to water sound speed. b) Corresponding simulation showing surface pressure and field mixture density contours.

Conclusions

A multi-phase CFD method has been presented and applied to a number of high density ratio developed- and super-cavitating flows. Several aspects of the method were outlined and demonstrated that enable convergent, accurate and efficient simulations of these flows. These include a differential model and preconditioning strategy with favorable eigensystem characteristics, a block implicit dual-time solution strategy, a three species formulation that separately accounts for condensable and non-condensable gases, higher order flux differencing with limiters and the embedding of this scheme in a parallel multi-block Navier-Stokes platform.

The two-dimensional/axisymmetric simulations presented verify the ability of the tool to accurately analyze steady-state and transient sheet- and super-cavity flows. The three-dimensional and compressible capability of the code was demonstrated as well.

As the authors proceed with this research, we are focusing on several areas including: 1) validation of the method for compressible constituent fields, 2) improved physical models for mass transfer and turbulence, 3) extended application and validation for steady and transient three-dimensional flows and 4) improved error damping through preconditioning and pseudo-time-stepping formulations that locally adapt to problem parameters.

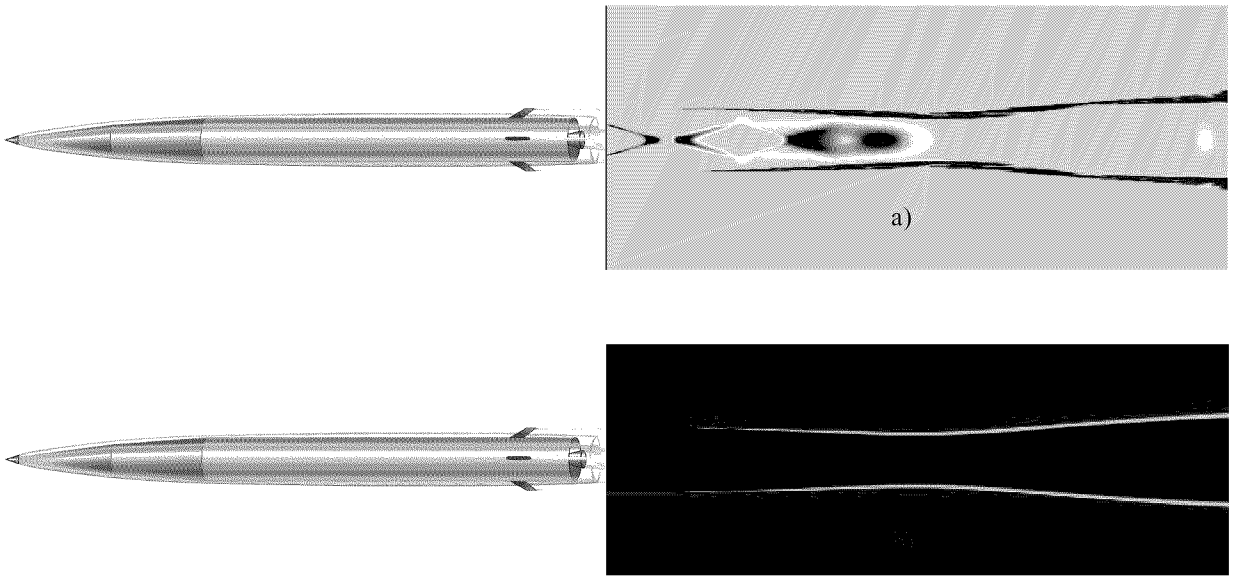


Figure 36. Cartoon vehicle and 3-stream, axisymmetric plume computation. Center jet (diameter=1, M=3 with respect to propellant sound speed) surrounded by cavity gas at free stream velocity (outer diameter=2, M<<1), surrounded by freestream liquid (Liquid to gas density ratio 1000, M<<1). a) mixture density contours, b) shock function, $\nabla \cdot \nabla \rho$, contours.

Acknowledgments

This work is supported by the United States Office of Naval Research with Dr. Kam Ng as contract monitor. This work was supported in part by a grant of HPC resources from the Arctic Region Supercomputing Center and in part by a grant of SGI Origin 2000 HPC time from the DoD HPC Center, Army Research Laboratory Major Shared Resource Center.

References

1. Ahuja, V., Hosangadi, A., Ungewitter, R., Dash, S.M. (1999) "A Hybrid Unstructured Mesh Solver for Multi-Fluid Mixtures, AIAA Paper 99-3330.
2. Anderson, W.K., Thomas, J.L., Van Leer, B. (1986) "Comparison of Finite Volume Flux Vector Splittings for the Euler Equations," *AIAA Journal*, Vol. 24, No. 9, pp.1453-1460.
3. Arndt, R., Song, C., Kjeldsen, M., He, J., Keller, A. (2000) "Instability of Partial Cavitation: A Numerical/Experimental Approach", presented at the 23rd Symposium on Naval Hydrodynamics, Val de Reuil, France.
4. Brennan, C.E., Cavitation and Bubble Dynamics, Oxford University Press, New York, 1995.
5. Brennan, C.E., Hydrodynamics of Pumps, Oxford University Press, England, 1994.
6. Chen, Y., Heister, S.D. (1994) "Two-Phase Modeling of Cavitated Flows," ASME FED-Vol. 190, pp.299-307.
7. Chorin, A.J. (1967) "A Numerical Method for Solving Incompressible Viscous Flow Problems," *Journal of Computational Physics*, Vol. 2, pp. 12-26.
8. Dellanoy, Y., Kueny, J.L. (1990) "Two-phase Flow Approach in Unsteady Cavitation Modeling," ASME FED-Vol. 98, pp.153-158.
9. Dieval, L., Pellone, C., Arnaud, M. (2000) "Advantages and Disadvantages of Different Techniques of Modeling of Supercavitation," Proceedings of Meeting on High Speed Hydrodynamics and Supercavitation, Grenoble, France.
10. Edwards, J.R. (2000) Published discussion to reference [19].
11. Garabedian, P.R. (1958) "Calculation of Axially Symmetric Cavities and Jets," Pac. J. of Math 6.
12. Grogger, H.A., Alajbegovic, A., (1998) "Calculation of the Cavitating Flow in Venturi Geometries Using Two Fluid Model," ASME Paper FEDSM 98-5295.

13. Hirsch, C. (1990) Numerical Computation of Internal and External Flows, Volume 2, John Wiley and Sons, New York.
14. Jameson, A., Schmidt, W., Turkel, E. (1981) "Numerical Solutions of the Euler Equations by Finite Volume Methods Using Runge-Kutta Time-Stepping Schemes," AIAA Paper 81-1259.
15. Kirchner, I. N. (2001) "Numerical Modeling of Supercavitating Flows," VKI Special Course on Supercavitating Flows, February.
16. Jones, W.P., Launder, B.E. (1972) "The Prediction of Laminarization with a Two-Equation Model of Turbulence," *International Journal of Heat and Mass Transfer*, Vol. 15, pp. 301-314.
17. Kunz, R.F., Siebert, B.W., Cope, W.K., Foster, N.F., Antal, S.P., Ettorre, S.M (1998) "A Coupled Phasic Exchange Algorithm for Three-Dimensional Multi-Field Analysis of Heated Flows with Mass Transfer," *Computers and Fluids*, Vol. 27, No. 7, pp. 741-768.
18. Kunz, R.F., Boger, D.A., Stinebring, D.R., Chyczewski, T.S., Lindau, J.W., Gibeling, H.J., Venkateswaran, S., Govindan, T.R. (1999) "A Preconditioned Navier-Stokes Method for Two-Phase Flows with Application to Cavitation Predication," AIAA Paper 99-3329, also *Computers and Fluids*, Vol. 29, No. 8, [Nov, 2000], pp. 849-875.
19. Lindau, J.W., Kunz, R.F., Gibeling, H.J. (2000) "Validation of High Reynolds Number, Unsteady Multi-Phase CFD Modeling for Naval Applications," presented at the 23rd Symposium on Naval Hydrodynamics, Val de Reuil, France.
20. Lindau, J.W., Kunz, R.F., Venkateswaran, S., Boger, D.A. (2001) "Application of a Preconditioned, Multiple-Species, Compressible, Navier-Stokes Model to Cavitating Flows", Submitted to the 4th International Symposium on Cavitation, Pasadena, California, 20-23 June.
21. Lindau, J.W., Venkateswaran, S., Kunz, R.F., Merkle, C.L. (2001) "Development of a Fully-Compressible Multi-Phase Reynolds-Averaged Navier-Stokes Model", AIAA Paper 2001-2648.
22. May, A. (1975) "Water Entry and the Cavity-Running Behaviour of Missiles," Naval Sea Systems Command Hydroballistics Advisory Committee TR-75-2.
23. Merkle, C.L., Feng, J., Buelow, P.E.O. (1998) "Computational Modeling of the Dynamics of Sheet Cavitation," Proceedings of 3rd International Symposium on Cavitation, Grenoble, France, pp. 307-311.
24. Orszag, S.A., Yakhot, V., Flannery, W.S., Boysan, F., Choudhury, D., Maruzewski, J., Patel, B. (1993) "Renormalization Group Modeling and Turbulence Simulations, Near Wall Turbulent Flows," Elsevier Science Publishers B.V., Amsterdam, The Netherlands.
25. Reboud, J. L., Delannoy, Y. (1994) "Two-Phase Flow Modeling of Unsteady Cavitation," Proceedings of 2nd International Symposium on Cavitation, Tokyo, Japan, pp. 39-44.
26. Reboud, J. L., Fortes-Patella, R., Hofman, M., Lohrberg, H., Ludwig, G., Stoffel, B. (1999) "Numerical and Experimental Investigations on the Self-Oscillating Behaviour of Cloud Cavitation," ASME Paper FEDSM99-7259, Proceedings of 3rd ASME/JSME Joint Fluids Engineering Conference.
27. Reichardt, H. (1946) "The Laws of Cavitation Bubbles at Axially Symmetrical Bodies in a Flow," Ministry of Aircraft Production Volkenrode, MAP-VG, Reports and Translations 766, Office of Naval Research.
28. Rogers, S. E., Chang, J. L. C., Kwak, D. (1989) "A Diagonal Algorithm for the Method of Pseudocompressibility," *Journal of Computational Physics*, Vol. 73, pp. 364-379.
29. Rouse, H., McNown, J. S. (1948) "Cavitation and Pressure Distribution, Head Forms at Zero Angle of Yaw," Studies in Engineering, Bulletin 32, State University of Iowa.
30. Saurel, R., Cocchi, J.P., Butler, P.B. (1999) "Numerical Study of Cavitation in the Wake of a Hypervelocity Underwater Projectile," *AIAA Journal of Propulsion and Power*, Vol. 15, No.4, pp. 513-520.
31. Schlichting, H. (1979) Boundary-Layer Theory, McGraw-Hill, New York.
32. Shin, B.R., Ikohagi, T. (1998) "A Numerical Study of Unsteady Cavitating Flows," Proceedings of 3rd International Symposium on Cavitation, Grenoble, France, pp. 301-306.
33. Shyy, Wei (2000) Personal communication and published discussion to reference [19].
34. Siebert, B.W., Maneri, C. C., Kunz, R.F., Edwards, D. P. (1995) "A Four-Field Model and CFD Implementation for Multi-Dimensional, Heated Two-Phase Flows," 2nd International Conference on Multiphase Flows, Kyoto, Japan.
35. Song, C., He, J., (1998) "Numerical Simulation of Cavitating Flows by Single-Phase Flow Approach," Proceedings of 3rd International Symposium on Cavitation, Grenoble, France, pp. 295-300.
36. Stinebring, D.R., Billet, M.L., Holl, J.W. (1983) "An Investigation of Cavity Cycling for Ventilated and Natural Cavities," TM 83-13, The Pennsylvania State University Applied Research Laboratory.
37. Stinebring, D.R. (1976) "Scaling of Cavitation Damage," M.S. Thesis, The Pennsylvania State University, University Park, Pennsylvania, August.
38. Stinebring, D.R., Billet, M.L., Lindau, J.W., Kunz, R.F. (2001) "Developed Cavitation-Cavity Dynamics," VKI Special Course on Supercavitating Flows, February.
39. Taylor, L. K., Arabshahi, A., Whitfield, D. L. (1995) "Unsteady Three-Dimensional Incompressible Navier-Stokes
40. Venkateswaran, S., Deshpande, M., Merkle, C.L. (1995) "The Application of Preconditioning to Reacting Flow

Computations," AIAA Paper 95-1673, from Proceedings of the 12th AIAA Computational Fluid Dynamics Conference.

41. Venkateswaran, S., Lindau, J.W., Kunz, R.F., Merkle, C.L. (2001) "Evaluation of Preconditioning Algorithms for the Computation of Multi-Phase Mixture Flows," AIAA Paper 2001-0279.
42. Venkateswaran, S., Merkle, C. L. (1995) "Dual Time Stepping and Preconditioning for Unsteady Computations," AIAA Paper 95-0078.
43. Van der Heul, D.R., Vuik, C., Wesseling, P. (2000) "Efficient Computation of Flow with Cavitation bay Compressible Pressure Correction", Proceedings of AMIF-ESF Workshop on Computing Methods for Two-Phase Flow, Aussois, France.
44. Vasin, A. (2000) "High Speed Body Motion in COmpressible Fluid," Proceedings of Meeting on High Speed Hydrodynamics and Supercavitation, Grenoble, France.
45. Whitfield, D. L., Taylor, L. K. (1994) "Numerical Solution of the Two-Dimensional Time-Dependent Incompressible Euler Equations," Mississippi State University CFD Laboratory Report MSSU-EIRS-ERC-93-14.

Control of Supercavitation Flow and Stability of Supercavitating Motion of Bodies

Yu. N. Savchenko
Ukrainian National Academy of Sciences - Institute of Hydromechanics
8/4 Zhelyabov str., 03057 Kiev
Ukraine

Introduction

Control of the supercavity parameters is necessary for maintenance of calculated regime of the supercavitation flow in unsteady conditions: at changing the velocity and depth of the body motion. The problem of cavitation flow control includes the two problems connected among themselves:

I) the control of cavity dimensions;

II) the control of forces on a cavitating body.

We consider sequentially both problems.

I) It is known [1, 2] that at small σ the mid-section diameter D_c and length L_c of the axisymmetrical cavity are determined by the cavitator diameter D_n, the drag coefficient c_x and the cavitation number:

$$\frac{D_c}{D_n} = \sqrt{\frac{c_{x0}\ (1+\sigma)}{\sigma}}, \qquad \frac{L_c}{D_n} = \frac{1}{\sigma}\sqrt{c_{x0}(1+\sigma)\ln\frac{1}{\sigma}}. \tag{1}$$

where the cavitation number $\sigma = 2(\rho g h - p_c)/\rho V^2$ is a an important parameter of supercavitating flows. Here, h, V are the depth and the speed of motion, respectively, and p_c is the cavity pressure.

At small cavitation numbers [6] the following approximate formula for the drag coefficient of a blunted cavitator is valid:

$$c_x = c_{x0}(1+\sigma), \tag{2}$$

where c_{x0} is the drag coefficient value for a given cavitator when $\sigma = 0$ (that is, for free streamline flow).

The validity of asymptotic relations (1) for models with disk cavitator moving with velocities $300 \div 1300$ m/s is confirmed by us experimentally [3].

It is visible from relations (1) that at constant D_n, h, V to control cavity dimensions it is possible by two ways:

1) changing the cavitation number σ; 2) changing the cavitator drag coefficient c_x.

Paper presented at the RTO AVT Lecture Series on "Supercavitating Flows", held at the von Kármán Institute (VKI) in Brussels, Belgium, 12-16 February 2001, and published in RTO EN-010.

1. Supercavitation flow control by gas blowing

The first way is effective at motion velocities $10 \div 100$ m/s and is realized by gas supply to the cavity, i.e. by increase p_c (so named the artificial cavitation or ventilation [5]). The method of gas-supply is widely applied in experimental researches for formation of long cavities at moderate flow speeds in the hydrodynamic tunnel (Fig.1).The Fig. 2 demonstrate dependencies $\sigma = \sigma(\overline{Q})$.

The value of gas-supply to the cavity Q is defined by dependence [2, 6]:

$$\overline{Q} = \frac{Q}{VD_n^2} = F(\sigma, Fr, \mathrm{Re}, We), \tag{3}$$

where Fr, Re, We are accordingly *Froude, Reynolds* and *Weber* numbers. The Fig. 3 demonstrate the cavity length – L control by gas flow rate $\overline{Q}$. In the region of strong influence of gravity the formula for supply value has the form [2]:

$$\overline{Q} = \frac{0.27}{\sigma[\sigma^3 Fr^4 - 2]}. \tag{4}$$

In the regimes close to vapor ones the structure of dependence (4) changes:

$$\overline{Q} = kVS\left(\frac{\sigma_\upsilon}{\sigma} - 1\right). \tag{5}$$

The region of effective control of air-supply in the artificial cavitation regime is limited by value $\sigma_{\min} = 1.41 g D_c / V^2$ from (4) and by vapor cavitation occurrence at $\sigma = \sigma_v$:

$$1.41 g D_c / V^2 < \sigma \le \sigma_\upsilon = \frac{2(p - p_\upsilon)}{\rho V^2}, \tag{6}$$

where p_υ is the pressure of saturated water vapor.

The motion in water with velocities $V >> 100$ m/s occurs in the regime of vapor or natural cavitation, then the gas-supply to the cavity becomes inefficient.

2. Supercavitation flow control by jet cavitator

According to the hydrodynamic scheme of supercavitation flow, the object is placed partially or fully inside a supercavity (Fig. 4a, b) formed by the nasal part (cavitator) [1, 4, 6]. In the case of a jet cavitator system, the cavity separates from the craft hull (Fig. 4c).

The comparatively new scheme (c) has in comparison with conventional schemes (a) and (b) the following advantages:

1) the hydrodynamic drag reduction due to the model in general has not points of contact with water (theoretically in twice in comparison with a solid disk cavitator at $\sigma \to 0$);

2) the possibility of control of cavity by water rate change in the nose jet.

For the first time *L.I.Sedov* offered the way of formation of cavities due to giving up the fluid jet toward to the mainstream (i.e. scheme of jet cavitator) [4]. He gave the estimation of drag coefficient of the jet cavitator, considering it as an inverted scheme of cavity with reentrant jet [14].

The scheme of cavitating flow around the body A with reentrant jet is presented in Fig. 5a. It is known as the *Efros - Hilbarg* scheme [14]. It is theoretically possible to think that the reentrant jet is absorbed by fictitious body B. Then the cavitation drag of body A is equal to:

$$X = \rho Q(V_\infty + V_c), \quad V_c = V_\infty \sqrt{1+\sigma}, \tag{7}$$

where $Q = SV_c$ is the volumetric water rate in the reentrant jet, S is the area of jet section, V_c is the velocity on the cavity surface (it is equal to velocity in the reentrant jet).

Passing on to the limit at $\sigma \to 0$ (thus the body B tends to the infinity), we obtain the cavitating drag of body A by *Kirchhoff* scheme :

$$X_0 = 2\rho Q V_\infty . \tag{8}$$

Changing the direction of all the velocities at $\sigma \to 0$, we obtain the scheme of cavitating flow around the body B with jet cavitator (Fig. 5b). The expenditure of energy expending by body on overcoming of cavitator drag is replaced by expenditure of energy on formation of opposing jet in this case. We obtain for jet momentum:

$$\rho Q V_\infty = \frac{X_0}{2}, \tag{9}$$

i.e. when $\sigma \to 0$, the opposing jet momentum necessary for cavity supporting is twice less than cavitating drag force of a solid cavitator.

We experimentally investigated the cavities formed by opposing liquid jet in the small hydrodynamic tunnel at the IHM UNAS at flow velocity 10 m/s. Thus the air is in addition supplied to the cavity because of small flow velocity. The experimental dependence of opposing jet length L_j from the nozzle to the frontal point of cavity on velocity in the jet $\overline{V}_j = V_j / V_\infty$ is presented in Fig. 6.

We note that the limit value obtained experimentally $V_j(L_j) \approx 0.75V_\infty$ at $L_j \to 0$ does not correspond to the classical scheme of jet collision with critical point [14], in which $\rho V_\infty^2 = \rho V_j^2$. The value $V_j(0) \approx 0.75V_\infty$ permits to assume that the scheme of jet collision with formation of critical region without breakdown points [14] is realized in the experiment. For such scheme the relation $\rho V_\infty^2 = 2\rho V_j^2$ should be fulfilled theoretically, whence $V_j = 0.707V_\infty$.

We mention yet for completeness about a cavitating flow scheme similar externally to the scheme where the cavity is formed with help of gas jet blown out from the model nose toward mainstream [5]. Thus these cavities relate to artificial (ventilated) cavities by classifications. To create cavity the gas jet with density ρ_g should be blown out with velocity V_g enabling to overcome the dynamic head of water mainstream $\rho V_\infty^2/2$. We have from the *Bernoulli* integral:

$$V_g > V_\infty \sqrt{\frac{\rho}{\rho_g}(1+\sigma)}. \tag{10}$$

If the air is used as a gas $\rho/\rho_g = 800$, then we obtain from (10) without account of air compressibility:

$$V_g > 28.3\left(1+\frac{\sigma}{2}\right)V_\infty.$$

It is visible that such way of cavity formation is really realized only at small V_∞.

The conducted experiments show that the cavities created due to opposing gas jet have the strongly disturbed surface and the powerful accompanying turbulent emulsion flow [5].

3. Supercavitation flow control by change of c_x

As it is was said above the cavity control method by means of gas-supply is not applied at very high velocities of motion in water and/or small model dimensions. Therefore, the research of possibility of cavity control by change of c_x is very interesting.

3.1. ESTIMATION OF DRAG OF AXISYMMETRIC CAVITATOR

The practical way of estimation of the drag of the axisymmetric cavitators consists in that the pressure distribution p along the generator of cavitator is taken from the solution of the two-dimensional problem on free streamline flow around the contour coinciding with a meridian section of the cavitator. Then the drag of the axisymmetric cavitator is defined by integration:

$$\tilde{c}_x = \frac{2\tilde{X}}{\rho V^2 \pi R_n^2}, \quad \tilde{X} = 2\pi \int_0^{R_n} (p - p_c) y dy, \tag{11}$$

where $R_n = D_n/2$.

It was shown in the work [17] that the values c_x for cones computed by given approximate way are close to the experimental data. We present also their comparisons with results of the numerical computation executed on basis of exact formulation of the problem [18]. For comparison we use the approximation formulae given in the work [19]:

$$
\begin{aligned}
c_x &= c_{x0} + (0.524 + 0.672\mu)\sigma, 0 \le \sigma \le 0.25, \\
&\qquad \frac{1}{12} \le \mu \le \frac{1}{2}, \\
c_{x0} &= 0.5 + 1.81(\mu - 0.25) - 2(\mu - 0.25)^2, \\
&\qquad \frac{1}{12} \le \mu \le \frac{1}{2} \\
c_{x0} &= \mu(0.915 + 9.5\mu), \ 0 < \mu < \frac{1}{2},
\end{aligned}
\tag{12}
$$

where $\mu\pi$ is the half angle of cone. When $\sigma \to 0$, the values c_{x0} are obtained by extrapolation method. A comparison of the experimental data with the results of "exact" [19] and approximate [17] computations is given in Table 1:

Table 1

$\pi\mu$ (deg.)	15	30	45	60	75	90
Exper.	0.15	0.35	0.47	0.61	0.72	0.82
c_{x0} [7]	0.1428	0.3353	0.5000	0.6369	0.7461	0.8275
$\widetilde{c}_{x0}$ [10]	0.2045	0.3758	0.5181	0.6350	0.7296	0.8053

We obtain the calculated formula for an arbitrary contour from (11):

$$
\widetilde{c}_{x0} = \frac{2}{R_n^2} \int_0^1 \overline{p}(\eta) y(\eta) \frac{dy}{d\eta} d\eta . \tag{13}
$$

3.2. CAVITATOR WITH VARIABLE DRAG

Both the length and the biggest diameter of cavity are proportional to $\sqrt{c_{x0}}$ as it is seen from the relations (1).

$$\frac{D_c}{D_n} = \sqrt{\frac{c_{x0}\ (1+\sigma)}{\sigma}}, \qquad \frac{L_c}{D_n} = \frac{1}{\sigma}\sqrt{c_{x0}(1+\sigma)\ln\frac{1}{\sigma}}. \tag{14}$$

Hence, the cavity shape should change similarly to self at changing the control parameter c_{x0} when D_n and σ are constant. It may be obtained by changing the cavitator shape at constant diameter of the cavitating edge.

We offer the sketch of the axisymmetric cavitator with variable geometry. The meridian section of the cavitator has the $\sum$ – shaped contour. The cavity drag coefficient is increased from $c_x(\beta)$ up to 1 for a cone at moving of the internal cone relatively to the outside cartridge with a cavitating edge, i.e. at increase of parameter x/D_n from 0.

The graphic of dependence c_{x0} on x/D_n is shown in Fig. 7 for $\sum$ – shaped contours.

The graphic of dependence of the ratio $\widetilde{c}_{x0}$ for axisymmetrical cavitators to theoretical value of the drag coefficient for disk 0.8053 on the dimensionless extension of cavitating edge x/D_n is shown in Fig. 8. Also, the experimental points are plotted there. As it is seen, the drag increases slower in the experiment than as the computation predicts at increase of x. It is explained that the closed zones of vortical motion of water are formed in the interior angles of cavitator in the experiment. Other words, the potential scheme of the free streamline flow with the critical point is not realized in this case, but the scheme of the flow with stagnant zones is realized [14].

The appearance of cavity at the two extreme positions of cone $(\sigma = 0.077, \mu = 1/3)$ is given in Fig. 9. At extending of cavitating edge from $x/D_n = 0$ to $x/D_n = 0.138$ in the experiment we obtained the increase of main dimensions of cavity on 35 %.

4. Stability of supercavitating motion of bodies

4.1. POSSIBLE FLOW SCHEMES

The analysis showed that the four different mechanisms of motion stabilization sequentially act at motion velocity increase.

1. Two-cavity flow scheme (Fig. 10a), $V \sim 70$ m/s.

In this case the hydrodynamic drag center is placed behind the mass center, and stabilizing moment of the force Y_2 acts to the model. It means that the classic condition of stability is fulfilled.

2. Stationary planing along the internal surface of cavity (Fig. 10b), $V \sim 50 \div 200$ m/s. To compensate the buoyancy losses the body's tail part is planing along the lower internal cavity surface. In this case the motion may be stable as a whole.

3. Impact interaction with cavity boundaries (Fig. 10c), $V \sim 300 \div 900$ m/s. Presence of initial perturbations of the model attack angle and the angular velocity causes to the impact of the model tail part against the internal boundary of cavity. The mathematical modeling showed that after this impact the model can perform steady or damped oscillations accompanied by periodic impacts of the tail part alternately against the upper and lower cavity walls. Then the motion can remain stable as a whole.

4. Aerodynamic interaction with vapour-splash medium of cavity (Fig. 10d), $V \sim 1000$ m/s **and higher**. At very high velocities the aerodynamic and splash forces of interaction with vapour filling the cavity and splashes near the cavity boundaries have considerable effect on the body motion. Since the clearance between the body surface and the cavity boundary usually is small compared to the cavity radius, we apply the known methods of near-wall aerodynamics to estimate the arising forces.

Statically stable contours

The pressure forces acting on the inclined contours in free streamline flow sum to the resultant force $\vec{F}$

and moment M_0 shown in Fig. 11.

The contour will be statically stable if these forces tend to turn the cavitator to decrease angle α relative to the mass center of the model. The condition of static stability has the form:

$$\delta = \arctan\frac{F_y}{F_x} > \alpha, \tag{15}$$

where F_x and F_y are the projections of the vector $\vec{F}$ onto the x- y-axes.

Computations have shown that a cavitator is statically stable if its contour is concave towards to the stream (in particular, inverted wedges with $\mu > 0.5$). A flat plate will be neutrally stable, $F_y / F_x = \tan\alpha$, if we do not take into account the moment M_0 induced by displacement of point of application of force $\vec{F}$ from the point C. Computations have shown that this moment is always stabilizing, but is very small in value. Convex contours (in particular, wedges with at $\mu < 0.5$) are statically unstable.

The force polars for wedges are shown in Fig. 12 for a series of values of wedge semiangle $\beta = \pi\mu$ in degrees. The characteristic stability regions are shown in Fig. 13. Wedges are statically stable for $\beta > 90^\circ$, and are statically unstable for $\beta < 90^\circ$. The lift of a wedge is equal to 0 irrespective of the attack angle for $\beta \approx 50^\circ 35'$ [9].

Computer program FLOWJET allows to select the best cavitator shape for static stability when the arbitrary c_y^α is maximum. The best cavitator from a practical point of view: (1) is statically stable; (2) has a maximal rotational derivative c_y^α; and (3) has a minimal drag coefficient c_{x0}.

4.2. DESIGNING THE SUPERCAVITATING (SC) MODELS

The supercavitation flow scheme is a special artificial scheme. It is necessary to know a cavity shape for successful realization of this scheme. This is necessary for optimal location of the body in the supercavity.

We consider two problems:

– calculation of a supercavity for a body of given shape and given motion regime;

– design of optimal body shape for the known supercavity.

Stage I. Inscribing the body into the cavity

According to the given motion regime – $V = V(t)$; $H = H(t)$ we calculate minimal and maximal cavitation numbers

$$\sigma_{\min} = \sigma(V_{\max}; H_{\min}); \quad \sigma_{\max} = \sigma(V_{\min}; H_{\max})$$

to construct minimal and maximal supercavity contours $R = F(Rn; \sigma)$ past a circular disk [16].

The main purpose of this stage is to inscribe the model into the minimal cavity contour. The minimal contour is determined by presence of points of contact of the model contour and the free cavity boundary in the tail part.

Fig. 14 presents results of the computation of cavity shape past disk cavitators around the body of revolution. These results are obtained with the help of software SCAV developed at IHM UNAS. The program permits to plot supercavities by given parameters: diameter and angle of the cavitator D_n; β; velocity V and depth H of the motion; the pressure in the cavity P_c.

At that we determine the clearance h between the body surface and the cavity boundary, ring area of this clearance along the whole body length, moment of inertia and body mass (Fig. 15).

The program also computes the distance and the velocity reduction from the starting velocity $V = V_0$ upon motion on inertia and displays graphs of changing the length L_c and diameter D_c of the supercavity as well.

Stage II. Optimization of the supercavitating body contour

This stage purpose is to optimize the clearance between the free cavity boundary and model.

During motion of the model by given regime ($V = V(t)$, $H = H(t)$) the supercavity shape will change according to changing the cavitation number

$$\sigma_{\min} \le \sigma \le \sigma_{\max}.$$

The clearance between the body and cavity boundary will be changed in certain range according to changing of σ.

Besides the clearance will be changed under action of possible angular oscillations of the model about the center of mass in supercavities with dimensions exceeding the minimal possible ones $(\sigma > \sigma_{\min})$.

Fig. 16 shows a PC-screen copy of optimization procedure for the model shape at its angular inclination ψ. Simultaneously, values of upper h_2 and lower h_1 clearances between the model and supercavity contours are shown there. The program STAB permits to determine the maximal angles of trim $\psi = \psi_{\max}$, points of touching the model with the cavity and the mass center location. A simple rule was developed for ensuring the stability of the supercavitating model motion at the IHM UNAS.

Rule of optimization of SC model shape

For certain ranges of varying the cavitation number $\sigma_{\min} \le \sigma \le \sigma_{\max}$ and angles of trim $\psi \le |\psi_{\max}|$, the optimal shape of the supercavitating model must not have points of touching with the supercavity contour which are situated in front of the model center of mass.

This requirement does not take into account the dynamics of the body and is based on principles of static stability. In the case of continuous flow the analogous rule of the stable motion maintenance requires location of a point of the hydrodynamic force application past the body center of mass. Both the rules guarantee against appearance of destabilizing moments directed to the possible angle of model deflection. This means that the induced total moment acting on the model always must has a sign opposite to a sign of angle ψ – accidental deflection of the model

$$Sgn\, M = -Sgn\, \psi\ .$$

4.3. EQUATIONS OF THE SCM DYNAMICS

The most effective method of investigation of the supercavitating body dynamics proved to be its direct simulation on a PC-screen (computer experiment). It permits to research the motion stability in interactive regime "researcher – computer" [16].

The complete mathematical model of the SCM motion includes a set of equations of solid body dynamics, equations to calculate the unsteady cavity shape and relations to calculate the acting forces.

A set of dynamic equations of the axisymmetric body motion in vertical plane without rotation in the body co-ordinate system $O_1 x_1 y_1$ is

$$m\left(\frac{d\vec{V}}{dt} + \vec{\omega} \times \vec{V}\right) = \Sigma \vec{F}\ , \tag{16}$$

$$I_c \frac{d\vec{\omega}}{dt} = \Sigma \vec{M}_z \tag{17}$$

where $\vec{V} = \{V_x, V_y, 0\}$ is the velocity of the SCM mass centre; $\vec{\omega} = \{0, 0, \omega\}$ is the angular velocity; m is the mass of model; I_c is the moment of inertia of model about mass centre.

Passing on to the integration along the longitudinal absolute co-ordinate x and adding obvious kinematic relations, we obtain the calculation set of five ordinary differential equations

$$V\cos(\psi-\alpha)\frac{dV_x}{dx}=\omega V_y+\frac{1}{m}\Sigma F_x, \tag{18}$$

$$V\cos(\psi-\alpha)\frac{dV_y}{dx}=-\omega V_x+\frac{1}{m}\Sigma F_y, \tag{19}$$

$$V\cos(\psi-\alpha)\frac{d\omega}{dx}=\frac{1}{I_c}\Sigma M_z, \tag{20}$$

$$V\cos(\psi-\alpha)\frac{d\psi}{dx}=\omega, \tag{21}$$

$$\frac{dy}{dx}=\tan(\psi-\alpha). \tag{22}$$

Here, ψ is the model pitch; α is the angle of attack; y is the ordinate of the SCM mass centre in the absolute co-ordinate system (see Fig. 17).

4.4. RELATIONS FOR FORCES AND MOMENTS

Two kinds of forces in right parts of Eqs. (18) – (20) are essential in considered velocity range (see Fig. 17):

– hydrodynamic force and moment on the cavitator $\vec{F}_n$, $\vec{M}_n$;

–hydrodynamic force and moment due to interaction between the SCM tail and internal cavity wall $\vec{F}_x$, $\vec{M}_x$.

Coefficients of the force projections acting on the cavitator-disk inclined to the stream at angle α are approximately calculated by formulae [2]:

$$c_x=c_{x0}\cos^2\alpha,\ \ c_y=c_{x0}\sin\alpha\ \cos^2\alpha. \tag{23}$$

For disk cavitators with plane perpendicular to the model axis, the vector $\vec{F}_n$ is always directed along the model axis. Therefore, the force on the cavitator does not create any moment. Formulae (23) agree with experiment for a disk and blunted cavitators when $\alpha<50^\circ$.

We use the approximate method [9] to calculate the hydrodynamic force on inclined non-disk cavitator. It is based on the exact solution of the two-dimensional problem on free jet flow around an inclined polygonal contour.

Process of interaction between the SCM tail and internal cavity wall is considered as unsteady planing of a prolate body along the curvilinear liquid boundary. The forces arising in this case are calculated basing on the hypothesis of plane sections [2]. The solution of the problem on immersion of the circular arc through the curvilinear boundary is used in this case [20].

If both the middle clearance $\Delta = R_c - R_s$ and the model immersion depth into the cavity surface h_k are small, formula for the cross component of the tail force in the body coordinate system was obtained in the form [20]

$$F_{sy} = \rho \pi R_s^2 V \left[V_1 \frac{\overline{h}\left(2+\overline{h}\right)}{\left(1+\overline{h}\right)^2} + V_2 \frac{2\overline{h}}{1+\overline{h}} \right], \tag{24}$$

where R_s is the stern section (transom) radius of the model; V_1 is the cross velocity of the model transom; $V_2 = -\partial R_c / \partial t$ is the velocity of the cavity boundary; $\overline{h} = -h_k / \Delta,\ k = 1.2;\ \ h_1 < 0,\ h_2 < 0$ is the model transom immersion into the lower and upper cavity boundaries, respectively.

The longitudinal component of force F_{sx} has viscous nature and is calculated by formulae

$$F_{sx} = \frac{\rho V^2}{2} S_w c_f \left(\mathrm{Re}\right), \tag{25}$$

where S_w is the area of washed part of the model; c_f is the viscous drag coefficient; Re is the *Reynolds* number.

If the motion velocity is very high $V > 1000$ m/s, then aerodynamic forces of interaction between the model body and vapour-gas-spray medium filling the cavity can essentially influence on the SCM dynamics [1]. Our evaluations have shown that this influence has damping character [20].

4.5. STABILITY OF SCM MOTION

Computer simulation with the STAB software allows to investigate the stability of SCM motion "as a whole", when the model oscillates within the cavity ricocheting by its tail from lower and upper cavity walls in turn.

The PC-screen view after execution of the function “Motion” is shown in Fig. 18, a. Here, *HX* is the dimensionless calculation step; $N = 10$ is the number of the model contacts with upper and lower cavity contours. The velocities V_x, V_y and ω are output in dimensionless by L, V_0 form (where L is length of the model). The angles ψ, α are output in radians. A signs of the coefficients show the direction of the force and moment action.

The PC-screen view after execution of the function “History” for the same model and starting data is shown in Fig. 18, b. The *y*-coordinates of the graphs are plotted in dimensionless form, the *x*-coordinate *x* is given in meters. As it is visible from graphs, the interaction of the SCM tail and water has behaviour of short-term impulses. It is displayed in discontinuous behaviour of functions $\omega(x)$ and $V_y(x)$ [16].

The performed analysis has shown that the motion stability of the SCM with a disk cavitator is determined by three dimensionless parameters:

$$\bar{I}_c = \frac{I_c}{mL^2}, \quad St = \frac{\omega_0 L}{V_0}, \quad \overline{\Delta} = \frac{R_c - R_s}{R_n}.$$

Value of the parameter $\overline{\Delta}$ is determined mainly by cavitator radius R_n for given model shape and weakly depends on starting velocity V_0.

After a number of calculations at constant values of $V_0, \bar{I}_c, x_2$ and varied values of R_n, ω_0, the plane of the parameters $\overline{\Delta}, St$ is divided on the zone I where motion is stable and the zone II where the motion is unstable. For dynamically similar models $\bar{I}_c = const$ the stability zones are equal.

The motion stability loss is visually perceived on the PC-screen as washing the frontal part of model and inadmissible great increase of the pitch ψ.

Also, the STAB software permits to simulate the regime of continuous planing the model along the lower cavity wall including the ventilated one and with working propulsor. In this case, the cavitator is fixed at the angle of δ to the model axis to compensate the moment of the force arising on the tail. Thrust of the propulsor is added to the right part of Eq. (18).

The computer simulation that the SCM motion in regime of continuous planing is unstable when the angle δ is constant.

4.6. COMPARISON WITH EXPERIMENT

We confirmed reality of the SCM self-stabilisation mechanism by ricocheting from the cavity walls by direct shooting the motion in water with velocities up to 1200 m/s [4, 6]. In experiment, its action appears in periodic supercavity surface perturbations which develop next according to the "independence principle". In Fig. 19, the experimental photographs of the model in moment of touch to the cavity wall (compare with Fig. 14, a) and the supercavity part perturbed after contact with model are shown. In this case, the exposure time of shooting was $3 \cdot 10^{-6}$.

Asymmetric washing the model occurs when the SCM motion loses stability. It results in impact increase of the hydrodynamic drag and deformation of model.

5. Schemes of the hydrodynamic stabilization and control of SC objects

5.1. SCHEME WITH FREE PLANING ALONG A CAVITY

This scheme (Fig. 20) of the vehicle motion is more favorable, because has the smallest washed part of the body and, hence, the lowest hydrodynamic drag. However, this scheme of motion will have essential distinctions in creation of stabilizing hydrodynamic forces.

At motion the vehicle is located in the cavity under some angle of attack α_A. It stipulates the appearance of lift on the tail part due to asymmetric washing the cylindrical part of the body. At motion with constant velocity V_∞ and depth H (or the pressure $P_0 = \rho g H$) we can choose the constructive parameters of the vehicle:

– position of gravity center;

– cavitator dimensions;

– deflection angle of α_P;

– gas-supply value of the artificial cavity Q or its length $L_C = F(Q)$ so that the basic conditions of the motion stability (equality of projection of all forces and moments acting on the body in the uniform rectilinear motion) are fulfilled:

$$\begin{aligned} Y_C + Y_B &= G - T\sin\alpha_A, \\ X_C + X_B &= T\cos\alpha_A, \\ M_C + M_B &= 0. \end{aligned} \tag{26}$$

The hydrodynamic forces on the cavitator at deflection on small angle α_C can be determined by formulae [13]

$$\begin{aligned} Y_C &= X_{C0}\cos\alpha_C \sin\alpha_C, \\ X_C &= X_{C0}\cos^2\alpha_C, \end{aligned} \tag{27}$$

where X_{C0} is the cavitator drag at $\alpha_C = 0$. For a disk:

$$X_{C0} = 0.82\frac{\rho V^2}{2}S_0,$$

where S_0 is the area of the cavitator section on the cavitating edge; $\alpha_C = \alpha_P - \alpha_A$ is the cavitator angle of attack; α_P is the positional angle of the cavitator fixation; α_A is the body's angle of attack; X_B is the drag of washed part of the body which includes the friction drag of the side surface X_F.

At this flow scheme it is possible to save the traditional principle of stabilization and control due to the tail fins and rudders, but with an additional condition - the cross stability preservation.

Really, at presence of roll angle, γ, the lift on the cavitator deflected on angle α_C will form the side force $Z_C = Y_C \sin\gamma$, which causes to the body yaw (Fig. 21).

The cross stabilization of the object can be obtained by following ways:

a) due to the location of mass center lower than a line connecting the points Y_C, Y_B of application of the forces (Fig. 22). The stabilizing moment M_γ arises at arising the roll γ, (Fig. 22). In this case it is possible to stabilize the object without fins at all at sufficient magnitude of M_γ

$$M_\gamma = G h_c \sin\gamma; \tag{28}$$

b) due to the hydrodynamic fins of roll (Fig. 23) creating the stabilizing moment.

A possible scheme of cross stabilization of the body within the cavity due to two fins is shown in Fig. 23.

There the tail part of the vehicle is equipped by two supercavitating fins creating hydrodynamic lifts: the right, Y_1 and left, Y_2. At possible angle of roll of the vehicle on angle \gamma the stabilizing moment M_γ must arise due to a difference of these forces caused by various immersion of the right and left fins into flow through the free cavity boundary. The total lift of the two fins must not exceed $10 \div 15$ of the total lift, Y_B, on the vehicle tail

$$Y_1 + Y_2 = 0.15 Y_B .$$

The hydrodynamic forces on fins in stable position arise under action of the hull slope about the cavity axis at gravity influence and also flow bend in the back cavity part caused by cavity floating-up effect.

Stabilization in horizontal plane is achieved due to using a number of factors:

– stabilizing influence of the hydrodynamic forces of washed part of the hull located past the mass center of supercavitating object (SCO);

– application of neutral stability cavitators (disk) relatively to angles of deviation in the horizontal plane;

– using the schemes of a self-stabilization by roll:

– low location of the mass center,

– V-shaped system of fins.

Stabilization of SCO in vertical plane is reached due to the following factors:

– the cavitator with deviation angle having stability about angular deviations in vertical plane (disk, cone $\beta > 110^\circ$) [14];

– stabilizing influence of the washed hull part located past the SCO mass center;

– stabilizing influence of the V-shaped system consisting of two fins located on the tail end of washed part of SCO.

The vehicle completely placed in the cavity is shown in the scheme in Fig. 20. The supporting hydrodynamic forces are created by deflecting statically stable cavitator [14], Y_C, and planing tail part of the vehicle, Y_B.

The low location of a point of the hydrodynamic force, Y_B, application hampers the execution of cross self-stabilization scheme by lowing the mass center *mc* below than a line connecting the points of the hydrodynamic force application on the cavitator, O_C, and on the tail, O_B, of the body (it is shown by dotted line in the scheme).

The considered stabilization schemes do not exclude the application of means of the active control of vehicle for it stabilization during motion.

For SCO control may be used general aerohydrodynamics principle – to realize the object control by using elements creating hydrodynamic side forces as wings, flaps, rudders, jets.

In SC flow scheme the cavitator is a convenient element for side force creation owing formulae (27).

SCO control in horizontal plane

- by cavitator deflection in horizontal plane;
- by cavitator rotation in corresponding side according scheme (Fig. 21);
- by SCO hull rotation in corresponding side by using active fins (Fig. 23).

SCO control in vertical plane

- by cavitator deflection in vertical plane according scheme in Fig. 20 and formula (27).

5.2. OPTIMIZATION OF FIN NUMBER

Traditional stabilization schemes of bodies of revolution with large aspect ratio require presence of two pairs of fins:
– the first pair to stabilize motion in horizontal plane;

– the second pair to stabilize motion in vertical plane [4].

Aerodynamic schemes for stabilization and control were developed to minimize the drag of aircraft and rockets. They have three elements located by 120° or T -shaped and also two elements at V -shaped location [4].

The most of the hydrodynamic high-speed vehicles of known designs have two pairs of fins and rudders for the motion stabilization reliability, control convenience [6] including supercavitating ones [9].

5.3. OPTIMIZATION OF FIN SHAPE

Use of the rudders and fins on supercavitating objects has essential features:
1) two-phase regime of flow around the part or whole fin installed past the artificial supercavity;

2) incomplete washing the fin at possible air layer on the supercavitating object hull in the fin mounting place;

3) high overloads at water entry and take off of the fins at oscillations of the cavity boundary or the body in the supercavity.

Presence of the two-phase flow promotes the flow separation from the frontal edge of the fin and cavity formation. It results in abrupt reduction of the fin lift.

The air layer presence on the hull in the fin mounting place also causes to the lift loss not only due to the loss of the fin interference with the hull. In the case of the plane wall this loss is equal to reduction of the effective aspect ratio λ in two times according to formula for C_y^α:

$$C_y^\alpha = \frac{2\pi}{1+\frac{2}{\lambda}}. \qquad (29)$$

High overloads at abrupt change of medium: water-gas-water require increased strength and increasing the fin profile thickness.

All these features of flow around the rudders and fins on the supercavitating body of revolution were investigated theoretically and experimentally at the IHM UNAS. These research results were development of two-phase profile stable for variable loads [12, 13] and recommendations for the fin shape [14].

All the rudders has wedge profile of the cross section $(\beta = 3^\circ \div 6^\circ)$ (Figs. 24, 25).

The experimental results show that the wedge profile gives more stable flow characteristics for regimes of presence of gas and water-air layers on the body hull. In this case the fins of small aspect ratio $\lambda \le 1$ are more preferable, because they have no separations in great range of angles of attack.

References

1. Garabedian P.R. Calculation of axially symmetric cavities and jets // Pac. J. Math, 1956. Vol. 6, N 4. P. 611 – 684.
2. Logvinovich G.V. Hydrodynamics of Flow with Free Boundaries.// Kiev, Naukova Dumka, 1969. 208 p. (in Russian)
3. Savchenko Yu.N., Semenenko V.N., Serebryakov V.V. Experimental Study of the Supercavitation Flows at Subsonic Flow Velocities // Doklady AN Ukrainy, 1992, N 2. pp 64 – 69 (in Russian).
4. Sedov L.I. About Ideal Fluid Flow around Body with Counter Jet // Doklady AN SSSR. Vol. 2066. N1. 1972. (in Russian)
5. Yegorov I.T., Sadovnikov Yu.M., Isayev I.I., Basin M.A. Artificial Cavitation. L.: Sudostroenie, 1971. 284 p. (in Russian)
6. Epshtein L.A. Methods of Theory of Dimensionality and Similarity in Problems of Ship Hydromechanics. L.: Sudostroenie. 1970. 207 p. (in Russian)
7. Deynekin Yu.P. Cavitating Flow around Body with Channel. //Hydromehanika. 1994. N. 68. P. 74 - 78 (in Russian).
8. Romanovsky V.I. Symmetric Jet Flow around Contour with Water-Channel //Trudy TZAGY. 1980. N. 2060. P. 31 – 53 (in Russian).
9. Savchenko Yu.N., Semenenko V.N., Naumova Ye.I. Hydrodynamic characteristic of polygonal contours at supercavitating flow// Reports of NAS of Ukraine. 1997. N 7. 97 – 103 (in Russian)
10. Savchenko Yu.N. On motion in water in supercavitation flow regimes//Hydromechanics. 1996. N 70. P. 105 –115 (in Russian)
11. Savchenko Yu.N., Semenenko V.N., Osipenko S.B. Mechanism of Cavity Interaction with Bubble Flow // Doklady AN Ukraini. 1985. N 9. P. 39 – 42 (in Russian).
12. Savchenko Yu.N. Investigation of high-speed supercavitating underwater motion of bodies // High Speed Body Motion in Water (AGARD Report 827). Proc. Fluid Dynamics Panel Workshop. – Kiev, 1997.
13. Vlasenko Yu.D. Experimental investigations of high-speed unsteady supercavitating flows. Proc. Third International Symp. on Cavitation. – Vol. 2. Grenoble (France). 1998. P. 39 – 44
14. Gurevich M.I. Theory of Ideal Fluid Jets (the second edition) N.: Nauka, 1979. 536 p. (in Russian).
15. Savchenko Yu.N., Vlasenko Yu.D., Semenenko V.N. Experimental study of high-speed cavitation flows// Hydromechanics. 1998. N 72. P. 103 – 111 (in Russian)

16. Semenenko V.N. Computer simulation of supercavitating body dynamics// Applied Hydromechanics. 2000. V 2, N 1. P. 57 – 62 (in Russian)

17. Plesset M.S., Shaffer P.A. Cavity drag in two and three dimensions// J. Appl. Phis., 1948. Vol.19, N 10.

18. Guzevsky L.G. Numerical Analysis of Cavitating Flow. Novosibirsk : 1979. (Preprint of Institute of Thermal physics SD of AS Of USSR; N 40 - 79. 36 p. (in Russian).

19. Guzevsky L.G. Approximation Dependencies for Axisymmetric Cavities behind the Cones // Hydrodynamic flows and Wave Processes. Novosibirsk, Institute of Thermophysics of SD of AS of USSR, 1983. P. 82 – 91 (in Russian).

20. Savchenko Yu.N., Semenenko V.N., Putilin S.I. Unsteady processes during supercavitating body motion// Applied Hydromechanics. 1999. V 1, N 1. P. 62 – 80 (in Russian).

21. Knapp R., Daily J., Hammet F. Cavitation. // Mir, Moscow, 1974, 687 p. (in Russian) .

22. Putilin S.I. Some features dynamics of supercavitating models. // J. of Applied hydromechanics, Vol. 2, No 3, 2000, pp. 65 –74.

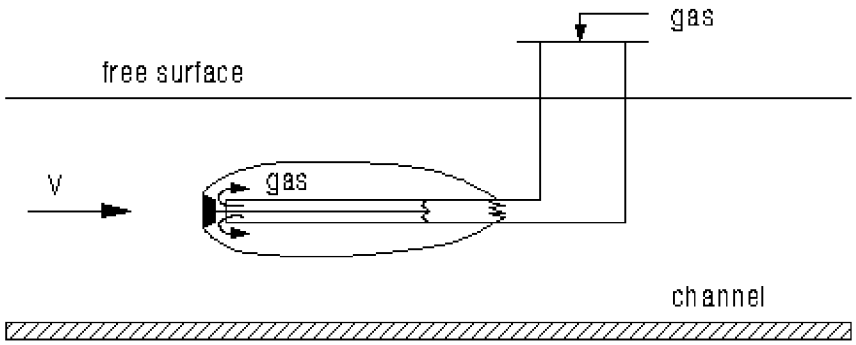


Fig. 1

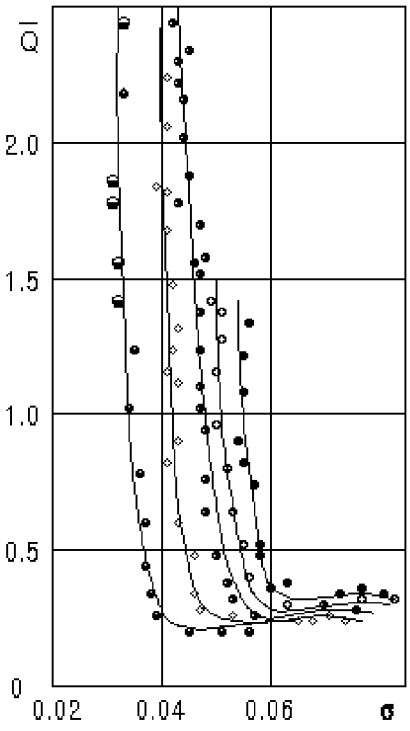


Fig. 2

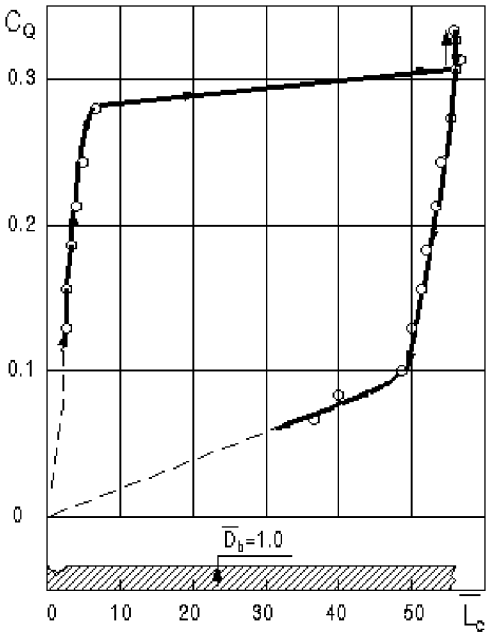


Fig. 3

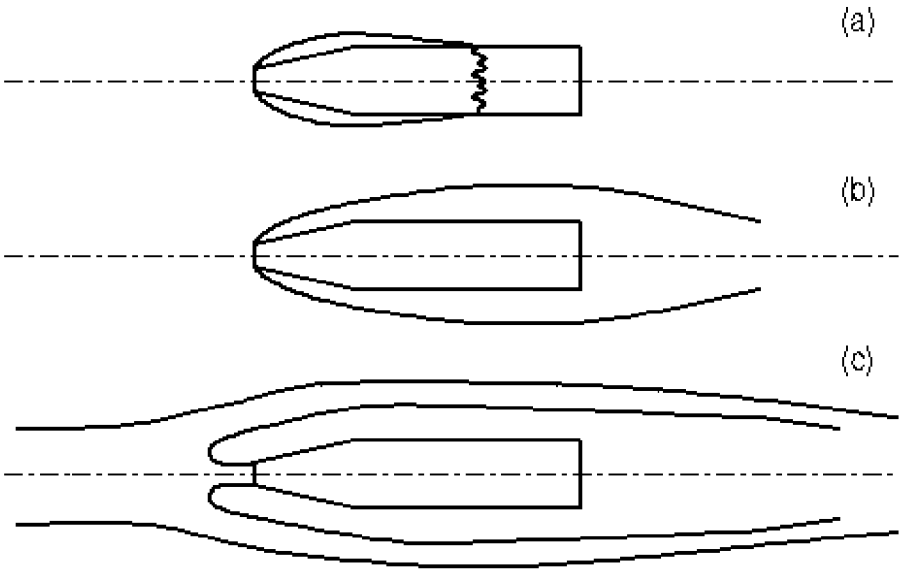


Fig. 4

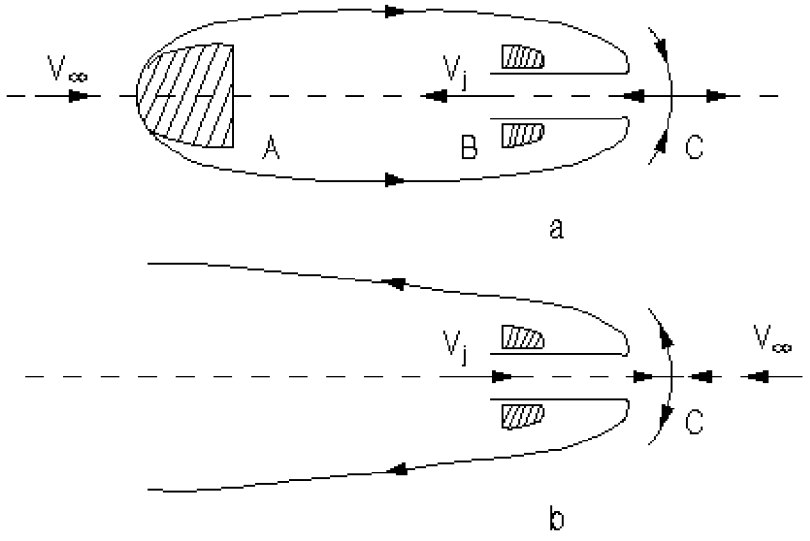


Fig. 5

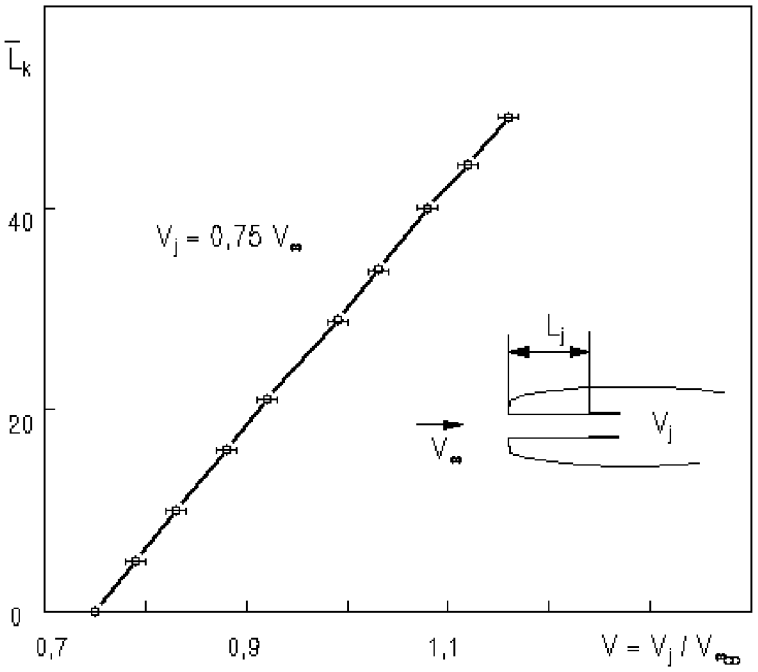

$\bar{L}_k$
40
20
0
$V_j = 0{,}75\ V_\infty$
L_j
V_j
V_∞
0,7
0,9
1,1
$V = V_j / V_\infty$

Fig. 6

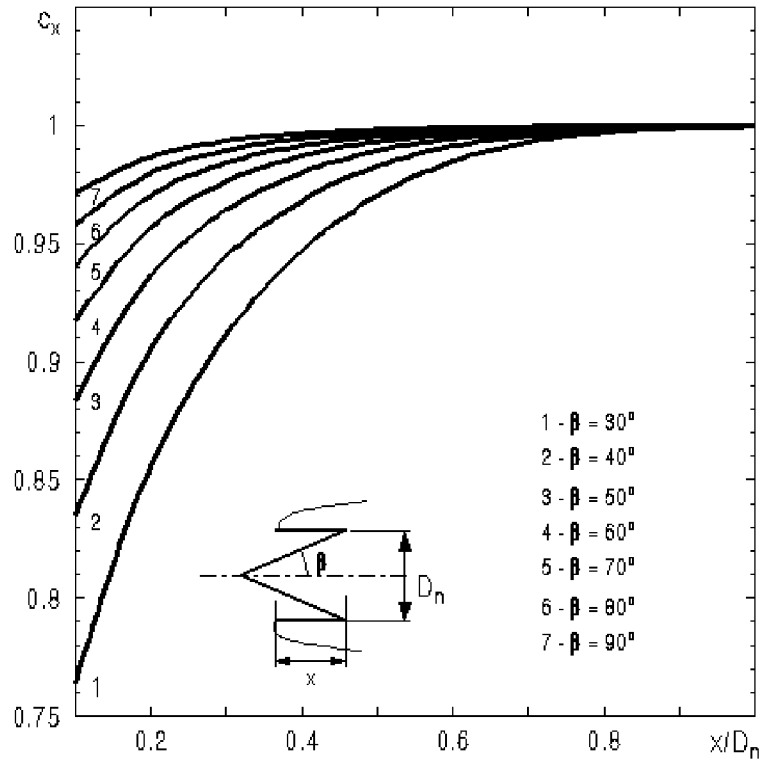

c_x
1
0.95
0.9
0.85
0.8
0.75
0.2
0.4
0.6
0.8
x/D_n
1
2
3
4
5
6
7
1 - β = 30°
2 - β = 40°
3 - β = 50°
4 - β = 60°
5 - β = 70°
6 - β = 80°
7 - β = 90°
β
D_n
x

Fig. 7

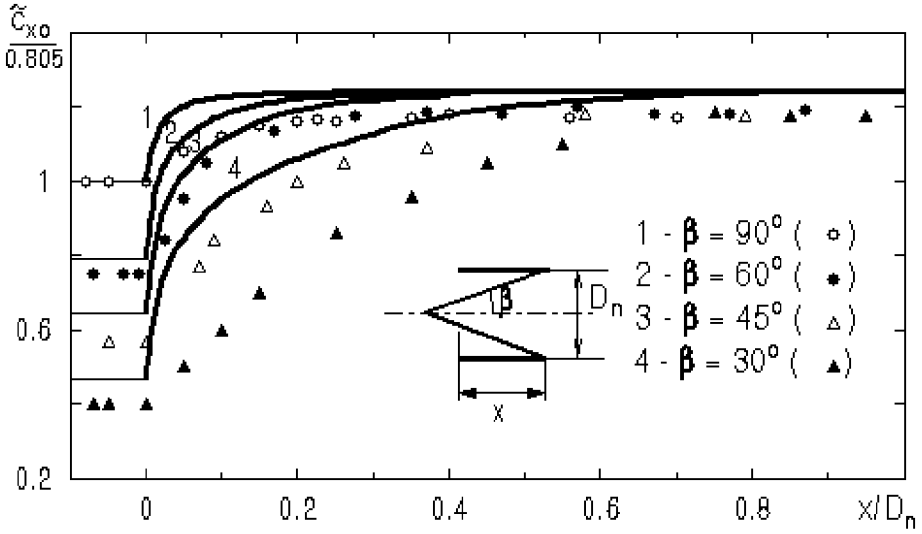

$\frac{\tilde{c}_{xo}}{0.805}$
1
0.6
0.2
0
0.2
0.4
0.6
0.8
x/D_n
1 - β = 90° (○)
2 - β = 60° (✱)
3 - β = 45° (△)
4 - β = 30° (▲)
β
D_n
x

Fig. 8

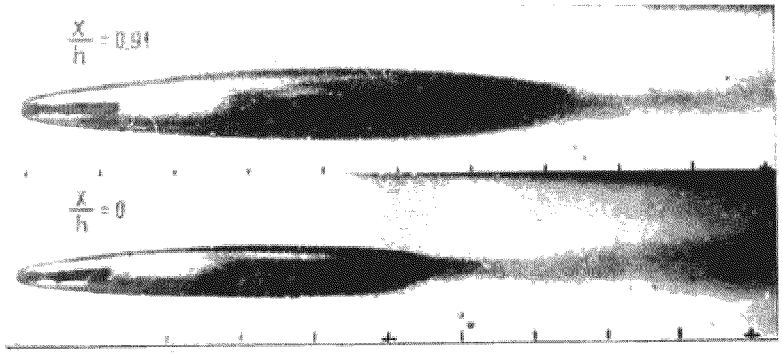

x/h = 0.91
x/h = 0

Fig. 9

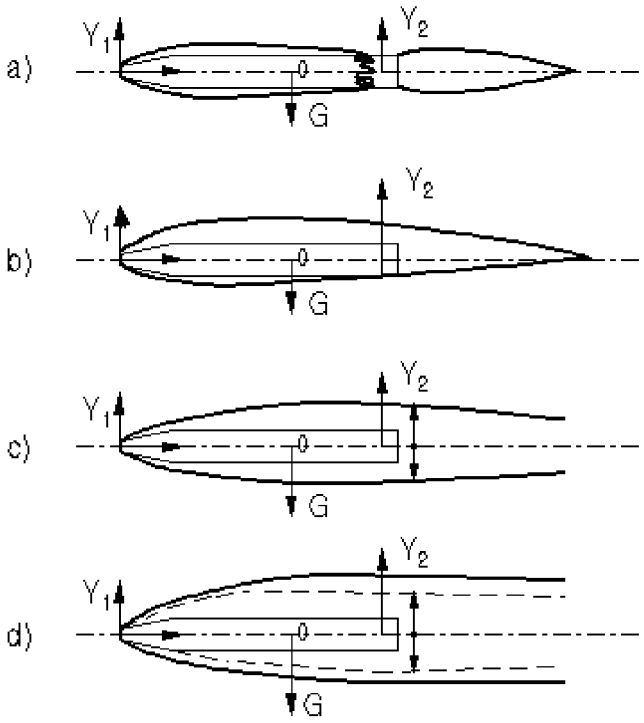


Fig. 10

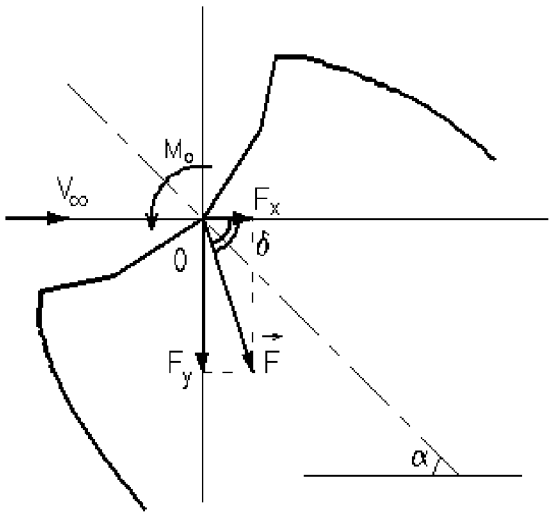


Fig. 11

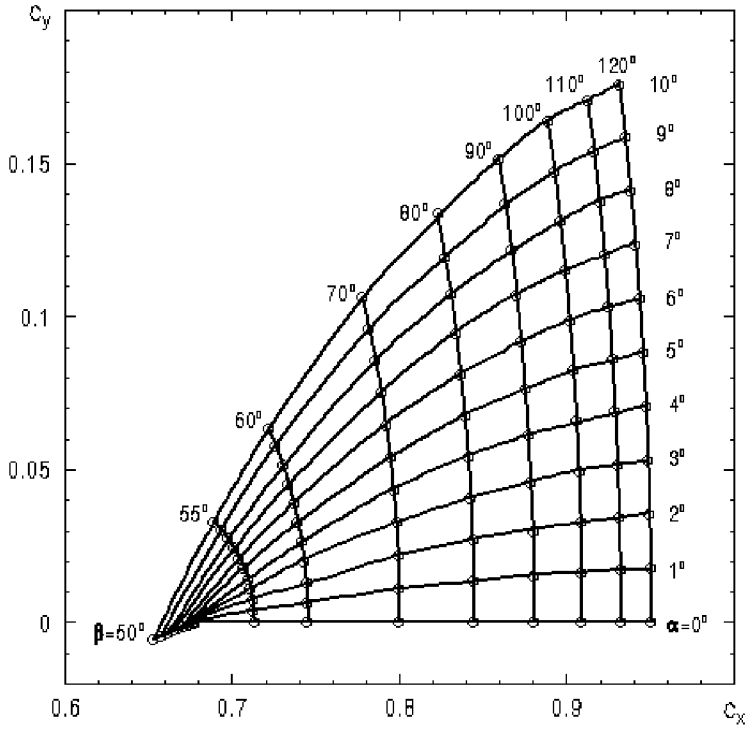

c_y
0.15
0.1
0.05
0
0.6
0.7
0.8
0.9
c_x
120°
110°
100°
90°
80°
70°
60°
55°
β=60°
10°
9°
8°
7°
6°
5°
4°
3°
2°
1°
α=0°

Fig. 12

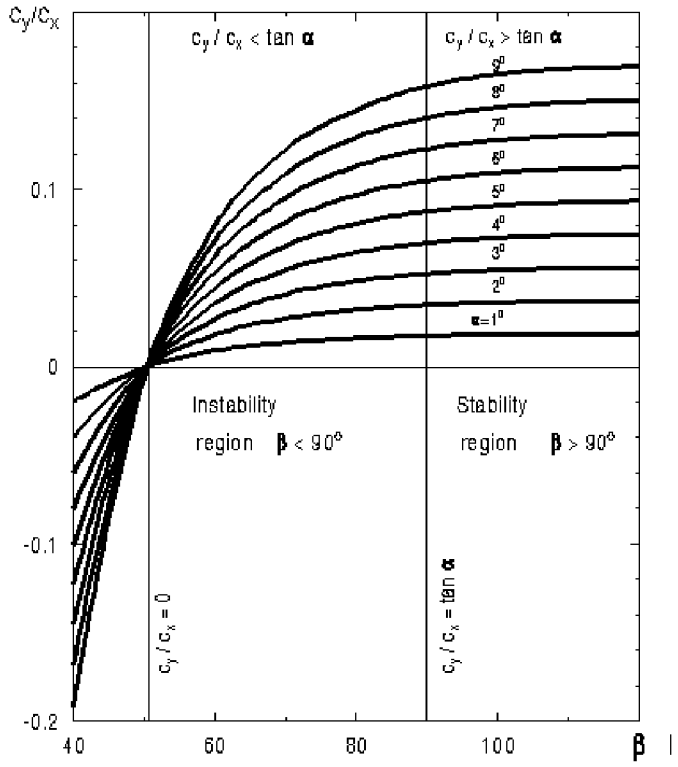

c_y/c_x
$c_y / c_x < \tan \alpha$
$c_y / c_x > \tan \alpha$
8°
7°
6°
5°
4°
3°
2°
α=1°
0.1
0
-0.1
-0.2
Instability
region β < 90°
Stability
region β > 90°
$c_y / c_x = 0$
$c_y / c_x = \tan \alpha$
40
60
80
100
β

Fig. 13

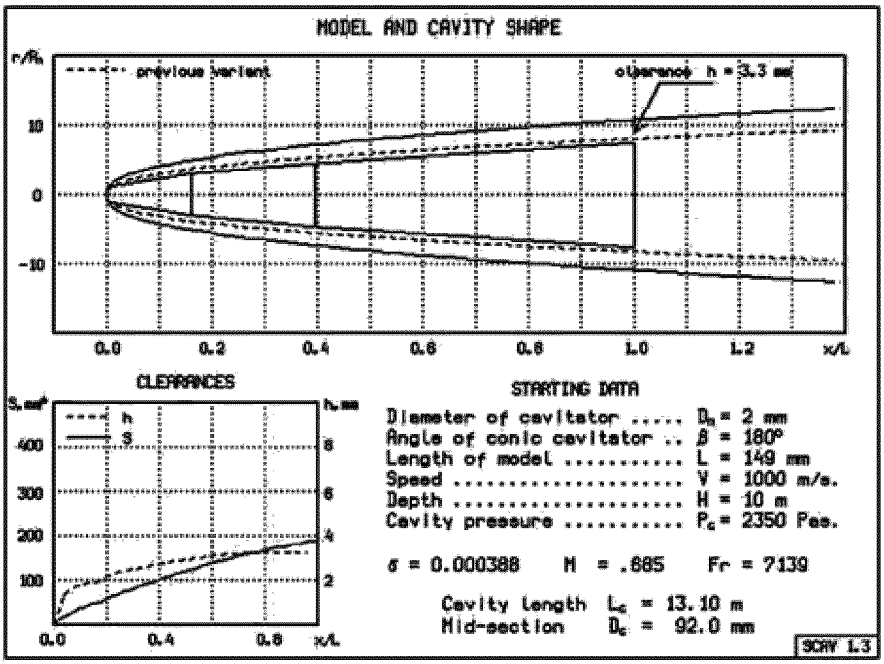

MODEL AND CAVITY SHAPE
previous variant
clearance h = 3.3 mm
CLEARANCES
STARTING DATA
Diameter of cavitator ..... D_n = 2 mm
Angle of conic cavitator .. β = 180°
Length of model ..... L = 149 mm
Speed ..... V = 1000 m/s.
Depth ..... H = 10 m
Cavity pressure ..... P_c = 2350 Pas.
σ = 0.000388 M = .885 Fr = 7139
Cavity length L_c = 13.10 m
Mid-section D_c = 92.0 mm
SCAV 1.3

Fig. 14

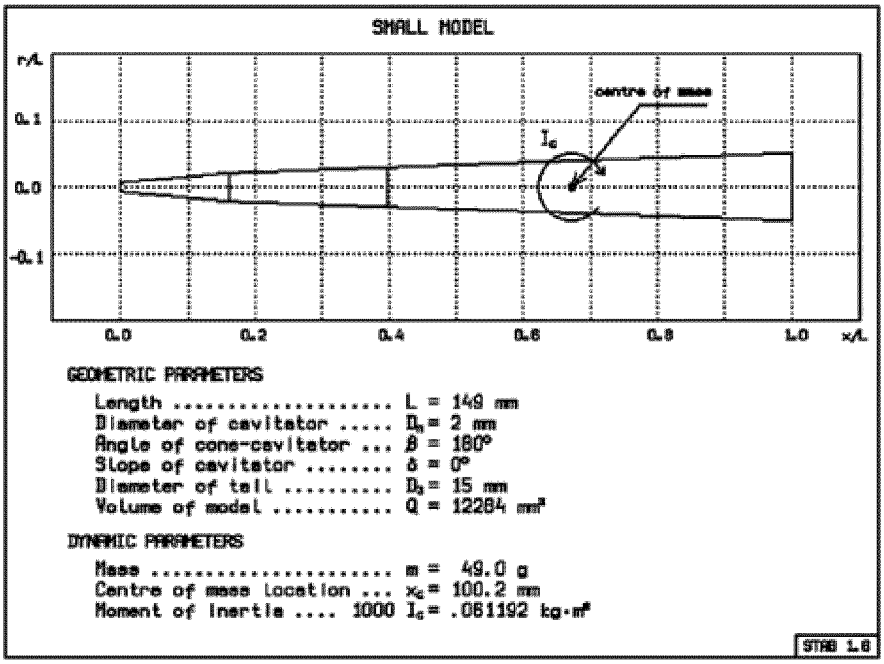

SMALL MODEL
centre of mass
GEOMETRIC PARAMETERS
Length ..... L = 149 mm
Diameter of cavitator ..... D_n = 2 mm
Angle of cone-cavitator ... β = 180°
Slope of cavitator ..... δ = 0°
Diameter of tail ..... D_b = 15 mm
Volume of model ..... Q = 12284 mm³
DYNAMIC PARAMETERS
Mass ..... m = 49.0 g
Centre of mass location ... x_c = 100.2 mm
Moment of inertia .... 1000 I_c = .081192 kg·m²
STAB 1.8

Fig. 15

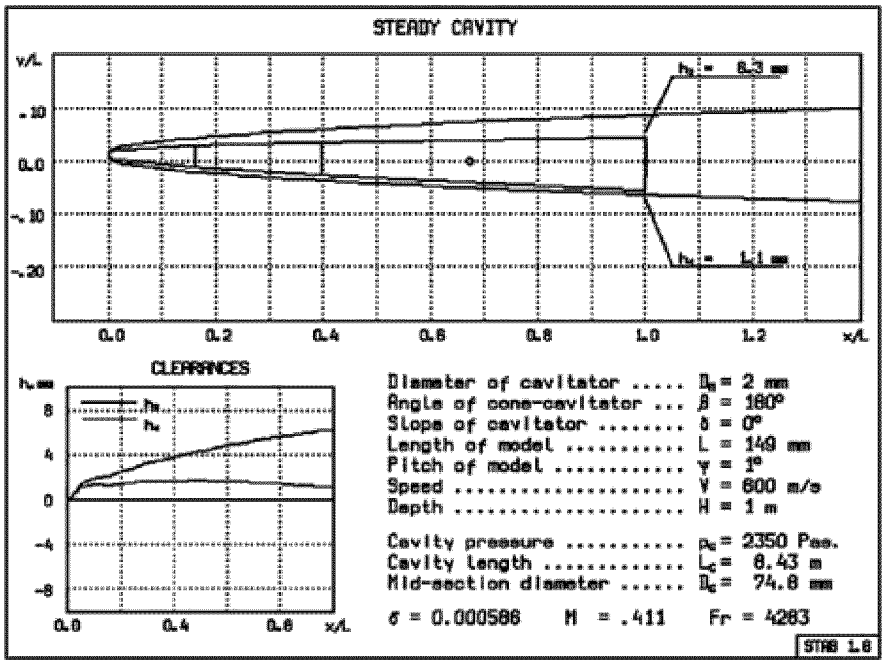

STEADY CAVITY
v/L
.10
0.0
-.10
-.20
0.0
0.2
0.4
0.6
0.8
1.0
1.2
x/L
CLEARANCES
h, mm
8
4
0
-4
-8
0.0
0.4
0.8
x/L
Diameter of cavitator ..... D0 = 2 mm
Angle of cone-cavitator ... β = 180°
Slope of cavitator ..... δ = 0°
Length of model ..... L = 149 mm
Pitch of model ..... ψ = 1°
Speed ..... V = 600 m/s
Depth ..... H = 1 m
Cavity pressure ..... pc = 2350 Pas.
Cavity length ..... Lc = 8.43 m
Mid-section diameter ..... Dc = 74.8 mm
σ = 0.000586 M = .411 Fr = 4283
STAB 1.8

Fig. 16

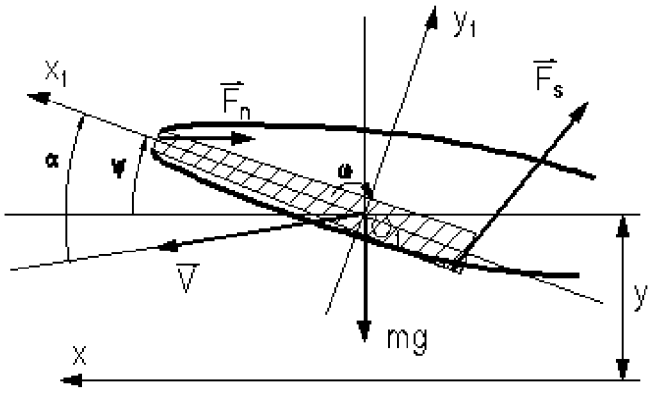

y1
x1
Fn
Fs
α
ψ
ω
V
y
mg
x

Fig. 17

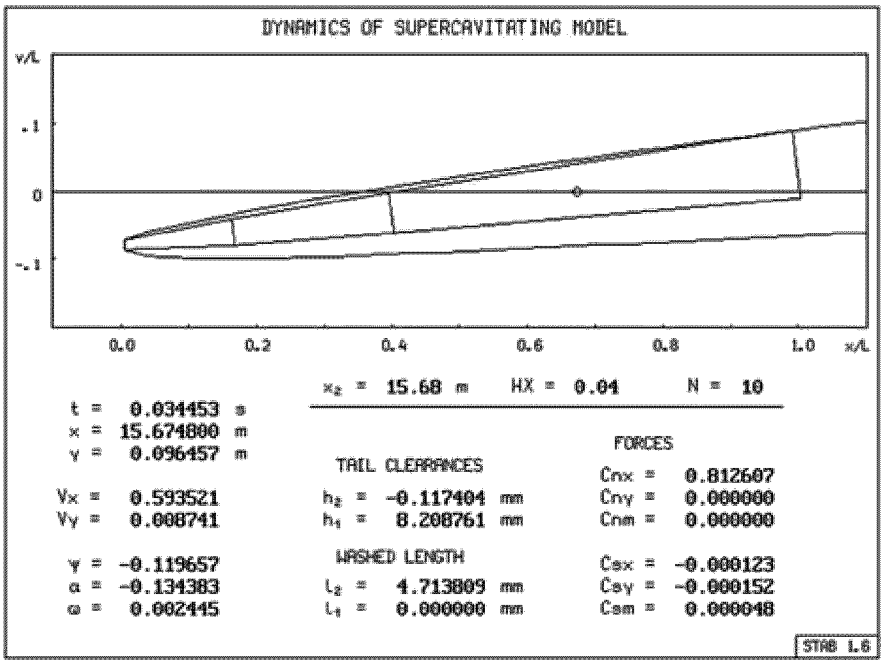


Fig. 18a

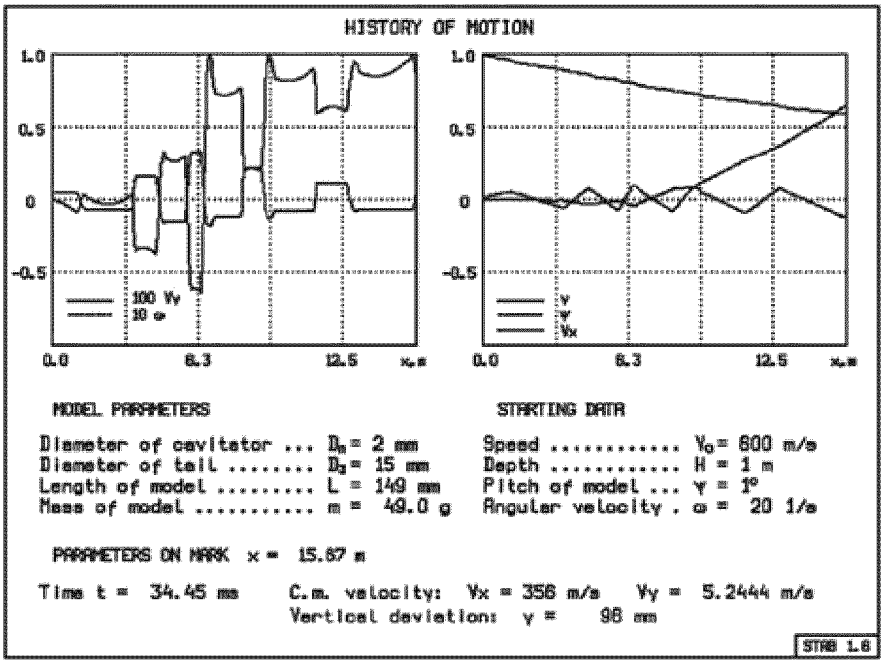


Fig. 18b

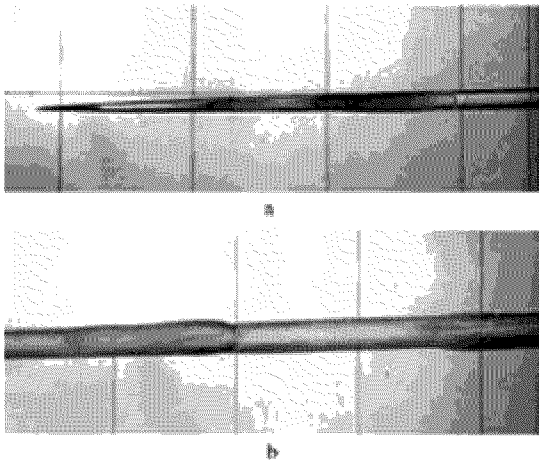


Fig. 19

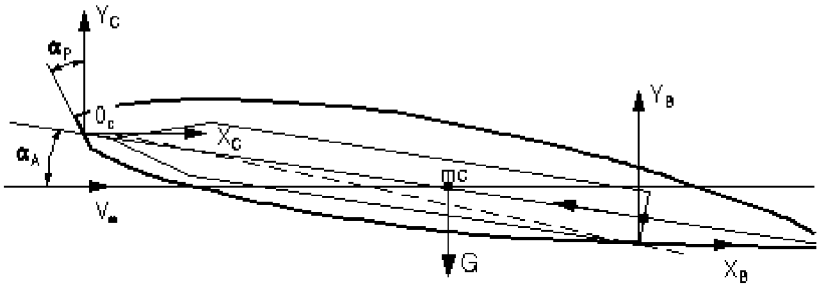


Fig. 20

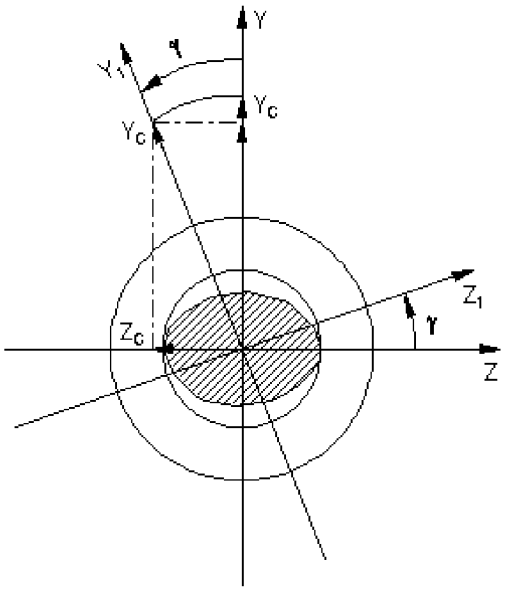


Fig. 21

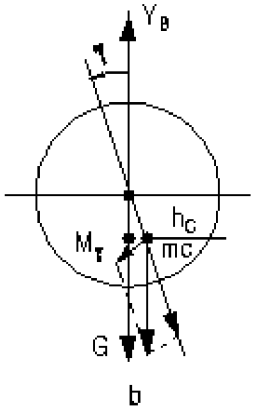


Fig. 22

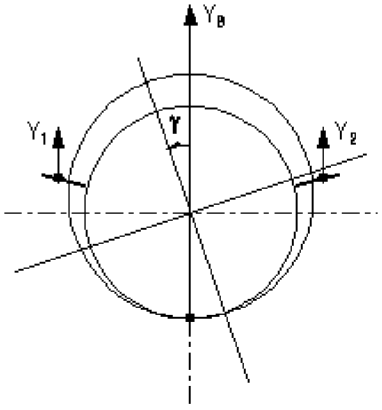
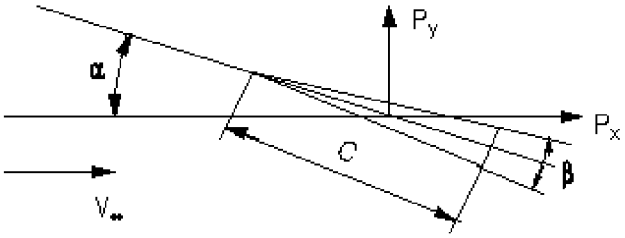


Fig. 23



$$A = \frac{S}{C^2}$$

Fig. 24

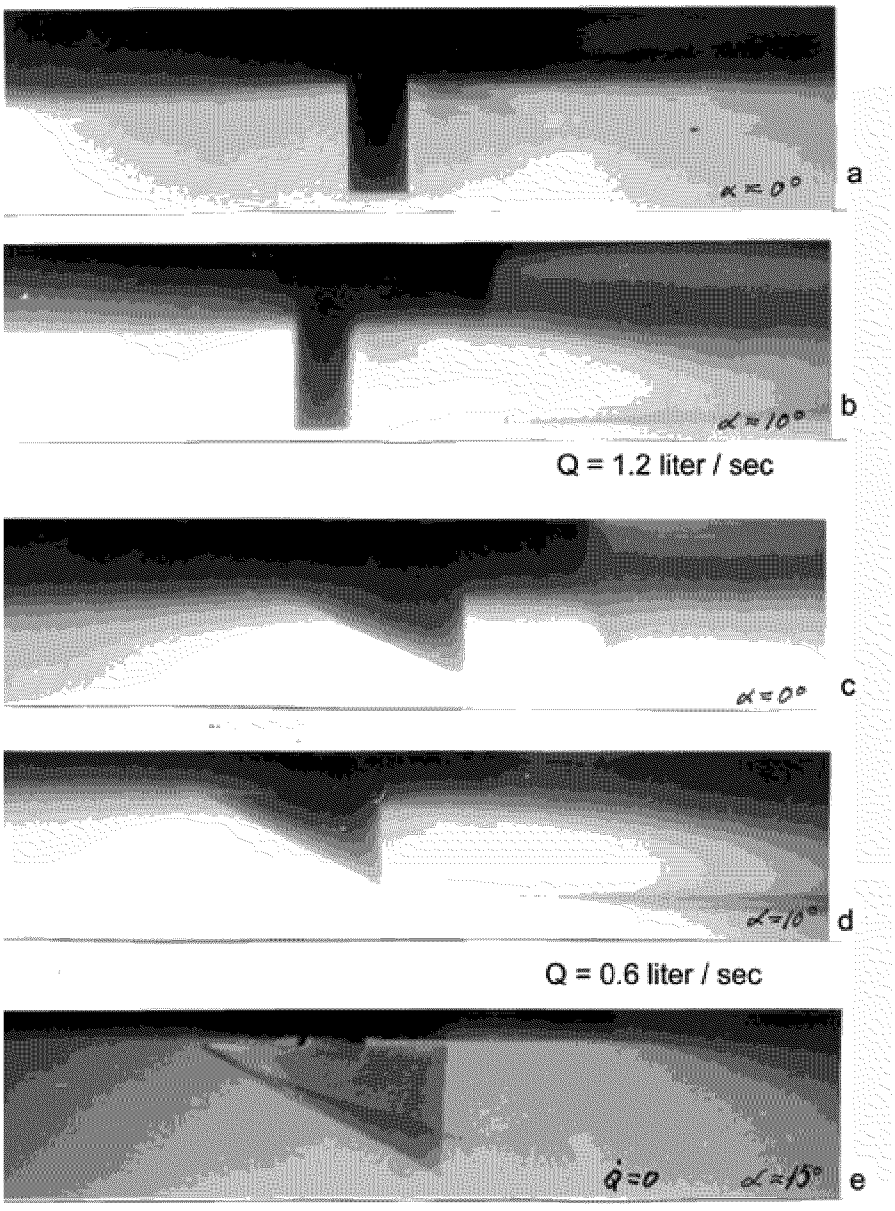


Fig. 25

This page has been deliberately left blank

Page intentionnellement blanche

Results of Selected Experiments Involving Supercavitating Flows

I.N. Kirschner, PhD[1]

Anteon/Engineering Technology Center
240 Oral School Road, Suite 105
Mystic, CT 06355
United States of America

SUMMARY

For much of the last decade, the Naval Undersea Warfare Center (NUWC) Division, Newport, Rhode Island, has conducted basic research and development involving supercavitating projectiles. Under this program, the theory of high-Mach-number underwater flows has been investigated and first-principles modeling of cavity development and projectile dynamics and stability have all been addressed.

To support these analytical efforts, a sophisticated experimental program has similarly matured. The NUWC Division Newport Supercavitating High-Speed Bodies (SHSB) Test Range has been designed to safely test underwater gun-launched projectiles traveling in excess of the speed of sound in water. This range was installed as an upgrade to a facility originally designed as a tow tank for testing tactical scale undersea vehicles. Currently the test range is 17 m long and approximately 4 m deep. Armor plates positioned ~1.5 m apart ensure that even unstable projectile trajectories are confined to the range.

This lecture describes the experimental facility and the tests performed there through the end of the author's tenure at NUWC circa December, 1998. A description of the test range, its instrumentation suite, and the extensive photographic capabilities developed to capture these high-speed projectiles are discussed. A summary of the experimental milestones through December, 1998, is also presented.

INTRODUCTION

An underwater test range was constructed in the NUWC tow tank and has been used in over 50 supercavitating high-speed projectile tests in support of the Supercavitating High-Speed Bodies (SHSB) program. This program involves basic research into very high-speed undersea projectiles. Application of supercavitation drag reduction at munitions scales can result in projectiles capable of supersonic velocities (exceeding 1500 m/s in water) over short ranges. The tests were executed by the SHSB Test Team at NUWC Division, Newport, Rhode Island, USA.

Important milestones in this program included the successful demonstration of 20-mm gun-launched underwater high-speed projectiles at the Langley Tow Tank in Hampton, Virginia in 1994 and the construction and test of an underwater test range for 30-mm gun-launched subsonic and supersonic projectiles at NUWC in 1996. The NUWC facility uses a 30-mm underwater gun launcher and is fully instrumented to provide the high-speed data and images necessary to conduct a comprehensive research program.

The experiments described here were performed in the NUWC building 1246 Tow Tank using a high-speed underwater gun launcher developed by NUWC and General Dynamics Armament Systems (GDAS, formerly Lockheed Martin Armament Systems). This launcher was integrated with the NUWC-developed test range and instrumentation package.

The overall objective of this experimental program is a better understanding of supercavitating high-speed flight and stability in flows over a range of cavitation numbers, and over underwater Mach numbers from near zero through and exceeding unity. Quantitative measurements are made to determine the projectile velocity time history, projectile drag, projectile trajectory, and spatial and temporal characteristics of the cavity. Qualitative observations result in a better understanding of projectile stability and the cavity structure, including external shock waves.

---

[1] These lecture notes are closely based on a previous publication by Hrubes, et al, (1998). The co-authors of that publication, J. Dana Hrubes, C.W. Henoch, C.M. Curtis, and P.J. Corriveau were essential to development of the information presented herein. They were supported in this effort by the NUWC Supercavitating High-Speed Bodies Test Team.

Paper presented at the RTO AVT Lecture Series on "Supercavitating Flows", held at the von Kármán Institute (VKI) in Brussels, Belgium, 12-16 February 2001, and published in RTO EN-010.

NUWC TEST FACILITY

The SHSB test facility is located at NUWC Division Newport. The tow tank is 49.4 m long by 6.1 m wide. The depth varies from 5.5 to 7.0 m. Its proximity to the research team makes it an ideal site for land-based high-speed undersea munitions and launcher testing. The range development task resulted in modification of this tank for the current program as well as for future SHSB programs.

The test hardware required to conduct the SHSB experiments was integrated with the test facility as depicted in the schematic diagram shown in figure 1. The underwater launcher is aimed to fire projectiles through 30.5 cm diameter holes in an array of armor baffle plates. Those projectiles that traverse the entire range are caught in a projectile catcher. If a projectile deviates more than about 15 cm from the nominal trajectory, the armor-plated baffle system stops the projectile and absorbs the energy so that it does not present a safety hazard.

Major hardware items include the underwater launcher system and mounting frame, projectiles, armor baffle plates, and a projectile catcher. Instrumentation includes witness screens, sensors and transducers, cameras (with enclosures and supports), video and analog data recorders, signal conditioners, a data acquisition and control computer, integrated circuitry, incandescent lamps, strobe lamps, a laser illumination system, and a launcher alignment system.

UNDERWATER LAUNCHER AND MOUNTING FRAME

The submerged gun launcher, or underwater firing fixture (UFF), currently consists of a 3.05m long, 30-mm smooth-bore barrel. The barrel diameter was chosen to accommodate the chamber pressures required to launch projectiles in excess of 1500 m/s. Prior to installing the smooth-bore gun, a 2.34 m long, 30 mm rifled GAU-8 Mann barrel was used. Figure 2 illustrates the gun assembly.

The gun is mounted in a box frame; this inner frame rides on rollers fixed to four rails, two above the frame and two below. These rails are mounted inside an outer frame that can be lowered in and out of the water while maintaining lateral position, and rests at the same position for every test firing. The inner frame rests against a heavy recoil plate that is hung aft of the frame. On firing, the inner frame moves aft along the rails within the outer frame, transferring no significant forces to the outer frame. The inner frame pushes the recoil absorption plate. The recoil velocity is decreased by acceleration of the mass of the plate, including the considerable added mass associated with fluid loading, while damping absorbs the recoil energy. A waterproof, pneumatically-operated breech with remote safe-and-arm features is screwed onto the end of the launcher barrel. High-pressure vents prevent damage to the barrel if it is fired when accidentally flooded. The gun launcher, mounted in the frame, is shown in figure 3.

To mitigate the effects of combustion gas ejection on the projectile cavity, the launcher bore is fitted with a 0.61m-long muzzle brake section of larger diameter, which allows the muzzle gases to expand before ejection into the free field. This decreases the pressure impulse on the projectile cavity, helping it to develop without transient collapse. The large-diameter muzzle brake also allows the cavity to develop behind the projectile without impinging on the face of the muzzle, further mitigating high transient launch pressures. In addition, the muzzle brake contains a sliding decelerator cylinder with a 21-mm hole to allow passage of the projectile. The remaining parasitic launch components are trapped by the decelerator, which exits the muzzle brake well after projectile passage.

A remote gun control unit allows the gun to be fired safely and initiates the computerized sequence critical to launch and data acquisition. At the discretion of the test director, the firing sequence can be aborted. The computerized sequencer starts the cameras and data recorders and activates capture and trigger mechanisms for cameras and stroboscopes.

PROJECTILE

Figure 4 is a photograph of the most successful projectile and sabot tested through December, 1998. The projectiles were designed in three phases. A concept design based on a semi-empirical model provided basic ballistics and hydrodynamics information. These results were refined using a mathematical model in a preliminary design cycle. Final design information was collected in a drawing package that included specifications of all dimensions, tolerances, and materials, along with precise estimates of mass properties.

The current projectile design has been developed through evolution over several years. Projectile materials have included maraging steel, tungsten, and titanium. Coupling materials have included aluminum, steel, titanium, and Ultem plastic.

PROJECTILE CONTAINMENT SYSTEM

The projectile containment system includes the armor plate baffle array and the projectile catcher. Armor plates roughly 1.22 m square by 2.54 cm thick with 30.5-cm holes are suspended every 1.52 m in the projectile path to provide effective termination of the projectile, should it travel off course. Each plate also has a 2.5-cm hole above the 30.5-cm hole to allow passage of a laser beam during plate alignment procedures.

A steel projectile catcher faced with a 1.22-m square baffle plate is suspended at the end of the array of armored baffle plates to stop those projectiles that traverse the entire range. The bucket is filled with steel plates, wood, and sand.

Since 1998, the range has been upgraded to extend the containment system (that is, the armor baffle plates) to the end of the tank, for a total length of approximately 45 m.

INSTRUMENTATION, CONTROL, DATA ACQUISITION, AND DATA PROCESSING

The range is instrumented to acquire both quantitative and qualitative data. Various launcher pressures are measured to assess launcher performance. Field pressures are measured to quantify perturbations due to the projectile, including any shock-wave system. The projectile displacement is measured using induction coils (for magnetized projectiles) or printed circuit break screens. Position, velocity, and drag are deduced from these measurements. Accelerometers measure motion of selected components in the tank. Induction coils and break screens are used to trigger components of various high-speed imaging systems.

Time and key range events are recorded by a computer-based data acquisition system and an analog tape recorder. Standard video and 35-mm cameras, a high-speed motion picture film camera, and high-speed intensified video imaging systems are available for each test. Illumination for each imager is provided by incandescent lamps, a copper vapor laser illumination system, or strobe lamps.

CONTROL AND DATA ACQUISITION COMPUTER SYSTEM

A desktop computer provides the platform for the data acquisition system. Data acquisition software configures two high-speed data acquisition boards, which control the data acquisition process in real time. The boards can each acquire up to 1.25 million samples per second, on up to eight differential channels. Each board has two analog timers and two digital channels, which are used to trigger other test functions such as camera shutters and the movie camera start signal, and which provide a reliable time basis for events throughout the duration of the test.

ANALOG DATA RECORDER

A 21-channel FM analog tape recorder is used as a backup for the computer data acquisition system. In the event that the computer fails to acquire some or all of the test data, the recorder is used to replay all data channels.

LAUNCHER PRESSURE AND MUZZLE VELOCITY SYSTEMS

Gas pressure at various locations in the launcher is measured by means of blast pressure transducers mounted in small ports in the barrel. Expected peak pressures are under 450 MPa in the chamber and under 70 MPa at the muzzle. Blast transducers are placed in the UFF to measure chamber pressure and pressure at various positions in the barrel. The blast transducer is a low-sensitivity, integrated-circuit, piezoelectric transducer with an output of 0.0102 mV per MPa and with high-pressure capability of more than 690 MPa. Two such sensors are screwed into the barrel velocity measurement holes to measure projectile velocity just before exit into the muzzle brake. The phasing between the pressure traces allow precise estimation of the projectile velocity.

UNDERWATER ACCELEROMETERS AND FIELD-PRESSURE TRANSDUCERS

Field-pressure sensors are mounted on a vibration-isolated rack downstream of the gun muzzle to measure dynamic pressure perturbations associated with passage of the projectile and shock system, if present. Acceleration of the recoil absorption plate and the first baffle plate are recorded by accelerometers mounted on those structures.

MOTION-DETECTION COILS

For tests where a magnetized steel projectile can be used, a voltage is induced by the magnetized projectile passing through a series of inductance coils for non-invasive velocity measurement. Velocity of the projectile is calculated using data from pairs of these coils. The coils are 45.7 cm in diameter and are mounted on a plastic post with the two active ends of the wire coil embedded and cabled to the instrumentation. The coils can also be used to trigger camera or illumination events.

BREAK-SCREEN MEMBRANES

Alternative velocity measurements are made using flexible mylar membranes on which continuous conductive circuits are printed. Each circuit is closed until broken by the projectile. These membranes double as witness screens, indicating projectile trajectory. Appropriate connecting circuitry was designed and assembled to produce signals for recording projectile velocity and for triggering instrumentation. When velocity coils are not used or the projectile is non-magnetic, break screens are mounted on each baffle plate to measure displacement and velocity.

WITNESS SCREENS

A system of witness screens is used to record the trajectory of each projectile during its passage downrange. Either mylar break screens or metal foils are mounted in frames. These frames are bolted to the containment baffles at known locations with respect to the nominal projectile trajectory. Pitch and yaw information can sometimes be deduced from the perforation shape.

GUN AND WITNESS-SCREEN ALIGNMENT SYSTEM

A laser bore-sighting technique is used for alignment of the launcher with the nominal trajectory. A blue-green laser enclosed in a waterproof housing is mounted securely to the gun barrel and co-aligned with the gun bore prior to each range alignment. The range is aligned by sighting the laser through 2.54 cm holes in each armor plate. The estimated cumulative error in the alignment of the range is +/-1.2 cm at the first plate and +/-1.8 cm at the tenth plate. In addition to range alignment, the 21-mm hole in the muzzle brake decelerator is aligned with the gun bore with an estimated accuracy of +/-0.03 cm.

CAMERA ENCLOSURES AND UNDERWATER PLATFORMS

Camera enclosures and support structures were fabricated to accommodate the cameras, the lights, and other necessary instrumentation. The enclosures are attached to platforms constructed of standard perforated metal framing, and are suspended at the desired depth and raised between tests for camera access. Other instrumentation, such as pressure transducers, are also attached to platforms. Cameras in close proximity to the gun muzzle are equipped with isolation-damped mountings to help protect the instruments from shock loading. Figure 5 illustrates some of the imager configurations.

IMAGING AND DATA ACQUISITION

Imaging and data acquisition at extremely high rates were critical to the success of this test program. This information has played a crucial role in post-test analysis leading to important design and operational changes. In addition, this information is important to the understanding of the physics of supercavitating bodies.

Imaging systems consisted of the following items: (1) Standard video (underwater and above water, full range coverage, incandescent lighting); (2) A high-speed 16-mm motion picture camera (10,000 frames/s, 15-W pulsed copper-vapor laser illumination, 100 ns pulse, front or shadow-graph lighting); (3) High-speed

gated, intensified video (incandescent or laser illumination); (4) 35-mm still cameras (front-lit, 50-mm lens, 3-μs front-lit stroboscope illumination); and, (5) 35-mm still cameras (50-mm lens, 3-μs shadow-graph stroboscope illumination). Each test used a variety of these imaging methods, but did not necessarily use all of them.

To use the resulting images for accurate measurements of cavity and projectile phenomena, image distortion must be assessed. The primary distortion issues are: (1) Optical distortion due to the flat window in front of the lens separating mediums of different indices of refraction; (2) Optical distortion of the image inside of a gas cavity in water; (3) Optical distortion due to movement of the projectile during the shutter or illumination period; and, (4) Camera lens distortion. Distortion sources 1 and 2 result primarily from the differences in the indices of refraction of the optical media: glass, air, and water.

TEST RESULTS

Over 50 projectiles were launched on the SHSB Test Range from the time the facility was completed through the end of the author's tenure at NUWC in December, 1998. Success criteria were based primarily on projectile performance and behavior. Calculated drag coefficient, stability of flight, and end-of-range residual kinetic energy were the major criteria. Results from each test have been used to guide an evolution leading toward an optimal design of the projectile and the launch package for the particular projectile configuration of interest. The primary projectile design parameters were the material (mass density), length-to-diameter ratio (aspect ratio), cavitator tip diameter, and overall shape (tail geometry, contour).

Figures 6 through 9 show several frames grabbed from some of the standard video cameras. Such single frames proved to yield a significant amount of important information regarding the projectile flight.

Figure 10 shows a sequence of shadow-graphs taken during one of the supersonic flights showing the shock wave produced in the water.

Figures 11 and 12 show two shadow-graphs captured using the 35-mm camera and a 3-μs stroboscope. These two images compare the flight of a normal and a damaged (hydrodynamically buckled) projectile as it passed the camera approximately 2.5 m from the gun muzzle exit.

Figures 13 and 14 show front-lit images captured using 35-mm cameras and 3-μs stroboscopes as the projectile reached a point approximately 5.5 m from the gun muzzle exit.

SUMMARY

A gun-launched underwater SHSB test range was constructed and has been used in extensive experimentation with supercavitating projectiles. Key results from this program have included the following:

- Successful design, construction, and operation of an indoor test range capable of launching supercavitating projectiles at velocities exceeding the speed of sound in water. In addition, an instrumentation and imaging suite has been integrated that provides the data necessary to perform basic research.
- Successful demonstration of fully submerged launch of supersonic, supercavitating projectiles at muzzle velocities up to 1550 m/s or Mach 1.03.
- Underwater, stable, subsonic and supersonic projectile flight has been demonstrated.
- Key parameters necessary for stable launch and flight have been identified.
- An understanding of launch dynamics has been acquired.
- Effects of varying projectile parameters and cavitator shape on subsonic and supersonic ballistics have been investigated.
- Good agreement of theory with experiment has been demonstrated.
- A tungsten projectile has been successfully launched underwater.

ACKNOWLEDGEMENTS

The material presented in this article was based on a previous publication (Hrubes, et al, 1998, listed in the references). In his role as Chief Engineer and Principal Investigator of the NUWC Supercavitating High-Speed Bodies program, the author of the current publication was supported by the NUWC Supercavitating

High-Speed Bodies Test Team led by Mr. J. Dana Hrubes, who served as Test Director. During various periods over the course of the program, Mr. C. Curtis and Dr. P. Corriveau served as Program Managers.

The author would like to acknowledge the sponsorship of the following organizations during the period discussed: the Office of Naval Research, the Defense Advanced Research Projects Agency, and the NUWC Division Newport In-House Laboratory Independent Research, Bid and Proposal, and Capital Purchase Programs. The enthusiastic guidance of the NUWC Technical Director, Dr. John Sirmalis, was essential to the success of this program.

Development of the current article was supported by Dr. Kam Ng (ONR), for which the author is especially grateful.

These lecture notes are dedicated to Prof. Yuri N. Savchenko and Mr. P. Kochendorfer, whose illuminating guidance in hydrodynamics and supercavitation has been inspirational.

REFERENCES AND BIBLIOGRAPHY

Hrubes, J.D., C.W. Henoch, I.N. Kirschner, C.M. Curtis, and P.J. Corriveau (1998) "NUWC Supercavitating High-Speed Bodies Test Range: Description and Test Results," *Proceedings of the 1998 ITTC Conference.*

Kirschner, I.N. (1997) "Supercavitating Projectile Experiments at Supersonic Speeds," abstract published in the *Proceedings of the NATO/AGARD Fluid Dynamics Panel Workshop on High Speed Body Motion in Water,* AGARD Report 827, Kiev, Ukraine.

Kirschner, I.N., K.W. Roth, J.D. Hrubes, L.M. Dean, and D.R. Stinebring (1996) "Progress in Supercavitating High Speed Projectiles Research," *Proceedings of the ASME & JSME Fluids Engineering Annual Conference & Exhibition, Cavitation and Multiphase Flow Forum,* FED 210, J. Katz and K. Farrell, editors, San Diego, CA.

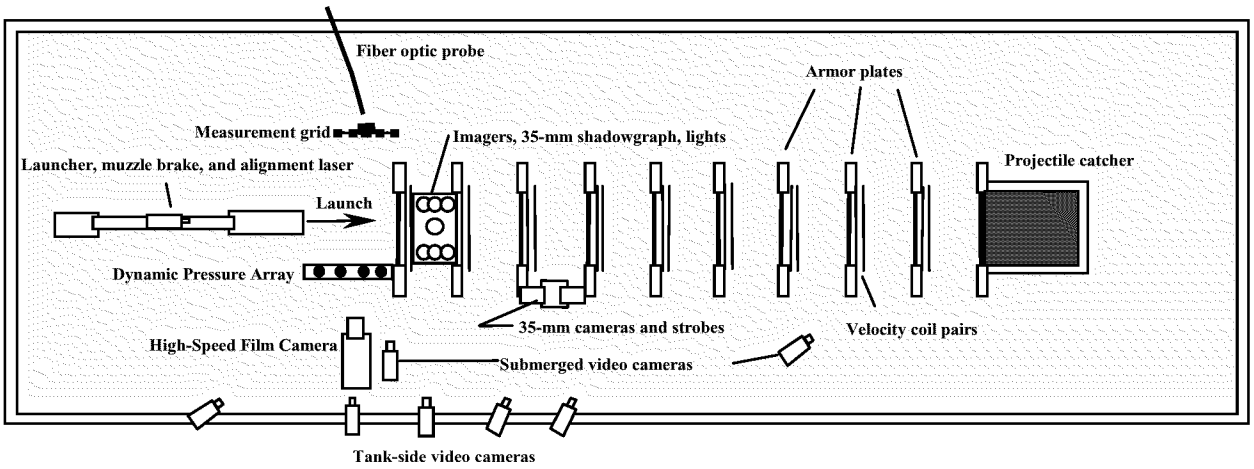


Figure 1. Schematic of SHSB test range

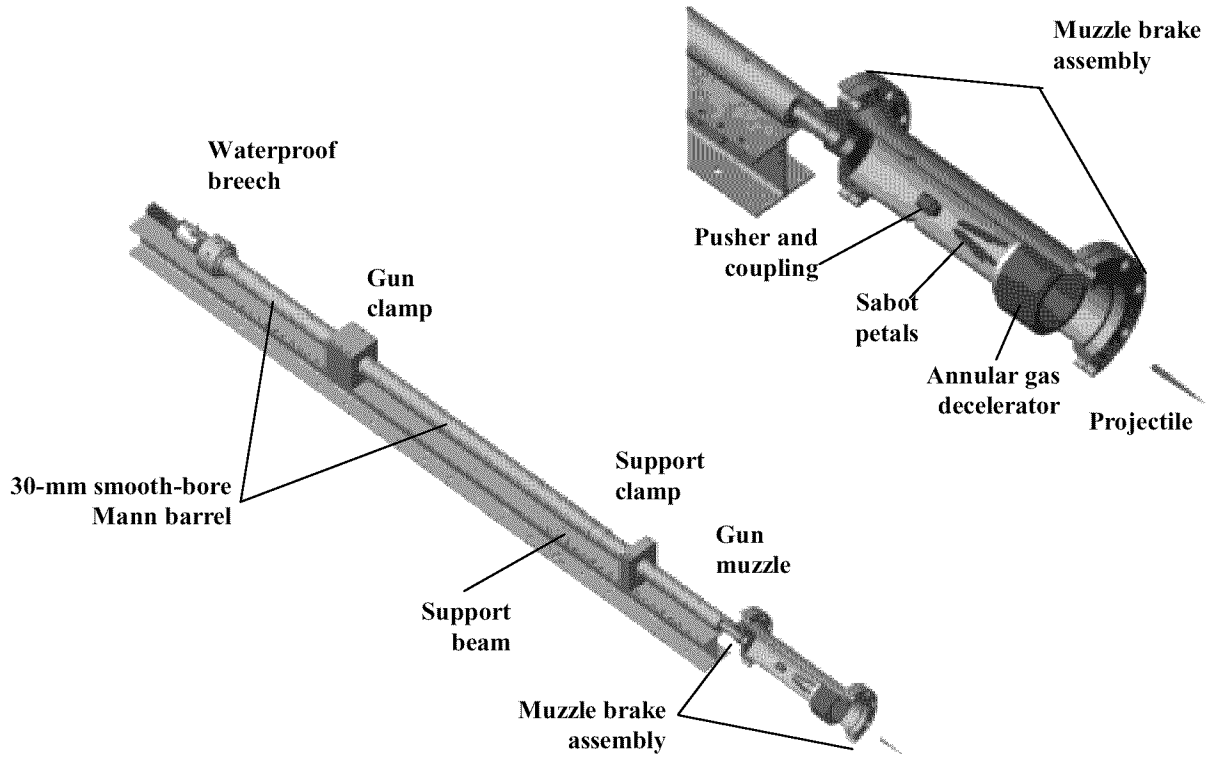
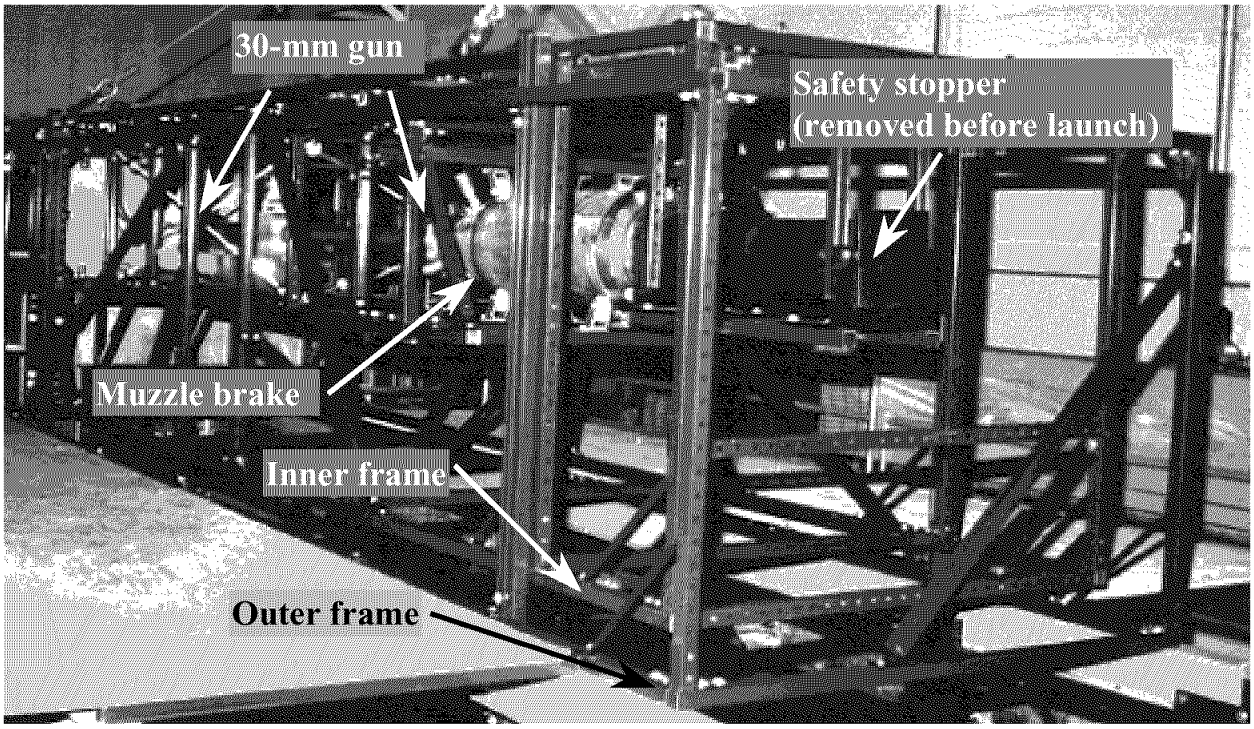


Figure 2. Schematic of 30-mm gun launcher and muzzle brake assembly



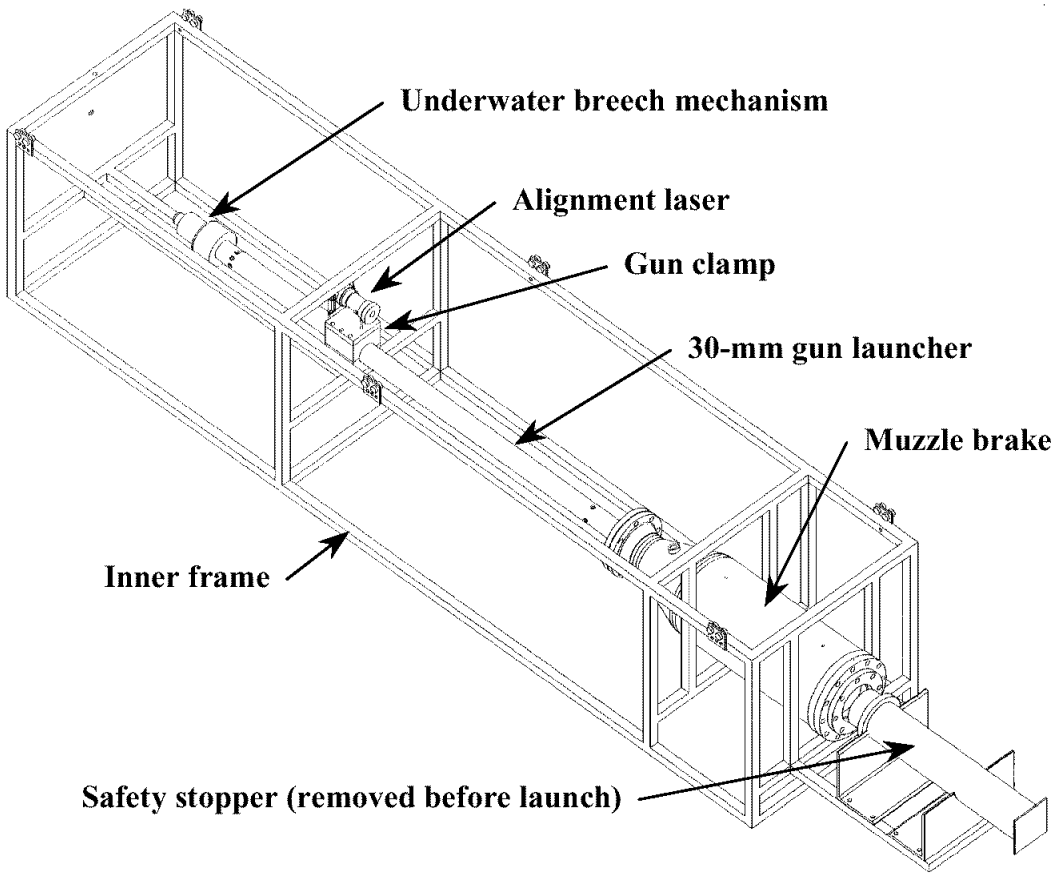


Figure 3. Photograph and schematic of launcher mounted in frame

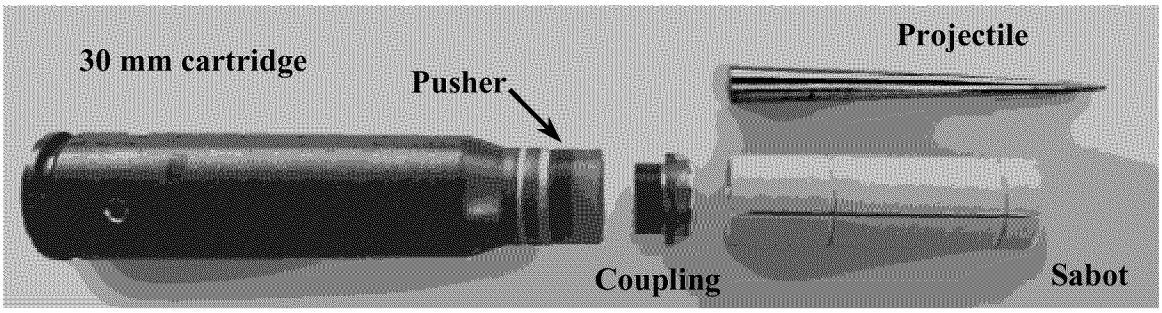


Figure 4. Successful 10:1 projectile launch package

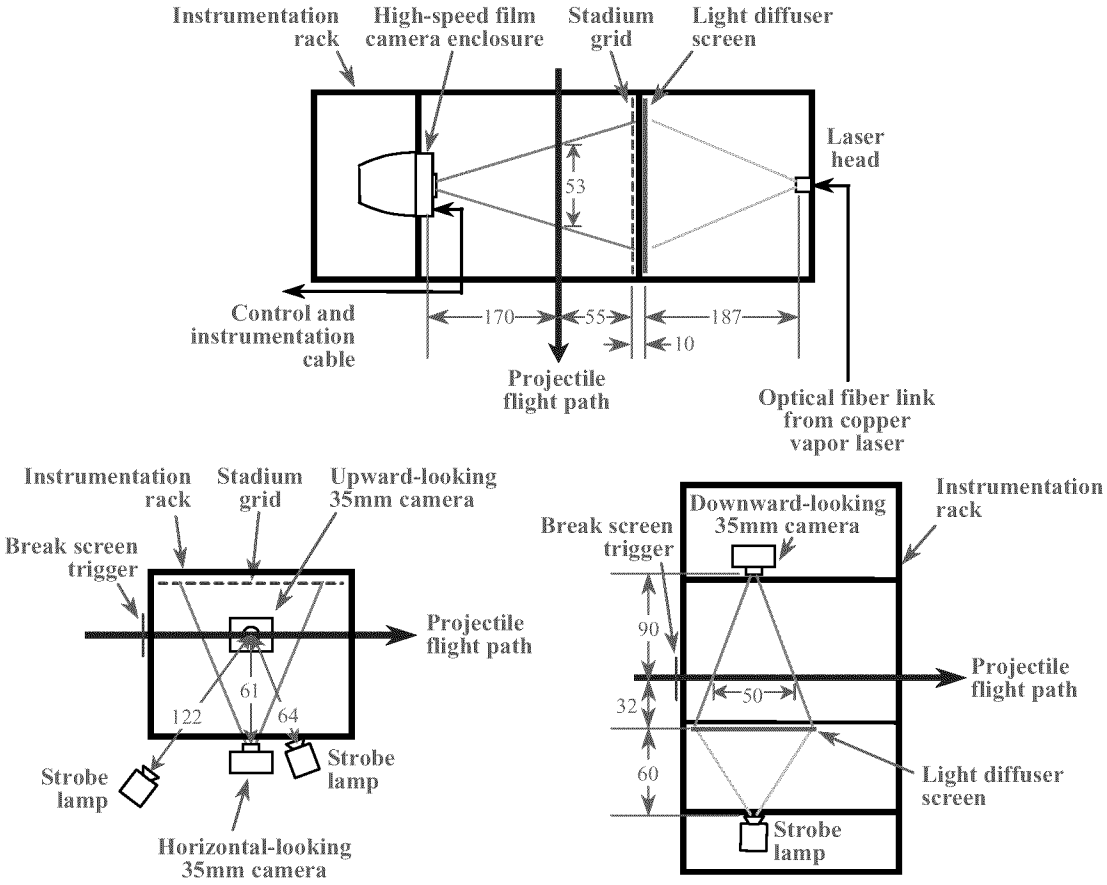


Figure 5. Various platform arrangements for high-speed imaging of projectile flight

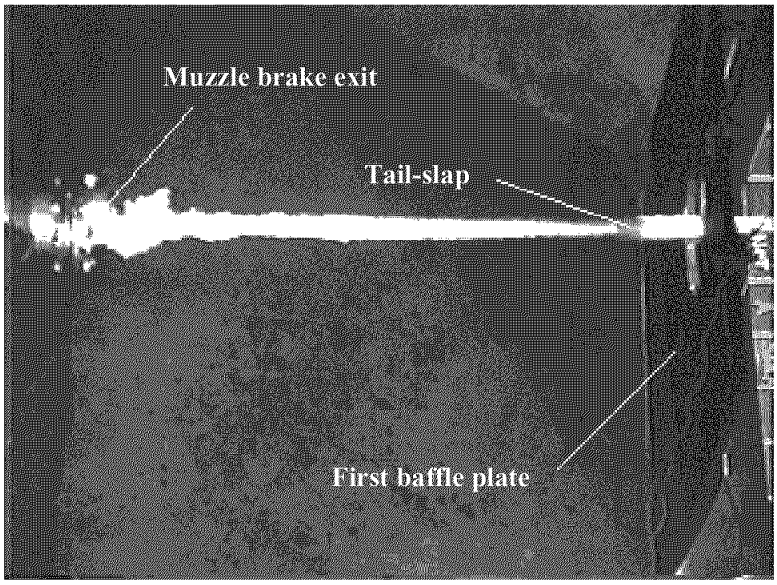


Figure 6. Projectile cavity – clean launch (standard front-lit video frame)

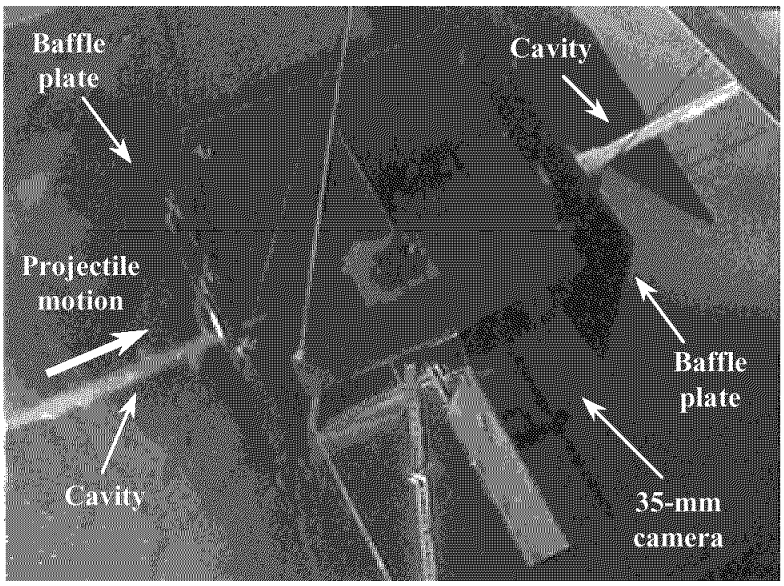


Figure 7. Projectile cavity – clean flight through instrumentation platform (standard front-lit video frame looking down)

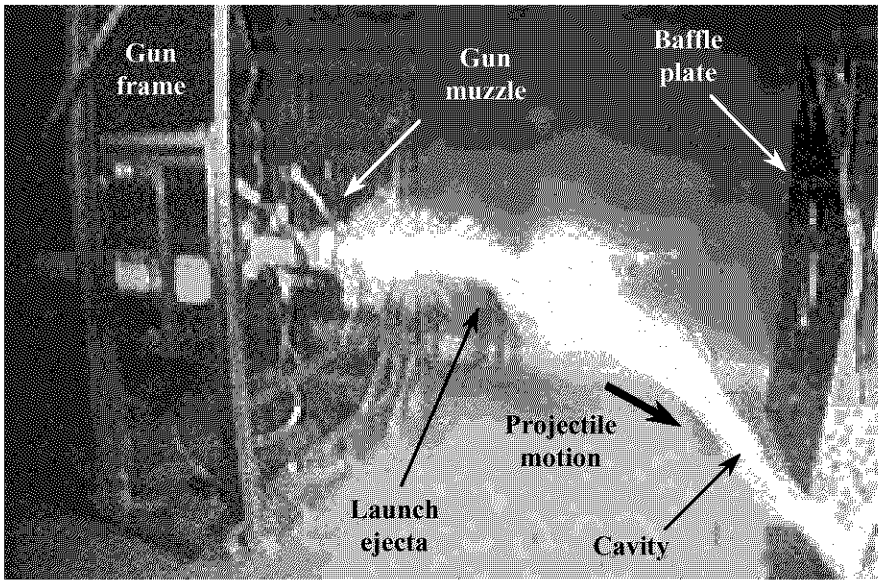


Figure 8. Projectile cavity – unstable flight (standard front-lit video frame)

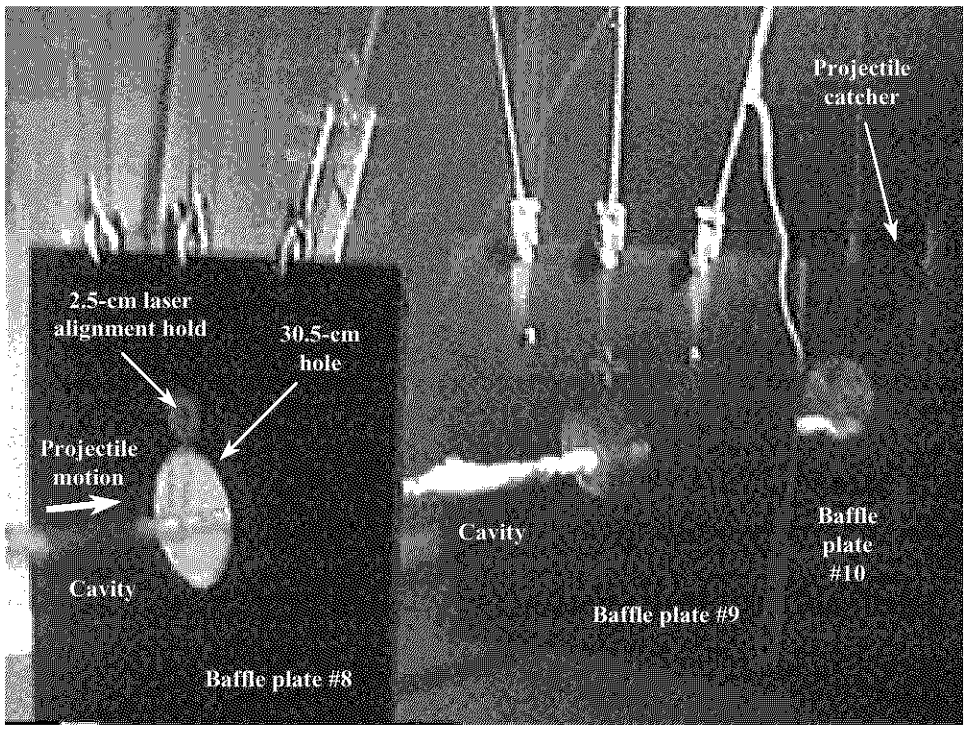


Figure 9. Projectile cavity – clean flight into catcher (standard front-lit video frame)

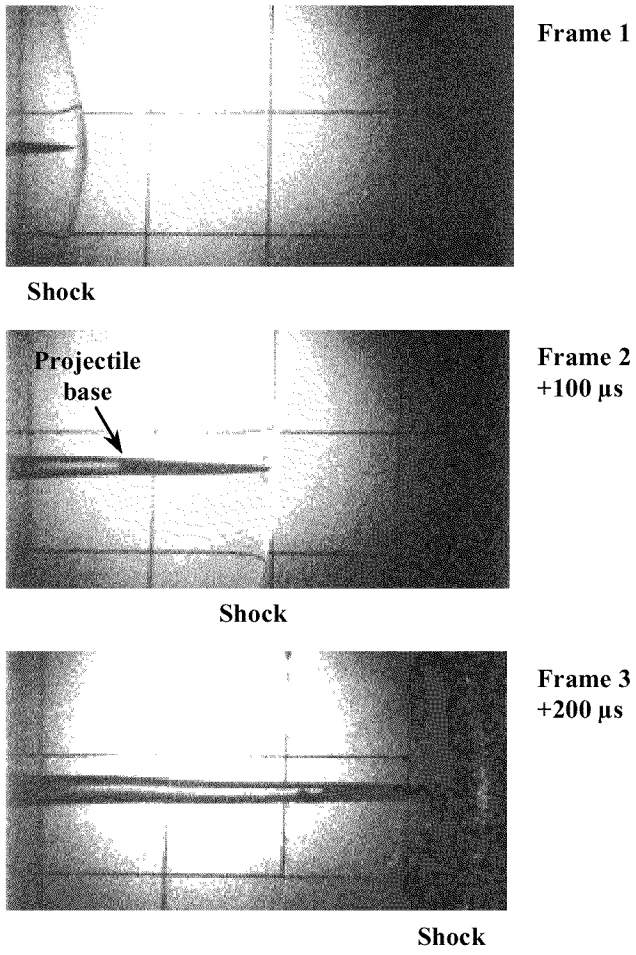


Figure 10. Projectile in supersonic flight (Mach number ~ 1.03; ~1549 m/s; high-speed shadow-graph film; 10,000 frames/s)

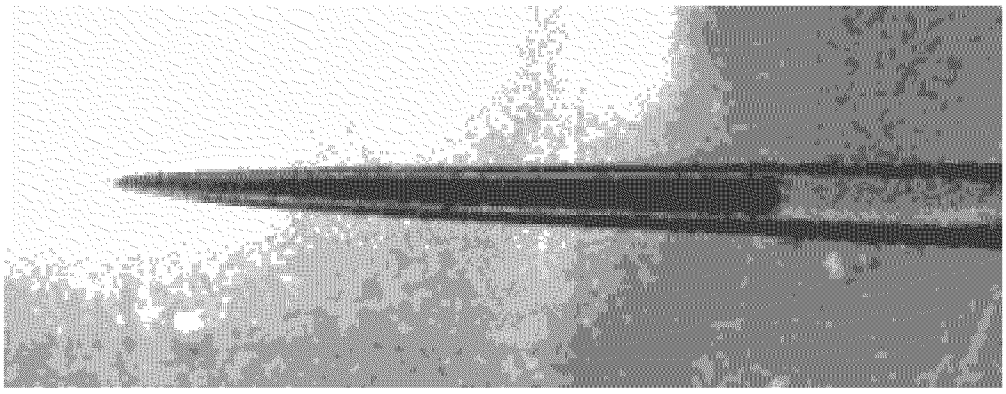


Figure 11. Projectile in cavity – clean flight (1200 m/s; 35-mm shadow-graph)

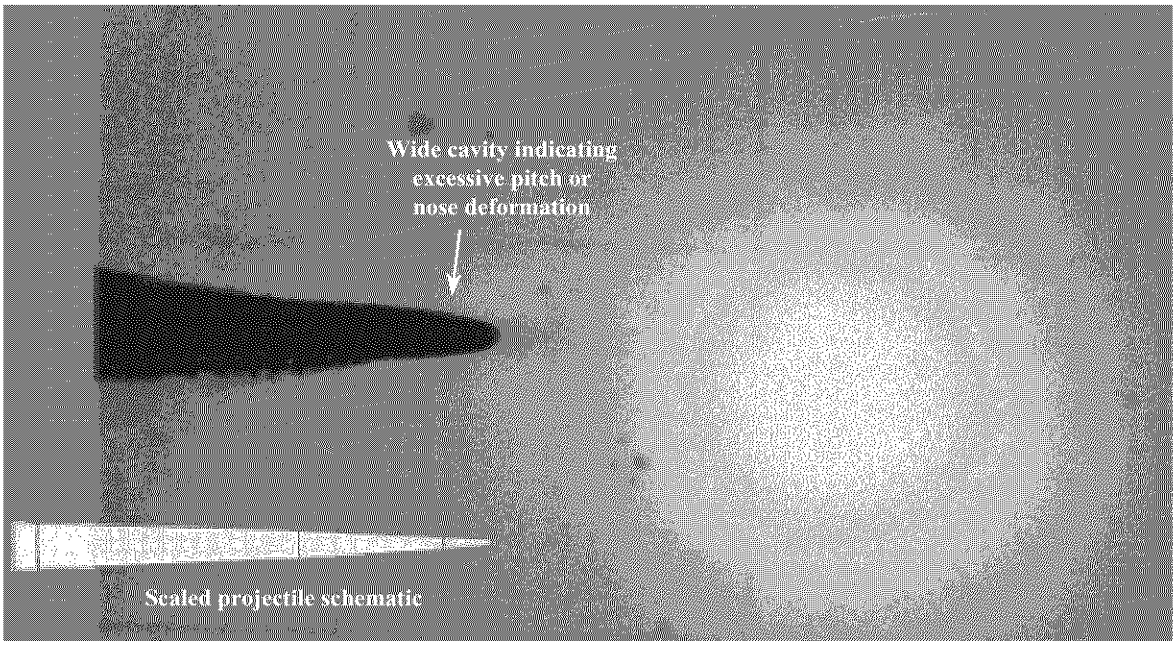


Figure 12. Projectile in cavity – damaged condition (35-mm shadow-graph)

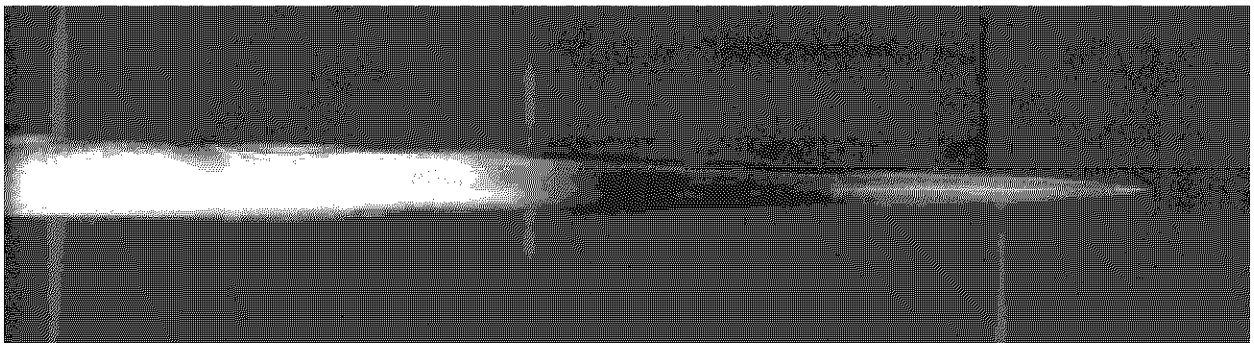


Figure 13. Projectile in cavity – clean flight (1200 m/s; 35-mm front-lit image)

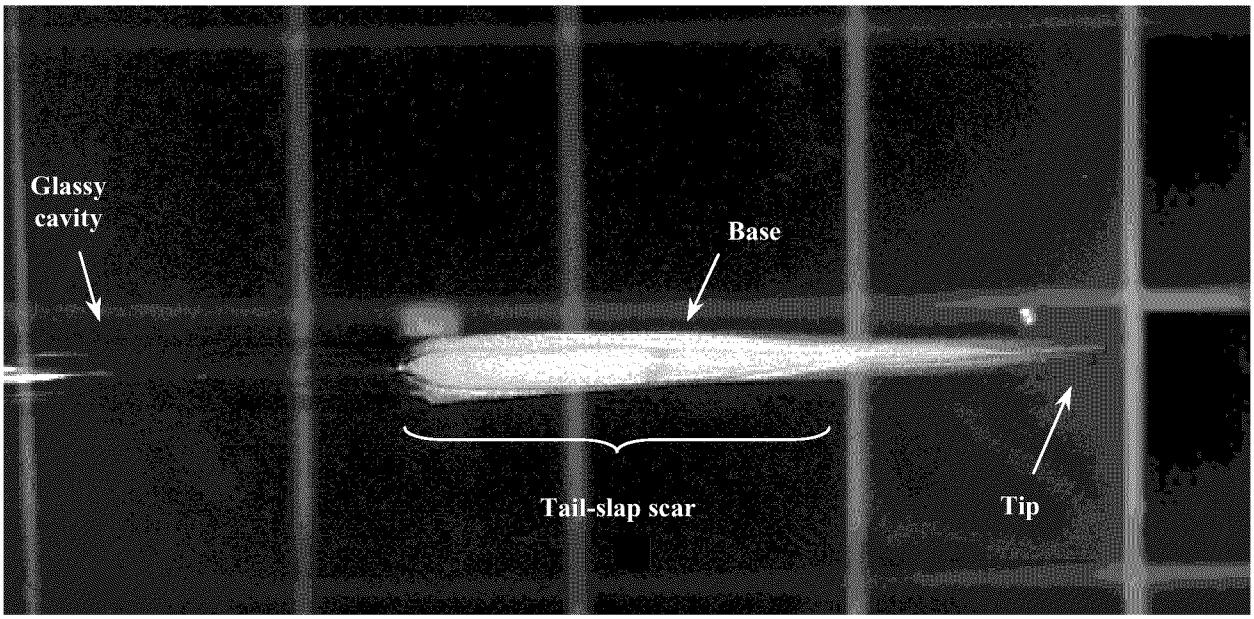


Figure 14. Projectile during a tail-slap event (1220 m/s; 35-mm front-lit image)

Supercavities in Compressible Fluid

A. D. Vasin

State SRC TsAGI, Moscow, Russia
17, Radio str., Moscow, Russia

Summary

The basic results obtained by the author in the theory of supercavities in compressible fluid have been presented. Some peculiarities of the theoretical methods application for the supersonic flows and their difference from the analogous flows in air have been noted. The basic correlations for the shock waves in the water are considered.

Axissymetric supercavities in sub- and supersonic compressible fluid have been researched using the asymptotic method. An integro-differential equation for the cavity profile was deduced. The outer solution was found and for the thin cone-cavitators the solution was obtained for the whole area of the flow.

Based of the modern numerical methods the algorithm of calculation of axisymmetric cavities in sub- and supersonic compressible fluid flow has been worked out. The results of calculation of axysimmetric supercavities downstream of a disk within the range of the Mach numbers $0 \le M \le 1.4$ have been represented. As a result of the analysis for the different Mach numbers the following was defined: the cavitation number, the cavitation drag ratio, the mid-section radius, the cavity shape, the distance of shock wave from a disk (for supersonic flow). The conical flows in a supersonic water stream have been calculated by the numerical method.

The results obtained by the author have been compared with the known experimental and theoretical results of other investigations.

Introduction

The axisymmetric and three-dimensional supercavities in incompressible fluid have been intensively studied since the early 1950's. A large amount of works have been published on three-dimensional supercavities in incompressible fluid. There were about several hundred of them. It should be noted that there have been a few publications on the three-dimensional supercavities in a compressible fluid (in contrast to the case of incompressible fluid). This situation is a result of both the absence of practical interest to this problem before 1980 and the complexity of the problem itself. The only work was Gurevich's work [1] that was published in 1947. In this work the expansion law for a cavity downstream of a body was examined for zero cavitation number and generalized to include the subsonic case.

Since the early 1980's in the USSR and in the USA the interest in supercavities in a compressible fluid has increased. The necessity to come up with the supercavities theory in a compressible fluid appeared. The following works have been made based on the slender body theory. These are the works: Yakimov [2,3], the author [4,5] and Serebryakov [6,7]. On the basis of the early numerical method Al'ev [8] has calculated the cavity past a thin cone. The theoretical investigations on two-dimensional supercavities in compressible fluid were carried out by Nishiyama [9].

The slender body theory has a limited application for calculation of supercavities in compressible fluid. For blunt cavitators such as a dusk or a blunt cone, this theory does not provide a way to obtain the complete data for the cavitation flow, for example, the cavity shape immediately downstream of the cavitator, and the cavitation drag. The linear equation for the potential of compressible fluid flow past

Paper presented at the RTO AVT Lecture Series on "Supercavitating Flows", held at the von Kármán Institute (VKI) in Brussels, Belgium, 12-16 February 2001, and published in RTO EN-010.

slender axisymmetric bodies is inapplicable on the transonic velocity range. Moreover, for the case of supersonic flow the slender body theory faces some major difficulties which is shown by the author's investigations.

The recent development of the numerical methods and widespread use of computers have made it possible to calculate compressible cavitation flows efficiently. It should be noted that the numerical calculations have been carried out by Zigangareeva and Kiselev [10] and by the author [11,12].

1. The application of the slender body theory for the investigation of supercavities in subsonic flow

The case of subsonic cavitation flow past a thin cone has been considered in chapter 2 of lecture #1. The Riabouchinsky scheme has been applied (Fig. 3 in lecture #1). An integro-differential equation for the cavity profile has the form of correlation (2.6) in lecture #1. In lecture #1 we have considered the case when the parameter of the cavity thinness has the same order as the parameter of the cavitator thinness ε equal to the ratio of the cone radius to its height. For the whole area of the flow the solution has been obtained by the method of expansion into asymptotic rows (rows have the form of correlations (2.6) in lecture #1). The first approximation of the cavity profile is represented by an ellipsoid of revolution (equation (2.9) in lecture #1). The second approximation is determined from the equation which was obtained after the equalization of members at ε^4 [13].

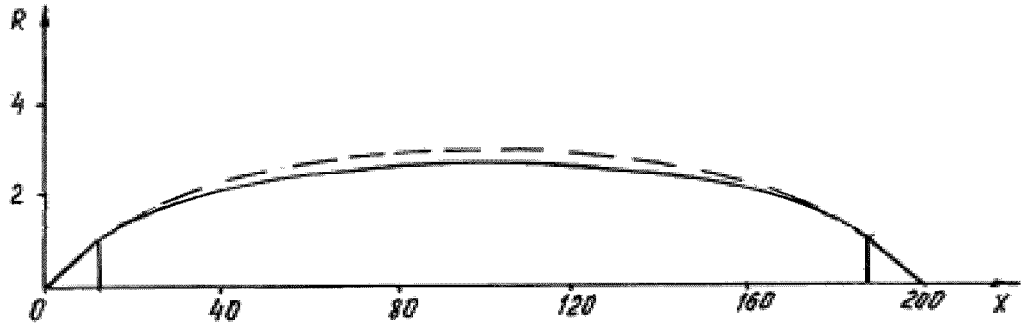


Fig. 1 Cavity profile in subsonic flow for the cone α=5°; the broken curve corresponds to the first approximation, the continuous curve corresponds to the second approximation

In Fig. 1 the broken curve corresponds to the first approximation of the cavity profile $R(x)$ past the cone with the apex half-angle equal to 5°. The total length L equals 200 (the geometric dimensions are scaled by the radius of the cone base, the description of the geometric dimensions is given in chapter 2 of lecture #1). The continuous curve corresponds to the second approximation of the cavity profile. From Fig.1 it is evident that the second approximation is close to the first one, i.e. the second members of asymptotic row are smaller than the first ones.

Besides, for the cavities past the thin cones the cavitation numbers σ are determined at the different Mach numbers M ($\sigma = 2(P_0 - P_k)/\rho V_0^2$, where P_0 is the free stream pressure. P_κ is the pressure within the cavity, ρ is the fluid density, V_0 is the free stream velocity; $M=V_0/a_0$, where a_0 is the free stream speed of sound). The dependences $\sigma(M)$ are determined at the constant cavity length L_k and the total length L equal to 200.

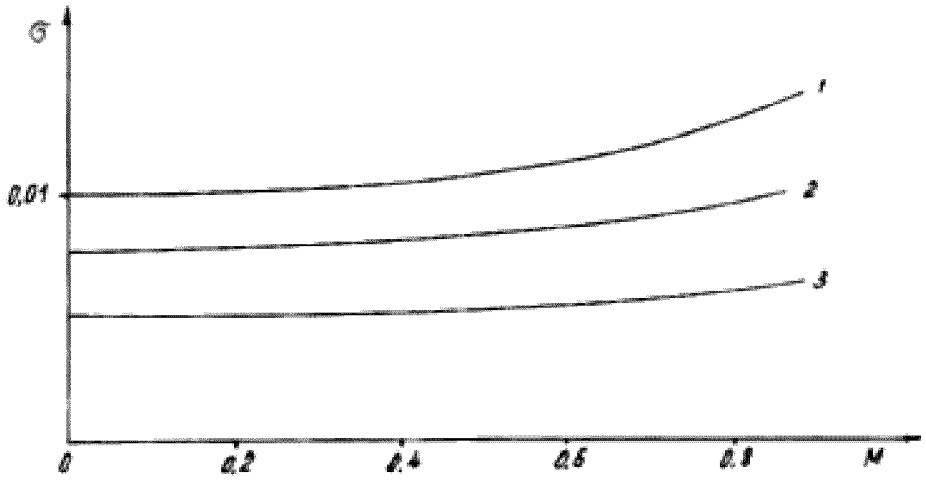


Fig. 2 Dependence of σ on M; curves 1-3 correspond to α=15°, 10° and 5°

In Fig.2 the dependences $\sigma(M)$ are shown at various cone apex half-angles α (curves 1-3 correspond to α=15°, 10° and 5° respectively). Thus, for the given cone at the constant value of L or L_k the cavitation number increases with the Mach number and the cavity profile remains invariable.

After implementation of the transformations analogous to the ones in chapter 2 of lecture 1 we can determine the expression for the pressure coefficient on the thin cone surface [13]. Integrating the pressure coefficient on the cone surface we obtain the cavitation drag coefficient C_x (normalized by the area of the cone base πR_n^2, where R_n is the radius of the cone base). In Fig. 3 the dependences $C_x(M)$ are shown at various cone apex half-angles (curves 1-3 correspond to α=15°, 10° and 5° respectively).

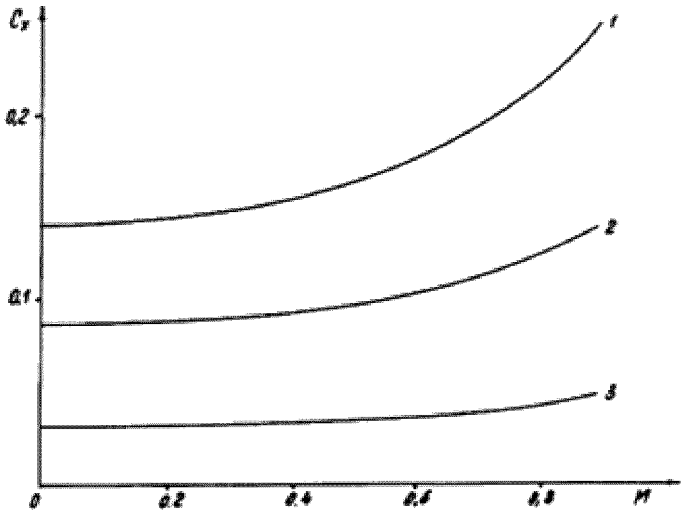


Fig. 3 Dependence C_x on M; curves 1-3 correspond to α=15°, 10°, 5°

The character of the dependences $C_x(M)$ (Fig.3) corresponds to one of the dependences $\sigma(M)$ (Fig.2). This is a consequence of the law of conservation of momentum applied to the cavity middle-section plane. The law of conservation of momentum can be written in the following form [14]

$$R_k = \sqrt{\frac{C_x}{k\sigma}} \tag{1.1}$$

where R_κ is the radius of the cavity mid-section normalized by the radius of the cone base, κ is the coefficient which value is close to 1 at the small cavitation numbers. In the first approximation we can neglect the dependence of κ on the Mach number. The solution for the thin cones has shown that at the constant value of L_k or L the value of R_κ remains the same at the variation of the Mach number. Then according to formula (1.1) the dependences $C_x(M)$ and $\sigma(M)$ must satisfy the following correlation

$$\frac{C_x(M)}{\sigma(M)} = const \tag{1.2}$$

where the constant is the function of α and L_k. The calculations have shown that correlation (1.2) is satisfied with sufficient accuracy at the Mach numbers on the interval $0 \le M \le 0.8$ [13]. The cavity past a thin cone in incompressible fluid (M=0) has been considered as a particular case. The value of the cone apex half-angle equals 15°. For this cone the results obtained based on the slender body theory have been compared with the results of the numerical calculation [15] for incompressible fluid. The comparison has shown good agreement of these results [13].

Let us consider the case when the parameter of the cavity thinness is far less than the parameter of the cavitator thinness. In this case we neglect the cavitator dimensions in comparison with the cavity dimensions. In order to determine the outer solution we assume that the radius of the cavitator equals zero. Let us place the origin of coordinates in the middle of the cavity length and the geometric dimensions normalize by the semi-length $L_k/2$. In this case integro-differential equation (2.6) in chapter 2 of lecture #1 takes the form [4,13]

$$\frac{u'^2}{2u} + u'' \ln\frac{(1-M^2)u}{4(1-x^2)} - \int_{-1}^{1} \frac{u''(x_1)-u''(x)}{|x-x_1|}dx_1 - \frac{u'(-1)}{1+x} + \frac{u'(1)}{1-x} = 2\sigma \tag{1.3}$$

$$u = R^2, \quad R(\pm 1) = 0, \quad R(0) = \varepsilon_1$$

where $\varepsilon_1 = 2R_k / L_k = 1/\lambda$ is the small parameter equal to the inverse amount of the cavity aspect ratio λ.

We seek the outer solution in the form of expansion into asymptotic rows with the small parameter ε_1. For the squared cavity radius and the cavitation number these rows have the form

$$R^2 = \varepsilon_1^2\left[R_0^2 + R_{-1}^2\left(\ln\frac{1}{\varepsilon_1^2}\right)^{-1} + R_{-2}^2\left(\ln\frac{1}{\varepsilon_1^2}\right)^{-2} + \ldots\right]$$

$$\sigma = \varepsilon_1^2 \left[\sigma_1 \left(\ln \frac{1}{\varepsilon_1^2} \right) + \sigma_0 + \sigma_{-1} \left(\ln \frac{1}{\varepsilon_1^2} \right)^{-1} + \ldots \right] \tag{1.4}$$

After substitution of (1.4) in (1.3) and conservation of the two members of the rows integro-differential equation (1.3) is transformed to two differential equations. Solving the differential equations we obtain the expression for the cavity profile and the dependence of the cavitation number on the cavity aspect ratio and the Mach number [4,13]

$$R^2 = \varepsilon_1^2 \left\{ \left(1 - x^2\right) + \frac{x^2 \ln 4 - \ln\left[(1+x)^{(1+x)}(1-x)^{(1-x)}\right]}{2 \ln \lambda} \right\}$$

$$\sigma = \frac{2}{\lambda^2} \ln \frac{\lambda}{\sqrt{e}\sqrt{1 - M^2}} \tag{1.5}$$

where e is the base of natural logarithms.

The first approximation of the cavity profile is an ellipsoid of revolution (as in incompressible fluid). From the first expression (1.5) it follows that the added member to an ellipsoid is small at the small cavitation numbers, for example, then λ=14.66 and σ=0.02 (M=0) the difference between the cavity shape and an ellipsoid of revolution does not exceed 1%. In general the cavity aspect ratio is dependent upon the cavitation and Mach numbers. From the second expression (1.5) it follows that at the constant value of the cavity aspect ratio the cavitation number increases along with the Mach number. The analogous dependence is obtained in the case of the subsonic cavitation flow past a thin cone. As the cavitation number decreases the influence of fluid compressibility on the cavity aspect ratio becomes insignificant.

Thus, the investigation carried out on the basis of the slender body theory has shown that in subsonic flow we can neglect the influence of the Mach number on the cavity shape: the cavity shape is described by an ellipsoid of revolution with sufficient accuracy (as in incompressible fluid). An ellipsoid of revolution is obtained from the outer solution (1.5) (when we neglect the cavitator dimensions in comparison with the cavity dimensions) and from the solution for the thin cones ((2.9) in lecture #1) (when the parameter of the cavity thinness has the same order as the parameter of the cavitator thinness). The Mach number mainly influences the value of the cavitation drag of the cavitator (the cavitation drag coefficient increases along with the Mach number). At the constant cavity length the cavitation number increases along with the Mach number according to the law of conservation of momentum.

2. The application of the slender body theory for the investigation of supercavities in supersonic flow

Let us consider the cavitation flow past a thin cone in supersonic stream. We apply the Riabouchinsky scheme (Fig. 3 in lecture #1). The linearized equation for the perturbed velocity potential in the cylindrical coordinate system is written as following [16]

$$-\left(M^2 - 1\right)\frac{\partial^2 \varphi}{\partial x^2} + \frac{\partial^2 \varphi}{\partial r^2} + \frac{1}{r}\frac{\partial \varphi}{\partial r} = 0 \tag{2.1}$$

where $\varphi = \varphi^* / V_0 R_n$ is the dimensionless perturbed velocity potential, φ^* is the perturbed velocity potential.

The geometric dimensions are scaled by the radius of the cone base (the description of the geometric dimensions is given in chapter 2 of lecture #1). For supersonic flow the perturbed velocity potential that satisfies equation (2.1) can be written in the form of integral [16]

$$\varphi = -\frac{1}{2\pi} \int_0^{x-\sqrt{M^2-1}r} \frac{q(x_1)dx_1}{\sqrt{(x-x_1)^2 - (M^2-1)r^2}} \tag{2.2}$$

where $q(x_1)$ is the intensity of sources and sinks on the axis of symmetry. Near the surfaces of the thin cavitator and the cavity potential (2.2) that satisfies the kinematic boundary condition has the following asymptotic representation [17]

$$\varphi = \frac{1}{4\pi} S'(x) \ln \frac{(M^2-1)r^2}{4x^2} - \frac{1}{2\pi} \int_0^x \frac{S'(x_1) - S'(x)}{x - x_1} dx_1 \tag{2.3}$$

where $S'(x)$ is the derivative of the dimensionless area of the cross section with respect to x coordinate.

For supersonic flow the dynamical boundary condition on the cavity surface has the same form as for subsonic flow [5] and is written as following

$$2\frac{\partial \varphi}{\partial x} + \left(\frac{\partial \varphi}{\partial r}\right)^2 = \sigma \tag{2.4}$$

Substituting (2.3) in (2.4) we obtain the integro-differential equation for the cavity profile past a thin cone in supersonic flow

$$\frac{u'^2}{4u} + \frac{u''}{2} \ln \frac{(M^2-1)u}{4x^2} - \int_o^l \frac{u_1''(x_1) - u''(x)}{x - x_1} dx_1 - \int_l^x \frac{u''(x_1) - u''(x)}{x - x_1} dx_1 = \sigma \tag{2.5}$$

$$u = R^2, \quad u_1 = R_1^2, \quad u_1'(0) = 0$$

We assume that the cone has the same thinness order as the cavity. The thinness order of the cone ε equals the ratio of the radius of the cone base to its height. We seek the solution for the whole area of the flow in the form of expansion into asymptotic rows with the small parameter ε. The rows have the form of correlations (1.4) if we substitute ε with ε_1. The boundary conditions are written in the same form as for subsonic flow [7,13]

$$x = l: \quad R = 1, \quad R' = \varepsilon$$

$$x = l + L_k : R = 1$$

After substitution of the asymptotic rows in (2.5) and conservation of the two members of rows integro-differential equation (2.5) is transformed to two differential equations. The first differential equation with the boundary conditions is written as follows

$$\frac{d^2 R_0^2}{dx^2} = -2\sigma_1$$
$$R_0^2(l) = l^2, R_0^2(l + L_k) = l^2, \quad \frac{dR_0^2}{dx}\Big|_{x=l} = 2l \tag{2.6}$$

The solution of equation (2.6) has the form

$$R_0^2 = \sigma_1 (a - x)(x - b)$$
$$\sigma_1 = \frac{2l}{L_k}, \quad a = \frac{L}{2} + \sqrt{\frac{L^2}{4} - \frac{lL}{2}}, \quad b = \frac{L}{2} - \sqrt{\frac{L^2}{4} - \frac{lL}{2}} \tag{2.7}$$

From expression (2.7) it follows that an ellipsoid of revolution is the first approximation of the cavity shape. The analogous result has been obtained in subsonic flow (expression (2.9) in lecture #1). The second approximation is determined from the differential equation which was obtained after equalization of members at ε^4.

In Fig. 4 the broken curve represents the first approximation of the cavity profile past the cone with the apex half-angle equal to 5°. The total length equals 200. The continuous curve represents the second approximation of the cavity profile.

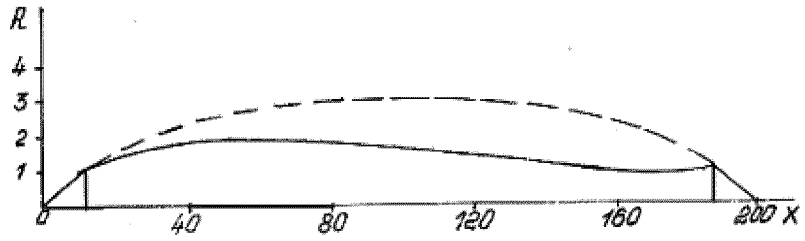


Fig. 4 Cavity profile in supersonic flow for the cone α=5°; the broken curve corresponds to the first approximation, the continuous curve corresponds to the second approximation

Figure 4 is analogous to Fig. 1 that illustrates the cavity profile past the same cone in subsonic flow. From Fig. 4 it follows that as distinct from subsonic flow (Fig. 1), in supersonic flow the second approximation of the cavity profile essentially differs from the first one, and the second members of asymptotic row are not smaller than the first ones. Besides, the unreal shape of the cavity contradicts with the physical laws of cavitation flows.

The analysis of this effect has shown that the slender body theory is not valid for the flow past the edge of the cone. In the supersonic flow the Prandtl-Meyer stream arises at the edge. The stream must turn at the angle that is dependent on the pressure within the cavity or the cavitation number. The

incline of a free stream line is less than the cone apex half-angle. It is impossible to satisfy this condition within the range of the slender body theory. The first peculiarity of the slender body theory application to the supersonic cavitation flow is its discrepancy with the boundary condition at the cavitator edge.

In order to determine the solution it is necessary to consider the supersonic flow around the cone, obtain the Mach number at its edge and match the Prandtl-Meyer stream with the cavitation flow. It is very difficult to carry out, as the cavity shape and the cavitation number are not known beforehand.

Let us determine the pressure coefficient on the surface of the thin cone in supersonic flow. The expression for the pressure coefficient has the form [16]

$$C_p = -2\frac{\partial \varphi}{\partial x} - \left(\frac{\partial \varphi}{\partial r}\right)^2 \tag{2.8}$$

where $C_p = 2(P_{con} - P_0)/\rho V_0^2$ is the pressure coefficient, P_{con} is the pressure on the cone surface.

After differentiating expression (2.3) the components of the perturbed velocity on the cone surface are written as following

$$\begin{aligned} \frac{\partial \varphi}{\partial x} &= \frac{\varepsilon^2}{2}\ln\frac{(M^2-1)\varepsilon^2}{4} \\ \frac{\partial \varphi}{\partial r} &= \varepsilon \end{aligned} \tag{2.9}$$

After substitution of (2.9) in (2.8) for the pressure coefficient we obtain the following expression

$$C_p = -\varepsilon^2\left[\ln\frac{(M^2-1)\varepsilon^2}{4} + 1\right] \tag{2.10}$$

Formula (2.10) coincides with the expression that defines the pressure coefficient on the thin cone in supersonic flow of air [16]. The pressure coefficient is connected to the cavitation drag coefficient by the following dependence

$$C_x = 2\varepsilon\int_0^l C_p R_1(x)dx + \sigma \tag{2.11}$$

where C_x is the cavitation drag coefficient normalized by the area of the cone base; $R_1(x) = \varepsilon x$ is the radius of the cone cross section.

The pressure coefficient is constant on the cone surface and expression (2.11) takes the form

$$C_x = C_p + \sigma \tag{2.12}$$

We can consider the coefficient C_p to be the cavitation drag coefficient at the zero cavitation number C_{xo}. The formula is written as follows

$$C_x = C_{xo} + \sigma \tag{2.13}$$

Expression (2.13) is the dependence of the cavitation drag coefficient on the cavitation number at the constant Mach number.

Let us consider the case when the parameter of the cavity thinness is far less than the parameter of the cavitator thinness. A similar case was considered for subsonic flow in chapter 1. Let us place the origin of coordinates in the middle of the cavity length and normalize the geometric dimensions by the semi-length $L_k/2$. Integro-differential equation (2.5) takes the form

$$\frac{u'^2}{4u} + \frac{u''}{2}\ln\frac{(M^2-1)u}{4(x+1)^2} - \int_{-1}^{x}\frac{u''(x_1)-u''(x)}{x-x_1}dx_1 - \frac{u'(-1)}{x+1} = \sigma$$
$$u = R^2, \quad R(\pm 1) = 0, \quad R(0) = \varepsilon_1 \tag{2.14}$$

where $\varepsilon_1 = 2R_k / L_k = 1/\lambda$ is the small parameter equal to the inverse amount of the cavity aspect ratio λ.

For determination of the outer solution we neglect the cavitator dimensions in comparison with the cavity dimensions (the radius of the caivtator equals zero in (2.14)). We seek the outer solution in the form of expansion into asymptotic rows with the small parameter ε_1. For the cavity radius squared and the cavitation number these rows have the form (1.4). After substitution of (1.4) in (2.14) and conservation of the two members of the rows integro-differential equation (2.14) is transformed to two differential equations. Solving the differential equations we obtain the expression for the cavity profile and the cavitation number dependence on the cavity aspect ratio and the Mach number

$$R^2 = \varepsilon_1^2\left\{(1-x^2) + \frac{x^2\ln 4 + \ln\left[(1+x)^{(x^2-x-2)}(1-x)^{(x-x^2)}\right]}{2\ln\lambda}\right\}$$
$$\sigma = \frac{2}{\lambda^2}\ln\frac{\lambda}{\sqrt{e}\sqrt{M^2-1}} \tag{2.15}$$

The comparison of the dependences (2.15) with the analogous ones (1.5) obtained for subsonic flow shows that in supersonic flow the first approximation of the cavity shape is an ellipsoid of revolution (as in incompressible fluid). The numerator of the second member in the asymptotic row (2.15) can be presented as the sum of two functions $f_1(x)$ and $f_2(x)$

$$f_1(x) = x^2\ln 4 - \ln\left[(1+x)^{(1+x)}(1-x)^{(1-x)}\right]$$
$$f_2(x) = \ln\left[(1+x)^{(x^2-1)}(1-x)^{(1-x^2)}\right]$$

The function $f_1(x)$ corresponds to the second approximation of the cavity profile in subsonic flow (1.5). In case of supersonic flow the odd function $f_2(x)$ is added to the even function $f_1(x)$ and the cavity becomes asymmetric relatively to the middle of its length. The cavity asymmetry is explained by the fact

that in supersonic flow the influence of sources and sinks spreads downstream only. The expression for $f_2(x)$ shows that $f_2(x)>0$ at $x<0$ and $f_2(x)<0$ at $x>0$, i.e. the cavity is thicker in the head than in the back part and the mid-section displaces ahead.

The calculations have shown that at the cavitation numbers that have the order 10^{-2} the second approximation of the cavity shape in (2.15) is close to the first one and the difference does not exceed several percent. From the second expression (2.15) it follows that the cavity aspect ratio is dependent upon the cavitation and Mach numbers. As the cavitation number decreases the influence of the fluid compressibility on the cavity aspect ratio becomes insignificant.

3. The application of the numerical methods for calculation of supercavities in subsonic flow

The modern numerical methods enable us to calculate the cavitation flows in compressible fluid efficiently. The author has worked out the algorithm of calculation of axisymmetric cavities in sub- and supersonic compressible fluid flow over a wide range of cavitation numbers [11,12].

Let us consider axisymmetric subsonic cavitation flow past a disk in accordance with the Riabouchinsky scheme; in this scheme the cavity is closed by a disk of the same dimensions as the cavitator disk (Fig. 5)

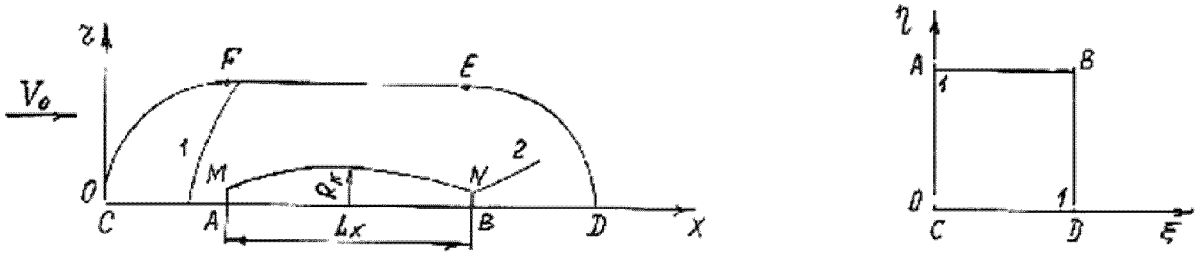


Fig. 5 Flow schematic and computation domain. 1 is the forward shock, 2 is the trailing shock

In view of the flow symmetry, we will examine the flow in a meridional plane. The problem consist in determining the shape of the cavity boundary MN that satisfy the constant velocity and impermeability conditions for a given cavity length L_k (see Fig. 5 where AM is the disk-cavitator, NB is the closing disk, CFED is the external boundary). The geometric dimensions are scaled by the disk radius. The external boundary CFED consists of three parts: CF and ED are parts of the circles with radius 120 and centers at the points A and B respectively; the segment FE is a parallel to the axis of symmetry and located at a distance of 120 from the latter. As the main equation we use the equation of continuity

$$\frac{\partial}{\partial x}(\rho v_x r)+\frac{\partial}{\partial r}(\rho v_r r)=0 \qquad (3.1)$$

where v_x and v_r are the velocity components in the x and r directions respectively. The flow velocity and liquid density are scaled by the free stream velocity V_0 and density ρ_0 respectively. In the

compressible case equation (3.1) is essentially nonlinear, and we will apply the finite-difference method to solve it. The density-velocity relationship is taken from the Bernoulli equation

$$\rho = \left[1 + \frac{(n-1)M^2}{2}\left(1 - v_x^2 - v_r^2\right)\right]^{1/(n-1)}, n = 7.15 \tag{3.2}$$

In order to make the formulation of the boundary conditions at the cavity surface more convenient, it makes sense to map the computational domain in x, r coordinates onto a unit square in ξ, η coordinates, conformity of the points is shown in Fig. 5. After mapping equation (3.1) takes the form [18]

$$\begin{aligned}
&\frac{\partial}{\partial\xi}\left(\frac{\rho r U^c}{J}\right) + \frac{\partial}{\partial\eta}\left(\frac{\rho r V^c}{J}\right) = 0 \\
&U^c = \frac{\partial\xi}{\partial x}v_x + \frac{\partial\xi}{\partial r}v_r, \quad V^c = \frac{\partial\eta}{\partial x}v_x + \frac{\partial\eta}{\partial r}v_r \\
&J = \frac{\partial\xi}{\partial x}\frac{\partial\eta}{\partial r} - \frac{\partial\xi}{\partial r}\frac{\partial\eta}{\partial x}
\end{aligned} \tag{3.3}$$

where U^c and V^c are the contravariant velocity components in the ξ and η directions, and J is the Jacobian of the mapping. We consider the flow to be potential and write the velocity components in the following form [18]

$$\begin{aligned}
&U^c = A_1\frac{\partial\Phi}{\partial\xi} + A_3\frac{\partial\Phi}{\partial\eta}, \quad V^c = A_3\frac{\partial\Phi}{\partial\xi} + A_2\frac{\partial\Phi}{\partial\eta} \\
&A_1 = \left(\frac{\partial\xi}{\partial x}\right)^2 + \left(\frac{\partial\xi}{\partial r}\right)^2, \quad A_2 = \left(\frac{\partial\eta}{\partial x}\right)^2 + \left(\frac{\partial\eta}{\partial r}\right)^2 \\
&A_3 = \frac{\partial\xi}{\partial x}\frac{\partial\eta}{\partial x} + \frac{\partial\xi}{\partial r}\frac{\partial\eta}{\partial r}
\end{aligned}$$

where Φ is the flow velocity potential and A_1, A_2, A_3 are metric coefficients. After mapping onto ξ, η plane equation (3.2) takes the form

$$\rho = \left[1 + \frac{(n-1)M^2}{2}\left(1 - \frac{\partial\Phi}{\partial\xi}U^c - \frac{\partial\Phi}{\partial\eta}V^c\right)\right]^{1/(n-1)} \tag{3.4}$$

The boundary condition is the following: the tangential velocity is constant on the cavity boundary MN, the impermeability condition is imposed on the segments CA, AM, NB and BD, the potential on the external boundary is equal to the free stream potential.

Thus, in order to determine the cavitation flow it is necessary to solve equation (3.3) onto a unit square with the given boundary conditions. The dependence of the density on the velocity (3.4) is added to equation (3.3). The entire computational domain (that is the unit square in the ξ,η plane) is divided by a network with steps $\Delta\xi$ and $\Delta\eta$ along ξ, and η directions.

The non-linear system of equations obtained as a result of the discretization was solved using the iteration method with approximate factorization [18]. Before proceeding to the calculations the first approximation for the cavity shape between the points M and N was preassigned and the computational network corresponding with the given cavity was constructed using an algebraic mapping technique [18]. The velocity on the cavity surface V_k was determined on each iteration stage using the values of the potentials Φ_N, Φ_M at the points N and M from the correlation

$$V_k = \left(\Phi_N - \Phi_M\right)/ s_N$$

s_N is the length of the arc measured from the disk edge M to the point N on the closing disk. The potential at the point on the cavity surface corresponding to s is given by the expression

$$\Phi(s) = V_k s + \Phi_M \tag{3.5}$$

where s is the arc length measured from the point M to the given point on the cavity surface. This expression was used for specifying the boundary conditions on the segment MN.

The iteration procedure turned out to be convergent; the discrepancy diminished, and the potential increment vanished as the number of the iteration cycles increased. However, in general, the obtained solution did not satisfy the impermeability condition on the cavity surface. In order to satisfy the impermeability condition the cavity shape was varied using the following way [11]. The normal flow velocity on the cavity surface was represented in the form - $\partial\Phi/\partial n=\partial\varphi/\partial n+\partial x/\partial n$ where φ is the perturbed velocity potential, x is the coordinate of a point on the cavity surface, n is the normal to the surface, and $\partial x/\partial n=\partial r/\partial s$. The cavity shape must satisfy the impermeability condition $\partial\Phi/\partial n$ =0 or

$$\frac{\partial r}{\partial s} = -\frac{\partial \varphi}{\partial n} \tag{3.6}$$

In [11] it is shown that for subsonic flow in view of cavity symmetry about the mid-section the iteration process of solving the system of two first order differential equations converges precisely to relation (3.6). The system has the form

$$\frac{\partial r}{\partial s} = -\frac{\partial \varphi}{\partial n}, \quad \frac{\partial x}{\partial s} = \sqrt{1 - \left(\frac{\partial r}{\partial s}\right)^2} \tag{3.7}$$

According to equations (3.7) the front half of the cavity had to be corrected.

The numerical analysis was performed for the constant cavity length L_k=199.96 that corresponds with the cavitation number 0.02 for incompressible fluid. The results of the numerical calculations were checked on the satisfaction of the mass and momentum conservation laws and were compared with the results obtained by the slender body theory. The numerical calculations show that in subsonic flow the

cavity shape is close to an ellipsoid of revolution and the dependence $\sigma(\lambda, M)$ is described by the the second expression (1.5) with sufficient accuracy. Moreover, the test calculations were performed to compare with results [15] for incompressible fluid (M=0, σ=0.02) and results [10] (M=0.5 σ=0.16). The comparison has shown a good agreement. For subsonic flow the cavity shape in the vicinity of the disk is shown in Fig. 4 in lecture #1. The continuous curve represents the calculations [15] for incompressible fluid. The author's numerical results are shown by points for different Mach numbers. In Fig. 5 in lecture #1 we compare the cavity profiles in compressible and incompressible fluid for the same cavitation number σ=0.0235. The continuous curve corresponds to the cavity profile in compressible fluid calculated by the numerical method for M=0.8; the broken curve corresponds to the cavity in incompressible fluid calculated by Logvinovich formula [14].

4. The application of the numerical methods for calculation of supercavities in supersonic flow

Let us consider axisymmetric supersonic cavitation flow past a disk in accordance with the Riabouchinsky scheme. The proposed flow scheme is presented in Fig. 5. In case of supersonic flow the shock waves appear (see Fig. 5, curve 1 is the forward shock formed upstream of the disk, and curve 2 is the trailing shock emanating from the closing disk edge). The forward shock is the most intense and nearly normal in the vicinity of the symmetry axis.

However, the shocks appearance does not break the condition that the flow is potential. In water over a wide range of pressures a shock adiabat agrees with the static one expressed by the Tait equation [19]. The special investigation on the analysis of the shock equations was carried out [20]. The analysis has shown that we can assume that the normal shock in water is isentropic and the flow is potential if Mach number does not exceed the value 2.2. In [20] it is shown that we can determine the density from the Bernoulli equation (3.2) in the whole area of the supersonic flow (at the known flow velocity).

Thus, the main equations for the calculation of the supersonic cavitation flow are equations (3.3) and (3.4) as in case of subsonic flow. We will apply the finite-difference method to solve these equations [12]. As distinct from the subsonic flow, in the supersonic flow the boundary conditions on the external boundary are the following: the potential is equal to the free stream potential only on the part of the external boundary where the normal velocity directed along the external normal is less than the velocity of sound. On the part of the external boundary where the normal velocity is more than the velocity of sound the potential is determined by interpolation of values in the nearest nodes of the computational network. As distinct from the subsonic flow, we apply the artificial viscosity so that the difference scheme will be stable in the supersonic area [18,21]. The artificial viscosity is introduced as a modification of density expression [12]. The modification is equivalent to upstream displacement of the computation domain nodes.

The non-linear system of equations obtained as a result of the discretization was solved using the iteration method with approximate factorization [12] (as in case of subsonic flow). The iteration procedure turned out to be convergent; the discrepancy diminished, and the potential increment vanished as the number of the iteration cycles increased. However, in general, the obtained solution did not satisfy the impermeability condition on the cavity surface. In case of subsonic flow the impermeability condition was satisfied by varying the cavity shape with the help of equations (3.7) which are first order differential equations, and since at subsonic flow velocities the cavity is symmetric with respect to the mid-section, a single boundary condition sufficed and only the front half of the cavity had to be corrected. However, at supersonic flow velocities the cavity is asymmetric and its shape must be corrected using second order differential equations subject to the boundary conditions

$$s = 0: \quad r = 1, \quad x = 0$$

$$s = s_N: \quad r = 1, \quad x = L_k$$

The cavity shape was corrected from the disk-cavitator edge towards the closing disk edge. The system of differential equations was derived by differentiating (3.7) with respect to s

$$\frac{\partial^2 r}{\partial s^2} = -\frac{\partial}{\partial s}\left(\frac{\partial \varphi}{\partial n}\right), \quad \frac{\partial^2 x}{\partial s^2} = -\frac{\partial r}{\partial s}\frac{\partial^2 r}{\partial s^2}\left[1-\left(\frac{\partial r}{\partial s}\right)^2\right]^{-1/2} \tag{4.1}$$

Note that the second derivative d^2r/dx^2 has a singularity near the disk edge, an accurate determination of the second derivatives in (4.1) presents considerable difficulties in this area. The calculation of the second derivatives near the disk edge was avoided by using equations (4.1) for $2<x<L_k-2$, and in the vicinity of the cavitator and closing disk the cavity shape was corrected using equations (3.7) (as in subsonic flow). As a result of the numerical solution the obtained cavity shape satisfied both the constant velocity condition (3.5) and the impermeability condition (3.6).

The numerical analysis was performed for the constant cavity length L_k=199.96 that corresponds with the cavitation number 0.02 for incompressible fluid. Calculations of supercavities downstream of a disk within the range of Mach numbers $1 \le M \le 1.4$ have been performed. As a result of the analysis for different Mach numbers the following characteristics were defined – the cavitation number, the cavitation drag ratio, the mid-section radius, the aspect ratio, the cavity shape, and the shock's distance from a disk.

The results of the numerical calculations of the supercavities in supersonic flow satisfy the mass and momentum conservation laws. For the supersonic flow the cavity shape defined by the numerical calculation is close to an ellipsoid of revolution. It agrees with the author's results obtained with the help of the slender body theory (see chapter 2). However, the results on asymmetry of the cavity shape (mid-section displacement relative to the middle of the cavity length) do not agree. While the numerical calculation yields a displacement directed downstream, in chapter 2 (the first expression (2.15)) an opposite displacement was obtained. The behavior of the dependence of σ on λ and M is also different: for constant L_k the calculated aspect ratio and σ increase with the increase in the Mach number (as in subsonic flow), whereas the second expression (2.15) yields the opposite. The discrepancy is due to the fact that the search for the second approximation to the cavity shape and the dependence $\sigma(\lambda, M)$ carried out in chapter 2 overstepped the limits of the slender body theory for supersonic flow. In fact, the first approximation (an ellipsoid of revolution) is not a slender body in the front part where the shock arises. The shock is not described by the small perturbation theory. This is the second peculiarity of the slender body theory application to the supersonic cavitation flows that should be noted.

The cavity profile in the vicinity of the disk is shown in Fig. 6.

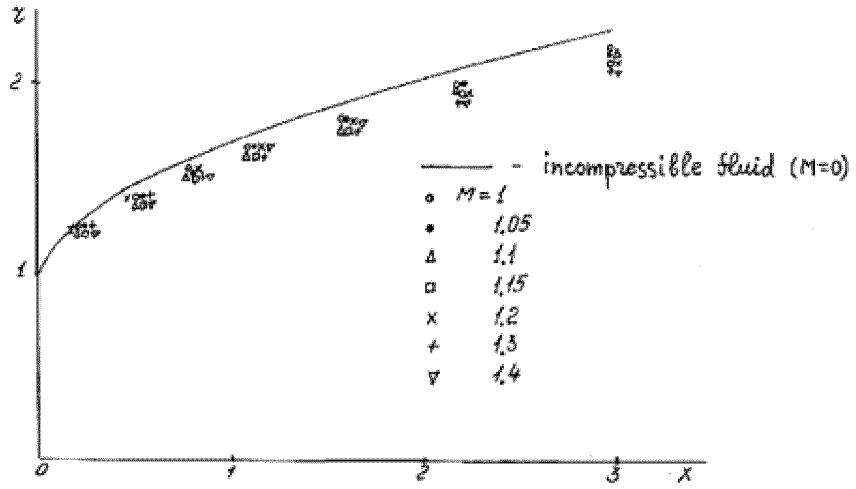


Fig. 6 The front of the cavity

The continuous curve represents the calculation for incompressible fluid [15]. The author's numerical results for supersonic flow are shown by points for different Mach numbers. It can be seen that in supersonic flow the cavity in initial regions is narrower than in incompressible flow. Narrowing of the cavity is related to the Prandtl-Meyer stream at the disk edge.

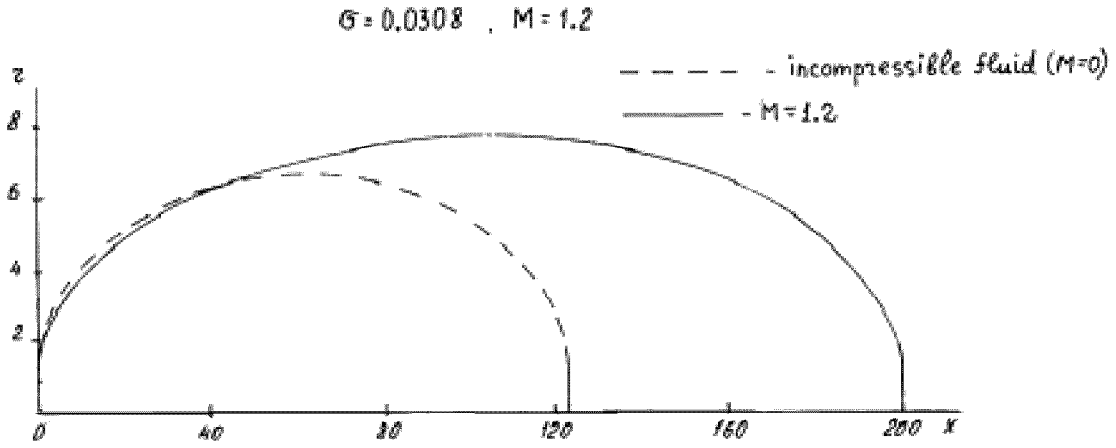


Fig. 7 Cavity profile

In Fig. 7 we compare the cavity profile in supersonic flow and incompressible fluid for the same cavitation number σ=0.0308. The continuous curve corresponds to the numerical method for M=1.2, the broken curve corresponds to the cavity in incompressible fluid. The maximum asymmetry to the cavity shape was observed for the Mach number equal to 1.1 (this case is illustrated in Fig. 8)

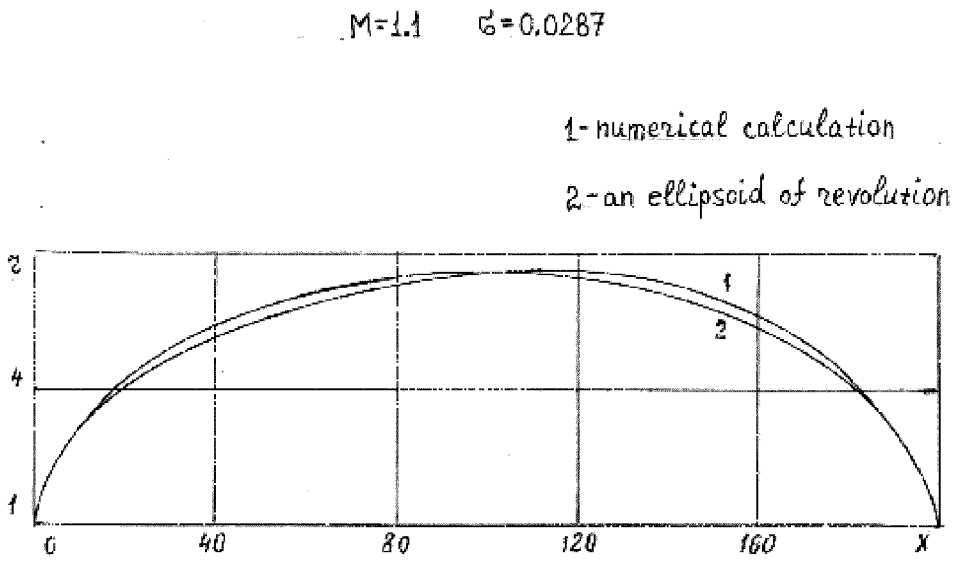


Fig. 8 Cavity profile

In Fig. 8 curve 1 corresponds to the numerical calculation, curve 2 corresponds to an ellipsoid of revolution (the origin is on the disk edge). From Fig. 8 it is evident that in the first approximation the cavity profile is close to an ellipsoid of revolution in supersonic flow.

The positions of the forward shock and the sonic line (where the local Mach number equals 1) were determined by numerical calculation. It was found that in case of supersonic cavitation flow past a disk the distance between the forward shock and the disk surface is much greater that in case of continuous supersonic air flow [12].

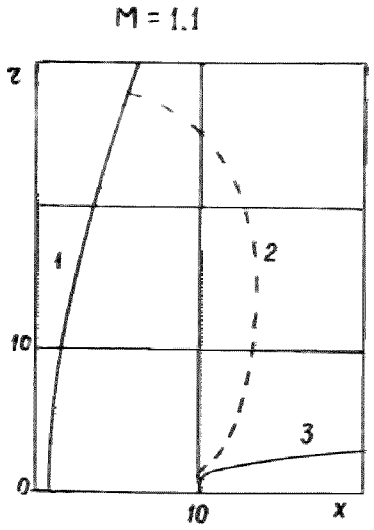


Fig. 9 Position of the forward shock for M=1.1. 1 is the forward shock, 2 is the sonic line and 3 is the cavity front profile.

As an example, in Fig. 9 the position of the forward shock is shown for the Mach number equal to 1.1. Curve 1 corresponds to the forward shock; curve 2 corresponds to the sonic line: curve 3 corresponds to the cavity front profile. The Mach number dependence of the cavitation drag coefficient of a disk at zero cavitation number C_{xo} is shown in Fig. 10 [12].

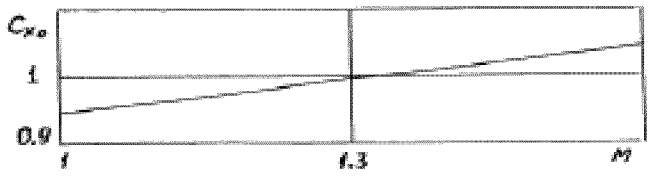


Fig. 10 Dependence of C_{xo} on M

Based on the numerical calculations we can conclude that the passing through the speed of sound does not result in a substantial variation in the cavity shape as compared with subsonic flow. In agreement with the slender body theory, the cavity shape in supersonic flow is close to an ellipsoid of revolution.

5. Shocks in a supersonic water stream

We will consider an oblique shock in a supersonic water flow, the double line in Fig. 11, where β is the angle between the direction of the undisturbed velocity V_0 and the shock, θ is the angle of deviation of the flow behind the shock, v_{no} and $v_{\tau o}$ are the normal and tangential components of the velocity ahead of the shock, and v_{n1} and $v_{\tau 1}$ are the velocity components behind the shock.

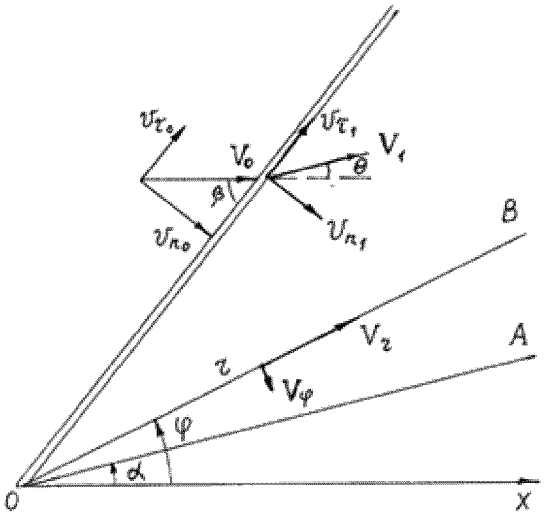


Fig. 11 Oblique shock and diagram of supersonic flow past a cone OA

The basic relations for the shock, namely, the mass and momentum conservation equations can be written as follows [22]

$$\rho_0 v_{no} = \rho_1 v_{n1} \tag{5.1}$$

$$\rho_0 v_{no}^2 + P_0 = \rho_1 v_{n1}^2 + P_1 \tag{5.2}$$

$$v_{\tau_0} = v_{\tau 1} \tag{5.3}$$

where P_0, ρ_0 are the pressure and the density ahead of the shock, and subscript 1 denotes the quantities behind the shock.

The equation of the shock adiabatic curve must be added to equations (5.1)-(5.3). It is well known [19] that at the pressures lower than $3 \cdot 10^3$ MPa the shock and the static adiabatic curves coincide and can be expressed by the Tait equation

$$\mathrm{P}_1 - \mathrm{P}_0 = B\left[\left(\frac{\rho_1}{\rho_0}\right)^n - 1\right], \quad B = \frac{\rho_0 a_0^2}{n}, \quad n = 7.15 \tag{5.4}$$

where a_0 is the speed of sound in the free stream ahead of the shock.

If on the shock front the pressure exceeds the value $3 \cdot 10^3$ MPa, the equation of the shock adiabatic curve can be written in the form [19]

$$\mathrm{P}_1 - \mathrm{P}_0 = d\left[\left(\frac{\rho_1}{\rho_0}\right)^k - 1\right], \quad d = 416MPa, \quad k = 6.29 \tag{5.5}$$

Behind the shock the speed of sound $\left(a_1^2 = dP/d\rho\right)$ can be determined from the static adiabat (5.4)

$$a_1^2 = a_0^2\left(\frac{\rho_1}{\rho_0}\right)^{n-1} \tag{5.6}$$

The expressions for determining the flow velocities ahead of the shock V_0 and behind it V_1 have the form

$$V_0 = \sqrt{v_{no}^2 + v_{\tau 0}^2}, \quad V_1 = \sqrt{v_{n1}^2 + v_{\tau 1}^2}$$

The dependences of the ratio of densities ρ_0/ρ_1 on the free stream Mach number ($M=V_0/a_0$) come from equations (5.1)-(5.3), (5.4) and (5.5) and can be written as follows

$$\begin{aligned} M^2 \sin^2\beta &= \left[\left(\frac{\rho_1}{\rho_0}\right)^n - 1\right]\left[n\left(1 - \frac{\rho_0}{\rho_1}\right)\right]^{-1} \\ M^2 \sin^2\beta &= \left[\left(\frac{\rho_1}{\rho_0}\right)^k - 1\right]\frac{d}{\rho_0 a_0^2}\left(1 - \frac{\rho_0}{\rho_1}\right)^{-1} \end{aligned} \tag{5.7}$$

We apply the first expression (5.7) when on the shock front the pressure does not exceed the value $3 \cdot 10^3$ MPa ($M\sin\beta \le 2.2$), the second expression (5.7) corresponds to the pressure that exceeds this value.

Let us consider a particular case that corresponds to the normal shock (β=90°). For this case the following correlations are satisfied

$$v_{\tau 0} = v_{\tau 1} = 0, \quad V_0 = v_{no}, \quad V_1 = v_{n1}, \quad \sin\beta = 1$$

The quantity of perturbed velocity u behind the shock is determined from the expression

$$u = V_0 - V_1 \tag{5.8}$$

The following is the way how we can calculate the flow parameters behind the normal shock. The value of the pressure on the shock front P_1 is given, then from (5.4) or (5.5) the ratio of densities ρ_1/ρ_0 is calculated. From expressions (5.7) the Mach number and velocity V_0 are determined , from (5.1) the value of velocity behind the shock V_1 is found. Then from equations (5.6) and (5.8) the speed of sound behind the shock a_1 and perturbed velocity u are determined. With the help of formulas (5.1), (5.2), (5.4)-(5.8) the author has calculated the flow parameters behind the normal shock on the pressure P_1 interval 490MPa≤P_1≤7840 MPa [20]. The results of this calculation have been compared with the results [23] obtained from the mass, momentum and energy conservation equations which were solved by the method of successive approximations. The flow parameters calculated by the author (V_0, u, a_1), and determined in [23] at the same values P_1 (V_0', u', a_1') are presented in the table.

TABLE

P_1, MPa	V_0, m/s	V_0', m/s	u, m/s	u', m/s	a_1, m/s	a_1', m/s
490	1967	1975	249	251	2221	2230
980	2310	2335	424	426	2734	2755
1470	2586	2630	568	567	3142	3175
1960	2823	2880	694	689	3491	3535
2450	3033	3110	808	798	3798	3855
2940	3223	3320	912	898	4075	4140
3430	3394	3510	1011	990	4343	4405
3920	3550	3690	1104	1075	4605	4650
4900	3836	4020	1277	1235	5088	5100
5880	4095	4325	1436	1380	5527	5505
6860	4333	4610	1583	1510	5931	5880
7840	4554	4885	1722	1625	6309	6240

From the table it is evident that the results obtained by the author is close to the results obtained in [23]. Consequently we can use expressions (5.4) and (5.5) for calculation of the shock adiabatic curve. It should be noted that T. Nishiyama in [9] applied the equations identical to the relations for a normal shock in air for calculation of a normal shock in water. In [24] it is shown that the equations in [9] are not applicable for calculating the shocks in water and they contradict with the well-known experimental and theoretical results.

Let us continue the consideration of the oblique shock. Expressions for the flow turning angle θ and the Mach number $M_1 = V_1 / a_1$ behind the shock can be determined from equations (5.1)-(5.3) and (5.6) and the geometric relations in Fig. 11.

$$\frac{tg(\beta-\theta)}{tg\beta} = \frac{\rho_0}{\rho_1}, \quad M_1 = \frac{M\sin\beta}{\sin(\beta-\theta)}\left(\frac{\rho_0}{\rho_1}\right)^{(n+1)/2} \tag{5.9}$$

The flow turning angle θ was calculated at Mach numbers on the interval $1.2 \le M \le 5$ [25]. The calculation was performed as follows. For the chosen value of M the interval of shock angle β (from Mach angle equal to arcsin $1/M$ to $\pi/2$) was divided into 200 parts; for the chosen values of M and β the ratio of densities ρ_0/ρ_1 was determined from (5.7) by half-division method. The value of ρ_0/ρ_1 was substituted in the first equation (5.9) and the value of θ was determined. The Mach number M_1 was determined from the second equation (5.9). In Fig. 12 we have reproduced the calculation results in the form of graphs of θ versus β at various M (continuous curves 1-8, the Mach numbers equal 1.2; 1.4; 1.6; 2; 2.5; 3; 4; 5 respectively).

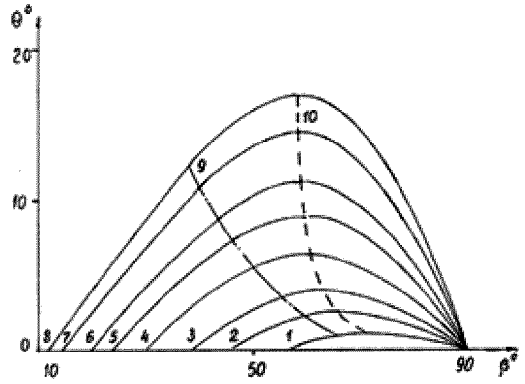


Fig.12 Dependence of θ on β; curves 1-8 correspond to-M=1.2; 1.4; 1.6; 2; 2.5; 3; 4 and 5; curve 9 and 10 correspond to M_1=1 and-$\theta=\theta^*$ respectively

The chain curve 9 separates the domains of supersonic flow behind the shock ($M_1>1$) and subsonic flow, the domains of supersonic flow are located to the left curve 9. The broken curve 10 corresponds to the maximum (critical) angles θ^*. The domain to the right of curve 10 corresponds to a detached shock. If the apex angle of the wedge exceeds the value of $2\theta^*$ then the flow around this body has the curved detached shock. In Fig. 13 curve 1 represents the graph of the critical angle θ^* as a function of M for a wedge.

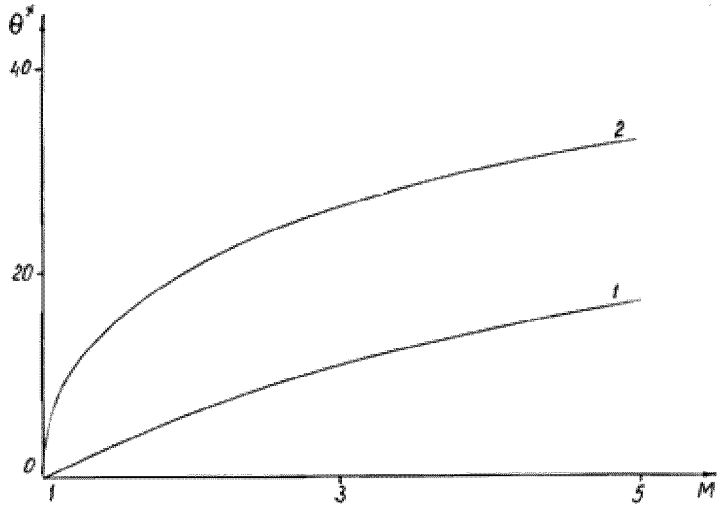


Fig.13 Dependence of θ^* on M; curves 1 and 2 correspond to flow past a wedge and cone respectively

6. Conical flows

Let us consider the axisymmetric conical flow formed behind a shock (Fig. 11) [25]; the line OA is the profile of the cone and α is its apex half-angle. The spherical coordinate system φ, r with the origin that lies at the apex of the cone and with x-axis directed along the symmetry axis is introduced. The angle φ is measured from the x-axis, r-coordinate equals the radius-vector drawn from the origin, OB is the intermediate conical surface, V_r is the component of the velocity directed along the radius-vector, V_φ is the component of the velocity directed along the perpendicular to the radius-vector.

The basic condition of the conical flow concludes that the flow parameters must be constant along the straight lines drawn from the apex of the cone. Consequently, any partial derivative of the flow parameters with respect to r – coordinate equals zero. The equations that define the kinematic parameters of the conical flow have been obtained from the continuity and Euler equations [22]

$$\frac{dV_\varphi}{d\varphi} = \frac{2a^2V_r + a^2V_\varphi ctg\varphi - V_rV_\varphi^2}{V_\varphi^2 - a^2}, \quad \frac{dV_r}{d\varphi} = V_\varphi \tag{6.1}$$

where a is the speed of sound at the given point of the flow.

For the velocity components $V_{\varphi 1}$ and V_{r1} the boundary conditions on the shock are written as follows

$$V_{\varphi 1} = -V_0 \sin\beta \frac{\rho_0}{\rho_1}, \quad V_{r1} = V_0 \cos\beta, \quad \varphi = \beta \tag{6.2}$$

The boundary conditions on the cone surface have the form

$$V_\varphi = 0, \quad V_r = V_{con}, \quad \varphi = \alpha \tag{6.3}$$

where V_{con} is the quantity of the velocity on the cone surface.

The speed of sound in the region behind the shock is determined from the Bernoulli equation

$$\frac{1}{2}\left(V_{\varphi 1}^2 + V_{r1}^2\right) + \frac{a_1^2}{n-1} = \frac{1}{2}\left(V_{\varphi}^2 + V_r^2\right) + \frac{a^2}{n-1} \tag{6.4}$$

The dependence of the density on the speed of sound has the form

$$\rho = \rho_1 \left(\frac{a}{a_1}\right)^{2/(n-1)} \tag{6.5}$$

The pressure in regions behind the shock is calculated from the static adiabatic curve at the known value of the density

$$P - P_1 = \frac{\rho_1 a_1^2}{n}\left[\left(\frac{\rho}{\rho_1}\right)^n - 1\right] \tag{6.6}$$

The conical flow behind the shock has been calculated in the following way. The system of equations (6.1), the boundary conditions (6.2) and (6.3) and equation (6.4) were reduced to the dimensionless form. The quantity of the velocity was normalized by the free stream speed of sound a_0 and we obtained the Mach number M as the dimensionless parameter. The Mach number was specified on the interval $1<M\leq 5$. For the chosen M the interval of shock angle β (from Mach number to $\pi/2$) was divided into 200 parts. Then for the chosen values of M and β from (5.7) and (6.1)-(6.4) the apex half-angle of the cone α was calculated. The system of differential equations (6.1) was solved by the numerical Runge-Kutta method. As the boundary condition we applied condition (6.2) and the step of angle change $_{\Delta}\varphi$ was equal to 0.25°. The condition (6.3) was used to determine the end of counting. The segment $[\varphi_i, \varphi_{i+1}]$ was determined on which the value of V_{φ} reversed sign. Then on this segment the value of α that corresponds to the condition $V_{\varphi}=0$ was found. As a result of these calculations for the fixed values of M we have obtained the dependences $\alpha(\beta)$, $M_{con}(\beta)$, $V_{con}(\beta)$ ($M_{con}=V_{con}/a_{con}$, where a_{con} is the speed of sound on the cone surface).

From the dependences $\alpha(\beta)$ the maximum angles α corresponding to the critical cone angles θ^* were determined for all values of M. If the cone apex half-angle α exceeds the value of θ^* then the supersonic flow around this body has the curved detached shock and the conical flow behind the shock is absent. In Fig. 13 curve 2 represents the graph of θ^* as a function of M. A comparison of the results in Fig. 13 with the results for air [22] shows that in supersonic water flow past a wedge or cone the critical angles are significantly less than those in an air flow past the same bodies.

For the visual representation the found values of β, α, V_{con} and M_{con} were treated and the dependences $\beta(M)$, $V_{con}(M)$ and $M_{con}(M)$ were obtained for the fixed values of α. The treatment was performed by interpolation. The values of cone angles α were chosen equal to 5°, 10°, 15°, 20°, 25° and 30°. Using the value of the velocity on the cone surface V_{con} the pressure coefficient C_p was calculated from equations (6.4), (6.5) and (6.6).

In Fig. 14 we have plotted graphs of the angle β of inclination of the shock as a function of M at cone angles $5°\leq\alpha\leq 30°$ (curves 1-6).

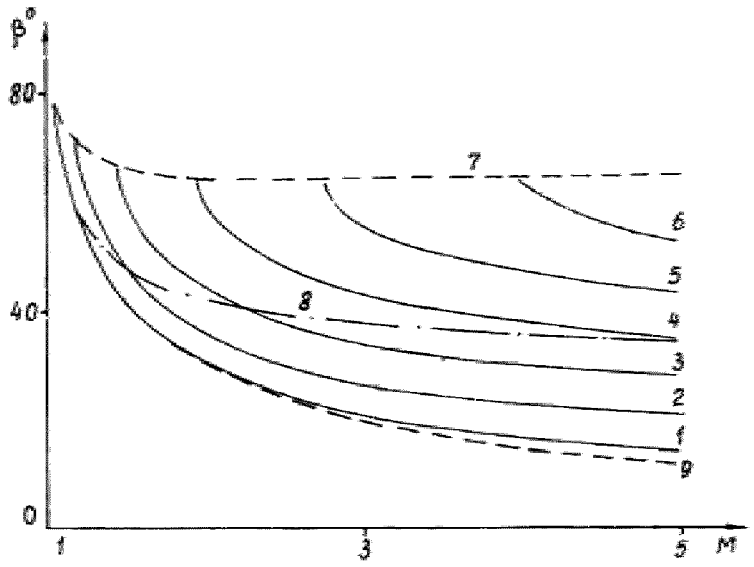


Fig. 14 Dependence of β on M; curves 1-6 correspond to α=5°, 10°, 15°, 20°, 25° and 30°; curve 7 corresponds to detachment of the shock from the apex of the cone; curve 8 corresponds to M_{con}=1; curve 9 corresponds to the Mach line ($sin\beta$=1/M)

The broken curve 7 corresponds to detachment of the bow shock from the apex of the cone. The chain curve 8 separates the domains of supersonic (M_{con}>1) and subsonic flows on the cone, the supersonic domain is located below curve 8. The broken curve 9 corresponds to the Mach angle ($sin\beta$=1/M). From Fig. 14 it is evident that the bow shock for the cone α=5° is Mach shock, it is close to the Mach line. We can assume that the flow around this cone is described by the small perturbation theory.

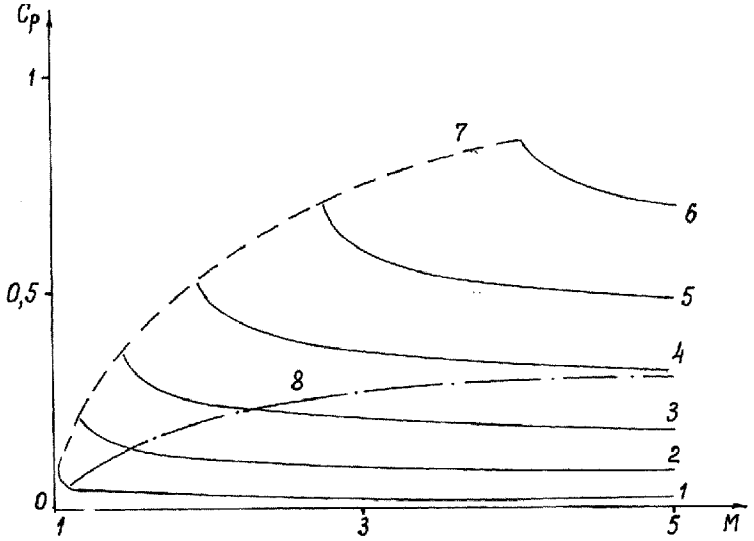


Fig. 15 Dependence of C_p on M; curves 1-6 correspond to α=5°, 10°, 15°, 20°, 25° and 30°; curve 7 corresponds to the detachment of the shock from the apex of the cone; curve 8 corresponds to M_{con}=1

In Fig.15 we have plotted graphs of the pressure coefficient C_p as a function of M for various cone angles (curves 1-6). The broken curve 7 and the chain curve 8 have the same meaning as those in Fig. 14; the supersonic domain is located below curve 8. In case of supersonic flow around the cone the drag coefficient C_x equals the pressure coefficient C_p at σ=0 (see chapter 2).

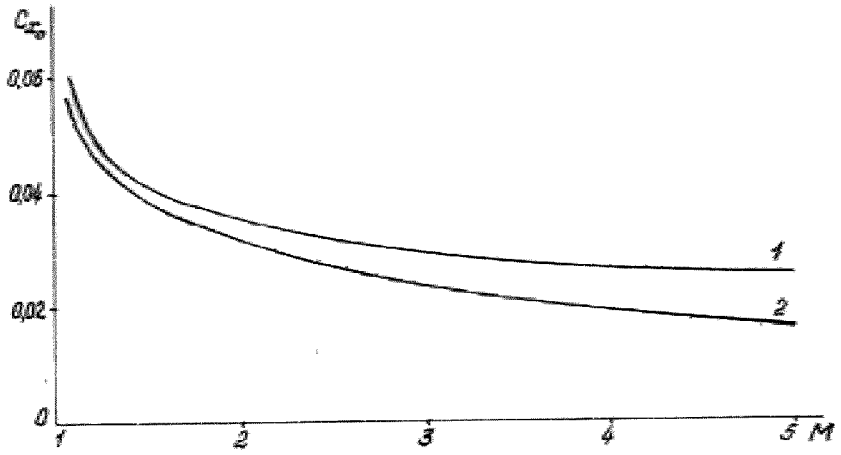


Fig. 16 Dependence of C_{xo} on M for the cone α=5°; curve 1 corresponds to numerical calculation; curve 2 corresponds to calculation from formula (2.10)

Let us compare the drag coefficient of the cones at σ=0 (C_{xo}=C_p) obtained in this chapter with the ones calculated based on the slender body theory (2.10). In Fig. 16 and Fig. 17 the dependences $C_{xo}(M)$ are shown for the cones α=5° and α=10° respectively. Curve 1 corresponds to the values of C_{xo} obtained in this chapter, curve 2 corresponds to the values of C_{xo} calculated by formula (2.10).

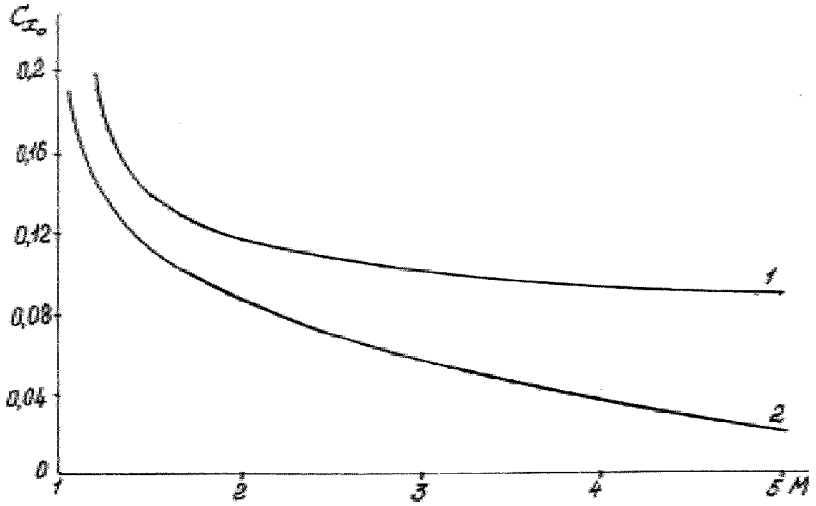


Fig. 17 Dependence of C_{xo} on M for the cone α=10°; curve 1 corresponds to numerical calculation; curve 2 corresponds to calculation from formula (2.10)

From Fig. 16 it follows that for the cone α=5° the results of the numerical calculation obtained by formulas (6.1)-(6.6) are close to the results obtained by formula (2.10) at the Mach numbers $1.1 \le M \le 3$. This conclusion agrees with Fig. 14 which shows that the bow shock for the cone α=5° is close to the Mach line.

From Fig. 17 we can see the significant discrepancy between the values of C_{xo} calculated by formulas (6.1)-(6.6) and the ones calculated by formula (2.10). We cannot consider the cone α=10° to be a slender body in supersonic water flow. The numerical calculation shows (Fig. 14, 15) that at the Mach numbers on the interval $1<M<1.2$ this cone has a detached shock and the velocity on the cone surface exceeds the speed of sound if the Mach number is greater than 1.46. This flow is not described by the small perturbation theory. The third peculiarity of the slender body theory application to the supersonic cavitation flow is restriction of its results. For the drag coefficient of thin cone-cavitators this theory provides the exact values if the cone apex half-angle does not exceed 5°.

7. The comparison of the theoretical results with the experimental data

In the experimental works [26, 27, 28] the cavitation flows formed at the high speed body motion in water have been investigated on the Mach number interval $0.1\le M\le 0.93$ (the body has a disk-cavitator). From the treatment of the experimental data we can conclude that in subsonic flow on the whole range of the Mach numbers the cavity is symmetrical with respect to the mid-section and the cavity profile is close to an ellipsoid of revolution. This conclusion agrees with the author's results obtained with the help of the slender body theory and the numerical methods. In Fig. 18 the continuous curve represents an ellipsoid of revolution; the points correspond to the experimental data [28] obtained on the Mach number interval $0.3\le M\le 0.93$; the cavitation numbers have the order $10^{-4}\div 10^{-3}$.

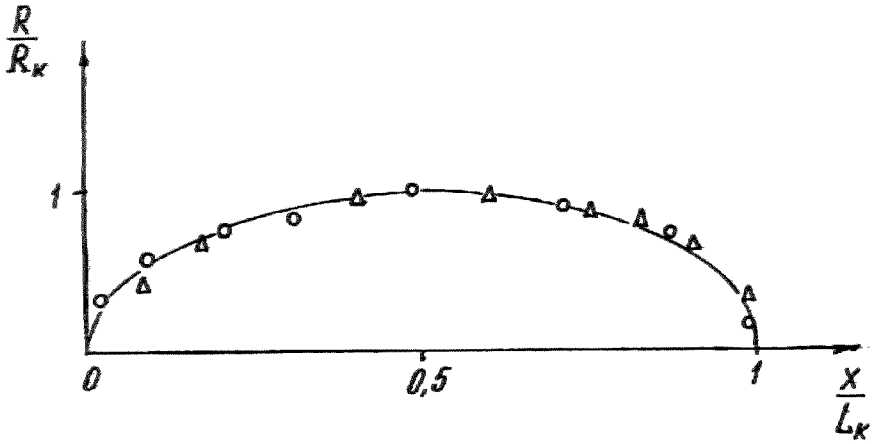


Fig. 18 Cavity profile; the continuous curve corresponds to an ellipsoid of revolution, the points correspond to the experimental data [28]

In [26, 27] the experimental values of the cavity dimensions obtained on the Mach number interval $0.1\le M\le 0.7$ and the cavitation number interval $10^{-4}<\sigma<10^{-2}$ have been compared with the asymptotic dependences at $\sigma\to 0$ [29]. The asymptotic formulas for the cavity mid-section radius and the cavity length scaled by the disk radius are written as follows [29]

$$R_k=\sqrt{\frac{C_x}{\sigma}},\quad L_k=\frac{2}{\sigma}\sqrt{C_x\ln\frac{1}{\sigma}} \tag{7.1}$$

In Fig. 19 the continuous curve represents the asymptotic dependence of the mid-section radius on the cavitation number (7.1); points 1 correspond to the experimental data [26, 27] (the Mach numbers are marked above the abscissa axis); points 2 correspond to the author's calculations [20].

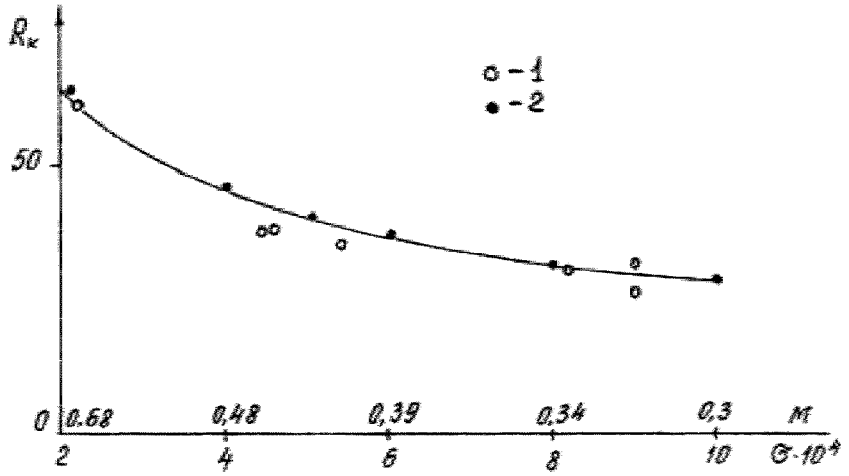


Fig. 19 Dependence of R_k on σ; the continuous curve corresponds to dependence (7.1); points 1 correspond to the experimental data [26, 27]; points 2 correspond to calculations [20]

In Fig. 20 the continuous curve represents the asymptotic dependence of the cavity length on the cavitation number (7.1); points 1 correspond to the experimental data [26, 27]; points 2 correspond to the author's calculations [20].

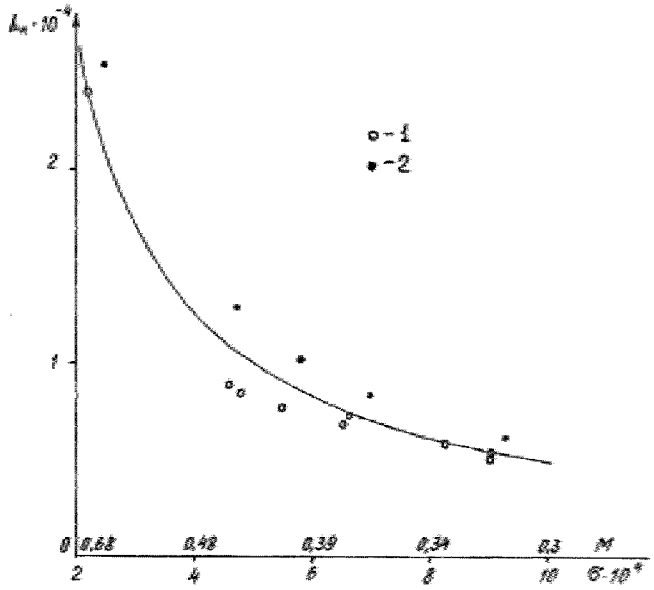


Fig. 20 Dependence of L_k on σ; the continuous curve corresponds to dependence (7.1); points 1 correspond to the experimental data [26, 27]; points 2 correspond to calculations [20]

From the examination of Fig. 18-20 we can conclude that the theoretical results agree with the experimental data.

In the United States and in the Institute of Hydromechanics (Ukraine) the tests are being carried out on the supersonic body motion in water. The quantitative experimental data are not presented, however, in 1998 a photograph of supersonic cavitation flow with a detached shock was published [30]. Also, the announcement was made in [30] that in the United States on July 17, 1997 the underwater

speed record was set (for the first time in water the speed of a body exceeds the speed of sound). The contour of the shock on the photograph shows that the Mach number is equal to 1.1 (or the speed of a body exceeds 1600m/s). In general, the image of the flow on the photograph corresponds to the author's theoretical result for the Mach number equal to 1.1 (Fig. 9).

Conclusions

The high speed cavitation flow in water has some peculiarities. The cavity has remarkable characteristics; it promotes not only the motion in water with small drag but also screens the body from shocks. On the cavity surface the constant velocity and the constant pressure conditions are satisfied, consequently the shocks are absent. The bow shock forms before the cavitator or on its apex (in case of thin cones), in the domain of cavity closure the trailing shock forms. For this scheme of flow the sharp change of the flow parameters does not take place on the transonic velocity range ($0.7<M<1.2$). As distinct from water, in air on the transonic velocity range the shocks form on the body surface and aerodynamic characteristics of body change considerably. In water on the transonic velocity range the parameters of the cavitation flow change smoothly as the Mach number increases. The passing though the speed of sound does not result in a substantial variation in the cavity shape as compared with subsonic flow. In spite of the small asymmetry of the shape about the mid-section the cavity shape in supersonic flow is close to an ellipsoid of revolution as it was before.

Water is rather law-compressible fluid as compared with air. In water many physical effects tied up with compressibility essentially differ from those in air. We can assume that the normal shock in water is isentropic and the flows are potential at the Mach numbers on the interval $1<M\leq2.2$. At the same Mach numbers the ratio of densities ρ_1/ρ_0 on the shock front in water is far less than that in air. As a result the distance between the forward shock and the cavitator surface in water is much greater than in case of continuous supersonic air flow. In supersonic water flow past a wedge or a cone the critical angles are significantly less than those in an air flow past the same bodies. The flow turning angle for the Prandtl-Meyer stream in water is far less than that in air at the same Mach numbers. All the factors mentioned above (the small losses of mechanical energy in the shocks, the considerable distance between the forward shock and the cavitator surface, the small deflection of flow in the stream about the cavitator edge) weakly prevent from the cavity expansion. In supersonic flow at the Mach numbers on the interval $1\leq M\leq1.4$ we do not observe the considerable narrowing and change of the cavity shape as compared with subsonic flow. The cavity expands in accordance with the law of conservation of energy in a liquid.

The slender body theory has a limited application for the investigation of the supersonic cavitation flows. First of all, in case of the thin cone-cavitators the solution obtained for the whole area of the flow is not valid for the flow past the cone edge. In the supersonic flow the Prandtl-Meyer stream forms at the edge. The stream must turn at the angle that is dependent upon the pressure within the cavity or the cavitation number. The incline of free stream line is less than the cone apex half-angle. It is impossible to satisfy this condition within the limits of the slender body theory. Secondly, for the outer solution the search for the second approximation to the cavity shape went beyond the limits of the slender body theory. In fact, the first approximation (an ellipsoid of revolution) is not a slender body in the front part where the shock forms. The shock is not described by the small perturbation theory. Thirdly, for the drag coefficient of thin cone-cavitators this theory provides the exact results if the cone apex half-angle does not exceed 5°.

As distinct from the supersonic flow the slender body theory is more applicable for investigation on subsonic water flow. For example, the author has determined the cavitation parameters in subsonic flow around thin cones with apex half-angle equal to 5°, 10° and 15°. These results satisfy the momentum conservation law and for the particular case of incompressible fluid ($M=0$) agree with the numerical calculations. For the case when the parameter of the cavity thinness is far less than the parameter of the cavitator thinness the outer solution was found for subsonic flow. The comparison between the results of outer solution and the results of numerical calculation has shown good agreement.

References

1. Gurevich M. I., "Half-Body with Finite Drag in Subsonic Flow", Tr.TsAGI, #653, 1947, pp 1-12. (in Russian)
2. Yakimov Yu. L., "Asymptotic Laws of Degeneration of Thin Cavity Shapes", Izv. Akad. Nauk SSSR, Mekh. Zhidk. Gaza, #3, 1981, pp 3-10. (reprinted in the USA)
3. Yakimov Yu. L., "Thin Cavitation Cavity in a Compressible Fluid", in Problems of Contemporary Mechanics, Pt.1, Moscow University Press, Moscow, 1983, pp 63-73. (in Russian)
4. Vasin A. D., "Thin Axisymmetric Cavities in Subsonic Compressible Flow", Izv. Akad. Nauk SSSR, Mekh. Zhidk. Gaza, #5, 1987, pp 174-177. (reprinted in the USA)
5. Vasin A. D., "Thin Axisymmetric Cavities in Supersonic Flow", Izv. Akad. Nauk SSSR, Mekh. Zhidk. Gaza, #1, 1989, pp 179-181. (reprinted in the USA)
6. Serebryakov V. V., "Asymptotic Solutions of Problems of Axisymmetrical Supercavitation Flow in Slender Body Approximation", in Hydrodynamics of High Speeds, Chuvash. University Press, Cheboksari, 1990, pp 99-111. (in Russian)
7. Serebryakov V. V., "Asymptotic Solutions of Axisymmetrical Problems of Subsonic and Supersonic Separated Water Flows with Zero Cavitation Numbers", Dokl. Akad. Nauk Ukraine, #9, 1992, pp 66-71 (in Russian)
8. Al'ev G. A., "Separated Transonic Water Flow past a Circular Cone", Izv. Akad. Nauk SSSR, Mekh. Zhidk. Gaza, #2, 1983, pp 152-154. (reprinted in the USA)
9. Nishiyama T. and Khan O. F., "Compressibility Effects on Cavitation in High Speed Liquid Flow (Second report – transonic and supersonic liquid flows)", Bull. JSME, v. 24, #190, 1981, pp 655-661.
10. Zigangareeva L. M. and Kiselev O. M., "Calculation of the Compressible Subsonic Cavitation Flow past a Circular Cone", Prikl. Mat. Mekh., v.58, #4, 1994, pp.93-107. (reprinted in the USA)
11. Vasin A. D., "Calculation of Axisymmetric Cavities Downstream of a Disk in Subsonic Compressible Fluid Flow", Izv. Rus. Akad. Nauk, Mekh. Zhidk. Gaza, #2, 1996, pp 94-103. (reprinted in the USA)
12. Vasin A. D., "Calculation of Axisymmetric Cavities Downstream of a Disk in Supersonic Flow", Izv. Rus. Akad. Nauk, Mekh. Zhidk. Gaza, #4, 1997, pp 54-62. (reprinted in the USA)
13. Vasin A. D., "Application of the Slender Body Theory to Investigate Developed Axisymmetric Cavitation Flows in a Subsonic Stream of Compressible Fluid", Applied hydromechanics, Kiev, v.2 (74), #3, 2000, pp 17-25. (in Russian)
14. Logvinovich G. V., "Hydrodynamics of Flows with Free Boundaries", Naukova Dumka, Kiev, 1969, 215 p. (in Russian)
15. Guzevskii L. G., "Plane and Axisymmetric Problems of Hydrodynamics with Free Surface", Dissertation for a doctor's degree, Institute of Thermal Physics, Siberian Branch of the USSR Academy of Sciences, Novosibirsk, 1987, 300 p. (in Russian).
16. Liepmann H. W. and Roshko A., "Elements of Gasdynamics", John Wiley & Sons, Inc., New York, 1957.
17. Ashley H. and Landahl M. "Aerodynamics of Wings and Bodies", Addison-Wesley Publishing Com., Inc., Massachusetts, 1966.
18. Fletcher C. A. J., "Computational Techniques for Fluid Dynamics", Springer Verlag, Berlin et al., 1988.

19. Zamyshlyaev B. V. and Yakovlev Yu. S., "Dynamic Loads in Underwater Explosions", Sudostroenie, Leningrad, 1967, 387 p. (in Russian)

20. Vasin A. D., "Problems of Hydrodynamics and Hydroelasticity at High Speed Body Motion in Water", Dissertation for a doctor's degree, TsAGI, Moscow, 1999, 282 p. (in Russian)

21. Holst T. L. and Ballhaus W. F., "Fast, Conservative Schemes for the Full Potential Equation Applied to Transonic Flows", AIAA Journal, v. 17, #2, 1979, pp 145-152.

22. Loitsyanskii L. G., "Mechanics of Liquids and Gases", Pergamon Press, Oxford, 1966.

23. Cole R. H., "Underwater Explosions", University Press, Princeton, 1948.

24. Vasin A. D., "High-Speed Body Motion in Compressible Fluid", in Proceedings of the Scientific Meeting on High-Speed Hydrodynamics and Supercavitation, Laboratoire des Ecoulements Geophysiques et Industriels, Grenoble, France, 2000.

25. Vasin A. D., "Shocks and Conical Flows in a Supersonic Water Stream", Izv. Rus. Akad. Nauk, Mekh. Zhidk. Gaza, #5, 1998, pp 196-199 (reprinted in the USA)

26. Savchenko Yu. N., Semenenko V. N. and Serebryakov V. V., "Experimental Check of Asymptotic Formulas for Axisymmetric Cavities at $\sigma \to 0$", in Problems of High-Speed Hydrodynamics, Chuvash. University Press, Cheboksari, 1993, pp 117-122. (in Russian)

27. Savchenko Yu. N., Semenenko V. N. and Serebryakov V. V., "Experimental Investigation of Developed Cavitating Flows at Subsonic Flow Velocities", Dokl. Akad. Nauk Ukraine, #2, 1993, pp 64-69. (in Russian)

28. Savchenko Yu. N., "Investigation of High-Speed Supercavitating Underwater Motion of Bodies", in "High-Speed Body Motion in Water", AGARD-R-827, 1998, Reference 20.

29. Garabedian P. R., "The Calculation of Axially Symmetric Cavities and Jets", Pacific J. Math., #6, 1956, pp 611-689.

30. Kirchner I. N., "Supercavitating Projectile Experiments at Supersonic Speeds", Abstract, in "High-Speed Body Motion in Water", AGARD-R-827, 1998, Reference 35.

This page has been deliberately left blank

Page intentionnellement blanche

Supercavitating Object Propulsion

Yu. N. Savchenko
Ukrainian National Academy of Sciences - Institute of Hydromechanics
8/4 Zhelyabov str., 03057 Kiev
Ukraine

1. SC vehicle as a result of tendencies of high speed vehicle development

In practice, the vehicle development is stipulated by a useful effect that is attained upon the vehicle operation.

The useful effect for transport ships consists in cargo transportation. Thus, the ship efficiency as vehicle efficiency will be determined by commercial effectiveness [22]

$$K_p = \frac{PV}{N},$$

where P is the payload, V is the velocity, N is the power.

The velocity and range are determining parameters for objects used for military and rescue purposes. In this case one can see that the hydrodynamic drag reduction positively influences on all main characteristics and increases the commercial effectiveness coefficient owing to consumed power decrease or increase of the velocity and range.

For surface vehicles, we clearly see a tendency of decreasing the waterline area and wetted surface of the hull due to dynamic means of maintenance of the hull on the water surface. There are ships with small waterline area SWATHS, hydrofoil ships, hovercrafts, ekranoplanes and hydroplanes.

In this case the energy consumption to realize the dynamic means of maintaining the hull on the water surface may be related to the controlling effect for the drag reduction.

One can see in Fig. 1 that the velocity and specific power of the vehicles increases at exiting the hull from the water.

The same way of reduction of the wetted surface of the hull due to developed artificial or vapor cavitation – supercavitation [10, 11, 15] may be used for underwater motion.

Calculations shows it is possible to obtain a twenty-fold advantage in the hydrodynamic drag when the velocity is equal to 100 m/sec, and cavitation number σ = 0.01, and 1000-fold advantage may be obtained when the cavitation number $\sigma = 10^{-4}$ [11].

$$\sigma = \frac{p_0 - p_c}{\rho V^2 / 2},$$

where p_0 is the hydrostatic pressure, p_c is the cavity pressure, which is equal to the saturated water vapor pressure $p_c = p_v$ at vapor cavitation.

Paper presented at the RTO AVT Lecture Series on "Supercavitating Flows", held at the von Kármán Institute (VKI) in Brussels, Belgium, 12-16 February 2001, and published in RTO EN-010.

Comparing the efficiency of the different methods of the hydrodynamic drag reduction with efficiency of the artificial and vapor supercavitation, one can see its advantage and, hence, perspective of its use [22]. Moreover, a vapor layer between the water and hull unites many methods of the drag reduction:

- Reduction of water adhesion to the surface or slippage;
- Effect of the movable surface (the gas flow velocity in the clearance may be equal to the water flow velocity);
- Change of the physical constants of BL (here, the medium density reduction);
- Gas blowing into the boundary layer (BL).

Here, – in the case of the artificial cavitation, the gas is blown through the solid surface of the object.

– in the case of vapor supercavitation, the gas arrives from the supercavity surface.

However, use of the supercavitation flow schemes requires respectively high specific power of the vehicle. So, when the velocity is equal to 100 m/sec, and cavitation numbers $\sigma = 0.05 \div 0.01$, specific available power will be of order $\frac{N}{D} = 2000 \div 4000$ H.p./t This is compared with specific power of the planing ships in the universal diagram of Gabrielly-Karman [22] (Fig. 2) .

2. Features of supercavitation

First of all, the supercavitation flow regime gives limitations for shape and dimensions of the hull of an underwater vehicle. They must correspond to the calculated supercavity shape. Therefore, formalization of the hull geometry will be performed by comparing the vehicle volume and surface with the supercavity volume and surface or with shapes of hulls of Reichhardt series having the constant pressure [19].

In this case dimensions of the vehicle having a shape of a body of revolution will be restricted by limiting dimensions of the supercavity. They are determined by known formulae for main supercavity dimensions [1]

$$D_c = D_n\sqrt{\frac{c_x}{\sigma}}; \qquad L_c = \frac{D_n}{\sigma}\sqrt{c_x \ln\frac{1}{\sigma}}; \qquad \lambda = \frac{L_c}{D_c} = \sqrt{\frac{\ln\frac{1}{\sigma}}{\sigma}}, \tag{1}$$

where cavitation number $\sigma = 2(p_0 - p_c)/\rho V^2$ is a main parameter of the supercavitation flows, p_0, p_c are pressures in the stream and in the cavity, respectively, and $c_x = c_{x0}(1+\sigma)$ is the coefficient of this cavitator in the form of a disk with diameter D_n, c_{x0} is the drag coefficient when $\sigma = 0$.

We should note that the supercavitation motion regime requires enough high motion velocity that is sufficient to form a supercavity where the vehicle hull is inscribed completely. This is explained by structure of the formulae for main supercavity dimensions (1):

$$\frac{D_c}{D_n} = V\sqrt{\frac{\rho c_x}{p_0 - p_c}}; \qquad \frac{L_c}{D_n} = \frac{\rho V^2}{p_0 - p_c}\sqrt{c_x \ln\frac{1}{\sigma}}. \tag{2}$$

The object calculated for given regime and inscribed into the calculated supercavity will need the attainment of this calculated velocity in the unseparated flow regime. During acceleration some difficult problems arise. These are:

– energetic problem connected with overcoming

the high hydrodynamic drag of the vehicle in unseparated flow;

– problem on ensuring the motion stability in

non-calculated flow regime.

The second essential feature of the supercavitation motion is a necessity to take into account the energy expenditure, volume and mass to ensure artificial regime of supercavitation, i.e. gas blowing into the cavity. This is inevitable upon the object acceleration up to the calculated velocity and maintaining the supercavity in sub-vapor supercavitation regimes when the pressure in the cavity is higher that the pressure of saturated water vapors. The necessity of the gas-supply into the cavity disappears at attainment of vapor supercavitation regimes when the supercavity is filled by water vapor.

The problem of interaction between the propeller and supercavity is sensitive to the velocity and pressure perturbations caused by working propeller. This may result in additional washing the hull and increasing the gas-supply rate.

In the general case the supercavitating vehicle motion may be considered as one consisting of three phases :

– phase 1 – the vehicle acceleration up to the calculated velocity;

– phase 2 – motion with constant velocity;

– phase 3 – motion on inertia.

The known applications of the supercavitation motion are used to attain the maximal motion range in phase 2 or in phase 3. In this case phase 1 is not essential to pass the distance, but has decisive significance in the propulsive sense, since requires development of the highest power exceeding multiply the power necessary for motion with constant calculated velocity.

3. Energy of SC vehicles in stationary motion

Energy of SC vehicles in the stationary motion will be determined by their hydrodynamic drag in steady flow. Since the vehicle hull will place in a vapor or gas cavity, the main component of the hydrodynamic drag is the cavitator drag. It is determined by formula

$$R_x = \frac{\rho V^2}{2} c_x S_n , \tag{3}$$

where ρ is the fluid density, V is the motion velocity, c_x is the cavitator drag coefficient (for disk $c_x = 0.82(1+\sigma)$, where σ is the cavitation number), $S_n = \frac{\pi D_n^2}{4}$ is the cavitator area.

Additional hydrodynamic drags can arise owing to using the schemes of supercavitation flow with partial or periodic washing the tail part of the object. Fig. 3 shows possible schemes of supercavitation flow around SCO:

a) scheme of flow with forming two cavities;

b) stationary planing along the inner cavity surface;

c) periodic impact interaction with the cavity walls;

d) aerodynamic interaction with vapor-splash medium of the cavity.

In the general case the total hydrodynamic drag of SCO may be represented with taking account of the cavitator drag (3) in the form

$$R_x = R_{xn} + R_{xF}, \tag{4}$$

where R_{xF} is the additional hydrodynamic drag of friction upon washing the hull. It may be equal $R_{xn} \cong 0.01 R_{xn}$ at the flow scheme d) (Fig. 3) and $R_{xn} \cong 0.5 R_{xn}$ at the flow scheme a) (Fig. 3).

When $V = Const$, the propeller thrust T must equalize the drag (4)

$$T = R_x. \tag{5}$$

If the propeller is one of rocket type, its thrust will be equal

$$T = \dot{m}_f Q_f, \tag{6}$$

where $\dot{m}_f = dm/dt$ is the mass rate of the fuel, Q_f is the specific impulse of the fuel.

For steady motion when $\dot{m}_f = Const$,

$$T = \frac{m_f}{t} Q_f. \tag{7}$$

Using the formulae (3) – (7), we obtain

$$V = \sqrt{\frac{2}{c_x \rho S_n}} \cdot \sqrt{\frac{m_f}{t} Q_f}. \tag{8}$$

Introducing the passed distance S in the form

$$S = Vt. \tag{9}$$

and define the volume due to the fuel

$$W_f = m_f / \rho_f = const, \tag{10}$$

we obtain for the passed distance that

$$S = \sqrt{\frac{2W_f}{c_x \rho S_n}} \cdot \sqrt{\rho_f Q_f t} = C_1 \sqrt{\rho_f Q_f t}\,, \tag{11}$$

where $\sqrt{\frac{2W_f}{c_x \rho S_n}} = C_1 = Const$, ρ_f is the fuel density.

One can see in the expression (11) that to attain the maximal range S it is necessary to apply fuels with maximal specific impulse Q_f and density ρ_f.

The vehicle velocity is obtained from expressions (3) and (5)

$$V = \sqrt{\frac{2}{c_x \rho}\left(\frac{T}{S_n}\right)}. \tag{12}$$

We can see from here that the velocity is proportional to ratio $(T/S_n)^{1/2}$.

We can obtain the estimation of maximal range from the assumption that whole cavity volume is filled by the vehicle hull, and the hull is filled by fuel with density ρ_f and specific impulse Q_f.

As since the cavities have a shape close to an ellipsoid with known diameter and length (1), it is possible to calculate the supercavitry volume W_c with taking account of the relation $L_c = \lambda D_c$ (1)

$$W_c = 0.71\pi R_c^2 L_c\,. \tag{13}$$

The SCO drag will be equal [1]

$$R_x = c_x \frac{\rho V^2}{2} S_n = k S_c \Delta P\,, \tag{14}$$

where $S_c = \pi R_c^2$ is the cavity mid-section area, $\Delta P = p_0 - p_c = \sigma \frac{\rho V^2}{2}$ is the pressure difference, $k = 0.96$.

The fuel mass in the cavity volume

$$m_f = \rho_f W_c = 0.71\pi R_c^2 L_c \rho_f\,. \tag{15}$$

Time, when the propeller is maintaining the necessary thrust, or the motion time is

$$t = \frac{Q_\Sigma}{R_x}, \tag{16}$$

where $Q_\Sigma = m_f Q_f$ is the total impulse of the fuel.

Hence, the maximal range of the motion S will be equal

$$S = tV = 1.4 \frac{\rho_f}{\rho} \frac{Q_f}{V} \frac{L_c}{\sigma} \tag{17}$$

or in the dimensionless form

$$\overline{S} = \frac{S}{L_c} = 1.4 \sigma^{-1} \frac{\rho_f}{\rho} \frac{Q_f}{V}. \tag{18}$$

If we assume that metal fuel of high efficiency is used ($\rho_f / \rho = 2.7$; $Q_f / V = 30$; $\sigma = 0.01$; $L_c = 10$ m), then the maximal range will be equal to

$$\overline{S} = 1.4 \cdot 100 \cdot 30 \cdot 2.7 = 11340$$

or in dimensional form $S = 113400$ m.

When the solid rocket fuel on the basis of nitrocellulose and nitroglycerin – JPN with density $\rho_f = 1.6$; $Q_f / V = 11$ is used, then the maximal range will be equal

$$\overline{S} = 1.4 \cdot 100 \cdot 1.6 \cdot 11 = 2464,$$

$$S = \overline{S} L_c = 24640 \text{ m}.$$

Calculation of maximally attainable range is represented in graphic form in Fig. 4. Here, the range S is represented as a dependence on velocity V and aspect ratio of the hull (cavity) $\lambda = L_c / D_c$ for specific impulses of the fuels Q_f = 230 sec and Q_f = 600 sec, depth H = 10 m, L_c = 10 m. If it is assumed that the strengthening (design) restriction of the hull aspect ratio is $\lambda \le 20$, then the maximal restriction on the motion range of SCO is $S_{\max} = 70$ km and on the velocity $V_{\max} = 200$ m/sec.

3.1. UNDERWATER VEHICLE PROPELLERS

Underwater vehicle propulsion is intended to transform chemical energy of the fuel into thermal energy. The latter transforms into mechanical energy – work for overcoming the hydrodynamic drag R_x (3).

When the motion is uniform, the thrust T of the propeller must equalize the hydrodynamic drag R_x

$$T = R_x . \tag{19}$$

In this case the useful power of the underwater vehicle propulsion will be equal to

$$N = TV . \tag{20}$$

The propulsion effectiveness is estimated by its total efficiency η representing the ratio of useful power N and all consumed power

$$\eta = \frac{TV}{I\dot{q}}, \tag{21}$$

where I is the mechanical equivalent of heat; $\dot{q}$ is the heat rate per time unit.

The coefficient η characterizes the propulsion perfection and is dependent of the fuel characteristics. In practice, the specific rate of the fuel is of importance. It is quantity of the fuel consumed per time unit at unit power. It is usually measured in g/kilo-Watt·hour. Since $\dot{q} = q \cdot \dot{m}_f$, where q is the caloric ability of the fuel; $\dot{m}_f$ is the fuel rate per a second.

Using (21), we obtain the relation for the specific rate of the fuel and efficiency η

$$\dot{q}_f = \frac{\dot{m}_f}{TV} = \frac{1}{I\,q\eta} . \tag{22}$$

One can see from (22) that the specific rate of the fuel $\dot{q}_f$ depends both on the propulsion characteristics η and on the fuel characteristics q. For diesels

$\dot{q}_f$ = 215 g/kW · h, for turbines $\dot{q}_f$ = 340 g/kW · h.

We well know specific powers of different propulsions used in the underwater vehicles [4]. There are

diesel propulsions	45 ÷ 90 W/kg	10 ÷ 30 W/ m^3
electro-accumulators	60 ÷ 100 W/kg	200
atomic propulsions	25 ÷ 200 W/kg	11.3
high-speed diesels	1.33 kW/kg	224 kW/ m^3
gas turbines	5.7 kW/kg	1700 kW/ m^3

It is known as well that the turbine or piston propulsion volume does not exceed 50% of the vehicle volume, whereas the fuel part in rockets exceeds 90%.

It is essential that the necessary specific power for supercavitating vehicles is calculated by formula

$$\rho_v = \frac{R_x V}{W_c} = \frac{R_x V}{0.67\pi R_c^2 L_c} = 0.71 \frac{\sigma \rho V^3}{L_c}. \qquad (23)$$

When $\sigma = 0.01$, $L_c = 10$ m, $\rho_v = 715$ kW/m^3 at V = 100 m/sec; $\rho_v = 5720$ kW/m^3 at V = 200 m/sec.

These values exceed on 2 – 3 orders the analogous values for diesel, electric, atomic propulsions. Therefore, the gas-turbine and jet propulsions with the metal fuel and using outboard water as a oxidizer and a cooler of the combustion products are considered perspective ones for the supercavitating vehicles at increased motion velocity. Such propulsions were investigated experimentally, and their high efficiency was confirmed [19].

At that, the increase of the velocity of SCO motion compared with vehicles at unseparated flow up to 100 – 200 m/sec do attractive the rocket schemes with solid fuel in view of the propulsion efficiency increase

(Fig. 5)

$$\eta_p = \left[1 + \frac{1}{2}\left(\frac{V_j - V}{V_j}\right)\right]^{-1}. \qquad (24)$$

Fig. 5 represents a graph of dependence of the propulsive efficiency for the jet propeller with solid fuel on the motion velocity at $V_j = 2040$ m/sec.

Reaction Al + water gives high temperature 10800K. Therefore, water must be supplied into the propeller in plenty. In this case the propulsion temperature reduction will occur according to the theoretical dependence on water gram-molecules n (Fig. 6a).

It is well known that to accelerate the reaction it is necessary to fluidize the metal and to transform the water into vapor. The calculation of the thermal processes is performed at condition that the temperature of the reaction products was reduced to 1250K. A scheme of the propulsion working on fuel Al with using the outboard water is shown in Fig. 6b. In the presented propulsion, the heat from combustion chamber is transmitted to aluminum to form a melt at temperature about 950K and to water to form vapor. The combustion products arrive on the turbine and after the turbine to outboard. In this case the propulsion efficiency will depend essentially on the excess pressure in the combustion chamber on the different depths. This is shown in graph in Fig. 7.

The graph in Fig. 7 gives the dependence of the specific output power of the propulsion with the fuel – aluminum + sea-water for different depths H = 305 ÷ 1525 m. For supercavitation motion regimes, the vapor exhaust will occur into the supercavity at pressure P = 0.02 kg/cm^3. This corresponds to the saturated vapor pressure at temperature 15°C. This pressure corresponds to the air pressure on height 23 km above sea level and ensures ideal conditions for work of propulsions with opened cycle independently on the object motion depth.

A scheme of the turbo-rotor propeller for supercavitating vehicle was considered to increase its efficiency at the Institute for Fluid Mechanics. Propellers with one or two turbo-rotors (Fig. 8, a,b,c) were tested there. It is shown in the scheme that the gas turbine and screw with three blades working in supercavitation regime were combined on one disk of the rotor. There also are shown section of the turbine blades and supercavitating screw sections.

Photographs in Fig. 9 a,b,c show models of the turbo-rotors in the hydro-tunnel and a picture of flow around the working turbo-rotors in the hydro-tunnel when the free stream velocity V = 10 m/sec at using the gas turbine with compressed air and at pressure to 6 kg/cm^2.

Preliminary experiments with turbo-rotor propellers showed real possibility of the propeller thrust increase on 20 % compared to the rocket scheme, although theoretical estimations point to possibility of double increase of the thrust. Therefore, possibility of attainment of optimal conditions for work of the turbine and supercavitating screw still will have to be realized.

3.2 FUEL FOR SCO

We can see from the previous analysis that the fuel for high-speed SCO must satisfy the heightened requirements to the specific characteristics Q_f and ρ_f. The specific characteristic - power/volume is the more important than the power/mass.

Work [21] considers schemes of turbo-prop of the hydro-jet propeller working on unitary solid fuel (Fig. 10, a), on two-component fuel (Fig. 10, b) and on hydro-reacting fuel on the basis of reaction between the magnesium and sea-water (Fig. 10, c).

Calculations showed that ratios of specific rates of the fuel transported on the board $\dot{m}_{fa} = \dfrac{\dot{m}_f}{T}$ in wide velocity range 20 ÷ 100 m/sec have constant values

$$\frac{\dot{m}_{fa}(schem\ b)}{\dot{m}_{fa}(schem\ a)} = 0.42; \quad \frac{\dot{m}_{fa}(schem\ c)}{\dot{m}_{fa}(schem\ a)} = 0.37.$$

The relations show that the hydro-reacting fuel on the vehicle board must be in 1.15 times less than the two-component one (scheme b) and in 2.7 times less than the solid unitary fuel (scheme a).

In rocket systems, where the fuel mass predominates, and weight and volume of the nozzle and combustion chamber are comparatively small, the propulsive characteristics of the system will be determined by the fuel characteristics – its specific impulse Q_f and density ρ_f.

The investigations showed that the chemical fuels using metals and sea-water as oxidizer, ballast and cooler are the most effective for underwater vehicles. This is stipulated that the metals ensures maximal energy at reaction with water [19, 21]

Al + sea-water → 3143 kW·hour/m^3 (1.18 kW·hour/kg),

Mg + sea-water → 1891 kW·hour/m^3 (1.05 kW·hour/kg),

Li + sea-water → 1092 kW·hour/m^3 (2.09 kW·hour/kg).

Reactions and main parameters are presented in Table [19, 21] Fig. 11.

In practice, Al is the best fuel, since it is proof and cheap. Aluminum melting temperature is 950K, and the combustion temperature in reaction with H_2O reaches 10800K.

Perspective of the fuels for the underwater vehicles is frequently estimated by theoretical value of specific work of the jet flow (kW·h/m^3). It is determined at fixed value of the balanced expansion and quantity of the injected sea-water sufficient to decrease the combustion product temperature to 1250K.

Dependence of the approximate theoretical values of the specific power with respect to mass ρ_1 and volume ρ_2 for *Al* at reaction with water

$$2Al + n \cdot H_2 0, \tag{25}$$

where n is the number of gram-molecules upon expansion of the combustion products from 206.9 to 10.14 kN/m^2, is presented in Fig. 12.

4. Calculation of supercavitating model motion range at inertial motion

Drag of a supercavitating model completely enveloped by a cavity is equal to a cavitator drag and calculated by formula

$$R_x = \frac{\rho V^2}{2} c_{xn} S_n, \tag{26}$$

where ρ is the fluid density; V is the model velocity; c_{xn} is the cavitator drag coefficient (for disk c_{xn} = 0.82 (1 + σ), where σ is the cavitation number); S_n is the cavitator area.

When cavitation number is small, it is possible to consider c_{xn} as constant one. Then the equation of motion of the model with mass *m* has the form

$$\frac{dV}{dt} = -kV^2, \tag{27}$$

where $k = \frac{\rho c_{xn} S_n}{2m}$.

Its solution gives dependence of motion time on velocity in the form

$$t(V) = \frac{1}{k}\left(\frac{1}{V} - \frac{1}{V_0}\right) \tag{28}$$

and dependence of passed range S on the velocity in the form

$$S(V) = \frac{1}{k} \ln \frac{V_0}{V} \quad , \tag{29}$$

where V_0 is the starting velocity of the model.

Hence, the model moves infinitely long and passes infinitely great distance. It is necessary to define criterion determining the finite point of the path to have sense of the range calculation.

Such criteria can be:

– the velocity reduction to certain value;

– decrease of the model momentum to certain value;

– disappearance of clearance between the model and cavity walls.

In essence, the second and third criteria are distinctive from the first one only by way of the final velocity definition. Thus, it is possible to consider the final velocity V_e definition as the most universal way of determination of the motion range S_e.

The range depends on the model mass m and cavitator radius r_p determining the drag for given velocities V_0 and V_e.

As the model must be located in the cavity, its maximal possible mass depends on the material density ρ_b, model length L and cross cavity dimensions determined by the cavitator radius.

Thus, the range is determined by

– material density;

– model length;

– cavitator radius.

Calculations necessary to determine the range can be executed due to the program SCAV [23]. The model shape is approximated by three truncated cones (Fig. 13, a) in this program. The program computes:

– the model characteristics: volume, mass center location and moment of inertia;

– the shape and dimensions of stationary supercavity past a disk or a conic cavitator at given velocity and depth of the motion;

– the clearances between the model and cavity boundary;

– the value of impact load acting to the model at water entry;

– the speed reduction of the supercavitating model moving on inertia;

– the basic dimensions of unsteady cavity (length and mid – section diameter) in any point of the distance.

The SCAV program (SuperCavity, Version 1.3) is intended to automatize designing the high-speed supercavitating models.

At experimental investigations of high-speed motion in water, the model shape must satisfy requirements of inscribing into a natural cavity and structural stability of the supercavitating motion regime. If we suppose that the model moves rectilinearly under action the cavitation drag only, then the process is described by the dimensionless equation of model motion on inertia

$$\frac{dV}{dt} = \frac{1}{Fr^2} - \frac{\rho \pi D_n^3 c_{x0}}{8m}\left[V^2 + \overline{p}_{atm} + \frac{2H}{Fr^2} - \overline{p}_c(t)\right],$$

where m is the mass of model; c_{x0} is the cavitation drag coefficient when $\sigma = 0$, p_{atm} is the atmospheric pressure; H is the immersion depth.

Fig. 13, a presents a copy of PC-screen after calculation of the model location in the cavity. The model shape and starting data correspond to the real experiment. The vertical scale of the image is increased for clearness.

In Fig. 13, b, graphs of changing the cavity length L_c and model velocity V in dependence on passed distance x are shown. The calculation was executed for titanic model at $D_n = 1.5$ mm, m = 49.0 g, $V_0 = 1000$ m/s. It is supposed that the model enters in water in point $x = 0$ and then moves on inertia. The initial rectilinear part of the graph $L_c(x)$ corresponds to the interval of the supercavity formation. Quasistationary magnitudes of $L_c(x)$ are plotted by dashed lines for comparison.

4.1. INERTIAL MOTION WITH PROPELLER

Motion of the model with propeller has two features. First, thrust T_p acts on the model. It compensates the drag. Second, the part of the model material with density ρ_b must be changed by fuel with density in 4 times lower. Therefore, the model mass with propeller, especially in the path end, is lower than the solid model mass.

The missile thrust can be determined from the relation behavior

$$T_p = -Q_f \frac{dm_f}{dt}, \tag{30}$$

where T_p is the propeller thrust; m_f is the fuel mass; Q_f is the specific impulse of the fuel. Usually, its value is expressed in kg_f/(kg/sec) or lb_f/(lb/sec). Numerical magnitudes are equal in the both cases.

Typical magnitudes of Q_f are in range from 200 to 500 kg_f/(kg/sec). Passing onto the system SI, we obtain

$$Q_f' = 9.81 Q_f \frac{n \cdot \sec}{kg} = 9.81 Q_f \frac{kg \cdot m}{\sec^2} \frac{\sec}{kg} = 9.81 Q_f \frac{m}{\sec}.$$

Impulse of force T_p during the motion time is

$$K_f = Q_f' m_f. \tag{31}$$

If the propeller chamber volume is equal to W_c, then the model mass decrease is

$\Delta m_0 = (\rho_b - \rho_f) W_c$ in beginning of the path;

$\Delta m_0 = \rho_b W_c$ in the path end.

As a result, the initial impulse is

$$K_1 = [m_0 - (\rho_b - \rho_f)W_c]V_0 . \tag{32}$$

During the propeller work the impulse K_f will be obtained by Eq. (31), and general available impulse will be

$$K_0 = W_c[\rho_f Q_f^{'} - (\rho_b - \rho_f)V_0] .$$

The expression in brackets vanishes at

$$V_{cr} = Q_f^{'} \frac{\rho_f}{\rho_b - \rho_f} . \tag{33}$$

When $V_0 < V_{cr}$, the initial impulse increases, and we can hope that the range increases. On the contrary, when $V_0 > V_{cr}$, it decreases, and we can wait for the model with propeller passes smaller distance than solid one.

4.2 INFLUENCE OF A MISSILE PROPELLER ON THE MODEL MOTION RANGE

Models h1 – h4 with length 250 mm and with length 150 mm were chosen as base-models to research influence of the missile propeller on the model motion range (Table1).

Table 1

Characteristics of models of a series h

N	L cm	R_n cm	R_e cm	m_o g	m_e g	W_f cm^3	M_f G	Δm %	m_f %
1	2	3	4	5	6	7	8	9	10
h1	25	0.05	0.7	156	115	5.3	98	27	6.3
h2	25	0.15	1.525	749	578	21.0	39	22	5.2
h3	15	0.15	1.225	277	227	6.5	12	18	4.3
h4	15	0.15	1.225	277	218	7.5	14	21	5.0

Note: m_o is the solid model mass; m_e is the mass of model with chamber; W_f is the chamber volume; m_f is the fuel mass.

It was accepted that the chambers having truncated cone shape were made in models to dispose the fuel. A diameter of the frontal base of the chamber was accepted equal to the half-diameter of the model in the place of the chamber base disposition. A diameter of the back base was accepted equal to the half-diameter of the tail part of the model.

As a result, four models were developed. They are designated as models of a series h. These models characteristics are given in Table1. Their schemes are shown in Fig. 14. Models h3 and h4 differs by the chamber dimension only.

The calculations were carried out by using the program CDILM. We varied the starting velocity of the model (1200, 1000, 800 and 600 m/s) and specific impulse of the fuel (200, 400 and 600 kg_f /(kg/sec)). The fuel density was accepted equal to 1.85 g/cm^3 in all the cases.

Calculations for the case, when the fuel density was equal to the model material density (7.85 g/cm^3), and its specific thrust was equal to zero, were performed for comparison. This case corresponds to the case of the solid model without propeller.

It is accepted in the calculations that the combustion occurs at constant velocity. All the fuel had burnt during the motion and the fuel combustion continued 1/2 sec to 1/12 sec.

Thus, the model was passing the greatest part of the path at the operating propeller.

One can see changing the model material on the fuel does not give an gain in the range for any model at specific impulse Q_f = 200. The most effective fuel gives some gain in the range from 30% at high starting velocity to 150 % at low one (Fig. 15).

5. Interaction between the propeller and supercavity

Problems on interaction between the propeller and a supercavity are weakly studied direction of the hydrodynamics and enough complex for theoretical and experimental investigation.

The similar problem on interaction between the propeller and ship is known in shipbuilding [16]. This interaction may be both positive:

– the system efficiency increasing at creation of the additional thrust on the hull by means of the pressure redistribution and negative;

– the entraining force increase on the hull and the interaction efficiency reduction of the system "hull-propeller" in dependence on construction of the propeller and hull, their mutual disposition and the propeller work regime.

In this case the propeller can influence on the cavity shape directly by changing its closure conditions, free surface structure and gas-leakage from the supercavity at its presence on the hull.

The following types should be noted among the constructive features of the propellers:

1. Gas jet.

1.1. Jet with condensable phase.

2. Water jet.

3. Screw.

3.1. Supercavitating screw.

4. Turboprop.

The following configurations are noted among the configurations of propellers about the supercavity:

1. The frontal disposition of the propeller or the

towing propeller located in the nose in front of the supercavity.

2. Tail disposition of the propeller or the pushing propeller past the supercavity.

5.1. DESCRIPTION OF PARAMETERS GOVERNING THE DYNAMICS OF CAVITY ENTRAINMENT

The supercavity as the flow form created by free streamlines is very sensitive to the external pressure fields, including the pressure fields formed by the propeller.

As is known from the hydromechanics [16], the propellers always forms jets of gas or fluid modeled by distributed sources and dipoles.

The scheme with ideal propeller [16] (Fig. 16) gives a typical picture of change of the flow parameters. In this case the additional fluid is not injected compared to the case of the jet (Fig. 16), and the working section of the propeller may e modeled by a surface of dipoles oriented so that they pumps the fluid from the zone in front of the propeller to the zone past the propeller. Thus, the pressure difference from $-\Delta P$ to $+\Delta P$ is created in the working section.

It is clear that in the case of interaction with the supercavity the frontal zone with reduced pressure $-\Delta P$ will entrain the cavity, and the cavity will be displaced from the zone with increased pressure $+\Delta P$. It is necessary to consider their joint influence in the real case when the flow is formed both by the hull and the propeller.

Since the propeller must only compensate the impulse loss caused by the hydrodynamic drag of the hull in the free stream, then main dimensionless criterion influencing on behavior of the flow around the propeller with taking the hull into account

$$\overline{T} = \frac{T}{R}, \tag{34}$$

where T is the propeller thrust, R is the hull drag. In this case it is necessary to distinguish three regimes.

When $\overline{T} > 1$, it is the acceleration regime. The thrust is higher than the hydrodynamic drag (the wake past the body has the positive impulse);

When $\overline{T} = 1$, it is the steady motion regime (the wake without impulse);

When $\overline{T} < 1$, it is the deceleration regime(the wake past the body has the negative impulse).

This criterion $\overline{T}$ is the most considerable, because the main consumption of the impulse and energy is included in the propeller thrust. This results in the basic change in the environmental fluid.

It is necessary together with this (34) to take into account the local flow parameters caused by propeller directly in the cavity closure zone.

5.2. CAVITY CLOSURE IN THE GAS JET ZONE OF THE PROPELLER

- **The gas jet is source of gas-supply into the supercavity**

At certain conditions of gas jet outflow, when the jet outflow velocity $\overline{V}_j$ is lower than the critical velocity $\overline{V}_{jCR}$

$$\overline{V}_j = \frac{V_j}{V_\infty} < \overline{V}_{jCR}, \tag{35}$$

the gas part may return from the jet boundary layer into the cavity and be the additional gas-supply.

- **The gas jet is the ejector (sink) sucking out the gas from the cavity**

This regime may be observed when $\overline{V}_j$ exceeds the critical velocity $\overline{V}_{jCR}$

$$\overline{V}_j = \frac{V_j}{V_\infty} > \overline{V}_{jCR}, \tag{36}$$

The criterion $\overline{V}_{jCR}$ depends on the place and conditions of the cavity closure. So the criterion $\overline{V}_j$ (35), (36) is the second parameter governing the dynamics of supercavity.

5.3. INTERACTION BETWEEN THE CAVITY AND PROPELLER. TAIL LOCATION OF THE PROPELLER

Experiments on study of the propeller influence on the cavity were carried out at the IHM on the special installation (Figs. 17, 18). On this installation the supercavity was formed by means of the ring cavitator on the hull with diameter D_m = 52 mm which is in front of the propeller with blades.

Pictures of flow around the model at different regimes of the propeller work at continuous gas-supply are shown in photos (Figs. 19, 20, 21).

5.4. FRONTAL LOCATION OF THE SCREW PROPELLER

Investigation of the propeller screw influence on the cavity was carried out on the special installation permitting to create the artificial cavity around the propeller tail cone at different regimes of the propeller screw work. A ratio of the screw and cavity diameter was $D_p = (2 \div 3)D_m$. The propeller screw is located in the nose part in front of the cavity. It is established in virtue of the fulfilled researches that the working propeller screw considerably changes the cavitation characteristics of the tail cone [15].

Results of the cavity testing for the working propeller screw are given in the form of dependencies of the relative parameters of the artificial cavity as function of the screw load coefficient $K_p = \frac{8K_1}{\pi\lambda_p^2}$, where K_1 is the thrust coefficient, and λ_p is the relative screw tread.

Changes of the cavity length $\overline{L} = \overline{L}_p / L_0$, cavitation number $\overline{\sigma} = \sigma_p / \sigma_0$ and air rate coefficient $\overline{Q} = Q_p / Q_0$, where L_0, σ and Q_0 are the isolated cavity parameters at absence of the propeller screws but at other the same conditions, are given in Figs. 22, 23, 24, respectively. As is shown in the graphs, the cavity length considerably decreases when the propeller screw is located in front of the cavity. It is about 30% of the isolated cavity length even at zero load of the screw and the same air rate. In this case the cavitation number increases but considerably slower than the cavity length changes. This is explained to that the propeller screw not only increases the pressure downstream and strongly swirls the stream. As a result, the cavity boundary is destroyed. To reach the same cavity length at the working propeller screw it is necessary to increase in some times the air rate. So, when $K_p = 0$, the consumable air rate must exceed in 2-3 times the corresponding value of Q_0 for the isolated cavity, and when $K_p = 0.3$, it is necessary to increase in 5 times the air rate (Fig. 24).

References

1. Epshtein L.A. Methods of theory of dimensionality and Similarity for problems of Ship Hydromechanics. –Leningrad, Sudostroenie, 1970, 207 p., (in Russian).
2. Gurevich M.I. Theory of jets of ideal fluid. – New-York – London, Academic Press, 1965.
3. Problems and methods of hydrodynamics of underwater foils and screws. – Kiev, Naukova dumka, 1966. – 160 p., (in Russian).
4. J. Nielsen. Missile aerodynamics. Mc. GRAW-HILL BOOK COMPANY, New York, Toronto, London, 1960. 474 c.
5. Borisyuk M.N. Problem on vertical hydrofoil. // J. Hydrodynamics of High Speeds. – Kiev, Naukova dumka, 1966. P. 59 - 74, (in Russian).
6. Pantov Ye.N., Mahin N.N., Sheremetov B.B. Foundations of theory of motion of underwater vehicles. Leningrad, Sudostroenie, 1973. – 211p., (in Russian).
7. Cascade wings. At edition of Belotserkovsky S.M. – Moscow, Mashinostroenie, 1985.-390 p., (in Russian).
8. Belotserkovsky S.M., Nisht M.N. Separated and continuous flow around slender wings in ideal fluid. – Moscow, Nauka, 1978. – 351 p., (in Russian).
9. Underwater projectile. Franklin A. Monson. US patent 3.915.092, 10.28.1975.
10. Logvinovich G.V. Hydrodynamics of flows with free boundaries. Kiev, Naukova dumka, 1969. – 208 p., (in Russian).
11. Savchenko Yu.N. Investigation of High-Speed Supercavitating Underwater Motion of Bodies. AGARD Report 827 "High Speed Body Motion in Water", 1998, FDP Wokrshop, Kiev. – P. 20-1 – 20-12.
12. Savchenko V.T. Reduction of overload on a body entering in water at high speed. AGARD Report 827, High Speed Body Motion in Water. Kiev, 1997. – P. 29-1 – 29-6.
13. Savchenko Yu. N., Putilin S.I., Savchenko V.T. Aerohydrofoil. Patent USSR, Inform Bull. 5, 1992.
14. Savchenko V.T. Hydrodynamic Characteristics of Rudders Operating in Air-Sea Interface. RTO AVT Symposium Papers "Fluid Dynamics Problems of Vehicles Operating near or in the Air-Sea Interface", Amsterdam, 1998. P. 17- 1 – 17-9.
15. Yegorov I.T. Artificial cavitation. – Leningrad, Sudostroenie, 1971, 283 p.
16. Voytkunski Ya.I. Handbook on ship theory. – Leningrad, Sudostroenie, 1960.
17. L.M. Milne-Tomson, C.B.E. Theoretical hydromechanics. – London, Macmillan & CO LTD, 1962.
18. Migirenko G.S. and others. Some ways of cavity flow control at low Froude numbers. Proc. of Symp. IUTAM.- Moscow, Nauka, 1973, p. 361 – 367.
19. Leonard Greiner. Underwater Missile Propulsion. – 1967. Compas Publ. Inc., VA, USA.
20. Putilin S.I. Some peculiarities of dynamics of supercavitating models. // J. of Applied mechanics. Vol. 2, No 3, 2000, pp. 65 – 74.
21. Ivchenko V.I., Grigoriev V.A., Prihodko N.A. Optimal hydroreactive systems. Krasnoyarsk Univ., 1985.
22. Savchenko Yu.N. Perspective of hydrodynamic drag reduction methods. // J. of Applied mechanics. Vol. 1, No 4, 1999, pp. 42 – 50.
23. Semenenko V.N. Dynamics of supercavitating bodies. Symp. on High-Speed Hydromechanics and Supercavitation.March 31, 2000, Grenoble, France, pp. 1 – 15.

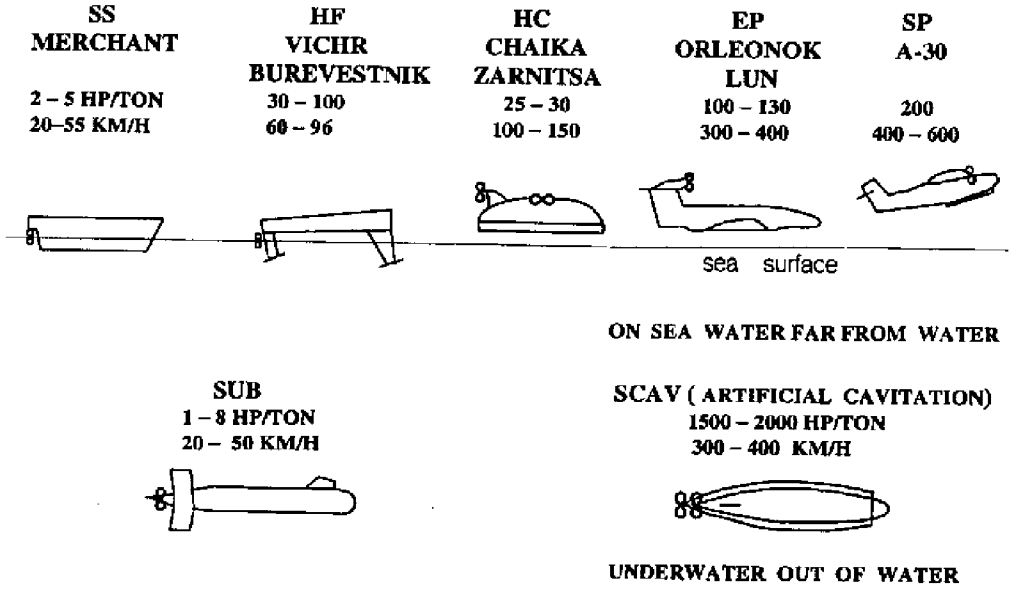

SS
MERCHANT
2 – 5 HP/TON
20–55 KM/H
HF
VICHR
BUREVESTNIK
30 – 100
60 – 96
HC
CHAIKA
ZARNITSA
25 – 30
100 – 150
EP
ORLEONOK
LUN
100 – 130
300 – 400
SP
A-30
200
400 – 600
sea surface
ON SEA WATER FAR FROM WATER
SUB
1 – 8 HP/TON
20 – 50 KM/H
SCAV (ARTIFICIAL CAVITATION)
1500 – 2000 HP/TON
300 – 400 KM/H
UNDERWATER OUT OF WATER

Fig. 1

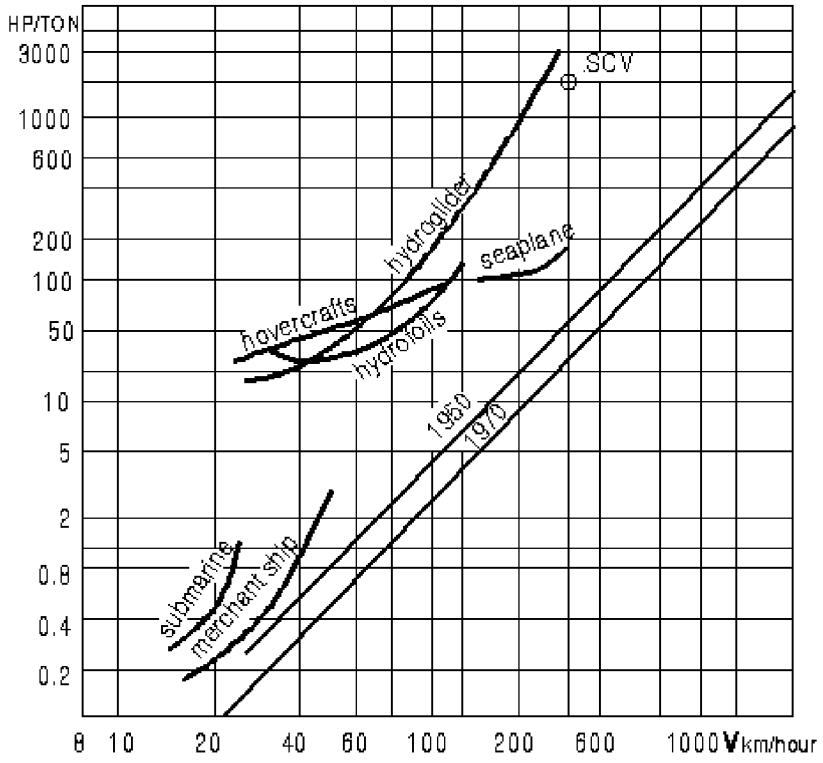

HP/TON
3000
1000
600
200
100
50
10
5
2
0.8
0.4
0.2
SCV
hydroglider
seaplane
hovercrafts
hydrofoils
1950
1970
submarine
merchant ship
8
10
20
40
60
100
200
600
1000
km/hour

Fig. 2

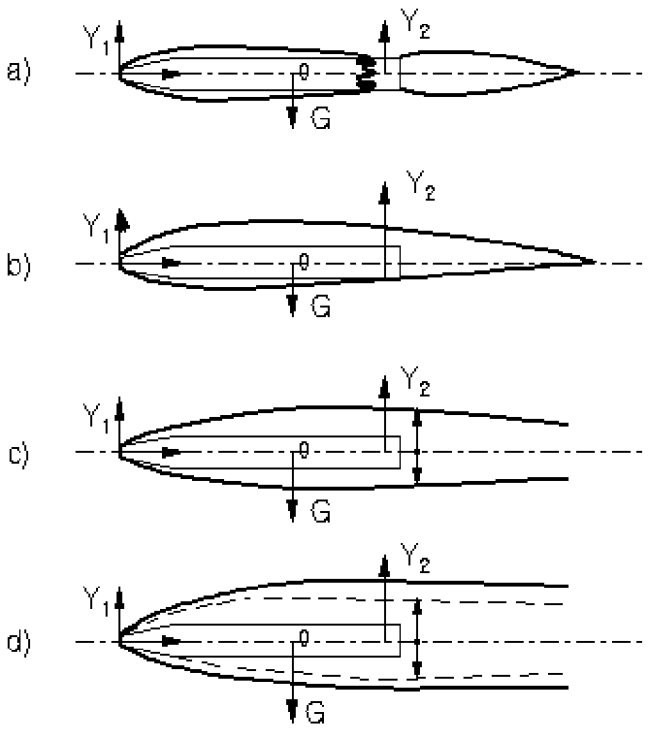

a)
b)
c)
d)
Y1
Y2
G

Fig. 3

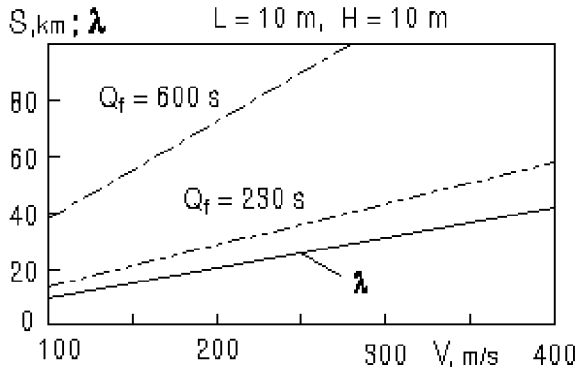

S,km; λ
L = 10 m, H = 10 m
Qf = 600 s
Qf = 250 s
λ
80
60
40
20
0
100
200
300
V, m/s
400

Fig. 4

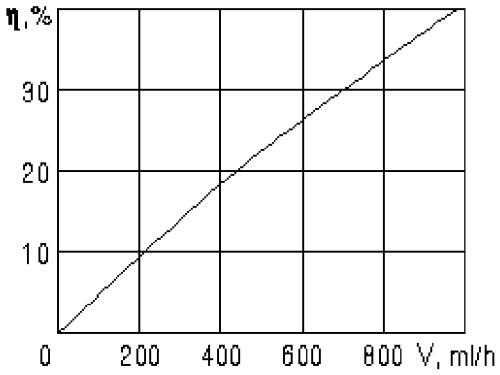

η, %
30
20
10
0
200
400
600
800
V, ml/h

Fig. 5

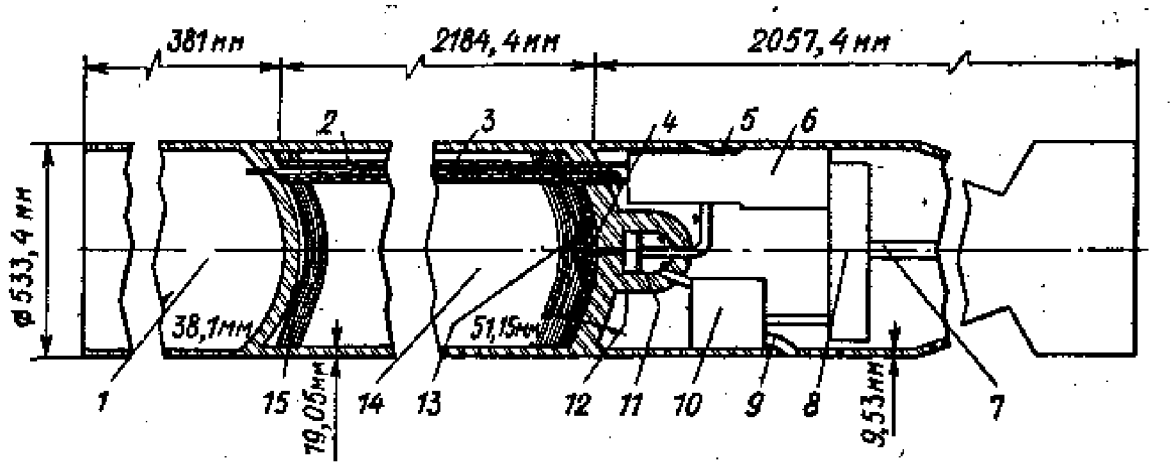

381 мм
2184,4 мм
2057,4 мм
ф 533,4 мм
38,1мм
51,15мм
19,05мм
9,53мм
1
2
3
4
5
6
7
8
9
10
11
12
13
14
15

Fig. 6b

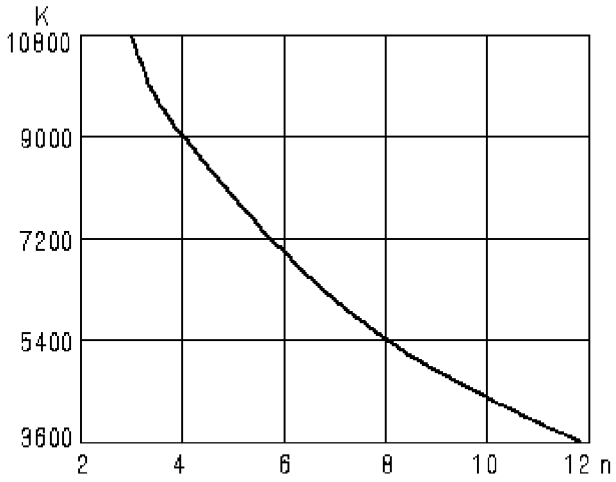

K
10800
9000
7200
5400
3600
2
4
6
8
10
12 n

Fig. 6a

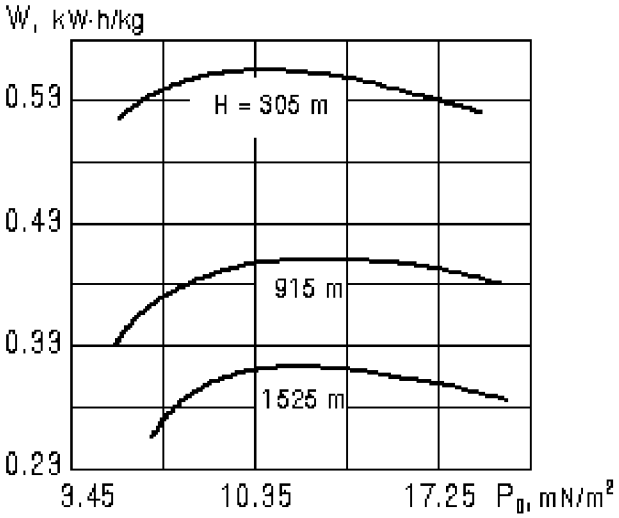

W, kW·h/kg
0.53
0.43
0.33
0.23
H = 305 m
915 m
1525 m
9.45
10.35
17.25
P0, mN/m²

Fig. 7

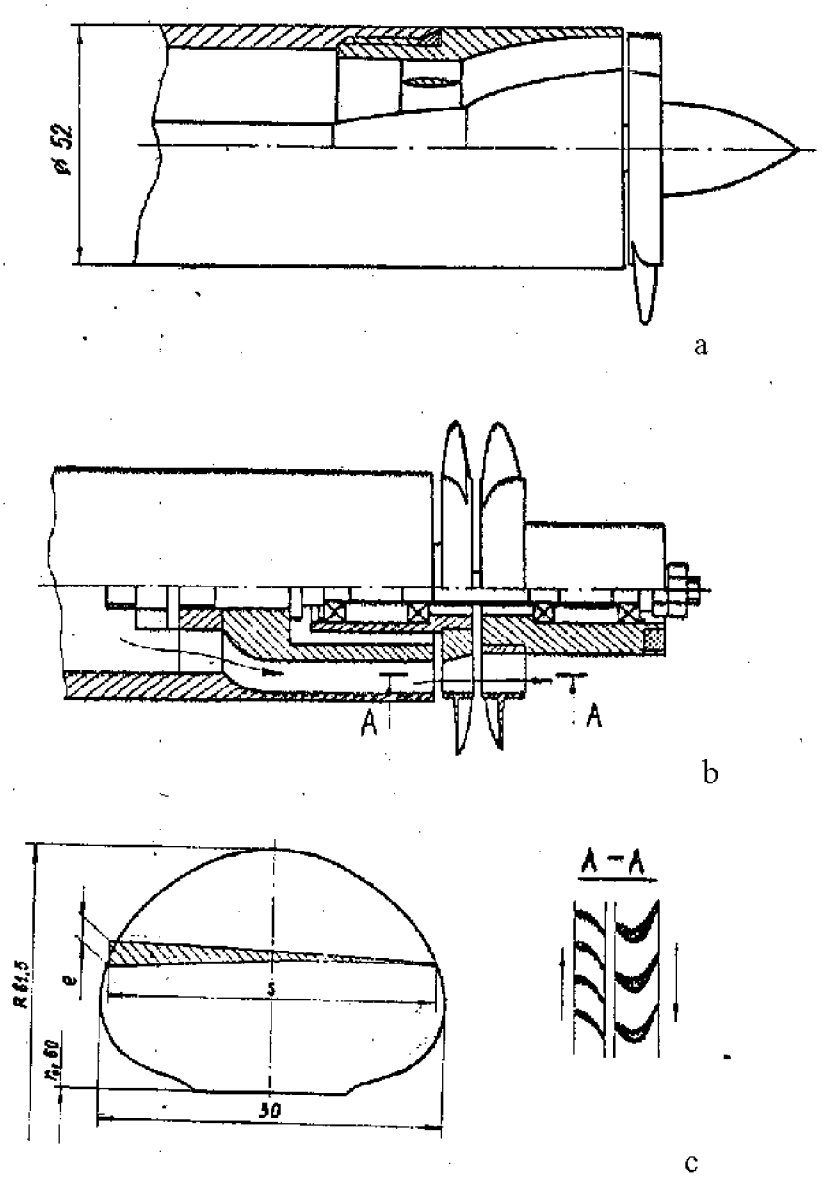


Fig. 8

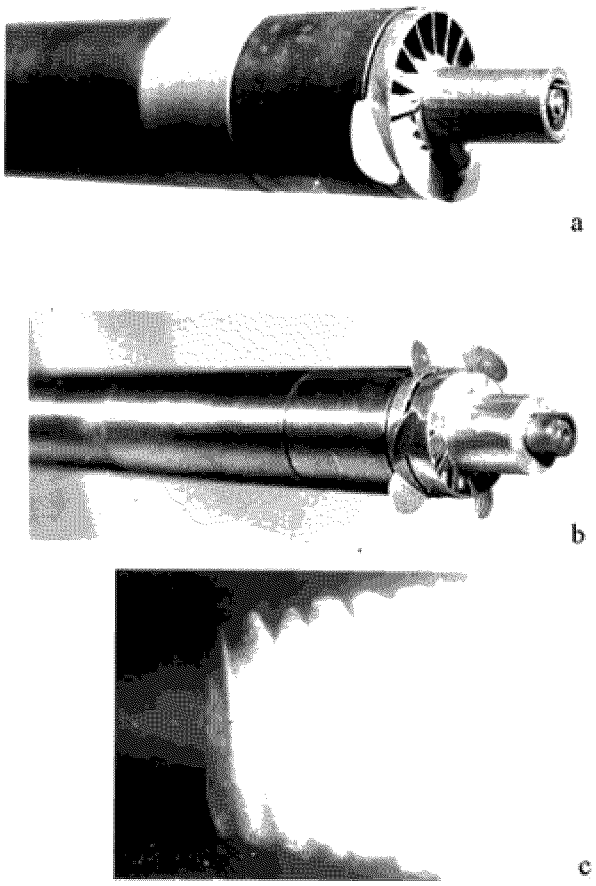


Fig. 9

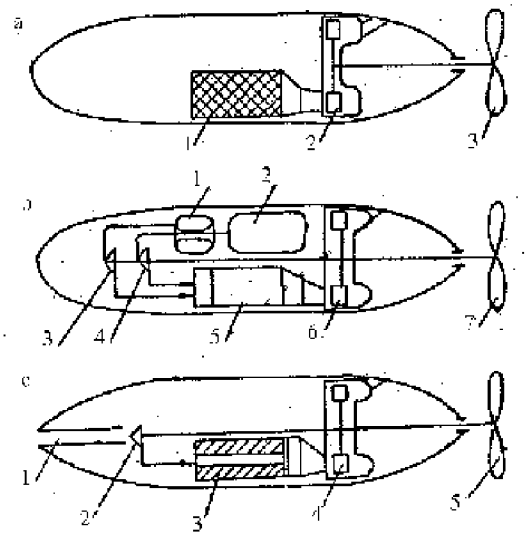


Fig. 10

Properties of different types of the fuel

Fuel	Chemical Formula	Density, g/cm3	Molecular weight	Temperature of melting	Temperature of boiling	Reaction	Molecular weight of reaction product	Quantity of evolved hydrogen, l/g,	Specific heat of reaction, Kcal/l	Theoretical velocity of flowing out, m/s	Theoretical specific impulse
Aluminum	Al	2.7	26.98	658	2500	$2Al + 1.5O_2 = Al_2O_3$	101.94	–	3730	5590	570
Aluminum	Al	2.7	26.98	658	2500	$Al + 3H_2O = Al(OH)_3 + 1.5H_2$	81.03	1.25	4150	5900	601
Magnesium	Mg	1.74	24.32	657	1102	$Mg + 0.5O_2 = MgO$	40.32	–	3623	5510	562
Magnesium	Mg	1.74	24.32	657	1102	$Mg + 2H_2O = Mg(OH)_2 + H_2$	60.32	0.924	3800	5640	575
Lithium	Li	0.534	6.94	179	1372	$2Li + 2H_2O = 2LiOH + H_2$	49.88	1.62	5340	6700	683

Fig. 11

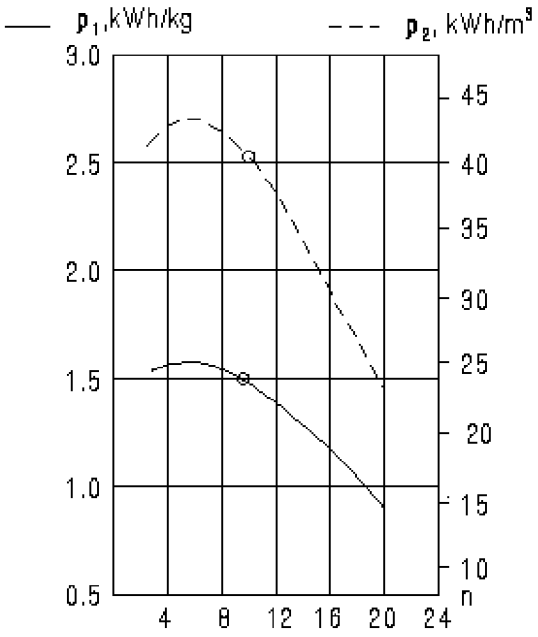


Fig. 12

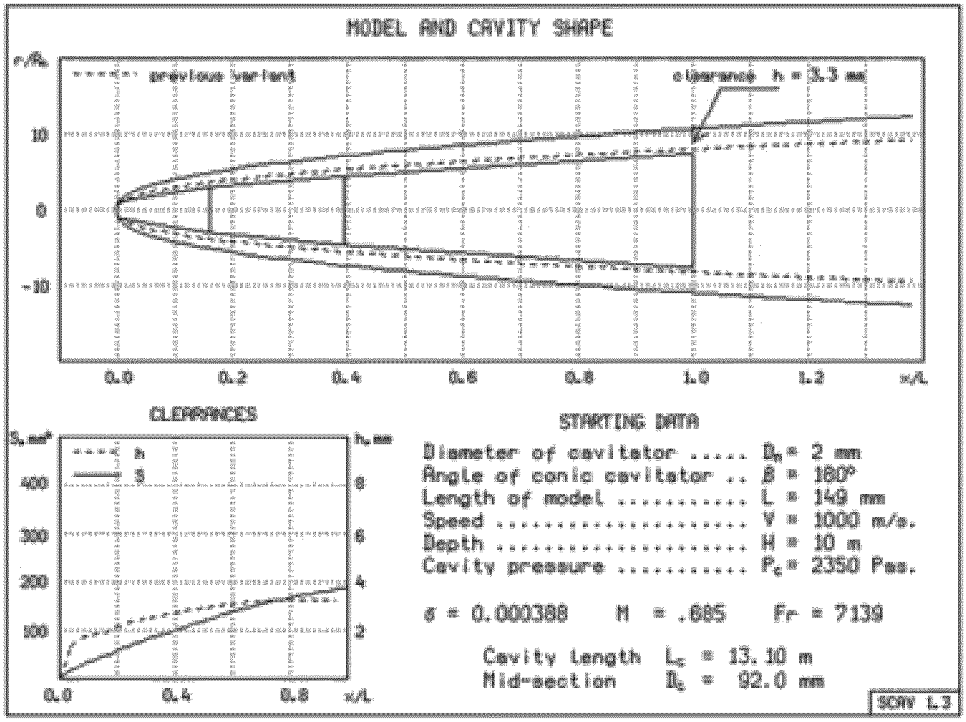


Fig. 13a

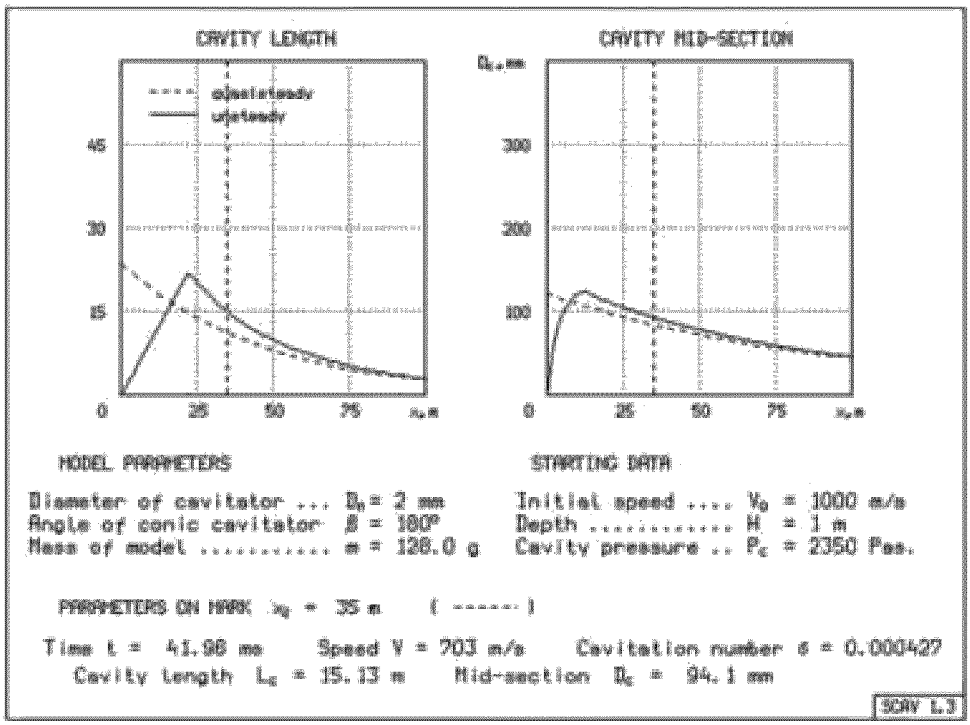


Fig. 13b

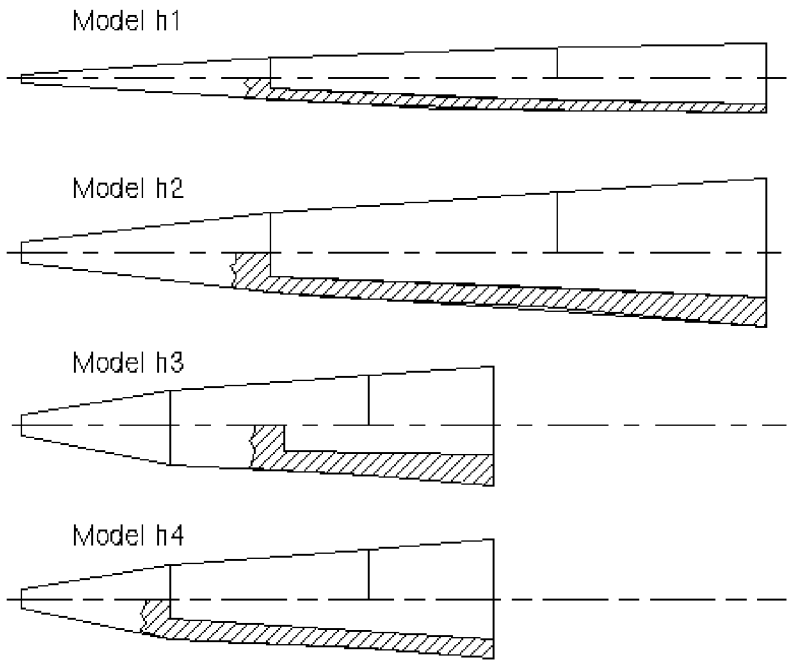

Model h1
Model h2
Model h3
Model h4

Fig. 14

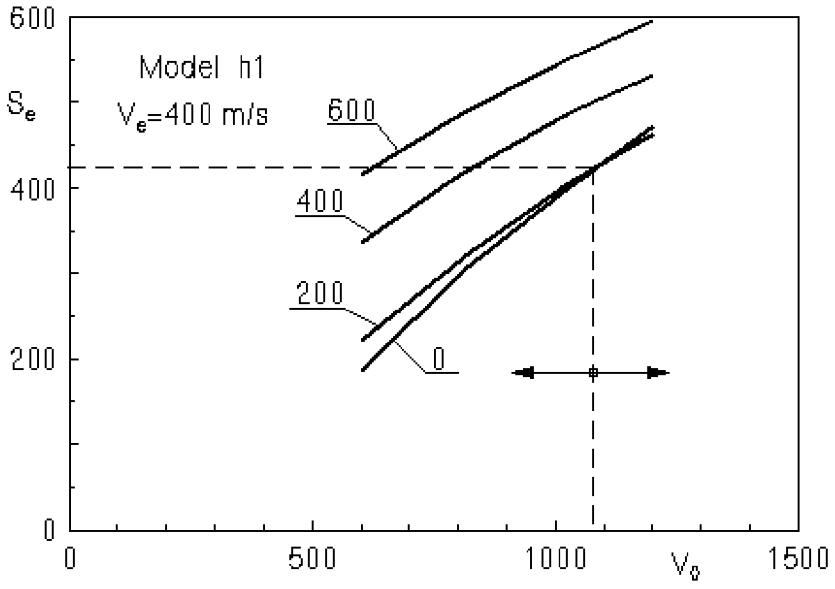

600
400
200
0
S_e
Model h1
V_e=400 m/s
600
400
200
0
0
500
1000
1500
V_0

Fig. 15

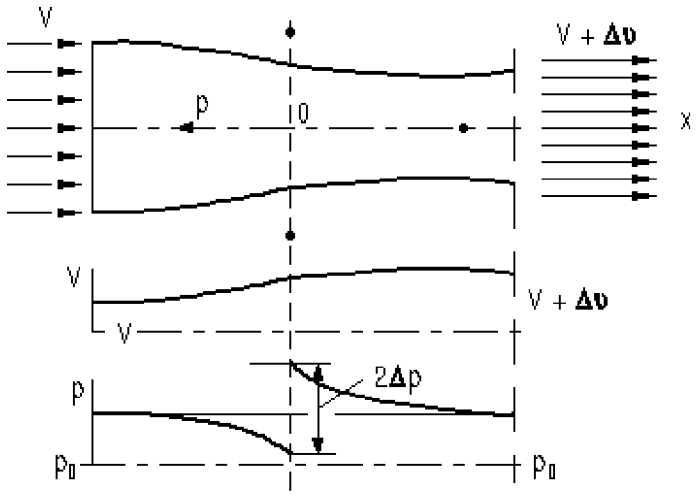


Fig. 16

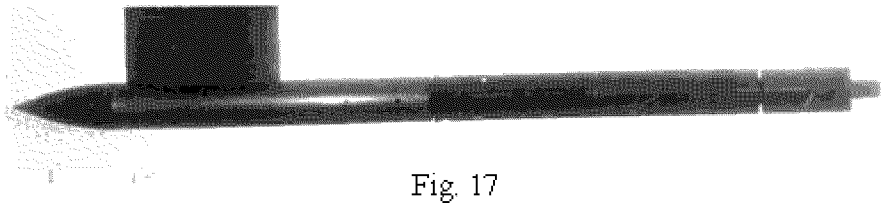


Fig. 17

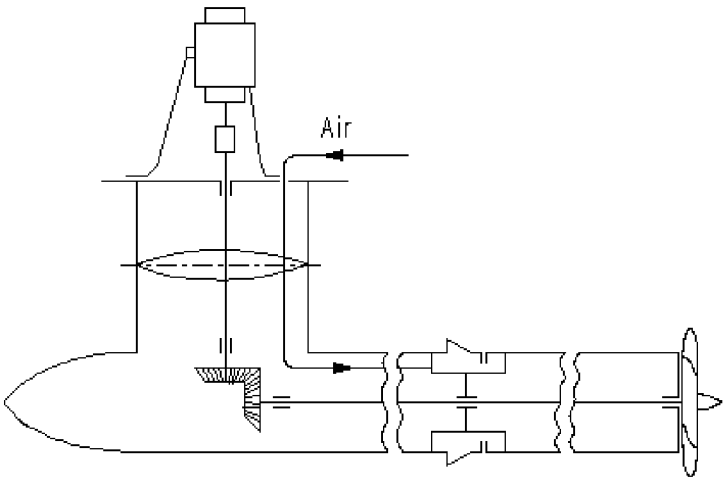


Fig. 18



Fig. 19

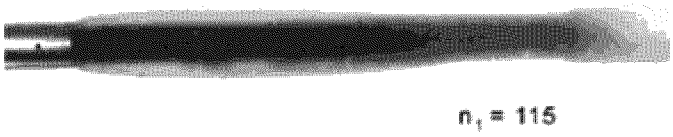


Fig. 20

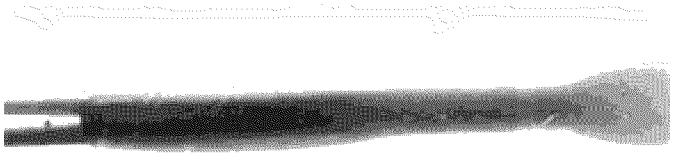


Fig. 21

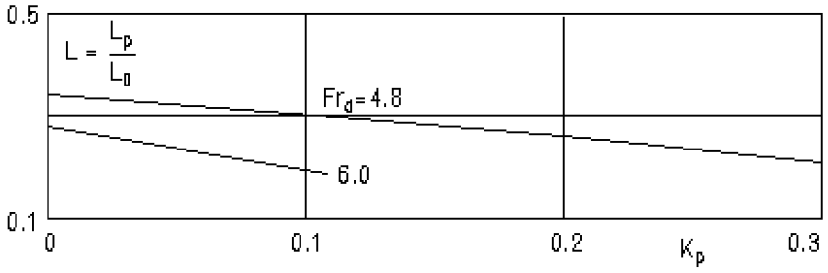


Fig. 22

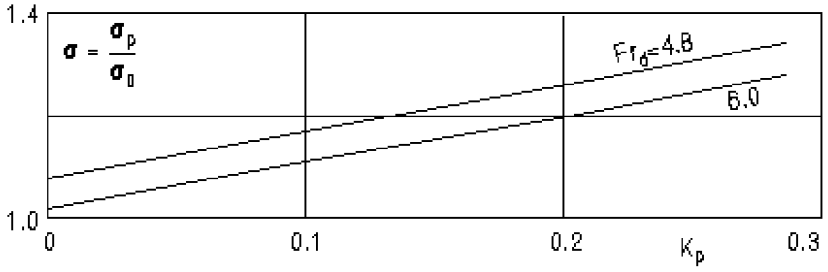

1.4
1.0
$\sigma = \frac{\sigma_p}{\sigma_0}$
Fr_d=4.8
6.0
0
0.1
0.2
K_p
0.3

Fig. 23

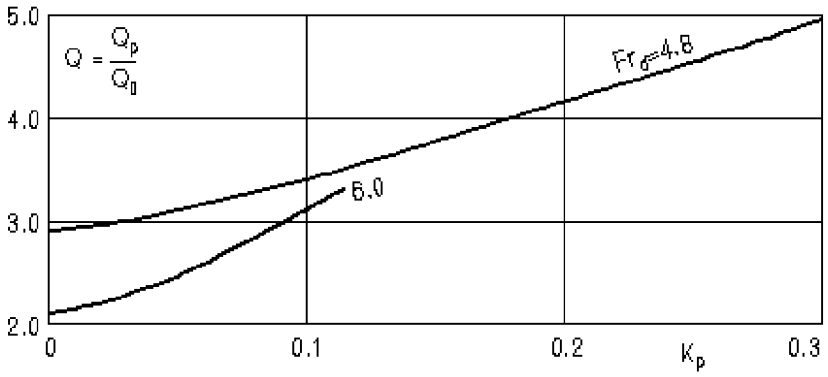

5.0
4.0
3.0
2.0
$Q = \frac{Q_p}{Q_0}$
Fr_d=4.8
6.0
0
0.1
0.2
K_p
0.3

Fig. 24

This page has been deliberately left blank

Page intentionnellement blanche

Supercavitating Flows: Small Perturbation Theory and Matched Asymptotics

Professor K.V. Rozhdestvensky
St.Petersburg State Marine Technical University
Lotsmanskaya str., 3
190008, St.Petersburg
Russia

Summary: The lecture discusses some applications of the theory of small perturbations as applied to supercavitating flows. In this context the linear theory is viewed as an outer expansion of a more complete nonlinear solution of the flow problem. In addition to comparing linear solutions for a supercavitating flat plate for different analogues of the cavity closure models, two examples are considered showing how to account for the presence of local flow regions where the perturbations are not small. In the first example a local asymptotic solution of the nonlinear flow problem in the vicinity of the leading edge is matched to the classical linear solution to provide a uniformly valid pressure distribution along a supercavitating flat plate. In the second example, the local nonlinear perturbation of the otherwise slightly perturbed flow is due to a spoiler fitted at the trailing edge of a flat plate.

1. Introduction

In a nonlinear steady 2-D problem formulation for a potential flow past a supercavitating body, one has to solve Laplace equation in the domain occupied by the fluid with the following conditions on the flow boundaries

- Slip condition on the wetted part of the body

$$\frac{\partial\varphi}{\partial x} = \frac{\mathrm{d}y}{\mathrm{d}x}\Big(1 + \frac{\partial\varphi}{\partial x}\Big), \qquad y = y_b(x), \tag{1}$$

  where φ is perturbation velocity potential, $y = y_b(x)$ is a function, describing the contour of the wetted part of the body in Cartesian coordinate system, x-axis being directed downstream. Note, that here all quantities and functions are non-dimensionalized with use of the characteristic length of the body and the velocity of the oncoming flow.

- Dynamic condition on the cavity

  The pressure on the boundary of the cavity is assumed constant wherefrom the corresponding pressure coefficient C_p should be taken equal in magnitude and opposite in sign to the cavitation number σ

$$C_p = C_{p_c} = 1 - (1 + \frac{\partial\varphi}{\partial x})^2 - \Big(\frac{\partial\varphi}{\partial y}\Big)^2 = -\sigma, \qquad y = y_c(x) \tag{2}$$

  where $y = y_c(x)$ describes the cavity contour, determined in the course of the problem solution.

- Kinematic condition on the cavity

  The cavity contour is a streamline, and, therefore, it should be subject to a slip condition, identical to (1).

- At the infinity the perturbation velocities should vanish.

In what follows we first consider a steady linearized flow problem for a supercavitating foil[1] using different linear analogues of the cavity closure schemes. Used in particular are the analogues of the *closed* cavity termination models (Riaboushinsky model, Efros-Gilbarg model, Tulin single-spiral vortex model), as well as those of Wu-Fabula and Tulin double-spiral vortex termination models. Then two examples are presented showing how the linearized (outer) solution can be supplemented by a nonlinear local (inner) solution in the flow regions when the perturbations are not necessarily small. These examples include: a uniformly valid solution of a flow problem for a flat plate at an angle of attack (zero cavitation number) and of that for a plate with a spoiler at the trailing edge. Both examples employ the method of matched asymptotic expansions (MAE), [2]. This technique consists in finding a local (inner) solution in the appropriately stretched coordinates, blending it smoothly to the outer (linear) solution, and, eventually obtaining a uniformly valid solution by additive composition of the inner and outer solutions.

[1]The term "supercavitating", as understood here, implies that the cavity extends beyond the trailing edge of the foil

Paper presented at the RTO AVT Lecture Series on "Supercavitating Flows", held at the von Kármán Institute (VKI) in Brussels, Belgium, 12-16 February 2001, and published in RTO EN-010.

2. Linear solution of the problem of a supercavitating flow past a thin foil with different closure schemes

Consider a linear problem of a steady supercavitating flow past a flat plate with different closure schemes. In what follows all quantities and functions are rendered nondimensional with use of the chord c of the plate and the velocity of the incoming flow U_o. To avoid complicated derivations when explaining the essential points of the lecture, one assumes that the cavity detaches from a sharp leading edge of the supercavitating foil of zero thickness. In most of the examples, discussed herein, the foil is represented by a flat plate at at an angle of attack.

Assume that the flow perturbations are small. Expanding previous nonlinear formulation, one easily shows that the linear flow problem for the perturbation velocity potential $\varphi = \varphi(x, y)$ is governed by the following equations

- Laplace equation
$$\frac{\partial^2 \varphi}{\partial x^2} + \frac{\partial^2 \varphi}{\partial y^2} = 0, \qquad (x, y) \in \mathcal{D}; \tag{3}$$

- Flow tangency condition on the wetted part of the foil
$$\frac{\partial \varphi}{\partial y} = \frac{\mathrm{d}y_o}{\mathrm{d}x}, \quad y = 0 - 0, \quad x \in (0, 1), \tag{4}$$
or, for a flat plate $y_o(x) = -\alpha x$,
$$\frac{\partial \varphi}{\partial y} = -\alpha, \quad y = 0 - 0, \quad x \in (0, 1),$$
where α is angle of attack (in radians);

- On the boundary of the cavity
As the linearized pressure coefficient is approximately equal to
$$C_p = \frac{2(p - p_o)}{\rho U_o^2} \approx -2\frac{\partial \varphi}{\partial x}, \tag{5}$$
and the cavitation number σ is defined as
$$\sigma = \frac{2(p_c - p_o)}{\rho U_o^2}, \tag{6}$$
where p_c and p_o are pressures in the cavity and at the upstream infinity. Then, the perturbed horizontal velocity on the boundary of the cavity should be
$$\frac{\partial \varphi}{\partial x} = \frac{1}{2}\sigma, \quad y = 0 \pm 0, \quad x \in (0, l) \quad \text{and} \quad x \in (1, l), \tag{7}$$
where l is the cavity length measured from the leading edge of the foil and related to the chord of the foil;

- Condition at infinity
$$\nabla \varphi = \vec{i}\,\frac{\partial \varphi}{\partial x} + \vec{j}\,\frac{\partial \varphi}{\partial y} \to 0, \quad \text{for} \quad x^2 + y^2 \to \infty, \tag{8}$$
where $\vec{i}$ and $\vec{j}$ are unit vectors of the axes x and y correspondingly.

It should be noted that the linearization implies that both α and σ tend to zero at the same speed, i.e. $\sigma = \mathrm{O}(\alpha)$. In order to use powerful methods of the complex functions' theory it is convenient to re-write the flow problem formulation, described previously, in terms of complex variables and functions. Instead of the perturbation velocity potential $\varphi = \varphi(x, y)$, introduce a complex potential $F = F(z) = \varphi(x, y) + \mathrm{i}\,\psi(x, y)$, where $\mathrm{i} = \sqrt{-1}$ is an imaginary unit, $z = x + \mathrm{i}\,y$ and $\psi(x, y)$ is a stream function. In this case the solution of the problem is reduced to finding an analytic function $\mathrm{d}F/\mathrm{d}z = w(z) = u(x, y) - \mathrm{i}\,v(x, y)$ in the domain $\mathcal{D}$ of the flow with the following boundary conditions on the flow boundaries

- On the wetted part of the plate
$$\Im w(z) = -v(x, y) = \alpha, \quad y = 0 - 0, \quad x \in (0, 1); \tag{9}$$

- On the cavity

$$\Re w(z) = u(x,y) = \frac{1}{2}\sigma, \quad y = 0 \pm 0, \quad x \in (0,l) \quad \text{and} \quad x \in (1,l); \tag{10}$$

- At infinity

$$w(z) \to 0, \quad \text{for} \quad z \to \infty. \tag{11}$$

2.1. Cavity closure models with a square root singularity

In the nonlinear formulation this type of the cavity closure models is characterized by presence of a stagnation point in the region of cavity termination, i.e. that of Riaboushinsky and Efros-Gilbarg (see Fig. 1(1) and Fig. 1 (2)). As discussed in [1] a linear analogue for all such models contains a square root singularity near the point of the cavity termination. Consider a corresponding flow problem solution following [1].
The linearized "physical" complex plane z of the flow past a foil with a trailing cavity of finite length is illustrated in Fig. 2. Note that in this plane *the plate plus the cavity* are represented by a slit $y = 0 \pm 0, x \in [0,l]$. To solve the problem, map the exterior of the slit in the complex plane z onto the upper half of the auxiliary complex plane $\zeta = \xi + \mathrm{i}\,\eta$ (see Fig. 2) with help of the function

$$\zeta = -\mathrm{i}a\sqrt{\frac{z}{z-l}}, \qquad a = \sqrt{l-1}. \tag{12}$$

The inverse function, i.e. $z = z(\zeta)$, can be written as

$$z = \frac{l\zeta^2}{\zeta^2 + a^2}. \tag{13}$$

The correspondence of the points in z and ζ planes can be seen from Fig. 2. Note that the point $z = l$, which represents the closure point of the cavity in the "physical" plane, passes into a point $\zeta = \infty$ in the auxiliary halfplane $\Im\zeta = \xi < 0$. In fact, for $z \to l$

$$\zeta \approx -\mathrm{i}a\sqrt{\frac{l}{z-l}} \to \infty. \tag{14}$$

On the other hand, the infinity of the "physical" plane, i.e. $z = \infty$ passes into the point $\zeta = -\mathrm{i}a$. Eventually, the wetted part of the slip coincides with the interval $\xi \in (0,1)$ whereas the upper and the lower boundary of the cavity in z plane are mapped onto the negative $\eta = 0 - 0, \xi < 0$ and positive $\eta = 0 - 0, \xi \in (1,\infty)$ parts of the real axis in the auxiliary plane.
In the context of the closure models it is important to specify the anticipated behavior of the complex conjugate velocity $w(\zeta)$ in the vicinity of the cavity closure point. It can be shown that the linear analogues of the nonlinear closure models, containing a stagnation point within the cavity termination zone, are characterized by a square root singularity of the perturbed velocity at the corresponding closure point (i.e. at $z = l$). Assuming that

$$\text{for} \quad z \to l \quad w(z) \approx \frac{\kappa}{\sqrt{z-l}}, \tag{15}$$

Accounting for the expression (14), it means that in the auxiliary plane

$$w[z(\zeta)] \approx -\frac{\kappa\zeta}{\mathrm{i}a\sqrt{l}} = \mathrm{i}A\zeta, \tag{16}$$

where A is a real constant to be determined.
It is convenient to solve the boundary problem for the function

$$w^*(z) = w(z) - \frac{1}{2}\sigma, \tag{17}$$

For this function $\Re w^*(z) = 0$ on the boundary of the cavity, i.e. on $\eta = 0 - 0$, $\xi < 0$ and $1 < \xi < \infty$. The latter fact simplifies the final expression for the solution. Note that the boundary conditions for $w^*(\zeta)$ on the real axis of the auxiliary complex plane ζ are *mixed*, prescribing $\Im w^*(\zeta)$ on one part of the axis and $\Re w^*(\zeta)$ on another part of the axis, see Fig. 2.
Assuming a quarter-root singularity $w(z) = \mathrm{O}(z^{-1/4})$ at the leading edge and square root zero $w(z) = \mathrm{O}[(1-z)^{1/2}]$ at the trailing edge, and using Keldysh-Sedov formula, one can derive the solution for the complex conjugate velocity in the form

$$w(\zeta) = \frac{1}{2}\sigma + \frac{\alpha}{\pi}\sqrt{\frac{1-\zeta}{\zeta}}\int_0^1 \sqrt{\frac{\xi}{1-\xi}}\frac{\mathrm{d}\xi}{\zeta-\xi}\,\mathrm{d}\xi + B\sqrt{\frac{1-\zeta}{\zeta}} + A\sqrt{\zeta(1-\zeta)}. \tag{18}$$

Note that B and A are real constants to be determined, and the last term in the formula is a permissible solution accounting for the required behaviour of the function $w(\zeta)$ for $\zeta \to \mathrm{i}A\zeta$.
After integration, one can obtain

$$w(\zeta) = \frac{1}{2}\sigma + (B-\alpha)\sqrt{\frac{1-\zeta}{\zeta}} + A\sqrt{\zeta(1-\zeta)}. \tag{19}$$

The solution thus obtained contains three unknown (real) parameters a, B and A. The first relationship between these parameters can be obtained by applying the infinity condition (8). For $\zeta \to -\mathrm{i}a$ the conjugate complex velocity should equal zero, i.e.

$$w(-\mathrm{i}a) = 0, \tag{20}$$

The latter complex equation is equivalent to the two real equations

$$\Re w(-\mathrm{i}a) = 0, \qquad \Im w(-\mathrm{i}a) = 0. \tag{21}$$

The remaining relationship necessary to determine all three unknowns of the solution can be obtained from the closure condition, which, in other words, is a requirement that the cavity should have finite length. The corresponding equation can be written as

$$\oint_{\mathcal{L}_z} \Im[w(z)]\,\mathrm{d}z = \Im \oint_{\mathcal{L}_z} w(z)\,\mathrm{d}z = \Im \oint_{\mathcal{L}_\zeta} w(\zeta)\frac{\mathrm{d}z}{\mathrm{d}\zeta}\,\mathrm{d}\zeta = 0, \tag{22}$$

where contour $\mathcal{L}_z$ encloses the slit $y = 0 \pm 0, x \in (0, l)$ and is passed in the clockwise direction, and the contour $\mathcal{L}_\zeta$ encloses the point $\zeta = -\mathrm{i}a$ and is passed in the clockwise direction. The derivative $\mathrm{d}z/\mathrm{d}\zeta$ can be derived from the expression (13) in the form

$$\frac{\mathrm{d}z}{\mathrm{d}\zeta} = \frac{2l\zeta}{\zeta^2 + a^2} - \frac{2l\zeta^3}{(\zeta^2 + a^2)^2}. \tag{23}$$

Treating the equation (22) is reduced to calculation of the imaginary part of the residue of the function $w(\zeta)\mathrm{d}z/\mathrm{d}\zeta$ at the point $\zeta = -\mathrm{i}a$, i.e.

$$\Im \oint_{\mathcal{L}_\zeta} w(\zeta)\frac{\mathrm{d}z}{\mathrm{d}\zeta}\,\mathrm{d}\zeta = \Im\Big\{2\pi\mathrm{i}\,\mathrm{Res}\Big[w(\zeta)\frac{\mathrm{d}z}{\mathrm{d}\zeta}\Big]\Big|_{\zeta=-ia}\Big\}. \tag{24}$$

Calculating the residue with use of the Taylor series of $w(\zeta)$ in the vicinity of $\zeta = -\mathrm{i}a$

$$w(\zeta) = \frac{\mathrm{d}w}{\mathrm{d}\zeta}\Big|_{\zeta=-ia}(\zeta + \mathrm{i}a) + \mathrm{O}[(\zeta + \mathrm{i}a)^2] \tag{25}$$

and the expression for the derivative of the inverse mapping function $z = z(\zeta)$, one comes to the following form of the equation (22)

$$\Im\Big\{\frac{\mathrm{d}w}{\mathrm{d}\zeta}\Big|_{\zeta=-ia}\Big\} = 0. \tag{26}$$

The lift coefficient can be derived by integrating the pressure over the slit in the "physical" plane, so that

$$C_y = \frac{2Y}{\rho U_o^2 c} = 2\Re \oint_{\mathcal{L}_z} w(z)\,\mathrm{d}z = 2\Re \oint_{\mathcal{L}_\zeta} w(\zeta)\frac{\mathrm{d}z}{\mathrm{d}\zeta}\,\mathrm{d}\zeta. \tag{27}$$

Similarly to the previous derivations leading to the equation (22), the calculation of the lift coefficient is reduced to that of the real part of the residue of the function $w(\zeta)\mathrm{d}z/\mathrm{d}\zeta$, which yields

$$C_y = 2\pi l a \Re\Big\{\frac{\mathrm{d}w}{\mathrm{d}\zeta}\Big|_{\zeta=-ia}\Big\} \tag{28}$$

The results obtained for the case of a flat plate at an angle of attack α have quite a simple form. After some algebra the expression for the lift coefficient becomes

$$Cy = \pi\alpha l\Big(\frac{\sqrt{l}}{\sqrt{l-1}} - 1\Big), \tag{29}$$

The relationship between cavitation number and length of the cavity is given by the formula

$$\bar{\sigma} = \frac{\sigma}{\alpha} = \frac{2}{a} = \frac{2}{\sqrt{l-1}}. \tag{30}$$

Note that both of the proceeding formulae imply that $l > 1$. Using the expressions, describing parametric dependences of the lift coefficient and the ratio σ/α on the nondimensional length of the cavity l, one can obtain the following formula

$$\frac{C_y}{\alpha} = \pi\Big(\sqrt{\frac{4}{\bar\sigma^2}+1} - \frac{2}{\bar\sigma}\Big)\Big(\frac{\bar\sigma}{2}+\frac{2}{\bar\sigma}\Big) \tag{31}$$

2.2. Wu-Fabula closure model

The solution, corresponding to Wu-Fabula cavity closure model (see Fig. 1(4)), can be easily derived from the previous solution by requiring a "smooth" termination at the point $z = l$, or $\zeta = \infty$. This is achieved by putting the real constant A equal to zero. The corresponding linearized "physical" plane is shown in Fig. 3. The resulting expressions for the lift coefficient and the ratio $\bar\sigma = \sigma/\alpha$ versus nondimensional length of the cavity are given by the formulae

$$\frac{C_y}{\alpha} = \frac{\pi\sqrt{l}}{\sqrt{l}+\sqrt{l-1}}, \tag{32}$$

$$\bar\sigma = \frac{\sigma}{\alpha} = \frac{2}{\sqrt{l}+\sqrt{l-1}}. \tag{33}$$

2.3. Tulin double spiral-vortex cavity closure model

In the double spiral-vortex model introduced by Tulin (Fig. 1(3)) it is assumed that the cavity termination is followed by a wake extending to the downstream infinity, [1]. Therewith, the cavity pressure turns abruptly into that of unperturbed flow. The corresponding linearized flow problem formulation is shown in Fig. 4. Note, that the linearization implies that the abscissas of the cavity termination points on the upper and the lower "banks" of the cut are identical. To formulate the relevant boundary problem for the perturbed conjugate complex velocity, map the exterior of the semi-infinite cut in the "physical" plane z onto the lower half plane $\Im\zeta = \xi < 0$ of the auxiliary plane ζ. This can be done by means of the function

$$\zeta = -\sqrt{z} \tag{34}$$

where the selected branch of the root transfers the point $z = 1 + \mathrm{i}(0-0)$ into the point $\zeta = -1 + \mathrm{i}(0+0)$. The correspondence of the points in z and ζ complex planes is indicated in Fig. 4. Note, that the termination points of the cavity $z = l + \mathrm{i}(0 \mp 0)$ are mapped respectingly into the points $\zeta = \pm b$, where $b = \sqrt{l}$. The boundary conditions for the conjugate complex velocity $w(\zeta)$ on the real axis $\Re\zeta = \xi$ of the auxiliary plane are shown in Fig. 4. Using Keldysh-Sedov formulae to solve this mixed boundary problem, one can derive the following expression

$$w(\zeta) = \frac{\alpha}{\pi}\sqrt{\frac{1-\zeta}{\zeta}}\int_0^1 \sqrt{\frac{\xi}{1-\xi}}\frac{\mathrm{d}\xi}{\zeta-\xi} + \frac{\sigma}{2\pi}\sqrt{\frac{1-\zeta}{\zeta}}\Big(\int_1^b + \int_{-b}^0\Big)\sqrt{\frac{\xi}{\xi-1}}\frac{\mathrm{d}\xi}{\zeta-\xi} + B\sqrt{\frac{1-\zeta}{\zeta}}, \tag{35}$$

where B is a real constant to be determined. Integrating, one obtains

$$w(\zeta) = (B-\alpha)\sqrt{\frac{1-\zeta}{\zeta}} + \frac{\sigma}{2\pi}\sqrt{\frac{1-\zeta}{\zeta}}\Big[\mathcal{F}(\zeta,\xi)\Big|_1^b + \mathcal{F}(\zeta,\xi)\Big|_{-b}^0\Big] + \mathrm{i}\alpha, \tag{36}$$

where

$$\mathcal{F}(\zeta,\xi) = \int\sqrt{\frac{\xi}{\xi-1}}\frac{\mathrm{d}\xi}{\zeta-\xi} = -2\ln\frac{\sqrt{\xi}+\sqrt{\xi-1}}{\sqrt{2}} + 2\sqrt{\frac{\zeta}{\zeta-1}}\ln\frac{\sqrt{\zeta(\xi-1)}+\sqrt{\xi(\zeta-1)}}{\sqrt{\zeta-\xi}} \tag{37}$$

Requiring that the perturbations vanish at the infinity, one obtains $B = 0$. After some additional algebra the expression for $w(\zeta)$ acquires the following form

$$w(\zeta) = \mathrm{i}\alpha\Big(1-\sqrt{\frac{\zeta-1}{\zeta}}\Big) - \frac{\mathrm{i}\sigma}{2\pi}\Big[2\sqrt{\frac{\zeta-1}{\zeta}}\ln\frac{\sqrt{b}+\sqrt{b-1}}{\sqrt{b}+\sqrt{b+1}} + \ln\frac{\zeta+b}{\zeta-b} + 2\ln\frac{\sqrt{\zeta(b-1)}+\sqrt{b(\zeta-1)}}{\sqrt{\zeta(b+1)}+\sqrt{b(\zeta-1)}}\Big] \tag{38}$$

Finally, the expression for the lift coefficient is obtained as

$$\frac{Cy}{\alpha} = \bar{\sigma} b \sqrt{b}(\sqrt{b+1} - \sqrt{b-1}), \quad \bar{\sigma} = \frac{\sigma}{\alpha} \tag{39}$$

where $b = \sqrt{l}$. The ratio $\bar{\sigma}$ versus l is described by the following formula

$$\frac{1}{\bar{\sigma}} = \frac{\alpha}{\sigma} = \frac{1}{\pi}\Big[\sqrt{b}(\sqrt{b-1} + \sqrt{b+1}) - \ln\frac{\sqrt{b}+\sqrt{b+1}}{\sqrt{b}+\sqrt{b-1}}\Big] \tag{40}$$

The previous two expressions can be viewed as a parametric dependence of the lift coefficient upon cavitation number and angle of attack, or rather as C_y/α as a function of σ/α for the linear supercavitating flow past a flat plate with a Tulin double spiral-vortex cavity closure scheme. Note that in order to find the relationship between the cavitation number σ and the length l of the cavity, it was assumed herein that the total drag of the cavity+wake system should be equal to zero. The latter statement can be formally expressed as

$$\Im \oint\limits_{\zeta=\infty} w^2(\zeta)\frac{\mathrm{d}z}{\mathrm{d}\zeta}\,\mathrm{d}\zeta = 0. \tag{41}$$

The corresponding calculation is reduced to finding the resudue of the integrand at the infinity in the auxiliary plane ζ.
Plotted in Fig. 5 are curves of lift coefficient related to angle of attack versus cavitation number related to angle of attack, i.e. $C_y/\alpha = f(\sigma/\alpha)$ for different linear analogues of the cavity closure scheme for the case of a flat plate. Presented in the Figure are the results:

1. For Tulin open closure scheme featuring two double-spiral vortices,
2. For a cavity scheme with a square-root singularity of perturbation velocity at the cavity termination points, and
3. Wu-Fabula cavity closure scheme (no singularity at the cavity termination point)

Plotted in the same Figure are experimental points, obtained by F.F. Bolotin and E.B. Anoufriev for a series of segment foils with different relative thickness $4.2, 5$ and 6%, [3]. It should be noted that in the case of the developed cavitation starting from the leading edge, the flow past the segment foil is equivalent to that of the flat plate. It follows from the comparison of test data with the calculated results that the correlation is fair not only for the case of developed cavitation (long cavities), but also for the transitional regime when $1 \le l \le 1.5$. Tulin double-spiral vortex scheme provides satisfactory results for the lift coefficient of flat plate up to $\sigma/\alpha \approx 6$, i.e. practically up the boundary of supercavitation. The experimental points are seen to be located between the schemes 1) and 2). Wu-Fabula scheme allows to obtain the magnitudes of C_y/α only for $\sigma/\alpha < 2$, i.e. for sufficiently long cavities. For σ/α close to 2, Wu-Fabula scheme gives somewhat excessive magnitudes of the lift coefficient.

2.4. The case of zero cavitation number - analogy with a fully wetted foil.

The simplest albeit practical case corresponds to zero cavitation number. Therewith the cavity becomes semi-infinite. The "physical" flow domain in z-plane is transformed onto an auxiliary lower half-plane $\Im\zeta = \eta < 0$ with the mapping function $\zeta = -\sqrt{z}$, discussed previously. As before, one can easily construct the solution of the ensuing boundary problem for $w(\zeta)$ with use of the Keldysh-Sedov formula. Restricting the analysis to the case of a flat plate, one comes to the following simple formula

$$w(\zeta) = \alpha\Big(\mathrm{i} - \sqrt{\frac{1-\zeta}{\zeta}}\Big), \tag{42}$$

which satisfies the requirement that the perturbed velocity should vanish at the infinity. The latter property of (42) can be easily verified. In fact for large $z \to \infty, \zeta \to \infty$

$$\sqrt{\frac{1-\zeta}{\zeta}} = \mathrm{i}\Big[1 - \frac{1}{2\zeta} + \mathrm{O}\Big(\frac{1}{\zeta^2}\Big)\Big], \quad w(\zeta) \sim \frac{\mathrm{i}}{2\zeta} \to 0. \tag{43}$$

In particular, the perturbed velocity distribution on the wetted (lower) side of the plate ($\zeta \to \xi - \mathrm{i}0, \xi \in (0,1)$) becomes

$$u(\xi, 0-0) = -\alpha\sqrt{\frac{1-\xi}{\xi}}, \tag{44}$$

Referring to the classical theory of a thin foil, one can conclude that the above result coincides with the perturbed velocity distribution on the lower side of a flat plate placed in a uniform flow in ζ-plane. This suggests a concept of an equivalence, existing between the original supercavitating flow in z plane and a fictitious non-cavitating (fully wetted) flow in ζ-plane, which was first indicated by Tulin.
It should be noted that since the fluid domain has been mapped entirely into the lower part of the ζ-plane, the region $\Im\zeta = \eta > 0$ has no physical significance. Mathematically, it can be regarded as the second Riemann sheet of the z-plane, or as the domain of the cavity. Owing to the fact that on the boundary of the cavity in ζ plane the real part of the conjugate complex velocity $w(\zeta)$ is zero, one can use the Schwartz reflection principle to continue $w(\zeta)$ across the real axis $\Re\zeta = \xi$ (excluding the cut $\xi \in (0,1)$), provided u is an odd function of η. To ensure that $w(\zeta) = u(\xi,\eta) + \mathrm{i}v(\xi,\eta)$ is analytic in the entire ζ-plane, it follows from the Cauchy-Riemann equations that v should be an even function of η. Thus, the appropriate reflections into the upper half-plane of ζ are given by

$$u(\xi,\eta) = -u(\xi,-\eta), \tag{45}$$

$$v(\xi,\eta) = v(\xi,-\eta) \tag{46}$$

The reflected boundary-value problem shown is mathematically identical to the lifting problem of a fully wetted thin foil. In both cases a Kutta-Zhukovsky condition should be imposed at the trailing edge, and the perturbation velocity should vanish at the infinity. *Thus, the solution of the supercavitating flow problem ($\sigma = 0$) in the complex plane z written in auxiliary complex variable ζ is identical to that of a fully wetted foil in ζ-plane.* This analogy enables to obtain the coefficients of hydrodynamic forces and moments of the supercavitating foil from those of a fictitious fully wetted foil. For example, to obtain the lift coefficient C_y of the supecavitating flat plate, one has to integrate the pressure coefficient along the wetted part of the plate, i.e.

$$C_y = \frac{2Y}{\rho U^2 c} = \int_0^1 C_p(x, 0-0)\,\mathrm{d}x = -2\int_0^1 u(x,0-0)\,\mathrm{d}x. \tag{47}$$

Passing over to the integration in ζ-plane ($x = \xi^2$), one derives from the previous line

$$C_y = -2\int_0^1 u(x,0-0)\,\mathrm{d}x = -2\int_0^1 u(\xi,0-0)\frac{\mathrm{d}x}{\mathrm{d}\xi}\,\mathrm{d}\xi == -4\int_0^1 u(\xi,0-0)\xi\,\mathrm{d}\xi \tag{48}$$

Accounting for the adopted reflection of u into the upper half-plane ζ, one can re-write (48) in the following way

$$C_y = -4\int_0^1 u(\xi,0-0)\xi\,\mathrm{d}\xi = 2\int_0^1 [u(\xi,0+0) - u(\xi,0-0)]\xi\,\mathrm{d}\xi =$$

$$\int_0^1 [C_p(\xi,0-0) - C_p(\xi,0+0)]\xi\,\mathrm{d}\xi = C_{m_\zeta}, \tag{49}$$

where C_{m_ζ} is a coefficient of the longitudinal hydrodynamic moment of a fictitious fully wetted foil of length $c_\zeta = \sqrt{c}$ in ζ-plane. This coefficient, calculated with respect to the leading edge of the fictitious plate, is defined as

$$C_{m_\zeta} = \frac{2M_\zeta}{\rho U^2 c_\zeta^2} = \frac{2M_\zeta}{\rho U^2\sqrt{c}\sqrt{c}}. \tag{50}$$

Similarly, one can show that the coefficient of the longitudinal hydrodynamic moment of a supercavitating foil ($\sigma = 0$) is equal to the coefficient of the third moment of the fictitious fully wetted foil.

$$C_m = \int^1 C_p(x,0-0)x\,\mathrm{d}x = \int_0^1 [C_p(\xi,0-0) - C_p(\xi,0+0)]\xi^3\,\mathrm{d}\xi \tag{51}$$

It can also be shown that the drag coefficient for the supercavitating foil can be found as

$$C_x = \frac{1}{8\pi}C_{y_\zeta}^2 \tag{52}$$

This useful equivalence was first established by Tulin and Burkart in 1955. For a supercavitating flat plate ($\sigma = 0$) at a given angle of attack α the corresponding calculations give

$$C_y = \frac{\pi\alpha}{2}, \quad C_m = \frac{5\pi\alpha}{32}, \quad C_x = \frac{\pi\alpha^2}{2} \tag{53}$$

It is interesting that the lift coefficient for the supercavitating flat plate is four times less than that of the fully wetted plate and two times less that for the case of a flat plate gliding on the surface. In comparison to the fully wetted flat plate, here the centre of pressure is shifted from the quarter-chord point to a position 5/16

of the chord downstream from the leading edge. Note that the drag coefficient of the supercavitating plate is seen to be equal to $C_y\alpha$, i.e. the total force is normal to the plate. This is different from the fully wetted case, where, according to D'Alembert paradox, the vector of the force, acting upon the foil, is strictly vertical due to the suction force at the leading edge and the resulting drag is zero. In the supercavitating case there is no suction force, since the square root singularity of the equivalent fully-wetted flow in the ζ-plane is reduced to a quarter-root singularity in the physical z-plane.

3. Uniformly valid asymptotic solution of the problem for the flow past a supercavitating flat plate

The linear theory reveals a quarter-root singularity of the perturbation velocity at the leading edge of a supercavitating foil. This defficiency can be corrected by a special consideration of the local region of the flow near the leading edge, as first done in [4].

3.1. Linear solution as a leading order outer expansion

Consider the perturbation velocity distribution along the wetted (lower) side of the supercavitating ($\sigma = 0$) flat plate, following from (44). In the auxiliary variable $\Re\zeta = \xi \in (0, 1)$ the horizontal component of w equals to

$$u(\xi, 0-0) = \Re w(\zeta) = -\alpha\sqrt{\frac{1-\xi}{\xi}} \tag{54}$$

As follows from the mapping function $\zeta = -\sqrt{z}$ the real variables x and ξ are related to each other as

$$\xi = \mp\sqrt{x}, \quad \text{for} \quad y = 0 \pm 0 \tag{55}$$

so that on the wetted side of the supercavitating plate $x \in (0, 1), y = 0-0$ the expression (54) can be re-written in terms of "physical" x coordinate

$$u(x, 0-0) = -\alpha\sqrt{\frac{1-\sqrt{x}}{\sqrt{x}}} \tag{56}$$

This expression shows explicitly the quarter-root singularity of the perturbation velocity (pressure) in the vicinity of the leading edge of the wetted side of the supercavitating flat plate. In fact, for $x \to 0+0$

$$u(x, 0-0) = -\frac{1}{2}\, C_p(x, 0-0) \sim -\alpha x^{-1/4} \tag{57}$$

Considering this linear theory solution as an *outer* expansion of a complete solution of a nonlinear problem for a flow past a supercavitating flat plate for $\alpha \to 0$, i.e.

$$u(x, 0-0) = u^o(x, \alpha) = \alpha u_1^o(x) + \mathrm{O}(\alpha^2), \quad u_1^o(x) = \mathrm{O}(1) \tag{58}$$

one can note that this asymptotic expansion loses uniform validity for sufficiently small x when the product $\alpha u_1^o(x)$ acquires the order of O(1). This takes place at distances from the leading edge of the order of $x = \mathrm{O}(\alpha^4)$. For the purpose of further analysis, one would need to have the expression for the ordinates of the upper boundary of the cavity from the linear theory. Recalling that for $z = x + \mathrm{i}(0+0), x > 0$ the ξ and x coordinates are related as $\xi = -\sqrt{x}, \xi < 0$, one arrives at the following *outer* expression for the vertical component of the conjugate complex perturbation velocity

$$v(x, 0+0) = \Im w(x) = v^o(x, \alpha) = -\alpha\Big(1 - \sqrt{\frac{1+\sqrt{x}}{\sqrt{x}}}\Big) =$$

$$-\alpha + \alpha v_1^o(x, 0+0) + \mathrm{O}(\alpha^2), \quad v_1^o = \mathrm{O}(1) \tag{59}$$

The *outer* expansion for the ordinates of the upper boundary of the cavity, measured with respect to the plate can be determined with use of the following formula

$$y_c^o(x, 0+0) = \alpha \int_0^x v_1^o(x, 0+0)\, \mathrm{d}x + \mathrm{O}(\alpha^2) = \alpha y_1^o(x, 0+0) + \mathrm{O}(\alpha^2). \tag{60}$$

Integrating this expression with account of the formula for $v_1^o(x, 0+0)$ gives the following expression for the *outer* contour of the upper boundary of the cavity

$$y_c^o(x, 0+0) \sim \alpha y_1^o(x, 0+0) = \frac{\alpha}{2}[(1+2\sqrt{x})\sqrt{x+\sqrt{x}} - \ln(\sqrt{1+\sqrt{x}} + \sqrt{\sqrt{x}})] \tag{61}$$

3.2. Inner expansion in the vicinity of the leading edge

As follows from the preceeding estimates, the linear solution is not valid in the vicinity of the leading edge of the supercavitating plate, having dimensions of the order of $\mathrm{O}(\alpha^4)$. As a result of this nonuniformity the pressure on the wetted side at the leading edge becomes unrealistically infinite. This also means that within the initial characteristic scale of the order of the length of the plate the stagnation point, located close to the leading edge is invisible. In order to the flow near this edge in more detail, introduce local (stretched) coordinates

$$X = \frac{x}{\alpha^4}, \quad Y = \frac{y}{\alpha^4}, \qquad Z = X + \mathrm{i}Y = \frac{z}{\alpha^4} \tag{62}$$

In these *inner* variables for $\alpha \to 0$ the training edge of the plate recedes to the infinity and the *inner* flow becomes as shown in Fig. 6. For zero cavitation number this flow is completely characterized by the distance s of the stagnation point from the leading edge of the plate. The inner problem is solved with use of the velocity hodograph method and conformal mappings.
Introduce the hodograph variable

$$r = \frac{1}{w^i} = \frac{\exp \mathrm{i}\theta}{q}, \tag{63}$$

where $w^i(Z, \alpha)$ is the conjugate complex velocity (of relative fluid motion) in the inner region of the flow, $q = |w^i|$ and $\theta = -\arg w^i$. To be able to determine the flow pattern in the nearfield using hodograph complex plane, one requires additionally an estimation of the behaviour of the angle θ of the tangent to the (upper) boundary of the cavity at the downstream infinity. Essentially, this is equivalent to estimating of the one-term *inner* limit of the one-term *outer* expansion. Replacing the *outer* variables in the expression (61), by the *inner* variables, i.e. $x = \alpha^4 X$ and $y = \alpha^4 Y$, and expanding for $X = \mathrm{O}(1)$ and $\alpha \to 0$, one obtains

$$y(x) = y(\alpha^4 X)\Big|_{\alpha \to 0} = y_c^{oi}(X, \alpha) =$$

$$\alpha^4 \Big[\frac{4}{3} X^{3/4} + \frac{2}{5} \alpha^2 X^{5/4} - \frac{1}{14} \alpha^4 X^{7/4} + \mathrm{O}(\alpha^6) \Big] \tag{64}$$

wherefrom the one-term *inner* expansion of the cavity contour in the form

$$Y = \frac{y_c^{oi}(X, \alpha)}{\alpha^4} = \frac{4}{3} X^{3/4} + \mathrm{O}(\alpha^2) \tag{65}$$

The inclination of this curve for $X \to \infty$ tends to zero, so that one can assume that $\theta = 0$ at the downstream infinity. The hodograph plane, shown in Fig. 7, is then transformed onto an auxiliary plane ζ in such a way that the images of the plate and the cavity be found on the real axis $\Im\zeta = \xi$, see Fig. 7.

$$\zeta = \frac{1}{2}\Big(r + \frac{1}{r}\Big). \tag{66}$$

To complete the procedure of obtaining the inner solution it is necessary to relate the complex potential *of relative motion* of the fluid

$$F^i = \varphi + \mathrm{i}\psi, \tag{67}$$

where φ and ψ are correspondingly the velocity potential and stream function (of relative motion) with the function w^i by means of an intermediate complex plane ζ. The complex potential plane F^i, shown in Fig. 7, is transformed onto ζ-plane with help of the function

$$F^i = \frac{A_i}{(\zeta - 1)^2}, \tag{68}$$

where A_i is a real constant. Using formulae (63) and (66), one comes to the following relationship

$$w^i = \zeta \pm \sqrt{\zeta^2 - 1}, \tag{69}$$

where the *plus* sign is used for $|\zeta| < 1$, and the *minus* sign should be taken for $|\zeta| \geq 1$.
The relationship between Z and w^i through complex variable ζ can be derived in the following way

$$\int_{Z_1}^{Z_2} \mathrm{d}Z = Z_2 - Z_1 = \int_{\zeta_1}^{\zeta_2} \frac{\mathrm{d}F^i}{\mathrm{d}\zeta} \frac{\mathrm{d}\zeta}{w^i}. \tag{70}$$

Using formulae (68) and (69) in combination with (70) and integrating from the leading edge to the stagnation point, one finds

$$A_i = \frac{12}{17}\,a \tag{71}$$

Making use of (70) one can find the following relationship between Z and $\zeta = \xi$ on the plate and the cavity in the following form

- On the plate, for $0 \le X \le a$,Y=0-0

$$\frac{X}{a} = \frac{24}{17}\Big[\frac{1}{2(\xi-1)^2} + \frac{1}{\xi-1} - \frac{1}{3}\frac{(\xi^2-1)^{3/2}}{(\xi-1)^3} + \frac{3}{8}\Big] \tag{72}$$

- On the plate, for $a \le X \le \infty$,Y=0-0

$$\frac{X}{a} = 1 + \frac{24}{17}\Big[\frac{1}{2(\xi-1)^2} + \frac{1}{\xi-1} + \frac{1}{3}\frac{(\xi^2-1)^{3/2}}{(\xi-1)^3} - \frac{1}{3}\Big] \tag{73}$$

- On the cavity, $-1 \le \xi \le 1$

$$\frac{Z}{a} = \frac{X}{a} + \mathrm{i}\frac{Y}{a} = \frac{24}{17}\Big[\frac{1}{2(\xi-1)^2} + \frac{1}{\xi-1} + \frac{3}{8} + \frac{\mathrm{i}}{3}\frac{(1-\xi^2)^{3/2}}{(1-\xi)^3}\Big] \tag{74}$$

The latter equation provides a parametric relationship between $Y = Y(\xi)$ and $X = X(\xi)$ on the cavity contour in inner variables.
Having determined the relationship $Z = Z(\zeta)$, described by (70), with account of (69) and (70) one can find an implicit expression for distribution of the velocity along the plate in the inner region

$$\frac{X}{a} = \frac{24}{17}\Big[\frac{2(u^i)^2}{(1-u^i)^4} + \frac{2u^i}{(1-u^i)^2} + \frac{1}{3}\Big(\frac{1+u^i}{1-u^i}\Big)^3 + \frac{3}{8}\Big], \quad \text{for} \quad 0 \le X \le a, \quad Y = 0-0; \tag{75}$$

and

$$\frac{X}{a} = 1 + \frac{24}{17}\Big[\frac{2(u^i)^2}{(1-u^i)^4} + \frac{2u^i}{(1-u^i)^2} + \frac{1}{3}\Big(\frac{1+u^i}{1-u^i}\Big)^3 - \frac{1}{3}\Big], \quad \text{for} \quad a \le X < \infty, \quad Y = 0-0. \tag{76}$$

3.3. Matching and additive composition

To determine the parameter a, entering the inner solution, one uses the *Van-Dyke asymptotic matching principle*, [2]. First of all, find a one-term inner representation of the two-term outer solution[2]

$$u^o \sim u^{oi} \sim 1 - \frac{\alpha}{x^{1/4}}. \tag{77}$$

On the other hand, take the outer representation of (75), (76) for u^i. Introducing $x = \alpha^4 X$, one can write

$$u^i \sim 1 - \alpha u_1^i + \mathrm{O}(\alpha^2). \tag{78}$$

Substituting this expression into (75) and (76) expanding it for $\alpha \to 0$ and x =fixed, one has

$$u^i \sim u^{io} \sim 1 - \alpha\Big(\frac{48a}{17x}\Big)^{1/4}. \tag{79}$$

Comparing formulae (77) and (79) gives

$$a = \frac{17}{48} \tag{80}$$

wherefrom one can see that the distance of the stagnation point from the leading edge is equal to $\alpha^4/4$.
Uniformly valid expression for the velocity u^c on the wetted side of the plate can be found by means of the additive composition of the outer (56) and inner (75),(76) solution, The latter procedure implies adding these solutions and substracting their common part (77), i.e.

$$u^c = u^i + u^o - u^{io} = u^i + u^o - u^{oi} = u^i - \frac{\alpha\sqrt{\sqrt{x}}}{1 + \sqrt{1-\sqrt{x}}} \tag{81}$$

The uniformly valid distribution of the pressure coefficient is calculated by means of the formula

$$\bar{C}_p^2 = 1 - (u^c)^2 \tag{82}$$

Figures 8 and 9 illustrate comparison of the pressure distributions, calculated using the formula (82) and the exact solution for $\alpha = 10^o$. The results of the linear theory are plotted with dot-and-dash line. The upper cavity shape (in stretched coordinates) in the immediate vicinity of the trailing edge of the supercavitating plate is shown in Fig. 10.

[2] Adding preliminarily the velocity of the incoming flow

4. Supercavitating foil with a spoiler

As another example of how the matched asymptotics technique can be used to complement the outer (linear) expansion of the solution in a local region of large flow perturbations is that of a flow past a supercavitating plate with a spoiler, [5], [6]. The spoiler is represented by a plate of a small relative height mounted upon the lifting surface either at the trailing edge on the pressure side or at an appropriate station on the suction side. The spoiler is usually oriented normally to the oncoming stream. The presence of the spoiler results both in local pressure rise due to creation of the stagnation zone in its vicinity, and redistribution of pressures around the entire foil, and, eventually, the additional lift occurs. Experiments of recent years have shown that the spoiler is one of the most effective, yet relatively simple devicess to enhance the lifting capacity of the supercavitating hydrofoils as well as the thrust of the supercavitating screw propellers. It is worth mentionning that Professor Tulin marked spoilers on one of the branches of his famous family tree of supercavitating flow theory, [6].

In the example below, considered is the case of a two-dimensional flow past a supercavitating foil with a spoiler of a small relative width ε at a trailing edge. For the sake of illustrating the procedure, the simplest case of zero cavitation number is considered. In the outer region (far from the spoiler in terms of its length) appropriate linear solutions are used incorporating an admissible (square root) singularity of unknown strength at the trailing edge. In the inner region (in the vicinity of the spoiler) the problem is reduced to that of a Kirchhoff type separated flow past a symmetric wedge. Asymptotic matching of the outer and inner solutions permits to determine hydrodynamic characteristics of the supercavitating foil with the spoiler.

Let the supercavitating foil be slightly curved and oriented to the flow at a small angle of attack α. As per foregoing, assume that the cavitation number $\sigma = 0$. The spoiler has a small relative width $\varepsilon << 1$ and is oriented at an arbitrary angle β to the foil at the trailing edge.

4.1. Flow near the spoiler (inner problem)

In the region near the spoiler introduce stretching of the local independent variables

$$X = \frac{x-1}{\varepsilon}, \qquad Y = \frac{y}{\varepsilon}, \qquad Z = X + \mathrm{i}Y. \tag{83}$$

Assume that the distance from the flow boundaries is of the order of the chord, i.e. O(1). Then, the pattern of the local flow does not depend on the type or on the number of the boundaries. It does not depend either on the distance of the trailing edge from the flow boundaries, and represents a flow past a semi-infinite horisontal flat plate with a spoiler of a unit width. Analytic continuation of this flow into the upper half-plane leads to a problem for a separated flow of unit velocity past a symmetric wedge. The solution of this classical problem can be obtained by the methods of the jet theory in an ideal fluid. Following [7] find the conjugate complex velocity $w^i(Z)$, by mapping the complex potential plane $F^i(Z) = \varphi^i + \mathrm{i}\psi^i$[3] and the logarithmic velocity hodograph plane $\omega = -\ln w = -\ln|w| + \mathrm{i}\theta$ upon auxiliary plane t (Fig. 11):

$$F(Z) = \varphi_o t^2, \qquad \omega = \frac{2\beta}{\pi}\ln\Big(\sqrt{1-\frac{1}{t^2}} + \frac{\mathrm{i}}{t}\Big), \tag{84}$$

where φ_o is a parameter related to the wedge angle β (in radians) by means of the following relationship

$$\varphi_o = \Big[2\int_0^1 \Big(\frac{\sqrt{1-t^2}+1}{t}\Big)^{2\beta/\pi} t\,\mathrm{d}t\Big]^{-1} \tag{85}$$

For better convergence of the integral in the denominator it is practical to to use it in the following alternative form

$$\int_0^1 \Big(\frac{\sqrt{1-t^2}+1}{t}\Big)^{2\beta/\pi} t\,\mathrm{d}t =$$

$$\int_0^1 t^{(1-2\beta/\pi)}\Big[\Big(\sqrt{1-t^2}+1\Big)^{2\beta/\pi} - 2^{2\beta/\pi}\Big]\,\mathrm{d}t + \frac{2^{2\beta/\pi-1}}{\pi-\beta/\pi} \tag{86}$$

The coordinates of the free boundary of the cavity, detaching from the spoiler (lower cheek of the wedge) can be calculated with use of the formula

$$Z = 2\varphi_o\int_{-1}^{t}\Big(\frac{\sqrt{1-t^2}+1}{t}\Big)^{2\beta/\pi} t\,\mathrm{d}t + \exp(-\mathrm{i}\beta) \tag{87}$$

[3] of relative fluid motion

In order to perfom the matching of the inner solution to the outer solution one has to obtain the asymptotics of the inner solution far the spoiler. With the purpose to perform the matching of the ordinates of the free boundary of the cavity[4] find the asymptotics of the free boundary for $X \to \infty$, $(t \to -\infty)$

$$Z(t) = X(t) + \mathrm{i}Y(t) \sim 2\varphi_o\Big(\frac{1}{2}t^2 + \frac{2\mathrm{i}\beta}{\pi}t\Big) + C^* \tag{88}$$

where

$$C^* = 2\varphi_o \int_1^\infty \Big[\Big(\sqrt{1-\frac{1}{\tau^2}} - \frac{\mathrm{i}}{\tau}\Big)^{2\beta/\pi} - 1\Big]\,\tau\,\mathrm{d}\tau \tag{89}$$

wherefrom

$$Y = \frac{y}{\varepsilon} \sim -\frac{4\beta}{\pi}\sqrt{\varphi_o X}, \quad \text{for} \quad X \to +\infty \tag{90}$$

Besides, estimating the outer limit of the inner solution, one can show that the outer description of the conjugate complex velocity has a square-root singularity at the point $x = 1$. In fact, expanding $w(t)$ and $Z(t)$ for large t, one can obtain

$$Z(t) \sim \varphi_o t^2 + \mathrm{O}(t), \tag{91}$$

and

$$w^i(t) = \exp\left[-\omega^i(t)\right] = \Big(\sqrt{1-\frac{1}{t^2}} + \frac{i}{t}\Big)^{-2\beta/\pi} \sim 1 - \frac{2\mathrm{i}\beta}{\pi t} + \mathrm{O}(\frac{1}{t^2}) \tag{92}$$

Excluding the auxiliary variable t from these two expressions, one can find

$$w^i(Z) = \frac{\mathrm{d}F^i}{\mathrm{d}Z} \sim 1 - \frac{2\mathrm{i}\beta\sqrt{\varphi_o}}{\pi\sqrt{Z}}, \qquad Z \to \infty \tag{93}$$

On the foil

$$Z = X = \frac{x-1}{\varepsilon} \tag{94}$$

Finally, one can evaluate the behaviour of w on the foil near the trailing edge

$$w \sim -\frac{2\beta\sqrt{\varphi_o}\sqrt{\varepsilon}}{\pi\sqrt{1-x}}, \quad \text{for} \quad x \to 1-0 \tag{95}$$

4.2. The outer (linearized) flow

For the simplest case of zero cavitation number ($\sigma = 0$) and angle of attack $\alpha << 1$ the flow field outside of the vicinity of the spoiler experiences small perturbations. The corresponding linear solution for the conjugate complex velocity can be written in the form

$$w(\zeta) = \alpha\Big(\mathrm{i} - \sqrt{\frac{1-\zeta}{\zeta}}\Big) - \frac{\mathrm{i}B_s}{\sqrt{\zeta(\zeta-1)}}, \tag{96}$$

Note that the foregoing expression differs from the solution for the foil without spoiler (42) by the last term, where B_s is a real constant. This latter term represents an admissible solution of the corresponding Riemann-Hilbert mixed boundary problem which

- has zero real part on $\zeta = \xi > 1$ and $\zeta = \xi < 0$, i.e. on the boundary of the cavity
- has zero imaginary part on $1 > \zeta = \xi > 0$, i.e. on the wetted part of the foil
- yields a square root singilarity of the type $1/\sqrt{x-1}$ at the point $\zeta = \xi = 1-0$, corresponding to the point $x = 1-0$. In other words, such a solution secures matching of the outer solution with the inner solution, discussed above

  In fact near that point ($\xi \to 1-0$, and $x \to 1-0$) the "spoiler" term behaves as

$$-\frac{\mathrm{i}B_s}{\sqrt{\xi(\xi-1)}} = -\frac{B_s}{\sqrt{\sqrt{x}\sqrt{1-\sqrt{x}}}} = -\frac{B_s\sqrt{1+\sqrt{x}}}{\sqrt{\sqrt{x}}\sqrt{1-x}} \sim -\frac{\sqrt{2}B_s}{\sqrt{1-x}}, \tag{97}$$

[4]Note that the matching can be performed with respect to other parameters of the flow, e.g. pressure or velocity on the foil

- yields a (proper) quarter-root singularity of the type $x^{-1/4}$ on the wetted side of the foil close to the leading edge.

  In fact, near the latter point one has

$$-\frac{\mathrm{i}B_s}{\sqrt{\xi(\xi-1)}} = -\frac{B_s}{\sqrt{\sqrt{x}\sqrt{1-\sqrt{x}}}} \sim -\frac{B_s}{x^{1/4}} \tag{98}$$

- complies with the requirement of the decay of the perturbation velocity at the infinity

The real constant B_s characterizes the strength of the square-root singularity at the point $x = 1$ and has to be determined from the matching procedure. Matching of the linearized outer solution and the inner solution can be performed in terms of the perturbation velocities, or in terms of the ordinates of the lower free boundary of the cavity detaching form the spoiler. Using the former option and employing the matching principle, one should equate the outer expansion w^{io} of the inner solution of with the inner expansion w^{oi} of the outer solution[5]. In other words, one should equate the expressions (95) and (97). As a result, the constant B_s is obtained in the form

$$B_s = \frac{\beta\sqrt{2\varphi_o}}{\pi}\sqrt{\varepsilon} \tag{99}$$

It is easy to verify that the matching could have been done in terms of the ordinates of the lower free boundary of the cavity. Find the asymptotics of the outer description of this boundary[6] near the spoiler, i.e. for $x \to 1-0$. Using the kinematic condition on the cavity $u = 0$

$$\frac{\mathrm{d}y}{\mathrm{d}x} = v = -\Im w = \frac{B_s}{\sqrt{\xi(1-\xi)}}, \quad (\xi = \sqrt{x}, x > 1, \xi > 1)$$

Integrating this expression one obtains

$$y = \int_1^x v\,\mathrm{d}x = \int_1^{\sqrt{x}} v(\xi)\frac{\mathrm{d}x}{\mathrm{d}\xi}\,\mathrm{d}\xi = 2\int_1^{\sqrt{x}} v(\xi)\xi\,\mathrm{d}\xi =$$

$$-B_s\{2\sqrt{\sqrt{x}(\sqrt{x}-1)} + \ln[2\sqrt{x}-1+2\sqrt{\sqrt{x}(\sqrt{x}-1)}]\}. \tag{100}$$

Asymptotic representation of (100) for $x \to 1-0$ is with use of the previously obtained magnitude of the constant B

$$y \sim -2\sqrt{2}B_s\sqrt{x-1} = -\frac{4\beta\sqrt{\varphi_o\varepsilon}}{\pi}\sqrt{x-1} \tag{101}$$

Re-writing (90) in terms of the outer variable x one can verify complete coincidence of the resulting expression with (101). This fact proves correctness of the matching procedure.
The additional lift coefficient due to presence of the spoiler

$$C_{y_s} = -2\Re\oint w_s(z)\,\mathrm{d}z = -\int_0^1 u_s(x)\,\mathrm{d}x = 2B\pi = 2\sqrt{2\varphi_o}\beta\sqrt{\varepsilon} \tag{102}$$

The drag coefficient due to presence of th spoiler in the case of flat plate and zero angle of attack is

$$C_{x_s} = -\Im\oint w^2(z)\,\mathrm{d}z = -\Im\oint w^2(\zeta)\frac{\mathrm{d}z}{\mathrm{d}\zeta}\,\mathrm{d}\zeta = 2\pi B_s^2 = \frac{4\varphi_o\beta^2}{\pi}\varepsilon \tag{103}$$

Some calculated results reflecting dependence of the spoiler contributions to the lift and drag coefficients on the spoiler installation angle β are presented in Fig. 12. For the case of non-zero angle of attack $\alpha \neq 0$ the resulting lift and drag coefficients can be determined with use of the known superposition rules

$$C_y = C_{y_\alpha} + C_{y_s} \tag{104}$$

$$C_x = (\sqrt{C_{x_\alpha}} + \sqrt{C_{x_s}})^2 \tag{105}$$

For the case of the flat plate the concrete expressions for these coefficients become

$$C_y = \frac{\pi\alpha}{2} + 2\sqrt{2\varphi_o}\beta\sqrt{\varepsilon} \tag{106}$$

[5]In the overlap regions
[6]Based on the possibility of linear superposition, it is sufficient to take the case of zero incidence

$$C_x = \Big(\sqrt{\frac{\pi}{2}}\alpha + 2\sqrt{\frac{\varphi_o}{\pi}}\beta\sqrt{\varepsilon}\Big)^2 \tag{107}$$

The spoiler contribution to the upper boundary of the cavity can be calculated by integrating the corresponding "upwash" $\Im w = v$ for $z = x + \mathrm{i}0, \zeta = \xi, \xi = -\sqrt{x}$, $x > 0$. Using (96), one has

$$y = \int_0^x v(x)\,\mathrm{d}x = \int_0^{-\sqrt{x}} v(\xi)\frac{\mathrm{d}x}{\mathrm{d}\xi}\,\mathrm{d}\xi = 2\int_0^{-\sqrt{x}} v(\xi)\xi\,\mathrm{d}\xi =$$

$$2B_s[\sqrt{x+\sqrt{x}} + \ln(\sqrt{1+\sqrt{x}} - \sqrt{\sqrt{x}})] \tag{108}$$

The structure of asymptotic solutions can be used for some useful estimates. One can evaluate e.g. optimal ratio angle of attack and relative length of the spoiler. Utilizing expressions (106) and (107) one can write the following formula

$$\frac{L}{D}\sqrt{\varepsilon} = \frac{C_y}{C_x} = \frac{a_\alpha\kappa + b_\varepsilon}{(c_\alpha\kappa + d_\varepsilon)^2 + c_f/\varepsilon} \tag{109}$$

where the coefficients $a_\alpha, c_\alpha, b_\varepsilon, d_\varepsilon$ can be easily determined comparing (106) and (107). Parameter κ is defined as

$$\kappa = \frac{\alpha}{\sqrt{\varepsilon}}, \tag{110}$$

and $c_f = c_f(Re)$ is a friction coefficient, which can be calculated as a function of Reynolds number with use of an appropriate formula. For example, assuming fulll turbulent regime of the flow past the wetted part of the cavitating plate, one can use the formula

$$c_f = \frac{0.455}{(\log Re)^{2.58}} \tag{111}$$

Differentiating (109) with respect to κ and equating the result to zero, one obtains the following *optimal* magnitude of κ

$$\kappa_{opt} = \frac{-c_\alpha b_\varepsilon + \sqrt{(c_\alpha b_\varepsilon - a_\alpha d_\varepsilon)^2 + c_f/\varepsilon}}{a_\alpha c_\alpha} \tag{112}$$

Note that for $c_f/\varepsilon \to 0$ one can assume that

$$\kappa_{opt} \to -\frac{d_\varepsilon}{c_\alpha} = -\frac{2\sqrt{2\varphi_o(\beta)}\beta}{\pi}, \tag{113}$$

so that the optimal ratio $\alpha/\sqrt{\varepsilon}$ is negative. The latter results means that to secure maximum lift-to-drag ratio, one has to provide a negative angle of attack, for example for a spoiler normal to the plate ($\beta = \pi/2$), $\alpha_{opt} = -0.748\sqrt{\varepsilon}$.

The value of κ_{opt} can be employed to calculate the maximum lift-to-drag ratio of a flat plate with a spoiler at the trailing edge. However, there exits a somewhat contradicting requirement of *univalence* which, in simple words, means that the upper side of the cavity generated by the optimal combination of the spoiler and (negative) angle of attack *should not intersect the plate*[7]. One can find the domain of univalence by considering the thickness of the cavity with respect to the plate. Using, the corresponding expressions (61) and (108) for the contributions to the ordinates of the upper side of the cavity due to angle of attack and presence of spoiler, one finds the aforementionned cavity thickness in the form

$$y_t(x) = y_\alpha^u + y_\varepsilon = \alpha f_\alpha(x) + \frac{\beta\sqrt{2\varphi_o(\beta)}}{\pi}\sqrt{\varepsilon}f_\varepsilon(x) \tag{114}$$

where

$$f_\alpha(x) = \frac{1}{2}[(1+2\sqrt{x})\sqrt{x+\sqrt{x}} - \ln(\sqrt{1+\sqrt{x}} + \sqrt{\sqrt{x}})] \tag{115}$$

$$f_\varepsilon(x) = 2[\sqrt{x+\sqrt{x}} + \ln(\sqrt{1+\sqrt{x}} - \sqrt{\sqrt{x}})] \tag{116}$$

Requiring that the cavity thickness be non-negative at the trailing edge of the plate ($y_t(1) \le 0$), one obtains the expression for the domain of univalence in terms of of the relationship between angle of attack and length of the spoiler

$$\kappa = \frac{\alpha}{\sqrt{\varepsilon}} \le -\frac{f_\varepsilon(1)}{f_\alpha(1)} = -N_o\beta\sqrt{\varphi_o(\beta)}, \tag{117}$$

[7]Condition of univalence for this case was first found by A.S. Achkinadze and G.M. Fridman

where

$$N_o = \frac{4\sqrt{2}}{\pi}\frac{\sqrt{2}+\ln(\sqrt{2}-1)}{3\sqrt{2}-\ln(\sqrt{2}+1)} \approx 0.285 \tag{118}$$

The optimal and "univalent"ratios $\alpha/\sqrt{\varepsilon}$ are plotted versus the spoiler installation angle β in Fig. 13. This Figure clearly shows that in a certain range of β the optimal ratio of the angle of attack and the length of the spoiler cannot be achieved in reality. The ("pedestrian") maximum of lift-to-drag ratio derived through optimisation of the ratio $\alpha/\sqrt{\varepsilon}$ is plotted in Fig. 14 together with the lift-to-drag ratio attainable within the regime of univalence.

5. Bibliography

[1] Tulin M.P. "Supercavitating Flows-Small Perturbation Theory", *Journal of Ship Research*, vol. 7, N 3, January 1964, pp. 16-37.
[2] Van-Dyke, M.D. "Perturbation Methods in Fluid Mechanics", *Parabolic Press, Palo Alto*, 1975.
[3] Bassin, M.A., Shadrin, V.P. "Hydrodynamics of a Wing Near an Interface", *Sudostroenie Publishers*, Leningrad, 1980, 303 p.
[4] Plotkin, A. "Leading Edge Correction for the Supercavitating Flat-Plate Hydrofoil", *Transaction ASME, JFE*, vol. 100, September 1978, pp. 276-280
[5] Rozhdestvensky, K.V., Fridman, G.M. "Asymptotic estimate of the influence of a spoiler upon hydrodynamic characteristics of supercavitating hydrofoils in presence of the interface", *Trudy Leningradskogo korablestroitelnogo instituta, Prikladnaya matematika i vychislytelnie systemi v sudostroenii*, Leningrad, 1989, pp. 96-111.
[6] Rozhdestvensky, K.V., Fridman, G.M. "Matched Asymptotics for Free Surface Lifting Flows with Spoilers", *In Mathematical Approaches in Hydrodynamics, SIAM volume dedicated to 65th Anniversary of M.P. Tulin, ed. Touvia Miloh*, 1991, pp. 499-517.
[7] Gurevich, M.M. "Theory of jets of the ideal fluid", *Nauka Publishers*, Moscow, 1979, 536 p.

Figures to "Supercavitating flows: small perturbation theory and matched asymptotics"

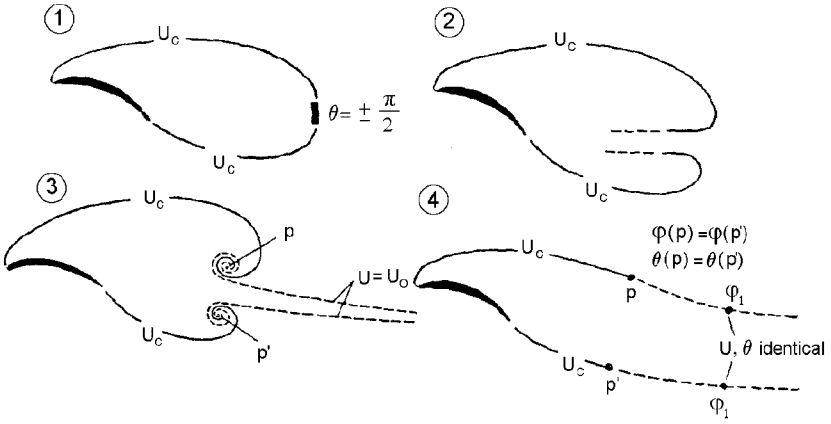


Fig. 1 Selected nonlinear cavity closure models (1 – Riaboushinsky model, 2 – Efros-Gilbarg model, 3 – Tulin double-spiral vortex model, 4 – Wu-Fabula model)

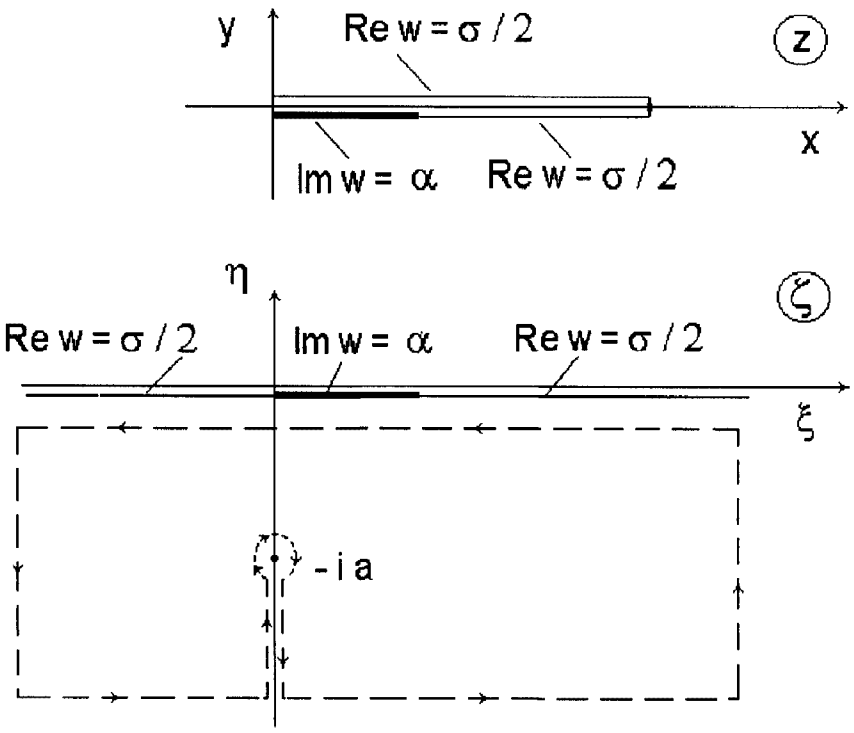


Fig. 2 Linearized "physical" complex plane z and auxiliary complex plane ζ for the case of closed cavity with singular termination. the ground

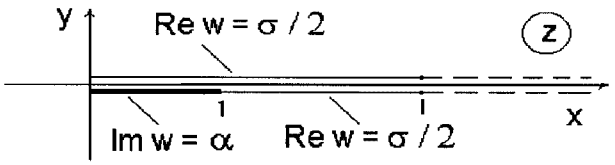


Fig. 3 Linearized "physical" complex plane z for the case of smooth cavity-wake transition (Wu-Fabula cavity closure scheme)

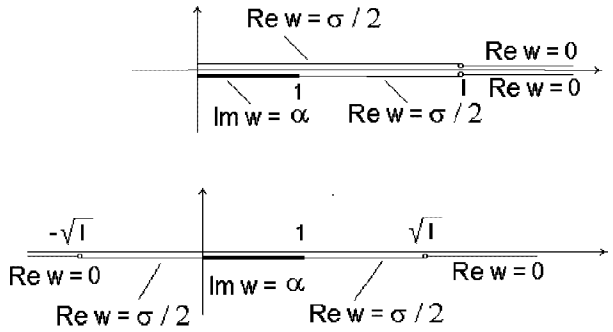


Fig. 4 Linearized "physical" complex plane z and auxiliary complex plane ζ for the case of cavity termination on Tulin double-spiral vortices

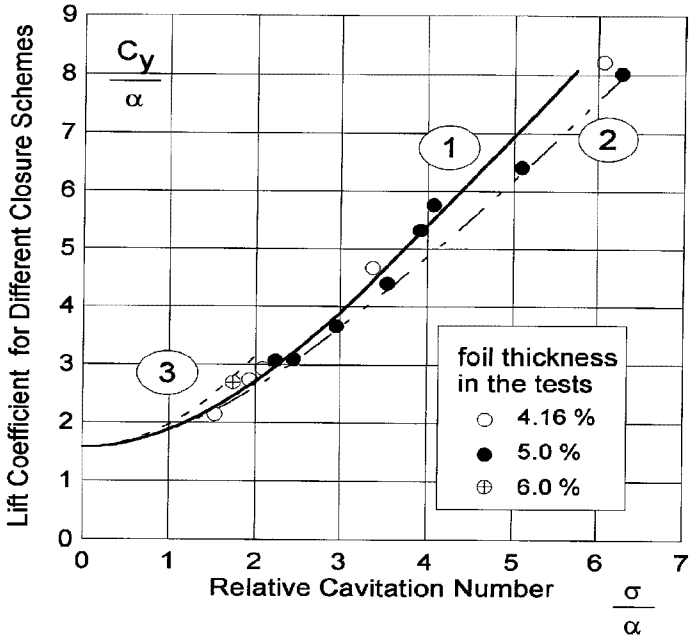


Fig. 5 Lift coefficient (C_y/α) of a supercavitating flat plate versus relative cavitation number σ/α for different linear analogues of the cavity closure models (1 – Tulin double-spiral vortex scheme, 2 – closed cavity scheme, 3 – Wu-Fabula scheme)

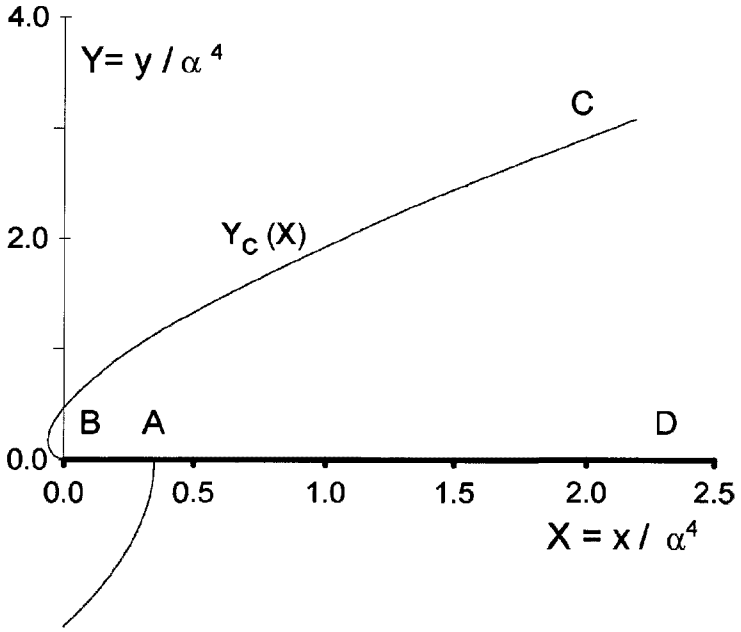


Fig. 6 Flow near the leading edge of supercavitating flat plate (inner region)

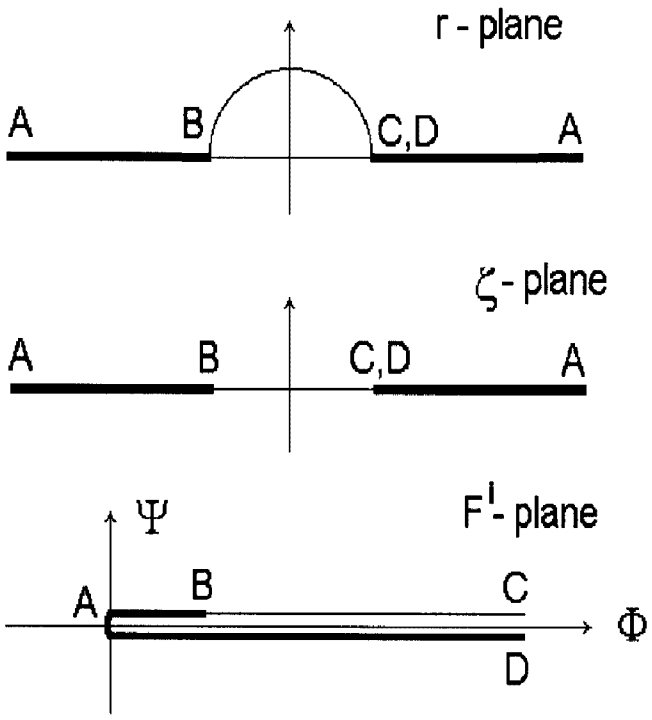


Fig. 7 Complex planes for the hodograph solution of the problem for the flow in the vicinity of the leading edge

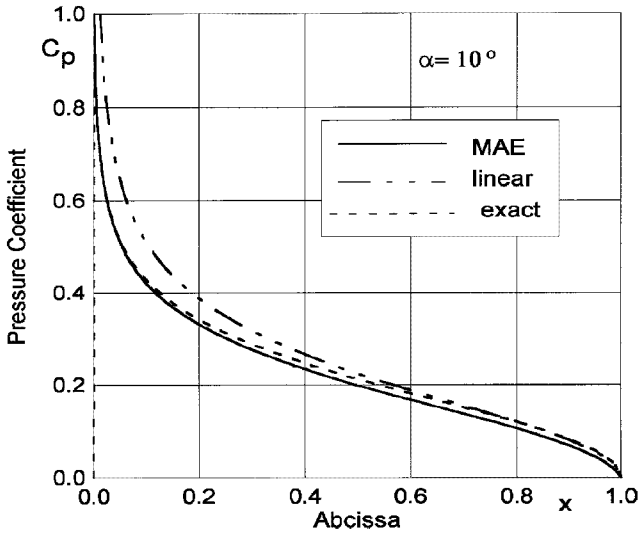


Fig. 8 Pressure distribution along supercavitating flat plate ($\alpha^o = 10^o$) (solid line – uniformly valid MAE, dashed line – exact solution, dot-and-dash line – linear theory)

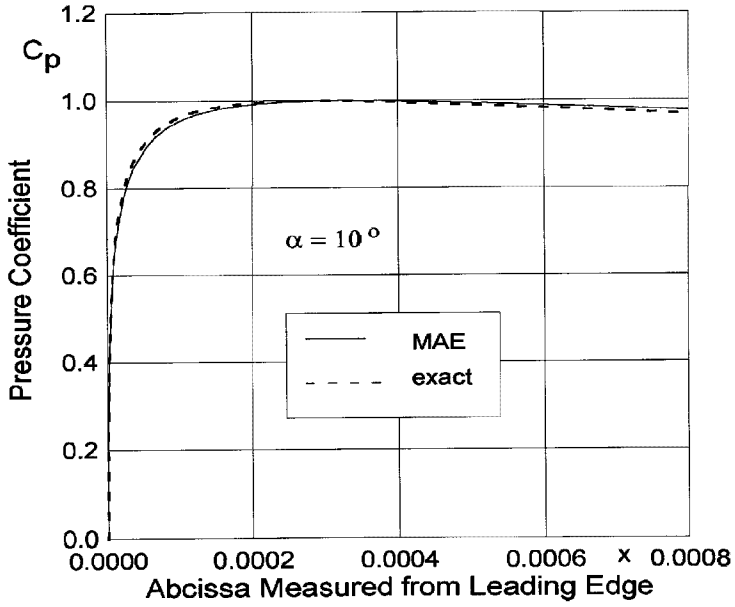


Fig. 9 Pressure distribution in the vicinity of the leading edge of a supercavitating flat plate for $\alpha^o = 10^o$ (solid line – MAE, dashed line – exact solution)

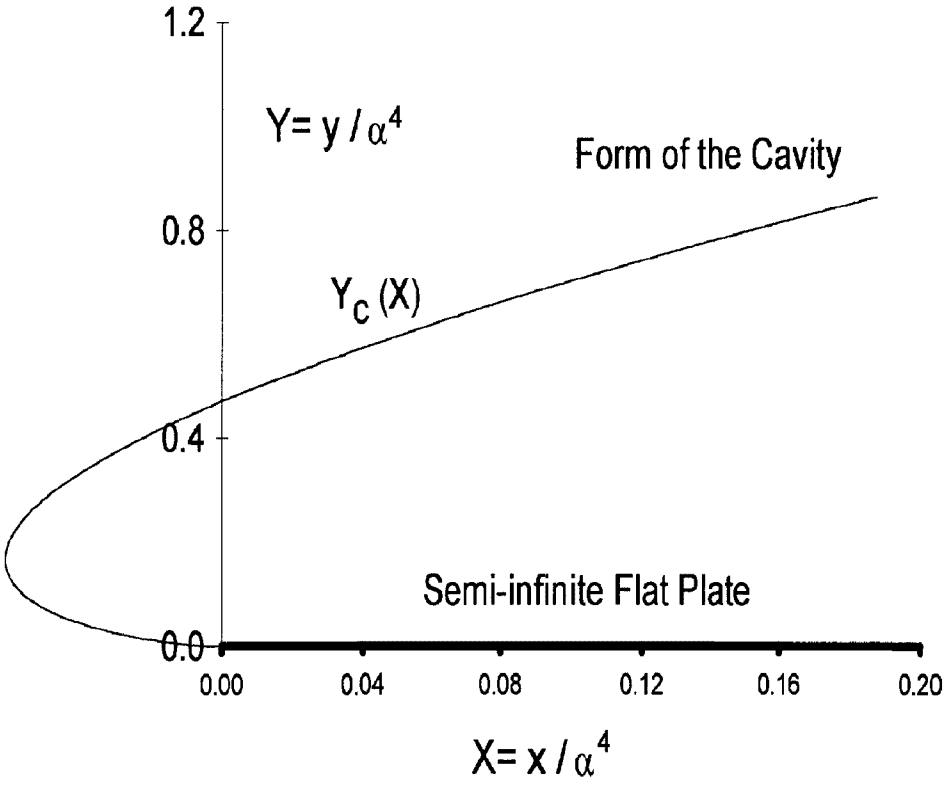


Fig. 10 Upper cavity shape in stretched coordinates in the immediate vicinity of the leading edge of supercavitating flat plate

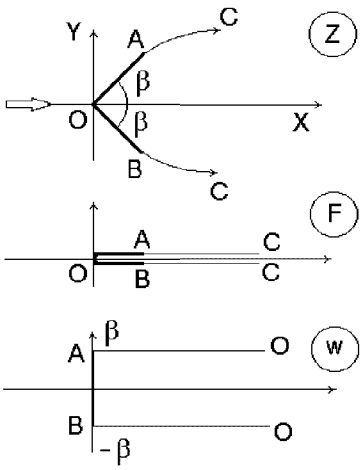


Fig. 11 "Physical" plane, complex potential plane and hodograph plane for the flow problem solution near the spoiler

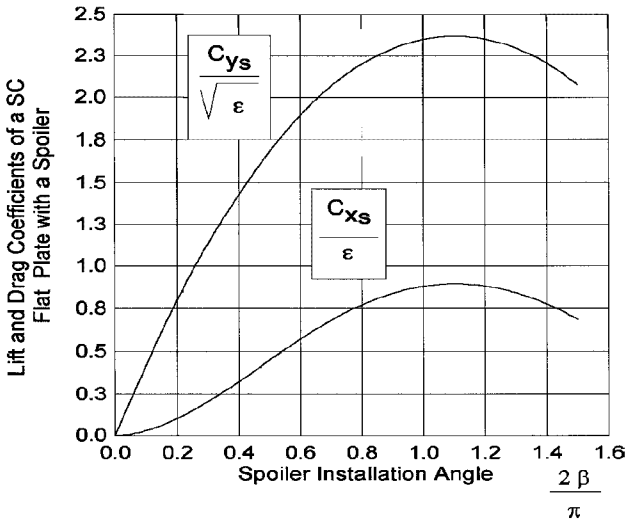


Fig. 12 Lift and drag coefficients of a supercavitating flat plate with a spoiler versus spoiler installation angle

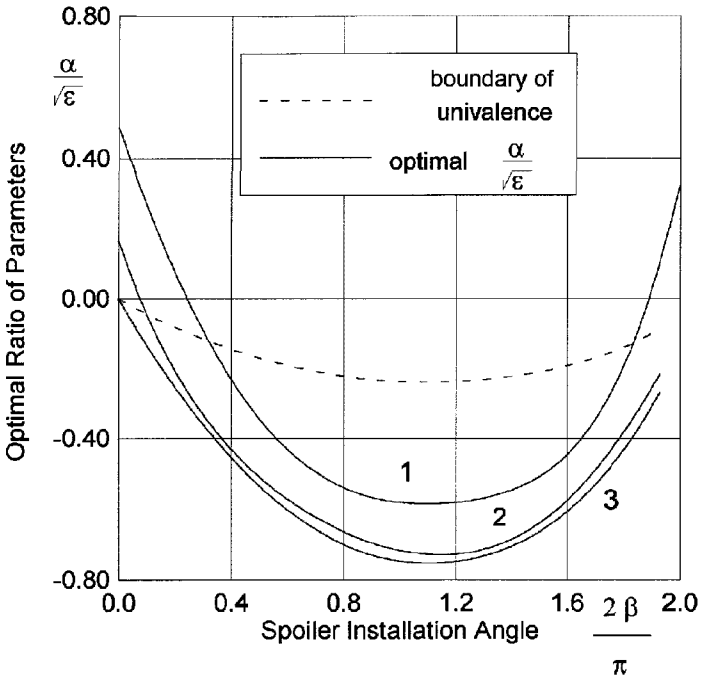


Fig. 13 Optimal and univalent ratios $\alpha/\sqrt{\varepsilon}$ versus the spoiler installation angle for a supercavitating flat plate with a spoiler at the trailing edge

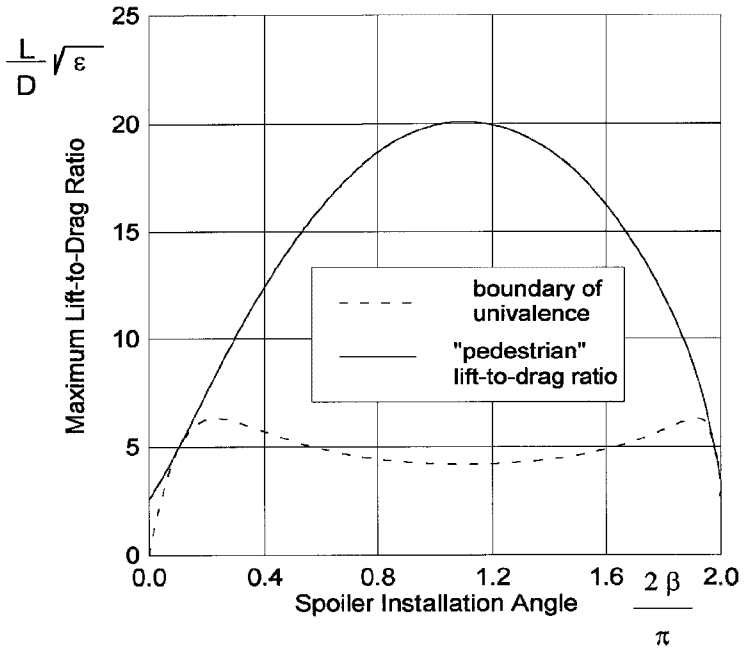


Fig. 14 Maximum "pedestrian" and "univalent" lift-to-drag ratios of a supercavitating flat plate with a spoiler versus the spoiler installation angle

Supercavitating Nonlinear Flow Problems: Matched Asymptotics

K.V. Rozhdestvensky & G.M. Fridman
Department of Applied Mathematics & Mathematical Modelling
St.Petersburg State Marine Technical University
Lotsmanskaya str., 3
190008, St.Petersburg
Russia

Summary: The purpose of the lecture is to demonstrate the method of Matched Asymptotic Expansion (MAE) to be efficiently applicable to various supercavitating flow problems. Two model problems were chosen to prove the statement. The first one is a problem of the flow around a supercavitating shock free hydrofoil with spoiler mounted on its trailing edge and wedge-like fully wetted leading edge. A gallery of local nonlinear edge solution is proposed for the inner flow problems in the vicinity of the spoiler as well as in the vicinity of the sharp or rounded cavitating leading edge. The second problem is supercavitating wing of large aspect ratio beneath the free surface. In both cases analytical solutions to nonlinear inner problem were applied to accomplish the matching procedure and to significantly extend the range of the flow parameters where asymptotic approach gives reliable results. Solutions obtained in the framework of the MAE method as well as linear and nonlinear theories are illustrated in the text by numerical data.

1. Introduction

The Matched Asymptotic Expansions (MAE) method is an appropriate solution technique for a wide variety of fluid mechanics problems. As a rule, the classical MAE method involves the following steps while solving a lifting flow (including cavitating one) problem:
a) to determine what the small parameters of the problem are and, depending on the answer to the question, subdivide the flow domain into a so-called farfield and a nearfield, that is, regions far from and in the vicinity of a source of singular perturbations; formulation of problems in those regions – outer and inner problems correspondingly. The main goal of the subdividing procedure is to simplify the outer problem as compared to a general one (for instance, such a simplification is brought about by the linearization procedure for all the boundary conditions in outer region), and to take into account as much nonlinear effects as possible in the nearfield.
b) a 'rough' asymptotic analysis of both outer and inner descriptions from the viewpoint of a solution class to the problems arising in those subdomains. For instance, a presence of the spoiler on the trailing edge of planing or cavitating hydrofoil dictates a non-traditional class (namely, $\infty - \infty$ instead of customary $\infty - 0$) of linearized outer solution to the corresponding mixed boundary problem. In the case of a cavitating problem that means that the function of complex conjugate velocity in the farfield has to have square root singularity on the trailing edge of the hydrofoil and $-1/4$ on the leading one, see Rozhdestvensky & Fridman [17];
c) solution of the outer lifting flow problem, in the flow region far from the inner zone. Such an outer asymptotic expansion is often derived under the assumption of small perturbations brought by a hydrofoil into the inflow. The assumption loses its correctness in the vicinity of the inner sub-region and so does the outer expansion. Outer solution contains some elements of uncertainty caused by the influence of local problem, as some significant features were omitted from consideration.
Note that the MAE method does not always require the outer problem to be linear and it is not a general restriction on its applicability. Examples as such are abound but here we to some degree confine ourselves by such an assumption.
d) solution of the inner flow problem, i.e. construction of a so-called inner asymptotic expansion which is correct in the local region and loses its correctness in the farfield. It should be pointed out that inner problem is usually considered in stretched local coordinates, the stretching factor being connected with a chosen small parameter. It is by taking advantage of the stretching procedure that the inner problem is also simplified, for instance, reducing of three–dimensional problem to two dimensions in the nearfield, neglecting the gravity, *etc.* This allows to apply a nonlinear approach to adequately describe the most important part of the flow domain. Because of the influence of the outer region, inner solution contains some unknown parameters, as well;
e) matching procedure for outer and inner expansions which is applied to 'blend' them and to take into account their interaction. This stage allows us to close the solution to the whole problem because all the unknown

Paper presented at the RTO AVT Lecture Series on "Supercavitating Flows", held at the von Kármán Institute (VKI) in Brussels, Belgium, 12-16 February 2001, and published in RTO EN-010.

parameters in the far- and nearfield are determined. Using the results obtained, a composite uniformly valid asymptotic solution to the problem under consideration is reached. Such a composite solution is shown to be correct in the whole flow domain and enables one to remove some intrinsic drawbacks of the purely linear description used in the outer region.
The advantages of such an asymptotic method of treating the lifting flow problems are easily seen and thoroughly discussed by many authors, see Van Dyke [24], Cole [2], Ogilvie [14], Rozhdestvensky [16], *etc.* In this connection a 'mathematical constructor' approach should be mentioned, advocated in Fridman [3] and Fridman & Rozhdestvensky [4, 17]. It is by applying this approach that one can pick up and then to combine the necessary outer and inner asymptotic expansions (just like standard 'mathematical parts' or the details of the whole construction) to obtain a desired everywhere correct solution.
It is a well known fact that the MAE method, being applied to the lifting flow problems, enables one to scrutinize those flow regions, where nonlinearities of the problem under consideration are concentrated and most pronounced, while outer flow domain, far from such zones of nonlinearity, can be described more or less sufficiently in the frameworks of an appropriate linear theory. In this case the outer description is certainly to retain some aftermaths of the linearization of the boundary conditions which, though, can be efficiently overcome by MAE technique.

2. Supercavitating shock free hydrofoil with spoiler

2.1 Problem formulation

Consider a cavitating problem for the hydrofoil with the spoiler, at arbitrary cavitation number, see figure 1, the influence of gravity being neglected. The Efros cavity closure model with re-entrant jet is adopted. The origin of the Cartesian coordinate system is taken at the plate's leading edge, x–axis being directed downstream and y upwards. There is an incident stream with speed V_∞ coming from the left. The region occupied by the fluid is bounded by the solid straight boundaries $[AC]$, $[OB]$ and arbitrarily arched portion (CO) given in the form $y = f(x)$ and the cavity surfaces (AE) and (BE), the intervals $[AC]$ and $[OB]$ being of the length $|AC| = l_{\rm w}$ and $|OB| = \varepsilon$. The hydrofoil chord $|OC|$ is chosen to be l. The incidence angle is α, the inclination angle of the spoiler with respect to the hydrofoil chord is β and the angle made by $[AC]$ and (CO) is γ.
It is of importance that the dividing streamline would meet the cavitating plate at the vertex of the wetted surface $(ACOB)$, namely at point C, to provide the shock–free cavitating mode. In this case the length of the upper wetted portion of the leading edge $l_{\rm w}$ is to be treated as an unknown parameter of the problem, the angle γ made by $[AC]$ and (CO) being given. Since the cavitation number $\sigma \geq 0$, the velocity absolute value on the free surfaces is $v_0 = v_\infty \sqrt{1+\sigma}$. The point at infinity on the re-entrant jet is denoted by E and is quite distinct from D, the point at infinity in the main stream. An additional stagnation point F appears in the flow pattern because of the re-entrant jet influence. That is why a double–sheeted Riemann surface is introduced, one sheet carrying the main flow pattern and the second including the jet. The direction of the jet at point E is determined by the angle μ, see figure 1. All the flow parameters are rendered nondimensional by using chord length l and velocity v_∞.

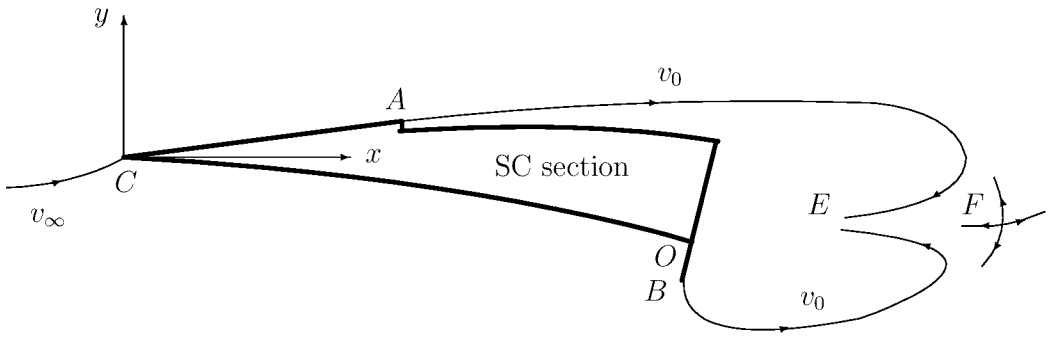


Figure 1: Shock free supercavitating hydrofoil with spoiler.

As is customary, the problem is considered to be solved when the velocity potential function $\varphi(x, y)$ is found. The harmonic function $\varphi(x, y)$, being the real part of an analytical function of complex potential $w = \varphi + i\psi$, has to satisfy the boundary kinematic (flow tangency) condition on the wetted length, the dynamic (pressure/velocity constancy) condition on the free surface and the condition at infinity.

Under assumption that the hydrofoil brings small perturbations into the inflow, subdivide the flow domain into a farfield (at distances of the order of O(1)) and nearfields (in the vicinity of the edges) we apply the MAE method.

2.2. Outer linear solution

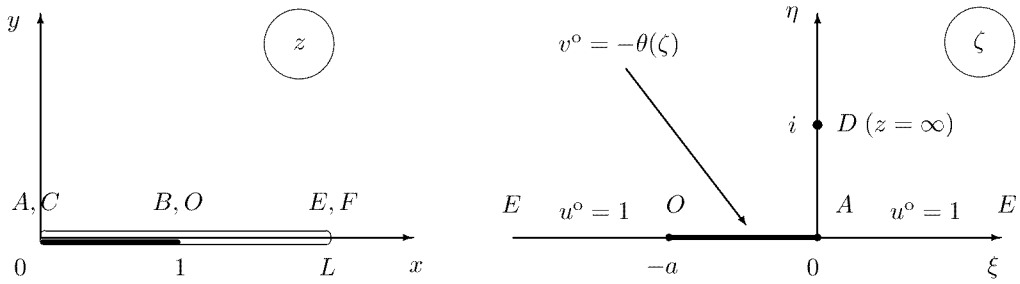
Assume that

$$\theta(x) = f'(x) = \mathrm{o}(1)\ , \quad \alpha = \mathrm{o}(1)\ , \quad \bar{\varepsilon} = \frac{\varepsilon}{l} = \mathrm{o}(1)\ , \quad \frac{l_{\mathrm{w}}}{l} = \mathrm{o}(\alpha)\ , \quad \sigma = \mathrm{o}(1)\ ,$$

that is, the hydrofoil and the cavity brings small perturbations into the inflow and therefore the linearization procedure has to be accomplished for the nonlinear boundary (dynamic and kinematic) conditions both on the free surfaces and on the wetted portion of the foil. Under those circumstances we can neglect the second order terms in all the equations and can formulate the linearized flow problem for supercavitating contour with spoiler [22, 21, 9, 10, 17]. All the wetted surface of the hydrofoil and the cavity appears as a slit of length L in the linearized plane $z = x + \mathrm{i}y$, where L actually is a linearized cavity extent. Boundary conditions for real and imaginary parts of the conjugate velocity χ^{o} are projected on the upper and lower boundaries of the slit, see figure 2, where

$$\chi^{\mathrm{o}}(z) = u^{\mathrm{o}} - i\, v^{\mathrm{o}} = \frac{\mathrm{d}w}{v_0\, \mathrm{d}z}\ ,$$

and $w(z) = \varphi + i\psi$ – function of the complex potential.



$$z = L\,\frac{\zeta^2}{1+\zeta^2}\ ; \quad \zeta = \sqrt{\frac{z}{L-z}}\ ; \quad a = \frac{1}{\sqrt{L-1}}$$

Figure 2: Physical and auxiliary planes.

The physical z-plane has to be mapped into the auxiliary upper semi-plane ζ where the mixed boundary value problem is formulated in $\infty - \infty$ class due to the presence of the spoiler located at the trailing edge of the foil. The class $\infty - \infty$ means that the function $\chi^{\mathrm{o}}(z)$ has to have square–root singularities for $z = 0$ and $z = 1$. Such a behaviour of the outer solution dictates by the asymptotic analysis of the flow problems arising in the vicinity of the leading and trailing edge with the spoiler done in the section that follows. The analysis also reveals that $l_{\mathrm{w}}/l \ll \alpha$ and therefore the kinematic boundary condition on the upper wetted portion $[AC]$ of the leading edge can be neglected correctly in the framework of the linear theory for all the wetted surface of the hydrofoil appears as a segment of unit length on the lower boundary of the slit in the physical z-plane (points A and C coincide and so do points B and O, and E and F).

Note that in the case of $l_{\mathrm{w}}/l = \mathrm{O}(1)$, the kinematic boundary condition on the upper wetted portion $[AC]$ has to be satisfied. To ensure shock free regime of the flow at the leading edge, the solution to the problem should behave at point C like $\sqrt{z}$ as $z \to 0$. Such a solution exists for unique value of the parameter l_{w}/l which becomes an unknown of the linear problem.

Back to the problem as $l_{\mathrm{w}}/l \ll \alpha$, apply Keldysh–Sedov formula for the upper semi-plane in $\infty - \infty$ class:

$$\chi^{\mathrm{o}}(\zeta) = 1 + \frac{i\,\mathcal{B}}{\sqrt{\zeta(\zeta+a)}} + \mathrm{i}\sqrt{\frac{\zeta+a}{\zeta}}\left(\frac{1}{\pi}\int\limits_0^a \sqrt{\frac{t}{a-t}}\,\frac{\theta(t)\,\mathrm{d}t}{\zeta+t} + \mathcal{A}\,\zeta + \mathcal{C}\right), \tag{1}$$

where $\mathcal{A}$, $\mathcal{B}$, $\mathcal{C}$ and $a = 1/\sqrt{L-1}$ are unknown parameters to be determined from the cavity closure condition and condition at infinity

$$\mathrm{Im} \oint\limits_{\zeta=i} \chi^{\circ}(\zeta) \frac{\mathrm{d}z}{\mathrm{d}\zeta} d\zeta = 0 \, ; \quad \chi^{\circ}(i) = 1 - \frac{\sigma}{2} \, ,$$

along with condition provided by the matching procedure in the vicinity of the spoiler. It is to be underlined that the solution provides a square-root singularity for χ° at cavity trailing edge $z = L$, $\zeta \to \infty$. It corresponds to the linearized closed cavity closure models: Riabouchinsky, Efros–Kreisel–Gilbarg, Tulin–Terentev (single spiral vortex).

Note that the simple non-quadrature approach can be proposed [21] for a wide range of the functions $y = f(x)$ characterizing the lower surface distribution of the hydrofoil.

It is obvious that the new function

$$\Omega(z) = \chi^{\circ}(z) - 1 + \mathrm{i}\,\theta(z)$$

where $\theta(x) = f'(x)$ is a tangential angle to the foil at point x, has pure real values on the wetted portion (as $x \in [0;1]$, $y = 0^{+}$) and pure imaginary values on the cavity surfaces, see figure 2. Let us assume that the wetted portion of the cavitating hydrofoil is a polynomial

$$f(x) = \sum_{i=0}^{n} a_i x^i$$

and therefore

$$\theta(x) = f'(x) = \sum_{i=1}^{n} i a_i x^{i-1} \, .$$

Then function

$$\Omega(\zeta) = \chi^{\circ}(\zeta) - 1 + \mathrm{i} \sum_{i=1}^{n} i a_i z^{i-1}(\zeta)$$

where $z(\zeta) = L\,\zeta^2/(1+\zeta^2)$, has to satisfy homogeneous boundary conditions on the upper semi-plane ζ in $\infty - \infty$ class. It should be pointed out that the multiplicity of a pole at the infinity $z \to \infty$ for the function $\Omega(z)$ is equal to $(n-1)$, i.e. to the degree of the polynomial $f'(x)$. That is why the solution can be derived without an integration procedure and is of the form

$$\chi^{\circ}(\zeta) = 1 + \frac{\mathrm{i}\,\mathcal{B}}{\sqrt{\zeta(\zeta+a)}} - \mathrm{i}\theta(z(\zeta)) + \mathrm{i}\sqrt{\frac{\zeta+a}{\zeta}} \left\{ \mathcal{A}\zeta + \mathcal{C} + \sum_{k=1}^{n-1} \left(\frac{\mathcal{D}_k + i\mathcal{E}_k}{(\zeta - i)^k} + \frac{\mathcal{D}_k - i\mathcal{E}_k}{(\zeta + i)^k} \right) \right\} . \tag{2}$$

Condition at infinity $z = \infty$ and at its image $\zeta = \mathrm{i}$ for function $\chi^{\circ}(\zeta)$

$$\lim_{\zeta \to \mathrm{i}} \big(\chi^{\circ}(\zeta) - 1 \big) = -\frac{\sigma}{2} \, ;$$

$$\lim_{\zeta \to \mathrm{i}} \Big\{ \big(\chi^{\circ}(\zeta) - 1 \big) (\zeta - \mathrm{i})^k \Big\} = 0 \quad \text{for } k = 1, \ldots, n-1 \, ,$$

linearized cavity closure condition re-written in the form

$$\mathrm{Im} \frac{\mathrm{d}\chi^{\circ}}{\mathrm{d}\zeta} (\mathrm{i}) = 0$$

along with the matching condition allow unknown parameters $\mathcal{A}$, $\mathcal{B}$, $\mathcal{C}$, $\mathcal{D}_k$, $\mathcal{E}_k$ and cavity extent L in (2) to be determined. So, the number $2n+2$ of unknowns coincides with that of conditions.

Once function $\chi^{\circ}(\zeta)$ is found (i.e. the unknowns of the outer problem are derived), the cavity volume is determined

$$z^{+}_{\mathrm{cav}}(x) = \int\limits_0^x \chi^{\circ}\Big(\sqrt{\frac{t}{L-t}} \Big) \mathrm{d}t \, , \qquad z^{-}_{\mathrm{cav}}(x) = \int\limits_1^x \chi^{\circ}\Big(-\sqrt{\frac{t}{L-t}} \Big) \mathrm{d}t + 1 - \mathrm{i}\, f(1) \, , \tag{3}$$

where superscripts $+$ and $-$ denote the upper and lower boundary of the cavity correspondingly.

All the hydrodynamic coefficients are also connected to $\chi^{\circ}(z)$:

$$C_p(x) = -2\,\mathrm{Re}\left\{\chi^{\circ}\Big(-\sqrt{\frac{x}{L-x}}\Big) - 1\right\}\,, \tag{4}$$

$$C_L = \int\limits_0^1 C_p(x)\,\mathrm{d}x = 2\,\mathrm{Re}\oint\limits_{\mathrm{i}} (\chi^{\circ}(\zeta) - 1)\,\frac{\mathrm{d}z}{\mathrm{d}\zeta}\,\mathrm{d}\zeta\,, \tag{5}$$

$$C_D = \int\limits_0^1 C_p(x)\,\theta(x)\,\mathrm{d}x\,. \tag{6}$$

Both classical and nonquadrature solutions to the supercavitating problem remain valid for the open cavity closure scheme (linearized analog of the Wu–Fabula model) as well. Such a model specifies the velocity field be continuous at the trailing edge of the cavity what means that the cavity and the trailing wake conjugates smoothly. From the mathematical point of view it corresponds to non-singular behaviour of $\chi^{\circ}(z)$ at point $z = L$ which implies the condition $\mathcal{A} = 0$ to be satisfied. Then the number of unknowns becomes $2n + 1$ and the cavity closure condition $\mathrm{Im}\,\dfrac{\mathrm{d}\chi^{\circ}}{\mathrm{d}\zeta}\,(\mathrm{i}) = 0$ should be neglected.

2.3. Inner nonlinear descriptions

2.3.1. A simplest spoiler problem. It was already mentioned above that outer asymptotic expansion loses its correctness in the vicinity of the spoiler as $z \to 1$ and inner description dictates the solution class of the outer one, namely $\infty - \infty$. The picture of the flow shown in figure 3 corresponds to stretching of local coordinates in this region by a factor $1/\bar{\varepsilon}$: $X = (x-1)/\bar{\varepsilon}$, $Y = y/\bar{\varepsilon}$, $\bar{\varepsilon} \to 0$. The region occupied by the fluid is bounded by the solid boundaries $[OB)$ and $[OA]$ and the free surface (AB), the interval $[OA]$ being of the unit length $|OA| = 1$. The absolute value of velocity V_∞^i at 'local' infinity and on the free surface (AB) is an unknown parameter to be determined through the matching procedure with outer problem. This is the simplest flow problem for a straight spoiler.

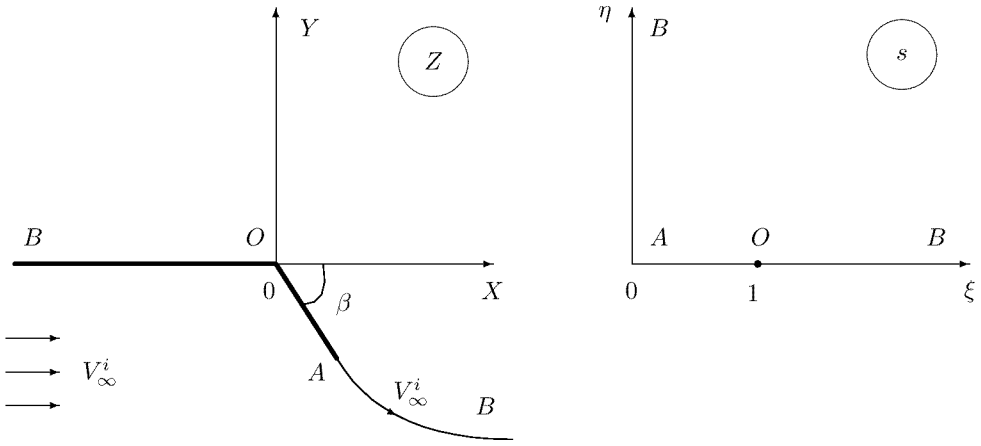


Figure 3: Flow pattern and auxiliary ζ-plane for the inner spoiler problem.

With the correspondence between physical and auxiliary planes (the first quadrant of the $\zeta = \xi + \mathrm{i}\eta$ plane is chosen as an image of the region occupied by the fluid), one can easily obtain the analytical inner nonlinear solution (following to Chaplygin method of singular points) in the form:

$$\chi^i(s) = \frac{\mathrm{d}w}{V_\infty^i \mathrm{d}Z} = \left(\frac{\zeta - 1}{\zeta + 1}\right)^{\beta/\pi}\,; \qquad \frac{\mathrm{d}w}{\mathrm{d}s} = N\,\zeta\,; \tag{7}$$

wherefrom

$$Z(s) = \frac{N}{V_\infty^i} \int_1^\zeta s \left(\frac{\zeta+1}{\zeta-1}\right)^{\beta/\pi} \mathrm{d}\zeta \,, \tag{8}$$

where N – unknown parameter to be determined from the condition $Z_A = Z(0) = \mathrm{e}^{-\mathrm{i}\beta}$ which yields

$$-\frac{N}{V_\infty^i} \int_0^1 \xi \left(\frac{1+\xi}{1-\xi}\right)^{\beta/\pi} \mathrm{d}\xi = -\frac{N_1}{U_1} R = 1 \,. \tag{9}$$

The pressure distribution coefficient ($0 \le \xi < \infty$) is

$$C_p^i = 1 - \left|\chi^i(\zeta)\right|^2 = 1 - \left|\frac{\xi-1}{\xi+1}\right|^{2\beta/\pi} \,, \tag{10}$$

where the value of ξ is obtained from the relationships between physical and auxiliary coordinates on the interval $[OB]$, see figure 3:

$$X(\eta) = \frac{N}{V_\infty^i} \int_1^\xi \xi \Big(\frac{\xi+1}{\xi-1}\Big)^{\beta/\pi} \mathrm{d}\xi \,, \qquad \xi \ge 1 \tag{11}$$

and on the interval $[OA]$:

$$|Z(\xi)| = -\frac{N}{V_\infty^i} \int_\xi^1 \xi \Big(\frac{1+\xi}{1-\xi}\Big)^{\beta/\pi} \mathrm{d}\xi \,, \quad 0 \le \xi \le 1 \tag{12}$$

The value of V_∞^i is the only unknown parameter left in this problem to be determined through the matching procedure.
It follows from (11) that $X \sim N\xi^2/(2V_\infty^i)$ as $X \to -\infty$ and $\xi \to +\infty$ and therefore velocity behaves as $X \to -\infty$

$$\frac{\mathrm{d}w}{\mathrm{d}Z} \sim V_\infty^i \left(1 - \frac{2\beta}{\pi}\frac{1}{\xi}\right) \sim V_\infty^i \left(1 - \frac{\sqrt{2}\,\beta}{\pi}\sqrt{\frac{-N}{V_\infty^i}}\,\frac{1}{\sqrt{-X}}\right). \tag{13}$$

If one assumes that $V_\infty^i = 1$, then coefficient $\mathcal{K}$ is

$$\mathcal{K} = \frac{\sqrt{2}\,\beta}{\pi}\sqrt{\frac{-N}{V_\infty^i}} = \frac{\sqrt{2}\,\beta}{\pi}\frac{1}{\sqrt{R}} \,,$$

see figure 4 for $\mathcal{K}(\beta)$ curve, which attains its maximum at $\beta \approx 1.734$ (or 99.34°).

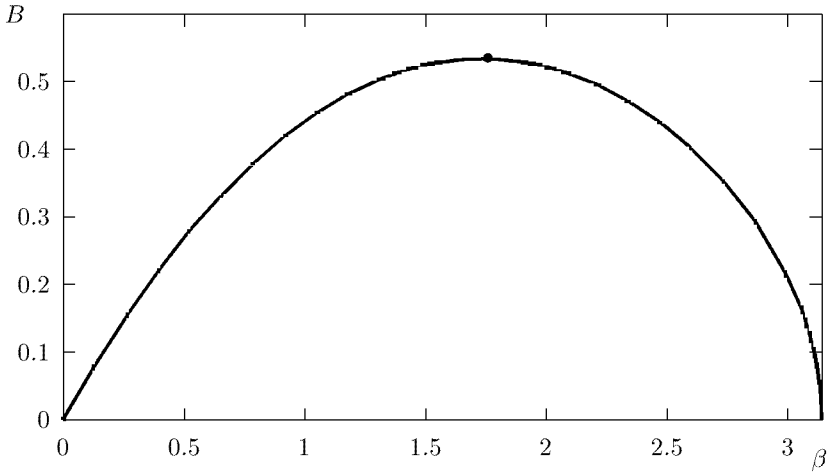


Figure 4: Parameter $\mathcal{K}$ versus β for the simplest inner spoiler problem.

2.3.2. Cavitating shock free leading edge Introduce a local stretched coordinate system in the vicinity of the wedge-like leading edge $Z = X + \mathrm{i}Y = z/l_{rmw}$, where $l_{rmw} \ll \alpha$ is the length of the upper wetted portion of the leading edge. As stagnation point coincides with the vertex of the wedge, value of l_{rmw} is unknown, but can be used as a stretching factor.

The flow pattern and corresponding auxiliary ζ-plane are depicted in figure 5. The flow region is bounded by semi-infinite line (OB), segment $[OC]$ and free surface (CD). Note that the interval $[OC]$ is of unit length because of the choice of the stretching factor. Like for the inner spoiler problem, the absolute value of velocity V^i_∞ at 'local' infinity and on the free surface (CB) is an unknown parameter to be determined through the matching procedure with outer problem.

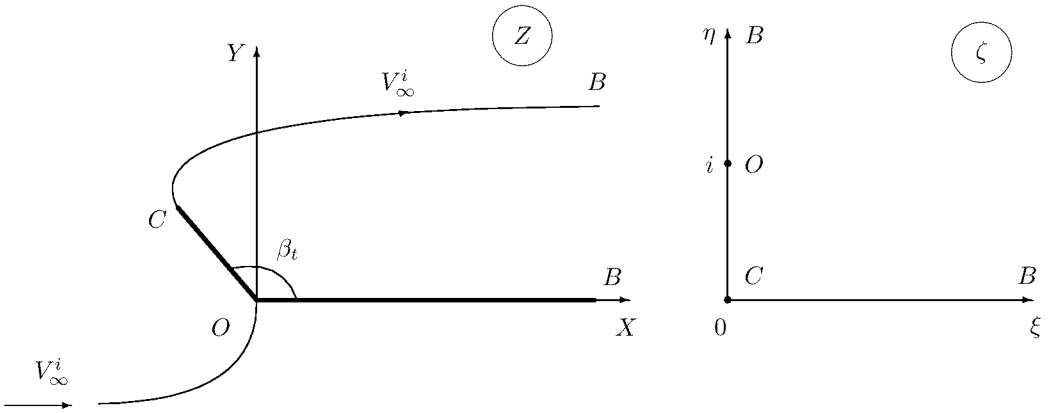


Figure 5: Flow pattern and auxiliary ζ-plane for the inner leading edge problem.

With the correspondence between physical and auxiliary planes (the first quadrant of the $\zeta = \xi + \mathrm{i}\eta$ plane is chosen as an image of the region occupied by the fluid), one can easily obtain the analytical inner nonlinear solution (following to Chaplygin method of singular points) in the form:

$$\chi^i(\zeta) = \frac{\mathrm{d}w}{V^i_\infty \mathrm{d}Z} = \left(\frac{\zeta - \mathrm{i}}{\zeta + \mathrm{i}}\right)^{\gamma/\pi}; \qquad \frac{\mathrm{d}w}{\mathrm{d}\zeta} = N\zeta(\zeta^2 + 1);$$
$$Z(\zeta) = \frac{N}{V^i_\infty} \int_{\mathrm{i}}^{\zeta} \zeta\,(\zeta^2 + 1) \left(\frac{\zeta + \mathrm{i}}{\zeta - \mathrm{i}}\right)^{\gamma/\pi} \mathrm{d}\zeta\,. \tag{14}$$

The length of the segment $[OC]$ $(|OC| = 1)$ is connected to the unknown parameter N through the relation

$$|CO| = \frac{N}{V^i_\infty} \int_0^1 t\,(1 - t^2) \left(\frac{1 + t}{1 - t}\right)^{\gamma/\pi} \mathrm{d}t = \frac{N}{V^i_\infty}\,Q\,. \tag{15}$$

It is seen that $X \sim N\eta^4/(4V^i_\infty)$ as $X \to +\infty$ and $Y = 0^-$ $(\xi = 0, \eta \to +\infty)$. Therefore the asymptotic structure of the inner solution at 'local' infinity as $X \to +\infty$ and $Y = 0^-$ is

$$\left|\frac{\mathrm{d}w}{\mathrm{d}Z}\right| \sim V^i_\infty \left(1 - \frac{2\gamma}{\pi}\frac{1}{\eta}\right) \sim V^i_\infty \left(1 - \frac{\sqrt{2}\,\gamma}{\pi} \sqrt[4]{\frac{N}{V^i_\infty}} \frac{1}{X^{1/4}}\right). \tag{16}$$

Such a behaviour corresponds to a well-known singularity '$-1/4$' arising in the framework of the linear cavitation theory at the leading edge of the hydrofoil.

Note that in the case of $\gamma = \pi$ the inner problem reduces to a well-known problem of the flow in the vicinity of the sharp leading edge of the cavitating hydrofoil considered by Plotkin [15] on the base of a hodograph method,

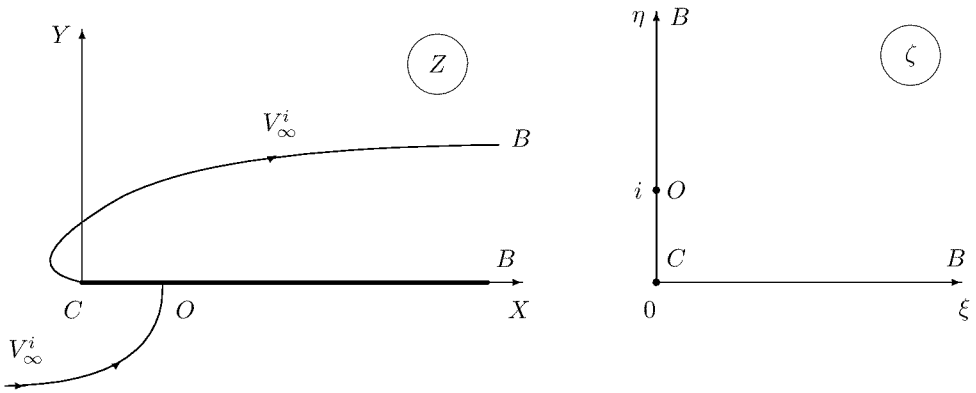


Figure 6: Flow pattern and auxiliary ζ-plane for the inner leading edge problem in the case of $\gamma = \pi$.

see figure 6. The solution presented below is appeared to be more efficient and convenient:

$$\chi^i(\zeta) = \frac{\mathrm{d}w}{V_\infty^i \mathrm{d}Z} = \frac{\zeta - \mathrm{i}}{\zeta + \mathrm{i}}; \qquad \frac{\mathrm{d}w}{\mathrm{d}\zeta} = N\zeta(\zeta^2 + 1)$$
$$Z(\zeta) = \frac{12}{17}\mathcal{L}\Big(\frac{1}{4}\zeta^4 + \frac{2}{3}\mathrm{i}\zeta^3 - \frac{1}{2}\zeta^2\Big); \tag{17}$$

where $\mathcal{L} = |OC|$ and, since $X \sim (3/17)\, L\eta^4$ as $X \to +\infty$ and $\eta \to +\infty$,

$$\left|\frac{\mathrm{d}w}{\mathrm{d}Z}\right| \sim V_\infty^i \left(1 - \frac{2}{\eta}\right) \sim V_\infty^i \left(1 - \sqrt[4]{\frac{48}{17}\,\mathcal{L}}\,\frac{1}{X^{1/4}}\right) \tag{18}$$

as $X \to +\infty$, $Y = 0^-$. The value of $\mathcal{L}$ and V_∞^i are to be determined through the matching procedure.

2.3.3. Cavity closure region It is obvious that outer linear solution loses its correctness in the vicinity of the cavity trailing edge as $z \to L$, where L is the cavity extent, provided a linearized closed cavity closure scheme (like Riabouchinsky, Tulin–Terentev or Efros–Kreizel–Gilbarg models) is adopted. The outer expression for the conjugate velocity $\chi^{\circ}(z)$ has a square-root singularity at $z = L$.

Since the latter linearized model is adopted in the outer region, a local nonlinear model is proposed of the flow in the close proximity of the re-entrant jet, see figure 7. The *upper half* of the flow pattern is shown in stretched and rotated local coordinates, the stretching factor being $1/\delta_e$, where δ_e is re-entrant jet width at infinity and rotating angle being γ_e, where angle γ_e describes a direction of re-entrant jet at infinity for Efros–Kreisel–Gilbarg cavity closure scheme. Since the flow pattern has axial symmetry, the streamline (AC) is substituted by the straight solid boundary (ABC). Then the region occupied by the fluid is bounded by free surface (AFC) and solid horizontal line (ABC), velocity vector at point D is directed downward. The dividing streamline meets the solid wall at stagnation point B. This streamline subdivides the flow into two parts: the first one is the main flow directed downstream with velocity V_∞^i at local infinity as $X \to +\infty$ and the second one forms a re-entrant jet of unit width at infinity at point A as $X \to -\infty$.

With the correspondence between the physical $z = x + \mathrm{i}y$ plane and auxiliary quadrant $\zeta = \xi + \mathrm{i}\eta$ shown in figure 7, the Chaplygin method allows us to write down the following solution:

$$\chi^i(\zeta) = \frac{\mathrm{d}w}{V_\infty^i \mathrm{d}Z} = \frac{\zeta - 1}{\zeta + 1}; \qquad \frac{\mathrm{d}w}{\mathrm{d}\zeta} = N\frac{\zeta^2 - 1}{\zeta}; \tag{19}$$

$$Z(\zeta) = \int_1^\zeta \frac{\mathrm{d}Z}{\mathrm{d}w}\frac{\mathrm{d}w}{\mathrm{d}\zeta}\mathrm{d}\zeta = \frac{N}{V_\infty^i}\left(\frac{\zeta^2}{2} + 2\zeta + \log\zeta - 2.5\right), \tag{20}$$

where unknown parameter N is connected to the flow rate in the jet at point A through the relation

$$N = \frac{2V_\infty^i}{\pi}\,. \tag{21}$$

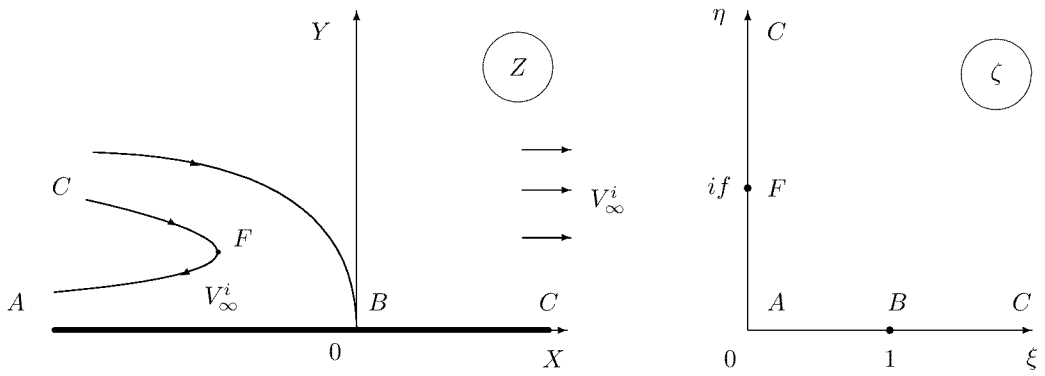


Figure 7: Flow pattern and auxiliary ζ-plane for the inner cavity closure problem.

It readily follows from condition $\chi^i(\mathrm{i}f) = i$ that $f = 1$ what gives the distance L^* between stagnation point B and normal projection of point F onto the horizontal line (ABC):

$$L^* = |\mathrm{Re}\,(Z(\mathrm{i}))| = \frac{6}{\pi}\,. \tag{22}$$

Both δ_e and V^i_∞ are to be determined through the matching procedure with outer linear solution.
It is seen that $X \sim \xi^2/\pi$ as $X \to +\infty$ and $\xi \to +\infty$, that is why

$$\frac{\mathrm{d}w}{\mathrm{d}Z} \sim V^i_\infty \left(1 - \frac{2}{\xi}\right) \sim V^i_\infty \left(1 - \frac{2}{\sqrt{\pi X}}\right), \tag{23}$$

which corresponds to the square-root singularity of the conjugate velocity for the outer linear expansion at the trailing edge of the cavity at $z = L$.

2.4. The matching procedure

It was mentioned above that outer solution loses its correctness in the vicinity of the hydrofoil and cavity edges ($z \to 0$, $z \to 1$ and $z \to L$) where function $\chi^{\mathrm{o}}(z)$ has singularities of 1/2 (square root) and 1/4 type. More to the point, the outer solution is not completed, for the number of unknowns is greater then the number of conditions and coefficient $\mathcal{B}$ in (1) or (2) is an unknown parameter. The main goal of the matching procedure is to close the whole problem (to determine all the parameters in outer and inner descriptions) and to get rid of the singularities of the linear outer solution.
Generally speaking, the matching procedure is carried out into three steps: the first one allows us to match asymptotic descriptions in the outer region and in the trailing edge region (the velocity $U_1 = V^i_\infty$ in expression (7) and the coefficient $\mathcal{B}$ in the equation (1) or (2) are determined); the second one matches the outer description with known value of $\mathcal{B}$ and leading edge expansion to yield the values of l_{w} and $U_2 = V^i_\infty$ in (14) and the third one enables re-entrant jet width δ_e and velocity $U_3 = V^i_\infty$ in (19) to be derived. Notation U_1, U_2 and U_3 is introduced to distinguish velocity absolute value in the local regions.
First, it is obvious that

$$\xi + a \sim \frac{La^3}{2}(1 - x)\,,$$

as $x \to 1^-$, $y = 0^-$ and $\xi \to -a^+$, $\eta = 0^+$ (see figure 2) and therefore the limiting form of (1) and (2) near the trailing edge with spoiler is

$$\chi_1^{\mathrm{o}i}(x) \sim 1 + \frac{\mathcal{B}}{\sqrt{a(a+\xi)}} \sim 1 + \frac{\sqrt{2}\,\mathcal{B}}{a^2\sqrt{L}}\,\frac{1}{\sqrt{1-x}}\,,$$

where $L = \cos^{-2}(\tau/2) > 1$ and $a = \cot(\tau/2)$.

Taking into account the fact that $X = (x-1)/\bar{\varepsilon}$, where $\bar{\varepsilon} = \varepsilon/l$ – is relative spoiler length this expression and formula (13) are compared to give

$$U_1 = V_0 = V_\infty\sqrt{1+\sigma}\ ;$$
$$\mathcal{B} = -\frac{\beta}{\pi}\cos\frac{\tau}{2}\sin^{-2}\frac{\tau}{2}\sqrt{\frac{\bar{\varepsilon}}{R}}\ , \tag{24}$$

where

$$R = \int\limits_0^1 \xi\Big(\frac{1+\xi}{1-\xi}\Big)^{\beta/\pi}\mathrm{d}\xi\,.$$

It is to be underlined that all the coefficients $\mathcal{A}$, $\mathcal{B}$, $\mathcal{C}$, $\mathcal{D}_k$, $\mathcal{E}_k$ in (1) and (2) are of the same order of magnitude. That is why $\bar{\varepsilon} = \mathrm{O}(\alpha^2)$ as $\mathcal{A} = \mathrm{O}(\alpha)$.

Second, it is seen that

$$\xi \sim -\sqrt{\frac{x}{L}}\ ,$$

as $x \to 0^+$, $y = 0^-$ and $\xi \to 0^-$, therefore the limiting form of the classical solution (1) near the leading edge is

$$\chi_2^{oi}(x) \sim 1 + \mathrm{i}\sqrt{\frac{a}{\xi}}\left(\frac{1}{\pi}\int\limits_0^a \frac{\theta(t)}{\sqrt{t(a-t)}}\mathrm{d}t + \frac{\mathcal{B}}{a} + \mathcal{C}\right) \sim 1 + \sqrt[4]{\frac{L}{a^2}}\left(\frac{a}{\pi}\int\limits_0^a \frac{\theta(t)}{\sqrt{t(a-t)}}\,dt + \mathcal{B} + a\mathcal{C}\right)\frac{1}{\sqrt[4]{x}}\ ,$$

and for nonquadrature solution (2) is

$$\chi_2^{oi}(x) \sim 1 + i\sqrt{\frac{a}{\xi}}\left\{\frac{\mathcal{B}}{a} + \mathcal{C} - 2\left(\mathcal{E}_1 + \mathcal{D}_2 - \mathcal{E}_3 - \mathcal{D}_4 + \mathcal{E}_5 + \mathcal{D}_6 - \ldots\right)\right\} \sim$$
$$\sim 1 + \sqrt[4]{\frac{L}{a^2}}\frac{1}{\sqrt[4]{x}}\left\{\mathcal{B} + a\mathcal{C} - 2a\left(\mathcal{E}_1 + \mathcal{D}_2 - \mathcal{E}_3 - \mathcal{D}_4 + \mathcal{E}_5 + \mathcal{D}_6 - \ldots\right)\right\},$$

the value of the coefficient B being given by (24).

The matching procedure for these expansions and expression (16) considering the fact that $Z = z/(l_\mathrm{w}/l)$ results in

$$U_2 = V_0 = V_\infty\sqrt{1+\sigma}\ ;$$
$$\frac{l_\mathrm{w}}{l} = \frac{\pi^4 Q}{4\gamma^4}\frac{L}{a^2}\left\{\mathcal{B} + a\mathcal{C} - 2a\left(\mathcal{E}_1 + \mathcal{D}_2 - \mathcal{E}_3 - \mathcal{D}_4 + \mathcal{E}_5 + \mathcal{D}_6 - \ldots\right)\right\}^4 \tag{25}$$

where

$$Q = \int\limits_0^1 t\,(1-t^2)\left(\frac{1+t}{1-t}\right)^{\gamma/\pi}\mathrm{d}t\,.$$

Note that $\mathcal{D}_k = \mathcal{E}_k = 0$, $k = 1, 2, \ldots$ in the case of the supercavitating shock free flat plate. Expressions (25) show the influence of flow parameters including spoiler geometry onto the length of the upper wetted portion of the leading edge l_w for a given value of angle γ. It follows from the latter equation (25) that $l_\mathrm{w}/l = \mathrm{O}(\alpha^4)$ as $\mathcal{C}$, $\mathcal{D}_k$, $\mathcal{E}_k$ are of the order of $\mathrm{O}(\alpha)$ and $\mathcal{B} = \mathrm{O}(\sqrt{\bar{\varepsilon}}) = \mathrm{O}(\alpha)$.

Third, in the vicinity of the cavity trailing edge $x \to L^-$, $y = 0^+$ and $\xi \to +\infty$, $\eta = 0^+$ (see figure 2)

$$\xi \sim \sqrt{\frac{L}{L-x}}\ ,$$

wherefrom the limiting form of outer solution (both classical and nonquadrature) is

$$\chi_3^{oi}(x) \sim 1 + \mathrm{i}\mathcal{A}\xi \sim 1 + \mathrm{i}\mathcal{A}\sqrt{\frac{L}{L-x}}\ .$$

Taking into account the fact that $X = (x-L)/(\delta_e/l)$, where δ_e/l is a half of the relative width of the re-entrant jet, this expression along with (23) are compared to yield

$$U_3 = V_0 = V_\infty\sqrt{1+\sigma}\ ; \qquad \frac{\delta_e}{l} = \frac{\pi}{4}\,L\,\mathcal{A}^2\ . \tag{26}$$

The expressions show relation between the width of the re-entrant jet and flow parameters (including spoiler length $\bar{\varepsilon}$ and inclination angle β). Note that $\delta_e/l = \mathrm{O}(\alpha^2)$ because of $\mathcal{A} = \mathrm{O}(\alpha)$.
The 'information stream' in the matching procedure is directed from the trailing edge of the hydrofoil to the leading one and to the trailing edge of the cavity as well. In fact, the spoiler geometry parameters β and $\bar{\varepsilon}$ dictate the value of the coefficient $\mathcal{B}$ which, in turn, defines the leading edge and re-entrant jet characteristics. The additive composite solution for the conjugate velocity can be constructed in a following manner:

$$\chi^{\mathrm{c}}(z) = \chi^{\mathrm{o}}(z) + \chi_1^{\mathrm{i}}(z) + \chi_2^{\mathrm{i}}(z) + \chi_3^{\mathrm{i}}(z) - \chi_1^{\mathrm{oi}}(z) - \chi_2^{\mathrm{oi}}(z) - \chi_3^{\mathrm{oi}}(z)\,, \tag{27}$$

where subscripts 1, 2, 3 correspond to local flow problems in the vicinity of the spoiler, leading edge and cavity trailing edge. Substituting composite solution χ^{c} instead of outer χ^{o} into formulae (3)–(6) enables one to derive hydrodynamic coefficients which are everywhere valid and to calculate correct flow pattern.

2.5. Exact solution to the nonlinear flat plate problem and asymptotic analysis

Consider a nonlinear problem of the flow around a supercavitating shock free flat plate. It is useful as a verification of the asymptotic results obtained in the previous sections. The problem under consideration is that of the theory of jets in an ideal fluid and has to be treated by corresponding methods. The physical $z = x+\mathrm{i}y$ and auxiliary ζ planes are shown in figure 8. The same notation is used as in section 2.1 where the general shock free cavitating problem is formulated. The velocity absolute value on the free surfaces is $v_0 = v_\infty\sqrt{1+\sigma}$. where $\sigma \geq 0$ is cavitation number. The region occupied by the fluid is bounded by solid segments $[AC]$, $CO]$ and $[OB]$ and cavity surfaces (BE) and (AE), point E is that at infinity (second Riemann sheet). Point at infinity F (first Riemann sheet) has the image $\zeta_0 = b + \mathrm{i}c$ and stagnation point F – image $\zeta_\infty = d + \mathrm{i}f$ on the first quadrant of the auxiliary ζ-plane.

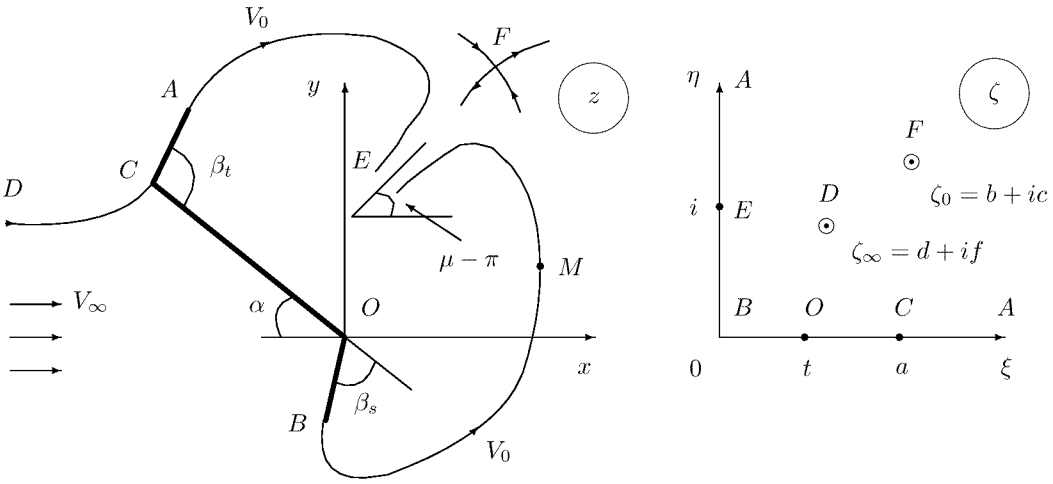


Figure 8: Flow pattern and auxiliary ζ-plane for the nonlinear shock free flat plate problem.

With the correspondence between the planes, the Chaplygin method allows us to write down the following exact solution:

$$\chi^{\mathrm{n}}(\zeta) = \frac{\mathrm{d}w}{v_0\mathrm{d}z} = e^{\mathrm{i}(\alpha-\gamma)}\left(\frac{\zeta-a}{\zeta+a}\right)^{\gamma/\pi}\left(\frac{\zeta-t}{\zeta+t}\right)^{\beta/\pi}\frac{(\zeta-\zeta_0)\,(\zeta-\bar{\zeta}_0)}{(\zeta+\zeta_0)\,(\zeta+\bar{\zeta}_0)}\,; \tag{28}$$

$$\frac{\mathrm{d}w}{\mathrm{d}\zeta} = N\frac{\zeta(\zeta^2-a^2)(\zeta^2-\zeta_0^2)(\zeta^2-\bar{\zeta}_0^2)}{(\zeta^2+1)(\zeta^2-\zeta_\infty^2)^2(\zeta^2-\bar{\zeta}_\infty^2)^2}\,, \tag{29}$$

wherefrom

$$z(\zeta) = \frac{N}{V_0}\,e^{\mathrm{i}(\gamma-\alpha)}\int_t^\zeta \frac{\zeta\,(\zeta+a)^{1+\gamma/\pi}\,(\zeta-a)^{1-\gamma/\pi}}{(\zeta^2+1)}\left(\frac{\zeta+t}{\zeta-t}\right)^{\beta/\pi}\cdot\frac{(\zeta+\zeta_0)^2(\zeta+\bar{\zeta}_0)^2}{(\zeta^2-\zeta_\infty^2)^2(\zeta^2-\bar{\zeta}_\infty^2)^2}\,d\zeta\,. \tag{30}$$

Five conditions

$$z_C = z(a) = l\,e^{\mathrm{i}(\pi-\alpha)}\,; \quad z_B = z(0) = \varepsilon\,e^{-\mathrm{i}(\alpha+\beta)}\,; \quad z_A - z_C = z(\infty) - z(a) = l_{\mathrm{w}}\,e^{\mathrm{i}(\gamma-\alpha)}\,;$$

$$\chi^{\mathrm{n}}(\zeta_\infty) = \frac{v_\infty}{v_0}\,; \quad \oint\limits_{\zeta_\infty} \frac{\mathrm{d}z}{\mathrm{d}\zeta}\,\mathrm{d}\zeta = 0$$

generate a system of seven nonlinear equations in eight real unknowns a, t, $\zeta_0 = b + \mathrm{i}c$, $\zeta_\infty = d + \mathrm{i}f$, N and l_{w}. An additional eighth condition is to be used to close the problem, namely connected with direction of the re-entrant jet at point E. Assume that angle μ is given, then the condition is

$$\chi^{\mathrm{n}}(\mathrm{i}) = e^{-\mathrm{i}\mu}\,,$$

or

$$\theta(1) = \mu\,, \tag{31}$$

where $\theta(\eta)$ denotes direction of velocity vector

$$\theta(\eta) = -\arg\chi(\mathrm{i}\eta) = -\alpha + \gamma - \frac{2\gamma}{\pi}\arctan\frac{a}{\eta} - 2\arctan\frac{b}{\eta - c} - 2\arctan\frac{b}{\eta + c} - \frac{2\beta}{\pi}\arctan\frac{t}{\eta}\,. \tag{32}$$

The pressure distribution coefficient is

$$C_p^{\mathrm{n}}(\xi) = 1 - |\chi^{\mathrm{n}}(\xi)|^2 = 1 - \left|\frac{\xi - a}{\xi + a}\right|^{2\gamma/\pi}\left(\frac{\xi^2 - 2b\xi + b^2 + c^2}{\xi^2 + 2b\xi + b^2 + c^2}\right)^2\left|\frac{\xi - t}{\xi + t}\right|^{2\beta/\pi}\,, \tag{33}$$

where $\xi = \mathrm{Re}\,(\zeta)$ is connected to z through relation (30). Lift and drag coefficients are

$$C_F = C_D + \mathrm{i}C_L = -\frac{\mathrm{i}}{l}\int\limits_0^\infty C_p^{\mathrm{n}}(\xi)\frac{\mathrm{d}z}{\mathrm{d}\xi}\,\mathrm{d}\xi = -\frac{\mathrm{i}}{l}(1+\sigma)\left(z_A - z_B - \frac{1}{v_0^2}\int\limits_0^\infty \frac{\mathrm{d}w}{\mathrm{d}\zeta}\overline{\frac{\mathrm{d}w}{\mathrm{d}z}}\,\mathrm{d}\xi\right). \tag{34}$$

On the other hand, using residue theory, one arrives at the following relationships (which are correct for an arbitrary cavitating hydrofoil):

$$C_D = \frac{2q}{v_\infty l}\left(1 - \frac{v_0}{v_\infty}\cos\mu\right)\,; \qquad C_L = \frac{2q}{v_\infty l}\left(\frac{\Gamma}{q} - \frac{v_0}{v_\infty}\sin\mu\right)\,, \tag{35}$$

where $q = 2\delta_e v_0$ denotes the flow rate in the re-entrant jet E (δ_e is *a half* of the width of the jet) and Γ is circulation along a large contour completely surrounding the cavitating foil and the cavity and enclosing most of the flow. Note that

$$\mathrm{res} = \oint\limits_{u_\infty} \frac{\mathrm{d}F}{\mathrm{d}\zeta}\mathrm{d}\zeta = \Gamma + iq$$

and, moreover,

$$q = \pi N\frac{(1+a^2)\,\left((1+b^2-c^2)^2 + 4b^2c^2\right)}{2\left((1+d^2-f^2)^2 + 4d^2f^2\right)^2}\,.$$

Another form of the force coefficient $C_F = C_D + \mathrm{i}C_L$ is

$$C_F = \frac{4\pi}{v_\infty}\left(-\sqrt{1+\sigma}\,\mathrm{e}^{\mathrm{i}\mu}\mathrm{Re}\,(\mathrm{res}) + \overline{\mathrm{res}}\right). \tag{36}$$

Let us analyse the solution to the problem under consideration in the case of $\alpha \to 0$, $\sigma \to 0$, $\varepsilon/l \to 0$ and $l_{\mathrm{w}}/l \to 0$, that is under assumption that hydrofoil brings small perturbations into the inflow. Thorough asymptotic analysis of the problem is given in [1] and below just final results are shown.
It is clear from what was done above that $a \to +\infty$, $\zeta_0 \to \mathrm{i}$ ($b \to 0$ and $c \to 1$) and $t \to 0$ if $\beta = \mathrm{O}(1)$ and $\gamma = \mathrm{O}(1)$.

Taking account of only linear terms in equations (28)–(32) under those circumstances results in $(c-1) \ll b$ (if $\mu = \pi + \mathrm{O}(\alpha)$) and

$$\sigma \sim 4fd_0\alpha + \frac{8\beta d_0}{\pi}\frac{1}{\sqrt{R}}\sqrt{\frac{\varepsilon}{l}}\,; \quad \frac{L_n}{l} \sim 4d_0^2 f^2$$

$$\frac{l_{\mathrm{w}}}{l} \sim \frac{\pi^4}{4\gamma^4}\frac{Q}{(f^2+d_0^2)^2}\left(d_0\frac{\sigma}{2} + f\alpha + \frac{\beta}{\pi}\frac{1}{\sqrt{R}}\sqrt{\frac{\varepsilon}{l}}\right)^4 \tag{37}$$

$$\frac{\delta_e}{l} \sim \frac{\pi}{16}\frac{1}{f^2 d_0^2}\left(f\frac{\sigma}{2} - d_0\,\alpha - \frac{2\beta}{\pi}\,f d_0\,\frac{1}{\sqrt{R}}\sqrt{\frac{\varepsilon}{l}}\right)^2$$

$$\frac{\mathrm{d}w}{v_\infty \mathrm{d}\tilde{z}} \sim 1 - \frac{2\gamma}{\pi}\frac{\zeta}{a} - 4b\,\frac{\zeta}{\zeta^2+1} - \frac{2\beta}{\pi}\frac{t}{\zeta}; \qquad \frac{\mathrm{d}w}{\mathrm{d}\zeta} \sim \frac{-Na^2\zeta(\zeta^2+1)}{\left(\zeta^4+2\zeta^2+(f^2+d_0^2)^2\right)^2}, \tag{38}$$

where L_n denotes 'nonlinear' cavity extent, $\tilde{z} = \mathrm{e}^{i\alpha}z$ and

$$d_0 = \sqrt{f^2-1}\,; \qquad R = \int\limits_0^1 \xi\Big(\frac{1+\xi}{1-\xi}\Big)^{\beta/\pi}\mathrm{d}\xi\,; \qquad Q = \int\limits_0^1 \xi(1-\xi^2)\Big(\frac{1+\xi}{1-\xi}\Big)^{\gamma/\pi}\mathrm{d}\xi\,. \tag{39}$$

The conformal mapping of the first quadrant of ζ–plane onto the upper semi–plane u has the following form

$$\zeta = \mathrm{i}\sqrt{\frac{u+u_0}{u}}\ ,$$

where $u_0 = 2d_0 f \sim \sqrt{L_n/l}$. Substituting this expression into (38) gives

$$\frac{\mathrm{d}w}{v_\infty \mathrm{d}\tilde{z}} \sim 1 - \mathrm{i}\,\frac{2\beta}{\pi}\,\frac{tu_0}{\sqrt{u\,(u+u_0)}} + \mathrm{i}\sqrt{\frac{u+u_0}{u}}\,\left(\frac{4b}{u_0}\,u - \frac{2\gamma}{\pi}\,\frac{1}{a} + \frac{2\beta}{\pi}\,t\right) \tag{40}$$

$$\frac{\mathrm{d}\tilde{z}}{\mathrm{d}u} \sim (L_n + l)\,\frac{2u}{(u^2+1)^2}\,. \tag{41}$$

Bearing in mind that 'linear' L and 'nonlinear' L_n cavity extent are connected to each other through the relation (due to a shift of coordinate systems)

$$L = 1 + \frac{L_n}{l}$$

and $L = \cos^{-2}(\tau/2)$, we find that

$$d_0 \to \frac{\sin\dfrac{\pi-\tau}{4}}{\sqrt{\sin\dfrac{\tau}{2}}}\,; \quad f \to \frac{\cos\dfrac{\pi-\tau}{4}}{\sqrt{\sin\dfrac{\tau}{2}}}\,.$$

Substituting these limits into asymptotic expansions obtained above gives expressions coinciding with those reduced from outer (2) and composite (27) solutions in the case of a supercavitating shock free flat plate when $f(x) = -\alpha x$ and $\mathcal{D}_k = \mathcal{E}_k = 0$. Moreover, the asymptotic and nonlinear approaches give the similar formulae for the width of re-entrant jet $2\delta_e$ and upper wetted portion of the leading edge l_{w}/l (compare (26) and (25) with (37)).

2.6. Numerical results

Mathematica for Windows computer mathematical environment was used to obtain all the numerical results shown in this section.

Flow pattern and hydrodynamic coefficients are given in figure 9 for nonlinear theory (NLT) and matched asymptotics (MAE) for a shock free flat plate. The flow parameters are chosen to be $\alpha = 10^{\mathrm{o}}$, $\sigma = 0.5$, $\bar{\varepsilon} = 0.05$, $\beta = 90^{\mathrm{o}}$, $\gamma = 60^{\mathrm{o}}$ and $\mu = 200^{\mathrm{o}}$. The position of stagnation point F is also shown.

Pressure distribution coefficient C_p is depicted for such a flat plate in figure 10 (for the same set of the flow parameters). Numerical results for the linear theory (outer asymptotic expansion $\chi^{\mathrm{o}}(z)$) is shown as well.

This page has been deliberately left blank

Page intentionnellement blanche

SUPERCAVITATING 2-D HYDROFOILS: PREDICTION OF PERFORMANCE AND DESIGN

Spyros A. Kinnas
Ocean Engineering Group, Department of Civil Engineering
The University of Texas at Austin, Austin, TX 78712, USA
http://cavity.ce.utexas.edu, email: kinnas@mail.utexas.edu

ABSTRACT

Recent numerical techniques for the prediction of cavitating flows, in linear and non-linear theories, are applied on super-cavitating 2-D, 3-D hydrofoils and propellers. Some of these techniques, when incorporated within a non-linear optimization algorithm, can lead to efficient super-cavitating hydrofoil or propeller designs. This lecture will address 2-D supercavitating hydrofoils.

1 INTRODUCTION

High-speed hydrofoil or propeller applications can benefit considerably, in terms of efficiency, by operating under super-cavitating, ventilating, or surface-piercing conditions, as shown in Fig. 1. A photograph from a super-cavitating hydrofoil experiment that was performed at MIT's variable pressure Marine Hydrodynamics Water Tunnel is shown in Fig. 2. Photographs of a modern surface-piercing propeller when out and in the water are shown in Fig. 3.

Cavitating or free-streamline flows were first addressed in nonlinear theory via the hodograph technique as introduced by Helmholtz, Kirchoff and Levi-Civita (Birkhoff & Zarantonello 1957)[1]. The cavity surface in steady flow was taken as a steamline with constant pressure (thus, constant velocity). The first problems to be addressed involved flows around bluff bodies at zero cavitation number.

The formulation of the cavitating flow around bodies at non-zero cavitation numbers created a lot of diversity on the cavity termination models. Some of the first known models were the Riabouchinsky end-plate model and the re-entrant jet model. Open wake models were introduced in an attempt to model the viscous cavity wake (Fabula 1962, Tulin 1964, Yamaguchi & Kato 1983, Rowe & Blottiaux 1993, Kato 1994). Some of the existing cavity termination models were already covered in previous lectures in this course.

Due to the difficulty of the hodograph technique in dealing with general body shapes, very few cases have been treated analytically. The hodograph technique was extended numerically to treat arbitrary geometries (Wu & Wang 1964) and later applied to the analysis of super-cavitating hydrofoils in the presence of a free surface (Furuya 1975a). This method however, still could not treat general shape three dimensional geometries.

The linearized cavity theory was introduced by (Tulin 1953) and became quickly very popular, as proven by the vast amount of publications[2] which made use of it.

Unfortunately, the linearized theory for partially cavitating hydrofoils predicts that by increasing the thickness of a hydrofoil, the extent and size of the cavity, for constant flow conditions, also increases. This contradicts the fact that thicker hydrofoils have larger leading edge radii which are known to delay cavitation inception and therefore are expected to develop smaller cavities. In addition, it is well known that linear theory grossly overpredicts the cavity extent and volume, especially in the case of partial cavitation.

(Tulin & Hsu 1980) developed the short cavity theory by considering the cavitating flow as a small perturbation on the nonlinear fully wetted flow. Thus, the nonlinear foil thickness effects were included in this

[1]The list of references is located at the end of the second lecture of Prof. Kinnas.
[2]An extended list of which may be found in (Tulin & Hsu 1980) or (Kinnas 1991).

Paper presented at the RTO AVT Lecture Series on "Supercavitating Flows", held at the von Kármán Institute (VKI) in Brussels, Belgium, 12-16 February 2001, and published in RTO EN-010.

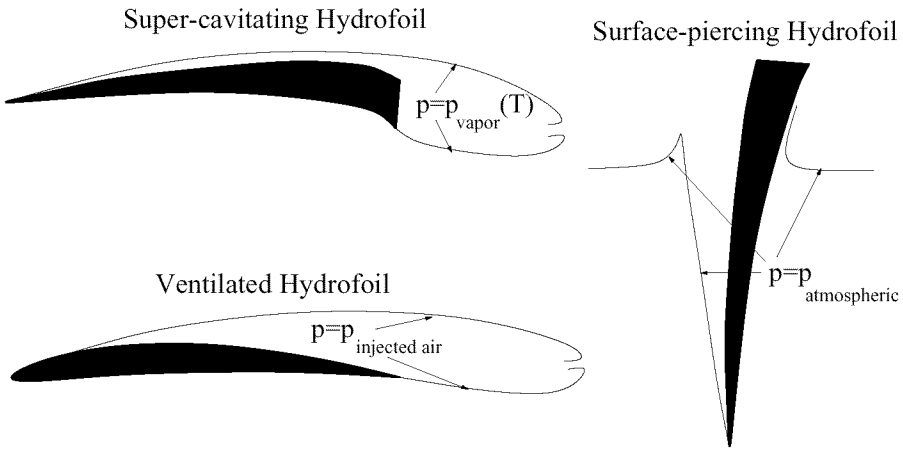


Figure 1: Schematic of different types of high-speed hydrofoils.

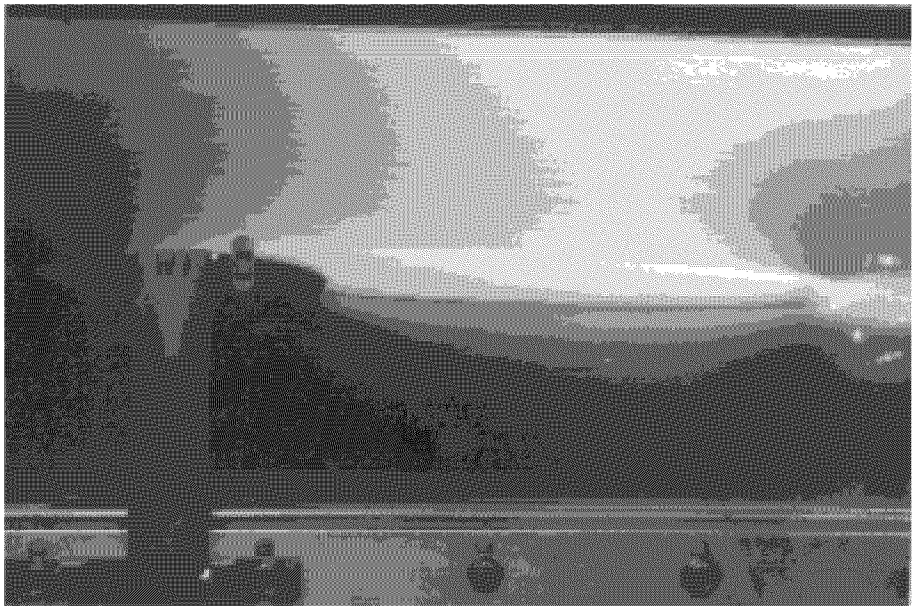


Figure 2: Photo of a supercavitating hydrofoil experiment inside MIT's Marine Hydrodynamics Water Tunnel, $l/c \approx 3$, from Kinnas & Mazel, 1993.

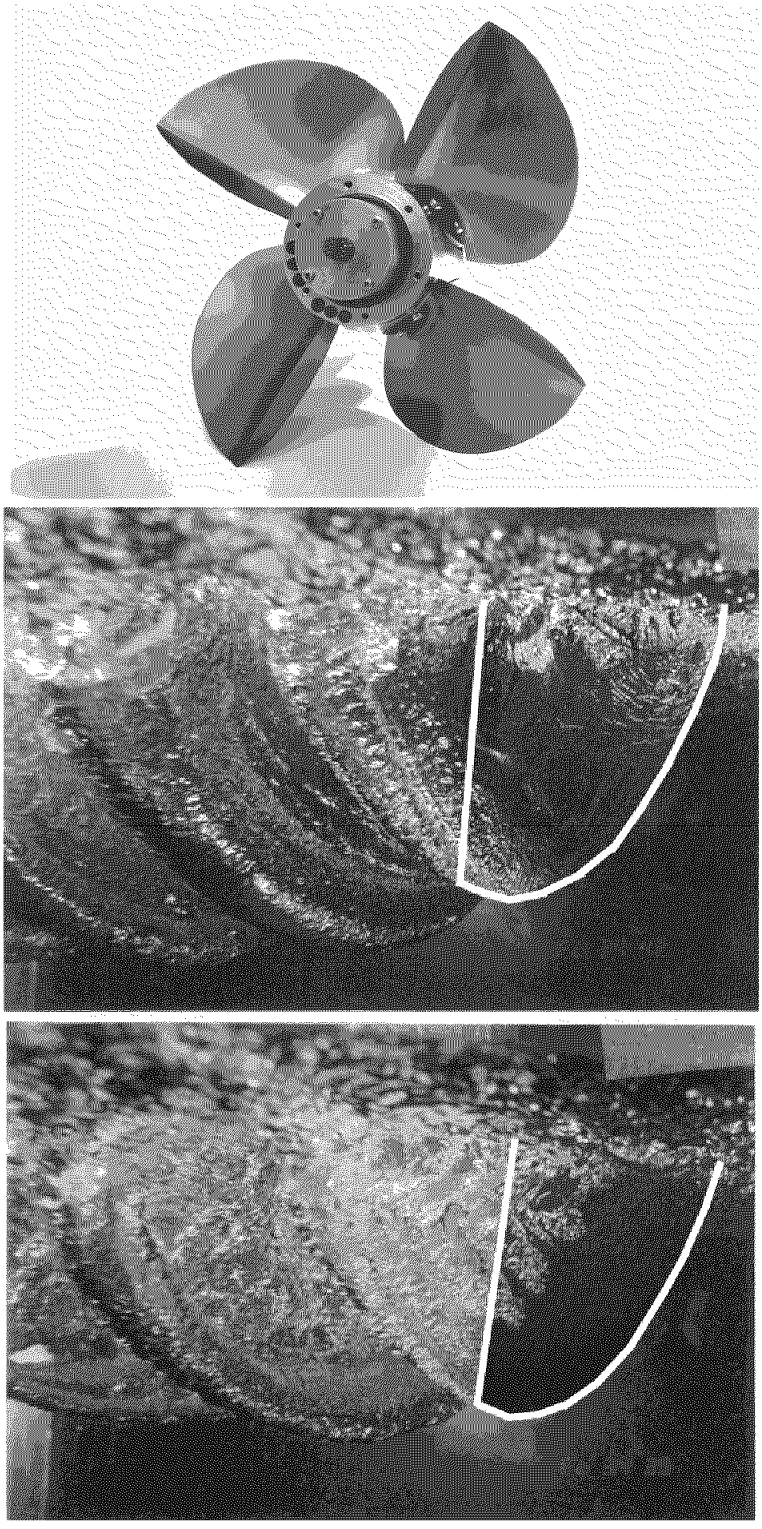


Figure 3: Photos of a surface-piercing propeller Model 841-B (top), and one of its blades after it has entered the free-surface, with leading edge detachment at $J_S = 0.9$ (middle), and with midchord detachment at $J_S = 1.0$ (bottom). For clarity, the blade has been outlined in the photos. From Olofsson (1996).

formulation. This method predicted that by increasing the thickness of a partially cavitating hydrofoil, the size of the cavity was reduced substantially for fixed flow conditions.

A nonlinear numerical method was employed to analyze cavitating hydrofoils by using surface vorticity techniques and by applying the exact boundary conditions on the cavity and on the foil (Uhlman 1987, Uhlman 1989). An end-plate cavity termination model was implemented. A reduction in the size of the cavity as the foil thickness increased was predicted, but not as drastic as that predicted in (Tulin & Hsu 1980). A surface vorticity technique to deal with thick foil sections which employed an open cavity model was developed in (Yamaguchi & Kato 1983). Similar boundary element method techniques were developed by (Lemonnier & Rowe 1988) and by (Rowe & Blottiaux 1993). Potential based boundary element methods were finally applied by (Kinnas & Fine 1991b, Kinnas & Fine 1993) and by (Lee et al 1992).

Three-dimensional flow effects around cavitating finite span hydrofoils were treated first in strip-theory via matching with an inner two-dimensional solution within either linear (Nishiyama 1970, Leehey 1971, Uhlman 1978, Van Houten 1982) or non-linear theory (Furuya 1975b).

The complete three-dimensional super-cavitating hydrofoil problem was first treated in linear theory via a numerical lifting surface approach based on the pressure source and doublet technique (Widnall 1966) and later via a vortex and source lattice technique (Jiang & Leehey 1977). In the latter work, an iterative scheme was introduced which determined the extent of the cavity by requiring the pressure distribution on the cavity to be constant along the span (in addition to being constant along the chord). A variational approach for determining the cavity planform was introduced in (Achkinadze & Fridman 1994).

Numerical boundary element methods within non-linear cavity theory were naturally extended to treat super-cavitating 3-D hydrofoils (Pellone & Rowe 1981) and 3-D hydrofoils with partial cavities (Kinnas & Fine 1993) or cavities with mixed (partial and super-cavities) planforms (Fine & Kinnas 1993a). Similar methods were also developed by (Kim et al 1994, Pellone & Peallat 1995).

The first effort to analyze the complete three dimensional unsteady flow around a cavitating propeller subject to a spatially non-uniform inflow was presented in (Lee 1979, Lee 1981, Breslin et al 1982). A source and vortex lattice lifting surface scheme was employed and the unsteady three dimensional *linearized* boundary conditions were applied on the cavity. The cavity planform was determined at each blade strip and each time step (i.e., blade angle) by searching for the cavity length which would produce the desired vapor pressure inside the cavity. The effect of the other strips was accounted for in an iterative sense by "sweeping" along the spanwise direction of the blade back and forth until the cavity shape converged. Similar methods were presented more recently by (Ishii 1992, Szantyr 1994, Kudo & Ukon 1994).

Unfortunately, all these 3-D methods are hampered by the inherent inability of linear cavity theory to predict the correct effect of blade thickness on cavity shape, as already mentioned. This deficiency was corrected in two dimensions in (Kinnas 1985, Kinnas 1991), where the *leading edge correction* was introduced in the linearized dynamic boundary condition on the cavity. The leading edge correction was subsequently applied to the three dimensional propeller solution (Kerwin et al 1986, Kinnas 1992b).

Non-linear methods based on an assumed semi-elliptic cavity sectional shape have also been applied (Stern & Vorus 1983) and (Van Gent 1994). Non-linear potential-based boundary element methods were finally applied to cavitating propellers in non-uniform flows by (Kinnas & Fine 1992, Fine & Kinnas 1993b), and more recently by (Kim & Lee 1996).

The inviscid cavity flow method was coupled with a boundary layer solver in the case of partial and super-cavitating 2-D hydrofoils by (Kinnas et al 1994). This allowed for the inclusion of the viscous boundary layer in the wake of the cavity and for determining the cavity detachment point based on the viscous flow upstream of the cavity.

Reynolds-Averaged Navier-Stokes solvers have also been applied in the case of the prediction of attached sheet cavitation on 2-D hydrodoils (Kubota et al 1989, Deshpande et al 1993). An overview of viscous flow solvers applied to cavitating flows may be found in (Kato 1996). However, these methods appear to be best suited for the prediction of cloud and or detached cavitation.

In these two lectures, linear and nonlinear methods for the prediction of super-cavitation on hydrofoils and propellers will be summarized, and some comparisons with experiments will be presented. Non-linear optimization techniques, applicable to the design of 2-D super-cavitating sections and super-cavitating propeller blades, will be also presented.

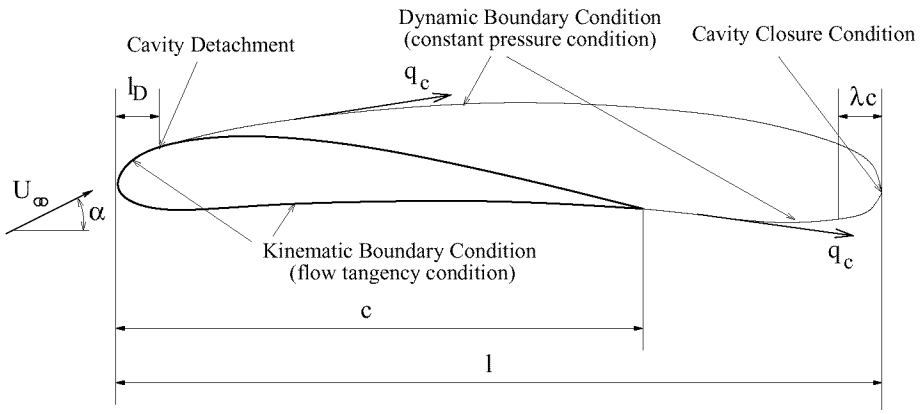


Figure 4: Formulation of the inviscid cavity flow problem

2 2-D HYDROFOIL

2.1 Formulation

Consider the 2-D super-cavitating hydrofoil[3], as shown in Fig. 4. Assuming inviscid and irrotational flow, the governing equation everywhere inside the fluid region is given by[4]:

$$\nabla^2\phi = 0 \tag{1}$$

where ϕ is the the perturbation potential defined from:

$$\mathbf{q} = \mathbf{U}_\infty + \nabla\phi \tag{2}$$

where $\mathbf{q}$ is the total velocity vector in the flow. In order to uniquely determine ϕ, the following boundary conditions are imposed:

- On the wetted foil surface, the following kinematic boundary condition is applied, which requires the fluid flow to be tangent to the surface of the foil. Therefore,

$$\frac{\partial\phi}{\partial n} = -\mathbf{U}_\infty \cdot \mathbf{n} \tag{3}$$

  where $\mathbf{n}$ is the surface unit normal vector.

- At infinity the perturbation velocities should go to zero.

$$\nabla\phi \to 0 \tag{4}$$

- The dynamic boundary condition specifies constant pressure on the cavity, or (via Bernoulli equation) constant cavity velocity q_c:

$$q_c = U_\infty\sqrt{1+\sigma} \tag{5}$$

  where the cavitation number, σ, is defined as:

$$\sigma = \frac{p_\infty - p_c}{\frac{\rho}{2}U_\infty^2} \tag{6}$$

  p_∞ is the pressure corresponding to a point in the free-stream and p_c is the pressure inside the cavity.

[3]The application of the methods to partially cavitating hydrofoils is straight-forward and the reader can find more details in (Kinnas 1998).

[4]The cavity is assumed to detach at a known location on the foil. A criterion for determining this location will be discussed in a later section.

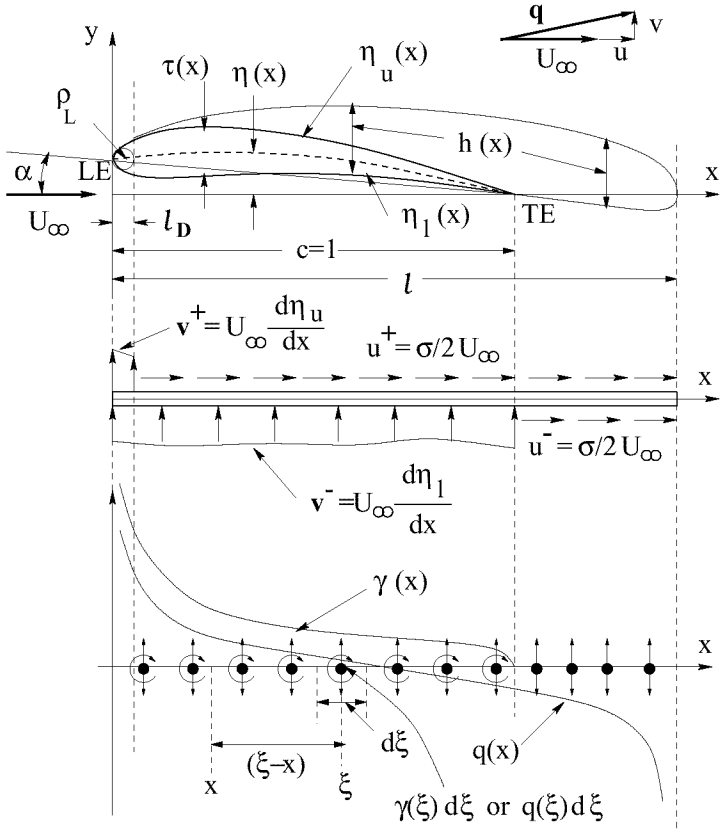


Figure 5: Supercavitating hydrofoil in linear theory.

- The following conditions at the trailing edge of the cavity:

  1. The cavity closes at its trailing edge. The inclusion of the viscous wake downstream of the cavity will be addressed in a later section.
  2. Near the trailing edge of the cavity, the pressure recovery termination model renders for the cavity velocity, q_{tr}, over a transition region λc:

$$q_{tr} = U_\infty \sqrt{1+\sigma}\,[1 - f(x)] \tag{7}$$

  where $f(x)$ is an algebraic function defined in (Kinnas & Fine 1993).

The problem of finding the cavitation number for given cavity extent, l, will be addressed first in the context of linear and nonlinear theories. A method for determining the cavity extent for given cavitation number will be described in a later section.

2.2 Linear theories

In this section, the linearized cavitating hydrofoil problem is formulated in terms of singular integral equations with respect to unknown vorticity and source distributions. These integral equations are inverted analytically in the case of general shape supercavitating hydrofoils. The cavitation number, the vorticity and source distributions are expressed in terms of integrals of quantities which depend *only* on the foil geometry and the cavity length. The procedure is summarized here. The details are given in (Kinnas 1992a) and (Kinnas & Fine 1991a).

We define as u and v the perturbation velocities tangent and normal to the direction of the incoming flow respectively, as shown in Figure 5. In the context of the linearized cavity theory the boundary conditions of the corresponding Hilbert problem are:

The kinematic boundary conditions:

$$v^- = U_\infty \frac{d\eta_l}{dx} \; ; \quad 0 < x < 1 \; , \; y = 0^- \tag{8}$$

$$v^+ = U_\infty \frac{d\eta_u}{dx} \; ; \quad 0 < x < l_D \; , \; y = 0^+ \tag{9}$$

The dynamic boundary conditions:

$$u^+ = \frac{\sigma}{2} U_\infty \; ; \quad l_D < x < l \; , \; y = 0^+ \tag{10}$$

$$u^- = \frac{\sigma}{2} U_\infty \; ; \quad 1 < x < l \; , \; y = 0^- \tag{11}$$

where $\eta_l(x)$ and $\eta_u(x)$ are the ordinates of the lower and upper hydrofoil surface, respectively, as shown in Figure 5. These boundary conditions can be expressed in terms of vorticity and source distributions [5] $\gamma(x)$ and $q(x)$, respectively, located on the slit $x \in [0, l]$.

$$v^- = -\frac{q}{2} + \frac{1}{2\pi} \int_0^1 \frac{\gamma(\xi) d\xi}{\xi - x} \tag{12}$$

$$u^+ = \frac{\gamma}{2} - \frac{1}{2\pi} \int_0^l \frac{q(\xi) d\xi}{\xi - x} \tag{13}$$

$$u^- = -\frac{\gamma}{2} - \frac{1}{2\pi} \int_0^l \frac{q(\xi) d\xi}{\xi - x} \tag{14}$$

By using equations (10), (11), (13), and (14) it can easily be shown that:

$$\gamma(x) = 0; \quad 1 < x < l \tag{15}$$

Finally, and with the use of the definitions:

$$\overline{\gamma}(x) = \frac{\gamma(x)}{\sigma U_\infty} \quad \text{and} \quad \overline{q}(x) = \frac{q(x)}{\sigma U_\infty} \; , \tag{16}$$

the complete boundary value problem becomes:

1. *Kinematic Boundary Conditions*

$$-\frac{\overline{q}}{2} + \frac{1}{2\pi} \int\!\!\!\!\!\!- \, _0^1 \frac{\overline{\gamma}(\xi) d\xi}{\xi - x} = \Theta_l^*(x) \; ; \; 0 < x < 1 \; , \; y = 0^- \tag{17}$$

$$\frac{\overline{q}}{2} + \frac{1}{2\pi} \int\!\!\!\!\!\!- \, _0^1 \frac{\overline{\gamma}(\xi) d\xi}{\xi - x} = \Theta_u^*(x) \; ; \; 0 < x < l_D \; , \; y = 0^+ \tag{18}$$

2. *Dynamic Boundary Condition*

$$\frac{\overline{\gamma}}{2} - \frac{1}{2\pi} \int\!\!\!\!\!\!- \, _0^l \frac{\overline{q}(\xi) d\xi}{\xi - x} = \frac{1}{2} \; ; \; l_D < x < l \; , \; y = 0^+ \tag{19}$$

3. *Kutta Condition*[6]

$$\overline{\gamma}(1) = 0 \tag{20}$$

[5] With $\int\!\!\!\!\!\!-$ designating the Cauchy principal value of the integral.

[6] The application of a Kutta condition may seem unnecessary due to the requirement of a finite pressure, thus velocity, at the foil trailing edge. Nevertheless, this condition is still required when inverting the integral equations.

4. *Cavity Closure Condition* [7]

$$\int_0^l \overline{q}(x)dx = 0 \tag{21}$$

where

$$\Theta_l^* = \frac{1}{\sigma}\frac{d\eta_l}{dx} \quad \text{and} \quad \Theta_u^* = \frac{1}{\sigma}\frac{d\eta_u}{dx} \tag{22}$$

2.2.1 Inversion of the Integral Equations - $l_D = 0$

In the case of leading edge detachment ($l_D = 0$), the singular integral equations of Cauchy type, (17) and (19), can be inverted to produce expressions for the unknown σ, $\overline{\gamma}(x)$ and $\overline{q}(x)$ in terms of the cavity length l and the lower hydrofoil surface $\eta_l(x)$, as follows (Kinnas 1992a):

First, equation (19) is inverted with respect to the unknown $\overline{q}(x)$ (Muskhelishvili 1946) to produce:

$$\overline{q}(x) = -\sqrt{\frac{x}{l-x}} + \frac{1}{\pi}\sqrt{\frac{x}{l-x}}\int_0^1 \sqrt{\frac{l-\xi}{\xi}}\,\frac{\overline{\gamma}(\xi)d\xi}{x-\xi} \tag{23}$$

where use of equation (15) has been made. Notice that the expression (23) corresponds to the unique solution to (19) which behaves like $1/\sqrt{l-x}$ at the trailing edge of the cavity (Wu's singularity (Wu 1957)). By substituting equation (23) in (17) and by using the substitutions:

$$z = \sqrt{\frac{x}{l-x}}, \quad \eta = \sqrt{\frac{\xi}{l-\xi}}, \quad t = \sqrt{\frac{1}{l-1}}, \tag{24}$$

we arrive at the following singular integral equation of Cauchy type for $\overline{\gamma}$:

$$\frac{1}{2\pi}\int_0^t \frac{\overline{\gamma}(\eta)d\eta}{(1+\eta^2)(z-\eta)} = \frac{z}{4(1+z^2)} - \frac{\Theta_l^*(z)}{2(1+z^2)} \tag{25}$$

Inversion of equation (25) with respect to the variable $\overline{\gamma}(\eta)/(1+\eta^2)$ renders finally:

$$\overline{\gamma}(z) = -\frac{(1+z^2)}{\pi}\sqrt{\frac{t-z}{z}}\int_0^t \sqrt{\frac{\eta}{t-\eta}}\,\frac{\frac{\pi}{2} - \Theta_l^*(\eta)}{(1+\eta^2)(z-\eta)}d\eta \tag{26}$$

Notice that $\overline{\gamma}(z)$ in equation (26) is the unique solution to (25) which satisfies the Kutta condition (20) at $z = t$.

The cavitation number σ is determined by satisfying the cavity closure condition (21). First, by substituting equation (23) in (21) and by using equation (15) we can get (Kinnas 1992a):

$$-\frac{\pi l}{2} + \int_0^1 \sqrt{\frac{l-\xi}{\xi}}\,\overline{\gamma}(\xi)d\xi = 0, \tag{27}$$

and by substituting equation (26) we can get the following general expression for σ (Kinnas 1992a):

$$\sigma = \frac{4\sqrt{2}r^4}{\pi(r^2+1)}\int_0^t \sqrt{\frac{\eta}{t-\eta}}\,\frac{\sqrt{r^2+1}+\eta\sqrt{r^2-1}}{(1+\eta^2)^2}\left[-\frac{d\eta_l}{dx}\right]d\eta \tag{28}$$

where: $r = \sqrt{1+t^2}$.

The source distribution can be derived by substituting equation (26) into equation (23) (Kinnas 1992a):

$$\begin{aligned}\overline{q}(z) \;=\; & -\Theta_l^*(z) + \sqrt{\frac{t+z}{z}}\,\frac{(\sqrt{r^2-1} - z\sqrt{r^2+1})}{2\sqrt{2}r^2} - \\ & \frac{1+z^2}{\pi}\sqrt{\frac{t+z}{z}}\int_0^t \sqrt{\frac{\omega}{t-\omega}}\,\frac{\Theta_l^*(\omega)d\omega}{(1+\omega^2)(z+\omega)}\end{aligned} \tag{29}$$

[7] We apply the linearized cavity closure condition in which the cavity is required to have zero thickness at its trailing edge. The present method can be extended to treat open cavities at the trailing edge with the openness of the cavity, possibly supplied from further knowledge of the viscous wake behind the cavity. The effects of viscosity will be addressed at a later section.

for $z < t$, and:

$$\begin{aligned}\overline{q}(z) \quad = \quad & \sqrt{\frac{t+z}{z}}\,\frac{(\sqrt{r^2-1}-z\sqrt{r^2+1})}{2\sqrt{2}r^2} - \\ & \frac{1+z^2}{\pi}\sqrt{\frac{t+z}{z}}\int_0^t \sqrt{\frac{\omega}{t-\omega}}\,\frac{\Theta_l^*(\omega)d\omega}{(1+\omega^2)(z+\omega)} - \\ & \sqrt{\frac{z-t}{z}}\,\frac{(z\sqrt{r^2+1}+\sqrt{r^2-1})}{2\sqrt{2}r^2} - \\ & \frac{1+z^2}{\pi}\sqrt{\frac{z-t}{z}}\int_0^t \sqrt{\frac{\omega}{t-\omega}}\,\frac{\Theta_l^*(\omega)d\omega}{(1+\omega^2)(z-\omega)}\end{aligned} \tag{30}$$

for $z > t$.

2.2.2 Inversion of the Integral Equations - $l_D > 0$

In this case, as shown in (Kinnas & Fine 1991a), equations (26), (29), and (30) still apply, after the following substitutions are made:

$$\text{replace } \overline{\gamma} \text{ with } \overline{\gamma} - 2(u_{cw}^+ - \frac{1}{2}) \;\; ; \; 0 < x < l_D \tag{31}$$

and

$$\text{replace } \Theta_l^* \text{ with } \Theta_l^* + F \tag{32}$$

with

$$F(x) \stackrel{\text{def}}{=} -\frac{1}{\pi}\int_0^{l_D} \frac{u_{cw}^+ - \frac{1}{2}}{\xi - x}d\xi \tag{33}$$

where u_{cw}^+ is the horizontal perturbation velocity on the wetted part on the suction side of the foil, divided by σU_∞. The value of u_{cw}^+ is determined by applying the kinematic boundary condition on the upper wetted part of the hydrofoil, equation (9). This is equivalent to requiring that the value of $q(x)$ for $0 < x < l_D$ is equal to the value of the thickness source in the case of wetted flow. A rather lengthy formula for u_{cw}^+, as well an expression for the modified value of σ are given in (Kinnas & Fine 1991a), and are not included in this lecture.

2.2.3 The cavity shape

The cavity thickness $h(x)$, which also includes the foil thickness as shown in Figure 5, is determined, within the framework of linearized theory, by integrating the equation:

$$U_\infty \frac{dh}{dx} = q(x) \tag{34}$$

The camber of the cavity in the wake, $c(x)$, is determined by integrating the following equation:

$$U_\infty \frac{dc}{dx} = v_w(x) \quad for \;\; 1 < x < l \tag{35}$$

where $v_w(x)$ is the normal perturbation velocity in the wake, given as follows:

$$v_w(x) = -\frac{1}{2\pi}\int_0^1 \frac{\gamma(\xi)d\xi}{x-\xi} \;\; ; \;\; 1 < x < l, \;\; y = 0 \tag{36}$$

By substituting equation (26) in (36) we can get v_w in terms of the hydrofoil geometry (Kinnas & Fine 1991a):

$$\frac{v_w(z)}{\sigma U_\infty} = \sqrt{\frac{t+z}{z}}\ \frac{(\sqrt{r^2-1}-z\sqrt{r^2+1})}{4\sqrt{2}r^2} - \frac{1+z^2}{2\pi}\sqrt{\frac{t+z}{z}}\int_0^t \sqrt{\frac{\omega}{t-\omega}}\ \frac{\Theta_l^*(\omega)d\omega}{(1+\omega^2)(z+\omega)} - \sqrt{\frac{z-t}{z}}\ \frac{(z\sqrt{r^2+1}+\sqrt{r^2-1})}{4\sqrt{2}r^2} - \frac{1+z^2}{2\pi}\sqrt{\frac{z-t}{z}}\int_0^t \sqrt{\frac{\omega}{t-\omega}}\ \frac{\Theta_l^*(\omega)d\omega}{(1+\omega^2)(z-\omega)} \tag{37}$$

The pressure distribution on the upper and lower cavity or foil surface is given, in the context of linear theory, as follows:

$$C_p^+ = -2\sigma\left[\frac{\overline{\gamma}}{2} - \frac{1}{2\pi}\int_0^l \frac{\overline{q}(\xi)d\xi}{\xi - x}\right]\ ;\ 0 < x < l\ ,\ y = 0^+ \tag{38}$$

$$C_p^- = -2\sigma\left[-\frac{\overline{\gamma}}{2} - \frac{1}{2\pi}\int_0^l \frac{\overline{q}(\xi)d\xi}{\xi - x}\right]\ ;\ 0 < x < l\ ,\ y = 0^- \tag{39}$$

where C_p is the pressure coefficient defined as:

$$C_p = \frac{p - p_\infty}{\frac{\rho}{2}U_\infty^2} \tag{40}$$

2.2.4 Numerical Integrations

The integrals in equations (28), (26), (29) and (30) are computed numerically with special care taken at the singularities of the integrands. We first define the transformation:

$$\eta = t\ \sin^2\left(\frac{\theta}{2}\right)\ \ ;\ \ 0 \le \eta \le t \text{ and } 0 \le \theta \le \pi \tag{41}$$

Next, we expess the involved integrals in terms of θ, thus avoiding the square root singularities of the integrands at $\eta = 0$ and $\eta = t$. The numerical integrations are then performed by applying Simpson's rule with K uniform intervals in θ.

To compute the principal value of the singular integral in equation (26), we first factor out the involved singularity as follows (Kinnas 1992a):

$$\int_0^t \sqrt{\frac{\eta}{t-\eta}}\ \frac{f(\eta)}{z-\eta}d\eta = \int_0^t \sqrt{\frac{\eta}{t-\eta}}\ \frac{f(\eta)-f(z)}{z-\eta}d\eta - \pi f(z) \tag{42}$$

where $f(\eta) = \frac{\frac{\eta}{2} - \Theta_l^*(\eta)}{1+\eta^2}$. Notice that the integrand in the integral of equation (42) is not singular anymore, and thus the integral is computed numerically by applying the same methodology described in the beginning of this section. As shown in (Kinnas 1992a), Simpson's rule produces very accurate values for the integrals even with five uniform intervals ($K = 5$).

2.2.5 The vortex/source-lattice method

A direct numerical method must be applied in the case of 3-D hydrofoils or propeller blades, as in (Lee 1979, Kinnas et al 1998a, Kosal 1999). In this case the involved integrals are disretized first, then the boundary conditions are applied at some appropriately selected control points (C.P.s), and finally, the resulting system of linear equations is inverted. The integrals in equations (17) and (19) are disretized over each segment i by replacing $\gamma(\xi)d\xi$ with $\gamma_i(X_{pv_{i+1}} - X_{pv_i})$, and $q(\xi)d\xi$ with $q_i(X_{ps_{i+1}} - X_{ps_i})$. Figure 6 shows two types of arrangements for the discrete vortices and sources and the correpsonding control points.

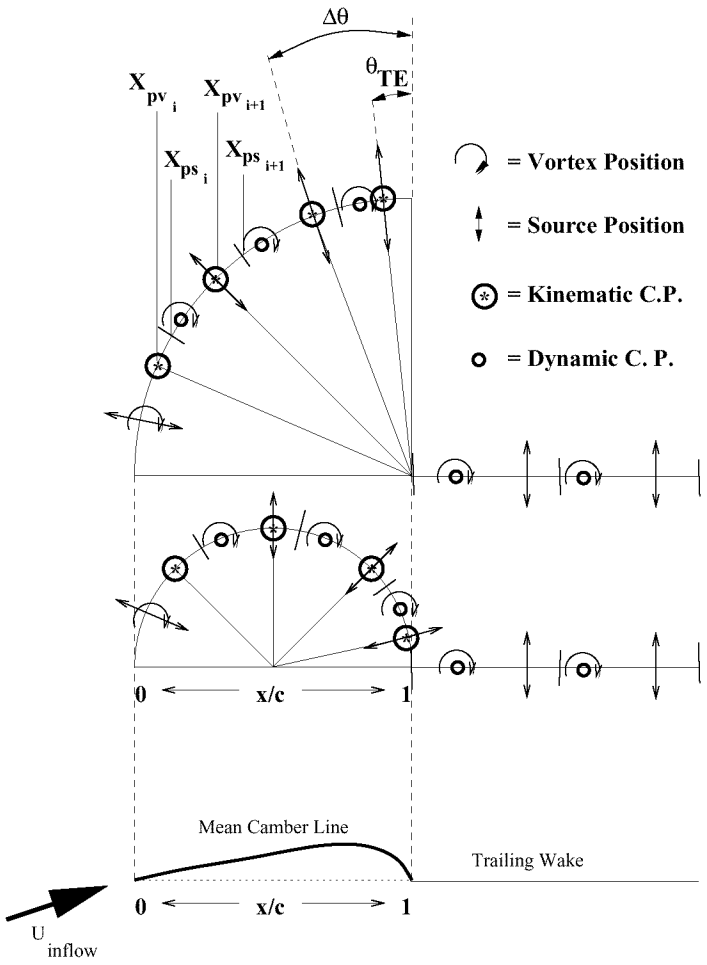


Figure 6: Half-cosine and full-cosine discretization scheme in the vortex/source-lattice method. The latter allows for a better representation of typical camber lines for super-cavitating hydrofoils.

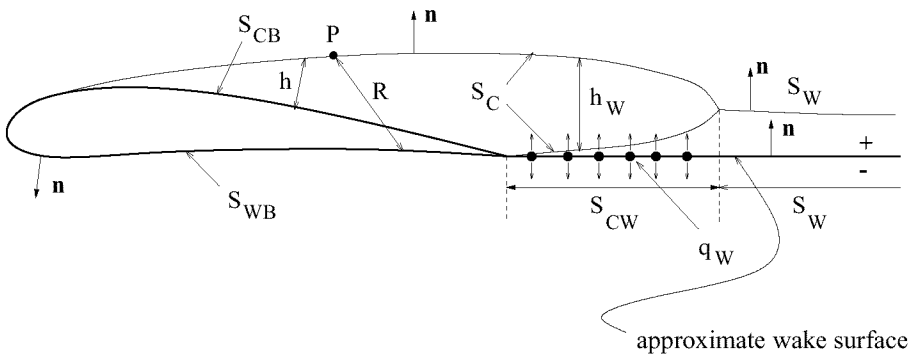


Figure 7: Super-cavitaitng non-linear theory. Definition of cavity, (wetted) body, and wake surfaces. The cavity sources in the wake are also shown in the case of the hybrid scheme.

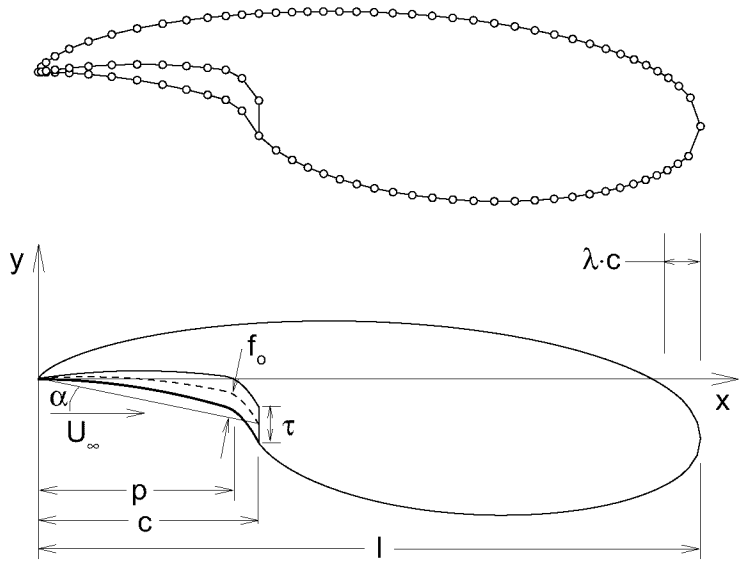


Figure 8: Super-cavitating hydrofoil. Definition of main parameters. Panel arrangement on the cavity and foil shown for $N = 80$.

2.3 Nonlinear theories

A potential based boundary element method which has applied has been applied for the analysis of cavitating hydrofoils in nonlinear cavity theory (Kinnas & Fine 1991b, Kinnas & Fine 1993, Fine & Kinnas 1993a), is summarized here, with emphasis on super-cavitating hydrofoils. The perturbation potential on the combined foil and cavity surface satisfies the following integral equation (Green's third identity):

$$\begin{aligned} \pi\phi_p &= \int_{S_{WB}\cup S_C} \left[\frac{\partial\phi}{\partial n}\ln R - \phi\frac{\partial \ln R}{\partial n}\right] dS \\ &- \int_{S_W} \Delta\phi_W \frac{\partial \ln R}{\partial n} dS \end{aligned} \tag{43}$$

$\mathbf{n}$ is a unit vector normal to the foil or cavity surface, S_{WB} is the wetted body (foil) surface, S_C, the cavity surface, and S_W is the trailing wake surface, as shown in Fig. 7. R is the distance between a point, P, and the point of integration over the wetted foil, cavity, or wake surface, as shown in Fig. 7.

The foil and cavity surface are discretized into flat panels, as shown in Fig. 8. The source and dipole strengths are assumed constant over each panel. On the wetted foil surface, the source strengths, which are proportional to $\partial\phi/\partial n$, are given by the kinematic boundary condition, equation (3). On the cavity, the dipole strengths, which are proportional to ϕ, are determined from the application of the dynamic boundary condition (5) and (7). For simplicity $\lambda = 0$ for the rest of this paper; the complete derivation is given in (Kinnas & Fine 1993). It should be noted that the length of the transition region λ has been found to affect the results only locally. In the case of $\lambda = 0$ and when a large number of panels is used the formation of a re-entrant is observed(Krishnaswamy 1999).

$$q_c = \mathbf{U}_\infty \cdot \mathbf{s} + \frac{\partial\phi}{\partial s} = U_\infty\sqrt{1+\sigma} \tag{44}$$

where s is the arclength along the cavity surface (measured from the cavity detachment point), and $\mathbf{s}$ is the unit vector tangent to the cavity surface. Integration of equation (44) renders the potential on the cavity surface:

$$\phi(s) = \phi(0) - \mathbf{U}_\infty \cdot \mathbf{s} + sU_\infty\sqrt{1+\sigma} \tag{45}$$

Where $\phi(0)$ is the potential at the leading edge of the cavity. In the numerical scheme $\phi(0)$ is expressed in terms of the (unknown) potentials on the wetted part of the foil in front of the cavity.

The potential jump, $\Delta\phi_w$, in the wake is determined via the following condition:

$$\Delta\phi_w = \phi^+_{CTE} - \phi^-_{CTE} \tag{46}$$

where ϕ^+_{CTE} and ϕ^-_{CTE} are the potentials at the upper and lower cavity trailing edge panels, respectively. In two dimensions the effect of the trailing wake surface is equivalent to the effect of a concentrated vortex at the cavity trailing edge with strength equal to $\Delta\phi_w$.

The integral equation (43) is applied at the panel mid-points together with equations (46). The resulting linear system of equations is inverted in order to provide the unknowns: (a) ϕ on the wetted foil, (b) $\partial\phi/\partial n$ on the cavity, and (c) the corresponding cavitation number σ. The cavity shape is determined in an iterative manner. In the first iteration the panels representing the cavity are placed on the foil surface directly under the cavity. In subsequent iterations the cavity shape is updated by an amount $h(s)$ (applied normal to the cavity surface) which is determined from integrating the following ordinary differential equation[8]:

$$q_c \frac{dh}{ds} = \mathbf{U}_\infty \cdot \mathbf{n} + \frac{\partial\phi}{\partial n} \tag{47}$$

In addition, the cavity closure condition is enforced by the following equation:

$$h(s_L) = \frac{1}{q_c} \int_0^{s_L} \left[\mathbf{U}_\infty \cdot \mathbf{n} + \frac{\partial\phi}{\partial n} \right] ds = 0 \tag{48}$$

s_L is the total arclength along the cavity surface.

The predicted cavity shapes and cavitation numbers have been found to converge quickly with number of iterations, especially in the case of super-cavitating hydrofoils.

This particular feature of the presented method makes it very attractive for 3-D and/or unsteady flow applications, where carrying more than one iterations would increase the computation time substantially. In fact the first iteration in the iterative scheme is determined by using the following *hybrid* scheme.

2.3.1 The hybrid scheme

In the case of 3-D hydrofoils and propeller blades, the following *hybrid* (combination of panel and source lattice method) scheme has been developed (Fine & Kinnas 1993a). In this scheme the panels representing the cavity are placed either on the foil surface underneath the cavity, S_{CB}, or on the approximate wake surface, S_{CW}, as shown in Fig. 7. Equation (43) then becomes(Fine & Kinnas 1993a):

$$\begin{aligned} \pi\phi_p &= \int_{S_B} \left[\frac{\partial\phi}{\partial n} \ln R - \phi \frac{\partial \ln R}{\partial n} \right] dS \\ + \int_{S_{CW}} q_W \ln R dS &- \int_{S_{CW} \cup S_W} \Delta\phi_W \frac{\partial \ln R}{\partial n} dS \\ & \text{for} \quad P \in S_B \end{aligned} \tag{49}$$

and

$$\begin{aligned} 2\pi\phi^+_p = \pi\Delta\phi_W &+ \int_{S_B} \left[\frac{\partial\phi}{\partial n} \ln R - \phi \frac{\partial \ln R}{\partial n} \right] dS \\ + \int_{S_{CW}} q_W \ln R dS &- \int_{S_{CW} \cup S_W} \Delta\phi_W \frac{\partial \ln R}{\partial n} dS \\ & \text{for} \quad P \in S_{CW} \end{aligned} \tag{50}$$

where $S_B = S_{WB} \cup S_{CB}$ is the surface of the whole foil, and q_W is the cavity source in the wake surface given as:

$$q_W = \frac{\partial\phi^+}{\partial n} - \frac{\partial\phi^-}{\partial n} = q_c \frac{dh_W}{ds} \tag{51}$$

[8] As shown in (Kinnas & Fine 1993) this equation is equivalent to the kinematic boundary condition on the cavity surface.

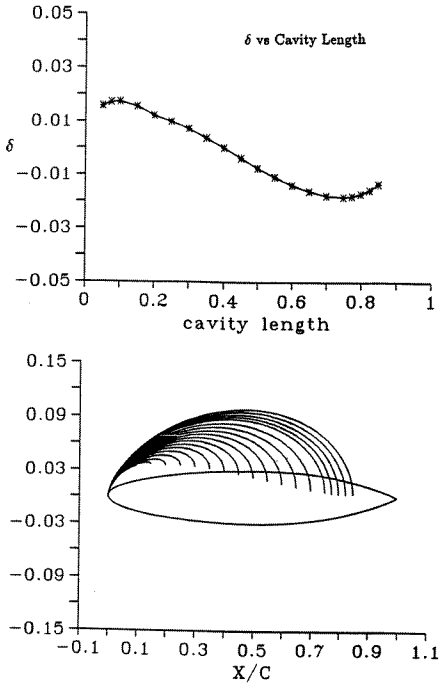


Figure 9: Predicted cavity trailing edge thickness and cavity shape for various cavity lengths at $\sigma = 1.097$ (corresponding to $l = 0.4$). From Kinnas and Fine, 1993.

where h_W is the cavity height measured normal to S_{CW}, as shown in Fig. 7. The cavity height h is measured normal to the foil surface for the part of the cavity that overlaps the foil, as also shown in Fig. 7.

The major advantage of the hybrid scheme is that it *can apply to all, wetted, partially, and super-cavitating flows alike* by utilizing the *same* panel discretization. In fact this scheme, as described in later sections, is applied on super-cavitating 3-D hydrofoils and propellers. In addition, this scheme has been found to predict the expected non-linear effect of foil thickness on the cavity shape in the case of partial cavitation (Kinnas & Fine 1993).

2.4 Cavity extent for given cavitation number

In the previous sections the cavity length was assumed to be known. In the case of linear theory, equation 28 can be inverted with respect to l for given σ. In the case of nonlinear theories the method can still be applied for the given σ and various "trial" cavity lengths. In this case though, due to the fact that the cavitation number is given (instead of being determined), the cavity closure condition, equation (48), or its equivalent $h_W(l) = 0$ in the case of the hybrid scheme, will not be satisfied.

$$\delta(l;\sigma) \equiv h_W(l) \neq 0 \tag{52}$$

This is shown for a partially cavitating hydrofoil in Fig. 9 where the predicted δ and the cavity shapes for fixed σ and different values of cavity length are shown. An iterative scheme has been developed (Kinnas & Fine 1993) for determining the cavity extent for given σ by searching for the cavity length, l, for which the cavity closes (within a specified tolerance) at its trailing edge[9]:

$$\delta(l;\sigma) = 0 \tag{53}$$

A comparison of predictions from applying the linear, the fully non-linear, and the hybrid cavity models to a super-cavitating hydrofoil is shown in Figure 10. All theories, including the conventional linear theory, appear

[9]An open cavity model can be readily implemented within this method by requiring the specified thickness at the cavity end.

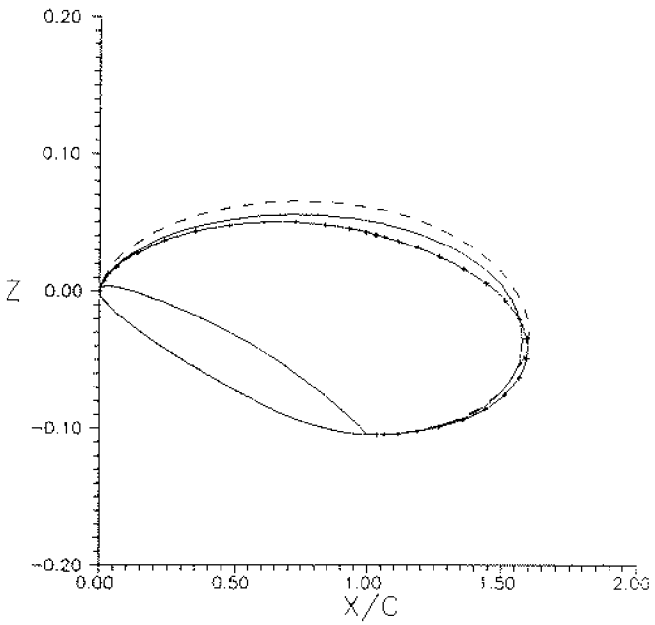


Figure 10: Comparison of predicted cavity shapes from linear (dashed), non-linear (solid) and hybrid (solid with dots) theories for NACA16004 at $\alpha = 6°$. (dotted) linear; $\alpha/\sigma = 0.44$. From Fine and Kinnas (1993a).

to predict the cavity shape within satisfactory accuracy. Note that linear theory overpredicts the slope of the cavity at the leading edge.

Finally, a comparison of predicted versus measured velocity profiles in the vicinity of a 2-D supercavity is shown in Figure 11. In the prediction the wall effects have been included by using a sufficient number of multiple images with respect to the horizontal tunnel walls (Kinnas & Mazel 1992).

2.5 Effects of viscosity

Consider a super-cavitating hydrofoil in viscous flow, as shown in Figure 12. We first solve the inviscid cavity flow in non-linear theory (Kinnas & Fine 1991b). We then apply the boundary layer equations on the compound foil, confined by the pressure side of the hydrofoil and the cavity boundary. A zero friction condition is applied everywhere on the cavity, as shown in Figure 12. The effects of viscosity may be included by including the following term on the right-hand side of equation 43:

$$+\int_{S_{WB} \cup S_C \cup S_W} \hat{\sigma} \ln R ds \tag{54}$$

where the blowing sources, $\hat{\sigma}$, are defined from (Hufford et al 1994):

$$\hat{\sigma} = \frac{dU_e \delta^\star}{ds} \tag{55}$$

where U_e is the edge velocity (in this case the same as the velocity predicted by the panel method when applied on the modified body that includes the displacement thickness) and $\delta^\star$ is the displacement thickess, which is determined from the boundary layer equations (Drela 1989).

Results from applying this method are shown in Figure 13. The resulting boundary layer displacement thickness is shown at the top of the figure. The pressure distributions in inviscid and viscous flow are also shown. Notice that viscosity has a very small effect on the pressure distribution. In other words, for super-cavitation, the cavitation number in viscous flow for given cavity length, l, is practically identical to that in inviscid flow. It should be noted that in the case of partial cavitation the effects of viscosity are much stronger than in the case of supercavitation (Kinnas et al 1994). The friction coefficient, C_f, on the pressure side of the foil and cavity, is also shown at the bottom part of Figure 13.

The lift and drag on the hydrofoil are evaluated by integrating the pressure forces acting on all sides of the hydrofoil (the constant cavity pressure is applied on the cavitating sides of the hydrofoil) as well as the frictional

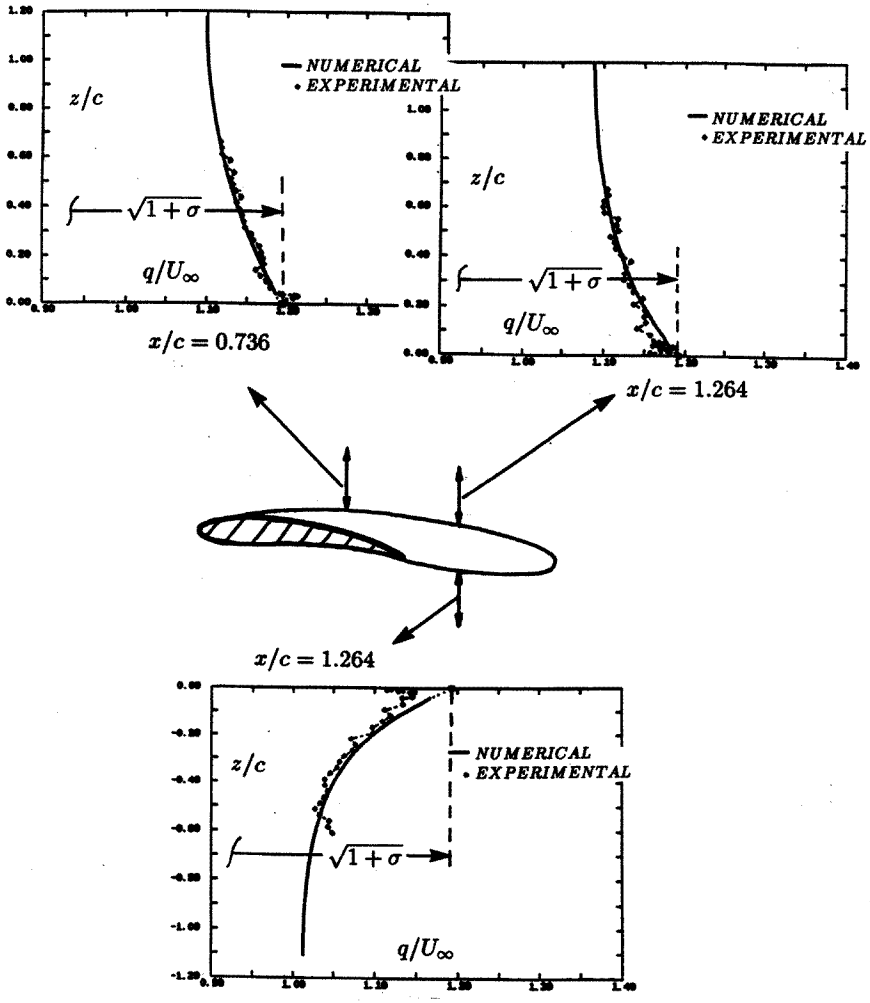


Figure 11: Numerical vs. experimental velocities as a function of the vertical distance from the cavity boundary at different chordwise locations. From Kinnas and Mazel (1993).

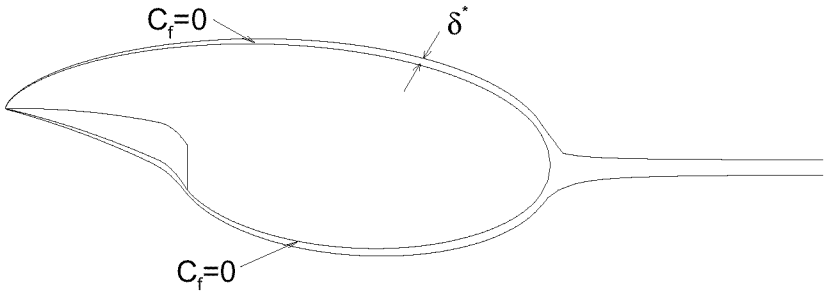


Figure 12: Super-cavitating hydrofoil with its boundary displacement thickness.

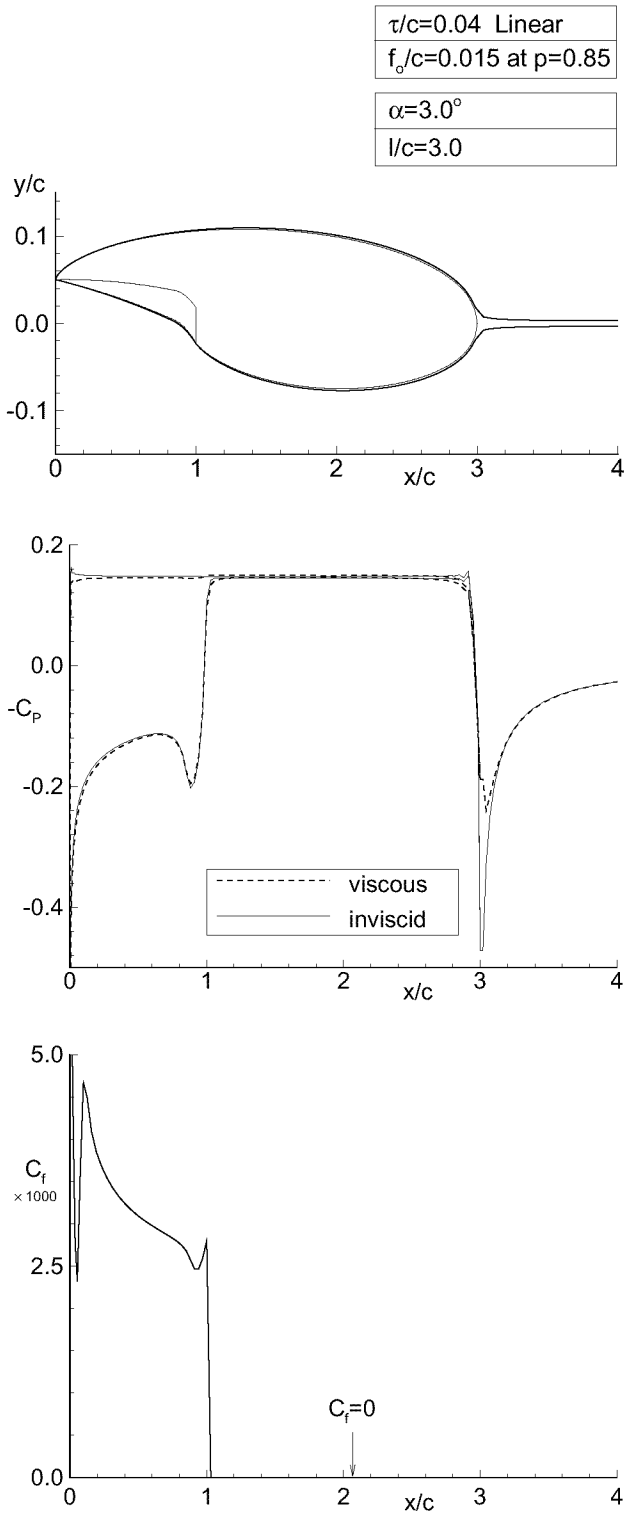


Figure 13: Super-cavitating hydrofoil in inviscid and viscous flow at $Re = 2 \times 10^7$. Cavity shape and boundary layer displacement thickness (top); pressure distributions (middle); and friction coefficient on the pressure side of the foil and cavity (bottom). All predicted by the present method.

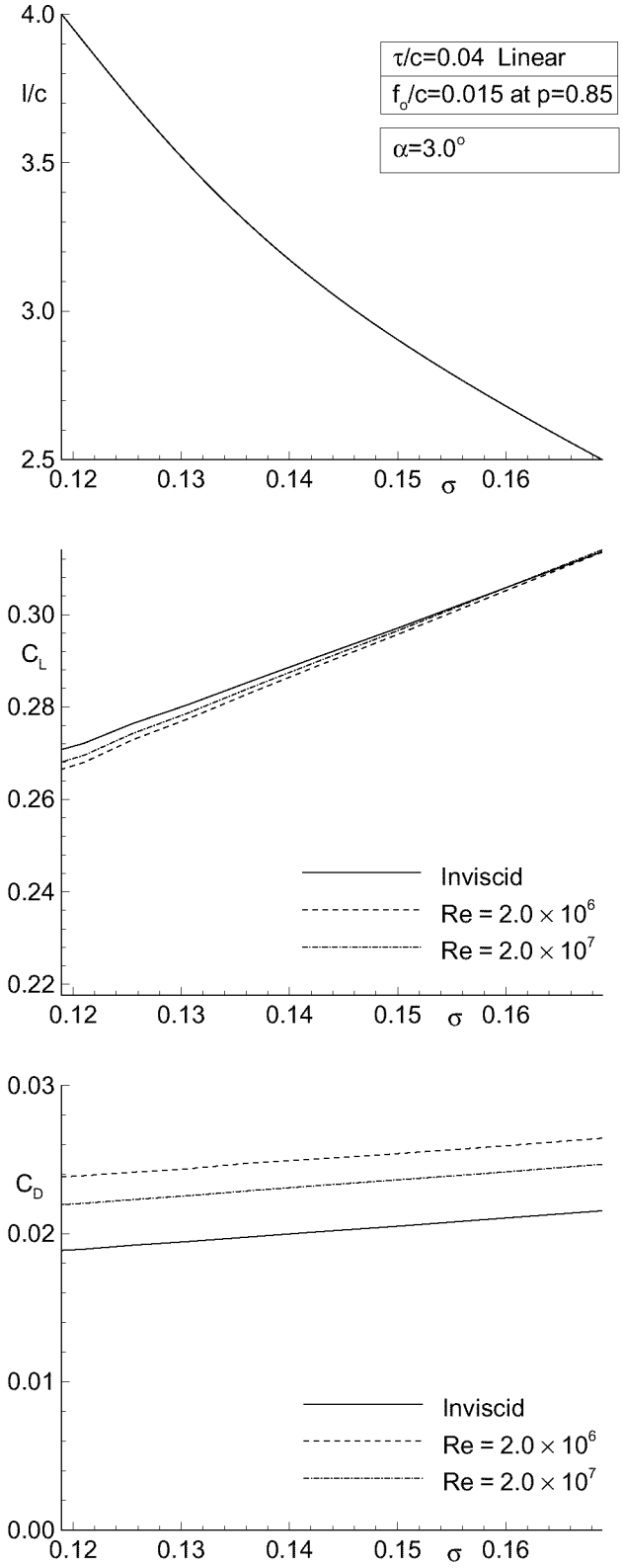


Figure 14: Cavity length, lift and drag coefficient versus cavitation number for a super-cavitating hydrofoil at $\alpha = 3^o$, in inviscid and viscous flow; predicted by the present method.

N	σ	V/c^2	C_L	C_D
100	0.145	0.365	0.282	0.0219
160	0.146	0.364	0.287	0.0223
200	0.146	0.363	0.292	0.0231

Table 1: Convergence of viscous cavity solution (σ, V/c^2, C_L and C_D) with number of panels. Super-cavitating hydrofoil; $\tau/c = 0.045$, $f_o/c = 0.015$, $p = 0.85$, $\alpha = 3^o$.

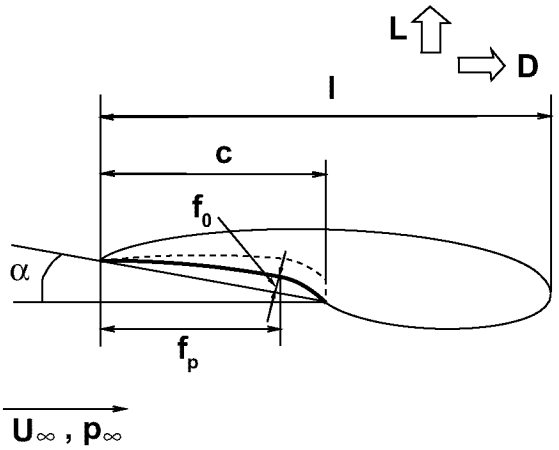


Figure 15: The main parameters in the design of a super-cavitating hydrofoil.

forces acting on the wetted side of the hydrofoil. The convergence of the cavity solution and the predicted forces with number of panels is given on Table 1.

Finally the predicted σ, C_L, and C_D vs. l curves are shown in Figure 14, for a super-cavitating section in inviscid flow and for two Reynolds numbers[10]. The super-cavitating section is a combination of a NACA 4digit camber form (with the maximum camber f_o at $x = p$) and a linear thickness form. The effect of viscosity on lift coefficient is shown to be very small.

3 DESIGN OF SURER-CAVITATING SECTIONS

3.1 Statement of the problem

We must determine the cavitating hydrofoil geometry and its operating condition (angle of attack, α), which produces the minimum drag, D, for specified design requirements.
The parameters that define the geometry of a super-cavitating hydrofoil, also shown in Figure 15, are:

- the chord, c
- the maximum camber, f_0, on the pressure side
- the location of the maximum camber, f_p

The design requirements taken into consideration in this paper are :

[10]Based on l.

- Sectional lift, $L_0(N/m)$
- Uniform forward velocity of the foil, $U_\infty(m/s)$
- Cavitation number, σ_0, defined as usual:

$$\sigma_0 = \frac{p_\infty - p_v}{\frac{1}{2}\rho U_\infty^2} \tag{56}$$

  where ρ is the fluid density, p_∞ is the ambient pressure, and p_v is the vapor pressure.
- Minimum section modulus of the foil, z_{min}
- Acceptable cavity length, l
- Acceptable cavity volume, V, or cavity height, h

The condition on the cavity length is necessary in order to avoid unstable cavities, usually being the long partial or the short super-cavities. The cavity volume/height constraints ensures acceptable positive cavity thickness (volume) in order to avoid very thin cavities (also negative thickness cavities) which are either non-physical or may turn into harmful bubble cavitation.

3.2 The hydrodynamic coefficients

The hydrofoil lift, L, and drag, D, acting on the hydrofoil, as shown in Figure 15, can be expressed in terms of lift and drag coefficients, C_L and C_D, respectively:

$$L = \frac{1}{2}\rho U_\infty^2 c C_L \tag{57}$$

$$D = \frac{1}{2}\rho U_\infty^2 c C_D \tag{58}$$

The drag coefficient, C_D, may be decomposed into two components.

$$C_D = C_D^i + C_D^v \tag{59}$$

where C_D^i is the inviscid cavity drag coefficient, and C_D^v is the viscous drag coefficient.

For known hydrofoil geometry, angle of attack, α, and cavity length, l, any hydrodynamic or cavity quantity, $\mathcal{Q}$ $(C_L, C_D^i, \sigma, V/c^2, ...)$, may be expressed as follows:

$$\mathcal{Q} = \mathcal{Q}(\alpha, \text{nondimensional foil geometry}, l/c) \tag{60}$$

Inviscid analysis methods are used to determine $\mathcal{Q}$. The analytical formulas of (Hanaoka 1964) could have been used. These expressions though are based on linearized cavity theory, which has been found to overpredict the cavity length and size substantially, especially in the case of partial cavitation. Instead, in this work the already described numerical non-linear cavity analysis method is utilized (Kinnas & Fine 1991b, Kinnas & Fine 1993). The shape of the cavity surface is determined in non-linear theory iteratively, with the use of a low-order potential based panel method. The (inviscid) forces are determined by integrating the pressures along the foil surface.

The viscous drag is determined by assuming a uniform friction coefficient, C_f, over the wetted part of the foil. C_f is expressed in terms of the Reynolds number ($Re = U_\infty c/\nu$, ν : kinematic viscosity) via the ITTC formula (Comstock 1967):

$$C_f = \frac{0.075}{(log_{10}Re - 2)^2} \tag{61}$$

During the optimization process, the chord length (also the Reynolds number) is not known, thus the value of C_f is updated at each optimization iteration.

Since only the lower surface of the foil determines the hydrodynamics of supercavitating flows, the thickness is not included as a parameter. The upper surface can be placed anywhere arbitrarily inside the cavity. Thus, when computing the section modulus of a foil, the upper cavity surface is considered as the upper surface of the

"compound" foil. It is reasonable to assume that the cavity always starts at the leading edge of the foil, since the supercavitating sections have a sharp leading edge. Furthermore, we deal with situations where the cavity detaches at the trailing edge of the foil on the pressure side. For the case of supercavitating sections, in addition to specifying the minimum section modulus of the compound section, the minimum allowable cavity height at the 10% of the chord length from the leading edge is specified via an inequality constraint. This ensures positive cavity thickness, as well as sufficient local strength at the sharp leading edge of the foil.

The relevant coefficients are expressed as follows:

$$\begin{aligned} C_L &= C_L(\alpha, f_0/c, f_p/c, l/c) \\ C_D^i &= C_D^i(\alpha, f_0/c, f_p/c, l/c) \\ \sigma &= \sigma(\alpha, f_0/c, f_p/c, l/c) \\ V/c^2 &= V/c^2(\alpha, f_0/c, f_p/c, l/c) \\ z/c^3 &= z/c^3(\alpha, f_0/c, f_p/c, l/c) \\ h_{10}/c &= h_{10}/c(\alpha, f_0/c, f_p/c, l/c) \end{aligned}$$

where h_{10} is the cavity height at the 10% of the chord length from the leading edge of the foil. Note that the section modulus is a function of all the geometry variables including the cavity length, whereas it is independent of the cavity length in the case of partial cavitation.

The coefficients are computed, as in the case of partial cavitation, for a number of foil geometries by using the analysis method of (Fine & Kinnas 1993a). The coefficients are again expressed by using second degree polynomials in terms of all the geometric parameters. For example,

$$\begin{aligned} C_L = C_{L_1}\alpha + C_{L_2}\alpha^2 + C_{L_3}\frac{f_0}{c} + C_{L_4}\left(\frac{f_0}{c}\right)^2 \\ + C_{L_5}\frac{f_p}{c} + C_{L_6}\left(\frac{f_p}{c}\right)^2 + C_{L_7}\frac{l'}{c} + C_{L_8}\left(\frac{l'}{c}\right)^2 \\ + C_{L_9}\alpha\frac{f_0}{c} + C_{L_{10}}\alpha\frac{f_p}{c} + C_{L_{11}}\alpha\frac{l'}{c} + C_{L_{12}}\frac{f_0}{c}\frac{f_p}{c} \\ + C_{L_{13}}\frac{f_0}{c}\frac{l'}{c} + C_{L_{14}}\frac{f_p}{c}\frac{l'}{c} + C_{L_{15}} \end{aligned} \tag{62}$$

where,

$$\frac{l'}{c} = \frac{1}{\sqrt{1-(c/l)^2} + 1 - (c/l)^2} \tag{63}$$

The variable transformation from l/c to l'/c is done knowing that C_L and C_D are linear in l'/c for the super-cavitating flat plate in linear theory, as described by (Geurst 1960). This transformation has been found to improve the accuracy of the interpolation substantially. The effect of the number of The accuracy of the interpolation for C_D may be seen in Figures 16.

3.3 The optimization problem

Consider the following general nonlinear optimization problem:

$$\begin{aligned} \text{minimize} \quad & f(\mathbf{x}) \\ \text{subject to} \quad & g_i(\mathbf{x}) \le 0 \quad i = 1, 2, \ldots, m \\ & h_i(\mathbf{x}) = 0 \quad i = 1, 2, \ldots, l \end{aligned} \tag{64}$$

where $f(\mathbf{x})$ is the objective function defined on $\mathcal{R}^n$. $\mathbf{x}$ is the solution vector of n components. $g_1(\mathbf{x}) \le 0, \ldots, g_m(\mathbf{x}) \le 0$ are inequality constraints defined on $\mathcal{R}^n$ and $h_1(\mathbf{x}) = 0, \ldots, h_l(\mathbf{x}) = 0$ are equality constraints also defined on $\mathcal{R}^n$.

The solution vector is defined as ($n = 5$):

$$\mathbf{x} = [\alpha, c, f_0, f_p, l]^T \tag{65}$$

The constraints are ($m = 3, l = 2$)

$$h_1(\mathbf{x}) = L(\mathbf{x}) - L_0 = 0 \quad (66)$$

$$h_2(\mathbf{x}) = \sigma(\mathbf{x}) - \sigma_0 = 0 \quad (67)$$

$$g_1(\mathbf{x}) = -\frac{l}{c} + \left(\frac{l}{c}\right)_{min} \leq 0 \quad (68)$$

$$g_2(\mathbf{x}) = -\frac{z(\mathbf{x})}{c^3} + \frac{z_{min}}{c^3} \leq 0 \quad (69)$$

$$g_3(\mathbf{x}) = -\frac{h_{10}(\mathbf{x})}{c} + \left(\frac{h_{10}}{c}\right)_{min} \leq 0 \quad (70)$$

3.4 The numerical optimization method

The method of multipliers is applied in which, first each of the inequality contraints, $g_i(\mathbf{x}) \leq 0$, is converted into an equality constraint with the introduction of the new variable, s_i:

$$g_i(\mathbf{x}) + s_i^2 = 0 \quad (71)$$

Then the augmented Langrangian penelty function is formed (Mishima & Kinnas 1996):

$$\begin{aligned} F(x_1, ..., s_1, ..., \lambda_1, ..., \tilde{\lambda}_1, ..., c_1, ..., \tilde{c}_1, ...) = \\ D(\mathbf{x}) + \Sigma\lambda_i h_i(\mathbf{x}) + \Sigma\tilde{\lambda}_i[g_i(\mathbf{x}) + s_i^2] \\ + \Sigma c_i h_i^2(\mathbf{x}) + \Sigma\tilde{c}_i[g_i(\mathbf{x}) + s_i^2]^2 \end{aligned} \quad (72)$$

where λ_i and $\tilde{\lambda}_i$ are the Langrange multipliers, and c_i and $\tilde{c}_i$ are penalty parameters. The parameters of the problem, the additional parameters (s_i), the Langrange multipliers, and the penalty parameters are determined by minimizing function F. A technique to minimize F is described in great detail in (Mishima & Kinnas 1996).

3.5 Effect of the initial guess on the optimum solution

In general, a nonlinear optimization problem is initial guess dependent. In other words, if there exist more than one local minimum to the objective function, any one of these minima may be obtained depending on the initial condition. Due to the special structure of the problem, no multiple solutions were found for the range of cavitation numbers that we studied. This uniqueness is attributed partly to the fact that the involved functions are quadratic, i.e. not wavy, and partly to the fact that the range of the solutions is known, so that a reasonable initial guess can be selected. Figure 17 shows that several different initial guesses lead to the same solution.

3.6 Results

A NACA 4 digit camber form and the Johnson five-term camber form are used. The NACA 4digit camber form (Abbott & Von Doenhoff 1959) has two parameters, which are the maximum camber f_0/c and the location of the maximum camber f_p/c, as shown in Figure 15. The values for the constraints are:

$$\left(\frac{l}{c}\right)_{min} = 1.15 \quad \left(\frac{h_{10}}{c}\right)_{min} = 0.01 \quad \left(\frac{z_{min}}{c^3}\right) = 7 \times 10^{-5} \quad (73)$$

The method is applied for fixed lift ($L_0 = 30,000 N/m$) and for a range of cavitation numbers between 0.15 and 0.7 (corresponding to approximate speeds of 70 and 30 knots, respectively[11]) for partial and supercavitating conditions. The resulting L/D for both cases are shown in Figure 18. As expected, for "low" σ a supercavitating section has larger L/D than a partially cavitating section, and the reverse holds for larger σ. Optimum partially and supercavitating sections are also shown in Figure 18.

Finally, we show in Figure 19, contour plots of L/D for optimum sections, designed by the present method, over a range of combinations of required lift and cavitation number. This graph is intended to help the designer decide as to what is the best solution (partially or supercavitating section), depending on the requirements.

[11]The cavitation number is inversely proportional to the square of the speed of the hydrofoil, for fixed ambient pressure and temperature conditions.

3.7 Comparison of the present to existing design methods

The designed sections, under given requirements, are compared to those designed from other methods. These methods are based on either the Tulin two-term or the Johnson five-term sections, given next:

$$\frac{y}{c} = \frac{A_1}{2}\left\{\frac{x}{c} + \frac{8}{3}\left(\frac{x}{c}\right)^{3/2} - 4\left(\frac{x}{c}\right)^2\right\} \quad \text{(Tulin two-term)} \tag{74}$$

$$\frac{y}{c} = \frac{A_1}{315}[210\left(\frac{x}{c}\right) - 2240\left(\frac{x}{c}\right)^{3/2} + 12600\left(\frac{x}{c}\right)^2 - 30912\left(\frac{x}{c}\right)^{5/2} + 35840\left(\frac{x}{c}\right)^3 - 15360\left(\frac{x}{c}\right)^{7/2}] \quad \text{(Johnson five-term)} \tag{75}$$

where A_1 is a parameter that relates the geometry to the lift coefficient.

As the number of terms included in the series increases, the loading moves towards the trailing edge. A useful formula for the finite cavitation number correction is given by (Ohba 1963/1964) as follows.

$$C_L = \sqrt{C_{L,\sigma=0}^2 + 0.85\sigma^2} + \sigma C_{L,\sigma=0} \tag{76}$$

where C_L is the required lift coefficient and $C_{L,\sigma=0}$ is the lift coefficient for zero cavitation number.

In Figure 20, the lift to drag ratio, L/D, is shown for the NACA 4dgt sections designed by the present method, Tulin's two-term sections, and Johnson's five-term sections, for various cavitation numbers. In the same figure we also show the L/D for the optimum Johnson section as designed by the present method. The corresponding lift coefficients are shown in Figure 21. For the design of Tulin sections and Johnson sections, the cavitation number and the lift coefficient are both specified, whereas in the present method, the cavitation number and the lift are given and the lift coefficient is determined as part of the solution. A representative section and its corresponding pressure distribution is shown in Figure 22.

3.8 Application to 3-D elliptic planform hydrofoils

As shown in (Kinnas et al 1995), a super-cavitating hydrofoil with elliptic planform and similar sections along its span (that are only scaled by the chord), can be designed by designing an equivalent 2-D section. If c and s_o are the maximum chord and span of the elliptic wing, the equivalent 2-D lift is given from:

$$L_{2D} = L_{3D}\frac{4}{\pi s_o} \tag{77}$$

If D_{2D} is the corresponding minimum value of the drag then D_{3D} will be given as:

$$D_{3D} = \frac{L_{3D}^2}{1/2\rho U_\infty^2 \pi s_o^2} + \frac{\pi s_o}{4} D_{2D} \tag{78}$$

The above equation can be re-written as:

$$\frac{D_{3D}}{L_{3D}} = \frac{L_{3D}}{1/2\rho U_\infty^2 \pi s_o^2} + \frac{D_{2D}}{L_{2D}} \tag{79}$$

Equation (79) implies that $(L/D)_{3D}$ will always be smaller than $(L/D)_{2D}$, i.e. the 3-D hydrofoil will always be *less* efficient than the 2-D hydrofoil.

The actual angle of attack α_{3D} will be related to that determined from the 2-D equivalent optimization problem as:

$$\alpha_{3D} = \alpha_{2D} + \frac{L_{3D}}{1/2\rho U_\infty^2 \pi s_o^2} \tag{80}$$

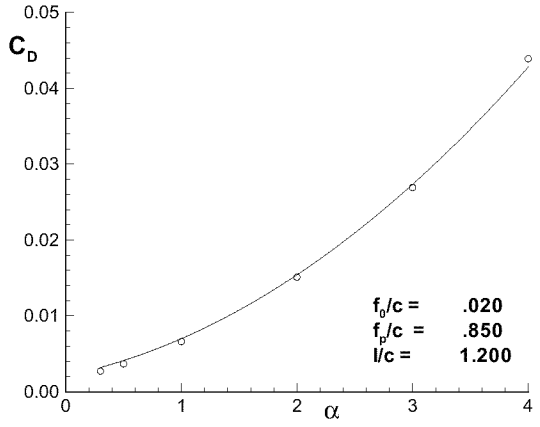


Figure 16: Accuracy of the interpolation : Supercavitation (C_D *vs* α), Range of parameters: $\alpha = 0.3 \sim 4.0$ deg (6 points), $f_0/c = 0.0 \sim 0.05$ (6 points), $f_p/c = 0.7 \sim 0.9$ (5 points), $l/c = 1.1 \sim 1.3$ (4 points)

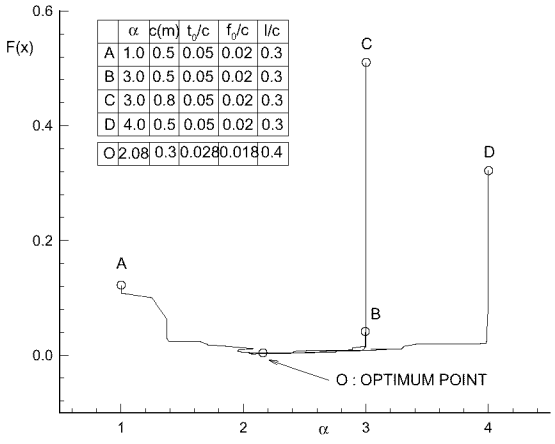


Figure 17: Sensitivity of the optimum solution on initial guesses , $L = 30,000(N/m), \sigma = 0.6, U_\infty = 18.2(m/s)$

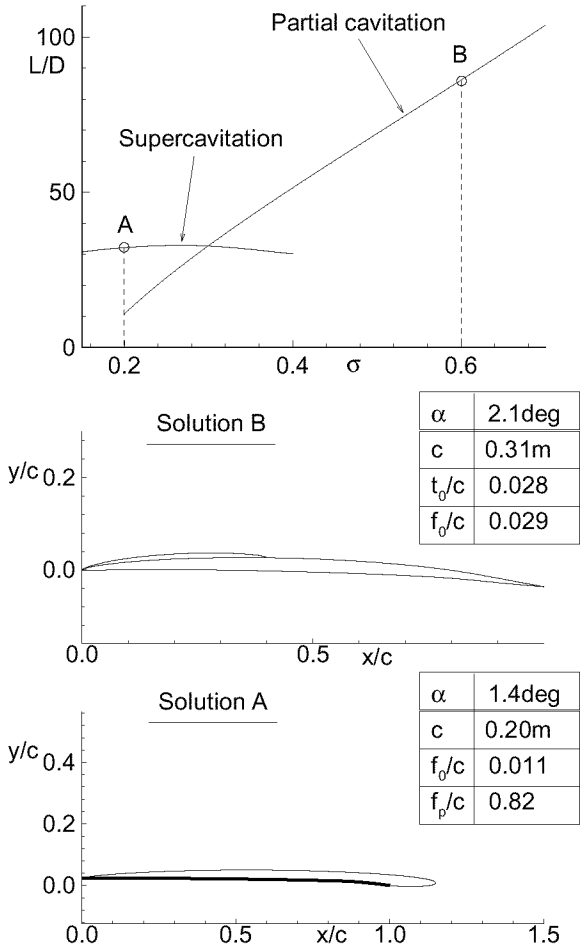


Figure 18: L/D for partially or super-cavitating foils designed by the present method; $L_0 = 30,000N/m$.

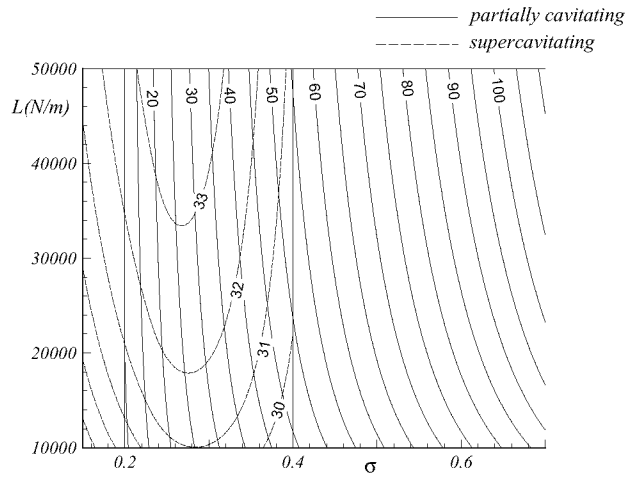


Figure 19: Contour plots of L/D for partially or super-cavitating foils designed by the present method.

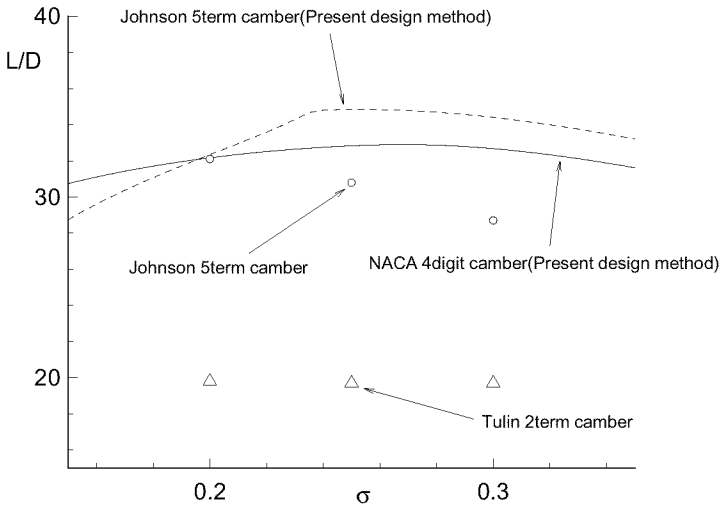


Figure 20: Comparison of L/D between designed sections and existing sections ($L = 30000(N/m), z_{min}/c^3 = 7.0 \times 10^{-5}$ (supercavitating)

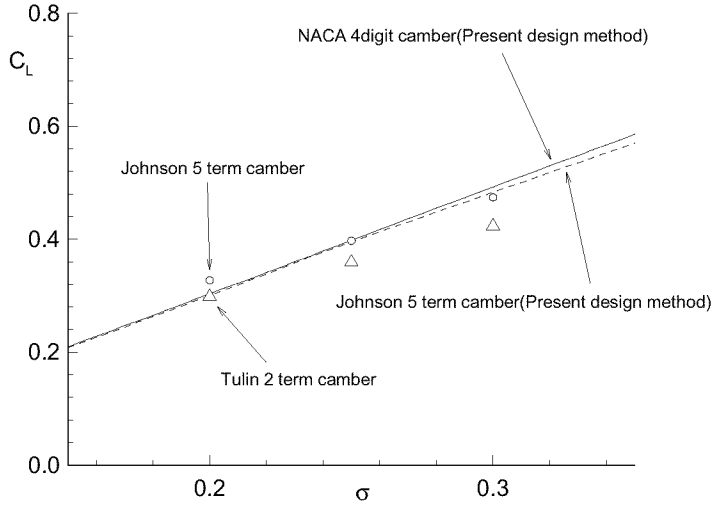


Figure 21: Comparison of C_L between designed sections and existing sections ($L = 30000(N/m), z_{min}/c^3 = 7.0 \times 10^{-5}$ (supercavitating)

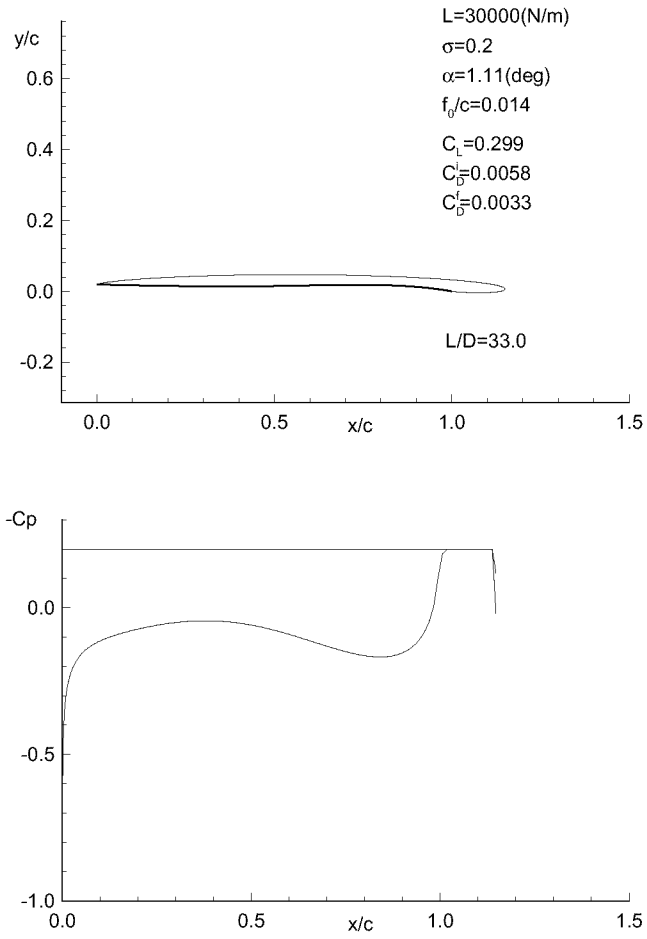


Figure 22: Optimum supercavitating section and corresponding pressure distribution; designed by the present method (Johnson five-term camber : $L = 30000(N/m), \sigma = 0.2, z_{min}/c^3 = 7.0 \times 10^{-5}$)

This page has been deliberately left blank

Page intentionnellement blanche

Supercavitating Propellers

A. S. Achkinadze
Ship Theory Department, Saint-Petersburg State Marine Technical University
3, Lotsmanskaya street, Saint-Petersburg 190008, Russia
E-mail: achkin@mail.ru

> "At about the same time (1955 г.) I first learned of the work of a Soviet scientist Pozdunin on cavitating propulsors, and also of the Russian term "supercavitation", and then on I began using this way of distinguishing cavitating flows with long trailing cavities from the other cavitating flows. At the beginning there were objections to use of this word, some preferred "developed cavitation", but soon the words "supercavitation" and "supercavitating" came into general use in the U.S.A. and worldwide."
>
> M.P. Tulin, 2000 [1]

1. Summary

The lecture covers the main stages of the development of the research in the field of supercavitating propellers (SCP) both experimental and theoretical. However, it should be viewed only as an introduction to this vast domain attempting to mainly give a notion of the relevant Russian research started in 1941 on the initiative of the academician V.L.Posdunin.

2. Historical notes and experimental investigation

2.1. TEST EQUIPMENT

The cavitation on a model of a screw propeller of just two inches in diameter was first observed by Sir Charles Parsons in 1894 during the tests of a model of the screw propeller of the steam turbine driven "*Turbinia*" (45-ton) in a small water tunnel invented by the researcher for this particular purpose [2]. In 1910 Sir Charles Parsons built the first cavitation tunnel of almost today's dimensions, where one could test the propeller models of a diameter of up 12 inches (304.8 mm). The first cavitation tunnel in Russia was launched in 1933. The first systematic tests of a series of the cavitating propellers with a segment-type sections were conducted by H.W.Lerbs in 1936 with use of the cavitation tunnel built specially for this purpose.

The principle of functioning of the cavitation tunnel, which represents a vertically mounted hermetically sealed variable-diameter tube, is extremely simple (Fig. 1). This experimental installation enables to conduct the force measurement and visual observations of models of the cavitating or

Paper presented at the RTO AVT Lecture Series on "Supercavitating Flows", held at the von Kármán Institute (VKI) in Brussels, Belgium, 12-16 February 2001, and published in RTO EN-010.

supercavitating screw propeller for given magnitudes of advance coefficient and axial cavitation number, which are taken equal to those of the full-size propellers for a regime under consideration. Therewith, it is assumed somewhat approximately that such modeling ensures similarity of the cavitation phenomena in the case of a sufficiently developed partial cavitation and in the case of supercavitation, which depend to a lesser degree on the vertical distribution of the hydrostatic pressure, viscosity, turbulence, air content and other factors not taken account of. Note that some of the forms of cavitation are either poorly modeled in cavitation tunnel, or require application of the special procedures for recalculation of the model results to those in full-scale. Examples include cavitation of the tip and axial vortices. Large difficulties occur when modeling of erosion, noise and vibration of the cavitating propeller.

Nonetheless, the most important factors (criteria) during in testing of the supercavitating propellers in the cavitation tunnel are the advance coefficient

$$J = V/(nD) \tag{1}$$

and axial cavitation number

$$\chi = (p_0 - p_v)/(0.5\rho V^2), \tag{2}$$

where p_0 - is hydrostatic pressure at the level of the SCP axis; p_v - pressure of saturated vapor of the fluid at the temperature of the testing, sometimes this value is taken to be equal the pressure of the vapor-fluid mixture in the cavity or the pressure above the free surface of the fluid for the case of superventilation of the cavity under consideration; ρ - fluid density; V- flow velocity in the working section of the cavitation tunnel; n – frequency of rotation; D – diameter of the SCP model.

Local cavitation number σ for cylindrical section of the blade, characterized by the radius r, differs form the axial cavitation number (2) in that in the denominator of the corresponding formula one finds a transport velocity of the blade points, belonging to the given cylindrical section V_E and a hydrostatic pressure is assumed to correspond to the level of the considered point of the corresponding blade section for its certain angular position $p_{or\theta}$, namely

$$\sigma = (p_{0r\theta} - p_v)/(0.5\rho V_E^2) \tag{3}$$

where $V_E^2 = V^2 + (2\pi nr)^2$.

It is obvious, that in the gravity field, when the screw propellers is rotating around a horizontal axis, the local cavitation number is variable for the given point of the considered section, varying during one revolution from a minimal magnitude (in the upper position of the considered point for its motion along a circular trajectory of a given radius) up to a maximal magnitude at a given radius (in the lower position of the considered point).

To control advance coefficient one can employ the velocity of the incoming flow in the working section of the cavitation tunnel (the latter can be varied, by changing the frequency of the axial pump mounted in the tunnel) or the frequency of rotation of the screw propeller model.

To adjust the axial cavitation number one can use a device with a vacuum pump, which enables to pump air out of the volume above the free surface of the fluid, in a special shaft located higher than the working section, i.e. where there is the only place with a free surface (other elements of the cavitation tunnel are hermetically sealed and completely filled with water). The pressure above the free surface in the aforementioned shaft decreases to a certain level, down to a certain value close to zero, which leads to a corresponding reduction of the magnitude of p_0, differing from the pressure above the free surface in a special shaft by the magnitude of the hydrostatic height of the fluid column under propeller model axis.

For proper modeling of the hydrostatic pressure distribution in height, or, speaking more exactly, to secure equality of the local cavitation numbers of the full size propeller and the model in all blade sections with account of gravity, it is necessary to additionally fulfill the equality of the Froude numbers for the model and full-size screw propeller. Absolute error in the determination of the local cavitation number, calculated with use on transfer velocity for the cylindrical blade section at a relative radius $\bar{r}$ (in

its upper position), occurring due to disregard of the inequality of Froude numbers, can be found through an almost obvious formula

$$\Delta\sigma = \{1/(n^2 D) - 1/[(n^*)^2 D^*]\}\, \bar{r}g / [J^2 + (\pi\bar{r})^2], \tag{3a}$$

where n^* and D^* - are the frequency of rotation and the diameter of the full-size screw propeller.

It is seen, that, accounting besides the equality of Froude numbers for another necessary requirement of the identity of advance coefficient for the model and full-size propeller, the aforementioned error can be reduced to zero if, first, the velocity in the working section of the cavitation tunnel would be $\sqrt{M}$ times less that the speed of the motion of the full-size propeller, and, secondly, the frequency of rotation of the model would be $\sqrt{M}$ times more than that of the full-size propeller, where M is the model scale, i.e. equal to the ratio of the diameter of the full-size propeller to that of the model propeller.

For example, if the speed of the full-size propeller equals 60 knots (30.87m/c), diameter 1.054 m., frequency of rotation is 1465 rpm (24.42 revolutions a second), then, for the simultaneous fulfillment of the identities of the Froude numbers and advance coefficient it is necessary to ensure the speed of 13.45 m/s in the working section and the frequency of rotation of 3363 rpm (56.05 revolutions a second) when testing in the cavitation tunnel a supercavitating propeller model of diameter 0.2 m. Note, that the results obtained for the model can, in principle, be realized for good experimental installations. But more often during the tests there are used smaller speed and frequency of rotation, which is acceptable only in those cases, when the arising error, in accordance with (3a), does not exceed reasonable limits narrowing with the reduction of the axial, and, correspondingly, local cavitation numbers.

The influence of the walls of the cavitation tunnel represents an obstacle for a proper modeling, because there are no such walls in the full-size situation. The effect of the walls of the cavitation tunnel may become unacceptably large especially when investigating the supercavitating regime, for which the flow blockage in the tunnel working section due to development of large cavities can noticeably influence the experimental results. Besides, the influence of the free surface (i.e. phenomena of ventilation and wave making) is as a matter of principle impossible to study in conventional cavitation tunnels. When investigating the supercavitating propulsors at small advance coefficients and small cavitation numbers the use of the cavitation tunnel becomes altogether impossible due to "blockage" of the cross section of the working section by the cavities. In order to conduct the experimental investigation in such cases there were built the cavitation basins [22], [23], which have sufficiently large cross section and a free surface, providing almost complete annihilation of the influence of walls, and enables studies of the influence of the free surface.

Note that out of the three existing in the world (cavitation) depressurized towing tanks the first one had been built in the 60s in Russia [22], having dimensional of 50x5x5 meters (length, width and depth correspondingly). In Holland was built a depressurized towing tank with dimensions 240x18x8 meters. More than 8 hours are needed to obtain vacuum constituting 4% of that of the atmospheric pressure [23].

However, the speed of the motion of model in the cavitation basins is restricted by approximately 4m/s, allowing to conduct the tests of the screw propeller model of the diameter 0.2 m in the operational regimes corresponding (based on equal Froude numbers) the speed of the full-size propeller not exceeding approximately 20 kn (assuming that the diameter of the full-size propeller is less than 1.2 m). For the experimental study of the supercavitating propellers at the regime of maximum speed it is far from being sufficient. Therefore the tests for such propellers in the cavitation basin can only be conducted without account of Froude numbers, but, as opposed to the cavitation tunnel, for any magnitudes of advance coefficient, including the regime of “blockage”. At present the cavitation basin is often used to study cavitation on a model of a conventional screw propeller, operating in the nonuniform following wake behind the hull of a ship model although this wake is known not to completely correspond to that of a full-size ship.

An alternative to cavitation basins which appeared in the 60s are cavitation tunnels with free water surface, enabling to account both for the presence of a free surface and the ship hull. For example Free-

surface Cavitation tunnel K27 in Berlin Technical University [35]. But it is difficult to receive the smooth condition of the free water surface in this equipment.

For this reason investigators returned to build the cavitation tunnel but differ on conventional tunnel with very big working section. The largest and most capable cavitation tunnel in the world is located in Memphis, Tennessee, USA, reaches 18 m/s, which allows to cover the speed range of the full-size propeller when testing up to the speeds of 70 kn. The cross section of the working section constitutes 3x3 m., which allows to test the propeller models together with that of ships in a scale from 1/10 to 1/20, and to decrease the influence of the walls down to an acceptable level [59].

The full-size experiment (to a very restricted extent) and mostly the propeller testing in the numerous conventional cavitation tunnels (there are approximately 66 tunnels in the world today [59]) constitute the main source of the contemporary experimental knowledge about the supercavitating and strongly cavitating screw propellers.

2.2. DEVELOPMENT AND TESTING OF A SERIES OF SUPERCAVITATING AND STRONGLY CAVITATING SCREW PROPELLERS, EXAMPLES OF THEIR USE FOR FULL-SIZE HYDROFOIL SHIPS

In the first part of the lecture let's dwell experimental investigations, connected with the development of a small number of full-size hydrofoil ships equipped with supercavatating propellers.

Cavitation of propulsors, leading to erosion, vibration, hydro-acoustic noise and undesired change of the hydrodynamic characteristics, represent a physical phenomenon, hindering the effort of the ship builders to increase the speed of both the conventional displacement ships and high-speed ships with dynamic principles of support. Sometimes, the whole set of technical problems accompanying occurrence and development of cavitation is called a "cavitation barrier".

In some cases it is possible to avoid the aforelisted consequences of the cavitation occurrence by way of designing a completely noncavitating propulsor. The proper selection of the expanded area ratio of the screw propeller has for a long time permitted to avoid (completely or partially) the development of the cavitation forms resulting in erosion of the screw propeller blades. However, as indicated in the documents of the command of the German Navy dated 1932, they did not manage to avoid strong erosion damage of the propellers of the destroyers and torpedo boats by the latter method [3]. In 200 hours of full-speed cruising the indicated screw propellers would acquire such a damage (erosion blisters of size of a fist), so that their replacement became inevitable. According to the present views [4], one can ensure an acceptable service resource of the screw propellers of ships up to the cruising speeds of 36 knots and even more by means of an optimal selection of the expanded area ratio, frequency of rotation and diameter, in combination with application of the skew contours and improved profiling as well as by taking measures to smooth out the nonuniformity of the following wake. The aforementioned measures can ensure complete absence of cavitation or its very insignificant development, which practically does not result in the erosion damage. For example, a prototype passenger hydrofoil "Taifun" (65t, 2x1750 hp, 100 passengers, [20]) with automatically controlled deeply submerged hydrofoils ship, built in Russia in 1971 reached a speed up to 44 knots with use of two non-cavitating screw propellers mounted on struts (pushing type arrangement)

However, in many cases, it is impossible to design a non-cavitating propulsor. For example, this is the case when the following peculiarities take place simultaneously or separately: high full speed, mounting of the screw propeller on an inclined shaft, nearness of the free surface, too large expanded area ratio (> 1.2), needed to avoid cavitation.

An alternative to the design of the non-cavitating propulsor is naturally an idea of designing a cavitating propulsor which is only to a small extent exposed to erosion and other negative consequences of cavitation. This idea was first set forth in 1941 for the purpose of design of the screw propellers of destroyers and similar ships by a Russian academician Valentin Lvovich Pozdunin [7],[8],[9].[10]. He

proposed to select a expanded area ratio, distribution of pitch, section curvature and the form of the sections (Fig. 2) in such a way, that the blades of the high- speed ship screw propeller should operate in the regime of supercavitation. More specifically, in such a regime when the cavities formed on the blades have a length exceeding the local chord, and, therefore close at a certain distance behind the blade (Fig. 3). Therewith, the erosion which usually occurs when the cavities close on the blade surface would not occurs in the supercavitating regime. If additionally, one minimizes the time of the transient ship regime for which the cavities have a length less than the local chords, the unfavorable consequences of the cavitation would not exceed reasonable limits.

Based on intensive experimental investigations in the cavitation tunnel Pozdunin revealed the main difficulties hindering the realization of his idea. First of all, it turned out to be of preference for the supercavitating propellers to employ a special wedge-type profiling (Fig. 4, 5), drastically different from the one traditionally used for the noncavitating screw propellers. Further on, in Russia they started to call supercavitating those propellers that have a wedge-type profiling. And to designate the supercavitating propellers with a segment-type profiling a term highly cavitating propellers was introduced.

The wedge-type profiling and the peculiarities of the flow past the SC propellers immediately gave birth to several problems. First of all, the problem of securing a local strength of thin wedge-type leading edges of the blades which would be sufficient for the full-size propeller. Secondly, the necessity of securing at the regime of full cruising a sufficient length and thickness of the cavity in all sections with a certain reserve for the cavitation occurrence on the pressure side of the blade. Thirdly, the necessity of securing of a sufficient thrust of the propulsor at the intermediate regimes, e.g. at the regime of the drag hump of the hydrofoil ship. The latter problem turned out to be rather important for the design of the hydrofoil ship as a whole and will be considered later in more detail, as there emerged historically two different ways of its solution, namely, the American one and the Russian one.

For the destroyers and torpedo boats the idea of Pozdunin was not realized, as it appeared in the process of experimental investigation that it is only reasonable to employ the SC propellers for by far larger magnitudes of the cruising speed, more specifically, at speeds higher than 50 knots, or for the local cavitation number at 0.7 of the propeller radius less than 0.045. In other words, with the purpose of obtaining sufficiently long cavities, if at all possible, it would be necessary to abruptly increase the angles of attack of the blade sections which would result in an unjustified augmentation of the cavitation drag and a sharp drop of the efficiency. The problem of erosion destruction of the screw propellers of the torpedo boats due to cavitation at the root sections of the blades, was successfully resolved by way of drilling anti-erosions orifices [11].

A complete realization of the Pozdunin's idea was effected in mid-50s by the researchers of the David Tailor Model Basin A.J. Tachmindji and W.B. Morgan [12], E.B.Caster [13] et al. As recollected by M.P.Tulin [1], these specialists started investigation of the SC propellers in the United States (1957) with a design by means of calculations (using quite an approximate lifting line theory) of a model of a two-blade SC propeller with wedge-type profiling. Therewith, the profile of the section was adopted in the form of the so-called 2-parametric optimal profile found with use of the linear two-dimensional theory of M.P.Tulin for zero cavitation number [14] (see Fig.5). Testing of this model completely confirmed sufficient accuracy of the adopted method of the design calculation. Further on this success allowed to develop by means of calculation series of 2, 3 and 4-blade SC propellers [13]. Testing of separate models in the cavitation tunnel also confirmed sufficient accuracy of the calculated results. For example, for the model of a supercavitating 3-blade screw propeller with expanded area ratio 0.5 and pitch ratio 1.57 there were obtained in the course of the experiment for a advance coefficient 1.125 and axial cavitation number 0.3 the thrust coefficient 0.140 and efficiency 0.685, which turned out to be just 2.2% less that the calculated one [12]. In 1962 under guidance of M.P.Tulin the specialists of the company "Hydronautics" successfully developed a 2-blade SC propeller for a gas-turbine hydrofoil ship "Denison" (80 ton, 60 knots, 10000 hp) [1],[15]. Therewith, the form of the pressure side coincided with that of the Tulin's 2-parametric foil, similarly to the aforementioned series, and the thickness was augmented up to the parabolic one. Especially big difficulties arised in securing a sufficient thrust at the regime of the drag hump, but this matter would be considered in more detail later on. Here we would only mention that these difficulties were connected with a phenomena of the flow "blockage" by the

cavities typical for the SC propellers at the magnitudes of advance coefficient significantly less than those corresponding to the maximum speed for the given ship project.

In mid-60s there was built a Canadian open ocean hydrofoil ship "HMCS Bras d'Or" (235 ton., 60 kn., 22000 hp) with two SC propellers [16]. When developing these propellers special attention was attached to the investigation of the local strength in the vicinity of the leading edge.

In 1958, i.e. practically at the same time as the U.S. specialists, a Krylov Institute researcher Yu.M.Sadovnikov conducted testing of a series "K" of the SC propellers with wedge-type profiling and symmetric contour [17],[18],[19],[20], comprising 15 two -blade models and 9 three-blade models of the 0.2 m. diameter. The propellers had a relative radius of the hub 0.165, expanded area ratio varied in the range 0.34-1.11, pitch ratio varied in the range 1.0-1.8, and the minimal axial cavitation number reached 0.3. The action curves of one model of this series are presented in Fig. 6. However, the full-size hydrofoil ship with the screw propeller of this series was never built, because for them problem of providing sufficient thurst at the drag hump regime was not solved for this series (see more details further on). The effective solution of the aforementioned problem in the Russian version (when the advance coefficient at the drag hump regime differs only slightly from that in full cruising speed due to drop in rpm) was solved by replacing the wedge-type profiling by the segment-type one (see, Fig.4). Further on, as indicated, adopted in the KSRI (and in Russia) was the term highly cavitating propellers for the SC propellers having the segment-type profiling.

Thus, the distinction between the highly cavitating propellers and the supercavitating propellers consists in the profiling (see Fig.4). In particular, instead of the wedge-type chordwise thickness distribution used is the segment distribution without shifting of the maximal thickness from the midchord (“CK” series) or with shifting of the maximal thickness 15% upstream of the midchord (“CK2” series).

The “CK” series is that of 3-blade highly cavitating screw propellers which was developed and tested in by V.D. Tsapin, and comprises 28 models with expanded area ratio in the range 0.65-1.10 and with pitch ratio in the range 1.0-2.2 [17]],[18],[19],[20]. Fig. 7 gives the characteristic curves for one of the models of this series, and the following Table 1 provides a comparison of the hydrodynamic characteristics of this model with the similar one of the series “K” of the supercavitating screw propellers, the characteristic curves of the latter being shown in Fig.6.

It can be seen from the Table that in the SC regime, when the hydrofoil ship has a maximal speed and the axial cavitation number is equal 0.3, the efficiency of the propeller with wedge-type profiling ("K" series) is 12 - 16% higher than that of the propellers with segment-type profiling ("CK" series). This can be explained by a smaller thickness of the leading edges for the wedge-type series, leading to the decrease of the cavity thickness and the cavitation drag of the propellers of this series. The general strength provided therewith is approximately the same at the expense of larger thickness of the trailing edges for the wedge-type series, although the local strength in the vicinity of these edges is noticeably lower.

Table 1. Comparison of characteristics of two screw propellers with an expanded area ratio 0.81/0.8 and pitch ratio 1.4, belonging to the series "K" of SC propellers with wedge-type profiling and a series "CK" of highly cavitating propellers with segment profiling (see Fig.6 and Fig,.7), (J-advance coefficient, K_T -thrust coefficient, η_0 -open water propeller efficiency)

J	Axial cavitation number	K_T "K"	K_T "CK"	η_0 "K"	η_0 "CK"	$\Delta\eta_0/\eta_0$ in %
0.8	0.3	-	-	-	-	-
0.9	0.3	-	-	-	-	-
1.0	0.3	0.100	0.095	0.600	0.533	12.6
1.1	0.3	0.115	0.103	0.655	0.565	15.9
1.2	0.3	0.098	0.099	0.630	0.560	12.5
0.8	1.0	0.225	0.215	0.562	0.515	9.1
0.9	1.0	0.230	0.248	0.620	0.588	5.4
1.0	1.0	0.200	0.250	0.640	0.660	-3.1
1.1	1.0	0.150	0.208	0.590	0.700	-18.6
1.2	1.0	0.100	0.161	0.520	0.709	-36.3
0.8	Atmosphere	0.315	0.348	0.560	0.562	-0.4
0.9	Atmosphere	0.250	0.300	0.618	0.619	-0.2
1.0	Atmosphere	0.200	0.253	0.625	0.667	-6.7
1.1	Atmosphere	0.150	0.208	0.620	0.700	-12.9
1.2	Atmosphere	0.100	0.161	0.575	0.709	-23.3

On the other hand the series "CK" with the segment profiling has much larger efficiency (more than 18% larger) as compared to the "K" series at the regime of drag hump, when the speed of the hydrofoil constitutes about 50-65% of the maximal speed, which corresponds e.g. to the axial cavitation number equal to 1.0 or slightly larger. Therewith, the advance coefficient only slightly differs from its magnitude 1.15, corresponding to the maximal efficiency of both screw propellers at the maximal speed regime. The case described herein corresponds to a Russian variant of the design of the hydrofoil ship, when the power plant (not having large reserve of power) allows a reduction of the frequency of rotation of the propeller at the drag hump (almost proportionally to the drop of the translational speed of ship) as a consequence of growth of the turning moment and, therefore the advance coefficient at the drag hump regime is only slightly less than its own magnitude at the maximal speed regime.

In the case under consideration the increased efficiency of the propeller at the drag hump regime becomes a decisive factor for choosing the series "CK", as the series "K", due to reduced efficiency and for available power simply does not provide sufficient thrust at the drag hump regime. Note that at the drag hump regime, the hydrofoil ship, as opposed to the displacement ship, has a drag, and hence a required thrust of propulsors close or even exceeding that of the maximum speed.

The U.S. approach to the considered problem of design of the hydrofoil ship radically differs from the Russian one described above. The power plant, for example, gas turbine, is chosen in such a way as to have a sufficient reserve of power to ensure constancy of the frequency of rotation of the propeller for all regimes from that of the maximal speed up to that of the drag hump. Then according to formula (1), the advance coefficient at the regime of drag hump would drop in comparison with that of the maximal speed some 50-35%, i.e. in proportion to the drop of the speed of the translational motion of the ship. Therewith, as follows from the Table 1 given above, (for axial cavitation number of 1.0 or higher) the efficiency of the propellers of the series "K" with wedge-type profiling is more than 9% higher than that of the series "CK" propellers with the segment-type profiling. Consequently, if one use the U.S. approach to the design, the preference should be given to the series "K" with wedge-type profiling which had been done in reality by the American and Canadian specialists when developing the SC propellers for the aforementioned hydrofoil ship "Denison" and an open ocean hydrofoil ship "HMCS Bras d'Or". It should

be noted, however, that the U.S. specialists encountered additional difficulties, related to peculiarities of operation of the SC propeller for small advance coefficient- the aforementioned "blockage" effect.

The comparison presented above was made for the two concrete propellers of the indicated two series, having identical number of blades, blade contours, expanded area ratios, pitch ratios, form of the pressure surface and magnitudes of the advance coefficient, but different distribution of the section thickness chordwise. More complete comparison requires analysis of both series, as the advance coefficients, pitch and expanded area ratios for each of the compared propellers are not necessarily equal, and may be taken as optimal for the corresponding series, i.e. may be taken correspondingly to the maximal efficiency for a given cavitation number. The data required for a more complete analysis are given in the Table 2.

Table 2. Comparison of characteristics of two 3-blade optimal screw propellers at axial cavitation number of 0.3, belonging to the series "K" of supercavitating screw propellers with wedge-type profiling and a series "CK" of highly cavitating screw propellers with segment-type profiling (J-advance coefficient, K_T -thrust coefficient, η_0 - open water propeller efficiency, A_E / A_0 -expanded area ratio, P/D-pitch/diameter ratio)

axial cavitation number	series	aim function	A_E / A_0	P/D	J	K_T	η_0	$K_{DT} = J/\sqrt{K_T}$	$1/K_{NT}^2 = \sqrt{K_T}/J^2$
0.3	"K"	max η_0	0.81	1.4	1.12	0.120	0.660	3.233	0.276
1.0	"K"	not opt	0.81	1.4	1.12	0.140	0.610		
1.0	"K"	not opt	0.81	1.4	0.70	0.195	0.490		
0.3	"CK"	max η_0	0.95	1.8	1.50	0.177	0.660	3.565	0.187
1.0	"CK"	not opt	0.95	1.8	1.50	0.209	0.706		
1.0	"CK"	not opt	0.95	1.8	0.90	0.290	0.457		

Comment: the last two columns contain the coefficients, which should be multiplied by the identical for both compared variants multiplier (if identical are the fluid density, thrust and the speed of advancement in free water) with the goal of determining the diameter and the frequency of rotation for the optimal (in efficiency) screw propeller of the corresponding series complying with the considered conditions.

A straitforward analysis of the data given in the Table 2 shows that, as opposed to comparison for the same advance coefficient and other identical parameters, in the case considered here of the maximal speed regime (and axial cavitation number equal to 0.3) no advantage is found in the maximal magnitude of the efficiency of the either series under comparison, because the efficiencies of the optimal wedge-type screw propeller of the "K" series and the optimal segment-type propeller of the "CK" series are identical and equal to 0.66. It should be recognized, however, that this magnitude is reached at different magnitudes of the advance coefficient, expanded area ratio and pitch ratio.

A deeper analysis shows that for given fluid density, thrust of the propeller and the speed of the ship, the optimal propeller of the "K" series would have 10% smaller diameter and 48% larger frequency of rotation as compared with the optimal series "CK" propeller. Increased frequency of rotation and reduced diameter (for identical other conditions) stipulate a substantial advantage of the series "K" propellers with the wedge-type profiling at the maximal speed regime.

The final choice of the series is again defined by the adopted variant of the design of the hydrofoil ship as a whole. If one use the Russian variant, when the advance coefficient at the drag hump regime is

only slightly different from that at the maximal speed regime, the preference should be given to the “CK” series with the segment profile, as it follows from the Table 2 that the efficiency of the propellers of this series at the drag hump regime in this case (axial cavitation number 1.0, J=1.5) is 15.7% higher than for the propellers of the “K” series. Notwithstanding the indicated advantages of the “K” series at the maximal speed regime, both in the case considered here and in the course of the analysis of the Table 1, the increased efficiency of the propellers at the drag hump regime becomes a crucial factor for selection of the “CK” series because the “K” series (due to reduced efficiency) for the lack of a sufficient reserve of power (Russian variant) simply cannot provide sufficient thrust at the drag hump regime.

On the other hand, if the U.S. approach is employed to the design of the hydrofoil ship as a whole, when both the frequency of rotation is almost constant, and the advance coefficient at the drag hump regime is much less than its magnitude at the maximal speed regime (in the Table 2 the magnitude of the advance coefficient is decreased on 40%) the preference when selecting the series should be given to the “K” series with wedge-type profiling because the efficiency of the propellers of this series at the drag hump is (axial cavitation number 1.0, J=0.7) is 7.2% higher than for the propellers of the series "CK".

Thus, the comparative analysis of the propeller series differing only in the shape of the section, both for the same advance coefficient (based on the Table 1), and for the propeller at the optimal advance coefficient (based on the Table 2), leads to one and the same conclusion. For almost constant advance coefficient (Russian variant) advantageous is the segment profiling, whereas for almost constant rpm (U.S. variant) the advantage is on the side of the wedge-type profiling.

Another important conclusion can be made on the basis of the foregoing material. When designing a supercavitating or a highly cavitating propeller for a hydrofoil ship the project optimization at the regime of maximal speed should be performed in such a way that a sufficient thrust be provided at the drag hump regime with account of the power plant available on board. In short, the high efficiency at the maximal speed regime is not the only requirement when designing a supercavitating or a highly cavitating propeller for a hydrofoil ship.

Further progress in the development of the supercavitating or a highly cavitating propeller in Russia was connected with a more complete utilization of the computational methods of the vortex theory. In 1970 A.A.Russetskiy and E.A.Fisher in the KSRI employed the lifting line theory with a number of corrections, including those to approximately account for the presence of cavities in the inter-blade space [17]. It is interesting to note that this approach was semi-empirical, as it made use of the experimental data for the determination of the cavities’ thickness at the trailing edge of the blade [24]. Most certainly, the mentioned experimental materials were valid only for the design of such propellers which differed but slightly from the tested ones.

Based on the described approach there was designed a small series of 3-blade highly cavitating propellers "CK2", comprising 4 models with expanded area ratio 0.9 and a radius-wise variable pitch ratio, varying in the range 0.9-1.6 at the radius 0.6. An interesting peculiarity of the form of the profiles of this series consisted in a shifting of the maximal of thickness and curvature of the pressure surface 15% from the midchord to trailing edge of cylindrical sections, while retaining of practically segment form for the corresponding distributions for the region of the leading and trailing edges. Therewith the thickness of the leading part of the profiles decreased, which served to augment the efficiency at the full speed regime, but, simultaneously, should diminish the strength in the region of the leading edges.

Table 3. Comparison of characteristics of the two 3-blade optimal screw propellers with axial cavitation number 0.3, belonging to the series of supercavitating "CK2" and the series of highly cavitating screw propellers "CK3" (J-advance coefficient, K_T -thrust coefficient, η_0 -open water propeller efficiency, A_E / A_0 -expanded area ratio, P/D-pitch/diameter ratio)

axial cavitation number	series	Goal function	A_E / A_0	P/D on r=0.6	J	K_T	η_0	$K_{DT} = J/\sqrt{K_T}$	$1/K_{NT}^2 = \sqrt{K_T}/J^2$
0.3	"CK2"	max η_0	0.95	1.36	1.08	0.115	0.645	3.185	0.291
1.0	"CK2"	not opt	0.95	1.36	1 .08	0.205	0.690		
1.0	"CK2"	not opt	0.95	1.36	0.70	0.165	0.470		
0.3	"CK3"	Max η_0	0.95	1.56	1.24	0.150	0.680	3.202	0.252
1.0	"CK3"	not opt	0.95	1.56	1.24	0.220	0.708		
1.0	"CK3"	not opt	0.95	1.56	0.60	0.175	0.360		

Comment: The last two columns contain the coefficients, which should be multiplied by the the same multiplier for the variants under comparison (if identical are fluid density, thrust and speed of translational motion in free water) with the goal of determining the diameter and the frequency of rotation for the optimal (in efficiency) screw propeller of a given series complying with conditions considered.

The results of the testing of the models of this series (see, Table 3) showed, that no gain was obtained. In the maximal magnitude of the efficiency in comparison with the "CK" series. However, one was able to reduce relative advance coefficient corresponding to the maximal efficiency (1.08 instead of 1.50 for the series "CK"), which led (inspire of the decrease of the thrust coefficient) to a possibility to reduce diameter of the optimal screw propeller for this series by 12% as compared to the optimal and identical in thrust screw propeller of the "CK" (therewith the frequency of rotation increased by 56%).

Comparing with the data of the Table 2 for a conditional drag hump regime, one can notice, that for the constant advance coefficient (Russian variant) the screw propeller of the "CK2" series has 2.3% less efficiency than the propellers of the "CK" series. At the expense of the shifting of the maximum of efficiency toward smaller advance coefficients the screw propellers of the "CK2" series have noticeably larger efficiency at the maximum speed regime when the axial cavitation number equals 0.3, as compared to the propellers of the "CK", if the comparison is conducted for the advance coefficient less then 1.2 (see Table 4). For example, for J=1.0 the augmentation of the efficiency constitutes 18.2%.

Table 4. Comparison of characteristics of three propellers with expanded area ratio 0.95 and pitch ratio 1.4, 1.36, 1.33, belonging to the series of highly cavitating propeller "СК", "СК2", "СК3" series correspondingly (J-advance coefficient, K_T-thrust coefficient, η_0-open water propeller efficiency)

J	axial cavitation number	K_T "СК"	K_T "СК2"	K_T "СК3"	η_0 "СК"	η_0 "СК2"	η_0 "СК2"
0.8	0.3	-		0.115	-	-	0.535
0.9	0.3	-	0.1	0.110	-	0.580	0.590
1.0	0.3	0.111	0.115	0.110	0.545	0.630	0.635
1.1	0.3	0.125	0.110	0.110	0.591	0.645	0.650
1.2	0.3	0.124	0.080	0.085	0.616	0.590	0.600
0.8	1.0	0.248	0.200	0.210	0.528	0.545	0.560
0.9	1.0	0.273	0.230	0.235	0.601	0.610	0.620
1.0	1.0	0.257	0.230	0.220	0.657	0.665	0.670
1.1	1.0	0.208	0.193	0.180	0.688	0.695	0.695
1.2	1.0	0.160	0.150	0.135	0.692	0.700	0.690
0.8	Atmosphere	0.356	0.330	0.340	0.555	0.770	0.585
0.9	Atmosphere	0.304	0.285	0.285	0.609	0.620	0.630
1.0	Atmosphere	0.257	0.238	0.230	0.657	0.665	0.670
1.1	Atmosphere	0.208	0.193	0.180	0.688	0.695	0.695
1.2	Atmosphere	0.160	0.150	0.135	0.692	0.700	0.690

In 1980 on the basis of the lifting surface theory for noncavitating propellers with account of the cavity thickness, modeled with a prescribed distribution of the simple layer (the intensity of which was approximately determined with use of the previously mentioned experimental data on measurement of the cavity thickness at the trailing edge [24], [17]) in the KSRI there was developed a small series of highly cavitating propellers “СК3". With the purpose of providing sufficient strength the thickness of the leading part of the profiles of this series was increased in comparison with the "СК2" series. The form of the profile was taken of segment-type and symmetric with respect to the midchord, as in the "СК" series, i.e. the idea of shifting the maximal of thickness and curvature was abolished in this series. Some data on this series are presented in the Table 3 and the Table 4. It is seen that the last of the considered series is the best from all viewpoints. For example, the optimal (in efficiency) at the regime of the maximal speed screw propeller of this series has a record-breaking high efficiency of 0.68, which is 3% higher than for the analogous magnitudes of the series "К" and "СК".

The last of the described series of highly cavitating propellers "СК3" (with the segment profiling) was directly employed at the beginning of the 80s during the design of the full-size highly cavitating propellers for the largest in the world (displacement about 465 t., power of gas turbines 3x18000 hp plus power of diesels 2x1100 hp and the speed of cruising of 63 knots [21]) of the Russian open ocean hydrofoil ship "Sokol". The highly cavitating screw propellers in number of 6 were mounted in pairs on three angular struts. The sense of rotation of each pair was opposite. At full speed the blades of the propellers operated in the regime of supercavitation, although the profiling adopted was the segment one (without shifting off the mid-chord of the maximal of thickness and curvature), and not of wedge-type, as proposed by academician Pozdunin.

The comparative tests of two projects of open ocean hydrofoil ships were conducted in Russia. Besides the hydrofoil ship "Sokol", tested was the hydrofoil ship "Uragan" (426 t., 2x18000 plus 2x1100, 60 kn.), which had two struts and four highly cavitating screw propellers of the "СК" series [21]. A complete set of full-size tests showed that, the hydrofoil ship “Sokol” has evident advantages as compared to the hydrofoil ship “Uragan” (mainly due to a better arrangement of wing system, and, after some improvements (in particular, the power was decreased down 2x20000 hp plus 8000 hp) the former

ship can be built in series. Until 1990 there were built 3 serial ship of "Sokol" type, after that the funding of the corresponding programme was stopped [21].

Thus, in Russia in the period of 1941-1980 there were carried out extensive experimental tests (tested were 4 series) of the suparcavitating and highly cavitating propellers.

The analysis of this materials revealed, in particular, an important peculiarity of such propellers, namely, for a given low cavitation number and at a given magnitude of the advance coefficient the increase of pitch for the supercavitating or highly cavitating propeller, as opposed to a noncavitating one, does not lead to a significant increase of the thrust coefficient. This shows that, firstly, use of variable pitch does not bring about the same effect usually anticipated for the noncavitating propeller, and, secondly, for a limited diameter of the SC propeller the thrust generated at the design regime may be insufficient for propelling the ship with a given speed for any choice of pitch.

With the goal of overcoming of the latter problem effective may become the application of the supercavitating propeller with a spoiler at a (rectilinear in radial direction) trailing edge. For the experimental investigation of models of such screw propellers there was developed and tested in the KSRI a model of 3-blades supercavitating propeller with expanded area ratio 0.8 and pitch ratio 1.4, having a wedge-type profiling and an asymmetric rectified contour with the trailing edge rectilinear in radial direction, adapted for mounting of a spoiler with regulated extenuation from -3% to +5% of the local chord. The tests of this mini series of supercavitating propellers with a spoiler showed that for a 2% spoiler (cavitation number 0.4, advance coefficient 1.2) the thrust coefficient increases as compared to the propeller without the spoiler 100% and reaches the value of 0.15. Therewith, the efficiency at the indicated advance coefficient even increases several percent, for smaller advance coefficients a drop of the efficiency of 2% accompanied by the growth of the thrust of 40-50%. The effect of the spoiler estimated in the latter experiment complies, at least quantitatively, with the results of theoretical research on the influence of a spoiler within an ideal fluid mathematical models [25] - [28], [31]. In particular, it was established by calculation that at the regime of its most favorable influence the spoiler provides a significant decrease of the cavity thickness in the inter-blade space, as compared to a similar profile without the spoiler. The latter effect corresponds to shifting of the center of action of the loading distribution chordwise in the direction of the trailing edge. Positive influence of such a shift upon the hydrodynamic lift-to-drag ratio of supercavitating foils at zero cavitation number was found by M.P.Tulin [14] back in 1955.

At the beginning of the 80s there was built and successfully tested a hydrofoil ship "Antaris" (200 t, 60 kn.) with supercavitating screw propellers with spoilers corresponding to the aforementioned mini-series. It is interesting to note that the propellers on this ship were installed on the inclined shafts, and, consequently, at speeds about 50 knots there was observed a breakthrough of the atmospheric air along the inclined shifts to the propeller blades. With the goal to secure a required thrust along with a possible ventilation there were chosen for this particular hydrofoil ship the supercavitating propellers with spoilers.

The story of the application of the supercavitating (or highly cavitating) screw propellers proper, which started successfully in 1962 from the hydrofoil ship "Denison", finishes over by the end of 80s, because the experience of operation of this screw propellers on the world largest serial hydrofoil ships of the "Sokol" type showed insufficient reliability of the shaft sealing on the nacelles and ensuing necessity in frequent repair. The problem of reliability become so acute that it was decided to equip the next projects of the Russian open ocean hydrofoil ships not with supercavitating propellers but with wateriest similarly to the U.S. hydrofoil ships "Tucumcari" and "Pegas".

However, these projects have not been realized. Further on, unfortunately, the interest toward the hydrofoil ships in the world dropped quite abruptly in connection with appearance of more prospective types of high-speed ships, such as catamarans, SES (Surface effect ships) and SWATH (Small water-plane area twin hull), for which the implementation of the supercavitating propellers proper is not preferable.

2.3. PRESENT DEVELOPMENT OF THE IDEAS OF ACADEMICIAN V.L. POZGUNIN

In spite of the evident end of the story of the application of the supercavitating propellers proper, the idea itself, lying in the basis of the development of supercavitating propellers and formulated in 1941 by V.L. Pozdunin as an idea for design of a cavitating (or ventilated) propulsor, less subject to erosion and othernegative consequences of the cavitation (or atmospheric ventilation), found its further evolution in the development of several new types of propulsors. Namely, highly-skewed cavitating propellers, trans-cavitating propellers, surface piercing propellers (or semi-submerged propellers) and ventilated wateriest, which are already in use or have good perspectives for their use on high-speed ships of different types.

Let's start our consideration with highly-skewed cavitating propellers, intended for the passenger hydrofoil ships of relatively small displacement, which haven inclined shaft and shallowly submerged hydrofoils. As established above, the supercavitating propellers have been used mostly on the sea-going hydrofoil ships, equipped with deeply submerged hydrofoils. However, the "cavitation barrier" is also encountered when designing propulsors for small passenger hydrofoil ships on shallowly submerged hydrofoils. The first of those ("Raketa", 25 t., 38 kn., 1200 hp, 66 passenger) was built in Russia by the design of R.E. Alexeev in 1957. In this case, inspite of moderate speed, it is not possible to avoid cavitation at the maximal speed regime because of the unsteadiness of the flow past the blades of the screw propellers, mounted on the inclined shaft (the angle of inclination of the shaftline varies for different projects in the range of 6-15 degrees). Moreover, in this case breakthrough of atmospheric air is possible through the suction zone along the inclined shaft to the blades of the propeller.

During the first stage of the investigation of this problem in the KSRI there was developed a special series of 5-blade screw propellers, adapted for operation in oblique flow field. These propellers were designed by E.P.Georgievskaya under guidance of Professor A.A.Rousetsky mostly for the purpose of securing the absence of cavitation, and, consequently, the absence of erosion on the pressure side of the blades [11]. Therewith, cavitation and erosion on the suction side could not be suppressed, although measures were taken to minimize it (the 5-blade propeller series consisted of 22 models with expanded area ratio 0.8; 1.1; 1.25; 1.4 and pitch ratio in the range of 1.1 - 1.55). However, use of 5-blade propellers of the indicated series did not provide in the considered case the realization of Posdunin's idea of designing a cavitating propulsor adapted to oblique flow and only slightly exposed to erosion and the other negative consequences of cavitation.

A direct use of the three-bladed supercavitating or highly cavitating propellers with symmetric contour, of the aforementioned series, did not give effect in the case of oblique flow, because unsteady form of cavitation in this case results in a qualitatively different mechanism of the appearance of erosional damage than in axial flow.

In the considered case of oblique flow the mechanism of the appearance of erosional damage, as it was found with use of high-speed photography [5], is connected with a periodical appearance and disappearance of a principally new type of unsteady cavities, which were proposed to be called "residual". In particular, it was found that the busted partial cavity the after further turning of the blade, when the zone of decreased pressure (corresponding to its occurrence conditions) is replaced by a zone of increased pressure, starts to close by way of moving its forward part to its tail part.

The latter does not have time to noticeably move downstream, because of the reestablishment of pressure behind the cavity and high speed of the process. Thus, the main distinctive feature of unsteady residual cavities consists in their collapsing only in their front part, disappearing in the region of its tail. In the region of its disappearance the residual cavity gives rise to an intensive erosion, and the corresponding erosional damage is most visible on the suction side of the 5-blade propeller of the indicated series tailored for operation in oblique flow. Deep understanding of the physics of the process accompanying the operation of the propeller in oblique flow enabled the specialists of the KSRI in 1983 to successfully realize in this complicated (due to oblique flow) case the idea of Posdunin of designing a propeller just slightly subject to erosion and other negative consequences of cavitation. This success was confirmed in September of 1983 in the process of full-size tests of a Russian passenger hydrofoil ship on shallowly submerged hydrofoils "Kometa" (1961, 118 passenger, 60 t., 2x1100 hp) with full cruising

speed of 35 kn., on which there were installed the specially developed highly-skewed cavitating propellers (HSCP) [5]. In the process of these investigations was designed a 3-blade HSCP operating on the inclined shaft (with angle 13 degree), having a expanded area ratio of 1.2, pitch ratio of 1.3 and diameter 0.67 m.

The working idea in this case consisted in the concept that for a properly chosen degree of skewing and form of the sections the cavity does not exist permanently as opposed to usual supercavitating propellers, but appears in the form of a dynamic film partial cavity at different moments of time and at different sections of the blade from its suction side, which is determined only by angular position of the considered blade at a given moment time (see Fig.8). The blade is designed in such a way that in the course of its turning (due to the skew and flow downwash), the residual cavity for each blade is dynamically shifting to peripheral sections end, eventually, closes outside of the surface of the cavity (see Fig.8). Therewith the formed front elements of the residual cavity are moving in the direction of the tail part. The latter forms at the end of the whole cycle right before the complete disappearance of the residual, and which finds itself outside the blade surface due to a special form of the blade. With such a closure mechanism of the unsteady residual cavities there is no erosion observed on the whole surface of the blade, although on the larger part of the sections there takes place a dynamically developing partial film-like residual cavity, which periodically (at every rotation) appears and disappears in its turn on every blade (see Fig. 8).

The full-size tests of the hydrofoil ship on a shallowly submerged hydrofoils "Kometa" with the two propellers thus designed showed, that the erosion in practically not observed on them, i.e. the service time of these propellers significantly exceeds that of the initially installed 5-blade custom screw propellers, corresponding to the series described above. Therewith, by means of optimization of the blade geometry the newly developed highly skewed cavitating screw propellers turned out to be 10 % more efficient, that the custom 5-blade propellers [5].

Close to the aforementioned type is a cavitating propulsor called a trans-cavitating propeller. An interesting investigation of a possibility of designing such propellers for the shallow-water ferries, having maximal speed in the range 30-35 kn., was performed by the Japanese researchers [36], [37]. They proposed to design a screw propeller having conventional sections (NACA or MAU) near the blade root and gradually much more pronounced wedge-type supercavitating sections when approaching the tip of the blade. Such mixed-type screw propellers were called "trans-cavitating propellers". In the trans-cavitating regime the suction side of the blade is covered by the cavity only at peripheral radial and is unsteady depending on the angular position of the blade, as the propeller operates in a tangentially nonuniform following wake. It should be noted that in the considered case due to restricted diameter the 4-blade skewed (skew at tip 36 degree) screw propellers were designed for a moderate loading (0.728), more exactly J=0.916(0.720), K_T =0.240(0.148), with the axial cavitation number equal to 1.048 or 1.371, which corresponds to the freely speed equal to 35 or 30 kn respectively. Tested altogether were 11 models of the propellers. The design was carried out with use of the method, enabling to control sheet cavitation on the propeller blades. On the basis of extensive experiments it was found that for a regime, corresponding to the ship speed of 30 kn, a noncavitating propeller with conventional profiling is better, and at the regime, corresponding to the ship speed of 35 kn is worse (in efficiency and the pressure fluctuations), than the proposed trans-cavitating propeller.

Pass over to consideration of the other two out of the listed propulsor types (surface piercing propellers and ventilated waterjets), which, in a general sense, can be viewed as a present stage of the development of the ideas of Pozdunin. The propeller operation on a high-speed ship is performed near a free surface (unless the special measures are taken, e.g. placing the propeller in zone of increased pressure under a hydrofoil), and, obviously, a possible breakthrough of the atmospheric air to the suction side of the blade can considerably diminish the thrust of the propulsor. This breakthrough is called atmospheric ventilation and is completely analogous to supercavitation, but for very low (practically vanishing) magnitudes of local cavitation number. Such low cavitation numbers correspond to the regime of atmospheric ventilation, because in this case the pressure in the cavity equals to atmospheric one, and not the pressure of saturated water vapor at the temperature during the tests, which, e.g for 4 degrees Centigrade constitutes just 0.8% of the atmospheric pressure.

Following the line of thinking of V.L. Pozdunin, in the cases, when the possibilities of avoiding ventilation of the blades of the propeller are exhausted, one may formulate a task of designing a ventilated propulsor, free of negative consequencies of ventilation (cavitation), i.e. free of a uncontrolled drop of the thrust and capable of working in the regime of atmospheric ventilation (in fact, this takes place at the regime of the extremely developed supercavitation, corresponding to almost zero magnitudes of local cavitation numbers). At present known are and have found applications two approaches of the technical realization of the formulated task. Consider these tasks in the same order, in which they started to be used on real high-speed ships.

One of the first applications of the surface piercing propellers (SPP) for the hydrofoil ships was realized in Russia in 1963 [29] with the goal of decreasing some 28% of the draft in floatation (as compared to the hydrofoil ship "Raketa") of the Russian river passenger hydrofoil ship "Raketa-M" (23t., 32.4 kn, 1200 hp, 50 passenger). The draft was decreased from 1.8m to 1.3m by varying the arrangement of the propeller relative to the stern hydrofoil. Therewith, diminished was the angle of inclination of the shaft from 12 to 5 degrees, the pitch of the screw propeller was increased from 0.815m to 0.91m, the expanded area ratio – from 1.0 to 1.45, and the number of blades and diameter remained the same 6 and 0.665 correspondingly [29]. The form of the blade contour was skew-like, the form of the profile was segment one. At maximum speed the propeller was partially immersed (80%), and its blades worked in the regime of atmospheric ventilation (atmospheric cavitation). The developed SPP provided a sufficient thrust on all regimes of the ship motion and turned out to be an acceptable technical solution applied later on on the passenger river hydrofoil ship "Belarus" (14.5t, 32.4 kn, 1200 hp,40 passengers).

These described applications of the first SPP were preceded by a development and testing of a model series of such propellers on a catamaran in open water, covering the range from от 3 to 6 blades, expanded area ratio from 0.685 to 1.285 and pitch ratio from 0.975 to 1.4. The modeling was performed in Froude number and advance coefficient. Almost zero magnitude of local cavitation numbers was provided at the expense of the regime of atmospheric ventilation and no vacuum was needed in this case above the free surface, as opposed to the case of supercavitating propeller, for which, as indicated, the modeling in cavitation number is required. All research was conducted under guidance of a Professor of Leningrad Institute of Water Transport A.M.Basin and an engineer of the Central Hydrofoil Bureau in Gorkiy A.I.Maskalik [30]. The maximum efficiency of this propeller series at a relative submergence of 0.5 turned out to be 0.48, and for the relative submergence of 0.8 turned out to be equal 0.50.

As another example of use of the SPP in Russia one can indicate a cutter "Mustang" (20t, 2x1600, 50kn.) built in mid-80s with a ventilated air cavity on the bottom. In this case the specialist of the KSRI under guidance of F.F.Bolotin managed to obtain higher SPP efficiency equal approximately to 0.6 at the maximal speed regime by means of implementation of the wedge-type profiling (instead of segment one used for the SPP of the hydrofoil ship "Raketa-M").

Operation of SPP on a high-speed ship is characterized by formation of considerable in size unsteady ventilated cavities and a substantial spray phenomenon, related to the process of crossing by each blade (two times per revolution) of free surface (see Fig.9).

In Switzerland Philip Rolla (of Rolla SP Propellers SA) developed and manufactured many SPPs for different high-speed ships. In 1991 were published the results of testing of the series of SPP (4-blades, expanded area ratio 0.8, pitch ratio varied from 0.9 to 1.6) developed by Philip Rolla. The tests were carried out by Professor Klaus F.L.Kruppa in the high-speed free-surface cavitation tunnel of Berlin Technical University [35].

A characteristic peculiarity of SPP is a growth of the efficiency with increase of the ship speed, illustrated in Fig.10 on an example of the cutter "Gentry-Transatlantic" (145 t., 10866 hp, 68 kn, length 33.5m.), which showed in July 1989 a record-breaking time (3733 min) of navigating across the Atlantics with one refueling. Two waterjets (2x3433h.p.) were used on this cutter, driven by the two diesels and one SPP (4000 hp), driven by gas turbine [32].

In Fig.10, borrowed from the aforementioned article, presented was a comparison of the efficiency of the waterjets of this cutter with the efficiency of SPP. One can see that the maximal efficiency of waterjets 0.68 is reached at a speed of 55 kn., and the efficiency of the SPP, also 0.68, has the maximum

magnitude at a speed of 70 kn., when the efficiency of there waterjets falls down to 0.55, that is 19% in comparison with the maximum. Therewith it is seen from the presented Figure that the efficiency of the SPP continues to grow up to the maximal speed (see Figure10), and obviously would continue to slowly rise for further growth of speed.

The growth of the efficiency with the speed represents a unique feature of the SPP and is explained by the influence of Froude number, as the local cavitation numbers, as indicated, are close to zero for the SPP blades, and, therefore, the caviotation number does not have any effect in this case. Note in passing that in the case of the supercavitating screw propeller of wedge-type profiling there takes place an opposite situation, i.e. Froude number does not practically influence, and the cavitation number becomes a decisive parameter. For example, according to the data on "K" series (see Table 1) the maximum efficiency of the supercavitating propeller with pitch ratio 1.4 for advance coefficient 1.1 is reached at the cavitation number about 0.4 is equal to 0.675. The indicated maximum for a concrete ship project corresponds to a certain speed so that for the supercavitating propeller there exists a usual maximum of the efficiency versus speed, which is completely analogous to that for the waterjet presented in Fig. 10.

The maximum speed shown by "Gentry-Transatlantic" in the process of its record cruise in good weather and empty fuel tanks, was equal to 74.8kn., and the average speed for the whole distance constituted 55kn. The considered cutter had one 5-blade SPP with the wedge-type profiling, a diameter of 0.914m., pitch ratio 1.36, expanded area ratio 1.05 and the nominal frequency of rotation 1900 revolutions per min. At the intermediate speed of 40kn. The efficiency of SPP (see Fig. 10) drops down to 0.46, i.e. 32% as compared to the maximum magnitude, which similarly to the supercavitating propellers with wedge-like profiling, is the main deficiency of the propulsors of this type.

Some possibilities of improvement of characteristics of the SPP in the intermediate speeds can be obtained by using the controlled pitch SPP (CPSPP). Two such 6-blade CPSPP of diameter 1.07m were installed in 1971 on the experimental skeg-type air cushion vehicle "SES-100B" (105t., 15020 hp, 90.3kn) and, during the full size tests ensured sufficient thrust (even larger the design thrust) at all regimes, starting from that at zero speed. It is interesting to mention that simultaneously in the U.S.A. there was built and tested an analogous experimental skeg-type air cushion vehicle "SES-100A" (114t., 12316 hp, 76 kn), equipped with two waterjets. The tests of both air cushion vehicles showed that for the speeds higher than 70 kn the CPSPP are considerably more efficient than the waterjets, as the speed of the waterjet variant turned out to be 10% less that of the propeller one even accounting for the 22% of excess of the power of the latter.

When developing the CPSPP for the air cushion vehicle "SES-100B" considerable attention had to be attached to the strength and vibration of thin wedge-like blades, accounting for the shock character of the loading at water entry with high frequency of rotation (at 80kn. about 1900 revolutions per min). Unsteadiness of the loading and its shock nature for the blade water entry and exit out of water is an incorrigible deficiency of the SPP, giving birth to serious problems in securing strength and reliability of the whole propulsor installation, especially difficult for solution in the case of increase of of the dimensions of ships.

For small sporting ships the SPP is a sufficiently reliable and wide-spread propulsor, e.g., sporting cutters of the type "FORMULA-1" always have the SPP as a propulsor, with diameter about 0.15m, frequency of rotation about 9000 rpm. This cutters-catamarans with aerodynamic unloading and power of the suspended engine of about 400hp. and the cutter weight (without fuel) of 0.4t reach a speed up to 120kn, and for them important is the unique property of the SPP to increase its efficiency with speed, more precisely with increase of Froude number. When passing to larger ships, as indicated previously, there comes to the foreground the problem of unsteady shock loading, occurring when the blades intersect the free surface.

The original means of the solution of this problem for ventilated propulsor by eliminating the causes of the appearance of unsteady loads is a new type of propulsor proposed in 1975 by a researcher of the KSRI M.A.Mavluydov. This propulsor was called a ventilated waterjet [18], [33]. In fact this is a waterjet with the above-water or partially above-water ejection of the jet, which has an axial pump at the end of the suction part of the waterjet tube which has contact with atmosphere. This pump operates in the

regime of atmospheric ventilation, i.e. for the local cavitation numbers close to zero. The blades of the pump should have a wedge-type profiling, sometimes with a cavitator on the suction surface (Fig. 11).

In terms of the peculiarities of hydrodynamic characteristics and the magnitude of the efficiency the ventilated watrejet is similar to the SPP. For example, it possesses to a full degree the aforementioned unique feature of the SPP to increase its efficiency with growth of the speed. However, as opposed to the SPP, during the operation of the ventilated waterjet absent are: the shock loads on the blades, large loads on the bearings and considerable unsteady lateral forces, acting upon the whole ship.

At the beginning of 80s in Russia were built an SES (140t, 2x3000 hp, 35 kn), equipped with two ventilated waterjets located behind the skegs, and a cutter with air cavity on the bottom "Serena" (100t, 2x3000 hp, 30 kn.), equipped by two ventilated waterjets with diameter of working wheel about 1.15m. The latter project is built in series is showed itself quite well in practical operation. The propulsive coefficient of the ventilated waterjets in this case at the full speed regime is equal approximately 0.7 [18].

A certain interest toward ventilated waterjets as a prospective type of propulsors was shown in 2000 by the specialists of the Naval Surface Warfare Center USA, Carderock Division [34].

3. Mathematical Modeling

3.1. PRELIMINARY COMMENTS

A necessity for theoretical investigations of hydrodynamics of the supercavitatin propellers was understood right after the formulation of the Pozdunin's idea, as engineers lacked the experience of the development of such propulsors. An intensive work was started begun in this direction in a number of countries. In Russia the pioneering research was carried out by V.F.Bavin, A.M.Basin, M.I.Gurevich, A.N.Ivanov, V.M.Ivchenko, V.M.Lavrientiev, A.D.Pernik, N.N.Polyakhov, O.V.Rozhdestvensky, A.A.Rousetsky, L.A.Epstein, D.A.Efros.

At first its seemed that supercavitating screw propellers would be more efficient than the noncavitating due to reduction of friction on the part of the blade covered by the cavity. However, more detailed theoretical investigations showed that for the supercavitating profiles having a wedge-type leading edge with cavity starting from the leading edge, the suction force is not realized, and therefore, together with the elimination of friction on the side of the blade covered with cavity there appears a specific pressure drag which was called "cavity drag". It turned out in practice that this drag component is comparable in magnitude with the "lost" friction drag. As a result the supecavitating screw propeller has an efficiency which is lower than that the same propeller at a larger advance coefficient and the same cavitation number, when rather than supercavities there occur on the blades partial cavities or no cavities at all depending on the magnitude of the considered cavitation number.

The principal problem of the theory in connection with the discovered new component of losses became that of the optimal distribution of loading along the blade (along radius and along the chord) with necessary account of the requirements on the sizes of the cavities forming on the blades. This problem was previously solved for noncavitating propellers. Therewith, important is both the length of the cavities, which should be larger than the maximum width of the blade (this is the main requirement of the flow regime, which is called supercavitation), and thickness, which should exceed the blade thickness complying with strength requirements. Let's call the formulated problem the problem of the design calculation of the supercavitating propeller (SCP) or the first problem.

The second albeit not less important problem is the so called analysis calculation, which enables obtaining by way of calculations all necessary characteristics of the designed propeller for any regime of its operation. This is a direct problem of hydrodynamic calculation of the SCP, when studied is a flow

past a propeller of a given configuration, given advance coefficient and given cavitation number. Therewith, Froude number is not accounted for and the fluid is assumed weightless, as, according to the aforementioned, the account of gravity leads to an unsteady flow problem, for which the local cavitation number, corresponding to a concrete point of the considered cylindrical section of the blade, is a variable, more exactly, a function of the time-dependent angular position of the blade for a horizontal position of the axis of the screw propeller. The importance of the analysis calculation is clear from that the SCP design obtained after the design calculation of the SCP should necessarily secure a sufficient thrust at the intermediate regimes, such as that of the drag hump for a hydrofoil ship. One can surely use the experiment in the cavitation tunnel to determine characteristics of the SCP, but for that one should manufacture the propeller which is impossible to do in the rhythm of the calculations and for many studied variants. Therefore, the actuality of the calculation methods is obvious. At the same time one should note that the complexity of the analysis calculation for SCP consists in necessity to calculate different regimes of flow past the blades bot without cavitation and with development of its different form.

To solve the two above formulated problems one can use mathematical models of different levels. Consider briefly some of the mathematical models developed as of now, not pretending to be complete and referring to the available publications.

3.2. REGRESSION MODELS OF HYDRODYNAMIC CHARACTERISTICS OF THE EXPERIMENTALLY INVESTIGATED SERIES OF THE SUPERCAVITATING PROPELLERS

The simplest albeit very actively employed mathematical models contain regression analysis, describing results of tests of systematic series of the SCP models. Presented in [38], [39] are the coefficients of the regression polynomials, obtained through the analysis of the following series of highly cavitating propellers:

-3-blade "CK" series of highly cavitating propellers [18], [19](Tsapin V.D., Sadovnikov Yu.M., 1955);

-5-blade series of the cavitating propellers adapted for oblique flow operation without erosion of the pressure side, [19](Georgievskaya E.G., Russetskiy A.A., 1965);

-3-blade series of screw propellers Newton R.N., Rader H.P. [40](1961);

-3-blade series of screw propellers Gawn R., Burrill L.C. [41](1957).

The regression polynomial, obtained separately for the thrust coefficient and the moment coefficient, represents these quantities versus advance coefficient, cavitation number, expanded area ratio and pitch ratio. Having such a mathematical model for a given series it is easy to construct the corresponding algorithms for the computer calculation within the design and analysis schemes. The main deficiency of such an approach consists in an impossibility of designing a propeller, going out (in any parameters) of the limit parameters of the series tested in the cavitation tunnel. For example, an impossibility to account for a nonuniformity of the flow coming upon the propeller if the tests of the aforementioned series were conducted in the uniform flow. Besides, there arises a question of design of the series proper and possibilities of their elaboration.

Within the regression mathematical models these questions cannot be solved. To solve them one should make use of different mathematical models of vortex theory of screw propellers. Let's consider in the following section one of the latter models, developed in 1985 in Leningrad Shipbuilding Institute (now Saint-Petersburg State Marine Technical University) by A.S.Achkinadze and A.S.Narvsky [47], [48], [49], [50], and solving the problem of design calculation of the supercavitating propeller on the basis of the lifting surface theory, and a liner theory of cavitating flows with use of the open model of the cavity closure.

3.3. LIFTING SURFACE THEORY AS A MATHEMATICAL MODEL FOR DESIGN CALCULATION OF SUPERCAVITATING PROPELLERS

Let assume that there are z (according to number of blades) symmetrically arranged proper helical surfaces with a common x-axis, oriented in direction of motion of the screw propeller. Designate one of these surfaces S and consider further on only this nominal surface, automatically accounting for the symmetry of the flow with respect to blades and a necessity of summing up all induced velocity contributions from all indicated z- surfaces.

The geometry of the nominal surface for a given x-axis is uniquely determined by pitch P_S, which is determined by a special algorithm, accounting for prescribed thrust coefficient, advance coefficient K_T, and the parameters of a given nonuniform velocity field. The indicated algorithm is called a Generalized Linear Model (GLM)[42] and is used successfully for the design of not only supercavitating but also noncavitating screw propellers [43], [54].

Take further on, following the linear theory of lifting surface, that the hydrodynamic singularities are continuously distributed upon the nominal surface within the blade and the wake behind it. Therewith, according to hypothesis of the potentiality, it is assumed that the considered fluid is potential in the whole flow domain except the surfaces occupied by hydrodynamic singularities (for all blades). The flow is assumed incompressible, inviscid, gravity-free, unbounded and steady (in a moving coordinate system, attached to a uniformly rotating and uniformly moving along x-axis screw propeller). Then, based on the theory of potential, knowing the potential induced by distributions of a simple layer with scalar intensity q, and a potentialof vortex surface layer of a vector intensity $\vec{\gamma}$, one can integrate over all corresponding domains and find direct value of the perturbation velocity vector:

due to a simple layer

$$\vec{W}_q(X_1,Y_1,Z_1) = grad\left(\frac{-1}{4\pi}\int_{S_q} q\left(\frac{1}{R}\right)dS\right) = \frac{-1}{4\pi}\int_{S_q} q\cdot grad\left(\frac{1}{R}\right)dS = \frac{1}{4\pi}\int_{S_q} q\frac{\vec{R}}{R^3}dS \tag{4}$$

due to a vortex layer (both attached and free)

$$\vec{W}_\gamma(X_1,Y_1,Z_1) = \frac{1}{4\pi}\int_{S_G}\frac{\vec{\gamma}\times\vec{R}}{R^3}dS \tag{5}$$

where $\vec{R}$ - radius vector, directed from the integrated element toward a point whre the velocity is calculated; S_q- is a part of the nominal surface upon which the simple layer is located; S_G- is a part of nominal surface on which the vortex layer is located.

As known from the theory of potential, in the points of the nominal surface, where the intensity of simple layer is not equal to zero, there is a jump of the normal component of the perturbation velocity and in the points of the nominal surface, where the intensity of vortex layer is not equal to zero, there is a jump of the tangential component of the perturbation velocity. With account of the latter consideration, one has:

For the normal component of the perturbation velocity on the pressure side of the nominal surface (normal vector is positive when directed from the pressure side to the suction side of the nominal surface)

$$W_n^- = W_{qn} + W_{\gamma n} + q/2 \tag{6}$$

for the tangential component, directed along the proper helical lines constituting the normal surface and designated by index τ, component of the perturbation velocity on the suction side of the nominal surface (positive when directed toward leading edge)

$$W_{\gamma\tau}^{+} = W_{\gamma\tau} - \gamma_r / 2 \tag{7}$$

To secure potential character of the flow outside of the considered system of singularities between the radial and tangential components of the vector $\vec{\gamma}$, which does not have a component normal to the nominal surface, there should be fulfilled a known relationship (which is equivalent to the condition of preservability of the vortices or equivalence to zero of surface divergence of vector $\vec{\gamma}$)

$$\gamma_\tau = \partial\Gamma / \partial r \tag{8}$$

where the intensity of the double layer, equivalent to the considered system of distributed continuos vortices equals

$$\Gamma(r,\xi) = -\int_{\xi_{LE}}^{\xi} \gamma_r(r,\xi) d\xi \tag{9}$$

The formulae presented are valid only for the case of absence of discretized vortex lines and zero magnitude of Γ on the contour of the blade and the vortex wake. In this case valid is the relationship, enabling to determine the equivalent vortex distribution for a given distribution of the double layer, namely

$$\vec{\gamma} = \vec{n} \times grad\Gamma \tag{10}$$

Besides the perturbation velocities there must be taken into attention a field of the transport velocity together with the moving coordinate system, which is rigidly connected with the rotating and transitionally moving screw propeller $\vec{V}_E$ and the incoming flow field $\vec{V}_\psi$, so that the field of relative velocity $\vec{V}_R$ in the moving and rigidly attached to the propeller coordinate system can be found with use of obvious formula

$$\vec{V}_R = \vec{W}_q + \vec{W}_\gamma + \vec{V}_\psi - \vec{V}_E \tag{11}$$

Using the corresponding Euler equations integral, the pressure in the fluid in the moving propeller-attached coordinate system can be determined, if found is the total field of perturbation velocity

$$\vec{W} = \vec{W}_q + \vec{W}_\gamma \tag{12}$$

using the formula

$$p - p_0 = -\rho \frac{(\vec{W} + \vec{V}_\Psi)^2}{2} + \rho \cdot \vec{V}_E (\vec{W} + \vec{V}_\Psi) \tag{13}$$

According to the linear approach, the induced velocity and the absolute velocity of the given oncoming flow are assumed being small magnitudes of the first order and the square of their geometric sum can be neglected, then one can derive

$$\begin{aligned} &p - p_0 = \rho \cdot \vec{V}_E (\vec{W} + \vec{V}_\Psi) = \\ &\rho V_{E\tau} W_\tau + \rho V_{E\tau} V_{\psi\tau} = \rho V_E W_\tau + \rho V_E V_{\psi\tau} \end{aligned} \tag{14}$$

where the index τ denotes the projections of the corresponding vectors upon the direction tangential to the proper helical lines constituting the nominal surface. It is more accurate to take the projections of the

induced and additional velocity on the direction of the vector $\vec{V}_E$, but the adopted tangential direction differs from the indicated one by a small angle (according the linear approach) so that the relevant error is of higher order of smallness than the retained terms.

Using the formula (3) for the local cavitation number σ and previous equality, one can obtain a linearized dynamic condition on the boundary of the cavity, which physically signifies a pressure identity for points of the cavity boundary with the pressure of the saturated fluid vapor ($p = p_V$),

$$W_\tau^+ / V_E = -\sigma / 2 - V_{\psi\tau} / V_E \quad \text{in } S_{CAV} \tag{15}$$

where S_{CAV} - is part of the suction side of the nominal surface, covered by the cavity in design regime. Note that the domain occupied by the cavity S_{CAV} does not coincide with the projection of the blade contour upon the nominal surface S_B (see Fig. 12).

When deriving (15) account was taken of the fluid being gravity-free, and, therefore, the pressure at the infinity, entering in the local cavitation number, coincides with the Euler integral constant ($p_{0r\theta} = p_0$). The pressure surface S_p of the supercavitating propeller is assumed free of cavitation at the design regime, and, therefore, on this surface (its form is to be determined in the solution process as that of the cavity) there should be fulfilled a kinematic condition of no-normal velocity, which without simplification in the most general way can be written as

$$\vec{V}_R \cdot \vec{n} = 0 \quad \text{in } S_p \tag{16}$$

Now all is ready for the formulation of the considered problem of the design calculation in its least general (basic) form (Formulation of Problem A), when there is no freedom of choice, and, consequently, no possibility to optimize the design.

The problem A consists in finding a geometry of the blades and cavities for a given distribution of loading along the blades of the supercavitating propeller. Therewith, given are the pitch of the nominal surface, the projection of the blade contour upon this surface, diameter of the hub (which is assumed to be infinite and cylindrical), advance coefficient and axial cavitation number χ (which, according to (2) and (3) with account of the absence of gravity forces, is related to σ by an obvious formula $\sigma = \chi \sin^2 \beta$, где $tg\beta = J/(\pi\bar{r})$

If the loading is prescribed, then prescribed is the intensity of the attached vortex layer (i.e. given is the radial component of the vector $\vec{\gamma}$) on the nominal surface within the blade or, which is the same, prescribed is the distribution of circulation along the radia and the blade chord. Unknown in this case is the intensity of the simple layer q, modeling the cavity. Thickness of the blade material in this case is not accounted for at all, as it is assumed that the cavity completely covers the suction side, starting from the leading edge. However, due to the absence of freedom in the choice of the distribution of loading along the blade the obtained solution of the problem A can give an unreal thickness from viewpoint of the strength of the blade, as no additional conditions are envisaged within the basic formulation.

After finding the platform of the cavity (i.e. after finding region S_{CAV}) and determination of the intensity of the simple layer q, distributed along this surface, one can easily find the form of the pressure side of the blade (i.e. find pitch distribution and the form of the pressure side of the section radius-wise) as well as all necessary hydrodynamic characteristics of the screw propeller under design.

Thus, the determination of the form of the cavity platform represent a central point of the problem A. To investigate this problem use a linear theory of cavitating flows and choose as a closure model the open model, proposed in linear two-dimensional case by Fabula [44] (a few months later a nonlinear formulation of an analogous model for the supervcavitation regime was published by Wu, and, for the regime of partial cavitation still a bit later by Bassanini). The choice of this model is not accidental.

As a matter of fact, the closed cavity model in the two-dimensional case predicts an unrealistic growth of lift coefficient of the supercavitating foil when the cavity closure region nears the trailing edge of the foil. This phenomena is called by some authors a "Geurst paradox" [45]. Comparison of the magnitudes of the lift coefficient for a 2-dimensional flat plate, obtained with help of the open and closed cavity closure models are presented in Fig.13. The advantage of the open model for the design regimes when the cavity length equals or nears unity ($\sigma/\alpha = 8\text{-}10$ for 2-d flat plate) is obvious. It is left to account that the indicated regime is the most characteristic flow regime for the blades of supercavitating propellers, because the maximal efficiency of these propulsors is reached exactly for a minimal cavity length at every section, i.e. for the minimal length of the cavity by the condition of the absence of erosion. This latter length, as indicated, should only slightly exceed the length of the corresponding chord. Application of the closed model in this case is either incorrect or requires special effort for overcoming the Geurst paradox.

The equation (15) is a 2-dimensional singular integral equation (SIE) with respect to the intensity of the simple layer q with an unknown domain of integration S_q (domain S_q for the sought solution should coincide with the domain covered by the cavity S_{CAV}). This equation is an equation of the considered problem A.

For uniqueness of the solution of the SIE it is necessary to specify the class of functions, in which one seeks the unknown function q and the loading is prescribed, i.e.given is the radial component of the vector of the vortex layer (i.e. the intensity of the attached vortex layer, which is prescribed within the blade). In accordance with the open model the function q should vanish at the rear boundary of the cavity and outside of the domain S_{CAV}. At the front boundary coinciding with the leading edge of the blade, the sought for function q should (the case of rounded leading edge is not considered here) have a quarter-root singularity as for a thin supercavitating plate in the two-dimensional case. Therewith, in all other points the unknown function q is assumed to be sufficiently smooth as a matter of existence of two-dimensional singular integrals.

A traditional approach (see e.g. the work of Kinnas [46]) to treatment of the formulated problem consists in organizing an iterative process with the goal of an approximate determination of the cavity platform. Authors of publications oftentimes attach little attention to matter of convergence, correctness (in the sense of dependence of the result on the initial approximation) and the efficiency of the indicated iterative process. In addition, use of traditional approach excludes a possibility to conduct (by setting free several parameters) a numerical optimization of the project with account of prescribed inequality conditions (it is clear that the conditions, securing sufficient thickness and length of the cavity, can be formulated in advance in form of inequalities).

In the period from 1974 through 1985 Achkinadze developed and (with Narvsky) applied for calculation of supercavitating propellers (for solution of the problem A and other problems) an untraditional method (the method of artificial varifational problem), which enabled using effective methods and programs of linear programming for numerical solution of the stated design problems [51], [47],[48]. Essentially, this untraditional approach allows (as opposed to the traditional one) to account for restrictions in form of the inequalities and (very effectively) organize iterations to determine the cavity's platform with use of the simplex method of linear programming.

Consider untraditional formulation of the problem A in that interesting for us case of the supercavitating regime whereby the cavities, starting at the sharp leading edge, have a length exceeding that of a corresponding local chord everywhere radius-wise, namely:

$$L_{CAV}/c > 1 \qquad \text{for } \bar{r} \in [\bar{r}_H; 1 \tag{17}$$

As it is difficult to say if this assumption is fulfilled, one would have a possibility to filter out the calculated results for the cases when it is not valid in the process of calculation.

Variational (nontraditional) formulation of the problem A differs from the traditional one, formulated above, by that:

Firstly, the integral equation (15) would now be satisfied only for the points of a given domain S_B, i.e. for the points corresponding to the suction side of the blade, namely

$$-W_\tau^+ / V_E = \sigma / 2 + V_{\psi\tau} / V_E \quad \text{in} \quad S_B \tag{18}$$

Secondly, for the domain outside of the blade the integral equation is replaced by a corresponding integral inequality

$$-W_\tau^+ / V_E \le \sigma / 2 + V_{\psi\tau} / V_E \quad \text{in} \quad S_{DET} \tag{19}$$

which should be satisfied not on the unknown part of the domain (outside of the blade) S_{CAV}, but on a simplified sufficiently stretched downstream (to embody the calculated cavity) and located outside of the blade domain S_{DET} (see Fig. 12). Note that the condition (19) possesses a universality, it is valid both for the points lying on the boundary of the cavity, and the points lying outside of the cavity, because the pressure outside of the boundaries of the cavity for natural cavitation in weightless fluid should necessarily be larger than in the cavity and upon its boundaries.

It should be noted that when replacing the condition (15) by a set of requirements (18) and (19) a multitude of admissible solutions of the considered problem widens considerably and becomes indefinite.

Thirdly, outside of the blade for the open cavity closure model it follows rigorously from the known property of stationary cavities in weightless fluid, namely from the property of convexity of the cavity [52]

$$q \ge 0 \quad \text{in } S_{DET} \tag{20}$$

Fourthly, behavior of the given function and sought for function in the vicinity of the sharp leading edge is regulated a

$$\begin{aligned} &\lim_{\xi \to \xi_0} \left[q(\xi;\bar{r}) \cdot (\xi - \xi_0)^{1/4} \right] = \\ &-\lim_{\xi \to \xi_0} \left[\gamma(\xi;\bar{r}) \cdot (\xi - \xi_0)^{1/4} \right] \ne \infty \end{aligned} \tag{21}$$

The latter requirement coincides with the traditional formulation of the problem and is further on used when linearizing functional of the artificial variational problem.

It is clear from comparison of the presented traditional and nontraditional formulations of the problem A, that, because of widening set of solutions when passing over from equality to inequality in the dynamic boundary condition, as indicated, the set of admissible solutions becomes infinite. With the goal of obtaining a single unique solution on the basis of nontraditional formulation, require a minimization of the artificial functional F over the multitude of solutions, satisfying the conditions (18)-(21). In this case the functional is adopted in the following form

$$F = \int_{S_B \cup S_{DET}} (W_\tau^+ / V_E + \sigma / 2 + V_{\psi\tau} / V_E)\, q \, ds \tag{22}$$

It is not difficult to check that, according to the conditions (18),(19),(20), the integrand equals zero in the domain S_B and both multiplyers under the integral sign are nonnegative in the domain S_{DET}, and,consequently, minF=0. Not complicated considerations show that the indicated minimal (zero) magnitude of the functional F is reached exactly on that very solution of the problem A which corresponds to the traditional formulation.

In fact the functional will differ from zero in the case, when there exists within S_{DET} an area element for which both multipliers in the integrand would be positive simultaneously. Exactly this can take place if on this area element there is simultaneously a simple layer and the pressure is higher than that in the cavity. The latter does not correspond to the traditional solution, for which outside of the cavity (on the surface of which the pressure is minimal and constant) sinks and sources should be absent. But if F

equals to zero, there are no such area elements in the area under control, and, consequently, the obtained solution corresponds to the traditional approach.

Thus, the described artificial variational formulation of the problem A is equivalent to the traditional one, presented earlier. It should be noted however that the artificial functional is not linear. Perform some transformations with the aim to obtain its linear form. With account of the previous relationships

$$F = \int\limits_{S_B \cup S_{DET}} (W_{q\tau} / V_E + W_{\gamma\tau} / V_E - \gamma_r / (2V_E) + \sigma / 2 + V_{\psi\tau} / V_E)\, q\, dS \tag{23}$$

One term can be eliminated, accounting for the equation

$$\int\limits_{S_B \cup S_{DET}} (W_{q\tau} / V_E)\, q\, dS = 0 \tag{24}$$

which can be proved by a interchanging the order of integration in the corresponding integral. It is important to have in mind, that the leading edge is assumed to be sharp (which is regulated by the condition (21)) and the suction force is not realized on it. Eventually one derives a complete linear form of the functional

$$F = \int\limits_{S_B \cup S_{DET}} [W_{\gamma\tau} / V_E - \gamma_r / (2V_E) + \sigma / 2 + V_{\psi\tau} / V_E]\, q\, dS \tag{25}$$

When stating a linearity, it is taken into account, that the intensity of the attached vortices γ_r is assumed to be prescribed within the blade, i.e. on S_B, and, therefore, all terms in the square brackets are given functions or can be calculated through them. The linear form of the functional allows (after discretization) to reduce the numerical solution of the problem A in its artificial variational formulation to the problem of linear programming.

In 1985 there was carried out with use of the simplex method of linear programming a numerical solution of the described problem A for a concrete supercavitating screw propeller [48], [49]. The model of the designed propeller was manufactured of silumin alloy, had a diameter 0.2 m (see Fig. 14) and was tested first in the cavitation tunnel of the KSRI, and then in the cavitation tunnel of the Gdansk Institute. Some of the input data, the results of the calculation and results of the experiment are given in the Table 5 and in the Fig. 15-18.

Table 5. The input data (first 5 lines) and the results of the verification calculation (problem A) of the supercavitating propeller N8401(Z=3; A_E/A_0=0.92; J=1.0; χ =0.25; K_T =0.084)

$\bar{r}$	0.265	0.404	0.595	0.786	0.925
c/R (preset)	1.045	1.245	1.416	1.355	0.939
δ (preset)	0.087	0.060	0.037	0.027	0.030
$\bar{\Gamma}$ (preset)	0.0145	0.0187	0.0213	0.0195	0.0129
C_L (preset)	0.1340	0.1170	0.0892	0.0680	0.0562
σ (preset)	0.1479	0.0957	0.0556	0.0352	0.0265
P/D (calcul.)	1.69	1.37	1.28	1.28	1.26
δ_P (calcul.)	-0.0007	0.0073	0.0124	0.0141	0.0124
L_{CAV}/c (calcul.)	1.000	1.000	1.080	1.160	1.000
$e_{CAV}(L)/c$ (calcul.)	0.282	0.140	0.076	0.084	0.069
$e_{CAV}(1)/c$ (calcul.)	0.282	0.140	0.074	0.075	0.058
$e_{CAV}(1)/c$ (exper.)	-	-	0.080	0.081	-

Comment: c - blade section chord length, R - propeller radius, δ -maximum blade section thickness-chord length ratio, $\bar{\Gamma}$ - non-dimensional circulation around blade section, C_L - lift coefficient, σ - local cavitation number, P/D - blade section pitch ratio, δ_P - maximum camber of blade presser surface, L_{CAV}/c - cavity length at some blade section- chord length ratio, $e_{CAV}(L)/c$ cavity thickness at a cavity termination point for given blade section-chord length ratio, $e_{CAV}(1)/c$ - cavity thickness at a blade section enter edge- chord length ratio.

Note additionally that the propeller reached its design regime. The experimental thrust coefficient was 0.0844 for a given magnitude 0.0840, the efficiency in the test was 0.543, i.e. 4% more than that obtained by calculations. A good correlation in forces confirmed a viability of the approximate correction, accounting for the loss of the part of the contour of integration when determining the circulation in a given cylindrical section of the blade, related to the presence of cavities in the inter-blade space. It is to be noted here that in the adopted cavity closure model, the supercavity terminates for a given cylindrical section in its widest cross-section and, further on there recedes to the infinity a helical-type stripe of the wake of constant width (measured along the cylinder surface), equal to the maximal thickness of the cavity. As the cavity thickness is unknown in advance the interaction process is envisaged within the problem solution algorithm to account for the indicated approximate correction (two steps appear to be sufficient). In the presented calculation the final correction resulted in the 18,6% reduction of the thrust compared to a purely linear approach.

The maximum difficulties when testing were connected with manufacturing of sharp leading edges, which (if of insufficient strength) could deform during the tests of the model in the cavitation tunnel. Therefore, when prescribing the loading there was secured a sufficient magnitude of the multiplier of the leading edge singularity. When manufacturing the model, in the vicinity of the leading edge the whole calculated gap between the cavity surface and the pressure side of the blade was filled by certain material. The thickness distribution of the remaining part of the section had a segment profiling (see Fig. 15). The law of the distribution of the circulation along the radius was assumed optimal, and found in the frame of the lifting line theory with use of the generalized optimality conditions obtained by Achkinadze in 1989 [42], [53], [54] and allowing to account for the radius-wise distribution of the cavitation drag of the blade.

Chord-wise distribution laws assumed close to a uniform one with a certain increase of the loading in the vicinity of the leading edge. In the process of the tests of the model in the cavitation tunnel there were made (except the force tests) drawings of the development of the cavity planform and thickness measurements at the cavity training edge. The correlation with the cavity planform calculations (see Fig, 16) and in the distribution of the cavity thickness along radius (see Fig. 15, Fig. 16, Fig. 17 and Table 5) at a design advance coefficient, equal to 1.0, and at a design cavitation number, equal to 0.25, turned out to be satisfactory. However, because of the thickening of the leading edge up to the calculated boundaries of the cavity (to the extent of 10% of the chord from the leading edge). At the design regime the cavity started not at the leading edge but 5-10% of the chord further downstream. This entails the following: at the design advance coefficient the whole (excepting the aforementioned region at the leading edge) suction side was covered by a dense bubbly cavitation, whereas the film-type cavity formed at a somewhat smaller (5% less) advance coefficients. There is a certain hope that, in the full-size situation the bubble cavitation would be replaced by a film-type one. The pressure side at a design advance ratio (J=1.0) was completely free of cavitation (see Fig. 18).

Later in Gdansk under guidance of Professor Szantyr and Dr. I.J.Dudziak were conducted the tests of this model of the supercavitating propeller in the conditions of oblique flow for axial cavitation number of 0.4, which is noticeably higher than the design one 0.25. However, for this out-of-design regime in the oblique flow the pressure surface was free of cavitation, which is an evidence of the sufficient reserve for avoidance of the cavitation occurrence on the pressure side within the considered project.

The efficiency of the tested screw propeller turned out (as foreseen by the calculations) close (a bit larger) to the efficiency of the propeller of "CK" series, although the section thickness of the designed propeller was taken noticeably larger (more exactly, the maximum blade section thickness-chord ratio was larger than that for the "CK" propeller series 16, 33 and 50 % for the sections corresponding to the relative radia 0.6, 0.8 0.95 correspondingly. Besides, near the leading edge the thickness was in fact larger for all cross-sections, located at the relative radia less than 0.8).

Further development of the described theoretical investigation was directed to obtaining such a form of the artificial functional, which coincides with the approximate (within lifting line theory) expression of the profile losses of the screw propeller due to just cavitation drag of the blades. Such a functional, as shown in the dissertation of Achkinadze [53](1993), has the following simple form

$$F_1 = \int\limits_{S_B \cup S_{DET}} (\sigma / 2)\, q \sin\beta \, dS \tag{26}$$

This functional is linear and should be minimized, although it no longer has a zero value. In obtaining such a form of the functional a number of assumptions were made. With the goal of evaluating the error introduced by these assumptions numerical solution of the problem A was obtained for the supercavitating propeller, described above. Comparison with the results, obtained with use of a completely rigorous form of the functional (25), showed an insignificant divergence in the obtained form of the cavity and the pressure side of the blade in the two compared cases.

The latter enables to pass over to the solution of the problem of the design calculation in a more complete (than for problem A) formulation, i.e. with account of restrictions on the thickness and length of the cavity, of the reserve of the cavitation avoidance on the pressure side etc., for given distribution of circulation along the radius (this distribution can be either prescribed arbitrarily or adopted optimal, as earlier with the utilization of the generalized optimum condition in the frame of the lifting line theory [42]).

Besides the geometry of the cavity in the considered case of a more complete formulation one can obtain optimal distribution of the attached vortex layer in the chordwise direction and a corresponding form of the pressure surface with use of the numerical method of linear programming. With such optimization the induced losses and friction losses remain unchanged and the profile losses, stipulated by the cavity drag, are minimized. The latter circumstance enables one to treat use of the functional in form (26) as an application of a certain variational principle (the principle of minimum cavitation drag), having a physical sense of minimization of cavitation drag of the blade sections of the supercavitating propeller

under design. The latter is valid at least for each section separately, which can be easily seen taking into attention the expression for the cavitation drag of the two-dimensional foil in the case of use of the open closure model of the cavity, namely

$$C_{DCAV} = \sigma\, e_{CAV}(L) \tag{27}$$

where $e_{CAV}(L)$ - is cavity thickness at a termination point related to the chord (for open model this is the largest magnitude of the cavity thickness), i.e. where terminates the simple layer modeling the cavity.

With use of the indicated more complete formulation were conducted design calculations of a systematic series of the optimal 3-blade supercavitating screw propellers with segment profiling. For practical use the results of this series were processed in form of the corrections for the influence of the lifting surface for supercavitating screw propellers [50], similarly to how it had been done previously for the noncavitating propellers. Given in Fig.19 is a (borrowed from the indicated work) comparison of the correction for the curvature of the mean line of the body "blade-cavity" for cylindrical sections of the supercavitating propellers with analogous correction for the mean line of cylindrical section of noncavitating screw propeller. It can be seen that for the supercavitating screw propeller the considered corrections depend on the cavitation number.

Considering concrete magnitudes, e.g. at a relative radius of 0.79, one sees that for the propeller of expanded area ratio 0.475 the curvature correction slightly exceeds the analogous one for noncavitating screw propeller. For the propellers of expanded area ratio 0.950 there exists a much bigger difference with the same trend. The value of corrections for noncavitating propellers are designated in Fig.19. by horizontal dashed lines separately for two expanded area ratios.

It seems that upon the augmentation of the cavitation number (for the same thrust coefficient) the magnitude of the corrections for the supercavitating propellers should tend to the magnitude of the analogous corrections for the noncavitating propellers, but this is not so. The explanation consists in that for an optimal supercavitating propeller required are sufficient thickness and length of the cavity. But, with growth of the cavitation number this requirement is more difficult to fulfill and the optimal pitch and curvature values grow. For reasonable magnitudes of cavitation number (for the designed propeller N8401 the ratio of the axial cavitation number to the thrust coefficient, not corrected for nonlinearity, equals 2.5) the corrections for curvature for the cavitating and noncavitating propellers for a expanded area ratio 0.475 differ insignificantly (less than 20%), which is indicative of a possibility to consider the blade and the cavity as a single lifting body in a flow of inviscid fluid. The latter possibility was contested by some specialists (Panchenkov).

When using the methods of optimization, such e.g. as a linear programming, there arises a need in smoothing the form of the pressure surface and even its artificial simplification, because, as a result of the design calculation with optimization, it can become excessively complicated, and the influence of this complication upon the efficiency of the propeller would be negligibly small. Achkinadze in 1974 [51] applied a principle of the minimum of cavitation drag to solve a two-dimensional problem of an optimal supercavitating section. He found that form the practical viewpoint it is sufficient to limit oneself to simple forms of the pressure surface, but one should (accurately enough) account for restrictions for the thickness and length of the cavity. Some examples of such calculations were published in [27].

Special attention deserves a proper choice of the optimal lift coefficient with account of the conditions, ensuring sufficient thickness of the cavity, as well with account of the friction drag C_f on the pressure side. For example, this problem was solved for a thin 2-dimensional arc at zero cavitation number. In particular, the following values were obtained for the optimal lift coefficient, angle of attack and curvature of the pressure side [27]

$$C_{LOPT} = 2.548\sqrt{C_f}\,; \quad \alpha_{OPT} = 0.1838\, C_{LOPT}\,; \qquad \delta_p = 0.1294\, C_{LOPT}$$

The approach described above is linear. As it becomes obvious in the course of time, the employed linear approach does not adequately allow to evaluate the effect of real (non sharp) leading edge. Recent developments in the field of optimal supercavitating profiles are connected with use of nonlinear approach and investigation of the influence of a spoiler, wedge-type leading edge and other nonlinearities [26].

Note an important circumstance, occurring in use of the improved propeller profiles. Improvement of hydrodynamic fineness of the section, measured by a relative variation (decrease) of the inverse fineness $\Delta\varepsilon/\varepsilon$, leads to the growth of efficiency of the supercavitating propeller by a quantity, which can be approximately estimated by means of a simple formula [53]

$$\Delta\eta_0/\eta_0 = -2\varepsilon\,(\Delta\varepsilon/\varepsilon) \tag{28}$$

if the inverse finenes is taken for the section at relative radius 0.7.

It follows straitforwardly from (28), that relative improvement of hydrodynamic fineness of the profile gives a relative improvement of the design of the propeller which K/2 less efficient (where $K=1/\varepsilon$ -hydrodynamic fineness of the supercavitating profile). For a hydrodynamic fineness of about 20 there takes place a 10 times reduction of the relative gain when passing from a profile to the propeller. Although the increase of the propeller efficiency is expensive, the increase of the efficiency of the supercavitating propeller by means of optimization of the profiles requires an improvement of their hydrodynamic fineness of not less than 10%, to obtain only a one percent growth in efficiency.

Conclusion

In conclusion, the author would like to express a hope that the experience in research and development in the field of he supercavitating screw propellers and similar propulsors, partly reflected in the presented lecture, would be called for and would be useful for the future. The author would also like to express his gratitude to his teachers: Professors V.M.Lavrientiev, V.V.Rozhdestvensky and A.A.Russetskiy, and to thank Professor J.A.Szantyr and Dr.I.J.Dudziak from Poland for the tests he had conducted in the cavitation tunnel of the SC propeller designed by the author.

References

1.Tulin M.P. 2000 Fifty years of supercavitating flow research in the U.S.: personal recollection. Applied hydromechanics, National Academy of Sciences of Ukraine Institute of Hydromechanics, Vol.2, Num.3, pp.100-107 (in Russian).

2.Burill W.C. 1951 Sir Charles Parsons and Cavitation. Transactions of the Institute of Marine Engineers, Vol.LXIII, No.8.

3.Springorum K. 1932 Hydromechanische Probleme des Schiffsantriebs, Hamburg, (p.331).

4.Jessup S.D., Wang H.-C. 1997 Propeller design and evaluation for a high speed patrol boat incorporating iterative analysis with panel method. Tr. P/S'97 Symposium, Sept. 23-24, Virginia Beach, USA, pp.11/1-20.

5.Georgievskaya E.P., Mavlyudov M.A., Hadjimikhalev V., Kozhukharov P. 1989 A new generation of cavitating propellers and their practical application to "Kometa" hydrofoil. Proc 4-th Internat. Symposium on PRADS-1989, Varna, Bulgaria, Vol.3, pp.123/ 1-11.

6.Kinnas S.A. 1996 An international consortium on high-speed propulsion. Marine Technology, Vol.33, No.3, pp.203-210.

7.Pozdunine V.L. 1941 Problems of ship propellers. Soviet Science, No.2.

8.Pozdunine V.L. 1944 On the working of supercavitating screw propellers. Tr. of INA, Vol.86.

9.Pozdunine V.L. 1944 On the working of supercavitating screw propellers. Doklady AN SSSR, Vol. XXXIX, №8, cc. 334-339.(in Russian)

10.Pozdunine V.L. 1947 The effectiveness of supercavitating propellers. Izvestia OTN AN SSSR, No.10. (in Russian)

11.Georgievskaya E.P. 1978 Screw propellers cavitation erosion. Leningrad "Sudostroenie Publ. House" 206 p.(in Russian)

12.Tachmindji A.J., Morgan W.B. 1958 The design and estimated performance of a series of supercavitating propellers. Proc. of the Second ONR Symposium on Naval Hydrodynamics, U.S., August.

13.Caster E.B. 1963 TMB 2,3 and 4-bladed supercavitating propeller series. DTMB Report 1637, January.

14.Tulin M.P., Burkart M.P. 1955 Linearized theory for flows about lifting foils at zero cavitation number. DTMB Report C-638, Feb.

15.Rosen G. High speed propellers. ISP, Vol.16, No.176, pp.110-116.

16.Davis B.V., English J.W. 1968 The evolution of a fully cavitating propeller for a high-speed hydrofoil ship. Proc. of the 7-th ONR symposium on naval hydrodynamics, Rome, August.

17.Mavlydov M.A., Rousetsky A.A., SadovnikovY.M., Fisher E.A. 1973 Propulsors for high speed ships. Leningrad "Sudostroenie Publ. House" 240 p.(in Russian)

18.Mavlydov M.A., Rousetsky A.A., SadovnikovY.M., Fisher E.A. 1982 Propulsors for high speed ships. Second revised and enlarged edition, Leningrad "Sudostroenie Publ. House" 280 p.(in Russian)

19.Ship Theory Handbook 1985 Ed. by Y.I.Voitkounski, Vol.3, Leningrad "Sudostroenie Publ. House" 540 p.(in Russian)

20.Ikonnikov V.V., Maskalik A.I. 1987 Unique feature of hydrofoil ships design and formation. Leningrad "Sudostroenie Publ. House" 318 p.(in Russian).

21.Rousetsky A.A. 2000 Alar ships (Крылатые корабли). Maritime Journal (Морской жупнал), "Sudostroenie Publ. House", pp. 46-49, N2 (in Russian)

22.Prishchemikhin Yu. N. 1969 Cavitation tank with remote testing operation. Tr. of the 12th ITTC, September.

23.Van Manen J.D. 1971 The effect of cavitation on the interaction between propeller and ship's hull. Proc. of the IUTAM Symposium, June 22-26, Leningrad, pp.305-328, "NAUKA", Chief Office PML, M., 1973.

24.Fisher E.A. 1966 Experemental determination of the screw propeller cavitation size. Tr. KSRI, Vol.231.(in Russian)

25.Achkinadze A.S., Fridman G.M 2000 Optimal profiles for supercavitating propeller screws with spoilers and fixed angle of frontal edge taper. Applied hydromechanics, Institute of Hydromechanics of NAS of Ukraine, volume 2 (74), number 3, pp.5-16 (in Russian).

26.Achkinadze A.S., Fridman G.M 2000 Optimal Sections for Supercavitating Propellers with Spoiler and Preset Leading Edge Angle. Proc. NCT'50 International Conference on Propeller Cavitation, 3-5 April, University of Newcastle, Newcastle upon Tyne, United Kingdom, pp. 263-274.

27.Achkinadze A.S., Fridman G.M 1995 On some aspects of design of supercavitating foils and propellers. Variation and asymptotic approach. Proc. An international conference on propeller cavitation to celebrate 100 years of propeller cavitation research (PROPCAV'95), 16-18 May, Newcastle upon Tyne, United Kingdom, p.163-174.

28.Rozhdestvensky K.V., Fridman G.M. 1991 Matched asymptotics for free surface lifting flows with spoilers. In book: Matched Asymptotics in hydrodynamics, SIAM.-Edited by T.Miloh, Philadelphia, pp.499-517.

29.Zaitsev N.A., Maskalik A.I. 1967 Fatherland hydrofoils. Second revised and enlarged edition, Leningrad "Sudostroenie Publ. House" 364 p.(in Russian)

30.Basin A.M., Goshev G.A. 1963 Experimental investigation of the semi-submerged propellers characters. Tr. of LIWT, Vol. X.

31.Baeva M.A., Mizina M.Y., Sadovnikov Y.M. 1981 Hydrodynamics characters of the cavitation profile with spoiler. Transactions of the Academician A.N.Krylov Scientific and Technical Shipbuilding Society, 1981, vol.358, p.44-60 (in Russian).

32.Rose J.C. 1993 Combination surface propeller and water jet systems. Pr. of the 3rd International Design Symposium on Yacht and Small Craft Design, Chianciano Terme, Italy.

33.Ibragimova T.B., Mavlydov M.A., Rousetsky A.A. 1995 Basic principles of propulsor efficiency comparisons. Pr. Third International Conference on Fast Sea Transportation.

34.McMahon J.F., Dai C.M., Gowing S., Lin G., Peterson F.P. 2000 Ventilated Waterjets for high speed ships. Proc.: SNAME Symposium "Propellers/Shafting'97", 20-21 September 2000, Virginia Beach, USA. pp.11/1-11/9.

35.Rose J.C., Kruppa C.F.L. 1991 Surface piercing propellers - methodical series model test results. Proc. of FAST'91, Trondheim, June.

36.Toyoda M., Kato H.,Yamaguchi H. 1999 Study on theoretical design method of trans-cavitating propeller. Journal of the SNA of Japan, Vol. 186, pp.41-49. (in Japan)

37.Ukon Y., Kudo T., Fujisawa J., Matsuda N. 1999 Experimental evaluation of trans-cavitating propellers. Journal of the SNA of Japan, Vol. 186, pp.51-58. (in Japan)

38.Kozhukharov P., Zlatev Z. 1983 Cavitating propeller characteristics and their use in propeller design. Proc. High-speed surface craft conference, London, May.

39.Kozhukharov P. 1983 Investigation and design on cavitating screw propellers operating in oblique flow. Ph. D. thesis, Leningrad, LKI (SMTU).

40.Newton R.N., Rader H.P. 1961 Performance data of propellers for high-speed craft. Tr. RINA, Vol.103.

41.Gawn R., Burrill L.C. 1957 Effect of cavitation on the performance of a series of 16 in. model propellers. Tr. INA, Vol.99, pp. 690-728.

42.Achkinadze A.S. 1989 Design of optimal screw propellers, turbines and freely rotating turbopropellers adapted for radially nonuniform swirled flow. Proc. Fourth Internat. Symposium on PRADS'89, 23-28 Oct. 1989, BSHC, Varna, Bulgaria, Vol. 3, p. 124/1-13 (in English).

43.Achkinadze A.S., Krasilnikov V.I., Stepanov I.E. 2000 A Hydrodynamic Design Procedure for Multi-Stage Blade-Row Propulsors Using Generalized Linear Model of the Vortex Wake. Proc.: SNAME Symposium "Propellers/Shafting'97", 20-21 September, Virginia Beach, USA. pp.20/1-20/21, (in English)

44.Fabula A.G. 1962 Thin-airfoil theory applied to hydrofoils with a single finite cavity and arbitrary free-streamline detachment. JFM, Vol.12, Part 2.

45.Geurst J.A. 1956 Linearized theory for partially cavitated hydrofoils. ISP, Vol.6, No.60, pp. 369-384.

46.Kinnas S.A., Kosal E.M. Young J. 1999 Computational techniques for the design and analysis of super-cavitating propellers. Pr. FAST'99, 31 August-2 September, Seattle, WA, USA.

47.Achkinadze A.S. 1983 Application of mathematical programming methods in the linear theory of cavity flows. Proc. 12th ses. SMSSH, BSHC, Varna, Bulgaria, 19-23 Sept., vol. 2, p. 32/1-19 (in Russian).

48.Achkinadze A.S., Narvsky A.S. 1985 Supercavitating propeller design equation in lifting surface theory and method of its solution. Proc. 14th ses. SMSSH, BSHC, Varna, Bulgaria, 23-29 Sept., vol. 1, p. 19/1-21.

49.Achkinadze A.S., Narvsky A.S. 1987 Calculation of cavitating propellers based on the lifting-surface theory. Proc. 4th Internat. congress IMAEM, BSHC, Varna, Bulgaria, 25-30 May, vol. 5, p. 158/1-15.

50.Achkinadze A.S., Narvsky A.S. 1989 Supercavitating propeller lifting-surface corrections. Proc. 18th ses. SMSSH, BSHC, Varna, Bulgaria, 25-30 Sept., vol. 1, p. 19/1-4.

51.Achkinadze A.S. 1974 Linear problem of supercavitating wing and problem of optimal wing's shape (variation approach). Transactions of the Academician A.N.Krylov Scientific and Technical Shipbuilding Society, Vol. 217, p.139-164 (in Russian).

52.Rozhdestvensky V.V. 1977 Cavitation. Textbook, Leningrad "Sudostroenie Publ. House", 247 p.

53.Achkinadze A.S. 1993 Design calculation of noncavitating and highly cavitating propellers with used vortex theory with take into acount load and radially nonuniform inflow. Thesis of Dr.I., Saint Petersburg State Marine Technical University, Saint Petersburg, Russia.

54.Achkinadze A.S., Krasilnikov V.I. 1997 A generalized optimum condition for wake adapted screw propellers. Proc.: SNAME Symposium "Propellers/Shafting'97", 23-24 September, Virginia Beach, USA. p.22/1-22/28.

55.Egorov I.T., Sadovnikov Y.M., Isaev I.I., Basin M.A. 1971 Artificial cavitation., Leningrad "Sudostroenie Publ. House" 280 p.(in Russian).

56.Kruppa C 1972 Testing of partially submerged propellers. 13th ITTC, Report of cavitation committee, Apendix V.

57.Claus F.L. Kruppa 1969 High speed propellers hydrodynamics and design. Textbook No.035, The Department of Naval Architecture and Marine Engineering, The University of Michigan College of Engineering, September, 78 p.

58.Comstock J.P., editor 1967 Principles of Naval Architecture. Published by SNAME, New York, p.827.

59.Etter R.J. 2000 State of the art - cavitation test facilities and experimental methods. NCT'50 International Conference on Propeller Cavitation, 3-5 April, University of Newcastle, Newcastle upon Tyne, United Kingdom.

Figures

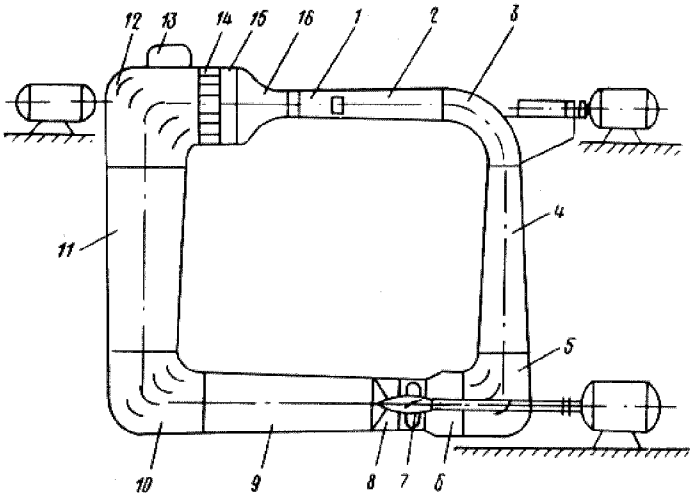


Fig.1. Cavitation tunnel
1.Working section
7.Impeller
8.Aline device
13.Variable pressure shaft
14.Honeycomb rectifier

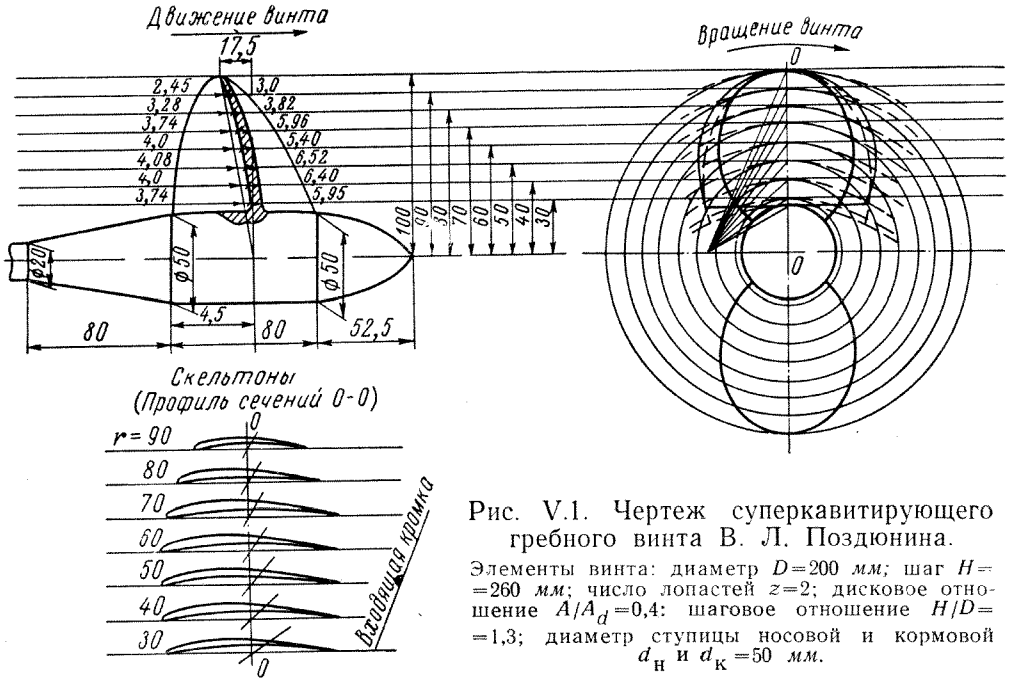


Рис. V.1. Чертеж суперкавитирующего гребного винта В. Л. Поздюнина.

Элементы винта: диаметр $D=200$ *мм;* шаг $H=260$ *мм*; число лопастей $z=2$; дисковое отношение $A/A_d=0,4$: шаговое отношение $H/D=1,3$; диаметр ступицы носовой и кормовой $d_н$ и $d_к=50$ *мм.*

Fig.2.Posdunine's supercavitating propeller drawing [55]
(D=0.2m., p=0.26m., A_E/A_0=0.4)



Fig.3.Propeller operating on supercavitating regime [16]

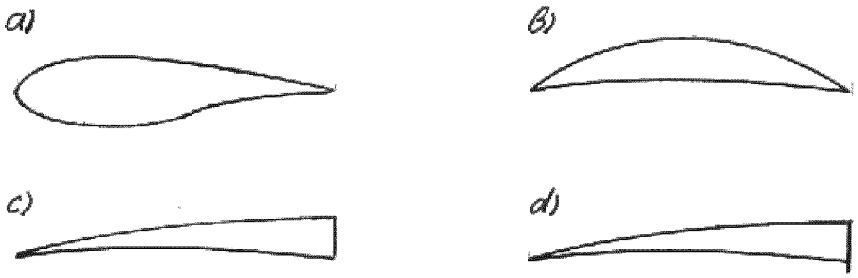


Fig.4.Blade section types
a)conventional
b)segment
c)wedge-shaped (supercavitating)
d)wedge-shaped with a spoiler (supercavitating with a spoiler)

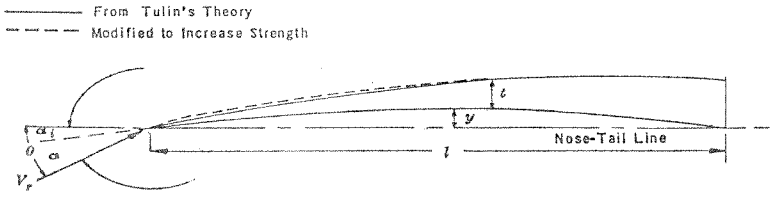


Fig.5.Tulin's patented two parameters supercavitating section
(C_L=0.2, α=2 degrees) [12]

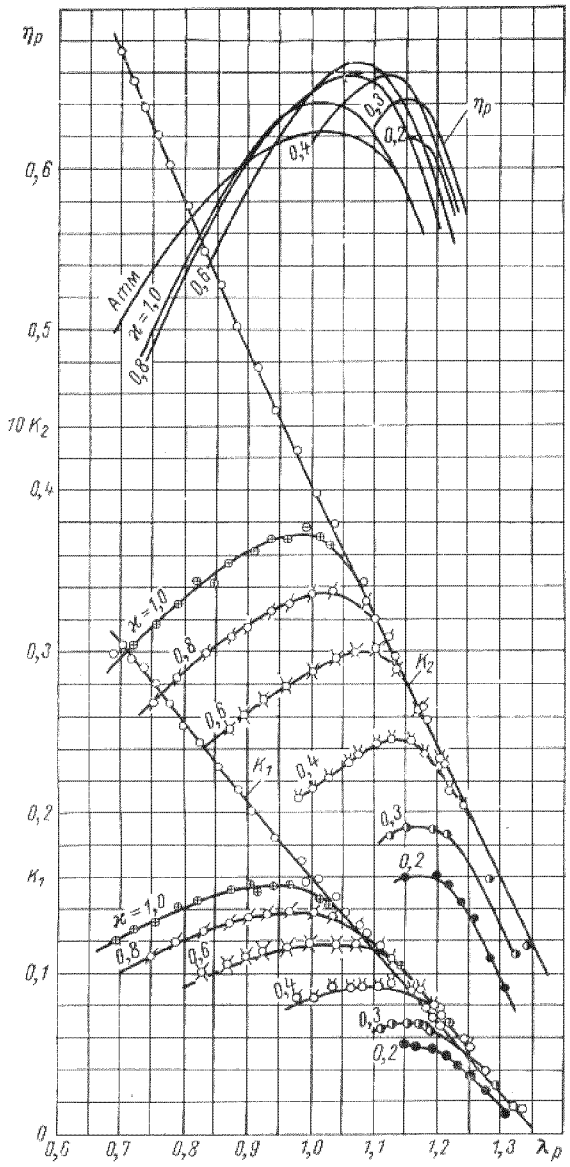


Fig.6. Characteristic curves for propeller of series "K" (z=3; A_E/A_0=0.81; P/D=1.4; wedge-shaped section type) [55]

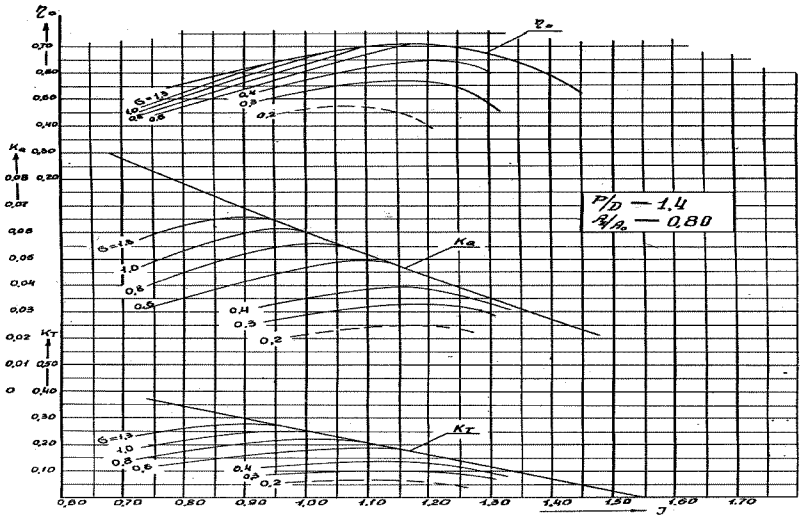


Fig.7. Characteristic curves for propeller of series "CK" (z=3; A_E/A_0=0.80; P/D=1.4; segment section type) [18]

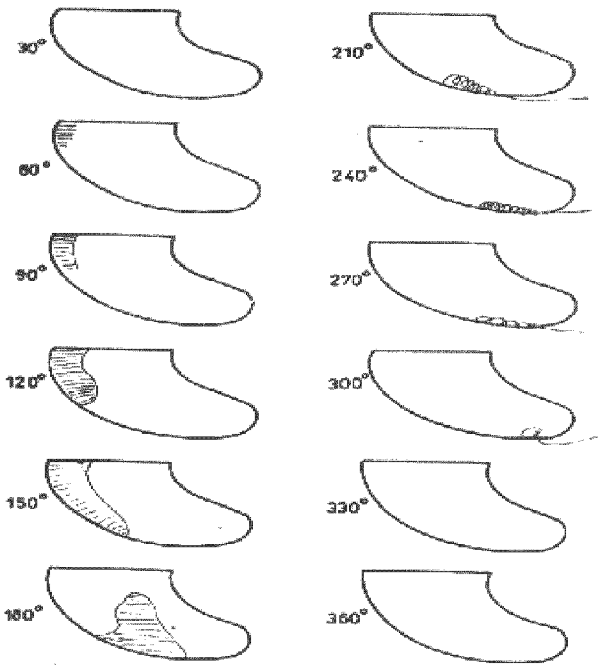


Fig.8.Face residual cavitation development at various blade phase angle in oblique flow 16 degrees (χ=0.65, J=1.0) [5]

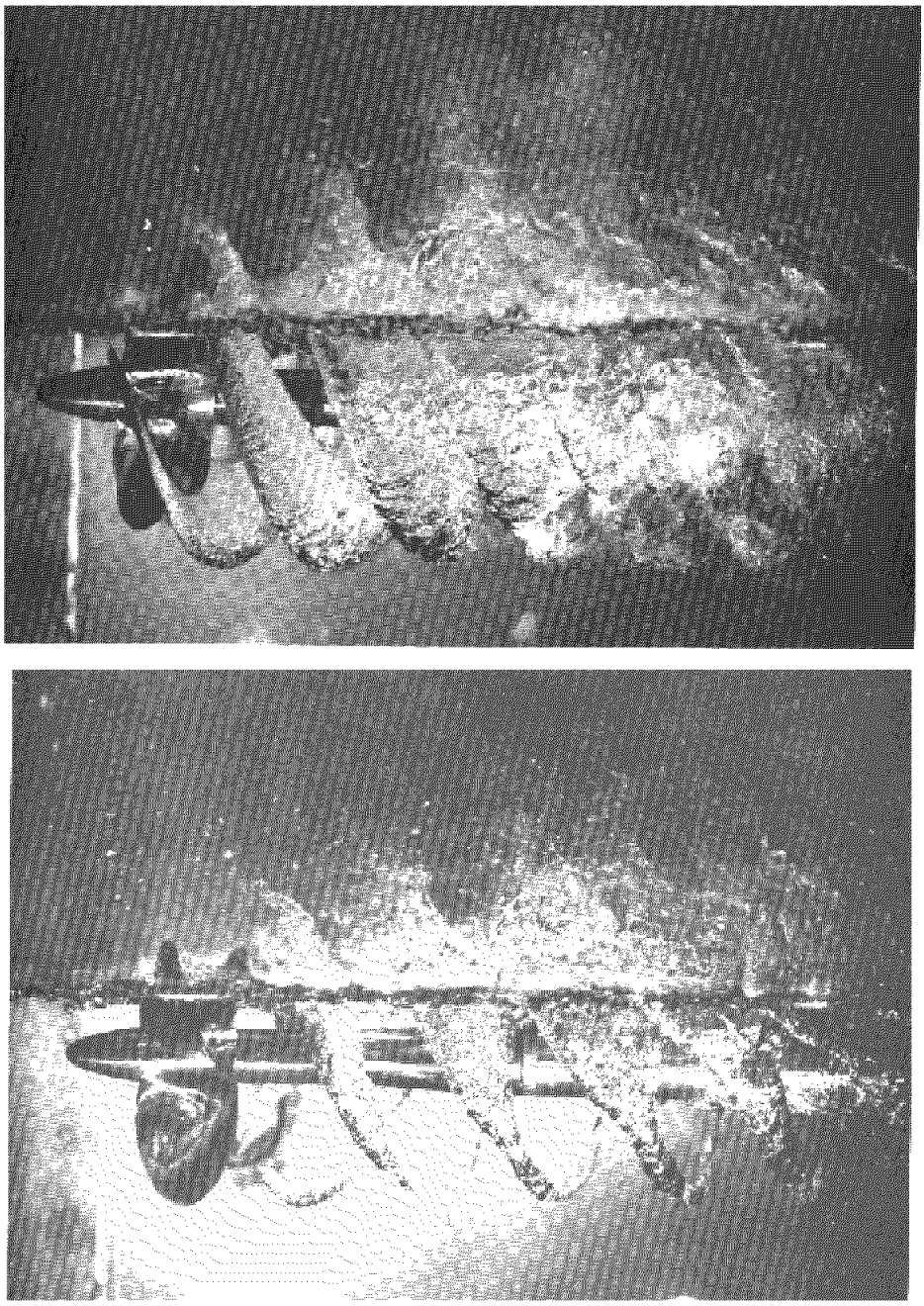


Fig.9.Surface piecing propellers in working regime.
(J=1.1 and 0.9; immersion 0.7D) [56]

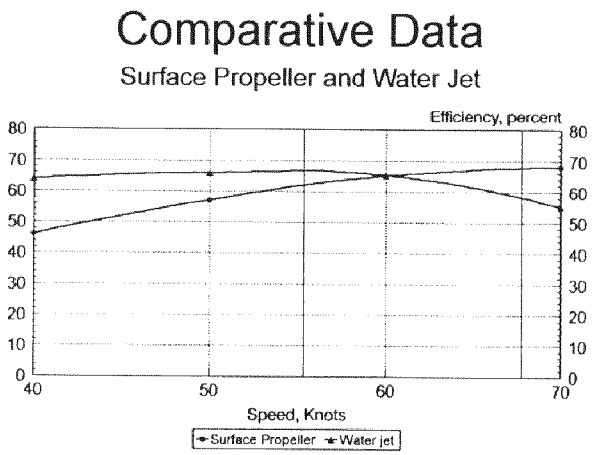


Fig.10.Efficiency versus ship speed (comparative data of SPP and water jet) [32]

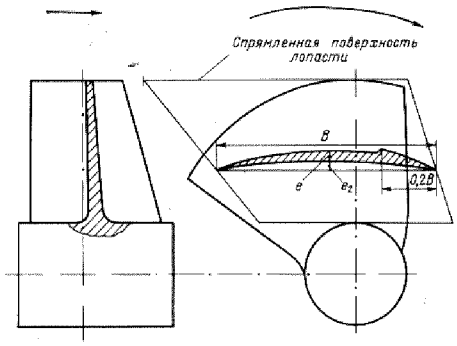


Fig.11.Blade geometry drawing of ventilated waterjet impeller blade [18]

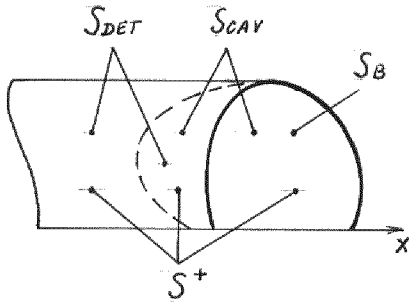


Fig.12. Domain nomenclature

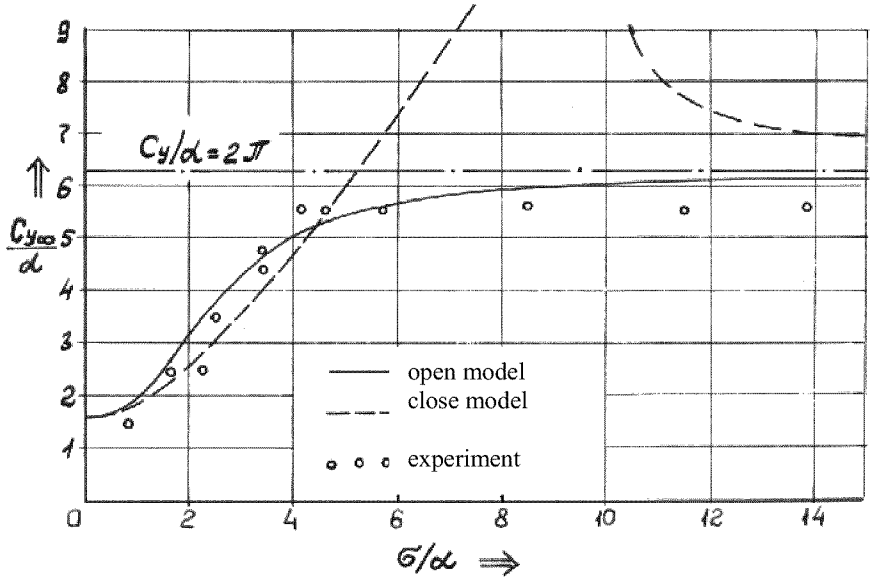


Fig.13.Lift coefficient-angle of attack ratio versus local cavitation number-angle of attack ratio for the supercavitating flat plate (comparative data of open and close cavitation models)

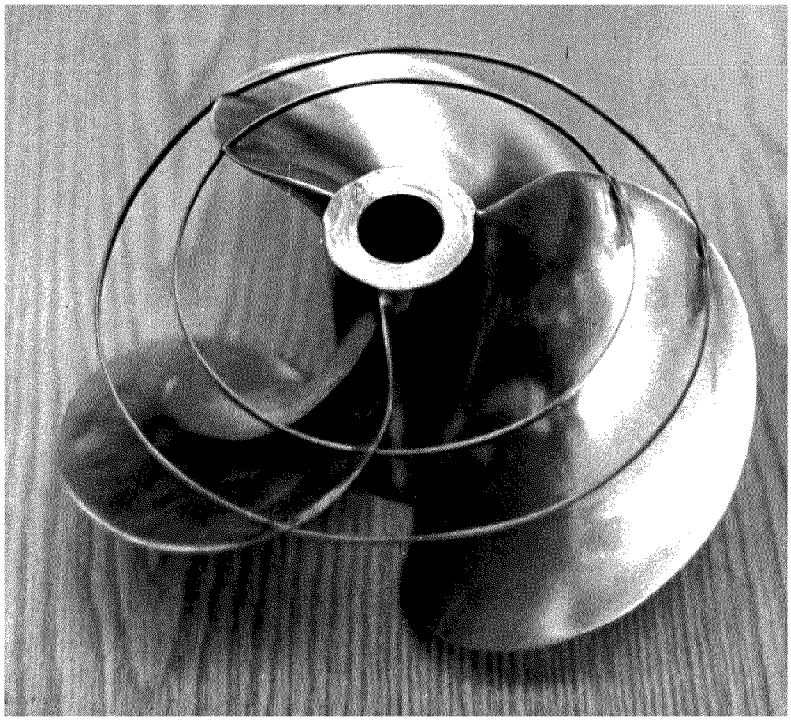


Fig.14.Designed in LSI supercavitating propeller model N8401 with cavity thickness measurer rings (z=3; A_E/A_0=0.92; P/D(0.6)=1.28; χ=0.25; J=1.0; K_T=0.084; segment section type)

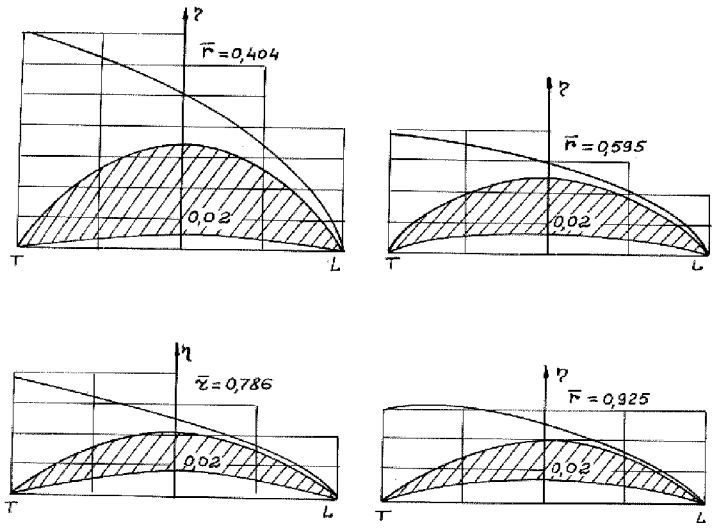


Fig.15.Cavity boundary and pressure surface calculation ordinates (multiply on 6.25) for supercavitating propeller N8401 at design regime [49]

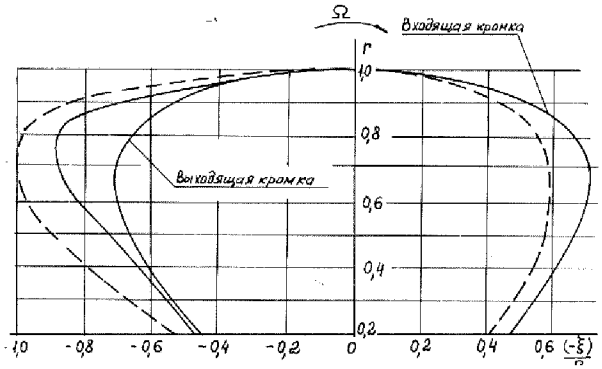


Fig.16.Cavity configuration for supercavitating propeller N8401 at design regime in sucking surface [49]

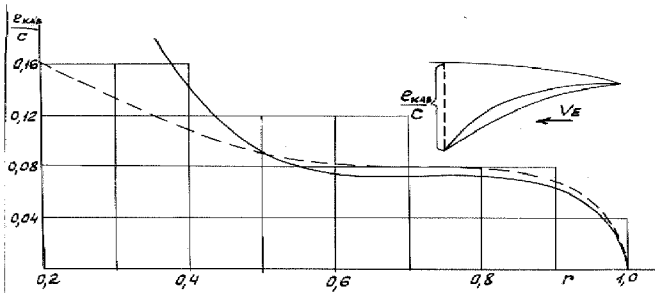


Fig.17.Radial cavity thickness distribution at blade trailing edge for supercavitating propeller N8401 at design regime [49]

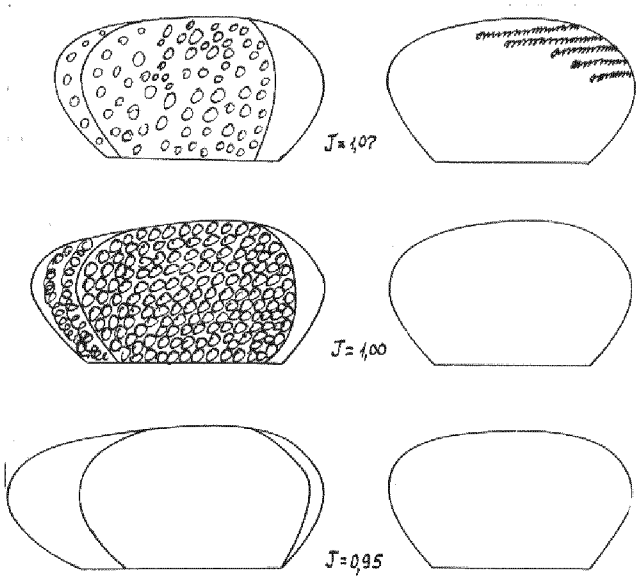


Fig.18. Blade surface cavitation development at various advance ratio for supercavitating propeller N8401 (pressure surface is on the right) [49]

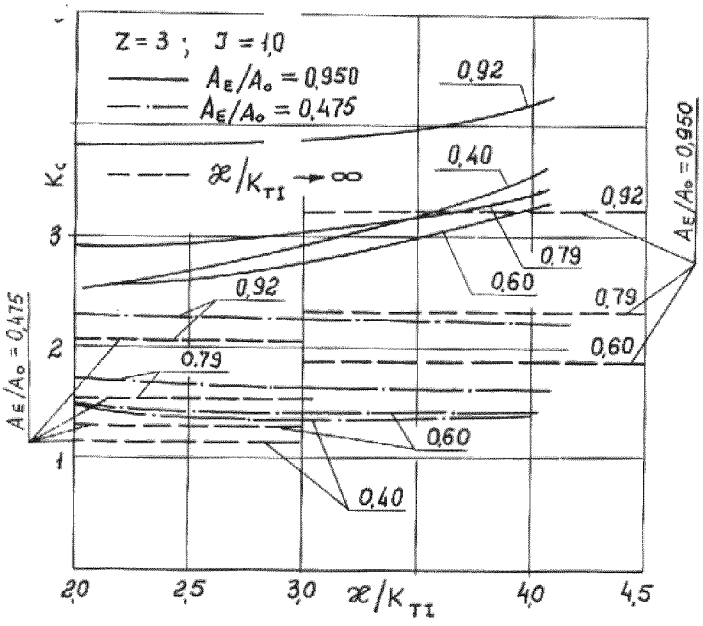


Fig.19.Correction for the camber of the blade cylindrical section central line together with the cavity (comparative data of supercavitating and non-cavitating propellers) [50]

SUPERCAVITATING 3-D HYDROFOILS AND PROPELLERS: PREDICTION OF PERFORMANCE AND DESIGN

Spyros A. Kinnas
Ocean Engineering Group, Department of Civil Engineering
The University of Texas at Austin, Austin, TX 78712, USA
http://cavity.ce.utexas.edu, email: kinnas@mail.utexas.edu

ABSTRACT

Recent numerical techniques for the prediction of cavitating flows, in linear and non-linear theories, are applied on super-cavitating 2-D, 3-D hydrofoils and propellers. Some of these techniques, when incorporated within a non-linear optimization algorithm, can lead to efficient supercavitating hydrofoil or propeller designs. This lecture will address 3-D supercavitating hydrofoils, supercavitating and surface-piercing propellers.[12]

NOMENCLATURE

α	Angle Of Attack For 3-D Hydrofoil
C_p	Pressure Coefficient, $C_p = (P - P_o)/(\frac{\rho}{2}n^2D^2)$
D	Propeller Diameter
η	Propeller efficiency, $\eta = \frac{K_T}{K_Q}\frac{J_S}{2\pi}$
F_r	Froude Number, $F_r = n^2D/g$
g	Gravitational Acceleration
Γ	Circulation Around Each Blade Section
h	Cavity Thickness Over The Blade Surface
h_w	Cavity Thickness Over The Wake Surface
J_S	Advance Ratio, $J_S = V_s/nD$
K_Q	Torque Coefficient, $K_Q = Q/\rho n^2D^5$
K_T	Thrust Coefficient, $K_T = T/\rho n^2D^4$
l	Cavity Length
n	Propeller Rotational Frequency (rev/s)
$\vec{n}$	Unit Normal Vector
ϕ	Perturbation Potential
P	Pressure
P_o	Pressure Far Upstream, at the Propeller Axis
P_v	Vapor Pressure of Water
P_∞	Pressure Far Upstream, at the Submergence Depth of the Hydrofoil
$\vec{q}$	Total Velocity
$\vec{q}_{in}$	Local Inflow Velocity (with respect to propeller-fixed coordinates system)
$\vec{q}_{wake}$	Effective Wake Inflow Velocity (with respect to ship-fixed coordinates system)
Q	Propeller Torque
ρ	Fluid Density
σ	Cavitation Number Based on U_∞, $\sigma = (P_\infty - P_v)/(\frac{\rho}{2}U_\infty^2)$
σ_n	Cavitation Number Based on n, $\sigma_n = (P_o - P_v)/(\frac{\rho}{2}n^2D^2)$
σ_v	Cavitation Number based on V_s, $\sigma_v = (P_o - P_v)/(\frac{\rho}{2}V_s^2)$
t	Time
T	Propeller Thrust
U_∞	Speed of Uniform Inflow for Hydrofoils
V_s	Ship Speed

[12] Sections, figures, equations and footnotes are numbered starting from the first lecture of Prof. Kinnas.

Paper presented at the RTO AVT Lecture Series on "Supercavitating Flows", held at the von Kármán Institute (VKI) in Brussels, Belgium, 12-16 February 2001, and published in RTO EN-010.

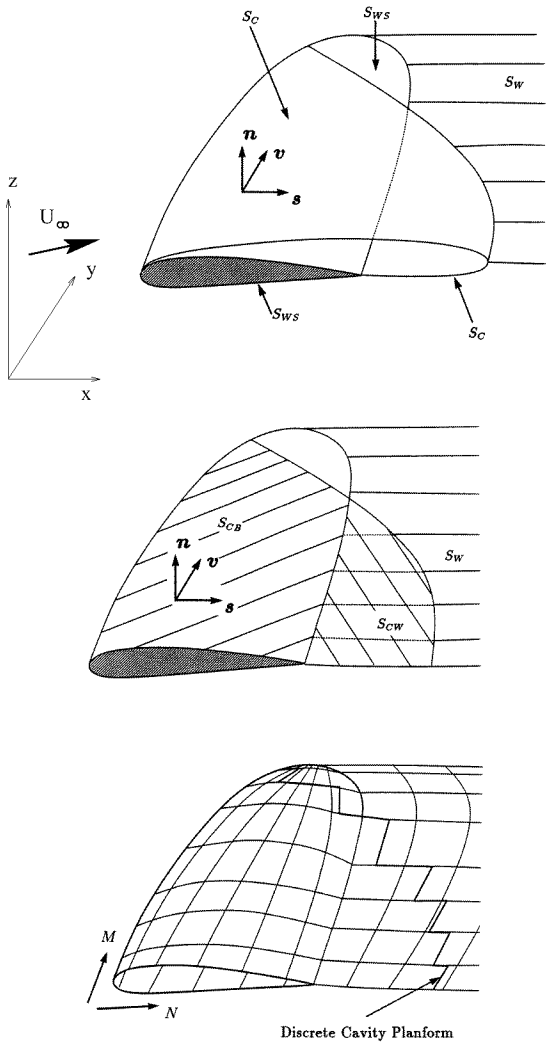


Figure 23: Definition of the "exact", the approximate, and the discretized 3-D cavity and foil surface.

4 3-D HYDROFOIL

4.1 Formulation

Consider now a 3-D hydrofoil which is subject to a uniform inflow $\mathbf{U}_\infty$ as shown in Fig. 23. The cavity surface is denoted with S_C, the wetted hydrofoil surface with S_{WS}, and the trailing wake surface with S_W. The total flow velocity field $\mathbf{q}(x, y, z)$, can be written in terms of the perturbation potential, $\phi(x, y, z)$, as follows:

$$\mathbf{q}(x, y, z) = \mathbf{U}_\infty + \nabla\phi(x, y, z). \tag{81}$$

In the next four sections the necessary equations and conditions for determining $\phi(x, y, z)$, as well as the cavity planform and shape are outlined. Only the non-linear cavity solution is described. References on linearized approaches have been given in the introduction.

4.1.1 The Green's formula

As in the case of the 2-D hydrofoil Green's third identity renders the following integral equation for $\phi(x, y, z)$:

$$2\pi\phi = \int_{S_{WS}\cup S_C}\left[\phi\frac{\partial G}{\partial n} - G\frac{\partial\phi}{\partial n}\right]dS + \int_{S_W}\Delta\phi_W\frac{\partial G}{\partial n}dS \quad (82)$$

$\mathbf{n}$ is the unit vector normal to the foil wetted surface, the cavity surface or the wake surface; $\Delta\phi$ is the potential jump across the wake sheet; $G = 1/R$ is the Green's function, where R is the distance between a point P and the point of integration along the foil and cavity surface.

Equation (82) should be applied on the "exact" cavity surface as shown in Fig. 23. Based on the fast convergence of the boundary element method with number of iterations in 2-D (as described in the previous section), only the solution from the hybrid scheme (i.e. the first iteration) is carried out. This is equivalent to applying Green's formula on an approximate surface, as shown in Fig. 23. This surface is comprised from the foil surface and the trailing wake surface. The treatment of a supercavity within this scheme is discussed in detail in (Fine & Kinnas 1993b). The approximate surface is discretized as shown at the bottom part of Fig. 23. Constant strength dipoles and sources are distributed on each of the wetted or cavitating flow quadrilateral panels. The strength of the source distribution on the wetted foil surface is expressed via the kinematic boundary condition:

$$\frac{\partial\phi}{\partial n} = -\mathbf{U}_\infty\cdot\mathbf{n}; \quad \text{on } S_{WS} \quad (83)$$

In the case of super-cavitation the cavity in the wake is modeled with constant strength line sources. Equation (82) is then split into two different formulations, on the part of the cavity over the foil, and on the part downstream of the trailing edge. The corresponding formulas are given in (Fine & Kinnas 1993a), and are similar to those given in equations (49) and (50).

4.1.2 The dynamic boundary condition

The dynamic boundary condition (DBC) requires that the pressure everywhere inside and on the cavity be constant and equal to the known cavity pressure, P_v. As in the case of 2-D hydrofoil, Bernoulli's equation will give:

$$q_c = U_\infty\sqrt{1+\sigma} \quad (84)$$

Where q_c is the magnitude of the cavity velocity $\mathbf{q}_c$. Note that for simplicity the hydrostatic terms, which would be important in the case of a vertical 3-D foil, have not been included.
The cavity velocity vector, $\mathbf{q}_c$, may also be expressed as follows (Kinnas & Fine 1993):

$$\mathbf{q}_c = \frac{V_s\left[\mathbf{s} - (\mathbf{s}\cdot\mathbf{v})\mathbf{v}\right] + V_v\left[\mathbf{v} - (\mathbf{s}\cdot\mathbf{v})\mathbf{s}\right]}{\|\mathbf{s}\times\mathbf{v}\|^2} \quad (85)$$

where s and v are the curvilinear coordinates[13] along the cavity surface (as shown in Fig. 23); $\mathbf{s}$ and $\mathbf{v}$ are the corresponding unit vectors; V_s and V_v are given as follows:

$$V_s = \frac{\partial\phi}{\partial s} + \mathbf{U}_\infty\cdot\mathbf{s}; \quad V_v = \frac{\partial\phi}{\partial v} + \mathbf{U}_\infty\cdot\mathbf{v} \quad (86)$$

Equations (84) and (85) may then be combined to form an equation which is quadratic in the unknown chordwise perturbation velocity, $\partial\phi/\partial s$. The solution to this quadratic[14] renders $\partial\phi/\partial s$ in terms of the cavitation number, the inflow velocity, and the unknown crossflow $\partial\phi/\partial v$:

$$\frac{\partial\phi}{\partial s} = -\mathbf{U}_\infty\cdot\mathbf{s} + V_v\cos\theta + \sin\theta\sqrt{q_c^2 - V_v^2} \quad (87)$$

with θ being the angle between s and v; q_c is given by equation (84). Equation (87) is integrated once to form a Dirichlet boundary condition on ϕ:

[13] In general non-orthogonal.
[14] The root which corresponds to cavity velocity vectors pointing downstream is selected.

$$\phi(s) = \phi(0) + \int_0^s [\text{right-hand-side of equ. (87)}]ds \tag{88}$$

The value of $\phi(0)$ in equation (88) at each strip is determined (as in the case of 2-D hydrofoil) via a cubic extrapolation in terms of the unknown potentials on the wetted panels on the same strip in front of the cavity.

The crossflow term, $\partial\phi/\partial v$, in equation (88) is included in an iterative sense (Kinnas & Fine 1993).

4.1.3 The cavity thickness distribution

The kinematic boundary condition on the cavity requires that the velocity normal to the cavity is zero (in the case of steady flows) , or, more generally (also valid in the case of unsteady flows), that the following substantial derivative is zero:

$$\frac{D}{Dt}(n-h) = \left(\frac{\partial}{\partial t} + \mathbf{q}_c \cdot \nabla\right)(n-h) = 0 \tag{89}$$

where n is the coordinate normal to the foil surface under the cavity (with unit vector $\mathbf{n}$) and $h(s,v,t)$ is the thickness of the cavity normal to the foil surface at the point (s,v) at time t. Expressing the gradient in terms of the local directional derivatives

$$\nabla = \frac{[\mathbf{s} - (\mathbf{s}\cdot\mathbf{v})\mathbf{v}]\frac{\partial}{\partial s} + [\mathbf{v} - (\mathbf{s}\cdot\mathbf{v})\mathbf{s}]\frac{\partial}{\partial v}}{\|\mathbf{s}\times\mathbf{v}\|^2} + \mathbf{n}\frac{\partial}{\partial n}, \tag{90}$$

and performing the dot product with $\mathbf{q}_c$ (as defined in (85)) and finally substituting the result in (89) yields the following partial differential equation for the cavity thickness:

$$\frac{\partial h}{\partial s}[V_s - \cos\theta V_v] + \frac{\partial h}{\partial v}[V_v - \cos\theta V_s] = \\ = \sin^2\theta(V_n - \frac{\partial h}{\partial t}) \tag{91}$$

where

$$V_n = \frac{\partial\phi}{\partial n} + \mathbf{U}_\infty \cdot \mathbf{n} \tag{92}$$

The partial differential equation (91) can be integrated over the entire cavity planform in order to provide the cavity thickness. In the case of steady flow (as considered in the beginning of this section) $\partial h/\partial t = 0$. In the part of the cavity downstream of the trailing edge a different formula, similar to that given in equation (51), is used for the cavity height, h_W (Fine & Kinnas 1993a).

4.1.4 The cavity planform

The extent (planform) of the 3-D cavity is not known and has to be determined as a part of the solution. This is accomplished by finding the appropriate $l(y)$ (cavity length at each spanwise location y) which satisfies the cavity closure condition for the given cavitation number, σ:

$$\delta(y;\sigma) = h(l(y), y) = 0 \tag{93}$$

4.2 Numerical aspects

The objective of the numerical analysis is to invert equation (82) subject to the conditions (83) and (88). The numerical implementation is described in detail in (Kinnas & Fine 1991b, Kinnas & Fine 1993, Fine & Kinnas 1993a). In brief, for given cavity planform, equation (82) is solved with respect to the unknown ϕ on the wetted foil and for the unknown $\partial\phi/\partial n$ on the cavity. The cavity height at the trailing edge of the used cavity planform are then determined by integrating equation (91). The cavity planform is adjusted accordingly and the solution is carried over again until the corresponding heights at the cavity end are equal to zero within some given tolerance. The numerics of the method have been extensively validated in (Kinnas & Fine 1993, Fine & Kinnas 1993a).

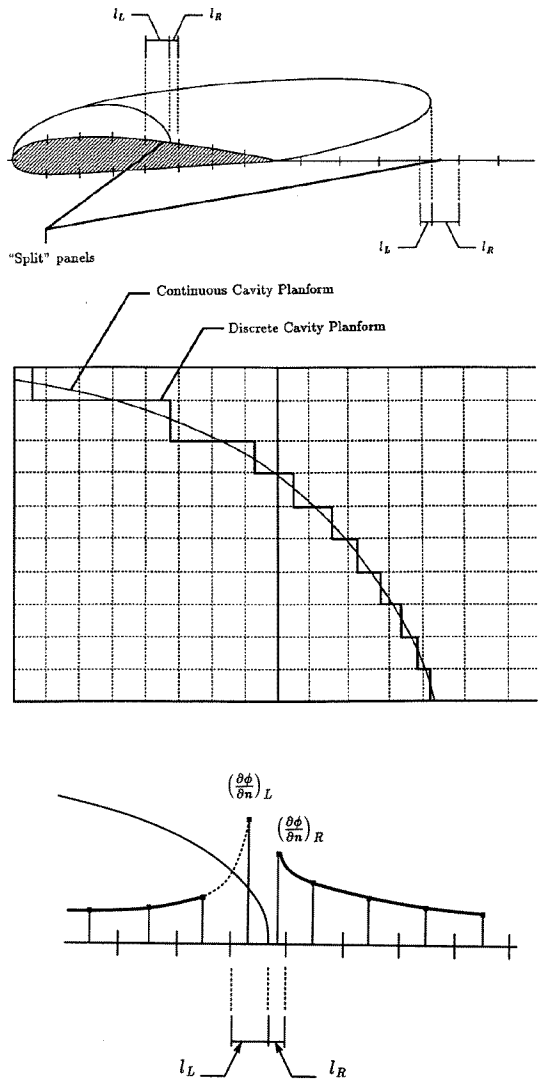


Figure 24: The split panel technique applied to the cavity trailing edge in three dimensions. The values (extrapolated from the side of the cavity) for $\partial\phi/\partial n$ into the two parts of the split panel are also shown.

4.2.1 The split panel technique

A very crucial issue in the numerical implementation was found to be related to the treatment of panels which were intersected by the cavity trailing edge. In order to avoid recomputing influence coefficients a technique was devised, namely the *split* panel technique (Kinnas & Fine 1993, Fine 1992), in which the intersected panel is treated as one panel with each of the ϕ and $\partial\phi/\partial n$ being determined as the weighted average of the values on the wetted and the cavitating part of the panel. This technique, as depicted on Fig. 24, provided substantial savings on computer time since the same panel discretization can handle arbitrary cavity planforms.

4.3 Multiplicity of Solutions

Equation (93) may accept more than one solutions, i.e. produce more than one cavity planforms for a given value of cavitation number. This is a very well known fact in two dimensions, where for some cavitation numbers there are three solutions (two partial cavities and one supercavity). The present method has also been found to predict multiple solutions in three dimensions (Kinnas & Fine 1992, Fine & Kinnas 1993a), as can be seen in Figure 25. Note that for $\sigma = 0.85$ two cavity planforms are predicted, one partial cavity and one mixed cavity (slightly supercavity at midspan). The partial cavity was produced when the initial guess was a

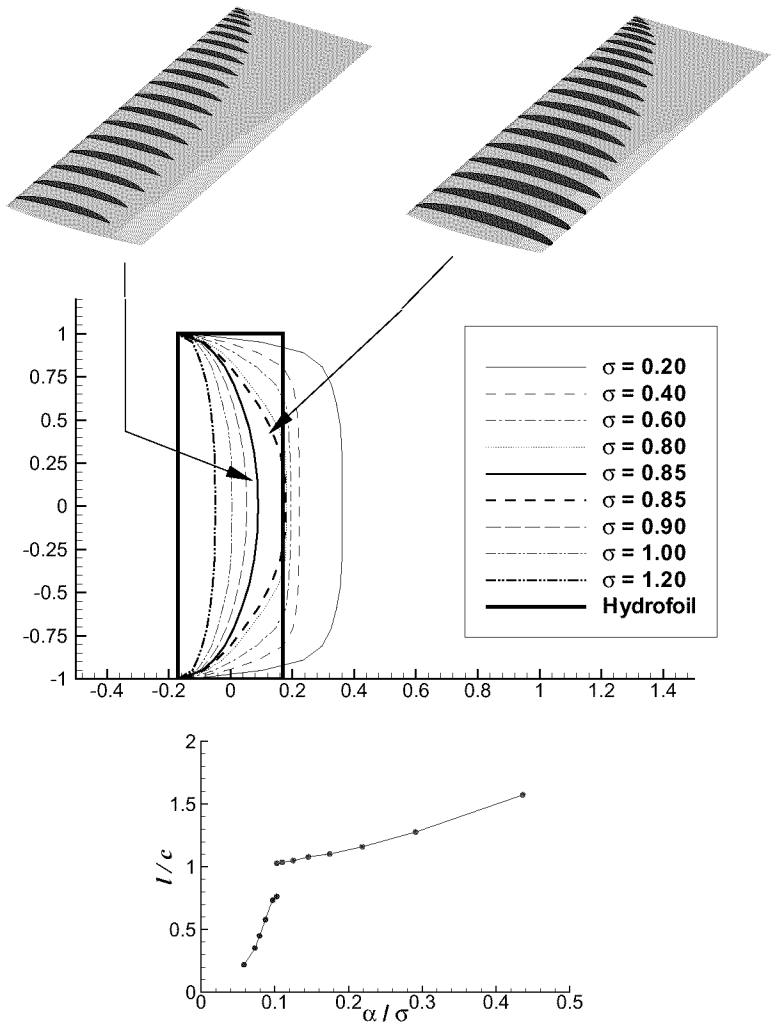


Figure 25: Multiple solutions in 3-D for $\sigma = 0.85$. The predicted cavity shapes are shown over half of the span at the top and the l_{max}/c vs. α/σ curve is shown at the bottom.

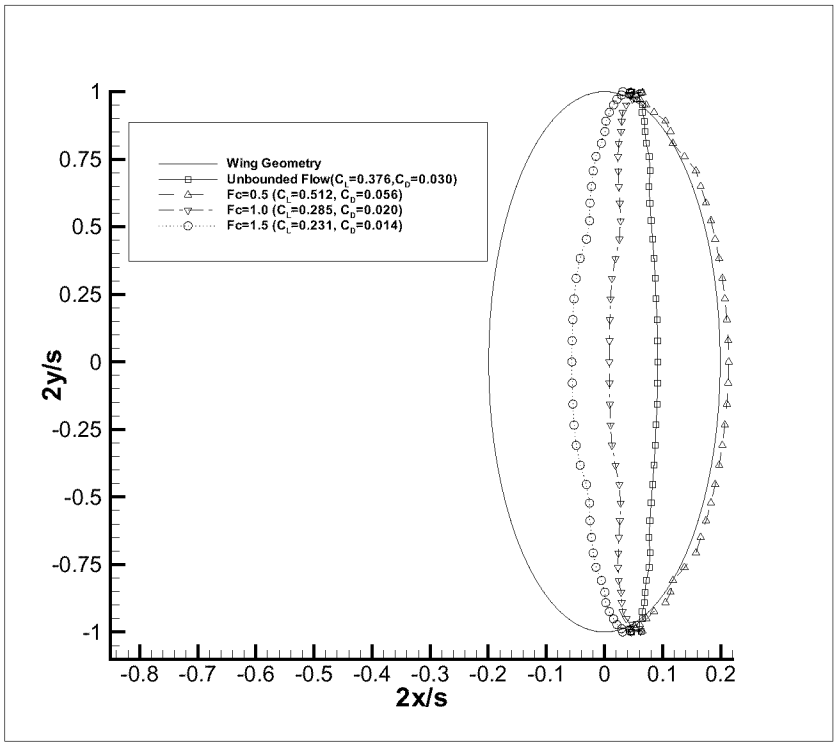


Figure 26: Froude number effect on predicted cavity planform and forces in the case the submergence depth at which the hydrofoil operates is equal to the chord length. From (Bal et al 2001).

partial cavity and the mixed cavity when the initial guess was a supercavity. The cavity length at midchord vs α/σ is also shown at the bottom part of Fig. 25. Note the striking similarity of this curve to the well known characteristic curve for a two dimensional cavitating flat plate (not shown in the Figure). This multiplicity of solutions in 3-D can also be confirmed from the observed instability on the cavity extent during experiments on cavitating 3-D foils as the cavity transitions from partial to super-cavitation.

4.4 Effects of free-surface

They are often substatial and can evaluated by using "negative" images with respect to the free-surface in the case of very large Froude number, $F_c = U_\infty/\sqrt{gc}$, where c is the maximum chord. In the case of finite Froude numbers the free-surface must also be modeled with panels (Bal et al 2001). A representative result from applying this method is shown in Fig. 26. Notice the strong dependence of the predicted cavity planform and forces on F_c.

4.5 Effects of tunnel walls

The effects of tunnel walls are known to be substantial (escpecially in the prediction of cavity extent) and need to be included, either by imaging of the hydrofoil and cavity with respect to the tunnel walls (in the case of 2-D flow and square section tunnel), or by modeling completely the tunnel boundaries in the numerical method (Choi & Kinnas 1998, Choi & Kinnas 1999, Kinnas et al 1998b, Kinnas et al 2000). The paneling on the 4990 3-D hydrofoil and the tunnel walls of the DTMB 36" circular section tunnel is shown in Figure 27.

Predicted cavity shapes, with and without the tunnel effects included, are shown for the 4990 3-D hydrofoil in Figure 28. Note the drastic effect of the tunnel walls on the predicted cavity shape. The predicted cavity plan-form when the tunnel effects are included appears to be very close to the observed, shown in Figure 29. However, there are flow phenomena at the root of the blade (re-entrant jet, cloud cavitation at the trailing edge) which are not modeled in the present method and thus not captured by the predictions. The predicted cavity with the tunnel effects included, as shown in Figure 28, has been determined by manually adjusting the cavity leading edge at each section along the span until two conditions are satisfied: (a) the cavity thickness is positive and (b) the pressures upstream of the cavity detachment are larger than the vapor pressure.

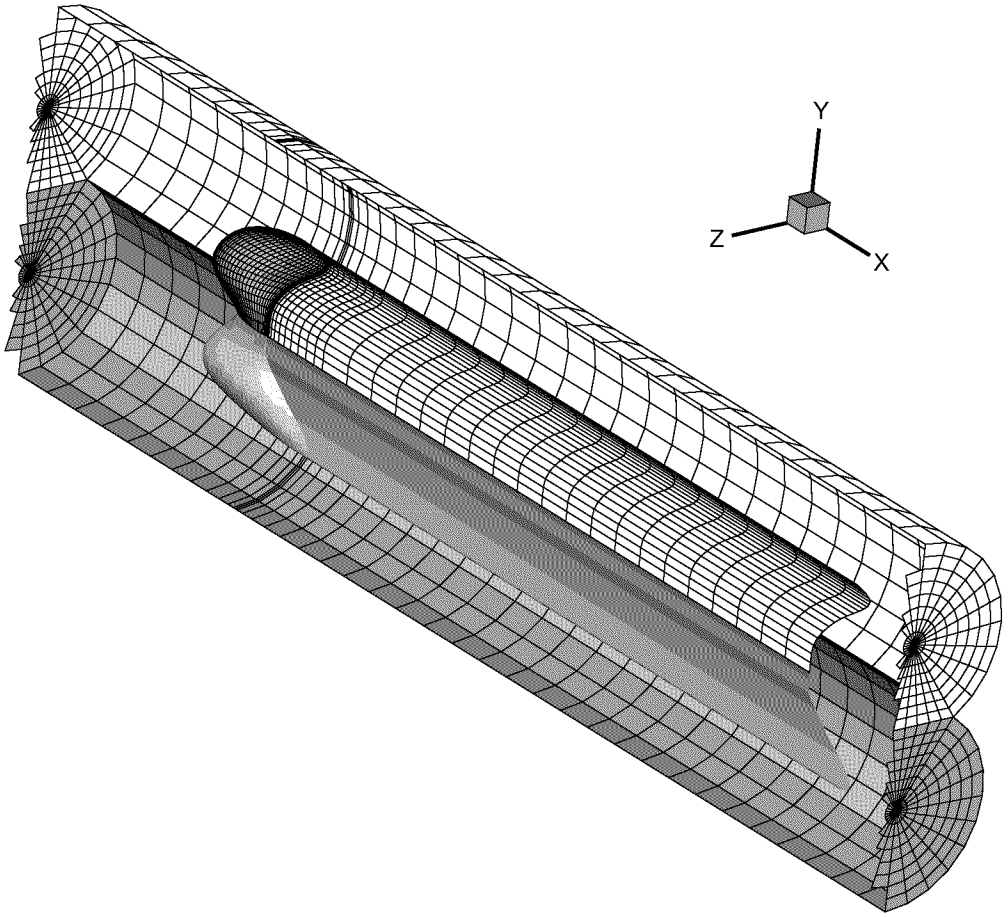


Figure 27: The grid on the 4990 hydrofoil, its trailing wake, and the DTMB 36" circular tunnel (the images with respect to the flat bottom of the tunnel are also shown). The flow goes from left to right. Only half of the tunnel panels are displayed.

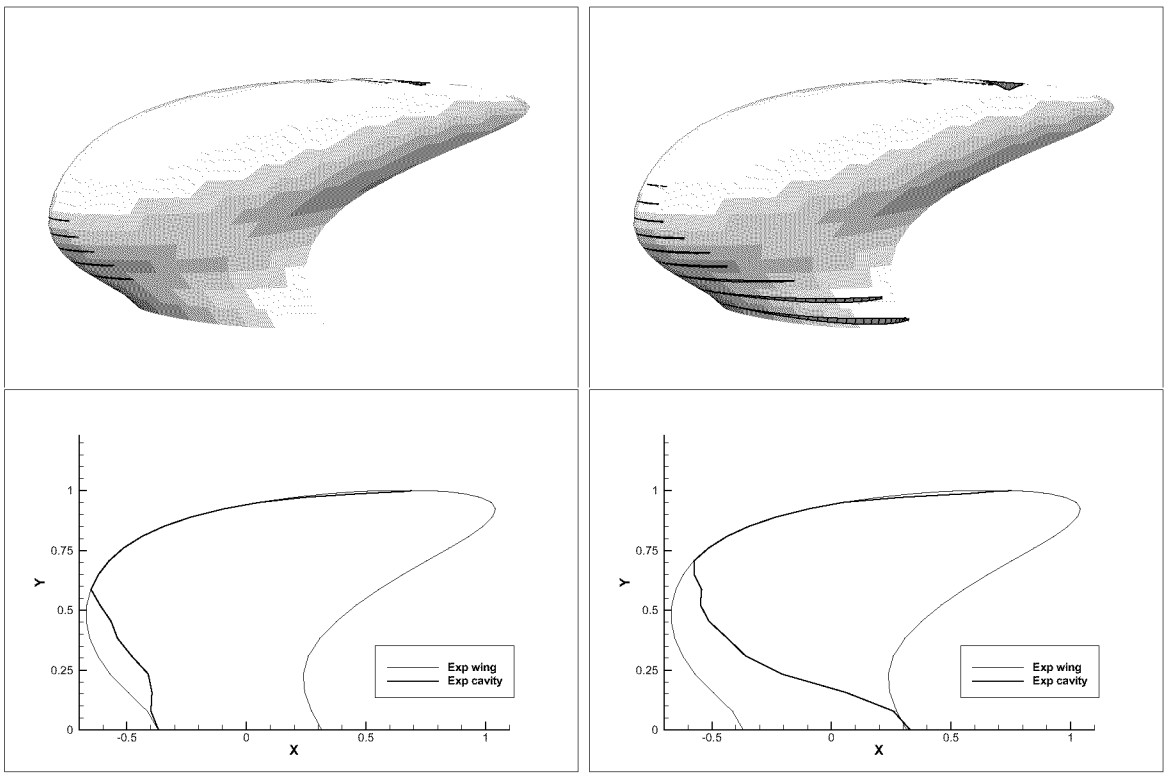


Figure 28: The predicted perspective (top) and expanded (bottom) cavity plan-forms *without* (left) and *with* (right) the tunnel wall effects for the 4990 hydrofoil; $\alpha = 0^o$, $\sigma = 0.62$. From (Kinnas et al 1998b).

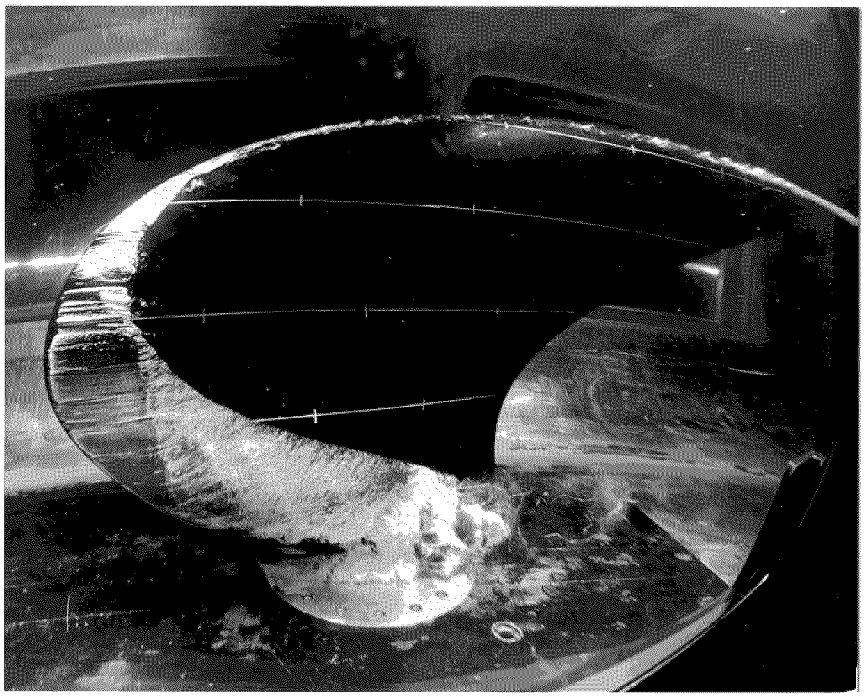


Figure 29: Photograph of the cavitating 4990 hydrofoil inside the DTMB 36inch cavitation tunnel; $\alpha = 0^o$, $\sigma = 0.62$. Courtesy of Dr. Rood of ONR and Dr. Jessup of DTMB. From (Kinnas et al 1998b).

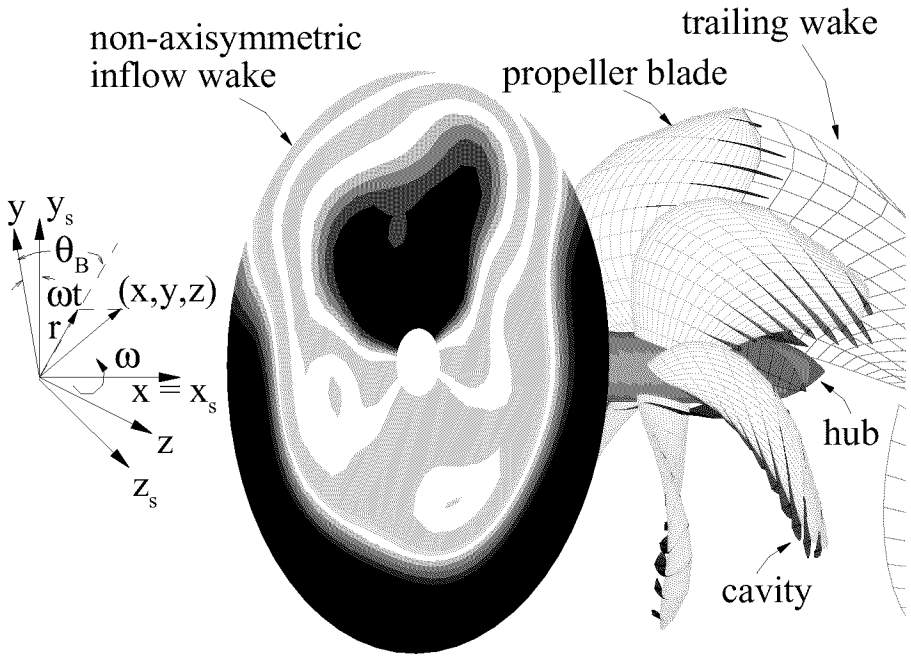


Figure 30: Propeller subjected to a general inflow wake. The propeller fixed (x, y, z) and ship fixed (x_s, y_s, z_s) coordinate systems are shown.

5 SUPER-CAVITATING PROPELLER

5.1 Formulation

This section summarizes the formulation of the cavitating flow around a propeller given by (Kinnas & Fine 1992) and (Fine 1992).

Consider a cavitating propeller subject to a general inflow wake, $\vec{q}_{wake}(x_s, y_s, z_s)$, as shown in Figure 30. The inflow wake is expressed in terms of the absolute (ship fixed) system of cylindrical coordinates (x_s, y_s, z_s). The inflow velocity, $\vec{q}_{in}$, with respect to the propeller fixed coordinates (x, y, z), can be expressed as the sum of the inflow wake velocity, $\vec{q}_{wake}$, and the propeller's angular velocity $\vec{\omega}$, at a given location $\vec{x}$:

$$\vec{q}_{in}(x, y, z, t) = \vec{q}_{wake}(x, r, \theta_B - \omega t) + \vec{\omega} \times \vec{x} \tag{94}$$

where $r = \sqrt{y^2 + z^2}$, $\theta_B = arctan(z/y)$ and $\vec{x} = (x, y, z)$. The inflow, $\vec{q}_{wake}$, is assumed to be the *effective wake*, i.e. it includes the interaction between the vorticity in the inflow and the propeller (Choi 2000), (Choi & Kinnas 2001). The resulting flow is assumed to be incompressible and inviscid. The total velocity field, $\vec{q}$, can be expressed in terms of $\vec{q}_{in}$ and the perturbation potential, ϕ, as follows:

$$\vec{q}(x, y, z, t) = \vec{q}_{in}(x, y, z, t) + \nabla\phi(x, y, z, t) \tag{95}$$

where ϕ satisfies the Laplace's equation in the fluid domain (i.e. $\nabla^2\phi = 0$). Note that in analyzing the flow around the propeller, the propeller fixed coordinates system is used.

5.1.1 Green's formula

The perturbation potential, ϕ, at every point p on the combined wetted blade and cavity surface, $S_{WB}(t) \cup S_C(t)$, must satisfy Green's third identity:

$$2\pi\phi_p(t) = \int\int_{S_{WB}(t) \cup S_C(t)} \left[\phi_q(t) \frac{\partial G(p;q)}{\partial n_q(t)} - G(p;q) \frac{\partial \phi_q(t)}{\partial n_q(t)} \right] dS$$

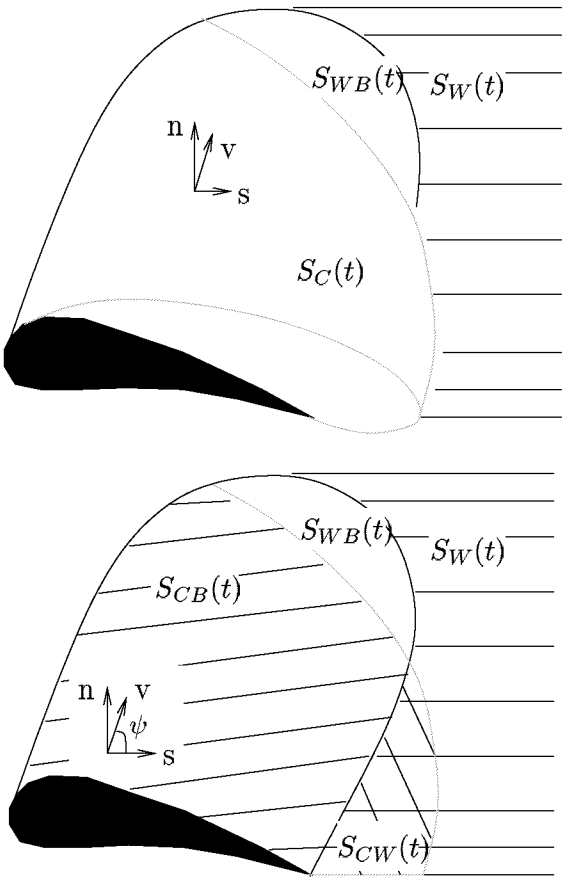


Figure 31: Top: Definition of the exact surface. Bottom: Definition of the approximated cavity surface.

$$+\int\int_{S_W(t)} \Delta\phi(r_q,\theta_q,t)\frac{\partial G(p;q)}{\partial n_q(t)}dS; \qquad p \in (S_{WB}(t) \cup S_C(t)) \tag{96}$$

where the subscript q corresponds to the variable point in the integration. $G(p;q) = 1/R(p;q)$ is the Green's function with $R(p;q)$ being the distance between points p and q. $\vec{n}_q$ is the unit vector normal to the integration surface. $\Delta\phi$ is the potential jump across the wake surface, $S_W(t)$. The definitions of S_{WB}, S_C and S_W are depicted in Fig. 31.

Eqn. 96 should be applied on the "exact" cavity surface S_C, as shown in the drawing at the top of Fig. 31. However, the cavity surface is not known and has to be determined as part of the solution. In this work, an approximated cavity surface, shown in the drawing at the bottom of Fig. 31, is used. The approximated cavity surface is comprised of the blade surface underneath the cavity on the blade, S_{CB}, and the portion of the wake surface which is overlapped by the cavity, S_{CW}. The justification for making this approximation, as well as a measure of its effect on the cavity solution can be found in (Kinnas & Fine 1993) and (Fine 1992).

Using the approximated cavity surface, Eqn. 96 may be decomposed into a summation of integrals over the blade surface, S_B ($\equiv S_{CB} + S_{WB}$), and the portion of the wake surface which is overlapped by the cavity, S_{CW}.

Field Points on S_B.

For field points on S_B, Eqn. 96 becomes:

$$2\pi\phi_p(t) = \int\int_{S_B}\left[\phi_q(t)\frac{\partial G(p;q)}{\partial n_q} - G(p;q)\frac{\partial \phi_q(t)}{\partial n_q}\right]dS - \int\int_{S_{CW}(t)} q_w(t)G(p;q)dS$$

$$+\int\int_{S_{CW}(t)\cup S_W(t)} \Delta\phi(r_q,\theta_q,t)\frac{\partial G(p;q)}{\partial n_q}dS; \qquad p\in S_B \tag{97}$$

where q_w is the cavity source distribution in the wake, defined as:

$$q_w(t) \equiv \frac{\partial \phi^+}{\partial n}(t) - \frac{\partial \phi^-}{\partial n}(t) \tag{98}$$

The superscripts "+" and "-" denote the upper and lower wake surface, respectively.

The geometry of the trailing wake is assumed to be invariant with time and taken to be the same as that corresponding to the circumferentially averaged flow (Kinnas & Hsin 1992). The dipole strength $\Delta\phi(r,\theta,t)$ in the wake is convected along the assumed wake model with angular speed ω:

$$\begin{aligned}
\Delta\phi(r,\theta,t) &= \Delta\phi_T\left(r_T, t-\frac{\theta-\theta_T}{\omega}\right); \quad t \geq \frac{\theta-\theta_T}{\omega} \\
\Delta\phi(r,\theta,t) &= \Delta\phi^S(r_T); \quad t < \frac{\theta-\theta_T}{\omega}
\end{aligned} \tag{99}$$

where r,θ are the cylindrical coordinates at any point in the trailing wake surface, S_W, and (r_T,θ_T) are the coordinates of the trailing edge at a point on the same streamline with (r,θ). $\Delta\phi^S$ is the steady flow potential jump in the wake when the propeller is subject to the circumferentially averaged flow.

The value of the dipole strength, $\Delta\phi_T(r_T,t)$, at the trailing edge of the blade at radius r_T and time t, will be given from the Morino's Kutta condition (Morino & Kuo 1974):

$$\Delta\phi_T(r_T,t) = \phi_T^+(r_T,t) - \phi_T^-(r_T,t) = \Gamma(r_T,t) \tag{100}$$

where $\phi_T^+(r_T,t)$ and $\phi_T^-(r_T,t)$ are the values of the potential at the upper (suction side) and lower (pressure side) blade trailing edge, respectively, at time t. Γ is the circulation around the blade section.

Recently, an iterative pressure Kutta condition (Kinnas & Hsin 1992) is applied for the analysis of unsteady fully wetted and cavitating propellers. The iterative pressure Kutta condition modifies $\Delta\phi_T(r_T,t)$ from that of Morino to achieve equality of pressures at both sides of the trailing edge everywhere on the blade (Young et al 2001).

Field Points on S_{CW}.

For field points on S_{CW}, the left-hand side of Eqn. 96 reduces to $2\pi\left[\phi_p^+(t)+\phi_p^-(t)\right]$, which can be expressed as $4\pi\phi_p^\pm(t) \mp 2\pi\Delta\phi_p(t)$ depending on if the equation is applied on the upper "+" or the lower "-" surface of the supercavitating region. This will render the following expression for $\phi_p^\pm$:

$$\begin{aligned}
4\pi\phi_p^\pm(t) &= \pm 2\pi\Delta\phi_p(t) \\
&+\int\int_{S_B}\left[\phi_q(t)\frac{\partial G(p;q)}{\partial n_q} - G(p;q)\frac{\partial\phi_q(t)}{\partial n_q}\right]dS \\
&-\int\int_{S_{CW}(t)} q_w(t)G(p;q)dS \\
&+\int\int_{S_{CW}(t)\cup S_W(t)} \Delta\phi(r_q,\theta_q,t)\frac{\partial G(p;q)}{\partial n_q}dS; \qquad p\in S_{CW}
\end{aligned} \tag{101}$$

5.1.2 Kinematic Boundary Condition on Wetted Part of the Blade

The kinematic boundary condition on the wetted portion of the blade defines the source strengths in terms of the known inflow velocity, $\vec{q}_{in}$:

$$\frac{\partial\phi_q}{\partial n_q} = -\vec{q}_{in}(x_q,y_q,z_q,t)\cdot\vec{n}_q \tag{102}$$

5.1.3 Dynamic Boundary Condition on Cavitating Surfaces

The dynamic boundary condition on the cavitating blade and wake surfaces requires the pressure everywhere on the cavity to be constant and equal to the vapor pressure, P_v. By applying Bernoulli's equation, the total velocity on the cavity, $\vec{q}_c$, can be expressed as follows:

$$\vec{q}_c{}^2 = n^2 D^2 \sigma_n + |\vec{q}_{wake}|^2 + \omega^2 r^2 - 2g y_s - 2\frac{\partial \phi}{\partial t} \tag{103}$$

where $\sigma_n \equiv (P_o - P_v)/(\frac{\rho}{2} n^2 D^2)$ is the cavitation number; ρ is the fluid density and r is the distance from the axis of rotation. P_o is the pressure far upstream on the shaft axis; g is the acceleration of gravity and y_s is the ship fixed coordinate, shown in Fig. 30. $n = \omega/2\pi$ and D are the propeller rotational frequency and diameter, respectively.

On the cavitating blade surface, the magnitude of the cavity velocity may also be written in terms of its projections along $\vec{s}$ (the chordwise) and $\vec{v}$ (the spanwise) grid directions on the blade surface:

$$|\vec{q}_c| \sin\psi = \sqrt{V_s^2 + V_v^2 - 2V_s V_v \cos\psi} \tag{104}$$

with:

$$V_s \equiv \frac{\partial \phi}{\partial s} + \vec{q}_{in} \cdot \vec{s} \qquad \text{and} \qquad V_v \equiv \frac{\partial \phi}{\partial v} + \vec{q}_{in} \cdot \vec{v} \tag{105}$$

where ψ is the angle between s and v directions, as shown in Fig. 31.

Combining Eqns. 103 and 104 renders the following expression for $\frac{\partial \phi}{\partial s}$:

$$\frac{\partial \phi}{\partial s} = -\vec{q}_{in} \cdot \vec{s} + V_v \cos\psi + \sin\psi \sqrt{|\vec{q}_c|^2 - V_v^2} \tag{106}$$

which can then be integrated to form a Dirichlet type boundary condition for ϕ. The unknown terms $\frac{\partial \phi}{\partial t}$ and $\frac{\partial \phi}{\partial v}$ on the right-hand side of Eqn. 106 are determined in an iterative manner.

On the cavitating wake surface, the coordinate $\vec{s}$ is assumed to follow the streamline [15]. Thus, the total cross flow velocity is assumed to be small, which renders the following expression for $\frac{\partial \phi}{\partial s}$:

$$\frac{\partial \phi}{\partial s} = -\vec{q}_{in} \cdot \vec{s} + |\vec{q}_c| \tag{107}$$

5.1.4 Kinematic Boundary Condition on Cavitating Surfaces

The kinematic boundary condition on the cavity requires the total velocity normal to the cavity to be zero. As shown in (Kinnas & Fine 1992), the kinematic boundary condition renders the following equation for the cavity thickness (h) on the blade:

$$\frac{\partial h}{\partial s}\left[V_s - \cos\psi V_v\right] + \frac{\partial h}{\partial v}\left[V_v - \cos\psi V_s\right] = \sin^2\psi \left(V_n - \frac{\partial h}{\partial t}\right) \tag{108}$$

where $V_n \equiv \frac{\partial \phi}{\partial n} + \vec{q}_{in} \cdot \vec{n}$ is the total normal velocity.

Assuming again that the spanwise crossflow velocity on the wake surface is small, the kinematic boundary condition reduces to the following equation for the cavity thickness (h_w) on the wake:

$$q_w(t) - \frac{\partial h_w}{\partial t} = |\vec{q}_c| \frac{\partial h_w}{\partial s} \tag{109}$$

where q_w is the cavity source distribution, defined by Eqn. 98.

The definitions of h and h_w are depicted in Fig. 32. The quantity h_w at the blade trailing edge is determined by interpolating the upper cavity surface over the blade and computing its normal offset from the wake sheet.

[15] It has been found by (Fine 1992) (Fine & Kinnas 1993b) that the effect of the crossflow term in the cavitating wake region has very little effect on the solution.

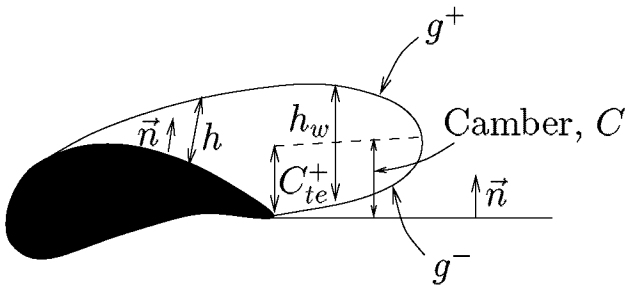


Figure 32: Definition of the cavity height on the blade and on the supercavitating wake.

5.1.5 Cavity Closure Condition

The extent of the unsteady cavity is unknown and has to be determined as part of the solution. The cavity length at each radius r is given by the function $l(r,t)$. For a given cavitation number, σ_n, the cavity planform $l(r,t)$ must satisfy the following requirement:

$$\delta\left(l(r,t),r;\sigma_n\right) \equiv h\left(l(r,t),r,t\right) = 0 \tag{110}$$

where δ is the cavity height at the trailing edge of the cavity. Eqn. 110 requires that the cavity closes at its trailing edge. This requirement is the basis of an iterative solution method that is used to find the cavity planform.

5.1.6 Solution Method

The unsteady cavity problem is solved by inverting Eqns. 97 and 101 subjected to conditions 99, 100, 102, 106, 107, and 110. The numerical implementation is described in detail in (Kinnas & Fine 1992), (Fine 1992), and (Kinnas & Fine 1993). In brief, for a given cavity planform, Green's formula is solved with respect to the unknown ϕ on the wetted blade surface and the unknown $\frac{\partial\phi}{\partial n}$ on the cavity surface. The cavity heights are then determined by integrating Eqns. 108 and 109. The correct cavity planform is obtained in an iterative manner by satisfying the cavity closure condition, Eqn. 110. The split-panel technique (Fine & Kinnas 1993a) (Kinnas & Fine 1993) is used to treat blade and wake panels that are intersected by the cavity trailing edge. Systematic convergence studies for various propeller geometries and flow conditions, as well as several comparisons with existing experiments of propellers in steady, unsteady, and cavitating flow are presented in (Young & Kinnas 2001).

5.2 Validation with experiments

In order to thoroughly validate PROPCAV, results from four different sets of experiments are presented.

To validate the supercavitation scheme in PROPCAV, predicted force coefficients are compared with experimental measurements (Matsuda et al 1994) for a supercavitating propeller. The test geometry is M.P.No.345(SRI), which is designed using SSPA charts under the following conditions: $J_S = 1.10$, $\sigma_v = 0.40$, and $K_T = 0.160$. It should be noted that the current version of PROPCAV modifies the suction side of the blade section aft of the midchord to render zero thickness at the trailing edge. This modification should not affect the results as long as the blade sections aft of the midchord are within the cavitation bubble.

The comparisons of the predicted versus measured thrust (K_T), torque (K_Q), and efficiency (η_p) are shown in Figure 33. The propeller geometry with the predicted cavities at $J_S = 1.3$ are shown in Figure 34. Also shown in Figure 34 are the predicted cavitating pressures along each radial strip at $J_S = 1.3$. It is worth noting that at this particular combination, there is substantial midchord detachment. Figure 34 indicates that the detachment search criterion in PROPCAV, which will be explained later, is satisfied since the cavity thickness is non-negative and the pressures everywhere on the wetted blade surfaces are above the vapor pressure. The comparisons shown on Figure 33 indicate that the predictions by PROPCAV agree very well with experimental data for values of $J_S \leq 1.2$. For $J_S > 1.2$, the comparisons are not as good because the cavities begin to detach aft of the midchord, where the suction side geometry was modified.

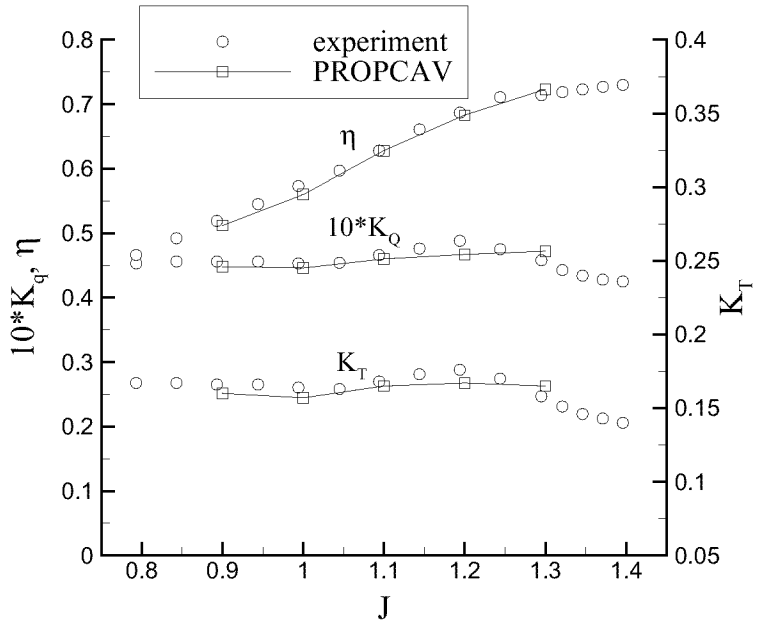


Figure 33: Comparison of the predicted and versus measured K_T, K_Q, and η for different advance coefficients. From (Young & Kinnas 2001).

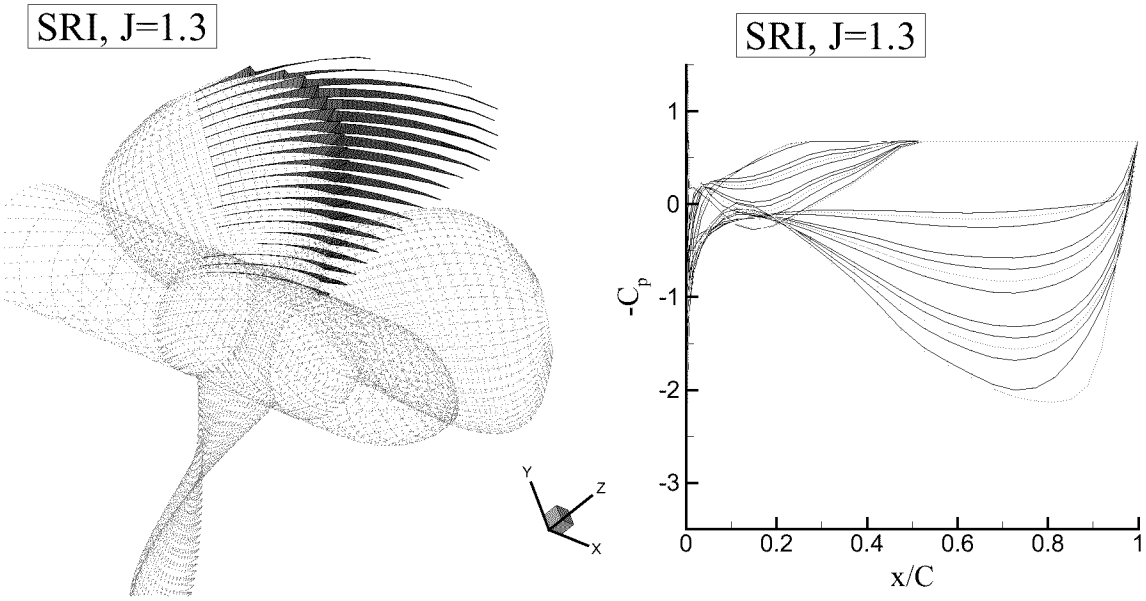


Figure 34: Geometry, cavitation pattern, and cavitating pressures for propeller SRI at $J_S = 1.3$. $\sigma_v = 0.4$. $\sigma_n = \sigma_v \times J_S^2$. From (Young & Kinnas 2001).

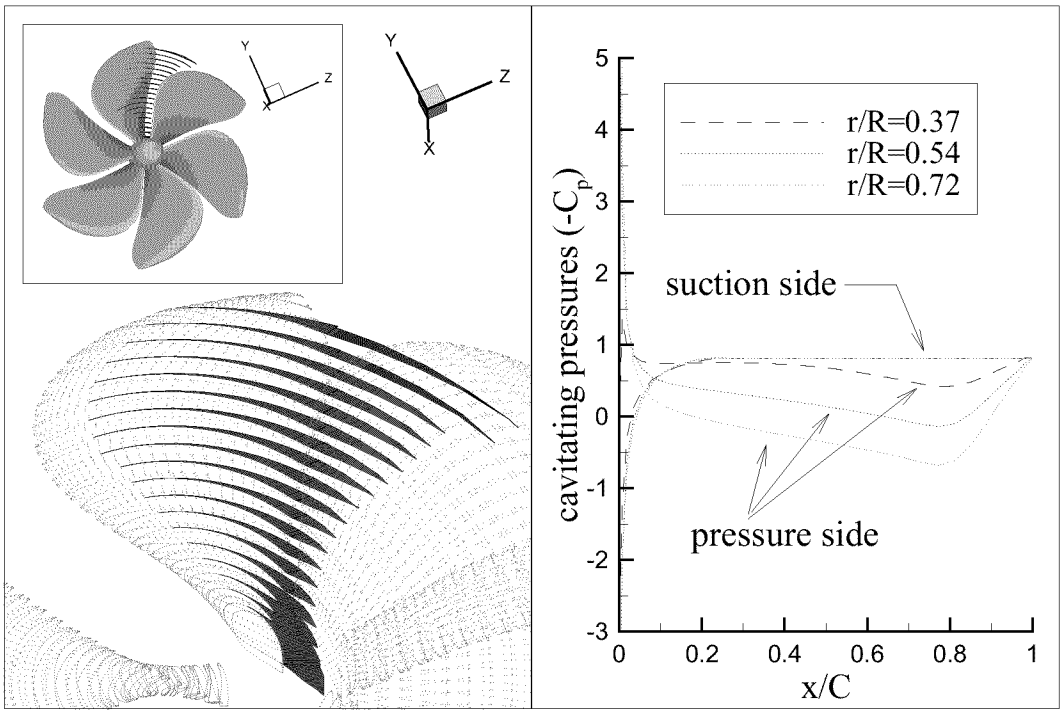


Figure 35: Cavity shape and pressures for propeller MW1. Mid-chord cavitation. The propeller is based on a design by Michigan Wheel Corporation, USA. $J_S = 1.224$. $\sigma_n = 0.8116$. $F_r = 26.6$. 60x20 panels. Uniform inflow. From (Young & Kinnas 2001).

5.3 Mid-chord detachment

The latest version of PROPCAV allows the cavity to detach from both the face (pressure side) and the back (suction side) of the blade. The initial detachment lines are obtained based on the fully wetted pressures. The detachment locations at each strip are then adjusted in the next revolution [16] according to the following criterion:

1. If the cavity at the strip has negative thickness, then the detachment location is moved towards the trailing edge of the blade.

2. If the pressure at a point upstream of the cavity is below the vapor pressure, then the detachment location is moved towards the leading edge of the blade.

It can be shown that the above criterion is equivalent to the Villat-Brillouin smooth detachment condition. Details of the formulation and convergence study for mid-chord detachment can be found in (Mueller 1998) and (Mueller & Kinnas 1999). An example of mid-chord cavitation for propeller MW1 [17] subjected to uniform inflow ($J_S = 1.224$, $\sigma = 0.8116$, $F_r = 26.6$) is shown in Fig. 35. Also shown in Fig. 35 are the corresponding cavitating pressures at three different strips along the span of the blade. It is worth noting that the predicted pressures on the suction side in front of the cavity detachment are higher than the vapor pressure. This indicates that the employed smooth detachment criterion works properly. However, the face side cavitating pressures near the leading edge are below the vapor pressure. This is because PROPCAV was only allowed to search for back cavitation. Had the option to search for face and back cavitation simultaneously (as explained in the next section) been on, PROPCAV would have also detected the expected face cavitation as shown in Figure 38.

5.4 Face and back cavitation

The latest version of PROPCAV allows the cavity to grow on both sides of the blade simultaneously. In this case, the dynamic boundary condition is applied on both cavity surfaces, and the kinematic boundary condition

[16] The solution is carried out over several complete revolutions of one blade, the "key" blade, with the effects of the other blades being accounted for in an iterative manner.

[17] The propeller geometry is based on a design by Michigan Wheel Corporation, USA (Young & Kinnas 2001).

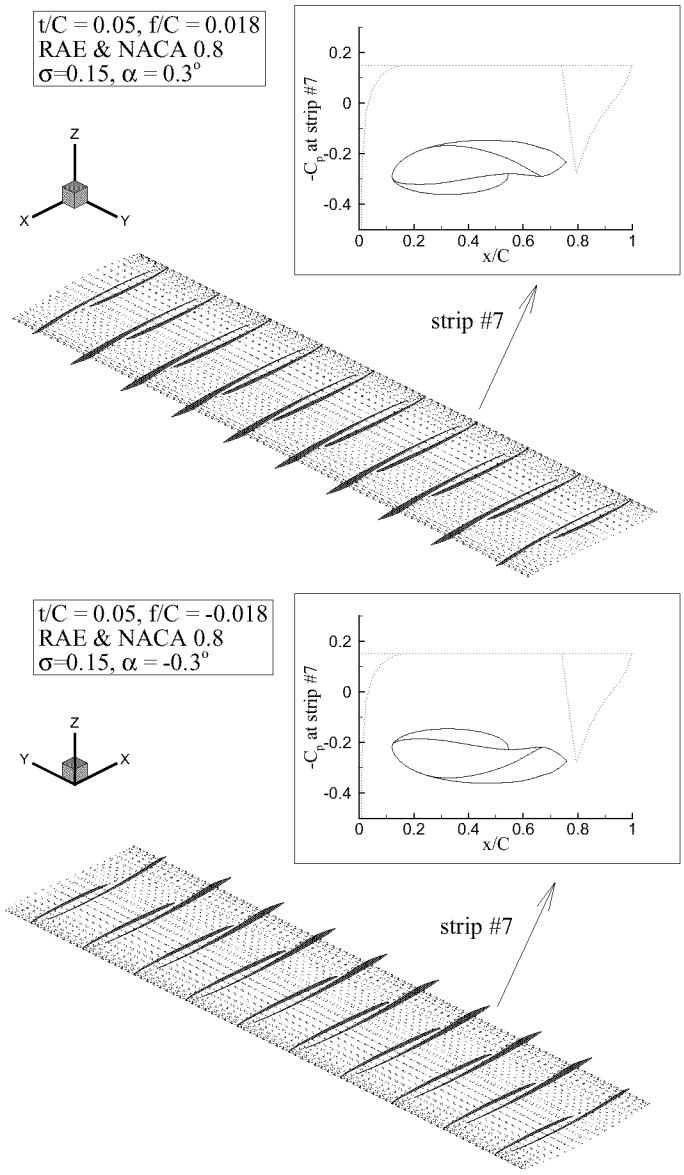


Figure 36: Validation of simultaneous face and back cavitation on an asymmetric rectangular hydrofoil. 50X10 panels. $\alpha = \pm 0.3^o$. $f/C = \pm 0.018$ (NACA0.8). $t/C = 0.05$ (RAE). $\sigma_v = 0.15$. From (Young & Kinnas 2001).

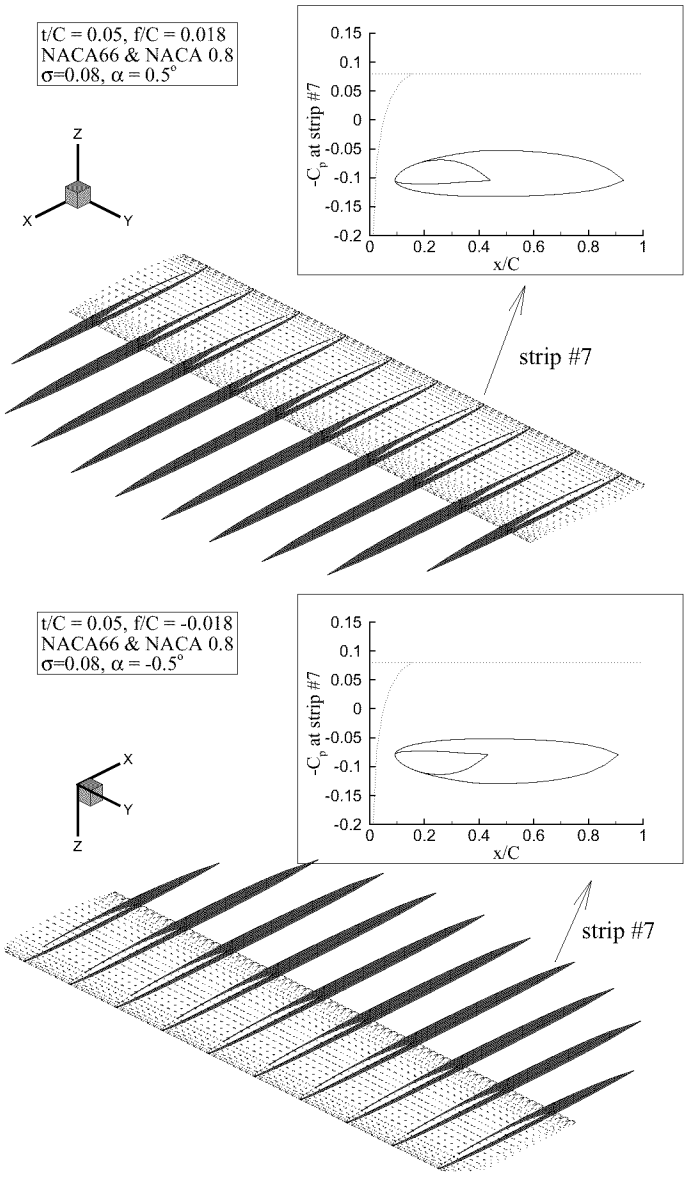


Figure 37: Validation of simultaneous face and back cavitation on an asymmetric rectangular hydrofoil. 50X10 panels. $\alpha = \pm 0.5^o$. $f/C = \pm 0.018$ (NACA0.8). $t/C = 0.05$ (NACA66). $\sigma_v = 0.08$. From (Young & Kinnas 2001).

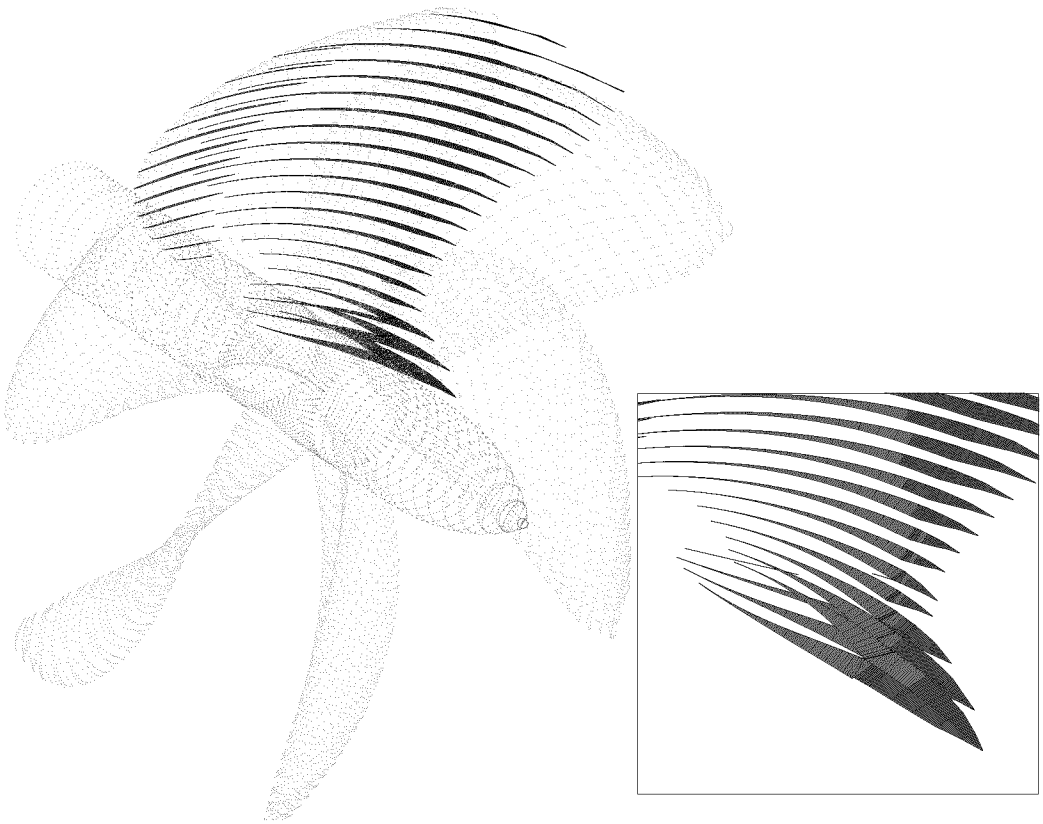


Figure 38: Predicted 3-D cavity shape for propeller MW1. The propeller is based on a design by Michigan Wheel Corporation, USA. 60x20 panels. $J_S = 1.224$. $\sigma_n = 0.8116$. $F_r = 25.6$. Uniform inflow.From (Young & Kinnas 2001).

is applied on the wetted blade surfaces. PROPCAV also has the ability to search for cavity detachments on both sides of the blade simultaneously.

Validation test for an asymmetric 3-D hydrofoil [18] with $\pm 1.8\%$ camber (f/C) and $\sigma_v = 0.15$ (based on the speed of the uniform inflow) at an angle of attack of $\pm 0.3^o$ is shown in Figure 36. As expected, the predicted cavity shapes are identical mirror images of each other. The same validation test was performed for another asymmetric 3-D hydrofoil at an angle of attack of $\pm 0.5^o$ with $\pm 1.8\%$ camber and $\sigma_v = 0.08$. The results are shown in Figure 37. Note that for both cases, the smooth detachment criterion are satisfied on both sides of the 3-D hydrofoil.

An example of simultaneous face and back cavitation for propeller MW1 is shown in Figure 38. The propeller geometry is based on a design by Michigan Wheel Corporation, USA (Young & Kinnas 2001). The flow conditions were as follows: $J_S = 1.224$, $\sigma_n = 0.8116$, uniform inflow. Notice that for this propeller, there is midchord supercavitation on the suction side of the blade, and leading partial cavitation as well as midchord supercavitation on the pressure side of the blade. To validate the solution, the convergence of the predicted cavities (on the back side of the blade) and forces with respect to the number of panels are shown in Figure 39.

[18] For validation studies, PROPCAV has an option where the numerical method is applied on a 3-D hydrofoil.

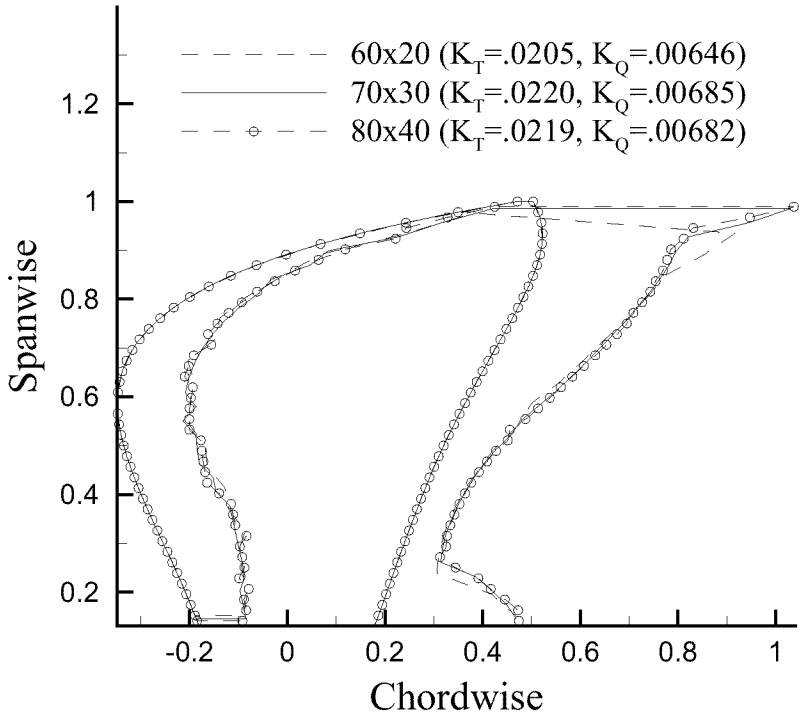
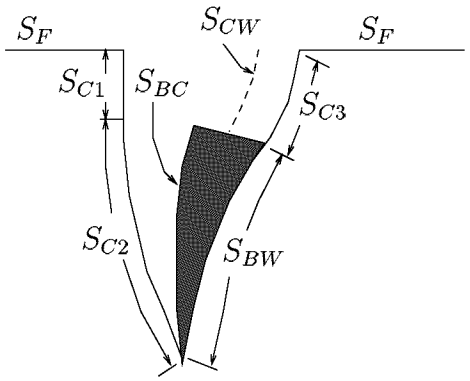


Figure 39: The convergence of predicted cavities (expanded view) and forces with respect to number of panels for propeller MW1. The propeller is based on a design by Michigan Wheel Corporation, USA. $J_S = 1.224$. $\sigma_n = 0.8116$. $F_r = 25.6$. Uniform inflow. From (Young & Kinnas 2001).



$$S \equiv S_F \cup S_{C1} \cup S_{C2} \cup S_{C3} \cup S_{BW}$$

Figure 40: Definition of exact and approximated flow boundary

6 SURFACE-PIERCING PROPELLER

6.1 Formulation

Consider a surface-piercing propeller subjected to a general non-axisymmetric inflow. For incompressible and inviscid flow, the perturbation potential, ϕ, at any time t satisfies Laplace's equation in the fluid domain:

$$\nabla^2\phi(x,y,z,t) = 0 \tag{111}$$

where (x,y,z) are the propeller fixed coordinates.

The perturbation potential, ϕ_p, at every point p on the combined wetted blade surface (S_{BW}), ventilated cavity surface ($S_{C1} \cup S_{C2} \cup S_{C3}$), and free surface ($S_F$), must satisfy Green's third identity:

$$2\pi\phi_p(t) = \int\int_{S(t)} \left[\phi_q(t)\frac{\partial G(p;q)}{\partial n_q(t)} - G(p;q)\frac{\partial \phi_q(t)}{\partial n_q(t)}\right] dS \tag{112}$$

where $S \equiv (S_{BW} \cup S_{C1} \cup S_{C2} \cup S_{C3} \cup S_F)$ is the combined surfaced as defined in the blade section example shown on Figure 40. The subscript q corresponds to the variable point in the integration. $G(p;q) = 1/R(p;q)$ is Green's function with $R(p;q)$ being the distance between points p and q. $\vec{n}_q$ is the unit vector normal to the integration surface.

Equation 112 should be applied on the "exact" cavity surface [19] ($S_{C1} \cup S_{C2} \cup S_{C3}$), as shown in Figure 40. However, the cavity surface is not known and has to be determined as part of the solution. In this work, an approximated cavity surface (on which the panels of the boundary element method are placed) is used. The approximated cavity surface is comprised of the blade surface underneath the cavity on the blade, $S_{C2} \rightarrow S_{BC}$, and the portion of the wake surface which is overlapped by the cavity, $(S_{C1} \cup S_{C3}) \rightarrow S_{CW}$. The definition of S_{BC} and S_{CW} are also shown in Figure 40. The justification for making this approximation, as well as a measure of its effect on the cavity solution, can be found in (Kinnas & Fine 1993) and (Fine 1992).

6.1.1 Linearized free surface boundary condition on the free surface, S_F

The linearized free surface boundary condition requires that:

$$\frac{\partial^2\phi}{\partial t^2} + g\frac{\partial\phi}{\partial\eta} = 0 \tag{113}$$

where η is the free surface elevation. Assuming infinite Froude number condition applies, Equation 113 reduces to:

$$\phi = 0 \qquad \text{on the free surface} \tag{114}$$

[19] The ventilated surface will be referred to as the cavity surface in this work.

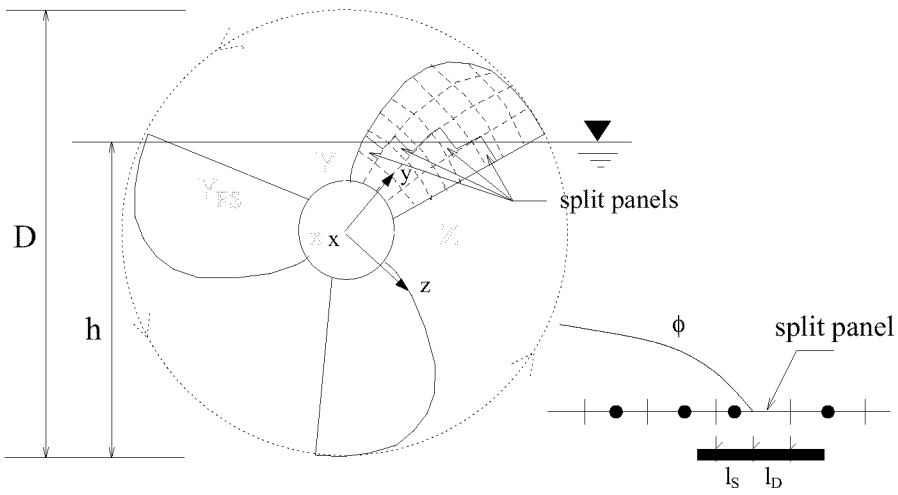


Figure 41: Definition of global (X,Y,Z) and local (x,y,z) coordinate systems and parameters for the split-panel technique.

Equation 114 implies that the "negative" image method can be used to account for the effect of the free surface. The infinite Froude number assumption is valid because surface-piercing propellers usually operate at very high speeds. (Shiba 1953) and (Yim 1974) have also concluded that gravity effects are negligible for Froude numbers greater than 3.

6.2 Solution algorithm

The unsteady ventilated cavity problem is solved by inverting equations 97 and 101 (where S_W should be eliminated from the limits of the integrals) subjected to the boundary conditions 99, 100, 108, 109, 106 (where σ_n in the expression for q_c, equation 103, must be evaluated by replacing P_v with the atmospheric pressure, P_{atm}, as this is the pressure inside the ventilated surface), and 114 (enforced via the negative images of the panels). On the wetted blade surface, ϕ is unknown and $\frac{\partial\phi}{\partial n}$ is known. On the ventilated cavity surface, ϕ is known and $\frac{\partial\phi}{\partial n}$ is unknown. To simplify the solution algorithm, ϕ and $\frac{\partial\phi}{\partial n}$ on the "dry" part of blades are set equal to zero. Thus, the number of unknowns is reduced to the number of fully submerged panels on the blade and on the wake. After solving Equations 97 and 101, the cavity heights are then determined by applying the kinematic boundary condition (Equation 108) on the ventilated cavity surface.

6.2.1 Split-panel technique

One of the difficulties in the numerical modeling of surface-piercing propellers involves the discretization of the blade and wake surfaces. The nature of the problem is highly unsteady due to the blades' entry to and exit from the free surface. The split-panel technique, which was introduced by (Kinnas & Fine 1993) for approximating the trailing edge of cavity planform. The partially submerged panels are *split* into a dry part and a submerged part, as shown in Figure 41. The lengths of the split-panels at their midspans are l_D and l_S, respectively. The source and dipole strengths on the split-panels (ϕ_{sp} and $\frac{\partial\phi}{\partial n}_{sp}$) are defined as weighted averages of the values on the dry part and the submerged part of the panel:

$$\begin{aligned} \phi_{sp} &= \frac{\phi_S l_S + \phi_D l_D}{l_S + l_D} \\ \frac{\partial\phi}{\partial n}_{sp} &= \frac{\frac{\partial\phi}{\partial n}_S l_S + \frac{\partial\phi}{\partial n}_D l_D}{l_S + l_D} \end{aligned} \tag{115}$$

The quantities ϕ_D and $\frac{\partial\phi}{\partial n}_D$ are set equal zero because they represent the dry part of the panel. If the split-panel is located on the wetted side of the blade, then $\frac{\partial\phi}{\partial n}_S$ is known via the kinematic boundary condition (Equation 89) and ϕ_S is extrapolated from adjacent panels; if the split-panel is located on the ventilated side of the blade, then ϕ_S is known via the dynamic boundary condition (Equation 103) and $\frac{\partial\phi}{\partial n}_S$ is extrapolated from adjacent panels.

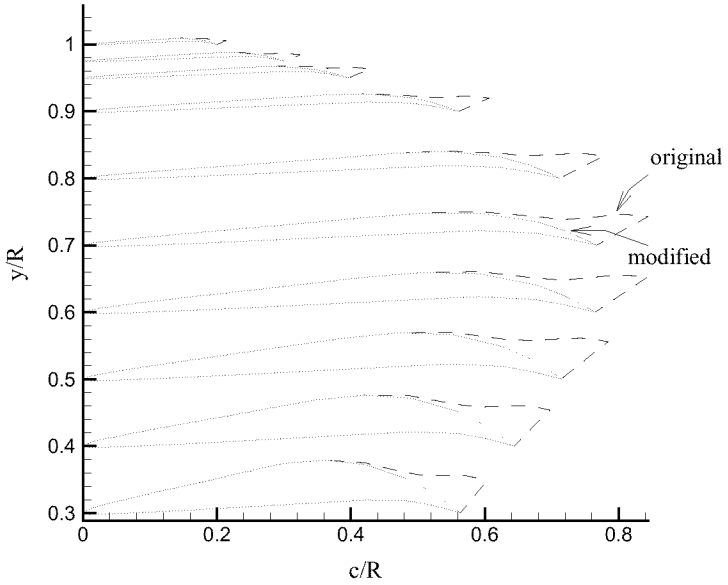


Figure 42: Original and modified (on the suction side aft the midchord) blade section geometry of propelle model 841-B.

The split-panel technique has the advantage that it allows the free surface to be relatively smooth without the added burden of recomputing influence coefficients at every timestep.

6.3 Results

In order to validate the new extension of PROPCAV, numerical results for the surface-piercing propeller model 841-B, already shown in Figure 3, are compared with experimental data. The experiments were conducted at the free-surface cavitation tunnel at KaMeWa of Sweden (Olofsson 1996). The flow conditions were as follows:

$$\begin{aligned} \textit{advance coefficient}: &\quad J_S = 0.8 \\ \textit{submergence ratio}: &\quad h/D = 0.33 \\ \textit{shaft yaw angle}: &\quad \psi = 0^o \\ \textit{shaft inclination angle}: &\quad \gamma = 0^o \end{aligned}$$

In the numerical calculation, the blade section was modified from the original aft of the midchord, as shown in Figure 42, in order to render zero trailing edge thickness. Furthermore, the code is still in the developmental stage. Thus, the current results do not include the effect of the partially submerged panels.

Preliminary force predictions for propeller model 841-B are shown in Figure 43 along with experimental data from (Olofsson 1996). The solid lines in Figure 43 represent the force coefficients predicted by PROPCAV at different blade angles. The symbols in Figure 43 represent the measured force coefficients. As shown in Figure 43, the maximum force coefficients predicted by PROPCAV seemed to be in reasonable agreement with experimental measurements. However, there are discrepancies at the blade entry and exit. The authors believe that the discrepancies at the blade entry are due to the effects of free surface up-ward jets and blade vibrations, both of which are not captured with the current numerical model. The discrepancies at the blade exit are probably due to the modified blade sections aft of the midchord and the change in free surface elevation. The sensitivity of the results on the discretization parameters can be found in (Young & Kinnas 2000).

The fully submerged panels for the key blade are shown in Figure 44. The resulting pressure contours on the wetted side of the blade are depicted in Figure 45. The predicted ventilated surface sections at different timesteps are shown in Figure 46.

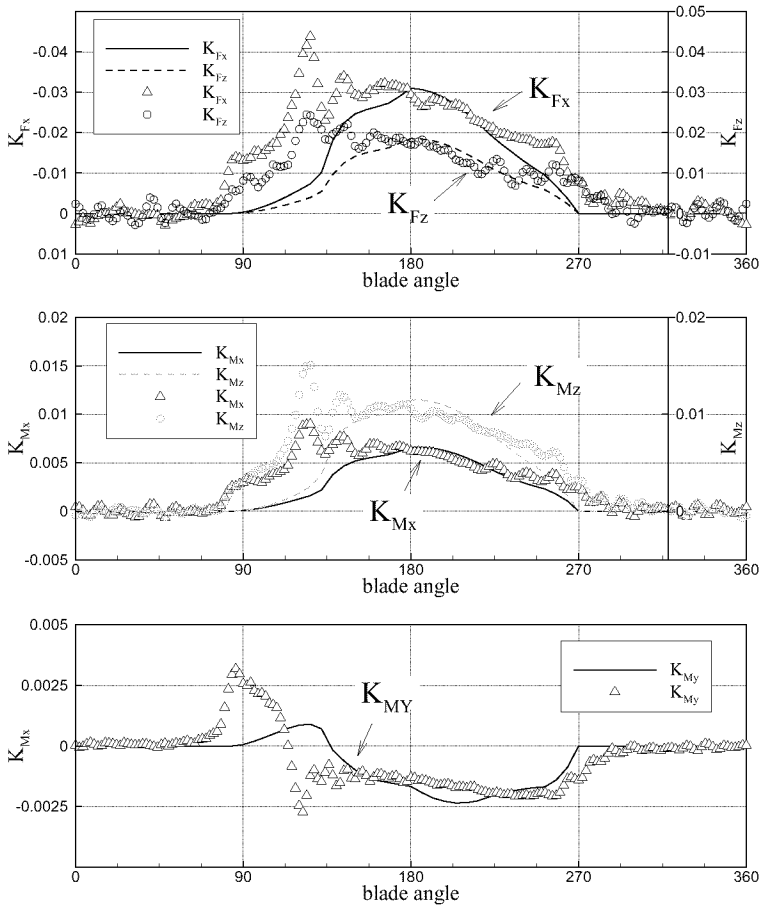


Figure 43: Preliminary comparison of the blade forces predicted by PROPCAV and by measurements from experiments. Propeller model 841-B. 4 Blades. $h/D = 0.33$. $J_S = 0.8$. 60x20 panels. $\Delta\theta = 6^o$.

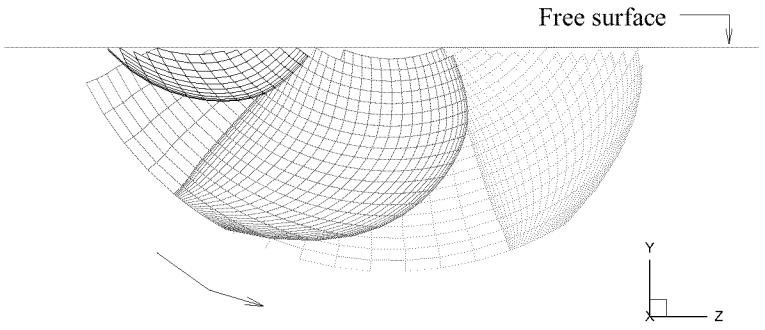


Figure 44: Fully submerged panels on the key blade at different time steps. Propeller model 841-B. 4 Blades. $h/D = 0.33$. $J_S = 0.8$. 60x20 panels. $\Delta\theta = 6^o$.

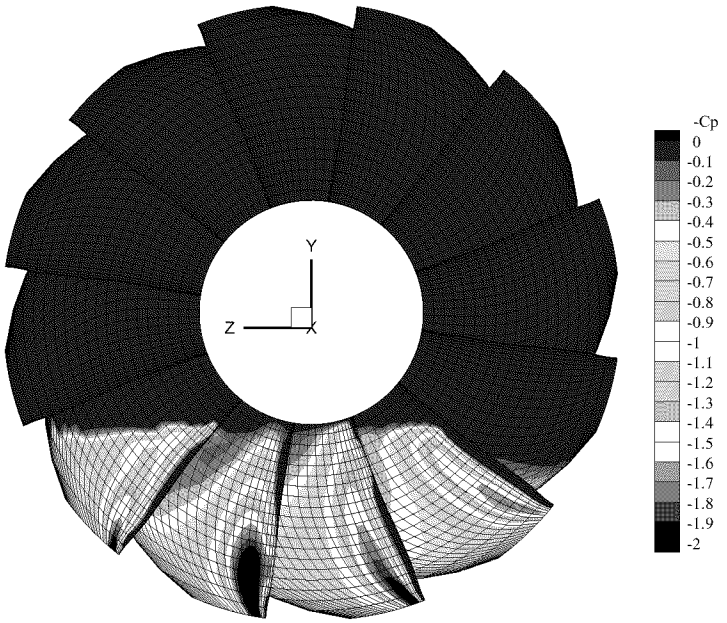


Figure 45: Preliminary pressure contours predicted by PROPCAV. Propeller model 841-B. 4 Blades. $h/D = 0.33$. $J_S = 0.8$. 60x20 panels. $\Delta\theta = 6^o$.

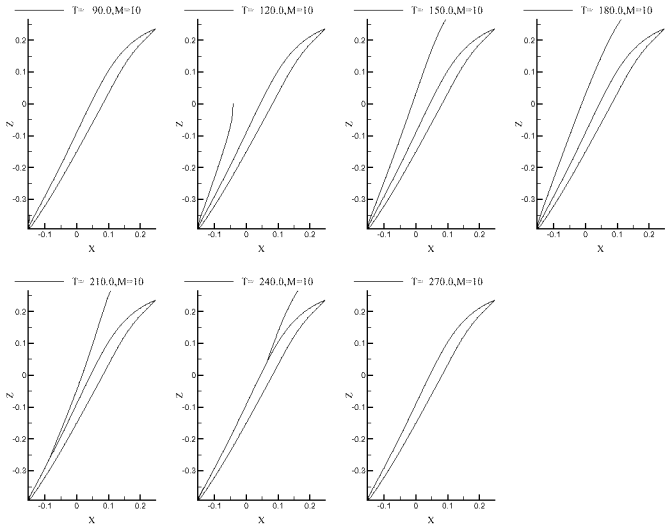


Figure 46: Preliminary ventilated surface sections at $r/R = 0.52$. Propeller model 841-B. 4 Blades. $h/D = 0.33$. $J_S = 0.8$. 60x20 panels. $\Delta\theta = 6^o$.

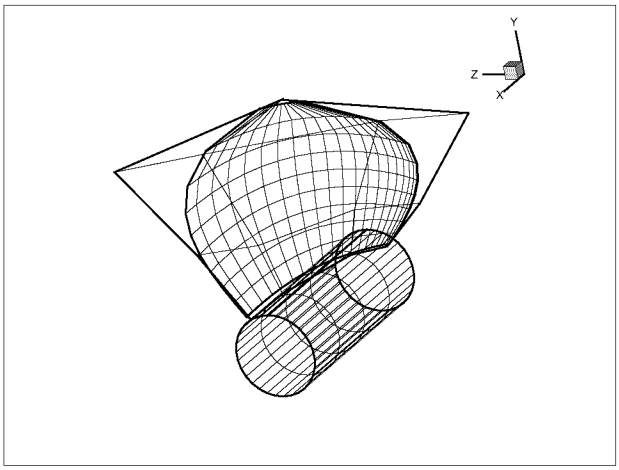


Figure 47: B-spline polygon and the paneled blade geometry in CAVOPT-3D/MPUF-3A.

7 DESIGN OF SUPER-CAVITATING PROPELLER

An optimization method (CAVOPT-3D), similar to that for supercavitating hydrofoil sections, has been developed (Mishima 1996, Mishima & Kinnas 1997). The coefficients of the objective function are determined in terms of second order Taylor expansions from the results of MPUF-3A, a vortex and source lattice method for cavitating propellers in unsteady flow (Kinnas et al 1998a). This method determines *both* the optimum cavitating propeller loading *and* the corresponding blade geometry at the same time. The blade mean camber surface is modeled with a 4x4 cubic B-spline vertex polygon net (Mishima 1996) (Griffin 1998), as shown in Figure 47. This allows the blade surface to be modeled with relatively few number of parameters when compared with the traditional method[20] of describing the blade geometry. The location of each of the B-Spline vertices, and thus the radial chord distribution, as well as the three-dimensional blade camber distribution, are determined during the design process. The skew distribution can be either fixed or specified (as parabolic or linear) up to a constant which can be also determined by the optimization. The maximum thickness to diameter ratio along the radial direction must be specified (using structural criteria) together with the blade thickness section shapes.

The objective function to be minimized is:

$$f(\mathbf{x}) = K_Q(\mathbf{x})$$

where $K_Q(\mathbf{x})$ is the torque coefficient obtained from *MPUF-3A*(Kinnas et al 1998a) and $\mathbf{x}$ is the design variable vector defining the the blade B-spline polygon (usually 13).

$$\mathbf{x} = [x_1, x_2, x_3, ..., x_{13}]^T$$

The equality constraint function is defined as

$$h_1(\mathbf{x}) = \frac{K_T(\mathbf{x}) - K_{To}}{K_{To}} = 0$$

where K_{To} is the required thrust coefficient and $K_T(\mathbf{x})$ is the computed thrust coefficient from *MPUF-3A*. The functions of the equality and inequality constraints are denoted as $h_i(\mathbf{x})$ and $g_i(\mathbf{x})$, respectively. *CAVOPT-3D* currently has the option of employing five inequality constraints, defined as

$$Cavity\ area \leq CAMAX$$
$$Face\ cavity\ area \leq FAMAX$$

[20]Span-wise values of pitch, rake, skew, chord, maximum thickness, maximum camber and chord-wise distributions of camber and thickness.

$$
\begin{aligned}
Max.skew &\leq SKMAX \\
Cavity\ volume\ velocity &\leq VVMAX \\
\sigma_n - (-C_{p,min}) &> PTOL
\end{aligned}
\tag{116}
$$

where the values on the left hand side are the values computed from *MPUF-3A* and the values on the right hand side are the user-specified limits to the left hand side values. The cavity area constraints CAMAX and FAMAX represent the maximum allowable back and face cavity area (as a fraction of the blade area), respectively. VVMAX corresponds to the maximum allowable blade rate cavity volume velocity harmonic, non-dimensionalized by nR^3. SKMAX corresponds to the maximum allowable skew at the tip of the blade. An option for quadratic or linear skew distribution is also available. $-C_{p,min}$ is the value of $-C_p$ at a location on the fully wetted part of the blade where the pressure is minimum (over all blade angles), and $PTOL$ is a specified tolerance.

The required input design variables required by *CAVOPT-3D* to set-up the design model are given as:

- advance coefficient (J_S)
- cavitation number (σ_n)
- Froude number (F_r)
- number of blades (Z)
- hub radius (r_H)
- required thrust coefficient (K_{To})
- inflow wake distribution

7.1 Application

The 3-D method has been applied extensively for the design of conventional propellers (Griffin & Kinnas 1998), (Kinnas et al 1999b), and more recently for the design of a supercavitating propeller (Kinnas et al 1999a). The SRI propeller Model No. 345 (Kudo & Ukon 1994), is used as the base for the supercavitating propeller design. It is identified here as the SRI/SSPA propeller, since the SSPA charts (Rutgersson 1979) were used to design it.

The original thickness distribution, as shown in Figure 48 has been used as input in *CAVOPT-3D*. We have forced leading-edge cavity detachment in *MPUF-3A*. The same design conditions as those of the SRI propeller are used for *CAVOPT-3D*.

These are:

$$
\begin{aligned}
J_S = 1.1,\ \sigma_n = 0.484,\ F_r = 5.0 \\
Z = 3,\ r_H/R = 0.19,\ K_{To} = 0.175
\end{aligned}
$$

Uniform inflow is used. For these conditions MPUF-3A predicts $K_T = 0.175$ and $\eta = 69.4\%$. The corresponding predicted cavity planform is shown in Figure 49.

The designed geometry by CAVOPT-3D is shown in Figures 50, 51, while a summary sheet from the design run is shown in Figure 52 (in which the predicted cavity planform is shown at the lower right bottom).

The following things should be noted:

- The new design has a substantially larger efficiency, 74.7%, i.e. increase in efficiency of over 7%.
- The new design has a wider blade area and a lower pitch (for the same thrust)
- The predicted cavities for the new design are thinner at the leading edge as well as at the trailing edge, thus resulting into a smaller cavity drag (thus higher efficiency overall). This design philosophy has actually been applied by (Vorus & Mitchell 1994).
- The new design may lead to midchord cavitation (due to the very thin cavities especially towards the outer radii) and this will increase its frictional drag, and degrade somewhat the expected higher efficiency.

This case, and some more shown in (Kosal 1999), demonstrate that that *CAVOPT-3D* can obtain blade geometries with higher values of efficiency when compared to geometries designed with other methods.

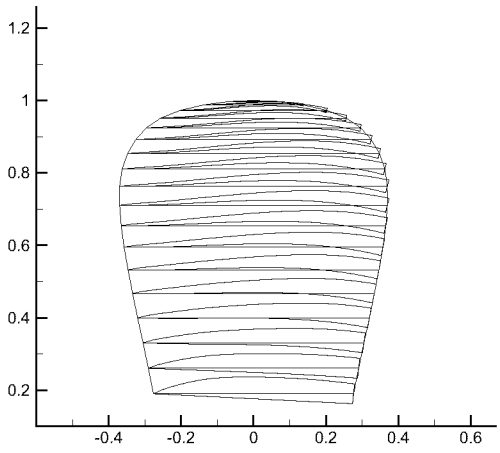


Figure 48: Blade contour and cross-sections of SRI/SSPA propeller.

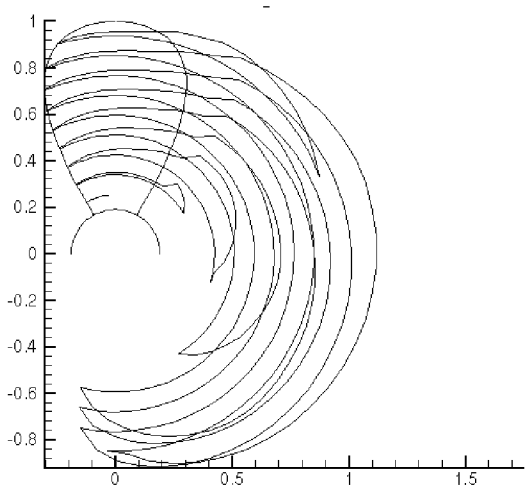


Figure 49: Cavity plan-form for SRI propeller;$J_S = 1.1$, $\sigma_n = 0.484$.

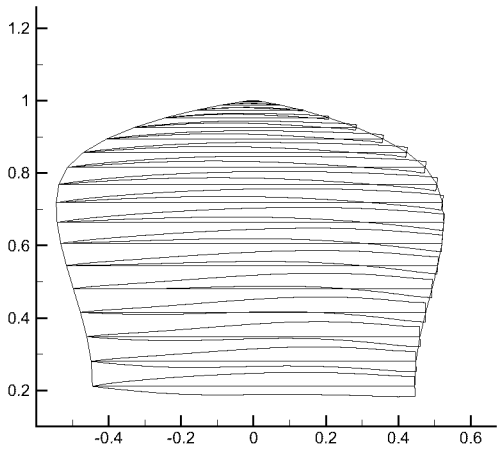


Figure 50: Blade contour and cross-sections of propeller design by CAVOPT-3D.

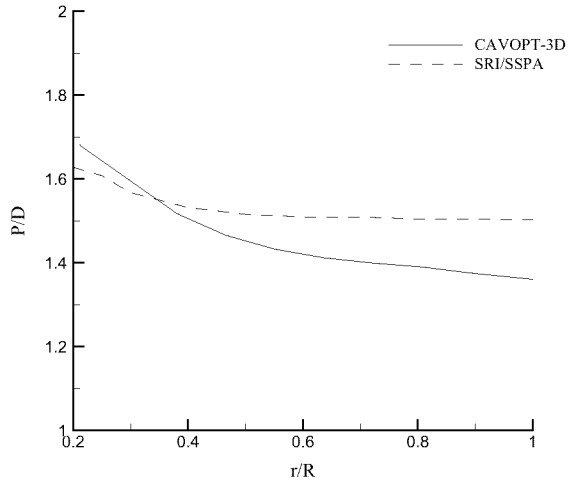


Figure 51: Pitch distributions for SRI/SSPA and CAVOPT-3D designs.

REFERENCES

ABBOTT, I. AND VON DOENHOFF, A. 1959 *Theory of Wing Sections.* Dover, New York.

ACHKINADZE, A. AND FRIDMAN, G. 1994 Artifical variation problems method for three-dimensional lifting cavity flows. *Proceedings:* Twentieth Symposium on Naval Hydrodynamics. August, 466–476.

BAL, S., KINNAS, S. AND LEE, H. 2001 Numerical analysis of 2-D and 3-D cavitating hydrofoils under a free surface. *Journal of Ship Research*, **45**, 1, March, 34–49.

BIRKHOFF, G. AND ZARANTONELLO, E. 1957 *Jets, Wakes and Cavities.* Academic Press Inc., New York.

BRESLIN, J., VAN HOUTEN, R., KERWIN, J. AND JOHNSSON, C.-A. 1982 Theoretical and experimental propeller-induced hull pressures arising from intermittent blade cavitation, loading, and thickness. *Trans. SNAME*, **90**.

CHOI, J.-K. AND KINNAS, S. 1998 Numerical water tunnel in two and three dimensions. *Journal of Ship Research*, **42**, 2, June, pp. 86–98.

CHOI, J.-K. AND KINNAS, S. 1999 Numerical model of a cavitating propeller inside of a tunnel. *Journal of Fluids Engineering*, **121**, June, 297–304.

CHOI, J.-K. AND KINNAS, S. 2001 Prediction of non-axisymmetric effective wake by a 3-D Euler solver. *Journal of Ship Research*, **45**, 1, March, 13–33.

CHOI, J. 2000 Vortical inflow – propeller interaction using unsteady three-dimensional euler solver. Doctoral dissertation, Department of Civil Engineering, The University of Texas at Austin. August.

COMSTOCK, J., Ed. 1967 *Principles of Naval Architecture.* Society of Naval Architects and Marine Engineers.

DESHPANDE, M., FENG, J. AND MERKLE, C. 1993 Navier-stokes analysis of 2-d cavity flow. *Proceedings:* Cavitation and Multiphse Flow Forum. FED-154, ASME, 149–155.

DRELA, M. 1989 Integral boundary layer formulation for blunt trailing edges. *AIAA paper*, **89-2200**.

FABULA, A. 1962 Thin-airfoil theory applied to hydrofoils with a single finite cavity and arbitrary free streamline detachment. *Journal of Fluid Mechanics*, **vol 12**, pp 227–240.

FINE, N. E. 1992 Nonlinear analysis of cavitating propellers in nonuniform flow. Doctoral dissertation, Department of Ocean Engineering, MIT. October.

FINE, N. AND KINNAS, S. 1993a A boundary element method for the analysis of the flow around 3-d cavitating hydrofoils. *Journal of Ship Research*, **37**, September, 213–224.

FINE, N. AND KINNAS, S. 1993b The nonlinear numerical prediction of unsteady sheet cavitation for propellers of extreme geometry. *Proceedings:* Sixth International Conference On Numerical Ship Hydrodynamics. August, 531–544.

FURUYA, O. 1975a Nonlinear calculation of arbitrarily shaped supercavitating hydrofoils near a free surface. *Journal of Fluid Mechanics*, **vol. 68**, pp 21–40.

FURUYA, O. 1975b Three-dimensional theory on supercavitating hydrofoils near a free surface. *Journal of Fluid Mechanics*, **71**, pp. 339–359.

GEURST, J. 1960 Linearized theory for fully cavitated hydrofoils. *International Shipbuilding Progress*, **vol 7**, No. 65, January.

GRIFFIN, P. 1998 Computational techniques for the design and analysis of cavitating propeller blades. Masters thesis, UT Austin, Dept. of Civil Engineering. May.

GRIFFIN, P. AND KINNAS, S. 1998 A design method for high-speed propulsor blades. *Journal of Fluids Engineering*, **120**, September, 556–562.

HANAOKA, T. 1964 Linearized theory of cavity flow past a hydrofoil of arbitrary shape. *Journal of the Society of Naval Architects, Japan*, **vol. 115**, June, pp. 56–74.

HUFFORD, G., DRELA, M. AND KERWIN, J. 1994 Viscous flow around marine propellers using boundary-layer strip theory. *Journal of Ship Research*, **38**, 1, March, pp. 52–62.

ISHII, N. 1992 Prediction of propeller performance and cavitation based on the numerical modeling of propeller vortex system. *Proceedings:* International Symposium on Propulsors and Cavitation. pp. 33–41.

JIANG, C. AND LEEHEY, P. 1977 A numerical method for determining forces and moments on supercavitating hydrofoils of finite span. *Proceedings:* Second Int'l Conf. Numer. Ship Hydrodynamics. September.

KATO, H. 1994 Recent advances in cavitating foil research. *Proceedings:* International Conference on Hydrodynamics. pp. 80–89.

KATO, H. 1996 *Cavitation.* Computational Mechanics Publications. in Advances in Marine Hydrodynamics. Chap. 5, pp 233–277.

KERWIN, J., KINNAS, S., WILSON, M. AND MCHUGH, J. 1986 Experimental and analytical techniques for the study of unsteady propeller sheet cavitation. *Proceedings:* Proceedings of the Sixteenth Symposium on Naval Hydrodynamics. July, 387–414.

KIM, Y.-G. AND LEE, C.-S. 1996 Prediction of unsteady performance of marine propellers with cavitation using surface-panel method. *Proceedings:* 21st Symposium on Naval Hydrodynamics. June.

KIM, Y.-G., LEE, C.-S. AND SUH, J.-C. 1994 Surface panel method for prediction of flow around a 3-d steady or unsteady cavitating hydrofoil. *Proceedings:* Second International Symposium on Cavitation. April 5-7, 113–120.

KINNAS, S. 1985 Non-linear corrections to the linear theory for the prediction of the cavitating flow around hydrofoils. Doctoral dissertation, Department of Ocean Engineering, MIT. May.

KINNAS, S. 1991 Leading-edge corrections to the linear theory of partially cavitating hydrofoils. *Journal of Ship Research*, **35**, 1, March, pp. 15–27.

KINNAS, S. 1992a Inversion of the source and vorticity equations for supercavitating hydrofoils. *Journal of Engineering Mathematics*, **26**, 349–361.

KINNAS, S. 1992b Leading edge correction to the linear theory of cavitating hydrofoils and propellers. *Proceedings:* Second International Symposium on Propeller and Cavitation. September.

KINNAS, S. 1998 Prediction of unsteady sheet cavitation. *Proceedings:* Third International Symposium on Cavitation. April 7-10, 19–36.

KINNAS, S. AND FINE, N. 1991a Analysis of the flow around supercavitating hydrofoils with midchord and face cavity detachment. *Journal of Ship Research*, **35**, 3, September, pp. 198–209.

KINNAS, S. AND FINE, N. 1991b Non-Linear Analysis of the Flow Around Partially or Super-Cavitating Hydrofoils by a Potential Based Panel Method. *Proceedings:* Boundary Integral Methods-Theory and Applications, Proceedings of the IABEM-90 Symposium, Rome, Italy, October 15-19, 1990. Springer-Verlag, Heidelberg, 289–300.

KINNAS, S. AND FINE, N. 1992 A nonlinear boundary element method for the analysis of unsteady propeller sheet cavitation. *Proceedings:* Nineteenth Symposium on Naval Hydrodynamics. August, 717–737.

KINNAS, S. AND FINE, N. 1993 A numerical nonlinear analysis of the flow around two- and three-dimensional partially cavitating hydrofoils. *Journal of Fluid Mechanics*, **254**, September, 151–181.

KINNAS, S. AND HSIN, C.-Y. 1992 A boundary element method for the analysis of the unsteady flow around extreme propeller geometries. *AIAA Journal*, **30**, 3, March, 688–696.

KINNAS, S. AND MAZEL, C. 1992 Numerical vs. experimental cavitation tunnel (a supercavitating hydrofoil experiment). *Proceedings:* 23rd American Towing Tank Conference. June 11-12.

KINNAS, S., MISHIMA, S. AND BREWER, W. 1994 Nonlinear analysis of viscous flow around cavitating hydrofoils. *Proceedings:* Twentieth Symposium on Naval Hydrodynamics. August, 446–465.

KINNAS, S., MISHIMA, S. AND SAVINEAU, C. 1995 Application of optimization techniques to the design of cavitating hydrofoils and wings. *Proceedings:* CAV'95 International Symposium on Cavitation. May 2-5, 135–143.

KINNAS, S., GRIFFIN, P., CHOI, J.-K. AND KOSAL, E. 1998a Automated design of propulsor blades for high-speed ocean vehicle applications. *Trans. SNAME*, **106**.

KINNAS, S., LEE, H. AND MUELLER, A. 1998b Prediction of propeller blade sheet and developed tip vortex cavitation. *Proceedings:* 22nd Symposium on Naval Hydrodynamics. August 9-14, 182–198.

KINNAS, S., KOSAL, E. AND YOUNG, J. 1999a Computational techniques for the design and analysis of super-cavitating propellers. *Proceedings:* FAST'99 - 5th International Conference on Fast Sea Transportation. August 31-September 2.

KINNAS, S., CHOI, J.-K., KOSAL, E., YOUNG, J. AND LEE, H. 1999b An integrated computational technique for the design of propellers with specified constraints on cavitation extent and hull pressure fluctuations. *Proceedings:* CFD99 - The International CFD Conference. June 5-7.

KINNAS, S., CHOI, J., LEE, H. AND YOUNG, J. 2000 Numerical Cavitation Tunnel. *Proceedings:* NCT'50, International Conference on Propeller Cavitation. April 3-5, 137–157.

KOSAL, E. 1999 Improvements and enhancements in the numerical analysis and design of cavitating propeller blades. Masters thesis, UT Austin, Dept. of Civil Engineering. May. Also, UT Ocean Eng. Report 99-1.

KRISHNASWAMY, P. 1999 Re-entrant jet and viscous flow modeling for partially cavitating hydrofoils. Technical report. No. 99-3. Ocean Eng. Group, Department of Civil Engineering, UT Austin. June.

KUBOTA, A., KATO, H. AND YAMAGUCHI, H. 1989 Finite difference analysis of unsteady cavitation on a two-dimensional hydrofoil. *Proceedings:* Fifth International Conference on Numerical Ship Hydrodynamics. September, 667–683.

KUDO, T. AND UKON, Y. 1994 Calculation of supercavitating propeller performance using a vortex-lattice method. *Proceedings:* Second International Symposium on Cavitation. April 5-7, 403–408.

LEE, C.-S. 1979 Prediction of steady and unsteady performance of marine propellers with or without cavitation by numerical lifting surface theory. Doctoral dissertation, M.I.T., Department of Ocean Engineering. May.

LEE, C.-S. 1981 Prediction of the transient cavitation on marine propellers. *Proceedings:* Thirteenth Symposium on Naval Hydrodynamics. 41–64.

LEE, C.-S., KIM, Y.-G. AND LEE, J.-T. 1992 A potential-based panel method for the analysis of a two-dimensional super- or partially- cavitating hydrofoil. *Journal of Ship Research*, **36**, 2, March, pp. 168–181.

LEEHEY, P. 1971 Supercavitating hydrofoil of finite span. *Proceedings:* IUTAM Symposium on Non-Steady Flow of Water at High Speeds. June, 277–298.

LEMONNIER, H. AND ROWE, A. 1988 Another approach in modelling cavitating flows. *Journal of Fluid Mechanics*, **vol 195**.

MATSUDA, N., KUROBE, Y., UKON, Y. AND KUDO, T. 1994 Experimental investigation into the performance of supercavitating propellers. *Papers of Ship Research Institute*, **31**, 5.

MISHIMA, S. 1996 Design of cavitating propeller blades in non-uniform flow by numerical optimization. Doctoral dissertation, M.I.T., Department of Ocean Engineering. September.

MISHIMA, S. AND KINNAS, S. 1996 A numerical optimization technique applied to the design of two-dimensional cavitating hydrofoil sections. *Journal of Ship Research*, **40**, 1, March, pp. 28–38.

MISHIMA, S. AND KINNAS, S. 1997 Application of a numerical optimization technique to the design of cavitating propellers in non-uniform flow. *Journal of Ship Research*, **41**, 2, June, pp. 93–107.

MORINO, L. AND KUO, C.-C. 1974 Subsonic Potential Aerodynamic for Complex Configurations : A General Theory. *AIAA Journal*, **vol 12**, no 2, February, pp 191–197.

MUELLER, A. 1998 Development of face and mid-chord cavitation models for the prediction of unsteady cavitation on a propeller. Masters thesis, UT Austin, Dept. of Civil Engineering. May.

MUELLER, A. AND KINNAS, S. 1999 Propeller sheet cavitation predictions using a panel method. *Journal of Fluids Engineering*, **121**, June, 282–288.

MUSKHELISHVILI, N. I. 1946 *Singular Integral Equations.* P. Noordhoff, Limited, Groningen, Holland.

NISHIYAMA, T. 1970 Lifting line theory of supercavitating hydrofoil of finite span. *ZAMM*, **50**, 645–653.

OHBA, R. 1963/1964 Theory on supercavitating hydrofoils at arbitrary cavitation coefficients. Technical report. Vol. 15. Institute of High Speed Mechanics, Tohoku University.

OLOFSSON, N. 1996 Force and flow characteristics of a partially submerged propeller. Doctoral dissertation, Department of Naval Architecture and Ocean Engineering, Chalmers University of Technology, Göteborg, Sweden. February.

PELLONE, C. AND PEALLAT, J. 1995 Non-linear analysis of three-dimensional partially cavitating hydrofoil. *Proceedings:* CAV'95 International Symposium on Cavitation. May 2-5, 433–440.

PELLONE, C. AND ROWE, A. 1981 Supercavitating hydrofoils in non-linear theory. *Proceedings:* Third International Conference on Numerical Ship Hydrodynamics. Basin d'essais des Carènes, Paris, France, June.

ROWE, A. AND BLOTTIAUX, O. 1993 Aspects of modeling partially cavitating hydrofoils. *Journal of Ship Research*, **37**, 1, pp. 34–48.

RUTGERSSON, O. 1979 Supercavitating propeller performance. SSPA Publication No. 82, Goteborg, Sweden.

SHIBA, H. 1953 Air-drawing of marine propellers. Technical report. 9. Transportation Technical Research Institute. August.

STERN, F. AND VORUS, W. 1983 A nonlinear method for predicting unsteady sheet cavitation on marine propellers. *Journal of Ship Research*, **38**, 1, pp. 56–74.

SZANTYR, J. 1994 A method for analysis of cavitating marine propellers in non-uniform flow. *International Shipbuilding Progress*, **41**, pp. 223–242.

TULIN, M. 1953 Steady two-dimensional cavity flows about slender bodies. Technical report. 834. DTMB. May.

TULIN, M. 1964 Supercavitating flows - small perturbation theory. *Journal of Ship Research*, **vol 7**, No. 3, pp. 16–37.

TULIN, M. AND HSU, C. 1980 New applications of cavity flow theory. *Proceedings:* 13th Symposium on Naval Hydrodynamics.

UHLMAN, J. 1978 A partially cavitated hydrofoil of finite span. *Journal of Fluids Engineering*, **100**, 3, September, pp. 353–354.

UHLMAN, J. 1987 The surface singularity method applied to partially cavitating hydrofoils. *Journal of Ship Research*, **vol 31**, No. 2, June, pp. 107–124.

UHLMAN, J. 1989 The surface singularity or boundary integral method applied to supercavitating hydrofoils. *Journal of Ship Research*, **vol 33**, No. 1, March, pp. 16–20.

VAN GENT, W. 1994 Pressure field analysis of a propeller with unsteady loading and sheet cavitation. *Proceedings:* Twentieth Symposium on Naval Hydrodynamics. August, 355–367.

VAN HOUTEN, R. 1982 The numerical prediction of unsteady sheet cavitation on high aspect ratio hydrofoils. *Proceedings:* 14th Symposium on Naval Hydrodynamics.

VORUS, W. AND MITCHELL, K. 1994 Engineering of power boat propellers. *Proceedings:* Propellers/Shafting '94 Symposium. Society of Naval Architects & Marine Engineers, Virginia Beach, VA, September 20-21, 1–16 (paper No. 12).

WIDNALL, S. 1966 Unsteady loads on supercavitating hydrofoils. *Journal of Ship Research*, **9**, pp. 107–118.

WU, T. 1957 A simple method for calculating the drag in the linear theory of cavity flows. Technical report. No. 85-5. California Institute of Technology, Hydrodynamics Laboratory. August.

WU, T. AND WANG, D. 1964 A wake model for free-streamline flow theory. part 2. cavity flows past obstacles of arbitrary profile. *Journal of Fluid Mechanics*, **vol 18**, pp 65–93.

YAMAGUCHI, H. AND KATO, H. 1983 On application of nonlinear cavity flow theory to thick foil sections. *Proceedings:* Second International Conference on Cavitation. IMechE, 167–174.

YIM, B. 1974 Linear theory on water entry and exit problems of a ventilating thin wedge. *Journal of Ship Research*, **18**, 1, pp. 1–11.

YOUNG, Y. AND KINNAS, S. 2000 Prediction of unsteady performance of surface-piercing propellers. *Proceedings:* Propellers/Shafting 2000 Symposium. Soc. Naval Arch. & Marine Engnrs., Virginia Beach, VA, September 20-21, 1–9 (paper No. 7).

YOUNG, Y. AND KINNAS, S. 2001 A BEM for the Prediction of Unsteady Midchord Face and/or Back Propeller Cavitation. *Journal of Fluids Engineering*, **123**, June. to appear.

YOUNG, Y., LEE, H. AND KINNAS, S. 2001 PROPCAV (version 1.2) user's manual and documentation. Technical report. No. 01-4. Ocean Engineering Group, UT Austin. January.

CAVOPT-3D (v 1.3) OUTPUT

mid28

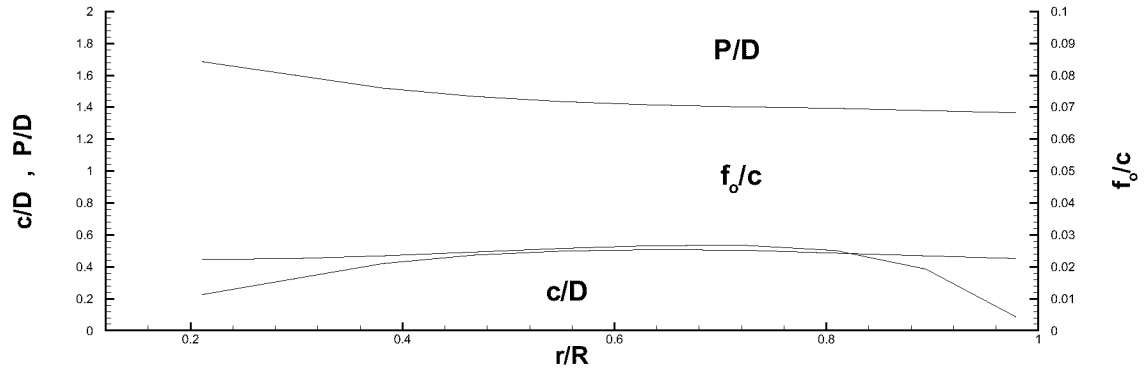
Design Conditions	Design Constraints	Design Parameters
$J_s = 1.100$	PTOL = -0.100	Chord Optimized
$\sigma_n = 0.484$		Skew Fixed (Skew from *.geo file)
$F_n = 5.000$		
NBLADE = 3.		
$r_H/R = 0.190$		
$K_{To} = 0.1750$		

MPUF-3A Parameters

```
MPUF-3A MIDCHORD/TIP/HUB/PROP CAVITATING SEPTEMBER 98 EDITION
------------------------------------------------------------
PROPELLER INPUT GEOMETRY FILE: sspa11  !geometry filename, wi.GEO
Header: -- Surface Piercing, Super-Cavitating Cross Section  11 radii (except 0
WAKE INPUT FILE: uniform !wake filename, withou.WAK
Header: SAMPLE WAKE FOR CAVOPT3D
NPROP=  1  IAXIS=  1  MXREV=  5  NFCON=  1  NN= 20
IHUB=  0 ILEON=  0  NX= 11 MCAM=  1 MTHK=  1 NBLADE=  3 IALIGN=  2
MM=  9  SJ=  1.1000  SIGMAN=  0.4840  FROUDE=  5.0000
```

Final Design

$\eta =$ 0.7468	Blade Angle at Max Cavity Volume = 150°	Max Back Cav Area/Blade Area = 1.2705
$K_Q =$ 0.0409	Max Cavity Vol/R^3 = 0.04588	Max Face Cav Area/Blade Area = 0.0000
$K_T =$ 0.1746	CVV = 0.08570	DPV = -0.06493



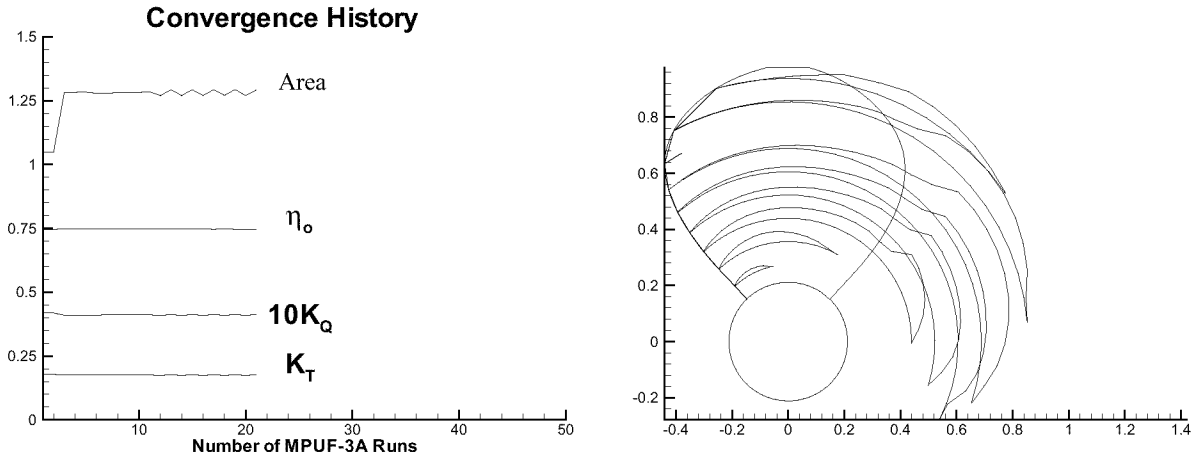


Figure 52: *CAVOPT-3D* design summary sheet. Note that this has been a quadratic run, i.e. a run that used the history of a previous run in which $PTOL = -0.3$.

REPORT DOCUMENTATION PAGE

1. Recipient's Reference	2. Originator's References	3. Further Reference	4. Security Classification of Document
	RTO-EN-010 AC/323(AVT-058)TP/45	ISBN 92-837-1074-6	UNCLASSIFIED/ UNLIMITED

5. Originator

Research and Technology Organisation
North Atlantic Treaty Organisation
BP 25, 7 rue Ancelle, F-92201 Neuilly-sur-Seine Cedex, France

6. Title

Supercavitating Flows

7. Presented at/sponsored by

the Applied Vehicle Technology Panel (AVT) in support of a VKI Lecture Series presented from 12-16 February 2001, at the von Kármán Institute in Brussels, Belgium.

8. Author(s)/Editor(s)	9. Date
Multiple	January 2002
10. Author's/Editor's Address	**11. Pages**
Multiple	558

12. Distribution Statement

There are no restrictions on the distribution of this document. Information about the availability of this and other RTO unclassified publications is given on the back cover.

13. Keywords/Descriptors

Cavitation	Flow distribution	Nonlinear flow
Cavities	High-speed hydrodynamics	Submarines
Cavity flow	Hydrodynamic configurations	Supercavitating flows
CFD (Computational Fluid Dynamics)	Hydrodynamic design	Supercavitating propellers
Compressible fluid	Hydrofoils	Supercavitation
Computerized simulation	Marine propellers	Torpedoes
Drag reduction	Naval architecture	Vortices
		Water flow

14. Abstract

The Lecture Series organized by NATO-RTO and VKI dealt with high speed hydrodynamics and the flow condition of supercavitation. This refers to the generation of large cavities around wetted bodies. Treated were theory, experiment and computation of:

- Supercavitating Motion,
- Variational Methods in Cavitational Flow,
- Independence of the Cavity Sections,
- Logvinovich's principle,
- Nonlinear Supercavitating Flows,
- Artificial Supercavitation,
- Dynamic Processes of Supercavitation,
- Oscillations of Ventilated Cavities,
- Cavity Dynamics,
- Multiphase CFD Modelling,
- Control of Supercavitation Flow,
- Stability of Supercavitating Motion,
- Supercavities in Compressible Fluid,
- Supercavitating Object Propulsion,
- Small Perturbation Theory,
- Supercavitating 2-D and 3-D Hydrofoils,
- Supercavitating Propellers.

Unfortunately only 15 of the original 18 presentations were available for print.

This page has been deliberately left blank

Page intentionnellement blanche

NORTH ATLANTIC TREATY ORGANISATION

RESEARCH AND TECHNOLOGY ORGANISATION
BP 25 • 7 RUE ANCELLE
F-92201 NEUILLY-SUR-SEINE CEDEX • FRANCE
Télécopie 0(1)55.61.22.99 • E-mail mailbox@rta.nato.int

DIFFUSION DES PUBLICATIONS
RTO NON CLASSIFIEES

L'Organisation pour la recherche et la technologie de l'OTAN (RTO), détient un stock limité de certaines de ses publications récentes, ainsi que de celles de l'ancien AGARD (Groupe consultatif pour la recherche et les réalisations aérospatiales de l'OTAN). Celles-ci pourront éventuellement être obtenues sous forme de copie papier. Pour de plus amples renseignements concernant l'achat de ces ouvrages, adressez-vous par lettre ou par télécopie à l'adresse indiquée ci-dessus. Veuillez ne pas téléphoner.

Des exemplaires supplémentaires peuvent parfois être obtenus auprès des centres nationaux de distribution indiqués ci-dessous. Si vous souhaitez recevoir toutes les publications de la RTO, ou simplement celles qui concernent certains Panels, vous pouvez demander d'être inclus sur la liste d'envoi de l'un de ces centres.

Les publications de la RTO et de l'AGARD sont en vente auprès des agences de vente indiquées ci-dessous, sous forme de photocopie ou de microfiche. Certains originaux peuvent également être obtenus auprès de CASI.

CENTRES DE DIFFUSION NATIONAUX

ALLEMAGNE
Streitkräfteamt / Abteilung III
Fachinformationszentrum der Bundeswehr, (FIZBw)
Friedrich-Ebert-Allee 34
D-53113 Bonn

BELGIQUE
Coordinateur RTO - VSL/RTO
Etat-Major de la Force Aérienne
Quartier Reine Elisabeth
Rue d'Evère, B-1140 Bruxelles

CANADA
Services d'information scientifique pour la défense (SISD)
R et D pour la défense Canada
Ministère de la Défense nationale
Ottawa, Ontario K1A 0K2

DANEMARK
Danish Defence Research Establishment
Ryvangs Allé 1, P.O. Box 2715
DK-2100 Copenhagen Ø

ESPAGNE
INTA (RTO/AGARD Publications)
Carretera de Torrejón a Ajalvir, Pk.4
28850 Torrejón de Ardoz - Madrid

ETATS-UNIS
NASA Center for AeroSpace Information (CASI)
Parkway Center
7121 Standard Drive
Hanover, MD 21076-1320

FRANCE
O.N.E.R.A. (ISP)
29, Avenue de la Division Leclerc
BP 72, 92322 Châtillon Cedex

GRECE (Correspondant)
Hellenic Ministry of National Defence
Defence Industry Research & Technology General Directorate
Technological R&D Directorate
D.Soutsou 40, GR-11521, Athens

HONGRIE
Department for Scientific Analysis
Institute of Military Technology
Ministry of Defence
H-1525 Budapest P O Box 26

ISLANDE
Director of Aviation
c/o Flugrad
Reykjavik

ITALIE
Centro di Documentazione Tecnico-Scientifica della Difesa
Via XX Settembre 123a
00187 Roma

LUXEMBOURG
Voir Belgique

NORVEGE
Norwegian Defence Research Establishment
Attn: Biblioteket
P.O. Box 25, NO-2007 Kjeller

PAYS-BAS
NDRCC
DGM/DWOO
P.O. Box 20701
2500 ES Den Haag

POLOGNE
Chief of International Cooperation Division
Research & Development Department
218 Niepodleglosci Av.
00-911 Warsaw

PORTUGAL
Estado Maior da Força Aérea
SDFA - Centro de Documentação
Alfragide
P-2720 Amadora

REPUBLIQUE TCHEQUE
DIC Czech Republic-NATO RTO
VTÚL a PVO Praha
Mladoboleslavská ul.
Praha 9, 197 06, Česká republika

ROYAUME-UNI
Dstl Knowledge Services
Kentigern House, Room 2246
65 Brown Street
Glasgow G2 8EX

TURQUIE
Millî Savunma Başkanliği (MSB)
ARGE Dairesi Başkanliği (MSB)
06650 Bakanliklar - Ankara

AGENCES DE VENTE

NASA Center for AeroSpace Information (CASI)
Parkway Center
7121 Standard Drive
Hanover, MD 21076-1320
Etats-Unis

The British Library Document Supply Centre
Boston Spa, Wetherby
West Yorkshire LS23 7BQ
Royaume-Uni

Canada Institute for Scientific and Technical Information (CISTI)
National Research Council
Document Delivery
Montreal Road, Building M-55
Ottawa K1A 0S2, Canada

Les demandes de documents RTO ou AGARD doivent comporter la dénomination "RTO" ou "AGARD" selon le cas, suivie du numéro de série (par exemple AGARD-AG-315). Des informations analogues, telles que le titre et la date de publication sont souhaitables. Des références bibliographiques complètes ainsi que des résumés des publications RTO et AGARD figurent dans les journaux suivants:

Scientific and Technical Aerospace Reports (STAR)
STAR peut être consulté en ligne au localisateur de ressources uniformes (URL) suivant:
http://www.sti.nasa.gov/Pubs/star/Star.html
STAR est édité par CASI dans le cadre du programme NASA d'information scientifique et technique (STI)
STI Program Office, MS 157A
NASA Langley Research Center
Hampton, Virginia 23681-0001
Etats-Unis

Government Reports Announcements & Index (GRA&I)
publié par le National Technical Information Service
Springfield
Virginia 2216
Etats-Unis
(accessible également en mode interactif dans la base de données bibliographiques en ligne du NTIS, et sur CD-ROM)

Imprimé par St-Joseph Ottawa/Hull
(Membre de la Corporation St-Joseph)
45, boul. Sacré-Cœur, Hull (Québec), Canada J8X 1C6

NORTH ATLANTIC TREATY ORGANISATION

RESEARCH AND TECHNOLOGY ORGANISATION
BP 25 • 7 RUE ANCELLE
F-92201 NEUILLY-SUR-SEINE CEDEX • FRANCE
Telefax 0(1)55.61.22.99 • E-mail mailbox@rta.nato.int

DISTRIBUTION OF UNCLASSIFIED RTO PUBLICATIONS

NATO's Research and Technology Organisation (RTO) holds limited quantities of some of its recent publications and those of the former AGARD (Advisory Group for Aerospace Research & Development of NATO), and these may be available for purchase in hard copy form. For more information, write or send a telefax to the address given above. **Please do not telephone**.

Further copies are sometimes available from the National Distribution Centres listed below. If you wish to receive all RTO publications, or just those relating to one or more specific RTO Panels, they may be willing to include you (or your organisation) in their distribution.

RTO and AGARD publications may be purchased from the Sales Agencies listed below, in photocopy or microfiche form. Original copies of some publications may be available from CASI.

NATIONAL DISTRIBUTION CENTRES

BELGIUM
Coordinateur RTO - VSL/RTO
Etat-Major de la Force Aérienne
Quartier Reine Elisabeth
Rue d'Evère, B-1140 Bruxelles

CANADA
Defence Scientific Information Services (DSIS)
Defence R&D Canada
Department of National Defence
Ottawa, Ontario K1A 0K2

CZECH REPUBLIC
DIC Czech Republic-NATO RTO
VTÚL a PVO Praha
Mladoboleslavská ul.
Praha 9, 197 06, Česká republika

DENMARK
Danish Defence Research Establishment
Ryvangs Allé 1, P.O. Box 2715
DK-2100 Copenhagen Ø

FRANCE
O.N.E.R.A. (ISP)
29 Avenue de la Division Leclerc
BP 72, 92322 Châtillon Cedex

GERMANY
Streitkräfteamt / Abteilung III
Fachinformationszentrum der Bundeswehr, (FIZBw)
Friedrich-Ebert-Allee 34
D-53113 Bonn

GREECE (Point of Contact)
Hellenic Ministry of National Defence
Defence Industry Research & Technology General Directorate
Technological R&D Directorate
D.Soutsou 40, GR-11521, Athens

HUNGARY
Department for Scientific Analysis
Institute of Military Technology
Ministry of Defence
H-1525 Budapest P O Box 26

ICELAND
Director of Aviation
c/o Flugrad
Reykjavik

ITALY
Centro di Documentazione Tecnico-Scientifica della Difesa
Via XX Settembre 123a
00187 Roma

LUXEMBOURG
See Belgium

NETHERLANDS
NDRCC
DGM/DWOO
P.O. Box 20701
2500 ES Den Haag

NORWAY
Norwegian Defence Research Establishment
Attn: Biblioteket
P.O. Box 25, NO-2007 Kjeller

POLAND
Chief of International Cooperation Division
Research & Development Department
218 Niepodleglosci Av.
00-911 Warsaw

PORTUGAL
Estado Maior da Força Aérea
SDFA - Centro de Documentação
Alfragide
P-2720 Amadora

SPAIN
INTA (RTO/AGARD Publications)
Carretera de Torrejón a Ajalvir, Pk.4
28850 Torrejón de Ardoz - Madrid

TURKEY
Millî Savunma Başkanliği (MSB)
ARGE Dairesi Başkanliği (MSB)
06650 Bakanliklar - Ankara

UNITED KINGDOM
Dstl Knowledge Services
Kentigern House, Room 2246
65 Brown Street
Glasgow G2 8EX

UNITED STATES
NASA Center for AeroSpace Information (CASI)
Parkway Center
7121 Standard Drive
Hanover, MD 21076-1320

SALES AGENCIES

NASA Center for AeroSpace Information (CASI)
Parkway Center
7121 Standard Drive
Hanover, MD 21076-1320
United States

The British Library Document Supply Centre
Boston Spa, Wetherby
West Yorkshire LS23 7BQ
United Kingdom

Canada Institute for Scientific and Technical Information (CISTI)
National Research Council
Document Delivery
Montreal Road, Building M-55
Ottawa K1A 0S2, Canada

Requests for RTO or AGARD documents should include the word 'RTO' or 'AGARD', as appropriate, followed by the serial number (for example AGARD-AG-315). Collateral information such as title and publication date is desirable. Full bibliographical references and abstracts of RTO and AGARD publications are given in the following journals:

Scientific and Technical Aerospace Reports (STAR)
STAR is available on-line at the following uniform resource locator:
http://www.sti.nasa.gov/Pubs/star/Star.html
STAR is published by CASI for the NASA Scientific and Technical Information (STI) Program
STI Program Office, MS 157A
NASA Langley Research Center
Hampton, Virginia 23681-0001
United States

Government Reports Announcements & Index (GRA&I)
published by the National Technical Information Service
Springfield
Virginia 22161
United States
(also available online in the NTIS Bibliographic Database or on CD-ROM)

Printed by St. Joseph Ottawa/Hull
(A St. Joseph Corporation Company)
45 Sacré-Cœur Blvd., Hull (Québec), Canada J8X 1C6

ISBN 92-837-1074-6